WOODHEAD PUBLISHING SERIES IN ENERGY



Materials for Ultra-Supercritical and Advanced Ultra-Supercritical Power Plants

Edited by Augusto Di Gianfrancesco

WP
WOODHEAD PUBLISHING

Materials for Ultra-Supercritical and Advanced Ultra-Supercritical Power Plants

Related titles

Ultra-Supercritical Coal Power Plants: Materials, Technologies and Optimization
(ISBN: 978-0-85709-116-1)

Coal-Fired Power Plant Materials: Performance and Life Assessment
(ISBN: 978-0-85709-431-5)

Clean Coal Engineering Technology
(ISBN: 978-1-85617-710-8)

Woodhead Publishing Series in Energy: Number 104

Materials for Ultra-Supercritical and Advanced Ultra-Supercritical Power Plants

Edited by

Augusto Di Gianfrancesco



AMSTERDAM • BOSTON • CAMBRIDGE • HEIDELBERG
LONDON • NEW YORK • OXFORD • PARIS • SAN DIEGO
SAN FRANCISCO • SINGAPORE • SYDNEY • TOKYO
Woodhead Publishing is an imprint of Elsevier



Woodhead Publishing is an imprint of Elsevier
The Officers' Mess Business Centre, Royston Road, Duxford, CB22 4QH, United Kingdom
50 Hampshire Street, 5th Floor, Cambridge, MA 02139, United States
The Boulevard, Langford Lane, Kidlington, OX5 1GB, United Kingdom

Copyright © 2017 Elsevier Ltd. All rights reserved.

No part of this publication may be reproduced or transmitted in any form or by any means, electronic or mechanical, including photocopying, recording, or any information storage and retrieval system, without permission in writing from the publisher. Details on how to seek permission, further information about the Publisher's permissions policies and our arrangements with organizations such as the Copyright Clearance Center and the Copyright Licensing Agency, can be found at our website: www.elsevier.com/permissions.

This book and the individual contributions contained in it are protected under copyright by the Publisher (other than as may be noted herein).

Notices
Knowledge and best practice in this field are constantly changing. As new research and experience broaden our understanding, changes in research methods, professional practices, or medical treatment may become necessary.

Practitioners and researchers must always rely on their own experience and knowledge in evaluating and using any information, methods, compounds, or experiments described herein. In using such information or methods they should be mindful of their own safety and the safety of others, including parties for whom they have a professional responsibility.

To the fullest extent of the law, neither the Publisher nor the authors, contributors, or editors, assume any liability for any injury and/or damage to persons or property as a matter of products liability, negligence or otherwise, or from any use or operation of any methods, products, instructions, or ideas contained in the material herein.

Library of Congress Cataloging-in-Publication Data
A catalog record for this book is available from the Library of Congress

British Library Cataloguing-in-Publication Data
A catalogue record for this book is available from the British Library

ISBN: 978-0-08-100552-1 (print)
ISBN: 978-0-08-100558-3 (online)

For information on all Woodhead Publishing publications visit our website at https://www.elsevier.com/



Publisher: Joe Hayton
Acquisition Editor: Sarah Hughes
Editorial Project Manager: Lucy Beg
Production Project Manager: Poulouse Joseph
Designer: Greg Harris

Typeset by TNQ Books and Journals

Contents

List of contributors xiii
Woodhead Publishing Series in Energy xv
Preface xxi

1 The fossil fuel power plants technology 1
A. Di Gianfrancesco
1.1 Types of thermal power station 1
1.2 The coal-fired power generation plants 6
1.3 The power generation trend: realizing decarbonization through efficiency gains 10
1.4 Fossil fuels classification 17
1.5 Power plant overview and main components 19
References 47

Part One Ultra-supercritical power plant materials 51

2 Low-alloyed steel grades for boilers in ultra-supercritical power plants 53
F. Masuyama
2.1 Introduction 53
2.2 Historical development of low-alloyed steels 53
2.3 Properties and metallurgy 57
2.4 Welding and forming 63
2.5 Service degradation 70
2.6 Conclusions 74
References 75

3 High-alloyed martensitic steel grades for boilers in ultra-supercritical power plants 77
J. Hald
3.1 Introduction 77
3.2 History of the high-alloyed martensitic steels 77
3.3 Basic properties and fabrication 79
3.4 Service experiences 84
3.5 Basic metallurgy and long-term microstructure stability 85

3.6 Microstructure instability: Z-phase **89**
3.7 Future perspectives **92**
References **95**

4 Austenitic steel grades for boilers in ultra-supercritical power plants 99
P. Barnard
4.1 Introduction **99**
4.2 Overview of austenitic steels **99**
4.3 Thermal fatigue **102**
4.4 Sensitization **103**
4.5 Strain-induced precipitation hardening **105**
4.6 Sigma-phase precipitation **108**
4.7 Stress corrosion cracking **109**
4.8 Stress relief cracking **111**
4.9 Secondary hardening **112**
4.10 Dissimilar metal welds **113**
4.11 Conclusions **116**
Acknowledgments **117**
References **117**

5 Martensitic steels for cast components in ultra-supercritical power plants 121
S. Roberts
5.1 Material requirements for ultra-supercritical application **121**
5.2 Why cast components are utilized for steam turbine applications **121**
5.3 Casting materials for ultra-supercritical applications **126**
5.4 Manufacturing challenges associated with production of heavy-wall martensitic 9%Cr steel castings **128**
5.5 Bigger, hotter, higher pressure **132**
5.6 Latest alloy developments and state-of-the-art technology **132**
5.7 What is next after ultra-supercritical? Cast materials for advanced ultra-supercritical applications? **134**
5.8 Summary **139**
References **140**

6 Martensitic steels for rotors in ultra-supercritical power plants 143
G. Zeiler
6.1 Introduction **143**
6.2 Common rotor material requirements **144**
6.3 Development of martensitic 9–12% Cr rotor steels for USC application **147**
6.4 Common materials for steam turbine rotors in Europe: fabrication and basic properties **155**
6.5 Present material development for application temperatures above 620°C **168**
6.6 Summary and conclusions **170**
References **171**

7 Steels and alloys for turbine blades in ultra-supercritical power plants 175
G. Lucacci
7.1 Introduction **175**
7.2 Commercial alloys **178**
7.3 Trends in USC steam turbine blading **189**
7.4 Coatings **193**
7.5 Conclusions **195**
References **195**

8 Technologies for chemical analyses, microstructural and inspection investigations 197
A. Di Gianfrancesco
8.1 Introduction **197**
8.2 Modeling tools **224**
8.3 Nondestructive testing **232**
References **243**

9 Welding technologies for ultra-supercritical power plant materials 247
S. Sorrentino
9.1 Introduction: welded fabrication of USC components **247**
9.2 Welding metallurgy of USC materials **252**
9.3 Weldments design, codes and standards, approvals **285**
9.4 Arc welding technology and consumables for USC materials **287**
9.5 Welding procedures, NDT, quality assurance, weldments testing **299**
9.6 Future trends **313**
List of acronyms **315**
Acknowledgments **315**
References **316**

Part Two Advanced ultra-supercritical power plant materials 321

10 New martensitic steels 323
F. Abe
10.1 Introduction **323**
10.2 Development history and utilization of 9 to 12Cr martensitic steels in coal power plants **324**
10.3 Basic methods of strengthening martensitic 9 to 12Cr steels in creep at elevated temperature **326**
10.4 Degradation in creep strength at long times **331**
10.5 Fundamental aspects of tempered martensitic microstructure and creep deformation **337**
10.6 New martensitic 9Cr steel **338**
10.7 Summary **368**
References **368**

11 New austenitic steels for the advanced USC power plants 375
M. Spiegel and P. Schraven
11.1 Introduction **375**
11.2 Future trends **376**
11.3 Sigma phase strengthened concept (Power Austenite) **377**
11.4 Summary **388**
References **390**

12 Sanicro 25: an advanced high-strength, heat-resistant austenitic stainless steel 391
G. Chai and U. Forsberg
12.1 Introduction **391**
12.2 Development of new high-strength austenitic material for high-efficiency coal-fired power plant **392**
12.3 Microstructure **394**
12.4 Creep and rupture behaviors **397**
12.5 Low-cycle fatigue properties **405**
12.6 High-temperature corrosion and steam oxidation behavior **407**
12.7 Weldability **410**
12.8 Fabricability **413**
12.9 Field experiences: testing in boilers **416**
12.10 Future trends **417**
12.11 Conclusions **418**
Acknowledgments **419**
References **419**

13 New Japanese materials for A-USC power plants 423
A. Di Gianfrancesco
13.1 Introduction **423**
13.2 Development of boiler tubes and pipes for advanced USC power plants: HR6W, HR35 **424**
13.3 Superalloys development in MHPS **443**
13.4 TOS1X **460**
References **466**

14 INCONEL alloy 740H 469
J.J. deBarbadillo
14.1 Background/introduction **469**
14.2 Composition **470**
14.3 Microstructure and phase stability **470**
14.4 Mechanical properties **474**

14.5 Corrosion properties **481**
14.6 Manufacturing of mill product forms **486**
14.7 Fabrication of components **490**
14.8 Casting **496**
14.9 Welding **496**
14.10 Summary **505**
References **506**

15 HAYNES 282 alloy **511**
K.L. Kruger
15.1 Introduction **511**
15.2 Conclusions **539**
15.3 Future trends **539**
Acknowledgments **539**
References **540**

16 Alloy 617 and derivatives **547**
J. Klöwer
16.1 Introduction **547**
16.2 Metallurgy of Alloy 617 **548**
16.3 Properties of Alloy 617 and derivatives **551**
16.4 Fabrication, heat treatment, and welding of Alloy 617 and derivatives **557**
16.5 Experiences from field testing **564**
16.6 Conclusions/outlook **565**
Acknowledgments **565**
References **565**

17 Alloy 263 **571**
A. Di Gianfrancesco
17.1 Introduction **571**
17.2 Physical metallurgy **571**
17.3 Physical properties **572**
17.4 Hot working **572**
17.5 Heat treatment **573**
17.6 Mechanical properties **573**
17.7 Microstructural analyses **573**
17.8 Weldability **578**
17.9 Examples of trial components manufacturing **579**
17.10 Long-term properties **586**
17.11 Chemistry optimization **586**
17.12 Corrosion and oxidation **592**
References **598**

18 Welding technologies for advanced ultra-supercritical power plants materials 601
S. Sorrentino
18.1 Introduction **601**
18.2 Experience accumulated in other industrial fields **602**
18.3 Weldability and welding metallurgy (ferritic, austenitic steels and nickel alloys) **602**
18.4 Arc welding consumables development, specific aspects of the welding procedures **614**
18.5 Dissimilar metal welding, repair welding **617**
18.6 Welding of A-USC valves, casings and cast components **619**
18.7 Welding of rotors; technologies, fabrication issues, non destructive testing **625**
18.8 Welding of boiler systems **627**
List of acronyms **635**
Acknowledgments **635**
References **635**

Part Three Materials' development programs worldwide 641

19 Worldwide overview and trend for clean and efficient use of coal 643
A. Di Gianfrancesco
19.1 Introduction **643**
19.2 The role of coal in future global energy needs **658**
19.3 Advantages and disadvantages of coal-fired for power plant boilers **661**
19.4 Carbon capture, use, and storage **667**
19.5 Why CCS **674**
19.6 Tackling climate change **676**
19.7 Industry experience **677**
19.8 Economic importance **677**
19.9 Affordability **678**
19.10 CCS project proposals **679**
19.11 Things about CCS **679**
19.12 Carbon dioxide reuse **679**
19.13 Key points of COP21: long-term goal **681**
19.14 Will coal be on the dole after COP21? **682**
19.15 Future energy: the electricity system now and decarbonized **684**
References **686**

20 The US DOE/OCDO A-USC materials technology R&D program 689
J.P. Shingledecker
20.1 Introduction **689**
20.2 US A-USC materials consortium **689**
20.3 Materials selection **693**

20.4 Boiler materials **697**
20.5 Turbine materials **702**
20.6 The future **706**
20.7 Conclusions **709**
Acknowledgments **709**
References **710**

21 The Chinese 700°C A-USC development program **715**
Z. Liu and X. Xie
21.1 Introduction **715**
21.2 The foundation of China's 700°C A-USC coal-fired power generation technology innovation consortium **716**
21.3 The fundamental consideration of China's 700°C A-USC coal-fired demo plant **717**
21.4 Boiler materials for China's 700°C A-USC coal-fired demo plant **719**
21.5 Steam turbine materials for China's 700°C A-USC coal-fired demo plant **725**
21.6 Pilot testing rig for China's 700°C A-USC coal-fired demo plant **726**
21.7 Structure stability of Inconel 740/740H **727**
21.8 Conclusions **730**
Acknowledgments **730**
References **731**

22 Advanced USC technology development in Japan **733**
M. Fukuda
22.1 Introduction **733**
22.2 Technology development of A-USC in Japan **737**
22.3 Summary and conclusion **753**
References **754**

23 A-USC R&D programs in other countries **755**
A. Di Gianfrancesco
23.1 Introduction **755**
23.2 Indian A-USC program **755**
23.3 Other countries **761**
References **770**

24 A-USC programs in the European Union **773**
A. Di Gianfrancesco and R. Blum
24.1 History of R&D programs on materials for USC and A-USC power plants **773**
24.2 EU steel development research programs for ultra-supercritical plants **775**
24.3 EU superalloys development research programs for advanced ultra-supercritical power plants **789**

24.4 New materials for steam generators with efficiencies above 50% (MARCKO DE 2) 1999–2004 **811**
24.5 Electron beam welding (EBW) **812**
24.6 KOMET 650 **812**
24.7 HWT I **814**
24.8 Post AD700 **814**
24.9 COMTES+ **815**
24.10 NextGenPower **827**
24.11 MACPLUS **831**
24.12 POEMA: production of coatings for new efficient and clean coal power plant materials **834**
24.13 "Partner steam power plant" for the regenerative power generation **835**
24.14 The European Creep Collaborative Committee (ECCC) **835**
24.15 Horizon 2020 **839**
24.16 European future **840**
24.17 Conclusions about the EU R&D activities **841**
References **842**

Index **847**

List of contributors

F. Abe National Institute for Materials Science, Japan

P. Barnard Boiler R&D Centre, Doosan Babcock, Tipton, West Midlands, United Kingdom

R. Blum Consultant (former Dong Energy), Denmark

G. Chai Sandvik Material Technology, Sandviken, Sweden; Linköping University, Linköping, Sweden

J.J. deBarbadillo Special Metals Corporation, Huntington, WV, United States

A. Di Gianfrancesco Materials & Technologies Consultant, Rome, Italy

U. Forsberg Sandvik Material Technology, Sandviken, Sweden

M. Fukuda Research Institute for Advanced Thermal Power Systems, Shinagawa, Tokyo, Japan

J. Hald Technical University of Denmark, Kgs. Lyngby, Denmark

J. Klöwer VDM Metals GmbH, Werdohl, Germany

K.L. Kruger Haynes International, Inc., Kokomo, IN, United States

Z. Liu China Iron and Steel Research Institute Group Co., Ltd, Beijing, China

G. Lucacci C Blade S.p.a. a SIFCO Industries Company, Maniago, Pordenone, Italy

F. Masuyama Kyushu Institute of Technology, Kitakyushu, Japan

S. Roberts Technical Director, Goodwin Steel Castings Ltd., Stoke-on-Trent, GBR

P. Schraven Salzgitter Mannesmann Stainless Tubes, Mülheim an der Ruhr, Germany

J.P. Shingledecker Electric Power Research Institute, Charlotte, NC, United States

S. Sorrentino Welding Consumables Research & Development, Air Liquide Welding, Italy

M. Spiegel Salzgitter Mannesmann Forschung GmbH, Duisburg, Germany

X. Xie University of Science & Technology Beijing, Beijing, China

G. Zeiler Bohler Edelstahl GmbH & Co KG, Kapfenberg, Austria

Woodhead Publishing Series in Energy

1 **Generating power at high efficiency: Combined cycle technology for sustainable energy production**
Eric Jeffs
2 **Advanced separation techniques for nuclear fuel reprocessing and radioactive waste treatment**
Edited by Kenneth L. Nash and Gregg J. Lumetta
3 **Bioalcohol production: Biochemical conversion of lignocellulosic biomass**
Edited by Keith W. Waldron
4 **Understanding and mitigating ageing in nuclear power plants: Materials and operational aspects of plant life management (PLiM)**
Edited by Philip G. Tipping
5 **Advanced power plant materials, design and technology**
Edited by Dermot Roddy
6 **Stand-alone and hybrid wind energy systems: Technology, energy storage and applications**
Edited by John K. Kaldellis
7 **Biodiesel science and technology: From soil to oil**
Jan C. J. Bart, Natale Palmeri and Stefano Cavallaro
8 **Developments and innovation in carbon dioxide (CO_2) capture and storage technology Volume 1: Carbon dioxide (CO_2) capture, transport and industrial applications**
Edited by M. Mercedes Maroto-Valer
9 **Geological repository systems for safe disposal of spent nuclear fuels and radioactive waste**
Edited by Joonhong Ahn and Michael J. Apted
10 **Wind energy systems: Optimising design and construction for safe and reliable operation**
Edited by John D. Sørensen and Jens N. Sørensen
11 **Solid oxide fuel cell technology: Principles, performance and operations**
Kevin Huang and John Bannister Goodenough
12 **Handbook of advanced radioactive waste conditioning technologies**
Edited by Michael I. Ojovan
13 **Membranes for clean and renewable power applications**
Edited by Annarosa Gugliuzza and Angelo Basile
14 **Materials for energy efficiency and thermal comfort in buildings**
Edited by Matthew R. Hall
15 **Handbook of biofuels production: Processes and technologies**
Edited by Rafael Luque, Juan Campelo and James Clark

16 **Developments and innovation in carbon dioxide (CO_2) capture and storage technology Volume 2: Carbon dioxide (CO_2) storage and utilisation**
Edited by M. Mercedes Maroto-Valer
17 **Oxy-fuel combustion for power generation and carbon dioxide (CO_2) capture**
Edited by Ligang Zheng
18 **Small and micro combined heat and power (CHP) systems: Advanced design, performance, materials and applications**
Edited by Robert Beith
19 **Advances in clean hydrocarbon fuel processing: Science and technology**
Edited by M. Rashid Khan
20 **Modern gas turbine systems: High efficiency, low emission, fuel flexible power generation**
Edited by Peter Jansohn
21 **Concentrating solar power technology: Principles, developments and applications**
Edited by Keith Lovegrove and Wes Stein
22 **Nuclear corrosion science and engineering**
Edited by Damien Féron
23 **Power plant life management and performance improvement**
Edited by John E. Oakey
24 **Electrical drives for direct drive renewable energy systems**
Edited by Markus Mueller and Henk Polinder
25 **Advanced membrane science and technology for sustainable energy and environmental applications**
Edited by Angelo Basile and Suzana Pereira Nunes
26 **Irradiation embrittlement of reactor pressure vessels (RPVs) in nuclear power plants**
Edited by Naoki Soneda
27 **High temperature superconductors (HTS) for energy applications**
Edited by Ziad Melhem
28 **Infrastructure and methodologies for the justification of nuclear power programmes**
Edited by Agustín Alonso
29 **Waste to energy conversion technology**
Edited by Naomi B. Klinghoffer and Marco J. Castaldi
30 **Polymer electrolyte membrane and direct methanol fuel cell technology Volume 1: Fundamentals and performance of low temperature fuel cells**
Edited by Christoph Hartnig and Christina Roth
31 **Polymer electrolyte membrane and direct methanol fuel cell technology Volume 2: *In situ* characterization techniques for low temperature fuel cells**
Edited by Christoph Hartnig and Christina Roth
32 **Combined cycle systems for near-zero emission power generation**
Edited by Ashok D. Rao
33 **Modern earth buildings: Materials, engineering, construction and applications**
Edited by Matthew R. Hall, Rick Lindsay and Meror Krayenhoff
34 **Metropolitan sustainability: Understanding and improving the urban environment**
Edited by Frank Zeman
35 **Functional materials for sustainable energy applications**
Edited by John A. Kilner, Stephen J. Skinner, Stuart J. C. Irvine and Peter P. Edwards

36 **Nuclear decommissioning: Planning, execution and international experience**
Edited by Michele Laraia
37 **Nuclear fuel cycle science and engineering**
Edited by Ian Crossland
38 **Electricity transmission, distribution and storage systems**
Edited by Ziad Melhem
39 **Advances in biodiesel production: Processes and technologies**
Edited by Rafael Luque and Juan A. Melero
40 **Biomass combustion science, technology and engineering**
Edited by Lasse Rosendahl
41 **Ultra-supercritical coal power plants: Materials, technologies and optimisation**
Edited by Dongke Zhang
42 **Radionuclide behaviour in the natural environment: Science, implications and lessons for the nuclear industry**
Edited by Christophe Poinssot and Horst Geckeis
43 **Calcium and chemical looping technology for power generation and carbon dioxide (CO_2) capture: Solid oxygen- and CO_2-carriers**
Paul Fennell and E. J. Anthony
44 **Materials' ageing and degradation in light water reactors: Mechanisms, and management**
Edited by K. L. Murty
45 **Structural alloys for power plants: Operational challenges and high-temperature materials**
Edited by Amir Shirzadi and Susan Jackson
46 **Biolubricants: Science and technology**
Jan C. J. Bart, Emanuele Gucciardi and Stefano Cavallaro
47 **Advances in wind turbine blade design and materials**
Edited by Povl Brøndsted and Rogier P. L. Nijssen
48 **Radioactive waste management and contaminated site clean-up: Processes, technologies and international experience**
Edited by William E. Lee, Michael I. Ojovan, Carol M. Jantzen
49 **Probabilistic safety assessment for optimum nuclear power plant life management (PLiM): Theory and application of reliability analysis methods for major power plant components**
Gennadij V. Arkadov, Alexander F. Getman and Andrei N. Rodionov
50 **The coal handbook: Towards cleaner production Volume 1: Coal production**
Edited by Dave Osborne
51 **The coal handbook: Towards cleaner production Volume 2: Coal utilisation**
Edited by Dave Osborne
52 **The biogas handbook: Science, production and applications**
Edited by Arthur Wellinger, Jerry Murphy and David Baxter
53 **Advances in biorefineries: Biomass and waste supply chain exploitation**
Edited by Keith Waldron
54 **Geological storage of carbon dioxide (CO_2): Geoscience, technologies, environmental aspects and legal frameworks**
Edited by Jon Gluyas and Simon Mathias
55 **Handbook of membrane reactors Volume 1: Fundamental materials science, design and optimisation**
Edited by Angelo Basile

56 **Handbook of membrane reactors Volume 2: Reactor types and industrial applications**
Edited by Angelo Basile
57 **Alternative fuels and advanced vehicle technologies for improved environmental performance: Towards zero carbon transportation**
Edited by Richard Folkson
58 **Handbook of microalgal bioprocess engineering**
Christopher Lan and Bei Wang
59 **Fluidized bed technologies for near-zero emission combustion and gasification**
Edited by Fabrizio Scala
60 **Managing nuclear projects: A comprehensive management resource**
Edited by Jas Devgun
61 **Handbook of Process Integration (PI): Minimisation of energy and water use, waste and emissions**
Edited by Jiří J. Klemeš
62 **Coal power plant materials and life assessment**
Edited by Ahmed Shibli
63 **Advances in hydrogen production, storage and distribution**
Edited by Ahmed Basile and Adolfo Iulianelli
64 **Handbook of small modular nuclear reactors**
Edited by Mario D. Carelli and Dan T. Ingersoll
65 **Superconductors in the power grid: Materials and applications**
Edited by Christopher Rey
66 **Advances in thermal energy storage systems: Methods and applications**
Edited by Luisa F. Cabeza
67 **Advances in batteries for medium and large-scale energy storage**
Edited by Chris Menictas, Maria Skyllas-Kazacos and Tuti Mariana Lim
68 **Palladium membrane technology for hydrogen production, carbon capture and other applications**
Edited by Aggelos Doukelis, Kyriakos Panopoulos, Antonios Koumanakos and Emmanouil Kakaras
69 **Gasification for synthetic fuel production: Fundamentals, processes and applications**
Edited by Rafael Luque and James G. Speight
70 **Renewable heating and cooling: Technologies and applications**
Edited by Gerhard Stryi-Hipp
71 **Environmental remediation and restoration of contaminated nuclear and NORM sites**
Edited by Leo van Velzen
72 **Eco-friendly innovation in electricity networks**
Edited by Jean-Luc Bessede
73 **The 2011 Fukushima nuclear power plant accident: How and why it happened**
Yotaro Hatamura, Seiji Abe, Masao Fuchigami and Naoto Kasahara. Translated by Kenji Iino
74 **Lignocellulose biorefinery engineering: Principles and applications**
Hongzhang Chen
75 **Advances in membrane technologies for water treatment: Materials, processes and applications**
Edited by Angelo Basile, Alfredo Cassano and Navin Rastogi

76 **Membrane reactors for energy applications and basic chemical production**
Edited by Angelo Basile, Luisa Di Paola, Faisal Hai and Vincenzo Piemonte
77 **Pervaporation, vapour permeation and membrane distillation: Principles and applications**
Edited by Angelo Basile, Alberto Figoli and Mohamed Khayet
78 **Safe and secure transport and storage of radioactive materials**
Edited by Ken Sorenson
79 **Reprocessing and recycling of spent nuclear fuel**
Edited by Robin Taylor
80 **Advances in battery technologies for electric vehicles**
Edited by Bruno Scrosati, Jürgen Garche and Werner Tillmetz
81 **Rechargeable lithium batteries: From fundamentals to applications**
Edited by Alejandro A. Franco
82 **Calcium and chemical looping technology for power generation and carbon dioxide (CO_2) capture**
Edited by Paul Fennell and Ben Anthony
83 **Compendium of hydrogen energy Volume 1: Hydrogen production and purificiation**
Edited by Velu Subramani, Angelo Basile and T. Nejat Veziroglu
84 **Compendium of hydrogen energy Volume 2: Hydrogen storage, transmission, transportation and infrastructure**
Edited by Ram Gupta, Angelo Basile and T. Nejat Veziroglu
85 **Compendium of hydrogen energy Volume 3: Hydrogen energy conversion**
Edited by Frano Barbir, Angelo Basile and T. Nejat Veziroglu
86 **Compendium of hydrogen energy Volume 4: Hydrogen use, safety and the hydrogen economy**
Edited by Michael Ball, Angelo Basile and T. Nejat Veziroglu
87 **Advanced district heating and cooling (DHC) systems**
Edited by Robin Wiltshire
88 **Microbial electrochemical and fuel cells: Fundamentals and applications**
Edited by Keith Scott and Eileen Hao Yu
89 **Renewable heating and cooling: Technologies and applications**
Edited by Gerhard Stryi-Hipp
90 **Small modular reactors: Nuclear power fad or future?**
Edited by Daniel T. Ingersoll
91 **Fuel flexible energy generation: Solid, liquid and gaseous fuels**
Edited by John Oakey
92 **Offshore wind farms: Technologies, design and operation**
Edited by Chong Ng & Li Ran
93 **Uranium for nuclear power: Resources, mining and transformation to fuel**
Edited by Ian Hore-Lacy
94 **Biomass supply chains for bioenergy and biorefining**
Edited by Jens Bo Holm-Nielsen and Ehiaze Augustine Ehimen
95 **Sustainable energy from salinity gradients**
Edited by Andrea Cipollina and Giorgio Micale
96 **Membrane technologies for biorefining**
Edited by Alberto Figoli, Alfredo Cassano and Angelo Basile
97 **Geothermal power generation: Developments and innovation**
Edited by Ronald DiPippo

98 **Handbook of biofuels' production: Processes and technologies (Second Edition)**
Edited by Rafael Luque, Carol Sze Ki Lin, Karen Wilson and James Clark
99 **Magnetic fusion energy: From experiments to power plants**
Edited by George H. Neilson
100 **Advances in ground-source heat pump systems**
Edited by Simon Rees
101 **Absorption-based post-combustion capture of carbon dioxide**
Edited by Paul Feron
102 **Advances in solar heating and cooling**
Edited by Ruzhu Wang and Tianshu Ge
103 **Handbook of Generation IV nuclear power reactors**
Edited by Igor Pioro
104 **Materials for ultra-supercritical and advanced ultra-supercritical power plants**
Edited by Augusto Di Gianfrancesco
105 **The performance of photovoltaic systems: Modelling, measurement and assessment**
Edited by Nicola Pearsall
106 **Structural materials for Generation IV nuclear reactors**
Edited by Pascal Yvon
107 **Organic rankine cycle (ORC) power systems: Technologies and applications**
Edited by Ennio Macchi and Marco Astolfi

Preface

This book summarizes the worldwide contributions about materials development for cleaner coal technologies in the fossil fuel power plant and the consequent sustainability for planet heart future.

The industrial use of steam for generation of energy started in the 18th century and was the main driving force for the industrial revolution. In the 20th century the consumption of fossil fuels and in particular of carbon for steam power generation plants guaranteed the development of the global economy.

Since beginning of the 21st century the world of energy production has changed in an unbelievable way: from an exponential increase of the energy demand due to the increase of the world population and economies, to the world financial crisis that generated a huge drop of the energy demand mainly in the Organisation for Economic Co-operation and Development (OECD) countries, through the implementation of the renewable sources.

The fossil-fueled power plants will continue for several years to guarantee the energy supply for the increasing demand in the emerging countries due to their urbanization and industrialization improvement.

Asia–Pacific is the largest market, by size, and it is estimated to grow at the highest rate due to a large number of power capacity expansion projects in China and India. To meet the growing demand for power, China alone is expected to add about 70–90 GW of capacity every year to its power generation sector, whereas India is expected to add about 10–20 GW every year.

These aspects seem in contrast with the final document issued in the last COP21 conference held in Paris at the end of 2015, where it was agreed to maintain the increase of global warming below 2°C in 2050.

Achieving CO_2 emission control while keeping electricity prices competitive and available for all the population in the world countries is a key economic and technical challenge for the world community. Renewable sources have to be improved jointly to the strategy for lowering CO_2 emission from coal-based power plants including primarily raising electricity generation efficiency. In fact, coal remains in the foreseeable future, 30–50 years, the dominant means of electric power generation.

The efficiency of the pulverized coal power plants (PP) increased a lot in the last 30 years from the efficiency range of 30% for the subcritical (SC) PP up to the last and most efficient ultra-supercritical (USC) PP operating with 46–47% efficiency. These improvements were mainly due to the availability of most performance materials developed in the last 40 years able now to operate up to 600–620°C with steam pressure up to 300 MPa. A further improvement of the efficiency will be obtained with

the introduction of the next PP generation called advanced USC (A-USC), targeting efficiency in the range of 50%, where the steam service condition will be over 700°C and pressure over 300 MPa.

An additional reduction of the emission will be obtained with the capture, the sequestration, and storage (CCS) of the CO_2 gas. In fact, it is expected that by 2030 the new coal-fired PP will be operating high-efficiency, low-emission technologies with CCS, associated with the drop-off of the older SC PPs having efficiencies lower than 40%.

It is expected that the first new-generation demonstration plants will be in operation by 2020 in China or India. Despite the first idea generated in the European Union about the A-USC PP, the several R&D programs carried out and the demonstrated production capabilities of the new materials/components, the construction of demonstration plant is not more scheduled in near future in European countries; this is due the incredible improvement of the renewable energy capacities developed in the last 10 years.

After my master's degree in chemical engineering, with a specialization in materials science, at the first Rome University "La Sapienza" in October 1982, I soon started my career at the beginning of 1983 as young researcher at Centro Sperimentale Metallurgico (CSM) (Metallurgy Experimental Center) in Rome, Italy. The CSM was founded in 1963 as the corporate research center of the Italian steel companies, which were at that time mainly public companies; also, Italian automotive and oil and gas companies were shareholders. The CSM changed the name to Centro Sviluppo Materiali (Materials Development Center), maintaining the same acronyms, and it was privatized in the 1990s as consequence of the privatization of the Italian steel companies. I have been employed at CSM since the end of 2014.

In my career, I have been fortunate to be involved practically in all the aspects concerning the steels and alloys for high-temperature applications in the power generation industries and in the aerospace engines.

In 1983, I was involved in the Italian team that produced the first European industrial heat of the steel grade 91. Then I started to investigate the effect of the alloy elements and the heat treatment times/temperatures on the mechanical properties; further, I studied the microstructural aspect and the mechanical properties of this steel and in particular the creep performance. In the 1980s, I started also the first integrated projects on this steel between the United Kingdom, Germany, and Italy sponsored by European Community. Therefore I contributed also in the investigation of microstructural evolution of this steel practically during my entire career at CSM, up to the discovery of the Z-phase also in this steel after very long-term aging.

I was also involved in the characterization, qualification, development, and pilot-scale production of the single-crystal, nickel-based superalloys and then in the titanium metal matrix composites for aircraft engines. At the end of the 1990s, my research activities turned back to the materials for power generation: tube, pipe, cast, and forged components made by steels and superalloys.

In 1991, I was one of the founders of the European Creep Collaborative Committee (ECCC) that is still alive and active to assess the European creep data for high-temperature materials. I was also active in the R&D COST actions for steel

development USC power plants and member of the management committee, as well as in the AD700 project, which was the first program in the world looking for materials to be applied in the A-USC PP.

During my working career, I was project leader of several national and EU programs, and I had the opportunity to attend several national and international Conferences, also as an invited speaker or member of scientific committee, to visit R&D centers, universities, and industrial plants in several countries. Therefore I had the opportunities to meet the main worldwide representatives of the scientific community in the field of high-temperature materials. This have been for me an incredible experience to learn, compare, discuss, and exchange my experience, improving my knowledge.

I am honored to be still in very good friendship with a lot of these colleagues around the world.

When in summer 2014 I was contacted by Elsevier Woodhead Publishing to be the editor of the book "Materials for ultra-supercritical and advanced ultra-supercritical power plants," I remained astonished and in the meantime honored by this nomination.

This opportunity arrived after the success of the third ECCC conference held in Rome in May 2014, organized also with my little contribution, practically at the end of my career at CSM, but not really at the end of my working life in materials science and technologies for sustainable energy.

I prepared a draft of the book structure based on three parts, containing in total 24 chapters that was positively approved by the Elsevier reviewers and described as follows.

In the first part of this book, in , Chapter 1, the evolution of the operating conditions and of the layout of the steam PPs are described, as well as the main components.

In the further chapters are described the current best available materials for the different PP sections. In addition are discussed the low-alloyed ferritic steels for the water wall, the high-alloyed martensitic steels for the headers, steam line, turbine rotor, casing, and blades, up to the austenitic steel used for the reheaters and superheaters. The joining technologies, methodologies for the materials control, and characterizations are also described.

The second and third part of the book, respectively, are dedicated to the new materials and R&D programs for the development of the next A-USC PP generation.

Chapters 9 and 10 are focused on the development of the new martensitic and austenitic steels, and the following chapter is dedicated to the several superalloys still under development and investigations for the most critical components operating in the more severe temperatures and pressure conditions. Also in the second part, a chapter is dedicated to the joining technologies for these materials and components.

In the third and last part of the book, the research programs still running around the world targeting the design, the development, and the operating of demonstrative A-USC PP are summarized.

Based on this structure, I started to think how to handle this huge and exiting job, and I asked to my worldwide colleagues and friends to give me support to write this book that is a summary of the knowledge in the field of steels and superalloys for coal-fired steam PP.

The feedback was enthusiastic; only a few chapters were reassigned to other very well-reputed authors, and two chapters have been written by me because I did not have positive feedback from all the contacted persons, and I wanted to maintain the original structure.

Therefore I make my personnel acknowledgments to all the team authors because they have made the best to give a simple and, in the meantime, detailed and updated description of the materials, of their properties, and of the R&D programs in which all have been and are currently involved.

I hope that a broad spectrum of readers may find this book interesting and useful. Please convey to me your comments and suggestions on any aspect of the present book.

My work was helped by the very high quality of the chapter drafts and by the excellent cooperation with all the authors and the Woodhead staff, who took care of all the boring duties.

My personnel acknowledgments are for Mrs. Sarah Hughes, Senior Acquisition Editor, for her tireless and extremely patient efforts to steer me through the preparation of this book. She has gone well above and beyond what could normally be expected to bring this work to fruition. I cannot express better my appreciation for her editorial assistance and her enthusiasm and encouragement.

I would like to thank all the Elsevier editorial team for the relevant support they gave me during the two years of job:

- Alex White, Editorial Project Manager
- Poulouse Joseph, Senior Project Manager
- Lucy Beg, Editorial Project Manager
- Joseph P. Hayton, Publisher, Engineering
- Shiva Meenakshi Sundaram, Senior Project Manager, Book Operations

A special acknowledgment goes to my friend Rudolph Blum for the unbelievable effort he gave me for this book.

The last, but not the least, acknowledgment goes to my beautiful wife Elena for patiently supporting me during this exiting adventure.

Augusto Di Gianfrancesco
Rome, Italy

The fossil fuel power plants technology

1

A. Di Gianfrancesco
Materials & Technologies Consultant, Rome, Italy

1.1 Types of thermal power station

The thermal power plants can be classified by the source of the energy used to generate the steam that it is expanded in the turbine to produce electricity.

1.1.1 Classification by heat source

- **Fossil fuel power stations** may also use a steam turbine generator, or in the case of natural gas-fired plants, they may use a combustion turbine. A coal-fired power station (Fig. 1.1) produces heat by burning coal in a steam boiler. The steam drives a steam turbine coupled to a generator producing electricity. The waste products of combustion include ash, sulfur dioxide, nitrogen oxides, and carbon dioxide. The ash is removed by filtration with an efficiency better than 99.9%, and all waste gases then can be removed by either catalytic transformation to harmless components or scrubbed and absorbed from the plume to reduce pollution by more than 90%. Natural gas can be used to produce energy by combustion in gas turbines. The hot exhaust gases from the gas turbine can be used for steam generation in a heat exchanger, a "heat recovery steam generation" (Fig. 1.2), and the steam is used in a steam turbine, thereby adding another 50% to the electricity generation. This concept called "combined cycle" can obtain very high efficiencies: up to 60%.

The fossil fuel power stations are currently the dominating plants for generation of energy production around the world.

- **A nuclear power plant** is a steam turbine plant where the steam is generated by a nuclear reactor (Fig. 1.3). About 10% of all electric generation worldwide is produced by nuclear power plants. In France, more than 75% of electricity consumption comes from nuclear energy, and in Japan, the nuclear installed electrical capacity in 2009 was able to produce 29%, with plans to increase to >50% in 2030, but after the Fukushima disaster, all the plants were scheduled to be shut down in a few years, and the rest of the world is very hesitant with respect to what role nuclear energy should have in future energy planning. On the contrary, in August 2015 the Sandai Nuclear Power Plant had been restarted, and several other reactors, passing the check of more restricted safety procedures, will also be in service again.
- **Geothermal power plants** use steam extracted from hot underground rocks (Fig. 1.4). This kind of energy plant only contributes a minor energy output compared with the global demand.

Materials for Ultra-Supercritical and Advanced Ultra-Supercritical Power Plants.
http://dx.doi.org/10.1016/B978-0-08-100552-1.00001-4
Copyright © 2017 Elsevier Ltd. All rights reserved.

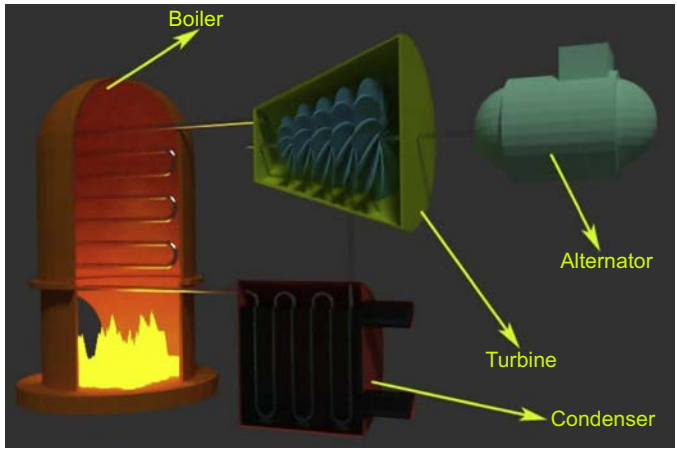


Figure 1.1 Scheme of coal-fired power plant.

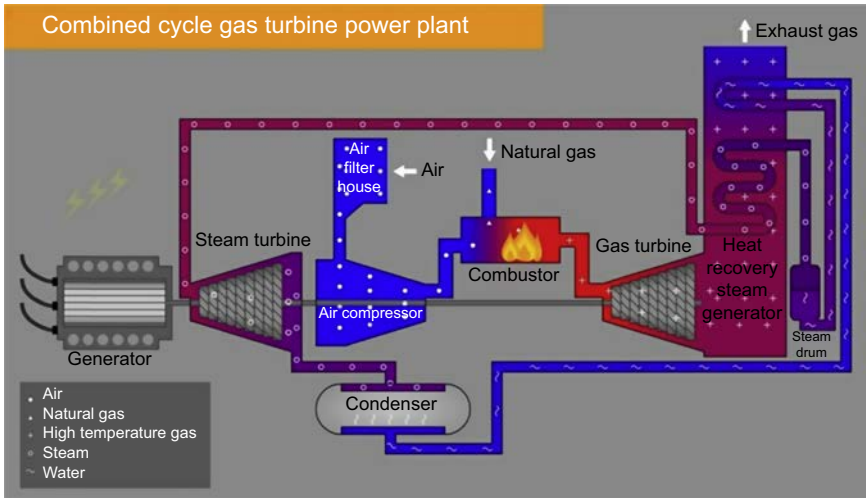


Figure 1.2 Scheme of heat recovery steam generator.

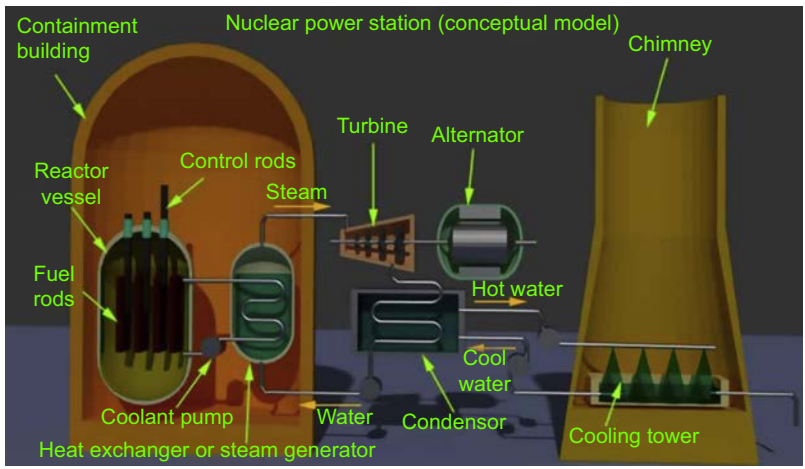


Figure 1.3 Scheme of a nuclear power plant.

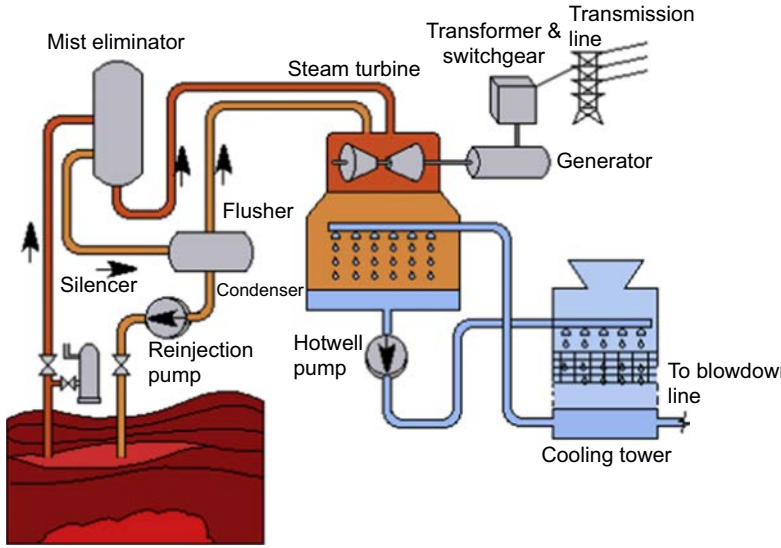


Figure 1.4 Scheme of geothermal power plant.

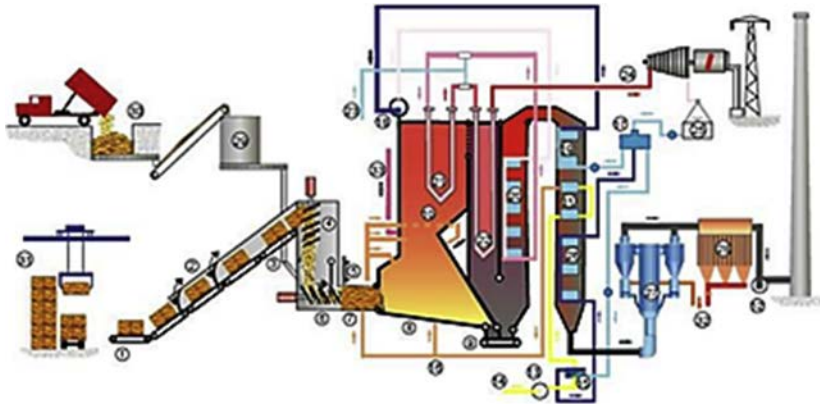


Figure 1.5 Scheme of a biomass power plant.

- **Biomass-fueled power plants** are fueled with wood pellets, wood chips, straw, and waste from the agricultural industry such as sugar cane and nut scale, municipal solid waste, landfill methane, or other forms of bio gas (Fig. 1.5).
- In **integrated steel mills**, blast furnace exhaust gas is a low-cost, although low-energy-density, fuel. This recycled gas is available to produce about 60% of the total electricity consumption.
- **Waste** heat from industrial processes is occasionally concentrated enough to use for power generation, usually in a steam boiler and turbine (Fig. 1.6).
- **Solar thermal** electric plants (Fig. 1.7) use sunlight to boil water and produce steam, which turns the generator.

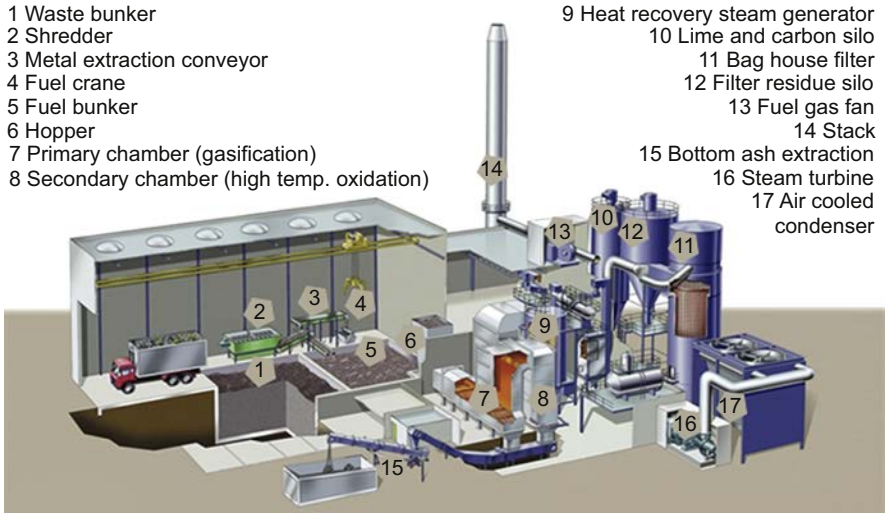


Figure 1.6 Waste generator power plant.

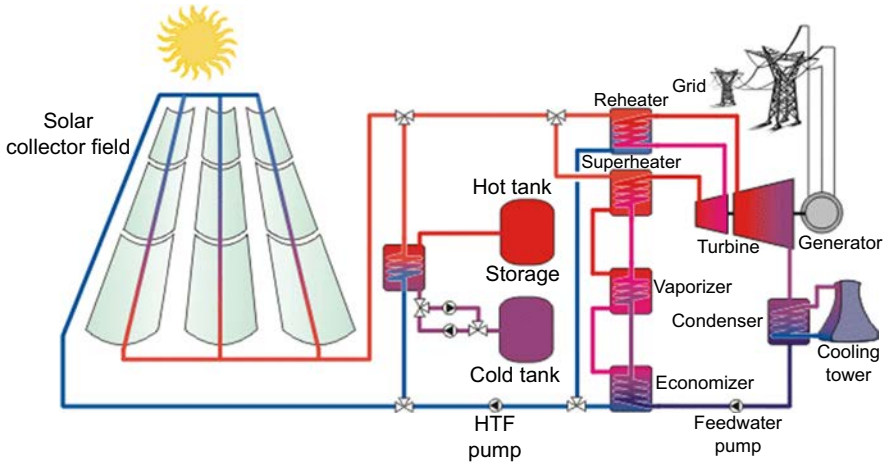


Figure 1.7 Solar thermal plant unit.

- **IGCC** *(integrated gasification combined cycle)* with carbon capture and storage (CCS) technology allows coal to be used to generate power as cleanly as natural gas. TEC will be among the first coal-fed facilities anywhere to meet this standard. IGCC technology has three basic components. In the gasification phase (Fig. 1.8), heat, pressure, pure oxygen, and water are used to break coal down into gas components and convert it into a clean synthetic gas (syngas).

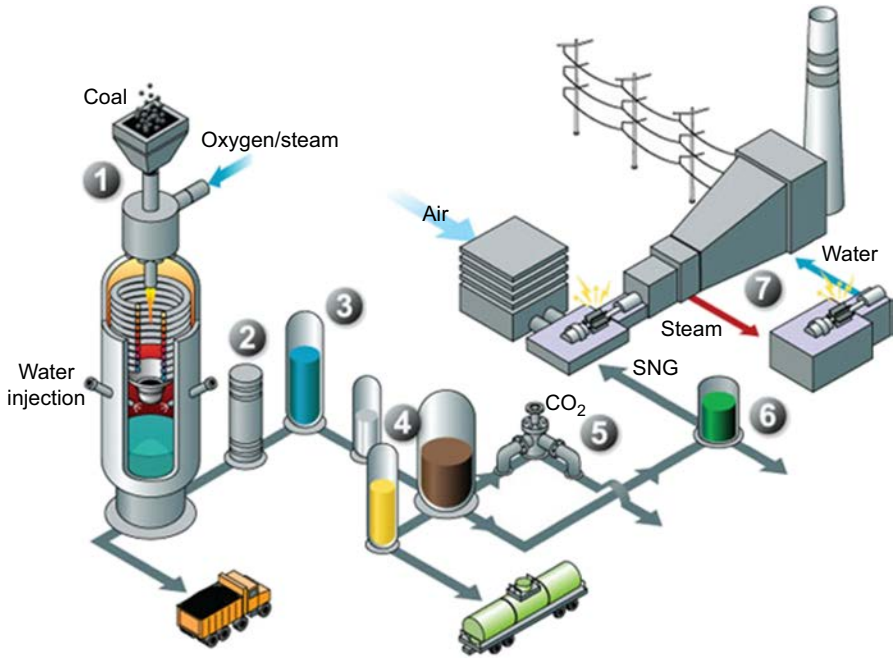


Figure 1.8 Integrated gasification combined-cycle.

1.1.2 Classification of power plants by duty

Power plants that can be dispatched (scheduled) to provide energy to a system include these:

- **Baseload power plants** run almost continually to provide that component of system load that does not vary during a day or week. Baseload plants can be highly optimized for low fuel cost, but they may not start or stop quickly during changes in system load. Examples of baseload plants would include large, modern, coal-fired and nuclear generating stations, or hydro plants with a predictable supply of water.
- **Peaking power plants** meet the daily peak load, which may only be for 1 or 2 h each day. While their incremental operating cost is always higher than base load plants, they are required to ensure security of the system during load peaks. Peaking plants include simple cycle industrial gas turbines and sometimes reciprocating internal combustion engines (mainly diesel), which can be started up rapidly when system peaks are predicted. Hydroelectric plants may also be designed for peaking use.
- **Intermediate load plants or load following power plants** are normally combined-cycle natural gas plants. But even advanced base load power plants can be optimized to operate as flexible as a gas turbine and even demonstrate rather high efficiency at part load. These plants can ramp up electricity production pretty efficiently but are most efficient when they run for a number of hours. They can economically follow the variations in the daily and weekly load, at lower cost than peaking plants, and with more flexibility than ordinary baseload plants.

It is the increase of the strongly unpredictable solar and wind power production capacity that calls for more flexibility of the fossil-fueled backup capacity. Thermo-mechanical fatigue damage in the thick section components due to the frequent startup and shutdown is a well-known problem in fossil-fueled plants if this new operation mode has not been met with adequate plant and operation modifications.

1.2 The coal-fired power generation plants

A coal-fired thermal power station is a power plant in which the prime mover is steam driven. Water is heated, turns into steam, and spins a steam turbine, which drives an electrical generator, as schematically shown in Fig. 1.9. After it passes through the turbine (one to three stage), the steam is condensed in a condenser and recycled to where it was heated; this is known as a Rankine cycle.

The efficiency of the Rankine cycle can be increased by introducing reheating of the steam after passage of the high-pressure turbine. Reheating not only improves the plant efficiency but also reduces the excessive moisture problem in low-pressure turbines. Reheating is commonly used in modern steam power plants, and for the USC plants or the A-USC plants, double reheating, where an additional reheating after the second turbine occurs, is adding another benefit to the plant efficiency.

The schematic and T-s diagram of the ideal reheat Rankine cycle is shown in Fig. 1.10(a) and (b).

The ideal reheat Rankine cycle differs from the simple, ideal Rankine cycle in that the expansion process take place in two stages. In first stage (the high-pressure turbine), steam is expanded isentropically to an intermediate pressure and sent back to the boiler where it is reheated at constant pressure, usually to the inlet temperature of the

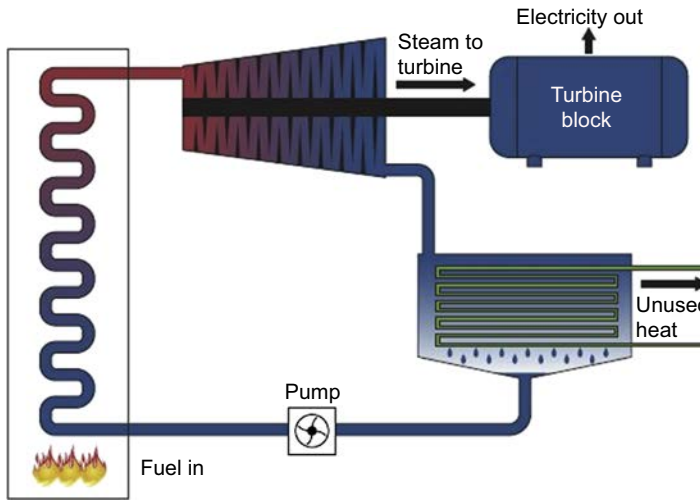


Figure 1.9 The steam cycle is at the heart of coal-fired power plant efficiency.

first turbine stage. Steam then expands isentropically in the second stage (low-pressure turbine) to the condenser pressure.

The energy efficiency of a conventional thermal power station, considered salable energy produced as a percent of the heating value of the fuel consumed, is typically 33% for the subcritical up to 48% for the most recent ultra-supercritical plants.

As with all heat engines, their efficiency is limited and governed by the laws of thermodynamics.

By comparison, most hydropower stations are about 90% efficient in converting the energy of falling water into electricity.

The greatest variation in the design of thermal power stations is due to the different fossil fuel resources generally used to heat the water. Some prefer to use the term energy center because such facilities convert forms of heat energy into electrical energy.

Certain thermal power plants also are designed to produce heat energy for industrial purposes of district heating, or desalination of water, in addition to generating electrical power.

Globally, fossil-fueled thermal power plants produce a large part of man-made CO_2 emissions to the atmosphere, and efforts to reduce these are varied and widespread.

A pulverized coal-fired boiler is an industrial or utility boiler that generates thermal energy by burning pulverized coal (also known as powdered coal or coal dust since it is as fine as face powder in cosmetic makeup) that is blown into the firebox.

The basic idea of a firing system using pulverized fuel is to use the whole volume of the furnace for the combustion of solid fuels. Coal is ground to the size of a fine grain, mixed with air, and burned in the flue gas flow.

Biomass and other materials, like waste, can also be added to the mixture. Coal contains mineral matter that is converted to ash during combustion. The ash is removed as bottom ash and fly ash. The bottom ash is removed at the furnace bottom.

This type of boiler dominates the electric power industry, providing steam to drive large turbines. Pulverized coal produces about 50% of the world's electric supply.

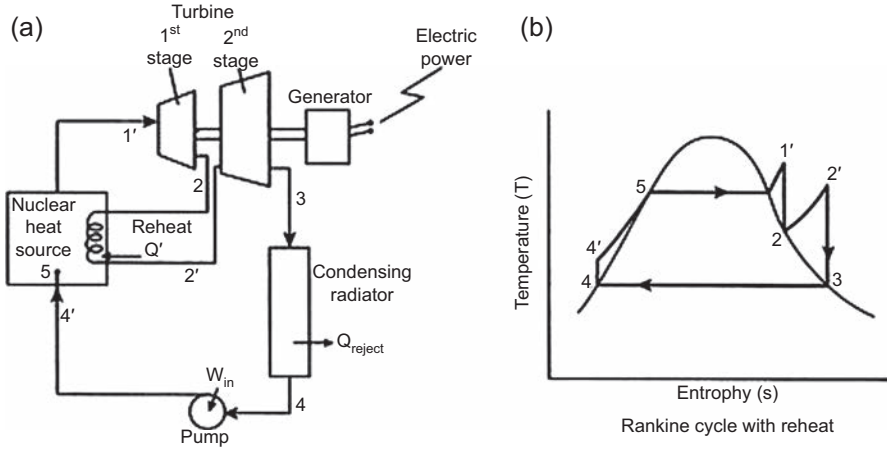


Figure 1.10 Ideal Rankine cycle [1].

The concept of burning coal that has been pulverized into a fine powder stems from the belief that if the coal is made fine enough, it will burn almost as easily and efficiently as a gas.

The feeding rate of coal according to the boiler demand and the amount of air available for drying and transporting the pulverized coal fuel is controlled by computers. Pieces of coal are crushed between balls or cylindrical rollers that move between two tracks or "races." The raw coal is then fed into the pulverizer along with air heated to about 330°C (650°F) from the boiler.

As the coal gets crushed by the rolling action, the hot air dries it and blows the usable fine coal powder out to be used as fuel. The powdered coal from the pulverizer is directly blown to a burner in the boiler.

The burner mixes the powdered coal in the air suspension with additional preheated combustion air and forces it out of a nozzle, similar in action to fuel being atomized by a fuel injector in modern cars. Under operating conditions, there is enough heat in the combustion zone to ignite all the incoming fuel.

Pulverized coal power plants are broken down into four categories, with operating temperatures and pressures as a function of the steam temperature and pressure:

- **Subcritical** pulverized coal (SubCPC) plants, below the critical point of water (540°C and 170–220 bar), have an operating efficiency <38%.
- **Supercritical** pulverized coal (SCPC) plants operate above the critical point, at 250 bar and 600/615°C, with an efficiency up to 42%.
- **Ultra-supercritical** pulverized coal plants operate above the critical point, at 300 bar and 620°C with efficiency in the 42–46% range.
- **Advanced ultra-supercritical** pulverized coal (A-USC PC) is the next generation, targeting operating efficiency >50% with steam temperature in the range of 700–760°C and pressure up to 350 bar.

Fig. 1.11 summarizes the trend in the operational parameters of the formerly listed power plants.

Supercritical power plants were in service in the late 1950s. But the technology did not really take off due to problems of reliability, especially from the metallurgical aspect.

Denmark was first in Europe to build ultra-supercritical (USC) plants, but Germany followed very soon after and later on also Italy. The USC plant with steam temperatures around 600°C is now considered state of the art in Europe, Japan, and China, whereas the United States has still not implemented this concept. It was the development of the steel grades 91 and later 92 for heavy section tubular components and derivatives for the cast and forged components that made this possible [2].

The main advantage between the subcritical, the supercritical, and the USC/A-USC units and the reason for a higher pressure operation is the increase in the thermodynamic efficiency of the Rankine cycle, as simply shown in Fig. 1.12. From subcritical to current state of art of USC, the efficiency increase is about 7%, targeting about 16% with the most optimistic A-USC project.

The single most important factor that determines the use of higher and higher pressure and temperatures is the availability of materials to withstand these conditions. Increases in operating pressure and temperatures have to go hand in hand with developments in metallurgy [3].

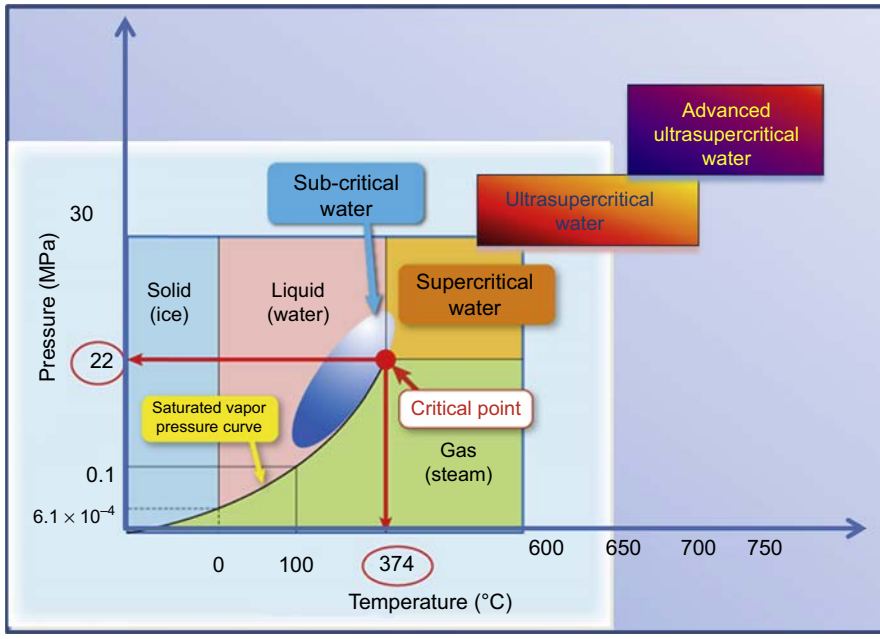


Figure 1.11 Water equilibrium diagram.

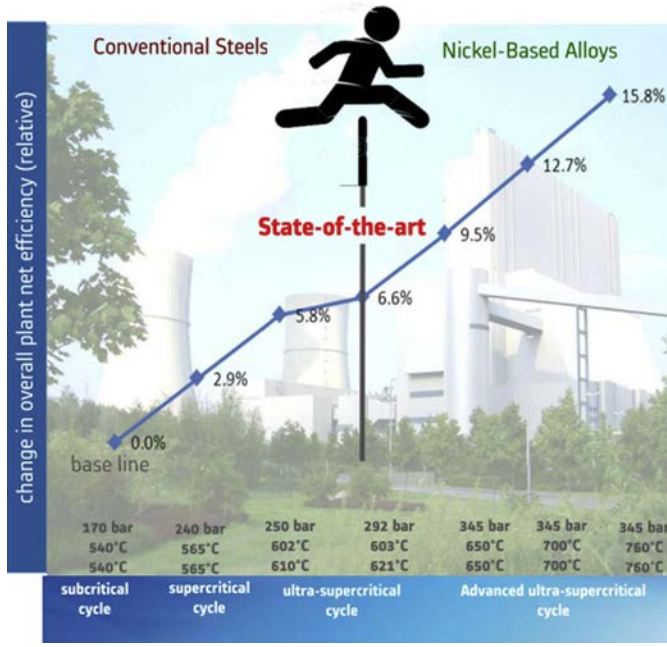


Figure 1.12 Increase of net efficiency from subcritical to A-USC power plants [4].

The last steel-based USC power plant is targeting a steam temperature in the range of 650°C. For the A-USC the use of nickel-based alloys is mandatory to reach a steam temperature over 700°C, both for creep and corrosion/oxidation properties. Fig. 1.13 summarizes the operating temperature and pressure of the different available material classes, and Fig. 1.14 shows the schematic view of the modified boiler for an A-USC power plant proposed by Babcock and Wilcox.

Fig. 1.15 shows how the ratio between ferritic, austenitic, and Ni-based materials for boiler components is changing when going from the supercritical to the advanced ultra-supercritical power plants.

The other chapters of this book will give detailed information about the materials currently available for the construction of the USC plants and the materials R&D activities around the world for the development and manufacture of components able to be used in the next generation of A-USC plants.

1.3 The power generation trend: realizing decarbonization through efficiency gains

Coal remains an important source of energy for the world, particularly for power generation. Therefore the advanced technology in power generation plants has to be adopted as fast as possible [8,9].

During the last two decades (1990–2012) the demand for coal has grown rapidly (Fig. 1.16), as has the demand for gas, oil, nuclear, and renewable energy sources. The increase of energy produced by coal is mainly due to the price and sources of coal in

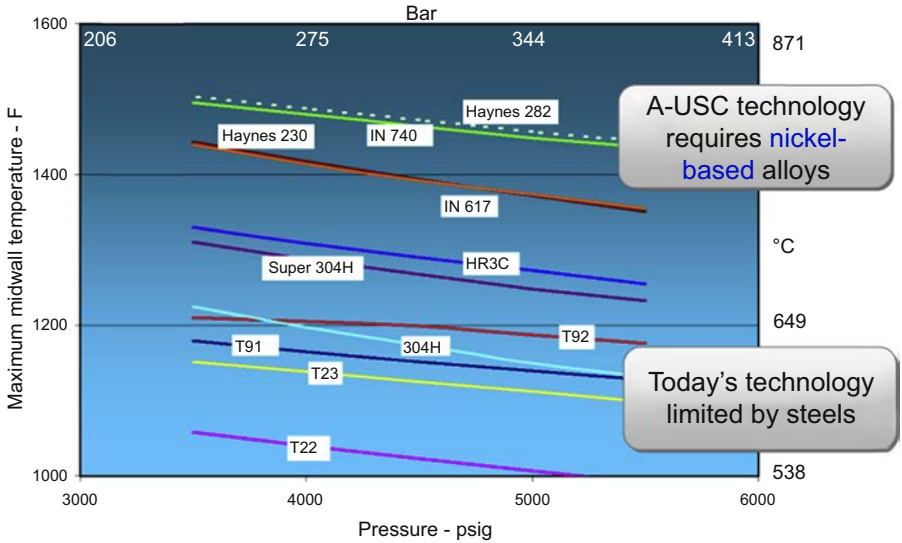


Figure 1.13 Maximum operating temperature and pressure of the different materials [5].

Asian countries and availability technology developed in the European Union and Japan for large USC plants [10].

Various projections for future growth in energy demand suggest that this trend will continue dominated by coal use in the emerging economies, particularly China and India.

New Policies Scenario of the World Energy Outlook broadly serves as the IEA baseline scenario. It takes account of broad policy commitments and plans that have been announced by countries, including national pledges to reduce greenhouse gas

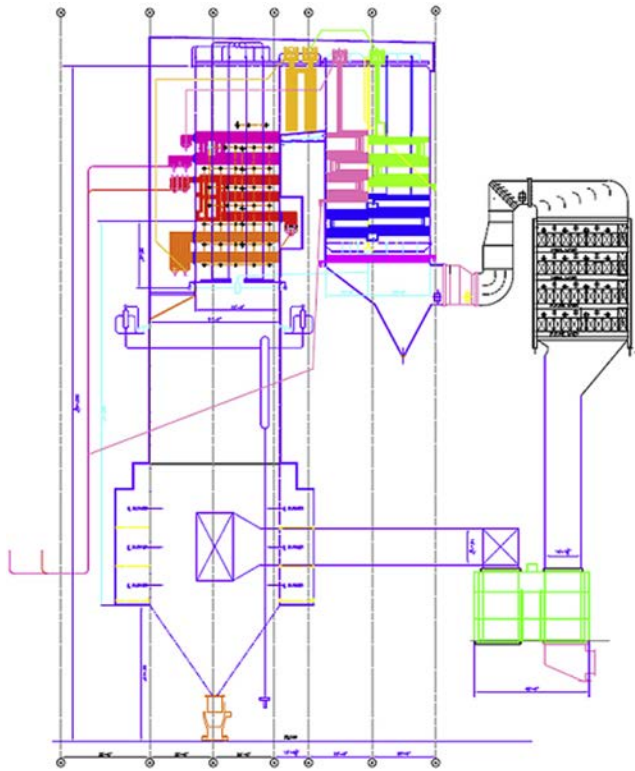


Figure 1.14 Conceptual design of 800-MW modified tower for an Advanced UltraSuperCritical Power Plant (A-USC PP) [6].

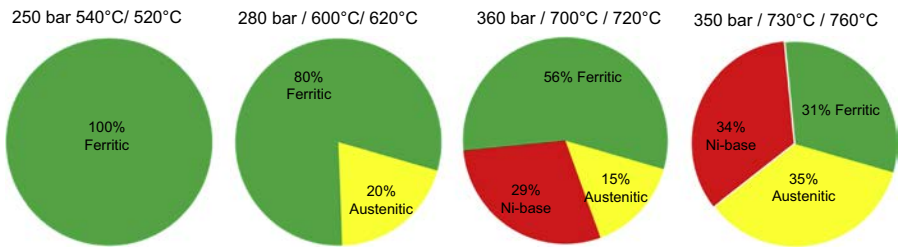


Figure 1.15 Materials used in SC, USC, and A-USC boiler [7].

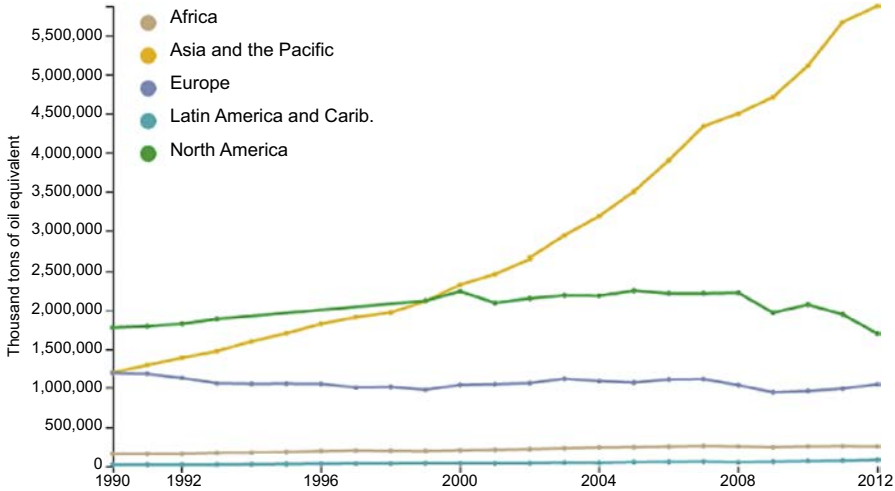


Figure 1.16 Electricity production from coal 1990–2012 (thousands tons of oil equivalents) [10].

(GHG) emissions and plans to phase out fossil energy subsidies, even if the measures to implement these commitments have yet to be identified or announced [11].

- **Current Policies Scenario** assumes no changes in policies from the midpoint of the year of publication (previously called the Reference Scenario).
- **450 Scenario** sets out an energy pathway consistent with the goal of limiting the global increase in temperature to 2°C by limiting the concentration of greenhouse gases in the atmosphere to around 450 parts per million of CO_2.
- **The 2°C Scenario (2DS)** is the focus of Energy Technology Perspectives. The 2DS describes an energy system consistent with an emissions trajectory that recent climate science research indicates would give an 80% chance of limiting average global temperature increase to 2°C. It sets the target of cutting energy-related CO_2 emissions by more than half by 2050 (compared with 2009) and ensuring that they continue to fall thereafter. Importantly, the 2DS acknowledges that transforming the energy sector is vital, but it is not the sole solution: the goal can only be achieved provided that CO_2 and GHG emissions in nonenergy sectors are also reduced. The 2DS is broadly consistent with the World Energy Outlook 450 Scenario through 2035 [11].
- **The 4°C Scenario (4DS)** takes into account recent pledges made by countries to limit emissions and step up efforts to improve energy efficiency. It serves as the primary benchmark in ETP 2012 when comparisons are made between scenarios. Projecting a long-term temperature rise of 4°C, the 4DS is broadly consistent with the World Energy Outlook New Policies Scenario through 2035 (IEA, 2011). In many respects, this is already an ambitious scenario that requires significant changes in policy and technologies. Moreover, capping the temperature increase at 4°C requires significant additional cuts in emissions in the period after 2050.
- **The 6°C Scenario (6DS)** is largely an extension of current trends. By 2050, energy use almost doubles (compared with 2009) and total GHG emissions rise even more. In the absence of efforts to stabilize atmospheric concentrations of GHGs, average global temperature rise is projected to be at least 6°C in the long term. The 6DS is broadly consistent with the World Energy Outlook Current Policy Scenario through 2035 (Fig. 1.17).

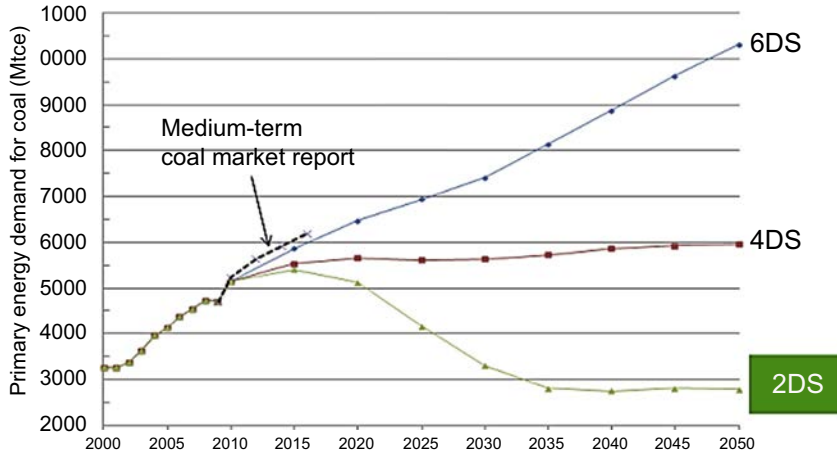
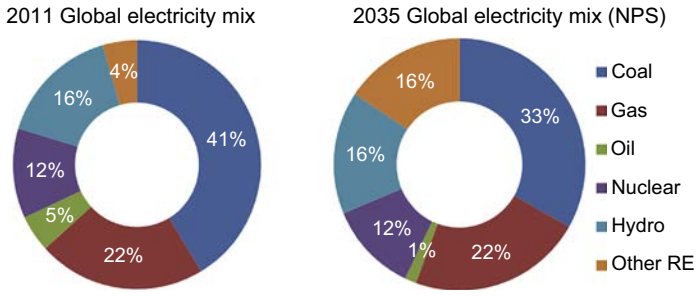


Figure 1.17 The size of the challenge is clear [11].



Data source: IEA (2013), *World Energy Outlook 2013*, OECD/IEA, Paris, France. (p.175)

Figure 1.18 Global electricity mix (current + projections) [10].

Nevertheless, while coal's share will fall to 33% in 2035, from 41% in 2011, coal remains the leading source of electricity generation in 2035 under the IEA New Policy Scenario (Fig. 1.18). Despite coal's drop in share, global coal demand will increase from 9140 TWh in 2011 to 12,312 TWh in 2035. Seventy-five percent of this growth will come from the power sector [10].

Continuing pressure to cut CO_2 emissions to mitigate the effects of climate change, specifically to limit the average rise in global temperature up to between 2°C, will require halving (from current levels) CO_2 emissions by 2100, as agreed in the last Paris COP21 conference.

To contribute to this goal, emissions from coal-fired power generation will need to be reduced by around 90% over this period: Cuts this deep will require CCS. In the International Energy Agency (IEA) 450 ppm CO_2 climate change scenario, around 3400 large-scale CCS plants must be operating globally by 2050 to abate the required amount of CO_2 emissions. At the same time, the growing need for energy, and its economic production and supply to the end user, must remain a central consideration in power plant construction and operation.

In 2012, the IEA concluded that, in general, larger, more efficient, and hence younger coal-fired power plants are most suited for an economic CCS retrofit. However, the agency also found that only around 29% of the existing installed global coal-fired fleet could be retrofitted with CCS. Furthermore, on average, the efficiency of existing global coal-fired capacity is comparatively low, at about 33% [net higher heating value (HHV) basis for all loads, all coals, and all steam conditions], although the recent establishment of large tranches of modern plants, particularly in China, is increasing this average value [8].

Operating at lower efficiency means that relatively large amounts of coal must be used to produce each unit of electricity. As coal consumption rises, so do the levels of CO_2 and other emissions. Upgrading existing plants and building new ***high-efficiency, low-emissions*** (**HELE**) coal-fired power plants addresses climate change concerns in two important ways. In the near term, emissions can be reduced by upgrading existing plants or building new HELE plants. Such plants emit almost 20% less CO_2 than a subcritical unit operating at a similar load. Over the longer term, HELE plants can further facilitate emission reductions because coal-fired plants operating at the highest efficiencies are also the most appropriate option for CCS retrofit. For these reasons, there is considerable global interest in HELE technologies. Fig. 1.19 illustrates the impact of employing progressively more effective HELE technologies and CCS on CO_2 abatement [presented in terms of lower heating value (LHV) at full load with hard coal] [8].

Supercritical plants can be found in 18 countries and are now the norm for new plants in industrialized nations; USC steam cycles are now the state of the art. A current coal-fired plant operating with a high-efficiency USC steam cycle not only has improved efficiency, but it is also more reliable and has a longer life expectancy.

Whereas the first supercritical units were relatively small (typically less than 400 MW_e), larger units of up to 1100 MW_e are now being built based on USC technology (such as the Neurath USC lignite-fired plant in Germany), and even larger units are planned.

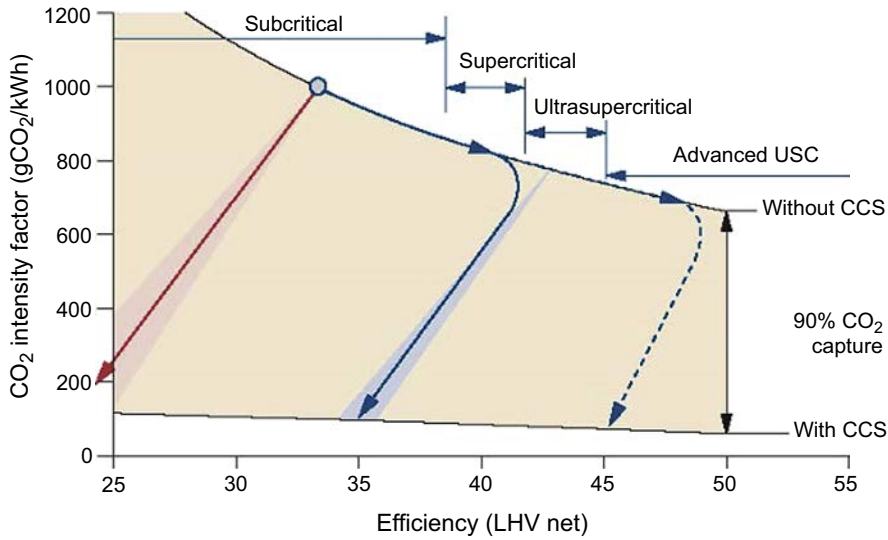


Figure 1.19 Reducing CO_2 emissions from pulverized coal-fired power generation [8].

Such a best available technology pulverized fossil-fired power plant would be fitted with high-quality selective catalytic reduction for NOx reduction, flue gas desulphurization for SO_2 reduction, and an electrostatic precipitator or baghouse filter, as appropriate, for particulates removal.

Developments in A-USC steam cycles are expected to continue this trend. A-USC coal-fired plants are designed with an inlet steam temperature to the turbine of 700–760°C. Average metal temperatures of the final superheater and final reheater could be higher, up to about 815°C. Nickel-based alloy materials are needed to meet this demanding requirement. Various research programs are underway to develop A-USC plants. If successful, a commercial A-USC-based plant would be expected to achieve efficiencies in the range of 45–52% (LHV [net], hard coal). A plant operating at 48% efficiency (HHV) would emit up to 28% less CO_2 than a subcritical plant, and up to 10% less than a corresponding USC plant. Commercial A-USC plants could be widely available by 2025, with the first units coming online in the near future.

To illustrate the potential of HELE technologies, Fig. 1.20 summarizes the impact of different steam-cycle conditions on an 800-MWe power station boiler burning hard coal and operating at an 80% capacity factor. Such a unit would generate 6 TWh of electricity annually and emit the quantities of CO_2 shown in the figure, depending on its steam-cycle conditions and corresponding efficiency. Thus, replacing a unit of this type operating with a subcritical steam cycle with a unit based on A-USC technology (under development) would result in savings of CO_2 in the region of 30% [8].

Another very important factor for the reduction of the CO_2 emission is the aging of the current available infrastructure: in fact, in main organization for economic cooperation and development (OECD) countries a relevant number of power plants are quite old and should be replaced by a new plant through a refurbishment program. The situation is clearly summarized in Fig. 1.21 [9]: Russia and the United States have

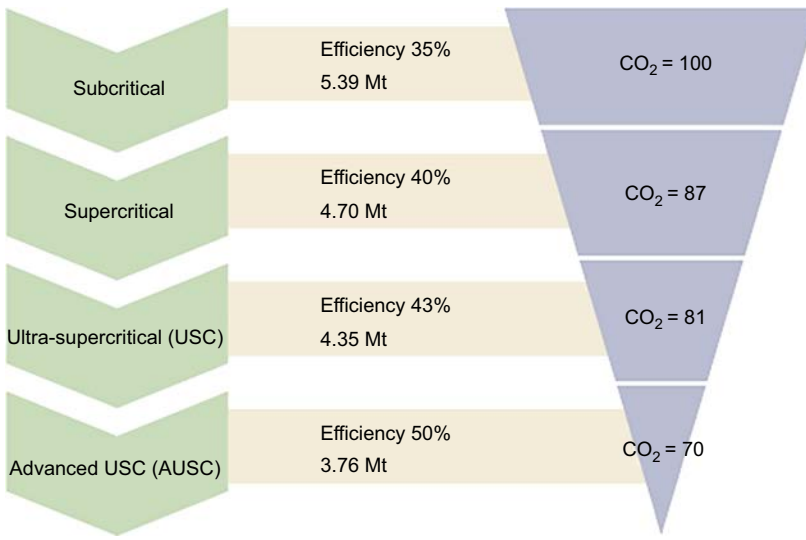


Figure 1.20 The impact of HELE technologies on CO_2 emissions [8].

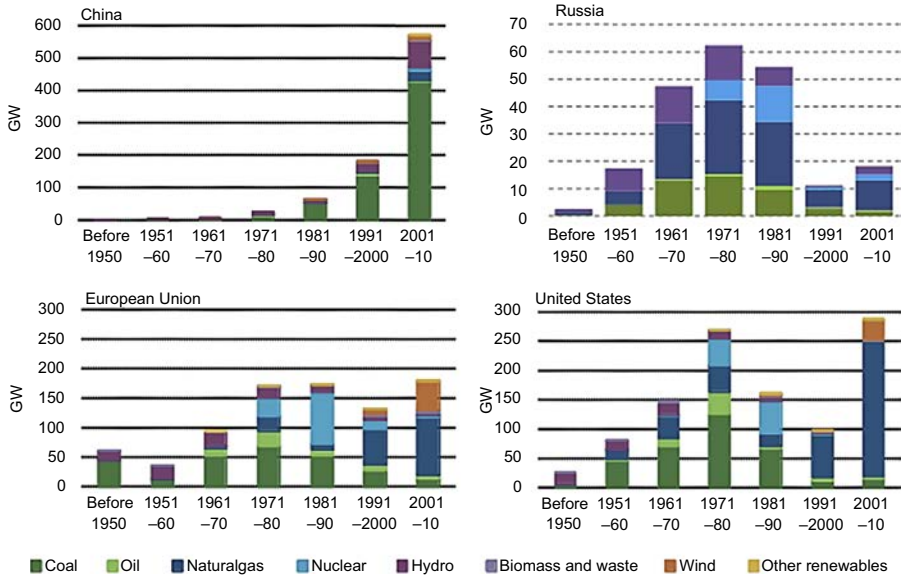


Figure 1.21 Age distribution of existing power plants [9].

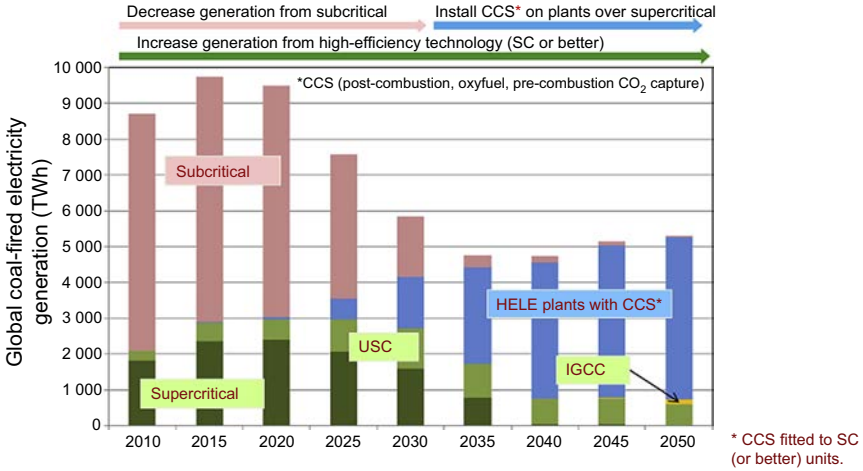


Figure 1.22 Three processes essential to achieve a low carbon scenario [9].

several old plants; the situation in the European Union is better, and in China, the main plant in operation is quite young.

Therefore the new IEA scenario that is quite in agreement with the results of the Cop21 Conference can be summarized, as shown in Fig. 1.22, as follows:

- dismantling of older subcritical power plants
- repowering of older subcritical and supercritical power plants with USC
- building only new USC power plants
- installation of CCS technology in the older and new power plants

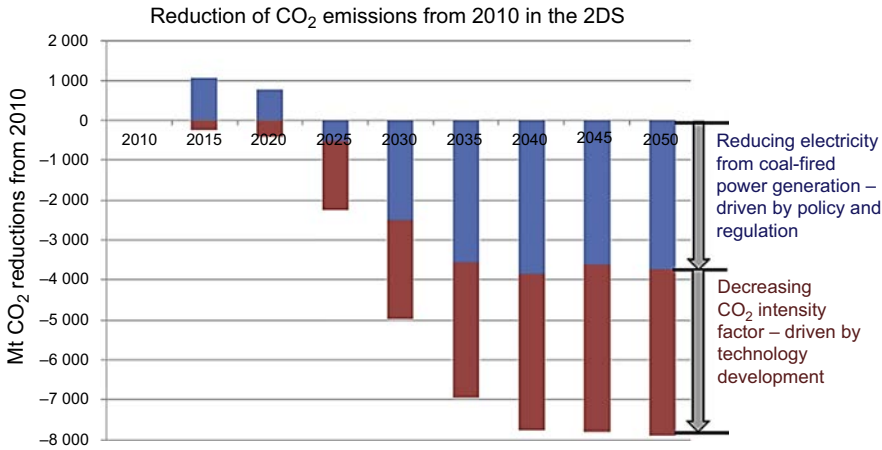


Figure 1.23 Reduction of CO_2 emissions from 2010 in the 2DS [9].

- development and commissioning of A-USC power plants after 2025 with CCS
- development of IGCC power plants
- installation of more renewable power plants

By following this method, a possible 8 Gt CO_2 reduction by 2050 could be reached (Fig. 1.23). In fact the Asian and Africa Countries that are requiring the increase of electricity from fossil fuel will reach the maximum in the next 20 years.

1.4 Fossil fuels classification

Coal comprises a different variety of a mix of solid carbon and mineral matters. It is characterized by density, carbon content, calorific value, volatiles, moisture, and specific quantity of the mineral impurities. Anthracite, bituminous coal, and lignite are the three main categories.

1.4.1 Anthracite

Anthracite ("coal-like") is a hard, very low content of volatile compact variety of coal that has a high luster. It has the highest carbon content (between 92.1% and 98%), the fewest impurities, and the highest calorific content of all types of coal, which also includes bituminous coal and lignite. Due to the lack of volatiles, it can only be burned in special boilers.

Anthracite has a history of use in blast furnaces for iron smelting; however, it lacks the pore space of metallurgical coke, which eventually replaced anthracite.

1.4.2 Bituminous coal or black coal

Bituminous coal or **black coal** is a relatively soft coal containing a tarlike substance called bitumen. It is of higher quality than lignite coal but of poorer quality than anthracite. Formation is usually the result of high pressure being exerted on lignite. Its

coloration can be black or sometimes dark brown; often there are well-defined bands of bright and dull material within the seams.

1.4.3 Subbituminous coal

Subbituminous coals are a type of coal whose properties range from those of lignite to those of bituminous coal and are used primarily as fuel for steam-electric power generation.

Subbituminous coals may be dull, dark brown to black, soft and crumbly at the lower end of the range, to bright jet-black, hard, and relatively strong at the upper end. They contain a high number of volatiles, which make it easy to ignite, and secure a stable combustion and 15–30% inherent moisture by weight and are non-coking (undergo little swelling upon heating).

1.4.4 Lignite

Lignite, often referred to as **brown coal**, is a soft brown combustible sedimentary rock that is formed from naturally compressed peat. It is considered the lowest rank of coal due to its relatively low heat content. It is mined in China, Bulgaria, Greece, Germany, Kosovo, Poland, Serbia, Russia, Turkey, the United States, Canada, India, Australia, and many other parts of Europe, and it is used almost exclusively as a fuel for steam-electric power generation. But it is also mined for its germanium content in China. The percentage of Germany's electricity that comes from lignite power plants is 26.3%, while in Greece, lignite provides about 50% of its power needs.

Lignite is brownish-black in color and has a carbon content of around 25–35%, a high inherent moisture content, sometimes as high as 66%, and an ash content ranging from 6% to 19%, compared with 6–12% for bituminous coal.

1.4.5 Natural gas

Natural gas is a fossil fuel formed when layers of buried plants, gases, and animals are exposed to intense heat and pressure over thousands of years. The energy that the plants originally obtained from the sun is stored in the form of chemical bonds in natural gas. Natural gas is a nonrenewable resource because it cannot be replenished on a human time frame. Natural gas is a hydrocarbon gas mixture consisting primarily of methane, but it commonly includes varying amounts of other higher alkanes and sometimes a lesser percentage of carbon dioxide, nitrogen, and/or hydrogen sulfide. Natural gas is an energy source often used for heating, cooking, and electricity generation. It is also used as fuel for vehicles and as a chemical feedstock in the manufacture of plastics and other commercially important organic chemicals.

Natural gas is found in deep underground rock formations or associated with other hydrocarbon reservoirs in coal beds and as methane clathrates. Petroleum is another resource and fossil fuel found in close proximity to and with natural gas. Most natural gas was created over time by two mechanisms: biogenic and thermogenic processes. Biogenic gas is created by methanogenic organisms in marshes, bogs, landfills, and

shallow sediments. Deeper in the earth, at greater temperature and pressure, thermogenic gas is created from buried organic material.

Before natural gas can be used as a fuel, it must be processed to remove impurities, including water, to meet the specifications of marketable natural gas. The by-products of this processing include ethane, propane, butanes, pentanes, and higher molecular weight hydrocarbons, hydrogen sulfide (which may be converted into pure sulfur), carbon dioxide, water vapor, and sometimes helium and nitrogen.

1.4.6 Petroleum

Petroleum, or **crude oil**, is any naturally occurring flammable mixture of hydrocarbons found in geologic formations, such as rock strata. Most petroleum is a fossil fuel, formed from the action of intense pressure and heat on buried dead zooplankton and algae. Technically, the term petroleum only refers to crude oil, but sometimes it is applied to describe any solid, liquid, or gaseous hydrocarbons.

1.5 Power plant overview and main components

Thermal power plant main sections.

The main thermal power plant sections, shown in Fig. 1.24, are these:

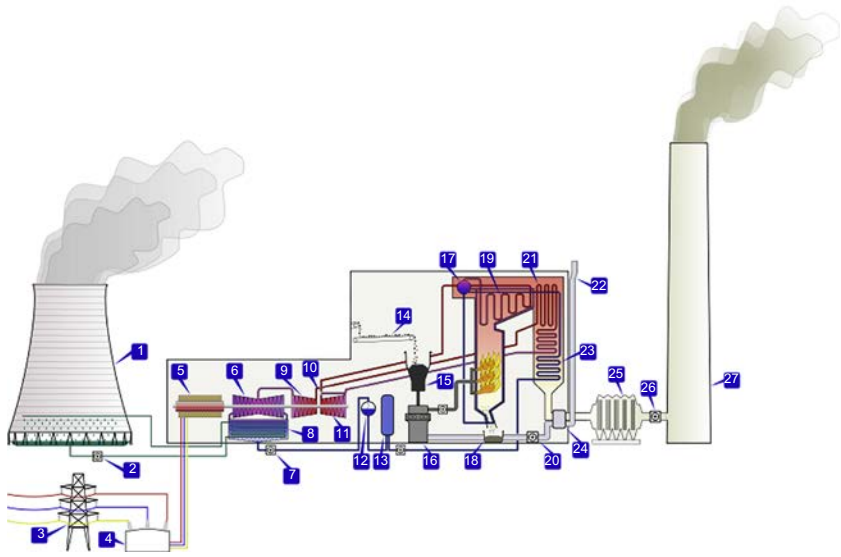
- boiler: water wall, superheater, reheater, header, economizer, drums (only for subcritical)
- steam line to connect boiler and turbine sections
- turbine (valves, casing, and rotor)
- condenser

1.5.1 Steam/water diagrams used in boiler calculations

Before we start the description of the sections and the components of a coal-fired power plant, it is important to have a basic knowledge of the water/steam conditions that are present in a boiler.

1.5.1.1 Temperature-heat (T-Q) diagram

The T-Q diagram is a useful tool for designing heat exchangers. It can also be used to present the heat transfer characteristics of an existing heat exchanger or heat exchanger network. The T-Q diagram consists of two axes: the current stream temperature on the *y*-axis and the amount of heat transferred on the *x*-axis. Sometimes the streams are marked with arrowheads to clarify the direction of the streams, but these are not necessary. Because heat cannot move from the colder stream to the hotter stream, according to the second law of thermodynamics, the directions of the streams are explicitly determined: the hot stream transfers its heat to the cold stream, thus the flow direction of the hot stream is toward lower temperature and the flow direction of the cold stream is toward higher temperatures. For the same reason, the hot stream is always above the cold stream in the T-Q diagram [13].



1. Cooling tower
2. Cooling water pump
3. Transmission line (3-phase)
4. Step-up transformer (3-phase)
5. Electrical generator (3-phase)
6. Low pressure steam turbine
7. Condensate pump
8. Surface condenser
9. Intermediate pressure steam turbine
10. Steam control valve
11. High pressure steam turbine
12. Deaerator
13. Feedwater heater
14. Coal conveyor
15. Coal hopper
16. Coal pulverizer
17. Boiler steam drum
18. Bottom ash hopper
19. Superheater
20. Forced draught (draft) fan
21. Reheater
22. Combustion air intake
23. Economiser
24. Air preheater
25. Precipitator
26. Induced draught (deraft) fan
27. Flue gas stock

Figure 1.24 Schematic overview of thermal power plants [12].

When designing or reviewing heat exchanger networks, the T-Q diagram gets useful. The T-Q diagram is therefore applied when designing boilers; the heat exchanger surface arrangement can especially be clearly visualized with a T-Q diagram (Fig. 1.25) for a USC plant with $T = 600°C$.

1.5.1.2 Temperature-entropy (T-s) diagram

The T-s diagram represents the various phases of steam/water with temperature as a function of the specific entropy. It is often used to visualize steam power processes. The T-s diagram is also commonly used for displaying reversible processes (or real processes simplified as reversible processes), which in the T-s diagram appear as closed curves (loop).

The left border, up to the critical point, is the border where the liquid is saturated (Fig. 1.26). That is, the water is still liquid and contains no steam. But if we go further

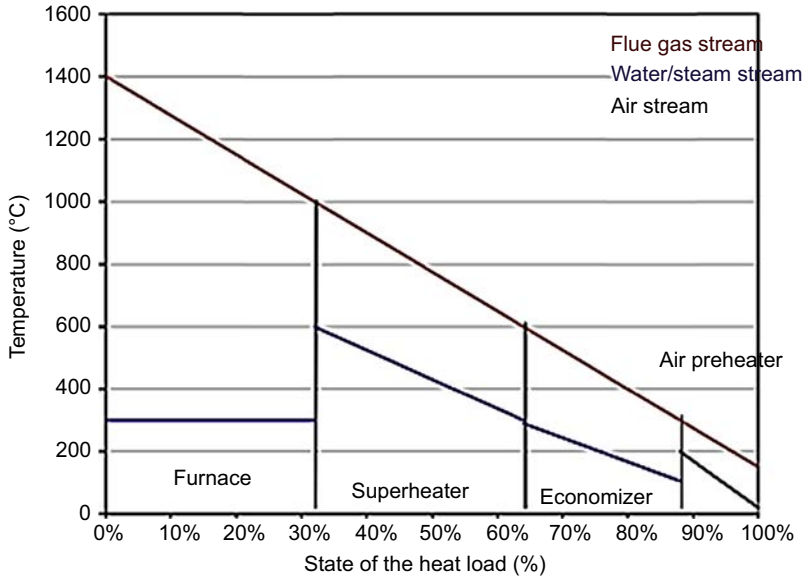


Figure 1.25 Example of a T-Q diagram representing the heat surfaces in a PCF boiler [13].

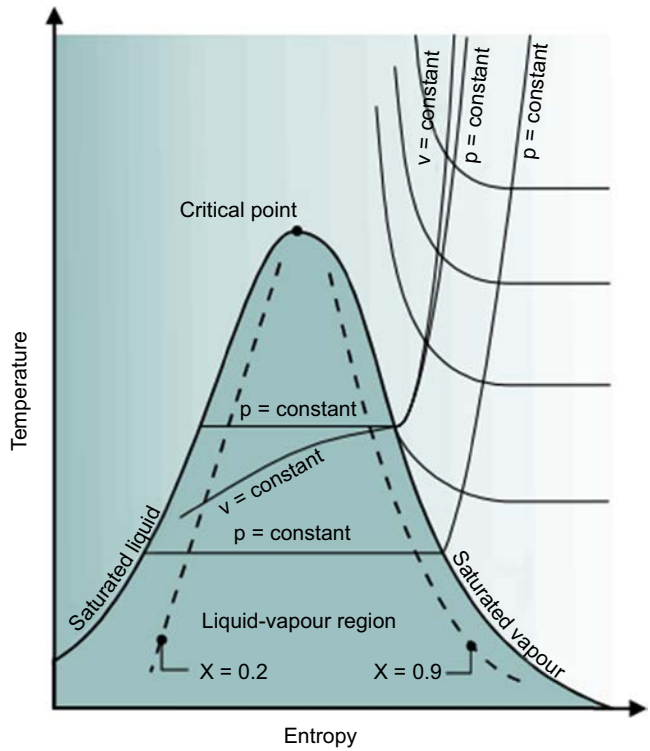


Figure 1.26 Simplified T-s diagram of steam/water [13].

right (increase the entropy), steam bubbles start to form in the water. In other words, saturated water starts to boil when heat is added and entropy is increased.

The enclosed region in the middle is the region where water is a mixture of vapor and liquid. Steam that contains water in any form, either as minute droplets, mist, or fog, is called wet steam. The quantity called "x" in the diagram represents the amount (percentage by weight) of dry vapor in the wet steam mixture. This quantity is called the *quality of steam.* For instance, if there is 10% moisture in the steam, the quality of the steam is 90% or 0.9. The temperature of wet steam is the same as dry saturated steam at the same pressure.

The right border, down from the critical point, is the line where steam is saturated. When steam is heated beyond that border, steam is called superheated. Water boils under constant temperature and pressure, so a horizontal line inside the enclosed region represents a vaporization process in the T-s diagram. The steam/water heating process in the boiler represented by the diagram in Fig. 1.25 can also be drawn in a T-s diagram (Fig. 1.27), if the boiler pressure is assumed to be, eg, 10 MPa.

1.5.1.3 Pressure-enthalpy (p-h) diagram

Another tool used in boiler calculation is the pressure-enthalpy diagram for steam/water (Fig. 1.28). With the p-h diagram, it is easy to visualize the partial shares of the total heat load on different heat exchanger surfaces in the boiler: drawing the steam heating process in the boiler onto the p-h diagram will give a horizontal line (if we simplify the process and set pressure losses to zero).

Fig. 1.29 shows the same boiler steam/water process from Fig. 1.27, drawn in the steam/water p-h diagram.

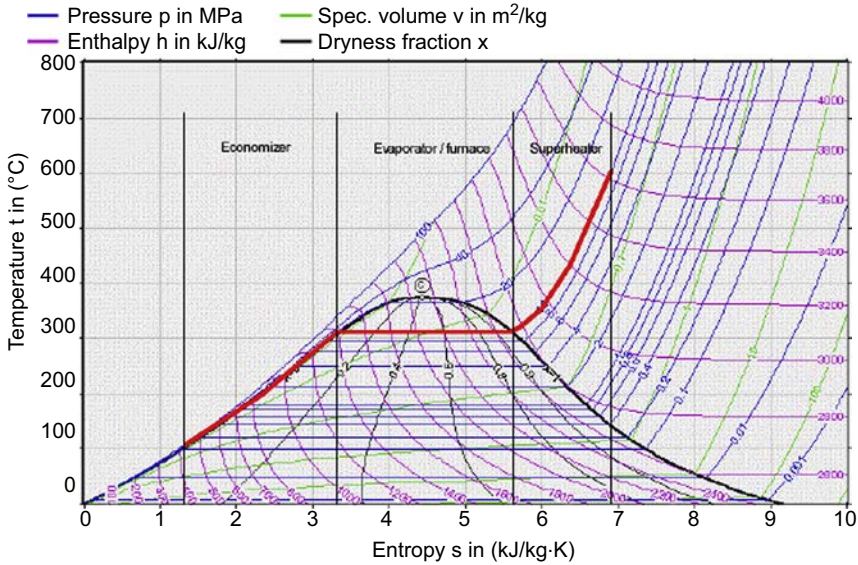


Figure 1.27 Detailed T-s diagram of the PCF boiler steam/water [13].

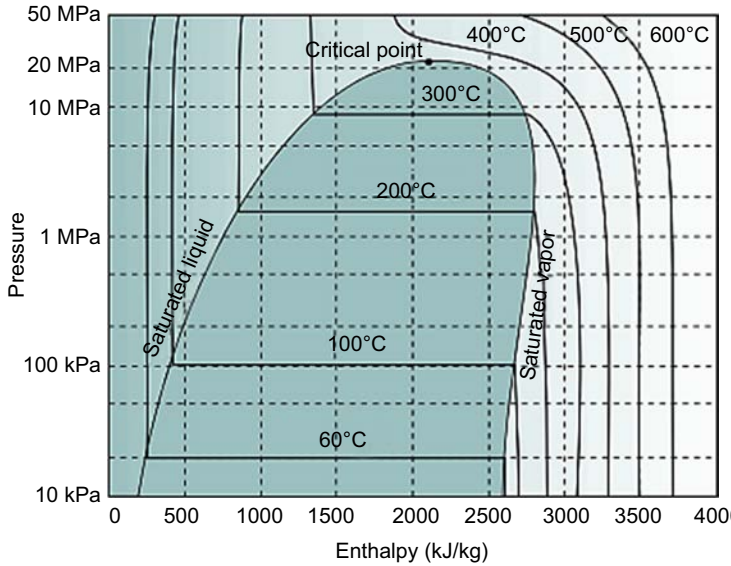


Figure 1.28 Simplified p-h diagram for steam/water [13].

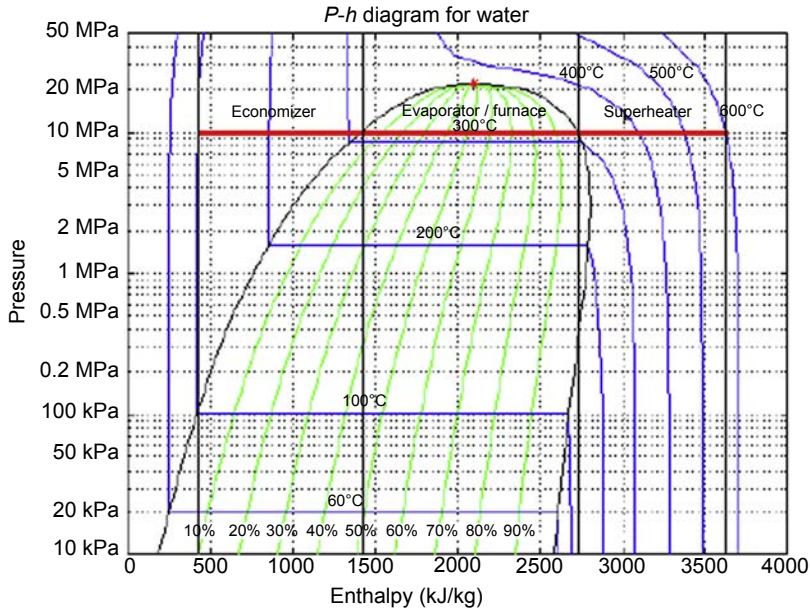


Figure 1.29 Detailed p-h diagram of the PCF boiler steam/water heating process (*red line*) from Fig. 1.27 [13].

1.5.1.4 Enthalpy-entropy (Mollier, h-s) diagram

The most frequently used tool for determining steam properties is probably the enthalpy-entropy (h-s) diagram, also called a Mollier diagram (Fig. 1.30). If two properties of the steam state are known (like pressure and temperature), the rest of the properties for steam (enthalpy, entropy, specific volume, and moisture content) can be read from the diagram. A more detailed h-s diagram can be found in Fig. 1.31. Since the diagram is very large, the diagram is usually found as two versions, consisting of zoomed portions of the original: one for steam properties (Fig. 1.30) and another for water properties.

1.5.2 Boiler

The boiler is a rectangular furnace about 15–25 m on a side and 40–80 m tall. Its walls are made of a web of high-pressure steel tubes about 30–58 mm in diameter. Pulverized coal is air-blown into the furnace through burners located at the four corners, or along one wall, or two opposite walls, and it is ignited to rapidly burn, forming a large fireball at the center.

The thermal radiation of the fireball heats the water that circulates through the boiler tubes near the boiler perimeter. The water circulation rate in the boiler is three to four times the throughput. As the water in the boiler circulates, it absorbs heat and changes into steam. In subcritical Power Plant (PP), it is separated from the water inside a drum at the top of

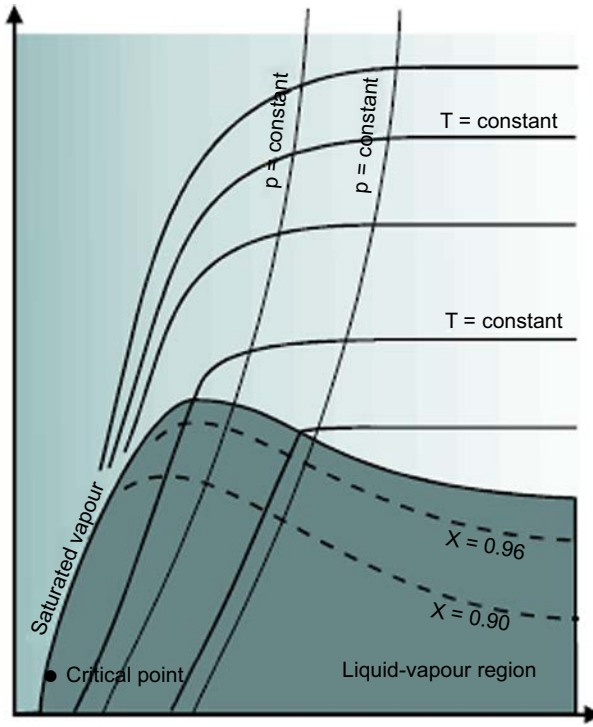


Figure 1.30 Mollier (h-s) diagram, simplified version [13].

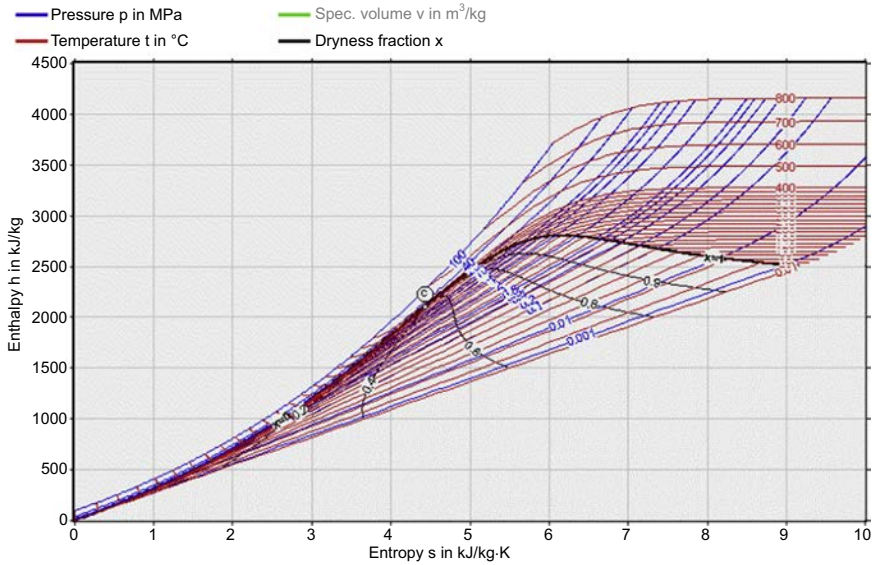


Figure 1.31 Large-scale Mollier h-s diagram for steam [13].

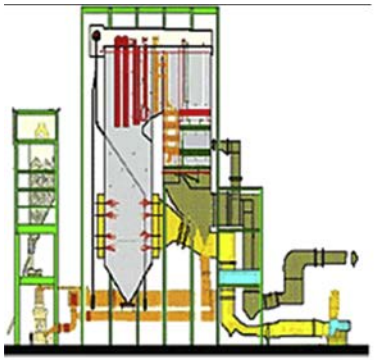
the furnace. The saturated steam is introduced into superheat pendant tubes that hang in the hottest part of the combustion gases as they exit the furnace. Here, the steam is superheated to 540–620°C to prepare it for the turbine. The schematic design of a subcritical PP (capacity of 1000 to 3175 TPH, pressure of subcritical SuperHeater (SH) and ReHeater (RH), and temperature up to 585°C) is proposed in Fig. 1.24. In Fig. 1.32, the schematic design of the subcritical, supercritical, and ultra-supercritical power plants are compared.

1.5.2.1 Water wall

The water walls surround the furnace and consist of tubes, with an outer diameter of typically 30–60 mm, welded together with fins (Fig. 1.33) to form a gas-tight containment of the hot flue gases. Tubes are exposed to the furnace flame, and inside the tubes, flowing water boils under high pressure. The tubes are automatically welded and preassembled as panels in a workshop and then welded together in the plant (Fig. 1.34). Water walls are also bent for the holes manufacture for burner's installation (Fig. 1.35). For example, the water walls of a 12 m × 12 m × 65 m large furnace in a recently built 400-MW coal-fired power plant consist of 58 km of tubes and fins weighing c. 350 tons excluding weld consumables.

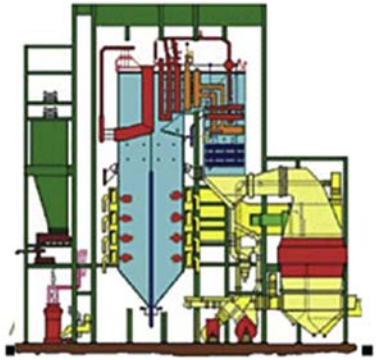
As a function of boiler designs, the tubes can be vertical or in a spiral position (Fig. 1.36): which one is chosen depends, in part, on the type of project under construction. The main advantages are described:

- spiral furnace tube:
  - benefits from the averaging of lateral heat absorption variation in each tube
  - simplified inlet header arrangement
  - use of smooth-bore tubing throughout entire furnace wall system



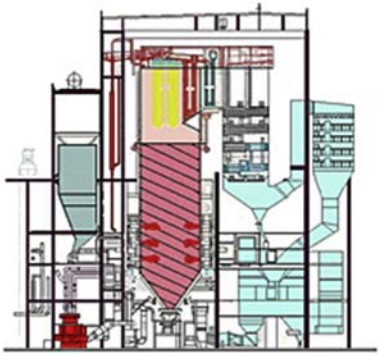
Subcritical two-pass type boiler characteristics:

Natural circulation
Two-pass type
High sub-critical pressure : SOP = 180bar(g)
Coal firing
Opposed wall fired
Divided back pass for R/H control



Supercritical boiler characteristics:

Once-through
Two-pass type
Supercritical pressure
Coal, oil and gas firing
Opposed wall fired
Gas-recycling



Ultra-supercritical boiler characteristics

Once-through
Two-pass type
Ultra supercritical pressure
SH and RH outlet temperature above 600°C
Coal firing
Opposed wall fired
Divided back pass for R/H control

Figure 1.32 Design differences in subcritical, supercritical, and ultra-supercritical power plants [14,15].

- no individual tube orifices
- large number of operating references

- vertical furnace tube:
  - simpler wind box openings
  - simpler furnace water wall support system
  - no intermediate furnace wall transition header
  - lower construction and maintenance costs
  - easier to identify and repair tube leaks

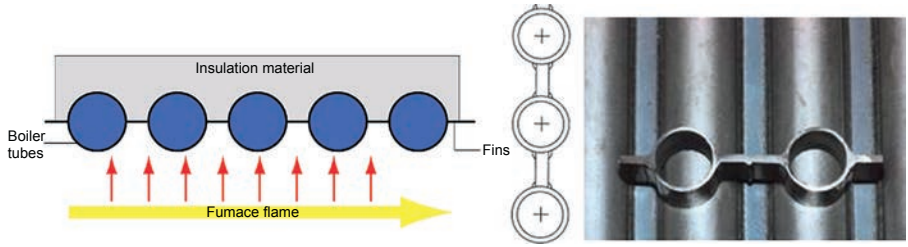


Figure 1.33 Water wall tubes.



Figure 1.34 Water wall panel [16] and preassembly in the workshop.

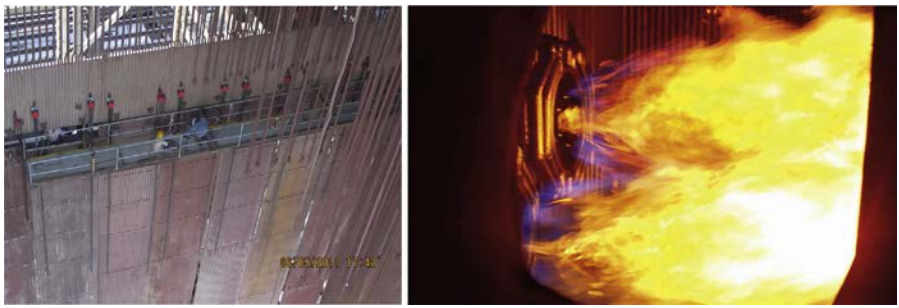


Figure 1.35 Water wall assembling in plants [17] and hole with operating burner [18].

Tubes can be smooth or also internally rifled to increase the heat exchange (Fig. 1.37). Usually, the rifled tubes are associated with vertical design. In the highly loaded furnace area, spiral-wound evaporator tubing is usually used with smooth tubes and high mass fluxes: approximately 2000–2500 kg/m^{3}s. As spiral-wound furnace tubing of this type is not self-supporting, it is reinforced with support straps that are welded to the tube wall with support blocks.

The water walls in boilers for subcritical steam conditions are generally configured as evaporators.

At increasing steam temperatures and pressures, the fraction of evaporator heating surfaces decreases, with the result that parts of the water walls must also be configured as superheaters, ie, downstream of the separator [21].

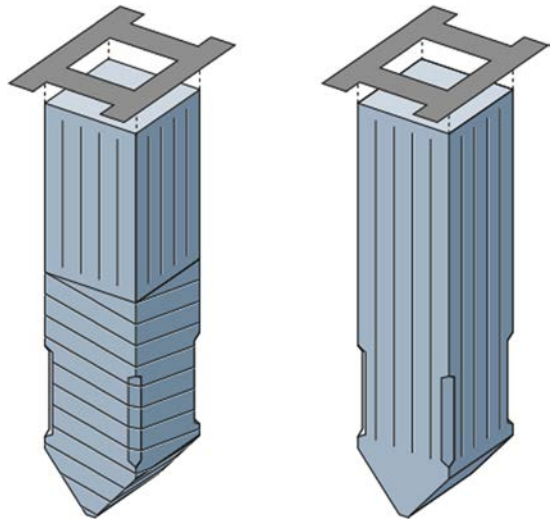


Figure 1.36 Spiral and vertical water wall design [18,19].

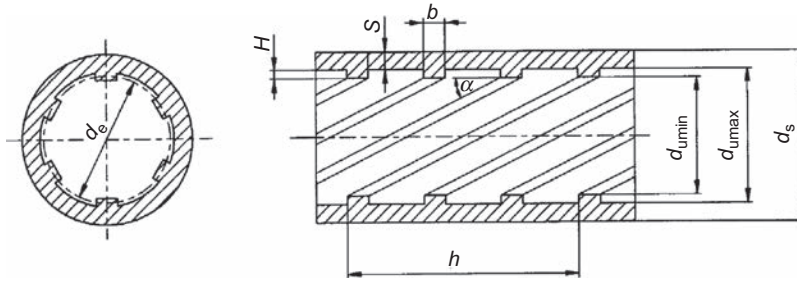


Figure 1.37 Example of characteristic dimensions of the rifled tubes [20].

High steam parameters also lead to higher material loading in the evaporator. The previously existing design reserves are no longer available, with the result that a detailed stress analysis is required for the design of the evaporator tubing in each case. As a result of the requisite large wall thicknesses, the design of highly loaded heating surface areas is in part no longer determined by the primary stresses due to internal pressure but rather by the secondary stresses due to restrained thermal expansion. The higher evaporator temperatures also result in increasing temperature differences between the tubes and support straps on startup and shutdown. This in turn leads to longer startup times, especially on cold start.

The "Benson Low Mass Flux" design developed by SIEMENS with design mass fluxes of approximately 1000 kg/m^{2}s and below and with vertical rifled evaporator

tubes requires no additional support structure and also does not impair plant flexibility in spite of wall outlet temperatures of approximately 500°C and above (Fig. 1.36(b)). In a design for main steam temperatures of 600°C and above, the creep strengths of the wall materials commonly used to date such as 13CrMo44 (T12) are no longer sufficient, necessitating the transition to new developments such as grade 23 or 24. This is already the case at steam pressures of 300 bar and above for lower design temperatures. Looking at primary stresses, the creep strengths of these materials, which require no post-welding heat treatment, permit steam temperatures up to 530°C in the furnace walls depending on main steam pressure, but the corrosion resistance and secondary stresses limit these values down to 500°C. Main steam temperatures of 630°. at moderate steam pressures are thus achievable in regard to the walls.

At higher steam temperatures, materials such as T91 or T92 are required, which must be heat-treated after welding. To minimize the manufacturing expenditure in such a design, the erection welds on evaporator tubes must be reduced to the absolute minimum possible. This is currently feasible only with vertical tubing. The relatively complex welds in the corners for spiral-wound furnace tubing are eliminated, and the individual wall segments are welded together only at the fins. Welding of tubes may become necessary only in the horizontal plane. Solutions are also available for this, which minimizes expenditure on heat treatment on erection. In all cases, it can be stated that the problems in the design of the water walls increase disproportionately with increasing steam pressures. A reduction of main steam pressure from 350 to 250 bar reduces the efficiency of a 700°C plant by 0.7 percentage points, but it also reduces the wall outlet temperature from 540°C to 500°C and makes a design with materials without post-weld heat treatment possible. Main steam pressures far above 250 bar should therefore be avoided, also in plants with high steam temperatures.

Evaporator/superheater dividing point: at high steam parameters the water walls can no longer be designed entirely as an evaporator [19].

The transition from evaporator walls to superheater walls then lies above the furnace. This transition must be designed to minimize the temperature differences between the evaporator and superheater sections of the walls that automatically result on water filling after shutdown, especially on water filling after an emergency shut down. Values of up to 80 K represent no cause for concern. For higher values, such as can occur at very high steam conditions as well as in large furnaces, a flexible connection, not necessarily welded gas-tight, should also be taken into consideration for this transition. Fig. 1.38 shows clearly the reduction of the red zone, where the evaporation is located, and the increase of the light brown zone where the steam is superheated before the inlet in the superheater panels.

The furnace water walls act as the evaporator, though not in the case of a supercritical unit. The evaporation end point can occur in various levels of the furnace depending on the boiler load, as shown in Fig. 1.38. The percentage of superheat in supercritical units is higher than subcritical units. Because of this, the furnace tubes act more as superheaters than water walls. This necessitates the use of a higher grade of materials, both for creep and corrosion/oxidation behaviors: therefore for the A-USC

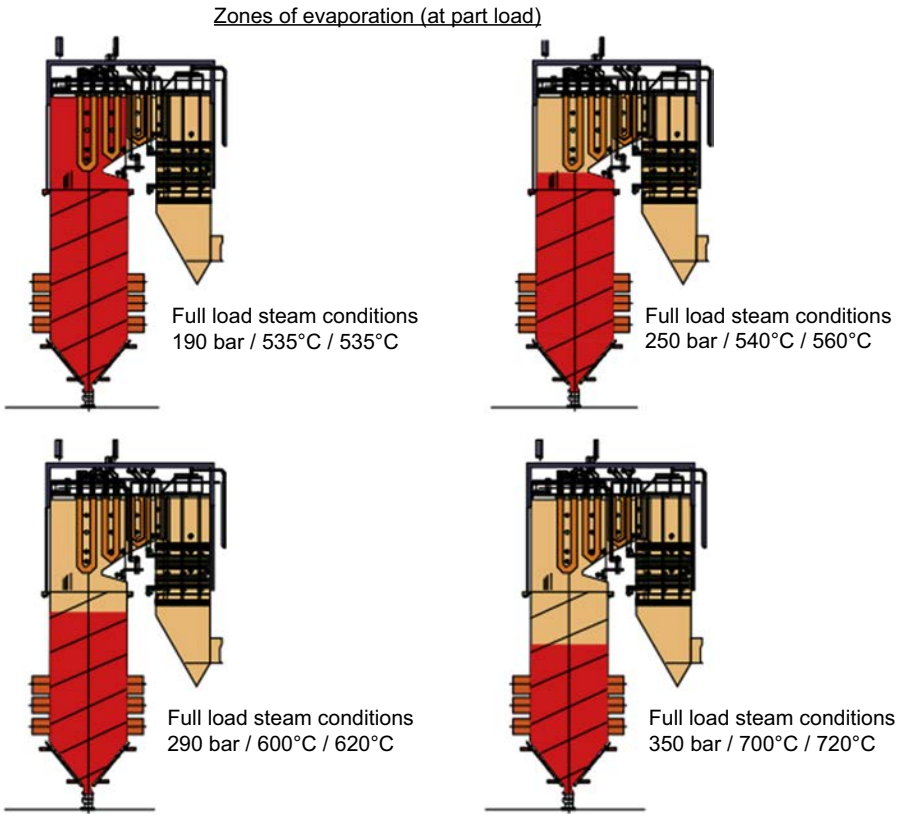


Figure 1.38 Increasing steam conditions lead to different evaporator designs [21].

PP, it will be necessary to use grade 92 or A617, thereby having respective problems like PWHT or high cost.

1.5.2.2 Drums

The drum itself is a large cylindrical vessel that functions as the storage and feeding point for water and the collection point for the water and steam mixture: Fig. 1.39 shows how a drum works. This is the largest and most important pressure part in the boiler and weighs in the range of 250 tons for 600-MW power plants (Fig. 1.40(a)). Drums are located in the top of the boiler tower (Fig. 1.40(b)).

In subcritical units the drum acts as a fixed evaporation end point. In the subcritical PP the drum also acts as separator and filter of the impurities coming from the inlet water in the plant and the water wall tube's internal corrosion deposit.

Supercritical boilers do not have a steam drum that separates the steam and the water because the water is fully transformed into steam and superheated in the water wall tubes. For this reason the water entering the boiler has to be of extremely high levels of purity. If the entering water quality is not good, carryover of impurities can result in turbine blade deposits.

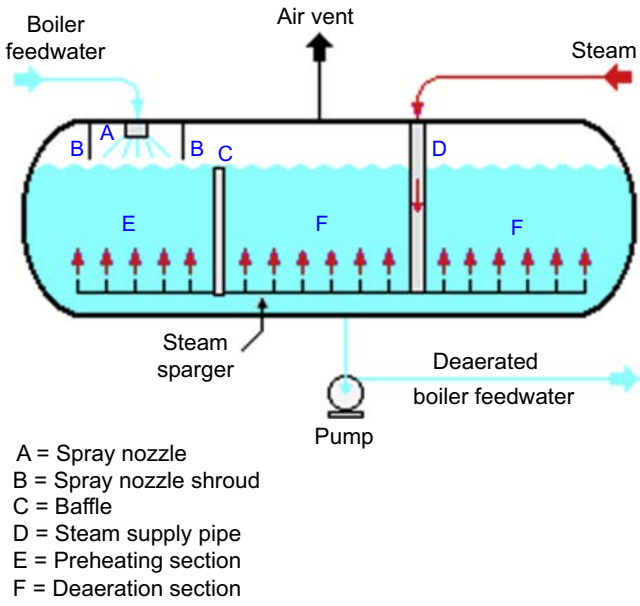


Figure 1.39 Schematic operation of a drum [22].

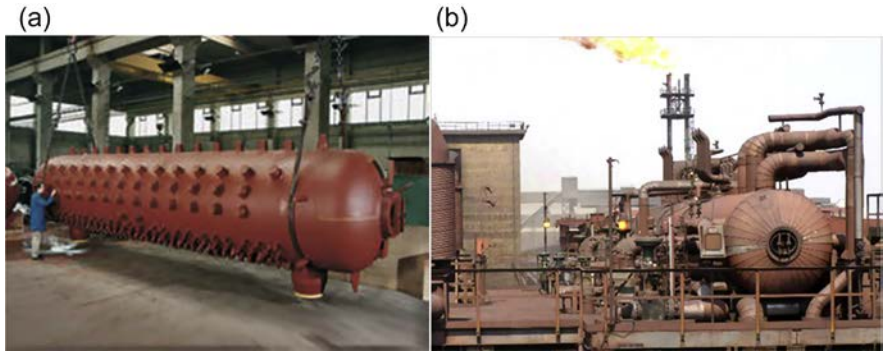


Figure 1.40 Boiler drums in workshop (a) [23] and in the top of a boiler tower (b) [24].

1.5.2.3 Superheater and reheater

Subcritical, supercritical, and USC modern fossil fuel power plants have **superheater** sections in the steam generating furnace. The steam passes through drying equipment inside the steam drum onto the superheater, a set of tubes in the furnace, to increase the temperature up to 538°C. Here, the steam picks up more energy from hot flue gases outside the tubing, and its temperature is now superheated above the saturation temperature.

In the case of SC and USC plants, the steam goes directly to the superheater section from the water walls, without passing in to the drum.

The superheated steam is then piped through the main steam lines to the valves before the high-pressure turbine.

The amount of superheat added to the steam is influenced by the location, arrangement, and amount of superheater surface installed, as well as the rating of the boiler. The superheater may consist of one or more stages of tube banks arranged to effectively transfer heat from the products of combustion. Superheaters are classified as convection, radiant, or a combination of these.

Nuclear-powered steam plants do not have such sections but produce steam at essentially saturated conditions. Experimental nuclear plants were equipped with fossil-fired superheaters in an attempt to improve overall plant operating cost.

Power plant furnaces may also have a **reheater** section containing tubes heated by hot flue gases outside the tubes. Exhaust steam from the high-pressure turbine is passed through these heated tubes to collect more energy before driving the intermediate- and then low-pressure turbines.

Some of the heat of the superheated steam is used to rotate the turbine, where it loses some of its energy. A reheater is also steam boiler component in which heat is added to this intermediate-pressure steam, which has given up some of its energy in expansion through the high-pressure turbine. The steam after reheating is used to rotate the second steam turbine, where the heat is converted to mechanical energy. This mechanical energy is used to run the alternator, which is coupled to turbine, thereby generating electrical energy.

From the construction point of view in the top of the boiler (RH and SH), the steam reaches the maximum temperature and pressure: c. 100 km of small and thin tubes are collected by welds to headers made of martensitic thick pipes. For the supercritical plant, where the temperature is up to 580°C, the tubes are made of grade 91 and 92; for the most advanced USC plant operating up to 620°C, it is necessary to use austenitic



Figure 1.41 Example of superheater bundles [25].

steels mainly for steam corrosion and flue gas oxidation matter. Fig. 1.41 shows an example of a finished superheater bundles ready to be installed in the plant.

Depending on designers, the superheater and reheater panels can be installed in vertical or horizontal position in the top of the boiler tower.

The tower radiant boiler can be arranged as follows:

- With a water-cooled, dry-bottom furnace and superheater, reheater, economizer, and air heater components, the tower radiant boiler design employs all horizontal convection surfaces (Fig. 1.42(a)).
- With a natural circulation, water-cooled, dry-bottom furnace and superheater, reheater, economizer, and air heater components, the Carolina radiant boiler design employs horizontal convection pass and vertical pendant heat transfer surfaces (Fig. 1.42(b)).

1.5.2.4 Header

Thick pipes with end cap and several holes for the connection of the superheater tube bundles with the steam line pipes are shown in Fig. 1.43, the schematic drawing of a header. Fig. 1.44 shows the header manufacturing in a workshop. In the case of a superheater made with austenitic steel, connecting pieces (black and white connectors; Fig. 1.45) are mandatory to be used for the joining with the header to avoid too high thermal stress in elements.

The headers are one of the most critical components due to the high stress concentration in the ligament welded joints and the end caps.

1.5.2.5 Steam line

The steam lines are a critical components system in the boiler tower: in particular the main steam and hot reheat lines are made by thick pipes that are necessary to transfer the steam from the top of the boiler to the steam turbine room, generally located at ground level. Fig. 1.46 shows the details of the operating conditions and dimensions of the high-pressure piping systems in the Neurath 1.00-MW lignite-fire power plant. The details of the amount, dimensions, and operating conditions of the different components are summarized in Fig. 1.46.

Fig. 1.47 shows an example of thermal vision that puts in evidence that the most critical points are the extrados and the welded joints: these are the most critical zones.

1.5.2.6 Steam valves

Valves are prevalent throughout a power plant, providing flow, pressure, level control, and process isolation capabilities. Valves are necessary to separate the different systems: boiler, condenser, boiler feed water reservoir, turbine, and bypass, as shown in Fig. 1.48, in the power plant in case of need to avoid disaster.

The most critical valves systems are between the boiler and the turbine where the components are operating at the higher steam and pressure conditions; these valves are made in alloyed steels and need internal coating to prevent erosion. Fig. 1.49 shows a schematic example of the valves systems in the turbine zone.

Perhaps no valve application is more mission critical than steam turbine stop and control valves (Fig. 1.50). Like the cruise control on an automobile, steam control valves regulate the amount of steam entering the turbine to maintain speed under a varying load.

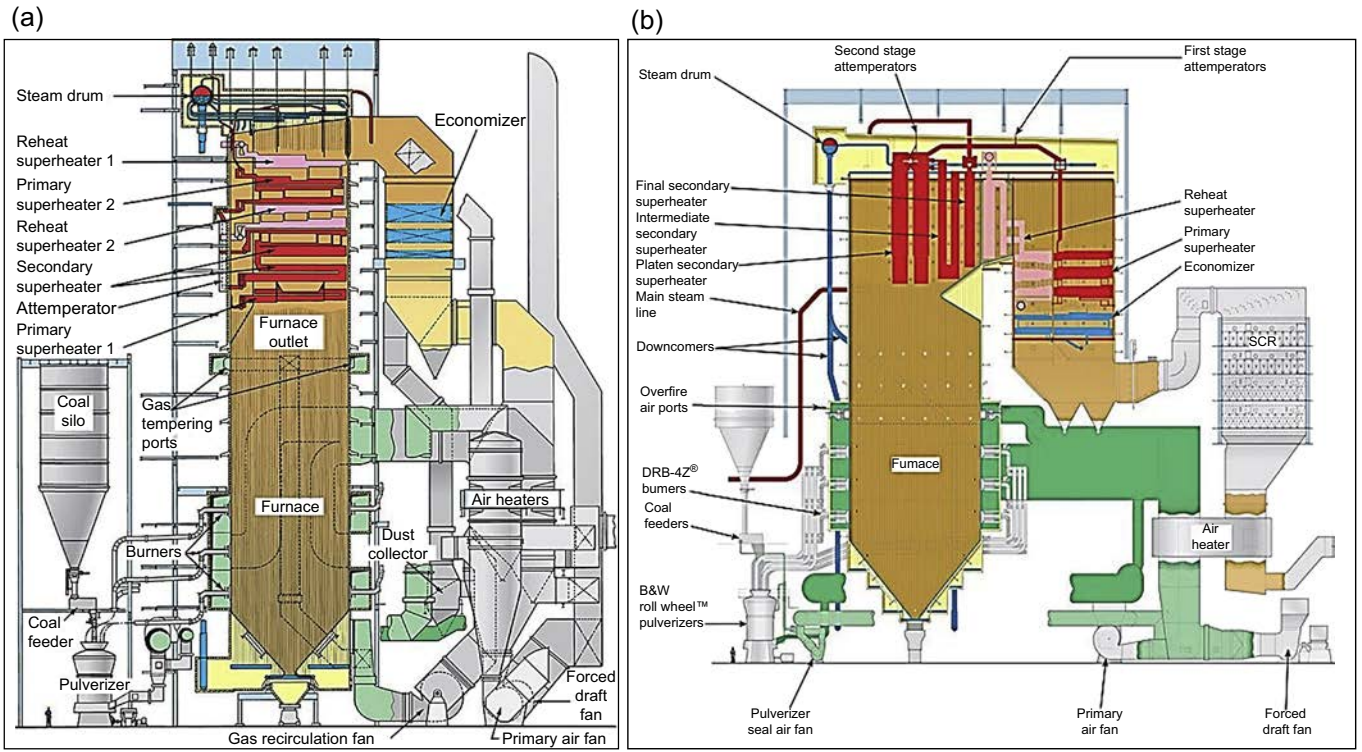


Figure 1.42 Examples of Babcock and Wilson tower radiant boiler SH-RH with horizontal (a) [25,26] and vertical (b) position [27].

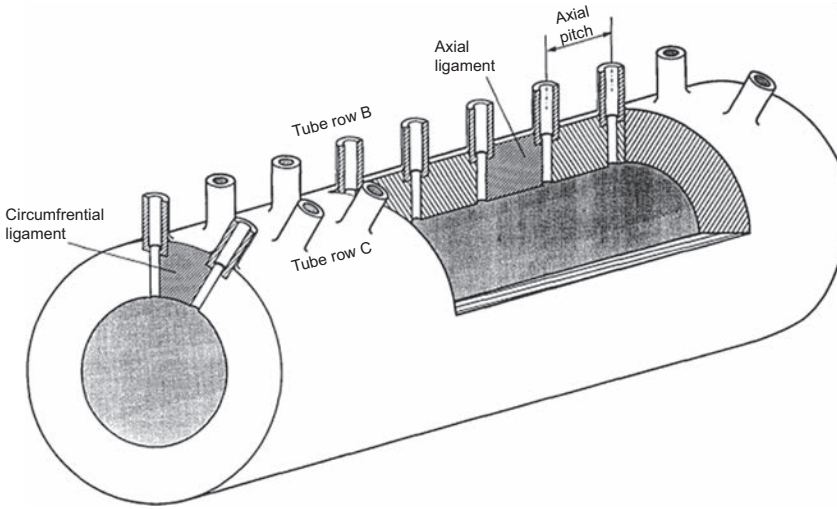


Figure 1.43 Schematic representation of header illustrating bore holes and ligaments [28].

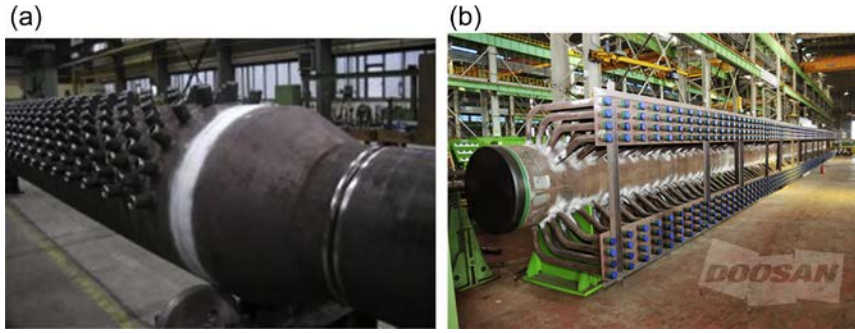
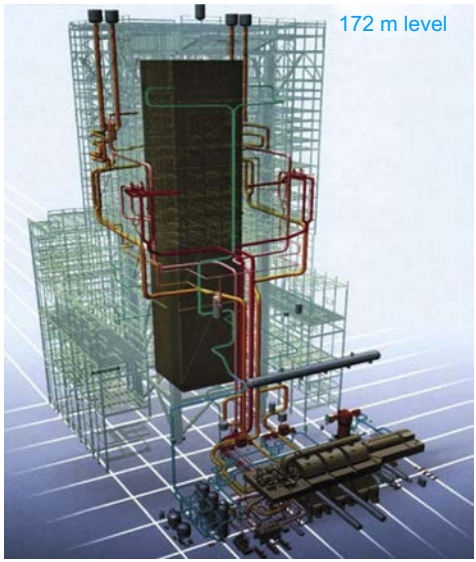


Figure 1.44 Example of headers during manufacturing and finished components: (a) Meeraner Dampfkesselbau [16]; (b) Doosan [29].



Figure 1.45 Example of connecting pieces (*black and white connectors*) between grade 91 (left) and austenitic steel X3CrNiMoN1713 (right) [16].



- Total material approx. 3,100 t / unit
- Pipes approx. 2,200 t
- Form pieces approx 115 t
- Fittings approx. 190 t
- Supports/hangers approx. 600 t
- Total pipe length approx. 11,000 m
- Main piping approx. 4,400 m
- Total circumferential welds approx. 7,000
- Total circumferential welds of main piping approx 1 400
  - Feed water: 430bar, 250°C, Φ 588mm, w.th 44mm
  - Main steam: 295bar, 610°C, Φ 549mm, w.th 97mm
  - Cold reheat: 75bar, 435°C, Φ 824mm, w.th 31mm
  - Hot reheat: 70bar, 615°C, Φ 806mm, w.th. 43mm

Figure 1.46 Main steam lines dimensions and operating conditions in 1.100-MW RWE Neurath lignite PP [30].

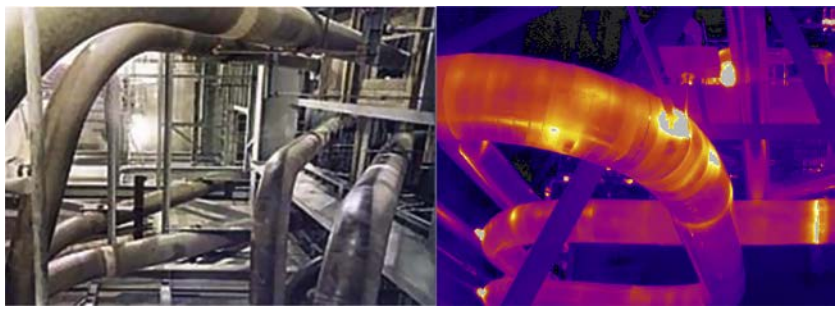


Figure 1.47 Main steam line [31] and thermal vision indication of some hot spots (*whiter zones*) [32].

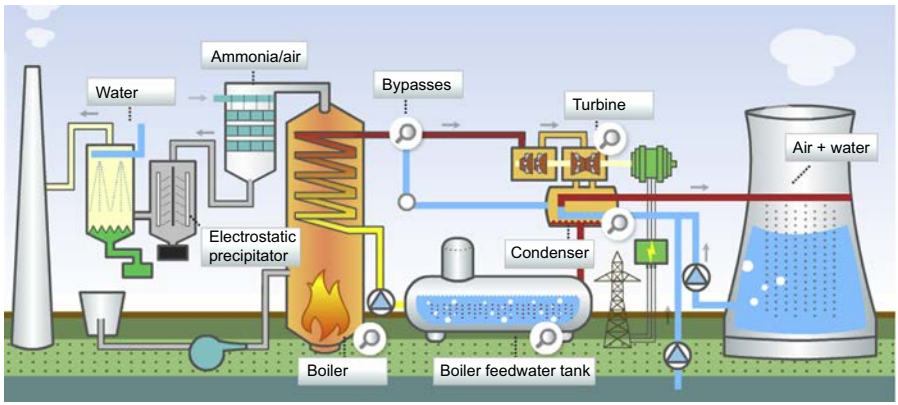


Figure 1.48 Location of the main valve systems in a power plant [27].

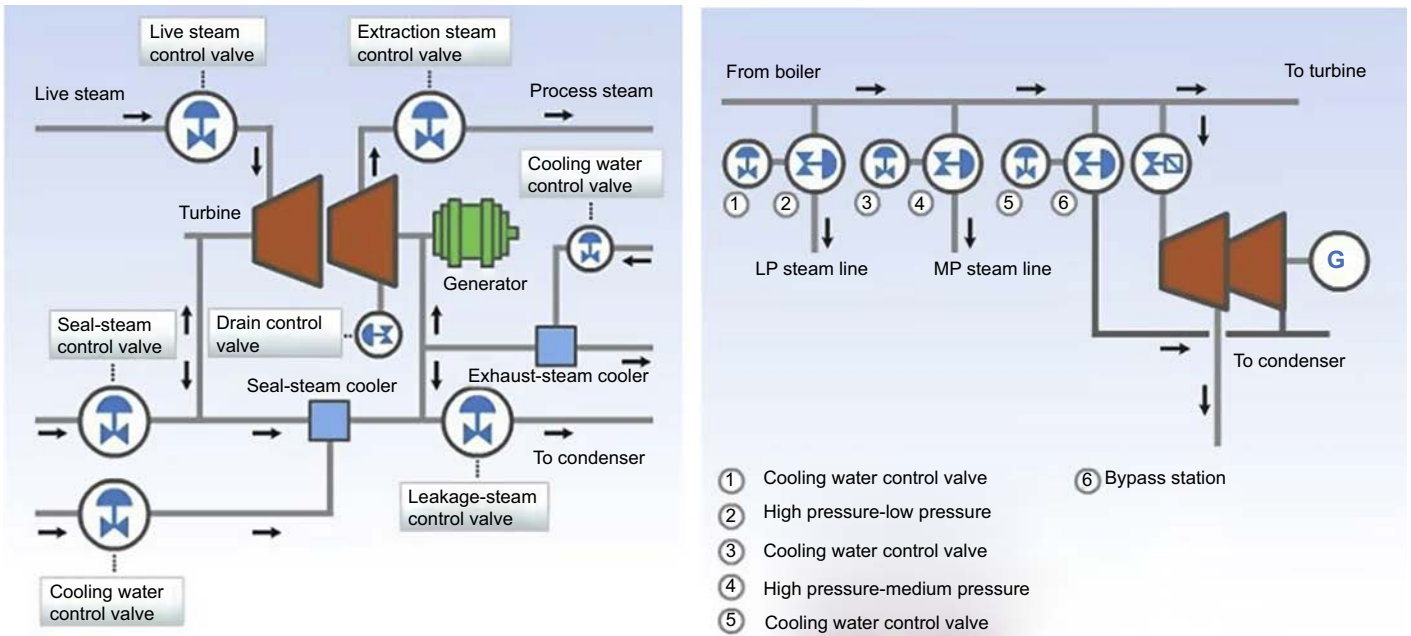


Figure 1.49 Schematic view of turbine and turbine bypass valves systems [27].

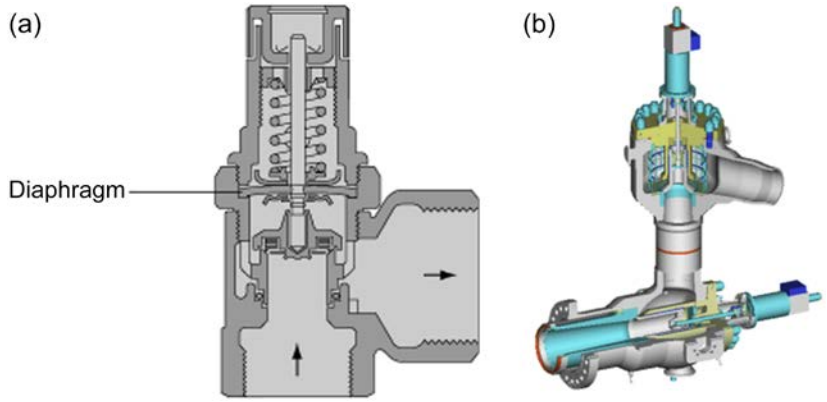


Figure 1.50 (a) Diaphragm sealed safety valve. (b) Stop and control valve [33].

Steam stop valves prevent steam from entering the turbine in emergency situations. Both require functional testing, including electronic control loops, if applicable.

1.5.3 Steam turbine section

1.5.3.1 Steam turbine

Steam turbines are made in a variety of sizes ranging from small <0.75-kW (1 < hp) units (rare) used as mechanical drives for pumps, compressors, and other shaft-driven equipment, to 1.500-MW (2,000,000 hp) turbines used to generate electricity. There are several classifications for modern steam turbines: these types include condensing, noncondensing, reheat, extraction, and induction:

- **Condensing turbines** are most commonly found in electrical power plants. These turbines exhaust steam in a partially condensed state, typically of a quality near 90%, at a pressure well below atmospheric to a condenser.
- **Noncondensing or back pressure turbines** are most widely used for process steam applications. The exhaust pressure is controlled by a regulating valve to suit the needs of the process steam pressure. These are commonly found at refineries, district heating units, pulp and paper plants, and desalination facilities where large amounts of low-pressure process steam are available.
- **Reheat turbines** are also used almost exclusively in electrical power plants. In a reheat turbine, steam flow exits from a high-pressure section of the turbine and is returned to the reheater boiler where additional superheat is added. The steam then goes back into an intermediate-pressure section of the turbine and continues its expansion. Using reheat in a cycle increases the work output from the turbine and also the expansion reaches conclusion before the steam condenses, thereby minimizing the erosion of the blades in last rows. In most of the cases, the maximum number of reheats employed in a cycle is two, as the cost of superheating the steam negates the increased the work output from turbine.
- **Extracting type turbines** are common in all applications. In an extracting type turbine, steam is released from various stages of the turbine and used for industrial process needs or sent to boiler feed water heaters to improve overall cycle efficiency. Extraction flows may be controlled with a valve or left uncontrolled.
- **Induction turbines** introduce low-pressure steam at an intermediate stage to produce additional power.

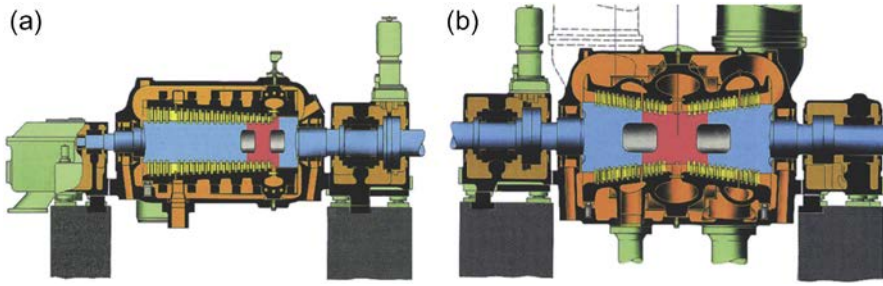


Figure 1.51 Alstom HP and IP turbines with welded rotors using 10% Cr steel in the hottest regions: (a) single flow, (b) double flux [34].

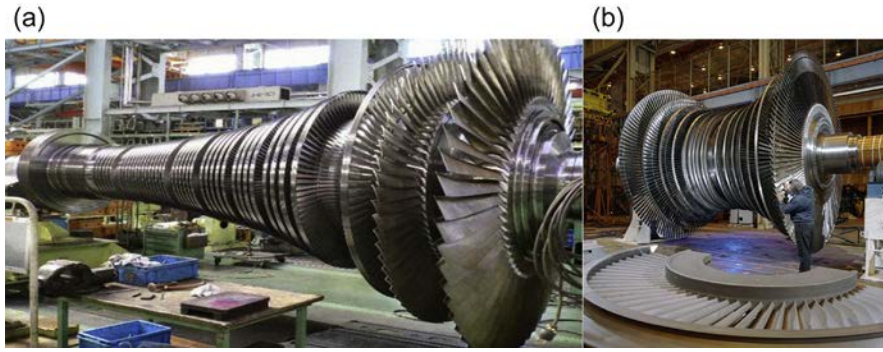


Figure 1.52 Rotor turbine: (a) single flux [35]; (b) two flow [36].

1.5.3.2 Casing or shaft arrangements

These arrangements include single-casing, tandem-compound, and cross-compound turbines. Single-casing units are the most basic style, where a single casing and shaft are coupled to a generator. Tandem-compound turbines are used where two or more casings are directly coupled together to drive a single generator. A cross-compound turbine arrangement features two or more shafts not in line driving two or more generators that often operate at different speeds. A cross-compound turbine is typically used for many large applications.

Single-flow rotors: Modern high pressure (HP) and intermediate pressure (IP) turbines for both conventional and supercritical applications at moderate temperatures use single-piece rotor forgings (Fig. 1.51(a)and 1.52(a)).

The application of welded rotor technology in these sections (with rotors made by welding together several forged sections to form a compact shaft with low body stresses) provides the capability to introduce 10% Cr steel sections for the hottest areas adjacent to the steam inlet zones of the HP and IP turbines, with conventional 1% CrMoV material for the outboard sections (Fig. 1.51(a)).

Two-flow rotors: The moving steam imparts both a tangential and axial thrust on the turbine shaft, but the axial thrust in a simple turbine is unopposed (Fig. 1.51(b),

Fig. 1.52(b)). To maintain the correct rotor position and balancing, this force must be counteracted by an opposing force. Either thrust bearings can be used for the shaft bearings, or the rotor can be designed so that the steam enters in the middle of the shaft and exits at both ends. The blades in each half face opposite directions, so the axial forces negate each other, but the tangential forces act together. This design of rotor is called two-flow or double-exhaust. This arrangement is common in low-pressure casings of a compound turbine.

Another example is Toshiba's tandem-compound, double-flow, condensing steam turbine that is typically applied to 2×1 and 3×1 combined-cycle configurations featuring F-, G-, or H-class gas turbines. These turbines range in output from 180 to 480 MW and feature last-stage blades lengths of 33.5, 35, 40, and 48 inches [37].

Performance of Toshiba's steam turbines is enhanced through several design features that improve turbine performance and increase durability. Chief among these features are advanced steam paths with optimized reaction stages, advanced sealing with sensitized packing, transonic vane profiles for last-stage blades, low bearing losses, and reduced pressure drop at the turbine inlets/outlets (Fig. 1.53).

For Doosan the basic construction of single reheat large steam turbines for coal-fired power plants was established over 30 years ago. This construction, designed originally for operating at conventional steam conditions, has achieved very high standards of reliability and operability through continuing development and feedback of operating experience. The same basic design therefore provides a very sound reference base for high-output applications at USC operating conditions, taking advantage of advanced materials and design refinements (see Fig. 1.54).

In Fig. 1.55 are presented some very complex cast for casing components of different steam turbine sizes, manufactured by different foundries, and the assembly of a rotor into a casing. The weight of the turbine valve casing can reach 100 ton.

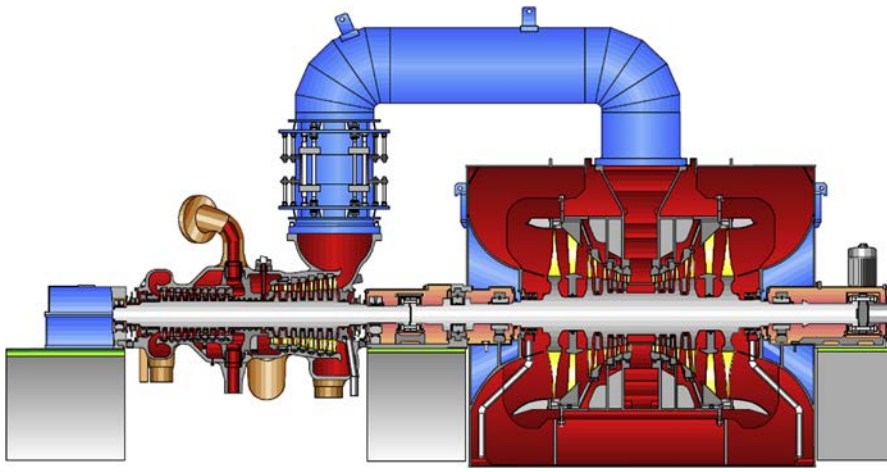


Figure 1.53 Toshiba's tandem-compound, double-flow, condensing steam turbines [37].

1.5.3.3 Turbine blades

The HP/IP/LP section blading is usually designed as these integrally shrouded blades (Fig. 1.56) and has, as a result, an elastically prestressed blade ring after assembly that is characterized by an excellent damping behavior during operation. Now the profiles are designed by highly efficient three-dimensional airfoil designs. Within the blade path section, interlocking labyrinth seals are applied.

Since the overall efficiency of steam turbine power plants is very strongly related to the turbine blading performance, it is necessary to design each turbine blade path individually—but within today's tight design lead times—to match the desired efficiency and performance levels in each particular application.

1.5.3.4 Economizer

Flue gases coming out of the boiler carry a lot of heat. The function of an economizer is to recover some of the heat from the heat carried away in the flue gases up the chimney and utilize it for heating the feed water to the boiler. It is placed in the passage of flue gases in between the exit from the boiler and the entry to the chimney.

Most of the sensible heat is absorbed in the economizer. These are a set of coils made from steel tubes located in the tail end of a boiler. The hot gases leaving the boiler furnace heat the water in the coils. The water temperature is slightly less than the saturation temperature. From the economizer the water is fed to the "drum."

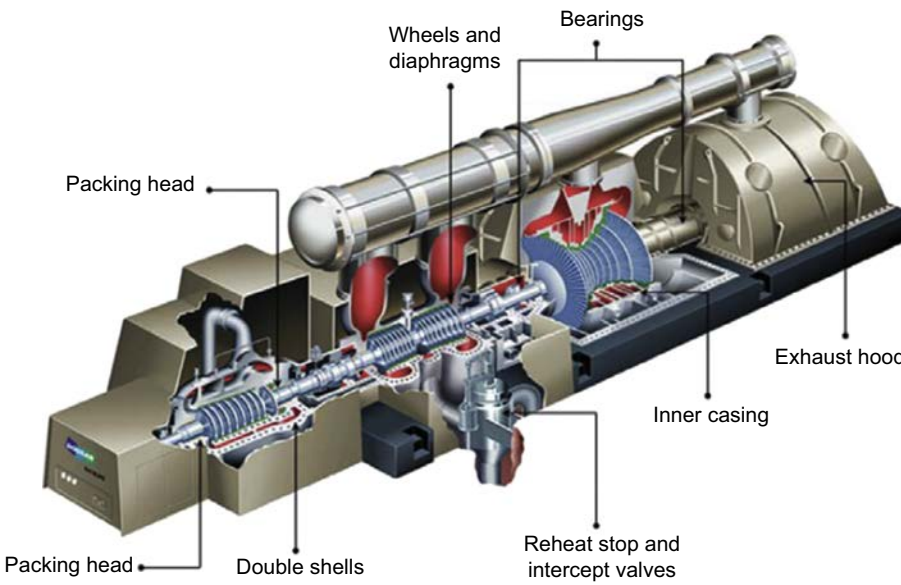


Figure 1.54 Doosan G-Series 4-Casings Turbine (up to 1100 MW) steam turbine for ASC steam conditions [37,38].



Steam turbine's outer casing with inlet and regulation valve fully assembled [39]



Outer casing for 350MW steam turbine [39]



Finish-machining ip outer casing [39]





Steam turbine casing, 45 t casing under final inspection [40]





Steam valve housing medium-pressure steam turbine inner casing made from the new material GX12CrMoCoVNbNB9–2–1 "CB2" [41]



Large steam turbine housing [41]





HP inner casing with rotor before and after assembly into the lower outer casing. [42]



Pilot valve housing made from a nickel-based alloy [43]

Figure 1.55 Examples of steam turbine components.

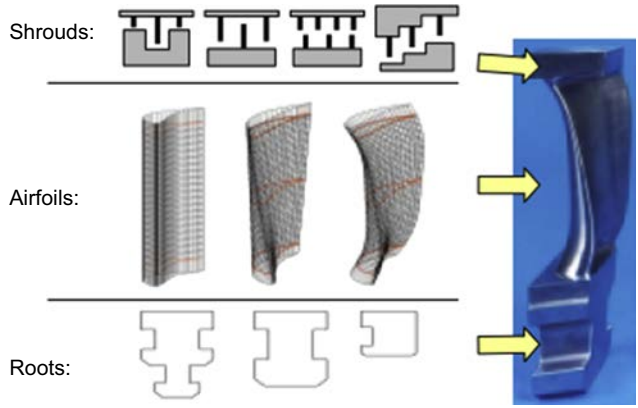


Figure 1.56 Modular concept of blade construction [44].



Figure 1.57 Economizer layout [45], manufacture in workshop, and installation [46].

The use of an economizer results in savings in coal consumption, an increase in steaming rate, and high boiler efficiency but needs extra investment and an increase in maintenance costs and floor area required for the plant. This is used in all modern plants. In this, a large number of small-diameter, thin-walled tubes are placed between two headers (Fig. 1.57). Feed water enters the tube through one header and leaves through the other. The flue gases flow outside the tubes, usually in counter flow.

From the economizer the water passes to the steam drum, and from there, it goes through downcomers to inlet headers at the bottom of the water walls. From these headers the water rises through the water walls of the furnace, where some of it is turned into steam, and the mixture of water and steam then reenters the steam drum. This process may be driven purely by natural circulation (because the water in the downcomers is denser than the water/steam mixture in the water walls) or assisted by pumps. In the steam drum, the water is returned to the downcomers, and the steam is passed through a series of steam separators and dryers that remove water droplets from the steam. The dry steam then flows into the superheater coils.

1.5.3.5 Attemperator

Attemperator desuperheaters reduce steam temperature by bringing superheated steam into direct contact with water. The steam is cooled through the evaporation of the water. Attemperator desuperheaters (Fig. 1.58) can be mounted either horizontally or vertically and are normally used for relatively steady load conditions where pressure losses must be minimized. These desuperheaters are a modification of the Venturi-type unit, without the Venturi tail, and they offer increased turndown when mounted vertically. While it is less costly and has negligible pressure losses, it normally does not have the rangeability of the Venturi-type unit.

1.5.3.6 Pipe fittings

Piping fittings are all the components that are necessary to assemble different components of power plants. There are usually made by forging and welding: Fig. 1.59 shows some examples of fitting pieces.

1.5.3.7 Condenser

Steam after the rotating steam turbine comes to the condenser. Condenser refers here to the shell and tube heat exchanger (or surface condenser) installed at the outlet of every steam turbine in thermal power stations of utility companies, generally. These condensers are heat exchangers that convert steam from its gaseous to its liquid state, also known as phase transition. In so doing, the latent heat of steam is given out from inside the condenser (Fig. 1.60). Where water is in short supply, an air cooled condenser is often used. An air cooled condenser is, however, significantly more expensive and cannot achieve as low a steam turbine backpressure (and therefore less efficient) as a surface condenser.

The purpose is to condense the outlet (or exhaust) steam from the steam turbine to obtain maximum efficiency and also to get the condensed steam in the form of pure water, otherwise known as condensate, back to the steam generator (or boiler) as boiler feed water.

In the following chapter of this book, the different authors will deeply describe the materials development that permits one to obtain the current commercial materials used in the recent USC power plants, as well as the current development in materials science and technologies to reach the next target for the A-USC power plants.

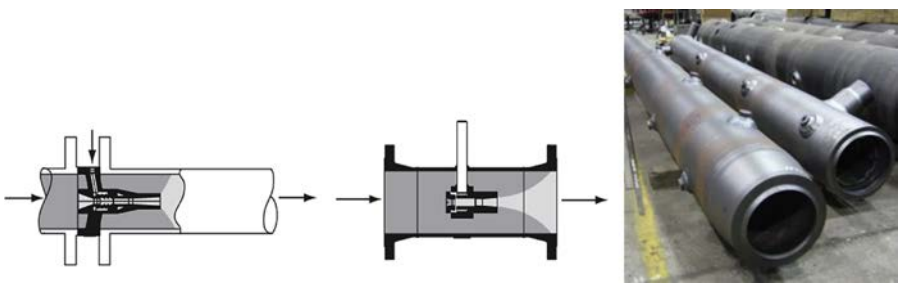


Figure 1.58 Attemperator schematic view [47] and component in workshop [16].



Figure 1.59 Examples of fitting pieces [16].

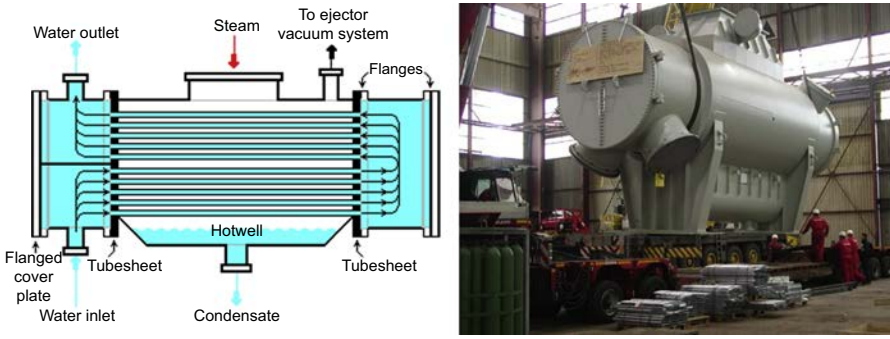


Figure 1.60 Condenser: schematic view [48] and assembled component ready for shipping [49].

1.5.4 The best available technology

"Higher process temperatures and pressures are mandatory to increase net efficiency and reduce CO_2 emissions" (as clearly shown in Fig. 1.61) is a sentence that will be used several times in this book by the different authors. As a consequence, these more severe operating conditions require better materials with higher demands for development, manufacturing, and fabrication.

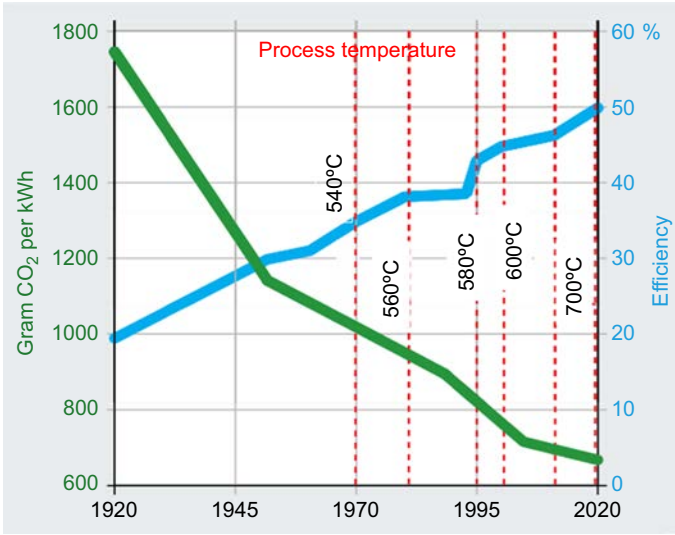


Figure 1.61 Development of efficiency and CO_2: emission in development of efficiency and CO_2 emission in coal-fired power plants [30].

In Fig. 1.61, it is possible to observe that there are some steps in the increase of efficiency due to the development of materials and consequent power plant technologies, which can be summarized as follows:

- the commercial availability of steel grade 91 at the beginning of 1990 with the development of USC plants up to 580°C,
- the further development of grade 92 and austenitic steels like Super304H with an increase of operating temperature up to 620°C [50]: **this is currently the best available technology base on steels,**
- the next introduction of a nickel-based alloy to reach ≥700°C for the A-USC plants.

Fig. 1.62 shows the creep behaviors of the different classes of materials used or candidates for the different plants.

The following chapters of Part 1 will describe the history of development of materials for the coal-fired generation plants, the characteristics of the current materials, the production routes, and welding procedure for the joining of the components of the USC plants.

Further, Part 2 of the book will describe the status of the development of the materials for the design and construction of the A-USC power plants.

Finally, Part 3 will described the current state of the art of A-USC programs around the world.

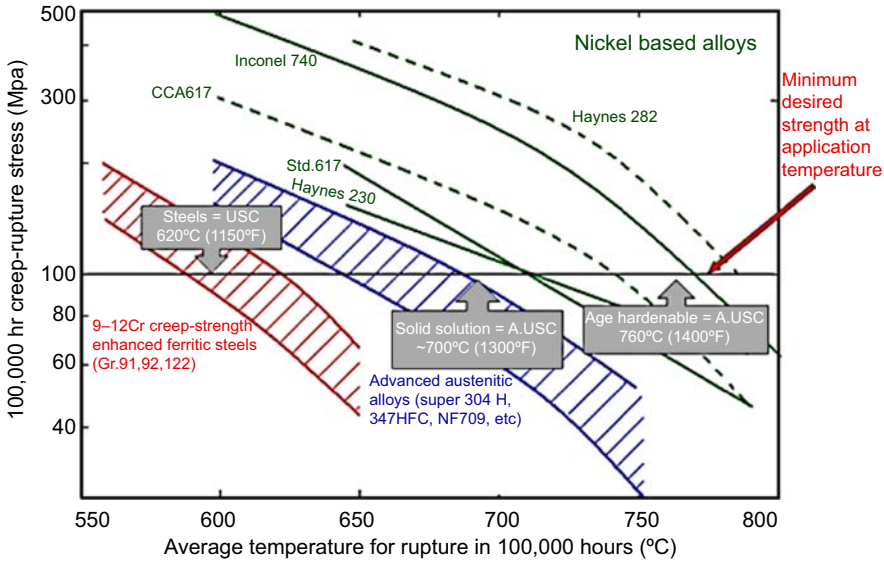


Figure 1.62 Relative stress rupture strength of steels and nickel alloys put forward as potential candidate alloys for USC and 700°C+A-USC plant operation [51].

References

[1] Unit 2 Steam Power Plant www.ignou.ac.in/upload/Unit-2-58.pdf.

[2] R. Blum: The European perspective and advancements for advanced USC, Sixth Int. Conf. on Advanced in Materials Technology for Fossil Power Plant: August 31–September 3, 2010 Santa Fe, New Mexico.

[3] Setting the Benchmark: the World's Most Efficient Coal-Fired Power Plants by Dawn Santoianni Managing director, Tau Technical Communications LLC. http://cornerstonemag.net/setting-the-benchmark-the-worlds-most-efficient-coal-fired-power-plants/.

[4] W. Zhang, Alstom Power USA Updates on Alstom's Clean Coal Technologies for Power Generation 2014 US – China Clean Energy Workshop, 15.09.2014, Taiyuan, China.

[5] R.M. Purgert, U.S. High efficiency strategies for clean coal systems operation & maintenance, in: Conference Sustainable Growth Strategies for Fuel and Efficiency New Delhi, India, February 2013.

[6] P.S. Weitzel, Steam generator for advanced ultra-supercritical power plants 700 to 760°C, in: Asme 2011 Power Conference, July 12–14, 2011. Denver, Colorado, U.S.A.

[7] F. Kluger, C. Hölzel, J. Marion, A. Skea; Alstom development of a-USC steam power plants; 2nd IEA CCC Rome, Italy, October 14, 2014.

[8] I. Barnes, Upgrading the Efficiency of the World's Coal Fleet to Reduce CO2 Emissions. http://cornerstonemag.net/upgrading-the-efficiency-of-the-worlds-coal-fleet-to-reduce-CO2-emissions/.

[9] K. Burnard, Global outlook: key findings from recently-launched hele coal roadmap, in: Cleaner and More Efficient Coal Technologies in Russia: Experts Meeting 10 December 2012, http://www.iea.org/media/workshops/keithburnard.pdf.

[10] Tulinov, Promotion of High-Efficiency, Low-Emissions Coal Technologies in Power Generation: http://www.unescap.org/sites/default/files/0_Tulinov_Ch.pdf.
[11] http://www.iea.org/publications/scenariosandprojections/.
[12] https://en.wikipedia.org/wiki/Thermal_power_station.
[13] S. Teir, A. Kulla; Boiler Calculations. http://www.energy.kth.se/compedu/webcompedu/ManualCopy/Steam_Boiler_Technology/Boiler_calculations/boiler_calculations.pdf.
[14] http://www.tbwes.com/products/subcritical-boilers/.
[15] http://www.stxhi.co.kr/Eng/Biz/fire_power.aspx.
[16] http://www.mdkb.de/.
[17] http://dguha1952.blogspot.it/2013/03/thermal-power-plant-boiler-pressure.html.
[18] http://www.sickinsight-online.de/gasanalysator-gm960-stopp-dem-korrosiven-kessel-wandfras/.
[19] http://alstomenergy.gepower.com/.
[20] D. Tucakovic, V. Stevanovic, T. Zivanovic: Thermal-Hydraulics of Evaporating Tubes in the Forced Circulation Loop of a Steam Boiler. http://www.mas.bg.ac.rs/_media/istrazivanje/fme/vol36/1/02_dtucakovic.pdf.
[21] J. Franke, R. Kral, Supercritical Boiler Technology for Future Market Conditions Presented at Parsons Conference 2003.
[22] http://www.studentstattle.in/feed-water-and-steam-circuit-of-boiler/.
[23] http://www.stabo-siegen.de/en/products/high-pressure-drums/.
[24] http://www.omegaboilers.com/our_projects.htm.
[25] http://www.fabprecision.com/offerings.aspx?panel=7.
[26] http://www.babcock.com/products/Pages/Tower-Radiant-Boiler.aspx.
[27] http://www.babcock.com/products/Pages/Carolina-Type-Radiant-Boiler.aspx.
[28] G. Nakoneczny, C. Schultz: Life assessment of high temperature components: American Power Conference Chicago, USA, April 18–20, 1995.
[29] http://www.doosan.com/doosanvina/en/pressRelease.do?cmd=viewPressRelease&no=20120208163056746480.
[30] R. Diehl, High Pressure Piping in Power Plants – Water/Steam Cycles: Capital Markets Day "Power Services" at Moorburg Power Plant, December 2, 2010.
[31] http://www.rohrbiegewerk.com/downloads/rohrbiege_dimensions.pdf.
[32] http://www.maverickinspection.com/services/infrared-thermography/sample-imagery/ir-piping/.
[33] http://www.arca-valve.com/index/lang/en/.
[34] Advanced Power Plant using High Efficiency Boiler/Turbine; Best Practice Brochure; BPB010, (January 2006).
[35] http://innal-my.blogspot.it/2014/12/part-main-of-steam-turbine.html.
[36] http://www.nytimes.com/2009/08/07/business/07electric.html?_r=0.
[37] http://www.toshiba.com/taes/products/steam-turbine–-generator-overview/tcdf-design.
[38] Doosan Steam Turbines: https://www.doosansteamturbine.
[39] http://www.cividalespa.com:81/en/mercato_energia.html.
[40] http://www.spezialguss.com/39.html?&L=1.
[41] Steel castings for the energy industry (>10 tons) http://www.voestalpine.com/stahl/en/Products/Products/Foundry-products/Steel-castings-for-the-energy-industry-10-tons.
[42] http://www.powermag.com/designing-an-ultrasupercritical-steam-turbine/?pagenum=4.
[43] Success for the Group KW 50 Plus Power Plant Project: http://www.voestalpine.com/blog/en/energy/success-group-kw-50-plus-power-plant-project/.
[44] http://www.energy.siemens.com/nl/pool/hq/energy-topics/pdfs/en/steam-turbines-power-plants/3_Design_and_Materials.pdf.

[45] http://www.globalspec.com/reference/73638/203279/appendix-d-improving-energy-efficiency-in-power-plant-operation.
[46] http://www.slideshare.net/sagnikchoudhury/mtps.
[47] http://www.s-k.com/pages/pro_08_02.html.
[48] http://www.slideshare.net/SHIVAJICHOUDHURY/condenser-in-thermal-power-plants.
[49] http://alfa-img.com/show/power-plant-condenser.html.
[50] H. Kimura, T. Sato, C. Bergins, S. Imano, E. Saito, Development of technologies for improving efficiency of large coal-fired thermal power plants, Hitachi Review 60 (7) (2011).
[51] Advanced Material Castings for High Temperature Coal Fired Steam Turbine Applications: www.goodwinsteelcastings.com.

This page intentionally left blank

Part One

Ultra-supercritical power plant materials

This page intentionally left blank

Low-alloyed steel grades for boilers in ultra-supercritical power plants

2

F. Masuyama
Kyushu Institute of Technology, Kitakyushu, Japan

2.1 Introduction

The ultra-supercritical power plants were introduced in the late of 1950s in the United States and Germany, and the highest steam parameters with 35 MPa (5000 psig) and 649°C/566°C (1200°F/1050°F) for superheaters/reheaters were realized to start commercial operation in 1960 at Eddystone power station unit No. 1 of Philadelphia Electric Power Company. At that time the high-temperature components were made of austenitic steels due to the base load operation, and the ferritic steels used there were conventional Cr-Mo low-alloyed steels such as 2.25Cr-1Mo steel (T22 in ASTM/ASME designation, the same hereinafter), which was the strongest in creep among the Cr-Mo low-alloyed steels for boiler applications. After that the steam temperature was reduced to 538–540°C of supercritical conditions until the end of 1980s for about 30 years. However, in the early 1980s the social requirement of resource saving and energy conservation forced the development of modern ultra-supercritical power plants with cyclic and swing loading due to the daily/weekly/monthly fluctuation in energy demand. Therefore austenitic steels were no longer the candidate material for high-temperature components because of the shortcomings of their low thermal conductivity and high thermal expansion coefficient, and high strength to substitute the austenitic steels was absolutely required to the ferritic steels. The development efforts of high-strength ferritic steels were conducted for the 9-12% Cr steels, followed by the study on the creep strength enhancement of low-alloyed steel grades, resulting in the development of steels such as 2.25Cr-1.6WVNb steel (T23) and 2.5Cr-1MoVBTi steel (T24). The application of T23 and T24 to the ultra-supercritical power boiler but also to the conventional type and heat recovery steam generator has yielded a great benefit to improve the plant efficiency and construction economy. In this sense the understanding of material properties and applications of both new steels is essential for the modern power plant technology.

2.2 Historical development of low-alloyed steels

2.2.1 Conventional low-alloyed steels

Development of low-alloy steels was required for the operation of power plants with steam parameters of 3.5 MPa and 450°C in the beginning of the 1920s. At the

Materials for Ultra-Supercritical and Advanced Ultra-Supercritical Power Plants.
http://dx.doi.org/10.1016/B978-0-08-100552-1.00002-6
Copyright © 2017 Elsevier Ltd. All rights reserved.

beginning of development, creep-strengthened low-alloyed steels were investigated with the alloying elements of Cr, Mo, V, and others such as Mn, Ni, and Si for tube, pipe, and forgings applications. In the 1930s, three steels with chemical compositions of 0.3–0.5Mo, 1Cr-0.5Mo steel [1], and 2.25Cr-1Mo steel [2] were introduced, followed by the development of 0.25V containing 0.5Mo steel and 0.5Cr-0.5Mo steel developed in 1950s, which could be used for boiler tube and pipe components [3]. An alloying element of molybdenum was recognized to increase the creep strength of carbon steel, and 0.3–0.5% of molybdenum content was used to improve the creep strength of the carbon steels with 0.15% of carbon. The alloying effect of Mo is the result of solution hardening and Mo_2C precipitation hardening of ferrite structure. The low-alloyed steels usually contain 0.5–1.0% of molybdenum to improve the creep strength, along with chromium contents between 0.5% and 9% for improved corrosion resistance, rupture ductility, and resistance against graphitization. Small additions of carbide formers such as vanadium, niobium, and titanium may also be added for precipitation strengthening and/or grain refinement. The conventional low-alloyed steels have still been used in boiler components operated under subcritical, supercritical, and ultra-supercritical pressure boiler up to the metal temperature of approximately 580°C. However, the allowable stresses are given to the temperature through to 650°C at maximum for 2.25Cr-1Mo steel, for example. The maximum use temperature is determined by boiler manufactures by their own design specification considering the high-temperature oxidation resistance. The alloy development efforts for conventional low-alloyed steels are well reported by several literatures [3,4].

2.2.2 Creep strength–enhanced low-alloyed steels

Many heat-resistant ferritic steels for power boilers have been developed during the last century. Fig. 2.1 shows the development progress of ferritic steels categorized into 2Cr, 9Cr, and 12Cr series. Of them, 2.25Cr-1Mo steel (T22) is the typical conventional low-alloyed steel developed in 1930s that has been used in the conventional and ultra-supercritical power boilers even at present. In the 1990s, creep strength–enhanced low-alloyed steels such as 2.25Cr-1.6WVNb steel (T23) and 2.5Cr-1MoVBTi steel (T24) have been developed, modifying the chemical composition and heat treatment of 2.25Cr-1Mo steel. The present and following sections will detail the development and properties of creep strength–enhanced low-alloyed steel; however, the strengthening and alloy design techniques for creep strength–enhanced low-alloyed steel were learned from the development of 9Cr and 12Cr steels.

Therefore this section at first introduces the development of 9Cr and 12Cr steels based on the development progress shown in Fig. 2.1. Regarding the 9Cr steels, HCM9M [5] is a low-carbon 9Cr-2Mo steel modified from 9Cr-1Mo (T9), and the strength of this steel is between those of T22 and TP304H austenitic steels, and it is used especially for reheater tubes in place of 18Cr-8Ni steels. Tempaloy F-9 [6], EM12 [7], and T91 [8] are also the modified 9Cr steels whose strengths have been enhanced by adding carbide forming elements such as V and Nb. Of these modified 9Cr-1Mo steels, T91 has the highest allowable stress and has already been extensively used all over the world as a material for heavy section components such as headers

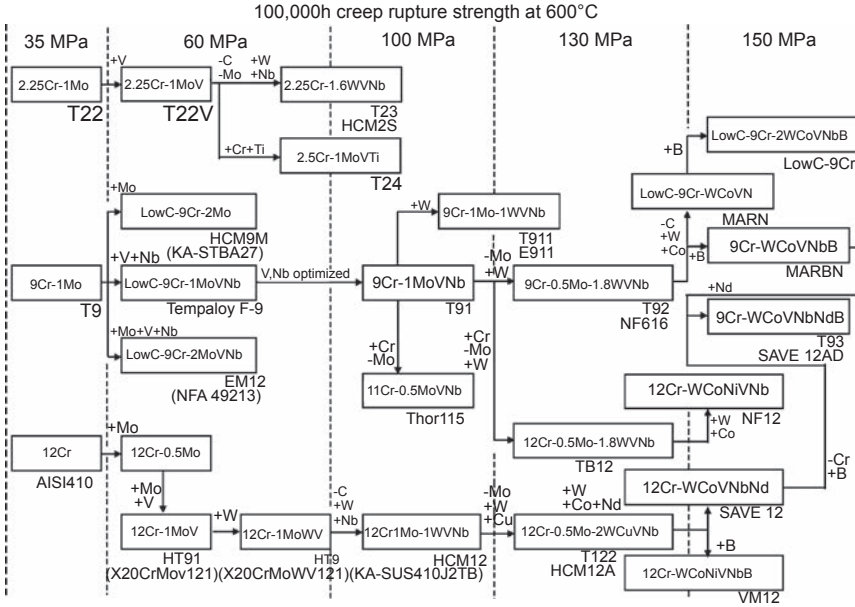


Figure 2.1 Development progress of ferritic boiler steels.

and steam pipes (ie, not limited in superheater tubing). The emergence of this steel has made it possible to fabricate high-pressure components for ultra-supercritical power plants up to 593°C (1100F) using a ferritic steel. NF616 (T92) [9], having an even higher allowable stress, was developed in the 1990s. This steel was obtained on the alloy design basis of substitution of W for Mo, decreasing the Mo content to 0.5% and adding 1.8% W, thus exhibiting the strongest creep among the modified 9Cr steels. This type of alloy design has been found to be excellent in terms of creep strengthening, and this method is commonly used in the most recently developed steels. This means that tungsten strengthening is more effective to increase creep resistance than molybdenum strengthening. It has already become possible to obtain 9Cr steels with remarkably high creep rupture strength, but they tend to be inferior for the use in the furnaces. This is because 9Cr steels cannot be used in a temperature range above about 625°C, taking into account the oxidation and corrosion resistance limiting temperature. Recently advanced creep strength–enhanced ferritic steels stronger in creep than T92 have been developed. Among those advanced creep strength–enhanced ferritic steels, T93 (SAVE12AD, ASME Code Case 2839 approved in October 2015) [10] is approximately 30% stronger in creep than T92, along with mitigating the susceptibility of Type IV creep damage. With respect to the 12Cr steels, HT91 (DIN, X20CrMoV121) [11] has extensively been used for superheater tubes, headers, and steam pipes, with extensive operating experience in Europe. However, this steel has not been used in Japan and the United States because the carbon content (as high as 0.2%) leads to poor weldability, and creep strength has not been found to be particularly good. Meanwhile, improved 12Cr steels for boilers have been developed by eliminating the drawbacks

of conventional 12Cr steels. HCM12 [12] and HCM12A [13] are examples of these improved 12Cr steels. HCM12 is a 12Cr steel with 1% Mo and 1% W having a duplex structure of delta ferrite and tempered martensite with improved weldability and creep strength. The stability of the creep strength of this steel has been designed by using precipitation strengthening with very fine VN precipitates and high-temperature tempering at over 800°C. The allowable stress is found to be somewhat superior to that of T91. This steel has already accumulated service experience over a period of more than 25 years and has been extensively used for superheater tubes particularly in chemical recovery boilers exposed to severe high-temperature corrosion attack. Development of the new steel for practical application must take into consideration not only creep strength but also oxidation resistance, weldability, and toughness. The roles of Mo, W, V, and Nb are extremely important in improving the creep strength of ferritic steels, and V and Nb addition are also important to set up at about 0.25% for V and about 0.05% for Nb to maximize the precipitation strengthening. The findings from the studies on development of creep strength–enhanced 9–12% Cr steels have been applied to develop the new high-strength low-alloyed steels in 1990–2000s. The low-carbon 2.25Cr-1.6W steel with V and Nb (HSM2S, T23) [14] and 2.5Cr-1MoVBTi steel (T24) [15] are the cost-effective creep strength–enhanced low-alloyed steels developed on the basis of the modern alloy design concept learned from 9–12% Cr steels. The creep strength of these steels at approximately 600°C is roughly twice as great as conventional low-alloyed steel such as T22. Since T22 was first used in the 1940s, a large quantity of this steel has been utilized for high-temperature components in power boilers up to approximately 580°C, and the utilization of T22 is accounted for over six decades. However, it has been clarified to improve the elevated temperature strength by the effect of alloying elements such as vanadium, niobium, titanium, molybdenum, and tungsten and optimization of the content of carbon, nitrogen, and boron. Conventional Cr-Mo low-alloyed steels usually contain 0.1% or more of carbon, which leads to considerable hardening during the weld heat cycles and requires prevention of weld-induced cracks by providing pre-weld and post-weld heat treatment. In view of this situation, the chemical optimization and heat treatment were investigated for the steels based on conventional 2.25Cr-1Mo steel and succeeded in developing new steels for boiler tubing applications, which exceeds 2.25Cr-1Mo steel in creep strength and is comparable to that of T91. As for the effect of chemical composition on creep strength of 2.25Cr-1Mo steel using the basic composition of 2.25Cr-0.25V-0.05Nb of which the vanadium and niobium content had been optimized by numerous studies on 9–12% Cr steel, such as T91, the influences of alloying elements such as molybdenum, tungsten, carbon, nitrogen, and boron on the creep strength were investigated. As the results of the study, it became clear that the creep strength can be greatly improved, with hardenability kept so low as to decrease the quenched hardness below 350 HV by reducing carbon content and by increasing the tungsten content considerably instead of reducing the molybdenum content. However, the addition of boron with keeping nitrogen as low as possible is effective to improve the hardenability to keep structure low-carbon bainitic and the creep strength over the long-term. Therefore, in case of T23 the tungsten content and molybdenum content were optimized to 1.6% and around 0.1%, respectively, and approximately 0.003%

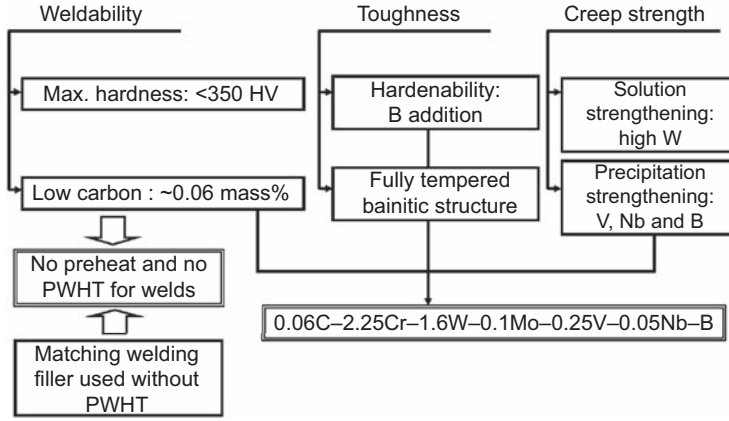


Figure 2.2 Alloy development concept of T23.

boron was added as an effective element. Fig. 2.2 shows the alloy design concept for T23 in the aspects of creep strengthening, toughness, and weldability. In case of T24, vanadium and titanium are used to employ the precipitation hardening for creep strengthening by the formation of carbide and carbonitride. Also, T24 contains boron to keep structure bainitic and improve creep strength, which becomes effective by the existence of titanium.

2.3 Properties and metallurgy

2.3.1 Steel grades in code and mechanical properties

Table 2.1 shows ASME/ASTM specifications for chemical composition of conventional low-alloyed steels (0.5Mo steel and 0.5-9Cr steels) including creep strength–enhanced low-alloyed steels such as T23 and T24, and high-strength 9Cr steel of T91. The conventional low-alloyed steels simply contain chemical elements of C, Si, Mn, Cr, and Mo, while the creep strength–enhanced ferritic steels contain additional elements from the variety of W, V, Nb, Ti, N, B, etc.

Table 2.2 demonstrates material designations of UNS number, ASME/ASTM, EN, and JIS, heat treatment conditions in specification, tensile properties at room temperature, and weld P-numbers, and its group numbers for the steels listed in Table 2.1.

The low-alloyed steels essentially have the improved creep strength by the addition of Mo and the enhanced corrosion resistance from Cr. The creep strength of low-alloyed steels is derived mainly from solid-solution strengthening of the matrix ferrite by C, Mo, and Cr and precipitation strengthening by carbides and carbonitrides when nitrogen is used as an alloying element along with V, Nb, and others. Creep strength, generally, but not always, increases with higher amounts of Mo and Cr. The effects of Cr and Mo on creep strength are complex. The low-alloyed steels are used primarily in product forms of tube, pipe, forgings, and plates for the high-temperature components of superheater/reheater tubes and pipe works in power plants. Conventional

Table 2.1 **Chemical requirements for low-alloyed steels**

Steels/ASME designation		Chemical composition (mass%)											
		C	Si	Mn	Ni	Cr	Mo	W	V	Nb	Ti	B	Others
C-0.5Mo	T1	0.10–0.20	0.10–0.50	0.30–0.80	–	–	0.44–0.65	–	–	–	–	–	–
0.5Cr-0.5Mo	T2	0.10–0.20	0.10–0.30	0.30–0.61	–	0.50–0.81	0.44–0.65	–	–	–	–	–	–
1Cr-0.5Mo	T12	0.05–0.15	0.5 max	0.30–0.61	–	0.80–1.25	0.44–0.65	–	–	–	–	–	–
1.25Cr-0.5MoSi	T11	0.05–0.15	0.50–1.00	0.30–0.60	–	1.00–1.50	0.44–0.65	–	–	–	–	–	–
2.25Cr-1 Mo	T22	0.05–0.15	0.50 max	0.30–0.60	–	1.90–2.60	0.87–1.13	–	–	–	–	–	–
2.25Cr-1.6WVNb	T23	0.04–0.10	0.50 max	0.10–0.60	0.40 max	190–2.60	0.05–0.30	1.45–1.75	0.20–0.30	0.02–0.08	0.010–0.060	0.0020–0.060	N 0.010max Al 0.030max
2.5Cr-1MoVBTi	T24	0.05–0.10	0.15–0.45	0.30–0.70	–	2.20–2.60	0.90–1.10	–	0.20–0.30	–	0.06–0.10	–	N 0.012max Al 0.02max
5Cr-0.5Mo	T5	0.15 max	0.50 max	0.30–0.60	–	4.00–6.00	0.45–0.65	–	–	–	–	–	–
9Cr-1Mo	T9	0.15 max	0.25–1.00	0.30–0.60	–	8.00–10.00	0.90–1.10	–	–	–	–	–	–
9Cr-1MoVNb	T91	0.07–0.14	0.20–0.50	0.30–0.60	0.40 max	8.0–9.5	0.85–1 0.05	–	0.18–0.25	0.06–0.10	0.01 max	–	N 0.030–0.070 Al 0.02max Zr 0.01max

Table 2.2 Material designation, heat treatment, room temperature tensile/yield strength, and P-number for low-alloyed steels

		Material designation, heat treatment, room temperature tensile/yield strength, and P-number						
Steels	**UNS**	**ASME/ ASTM**	**EN**	**JIS**	**Heat treatment**	**TS**	**YS**	**P-No.- Gr. No.**
C-0.5Mo	K11522	T1	16Mo5	STBA12	Full/isothermal ann. 650°C min. subc. ann.	380	205	3-1
0.5Cr-0.5Mo	K11547	T2	–	STBA20	Full/isothermal ann. 650–730°C subc. ann.	415	205	3-1
1Cr-0.5Mo	K11562	T12	13CrMo4-4	STBA22	Full/isothermal ann. 650–730°C subc. ann.	415	220	4-1
1.25Cr-0.5MoSi	K11597	T11	13CrMo4-5	STBA23	Full/isothermal ann. 650°C min. subc. ann.	415	205	4-1
Z25Cr-1Mo	K21590	T22	10CrMo9-10	STBA24	Full/isothermal ann. 675°C min. subc. ann.	415	205	5A-1
2.25Cr-1.6WVNb	K40712	T23	–	KA-STBA24J1	1040–1020°C normal. 730–800°C temper	510	400	15C
2.5Cr-IMoVBTi	K30736	T24	7CrMoVTiB10-10	–	980–1080°C normal. 720–775°C temper	585	415	15C
5Cr-0.5Mo	K41545	T5	–	STBA25	Full/isothermal ann. 675°C min. subc. ann.	415	205	5B-1
9Cr-1Mo	K90941	T9	–	STBA26	Full/isothermal ann. 675°C min. subc. ann.	415	205	5B-1
9Cr-1MoVNb	K90901	T91	X10CiMoVNb9-1	KA-STBA28	1040–1080°C normal. 730–800°C temper	585	415	15E-1

ann, annealing; *min*, minimum; *subc,* subcritical; *normal,* normalizing.

ferritic boiler tubes are used mostly in the annealed condition in ASME Code, whereas pipes are used mostly in the normalized and tempered condition. Bend sections used in pipe, however, are closer to an annealed condition than to a normalized condition. As a result of the cooling rates employed in these treatments, the microstructures of conventional low-alloyed steels may vary from ferrite and pearlite structure to ferrite and bainite structure. Bainite structures have better creep resistance under high-stress, short-time conditions but degrade more rapidly at high temperatures than ferrite and pearlite structure. As a result, ferrite and pearlite structure has better creep resistance to long-term and low stress conditions. Because both microstructures will eventually spheroidize, it is expected that over long service lives the two microstructures will converge to similar creep strengths. The 0.5Mo steel with 0.15% C (T1) is used for piping and superheater tubes operating at metal temperatures to 450°C. Above this temperature, spheroidization and graphitization may increase the possibility of failure in service. Use of carbon-molybdenum steel has been largely discontinued for higher temperatures because of graphitization. Cr-Mo steels are highly resistant to graphitization and are therefore preferred for service above 450°C. The 1Cr-0.5Mo steel (T12) is used for boiler tubes and piping for service temperature to 510°C or 540°C. The similar 1.25Cr-0.5Mo steel (T11) is used up to 560°C and has comparable stress rupture and creep properties as that of T12. The 2.25Cr-1Mo steel (T22) has better oxidation resistance and creep strength than the steels mentioned above. T22 is a highly favored alloy for service up to about 600°C in power boiler. The 5-9% Cr steel (T5 and T9) are generally lower in stress rupture and creep strength than T22 because the strength at elevated temperature typically drops off with an increase in chromium, except in recently developed creep strength–enhanced ferritic steels. However, this may not always be the case, depending on the service temperature and exposure. Heat treatment is also an important factor. The main advantage of these steels is the improved oxidation resistance from the increased chromium content. Regarding the application of the steels, the literature is quoted as [16] revising the maximum use temperatures to 560°C from 590°C for T11 and to about 580°C from 650°C for T22, respectively, for boiler applications. Figs. 2.3 and 2.4, respectively, show allowable stresses against temperatures for T22 and lower conventional grades and for creep strength–enhanced ferritic steels (T23, T24, and T91) in comparison with T22, T5, and T9. From the figures, it is clear that among the conventional low-alloyed steels including T5 and T9, T22 is strongest in allowable stresses, and T23 and T24 have excellent strength as twice of those of T22 at the temperature up to 625°C, and as 80% of those of T91. In ASME Code Case the allowable stress at the 650°C for T23 is conservatively set to the same value as that of T22, while the creep strength of T23 at 650°C is almost twice of that of T22.

2.3.2 Heat treatment and metallurgy

As shown in Table 2.2, conventional low-alloyed steels shall be fully or isothermally annealed, or normalized and tempered at the temperatures listed. The boiler tubes are usually isothermally annealed to obtain stable ferrite and pearlite structure; however, the pipes with relatively thick sections are normalized and tempered to obtain ferrite

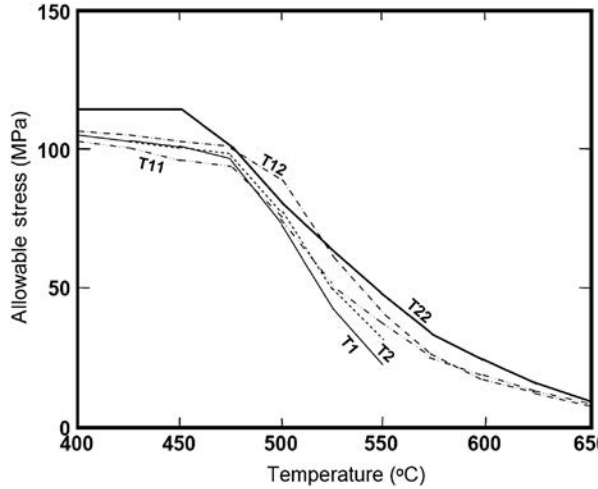


Figure 2.3 Comparison of allowable stresses for conventional low-alloyed steels.

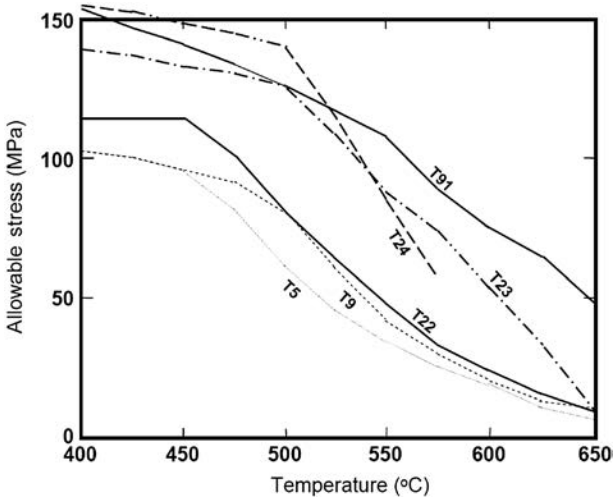


Figure 2.4 Comparison of allowable stresses for creep strength–enhanced low-alloyed steels in comparison with T22 and 5-9Cr steels.

and bainite structures or single bainite structures. On the other hand, developed creep strength–enhanced ferritic steels are normalized and tempered at indicated temperature ranges. According to the ASME Section IX, QW/QB-492 "Definition," the creep strength enhanced ferritic steels is defined as "a family of ferritic steels whose creep temperature strength is enhanced by the creation of a precise condition of microstructure, specifically martensite or bainite, which is stabilized during tempering by controlled precipitation of temper-resistant carbides, carbonitrides, or other stable and/or meta-stable phases." Therefore the heat treatment for the creep strength–enhanced

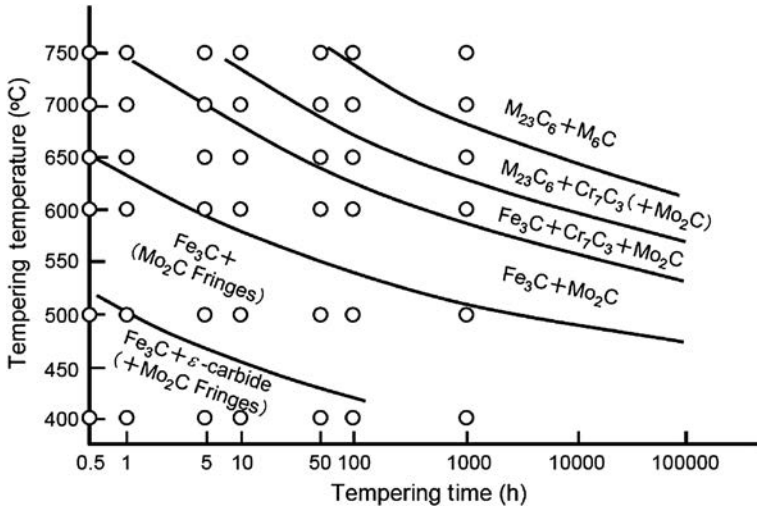


Figure 2.5 Isothermal diagrams showing the sequence of carbide formation on tempering the normalized T22.

low-alloyed steels must be carefully controlled in accordance with code specifications. In the case of conventional low-alloyed steel, microstructural evolution during heat treatment is caused by the carbide reaction at the tempering temperatures and times. Fig. 2.5 [17] is the isothermal diagram showing the sequence of carbide formation on tempering of the normalized 2.25Cr-1Mo steel (T22). For normalized conditions, T22 contains pro-eutectoid ferrite and bainite. And no carbides are present in the ferrite, but plate-like and lath-like carbides are extracted from the bainite structure, which is thought to be partly ε-carbide and partly cementite. Fringes of acicular Mo_2C are observed on the ferrite side of some of the bainite/ferrite boundaries. During tempering, various carbides precipitate depending on the temperature and tempering duration, as shown in Fig. 2.5.

Figs. 2.6 and 2.7 [18], respectively, show continuous cooling transformation diagrams for T23 and T24. The Ac1 and Ac3 transformation temperatures for both steels are almost the same. And bainite transformation temperatures are about 600°C and 550°C, respectively, for T23 and T24.

Fig. 2.8 [19] shows light optical micrograph and transmission electron micrograph for T23 that are exhibiting tempered bainite structure and very fine carbides of (V, Nb) C and M_6C dispersed in the matrix, which are determined by the chemical analysis of extracted residues. The dispersed fine precipitates are also confirmed to be formed as interphase precipitates during bainite transformation from austenite.

Fig. 2.9 [20] shows hardness measurement results for T23 specimens as-normalized condition in terms of cooling rate comparing with T22. At the rapid cooling conditions faster than 5°C/s, T22 is harder than T23 due to the martensite formation by quenching; however, the hardness remarkably drops to 250-130 HV when cooled slower than 5°C/s. On the other hand, T23 as normalized shows stable hardness 270–330 HV at the cooling rate between 0.1 and close to 100°C/s. This means T23 has adequate hardenability against the wide range of cooling rate. Fig. 2.10 [20] shows

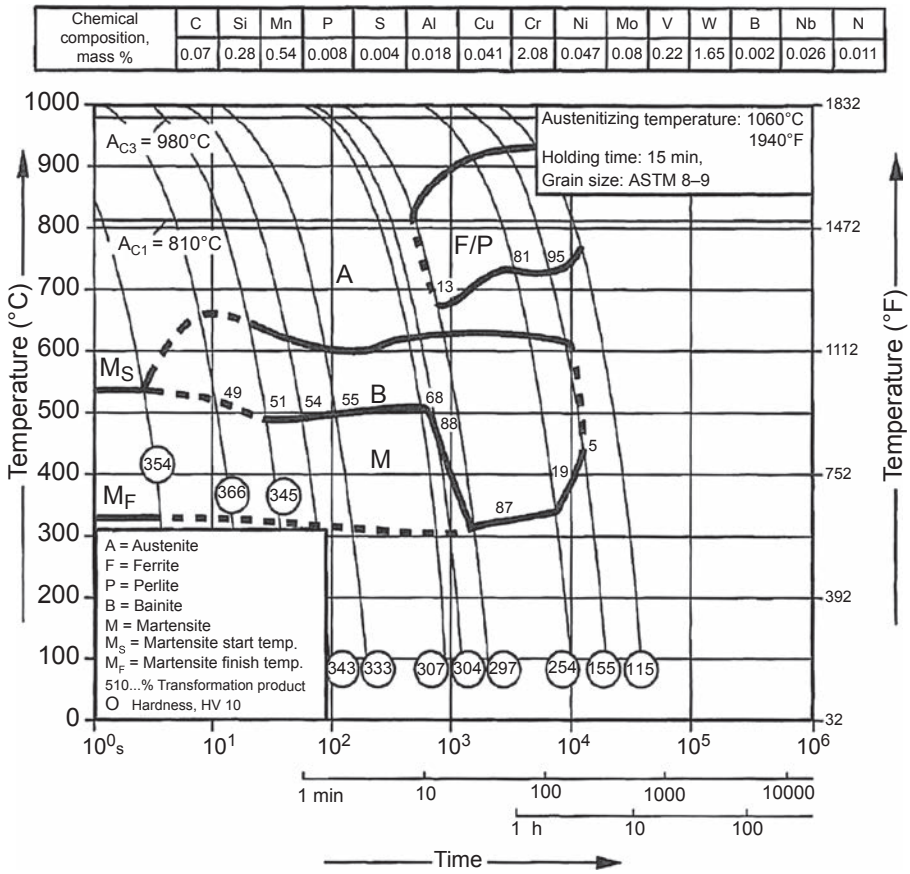


Figure 2.6 Continuous cooling transformation diagrams for T23.

the effect of cooling rate after normalizing on the microstructures of T23. The cooling rate of 0.2°C/s and faster does not form ferrite gain; however, 50% and 5% ferrite are observed at the cooling rate of 0.01°C/s and 0.03°C/s, respectively.

Fig. 2.11 [20] shows the relationship between 100,000 h creep rupture strength extrapolated at given temperatures and cooling rate after normalizing for normalized and tempered T23. The creep rupture strength decreases at the cooling rate slower than 0.1°C/s due to the ferrite formation. From these facts in the case of T23, cooling rate after normalizing is recommended to be 0.1°C/s at minimum to satisfy the required creep strength.

2.4 Welding and forming

2.4.1 Welding and properties of welds

The lower content of carbon such as 0.06% and 0.08%, respectively, in T23 and T24 leads to reduce the maximum as-welded hardness in the welds down to around 350 HV. This suppresses the occurrence of hydrogen cracking or cold cracking in the

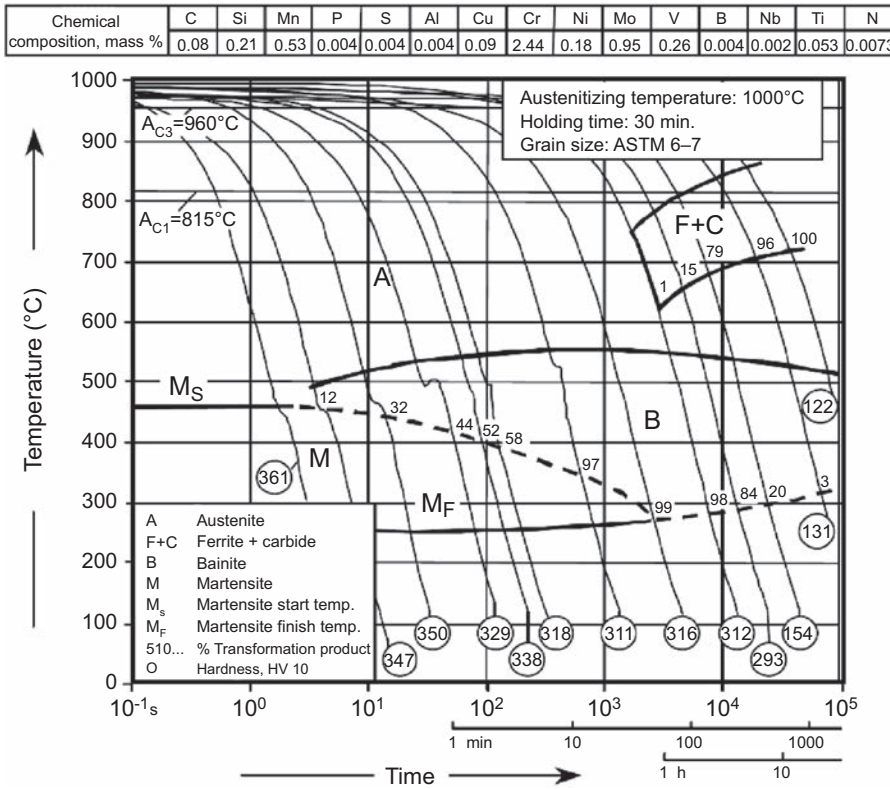


Figure 2.7 Continuous cooling transformation diagrams for T24.

welds. Conventional low-alloyed steels with carbon content of 0.10–0.15% having maximum as-welded hardness of about 400 HV and higher have the susceptibility to suffer this type of weld cracking, and to avoid this failure, preheating in the temperature range of 150–250°C is applied before welding. Fig. 2.12 [21] compares the cold cracking susceptibility between T23 and the conventional steels, T22 and T91 in the Y-groove restraint weld cracking test. The minimum preheating temperatures for complete prevention of weld cracking for T22 and T91 are 300°C and 175°C, respectively, whereas no cracking occurred in T23 even at room temperature or under any preheating conditions. This test result reveals that the T23 has excellent weldability, which may not be expected in the case of conventional low-alloyed steels. However, in the codes and standards for welding, the materials are categorized into several groups, which may need preheating and/or post-weld heat treatment. When T23 and T24 were covered by the ASME Code Case, both steels were categorized into P-number 5A, the same as T22, which require the preheating and post-weld heat treatment; however, the new P-numbers such as P-number 15 were developed for those creep strength–enhanced ferritic steels, and T23 and T24 were categorized into P-15C, which also requires preheating and post-weld heat treatment.

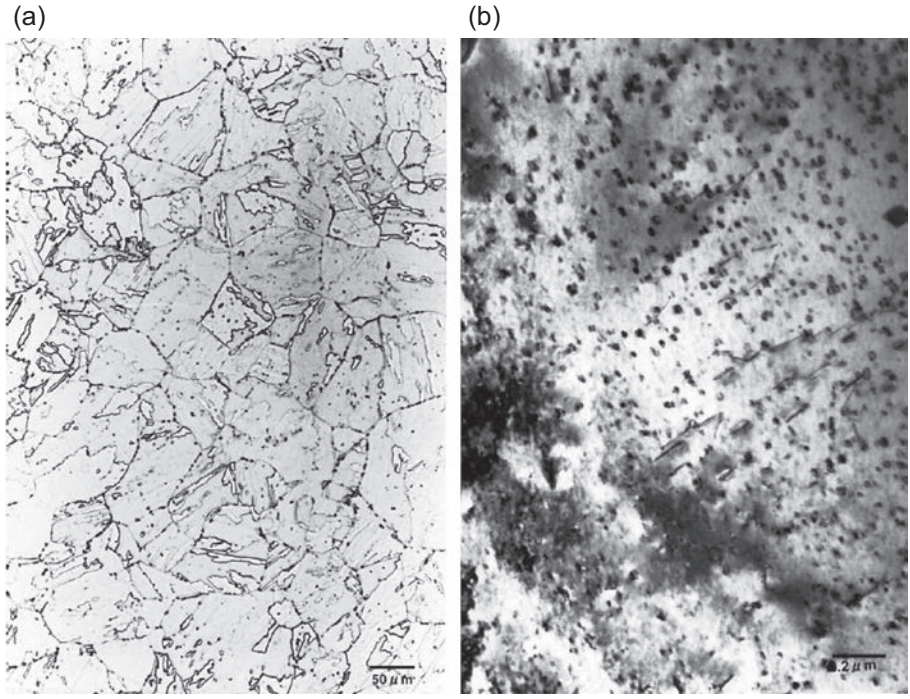


Figure 2.8 Microstructures of T23.

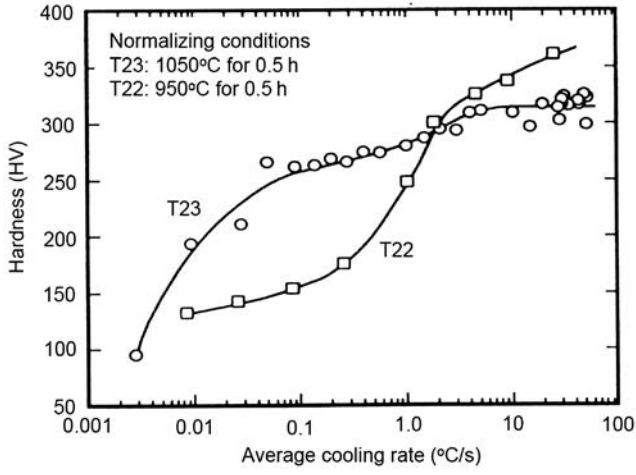


Figure 2.9 Effect of cooling rate after normalizing on hardness of T23 in comparison with T22.

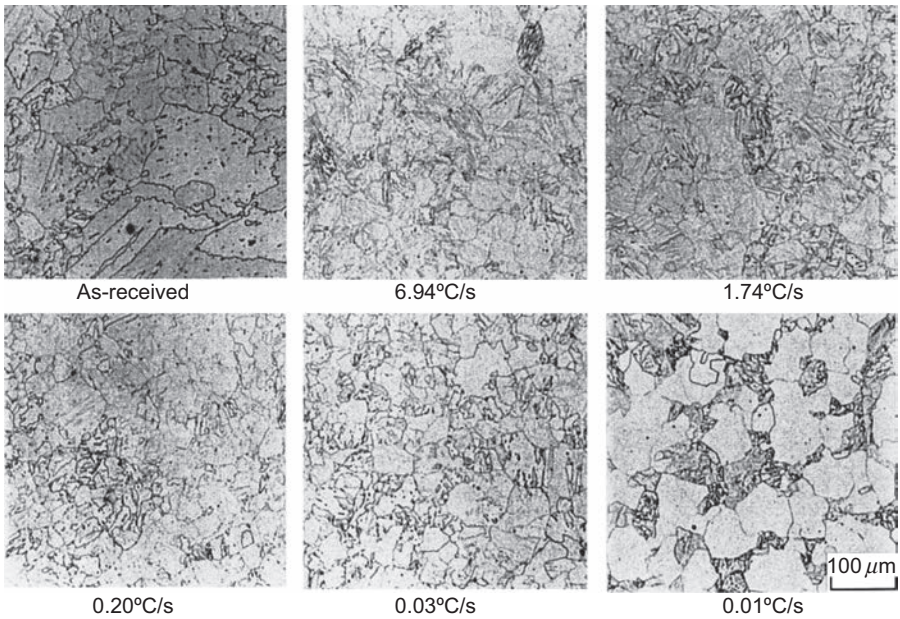


Figure 2.10 Effect of cooling rate after normalizing on microstructures of T23 (normalized at 1050°C, followed by tempering at 770°C).

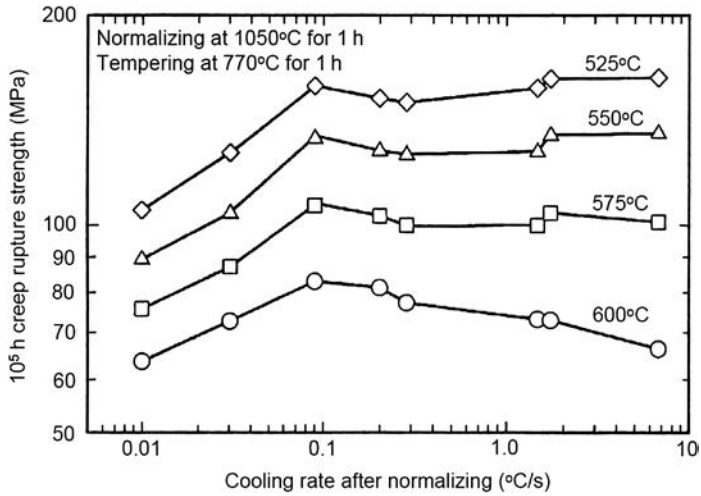


Figure 2.11 Effect of cooling rate after normalizing on 10^5 h creep rupture strength of T23.

Welding of T23 and T24 can be conducted by several processes such as shielded metal arc welding (SMAW), gas tungsten arc welding (GTAW), submerged arc welding, flux cored arc welding, and gas metal arc welding. Various manufacturers, for example, Metrode, Böhler, and Air Liquide, produce welding consumables for all

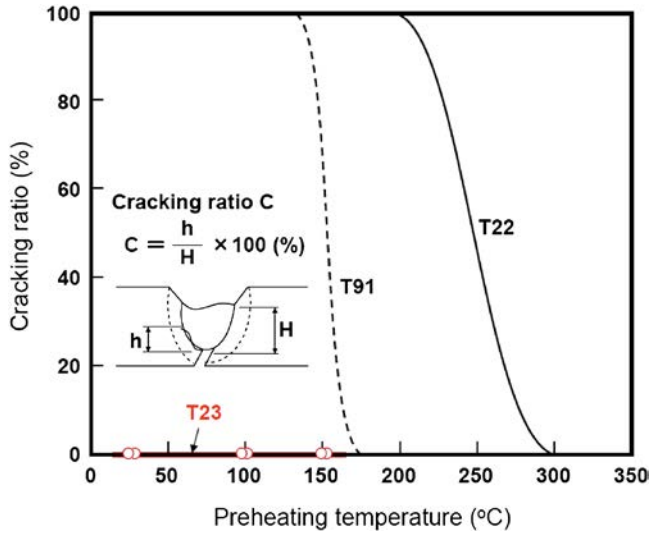


Figure 2.12 Comparison of Y-groove weld cracking ratio between T23 and conventional steels, T22 and T91.

these processes. For the T23 steel grades, all three manufacturers have welding consumables, but only Metrode indicates where the manual metal arc (MMA) and tungsten inert gas/metal inert gas (TIG/MIG) welds can be used without application of post-weld heat treatment. It is noted that Metrode shows a nickel content of ~0.5%, which is added to improve the toughness of as-deposited weld metal for relatively low toughness in as-welded condition for MMA and TIG/MIG consumables. Although Böhler does not show nickel as an addition in their consumables, there are several publications from other sources that indicate the "need" for such an addition to improve toughness [4]. According to the weld performance test results of T23 [21], the tensile, side bend, and Charpy impact for the welded joint using matching filler metal, all of the tensile specimens ruptured in the base metal exceeding the specified strength, and it was satisfactory in side bending. Charpy impact properties of weld metal as-welded condition averaged around 200 J for GTAW and 30 J for SMAW. The transition temperatures measured in the Charpy impact tests were −39°C for as-welded condition and −35°C for post-weld heat treated at 715°C for 0.5 h. The microstructures in the welds including weld metal, heat-affected zone, and base metal showed homogeneous bainite for each welded joint. The creep rupture test results are shown in Fig. 2.13 [21] for T23 welded joint manufactured by GTAW and SMAW as-welded condition in comparison with the data band for the base metal. The creep rupture strength of welded joint is well within the scatter band for the base metal at temperatures of 550°C, 600°C, and 650°C.

Stress relief or reheat cracking susceptibility is one of the weldability issues as well as hydrogen or cold cracking susceptibility. High-strength T23 and T24 may be used for manufacturing of constrained construction such as the water wall of boiler components by welding. The welding under the severe constrained conditions leads to cause

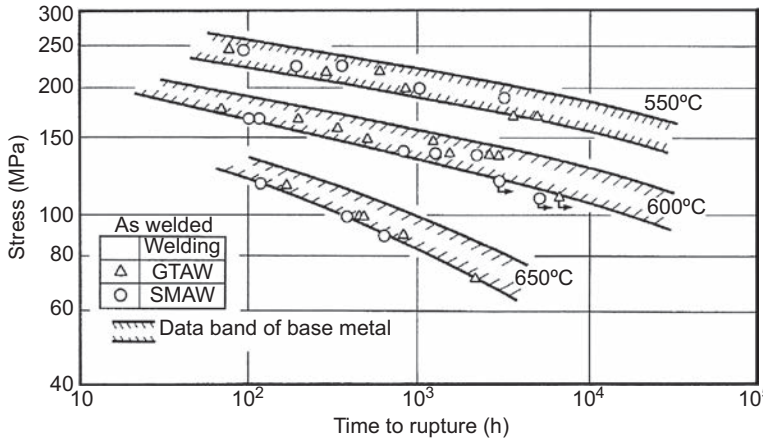


Figure 2.13 Creep rupture properties of T23 welded joint as-welded.

stress relief or reheat cracking in especially high-strength low-alloyed steels; therefore the reheat cracking of T23 and T24 was investigated by several researches [22,23]. This type of cracking is caused by coarse-grain structure in the heat-affected zone and brittleness of the structure. According to the investigation results, T23 is more susceptible to reheat cracking than T22 over the range of weld thermal simulation and tempering schedules tested for the original chemical composition of T23 [22]. The thick-section multipass welds made using filler metal with the chemical composition closer to T24 are less susceptible to reheat cracking than matching T23 welds [23]. Based on the comprehensive reheat cracking investigation, the chemical composition of T23 has been modified to add a small amount of titanium, which improves reheat cracking susceptibility [24].

2.4.2 Forming and properties of formed metal

Bending formability is an important performance for boiler tubing fabricated into superheater/reheater panels and water wall panels. Three types of bending procedures for tubes—cold bend, hot bend, and flat bend—are usually used for fabrication of boiler components. The typical bending conditions for the three types are as follows: (1) cold bend at room temperature with bending radius of 2.5D, (2) hot bend at the temperature of about 700°C on the intrados-side only of bending with bending radius of 1.5D, and (3) flat bending by die forming of hot bent tube at the temperature above 900°C with 0.5D (this means flatting of tube), where D is the outside diameter of tube [21]. These bending conditions are also applied to the conventional low-alloyed steel tubes. By the dimensional measurement on the section of bent tubes, it was revealed that the ellipticities of the cold and hot bent tubes were approximately 3% at maximum, and about 8% for flat bent tube at maximum. The measured values are almost same as those of conventional T22 and T91 tubes, and in acceptable ranges for practical use. The hardness measurement on the section of bent tubes demonstrated that

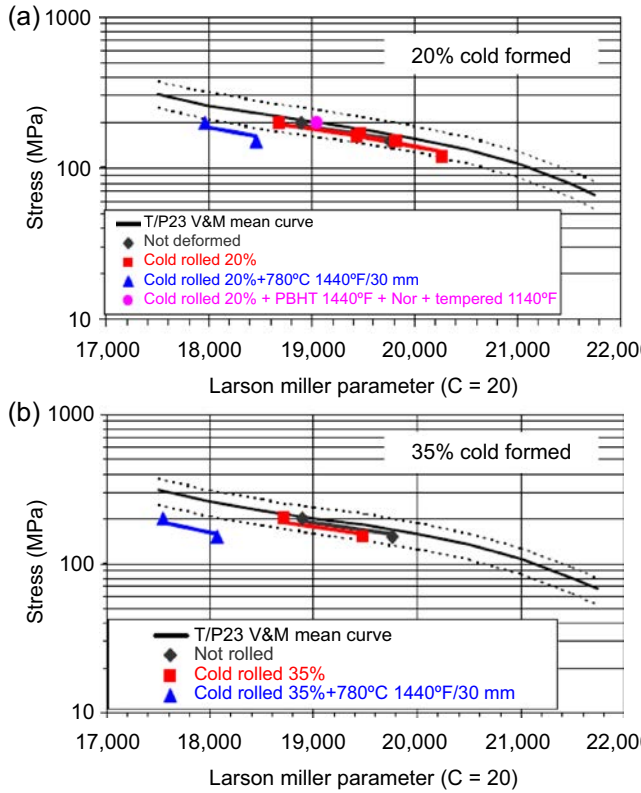


Figure 2.14 Effect of cold forming on creep rupture strength of T23.

the cold and hot bent tube had values of 170–190 HV on each circumferential position (eg, tension, compression, and neutral position) showing no bending effect on the hardness, while the flat bent tube showed a hardness of 300–310 HV due to direct quenching during the die forming. The microstructures under the conditions of cold bend and hot bend showed homogeneous fine bainite in the circumferential area of the tubes; meanwhile, the flat bent tube exhibited coarsening of grains due to heating for die forming at the temperature beyond Ac3, but the bainite structure of the tube was well maintained.

Fig. 2.14 [25] shows effect of cold forming on the creep rupture strength of T23. From the figure, it is clear that cold forming at higher strain induces great drop of creep rupture strength and renormalizing and tempering is necessary to recover the creep strength of cold-formed metal.

This kind of creep strength degradation by cold forming is well known for austenitic steels and T91, and the post-forming rules are specified for austenitic steels in ASME Section I, PG-19 and PG-20 for austenitic steels and T91, respectively. Also creep strength–enhanced ferritic steels covered by ASME Code Case have similar rules in their own Code Case individually. As for T23 and T24, Code Cases (2199-6

for T23 and 2540 for T24) state that all cold-formed material with a thickness less than 13 mm, which is designed for service at nominal temperature of 480°C or higher, shall be heat treated in accordance with the following rules. "Cold bending or forming is defined as any method that produces strain in the material and is performed at a temperature below 605°C for T23 or 650°C for T24. The calculation of cold strains shall be made as described in Section I, PG-19." The rules for T23 are "(1) strain greater than 20%: renormalizing and tempering, (2) strain 20% and less but greater than 5%: shall not exposed to temperature between 720 and 1040°C during fabrication or erection, and others." The rules for T24 are "(1) strain greater than 28%: stress reliving at a temperature between 650 and 750°C, (2) strain greater than 17% for tubes of diameter greater than 76.1 mm: renormalizing and tempering, and (3) all material formed at or above 650°C: renormalizing and tempering."

2.5 Service degradation

2.5.1 Creep degradation

T23 and T24 have already been practically used worldwide in the conventional type and ultra-supercritical type power boilers including heat recovery steam generators in gas turbine combined cycle power plants. The extensive use of both steels has brought great benefit of economy and environmental protection by increasing thermal efficiency. However, there exist some reports on the failure due to fabrication problems and poor technical management for the room temperature behavior of the steels such as stress corrosion cracking and reheat cracking. Regarding the high-temperature service exposure experience or performance, there are few reports on failure or trouble such as creep degradation so far. According to the service exposure test results [26] and creep degradation test results [27] on T23, we can confirm the long-term material properties and performances of creep strength–enhanced low-alloyed steels. The field exposure tests for up to 10 years (79,000 h) was conducted using a 156-MW power boiler with 571°C superheater outlet temperature and 543°C reheater outlet temperature. The creep rupture tests for ex-serviced T23 at 550°C and 600°C (Fig. 2.15) demonstrate that the base metal fell in the lower band of virgin material, although the welded joint was slightly lower than that of base metal similarly as other creep strength–enhanced ferritic steels but not so significant comparing with T91, and the test pieces taken from fire side showed greater reduction of creep rupture strength than those taken from rear side of flue gas. With respect to the yield strength and tensile strength in tensile tests the exposed material showed slightly lower after 1-year exposure than virgin material, but the strengths after 3-year, 6-year, and 10-year exposure were almost the same as that after 1-year serviced material. Charpy impact properties at 0°C changed corresponding to service duration. The impact values in base metal decreased to approximately half of the initial values after 1-year service; little change occurred with further exposure. The impact values for weld metal without post-weld heat treatment were scattered, but they were superior to the values for base metal.

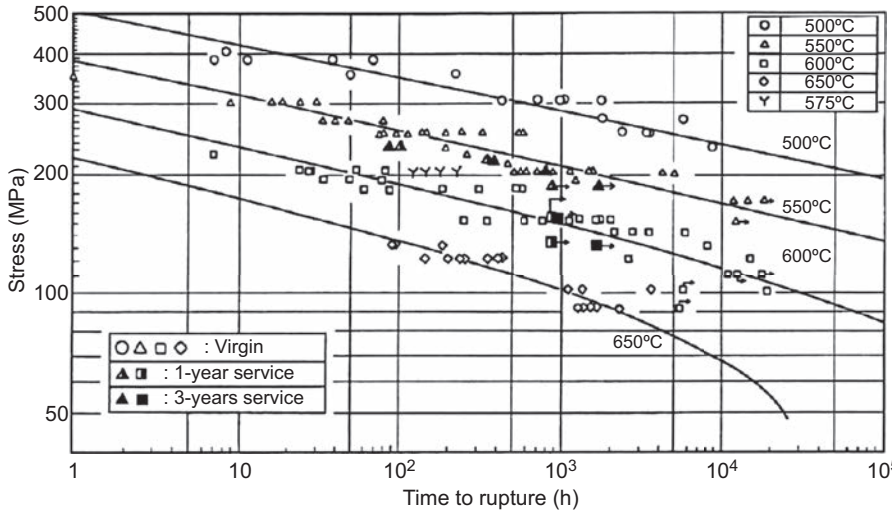


Figure 2.15 Creep rupture properties of ex-serviced T23.

Creep degradation tests, which mean creep interrupting tests using cross-weld specimens from T23 tube material (for standard-size specimen) and pipe material (for large-size specimen with 30 mm by 30 mm section), were conducted to investigate the creep degradation process in the welds in comparison with its base metal [27]. The test conditions were 80 MPa for base metal and 70 MPa for welds at 650°C. The rupture times for creep specimens were 4042 h for base metal and 2662 h for standard-size cross-weld specimens from welds and 3153 h for large-size cross-weld specimens taken from welded joints. The creep rupture strength of welds is weaker than that of base metal even for the lower test stress than base metal. Standard-size cross-weld specimens were ruptured at 3 mm away from weld fusion line in the heat-affected zone, and it was obvious that the specimens ruptured in the fine-grain heat-affected zone as typical Type IV failure. The hardness measured on the interrupted base metal continuously reduced from 188 HV to 138 HV at rupture in gage portion due to the creep stress; however, the grip portion reduced hardness only 15 Hv due to aging without stress. Fig. 2.16 shows microstructures of base metal at various interrupted life fractions. Creep cavities were observed beyond the creep life fraction of 0.65; creep cavities tend to generate on the grain boundary perpendicular to the stress axis. Creep cavities were also observed in the creep-interrupted cross-weld specimens in the coarse-grain heat-affected zone and fine-grain heat-affected zone at the creep life fraction of 0.71.

2.5.2 Steam oxidation

Oxidation due to superheated steam is an especially serious problem in boilers with high steam temperatures, which have become increasingly common in the ultra-supercritical power plants. Damage resulting from steam oxidation includes tube

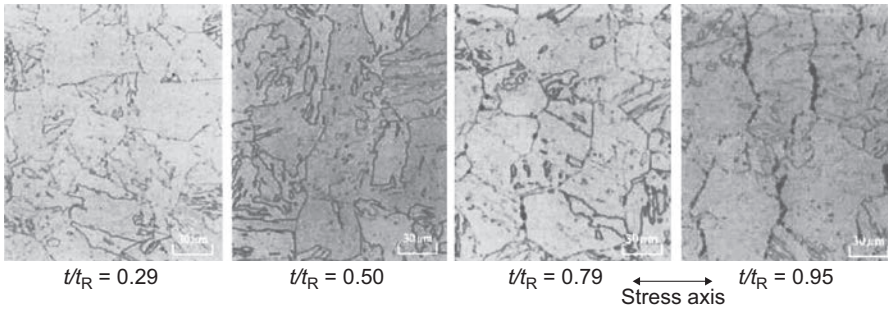


Figure 2.16 Microstructural changes of T23 base metal in terms of creep-interrupted fraction.

blockage caused by the exfoliation and buildup of scale. This leads to creep damage induced by overheating of affected tubes as well as particle erosion in turbine-side equipment downstream from the boiler due to dispersion of scale. The formation and exfoliation behavior of steam oxidation scale are quite different for ferritic and austenitic steels, respectively. In the past, because the damage resulting from steam oxidation was not as severe in cases involving ferritic steels as compared to austenitic steels, ferritic-related research was relatively sparse. Recently, however, considerable research has been conducted on creep strength–enhanced ferritic steels, particularly on T91. As the thermal expansion coefficient differential between ferritic steels and scale is less than with austenitic steels, scale does not reach the exfoliation limit thickness until considerable time has elapsed. Nevertheless, scale exfoliation has been confirmed for low-alloyed steels after long-term usage of over 100,000 h. The scale on low-alloyed steels is known to have a dual-layer structure with exfoliation occurring when the thickness reaches approximately 500 μm. The scale formed on low-alloyed steels is different from austenitic steels in exfoliation manner. That is to say all layers on the low-alloyed steels exfoliate simultaneously, and the scale is hard. In terms of the steam oxidation behavior of ferritic steels in actual use, T91 is treated here as a representative example. Exfoliation has not occurred with respect to the steam oxidation scale in any of these cases, with the structures consisting of an inner and outer layer (dual-layer structure). More detailed observation reveals that the outer layer consists of interior layer scale (magnetite, Fe_3O_4) and a thin layer of hematite (Fe_2O_3) in the most outer layer covering over the magnetite. This is considered to be due to the scale interface that develops between the inner and outer scale layers accompanying scale growth as well as the formation of numerous voids in the outer layer, inhibiting the supply of Fe^{2-} and 2e to the scale from the base metal during the process of scale formation. As for the time-wise change in the thickness of steam oxidation scale, the thickness is dependent on temperature and time with scale growth conforming to the parabolic rate law at a constant temperature expressed by the relationship between total scale thickness, X, and time, t, as $X^2 = K_p \cdot t$ (where K_p is an oxidation rate constant expressed by the equation, $K_p = A\exp(-Q/RT)$, where A is the frequency factor, Q the apparent activation energy, R the gas constant, and T the absolute temperature). Fig. 2.17 [28] shows weight gain vs. time curves for T91 and T22 at temperatures of 600°C, 650°C,

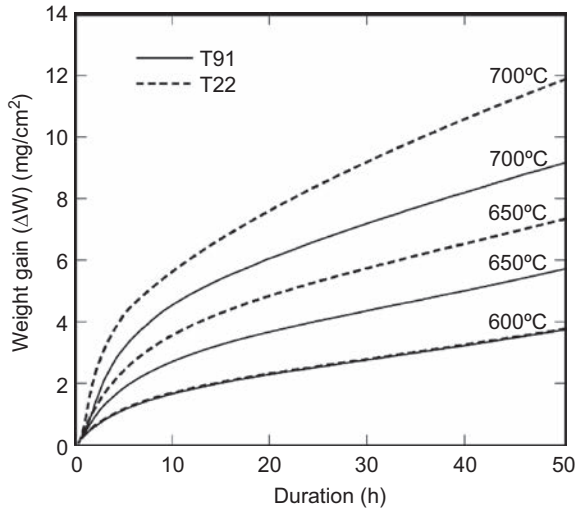


Figure 2.17 Weight gain vs. time curves for T91 and T22 in steam oxidation tests.

and 700°C. The oxidation growth curves all follow the parabolic rate law over the test time up to 50 h. The weight gain of T91 is smaller than that of T22 at the temperatures tested, with the exception of 600°C. This test result suggests that the steam oxidation resistance of T22 is almost similar to that of T91 up to 600°C.

In a power boiler, carbon steel is used in superheaters operated up to 450°C, and 0.5Mo or Cr-Mo low-alloyed steels are used for higher steam conditions. In 16MPa, 566°C class boilers, however, the metal temperature of the highest temperature components is in excess of 560°C, meaning that the strength and corrosion resistance of Cr-Mo low-alloyed steels become unsatisfactory, and 18Cr-8Ni stainless steels must be used. As the selection of materials for a superheater depends on temperature and pressure, these materials change from carbon steel to Cr-Mo low-alloyed steel to 18Cr-8Ni stainless steel in supercritical boilers as temperatures become higher. The maximum use temperature for each material is generally determined by the oxidation resistance limit temperature, and newly developed creep strength–enhanced low-alloyed steels and 9Cr steels are being used to replace existing conventional low-alloyed steels according to their corrosion resistance limit temperatures (often depending on the content of Cr). The reheater is similar in structure and function to a superheater, and it is normally positioned on the gas downstream side of the superheater, serving to boost turbine thermal efficiency by reheating steam that has already done work in a high-pressure turbine, having expanded and fallen to nearly the saturation temperature, and sending this reheated steam to a medium- or low-pressure turbine. The main difference as compared to a superheater is that the steam pressure is lower and the volume is greater, such that the design must limit steam pressure loss. The reheater is installed mainly in plants with capacities of 75 MW and over, and while reheater steam temperatures have been the same as those of superheaters (538°C or 566°C), temperatures of 600–620°C have recently been realized, and the trend toward

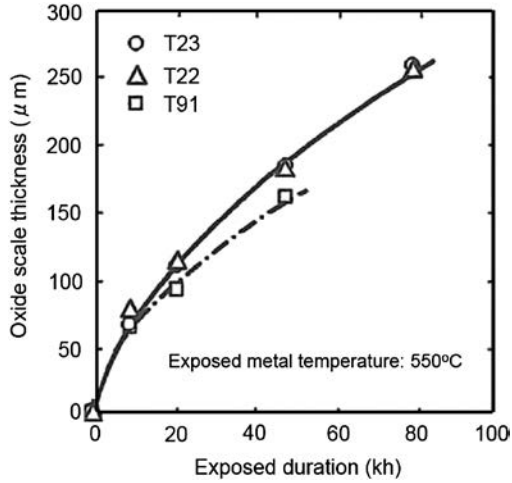


Figure 2.18 Changes in steam oxidation scale thickness in terms of exposure duration for T23 in comparison with T22 and T91.

higher temperatures is no different from the case of superheaters. In 538°C class boilers, mainly 1.25Cr-0.5Mo (T11) and 2.25Cr-1Mo (T22) are used, while 9Cr-1Mo (T9), having superior corrosion resistance, was also adopted for a time. However, a disadvantage of this material is high susceptibility to weld cracking, and it is now used hardly at all. Instead of these conventional low-alloyed steels, creep strength–enhanced low-alloyed steels T23 and T24 are used recently in conjunction with the new 9Cr steels such as T91 and T92. Therefore when the tube materials are used as superheaters and reheaters in power boilers, the steam oxidation property of the steels should be taken into consideration for materials selection. In general, however, the steam oxidation resistance of tube steels depends on the Cr content of the alloy, as mentioned earlier. In this sense the steam oxidation resistance of T23 and T24 is roughly assumed to be the same as that of T22. According to the field exposure test in the power boiler [26], steam oxidation scale growth behavior of T23 over 10 years is almost the same as that of T22 and a little bit less resistant than T91 at the estimated exposure metal temperature of 550°C, as shown in Fig. 2.18.

2.6 Conclusions

In the power boiler, conventional low-alloyed steels are still important materials to be used in the high-temperature weld construction components such as water walls, superheater/reheater tubes, and steam pipes for not only subcritical/supercritical but also ultra-supercritical steam conditions at temperatures below about 560°C. However, at the higher temperature services the conventional low-alloyed steels should have a thick wall and larger diameter, which causes difficulty of manufacturing and fabrication. In the last three decades, alloy development R&D for low-alloyed steel has actively been

conducted along with the development of high-strength 9–12% Cr steels and austenitic steels. As a result, creep strength–enhanced low-alloyed steels represented by T23 and T24 have been developed and applied to realize the modern power plant of ultra-supercritical and heat recovery steam generator of gas turbine combined cycle systems. By use of both creep strength–enhanced low-alloyed steels, the high-temperature weld construction components could be made smart with thinner walls and easier manufacturing and fabrication. The understanding of material properties and applications such as fundamental aspects of metallurgy and fabrication/service technology of both new steels is essential for the modern power plant technology. The creep rupture strength of creep strength–enhanced low-alloyed steels is almost twice of that of T22, strongest among the conventional low-alloyed steels. This realizes the great reduction of wall thickness and diameter of tubes and pipes that fit the frequent start–stop cyclic operations of modern power plants. The relatively lower carbon content of both steels improves weldability to minimize the susceptibility of hydrogen assist cold cracking; however, there exists some risk of the occurrence of reheat cracking due to the high-strength material and grain coarsening and stress corrosion cracking. The reheat cracking resistance in the creep strength–enhanced low-alloyed steels is now suppressed by the minor modification of chemical compositions. And also the stress corrosion cracking problem should be solved by well-managed fabrication conditions and environment control. Presently the new creep strength–enhanced low-alloyed steels T23 and T24 have extensively been used worldwide to achieve great benefit to improve plant efficiency and economical construction of modern power plants.

References

[1] K. Baumann, U. Gramberg, VGB Kraftwergstechnik 57 (1977) 699.
[2] J. Orr, F.R. Beckitt, A. Met, G.D. Fawkes, in: Proceedings of BNES (British Nuclear Energy Society) Conference on Ferritic Steels for First Reactor Steam Generator, London, 1977.
[3] K.-H. Mayer, F. Masuyama, The development of creep resistant steels, in: F. Abe, T.-U. Kern, R. Viswanathan (Eds.), Creep Resistant Steels, Woodhead Publishing Ltd, Cambridge, UK, 2008.
[4] S. Paddea, F. Masuyama, A. Shibli, T23 and T24 – new generation low alloyed steels, in: A. Shibli (Ed.), Coal Power Plant Materials and Life Assessment, Developments and Applications, Woodhead Publishing Ltd, Cambridge, UK, 2014.
[5] T. Yukitoshi, H. Yuzawa, K. Yoshikawa, T. Daikoku, N. Tsuruta, F. Masuyama, Thermal and Nuclear Power 31 (1980) 34.
[6] K. Kinoshita, NKK Technical Report, 1964, p. 602.
[7] M. Ivenel, Revie Generule Term, 1964, p. 555.
[8] V.K. Sikka, C.T. Ward, K.C. Thomas, in: ASME Int. Conf. Production, Fabrication, Properties and Applications, Warrendale, PA, 1981.
[9] M. Sakakibara, H. Masumoto, T. Ogawa, T. Takahashi, T. Fujita, Thermal and Nuclear Power 38 (1987) 841.
[10] T. Hamaguchi, H. Okada, H. Semba, H. Hirata, A. Iseda, M. Yoshizawa, in: Proceedings 41st MPA-Seminar, October 5–6, 2015. [Stuttgart, Germany].

[11] G. Kalwa, K. Harrmann, J.K. Janssen, in: Topical Conf. Ferritic Alloys for Use in Nuclear Energy Tech., Metall. Soc, ASME, Snowbird, Utah, 1983.
[12] A. Iseda, H. Teranishi, K. Yoshikawa, F. Masuyama, T. Daikoku, H. Haneda, Thermal and Nuclear Power 39 (1988) 897.
[13] A. Iseda, Y. Sawaragi, S. Kato, F. Masuyama, in: Proc. 5th Int. Conf. Creep of Materials, Creep Characterization, Damage and Life Assessment, ASM Int, Metal Park, OH, 1992, p. 389.
[14] F. Masuyama, T. Yokoyama, Y. Sawaragi, A. Iseda, in: Proc. CSPF-JSME-ASME Int. Conf. Power Engineering, vol. 1, 1995, p. 1093. Shanghai, China, November 22–26, .
[15] W. Bendick, F. Destiayes, K. Haarmann, J.C. Villant, PWR Vol. 33, 1998 Int. Joint Power Generation Conf., vol. 2, ASME, 1998.
[16] Metals Handbook, nineth ed., Properties and Selection of Iron and Steels, vol. 1, 1987.
[17] R.G. Baker, J. Nutting, Iron and Steel Institute, July, 1959, p. 257.
[18] F. Deshayes, W. Bendick, K. Haarmann, J.C. Vaillant, in: J. Lecomte-Beckers et al. (Ed.), Materials for Advanced Power Engineering 1998, vol. 1, 1998, p. 1501.
[19] F. Masuyama, T. Yokoyama, Y. Sawaragi, A. Iseda, in: J. Lecomte-Beckers et al. (Ed.), Materials for Advanced Power Engineering, 1998, Part 1, 1994, p. 174.
[20] N. Komai, T. Imazato, F. Masuyama, ISIJ International 41 (Supplement) (2001) S91.
[21] F. Masuyama, T. Ypokoyama, Y. Sawaragi, A. Iseda, PVP Vol. 288, Service Experience and Reliability Improvement, Nuclear, Fossil, and Petrochemical Plants, ASME, 1994, p. 141.
[22] P. Navasamaa, J. Salonen, Welding in the World-Research Supplement 52 (2008) 68.
[23] J.G. Nawrocki, J.N. Dupont, A.R. Marder, Welding Journal 79 (2000) 355.
[24] N. Komai, F. Masuyama, T. Yokoyama, US Patent 5814274 (1988).
[25] J. Gabrel, W. Bendick, C. Zakine, B. Vandenberghe, in: PVP Vol. 9, 8th Int. Conf. on creep and Fatigue, CREEP-2007, 2007, p. 189.
[26] N. Komai, F. Masuyama, M. Igarashi, Trans. ASME, Journal of Pressure Vessel Technology 127 (2005) 190.
[27] N. Komai, F. Masuyama, in: Proc. EPRI Int. Conf. on Advances in Life Assessment and Optimization of Fossil Power Plants, Orland, FL, March 11–13, 2002.
[28] T. Murai, K. Arakkawa, K. Chiku, T. Shirane, F. Masuyama, in: 3rd Int. Conf. Advanced Structural Steels, 2006, p. 570.

High-alloyed martensitic steel grades for boilers in ultra-supercritical power plants

3

J. Hald
Technical University of Denmark, Kgs. Lyngby, Denmark

3.1 Introduction

Martensitic 9–12% Cr steels are used for the hottest parts in steam boilers, ie, main steam and hot reheat lines, outlet headers, and superheaters. Their high tensile and creep strength, good corrosion and oxidation resistance, high thermal conductivity, and low thermal expansion in combination with relatively low cost make them ideal for this application.

The creep strength of these alloys sets a physical limitation on the achievable thermal efficiency of steam power plants. This material property defines the maximum steam pressure and temperature at which highly stressed pressurized components can be designed with a wall thickness low enough to allow fast temperature changes during boiler start up and load changes.

The introduction of martensitic 12% CrMoV steels for thick-section boiler components enabled the construction of the first flexible supercritical power plants in the 1980s. The introduction of the creep strength–enhanced 9% Cr martensitic steels P91 and P92 in the 1990s and 2000s was the basis for the development of ultra-supercritical power plants with 600°C live steam temperature, which is state of the art today. The failure to develop microstructurally stable 12% Cr steels for steam temperatures higher than 600°C initiated the idea to introduce Ni-base alloys for 700°C A-USC power plants.

3.2 History of the high-alloyed martensitic steels

Historically, martensitic steels with 12% Cr have been used for their good corrosion resistance since the beginning of the last century [1]. Dedicated research on development of creep-resistant high-temperature steels was initiated in the 1920s mainly driven by (petro)chemical industry. It was initially believed that short-term tests of a few hundred hours could be used to determine a creep limit stress, from which

Materials for Ultra-Supercritical and Advanced Ultra-Supercritical Power Plants.
http://dx.doi.org/10.1016/B978-0-08-100552-1.00003-8
Copyright © 2017 Elsevier Ltd. All rights reserved.

strength values for design could be derived. However, this led to development of creep brittle materials, and a spectacular failure of CrNiMo bolts in 1937 forced the industry to reconsider the design basis for pressure equipment [2]. This led to the recognition that long-term creep testing is inevitable for safe qualification of creep strength values. Consequently, the industry established test facilities for long-term creep testing, which have formed the basis for all steel developments and qualifications since then [3].

The first development of a martensitic 9% Cr high temperature steel was described in 1936 by Newell from Babcock & Wilcox in the United States [4]. The aim was to develop an "intermediate" tube alloy to fill the gap between 18% Cr-8% Ni austenitic steels and 5% Cr steels in the refinery and chemical industries. Elements like V, W, and Mo were added to a 0.15% C-9% Cr steel, and creep tests were carried out by Professor Norton with his new device for long-term testing [5]. Mo addition proved to be the most economical way to improve creep strength, and the development resulted in a 9% Cr-1.5% Mo steel with creep strength and corrosion resistance between the 5% Cr and 18-8 steels [4]. This alloy is the forerunner for the 9Cr-1Mo tube and pipe alloy T/P9 later included in standards and applied for superheaters and boiler components.

The goal for development of the first 12% CrMoV steel for boiler and steam pipe applications in Germany around 1950 was to find a steel that could fill the gap between ferrite-pearlite low-alloy steels and 16–18% CrNi austenitic steels. Additions of carbide-forming elements W, Mo, and V to 13% CrMo steels led to the X20CrMoV121 composition, which was found to have high creep strength [6]. 12% CrMoV steels had previously been used for forged and cast components in steam turbines and jet engines, but since they could not to be welded without cracking, steam boiler application was not possible. Suitable weld procedures were developed in the mid-1950s, and the steel found wide application in power plants in continental Europe, where it was introduced from the early 1960s [7]. The creep strength of the X20CrMoV121 steel is doubled as compared to the low-alloy 2.25CrMo and ½CrMoV steels, and this enabled the construction of larger boilers, as well as of the first flexible supercritical boilers. In 1992 the limits for steam parameters with the steel was reached at the 400-MW boiler Esbjerg in Denmark, operating with live steam parameters of 250 bar and 560°C.

In Belgium the first Nb-alloyed tube steel EM12 was developed from 1955 on the basis of the 9Cr-1Mo steel [8]. The composition with 0.1% C, 9% Cr, 2% Mo, V, and Nb had a duplex microstructure of martensite and δ-ferrite. It was adapted in French standards and found application in superheaters from 1970 and onward.

In the 1970s, a strong focus on the development of nuclear power plants of the LMFBR type intensified the development of martensitic alloys of the 9Cr type, since they have low activation in radiation and good resistance to corrosion in liquid sodium. This led to development of the 9Cr-2Mo steel HCM9M by Sumitomo and Mitsubishi in Japan [9] and to initiation of a large development program in the United States in collaboration between ORNL and Combustion Engineering [10]. The US program gave a breakthrough with the steel Grade 91 or P91, which was a modification of the 9Cr-1Mo steel P9. Marked increases of the creep rupture strength were obtained by balanced additions of V and Nb combined with deliberate alloying with N, which was specified for the first time in a commercial martensitic creep-resistant steel [11].

After code approval by ASME in 1984 the steel found wide application in fossil power, where it laid the foundation for the first ultra-supercritical power plants. The world's first USC application was in 1988 in the 700-MW Kawagoe power plant in Japan with live steam parameters of 310 bar and 566°C, and the first USC application in Europe was in the 400-MW Skærbæk and Nordjylland power plants in Denmark, commissioned in 1997 and 1998 with live steam parameters of 280 bar and 580°C. With the P91 steel, large-scale application of martensitic steels in steam pipes and outlet headers of fossil power plants became widespread outside continental Europe.

In Japan a long-lasting activity to develop improved 9–12% Cr steels had been ongoing at Tokyo University since the early 1950s led by prof. T. Fujita. This resulted in the first boron-alloyed 10% Cr steel named TAF, which is still the strongest creep-resistant alloy in this class of materials. In 1986, Fujita published the first results on development of the boiler steel TB9, which was derived from the TAF steel [12]. By optimization of the Mo and W contents and addition of B to a steel quite similar to Grade 91, a 25% increase of the creep rupture strength was achieved. The steel was further developed in collaboration with Nippon Steel Corporation under the name NF616 [13,14]. Full qualification and standardization was achieved in international R&D projects led by EPRI [15], and in 1994 the steel was included in the ASME codes under the name Grade 92 or P92 for pipes. First use of the steel in a full-scale USC power plant was in the 400-MW Avedøre 2 in Denmark, which was commissioned in 2001 with live steam parameters of 290 bar and 580°C. P92 is currently the strongest commercially available steam pipe steel, and it has enabled the construction of several USC power plants with live steam parameters up to 300 bar and 600°C, and sizes up to more than 1 GW.

All of the successful creep strength–enhanced martensitic steels are modified 9% Cr steels. It was clear early on that Cr contents of 11–12 wt% would be necessary to obtain intrinsic protection against steam oxidation at temperatures significantly higher than 600°C. Attempts were made to develop 12% Cr steels, like the experimental NF12 [16] and the standardized steels P122 [15] and VM12 [17]. None of these steels could reach the strength of Grade 92, since the long-term creep strength of the 11–12% Cr steels collapsed to strength levels of Grade 91, Fig. 3.1. The failure to develop strong, stable high-Cr martensitic steels led to the idea that Ni-base alloys should be introduced to increase steam parameters to higher values than the 300 bar and 600°C.

3.3 Basic properties and fabrication

3.3.1 Chemical composition

Typical chemical composition and heat treatments of alloys discussed earlier is shown in Table 3.1. The gradual development toward more and more complicated alloy compositions is clear. It is also clear that the improvements of strength have mainly been achieved through minor alloy additions. All of the martensitic pressure vessel steels are normalized and tempered at relatively high tempering temperatures to achieve the best balance between strength and high toughness.

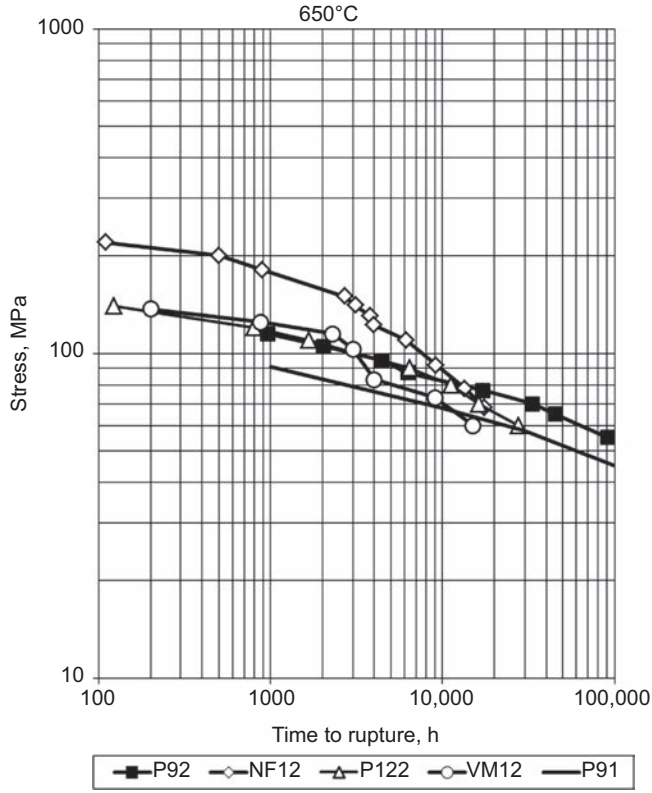


Figure 3.1 Creep rupture strength of P91, P92 and three 11–12% Cr steels at 650°C.

3.3.2 Physical properties

In Fig. 3.2, yield stress, thermal expansion, and thermal conductivity of the steels X20 and P92 are compared with the austenitic steel X8 CrNiMoNb 16 16 (X8). It is clear that even though the austenitic steels have superior creep strength, their low yield strength, high thermal expansion, and low thermal conductivity make them susceptible to thermal fatigue damage. Thus they cannot be used for thick-section components in thermal power plants.

3.3.3 Long-term mechanical properties

Long-term creep testing is needed to document the creep strength values of the alloys for use in pressure vessel design. Standards allow extrapolation by a factor of three in time from the longest creep rupture times of at least three heats of the material [18]. This means that creep tests up to 30,000 h (3.4 years) are needed to establish the 100,000 h mean strength values for pressure vessel design.

The comprehensive long-term testing effort for standardization is often shared between several laboratories to enlarge the databases. In Europe, this is done in

Table 3.1 Chemical compositions (mass%, bal. Fe) and typical heat treatments of 9–12% Cr steam pipe steels

Mass %	9Cr1Mo	X20	EM12	P91	P92	NF12	P122	VM12
C	0.11	0.2	0.11	0.1	0.1	0.09	0.1	0.12
Si	0.5	0.3	0.4	0.3	0.3	0.2	0.3	0.5
Mn	0.5	0.5	1	0.45	0.45	0.5	0.45	0.3
Cr	9	11	9.5	9	9	11	11	11.5
Mo	1	1	2	1	0.45	0.15	0.45	0.3
W					1.75	2.6	2	1.5
Ni		0.5		<0.2	<0.4	0.1	<0.5	0.25
Co						2.5		1.6
Cu							1	
V		0.3	0.3	0.2	0.2	0.2	0.25	0.25
Nb			0.4	0.08	0.06	0.06	0.07	0.06
N				0.05	0.05	0.07	0.07	0.05
B					0.003	0.004	0.003	0.005
Norm	950°C	1050°C	1100°C	1050°C	1065°C	1150°C	1050°C	1060°C
Temp	700°C	750°C	750°C	750°C	770°C	770°C	770°C	780°C

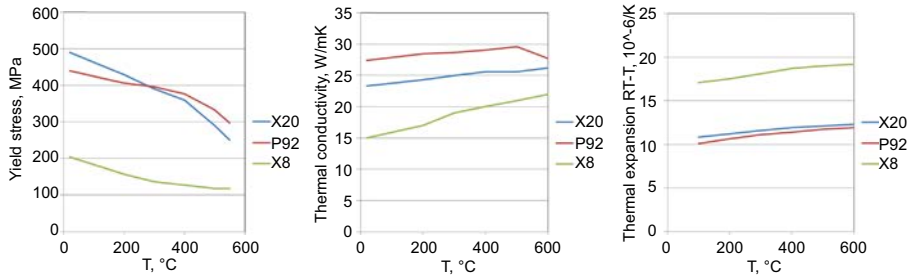


Figure 3.2 Yield strength, thermal conductivity, and thermal expansion of the martensitic 12% CrMoV steel X20, the martensitic 9% CrW steel P92, and the austenitic 16% Cr16Ni steel X8.

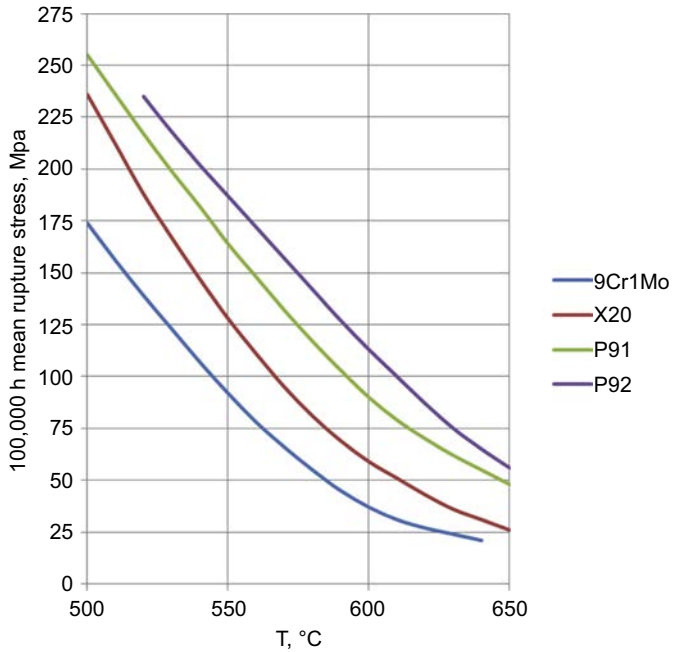


Figure 3.3 100,000 h mean rupture stress for commercial martensitic boiler and steam pipe steels according to ECCC.

the European Creep Collaborative Committee ECCC, which also performs the data assessments (extrapolation) to establish strength values [19].

Fig. 3.3 shows 100,000 h mean rupture strengths for the steam pipe alloys 9Cr1Mo, X20, P91, and P92 according to the most recent assessments by ECCC. All of these materials have now been tested to rupture times of more than 100,000 h (11.4 years) and show stable long-term creep behavior. As a good rule of thumb, 100,000 h mean rupture strength of 100 MPa is needed to enable the design of sufficiently thin components of ferritic/martensitic steels for flexible operation of USC power plants. It is seen that the materials development supports the increase of steam temperature from 540°C up to 620°C based on the improved creep rupture strength.

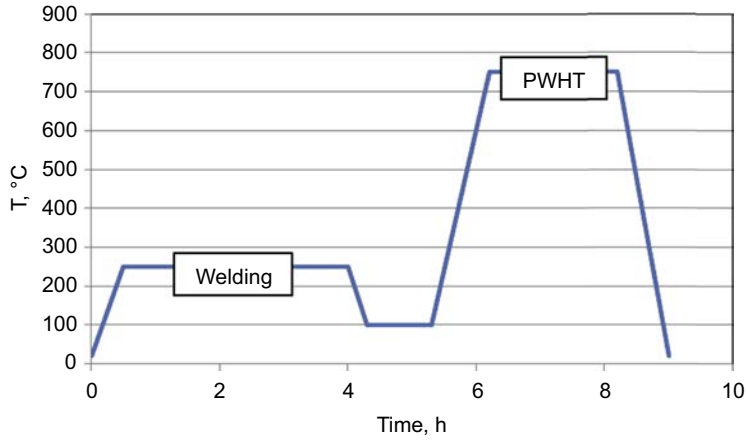


Figure 3.4 Temperatures during welding of martensitic 9–12% Cr steels.

3.3.4 Weldability and weld procedures

The martensitic steels were for long considered not to be weldable in thick sections. Since these steels air-harden to martensite, constrained welds in thick-section components may crack when cooled to room temperature either directly after welding or after post-weld heat treatment. This prevented the use of thick-section 12% CrMoV steels for steam pipes until the problem was solved for the steel X20CrMoV121 in 1957 [6]. The martensitic transformation of the X20 steel with 0.2wt%C takes place in the range Ms–Mf≈270°C–50°C upon air cooling of components with thicknesses up to ≈100 mm. By preheating to 250°C and keeping the interpass temperature above this level, martensitic transformation during welding can be prevented, and the martensitic transformation takes place during cooling after welding. It is important to cool below 150°C to transform >90% of the weld to martensite. Otherwise, untransformed martensite (austenite) can survive the post-weld heat treatment, and the martensitic transformation will take place during cooling after post-weld heat treatment with risk of crack formation. Typical temperatures during welding of martensitic 9–12% Cr steels are shown in Fig. 3.4.

When these precautions are followed the martensitic 9–12% Cr steels have good weldability for all generally used processes in boiler and steam pipe welding. Matching weld consumables have been developed, which provide good impact toughness and creep strength of weld metals.

3.3.4.1 Type IV cracking

Similar to the low-alloy ferritic steels, the intercritical heated part, or the fine-grain zone, in the heat-affected zone (HAZ) of welds in martensitic steels will lose creep strength as a result of welding [20]. Creep tests on cross-weld specimens of steels X20, P91, and P92 show that the martensitic steel welds can show considerable loss of strength compared to parent materials, depending on test temperatures and stresses.

This means that welds loaded with high stresses in the cross-weld direction will have shorter creep life than parent materials, and they will fail by creep damage development in the HAZ. This is known as type IV cracking. However, cross-weld stresses acting on circumferential welds in steam pipes are only 50% of the hoop stress, and such welds will only suffer Type IV cracking if they experience surplus cross-weld stresses, eg, by bending stresses induced from the pipe system (system stresses). Geometrically more complex welded components in steam pipe systems like T- or Y-joints or longitudinally welded pipes can experience higher cross-weld stresses and may be more prone to Type IV cracking than circumferential welds.

Creep damage development in welds can be followed by replica inspections, which provide ample time for repair or replacement of damaged welds and good control of Type IV cracking problems in power plants.

3.4 Service experiences

Service experience with low-alloyed steam pipe steels 14MoV63 (½Cr½Mo¼V), 13CrMo44 (1Cr½Mo), and 10CrMo910 (2¼Cr1Mo) have shown relatively high occurrence of Type IV cracking in up to 10% of all welds well before 100,000 h of plant operation [21].

The first installed steam pipes with steel X20CrMoV121 have now been in operation for more than 300,000 h at 535°C, and a number of supercritical plants have passed 150,000–200,000 h of operation at 540–560°C. Reviews of damage experience with the X20 steel have shown an exceptionally low occurrence of Type IV cracking for this steel, with many plants showing total absence of type IV cracking [22–24].

A number of reasons can be given for this behavior: The quality of pipe hanger systems has been improved compared to the older power stations with pipe systems made of low-alloyed steel, and more attention has been paid to the design of the pipe system to reduce system stresses. This has contributed to the suppression of type IV cracks. Also the fact that a stronger steel can be less sensitive to type IV cracking is of significance here [25].

The very low defect rate of welds means that the overall service performance of the X20CrMoV121 steel in steam pipes must be characterized as excellent. There have, however, been a few parent material problems with the steel caused by incorrect production heat treatments leading to low creep strength material in some components, in particular, in steam pipe bends [21].

Service experiences with steel Grade 91 have been more mixed. The first large-scale use of the material in Europe was a major replacement program for steam outlet headers in UK power plants in the early 1990s. After 50,000–80,000 operating hours at 560°C steam temperature, severe type IV cracking was observed in more than 10% of all welds in these headers. The occurrence of the cracking, mainly in header-stub welds, indicated that it was driven by internal pressure, Fig. 3.5. It was found that, in general, the parent materials delivered for the header replacement program contained a high concentration of Al, which led to low strength of the parent metals [26,27].



Figure 3.5 Type IV crack in a stub weld of a steel Grade 91 steam outlet header.

As a consequence the Al content in the steel specifications was reduced from originally 0.04 wt% to 0.02 wt%.

The Danish USC plants with steel Grade 91 have now been in operation up to more than 115,000 h, at 280 bar and 580°C, and regular inspections have so far revealed no type IV cracks.

The Danish Avedøre power plant with P92 steam lines has been operating under reduced steam temperature due to biomass firing. The longest operating experience with steel Grade 92 in steam pipes operating under USC steam conditions is in the three 660 MW units at the Torrevaldiga power plant in Italy, which opened in 2008 with steam conditions of 600°C and 250 bar.

3.5 Basic metallurgy and long-term microstructure stability

As seen from the Fe-Cr phase diagram, 0.1% C steels with up to 12% Cr can be fully transformed to austenite (γ) during heating to 1200–1400 K (≈900–1200°C), Fig. 3.6. Air cooling of 9–12% Cr steels with section thickness up to 100 mm will result in transformation to hard and brittle martensite, since Cr contents larger than 5–7% suppress bainite transformations due to interaction between Cr and carbon. A minimum of 9% Cr is added to the martensitic steels for oxidation resistance.

Several different alloying elements are added to the steels to achieve optimum properties. These elements will increase the stability range of either the austenite phase (γ) (Ni, Mn, Co, Cu, C, N) or the ferrite phase (α) (Cr, Si, Mo, W, V, Al, Nb, Ta, Ti, B). An improper balance between ferrite and austenite stabilizing elements may promote ferrite in the steels (often termed δ-ferrite). Steels with large contents of δ-ferrite may be prone to embrittlement due to formation of σ-phase or by spinodal decomposition of the matrix to form α-Cr (475°C embrittlement).

Thermodynamic equilibrium calculations usually provide accurate predictions of stable phases in the 9–12% Cr steels. However, they were found to be inaccurate for the prediction of δ-ferrite occurrence. This is because the steels solidify as ferrite,

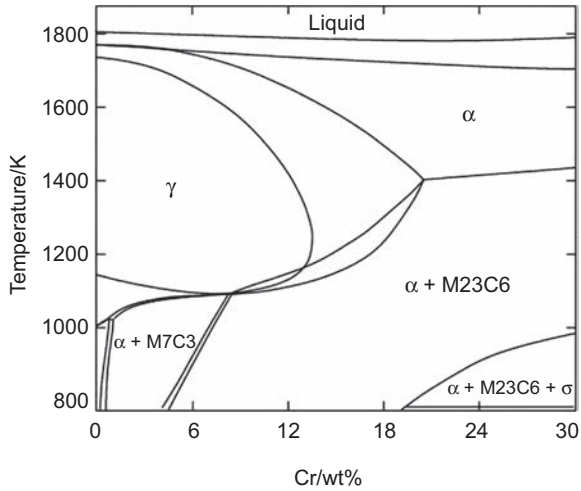


Figure 3.6 Phase diagram for Fe-Cr steels with 0.1 wt%C.

Fig. 3.6, and then, during cooling, δ-ferrite transforms into γ-austenite by a diffusion controlled growth process. This process can be slow, and thus δ-ferrite can remain in the steel at low temperatures as a nonequilibrium phase, Dissolution of δ-ferrite during consecutive normalizing is also a slow process, and this may leave δ-ferrite in the steel.

Since δ-ferrite is not necessarily an equilibrium phase, empirical formulas such as the one derived by Ryu and Yu [28] provide much more accurate predictions of the amount of δ-ferrite observed in 9–12% Cr steels:

$$Cr_{eq}(\%) = Cr + 0.8\,Si + 2\,Mo + 1\,W + 4\,V + 2\,Nb + 1.7\,Al + 60\,B + 2\,Ti + 1\,Ta - 2\,Ni - 0.4\,Mn - 0.6\,Co - 0.6\,Cu - 20\,N - 20\,C$$

Chemical composition should be entered in weight %. The Cr_{eq} should be <10% to avoid δ-ferrite and 100% δ-ferrite forms when $Cr_{eq} > 17.7\%$.

If $10\% < Cr_{eq} < 12\%$, the amount of δ-ferrite can be estimated from:

$$\text{Vol \% } \delta\text{-ferrite} = 340.34 - 71.75\,(Cr_{eq}) + 3.77(Cr_{eq})^2$$

The normal microstructure of the 9–12% Cr steels is tempered martensite formed during the final normalizing and tempering heat treatment. The tempered martensite consists of prior austenite grains separated by high-angle grain boundaries. Prior austenite grains are subdivided by high-angle boundaries into blocks of martensite laths [29]. After tempering the blocks consist of ferrite subgrains with an average width of 0.3–0.5 μm separated by low-angle boundaries. The dislocation density of the tempered martensite is high (in the order of $10^{14}\,m^{-2}$), Fig. 3.7.

Carbide and nitride particles precipitate in the steels during tempering, on prior austenite grain boundaries, block boundaries, and ferrite subgrain boundaries and on

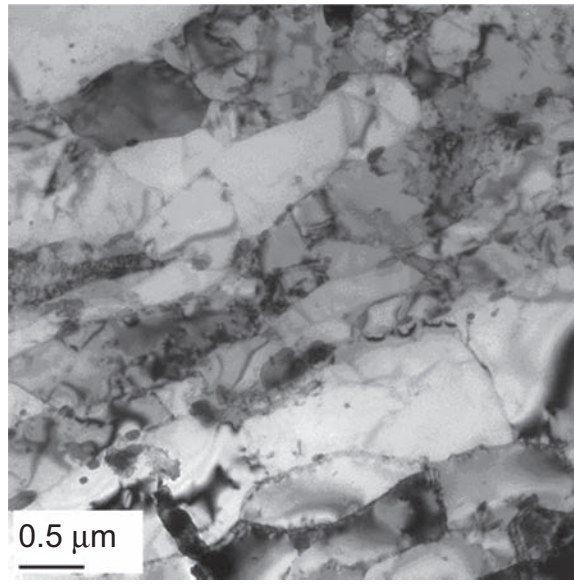


Figure 3.7 Steel P92. Tempered martensite microstructure as observed in transmission electron microscope.

dislocations inside subgrains. When the steels are put into operation in power plants at temperatures below the final tempering temperature, further particles may precipitate, which are thermodynamically unstable at the tempering temperature, eg, the intermetallic Laves phase.

3.5.1 Microstructure stability

Historically, it has often been assumed that for isothermal creep rupture tests a linear relation would exist between the logarithm of time to rupture and the logarithm of stress if the tested material was *metallurgically stable*. Inspections of creep rupture data for all technical high temperature steels show that none of these are metallurgically stable at relevant temperatures. It has been tried with some success to explain the deviations from linearity by a change in fracture mechanism from ductile fracture at shorter testing times to intergranular cavitation at longer testing times. Further explanations include changes in the controlling creep mechanism of the steel from dislocation creep to viscous creep.

The technically interesting stress and temperature ranges for creep testing and service exposure of the 9–12% Cr steels are 250–20 MPa at 500–700°C. Relevant loading conditions in this range will lead to rupture times between 100 and 300,000 h and minimum creep rates between $3 \cdot 10^{-6}$ and $5 \cdot 10^{-12} \cdot s^{-1}$. In the authors opinion, there are strong indications that the dominant creep mechanism in the whole of the technically relevant stress/temperature range is dislocation creep.

During creep the subgrains grow, and the dislocation density decreases with strain accumulation in a similar manner for all the 9–12% Cr steels [30]. It is then the ability

of a steel to *maintain* a small subgrain size and a high dislocation density for a long time at stress and temperature, which is significant to high creep strength. This indicates that microstructural explanations for the improved creep strength of the new 9–12% Cr steels should be found in mechanisms that retard the migration of dislocations and subgrain boundaries, and thus delay the accumulation of creep strain with time. Such mechanisms include (1) solid solution strengthening by formation of clouds of solute atoms around dislocations, and (2) interactions with precipitate particles.

Solid solution strengthening has often been referred to in discussions of the effect of Mo and W on creep strength of 9–12% Cr steels. It has long been clear that during creep exposure at temperatures around 600–650°C, most of the Mo and W in the steels will precipitate as intermetallic Laves phase ($(Fe,Cr)_2(Mo,W)$). The dominating opinion was that this would cause creep instability in the steels because the solid solution strengthening effect from Mo and W would be lost, and the precipitation strengthening effect from Laves phase was believed to be insignificant. This opinion seemed to be supported by the breakdown of long-term creep strength of some W-alloyed 9-11% Cr steels, and by the excellent long-term stability of Mo-alloyed 9% CrB steels (Mo causes less Laves phase precipitation than W). However, the excellent long-term stability of the W-alloyed 9% CrW steels P92 and MARBN seemed to contradict the opinion. Furthermore, experimental evidence to demonstrate significant solid solution strengthening from W in 9–12% Cr steels is sparse.

Precipitation hardening by pinning of dislocations and subgrain boundaries should be regarded as the most significant strengthening mechanism in 9–12% Cr steels, and microstructure stability of the 9–12% Cr steels under creep load is thus equivalent to precipitate stability. This is consistent with two findings: (1) the compositional changes, which have doubled the creep strength of the 9–12% Cr steels, have also resulted in clear changes in the precipitate populations, and (2) breakdowns in creep stability presented next can be explained by unexpected precipitate reactions.

The new 9–12% Cr steels contain several precipitate types, which form either during the final normalizing and tempering heat treatment or during subsequent creep, see Table 3.2.

3.5.2 Precipitate stability

Experimental measurements and models of particle size evolution of individual precipitate types have been used to evaluate the precipitate stability of a number of 9–12% Cr steels. Fig. 3.8 shows evaluations by measurements and modeling of the evolution in mean particle size of precipitates in steels P91 and P92 at 600°C [31]. In both steels the MX carbonitrides show a similar very high stability against coarsening. The $M_{23}C_6$ carbides show considerable coarsening in steel P91, whereas in steel P92 this carbide is highly stable; this is attributed to the presence of B in steel P92, which seems to improve the carbide coarsening stability.

Large differences are found between the Laves phase particle sizes in the two steels. After an initial growth phase of approximately 10,000 h, the Laves phase particles in steel P92 are more stable against coarsening than the $M_{23}C_6$ carbides in steel P91. In steel P91 the Laves phase particles grow to very large sizes during an extended growth phase, which lasts approximately 30,000 h. The observed differences in particle

Table 3.2 Main precipitates in some 9–12% Cr steels

Steel	Precipitate	Formula	Remark
12CrMoV	$M_{23}C_6$	$(Cr,Fe,Mo)_{23}C_6$	Precipitate during tempering
P91	$M_{23}C_6$	$(Cr,Fe,Mo)_{23}C_6$	Precipitate during tempering
	MX	(Nb,V)(N,C)	Undissolved during austenitization
	MX	(V,Nb)(N,C)	Precipitate during tempering
	Laves phase	$(Fe,Cr)_2Mo$	Precipitate during creep ($T<650°C$)
P92	$M_{23}C_6$	$(Cr,Fe,Mo,W)_{23}C_6$	Precipitate during tempering
	MX	(Nb,V)(N,C)	Undissolved during austenitization
	MX	(V,Nb)(N,C)	Precipitate during tempering
	Laves phase	$(Fe,Cr)_2(Mo,W)$	Precipitate during creep ($T<720°C$)

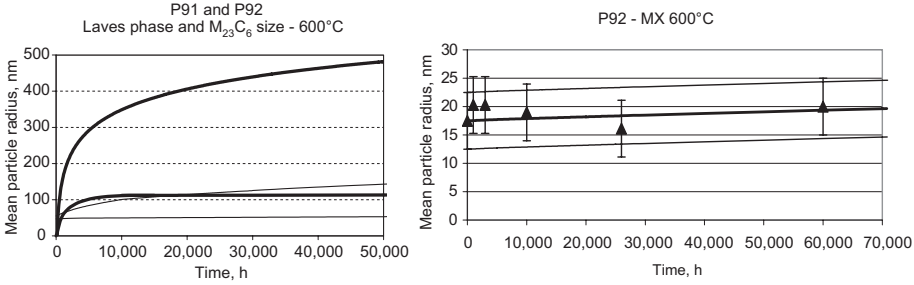


Figure 3.8 Left: Particle sizes of $M_{23}C_6$ (*thin lines*) and Laves phase (*thick lines*) in steels P91 and P92. Right: Size evolution of MX particles in steel P92. A similar MX evolution is observed in P91.

stability can explain the observed differences in creep rupture strength between the steels. The Laves phases in steel P92 produce a significant precipitate strengthening effect, which together with the observed high stability of the $M_{23}C_6$ carbides provide the high creep strength of this steel. The MX precipitates appear to be extremely stable against coarsening and could probably be characterized as the backbone of the long-term stability of the new 9–12% Cr steels.

3.6 Microstructure instability: Z-phase

All new 9–12% Cr creep-resistant steels developed in the last 35 years contain balanced additions of nitrogen (0.03–0.07 wt%) and nitride formers V (0.2–0.25 wt%) and Nb (0.05–0.07 wt%), which led to improved creep strength and excellent microstructure stability of 9–10% Cr steels.

However, it is now well understood that the Cr(V,Nb)N Z-phase nitrides are thermodynamically more stable than the (V,Nb)N nitrides, and that a nitride transformation from (V,Nb)N to Cr(V,Nb)N nitrides can take place in the 9–12% Cr steels. Since the Cr(V,Nb)N Z-phase nitrides can grow fast to very large (micron) sizes, the Z-phase transformation can lead to a significant loss of precipitation strengthening [32–35].

Systematic investigations of a large number of 9–12% Cr steels have revealed kinetics, driving forces, and transformation mechanisms for the Z-phase transformation [34–36]. It is clear that increased Cr content strongly accelerates the transformation. In 12% Cr steels, the transformation is often complete before 30,000 h at 600°C, whereas in a 9% Cr steel, it can take several 100,000 h. This explains the lack of success to develop a stable 12% Cr steel, which bases high creep strength on (V,Nb)N nitride precipitates.

Further, contents of Ni and Co accelerate Z-phase transformation [37–39], which means that a steel with 9% Cr and 3% Co can show complete Z-phase transformation after 30,000 h at 650°C [40,41].

A thermodynamic model of the Z-phase was developed based on experimental observations. It shows that Z-phase is a stable nitride in 9–12% Cr steels alloyed with conventional amounts of V, Nb, and N [36]. This means that it is the kinetics of the Z-phase precipitation that controls the microstructure stability of the steels. Calculations of driving force for Z-phase formation with the thermodynamic model were used to estimate the influence of individual alloying elements on Z-phase precipitation rate. They indicated a strong accelerating effect of Cr on Z-phase formation similar to experimental observations. Furthermore, the calculations indicated that an increase of the C content would delay the Z-phase formation, since C ties up Cr in carbides and thus reduces the amount of Cr available for Z-phase formation. Co accelerates Z-phase formation by an increase of the Cr activity in the steels matrix, whereas the accelerating effect of Ni is not well explained.

TTP diagrams for Z-phase formation in commercial 9–12% Cr steel grades were published by Sawada et al. in 2007 [35]. They confirmed the accelerating effect of Cr on Z-phase formation and indicated that the nose of the TTP diagrams lies at 650°C. More recent studies of TTP diagrams for 9Cr and 12Cr model alloys indicate that the nose moves to lower temperatures around 600°C for reduced Cr contents, Fig. 3.9 [42].

Microstructure studies of the formation mechanism of Z-phase have shown that the Z-phase does not nucleate on its own in martensitic steels. Instead, it forms by diffusion of Cr from the steel matrix into the MN particles [43]. This slowly transforms the MN particles into Z-phases [44], Fig. 3.10.

On the atomic scale, this transformation is seen as the formation of double atomic layers of Cr inside the MN cubic crystal. These Cr planes gradually transform the MN crystal into the tetragonal Z-phase crystal, Fig. 3.11.

The fact that Z-phase forms only from preexisting MN particles explains the sluggish nature of Z-phase precipitation in 9-12% CrVNbN steels. Furthermore, it explains the observations that when applying low tempering temperatures to martensitic steels, which result in the formation of hexagonal M_2N precipitates (mainly Cr_2N) rather than the cubic MN in the as-tempered steel, the Z-phase formation is significantly delayed

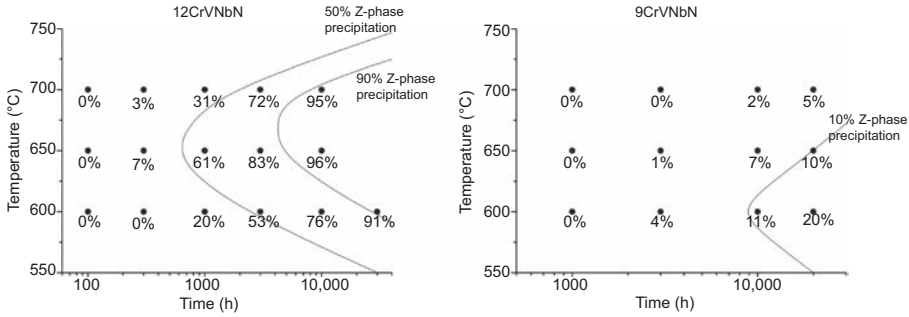


Figure 3.9 Relative amount of MN transformed to Z-phase in 12% CrNbVN and 9% CrNbVN model alloys [42].

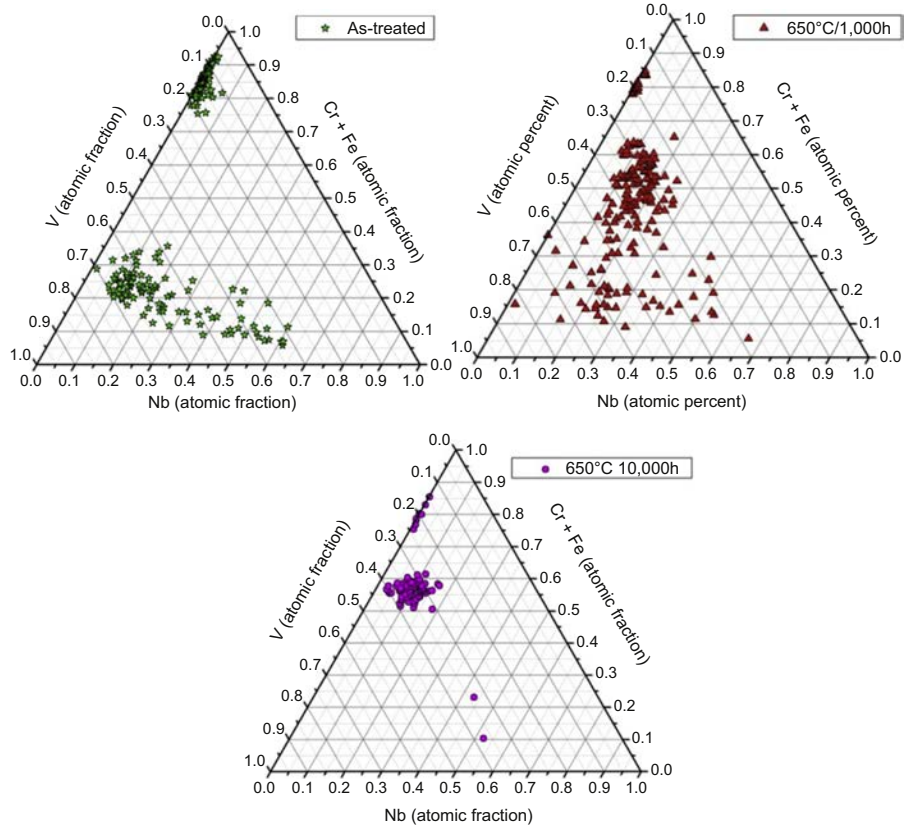


Figure 3.10 Evolution of chemical composition of Nitrides in a 12% CrVNbN alloy during aging up to 10,000 h at 650°C [44].

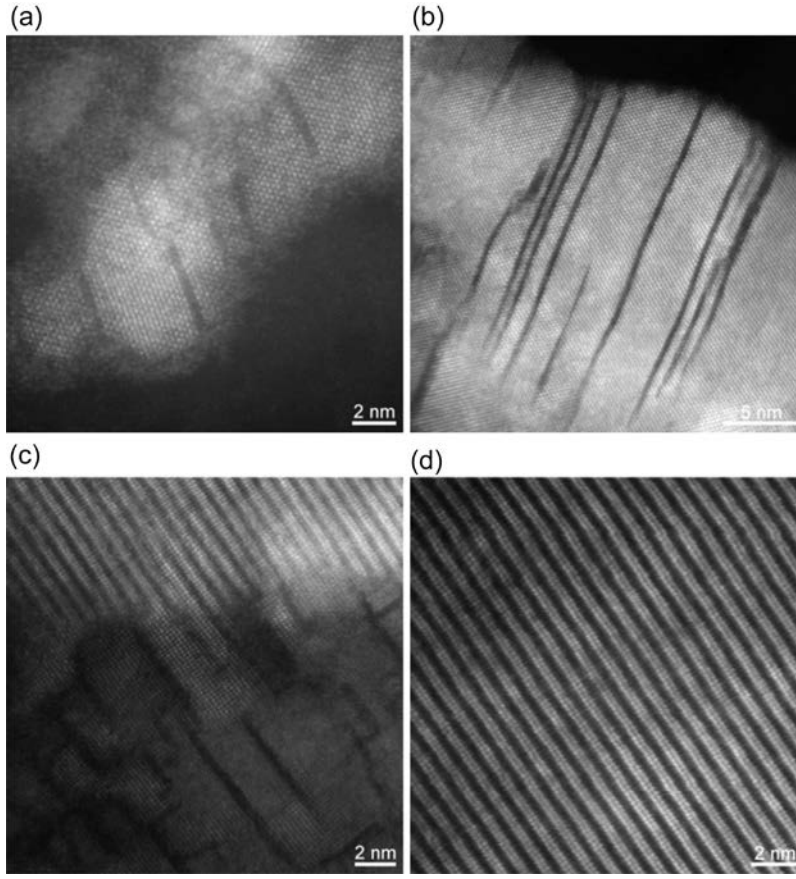


Figure 3.11 Atomic scale images of the transformation of a cubic TaN (a) into a tetragonal CrTaN Z-phase (d). Double atomic layers of Cr (*dark*) form in the MN crystal [45].

during creep. The M_2N needs to dissolve, and MN needs to precipitate before Z-phase can form by transformation of the MN particles.

Once a (V,Nb)N particle has transformed into a Cr(V,Nb)N Z-phase, it can grow relatively fast. Large Z-phase particles of 0.5 µm diameter were observed after 15,000 h at 650°C in 12% Cr steels [34] and after 30,000 h at 650°C in 9% Cr steels [46]. During growth the Z-phase consumes the fine MN particles.

3.7 Future perspectives

The Z-phase transformation effectively prevents the development of strong stable 11–12% Cr steels, which rely on precipitation of fine (V,Nb)N nitrides for high creep strength. This means that a development strategy for 11–12% Cr steels has to rely on

other precipitates than (V,Nb)N. This could involve either using the Z-phase itself as a strengthening agent or elimination of the Z-phase from the steels.

The formation mechanism for Z-phases is not traditional nucleation and growth like most other precipitate phases. Instead, the Z-phase forms only by diffusion of Cr into preexisting MN nitrides. Coarse Z-phases form by fast growth of fully transformed particles, including the consumption of other fine MN, which dissolve [43–45]. This understanding led to the idea that a strong acceleration of the Z-phase transformation could provide a fine distribution of Z-phase particles with high particle strengthening. Considerations indicated that Z-phase coarsening would be rather similar to MN [47].

Driving force calculations by thermodynamic modeling indicated that steels with low carbon content and high Cr content could show fast transformation of Nb- or Ta-based MN into Z-phase [36], and test alloys were designed, Table 3.3.

Experiences with the first test alloys of Z-phase strengthened steels revealed basic challenges:

- The steel should have high Cr and very low carbon content to form only nitrides, which can transform quickly into Z-phase.
- High Cr content and low carbon content will stabilize δ-ferrite.
- Elements, which suppress δ-ferrite (stabilize austenite), lower the Ac1 temperature.
- Low carbon removes Cr carbides from the steel. Thus, other precipitates should be added for strength.

Isothermal annealing experiments showed that CrTaN Z-phases were stable up to 10,000 h at 650°C, Fig. 3.12. NbN Z-phases were less stable. Increase of the carbon content in steel ZL3 led to slower Z-phase transformation and coarser Z-phase particles.

The low carbon content in Z-phase-forming steels means that no or only very small amounts of $M_{23}C_6$ carbides form in the steels. Instead, a high amount of W is added to form Laves phase $(Fe,Cr)_2W$ for precipitation hardening. However, in the Z4 steel the Laves phase precipitated in a continuous film along prior austenite grain boundaries during tempering. Consequently, this steel had very low impact toughness at room temperature. The ZL3 steel has lower W content and good impact toughness.

Creep tests on steel Z4 show strength similar to steel P92 up to more than 10,000 h, Fig. 3.12. The ZL3 steel with improved toughness shows lower strength between P91 and P92 due to slow Z-phase transformation and lower content of Laves phase. Ongoing research aims to optimize carbon, Co, and W contents in the steels. Results so far indicate that higher creep strength than for steel P92 can be achieved [48].

3.7.1 Nitride-free steel

Another option to design a strong, stable 12% Cr steel is to eliminate nitrides, which could transform into Z-phase. It is known that only V-, Nb-, or Ta-based MN nitrides can transform to Z-phase CrMN [49].

Belgorod State University in Russia designed a 10% Cr steel, which shows excellent creep stability up to more than 40,000 h at 650°C/120 MPa. The results indicate that this steel could reach the creep strength target of 100 MPa for 10^5 h at 650°C

Table 3.3 Chemical compositions of the first Z-phase strengthened steels

	wt%, bal. Fe											
	Cr	**C**	**B**	**Ta**	**Nb**	**N**	**W**	**Ni**	**Co**	**Cu**	**Mn**	**Si**
Z3	11.64	0.005	0.004	0	0.26	0.036	2.82	1.47	5.4	0	0.49	0.3
Z4	11.79	0.005	0.004	0.39	0	0.033	2.9	0.5	7.3	0	0.48	0.3
ZL3	12.1	0.06	0.0063	0.36	0	0.049	2.47	0.19	3.5	1.95	0.21	0.31

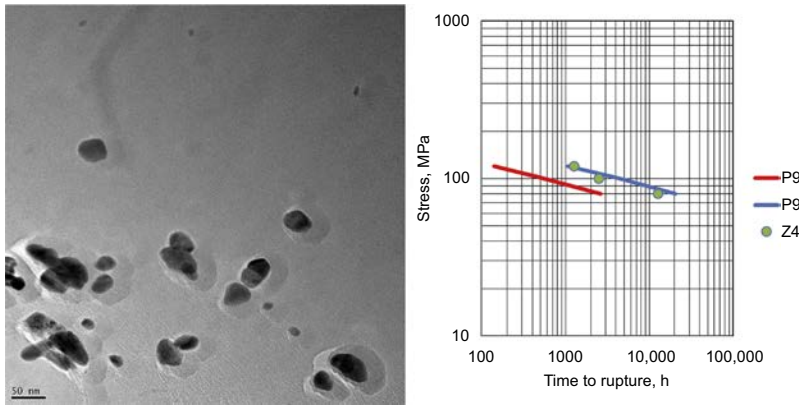


Figure 3.12 Fine CrTaN Z-phase particles in steel Z4 after aging 650°C/10,000 h (*left*) and creep rupture tests on steel Z4 at 650°C (*right*).

[50–52]. Alloy design is based on the TOS 110 steel earlier developed at Toshiba [53], but the composition has been altered with reduced nitrogen and addition of titanium. This means that TiN is the only nitride, which forms in the steel, and TiN cannot transform into Z-phase. Thus, the elimination of the Z-phase transformation could be an explanation for the excellent long-term microstructure stability of the steel. This means that it could be possible to increase the Cr content of such steels without introducing microstructure instability. Work is ongoing to design and test 11–12% Cr steels based on the ideas to eliminate nitrides, which could transform into Z-phase.

References

[1] H. Krainer, Technische Mitteilungen Krupp 20 (1962) 165–179.
[2] J. Ewald, W. Bendick, J. Granacher, K. Maile, B. Melzer, K.H. Mayer, et al., 50 Years of Joint German Activities in the Area of Creep Resistant Materials, 22. Vortragsveranstaltung AWS, 26, VDEh, Düsseldorf, November 1999, pp. 83–113.
[3] A. Thum, K. Richard, Archiv Für das Eisenhüttenwesen 28 (5–6) (1957) 1–13.
[4] H.D. Newell, Metal Progress (February 1936) 5–55.
[5] F.H. Norton, J.A. Fellows, Metal Progress (October 1933) 41–43.
[6] E. Kauhausen, P. Kaesmacher, Schweissen und Schneiden 9 (9) (1957) 414–419.
[7] H. Jesper, H.R. Kautz, Eigenschaften, Verabeitung und Bewährung des Stahles X20 CrMo(W)V 12 1 im Kraftwerk, V9, VGB-Werkstofftagung, Essen, 1985, pp. 274–316.
[8] M. Caubo, J. Mathonet, Revue de Métallurgie (May 1969) 345–360.
[9] T. Yukitoshi, K. Yoshikawa, T. Daikoku, F. Masuyama, Journal of Materials for Energy Systems 4 (2) (1982) 99–109.
[10] G.C. Bodine, R.E. McDonald, in: A.K. Khare (Ed.), Proc. Ferritic Steels for High Temperature Application, ASM, Metals Park Ohio, 1983, pp. 9–19.
[11] V.K. Sikka, C.T. Ward, K.C. Thomas, in: A.K. Khare (Ed.), Proc. Ferritic Steels for High Temperature Application, ASM, Metals Park Ohio, 1983, pp. 65–84.
[12] T. Fujita, Metal Progress (August 1986) 33–40.

[13] H. Masumoto, M. Sakakibara, H. Sakurai, T. Fujita, in: EPRI 1st Int. Conf. Improved Coal-Fired power plants, Palo Alto, 1986, pp. 203–218.
[14] H. Masumoto, H. Naoi, T. Takahashi, S. Akari, T. Ogawa, T. Fujita, in: EPRI 2nd Int. Conf. Improved Coal-Fired Power Plants, Palo Alto, 1988, pp. 3–10.
[15] E. Metcalfe (Ed.), New Steels for Advanced Plant up to 620°C EPRI/National Power Conference, London, May 1995.
[16] H. Naoi, M. Ohgami, H. Mimura, T. Fujita, Materials for Advanced power Engineering 1994, October 3–6, 1994, Liege.
[17] Vallourec VM12-SHC Technical-Datasheet.
[18] International Standard ISO 6303-1981 (E).
[19] http://eccc.c-s-m.it/.
[20] J. Hald, in: A. Strang, J. Cawley, G.W. Greenwood (Eds.), Proc. Conf. Microstructural Stability of Creep Resistant Alloys for High Temperature Plant Applications, Sheffield, 1997, The Institute of Materials, 1998, pp. 173–184.
[21] J. Hald, K.E. Poulsen, in: Proc. Conf. VGB-ESKOM International Materials Conference, 2000. Pretoria, South Africa, September 18–20.
[22] J. Storesund, K. Borggreen, Värmeforsk report M4-207, 2003, Stockholm.
[23] J. Storesund, K. Borggreen, W. Zang, H. Nilsson, Å. Samuelson, Värmeforsk report M4-306, 2004, Stockholm.
[24] S. Brett, S. Holmström, J. Hald, U. Borg, S. Aa Jensen, R. Van Vulpen, et al., Värmeforsk report M8-803, 2011, Stockholm.
[25] C.J. Middelton, in: Proc. Conf, "Power Plants of the 90's, IMechE, London, 1990.
[26] S.J. Brett, in: EPRI – 4th Int. Conf. on Advances in Materials Technology for Fossil Power Plants, South Carolina, October 25–28 2004.
[27] S.J. Brett, D.L. Oates, C. Johnson, in: ECCC Conference: Creep & fracture in high temperature components – design & Life Assessment Issues, IMechE, London, 2005. September 12–14.
[28] S.H. Ryu, J. Yu, Metallurgical and Materials Transactions A 29A (June 1998) 1573–1578.
[29] F. Abe, Current Opinion in Solid State and Materials Science 8 (2004) 305.
[30] S. Straub, Verformungsverhalten und Mikrostruktur warmfester martensitischer 12%-Chromstähle, 1995, 405, VDI Forschungsberichte 5, VDI Verlag, Düsseldorf.
[31] J. Hald, L. Korcakova, ISIJ International 43 (3) (2003) 420.
[32] E. Schnabel, P. Schwaab, H. Weber, Stahl und Eisen 107 (1987) 691–696.
[33] A. Strang, V. Vodarek, Materials Science and Technology 12 (1996) 552.
[34] H.K. Danielsen, J. Hald, Energy Material 1 (2006) 49.
[35] K. Sawada, H. Kushima, K. Kimura, M. Tabuchi, ISIJ International 47 (5) (2007) 733–739.
[36] H.K. Danielsen, J. Hald, Computer Coupling of Phase Diagrams and Thermochemistry 31 (4) (2007) 505–551.
[37] A. Strang, V. Vodarek, in: A. Strang et al. (Ed.), Microstructural Development and Stability in High Chromium Ferritic Power Plant Steels, 1, The Institute of Materials, London, 1997, pp. 31–52.
[38] L. Helis, Y. Toda, T. Hara, H. Miyazaki, F. Abe, in: 34th MPA Seminar, Stuttgart, Germany, 2008. 9.1–9.20.
[39] F. Kaufmann, G. Zies, K. Maile, S. Straub, K. H Mayer, in: 34th MPA Seminar, Stuttgart, Germany, 2008. 4.1–4.14.
[40] P. Mayr, I. Holzer, M. Albu, G. Kothleitner, H. Cerjak, S. M Allen, in: Proc. 6th International Conf. Advances in Materials Technology for Fossil Power Plants 2010, ASM International, 2011, pp. 640–653.

[41] P. Mayr, F. Méndez Martin, M. Albu, H. Cerjak, Materials at High Temperatures 27 (1) (2010) 67–72.
[42] H.K. Danielsen, P.E. Di Nunzio, J. Hald, Metallurgical and Materials Transactions A 44A (2013) 2445–2452.
[43] H.K. Danielsen, J. Hald, Materials Science and Engineering A 505 (2009) 169–177.
[44] L. Cipolla, H. K Danielsen, D. Venditti, P.E. Di Nunzio, J. Hald, M.A.J. Somers, Acta Materialia 58 (2010) 669–679.
[45] H.K. Danielsen, J. Hald, M.A.J. Somers, Scripta Materialia 66 (2012) 261–264.
[46] K. Sawada, H. Kushima, K. Kimura, ISIJ International 46 (5) (2006) 769–775.
[47] H.K. Danielsen, J. Hald, VGB powerTech 89 (2009) 68.
[48] European Union FP7 Project Z-Ultra (GA Nr 309916), (2013).
[49] H.K. Danielsen, J. Hald, Scripta Materialia 60 (2009) 811.
[50] N. Dudova, R. Kaibyshev, ISIJ International 51 (5) (2011) 826.
[51] N. Dudova, R. Mishnev, R. Kaibyshev, ISIJ International 51 (11) (2011) 1912.
[52] R. Mishnev, N. Dudova, R. Kaibyshev, in: Proc. 3rd International ECCC Conference Creep & Fracture 2014, Paper #66, Rome, 2014.
[53] Y. Tsuda, M. Yamada, R. Ishi, O. Wanatabe, M. Miyazaki, J. Lecompte-Beckers, et al., in: 6th Liége Conference. Materials for Advanced Power Engineering 1998, 1998, p. 331.

This page intentionally left blank

Austenitic steel grades for boilers in ultra-supercritical power plants

4

P. Barnard
Boiler R&D Centre, Doosan Babcock, Tipton, West Midlands, United Kingdom

4.1 Introduction

In any thermal power plant, cost, temperature, pressure, and environmental factors dictate the alloy selection through the plant. Second-order factors in alloy selection may include past experience, weld/fabricability, and availability. At low temperature and/or pressure, there is a large choice of materials, but as temperature and/or pressure increase, the alloy selection becomes more restricted. For high-temperature application, the main considerations are corrosion resistance (of which steam-side oxidation is the main corrosion), creep strength, and microstructural stability. In boiler applications the main protection against steam-side oxidation is the formation of a dense protective Cr_2O_3 oxide scale. This can be enhanced by increased Cr content of the alloy and/or enhanced Cr diffusion, eg, surface shot peening and use of fine-grained material. Microstructural stability of the austenitic alloys can be enhanced by the addition of austenite stabilizing elements and for creep strength either solid solution strengthening and/or second phase precipitates to restrict plastic deformation.

Although corrosion resistance and creep may be the main alloy selection criteria, component failure in service is often associated with mechanisms other than corrosion and/or creep. This chapter looks at some of these mechanisms that effect the use of austenitic steels in high-temperature pressure parts and some of the generic issues associated with this class of alloy. Also within this chapter, we will examine some of the main failure mechanisms associated with the fabrication of components and from operation.

If the reader requires more information on the history/evolution of stainless steels, they are referred to [1,2]. A good summary of austenitic alloys in power plants is given in reference [3].

4.2 Overview of austenitic steels

There is a range of austenite-forming matrices; most notably in the context of boiler alloys are the Fe-, Ni-, and Co-based alloys. In this chapter, when we refer to austenitics, we are only discussing those based upon Fe. The austenitic steels generally have compositions highlighted by the Schaeffler diagram, see Fig. 4.1 [4]. Although

Materials for Ultra-Supercritical and Advanced Ultra-Supercritical Power Plants.
http://dx.doi.org/10.1016/B978-0-08-100552-1.00004-X
Copyright © 2017 Elsevier Ltd. All rights reserved.

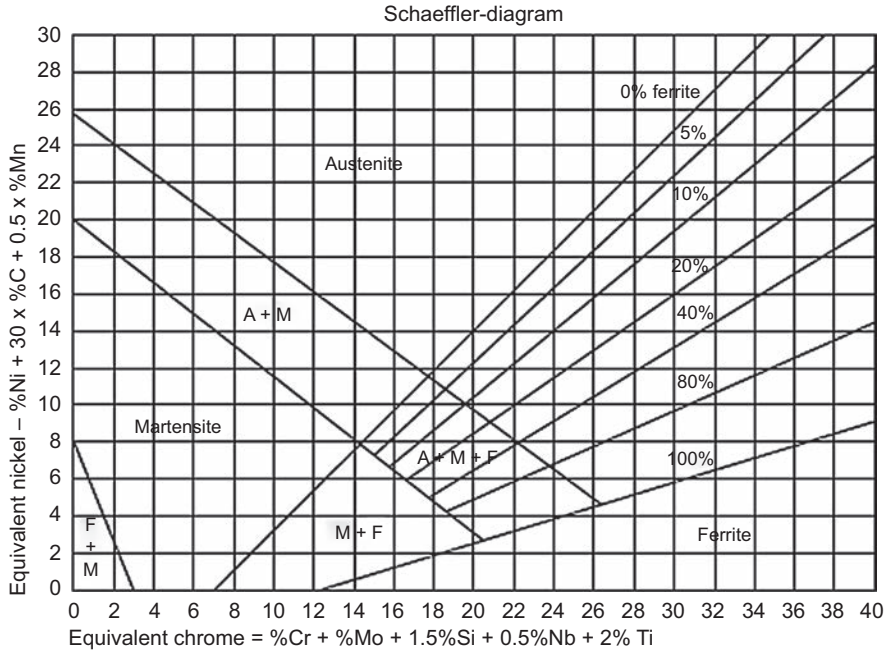


Figure 4.1 Schaeffler diagram for weld metal [4].

specifically for weld metal, this diagram gives an indication of the austenite stabilizing elements, on the vertical axis, and the ferrite stabilizing elements on the horizontal axis, which is relevant for wrought product as well.

A wide range of austenitic steels have been used for many years in boiler applications for tubing, ie, heat transfer surfaces, and for piping, ie, transport of fluid without heat transfer. A comparison of the creep performance of ferritic and austenitic steels and Ni-based alloys is given in Fig. 4.2. Steam-side oxidation resistance is often attributed to Cr content, as per Fig. 4.3.

Generally, austenitic steels are characterized by having good ductility, a low yield stress, and relatively high ultimate tensile strength compared to carbon steel. Other favorable characteristics are that welding has little effect on mechanical properties and normally post-weld heat treatment (PWHT) is not necessary, except where stress corrosion cracking may be an issue. Austenitic steels are not susceptible to hydrogen embrittlement, therefore in most cases, pre- and post-weld heating is also unnecessary.

Other than the cost of austenitic alloys, the main disadvantage for their use is the high coefficient of expansion and low thermal diffusivity, ie, thermal fatigue and high residual stresses in dissimilar metal welds (DMW). Other considerations include alloy sensitization, stress corrosion cracking, stress relief cracking, secondary hardening, and strain-induced precipitation hardening (SIPH). For the rest of this chapter, we will examine some of these disadvantages to see how they manifest themselves in service or during component manufacture.

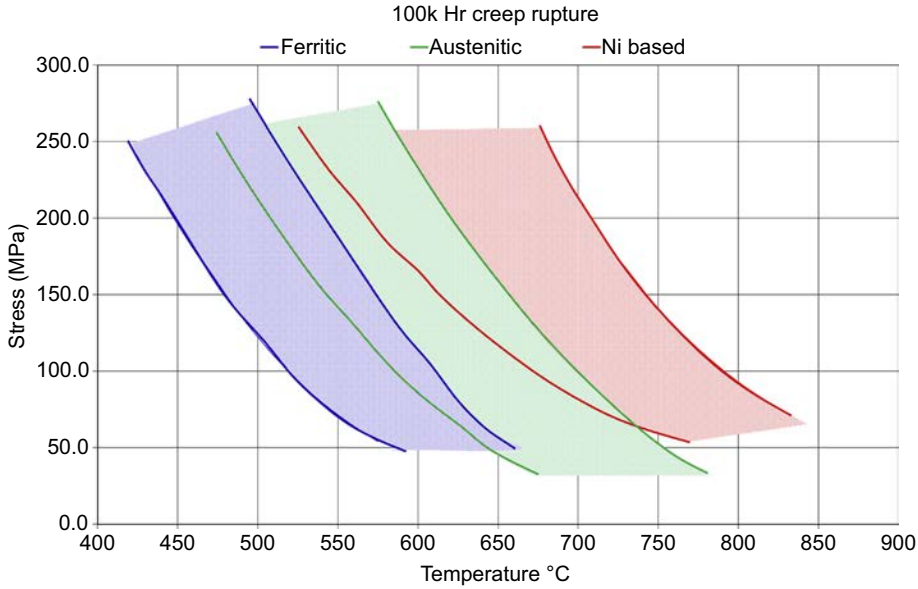


Figure 4.2 Envelopes of 100,000 h creep rupture for the three main alloy classes. Compiled from literature and internal Doosan data.

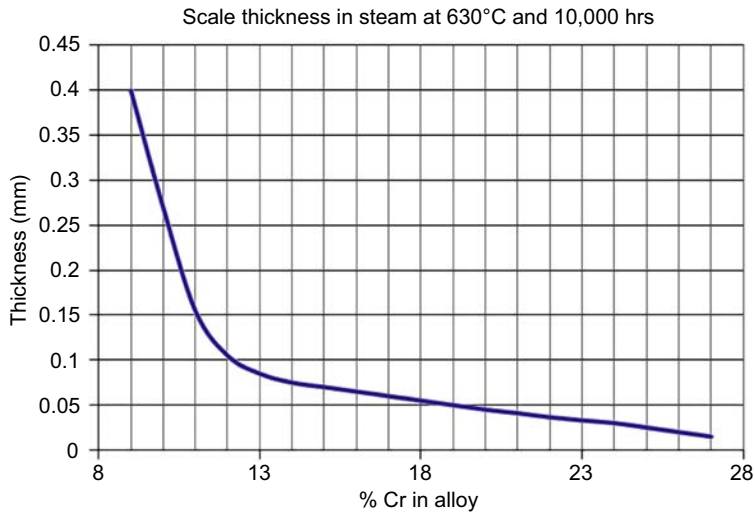


Figure 4.3 Generic plot of oxidation versus the Cr content of the alloy. Compiled from literature and internal Doosan data.

4.3 Thermal fatigue

Thermal fatigue is driven by thermally induced stresses arriving from thermal cycles during operation. These induced stresses are a function of $\alpha\Delta T$, ie, the product of coefficient of thermal expansion, α, and the temperature differential, ΔT. ΔT is composed of two parts: the globe temperature differential, ie, boiler operating temperature, and local temperature differential within the component, eg, through wall temperature gradient, which is a function of the thermal conductivity, k, of the material. Typical values for the three classes of materials are given in Table 4.1.

In the use of austenitic steels in areas of little constraint, eg, superheater (SH) or reheater (RH) tubing, there is little chance of thermal fatigue. In these types of components the expansion is allowed without constraint, and the wall thickness, typically 6–9 mm, offers limited ΔT. Even where these components are joined to a ferritic alloy, the stresses across the DMW are sufficiently small not to induce thermal fatigue.

Although thermal fatigue is more of a consideration for thick-section components, even for thin sections where high ΔT is a function of operation, thermal fatigue may be a significant issue. An example of this would be soot blowers where low-temperature steam is sprayed periodically on furnace walls or tube banks to induce spallation of ash deposits. The soot blowers themselves sit within the main gas path, thereby experiencing considerable ΔT, which often leads to the typical mud crack appearance of the blower inner surface, as shown in Fig. 4.4. These surface cracks often act as stress-relieving cracks and become none propagating, but as shown in Fig. 4.4, through-wall cracks can occur in extreme circumstances. Fig. 4.4 also shows the classic uniform depth of none propagating thermal fatigue cracks and that the crack propagation is mixed mode, ie, intragranular and intergranular.

Examples of thermal fatigue in thick sections are rare since very few components made from austenitic alloys have entered service. One example was the use of 316H for the main steam line (228.6 mm OD × 63.5 mm WT) for Eddystone Unit 1 designed for operation at 654°C and 36.5 MPa [3]. It is reported that a combination of thermal fatigue cracking in the thick-section 316H main steam line and fireside corrosion of the superheater tubes led to the unit being downgraded to 632°C and 31 MPa. In Masuyama et al.'s publication on the failure investigation [5] the cause of the main steam line failure after 130,520 h was attributed to a combination of creep and thermal fatigue.

Table 4.1 Comparison of typical thermal properties relating to thermal fatigue

Material type	Thermal conductivity	Coefficient of thermal expansion
Ferritic steel	High (~50W/m°C)	Low (~11×10^{-6})
Austenitic steel	Low (~16W/m°C)	High (~18×10^{-6})
Nickel alloy	Moderate (~24W/m°C)	Moderate (~14.7×10^{-6})

Compiled from literature and internal Doosan data.

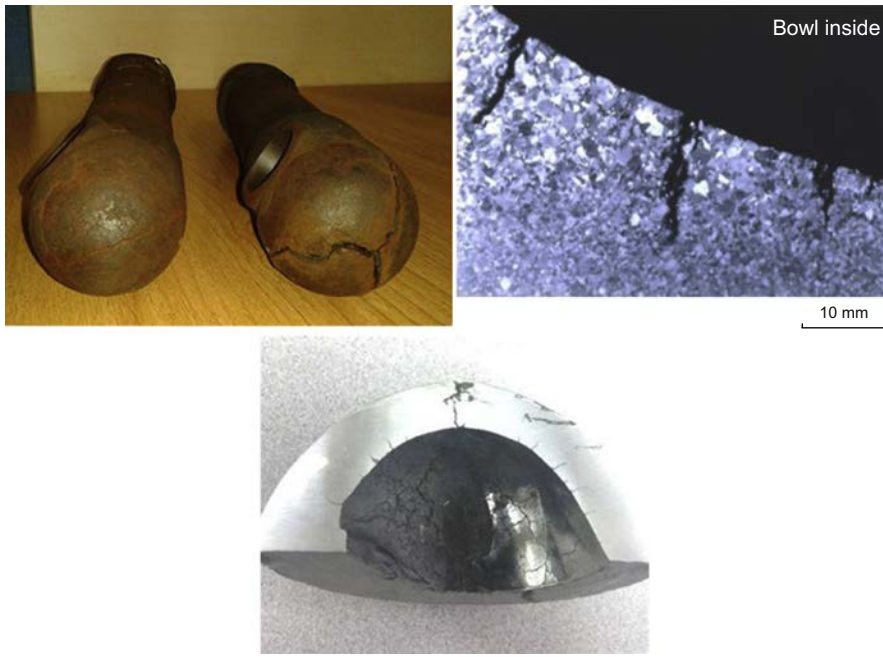


Figure 4.4 Thermal fatigue of a cast wall blower; top left shows the end of blower with through-wall cracking; lower shows a section through the end showing the "mud" cracked inner surface; top right shows close-up of the inner surface cracks.

4.4 Sensitization

All alloys are effectively a matrix with various chemical elements in solution. The solubility of these elements changes with temperature, which can lead to some elements coming out of solution to produce additional phases. As temperature reduces from the liquidus, more and more elements come out of solution, increasing the number of additional phase particles. For particles to form and/or have appreciable size, there may be a need for the insoluble elements to diffuse through the matrix. The diffusion rate of these insoluble elements slowly reduces with temperature.

For the austenitic steels, when held at a temperature c. 450–750°C, carbon comes out of solution, and the diffusion rates are sufficient for chromium carbide precipitation at the grain boundaries. For the chromium carbide to precipitate, chromium from the surrounding matrix diffuses to the grain boundary, leading to a chromium-depleted zone around the grain boundaries, as shown in Fig. 4.5, reproduced from references [6,7]. These chromium-deleted regions are less protected against environmental corrosion/oxidation so are sensitive to grain boundary corrosion: the steel has become sensitized to environmental attack [8,9]. Sensitization is therefore a process where regions within the grain, close to the grain boundaries, have significantly reduced corrosion resitance.

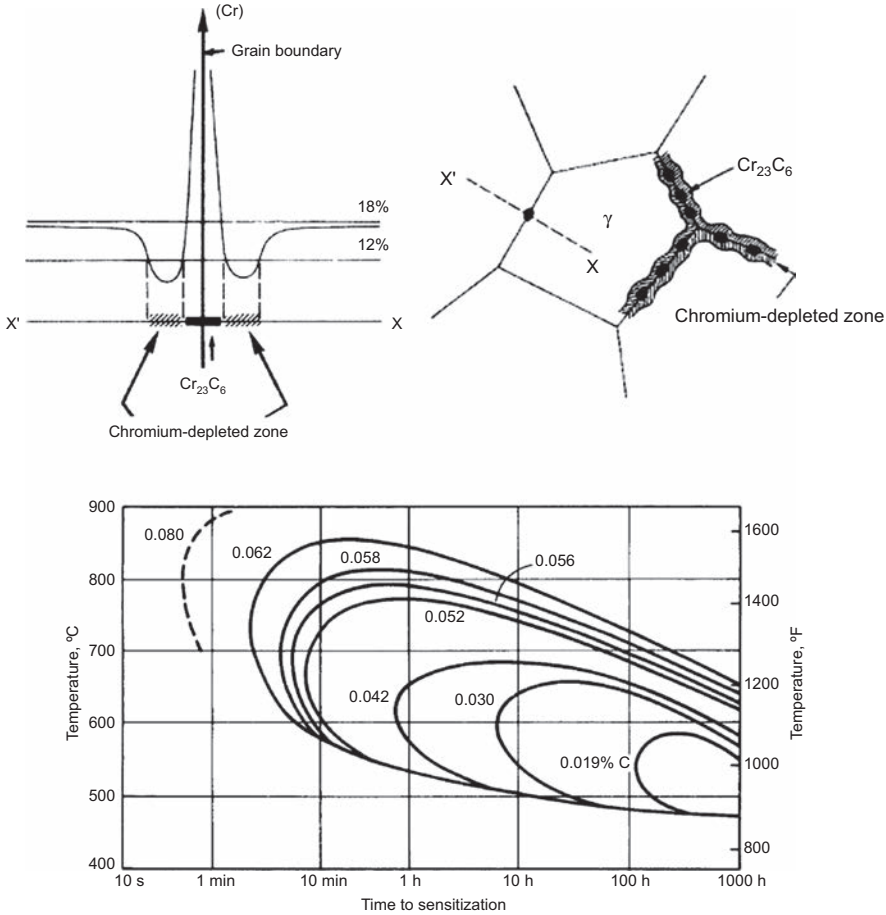


Figure 4.5 Cr depletion at grain boundaries leading to sensitization. Top images show the mechanism, and the lower image shows rate of sensitization for a particular alloy.
Top images reproduced from reference F. Masuyama, et al., Findings on creep-fatigue damage in pressure parts of long-term service-exposed thermal power plants, Journal of Pressure Vessel Technology, ASME, 107 (1985) 260; and the bottom image reproduced from reference M. McGuire, Stainless steels for design engineers, Austenitic Stainless Steel, ASM, (2008), (Chapter 6), with permission from ASM.

Sensitization is a through-thickness effect, so once corrosion attack has started, it is progressive with the grain boundaries being corroded, grains becoming isolated, and becoming detached from the surface. This effect is similar to metal dusting, although the mechanism of grain boundary corrosion is different. Sensitization not only occurs during service but also during any thermal treatment, eg, during welding or annealing after cold-working [10]. During welding, as you move away from the fusion line, regions of the parent metal will experience the temperature where sensitization can occur. Similarly, after cold work using localized heating pads for re-solutioning, some

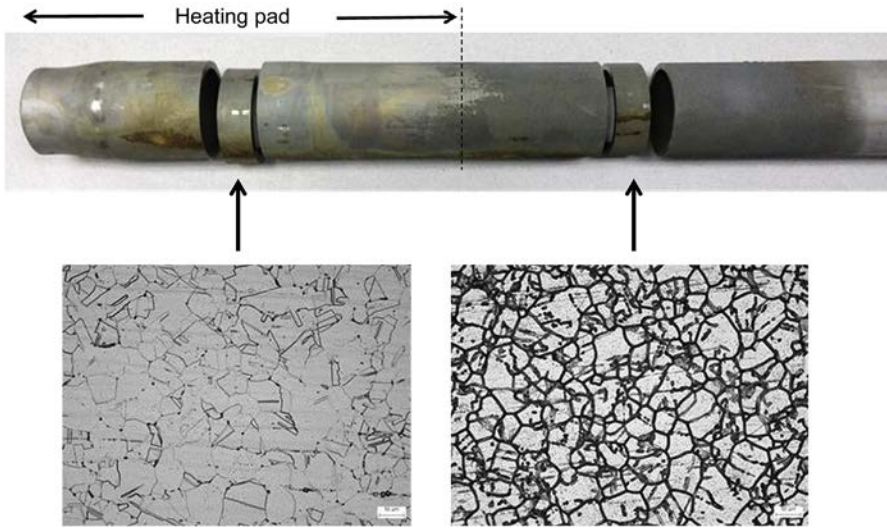


Figure 4.6 Swagged SA-213 TP304H tube after re-solutioning at 1070°C for 18 min. Bottom left shows a re-solutioned microstructure and bottom right carbide-decorated grain boundaries.

regions outside the pads will be exposed to this critical temperature, effectively forming a defective part; an example of this is given in Fig. 4.6.

The main mechanism to reduce sensitization is to reduce the formation of chromium carbides. This can be achieved by a reduction of the carbon content or the addition of carbide forming elements, eg, niobium and titanium, which form carbides in preference to the chromium, or the reduction in the time spent in the critical temperature range. The importance of carbide formers can be seen in the composition of the main austenitic steels used in boiler applications; see Table 4.2. Most of these alloys have between 0.04 and 0.1C, which from the lower image in Fig. 4.5 would lead to sensitization within minutes at the critical temperature. Many of these alloys listed in Table 4.2 specify significant additions of Nb and/or Ti, which are carbide formers in preference to Cr.

4.5 Strain-induced precipitation hardening

Cold-forming is an efficient way to produce pipe bends because of the low cost of production, limited time requirements to produce the bends, and because multiple bends are possible during cold-forming. Where the bending is kept within code or code case allowables, then subsequent post-bend heat treatment (PBHT) is not mandated [11]. Where PBHT is mandated by the code, or by company internal procedure, the cold-formed material should be annealed above the AC_1 temperature. Where the whole component cannot undergo PBHT, eg, on site, then the sub-solvus annealed material outside the heating pads may have reduced creep strength [12].

Table 4.2 Composition of typical austenitic steels used in boiler application

Material	C	Si	Mn	Cr	Ni	Mo	V	Nb
SAVE 12[a]	0.01	0.3	0.2	11			0.2	0.07
A286	0.08 max	1.0 max	2.0 max	13.5–16.0	24.0–27.0	1.0–1.5	0.10–0.50	
Esshete 1250	0.06–0.15	0.20–1.00	5.50–7.00	14.0–16.0	9.0–11.0	0.80–1.20	0.15–0.40	0.75–1.25
TP316	0.08 max	1.00 max	2.00 max	16.0–18.0	10.0–14.0	2.00–3.00		
TP316H	0.04–0.10	1.00 max	2.00 max	16.0–18.0	10.0–14.0	2.00–3.00		
TP316L	0.03 max	1.0 max	2.0 max	16.0–18.0	10.0–14.0	2.00–3.00		
Super 304H	0.07–0.13	0.3 max	1.0 max	17.0–19.0	7.5–10.5			
TP321	0.08 max	0.75 max	2.0 max	17.0–19.0	9.0–12.0			
TP321H	0.04 min	1.00 max	2.00 max	17.0–19.0	9.0–12.0			
TP347	0.08 max	1.00 max	2.00 max	17.0–19.0	9.0–13.0			10×%C
TP347H	0.04 min	1.00 max	2.00 max	17.0–19.0	9.0–13.0			
TP347HFG	0.04–0.10	0.75 max	2.00 max	17.0–20.0	9.0–13.0			8×%C
TP304	0.08 max	1.00 max	2.00 max	18.0–20.0	8.0–12.0			
TP304H	0.04 min	1.00 max	2.00 max	18.0–20.0	8.0–12.0			
Alloy 800H	0.05–0.10	0.7 max	1.50 max	19.0–22.0	30.0–34.0			
NF709	0.04–0.10	0.75 max	1.50 max	19.0–22.0	23.0–27.0	1.00–2.00		0.10–0.40
SANICRO 25	0.04–0.10	0.40 max	0.60 max	21.5–23.5	23.5–26.5			0.40–0.60
SAVE 25[a]	0.1	0.1	1	23	18			0.45
HR3C	0.04–0.10	0.75 max	2.00 max	24.0–26.0	17.0–23.0			0.20–0.60
TP310NbN (HR3C)	0.04–0.10	0.75 max	2.00 max	24.0–26.0	17.0–23.0			0.20–0.60
SANICRO28	0.02 max	0.6 max	2.0 max	26.0–28.0	29.5–32.5	3.0–4.0		

[a]Nominal values.
Compiled from literature and internal Doosan data.

Ti	Al	W	Co	N	B	Cu	P	S	Others
		3	3	0.04					Ta 0.07; Nd 0.04
1.90–2.35	0.35 max				0.001–0.01 0.003–0.006			0.030 max	
	0.001–0.03			0.05–0.12	0.001–0.010	2.5–3.5			
5×%C–0.60 5×%C				0.10 max			0.045 max	0.030 max	
0.25–0.65	0.25–0.65		0.5 max	0.03 max		0.50 max	0.015 max	0.010 max	(Ni+Co) 30.0–34.0
0.02–0.20				0.10–0.20	0.002–0.004				
		3.0–4.0	1.0–2.0	0.20–0.30	0.002–0.008	2.5–3.5	0.025 max	0.015 max	
		1.5		0.2		3			
				0.15–0.30					
				0.15–0.30					
						0.5–1.5	0.025 max	0.010 max	

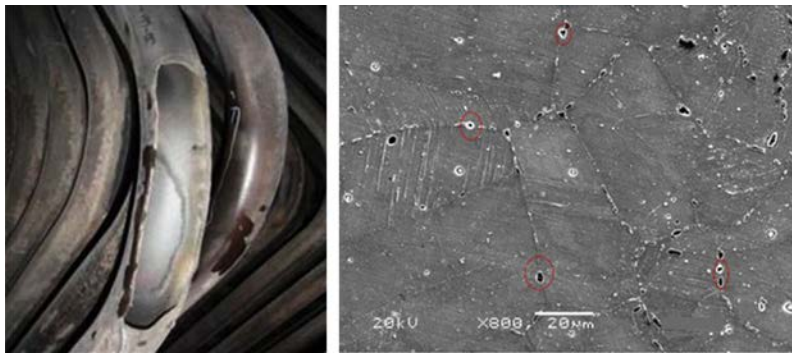


Figure 4.7 SIPH failure in RH tubing. Left, macroscopic view; right, void formation at grain boundaries.

The mechanism for SIPH is effectively precipitation of particles at dislocations, twin boundaries, and stacking faults induced by the cold work. This precipitation leads to an increase in hardness and reduction in ductility [13,14], with ductility being defined as strain to failure. These fine precipitates are a combination of carbides, nitrides, and carbonitrides, designated MX (M, metallic atom and X, non-metallic atom) precipitates [15]. The work of van Wortel on relaxation cracking [16] demonstrated that this effectively produced a high yield stress intragranular region and a denuded low yield stress grain boundary region, where the precipitates had been adsorbed into the grain boundary carbides. This means that all the creep deformation is restricted to a narrow zone along the grain boundary, which although it may be very ductile gives a low ductile global failure due to the small volume fraction of the denuded zone.

The ASME Code defined strain before PBHT is mandated in an attempt to restrict the number of dislocations, twin boundaries, and stacking faults and hence the number of MX precipitates. Other ways to reduce the susceptibility of SIPH is alloy selection (Moody [15] and Van Wortel [16] show that some austenitic steels are less sensitive) or over-aging of the MX particles to coarsen the particles and increase the particle spacing [16,17], ie, easier dislocation movement.

Even keeping to the ASME Code allowables, there is no guarantee of eliminating the sensitivity to SIPH; see, for example, Fig. 4.7. In this example, we have SIPH on the extrados of TP347H RH tubing operating at a metal temperature of ca. 635°C. The strain after bending was c. 14.7%, ie, below the 15% allowable [11], therefore no PBHT was performed. SIPH is probably the number one cause of tube failure within the superheater and reheater regions of the boiler, followed by failure of the creep weak region generated by the sub-solvus annealed material mentioned in the first paragraph of this section.

4.6 Sigma-phase precipitation

There are a number of intermetallic phases that can precipitate in austenitic stainless steels, most notable being chi and sigma. These incoherent phases tend to form within delta ferrite and/or at grain boundaries [18,19] and can be prevalent in alloys

that contain additions of molybdenum, titanium, and niobium (Types 316, 321, and 347). Sigma is a chromium-rich phase (Fe_2Cr) that is very hard and brittle and can significantly reduce toughness and ductility [20]. Sigma forms most rapidly at approximately 800°C, but generally in the range of 650–950°C. The initiation of sigma formation is likely to be very sluggish in fully austenitic steel but will form more rapidly when ferrite is present since ferrite is chromium-rich [18].

There is still debate regarding the formation of sigma since for different alloys sigma can evolve from the chi (χ) phase [18], in carbon-depleted regions around $M_{23}C_6$, in nitrogen depleted regions around Cr_2N [21], from delta ferrite due to their high-volume fractions of Cr and Mo [19]. Most likely, there is no single mechanism, and all initiation sites may be simultaneously active [22], but Cr appears the common factor. For boiler applications, chi and/or sigma-phase embrittlement is a problem of service aging where service temperatures move above c. 650°C. Care is needed to ensure forging operations are above 1000°C to prevent rapid formation of these intermetallic phases [23]. Fig. 4.8 shows an example of grain boundary sigma-phase precipitation in 347 H after aging at 700°C for ca. 15,000 h.

An alloy's equivalent chromium content, Cr_{eq}, is given by

$$Cr_{eq} = Cr + 0.31Mn + 1.76Mo + 0.97W + 2.02V + 1.58Si + 2.4Ti + 1.76Nb + 1.22Ta - 0.226Ni - 0.177Co$$

If the Cr_{eq} value is greater than 17–18 wt%, there is a strong tendency for sigma phase formation [24]. Selecting an alloy for operation within the 650–950°C temperature range, the composition and sensitivity to sigma phase formation needs to be considered. It should also be noted that since sigma phase can form from $M_{23}C_6$ and these are induced by SIPH, it follows that sigma phase initiates more rapidly where the material has been cold worked.

Weld repair of sigma-phase embrittled material can cause significant problems, namely cracking, from the toe of the weld or close to the fusion line due to a combination of low ductility and solidification strains from the weld. Apart from replacement the only solution is to re-solution the material in the weld region to dissolve the sigma phase, after which conventional welding procedures can be used.

4.7 Stress corrosion cracking

Stress corrosion cracking (SCC) of austenitic alloys has been the subject of many publications; reasonable overviews of SCC initiation and crack growth are given in [25,26]. Generally, SCC is a low-temperature effect where there is accelerated corrosion of the grain boundaries, eg, after sensitization where the regions around the Cr carbides are denuded of Cr. Operating temperatures are usually too low for diffusion rates of Cr replenishment to be of significance. Generally, austenitic materials tend not to be susceptible to SCC in boiler environments because high-temperature service ensures Cr diffusion can reduce the effects of Cr depletion due to carbide formation. Where SCC may become active is during shutdowns with chloride species condensing out and attacking the passivation layer. The use of "stabilized" steels, ie, additions of

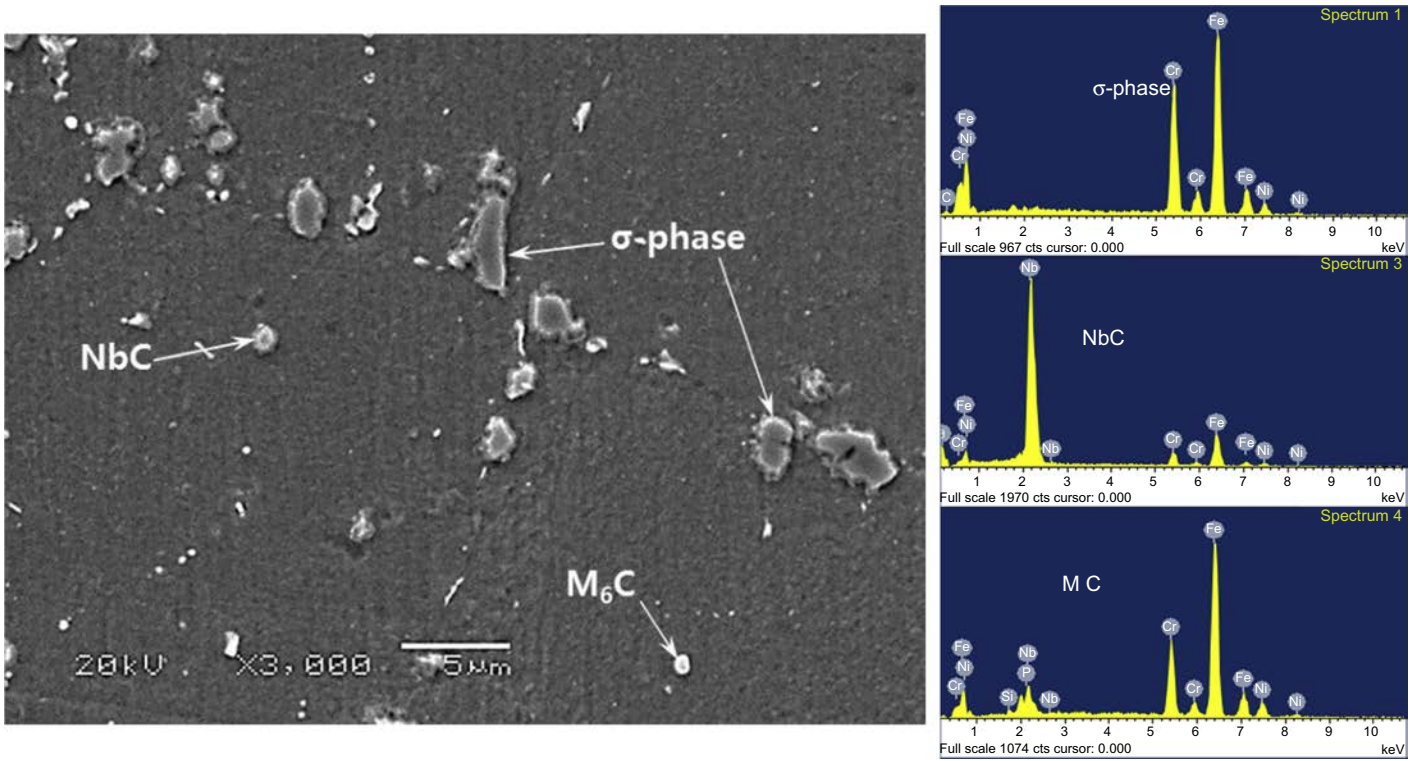


Figure 4.8 Grain boundary precipitation of sigma phase in 347 H after ca. 15 kh at high temperature.

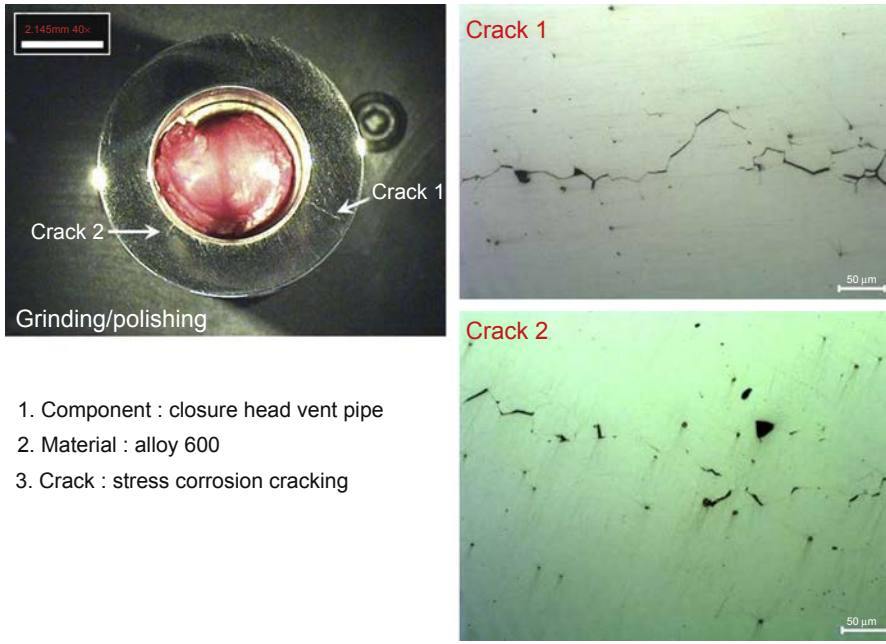


Figure 4.9 Example of SCC in Alloy 600 showing the intergranular crack path.

Ti, NB, and other carbide formers that form carbide in preference to Cr, eg, 347 and 321, are used to mitigate the possibility of SCC [27].

One particular form of SCC, namely hydrogen-induced cracking (HIC), although an issue for high-strength steels is not of major concern for austenitics since the solubility of hydrogen is greater in the austenitic matrix rather than the martensitic/ferritic matrix [28]. Where a material has been sensitized, there is the possibility of HIC being an issue [29], particularly in the weld region where hydrogen trapping is increased due to the local residual stress. Fig. 4.9 highlights the brittle nature of SCC where crack propagation tends to be intergranular in nature, with this example showing no signs of branching.

4.8 Stress relief cracking

Stress relief cracking is defined as intergranular cracking in the heat-affected zone (HAZ) or weld metal that occurs during PWHT or during high-temperature service. The difference between this embrittlement during PWHT and service is not just one of time but also mechanism.

Stress relief cracking during PWHT, also known as reheat cracking, is essentially grain boundary embrittlement due to carbide precipitation during the PWHT [30,31]. The main purpose of the PWHT is to relieve the stresses built up during welding. The PWHT temperature and time are selected to unsure that stress relief via dislocation

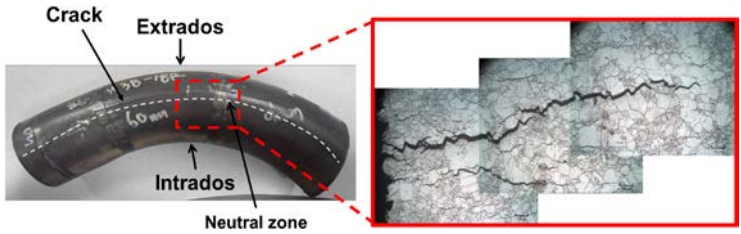


Figure 4.10 Relaxation cracking along neutral zone of a 347H tube.

movement is both sufficiently rapid and complete by the end of the PWHT. As the stresses are relaxed via dislocation movement, the newly decorated grain boundaries act as dislocation sinks and/or result in dislocation pile-up causing back stress. Either way the grain boundaries are unable to tolerate the strain redistribution leading to decohesion of the boundaries, ie, low ductility fracture mechanism.

Stress relief cracking in service, also known as relaxation cracking and/or hold time cracking, is essentially a secondary hardening of the grains coupled with the carbide precipitation on the grain boundary. The carbide precipitation consumes the secondary hardening elements, leading to a denuded, relatively weak grain boundary zone. With the intragranular regions being strengthened by the secondary hardening, all the service-induced deformation is constrained to the weak narrow grain boundary region leading to an apparent intergranular brittle failure [16]. The secondary hardening may be an SIPH mechanism and/or addition phases coming out of solution as the alloy moves to equilibrium; see section on secondary hardening. Fig. 4.10 shows an example of relaxation cracking on the natural axis of a 347H bend and also shows the intergranular nature of the crack.

4.9 Secondary hardening

During the manufacture of the alloy and component, insufficient time has occurred for the material to reach equilibrium. By equilibrium, we mean the volume fractions and specific phases present in the alloy such that entropy (sometimes called free energy) has reached a minimum [32]. The thermal treatments after alloy manufacture/forming are usually higher than service operation temperature. At these higher temperatures the matrix is able to hold in solution a higher concentration of secondary elements than it can at service temperature. Therefore at the reduced operating temperature, additional elements will come out of solution during service, forming additional phases and/or additional precipitates. These additional phases and/or precipitates invariably lead to hardening of the material [33–35].

Some alloys, for example TP347, are designed to experience this secondary hardening during the thermal treatments prior to service [33], while others are designed to age harden during service, for example Sanicro 25, as shown in Fig. 4.11 [36]. The purpose of this secondary hardening either prior to service or during service is to enhance the high-temperature creep resistance of these alloys [35]. These strengthening

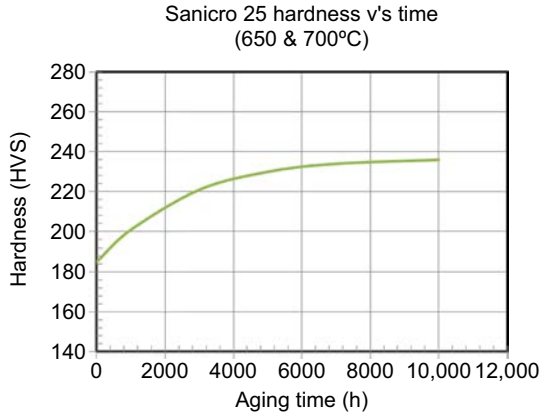


Figure 4.11 Increase in hardness of Sanicro 25 as a function of time as a result of secondary hardening caused by Laves phase precipitation.

phases, mainly carbides and/or carbonitrides, or Laves phase, Fe_2M, form both within the grains and on grain boundaries and operate to either pin dislocations within the grains or pin the grain boundaries.

Secondary hardening can lead to a significant reduction in ductility and toughness; for example, Nikulin et al. [37] attribute the reduction for 18/8 type materials to $M_{23}C_6$, Laves and Z-phase formation mainly on the grain boundaries. Another consideration that has received little attention is the volumetric change that can occur with secondary hardening, in particular the phenomena of negative creep, ie, volumetric shrinkage. Negative creep has been well reported and researched for Ni-based alloys [38], while for Fe-based austenitic materials, little seems to have been reported for many years, although the effects may be just as significant for the Fe-based austenitic alloys as the Ni-based austenitic alloys [39].

4.10 Dissimilar metal welds

DMWs are defined as a joint between two different classes of materials, ie, ferritic to austenitic steels or austenitic steel to nickel alloy. Historically, there has been no service experience with austenitic to nickel joints, but for future plants operating under hyper-supercritical (HSC) conditions, there needs to be consideration of austenitic to nickel joints. Note HSC is also known as advanced ultra-supercritical (A-USC). The obvious issues with DMW are differences in composition, differences in properties, and differences in pre- and post-weld heat treatments.

When we talk about composition, the issue here is one of weld consumable selection to be compatible with both parent metals. For the ferritic to austenitic joints the most likely ferritic material is a 9% Cr creep strength–enhanced ferritic alloy, ie, T/P91 or T/P92. The use of austenitic filler metals is problematic due to carbon diffusion into the weld metal from the ferritic parent leaving a weak zone in the ferritic material

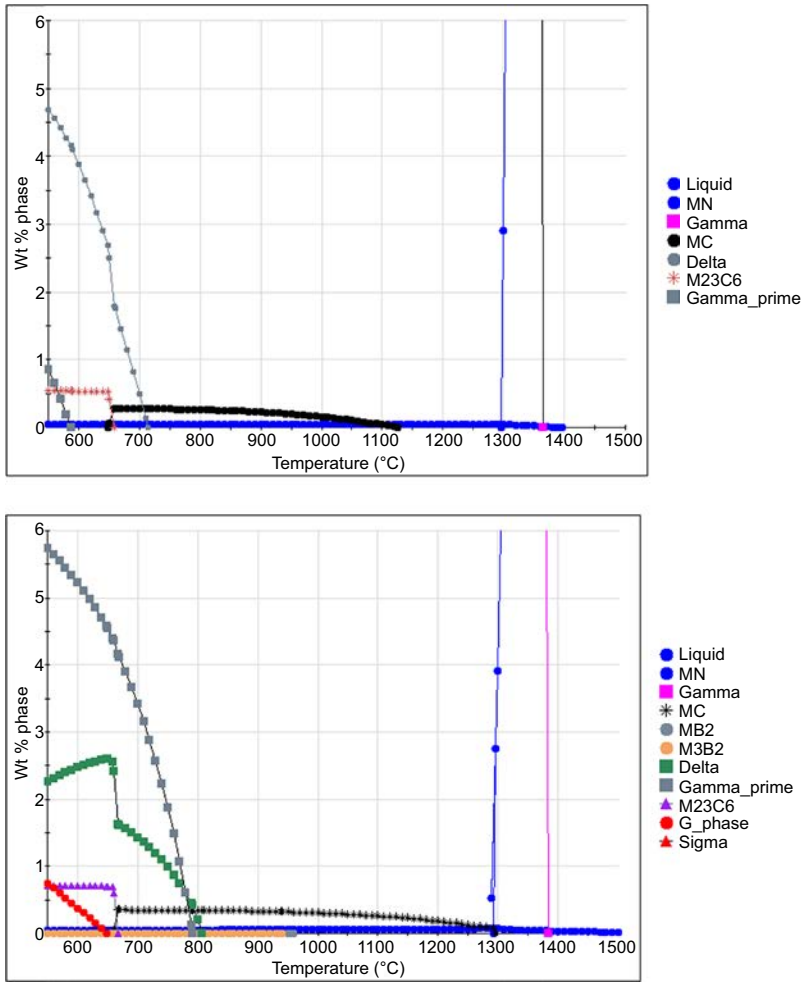


Figure 4.12 Effect of dilution on the predicted equilibrium phase diagram: top is for Filler Metal 82, and lower is for 316H/FM82/IN740H with a 45% mix from both parents.

close to the fusion line [40,41]. Similarly, using a ferritic consumable carbon migration from the weld metal to the austenitic parent leaves a weak zone within the weld metal close to the fusion line. The standard solution is to use a nickel filler, most often Inconel 82/182 (ERNiCr3). For the austenitic to nickel joint, again, Inconel 82/182 is the standard consumable; an example of the possible equilibrium phases in the mixed zone typical of the root pass is given in Fig. 4.12 [42]. The microstructure of the weld and HAZ regions both post-welding and its evolution with time and temperature is the subject of many publications, for example [43–45]. Each combination of parent, consumable, and welding process seems to yield a unique microstructure, so generic findings are yet to be defined.

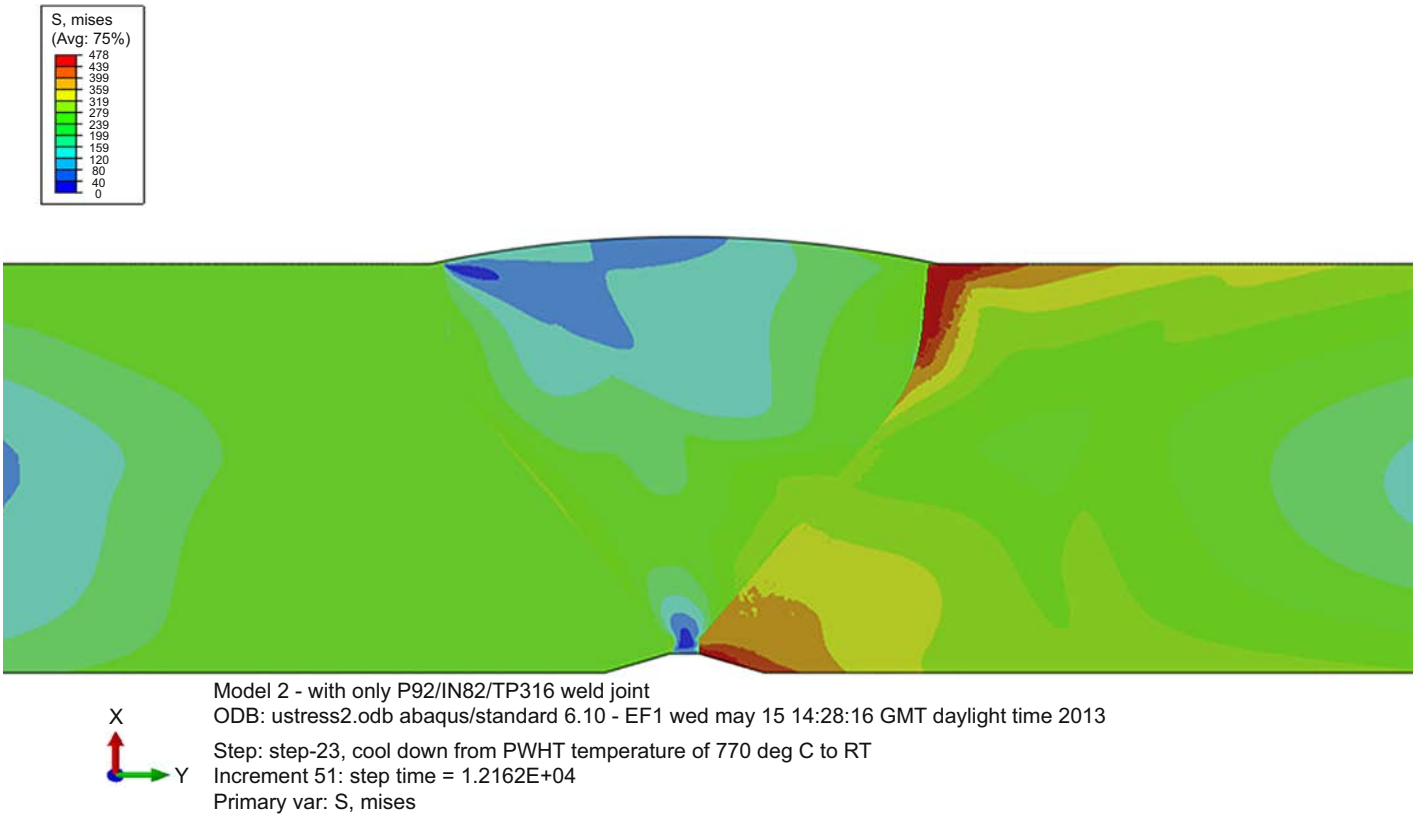


Figure 4.13 P92/TP316H weld joint: Mises stress prediction at room temperature after welding.

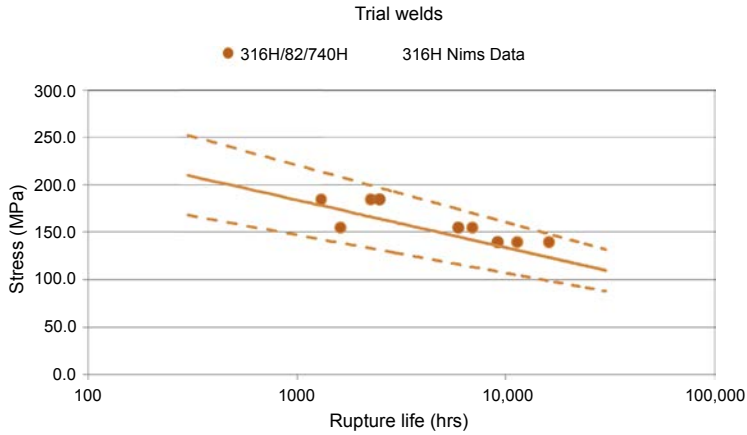


Figure 4.14 X-weld creep data, individual data points, plotted against 316H parent data scatter bands derived from Nims database, *solid and dashed lines*.

For thin-section superheater and reheater tubing a single- or two-pass GTAW process is normal with a PWHT of 1 h at 740–760°C, and issues associated with differences in material properties and heat treatments pose less of a problem than for the thick-section components. When we look at thick-section components, the difference in thermo-physical properties, in particular the coefficient of thermal expansion mismatch, between the ferritic and austenitic alloys becomes very significant. This thermal expansion mismatch can lead to significant residual stresses; an example is shown in Fig. 4.13 of a finite element analysis (FEA) of a joint between P92 and P316H. The residual stresses in the 316H are predicted to be above its ultimate strength, with the highest stresses predicted to be at the toe of the weld for both the root and cap of the weld. Much research has been conducted on ways to reduce these stresses including surface cladding, buttering, and PWHT to varying degrees of success [46].

Of most importance is the effect of this DMW on the creep properties of the joint. As this is a joint between two metals with different creep strengths, provided the X-weld failure occurs in the weaker of the parent, details of the microstructure and residual stress distribution are of academic interest rather than of engineering interest. Fig. 4.14 shows data for X-weld creep data for a 316H/IN740H combination welded using Alloy 82 consumable plotted against 316H parent data contained within the Nims database. Since the X-weld falls within the expected scatter bands, it may be concluded that failure of the X-weld occurs in the 316H parent material.

4.11 Conclusions

This chapter does not attempt to capture all data, from the thousands of publications, on the topic related to the use of iron-based austenitic materials for boiler applications but rather highlights some of the issues that need to be considered during material selection and component manufacture.

One major section deliberately not addressed was that of fatigue/creep and creep/fatigue interactions. This is of particular significance for the DMW joints, where careful design will be required. This is the main reason this topic has been deliberately omitted, ie, design has such a major effect on fatigue/creep and creep/fatigue, we tread heavily on commercial confidentiality. Also fatigue/creep and creep/fatigue interactions fit more comfortably under structural integrity rather than materials.

Acknowledgments

This chapter includes many works conducted by my colleagues within the Doosan family, in particular Dr Paul Moody and Dr Tamba Dauda from the UK and Dr Byeongook Kong, Mr Cheolhong Joo, and Mr Sunwoo Ryu from Korea. The assistance from my colleagues in the preparation of this chapter is much appreciated.

References

[1] D. Peckner, I. Bernstein, Handbook of Stainless Steels, McGraw-Hill, New York, 1977.
[2] C. Kovach, High performance stainless steels, NiDI (1998).
[3] Anon, State of Knowledge for Advanced Austenitics, EPRI, Palo Alto, CA, 2009, p. 1020241.
[4] Anon, "Application of the Schaeffler diagram", Dacapo Stainless, Technical Data. http://dacapo.com/uploads/documents/40-document.pdf.
[5] F. Masuyama, et al., Findings on creep-fatigue damage in pressure parts of long-term service-exposed thermal power plants, Journal of Pressure Vessel Technology, ASME 107 (1985) 260.
[6] M. McGuire, Stainless steels for design engineers, Austenitic Stainless Steel, ASM (2008) (Chapter 6).
[7] A. Inoxidables, Les Editions de Physique, Les Ulis, Paris, 1993, p. 410.
[8] M. Abd Rashid, et al., formation of $Cr_{23}C_6$ during the sensitization of AISI 304 stainless steel and its effect to pitting corrosion, International Journal of Electrochemical Science 7 (2012) 9465–9477.
[9] P. Atanda, A. Fatudimu, O. Oluwole, Sensitisation study of normalized 316L stainless steel, Journal of Minerals & Materials Characterization & Engineering 9 (1) (2010) 13–23.
[10] B. Chen, P.E.J. Flewitt, D.J. Smith, Microstructural sensitivity of 316H austenitic stainless steel: residual stress relaxation and grain boundary fracture, Materials Science and Engineering A 527 (2010) 7387–7399.
[11] ASME Boiler and Pressure Vessel Code, Section I, Table PG-19, Post Cold-Forming Strain Limits and Heat-Treatment Requirements, 2013.
[12] B. Kartik, et al., Effect of high temperature ageing on microstructure and mechanical properties of a nickel-free high nitrogen austenitic stainless steel, Materials Science & Engineering A 642 (2015) 288–296.
[13] EPRI Interim Report 1017607, Strain Induced Precipitation Hardening of Stainless Steels – Material Degradation and Service Experience, December 2009.
[14] A. Farahat, T. El-Bitar, Effect of Nb, Ti and cold deformation on microstructure and mechanical properties of austenitic stainless steels, Materials Science & Engineering A (2008).

[15] P. Moody, Strain induced hardening of advanced austenitic stainless steels–evaluation of creep properties, Sixth International Conference on Advances in Materials Technology for Fossil Power Plants, EPRI (2010).
[16] J. van Wortel, Prevention of Relaxation Cracking by Material Selection and/or Heat Treatment, TNO Final Report RC 00–42A, November 2000.
[17] EPRI Technical Report 1019777, Strain-Induced Precipitation Hardening in Stainless Steels: Evaluation of Field Heat Treatment, December 2010.
[18] R.L. Plauta, et al., A short review on wrought austenitic stainless steels at high temperatures: processing, microstructure, properties and performance, Materials Research 10 (4) (2007) 453–460.
[19] E.J. Chun, et al., Precipitation of sigma and chi phases in δ-ferrite of Type 316FR weld metals, Materials Characterization 86 (2013) 152–166.
[20] J. Anburaj, et al., Ageing of forged super austenitic stainless steel: precipitate phases and mechanical properties, Materials Science and Engineering A 535 (2012) 99–107.
[21] T.H. Lee, et al., Precipitation of σ-phase in high-nitrogen austenitic 18Cr–18Mn–2Mo–0.9N stainless steel during isothermal aging, Scripta Materialia 50 (2004) 1325–1328.
[22] A. Perron, et al., Understanding sigma-phase precipitation in a stabilized austenitic stainless steel (316Nb) through complementary CALPHAD-based and experimental investigations, Acta Materialia 79 (2014) 16–29.
[23] C.C. Hsieh, et al., Precipitation behavior of σ phase in 19Cr–9Ni–2Mn and 18Cr–0.75Si stainless steels hot-rolled at 800°C with various reduction ratios, Materials Science and Engineering A 467 (2007) 181–189.
[24] S. Roychowdhury, et al., σ-phase induced embrittlement in titanium containing austenitic stainless steel tie-bars in a condenser, Engineering Failure Analysis 25 (2012) 123–132.
[25] Y. Prawoto, et al., Effect of microstructures on SCC of steel: field failure analysis case study and laboratory test result, Engineering Failure Analysis 18 (2011) 1858–1866.
[26] Guides to Good Practice in Corrosion Control – Stress Corrosion Cracking, NPL Guideline, 2000.
[27] R. Viswanathan, Damage mechanisms and life assessment of high temperature components, ASM International (1989).
[28] C.L. Lai, et al., Effect of microstructure on hydrogen embrittlement of various stainless steels, Materials Science & Engineering A584 (2013) 14–20.
[29] J. Neuharth, M. Cavalli, Investigation of high-temperature hydrogen embrittlement of sensitized austenitic stainless steels, Engineering Failure Analysis 49 (2015) 49–56.
[30] A. Dhooge, A. Vinckier, Reheat cracking-a review of recent studies, International Journal of Pressure Vessels and Piping 27 (1987) 239–269.
[31] S. Ghiya, et al., Stress relief cracking in advanced steel material- overview, Proceedings of the World Congress on Engineering II (2009) 978–988.
[32] W.D. Callister, in: Materials Science and Engineering an Introduction, seventh ed., John Wiley & Sons, 2007.
[33] C.Y. Chi, et al., The precipitation strengthening behaviour of Cu-rich phase in Nb contained advanced Fe–Cr–Ni type austenitic heat resistant steel for USC power plant application, Progress in Natural Science: Materials International 22 (3) (June 2012) 175–185.
[34] C. Solenthaler, et al., Precipitation strengthening of nb-stabilized TP347 austenitic steel by a dispersion of secondary nb(C,N) formed upon a short-term hardening heat treatment, Materials Science & Engineering A 647 (October 28, 2015) 294–302.
[35] S.W. Chen, et al., Precipitation behavior of Fe2Nb Laves phase on grain boundaries in austenitic heat resistant steels, Materials Science & Engineering A 616 (October 20, 2014) 183–188.

[36] G. Chai, Private Communication, Sandvik Global Group Expert, 2015.
[37] I. Nikulin, et al., Effect of high-temperature exposure on the mechanical properties of 18Cr–8Ni–W–Nb–V–N stainless steel, Materials Science and Engineering A 554 (September 30, 2012) 61–66.
[38] A. Marucco, B. Nath, The consequences of ordering on negative creep and flow of nickel based alloys, Mechanical Behaviour of Materials V (1988) 949–956.
[39] A.M. Parshin, I.E. Kolosov, The nature of negative creep in austenitic steels Kh18N22V2T2 and Kh12N20T3R, Metallovedenie i Termicheskaya Obrabotka Metallov 12 (December, 1968) 26–29.
[40] L. Falat, et al., Microstructure and creep characteristics of dissimilar T91/TP316H martensitic/austenitic welded joint with Ni-based weld metal, Materials Characterization 72 (2012) 15–23.
[41] J. Cao, et al., Microstructure and mechanical properties of dissimilar materials joints between T92 martensitic and S304H austenitic steels, Materials and Design 32 (2011) 2763–2770.
[42] R. Gollihue, Private communication, Special Metals (2014).
[43] R. Mittal, B. Sidhu, Microstructures and mechanical properties of dissimilar T91/347H steel weldments, Journal of Materials Processing Technology 220 (2015) 76–86.
[44] P. Šohaj, R. Foret, Microstructural Stability of 316Ti/P92 and 17242/P91 Weld Joints, Metal, Czech Republic, Brno, 2011.
[45] W. Wang, et al., Microstructures and microhardness at fusion boundary of 316 stainless steel/Inconel 182 dissimilar welding, Materials Characterization 107 (2015) 255–261.
[46] D. Deng, et al., Prediction of residual stresses in a dissimilar metal welded pipe with considering cladding, buttering and post weld heat treatment, Computational Materials Science 47 (2009) 398–408.

This page intentionally left blank

Martensitic steels for cast components in ultra-supercritical power plants

5

S. Roberts
Technical Director, Goodwin Steel Castings Ltd., Stoke-on-Trent, GBR

5.1 Material requirements for ultra-supercritical application

The material requirements for ultra-supercritical (USC) power plant operation are more arduous than for supercritical operation due to the higher temperatures and pressures involved. Ultra-supercritical conditions are typically 600°C for main steam temperature with steam pressures up to 28.5 MPa and reheat steam temperatures of 620°C. Design life is a key factor and for most new plants this is typically 250,000 h or 30 years.

Supercritical operation of power plants during the 1980s used steam temperatures of around 550°C, leading to around 40% thermal efficiencies. Today's USC steam conditions now give a net efficiency of greater than 44% and up to 46% (Fig. 5.1). Siemens reports that just a 1% gain in efficiency for a typical 700 MW plant reduces 30-year lifetime emissions by 2000*t* NO_x, 2000*t* SO_2, 500*t* particulates, and 2.5 million tons CO_2 [1].

Materials held at high temperatures and pressures for prolonged periods of time and at constant stress experience creep phenomena. Turbine operation, which very much fits with these service conditions, operates with material that exhibits creep-dominated failure. For this very reason turbine material selection is strongly influenced by high-temperature creep properties.

Castings for operation at subcritical and supercritical condition have traditionally been manufactured from chrome molybdenum (Cr-Mo) and chrome molybdenum vanadium (Cr-Mo-V) steels. These steels have been successfully operated for many years in sub- and supercritical plants but unfortunately have insufficient creep strength to operate at USC conditions. Therefore, the range of steels known as the 9%Cr steels are favored for USC application.

5.2 Why cast components are utilized for steam turbine applications

The casting process is a very cost-effective way of producing near net-shape components, which can be intricate in geometry. The science of casting is in the ability to

Materials for Ultra-Supercritical and Advanced Ultra-Supercritical Power Plants.
http://dx.doi.org/10.1016/B978-0-08-100552-1.00005-1
Copyright © 2017 Elsevier Ltd. All rights reserved.

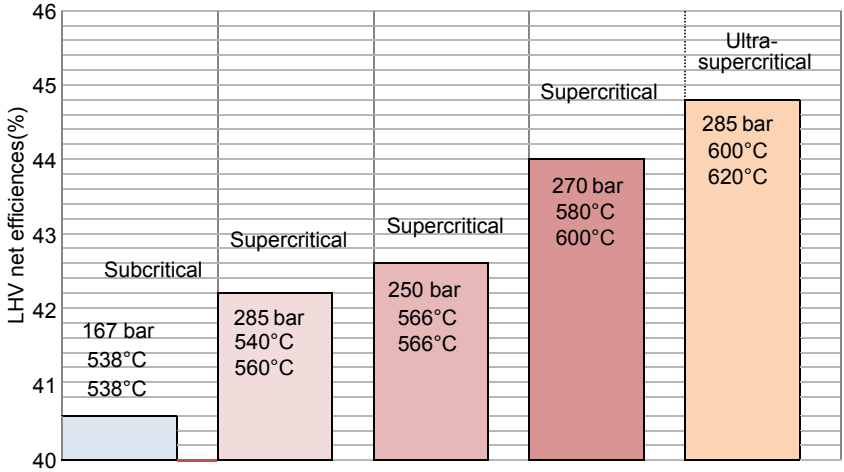


Figure 5.1 Net efficiencies versus operation condition of plant.

produce a correctly dimensioned component with acceptable chemistry and physical properties with the required surface and volumetric integrity.

This sounds quite simple until we consider the founder has to overcome both solidification shrinkage and solid contraction during the cooling process from liquid to room temperatures. These factors cause certain complications that the foundry has to overcome during manufacture.

In its simplest form the basic sand casting process is where a wooden, resin, metal, or other suitable material pattern representing the geometry of the component is manufactured and used to produce a sand mold. The sand, which can be silica, zircon, chromite, or even synthetic sand, is coated with some form of binder system whereby the binder can be hardened so each sand grain adheres to the next. The sand itself is graded and mixed to the required blend. This often will contain a combination of small, medium, and large sand grains to suit the particular foundry's permeability needs and surface quality requirements.

There are many sand systems to suit different applications (a system being a sand/binder combination), but most modern steel foundries will use a chemically bonded air set system with low gas evolution. The sand system is a vitally important part of the foundry process for producing quality castings and it is regularly monitored to ensure all operating parameters are within the specified tolerance. Fig. 5.2 shows a wooden pattern within a molding box during the molding process, where the molding box is being filled with resin-coated sand.

Once the sand is set (i.e., the binder is hardened), the pattern can be removed to reveal a mold cavity. Fig. 5.3 details the bottom section of a two-part mold with a simple cylindrical core in place above one-half of the mold cavity. The sand is contained within a metal molding box that is reusable, while the sand mold and core are only single use. Most molds are made from a number of sections, the simplest mold being a top and bottom section with the mold cavity between the two mating parts. When a



Figure 5.2 Showing the molding box and pattern equipment for a valve component.

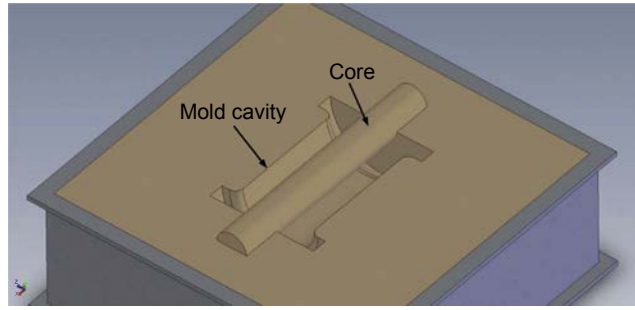


Figure 5.3 Shows a diagram of a simple bottom (drag) section of a two part mold.

hole is required within a component, such as the internal bore of a valve, then a sand core is positioned within the mold to produce this geometry. Foundries may use different sand system parameters and materials for cores.

The sand surface in contact with the molten metal, without further protection, is often not impermeable enough to prevent molten metal ingress, especially in heavy sections and where high ferro-static pressures are encountered. In such cases a mold coating is applied to the mold surface by brushing, flood coating, or spraying. The coating is normally water or alcohol based, depending on the foundry's production requirements, and within this coating liquid are fine suspended refractory particles that adhere to the mold surface offering a barrier to the molten metal.

The pattern equipment is designed to compensate for solid-state contraction, which is the amount the casting contracts through solid-state cooling through to room temperature. This means the pattern equipment has to be larger than the actual component produced, typically by a factor of 2–2.5% on most linear dimensions.

For the highest quality components, the molten metal is poured into the mold through a ceramic refractory running system, which introduces the metal into the mold in a controlled manner. The design of this system is such as to prevent turbulence and high-velocity defects and it is of sufficient refractoriness to prevent erosion defects. This ceramic hollowware is sized to suit the requirements of the particular casting

being produced and offers a much improved cleanliness solution for pouring than using a conventional sand runner system alone.

Liquid shrinkage is different for each material manufactured and typically is in the region of 3–7% for steels and nickel alloys, respectively. Liquid shrinkage is the reason the founder requires liquid metal reservoirs called feeders or risers, which provide feed metal to a solidifying casting.

Steel castings require correctly positioned feeders to prevent liquid shrinkage causing leak paths, detected by pressure testing, forming in the internal volume of the component.

The position and sizing of the liquid feeders, solidification aids such as chills and pads, along with the runner system and pouring orientation, all form part of the foundry method design for a particular component. The modern foundry uses solidification simulation software to aid method design.

When producing an item for the first time, most foundries will produce a prototype or sample casting to prove the method design before commencing full production of subsequent items. These software programs increase the foundry's success rate in producing methods for new components where multiple iterations of actual manufactured prototypes can be reduced. This reduces overall costs and lead times. Fig. 5.4 shows an example of a filling simulation (left) and solidification simulation (right) for a demonstration steam valve component.

Modern simulation software can also have a fluid-modeling element, which enables the simulation of the filling/pouring of the mold. A visual representation of a mold cavity being filled and the casting subsequently solidifying and cooling could only previously be visualized in the imagination of the methods engineer,

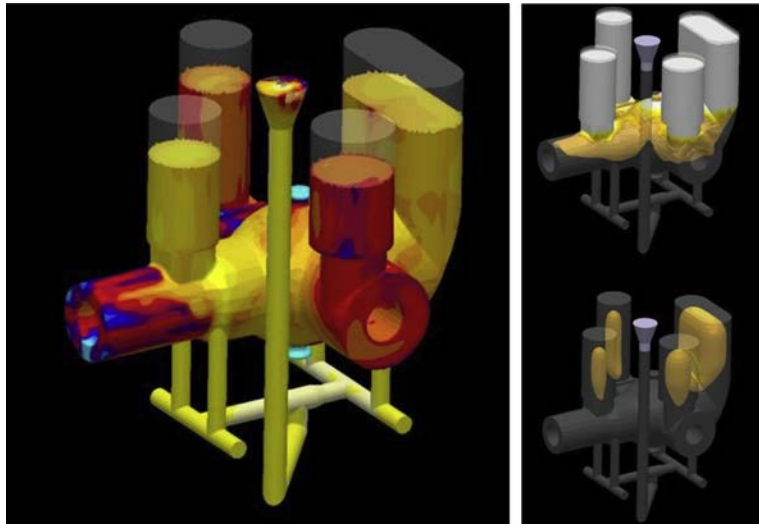


Figure 5.4 Typical casting method and solidification simulation showing the castings, feeders, and runner system as the casting is filled and subsequent solidification simulated using solidification software.

but modern computing power and finite element analysis has enabled the foundry industry to take advantage of these techniques to improve castings quality and reproducibility. Prior to the use of simulation software, the methods engineer used empirical-based calculation programs for the size and placement of feeders, or first principle empirical modulus-based tables, painstakingly created from actual experimentation.

Fig. 5.5 shows in the form of a simple flow chart the basic casting processing steps required to produce a single piece casting. The flow chart does not show the additional steps necessary if the casting is part of an assembly, where subsequent steps are required to cover fabrication welding and nondestructive testing (NDT).

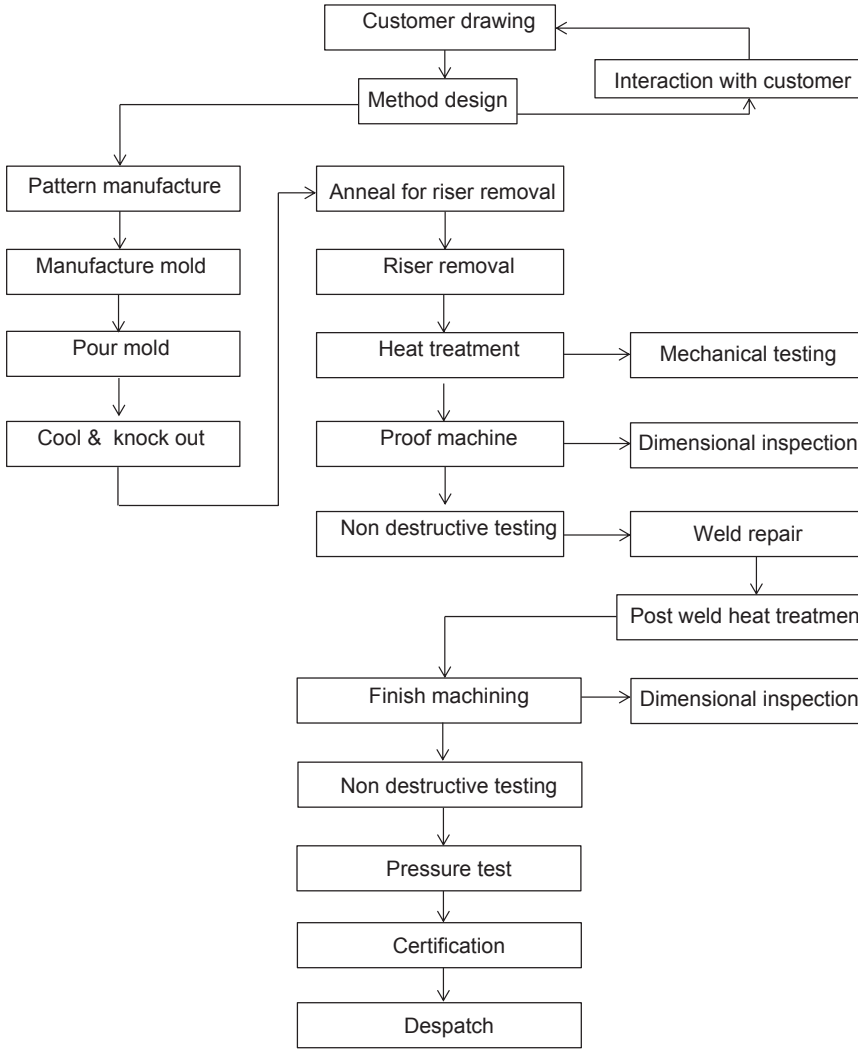


Figure 5.5 Flow chart of basic casting process steps.

A high integrity cast valve or casing can have distinct technical advantages over a wrought product such as a forging.

Advantages of a casting compared with wrought components:

1. Complex geometry components can be produced to near net shape, which is not possible for any wrought product without exceptional machining costs.
2. Machining costs are dramatically reduced, as costly machining operations are minimized when cast components are produced to near net shape.
3. Wrought products have directional mechanical properties and have to be tested in both longitudinal and transverse directions, while castings have equiaxed grain morphology and for all intents and purposes have equal mechanical properties in all directions.
4. Castings do not suffer from lamination defects associated with wrought material processing techniques, which can be difficult to detect by NDT techniques.
5. Cast materials are less sensitive to steel cleanliness such as inclusion defects, as inclusions in wrought alloys can be exaggerated during the working processes, which elongate inclusions, making their morphology linear rather than rounded. This linear/stringer morphology is very much more of a concern than a rounded inclusion, as linear stringer defects can present as weak fracture planes within an incorrectly processed wrought material.
6. Castings have inherently larger grain size than their equivalent wrought components, and there is certain evidence to support that larger grain size materials can have higher creep properties than those with smaller grain size.
7. Castings have fillet radii to reduce stresses at geometry junctions, unlike fabrications that have high stresses at welded junctions.
8. Fabrications have many construction welds that require in-service inspection. Good quality castings have fewer construction welds and far less in-service inspection requirements.

5.3 Casting materials for ultra-supercritical applications

5.3.1 Casting materials grades

As previously mentioned, current power station efficiencies are in the range of 38–46% using conventional ferritic steels. Generally the operating temperature range of these materials is from 540 to 580°C. Table 5.1 details typical high-pressure valve and casing materials. The series of 9%Cr steels have distinct advantages over their conventional ferritic steel counterparts that allow their operation at higher temperature and pressure.

5.3.2 9%Cr steels: how do they work?

It was found that an increase in chromium (Cr) to over 7% added to a Cr-Mo steel composition, which would have typically contained 2.5%Cr, produced a group of materials having a fine martensitic lath microstructure characterized by high dislocation density and stabilized by $M_{23}C_6$ precipitates. Then, when this material was hardened and suitably tempered, a large increase in strength over conventional 2.25%Cr-Mo steel was observed. This group of materials are known as unmodified 9%Cr steel [2].

Then, when niobium, vanadium, nitrogen, tungsten and later boron were added to the material, even further improvements in creep strength were observed. When the material is tempered, this results in the precipitation of niobium, vanadium and

Table 5.1 Typical valve and casing material grades

Steel grade	C	Si	Mn	Ni	Cr	Mo	V	Nb	Other
Supercritical materials									
G17CrMo5-5 1¼Cr; ½Mo steel (Cr-Mo)	0.17	0.40	0.75	0.4x	1.25	0.55	–	–	
G17CrMoV5-10 1¼Cr; 1Mo; ¼V steel (Cr-Mo-V)	0.17	0.45	0.70	0.4x	1.35	1.0	0.25	–	Al <0.025
G17CrMo9-10 2¼Cr; 1Mo steel (Cr-Mo)	0.17	0.50	0.70	0.4x	2.25	1.0	0.02	–	Al <0.025
Ultra-supercritical materials									
G-X12CrMoVNbN9-1 P91/C12A type 9%Cr steel	0.12	0.30	0.60	0.4x	9.50	1.0	0.25	0.06	N:0.05
G-X12CrMoWVNb10-1-1 E911 type 9%Cr steel	0.12	0.25	0.75	0.60	10.0	1.0	0.25	0.06	W:1; N:0.05
GX-13CrMoCoVNbNB9 CB2 type 9%Cr steel with Boron	Nominal composition 9%Cr/1% Co/1.5% Mo, + V,Nb,B,N								
MarBN steel 9% Cr steel with Boron	Nominal composition 9%Cr/3% W/3% Co + V,Nb,B,N								

carbonitrides, which act as anchors to maintain excellent creep strength at high temperature. These steels are known as modified 9%Cr steels. These materials form the basis of most high-temperature steels used in USC power plants today, with some exceptions.

5.3.3 Modified 9%Cr steel: benefits over conventional ferritic steels

1. Higher stress rupture strength of 9%Cr steel facilitates the use of increased steam temperature and pressures. In general, compared to G17CrMoV5-10, a significant improvement in creep strength reached corresponds to an increase in operating temperature of 30–50°C.
2. Significant corrosion resistance improvement is observed with 9%Cr steels compared to 2.25%CrMo and 1CrMoV steels; this is associated with the higher chrome content of around 9%.
3. Significantly longer component life can be expected for a given creep and fatigue duty.
4. Reduced wall thickness can be used for the same design conditions, leading to lower thermal storage and reduced thermal stress.

Point 4 is very important as smaller section components require less time to reach thermal equilibrium within the power station and so are less likely to be thermo-mechanically damaged during turbine cycling. The ability to cycle the plant more frequently is becoming an important feature for operators to follow grid loading demands [2].

Cast grades of modified 9%Cr steels designated GX12CrMoVNbN9-1 (cast P91) and GX12CrMoWVNbN10-1-1 (cast E911) were developed in the Electric Power Research Institute (EPRI) program EPRI 1403-15 and European COST 501 program respectively. Modified 9%Cr steels GX12CrMoVNbN10-1-1 and GX-12CrMoVNbN9-1 have been utilized in Europe and Asia for the production of large castings for casings and valve bodies for both high-pressure and intermediate-pressure turbines. Specifically in Japan, cast valve bodies have been manufactured in GX12CrMoVNbN10-1-1 and GX-12CrMoVNbN9-1, but also in alloys such as 9%CrVNbW (TF1) and 12CrMoVNb (TOS 301) [4].

Fig. 5.6 shows a typical suit of finish machined castings manufactured in GX-12CrMoVNbN9-1. These components are high-pressure USC main steam valves (left and right). The main steam valves (tallest components in the picture) each are manufactured from two castings and three small spool piece forgings.

5.4 Manufacturing challenges associated with production of heavy-wall martensitic 9%Cr steel castings

9%Cr steels, compared to conventional ferritic steels used for supercritical applications, require a higher level of manufacturing skill set and additional controls. The following sections summarize the main manufacturing differences.



Figure 5.6 Main steam valves (800-MW) and ancillary components material GX12CrMoVNbN9-1 (cast P91).

5.4.1 Chemistry

9%Cr steels have more stringent chemistry requirements than conventional Cr-Mo and Cr-Mo-V ferritic steels. This means the melting and steel-making process employed needs to exhibit a higher level of chemical control during melting and subsequent refinement stages. The chemical specification ranges are also much tighter and consequently a higher level of analytical accuracy is also required when performing analysis. The narrow chemistry ranges are required as small changes in melt chemistry can affect the creep properties of the material, so careful control is required to ensure the consistency of high-temperature properties.

Trace elements have to also be strictly controlled and deoxidation of the steel is very different than that used for conventional ferritic supercritical steels.

5.4.2 Heat treatment and microstructural control

The final microstructure of the 9%Cr steels is tempered martensite with controlled delta ferrite. Delta ferrite is detrimental to creep life and is avoided by chemistry balance and heat treatment parameters. Like supercritical grades, 9%Cr steels require an initial austenitization followed by rapid cooling, usually using forced air blasting. The hardened material is then tempered (Fig. 5.7) to achieve a microstructure of tempered martensite, resulting in a material with an excellent balance of strength while maintaining acceptable levels of room-temperature toughness. Table 5.2 shows the typical room mechanical properties that are achieved with 9%Cr steel castings.

9%Cr steel castings often receive a double temper treatment. The martensite finish (MF) temperature is relatively low compared to Cr-Mo and Cr-Mo-V steels, and this needs to be taken into account before tempering and post-weld heat treatment are performed.

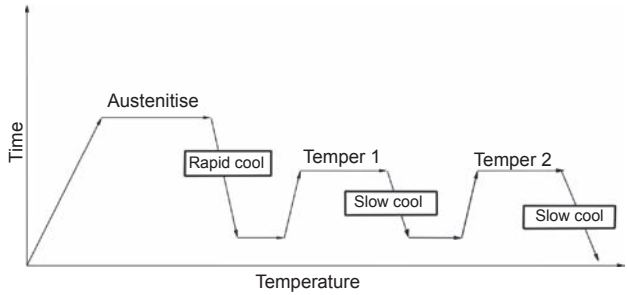


Figure 5.7 Schematic quality heat treatment for modified 9%Cr steels.

Table 5.2 Typical mechanical properties of cast grades of 9%Cr steel

9%Cr steel grade	UTS (N/mm^2)	Yield (N/mm^2)	Elongation (%)	Impacts RT (J)
G-X12CrMoVNbN9-1 (C12A type)	720	500	25	60
G-X12CrMoWVNbN10-1-1 (E911 type)	760	550	26	80
GX-13CrMoCoVNbNB-9 (CB2)	720	565	20	50

5.4.3 Melting techniques and secondary refinement

The more conventional supercritical materials can be produced by a variety of melting techniques, including electric induction melting and electric arc furnace. For the USC series of materials, these typically require secondary refinement such as argon oxygen decarburization (Fig. 5.8), vacuum oxygen decarburization, or ladle furnace refining. This is due to the much tighter chemical control required and the lower residual gas and higher cleanliness levels necessary to produce successful castings.

5.4.4 Weld repair

Weldability is an important consideration for turbine castings as most components have to be welded either as a function of a weld repair or as a fabrication weld to another casting or forged transition piece.

Welding martensitic materials using close-matching filler compositions results in very high hardness in the weld and heat-affected zone in the "as welded" condition. This results in unacceptably low toughness and high risk of brittle fracture if not suitably conditioned by post-weld heat treatment. Due to martensitic transformations and residual welding mechanical stresses caused by restraint, the weld and parent material are in a highly stressed condition prior to post-weld heat treatment. Consequently cooling and heating rates during post-weld heat treatment must be carefully controlled to reduce the risk of stress cracking. Castings are always preheated prior to welding to reduce the thermal gradient between base materials and weld pool. Interpass



Figure 5.8 Ten-ton capacity argon oxygen decarburization vessel in operation at Goodwin Steel Castings Ltd after tapping.

temperatures have to be maintained to prevent hydrogen pickup and the risk of subsequent hydrogen cracking. After welding controlled cooling is required to ensure full microstructural transformation prior to post-weld heat treatment. Filler materials must be low hydrogen to prevent hydrogen pickup during welding operations.

5.4.4.1 Post-weld heat treatment

Correct tempering of 9%Cr steel weld is essential. Post-weld heat treatment is generally governed by the Larson Miller parameter (LMP), where tempering temperature (P) should be controlled to achieve adequate tempering for P91 type cast steel [2].

5.4.4.2 Over-tempering

This is where the post-weld heat treatment (PWHT) temperature is too high, the material is heated to above the lower critical transformation temperature (AC1) and martensite starts to transform back to austenite. When 9%Cr steels are exposed to this temperature during PWHT regimes, martensite will partially re-austenitize and on cooling will reform martensite. Additionally, the carbonitride precipitates are coarsened, but they do not fully dissolve back into solution. These results generate a low-ductility material that lacks the pinning effect of the precipitates, resulting in substantially reduced creep properties.

5.4.4.3 Under-tempering

This is where the PWHT temperature is too low and results in under-tempered material with high hardness and low ductility. This material condition can lead to brittle fracture and stress corrosion cracking.

5.5 Bigger, hotter, higher pressure

In general, turbine sizes have increased in recent times where 660- to 1000-MW USC units are more commonplace for new builds than previous supercritical 300-MW or 550-MW units. This has resulted in the requirement for larger castings, with heavier wall thickness operating at higher temperatures, with even larger fabrication welds. Today's state-of-the-art 660- to 1000-MW power plant requires high-pressure stop and control valve assembled configurations weighing in excess of 50,000 kg (Fig. 5.9), with individual castings and reheat steam valves with individual weights in excess of 18,000 kg.

New, state-of-the-art higher efficiency 660- to 1000-MW USC turbines have now been developed with reheat steam temperature up to 620/625°C to increase plant efficiency and reduce emissions even further. Traditional 9%Cr cast steel cannot fulfill current design requirements for inner casings and valve bodies up to 620°C, so new steels have been developed worldwide to facilitate the increased creep strength required.

5.6 Latest alloy developments and state-of-the-art technology

5.6.1 CB2 type 9%Cr steel (GX-13CrMoCoVNbNB9)

This steel was developed within the European COST activity COST 522 (1998–2003). The steel is a 9%Cr steel with a controlled boron and nitrogen addition. It was designed for cast and forged components operating in advanced power plants with operational steam temperatures up to 620°C with enhanced creep strength when compare to conventional modified 9%Cr steels like cast P91 and E911.

The development of the CB2 alloy focused on these points:

1. Nickel (Ni) content was reduced to improve creep strength.
2. Stability and creep strength was improved by adding boron (B) while simultaneously modifying the nitrogen (N) content.



Figure 5.9 One thousand-MW unit comprised of eight castings (unit weight 49,000 kg); material: GX12CrMoWVNbN10-1-1 (cast E911).

3. To compensate for low Ni content, the addition of Cobalt (Co) was utilized to counteract the formation of delta ferrite.
4. Molybdenum content was increased and Tungsten (W) was removed to provide additional stability and improved creep strength.
5. Previously proven elements, carbon, vanadium and niobium, were optimized.

Just as with conventional modified 9%Cr steels the main creep strength is derived from the occurrence of Cr-rich carbides at prior austenite grain boundaries and MX such as vanadium nitrides within grains to give a "pinning effect" to inhibit dislocation movement. However, in addition to this, CB2 utilizes a small addition of boron (~100 ppm) that greatly helps the creep strength by reducing the coarsening effect of the Cr-rich carbides. CB2 has an advantage of about 25°C over grade 91 [3]. CB2 is now a fully commercialized cast 9%Cr steel, and many new power plants built worldwide utilize this alloy for high- and intermediate-pressure casings and main steam valves for operation temperature up to 620/625°C [6,7].

5.6.2 MarBN steels

The name MarBN is derived from the following: martensitic microstructure and Boron/Nitrogen control. MarBN steel was originally proposed by Prof. Fujio Abe of the Japanese research organization NIMS [10]. Abe's development was also based on a novel alloy formulation: 9%Cr, 3% W, 3% Co. This was claimed to be superior to alternative alloy bases such as P92 (9%Cr, 1.5–2% W, 0.5% Mo).

Abe's original work has been expanded and a new enhanced steel has been produced as full-size prototype components within the UK IMPACT [12] and INMAP [13] projects. The steel produced is a modified 9%Cr steel with chemical concentration of Co and W higher than that of both CB2 and P92. Typically the chemistry of MarBN 9%Cr steel is nominally 2–3% Co, 3% W, with controlled B and N additions (see Table 5.2). The B addition is designed to segregate to interfaces and stabilize the carbide structure from coarsening under creep conditions, while nitrogen is important to promote the formation of finely dispersed MX particles that strengthen the martensitic matrix.

The foundry's ability to precisely control the elements that promote matrix strengthening, which are measured in parts per million, are vital in ensuring the correct enhanced creep performance of the alloy. Precise heat treatment control is essential for obtaining optimal microstructures for ultimate creep strength.

Testing of the prototype casting within the IMPACT project demonstrated that MarBN steel has a temperature advantage over CB2 and P92 on the order of 25°C, making the operation of the steel at 650°C a realistic possibility [4,11]. Fig. 5.10 shows the perceived maximum operating temperature for state-of-the-art 9%Cr steels.

Fig. 5.11 shows a demonstration casting produced in MarBN steel as part of the UK-funded INMAP project. The purpose of the casting is to evaluate the upscaling of production capability to a full-scale component and to demonstrate successful manufacturability of this new 9%Cr steel material in the cast form.

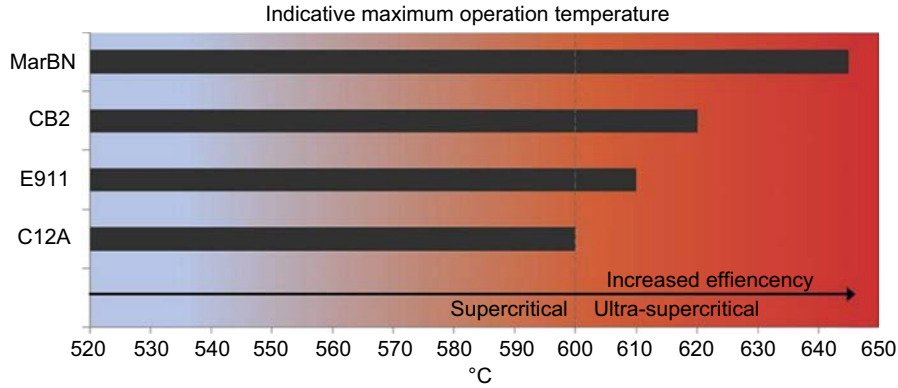


Figure 5.10 A graphical representation of the indicative maximum operating temperatures of common 9%Cr steel casting grades, state of the art grades and MarBN steel still underdevelopment.



Figure 5.11 MarBN steel casting produced within the UK INMAP project. Project partners are Alstom, Goodwin Steel Castings Ltd, and Applied Inspection Ltd.

5.7 What is next after ultra-supercritical? Cast materials for advanced ultra-supercritical applications?

The current USC operation temperature limit for 9%Cr steels is around 625°C, and this may be increased to around 650°C with the introduction and commercialization of new steels such as MarBN steel. However, it is unlikely that steels will ever have sufficient creep strength and oxidation resistance to operate much higher than this temperature, and therefore, beyond 680°C, only nickel alloys are likely to maintain sufficient high-temperature properties. So for advanced ultra-supercritical applications (A-USC), development focus has concentrated on nickel alloys. For castings, this has concentrated on two main groups: solid solution strengthened alloys and

Table 5.3 Chemistry of candidate advanced ultra-supercritical applications cast Ni alloys

Alloy name	Ni	Cr	Mo	Co	Nb	Al	Ti	Other
A625	BAL	21.0	9.0	–	3.5	–	–	5% Fe max
A617	BAL	22.0	9.0	12.0	–	1.0	0.5	3% Fe max; 0.006% B
A230	BAL	22.0	2.0	4.0	–	0.3	–	3% Fe max; 14% W
A263	BAL	20.0	6.0	20.0	–	0.5	2.2	0.7% Fe max
Inconel 740H	BAL	25.0	0.1	20.0	1.50	1.35	1.35	3% Fe max; 0.006% B max
Haynes 282	BAL	19.5	8.0	10.0	–	1.4	2.1	1.5% Fe max; 0.005% B max
Goodwin G130	BAL	24.5	0.25	19.5	0.25	1.5	1.45	Ta: Added
Toshiba TOS-3X	Proprietary alloy of Toshiba							

TOS-3X is a Toshiba proprietary alloy similar to Toshiba rotor alloy TOS-1X.
Inconel 740H is the property of Special Metals Corporation.
Haynes 282 is the property of Haynes International.
Alloy G130 is the property of Goodwin Steel Castings Ltd

precipitation hardened alloys. Table 5.3 details common candidate alloys that have been investigated for the use in environments.

Solidification prediction, melting/refining, NDT, fabrication welding, PWHT and machining are all more technically difficult for nickel alloys than for conventional steels. This means the manufacturer producing these cast alloys needs to have the specialist knowhow and understanding required for nickel alloy production, which is very different from the skillset required for the production of steel castings, especially when heavy-section nickel alloy castings are required.

Solid solution–strengthened alloys like A625 are well known within the casting industry; for example, ASTM A494 CW6MC is the equivalent of A625, and for many years these alloys have been manufactured as components for the oil and gas industry along with Hastelloy grades where the chemical corrosion resistance of the alloy has been utilized. The high-temperature properties of these oil and gas industry materials are not normally so important; in fact the low-temperature properties are much more important, as operation is often at subzero temperatures.

Additionally, the oil and gas components are relatively small and have thinner sections compared to those required in the power generation industry, where section sizes are required between 150 and 300 mm. This is because as valve sizes increase in the oil and gas industry often a carbon steel valve with nickel alloy cladding becomes a more cost-effective route than one produced completely in nickel alloy. By contrast, the power industry the whole component's high-temperature creep properties are required throughout the full section of the casting. So the option of utilizing a lower cost alloy for noncontact parts is not possible.

This requirement for an increase in section size for nickel alloy cast components constitutes a step change in the technology required to produce such a high-integrity component. This is because nickel alloy castings are not as easily scalable as their steel

counterparts. So work has been undertaken in various worldwide projects (Table 5.4) to upscale the manufacturability of large nickel alloy castings as such thick-section castings and welds will be a necessity for the A-USC turbine.

This work has culminated in some very large successful castings being produced by just a handful of specialized foundries.

A-USC parameters are commonly said to be 100,000 h at 700°C and 100 MPa. The main candidate alloys for this application are alloys A625 and A617. Both have good castability, with A625 being the easier of the two to produce as a casting due to the lower titanium and aluminium levels. Alloy A617 is more difficult to cast in air and requires other special precautions [9].

Fig. 5.12 shows a very large alloy 625 high-pressure casing casting made for the national A-USC project. Fig. 5.13 shows a picture of the alloy A617 nozzle box produced in the proof machine condition prior to sectioning for characterization and testing.

Table 5.4 Worldwide advanced ultra-supercritical applications projects involving cast materials for steam turbines

Project	Year	Country	Potential casting alloys
AD700	1996	Europe	A625 and A617
European Comtes 50+	2003	Europe	A625
US 1400°F project	2001	USA	Haynes 282
Cool Earth [5,9]	2008	Japan	A625
China National 700°C Project	2010	China	A625 & A617
Nextgen Power [8]	2010	Europe	Haynes 282, A263, Inconel 740H, Goodwin G130
MACPLUS	2011	Europe	GoodwinG130
Indian National Project	2010	India	A625
Korean National Project	–	South Korea	To be confirmed



Figure 5.12 Nickel Alloy A625 HP Casing manufactured by Goodwin Steel Castings Ltd (UK) for (maximum section size ≥ 400 mm; casting weight 10,500 kg).

Mitsubishi Heavy Industries (MHI) reported in 2013 successful results of trial nozzle box castings produced in alloy A625 and A617 with a very low level of defects after NDT, and excellent through-section mechanical properties meeting MHI's target A-USC criteria for creep strength after medium-term testing [5].

The standard methods for casting nondestructive inspection are magnetic particle inspection for surface inspection and ultrasonic inspection (UT) for casting volumetric inspection (Table 5.5). With nickel alloy castings, because of the large grain size compared to a corresponding wrought component, UT is not able to achieve a suitable sensitivity and so cannot be used as a means of volumetric inspection [14]. Some work has been performed on phased array UT techniques for the inspection of nickel alloys,



Figure 5.13 Nozzle box casting (alloy A617; weight 1500 kg) manufactured using the patented induction feeder system.

Table 5.5 Typical nondestructive testing options

Location	Coverage	Steels	Nickel alloys
Casting cast surface inspection	100%	MT	PT
Machined surface inspection	100%	PT	PT
Casting volumetric inspection	100%	UT	RT
Weld preparations	Weld prep 75–100 mm	RT	RT
Weld repairs	Repair area + parent	UT[a] + MT	RT[a] + PT
Construction welds	Weld + parent	UT or RT + MT	RT + PT
In-service inspection	As required	UT + MT	RT + PT

MT, magnetic particle inspection; *PT*, penetrant inspection; *RT*, radiographic inspection; *UT*, ultrasonic inspection.
[a]Weld repairs are generally reinspected by the technique that originally disclosed the defect. Except when UT or RT is performed on a weld repair, surface inspection by MT or PT is always also repeated.



Figure 5.14 A linear accelerator X-ray facility at Goodwin Steel Castings Ltd (United Kingdom).

but at this time the author has not seen evidence that this technique can be adopted for thick-section castings (ie, >100 mm). For the volumetric inspection of nickel alloy castings, radiography is the preferred technique. However, only high-powered X-rays such as those generated by a linear accelerator should be used for the inspection of heavy-walled nickel alloy castings, as exposure times are much greater than those used for steels (Fig. 5.14).

Precipitation-hardened Ni alloys are favored for higher temperature application due to their higher creep strength. These are nickel alloys generally in the Ni-Cr-Co group, which are strengthened by gamma prime. Additions of aluminium and titanium in these series of alloys combine with nickel to form the intermetallic compound $Ni_3(Ti,Al)$ or gamma prime (γ'). Gamma prime inhibits slip and creep effectively at elevated temperatures, making these alloys higher in creep strength than those predominantly strengthened by solid solution strengthening alone like A625 and A617. The heat treatment of these series of alloys differs from the solid solution–strengthened alloys, as an aging treatment is required to precipitate the gamma prime subsequent to some form of solution treatment.

Production of heavy section castings in precipitation-hardened nickel alloys are still in its infancy with just a few foundries worldwide producing prototype components for evaluation. Most of the candidate nickel alloys selected for investigation have their heritage in thin section wrought products for the petrochemical or aero industries. To the authors best knowledge, only Toshiba alloy TOS-3X and Goodwin Alloy G130 are specifically designed for A-USC turbine castings. While TOS-3X and G130 were the only alloys specifically designed for castings, there may be others [8].

In the author's experience it is not always possible to successfully cast the wrought alloy as a casting without some chemistry modifications. This is because the pouring, solidification, and subsequent solid metal processing are all fundamentally different for a wrought product compared to a cast product. This means that chemistries ideally

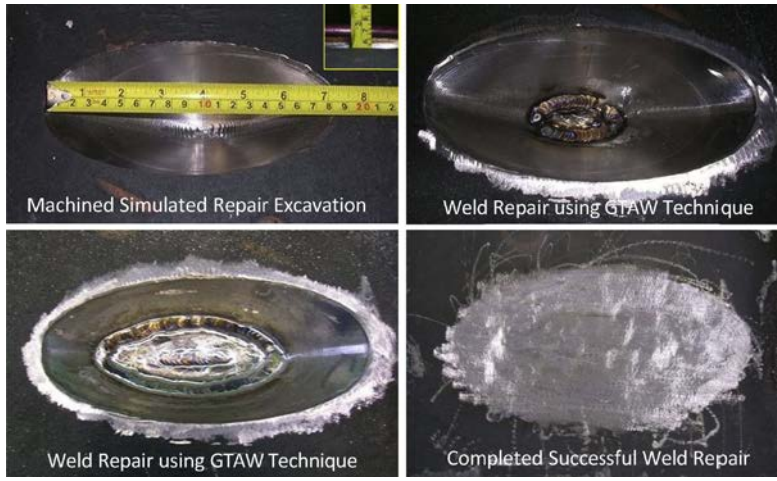


Figure 5.15 A simulated weld repair in an Inconel 740 casting.

suited to fast cooling, and hot or cold working, do not always work for a slowly cooled sand casting with no subsequent hot or cold work.

Weld repair of precipitation hardened nickel alloy castings and construction welds to join these casting together is not yet well explored. Much more is known about the fabrication of wrought boiler piping. However, trials have/are being performed in research and development programs for both weld repair and fabrication welding of castings (Fig. 5.15). These alloys are known to be far more challenging to weld than conventional solid solution-strengthened nickel alloys. This is partly associated with the inherent lower ductility of these materials and the limitation on welding techniques that can be used for welding.

Due to the high proportions of aluminium and titanium in the weld metal, techniques that provide inert gas protection are the ones favored for producing successful welds, such as gas tungsten arc welding (GTAW). This means conventional techniques for welding large castings in the power industry such as shielded metal arc welding (SMAW) and flux cored arc welding (FCAW) cannot be used, as these techniques cannot offer sufficient protection against oxidation of the weld pool and the resulting loss of gamma prime strengthening elements.

The disadvantage of using techniques such as GTAW for casting repairs is the poor deposition rates achieved compared to SMAW and FCAW. This means welds take much longer to complete, and therefore costs are higher, and processing times are much longer.

5.8 Summary

Castings continue to a play an important role in the manufacture of steam valves, casings and ancillary parts for the steam turbines for both USC and almost certainly with new technology A-USC application plants. The casting process is favorably utilized

for the manufacture of these components, as it is remains the most cost-effective method of producing complex geometry near net-shape components with material characteristics that withstand the high temperature and stress environments within a steam turbine. The resulting cast components can often exhibit clear advantages over similar components produced by a wrought process.

The new casting alloys being developed for 650°C and 700°C plus turbine operation require much tighter chemical and processing parameter control than previous conventional power plant grades. Therefore, to ensure acceptable material performance, the selection of technically competent foundries for the supply of these new casting alloys will be paramount for their successful procurement.

References

[1] Power Technology.com, Yuhuan 1,000 MW Ultra-Supercritical Pressure Boilers, China201D.

[2] S. Birks, Advanced material castings for high temperature coal fired steam turbine applications, Foundry Trade Journal (August 2011).

[3] B. Scarlin, The European efforts in material development for 650°C USC power plant – COST 522. Advances in materials technology for fossil power plants, in: Proceedings From EPRI 2004, vol. 1(1), 2005, p. 84.

[4] R. Vanstone, KMM-VIN Newsletter (July 2014) issue 10.

[5] Y. Hirakawa, Y. Kadoya, S. Nishimoto, Y. Tanaka, Trial Production of Alloy 625 and Alloy 617 Casting Components for Advanced 700°C Class Steam Turbines, Mitsubishi Heavy Industries Ltd., Takasago, Hyogo, Japan.

[6] M. Staubli, R. Hanus, T. Weber, K.-H. Mayer. T.-U. Kern, The European Efforts in Development of New High Temperature Casing Materials – COST 536.

[7] L. Sonfeng, S. Hongwei, J. Guoqing, M. Linbo, W. Weili, X. Cunguan, The Application of 9% Cr Steel Casting Steel With Co and B Addition for 620°C Steam Turbine, Shanghai Electric Power Generation Equipment Co Ltd.

[8] R. Leese, S. Roberts, in: Liege conference paper 2014, Developments of Castable Precipitation Hardened Ni-Base Alloys for 750°C Technology Within Nextgen Power Project, 2014.

[9] S. Birks, S. Roberts, R. Leese, EPRI Conference on Advances in Materials Technology for Fossil Power Plants, Waikoloa, Hawaii, in: Paper, Advances in Ni Alloy Casting Production for +700°C Applications, 2013.

[10] F. Abe, M. Tabuchi, H. Semba, M. Igarashi, M. Yoshizawa, N. Komai, et al., Feasibility of MARBN steel for application to thick section boiler components in USC power plant at 650°C, in: Proceedings of the 5th International conference on Advances in Materials Technology for Fossil Power Plants (5th EPRI Conference), October 3–5, 2007. Marco Island Florida, USA, .

[11] C. Degnan, State of the art of MarBN steel, in: VGB Workshop: Materials and Quality Assurance, Laborelec GDF Suez, Linkebeek, Belgium, April 29–30, 2013.

[12] IMPACT Project – (Innovative Materials, Design and Monitoring of Power Plant to Accommodate Carbon Capture) is a 4-year, UK collaborative R&D project, UK Technology Strategy Board (TSB), December 2013.

[13] INMAP Project – Industrialisation of Novel MarBN Steel for Advanced Power Plants is a 2 year R&D project, UK Technology Strategy board (TSB), 2014.
[14] S. Roberts, Steam turbine castings, Casting's Buyer (August 2011).

All trade marks are the property of their respective owners Inconel 740H is the property of Special metals Corporation, Haynes 282 is the property of Haynes International, Goodwin G130 is the property of Goodwin Steel Castings Ltd, and Toshiba TOS-3X is the property of Toshiba Corporation.

This page intentionally left blank

Martensitic steels for rotors in ultra-supercritical power plants

6

G. Zeiler
Bohler Edelstahl GmbH & Co KG, Kapfenberg, Austria

6.1 Introduction

Energy is a basic necessity for a high standard of living in each country. To preserve the environment for future generations and to protect health of humanity and other living beings, energy production itself is faced with the introduction of stringent emission regulations.

That is why in the next decades renewable energy resources such as wind and solar energies will have to be increased. Fossil fuels, such as coal, oil, and natural gas will nevertheless still play an important role as an energy provider in developed countries, also as a weather-independent basic supply and to cover periods where a maximum of demand is required.

Especially in large developing countries like India and China, the demand for coal-fired power plants will continue its expansion due to the regional deposits of coal in the near future.

This continuous trend toward more economic electricity production parallel to reduced environmental pollution can only be sustained by improving the thermal efficiency of power generation plants. The efficiency is increased by raising the temperature as well as the pressure of the steam, which finally results in the need for materials with improved high-temperature capability for the boiler and turbine design.

To minimize investment costs, which of course influences the effective cost of electricity generation, martensitic steels for all major components in boiler and turbine have to be used as much as possible. Specifically, steels of the 9–12% Cr class are required with high long-term creep strength and oxidation resistance in steam, along with not too complex manufacturing processes.

During the last 25–30 years, enormous efforts, especially in development of new materials, were made to establish the technology for the new ultra-supercritical (USC) power plants, which are the standard of today's fossil-fired power generation plants. The basic necessity for realization was to increase temperature and pressure of the inlet steam into the turbine combined with single and/or double overheating. Steam temperature of 600–610°C, 630°C overheating temperature, and overcritical steam pressures of about 300 bar could be realized [1–3].

As an example, the profit on thermal efficiency in a 600°C/300 bar power station with double overheating in comparison to the traditional 540°C/185 bar power

Materials for Ultra-Supercritical and Advanced Ultra-Supercritical Power Plants.
http://dx.doi.org/10.1016/B978-0-08-100552-1.00006-3
Copyright © 2017 Elsevier Ltd. All rights reserved.

plants with single overheating is more than 8%, and in parallel the CO_2 emission can be reduced by about 20%, which has a significant impact on environmental aspects [4].

From this point of view, the USC power plants are playing an important role in power generation systems with high thermal performance.

Resulting from the oil crises in the 1970 years, the topic of reducing CO_2 emissions, a careful dealing with resources and the more and more upcoming international competition led to the demand after flexible and cost-convenient fossil-fired steam power plants. To fulfil all these aspects, improved and advanced ferritic martensitic 9–12% Cr steels for all the key components in the hot sections of the power station became necessary, and research and development programs were initiated in the highly developed countries in Europe, United States of America, and Japan (Fig. 6.1) [4,5].

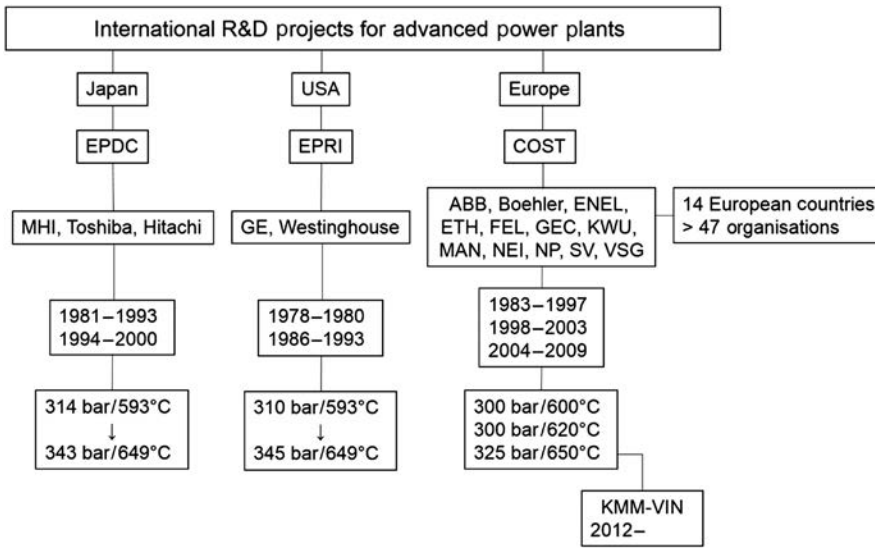


Figure 6.1 International R&D projects for development of improved creep resistant steels.

6.2 Common rotor material requirements

As in nearly all areas of technique, but especially in the field of energy machines operating at higher temperatures, the realization of these machines and their physical processes is strongly related to the availability of suitable materials. The improvement in efficiency and performance of modern steam power engines can only be achieved by raising the temperature as well as the pressure of the steam generated in the boiler. To withstand these advanced operating conditions, materials are required with improvements:

- high-temperature capability,
- oxidation resistance in steam,

- weldability,
- low costs,
- good availability and easy to fabricate.

To define the specific requirements/loads for steam turbine rotors, we have to consider several basic types of steam turbines. In general, we have to differentiate between high-pressure (HP), intermediate-pressure (IP), and low-pressure (LP) turbines, where each is operating in a specific temperature/pressure range, shown in Fig. 6.2, for power ranges up to 1000 MW [6] and a typical configuration of a turbine train (Fig. 6.3).

Turbine	Temperature (°C)	Pressure (bar)
High pressure (HP)	≥ 530	180
Intermediate pressure (IP)	≥ 530	30
Low pressure (LP)	≤ 350	10

Figure 6.2 Typical temperature and pressure parameters for subcritical steam turbines.

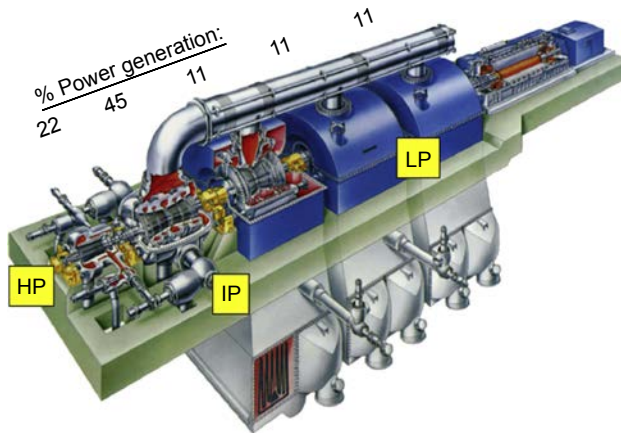


Figure 6.3 Typical Siemens steam turbine arrangement with high-pressure (*HP*), intermediate-pressure (*IP*), and low-pressure parts (*LP*).
Siemens AG, Power Generation.

Further solutions for power generation with steam turbines are combined HP-IP and IP-LP turbines for the smaller power range for combined cycle power plants (CCPP). The rotors are hereby in monoblock or welded rotor design [2] (Fig. 6.4).



Figure 6.4 High-pressure turbine with combined intermediate-low pressure in welded design. Siemens AG, Power Generation.

To fulfil the various customer needs for an advanced power plant, specific design requirements have to be met.

The most important components in turbo-sets like rotors, casings, valves, bolts, blades, and pipes are differently loaded, and as a consequence, specific property profiles have to be considered.

Next, the basic material requirements for HP and IP steam turbine components are listed:

- static strength (tensile strength),
- creep rupture strength,
- fracture toughness,
- low cycle fatigue (LCF),
- high cycle fatigue (HCF),
- creep crack growth,
- fatigue crack growth,
- erosion and oxidation behavior.

Today, advanced USC turbines are operating with temperatures from 580–600°C and a maximum steam pressure of 300 bar. However, the maximum possible operating temperatures of the developed materials are not fully used yet.

HP and IP rotor forgings, which can reach diameters of up to 1200 mm, need to be manufactured in well-selected materials to meet all property requirements. Creep behavior plays an important role for areas such as the rotor center and the blade attachment, whereas the fatigue resistance is mainly considered in the surface regions [6].

Especially, the material class of the 9–12% CrMoV steels, used in power plants since the late 1950s, were identified with many advantageous properties and a big potential for improvement. Their mechanical and physical property profile made it possible to go for temperatures $T > 600$°C, and the target of material development in Europe was defined as follows [4,6–7]:

- 100,000 h creep rupture strength at 600–620°C and 100 MPa design stress,
- good creep rupture ductility with > 10% elongation and no notch sensitivity,

- good through-hardenability up to at least 1200 mm diameter,
- 0.2% yield strength of at least 700 MPa,
- other properties should not be worse than those of conventional 12% and 1% CrMoV rotor steels.

The way and chronology of development for achieving this goal is now described in the following paragraphs.

6.3 Development of martensitic 9–12% Cr rotor steels for USC application

12% Cr steels, alloyed with Mo and V, have been used in power plants since the middle of the 20th century. The German alloy X21CrMoV12 1, strengthened by solid solution and precipitation of $M_{23}C_6$ and a small amount of V(C, N), was first used for blades, forgings, and castings in the 1950s, and after solving the weldability problems, the steel has been introduced successfully also for tubes and pipes in power plants. Since 1955, European turbine producers have manufactured numerous rotors of the material X21CrMoV 12 1, specified in SEW 555, with diameters up to 1300 mm and weights up to 35 metric tons. The 0.2% yield strength was in the range of 500–650 MPa at operating temperatures of maximum 580°C (560–600°C steam inlet temperature). In this temperature range, the X21 steel showed a clear advantage in comparison to 1% CrMoV steels [7,8].

At the end of the 1950s, two 12% CrMoV rotor steels were also developed in the United States for HP and IP rotors. One of them is alloyed with 1% tungsten and the other with additions of niobium and nitrogen (Fig. 6.5). At this time the big potential of the 12% Cr steel class for high long-term creep strength and oxidation resistance in steam was found, and a further milestone in development history was the introduction of the tube and pipe steel T/P91 in the late 1970s by Combustion Engineering and Oak Ridge National Laboratories in the United States.

Steel	Source	C	Si	Mn	Cr	Mo	Ni	W	V	Nb	N	Creep rupture strength at 600°C/10^5 h (MPa)
		(weight %)										
12%CrMoV	SEW 555	0.22	0.25	0.50	12.0	1.0	0.50	–	0.30	–	–	59
13%CrMoWV	USA	0.22	0.40	0.80	13.0	1.0	0.75	1.0	0.25	–	–	
11%CrMoVNbN	USA	0.18	0.25	0.70	10.5	1.0	0.70	–	0.20	0.08	0.06	85

Figure 6.5 Standard and developed 10–12% Cr steels for HP and IP steam turbine rotors.

At the same time, development work has been going on in Japan, led by Prof. T. Fujita at Tokyo University. Based on the highly creep-resistant 12% Cr steels, developed in Europe and the United States, Fujita started to investigate to what extent alloying elements could improve the creep strength for 600°C application. This was found by alloying and balancing the steel composition with Nb, N, and W, whereas the strengthening was mainly pursued by solid solution with W. In the middle of the 1980s, this led to new alloys for turbine rotor forgings TR 1100, 1150, and 1200, as

well as to the pipe steel NF616 (P92 according to ASME code) developed together with Nippon Steel Corporation (Fig. 6.6) [7,8].

Steel	Source	C	Si	Mn	Cr	Mo	Ni	W	V	Nb	N	Creep rupture strength at 600°C/10^5 h (MPa)
		(weight %)										
TR1100 (TMK1)	Japan	0.14	0.05	0.50	10.3	1.50	0.60	–	0.17	0.05	0.04	90
TR1150 (TMK2)	Japan	0.14	0.05	0.50	10.3	0.50	0.70	1.80	0.17	0.05	0.04	90
TR1200	Japan	0.12	0.05	0.50	11.3	0.30	0.80	1.80	0.20	0.05	0.06	125

Figure 6.6 Newer developed 10–12% Cr steam turbine rotor steels in Japan.

The compositions of the steels TR 1100, 1150, and 1200 were selected on the basis of short-term creep tests with less than 10,000 h and were supposed to have enough creep strength for the application at temperatures up to 593, 621, and 648°C according to 1100, 1150, and 1200°F.

Nevertheless, it has to be pointed out that extrapolation of short-term creep results to 100,000 h is very difficult and dangerous for these complex alloyed steels. Reliable data on the creep strength can only be provided after very long testing times. This was the conclusion of a critical evaluation of published creep results by Newhouse and Greenfield [7].

The steel TMK 1 or TR 1100 was then selected for the first big forging for industrial use for the HP rotor of the 50-MW demonstration plant at Wakamatsu [7]. The rotor weighed 28 metric tons with a barrel diameter of 980 mm. With the applied heat treatment of 1100°C/oil + 550°C/FC + 680°C/FC, a 0.2% yield strength of 745 MPa, and an impact energy of 32 J, respectively, +25°C FATT could be achieved in the center of the rotor [9].

In sequence, further optimizations for improving the creep strength were done by defining the optimum content of C, N, and Cr as well as a careful balancing of Mo and W, whereby the Mo equivalent = Mo + 0.5 W was determined to be the significant parameter [7].

The developments in the United States and Japan have been followed up in Europe in the COST (COST = **co**operation in **s**cience and **t**echnology) programs: COST 501 (1983–1997), COST 522 (1997–2003), and COST 536 (2004–2009). In these programs, new ferritic creep resistant 9–12% CrMoV steels for turbine forgings, castings, and pipework were developed and characterized. Carried out under the frame of the European community, the participants consisted of power station manufacturers, manufacturers of forgings, castings, pipework, and welding consumables, power station operators, and research institutes as well as testing institutes and utilities.

It started in the 1980s with the first round and targeted a creep strength of 100 MPa for 100,000 h at 600°C. At the beginning, the approach was more or less empirical and concentrated at that time on the effect of boron additions and on a review of existing 9–12% Cr steel grades including worldwide development activities. In addition, the steelmaking developments in Europe and the forgemasters' experiences on 9–12% Cr as well as the careful balancing of Ni and Cr equivalents to avoid δ-ferrite were of big

importance. Furthermore, Al should be kept as low as possible, particularly due to the high affinity to N to enable a high amount of VN precipitates.

After this review, five grades of steel (called A to E) were identified as candidates for development, and small melts were produced for characterization of the materials. The alloy concept hereby was the addition of N, B, W, W + Mo, and Mo. Thereby the main requirements were to carry out long-term creep tests to avoid the uncertainty of extrapolation from short-time tests and to manufacture full-size rotors to get experience in manufacturing of these new steels, as well as getting the knowledge about the properties of the inner and outer regions of a real component.

After careful analysis of all results the two most promising candidate alloys E (1%Mo and 1%W) and F (1.5% Mo) were selected for the manufacture of trial rotor forgings with barrel diameters up to 1200 mm, in addition to the already produced first trial rotor B2 (1.5% Mo, 100 ppm B) (Fig. 6.7 and 6.8). A lot of testing work was

Steel	C	Si	Mn	Cr	Mo	Ni	W	V	Nb	N	B	Creep rupture strength at 600°C/10^5 h (MPa)
						(weight %)						
Cost B2	0.17	0.07	0.06	9.3	1.55	0.12	–	0.27	0.06	0.015	0.010	122
Cost E	0.12	0.10	0.45	10.3	1.05	0.75	0.90	0.18	0.05	0.05	–	95
Cost F	0.12	0.10	0.50	10.3	1.50	0.60	–	0.18	0.05	0.05	–	95

Figure 6.7 Within COST developed 10–12% Cr steels for steam turbine rotors.

performed on the materials, and they showed much improved creep strength and resistance to embrittlement in operation [10].

Meanwhile, these improved steels are in commercial operation in advanced European power stations and have made it possible to increase the operating steam temperatures from well-known 530–565°C up to 580–600°C with a corresponding increase in thermal efficiency.

The trend to even higher steam conditions was the subject of the COST 522 program, which explored the possibilities of stabilizing the tempered martensitic microstructure through addition of small quantities of boron.

In addition, Co was added up to 1.3% to reduce Ni and Mn, due to their detrimental effect on creep rupture strength, and limiting the risk of δ-ferrite formation. Furthermore, increased Cr levels up to 11% for better oxidation resistance were introduced, and a full program of screening tests was performed. From all these variants, only one alloy showed the best behavior and led to a new modified steel called "FB2", first produced as a trial melt (Fig. 6.9), and after getting very promising properties, a scale-up to industrial heat with the manufacture of the first trial rotor forging followed [11,12] (Fig. 6.10).

In total, three trial full-size rotor forgings have been manufactured applying three different melting routes.

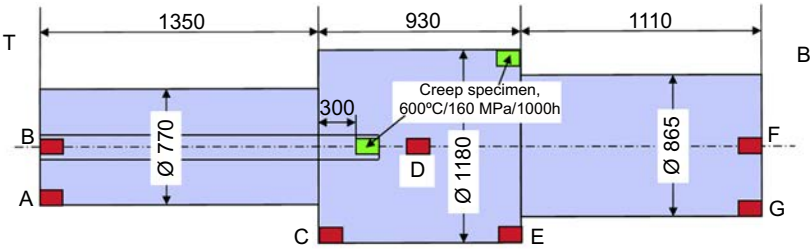
The first, manufactured by Bohler Edelstahl/Austria in 2001, used a 29-metric ton ingot via the BEST (Bohler electro slag toping) melting route, Saarschmiede/Germany a 56-mt ESR (Electro slag remelting) ingot, and Società delle Fucine/Italy has

Rotor	Manufacturer	Melting process	D_{max} (mm) / Ingot weight (kg)	Heat treatment	Periphery, tangential, body top end				Centre, radial, midsection of body			
					UTS (MPa)	0.2%YS (MPa)	Charpy (J)	FATT (°C)	UTS (MPa)	0.2%YS (MPa)	Charpy (J)	FATT (°C)
B2	Bohler Kapfenberg (A)	ESR	840 / 15,000	1100°C/oil + 590°C + 700°C	801	642	22	+45	813	651	33	+60
E	Saarschmiede Voelklingen (Ge)	ESR	1200	1070°C/oil + 570°C + 690°C + 715°C	914	801	27	+55	875	744	86	+5
			42,000		783	647	76	+20	785	633	146	–10
F	Forgemaster Eng. Sheffield (UK)	VCD	1200	1070°C/oil + 570°C + 680°C + 710°C	892	770	55	+30	855	729	42	+40
			45,000		737	600	99	–2	764	609	75	+5

Figure 6.8 Basic data and mechanical properties at RT of COST rotors B2, E, and F (COST 501/II Program).

Steel	C	Si	Mn	Cr	Mo	W	Ni	Co	V	Nb	N	B
FB2 test melt	0.13	0.05	0.82	9.32	1.47	–	0.16	0.96	0.20	0.050	0.019	0.0085
FB2 trial rotor	0.13	0.09	0.33	9.08	1.43	–	0.16	1.26	0.22	0.054	0.022	0.0076

Figure 6.9 Chemical compositions of steel FB2 [wt%].



	A	B	C	D	E	F	G
RT:							
UTS (N/mm²)	835	838	825	863	824	838	834
0,2YS (N/mm²)	713	703	700	730	702	708	715
EL (%)	15	14	17	13	16	12	16
RA (%)	56	44	61	40	56	32	56
Charpy (J)	30, 35, 30	26, 28, 22	35, 33, 31	27, 21, 23	37, 40, 28	26, 24, 23	31, 56, 35
FATT (°C)	+52	+64	+36	+67	+49	+65	+48
625°C:							
UTS (N/mm²)	437	366	417	368	429	416	450
0,2YS (N/mm²)	381	323	361	308	362	359	390
EL (%)	19	19	21	29	20	16	19
RA (%)	62	79	70	79	69	68	70
Grain size (ASTM)	2–0	1–0	3–1	1–0	2–0	1–0	2–0

S, surface, tang.; *C*, center, transversal

QHT: 1100°C/spray quenching + 570°C/AC + 700°C/AC

Figure 6.10 Mechanical properties of first trial rotor FB2 by Bohler.

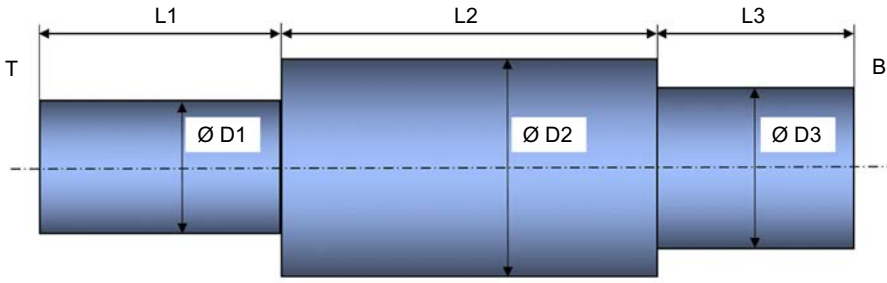
applied the steelmaking process VCD with an ingot weight of 53 mt [6,13,14] (Figs. 6.11 and 6.12).

The results of creep tests showed that all data lies in one narrow scatter band, confirming the trial melt behavior of FB2. In Fig. 6.13 the values are all above the rotor B2 line, the boron containing steel from COST 501, and the basis for the development of FB2.

The very good creep behavior of steel FB2 can be attributed to characteristic microstructural features and their stability under the influence of temperature and stress.

The microstructure in the quality heat-treated condition in general consists of tempered martensite and precipitates, mainly $M_{23}C_6$ carbides representing the dominant particle type.

During creep, in general, the dislocation density decreases, subgrains form and grow, $M_{23}C_6$ particles coarsen, the martensite laths become much wider, and also new



Manufacturer	Melting process	D1 (mm)	D2 (mm)	D3 (mm)	L1 (mm)	L2 (mm)	L3 (mm)	MDDS (mm) D1/D2/D3
Bohler Kapfenberg (Austria)	BEST	770	1180	865	1350	930	1110	1.2/1.8/1.3
Societa delle Fucine Terni (Italy)	EAF/VCD	925	1110	790	800	2750	830	1.0/1.5/1.5
Saarschmiede Voelklingen (Germany)	ESR	800	1215	1050	1085	2130	800	1.5/2.0/1.7

MDDS, minimal detectable defect size

Figure 6.11 COST FB2 trial rotor forgings: dimensions and minimum detectable defect size (MDDS) results.

phases as the Laves phase appear. Not so in FB2, the good high temperature stability is caused by the following:

- a martensitic structure with narrow martensite laths, which are decorated with and therefore stabilized by $M_{23}C_6$ carbides, stabilized itself by boron [15],
- a high dislocation density, which is preserved for longer times,
- and Nb, V carbonitrides (up to about 1 µm), which avoid grain growth during austenitization and are stable during creep [16].

A representative TEM image of steel FB2 is shown in Fig. 6.14 [17].

Under the influence of temperature, Laves phase also appears in FB2, but it is very small (0.6–0.8 µm) and homogeneously distributed, and therefore has no negative effect on creep.

All in all, it can be stated that materials for USC power plants have been developed with the goal to provide environmentally friendly power plants with low consumption of primary energy and the lowest rate of emissions. These newly developed material grades are highly creep-resistant martensitic materials for the use of up to 625°C and

Rotor	Manufacturer	Melting process	D_{max} (mm) / Ingot weight (kg)	Heat treatment	Test temp. (°C)	Periphery, tangential, body end							Core, radial, midsection body (* body end)						
						UTS (MPa)	0.2%YS (MPa)	EL (%)	RA (%)	Charpy (J)	FATT (°C)	Grain size (ASTM)	UTS (MPa)	0.2%YS (MPa)	EL (%)	RA (%)	Charpy (J)	FATT (°C)	Grain size (ASTM)
FB2	Boehler Kapfenberg (Austria)	BEST	1180 / 29,000	1100°C/spray Q + 570°C + 700°C	RT	824	702	16	56	37	+49	0–2	863	730	13	40	23	+67	0–1
					+625	378	332	21	82				368	308	29	79			
	Societa delle Fucine Terni (Italy)	EAF / VCD	1110 / 53,000	1100°C/oil + 570°C + 700°C	RT	776	656	20	62	14	+90	0–2	803	682	13	39	12	+94	
					+625	449	434	17	77				445	428	22	79			
	Saarschmiede Voelklingen (Germany)	ESR	1215 / 56,000	1100°C/oil + 570°C + 700°C	RT	846	720	15	56	36	+47	00–2	843 *	710	13	45	29	+58	< 00 = 70% > 00–2 = 30%
					+625	464	392	27	84				465 *	396	23	70			

Figure 6.12 Basic data and mechanical properties at RT of COST rotors FB2 (COST 522 Program).

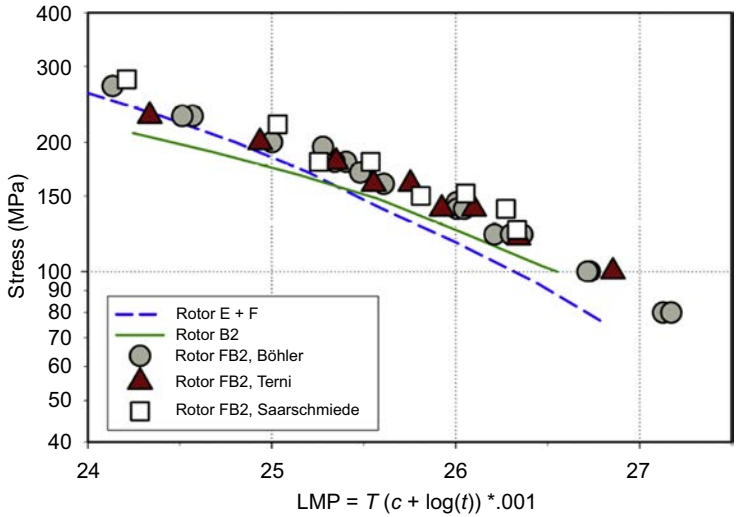


Figure 6.13 Creep rupture strength of COST FB2 test rotors in comparison to other COST rotor alloys [14].

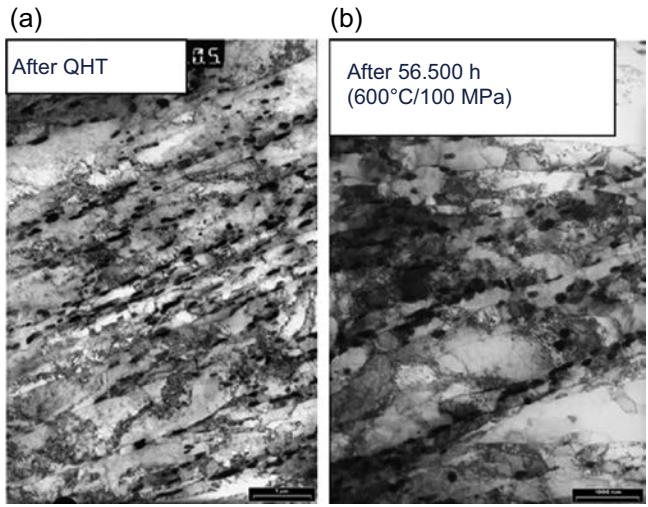


Figure 6.14 Microstructure of FB2: after being quality heat treated (QHT) (a); gauge section (b) (600°C, 100 MPa) after 56.500 h [17].

steam pressures above 300 bar. Fig. 6.15 [18] shows the steps in the development of materials for USC power plants with respect to increasing steam temperatures.

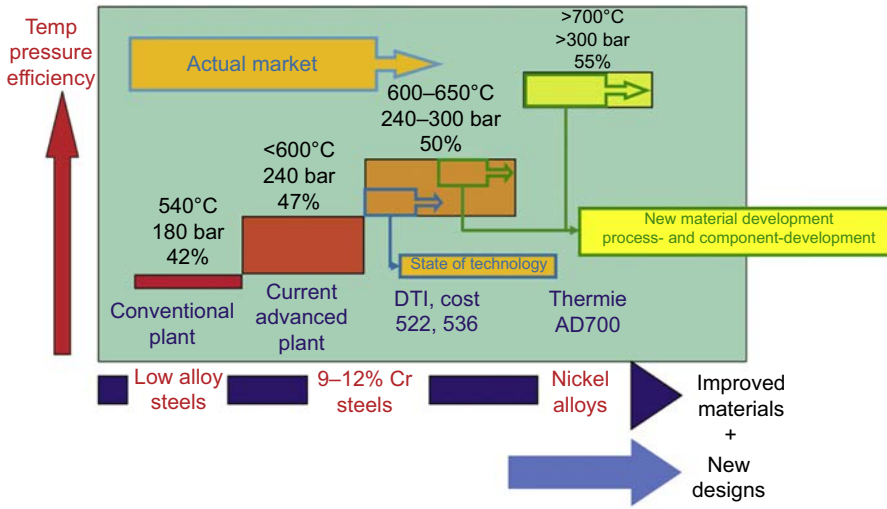


Figure 6.15 Steps in the development of the materials for USCs.
Voest Alpine AG, Foundry Linz; C. Lochbichler, F. Füreder Kitzmüller, G. Zeiler, S. Paul, J. Klarner, T. Vogl, et al, Know how and process development for components used in (A) USC power plants, 10th Liege cost Conference on materials for advanced power Engineering, September 14th–17th 2014, 2014 [Liege, Belgium].

6.4 Common materials for steam turbine rotors in Europe: fabrication and basic properties

All the efforts undertaken in the European research activities COST 501/522 have been very successful and led to three new modified creep-resistant chromium steels: COST grade E (10% CrMoWVNbN), grade F (10% CrMoVNbN), followed by FB2 (9% CrMoVNbNB).

These improved steels have become well established and qualified and are now in commercial operation in advanced European fossil-fired power stations. They have made it possible to increase the operating steam temperatures from widely known 530–565°C up to 580–610°C with a corresponding increase in thermal efficiency from previous 30–35% to now 42–47%, connected with approximately 30% CO_2 reduction [19].

6.4.1 COST E and COST F rotor forgings for 600°C steam temperature

In the early 1990s, industrial production of these newly developed 9–10% Cr steels became ongoing in Europe and in Japan.

As described in Section 6.3, the development occurred very carefully, starting with investigation of several test melts and determination of candidate materials up to the manufacturing of pilot components with real dimensions followed by testing times up to 30,000 h. This succeeded the preconditions to realize 14 European steam power plants with advanced steam parameters and power ranges up to 950 MW [4]. The increase of the steam parameter from 540°C up to 610°C occurred systematically in a way that the property potential of the new steels did not need to be exploited for the first plants.

All the three European forgemasters involved in the COST 501 programs—Sheffield Forgemasters, Saarschmiede, and Bohler Edelstahl—were predestined for the manufacturing of the first rotor forgings, based on their knowledge and experiences gained in the COST action, when manufacturing the prototype forgings. Depending on the forgemasters specific equipment, the melting routes ranged from conventional ingot casting over the BEST process up to ESR with ingot weights up to 108 metric tons [20–22] at the beginning. To date, ingot weights up to 154 metric tons have already been realized [23].

Bohler Edelstahl, for many years a premium supplier of forged components for the power generation industry, mainly applied the melting route over the BEST process, a process with special measures to improve the ingot homogeneity in comparison to conventional casted ingots (Fig. 6.16).

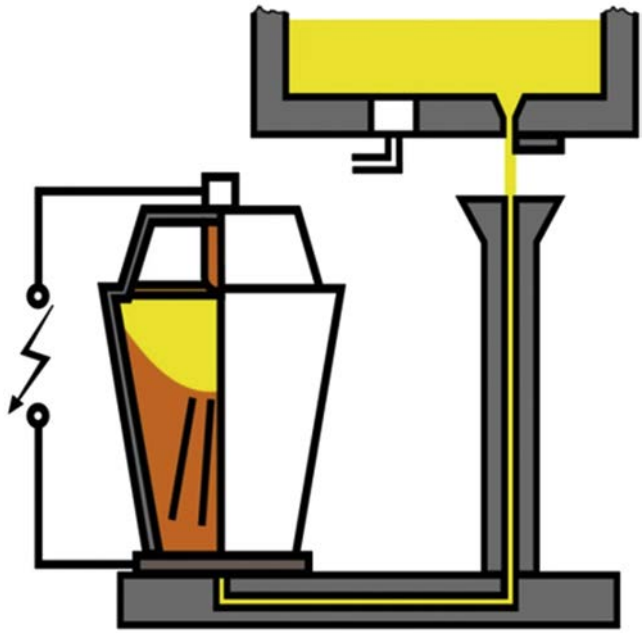


Figure 6.16 Bohler electro slag topping (schematic).

A water-cooled ring is placed at the top end of a forging ingot mold. The mold is filled with liquid steel via a bottom pouring process. Afterward, the steel surface is covered with a slag of a special chemical composition. A consumable electrode is immersed into the slag, electrical energy is applied to the system, the slag is heated up, and the electrode begins to melt. Droplets of the melting electrode fall into the liquid pool of the solidifying ingot, compensating for shrinkage and influencing the solidification process in a positive way.

Ingots produced by this process are free from V-segregations, and the structure of A-segregations is similar to ESR-ingots. Homogeneity and cleanliness is better than in conventional casted ingots but not as good as ESR material.

The ingot weights were up to a maximum 48 metric tons, suitable for HP rotors in monoblock construction and shaft parts for welded rotor constructions.

A similar ingot-making process, developed by JCFC in Japan, is the ESHT (**e**lectro **s**lag **h**ot **t**opping) process. High-Cr steel rotor forgings with good homogeneity, sufficient cleanliness, and also good mechanical properties including creep rupture strength could be confirmed [22,24].

The second applied melting route used so far is the PESR (**p**rotective gas **e**lectro **s**lag **r**emelting) process, with a maximum possible ingot weight of 32 mt due to the equipment and possibilities at Bohler Edelstahl (Fig. 6.17).

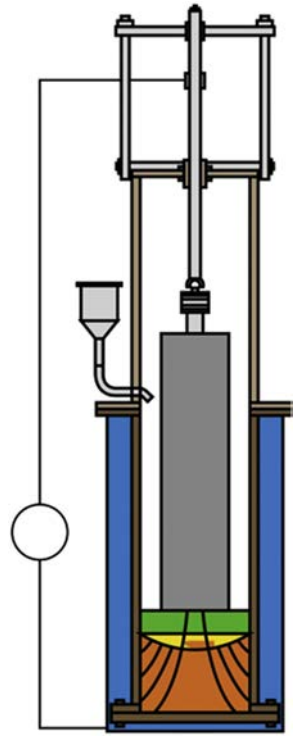


Figure 6.17 Protective gas electro slag remelting (schematic).

Remelting takes place in a leak-proof chamber similar to the VAR process. Before starting remelting, the chamber is evacuated to a pressure lower than 10 mbar and flooded successively with protective gases argon and nitrogen. The reactive slag is first melted by the use of an electric arc. Once this has occurred the normal ESR process takes place with the advantage of the total absence of oxygen in the atmosphere above the slag surface and around the electrode. In that manner, no oxidation can take place, and this results in a very uniform quality of the remelted steel from bottom to top of the ingot. PESR is the desired remelting process for components made of super clean, creep-resistant 10% Cr steels with reduced Si and Al contents.

After heating the ingots to forging temperature, they are forged on a forging press, mainly by multiple upsetting operations followed by cogging and forging to the final shape. The number of upsetting operations is hereby strongly dependent on melting route, ingot weight, size, and final rotor forging dimensions. Especially in the case when large ingots are needed, the manufacturing parameters such as the forging temperature, soaking time, and deformation rate for the first forging steps are very important to ensure a defect-free forging and suitable microstructure. To optimize the forging sequence and improve the reproducibility of the forging process, FEM modelling can be a very helpful instrument to develop the optimal forging technology. Achieving a largely uniform deformation resulting in uniform microstructure and grain size distribution is one of the preconditions to achieve the high requirements on mechanical properties and ultrasonic detectability (Fig. 6.18).

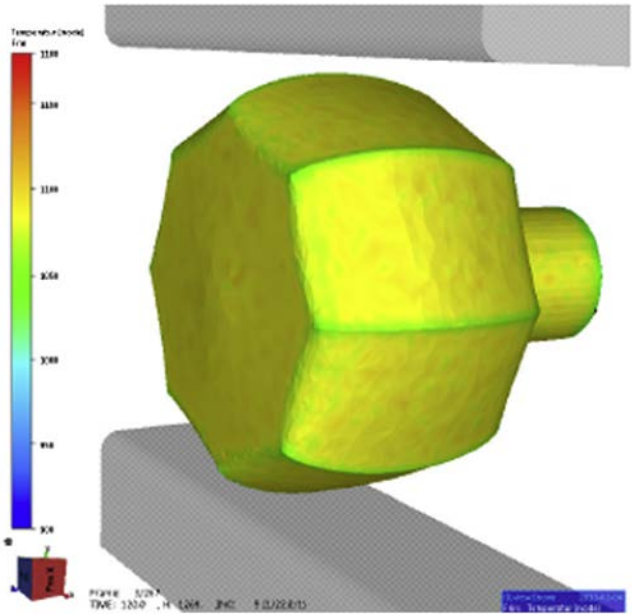


Figure 6.18 FEM model for optimized forging steps (schematic).

When forged, the rotors are preliminary heat treated, which is a very important heat treatment step to allow optimum ultrasonic testing of the material/forgings in the quality heat-treated (QHT) condition. This can be carried out in different ways; meanwhile, pearlitic phase transformation has become a common procedure [11,23,25,26]. After pre-machining, the quality heat treatment to adjust a yield strength $\geq 700\,N/mm^2$ is performed, followed by final machining to delivery contour and testing including heat stability test prior to shipment.

The quality heat treatment (Fig. 6.19) consists of these steps:

austenitizing: 1050°C–1100°C/oil or polymer or water-spray quenched
first tempering: 570°C/air cooled, to complete the martensitic transformation
second tempering: 690–700°C/FC, AC, to adjust the desired properties

The soaking times have to be defined according to the largest diameters of the rotor forgings.

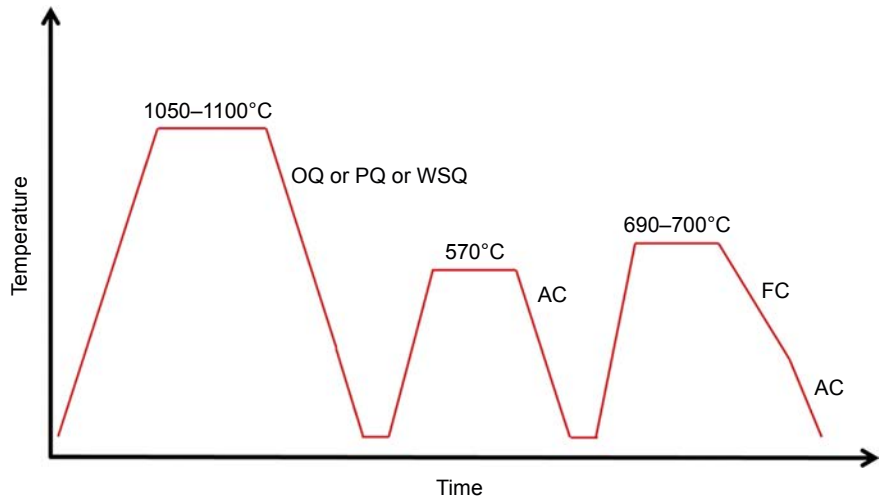


Figure 6.19 Quality HT cycle (schematic).

Typical test results are summarized in Fig. 6.20.

Beside the mechanical properties, which have to be fulfilled, the ultrasonic detectability including sound attenuation is an important criterion for the quality of rotor forgings and therefore forms part of the specifications. Detectable flaw size values of minimum 1 mm for diameters ≤ 800 and 1.5 mm for diameters ≥ 800 mm are required and achievable (Fig. 6.21).

To date, these new steels have been introduced in highly efficient USC power plants with a total capacity of about 187 GW worldwide [IEA WEO 2013]. COST E and F are meanwhile specified in the German standard SEW 555 with the steel numbers 1.4906 (grade E) and 1.4902 (grade F). Bohler manufactured more than

Steel	Melting process	Body (mm) / Ingot weight (kg)	Q-heat treatment	Periphery, tangential, body end						Core of journal, radial, body end side						MDDS body PHT (mm)	MDDS body QHT (mm)	Sound attenuation 2 / 4 / 5 MHz (dB/m)
				UTS (MPa)	0.2%YS (MPa)	EL (%)	RA (%)	Charpy (J)	FATT (°C)	UTS (MPa)	0.2%YS (MPa)	EL (%)	RA (%)	Charpy (J)	FATT (°C)			
E	BEST	1020 / 44,000	1080 °C/oil + 570 °C + 705 °C	842	718	19	63	87		867	740	19	63	45	+37	2.0	1.0	0.5 / 2.0 / 4.0
E	ESR	1300 / n/a	n/a	866	744	18	59	49		878	743	18	56	52	+34		1.2	1.9 / 3.5 / 5.0
E	ESR	1240 / 154,000	n/a	862	736	18	60	87		854	730	15	60	80	+18		1.0	1.3 / 4.4 / 4.5
E	ESHT-J	1280 / 69,500	1090 °C/oil + 570 °C + 685 °C	896	780	20	60	37	+30	903	782	16	47	34	+27		0.9	0.4 / n/a / 4.6
F	ESR	1410 / 115,000	1090 °C/oil + 570 °C + 690 °C	875	740	18	56		+17							3.4	1.4	0.4 / n/a / n/a
F	ESR	1370 / 115,000	1090 °C/oil + 570 °C + 690 °C	873	741	18	59		+22							3.4	1.4	0.8 / n/a / n/a

MDDS, minimal detectable defect size; *PHT* , preliminary heat treatment (= pearlitic transformation); *QHT*, quality heat treatment

Figure 6.20 Basic data and mechanical properties at RT of COST rotors E and F from different suppliers [23,25,26].

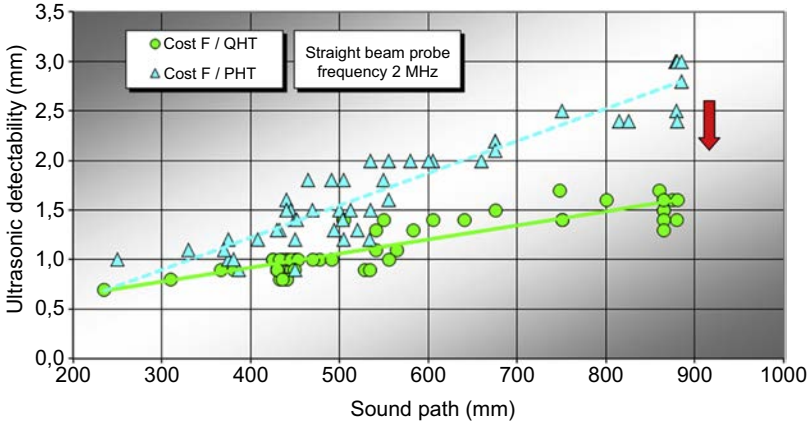


Figure 6.21 Ultrasonic detectability versus sound path (COST F steel).

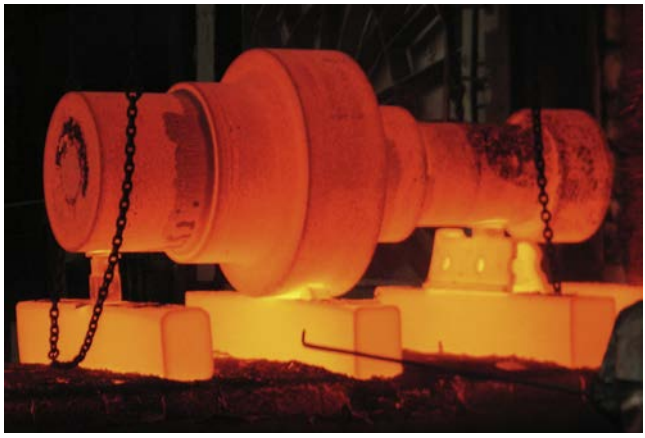


Figure 6.22 Shaft component at QHT, COST steel F.



Figure 6.23 Shaft component machined, COST steel E.



Figure 6.24 HP rotor at final forging, COST steel E.

480 rotor forgings out of COST steels type E and F, namely high-pressure shafts as well as shaft components for welded rotor constructions with diameters from 700 to 1180 mm and shaft ends with flange diameters of up to 1800 mm (Figs. 6.22–6.24).

6.4.2 COST FB2 for up to 620°C

After the successful development of COST type E, F, and B2 material within COST 501 (1983–1997), the subsequent COST 522 action (1998–2003) followed the trend to develop materials for even higher steam temperatures (Fig. 6.25).

Trial rotor	0.2%YS (MPa)	Max. testing time (h)	CRS at 600°C/10^5h (MPa)
B2	> 600	131,000	122
E	> 700	106,000	95
F	> 700	115,000	95
FB2	> 700	60,000	125

Figure 6.25 100,000 h creep rupture strength of COST type E, F, B2, and FB2 steels.

Based on the composition of the boron-alloyed B2 steel, which showed the highest creep resistance of the three steels [19], a new modified steel called "FB2" with the addition of Co has been developed and first produced as a trial melt by Bohler Edelstahl. The very promising properties of this FB2 test material led to an upscale to industrial heat and the manufacture of a full-size trial rotor forging with a final weight of 17,000 kg, again manufactured by Bohler Edelstahl. Then forgings from Società delle Fucine Terni and Saarschmiede followed [6,12–14].

The excellent creep resistance of FB2 and the successful transformation of trial melt behavior to large components led to the start of industrial production for new USC power plant projects in Germany, the United States, and Asia, starting in 2007 (Fig. 6.26).

Power plant	Component	D_{max} (mm)	Delivery weight (kg)
Hempstaed	Rotor part	980	6500
Hempstaed	Rotor part	860	6500
Neurath F	Rotor part	1064	9200
Boxberg	Rotor part	1022	7000
Karlsruhe	Rotor part	1112	10400
Sostanji	Rotor part	1066	8700
Manju	Rotor part	1056	9700

Figure 6.26 First USC power plants using FB2 in turbines.

Again, as already described in the previous chapter for the 600°C materials COST type E and F, the melting route for FB2 steel is also ranging from conventional ingot casting with ingot weights of up to approximately 30 metric tons for smaller shaft dimensions over BEST process [11,12,17,21] or equivalent ESHT [27–29] up to ESR with ingot weights up to 90 metric tons [30–32]. Therefore the melting/remelting know-how in combination with the specific steelmaking equipment of the forgemasters are of great importance to fabricate a highly homogeneous and uniform ingot with a good boron distribution from top to bottom and also over the whole cross-section of the ingot. This is not very easy to adjust for FB2 type steel, but these are basic necessities to gain the excellent creep rupture strength properties for the forging.

The basic manufacturing steps for FB2 rotor forgings are quite similar to those for type E or F forgings and are roughly described for a conventional ingot as follows [17]:

Melting the steel in an electric arc furnace (EAF), then ladle furnace (LF) followed by argon oxygen decarburization (AOD) and LF with vacuum degassing (VD), casting the ingot by bottom pouring process, hot forming, preliminary heat treatment, pre-machining, ultrasonic testing, QHT, machining, and final testing (Fig. 6.27).

Considering the fabrication of larger forgings with the need of heavier ingots, the use of BEST or even better remelted (PESR) materials due to a better consolidation of the ingots combined with less segregations and a better homogeneity of the later on product is advisable.

The ingot is then heated up to forging temperature and forged on a forging press by multiple upsetting operations followed by cogging and forging to the final shape. All the considerations about deformation rates—described under Section 6.4.1—are also fully valid for FB2 forgings, whereby forging temperatures have to be set much more carefully to not damage the microstructure. It is of great importance to avoid delta ferrite, which can occur depending on the actual chemical composition beginning at 1180°C and above [31]. Forging temperatures and soaking times have to be tuned very well and adapted to each deformation step.

When forging is finished, the preliminary heat treatment (PHT) has to be carried out to cool down the forging to room temperature. Meanwhile, it is well known that

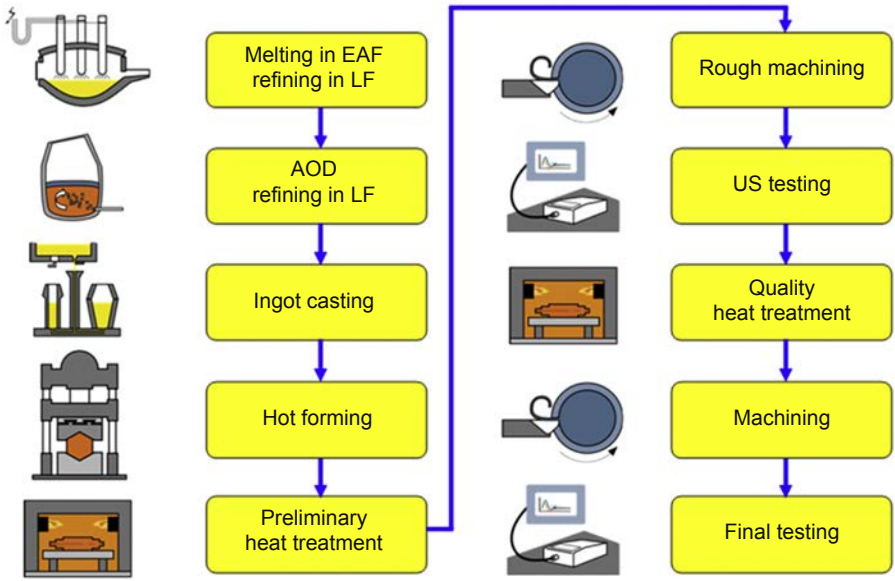


Figure 6.27 Principal flow chart of FB2 rotor manufacturing route.

boron-alloyed steels have to be austenitized at higher temperatures to generate the expected high creep resistance. The disadvantage, when all precipitates are in solid solution at austenitizing temperature, is grain coarsening and later on a bad ultrasonic detectability, worse than COST E or F materials. A simple martensitic transformation is only sufficient in case of smaller cross-sections because there is not so much improvement in grain size expected. For large forgings, a pearlitic transformation, similar to that applied on the 600°C class 10% Cr rotor forgings, has meanwhile become evident and is much more efficient to get a finer grain after quality heat treatment followed by an improvement of the minimum detectable defect size (MDDS) [27,28,31–33].

The microstructure obtained after pearlitic transformation consists of ferrite, fine $M_{23}C(B)_6$, and eutectoid structure at the prior austenite grain boundaries.

After pre-machining the rotors to achieve a defect-free surface, ultrasonic tests are performed to confirm the internal quality of the forgings. Then the quality heat treatment (Fig. 6.28) for adjusting the mechanical properties has to be carried out by austenitizing at 1100°C/rapid cooling (oil or polymer or spray quenching, depending on the facilities) and double tempering to the target 0.2% yield strength of ≥650 N/mm^2. Double annealing has to be performed to ensure a totally annealed martensitic microstructure.

The rotors are then machined and checked (Fig. 6.29) using ultrasonic testing to determine the MDDS. Usual measured MDDS values range from 1.5 mm for a smaller part with ∅ 860 mm up to 2.2 mm for parts with a diameter of 1120 mm up to 1200 mm, respectively, when applying martensitic transformation as a PHT. There is only a small improvement in MDDS of approximately 0.8 mm when comparing with the preliminary heat-treated condition [17,33,34].

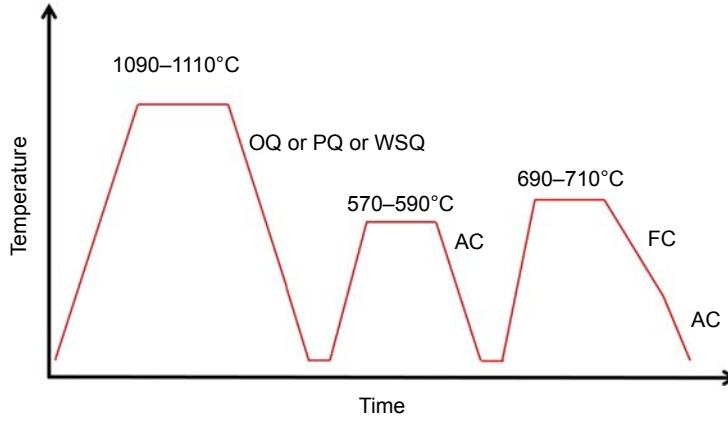


Figure 6.28 Quality HT cycle (schematic).



Figure 6.29 Quality heat-treated and machined FB2 forging; final weight 9.2 mt.

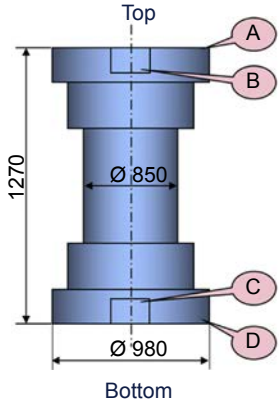
It is reported [27,32,33,35] that by applying (isothermal) pearlitic transformation the grain transformation process results in a significant improvement of the minimum detectable defect size of 1.1–1.3 mm for a rotor barrel diameter of 1200 mm (Fig. 6.30).

All turbine rotors are subjected to mechanical technological testing to ensure their suitability for use. Usually the properties are checked at different test positions, depending on the shape of the rotor forging; specimens in tangential direction from the outer segments on both ends, from the barrel diameter, from the core when taking a core sample, and in some cases specimens are taken from a near-center test ring from the face end. Typical test results of basic strength and toughness properties are summarized in Fig. 6.31.

Manufacturer	D_{max} (barrel) (mm)	Preliminary heat treatment	Quality heat treatment (°C)	MDDS (mm)
Boehler (trial rotor)	1180	Martensitic transformation	1100 570 700	1,8
Boehler	980	Martensitic transformation	1100 570 690	1,7
Saarschmiede	1115	Martensitic transformation	1100 570 700	2,0
Saarschmiede	1250	Martensitic transformation	1100 570 700	2,0
JCFC, Japan	1280	Pearlitic transformation	1095 570 660	1,5
Saarschmiede	1185	Pearlitic transformation	1100 570 690	1,3
Saarschmiede	1205	Pearlitic transformation	1100	1,1

MDDS, minimal detectable defect size

Figure 6.30 Achievable detectable flaw sizes.



	Test position			
	Edge		Centre	
	A	D	B	C
TS (MPa)	814	819	810	812
0,2%YS (MPa)	681	687	680	684
EL (%)	16	17	17	17
RA (%)	53	55	54	55
CVN, RT (J)	23, 36, 37	34, 38, 36	32, 30, 36	32, 37, 35
CVN, +40°C (J)	55, 70, 53	48, 56, 54	48, 55, 52	50, 47, 56
FATT (°C)	54	58	58	60

Detectable flaw size:
1,7 mm (Ø 980 mm)

Figure 6.31 Mechanical properties of an FB2 rotor forging.

The microstructure, checked at the edge as well as center and/or near-center positions, consisted of tempered martensite with grain sizes of 0–2 according to ASTM E112 in the edge and about 00 in the near-center areas [17,27,33,34]. No δ-ferrite could be observed, but the microstructure contained some small isolated boron nitrides, which are not avoidable and expected not to be detrimental.

It has to be taken into consideration that adjusting the correct chemical composition is not enough to gain the excellent creep rupture strength of the steel. Boron has to be in solid solution to stabilize the $M_{23}C_6$ carbides for a high level of creep resistance.

In addition, nitrogen is necessary for the formation of the MX precipitates, which are basically Nb, V-carbo nitrides. If there are too many boron nitrides (BN) in the microstructure, especially clusters, the creep properties will not achieve the expected level due to a lack of B and N in the matrix. B and N have therefore to be balanced very carefully.

All the results in Fig. 6.32 have been achieved by industrial melts based on 9–12% Cr steels. Larger BN are present among and above the *red line*; smaller isolated ones among the *blue line*. Having N contents below the *blue dotted line*, there is no BN formation observed.

To check and roughly verify the creep behavior, short-term creep tests and observing the creep strain is a good tool to do so. Fig. 6.33 shows the results achieved on

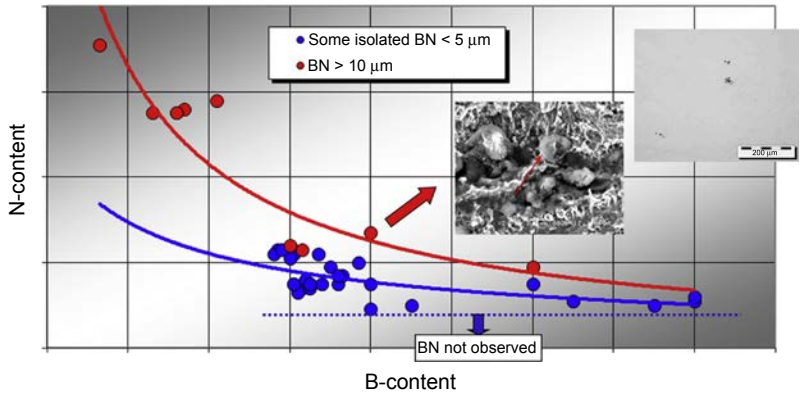


Figure 6.32 Influence of boron and nitrogen on BN generation.

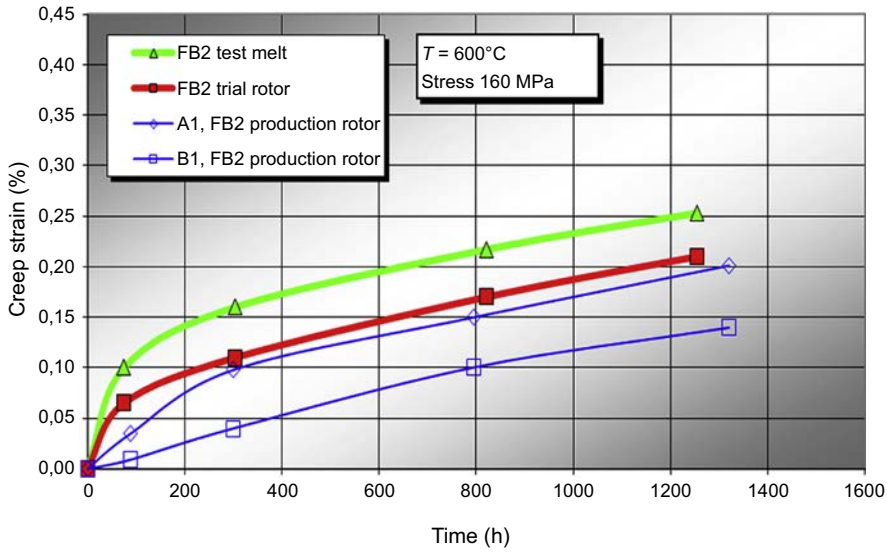


Figure 6.33 Short-term creep testing in comparison to FB2 trial melt and trial rotor forging.

the shaft in Fig. 6.31 and compared with the creep behavior achieved on the FB2 trial melt, respectively, the FB2 trial rotor forging from the COST program. Test specimens were taken from the edge and near-center location and tested at 600°C and 160 MPa load for 1300 h. The results, plotted as a creep strain versus time curve, are good in line with the FB2 trial rotor.

All in all, great efforts have been made to increase the thermal efficiency by increasing the operating temperature of steam power engines to currently 620°C. Research work as well as first industrial manufacturing showed and confirmed the suitability of these steels for use at high temperatures, and FB2 is now going to be the material for the next turbine generation.

6.5 Present material development for application temperatures above 620°C

Over the past 50 years, new, improved creep-resistant martensitic 9% Cr steels have been developed and successfully introduced in power plants. The maximum achievable steam conditions could be improved from subcritical 180 bar and 540°C up to ultra-supercritical values of 300 bar and 600–620°C, now being introduced worldwide with unit sizes of up to 1100 MW. In comparison to the X21 material, the creep rupture strength of the last generation of 9–10% Cr steels were nearly doubled [19], and currently the best and most stable alloy for rotor forgings is the FB2 material (Fig. 6.34).

A further increase of the steam parameters up to the aim of 325 bar and 650°C needs again to double the creep strength of the currently best martensitic Cr steel FB2. In parallel, the resistance against steam oxidation at such high temperatures has

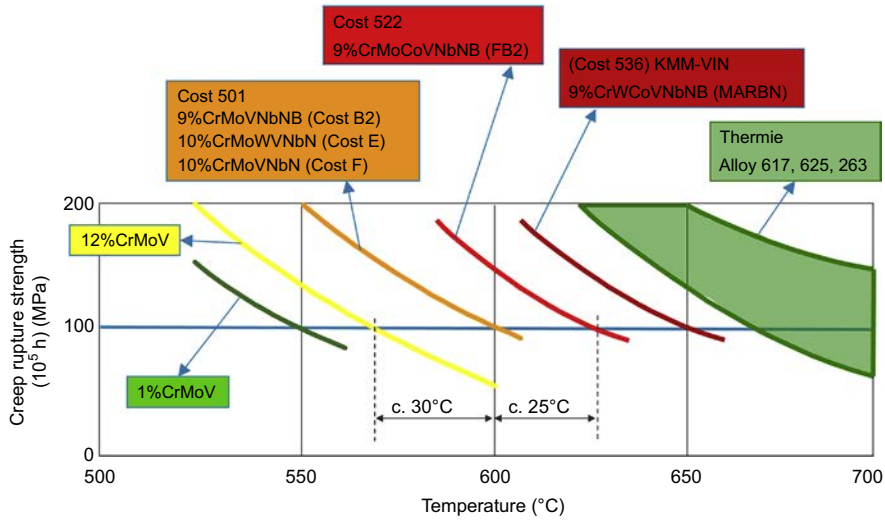


Figure 6.34 100,000 h creep rupture strength of the newly developed European steels.

to be taken already into consideration, and 9% Cr steels have to be surface coated. Within the last COST action, COST 536 (2004–2009), all attempts to make stronger 9–12% Cr steels have led to breakdowns in long-term creep strength properties [6]. However, achievements have been made in better understanding of microstructural stability; especially the effect of B and N on long-term creep properties, and these two elements have to be balanced very well to avoid BNs (Fig. 6.35). This was the basis for a series of new, stronger 9% Cr test alloys for predicted improved creep strength, developed at the end of the COST program and now being investigated and optimized in the current KMM-VIN action, the continuation of the COST program [19].

Steel	C	Si	Mn	Cr	Mo	Ni	Co	W	V	Nb	N	B
MARBN	0.078	0.31	0.49	8.88	–	–	3.00	2.85	0.20	0.051	0.0079	0.0135
MARN	0.002	0.29	0.51	9.19	–	–	3.09	2.96	0.20	0.060	0.0490	0.0070

Figure 6.35 Chemical compositions of newly developed 9% Cr steels [wt%].

These new low-carbon martensitic steels, alloyed with boron and nitrogen, so-called MARBN steels, are one of the preferred materials showing a big potential for further increase in creep resistance and having good chances for reaching the target of 650°C. However, the development and long-term testing takes at least another 10 years to be ready for their introduction into industrial fabrication.

Two test alloys with 3.5 metric tons each, FB2-2LN and NPM1, have been manufactured by PESR process at Bohler Edelstahl, forged to square 250 mm and preliminarily heat treated. These alloys are now in the phase of investigation and optimization; running research activities have the goal to create improved microstructures, influencing the mechanical properties at high temperatures. One important tool for that is an optimized heat treatment, to adjust a specific prior austenite grain size and in sequence cooling to a temperature between Ms and Mf to get about 80% martensite and the remaining austenite transforms into 20% Bainite, a heat treatment called IsoMar [36,37] (Fig. 6.36).

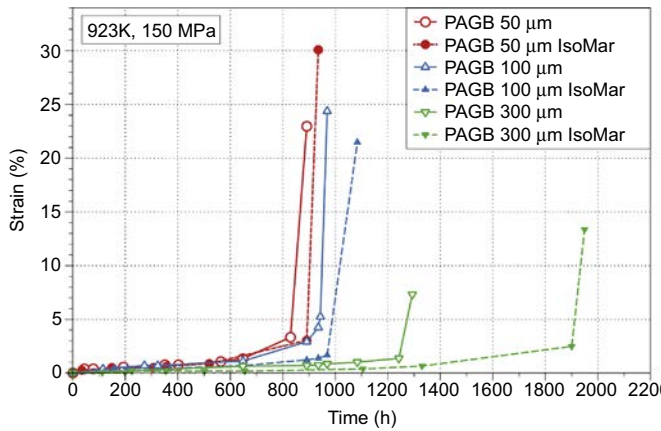


Figure 6.36 Creep curves of FB2-2 LN steel for three different prior austenite grain boundaries (PAGB) and two types of microstructure [36].

As comparative creep test results have shown, the time to rupture of the selected MARBN steels could be increased by more than 10% when having adjusted this advanced microstructure.

One of the new alloy concepts is Z-phase (Cr (V, Nb) N)-strengthened steel. Z-phase precipitation is normally detrimental to the creep strength as it dissolves finely distributed MX particles. The precondition for a Z-phase-strengthened steel would be very finely distributed Z-phase, which should be stable and showing no or only a small coarsening effect during operating time [38].

Also, investigations on experimental alloys based on 15% Cr (Japan) with dual phases of ferrite and martensite and precipitation hardened by intermetallic phases like Laves phase and carbide $Cr_{23}C_6$ as well as the 22% Cr class (Germany) are currently being carried out [39,40] (Fig. 6.37). Nevertheless, these materials are at the beginning of development on a laboratory scale and still have to be tested long-term and, if successful, finally transferred into industrial production and tested on real components again. This will need at least a further 15–20 years, but there are good prospects for the realization of 650°C steam power plants, and these martensitic alloys could be an alternative to the very expensive and possibly risky application of Ni-based alloys.

Steel	Source	C	Si	Mn	Cr	Mo	Ni	Co	W	V	Nb	N	B	Ti	La
15Cr–3Co–1.2Ni	Japan	0.049	–	–	15.02	1.00	1.21	2.96	6.04	0.20	0.051	0.042	0.0028	–	–
15Cr–3Co–2.0Ni	Japan	0.048	–	–	14.96	1.00	2.00	2.98	6.07	0.20	0.050	0.036	0.0029	–	–
Crofer 22H	Germany	0.007	0.21	0.43	22.93	–	–	–	1.94	–	0.510	0.015	–	0.07	0.08

Figure 6.37 Experimental steels based on 15/22% Cr in Japan/Europe [wt%].

6.6 Summary and conclusions

The improvement in efficiency and performance of modern steam power engines can only be achieved by raising the temperature as well as the pressure of the steam generated in the boiler.

During the last four decades, enormous efforts, especially in development of new materials, were made to establish the technology for the new **u**ltra-**s**uper**c**ritical (USC) power plants. The basic necessity for realization was to increase temperature and pressure of the inlet steam into the turbine, which called for the need of new materials with improved high-temperature capability.

Specifically, the 9–12% Cr grades steels have the potential for high long-term creep strength and oxidation resistance in steam. To develop improved and advanced ferritic martensitic 9–12% Cr steels for all the key components in the hot sections of the power station, research and development programs were initiated in Europe, United States, and Japan.

In Europe, the main efforts to improve this steel class were concentrated in the COST programs and led to the development of new ferritic steels for forgings, casting, and pipework. For steam turbine rotors, three modified creep resistant chromium steels—COST grade E (10% CrMoWVNbN), grade F (10% CrMoVNbN) and FB2

(9% CrMoVNbNB)—were developed and characterized. These improved steels have become well established and qualified and are now in commercial operation in advanced fossil-fired power stations. They have made it possible to increase the operating steam temperatures from the supercritical plant with 540°C steam temperature and 250 bar steam pressure to the first generation of ultra-supercritical with 580°C/270 bar and finally to the second generation of USC plants with 600–620°C and 300 bar steam pressure.

References

[1] K.H. Mayer, R. Blum, P. Hillenbrand, T.U. Kern, M. Staubli, Development steps of new steels for advanced steam power plants, in: 7th Liege Cost Conference, 29 September–October 2002. Liege, Belgium.

[2] T.U. Kern, K. Wieghardt, H. Kirchner, Material and design solutions for advanced steam power plants, in: 4th International Conference on Advances in Materials Technology for Fossil Power Plants (EPRI), Conference CD, Hilton Head Island, South Carolina, USA, October 25–28, 2004, pp. 20–34.

[3] B. Scarlin, T.U. Kern, M. Staubli, The European efforts in material development for 650°C USC power plants – cost 522, in: 4th International Conference on Advances in Materials Technology for Fossil Power Plants (EPRI), Conference CD, Hilton Head Island, South Carolina, USA, October 25–28, 2004, pp. 80–99.

[4] K.H. Mayer, Final report VGB research project No. 158 "New Materials for steam Turbines", ALSTOM Energie GmbH, Nürnberg, 2001.

[5] F. Masuyama, Alloy development and material issues with increasing steam temperature, in: 4th International Conference on Advances in Materials Technology for Fossil Power Plants (EPRI), Conference CD, Hilton Head Island, South Carolina, USA, October 25–28, 2004, pp. 35–50.

[6] T.U. Kern, M. Staubli, K.H. Mayer, B. Donth, G. Zeiler, A. Di Gianfrancesco, The European effort in development of new high temperature rotor materials – cost 536, in: 8th Liege Cost Conference, September 18–20, 2006. Liege, Belgium.

[7] C. Berger, R.W. Vanstone, Development of high strength 9–12% CrMoV steels for high temperature rotor forgings – a collaborative European effort in COST 501/II, in: 3rd Int. Conference on Improved Coal-Fired Power Plants, EPRI-Meeting, San Francisco, April 2–4, 1991 and at Conference on Materials for Combined Cycle Power Plant, June 1991. Sheffield, England.

[8] J. Hald, Metallurgy and creep properties of new 9–12% Cr steels, Steel Research 67 (9) (1996) 369–374.

[9] K. Furuja, A. Hizume, Y. Takeda, Y. Takano, H. Yokota, A. Suzuki, et al., Advanced 12Cr steel rotors developed for EPDC Wakamatsu's ultra high temperature turbine project, in: 2nd Int. Conference on Improved Coal-Fired Power Plants, Palo Alto, California, November 2–4, 1988.

[10] C. Berger, K.H. Mayer, R.B. Scarlin, D. Thornton, New ferritic 10% CrMo(W)V(B) NbN rotor Steels for advanced power plants, in: Int. Joint Power Generation Conference, Atlanta, Georgia, October 18–22, 1992.

[11] G. Zeiler, W. Meyer, K. Spiradek-Hahn, Ch Stocker, 9–12% chromium steel forgings for power generation plants – experiences in manufacturing and long-term mechanical & microstructural testing, in: 15th International Forgemasters Meeting, Conference Proceedings, Kobe, Japan, October 26–29, 2003, pp. 248–255.

[12] G. Zeiler, W. Meyer, K. Spiradek-Hahn, J. Wosik, Experiences in manufacturing and long-term mechanical & microstructural testing on 9–12% chromium steel forgings for power generation plants, in: 4th International Conference on Advances in Materials Technology for Fossil Power Plants (EPRI), Conference CD, Hilton Head Island, South Carolina, USA, October 25–28, 2004, pp. 222–236.

[13] A. Di Gianfrancesco, L. Cipolla, D. Venditti, S. Neri, M. Calderini, High temperature properties and creep behaviour of a CrMoCoB (FB2) steel trial rotor, in: 17th International Forgemasters Meeting, Conference Proceedings, November 03–07, 2008, pp. 309–315. Santander, Spain.

[14] T.U. Kern, B. Scarlin, B. Donth, G. Zeiler, A. Di Gianfrancesco, The European cost 536 project for the development of new high temperature rotor materials, in: 17th International Forgemasters Meeting, Conference Proceedings, November 03–07, 2008, pp. 316–320. Santander, Spain.

[15] L. Lundin, High Resolution Microanalysis of Creep Resistant 9–12% Chromium Steels (Ph.D. thesis), Chalmers University, Goeteborg, 1995.

[16] F. Kager, N. Boeck, K. Spiradek-Hahn, S. Hoefinger, M. Brabetz, G. Zeiler, Superior long-term creep behaviour and microstructural evolution of 9% Cr-Steels with boron, in: 8th Liege COST Conference, September 18–20, 2006. Liege.

[17] G. Zeiler, A. Putschoegl, Experiences in manufacturing of forgings for power generation application, in: 18th International Forgemasters Meeting, Conference Proceedings, Pittsburgh, PA, USA, September 12–15, 2011, pp. 199–205.

[18] C. Lochbichler, F. Füreder Kitzmüller, G. Zeiler, S. Paul, J. Klarner, T. Vogl, et al., Know how and process development for components used in (A) USC power plants, in: 10th Liege Cost Conference on Materials for Advanced Power Engineering, September 14–17, 2014. Liege, Belgium.

[19] J. Hald, Development status and future possibilities for martensitic creep resistant steels, in: 9th Liege Cost Conference on Materials for Advanced Power Engineering, September 18–20, 2010. Liege, Belgium.

[20] K.H. Mayer, T.U. Kern, K.H. Schoenfeld, M. Staubli, E. Tolksdorf, Long-term investigations of specimen of 8 production rotors manufactured of the advanced martensitic 10% Cr-Steels X12CrMo(W)VNbN 10 1 1, in: 14th International Forgemasters Meeting Conference Proceedings, September 03–08, 2000, pp. 277–282. Wiesbaden, Germany.

[21] W. Meyer, G. Zeiler, R. Bauer, Recent developments on 9 to 12% chromium steel open die forgings for steam and gas turbine applications at Boehler, in: 14th International Forgemasters Meeting Conference Proceedings, September 03–08, 2000, pp. 290–294. Wiesbaden, Germany.

[22] M. Mikami, K. Morinaka, Y. Okamura, S. Tanimoto, Y. Wakeshima, R. Magoshi, et al., Manufacturing of 12%Cr rotor forgings for high temperature steam turbines from electro slag hot topped ingot, in: 14th International Forgemasters Meeting Conference Proceedings, September 03–08, 2000, pp. 295–300. Wiesbaden, Germany.

[23] N. Blaes, K.H. Schönfeld, D. Bokelmann, High temperature steel forgings for power generation machinery, in: 15th International Forgemasters Meeting, Conference Proceedings, Kobe, Japan, October 26–29, 2003, pp. 219–226.

[24] S. Nozu, K. Morinaka, H. Naruse, T. Muraoka, Manufacturing technology of 12%Cr steel alloyed with boron large ingot for power generator, in: 15th International Forgemasters Meeting, Conference Proceedings, Kobe, Japan, October 26–29, 2003, pp. 276–281.

[25] Y. Wakeshima, M. Mikami, Manufacturing of trial rotor forgings of cost E steel (X12CrMoWVNbN10-1-1), in: 16th International Forgemasters Meeting, Conference Proceedings, Sheffield, UK, October 15–19, 2006, pp. 375–382.

[26] N. Blaes, D. Bokelmann, P. Braun, B. Donth, G. Weides, Y. Hirakawa, et al., Largest turbine rotors ever manufactured from 10%Cr steels, in: 16th International Forgemasters Meeting, Conference Proceedings, Sheffield, UK, October 15–19, 2006, pp. 383–391.

[27] K. Kawano, Y. Wakeshima, T. Miyata, Y. Okamura, F. Gatazka, S.L. Breitenbach, Manufacturing of COST-FB2 trial rotor forgings, in: 17th International Forgemasters Meeting, Conference Proceedings, November 03–07, 2008, pp. 303–308. Santander, Spain.

[28] K. Kawano, T. Miyata, T. Satoh, T. Nakano, S. Nishimoto, A. Matsuo, et al., Manufacturing of advanced 12%Cr steel forgings for steam turbines, in: 18th International Forgemasters Meeting, Conference Proceedings, Pittsburgh, PA, USA, September 12–15, 2011, pp. 239–243.

[29] M. Nakano, K. Kawano, M. Mikami, Manufacturing of trial rotor forging of 9%Cr steel containing Co and B (X13CrMoCoVNbNB9-2-1) for ultrasupercritical steam turbines, in: 7th International Conference on Advances in Materials Technology for Fossil Power Plants (EPRI), Conference Proceedings, Waikoloa, Hawaii, USA, October 22–25, 2013, pp. 321–332.

[30] N. Blaes, B. Donth, A. Diwo, D. Bokelmann, Rotor forgings for steam turbines with high efficiency, in: 7th International Conference on Advances in Materials Technology for Fossil Power Plants (EPRI), Conference Proceedings, Waikoloa, Hawaii, USA, October 22–25, 2013, pp. 448–458.

[31] V. Vicario, T. Brambilla, M. Colnaghi: Large COST FB2 rotors produced from ESR ingots: manufacturing and characterization, in: 19th International Forgemasters Meeting, Conference Proceedings, Tokyo, Japan, September 29–October 03, 2014, pp. 328–332.

[32] N. Blaes, D. Bokelmann, A. Diwo, B. Donth, H.E.S. Atmadja, Advanced rotor forgings for highly efficient steam turbines, in: 19th International Forgemasters Meeting, Conference Proceedings, Tokyo, Japan, September 29–October 03, 2014, pp. 349–353.

[33] N. Blaes, B. Donth, A. Diwo, D. Bokelmann, Rotor forgings for supercritical and ultrasupercritical fossil power plants, in: 18th International Forgemasters Meeting, Conference Proceedings, Pittsburgh, PA, USA, September 12–15, 2011, pp. 233–238.

[34] G. Zeiler, A. Putschoegl, Gas and steam turbine forgings for high efficient fossil power plants, in: 7th International Conference on Advances in Materials Technology for Fossil Power Plants (EPRI), Conference Proceedings, Waikoloa, Hawaii, USA, October 22–25, 2013, pp. 281–292.

[35] N. Ryu, Y. Nakamura, Y. Wakeshima, H. Yamaguchi, T. Miyata, K. Kawano, Manufacturing experiences of high chromium rotor forgings made from large ESR ingot, in: 19th International Forgemasters Meeting, Conference Proceedings, Tokyo, Japan, September 29–October 03, 2014, pp. 323–327.

[36] E. Plesiutschnig, C. Beal, S. Paul, G. Zeiler, S. Mitsche, C. Sommitsch, Advanced microstructures for increased creep rupture strength of MARBN Steels, in: Thermec 2013, 8th International Conference on Processing & Manufacturing of Advanced Materials, Processing, Fabrication, Properties, Applications, Conference Proceedings, Las Vegas, USA, December 02–06, 2013, pp. 1867–1871.

[37] S. Paul, G. Zeiler, A. Putschoegl, E. Plesiutschnig, Development of high creep resistant MARBN steels for forged components in high efficient fossil-fired power plants, in: 19th International Forgemasters Meeting, Conference Proceedings, Tokyo, Japan, September 29–October 03, 2014, pp. 338–342.

[38] H.K. Danielsen, Precipitation process of Z-phase in 9–12%Cr steels, in: 7th International Conference on Advances in Materials Technology for Fossil Power Plants (EPRI), Conference Proceedings, Waikoloa, Hawaii, USA, October 22–25, 2013, pp. 1104–1115.

[39] M. Shibuja, Y. Toda, K. Sawada, H. Kushima, K. Kimura, Effect of precipitation behaviour on creep strength of 15%Cr ferritic steels at high temperature between 923 and 1023K, Materials Science & Engineering A592 (2014) 1–5.
[40] B. Kuhn, M. Talik, L. Niewolak, J. Zurek, H. Hattendorf, P.J. Ennis, et al., Development of high chromium ferritic steels strengthened by intermetallic phases, Materials Science & Engineering A594 (2014) 372–380.

Steels and alloys for turbine blades in ultra-supercritical power plants

7

G. Lucacci
C Blade S.p.a. a SIFCO Industries Company, Maniago, Pordenone, Italy

7.1 Introduction

Blades are the only parts of a turbine that are able to convert the energy in form of heat and kinetic energy in the steam to useful mechanical work of the shaft. In general, designers of steam turbines should take into primary account the set of concurrent conditions that result in the highest imposed loads on individual turbine components. In service the blades are subjected to cyclic load, with dynamic centripetal forces acting especially on the thin airfoil sections. Moreover, a relatively recent feature that has risen in steam turbines working is the ever higher frequency of on-off switching, which is needed to compensate the temporary drops and peaks of energy supplied by the ever-increasing renewable energy generators [1]. These factors put rotating blades among the most critical components in useful life assessment of a steam turbine.

The final quantity, size, and shape of the blades are the resulting data of a design process that takes into account all the relevant operational variables such as power output, speed, and steam parameters. Pressure and temperature are therefore parameters of primary importance in the blades design, specifically in the selection of constituent materials. Operating at high pressures and temperatures, ultra-supercritical (USC) steam turbine blades must possess a set of properties that differs significantly from the one of blades assembled in subcritical and supercritical plants. Before going into detail about the blades materials selection process, it seems useful to briefly describe their construction features.

All moving blades of a steam turbine can be broken down into a set of basic features: the airfoil, the root, the shroud, and one to many damping pins, the last two not always being present.

The airfoil is the most important portion as far as the machine working. It is the portion that does the useful work; therefore it is subject to the highest loads, both steady and unsteady. In addition to being the critical area as far as reliability of the whole part, there are critical attributes to it that have a major influence on the efficiency of the machine, namely position and shape accuracy of the body and the edges, surface roughness, and surface cleanliness.

The root is the primary mechanical attachment between the blade and the disk. It is the portion of the object that transmits the work to the disk and then in turn to the shaft. Its purpose is to keep the blade against centrifugal forces that are generated through the rotation of the disk. Roots can be divided into three categories of form: circumferential or tangential dovetail roots, axial or fir-tree roots, and pinned roots. In general,

Materials for Ultra-Supercritical and Advanced Ultra-Supercritical Power Plants.
http://dx.doi.org/10.1016/B978-0-08-100552-1.00007-5
Copyright © 2017 Elsevier Ltd. All rights reserved.



Figure 7.1 Detail of fir-tree roots.

dovetail roots are easy to produce, while axial roots, of which an example is shown in Fig. 7.1, are more resistant, especially in conditions of high rotational speed or high centrifugal forces, for example acting on long, last-stage low-pressure (LP) turbine blades. Pinned roots represent an alternative to the aforementioned designs where very close machining tolerances do not count as much.

The shroud is always more frequently included in the overall blade design, especially in requiring exercise conditions, due to the improvements it brings to structural stiffness and vibration damping. In addition, it contributes to lower the amount of tip leakage and secondary flows. They can be riveted, which means a separate component attached to the blade by peened tenons, integral, which means it is an integral part of the blade, or z-lock, which is a special version of integral shroud with interlocked contacting surfaces.

Additional damping devices may be added to the design, such as wires that form a 360° ring connecting each blade together or integral individual dampers placed, for instance, at half-height of the airfoil, with the function to span the individual gaps from blade to blade.

Coming to constituent materials, blades and vanes for subcritical and supercritical steam turbines are generally made of stainless steel. This is true for all the original equipment manufacturers (OEMs) currently on the market. The set of steel grades that are used is relatively small, despite the wide range of exercise conditions those components have to sustain. Generally, the starting material is wrought, and blades are produced either via machining steel bar blanks to final dimension or going through a stage of envelope forging (see Fig. 7.2) before machining to final dimensions, the latter process resulting in more reliable material features besides being economically convenient, especially where large portions of bar material should be milled off.

The properties required on blades are different from those on other components such as boilers and piping. Tensile and fatigue strengths are perhaps the most intuitive ones, due to the high centrifugal and bending forces in play. Although, ductility is also an important property since small plastic deformations especially in the start-up of a turbine can help improving the coupling between blade root and disk slot [2]. For the



Figure 7.2 Hammer-forging of a steam turbine blade and detail of coordinates-measuring machine dimensional control of the finished part.

alloys employed in the blades production, higher ductility goes together with higher level of adsorbed energy before rupture, both in static and impact load conditions at room temperature, and this feature is favorable in unsteady work conditions. For this reason, steels for turbine blading are normally heat treated to lower slightly their absolute mechanical strength in return for improved toughness.

When considering turbine blades working in ultra-supercritical conditions, the design perspective must change remarkably. In principle, properties such as impact toughness at room temperature lose importance in favor of creep strength and stress rupture hot corrosion resistance at high temperature. In choosing constituent materials for USC steam turbine blades, two options represent the main guidelines from an engineering perspective. One is considering alloys that are similar to the common ones, such as 12% Cr steels with relatively small chemical modifications, due to their wide availability on the market and relatively low price. The downside of this choice is still the limitation in exercise temperature such components would bear and a shorter life cycle, with consequent need for more frequent replacements. Nonetheless, to protect turbine blades from excessive heat transfer, other solutions can be applied, such as mechanically shielding them [3]. The second option is considering superalloys that combine good resistance to oxidation and to creep with effective hardening mechanisms, such as precipitation of secondary phases. These alloys are normally derived from gas turbine experience. In general terms, performance of such materials in tough conditions is significantly higher, although costs rise (raw materials, production, exercise, etc.).

Efforts have been made through the past decades, which can be read as a tentative to find a compromise solution for turbine blades material. Highly alloyed steels with increased thermo-mechanical performances were developed. It has been reported [4] how the concept leading the design of such alloys must first of all take into consideration a good chemical match with the rotor constitutive alloy to not to have differential thermal expansions and therefore generation of dimensional mismatches and vibration systems. Although the blades are relatively easy components to handle in production, they can have features that are not possible on very big parts in terms of chemical mix, such as additions of Nb and W (grades TOS202 and TOS203) in higher amounts compared to the respective rotor alloys. Such modifications contribute to increase the resistance to creep strength.

7.2 Commercial alloys

7.2.1 Stainless steels: compositions, processes, properties, and uses

The commonly used family of alloys for steam turbine blades is stainless steel, specifically wrought martensitic. Martensitic stainless steels are essentially iron, chromium, and carbon alloys that exhibit a martensitic transformation when cooled from enough high temperature to room temperature. The chromium content generally ranges between 10.5% and 18%, while the carbon content can reach 1.2%, although for turbine blades application it is always kept below 0.3% not to affect ductility of the parts. They are ferromagnetic, and generally they possess corrosion resistance only in mildly aggressive environments. They are weldable. In most cases, additions of elements such as Ni, Mo, V, W, and Nb are made to modulate the response of the material after heat treatment. In the following paragraphs the features of the most important categories of stainless steels used for turbine blades are described.

7.2.1.1 Basic 12% Cr steels

The steels of this category contain around 12% in weight of chromium, a medium to high content of carbon, and none to few other alloying elements, besides the common ones like Mn and Si. They are extensively used in the production of blades, especially in high-pressure (HP) sections of USC steam turbines. Table 7.1 introduces some of the main chemical compositions commercially used.

Despite their relatively poor alloying condition, non-coated, basic 12% Cr steels are able to resist the higher temperatures encountered in subcritical and supercritical steam turbines, and their resistance to corrosion and mechanical properties are sufficient for such applications. Table 7.2 summarizes the main mechanical properties required for turbine blades applications.

Their relatively low price makes 12% Cr steels of commercial interest both for small and big last-stage blades, even though in this case limitations must apply to rotational forces into play.

For higher temperature applications, basic 12% Cr steels can be coated or otherwise shielded. Although, for instance, the addition of Nb up to 0.30% to standard AISI 403 steel is normally judged enough by the designers to use this alloy to make blades of the hot stages in USC steam turbines, HP sections, of currently marketed generation (up to 566°C reheat steam temperature). In fact, 403 Cb retains up to 400 MPa yield strength up to said temperature in the hardened and tempered condition; therefore it is judged suitable at least for small dimension components.

The production route of 12% Cr steels for turbine blades is well standardized. It normally consists of melting in electric-arc furnace, elaboration in ladle furnace, vacuum treatment, bottom casting, and lamination. Electro-slag remelting of these alloys is rarely required. Parts are always heat treated to produce a tempered martensitic structure. Tempering temperatures are generally higher than for other products made of 12% Cr steel, such as knives, because for turbine blades a higher level of ductility is pursued, and specifically in the case of USC steam turbines, the tempering temperature must be

Table 7.1 **Chemical composition of the commercial steels used for blade manufacture**

	C	Si	Mn	P	S	Cr	Ni	Mo	Nb
X12Cr13 (Mod)	0.10–0.15	0.50	0.30–0.60	0.020	0.015	11.50–13.00			
X12Cr13 + Mo	0.10–0.15	0.50	0.30–0.60	0.025	0.025	11.5–13.00		0.40–0.60	
X20Cr13 (Mod)	0.17–0.20	0.10–0.50	0.30–0.80	0.025	0.020	12.50–14.00	0.30–0.80		
403 Cb	0.10–0.15	0.5	0.30–0.60	0.025	0.015	11.50–13.00			0.05–0.30

Table 7.2 **Mechanical properties of the commercial steels**

	$R_{p_{0,2}}$ [MPa]	R_m [MPa]	A_5 [%]	Z [%]	KV [J]	Avg. grain size [ASTM E 112 points]	δ-ferrite amount [%]	Severity of thin type inclusions [ASTM E 45 points]	Severity of heavy type inclusions [ASTM E 45 points]
X12Cr13 (Mod)	550	690	18	60	63	5	<5%	2	1.5
X12Cr13 + Mo	575	700	18	60	63	5	<5%	2	1.5
X20Cr13 (Mod)	600	800–950	15	50	20	4	<5%	2	1.5
403 Cb	660	790	15	50	20	4	<5%	2	1.5

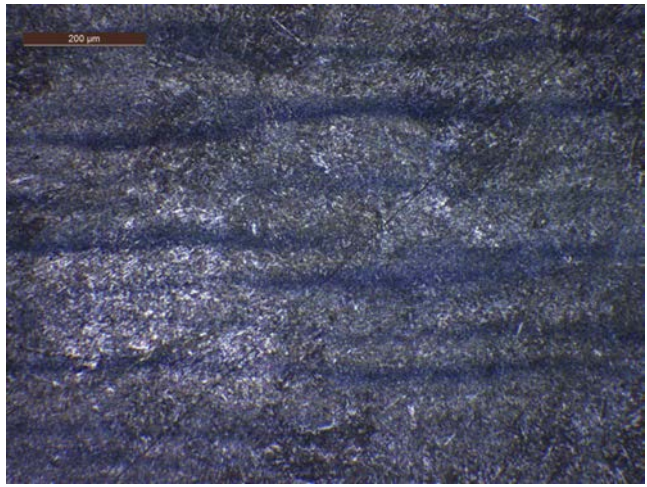


Figure 7.3 Banding detail of segregated microstructure in X20Cr13 steel.

well above the service temperature the components would work at due to dimensional stability issues. Due to the low alloying elements amounts, these alloys are sensitive to the occurrence of $M_{23}C_6$ precipitates, especially at austenitic grain boundaries; therefore care must be put in cooling rates of the pieces especially after tempering. Chemical segregation is another side effect due to the poor microstructural control. Banding as shown in Fig. 7.3 is a common feature detected on such steels, which is the combination of chemical segregation and directionality given by the process of bar lamination. The effects of banding are shown in mechanical behavior of the material, resulting in generally less ductility and especially showing high directionality of properties. Moreover, segregated bands can reach the surface of the parts after machining operations, resulting in unacceptable indications detected, for example, through magnetic particle inspection.

A treatment of homogenization of the starting ingot can solve this problem; nonetheless the relatively low engineering requirements on such steels make those concerns less critical than in other turbine sections. Another aspect that makes 12% Cr steels interesting is their relative ease in being machined. As discussed before, small moving blades are normally machined from bar blanks since this is the most convenient production route. Compared to other more alloyed steel grades, 12% Cr steels do not need the same attention, and this results, for example, in higher feed rates, lower tools and inserts consumption, and overall lower cost of production.

7.2.1.2 9–12% Cr steels and precipitation hardenable (PH) steels

These two categories of stainless steels represent an evolution of the previous one in terms of chemical composition and are of much higher interest for USC steam turbines. Their higher thermomechanical performances make them suitable for all the types of turbine blades encountered in subcritical and supercritical steam turbines. In USC steam turbines, 9–12% Cr steels are employed in all sections of the turbine. For HP section, alloys with a high content of heat-resistant elements are used, while in intermediate-pressure (IP) and LP sections, steels with very high resistance and toughness at low to medium temperatures

are employed due to the bigger dimensions of the blades compared to HP section, and therefore to the higher engineering requirements at low temperatures to be guaranteed. PH steels are more and more acquiring interest, specifically for LP last stages turbine blades due to their high yield strength to weight ratio and high and low cycle fatigue resistance.

9–12% Cr steels present lower levels of chromium, and in many cases, the increase of mechanical properties does not rely only on the increase of martensite hardness but also on secondary hardening phenomena, like precipitation of carbides, carbonitrides, and Laves phases. Therefore some compositions are allowed to have very low carbon contents. Table 7.3 introduces some of the main chemical compositions commercially used.

The addition of solid solution strengtheners and carbide formers elements, such as Nb and W, have the purpose to specifically increase the thermal resistance; therefore such alloys are employed for blades of HP and IP first stages of the turbine. Steel grades containing Ni, Mo, and V in amounts up to 3%, 2%, and 0.5%, respectively, see an increase of performance in the hardened and tempered state mostly at intermediate to low temperature thanks to the beneficial effect of the elements to the steel matrix. For example, the typical value of fracture appearance transition temperatures ($FATT_{50}$) required for X12CrNiMoV12-3 is below −35°C. For these reasons, those steel grades can be used for the production of the LP stages.

The production routes of 9–12% Cr steels do not differ in principle compared to the ones for 12% Cr steels. Nonetheless, given the higher alloying level, the occurrence of the typical defects of 12% Cr steels is facilitated. The chemical analysis of some 9–12% Cr alloys must be carefully controlled to not generate a high amount of δ-ferrite that after the lamination operations would align in the form of stringers parallel to the main axis of the bar. Alignments of niobium carbonitrides can be formed as well, and all these aspects are able to affect material isotropy. An example of heavily affected microstructure is shown in Fig. 7.4.

To reduce the segregations and to reduce the severity of nonmetallic inclusions, electro-slag remelting has been traditionally adopted within the production process of the steel grades for moving parts. Although, currently, this choice is not seen as mandatory by many OEMs, since the improvements in process control often result in comparable quality between remelted and non-remelted steels.

Martensitic PH grades have been extensively used for moving blades for land turbines in the past decades. Nonetheless, their utilization is increasing more and more for the low-temperature sections of turbines. Their use for blades is extensive in USC steam plants, specifically for last stage LP turbine of big-size plants, which means output from 660 MW upward, due to their especially high fatigue resistance. Those alloys represent a more competitive option compared, for instance, to titanium alloys. Table 7.4 introduces some of the main chemical compositions used optimized for turbine blades.

The most popular PH grades for turbine blades are the so-called 17-4 PH and GTD450. In those cases, the production process most of the time involves at least electro-slag remelting to guarantee good homogenization of the constituents, besides low inclusions severity not to affect mechanical performance. Special care must be taken in the alloy addition and during solidification phase to avoid precipitation of δ-ferrite. As a matter of fact, those grades have a strong tendency to form such a secondary phase due to the very low content of carbon and high content of ferrite stabilizers. δ-ferrite can be formed also under specific conditions of deformation rates and temperature

Table 7.3 Main chemical composition of 9–12% Cr steels

	C	Si	Mn	P	S	Cr	Ni	Mo	V	W	Nb
AISI 422 (Mod.)	0.20	0.50	1.00	0.025	0.025	11.00–12.50	0.50–1.00	0.90–1.25	0.20–0.30	0.90–1.25	
X22CrNiMoV12-1	0.18–0.24	0.10–0.50	0.40–0.90	0.025	0.015	11.00–12.50	0.30–0.80	0.80–1.20	0.25–0.35		
X12CrNiMoV12-3	0.10–0.13	0.10–0.35	0.60–0.90	0.020	0.008	11.40–12.00	2.30–2.80	1.60–1.80	0.25–0.40		0.05–0.10
15Х11МФ	0.12–0.18	0.5	0.7	0.030	0.025	10.00–11.00	0.6	0.60–0.80	0.25–0.40		
15Х12ВНМФ	0.12–0.18	0.40	0.50–0.90	0.030	0.025	11.00–13.00		0.50–0.70	0.15–0.30	0.70–1.10	

Table 7.4 Chemical composition of PH steels

	C	Si	Mn	P	S	Cr	Ni	Mo	Cu	Nb
17-4 PH	0.050	0.10–0.35	0.30–0.60	0.025	0.005	15.00–16.00	4.20–5.00		3.00–3.70	0.20–0.35
GTD 450	0.025–0.050	0.50	0.50–0.80	0.020	0.005	14.00–15.00	6.00–7.00	0.50–1.00	1.25–1.75	0.30–0.50
14-5 PH	0.070	0.50	0.30–0.80	0.020	0.015	13.50–16.00	5.00–6.00	1.20–2.00	1.20–2.00	0.15–0.50

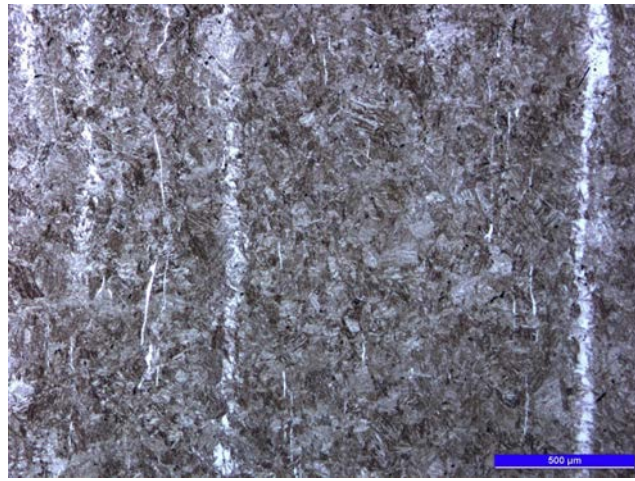


Figure 7.4 Segregated microstructure in a low-carbon 9–12% Cr steel. Presence of δ-ferrite and white martensite, enriched in α-stabilizing elements.

during hot working; therefore temperatures should never go beyond 1175°C. PH steels can be heat treated in various ways for turbine blades applications. The two options that are normally specified are either a standard solution annealing + overaging at 650°C or a modified H1075 with a double annealing stage before precipitation. This last heat treatment route results in properties that are very well tailored on demanding turbine blades application, resulting in very high yield strength (>930 MPa) and high-cycle fatigue and very high ductility. Although, due to the low temperatures required for precipitation hardening, these steels can only be used for low-temperature applications.

7.2.2 Titanium alloys: compositions, processes, properties, and uses

7.2.2.1 Ti-6Al-4V (Grade 5)

Introduction of titanium blading into low-pressure steam turbines started in the early 1960s. The evolution of this application has proceeded since then, and by now using alloys such as Ti-6Al-4V as constituent material of last-stage LP blades represents a viable commercial solution. Those blades are employed by standard in many new generation USC steam turbine designs, specifically the ones designed for outputs of 1000 MW and above [5], thanks to their intrinsic properties. Since titanium density is approximately 60% of that of martensitic stainless steels, centrifugal stresses in operation are reduced; therefore, blades are able to sustain higher tensile stresses. This means that longer airfoils can be designed for high-speed applications, with reported increase in reheat steam temperature of 20°C and overall efficiency increase of about 2%. In addition, resistance to droplet erosion of titanium alloys is higher than that of martensitic stainless steels; therefore the efforts in finding and applying effective leading edge protection on blades are saved.

Ti-6Al-4V is the alloy of main interest due to its properties and availability in the market. For turbine blades applications, restrictions in chemical compositions are sometimes applied, especially in the content of residuals and gases in the final product. For example, combined amount of Cr and Mn is sometimes specified for < 0.15%, combined amount of Cu and Ni is sometimes specified for < 0.10%, and so on. The production of the raw material generally follows vacuum induction melting with subsequent multiple electro-slag remelting or, more often, up to triple vacuum-arc remelting. Ingot breakdown and subsequent deformation steps follow a specific process called bimodal forging. The first deformation is made in a range of temperatures beyond β-transus, followed by a rapid cooling in water. Deformation into bars is then performed at a temperature just below β-transus, at which α and β crystalline structures coexist. Heat treatment following deformation steps consists of a recrystallization annealing at 950°C. The outcome is an $\alpha+\beta$ microstructure that has a much smaller average grain size if compared to a conventional production constantly in a $\alpha+\beta$ temperature range. Raw material bimodal microstructure is essential for the production of blades that possess bimodal microstructure too. Since the use of Ti-6Al-4V is mostly for very big-size parts and due to the high raw material cost, blades are commonly forged from raw billets and then machined. Forging is performed in various steps involving upsetting of the blade root, rough preforming, and finish forging. Due to the relatively low working temperature and to the hcp crystalline structure of titanium, flow stress is very high if compared to that of stainless steel. Moreover, overheating due to friction of the surfaces and generation of adiabatic bands inside the piece may occur, with harmful effects on surface integrity and mechanical performance. Conditions of heating are very important too to avoid gas entrapment within the material. Another issue to take into consideration is the impossibility to cold-straighten titanium blades, due to the low Young's modulus and high springback effect. In case parts do not meet dimensional requirements the only viable option is the creep straightening, which implies holding the piece into position, normally by means of heat-resistant dies, at a temperature above 700°C for a time that allows material to flow into final position. Machinability of Ti-6Al-4V after the described production process is very poor. Just as in hot deformation, milling may result in overheating if proper cooling is not applied to the piece and residual stresses. It is also fundamental to completely remove the surface oxide (α-case) that forms during hot working to prevent excessive tool consumption. This can be achieved through thorough sand blasting or pickling.

7.2.3 Heat-resistant alloys: compositions, processes, properties, and uses

The main elements of the chemical composition of the superalloys used or candidate for the steam turbine blades are summarized in Table 7.5.

7.2.3.1 Nimonic 80A

Nimonic 80A is the current first commercial option for USC steam turbines built by an important OEM (Siemens) and its licensees [6]. The alloy is designed for usage in 1000 -MW plants for the first HP stages, having to resist for at least 10^5 h to steam

Table 7.5 **Chemical composition of superalloys for blades**

Ni + Co	Cr	Ti	Nb + Ta	Al	Fe	Mn	Si	Cu	C	P	S	Co	Mo	W	B
Bal	18.00–21.00	1.80–2.70		1.00–1.80	3.0	1.0	1.00	0.2	0.10		0.015	2.00			0.008
70.00	14.00–17.00	2.00–2.75	0.70–1.20	0.40–1.00	5.0–9.0	1.00	0.50	0.5	0.08		0.01				
Bal	18.00–20.00	2.90–3.25		1.80–2.30	0.8	0.15	0.15	0.1	0.02–0.06	0.010	0.005	11.00–14.00	5.5–7.0	0.80–1.20	0.004–0.010

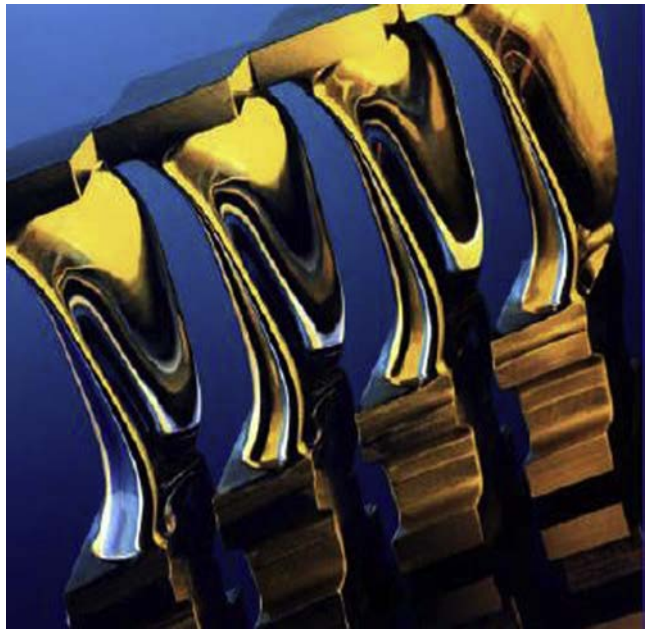


Figure 7.5 USC HP first-stage blades in Nimonic 80A [14].

flows of 25 MPa at 600°C. Blades made of such alloy are shown in Fig. 7.5, from which the optimized design of the airfoil can also be noticed.

Although it started as a material for aerospace applications, by applying strict specifications to chemical composition and heat treatment, mechanical performance can be optimized for the somehow more demanding applications in land-based steam turbines. As reported [9], chemical composition must guarantee a minimum level of γ' stabilizers (for this alloy only Al and Ti) of 3.50%. Gas content (H, O, N) must be kept as low as possible and addition of nonstandard elements for superalloys such as Mg and B are made to refine the average grain. Production of raw material provides for vacuum induction melting followed by electro-slag remelting in Ar-protected atmosphere (PESR). Heat treatment consists of a solubilization step at 1080°C followed by an intermediate annealing at 845°C for 24 h and a precipitation hardening step at 700°C for 16 h. The properties of final parts are normally investigated both at high and low temperatures. Typical requirements are for minimum hardness of 260 HB, minimum yield strength of 600 MPa, and UTS between 1100 and 1300 MPa. ISO-V impact energy is also specified to be above 20 J. As for high-temperature testing, stress rupture at 750°C and load of 310 MPa should occur in not less than 100 h and with an elongation at breakage of no less than 4%.

7.2.3.2 Inconel X-750

Inconel X-750 has been used in the past, especially for forged gas turbine blades, but it has the potential to be employed in USC steam turbine applications. As a matter of fact, the alloy in its solution annealed and aged condition is intended for service at

temperatures above 593°C. It is a PH alloy with a high content of Ni that improves its corrosion resistance also at cryogenic temperatures. The alloy in its forged turbine blade fashion has the chemical composition as per proprietary specification shown in Table 7.5.

For energy purposes the alloy is produced via vacuum induction melting and multiple consumable electrode remelting. After forging, the material is solution annealed at 1150°C for a suitable time, then stabilized at around 840°C for 8 h and finally aged around 700°C for 20 h. Stress rupture test is normally performed at 730°C, and applied stress of 310 MPa with the following limits to guarantee the following:

- minimum rupture time [h]: 100
- minimum elongation A_4 [%]: 5
- minimum reduction of area [%]: 5

7.2.3.3 Udimet 520

Udimet U-520 has replaced Inconel X-750 in many new designs for its somehow more suitable properties for applications such as moving parts at high temperatures. The alloy is still a PH, but with higher content in γ' stabilizers, which results in higher stability at service temperatures. The chemical composition for turbine blades application is shown in Table 7.5.

Raw material production is the same as for Inconel X-750, while heat treatment sees a higher final aging temperature up to 760°C for 12 h. Due to the higher thermomechanical resistance of the alloy, the stress rupture test is prescribed at around 800°C and at an applied stress of 345 MPa with the following limit to guarantee the following:

- minimum rupture time [h]: 150
- minimum elongation A_4 [%]: 7
- minimum reduction of area [%]: 7

7.2.3.4 Other special alloys

A significant number of alloys for high-temperature turbine blades have been developed since the 1960s in the Soviet Union and Russia. Table 7.6 summarizes the most popular alloys that are used in this application.

Such alloys were specifically developed for gas turbines, but thanks to their chemical composition, they are suitable for USC applications as well. With respect to Nimonic 80A, mentioned alloys have the potential to resist in even more critical conditions of temperature and stresses. Although, their availability on the market, at least outside the former USSR region, is lacking, and therefore they are commercially less attractive than other similar alloys. The hardening mechanism is in most cases through precipitation of γ' phase, which explains the considerable amounts of Al and Ti added. Heat treatments normally consist of a solubilization followed by one to many stabilization and aging steps. Materials performances are normally not specified for these alloys at room temperature; instead strict requirements are applied to both strengths at high temperature and stress rupture. Table 7.7 summarizes typical properties that are required for those superalloys.

Table 7.6 **Russian chemical compositions for turbine blades**

	C	Si	Mn	Cr	Fe	Ti	Al	W	Mo	V	S	P	Ce	B	Ni
ХН70ВМТЮ	0.12	0.55	0.50	13.00–16.00	5.0	1.8–2.3	1.7–2.3	5.0–7.0	2.0–4.0	0.10–0.50	0.01	0.015	0.02	0.02	Bal
ХН60ВМЮВТ	0.04–0.09	0.50	0.50	17.0–19.0	4.0	2.0–3.0	3.0–4.0	2.5–4.0	5.0–7.0						
ХН70ВМТЮФ	0.04–0.10	0.60	0.50	13.00–16.00	5.0	1.7–2.2	2.4–2.9	5.0–7.0	2.5–4.0	0.2–1.0					

Table 7.7 **Mechanical properties of Russian alloys**

	Hardness [HB]	Creep-rupture life [h]	Test stress [MPa]	Test temperature [°C]
ХН70ВМТЮ	269–341	40	490	700
ХН60ВМЮВТ	285–363	50	195	900
ХН70ВМТЮФ	269–341	50	265	850

7.3 Trends in USC steam turbine blading

7.3.1 Chemical optimizations of 9–12% Cr steels

The option of optimizing the chemical compositions of steels to be used for USC steam turbine blades has been constantly pursued from the 1960s on, with the purpose to obtain a material able to withstand exercising conditions of USC steam turbines at a lower raw material and production cost. The first heat-resistant steel that was employed for HP turbine blades was the AISI 422 and its European correspondent Wk. 1.4923, although it was generally designed to work at temperatures below 550°C. Further increase in creep resistance at high temperature was pursued by adding to the alloy significant amounts of Nb. This route was followed specifically for small forgings such as turbine blades due to their relative ease of production if compared to other very big components such as rotors. The presence of Nb in amounts of 0.30 to 0.45% in weight allowed the consistent precipitation Nb nitrides and Nb carbonitrides. Resulting mechanical resistance at high temperatures after heat treatment is dramatically improved, but not as good of improvements are observed in the long-term. Examples of high-Nb steels that were used for USC steam turbine blades are described in Table 7.8.

Addition of B up to 400 ppm has been proven to stabilize the steel microstructure [7] through the precipitation of $M_{23}(C, B)_6$. Up to now, the better optimized chemical composition for turbine blades in terms of mechanical properties is still represented by TOS203 (Table 7.9), developed by the EPDC, TEPCO, and EPRI consortium in the early 2000s.

Further efforts have been made in finding chemical compositions that would improve important aspects in the production process, such as decreasing the tendency to form harmful segregations of alloying elements during ingot solidification. From this, the trend was to evaluate the creep resistance of many experimental steel grades with decreased amount of Nb and, for instance, a higher amount of Mo and V. Steels developed under European COST projects belong to this category. In any case, such steels have been used to produce turbine rotors [8], and despite the high creep resistance at relevant stress levels, their eligibility as turbine blade material still needs to be verified, in particular as far as high-temperature stress rupture resistance.

In general, extensive studies have been carried out through the last decades to point out the main factors that affect creep resistance in such steels, and it has been proven how an optimum control of alloying elements and grain size, among other features, is the key to increase service life of moving parts in the turbine.

7.3.2 Nickel-based superalloys as candidate materials for A-USC blades

Commercialization of advanced ultra-supercritical steam turbines working at pressures of over 30 MPa and at temperatures of over 700°C is considered the most promising step in the development of power generation technology, specifically in thermal power generation. The need to reduce CO_2 emissions of coal-fired plants can only be pursued with the increase of specific output of the plants, and the opportunity that new heat-resistant alloys give in this field will certainly be exploited to this scope in the future.

Table 7.8 New 9–12% Cr steels for turbine blades

	C	Si	Ni	Nb	N	Mn	Cr	Mo	V	Co	B
H-46	0.15–0.20	0.20–0.60	0.30–0.60	0.20–0.60	0.04–0.10	0.50–0.80	10.0–14.0	0.50–1.00	0.20–0.40		
FV448	0.15		0.7	0.3			11	0.7	0.25	6	0.005
X19CrNiMoNbV11-1	0.17–0.25	0.80	1.00	0.20–0.60		1.00	10.0–12.0	0.6–1.25	0.10–0.40		

Table 7.9 Chemical composition of Japanese TOS203

C	Si	Mn	Ni	Cr	Mo	V	Nb	N	W	Co	B	Re
0.11	0.05	0.5	0.6	10.5	0.10	0.2	0.1	0.03	2.5	1.0	0.01	0.2

Table 7.10 Chemical composition of superalloys for A-USC blades

	C	Si	Cu	Fe	Mn	Cr	Ti	Al	Co	Mo	Pb	S	B	Zr	Ni
Nimonic 105	0.17	1.0	0.2	1.0	1.0	14.0–15.7	0.9–1.5	4.5–4.9	18.0–22.0	4.5–5.5	0.0015	0.010	0.003–0.010	0.15	Bal
Haynes 282	0.06	0.15		1.5	0.3	20	2.1	1.5	10	8.5			0.005		
Waspaloy	0.02–0.10	0.75	0.50	2.0	1.0	18.00–21.00	2.75–3.25	1.20–1.60	12.00–15.00	3.50–5.00		0.030	0.003–0.01	0.02–0.12	Bal

As known, many research projects bringing together public institutions and private corporations have been carried out on a global basis since the mid-2000s. Among them, European, US, Japanese, Chinese, and Indian programs are the most relevant. The issue of materials for A-USC steam turbine blades is one of the most critical, even though developments as far as other components that are more complex to produce appear more problematic and therefore in need of more attention. The most remarkable effort in guiding the materials selection for A-USC turbine blades is possibly the one made by the US program [9]. The main criteria for materials constituting turbine blades were established as minimum yield strength of 400 MPa and 10^5 h of creep life (100 MPa minimum) at the target steam inlet temperature of 760°C. After an initial screening through simulation tools, a set of five alloys were selected for further evaluations. The laboratory testing resulted in a ranking of the most promising alloys. Nimonic 105 showed the higher performance, with Haynes 282 and Waspaloy possessing the minimum requirements as well and therefore being considered as alternatives. In the Table 7.10 the chemical compositions of the three alloys are shown.

The general purpose is to develop nickel-based superalloys with the highest possible amount of alloying elements that promote the hardenability through development of γ' structure (see Fig. 7.6) and at the same time allowing stable production outputs in terms of material quality. Solution-strengthened alloys, such as Inconel 617, are not an option for steam turbine blades due to their insufficient stress rupture properties at service temperatures.

Nimonic 105 is a wrought nickel-cobalt-chromium-based superalloy with a high concentration of elements promoting the precipitation of $Ni_3(Al,Ti)$ intermetallics and carbides. The standard production makes use of vacuum induction melting and

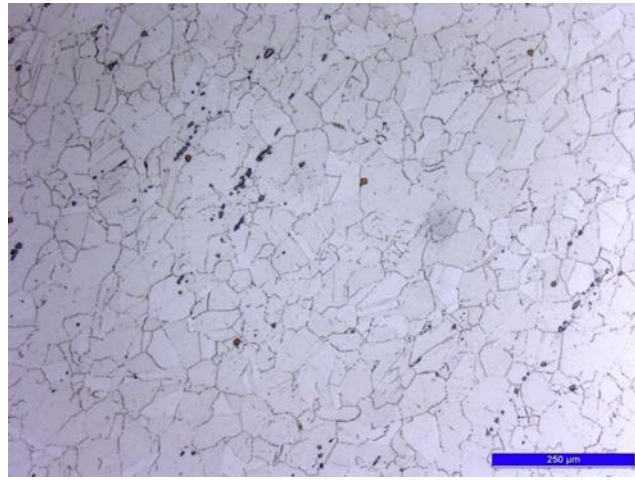


Figure 7.6 Typical microstructure of a nickel-based superalloy after precipitation hardening treatment.

subsequent multiple remelting. Homogenization treatments are always needed in particular to avoid micro-segregations across the fcc dendrites. Experimental optimized homogenization treatments have been reported in the literature [10], which proves the importance of such a production phase. Hot working temperatures range in the interval of 1050–1200°C. The operations are critical both during deformation due to hot tearing tendency and during cooling to room temperature due to its tendency to surface cracking for thermal stress. To obtain the higher performance in terms of creep resistance at temperatures well above 700°C, the alloy is heat treated through a solubilization step at 1150°C for a time depending on maximum part thickness and air-cooling to room temperature, followed by an intermediate annealing at 1050°C for 16 h and air-cooling to room temperature and the final precipitation hardening step at 850°C for 16 h and air-cooling to room temperature. A different and more simple heat treatment can be performed when working temperatures are not as demanding or for smaller components such as bolts. Machining this alloy is also difficult due to the high resulting hardness (up to 385 HV) but mostly to the fcc crystal structure that promotes work-hardening; therefore very low cutting speeds are normally prescribed.

Haynes 282 is the best alternative to Nimonic 105 for turbine blades, but it is considered an alloy of interest also for other parts of A-USC steam turbines, either forged or cast. For example, it is currently being scaled up to produce rotor disks [11]. Although specific properties in creep resistance at temperatures that are typical of USC inlet steam are lower than those of Nimonic 105, this newly developed alloy (2006) is appreciated for combining excellent properties with a better weldability and formability. The tendency to generate segregations is lower if compared to Nimonic 105, and the alloy is reported to have better strain-age cracking, which is a general problem to many γ'-strengthened alloys. The production route is the same of the precedent alloy. As said, workability is higher than other similar alloys due to the optimized balance of γ'-formers. Heat treatment generally consists of a solubilization step at 1150°C followed by an intermediate annealing at 1010°C for 2 h and a precipitation hardening step at 790°C for 8 h. It can be noted from the heat treatments parameters that the production of such alloy is less heavy compared to Nimonic 105 especially in terms of soaking times for each step. Machining presents the same problematics as other nickel superalloys. It is generally advised that the parts undergo rough machining in the solubilized state and finishing after the final treatment.

Waspaloy represents the second alternative for A-USC turbine blades. It is a well-known age-hardenable superalloy in possession of the minimum requirements for that application as far as creep resistance. It was primarily designed for land and aero-gas turbines applications. The standard heat treatment characterizing this alloy requires a solubilization at a lower temperature compared to Nimonic 105 and Haynes 282 (1080°C) due to the low amount of alloy constituents, followed by stabilization at 845°C for 24 h and age hardening at 760°C for 16 h. Cooling especially from hot working temperature is the most critical among the three described alloys due to surface cracking occurrence.

7.4 Coatings

7.4.1 Innovative TBCs and erosion-resistant coatings (500)

The working conditions of A-USC steam turbine blades have the potential to affect surface integrity of blades airfoils in a relatively short time. In turn, this would cause problems especially in the steam path accuracy, which is very carefully designed to increase working efficiency of the machine, and eventually unbalancing the whole bladed disk. Therefore one of the main research fields regarding blades, besides constituent bulk materials, is about protective coatings. Besides the problems of erosion faced also in subcritical plants, high temperatures may result in significant surface oxidation and coating softening and loss of resistance toward erosion particles. Therefore those two issues are under evaluation and leading the experimental studies. As reported [12], since the choice for bulk materials is directed to thermomechanical-resistant alloys, oxidation and corrosion at high temperature does not seem as the main problem for the bulk, at least not alone. Instead, erosion has been demonstrated to affect significantly in the short term constituent materials, as high temperatures and pressures represent an incentive to the degradation of the material. Currently used coatings proved unsuitable to guarantee sufficient life time, and a number of novel coatings were tested. T400-C (Tribaloy) resulted as the best candidate due to its good resistance to both erosion and oxidation at 760°C. Coatings of the Tribaloy series are nickel- or cobalt-based alloys with significant presence of alloying elements, which in case of T400-C are Mo (≈26%), Cr (≈14%), and Si (≈3%) [13]. It is a hyper-eutectic alloy containing a large volume of hard, intermetallic Laves phases distributed in a softer solid solution matrix. Varying the amount of the alloying elements, the properties of the coatings can be dramatically tuned, from higher oxidation resistance, through the addition of Cr forming a protective surface passivating film, to higher wear resistance, through the addition of Mo that increases matrix hardness and through the addition of Si that increases the volume fraction of intermetallic phases. Another field of constant development is referred to deposition technologies.

7.4.2 Leading edge protection (1000)

Last-stage LP turbine blades are more subjected to the deleterious effects of water droplets erosion. This is a different phenomenon compared to the previously described, where erosion comes especially from hard particles detached from pipes and other components that are in contact with steam. As for last stage LP turbines, the steam is found in a near-liquid state, and due to the high rotational speed, small liquid droplets are able to deteriorate the blade especially where they hit it, which is the top leading edge of the airfoil. As a general guideline, last-stage LP turbine blades being manufactured are always harder steels and alloys. For example, GTD steel 450 is prescribed especially for 41″ and over blades, generally being designed for very high output plants (over 800 MW). General prescriptions for such materials used in turbine blades applications are for an H950 heat treatment that is aging at a relatively low temperature, resulting in hardness levels of over 400 HB. Although, an increase of hardness of the leading edge is being more and more pursued by means of surface modifications, which currently consists of two options: surface

hardening, for example, flame or laser hardening, or Stellite gr. 6 brazing or cladding. The first process is only applied to hardenable steels, and it consists of a controlled heating of the leading edge to reach austenitization, followed by a rapid cooling. The part is then annealed at a temperature of about 250°C and slowly cooled to relieve any stress that can be generated in the hardening process. The whole surface hardening process is performed after the part has undergone bulk heat treatment as per prescriptions. The final appearance of the processed part is shown in Fig. 7.7. Bulk material properties are not modified in the surface hardening process and in the following annealing treatment since its temperature is much lower than the generally required tempering temperature. Generally, quality prescriptions include a nondestructive hardness check, normally performed through Vickers microindentation (0.3 kg). A series of micro-hardness checks is sometimes prescribed to evaluate the exact geometry of the hardened area, both copying the section perimeter and going in depth. Minimum prescribed hardness Vickers values depend on the steel grade and specifically on the hardenability, although they can reach up to over 500 HV. Other quality controls commonly required are micro- and macrostructure analysis of sample blades. Lately, techniques have been developed and optimized for surface hardening of PH steels. This was a major breakthrough since PH steels are specifically used where high rotational speeds are used due to their good toughness, and therefore water droplet erosion becomes even more critical. Such steels require first of all higher processing temperatures to obtain a complete solubilization of constituents and therefore a more homogeneous final result. Following heat treatment does not only have the purpose to relieve stresses, but it is a proper aging treatment at temperatures of below 500°C. Such aging treatment does not affect the material properties, since aging temperatures for turbine blades are generally higher. In the case of PH steels, resulting surface hardness depends on the content of Cu, which together with iron is the constituent of the characterizing intermetallics.



Figure 7.7 33.5″ L-0 blade with laser-hardened leading edge.

Stellite gr. 6 has been used as anti-wear coating for decades. It is an alloy of chromium and cobalt with significant additions of other elements to increase its mechanical resistance. It is used for its good properties both in terms of corrosion and erosion resistance (hardness of around 380 HV). Commonly, Stellite gr. 6 strips of various shapes were applied on the leading edge through brazing. Some designs also allowed the application of Stellite gr. 6 in form of separate blocks forming a row. However, this practice was discontinued due to safety issues connected with the use of specific brazing alloys containing cadmium. Currently, the most promising alternative makes use of laser to melt the alloy in the form of powder to the surface. This process allows a very accurate control of the coating thickness, and considerable improvements as far as coating adhesion to the moving parts have been observed if compared to the brazing. Moreover, typical issues concerning brazing such as incomplete penetration of brazing alloy, shield overheating, or cracking do not occur. On the other hand, a trade-off must be found between process overall duration, which is connected to the thickness growth by pass, and risk of part warping.

7.5 Conclusions

Among the various efforts that are being made worldwide to develop and validate new technologies for ultra-supercritical and advanced ultra-supercritical power plants, always finding better solutions in turbine blading is of primary importance. As discussed in this chapter, a multidisciplinary approach is needed to guarantee the fulfillment of the design specifications at each stage of the turbine and to overcome the different critical working issues moving parts are subjected to, such as high cyclic stresses, high temperatures, particle and droplet erosion, hot corrosion, etc.

Currently, USC and A-USC steam turbine blades can be designed in martensitic stainless steels, superalloys, and titanium alloys, depending on the dimension and shape of the component but most of all on where they are assembled within the turbine and specifically how they will work. In view of an ever increasing plant efficiency through increased inlet and reheat steam temperatures and increased annular areas of LP turbines, the most suitable candidates for HP and potentially IP turbine blades are the strongest precipitation hardening nickel superalloys, while for bigger LP blades, especially last-stage blades, PH steels or titanium alloys appear as the best options. However, to see these trends take place, production routes will have to be constantly optimized and stabilized to obtain the sought final microstructures in the components and at the same time to reach competitive costs.

References

[1] V. Casamassima, M. Benini, A. Cammi, Incidenza delle fonti rinnovabili non programmabili sull'esercizio dei cicli combinati – nuovi stimoli per lo studio e la modellazione dei materiali, in: Proceedings From the Workshop "Sfide per i Materiali Nella Generazione Termica di Energia del XXI Secolo" by the Italian Metallurgy Association (AIM), 2013.

[2] M. Singh, G. Lucas, Blade Design & Analysis for Steam Turbines, McGraw-Hill, 2011.

[3] K. Nakamura, T. Tabei, T. Takano, Recent Technologies for Steam Turbines, Energy Solution Group, Fuji Electric Systems Co., Ltd.
[4] M. Fukuda, Y. Tsuda, K. Yamashita, Y. Shinozaki, T. Takahashi, Materials and design for advanced high temperature steam turbines, in: Proceedings From the Fourth International Conference on Advances in Materials Technology for Fossil Power Plants, October 2004.
[5] S. Senoo, K. Asai, A. Kurosawa, G. Lee, Titanium 50-inch and 60-inch last-stage blades for steam turbines, Hitachi Review 62 (2013).
[6] H. Shen, W. Wang, Z. Wang, L. Zhang, X. Xie, S. Fu, The application of Ni-base alloy nimonic 80A for buckets of USC steam turbine in China, advances in materials technology for fossil power plants, in: Proceedings from the 5th International Conference, 2008, pp. 402–412.
[7] A. Golpayegani, F. Liu, H. Svensson, M. Andersson, H.O. Andrén, Microstructure of a creep-resistant 10 Pct. Chromium steel containing 250 ppm Boron, Metallurgical and Materials Transactions A 42A (2011) 940–951.
[8] See note [4].
[9] R. Viswanathan, J. Shingledecker, J. Hawk, S. Goodstine, Effect of creep in advanced materials for use in ultrasupercritical coal power plants, in: Proceedings from the 2nd ECCC Creep Conference, 2009.
[10] D. Jablonski, C.J. Cowen, Homogenizing a nickel-based superalloy: thermodynamic and kinetic simulation and experimental results, Metallurgical and Materials Transactions B 40B (2009) 182–186.
[11] R. Schwant, C. Shen, M. Soare, New materials enable unprecedented improvement in turbine performance, Advanced Materials & Processes 171 (1) (January 2013) 18.
[12] P. Rawls, B. Purgert, J. Shingledecker, Advanced Ultra Super Critical, Turbomachinery International, March/April 2011.
[13] S. Nsoesie, R. Liu, K. Jiang, M. Liang, High-temperature hardness and wear resistance of cobalt-based tribaloy alloys, International Journal of Material and Mechanical Engineering 2 (3) (August 2013).
[14] https://www.cee.siemens.com/web/ua/ru/production_energy/Documents/Service_High%20Performance%20Blading%20for%20Steam%20Turbines.pdf.

Technologies for chemical analyses, microstructural and inspection investigations

8

A. Di Gianfrancesco
Materials & Technologies Consultant, Rome, Italy

8.1 Introduction

The chemical and microstructural analyses, jointly with the nondestructive testing (NDT) technics and methodologies, have been, are, and will be fundamental for the development and qualification of materials and components. In this chapter the main techniques will be presented, briefly discussed, and some examples of application in the field of materials for power generation will be given.

The chemical analyses are crucial during the manufacturing processes and have to be carried out step by step to guarantee the final chemistry in respect to the materials standards and requirements.

The current steels and in particular the superalloys are now produced with an electric arc furnace followed by chemical adjustment in a ladle furnace and/or in vacuum oxygen degassing. The produced ingots to be transformed into forged components are remelted in ESR (electro slag remelting) in air, that could generate modification in the alloy chemistry, or in argon atmosphere to prevent it. Impurities and trace elements, like boron and nitrogen, are very critical for steel stability with very strict chemical windows.

For superalloys the process steps can be more complex with primary melting in vacuum induction melting followed by single or double remelting by ESR and vacuum arc remelting. For the production of superalloys ingots, the criticism is the homogeneity of the chemistry in the whole section to avoid the formation of freckles. In the superalloys, several impurity elements have to be strictly maintained lower than 10 ppm and in some case lower than 1 ppm.

The microstructural analyses are essential to guarantee the quality of the components and the respect of the homogeneity in the whole component: starting from the grain size up to the fine precipitation after the quality heat treatment that steels and superalloys must have to assure their performance in service.

Technology and the computer software development have improved the capabilities of the electronic instruments and generated new instruments able to investigate in deeper detail the microstructures and the phases up to the atomic levels.

Materials for Ultra-Supercritical and Advanced Ultra-Supercritical Power Plants.
http://dx.doi.org/10.1016/B978-0-08-100552-1.00008-7
Copyright © 2017 Elsevier Ltd. All rights reserved.

The nondestructive analyses also have taken great advantages from the technologies, hardware, and software greatly improving the capability to find very small defects also in big components, granting the quality of the components and avoiding failure in service.

8.1.1 Chemical analysis on bulk

The bulk analyses to determine the chemical of materials are fundamental for the main alloy elements and are becoming more and more crucial to identify the correct content of impurities and trace elements.

Material identification, characterization, and verification are essential for businesses to ensure their materials or products have been manufactured to the correct alloy grade and conform to national or international codes and standards. Metal chemical analysis is also used in reverse engineering to determine the alloys used to produce a component and in failure investigations to establish whether the correct alloy was used.

In Table 8.1 are summarized the most used technics for the chemical analyses of the metals, with the dimension and minimum weight necessary and the detection limits

Table 8.1 Most used technics for chemical analyses of the metals

Test	Sample	Materials	Detection limits
Optical emission spectroscopy (OES)	Solid samples Min. Diameter 12 mm Min. Thickness 0.5 mm	Iron, nickel, and cobalt-based alloys	>0.0002%, depending on element and sample. Elements include: Ag, Al, As, B, Bi, C, Ca, Ce, Co, Cr, Cu, Fe, Mg, Mn, Mo, N, Nb, Ni, P, Pb, S, Sb, Si, Sn, Te, Ti, V, W, Zn, Zr
Combustion (LECO)	Solid samples, turnings, or powders. Minimum weight 5 g	Ferrous alloys	C: 0.0002–10.0% S: 0.0002–1.0%
Atomic absorption	Solid samples, turnings, powders, or solutions Minimum weight 10 g	Ferrous alloys Non-ferrous alloys	>0.0005%, depending on element and sample Elements include: Ag, Al, As, B, Be, Bi, Ca, Cd, Ce, Co, Cr, Cu, Fe, Mg, Mn, Mo, Nb, Ni, Pb, Sb, Si, Se, Sn, Sr, Ta,Te, Ti, V, W, Zn, Zr
SEM/EDS	Solid samples or powders Very small samples possible	Ferrous alloys Non-ferrous alloys	>0.1%, depending on element and sample Elements with atomic number ≥5
X-ray diffraction	Solid samples or powders	Crystalline solids	>1.0%, depending on phase and sample

Table 8.2 Main ASTM standards used for the metal chemical analyses

ASTM E350-95	Standard test methods for chemical analysis of carbon steel, low-alloy steel, silicon electrical steel, ingot iron, and wrought iron
ASTM E351-93	Standard test methods for chemical analysis of cast iron, all types
ASTM E353-93	Standard test methods for chemical analysis of stainless, heat-resistant, maraging, and other similar chromium-nickel-iron alloys
ASTM E354-93	Standard test methods for chemical analysis of high-temperature, electrical, magnetic, and other similar iron, nickel, and cobalt alloys
ASTM E415-99a	Standard test method for optical emission vacuum spectrometric analysis of carbon and low-alloy steel
ASTM E1999-99e1	Standard test method for analysis of cast iron using optical emission spectrometry

for the elements. In Table 8.2 are reported the main ASTM standards used for the metal chemical analyses.

8.1.2 Microstructural investigations

Microstructural investigations (XRD, LM, SEM, FIB, TEM, EFTEM, 3D APFIM, etc.) of specimens of virgin/as treated condition, after aging, and after long-term creep testing of base material and welds identified precipitation strengthening as the key mechanism to stabilize the tempered martensitic structure in the steel or the γ' phase in superalloys against creep. Microstructure and creep modeling based on thermodynamic equilibrium and multicomponent diffusion modeling using software such as Thermo-Calc, DICTRA, and MatCalc have supported the understanding of microstructure–property relationships of martensitic and austenitic steels, as well as, nickel-based superalloys. However, the definition of new alloy compositions has not significantly advanced beyond a trial-and-error approach.

8.1.3 Metallography

Metallography is the study of the physical structure and components of metals, typically using microscopy. The surface of a metallographic specimen is prepared by various methods of grinding, polishing, and etching. After preparation, it is often analyzed using optical or electron microscopy. Using only metallographic techniques, a skilled technician can identify alloys and predict material properties.

Mechanical preparation is the most common preparation method. Successively finer abrasive particles are used to remove material from the sample surface until the desired surface quality is achieved. Many different machines are available for doing this grinding and polishing, and they are able to meet different demands for quality, capacity, and reproducibility (Fig. 8.1).

A systematic preparation method is the easiest way to achieve the true structure. Sample preparation must therefore pursue rules that are suitable for most materials. Different materials with similar properties (hardness and ductility) will respond alike and thus require the same consumables during preparation.



Figure 8.1 Abrasive cutters, compression mounting presses, automated polishing heads, metallurgical microscopes, and hardness testers [1].

Metallographic specimens are typically "mounted" using a hot compression thermosetting resin. In the past, phenolic thermosetting resins have been used, but modern epoxy is becoming more popular because reduced shrinkage during curing results in a better mount with superior edge retention. A typical mounting cycle will compress the specimen and mounting media to 28 MPa (4000 psi) and heat to a temperature of 177°C (350°F). When specimens are very sensitive to temperature, "cold mounts" may be made with a two-part epoxy resin. Mounting a specimen provides a safe, standardized, and ergonomic way by which to hold a sample during the grinding and polishing operations. After mounting, the specimen is wet ground to reveal the surface of the metal. The specimen is successively ground with finer and finer abrasive media. Silicon carbide abrasive paper was the first method of grinding and is still used today. Many metallographers, however, prefer to use a diamond grit suspension that is dosed onto a reusable fabric pad throughout the polishing process. Diamond grit in suspension might start at 9 μm and finish at 1 μm. Generally, polishing with diamond suspension gives finer results than using silicon carbide papers, especially with revealing porosity, which silicon carbide paper sometimes "smear" over. After grinding the specimen, polishing is performed. Typically, a specimen is polished with a slurry of alumina, silica, or diamond on a napless cloth to produce a scratch-free mirror finish, free from smear, drag, or pull-outs and with minimal deformation remaining from the preparation process.

After polishing, certain microstructural constituents can be seen with the microscope, eg, inclusions and nitrides. If the crystal structure is non-cubic (eg, a metal with a hexagonal close-packed crystal structure, such as Ti or Zr), the microstructure can be revealed without etching using crossed polarized light (light microscopy). Otherwise, the microstructural constituents of the specimen are revealed by using a suitable chemical or electrolytic etchant.

8.1.4 Microscopy

Microscopy is the technical field of using microscopes to view samples and objects that cannot be seen with the unaided eye (objects that are not within the resolution range of the normal eye). There are three well-known branches of microscopy: optical, electron, and scanning probe microscopy.

Optical and electron microscopy involve the diffraction, reflection, or refraction of electromagnetic radiation/electron beams interacting with the specimen and the

subsequent collection of this scattered radiation or another signal to create an image. This process may be carried out by wide-field irradiation of the sample (eg, standard light microscopy and transmission electron microscopy) or by scanning of a fine beam over the sample (eg, confocal laser scanning microscopy and scanning electron microscopy). Scanning probe microscopy involves the interaction of a scanning probe with the surface of the object of interest. The development of microscopy revolutionized biology and remains an essential technique in the life and physical sciences.

8.1.4.1 Light optical microscopy

The optical microscope, often referred to as the "light optical microscope," is a type of microscope that uses visible light and a system of lenses to magnify images of small samples. Optical microscopes are the oldest design of microscope and were possibly designed in their present compound form in the 17th century. Basic optical microscopes can be very simple, although there are many complex designs that aim to improve resolution and sample contrast. Historically, optical microscopes were easy to develop and are popular because they use visible light, so samples may be directly observed by the eye.

The image from an optical microscope can be captured by normal light-sensitive cameras to generate a micrograph. Originally, images were captured by photographic film but modern developments in complementary metal-oxide-semiconductor and charge-coupled device (CCD) cameras allow the capture of digital images (Fig. 8.2).

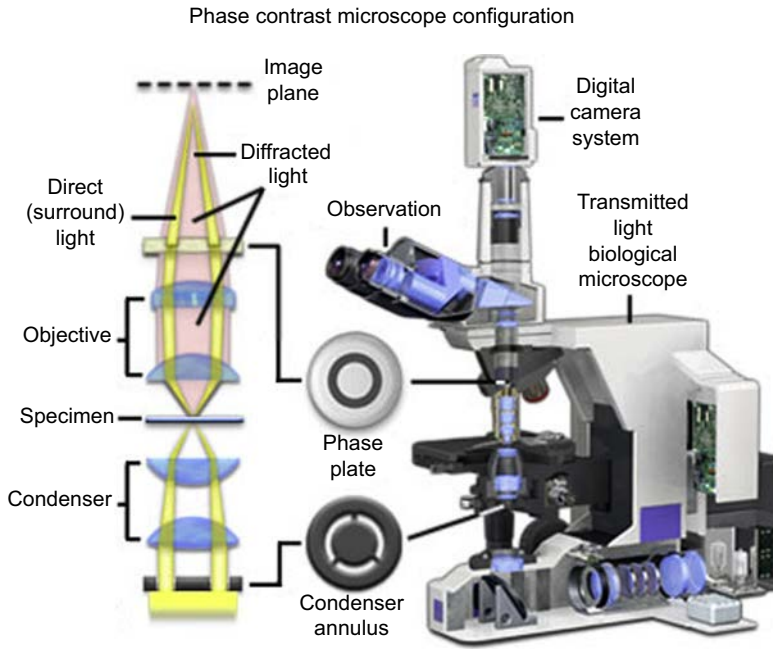


Figure 8.2 Light microscope [2].

Purely digital microscopes are now available that use a CCD camera to examine a sample, showing the resulting image directly on a computer screen without the need for eyepieces. In Fig. 8.3 are presented two examples of grade 91 martensitic steel and A617 superalloy light microstructures.

Alternatives to optical microscopy that do not use visible light include scanning electron microscopy and transmission electron microscopy.

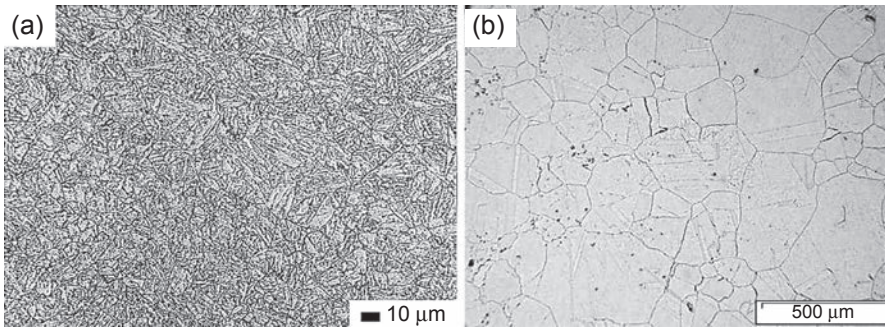


Figure 8.3 Martensitic structure of grade 91 (a) in as-treated condition and IN617 (b) solution-treated and aged 670°C/10 Hrs/AC (right) [3,4].

8.1.4.2 Scanning electron microscopy

A scanning electron microscope (SEM) is a type of electron microscope that produces images of a sample by scanning it with a focused beam of electrons (Fig. 8.4(a) and (b)). The electrons interact with atoms in the sample, producing various signals that can be detected and that contain information about the sample's surface topography and composition. The electron beam is generally scanned in a raster scan pattern, and the beam's position is combined with the detected signal to produce an image. SEM can achieve resolution better than 1 nm. Specimens can be observed in high vacuum, in low vacuum, and (in environmental SEM) in wet conditions.

The most common mode of detection is by secondary electrons emitted by atoms excited by the electron beam. The number of secondary electrons is a function of the angle between the surface and the beam. On a flat surface, the plume of secondary electrons is mostly contained by the sample, but on a tilted surface, the plume is partially exposed and more electrons are emitted. By scanning the sample and detecting the secondary electrons, an image displaying the tilt of the surface is created.

Fig. 8.4(c) and (d) show some examples of microstructures of grade 91 and IN740 in the as-treated condition.

Energy-dispersive X-ray spectroscopy (EDS, EDX, or XEDS) is an analytical technique used for the elemental analysis or chemical characterization of a metal sample. It relies on the investigation of an interaction of some source of X-ray excitation and a metal sample. Its characterization capabilities are due in large part to the fundamental principle that each element has a unique atomic structure allowing a unique set of peaks on its X-ray spectrum. To stimulate the emission of characteristic X-rays from a specimen, a high-energy

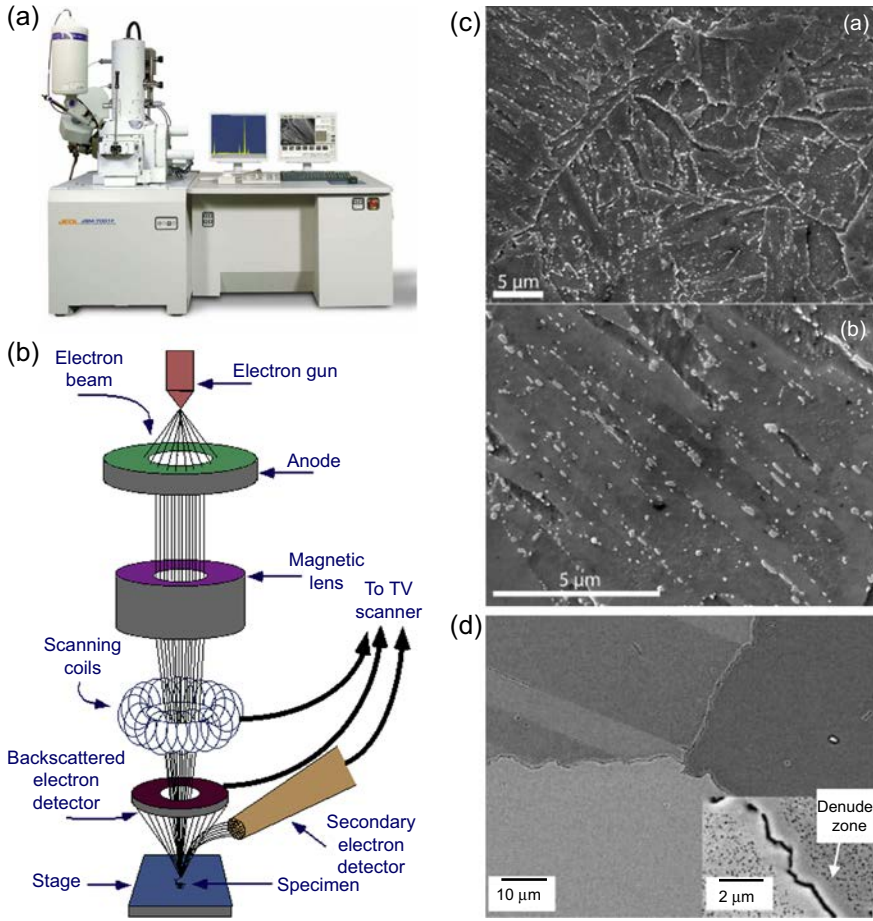


Figure 8.4 SEM layout (a), physical principle (b), and typical pictures SEM micrographs for the as-treated T91 (c) and IN740 (d) [5–8].

beam of charged particles such as electrons or protons, or a beam of X-rays, is focused into the sample being studied. At rest, an atom within the sample contains ground state (or unexcited) electrons in discrete energy levels or electron shells bound to the nucleus. The incident beam may excite an electron in an inner shell, ejecting it from the shell while creating an electron hole where the electron was. An electron from an outer, higher-energy shell then fills the hole, and the difference in energy between the higher-energy shell and the lower energy shell may be released in the form of an X-ray. The number and energy of the X-rays emitted from a specimen can be measured by an energy-dispersive spectrometer. As the energy of the X-rays is characteristic of the difference in energy between the two shells, and of the atomic structure of the element from which they were emitted, this allows the elemental composition of the specimen to be measured in the EDS spectrum of the mineral crust of the vent shrimp.

8.1.4.3 Field-emission gun scanning electron microscope

In the **field-emission gun scanning electron microscope (FEG-SEM)**, the function of the gun is to produce an extremely narrow beam of electrons of precisely controlled energy (Fig. 8.5). It is called a "field-emission" gun because an electric field causes high-energy electrons to be emitted from a tungsten filament emitter having a point as small as 10 nm. State-of-the art field-emission guns feature a Schottky emitter, which is made of a tungsten filament with a tip as small as 10 nm, coated with a thin layer of zirconium oxide to raise electrical conductivity. As a result, this FEG-SEM provides higher spatial resolution, better reliability, improved signal-to-noise ratio, and longer life than previous technologies.

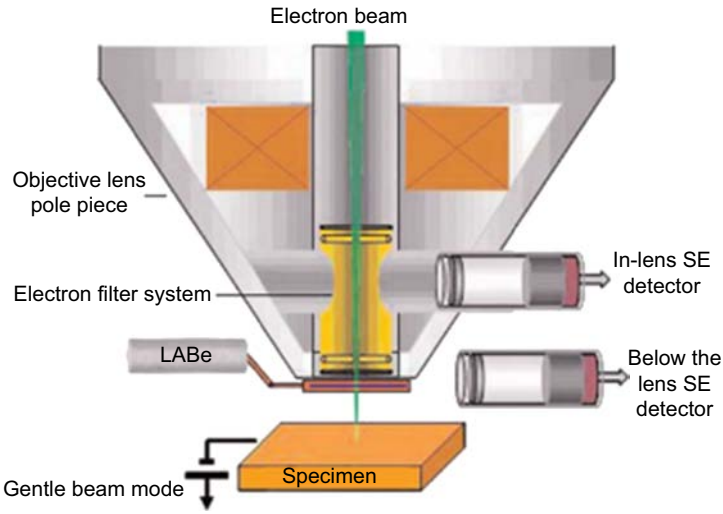


Figure 8.5 General schematic of the detector system in the JSM-7600F [9].

Electron detectors of various types convert secondary electrons (SE) and backscattered electrons (BE) into photons, which are then converted into an electrical signal. Detector types include large-area scintillator detectors, BE-to-SE conversion detectors, and solid-state diode detectors. Additional detectors include a cathodoluminescence detector (photomultiplier) and acoustic or infrared detectors. Energy dispersive X-ray detectors made of silicon or germanium enable the qualitative and quantitative analysis of elements having an atomic number greater than five.

Imaging and characterization of nanomaterials, composites, and biological specimens require operation in the low and ultra-low kV range in FEG-SEM for both imaging and analytical modes. The state-of-the-art FEG-SEM should show high resolution with various detectors at a wide range of accelerating voltages. It should also provide fast and reliable microanalysis at low kV at high probe currents, without loss of spatial resolution and with ease of operation [9].

Fig. 8.6 shows a comparison of the microstructure of the grade 91 in as-treated condition and after long-term (>110 kh) creep at 600°C with EDS analysis spectra of the matrix and $M_{23}C_6$ and Laves particles.

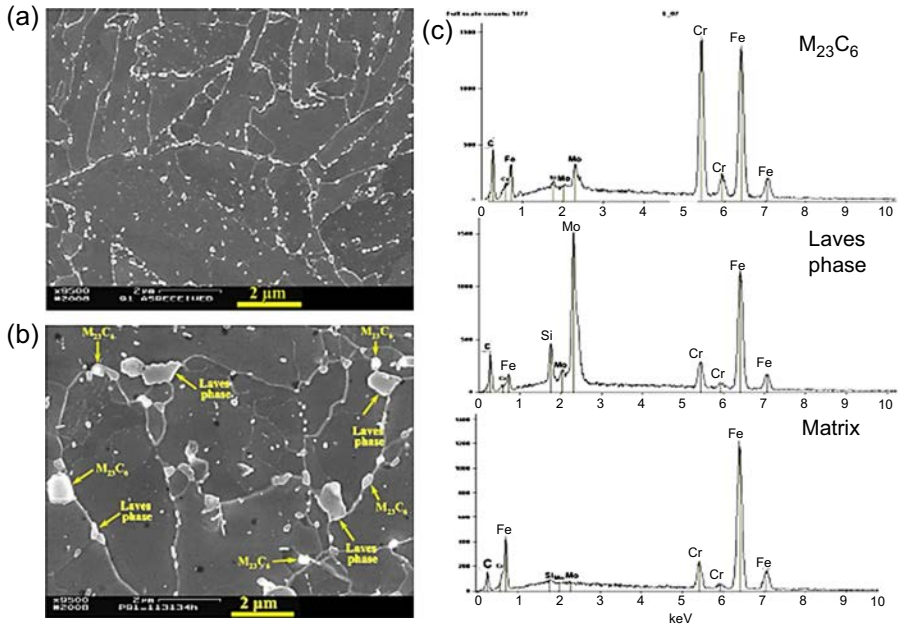


Figure 8.6 Microstructure of the (a) as received P91, (b) after creep at 600°C for 113,431 h (gauge); (c) typical EDS (FEG-SEM) spectra for $M_{23}C_6$ carbides, Laves phases, and matrix, respectively [10].

8.1.4.4 Electron backscatter diffraction

Electron backscatter diffraction (**EBSD**), also known as **backscatter Kikuchi diffraction,** is a microstructural-crystallographic technique used to examine the crystallographic orientation of many materials, which can be used to elucidate texture or preferred orientation of any crystalline or polycrystalline material. EBSD can be used to index and identify the seven crystal systems, and as such, it is applied to crystal orientation mapping, defect studies, phase identification, grain boundary and morphology studies, regional heterogeneity investigations, material discrimination, micro-strain mapping, and using complementary techniques, physicochemical identification. Traditionally, these types of studies have been carried out using X-ray diffraction (XRD), neutron diffraction, and/or electron diffraction in a TEM.

Experimentally, EBSD is conducted using a SEM equipped with an EBSD detector containing at least a phosphor screen, compact lens, and low-light CCD camera chip (Fig. 8.7). Commercially available EBSD systems typically come with one of two different CCD cameras: for fast measurements the CCD chip has a native resolution of 640×480 pixels; for slower, and more sensitive measurements, the CCD chip resolution can go up to 1600×1200 pixels. However, with higher resolutions the readouts are more time-consuming. The biggest advantage of the high-resolution detectors is their higher sensitivity. For texture and orientation measurements, the images are binned to reduce their size and reduce computational times. Thus, the transfer and interpretation of up to almost 1000 images per second is possible if the diffraction signal is sufficient.

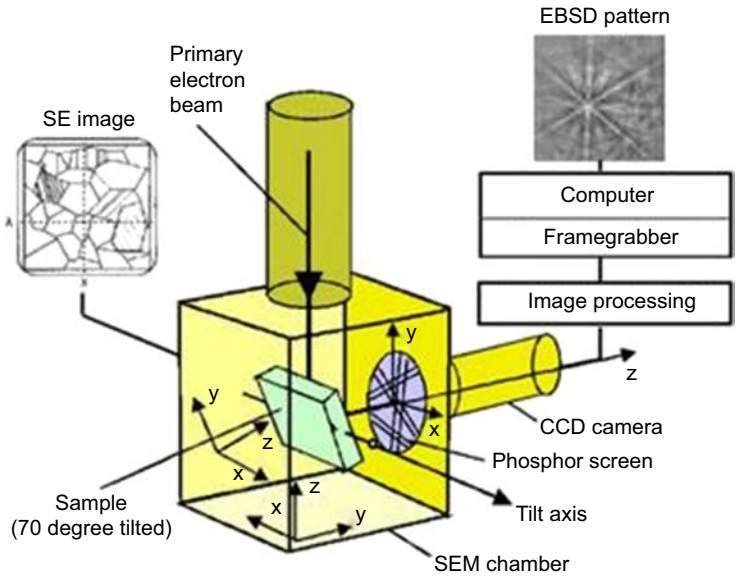


Figure 8.7 Principle of EBSD pattern formation and scheme of measurement [11].

For an EBSD measurement, a flat/polished crystalline specimen is placed in the SEM chamber at a highly tilted angle (~70° from horizontal) toward the diffraction camera, to increase the contrast in the resultant electron backscatter diffraction pattern. The phosphor screen is located within the specimen chamber of the SEM at an angle off approximately 90° to the pole piece and is coupled to a compact lens that focuses the image from the phosphor screen onto the CCD camera. In this configuration, some of the electrons that enter the sample backscatter and may escape. As these electrons leave the sample, they may exit at the Bragg condition related to the spacing of the periodic atomic lattice planes of the crystalline structure and diffract. These diffracted electrons can escape the material, and some will collide and excite the phosphor causing it to fluoresce.

An electron backscatter diffraction pattern (EBSDP) is formed when many different planes diffract different electrons to form Kikuchi bands, which correspond to each of the lattice diffracting planes. If the system geometry is well described, it is possible to relate the bands present in the EBSP to the underlying crystal phase and orientation of the material within the electron interaction volume. Each band can be indexed individually by the Miller indices of the diffracting plane that formed it. In most materials, only three bands/planes that intercept are required to describe a unique solution to the crystal orientation (based upon their interplanar angles), and most commercial systems use lookup tables with international crystal databases to perform indexing.

While this “geometric” description related to the kinematic solution (using the Bragg condition) is very powerful and useful for orientation and texture analysis, it

only describes the geometry of the crystalline lattice and ignores many physical processes involved within the diffracting material. To adequately describe finer features within the EBSDP, one must use a many beam dynamical model (eg, the variation in band intensities in an experimental pattern does not fit the kinematic solution related to the structure factor).

Fig. 8.8 shows an example of the EBSD map on steel grade 91 sample in as-received conditions.

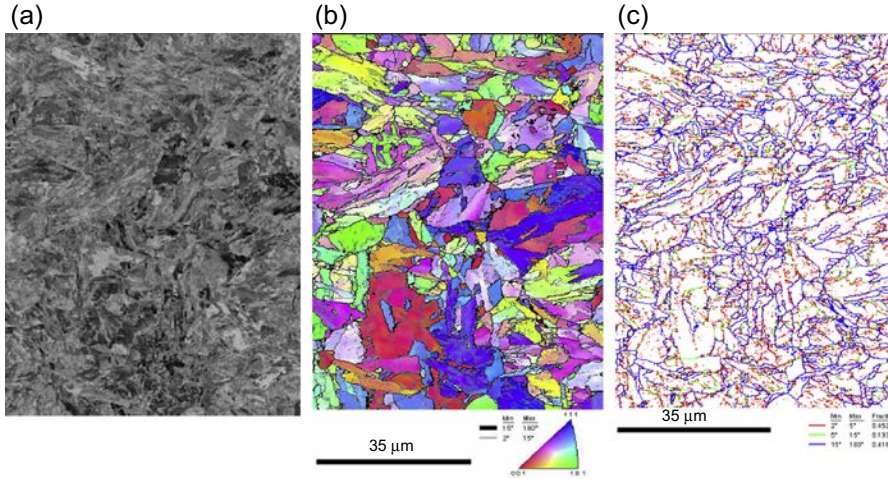


Figure 8.8 Microstructure of the as-received P91 steel: (a) SEM-BSE micrograph; (b) inverse pole figure with orientation of sample normal in the crystal frame as key color; (c) EBSD boundary map [10].

8.1.4.5 Focused ion beam

Focused ion beam, also known as FIB, is a technique used particularly in the semiconductor industry, materials science, and increasingly in the biological field for site-specific analysis, deposition, and ablation of materials. An FIB setup (Fig. 8.9) is a scientific instrument that resembles a SEM. However, while the SEM uses a focused beam of electrons to image the sample in the chamber, an FIB setup uses a focused beam of ions instead. FIB can also be incorporated in a system with both electron and ion beam columns, allowing the same feature to be investigated using either of the beams. FIB should not be confused with using a beam of focused ions for direct write lithography (such as in proton beam writing). These are generally quite different systems where the material is modified by other mechanisms.

FIB technology has become a very powerful tool for TEM sample preparation in steel metallography. The preparation of TEM samples of well-localized sites allows one to directly investigate special points of interest, eg, grain boundaries. The FIB system uses a Ga^+ ion beam to raster over the surface of a sample in a similar way as the electron beam in a SEM does. The high-energy ion beam allows the milling of

small ditches in the sample at well-localized sites, so that samples, sufficiently thin for TEM investigation, can be cut out of the bulk material. Fig. 8.10 shows TEM sample preparation, located in a triple point of prior austenite grain boundary, using FIB technology on NPM1 base material. For this investigation, an FEI dual-beam UHR FEG-SEM/FIB is used [12].

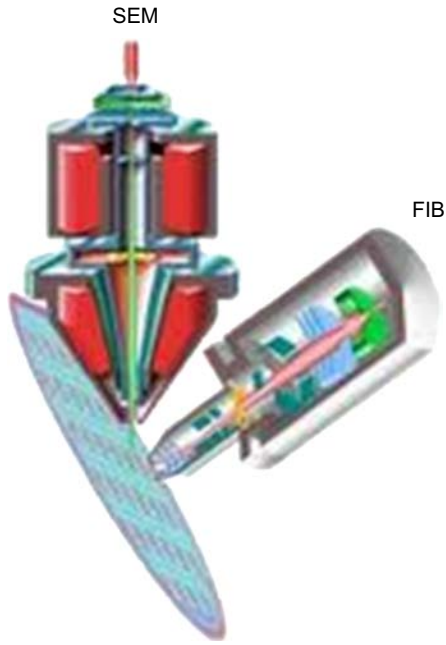


Figure 8.9 FIB work station [11].

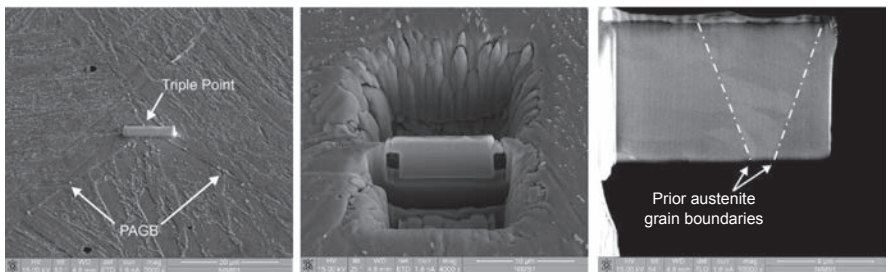


Figure 8.10 TEM specimen preparation using FIB technology on NPM1 base material [12,13].

8.1.4.6 Field-emission gun scanning electron microscope and ion beam system (FIBSEM)

FIBSEM is an instrument that can be also used for both characterizing the grain structure and the carbide population using ion beam etching [14,15]. Operating FIBSEM in

ion image mode, adjusting the image parameters, it is possible to achieve a good contrast between the particles and the matrix present in steels and alloys. The developments of software now available in the new instruments are then able to measure the particles sizes and the populations, using also the grayscale discrimination. Fig. 8.11 shows an example of FIBSEM images on grade 92 steel in as-received condition and after an additional stress-relieving treatments of 16 h at 765°C with the associated EBDS maps: the change in microstructure and precipitation due to the additional heat treatment is clear.

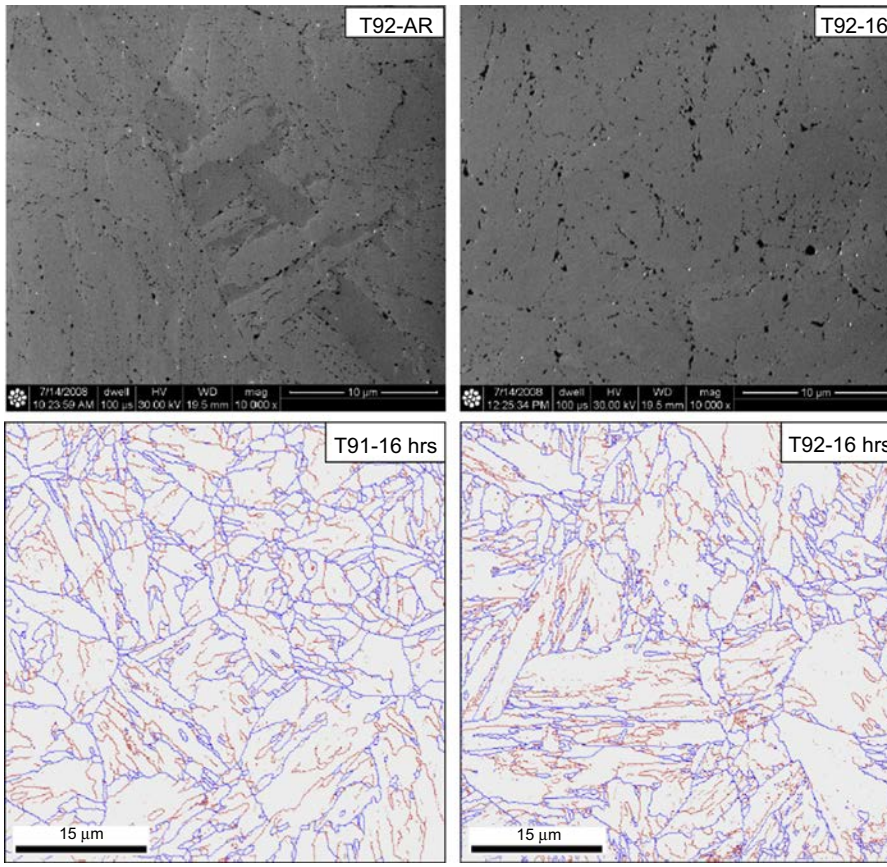


Figure 8.11 Focused ion beam–induced secondary electron images for grade 92. Upper: the particles visible in the image correspond to $M_{23}C_6$. Lower: EBSD-derived boundary maps: low-angle boundaries, defined to be from 2–15 degree are shown in *red*, and high-angle boundaries, 15–180 degree, are shown in *blue* [14].

8.1.4.7 Transmission electron microscopy (TEM)

TEM is a microscopy technique whereby a beam of electrons is transmitted through an ultra-thin specimen, interacting with the specimen as it passes through. An image

is formed from the interaction of the electrons transmitted through the specimen; the image is magnified and focused onto an imaging device, such as a fluorescent screen, on a layer of photographic film, or to be detected by a sensor such as a CCD camera (Fig. 8.12).

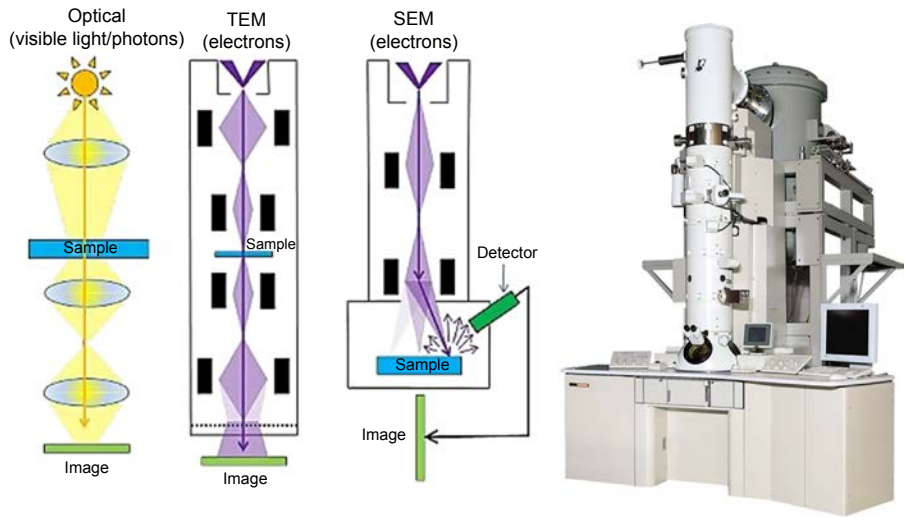


Figure 8.12 Difference in operating principles of optical, TEM, SEM [12], and JEOL 3200FS–HR [16].

TEMs are capable of imaging at a significantly higher resolution than light microscopes, owing to the small de Broglie wavelength of electrons. This enables the instrument's user to examine fine detail, even as small as a single column of atoms, which is thousands of times smaller than the smallest resolvable object in a light microscope. TEM forms a major analysis method in a range of scientific fields, in both physical and biological sciences. TEMs find application in cancer research, virology, and materials science, as well as pollution, nanotechnology, and semiconductor research.

At smaller magnifications, TEM image contrast is due to absorption of electrons in the material due to the thickness and composition of the material. At higher magnifications, complex wave interactions modulate the intensity of the image, requiring expert analysis of observed images. Alternate modes of use allow for the TEM to observe modulations in chemical identity, crystal orientation, electronic structure, and sample-induced electron phase shift as well as the regular absorption-based imaging.

SEMs and TEMs differ from conventional light microscopes in that they employ electrons rather than photons to irradiate material and produce images.

Fig. 8.13 shows the martensitic microstructure, by thin foil, and the precipitate population, by extraction replica, of the FB2 steel for rotor applications in the as-received conditions.

Fig. 8.14 shows an example of the γ' particles in Haynes 282 in the dendritic and interdentritic zones with the electron diffraction pattern.

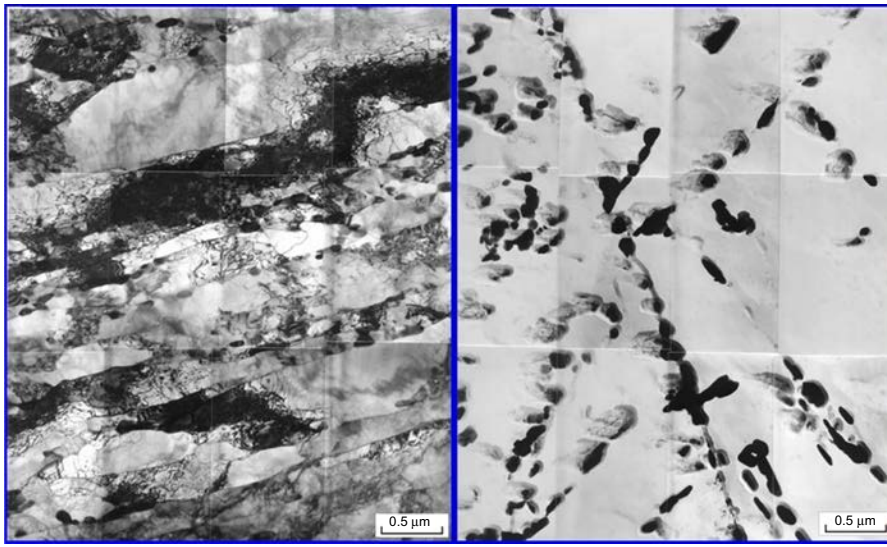


Figure 8.13 FB2 rotor steel microstructure (thin foil) and precipitation (extraction replica) after heat treatment [18].

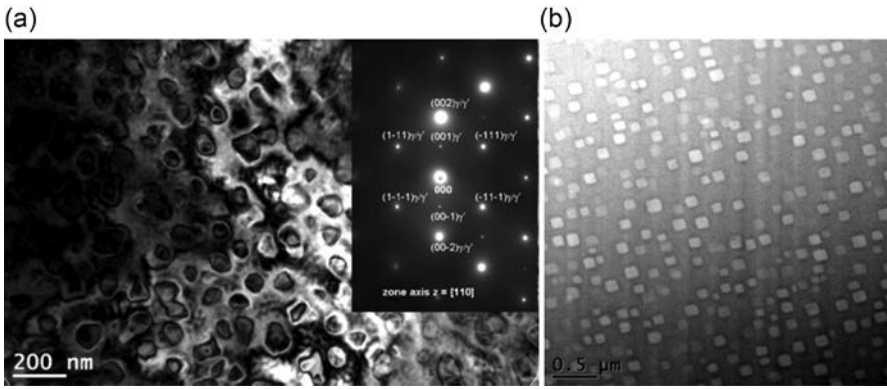


Figure 8.14 A BF TEM image and selected area electron diffraction pattern for γ/γ′ type microstructure in the as-cast Haynes 282 superalloy: (a) dendrite and (b) interdendritic area [19].

8.1.4.8 Scanning transmission electron microscope (STEM)

A **STEM** combines the capabilities of both an SEM and a TEM (Fig. 8.15). The electron beam is transmitted across the sample to create an image (TEM) while it also scans a small region on the sample (SEM). The ability to scan the electron beams allows the user to analyze the sample with various techniques such as **electron energy loss spectroscopy (EELS)** and **energy dispersive X-ray (EDX)** spectroscopy, which are useful tools to understand the nature of the materials in the sample [20].

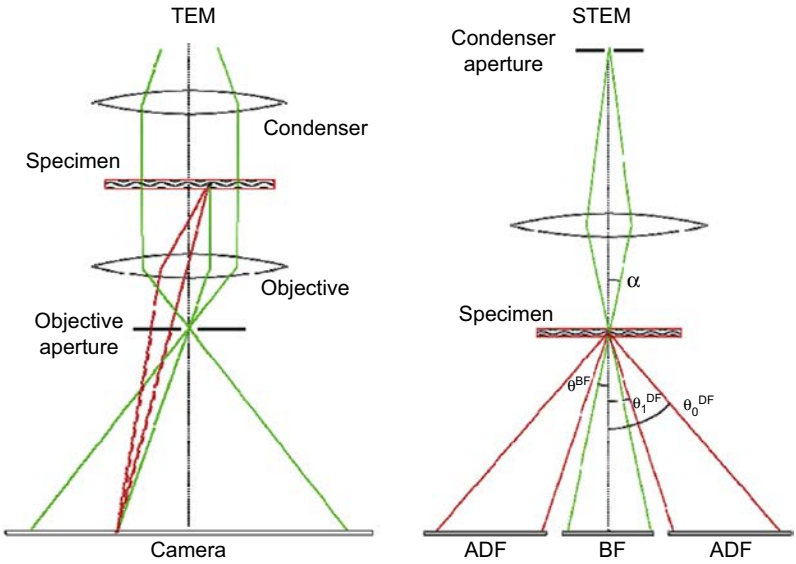


Figure 8.15 Difference in operating principles TEM and STEM [21].

8.1.4.9 *Energy-filtered transmission electron microscopy*

The development of modern materials is becoming increasingly reliant on the accurate chemical analysis on the nanoscale. One technique that is well suited to mapping the chemical distribution at high resolution is energy-filtered TEM (EFTEM) in which an image is formed using only electrons that have suffered an energy loss characteristic of the element of interest, typically an ionization edge in the 100–1000 eV range. We have found that by acquiring a series of EFTEM images across a large range of energy loss, conventional spectroscopic techniques may be applied to such a series to improve quantification. This hybrid approach is known as "image spectroscopy" (Fig. 8.16).

From EELS to EFTEM: Inelastic interactions with the specimen will lead to a loss of energy of the incident electrons, and this loss will be related to the chemical and electrical makeup of the specimen. By dispersing transmitted electrons using a magnetic prism an electron energy loss (EEL) spectrum can be recorded. After dispersion a series of lenses can be used to reform an image using electrons whose loss is defined by a slit in the spectral plane: a technique known as EFTEM [23].

Fig. 8.17 shows an example EFTEM analysis on grade 91 aged over 100 kh at 600°C: the possibility to identify the precipitates $M_{23}C_6$ and MX and associate main elements with the particles using the mapping of the single elements is evident.

Other examples of the potentiality of investigations that can be done are now reported.

In a sample from head creep specimens broken after 104 k at 600°C, a small hybrid (MX in transformation to Z-phase) particle with a V-rich core and a Cr-rich rim have been analyzed (Fig. 8.18). In addition to the high annular angular dark field (HAADF) image of the particle (Fig. 8.18(a)), the EFTEM thickness map

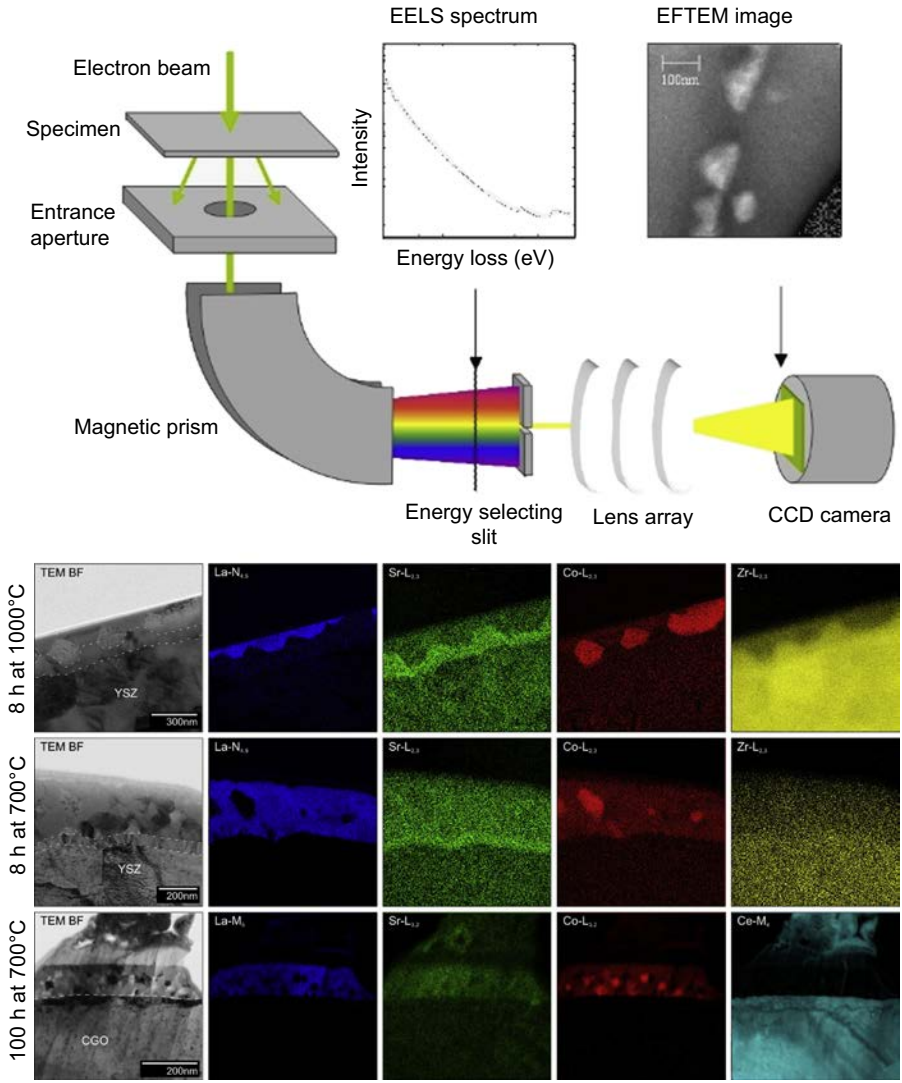


Figure 8.16 A schematic of the EELS and EFTEM experimental setup for a Gatan imaging filter [22,23].

and the vanadium map of the hybrid particle have been obtained, as shown in Fig. 8.18(b) and (c), respectively. The variation in composition within the particle was also investigated using an EDS line scan with 50 measurements (Fig. 8.19). The chemical composition gradually varies within the precipitate: there is an area with an MX-like composition in the middle (V: ~50 at%; Cr: ~30 at%), while the "wings" of the particle have a Z-phase like composition (V: ~35 at%; Cr: ~55 at%). Between the core and the outer particle surface a relatively smooth Cr and V gradient was measured [18].

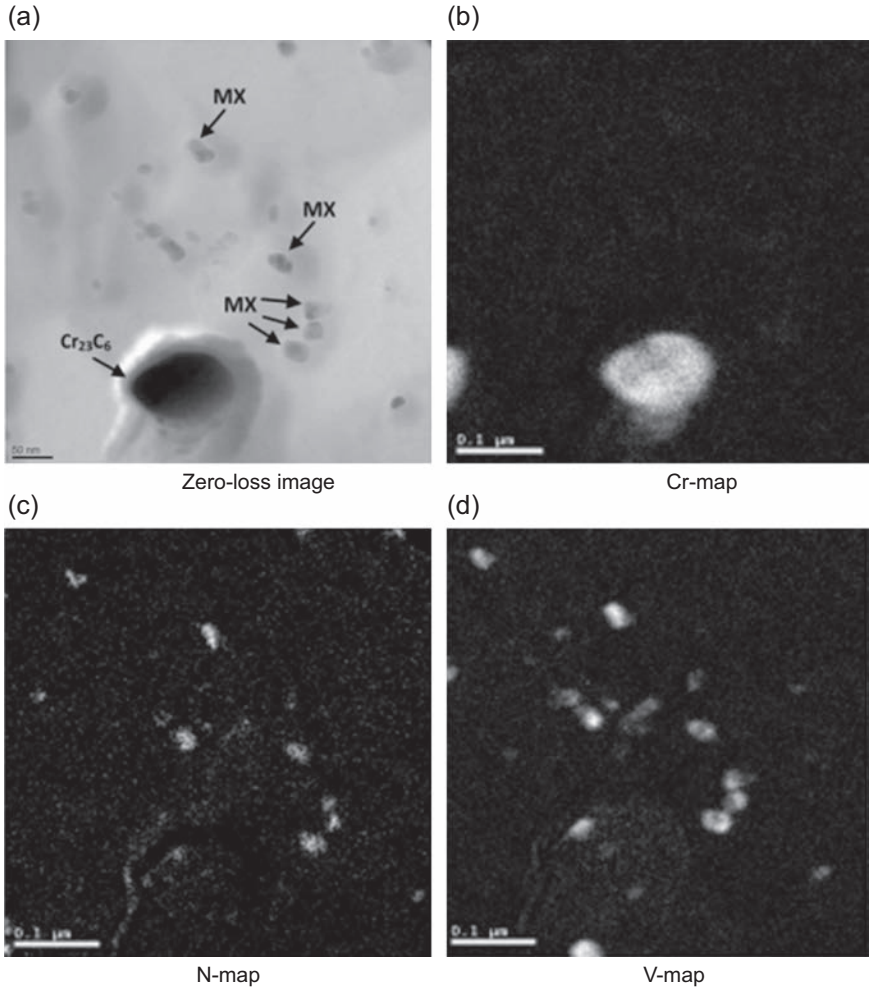


Figure 8.17 (a) Zero-loss image and jump ratio images of (b) chromium, (c) nitrogen, and (d) vanadium map on a frame of 600°C/104 kh aged P91 sample (investigation carried out on extraction replica) [17].

The investigation capability offered by the new EFTEM has been also used to analyze, eg, the recovery of the martensite around the PAGB (prior austenite grain boundary) in grade 91 steel as function of time at 600°C [24,25], using creep specimen heads. Precipitate distributions in the extracted carbon replicas are shown in Fig. 8.20. The *dashed line* indicates the PAGB predicted on the basis of precipitate distribution. Before creep, a large number of fine precipitates were located around the PAGB and inside the prior austenite grains. The precipitate particles apparently became coarse during creep. The number of very fine precipitates with weak contrast tended to decrease after 50,000 h.

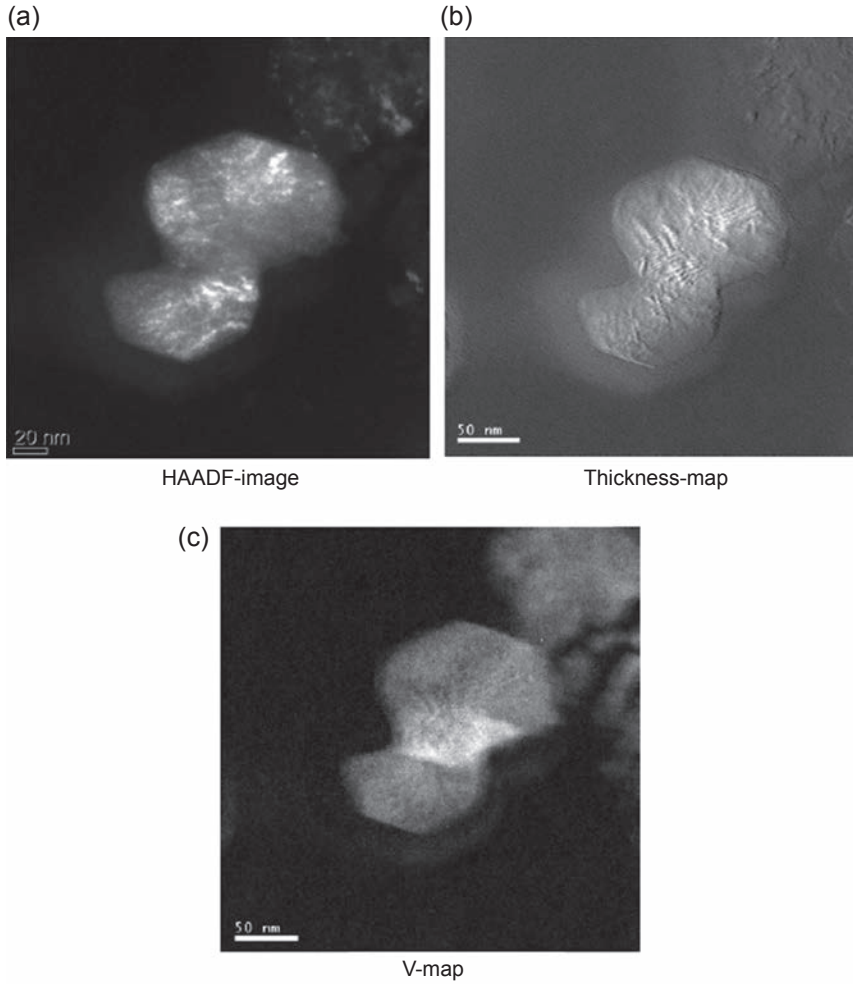


Figure 8.18 Hybrid MX/Z-phase particle in P91 600°C/104 kh sample: (a) HAADF image, (b) thickness map, and (c) vanadium map of the particle (investigation carried out on extraction replica) [17].

Fig. 8.21 shows the results obtained from the Cr, V, and Nb elemental maps. $(Fe,Cr)_{23}C_6$, VX, and NbX could be detected in the Cr, V, and Nb maps, respectively.

In addition, many particles were observed in the Cr and V maps; the results of EDX analysis confirmed that these particles were Z-phase [Cr(V,Nb)N] particles. In Fig. 8.21, the *red*, *blue*, *green*, and *white* particles correspond to $(Fe,Cr)_{23}C_6$, VX, NbX, and Z-phase, respectively.

It was clear that the size of the $(Fe,Cr)_{23}C_6$ particles gradually increased with time. Z-phase formation could be clearly observed after 30,000 h. The Z-phase particles gradually increased in size during creep after 30,000 h and finally became very large,

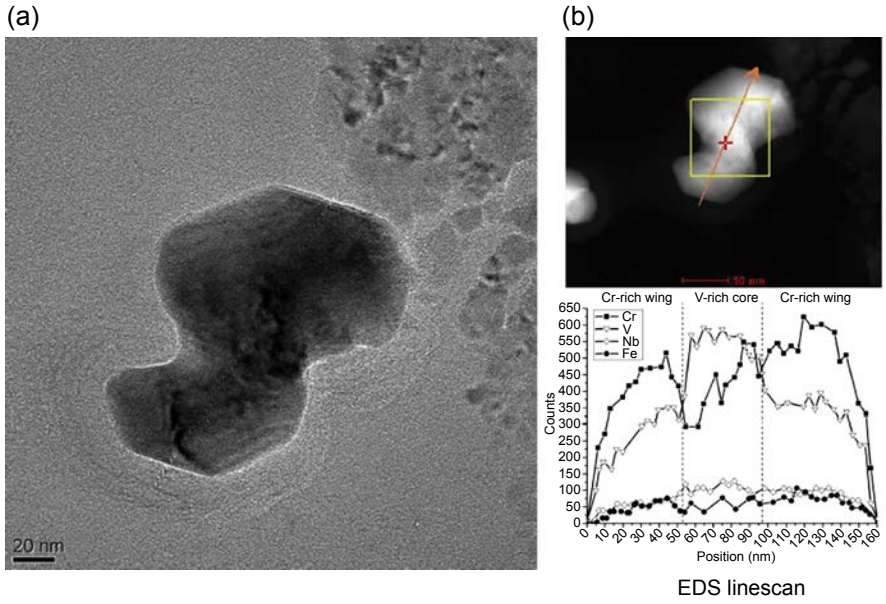


Figure 8.19 (a) Bright field image of the hybrid particle in 600°C/104 kh sample; (b) line scan along main particle axis: Nb, Fe, Cr, and V EDS counts [17].

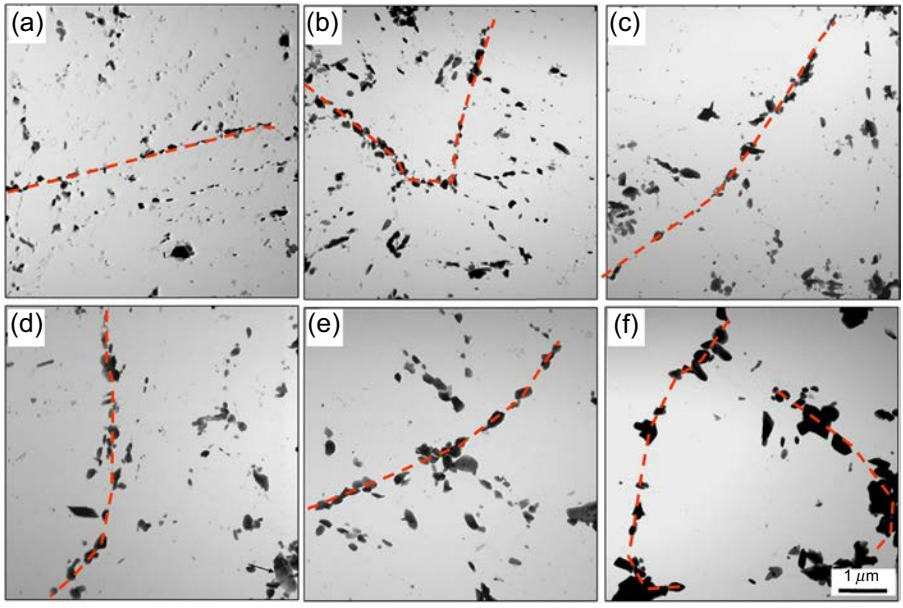


Figure 8.20 Change of precipitates distributions on carbon extracted replica during creep. (a) As temperature, (b) 9992 h, (c) 30,030 h, (d) 50,064 h, (e) 70,000 h, and (f) 80,736.8 h [24,25].

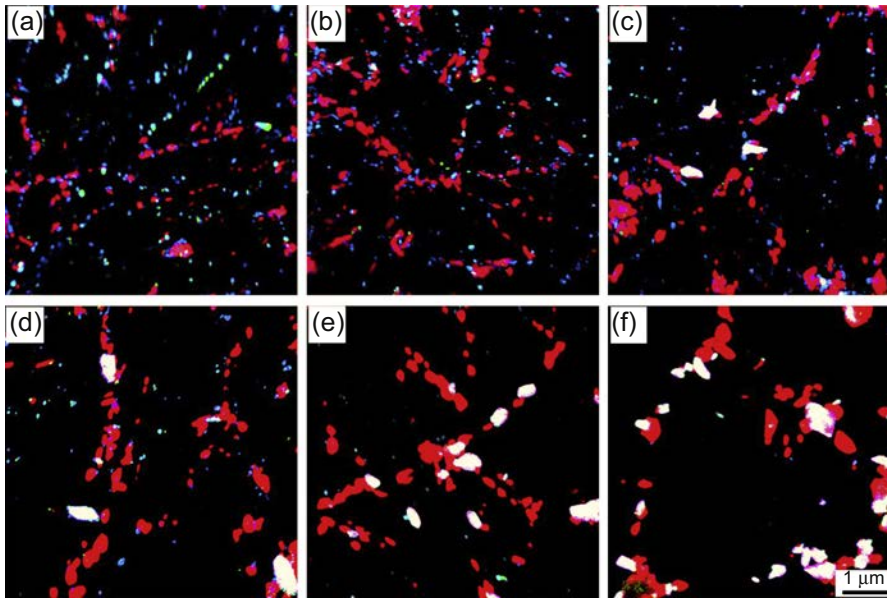


Figure 8.21 Precipitates distributions based on the results of elemental maps of Cr, V, and Nb. (a) As temperature, (b) 9992 h, (c) 30,030 h, (d) 50,064 h, (e) 70,000 h, and (f) 80,736.8 h. *Red*: M23C6, *blue*: V-rich MX, *green*: Nb-rich MX, *white*: Z-phase [24,25].

similar to $(Fe,Cr)_{23}C_6$ particles, after creep rupture. On the other hand, the number of VX and NbX particles appeared to decrease after 50,000 h. In short, we could state that during Z-phase formation, the VX and NbX particles were consumed.

8.1.4.10 APFIM

The atom probe is a microscope used in material science that was invented in 1967 by Erwin Wilhelm Müller, J. A. Panitz, and S. Brooks McLane. The atom probe is closely related to the method of field ion microscopy, which is the first microscopic method to achieve atomic resolution, occurring in 1951.

Atom probes are unlike conventional optical or electron microscopes, in that the magnification effect comes from the magnification provided by a highly curved electric field, rather than by the manipulation of radiation paths. Technically, the method is destructive in nature, removing ions from a sample surface to image and identify them, generating magnifications sufficient to observe individual atoms as they are removed from the sample surface. Through coupling of this magnification method with time of flight MS, ions evaporated by application of electric pulses can have their mass-to-charge ratio computed.

Through successive evaporation of material, layers of atoms are removed from a specimen, allowing for probing not only of the surface but also through the material itself. Computer methods are utilized to rebuild a three-dimensional view of

the sample, prior to it being evaporated, providing atomic-scale information on the structure of a sample, as well as providing the type atomic species information. The instrument allows the three-dimensional reconstruction of up to hundreds of millions of atoms from a sharp tip (corresponding to specimen volumes of 10,000–1,000,000 nm^3). Visualization of data obtained from an atom probe shows each point represents a reconducted atom position from detected evaporated ions.

Fig. 8.22 shows an APT acquisition with MX precipitates on FT3B experimental steel, having as parent the FB2 steel, and containing 250 ppm of boron [26]. The iso-concentration surfaces of VN^{2+} molecular ions are used to study the MX precipitates. It can be observed from Fig. 8.14 that the precipitates have a disk-shaped morphology. The size of the precipitates varies from approximately 5 nm up to 15 nm in diameter with a thickness of a few nanometers, which corresponds to the dimensions obtained from TEM. In Fig. 8.22, a somewhat larger precipitate (20 nm) is found that probably belongs to the family of larger MX precipitates. The number density of MX is approximately $4.5 \times 10^{22}\ m^{-3}$. This result is based on a total analysis volume of more than $10^6\ nm^3$ from 11 different APT tips. *At present, it is not possible to give a quantitative analysis of MX precipitates because of several experimental difficulties.* These difficulties include overlap between isotopes (eg, N^+ and Si^{2+}) in the mass spectrum and, above all, trajectory effects resulting from precipitates protruding from the specimen

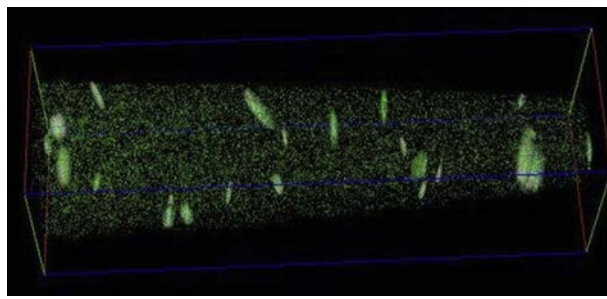


Figure 8.22 APT analysis of steel FT3B after tempering at 963 K (690°C) for 2 h including 23 MX precipitates. The size of the analyzed volume is $39 \times 39 \times 153\ nm^3$ and contains 10 million atoms. The dots represent vanadium atoms and each VN precipitate is enclosed by surface [26].

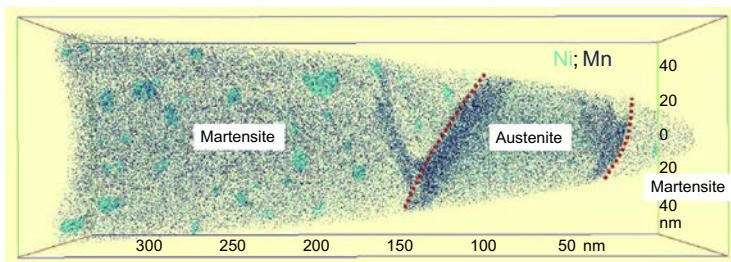


Figure 8.23 Ni atoms *(cyan symbols)* are accumulated in precipitates in the martensitic grains (left- and right-hand side). The precipitate-free austenite (right-hand center) is bordered by plate-like zones that are characterized by strong Mn enrichment *(blue symbol)*. *Red dotted lines* illustrate the suggested crystallographic positions of the phase boundaries between martensite and austenite [28].

surface during analysis. However, qualitatively, the precipitates were rich in vanadium, niobium, molybdenum, chromium, and nitrogen. A high chromium content in small VN precipitates has been observed in martensitic chromium steels before [27] as well as in many types of MX precipitates in austenitic steels [29].

An example of 20-nm-thick middle layer slice through the APT reconstruction of the maraging TRIP steel is shown in Fig. 8.23.

8.1.5 Surface analysis

8.1.5.1 Auger electron spectroscopy (AES)

AES is a common analytical technique used specifically in the study of surfaces and, more generally, in the area of materials science. Underlying the spectroscopic technique is the Auger effect, as it has come to be called, which is based on the analysis of energetic

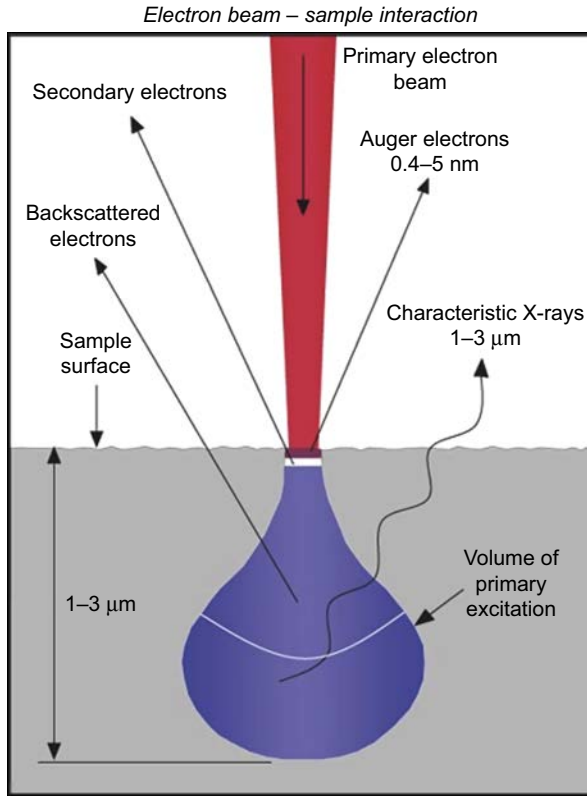


Figure 8.24 Auger electron spectroscopy [30].

electrons emitted from an excited atom after a series of internal relaxation events (Fig. 8.24). The Auger effect was discovered independently by both Lise Meitner and Pierre Auger in the 1920s. Though the discovery was made by Meitner and initially reported in the journal Zeitschrift für Physik in 1922, Auger is credited with the discovery in most

of the scientific community. Until the early 1950s, Auger transitions were considered nuisance effects by spectroscopists, not containing much relevant material information, but studied so as to explain anomalies in X-ray spectroscopy data. Since 1953, however, AES has become a practical and straightforward characterization technique for probing chemical and compositional surface environments and has found applications in metallurgy, gas-phase chemistry, and throughout the microelectronics industry.

8.1.5.2 Glow discharge optical emission spectroscopy

In glow discharge optical emission spectroscopy, a glow discharge is a plasma formed by the passage of electric current through a low-pressure gas (Fig. 8.25). It is created by applying a voltage between two metal electrodes in a glass tube containing gas. When the voltage exceeds a certain value, called the striking voltage, the gas in the tube ionizes, becoming a plasma, and it begins conducting electricity, causing it to glow with a colored light. The color depends on the gas used. Glow discharge is widely used as a source of light in devices such as neon lights, fluorescent lamps, and plasma-screen televisions. Analyzing the light produced by spectroscopy can reveal much about the atomic interactions in the gas, so glow discharge is used in plasma physics and analytical chemistry. It is also used in the surface treatment technique called sputtering.

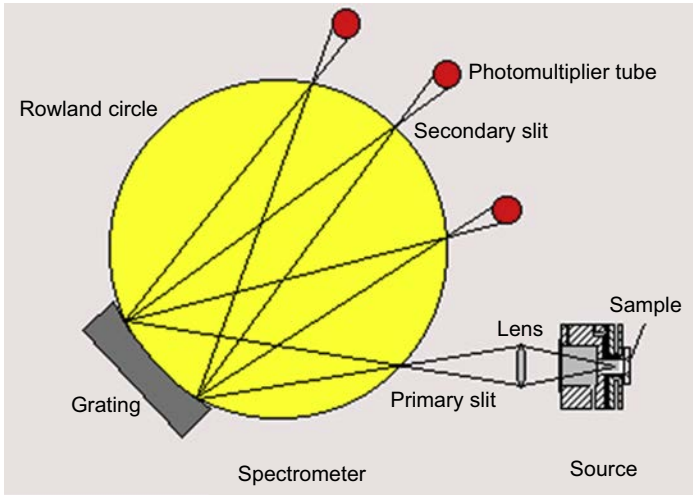


Figure 8.25 Glow discharge optical emission spectroscopy [31].

8.1.5.3 Electron microprobe

An electron microprobe (EMP), also known as an **electron probe microanalyzer (EPMA)** or **electron micro probe analyzer (EMPA)**, is an analytical tool used to nondestructively determine the chemical composition of small volumes of solid materials. It works similarly to a SEM: the sample is bombarded with an electron beam, emitting X-rays at wavelengths characteristic to the elements being analyzed (Fig. 8.26). This enables the abundances of elements present within small sample volumes

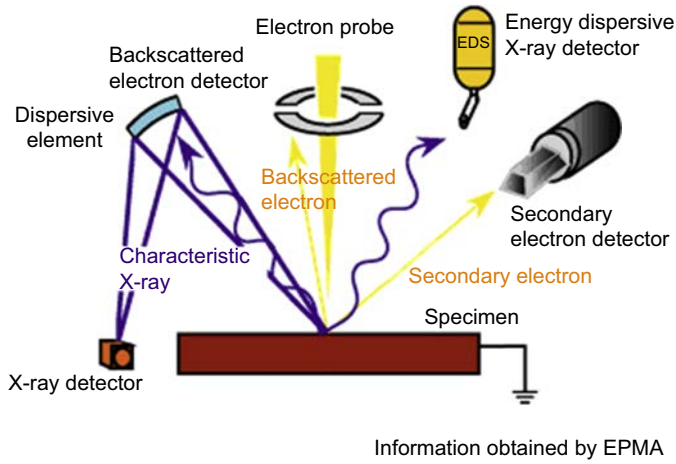


Figure 8.26 Electron probe microanalyzer [32].

(typically 10–30 cubic micrometers or less) to be determined. The concentrations of elements from boron to plutonium can be measured at levels as low as 100 parts per million (ppm). Recent improvements on EMPAs can accurately measure elemental concentrations of approximately 10 ppm.

8.1.5.4 Secondary ion mass spectrometry (SIMS)

SIMS is the most sensitive elemental and isotopic surface microanalysis technique [33]. When a solid sample is sputtered by primary ions of a few keV energy, a fraction of the

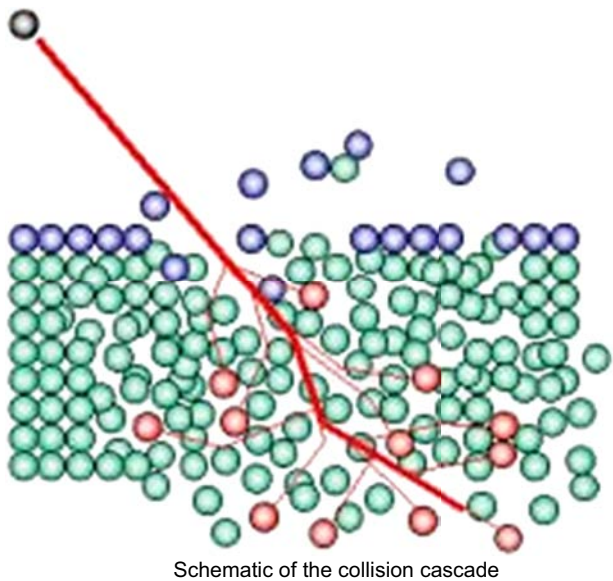


Figure 8.27 Secondary ion mass spectrometry [33].

particles emitted from the target is ionized (Fig. 8.27). **SIMS** consists of analyzing these secondary ions with a mass spectrometer. Secondary ion emission by a solid surface under ion bombardment supplies information about the **elemental, isotopic, and molecular composition** of its uppermost atomic layers. The secondary ion yields will vary greatly according to the chemical environment and the sputtering conditions (ion, energy, angle). This can add complexity to the quantitative aspect of the technique. SIMS is nevertheless recognized as the most sensitive elemental and isotopic surface analysis technique.

The SIMS technique provides a unique combination of extremely **high sensitivity** for all elements from hydrogen to uranium and above (detection limit down to ppb level for many elements), **high lateral resolution** imaging (down to 40 nm), and a very low background that allows **high dynamic range** (more than five decades). This technique is "destructive" by its nature (sputtering of material). It can be applied to any type of material (insulators, semiconductors, metals) that can stay under vacuum.

8.1.5.5 X-ray photoelectron spectroscopy (XPS)

XPS is a sensitive and surface-sensitive quantitative spectroscopic technique that measures the elemental composition, empirical formula, chemical state, and electronic state-of-the-art elements that exist within a material. XPS spectra are obtained by irradiating a material with a beam of X-rays while measuring the kinetic energy and number of electrons that escape from the top 0–10 nm of the material being analyzed. XPS requires ultra-high vacuum (UHV) conditions.

XPS is a surface chemical analysis technique that can be used to analyze the surface chemistry of a material in its "as-received" state or after some treatment, eg, fracturing, cutting, or scraping in air or UHV to expose the bulk chemistry, ion beam etching to clean off some of the surface contamination, exposure to heat to study the changes due to heating, exposure to reactive gases or solutions, exposure to ion beam implant, or exposure to ultraviolet light (Fig. 8.28).

- XPS is also known as ESCA (electron spectroscopy for chemical analysis), an abbreviation introduced by Kai Siegbahn's research group to emphasize the chemical (rather than merely elemental) information that the technique provides.
- In principle XPS detects all elements. In practice, using typical laboratory-scale X-ray sources, XPS detects all elements with an atomic number (Z) of 3 (lithium) and above. It cannot easily detect hydrogen ($Z=1$) or helium ($Z=2$) because the binding energy of these electrons is so small compared to the excitation energy of the X-ray photon; hence the absorption efficiency is very small. Ultraviolet photoelectron spectroscopy is better suited for studying these elements since there is a better match in excitation and ionization energies, hence a larger absorption efficiency and ionization cross-section.
- Detection limits for most of the elements are in the parts per thousand range. Detection limits of parts per million (ppm) are possible but require special conditions: concentration at top surface or very long collection time (overnight).
- XPS is routinely used to analyze inorganic compounds, metal alloys, semiconductors, polymers, elements, catalysts, glasses, ceramics, paints, papers, inks, woods, plant parts, makeup, teeth, bones, medical implants, bio-materials, viscous oils, glues, ion-modified materials, and many others.

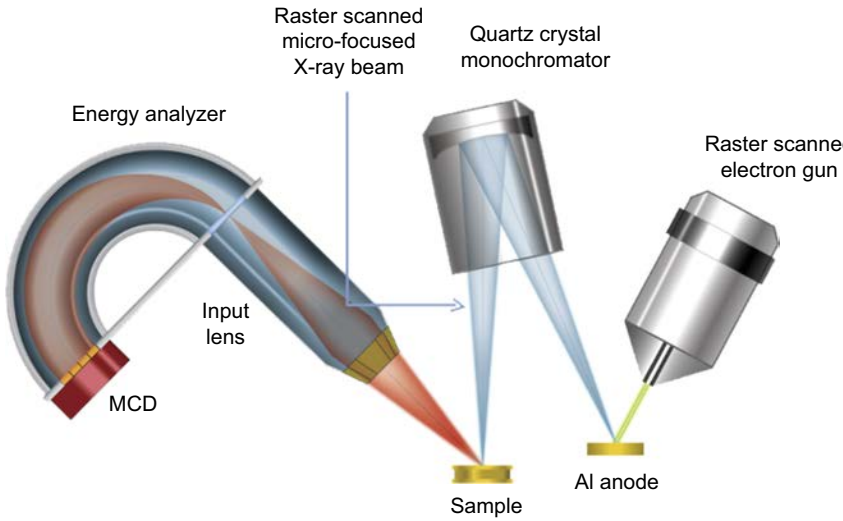


Figure 8.28 Surface analysis through XPS technique [33,34].

8.1.5.6 X-ray diffraction

XRD is a nondestructive technique for characterizing crystalline materials. Typically, XRD is used for the identification of a crystalline phase or mineral. However, it can also provide information on structures, preferred crystal orientation, and other structural parameters, such as average grain size and strain distribution.

XRD patterns are produced by a goniometer, which is rotated at specific angles while bombarding the sample material with X-rays. The diffraction pattern peak intensities are determined by the distribution of atoms within the lattice. The XRD pattern is specific to the periodic atomic arrangements in a given material, which is compared to the ICDD standard database of XRD patterns for phase identification (Fig. 8.29).

XRD can be used for the identification of powdered metals and mineral compounds, for the quantification of primary and minority crystalline phases, the quantification of preferred orientation, the measurement of residual stress in metal and ceramics, and the measurement of the crystalline size. It is enough to have a gram of material (minimum), which must be ground into a powder.

Fig. 8.30 shows an example of XRD diffractogram of the precipitates present in a grade 92 crept sample after 57,715 at 650°C. The specimen was previously analyzed by TEM and $M_{23}C_6$, MX, Laves, and also some MX/Z-phase particles were identified by EDS measurements. To complete the analyses the specimen was electrolytically dissolved, and the residual powders (extracted precipitates) have been analyzed by XRD. The diffractogram confirms the presence of Z-phase: the Cr(V,Nb)N peak is small but evident.

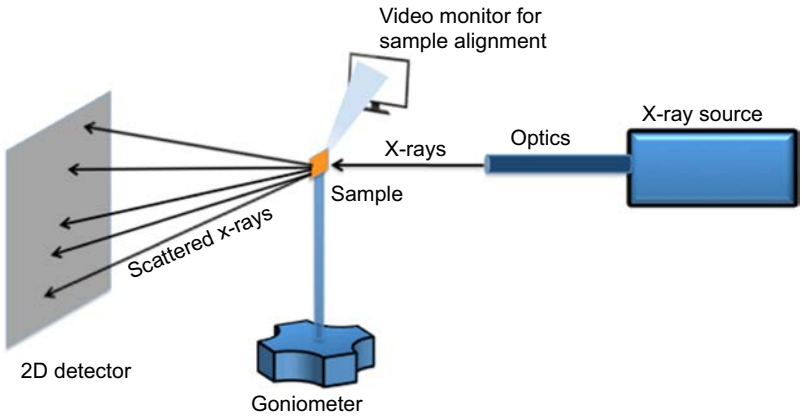


Figure 8.29 X-ray crystallography [35].

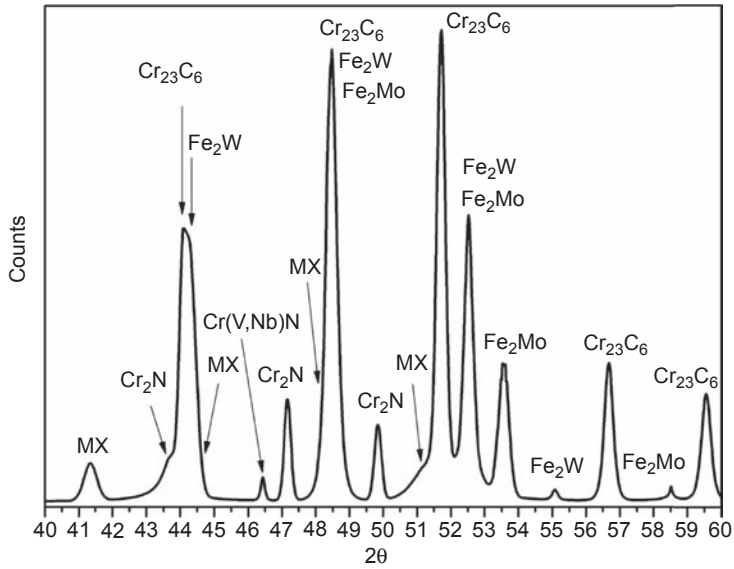


Figure 8.30 XRD diffractogram of P92 aged sample after 57,715 h at 650°C [36].

8.2 Modeling tools

8.2.1 Thermo-Calc

Thermo-Calc [37] has over the past 30 years gained a world-wide reputation as the best and most powerful software package for thermodynamic calculations. It is widely used for a variety of calculations, including calculating the following:

- stable and metastable heterogeneous phase equilibria
- amounts of phases and their compositions
- thermochemical data such as enthalpies, heat capacity, and activities

- transformation temperatures, such as liquidus and solidus
- driving force for phase transformations
- phase diagrams (binary, ternary, and multicomponent)
- solidification applying the Scheil-Gulliver model
- thermodynamic properties of chemical reactions

All calculations are based on thermodynamic data that is supplied in a database. There exists a wide selection of high-quality databases for various purposes that include many different materials. The databases are produced by experts through critical assessment and systematic evaluation of experimental and theoretical data following the well-established CALPHAD technique.

Fig. 8.31 shows an example of the Thermo-Calc calculations for steel grade 91 that indicates a decrease in the volume fraction of precipitates around A_{C1} temperature (ferritic-austenitic transformation).

Another example of use of Thermo-Calc was made by Aubert and Duval: three conditions were defined to optimize the Nimonic C-263 composition. The first condition was defined to improve microstructure stability at 750°C and so to remove η phase

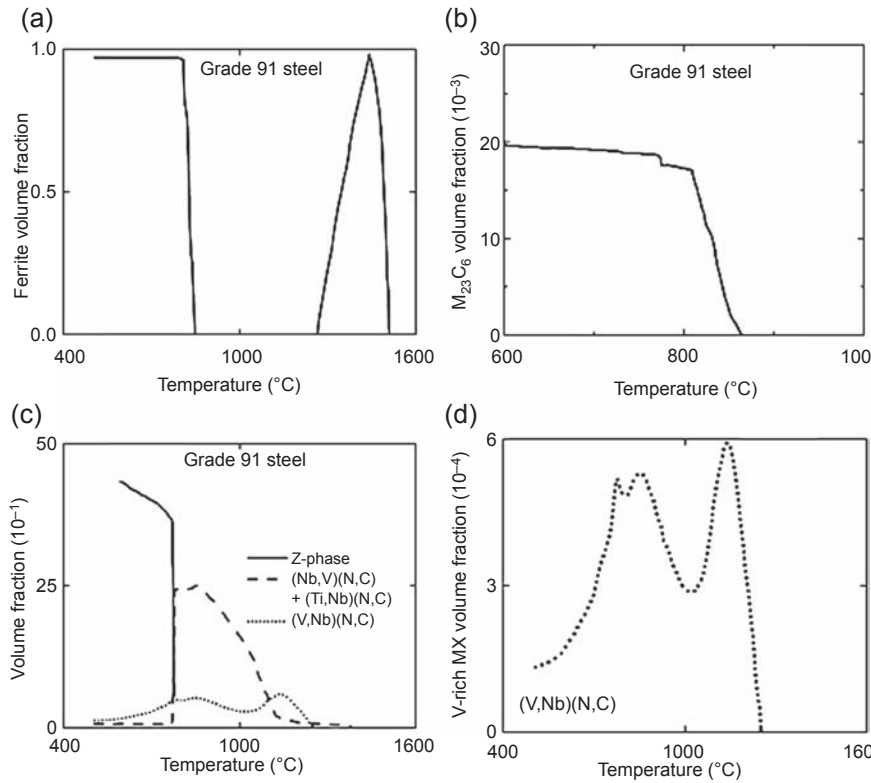


Figure 8.31 Evolutions of (a) the ferrite phase; (b) $M_{23}C_6$ precipitate; (c) Z-phase, Nb-rich MX, V-rich MX, and Ti-rich MX precipitates; and (d) high-resolution plot of (V,Nb)(N,C) precipitate as a function of temperature [3].

formation. Then, the second and third conditions concern process properties (workability, weldability, etc.), which were expected to be as good as those of Nimonic C-263. To satisfy these conditions, γ′ solvus and γ′ content at 750°C have to be similar to those of Nimonic C-263. As we know, formation of η and γ′ phases are linked to Ti and Al contents. Consequently, Thermo-Calc software with the database TCNI5 was used to define Ti-Al couples that satisfy the previous conditions [38].

The stability window of η phase for Nimonic C-263 composition as a function of Ti and Al contents was determined and the boundary of the domain is plotted on Fig. 8.32(a) (*dashed line*). The Ti-Al couple for Nimonic C-263 is also reported on Fig. 8.32, and it appears that Nimonic C-263 lies in the stability window for η phase. Nimonic C-263 γ′ solvus calculated by Thermo-Calc was found to be equal to 900°C. Simulations were then made to determine all Ti-Al couples, which allow 900°C as γ′ solvus, and the results were plotted on Fig. 8.32(a) (*solid line*). Nimonic C-263 γ′ content was calculated to be equal to 10 at% at 750°C. As for γ′ solvus, Ti-Al couples which allow 10 at% of γ′ content at 750°C were determined and plotted in Fig. 8.32(a) (*dashed line*). Simulations were also performed for 9 at% and 11 at% γ′ content at 750°C to surround the 10 at% line. Fig. 8.32(b)–(d) shows, respectively, the microstructure of the basic composition with η-phase and the microstructure of the trial and industrial test without η-phase after 750°C for 3000 h.

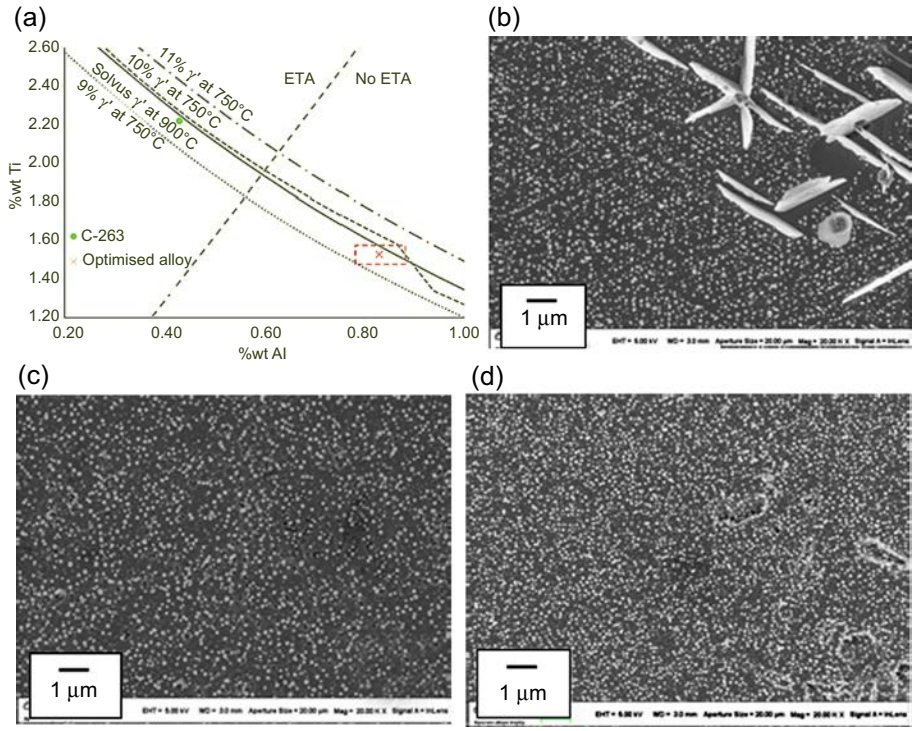


Figure 8.32 Thermo-Calc simulations to define stability window of η phase, γ′ solvus, and γ′ content at 750°C. SEM micrographs of samples aged at 750°C for 3000 h. (a) Nimonic C-263; (b) optimized alloy (trial test); (c) optimized alloy (industrial test) [38].

8.2.2 DICTRA

DICTRA is software for accurate simulation of diffusion controlled reactions in multicomponent alloy systems, which is based on numerical solution of the multicomponent diffusion equations.

DICTRA [39] is a sophisticated software for accurate simulations of diffusion in multicomponent alloy systems. Many different processes can be simulated (Fig. 8.33):

- homogenization of alloys
- carburizing and decarburizing of steels
- microsegregation during solidification
- carbide dissolution during austenitization of steels
- coarsening of precipitates

DICTRA requires Thermo-Calc for necessary thermodynamic calculations and is available as an add-on to a Thermo-Calc license. The DICTRA software has been applied to numerous problems of practical and scientific interest.

The simulations with DICTRA require these databases:

- thermodynamic data (used in Thermo-Calc)
- kinetic data (used in DICTRA)

There are databases available for different materials and applications such as steel, nickel superalloys, or aluminum. Some examples of cases that have been simulated using DICTRA include micro-segregation during solidification, homogenization of alloys, growth/dissolution of carbides, nitrides, and intermetallic phases, coarsening of precipitate phases, interdiffusion in compounds (eg, coating systems), austenite to ferrite transformations in steel, carburization, nitriding, and carbonitriding of high-temperature alloys and steels, post-weld heat treatment, and sintering of cemented-carbides.

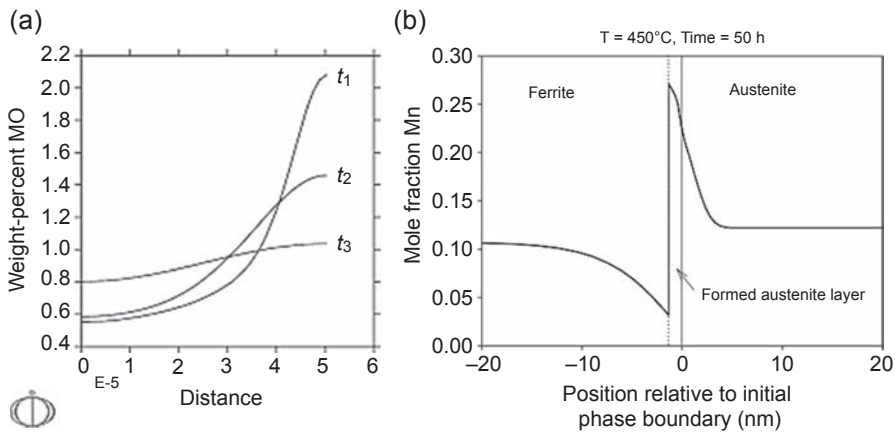


Figure 8.33 Example of DICTRA applications: (a) homogenization of alloys; (b) Mn distribution at the martensite/austenite phase boundary [28,39].

8.2.2.1 Linking fundamental models to critically assessed thermodynamic and kinetic data

To allow simulations to be performed with realistic conditions on alloys of practical importance, emphasis during the development of DICTRA has been on linking fundamental models to critically assessed thermodynamic and kinetic data. As a result, DICTRA is very general, and it is primarily the access to thermodynamic and kinetic data that determines if a problem can be simulated or not. This is, of course, under the assumption that the problem in question is diffusion controlled and that all other basic model assumptions are met.

To perform a DICTRA simulation, both a thermodynamic and a kinetic database are needed. The thermodynamic database is the same as used by Thermo-Calc, whereas the kinetic database is an additional database that contains information about the atomic mobility of individual components in relevant phases. The kinetic databases are created through an assessment procedure similar to the one that is used for thermodynamic databases.

It should also be emphasized that simulations are one-dimensional and that three different geometries, ie, planar, cylindrical, and spherical, can be used. This is sufficient to model many cases of interest. A cylindrical geometry may, eg, be used both for modeling of diffusion through a tube wall, as well as the dissolution of a rod-shaped precipitate.

8.2.3 CALPHAD

CALPHAD [40] stands for *CALculation of PHAse Diagrams*. An equilibrium phase diagram is usually a diagram with axes for temperature and composition of a chemical system. It shows the regions where substances or solutions (ie, phases) are stable and regions where two or more of them coexist. Phase diagrams are a very powerful tool for predicting the state of a system under different conditions and were initially a graphical method to rationalize experimental information on states of equilibrium. The CALPHAD approach is based on the fact that a phase diagram is a manifestation of the equilibrium thermodynamic properties of the system, which are the sum of the properties of the individual phases. It is thus possible to calculate a phase diagram by first assessing the thermodynamic properties of all the phases in a system.

The design of industrial processes requires reliable thermodynamic data. CALPHAD (computer coupling of phase diagrams and thermochemistry) aims to promote computational thermodynamics through development of models to represent thermodynamic properties for various phases that permit prediction of properties of multicomponent systems from those of binary and ternary subsystems, critical assessment of data and their incorporation into self-consistent databases, development of software to optimize and derive thermodynamic parameters, and the development and use of databanks for calculations to improve understanding of various industrial and technological processes. This work is disseminated through the CALPHAD journal and its annual conference. Contributions of high quality in these and related fields, especially the fields of first-principles calculations, experimental

measurements of thermochemical and phase equilibrium data, phase transformations, and the process and materials designs that the CALPHAD works are based on or used for, are welcome.

8.2.4 JMatPro

JMatPro [41] is simulation software that calculates a wide range of materials properties for alloys and is particularly aimed at multicomponent alloys used in industrial practice. Using JMatPro you can make calculations for stable and metastable phase equilibrium, solidification behavior and properties, mechanical properties, thermo-physical and physical properties, phase transformations, and chemical properties.

Various material/alloy types currently available in JMatPro are Al, Mg, Fe (general steels, stainless steels, cast iron), Ti, Ni, Co, Zr, and solder alloys.

With JMatPro, stable and metastable phase equilibria calculations can be performed, such as temperature and concentration stepping and metastable phase calculations.

Solification calculation based on a modified Scheil-Gulliver model to include fast C and N diffusion in steels and solid-state transformations can be done, and thermo-physical and physical properties during solidification (enthalpy, specific heat, latent heat, density, thermal expansion, volume change, thermal conductivity, electrical conductivity and resistivity, liquid viscosity, liquid diffusivity, Poisson's ratio, and Young's/bulk/shear moduli) can be evaluated.

JMatPro is able to evaluate the mechanical properties, the thermo-physical and physical properties, and the phase transformations.

8.2.5 MATCALC

MatCalc is an *ongoing project* [42]: one that was initiated in 1993 with a PhD thesis addressing the simulation of precipitation kinetics in steel. Over many years, it has evolved into a software project for computer simulation of phase transformations in metallic systems. The topics covered by the MatCalc project include these:

- constrained and unconstrained phase equilibria
- precipitation kinetics
- long-range diffusion
- simultaneous diffusion and precipitation
- phase transformations/moving phase boundaries
- lattice Metropolis and kinetic Monte Carlo

The thermodynamic foundation of MatCalc is the CALPHAD method and (unencrypted) CALPHAD-type databases. The kinetic modules of MatCalc are developed within the framework of solid-state phase transformations, with particular focus on computational efficiency and applicability to multicomponent systems.

The kinetics of phase transformations are controlled by distinct physical mechanisms. We want to identify and understand the relevant processes, describe them rigorously in a mathematical framework, and cast them into efficient models and algorithms that can be solved on desktop computers.

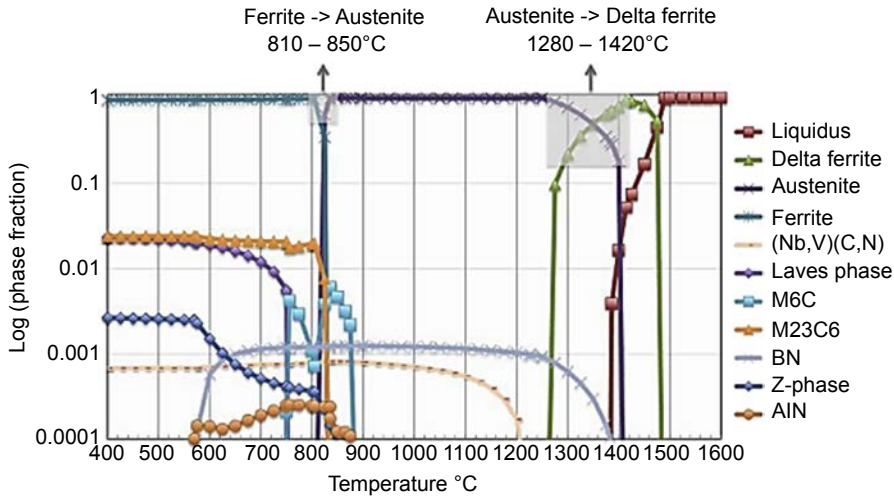


Figure 8.34 Thermodynamic equilibrium calculations of a MarBN steel using the software MatCalc [43].

MATCALC aims at avoiding unknown phenomenological coefficients and tries to substitute them with (parameter-free) physical models wherever possible. If no appropriate models are at hand, we try to develop them in our team.

MATCALC's aim is to develop sound theoretical concepts and transparent, efficient, and enjoyable scientific software for application in computational microstructure evolution.

The latest version of the software is always available in the download section of their Website. MatCalc can be used in a stand-alone GUI or command-line version. It is also available in the form of libraries that can be linked to general-purpose software, such as MatLAB, or your own code.

Fig. 8.34 shows an example of the MatCalc thermodynamic equilibrium calculation for MarBN steel.

Fig. 8.35 shows the simplified thermal history of P92 type steel [44] during heat treatment: cooling from austenitizing, tempering, and annealing at 600°C. The experimental data points represent the phase fractions of VN and Laves phase and the mean radii of VN, $M_{23}C_6$ and Laves phase according to Ref. [45]. For better visualization, the time scale is linear up to the beginning of annealing (~71 h) and then logarithmic. The *dotted lines* indicate the matrix phase transformation from austenite to ferrite and vice versa. The *green dashed line* in the annealing section is the sum of the VN phase fractions.

8.2.5.1 Austenitizing (1070–250°C)

When the temperature decreases, NbC and VN1 precipitates nucleate and grow rapidly. The precipitates deplete the matrix from V, N, and especially Nb, which slows down the growth of the large NbC and VN1.

8.2.5.2 Tempering (250–770°C: 2 h 250°C)

During tempering, the NbC and VN1 populations grow and the phase fraction increases. The newly introduced VN2 precipitates first grow but show a coarsening behavior overlapped by dissolution at the top temperature. The large VN1 precipitates are more stable and grow at the expense of the much smaller VN2 (Gibbs Thomson effect). The $M_{23}C_6$ precipitates coarsen, which can clearly be seen in Fig. 8.35(b)–(d). The phase fraction stays constant, while the mean radius rises, and the number density drops. As can be seen in Fig. 8.35(b), Laves phase does not reach important phase fractions; however, it reaches a number density of about $3 \times 10^{19}\,m^{-3}$, but the mean radii stay well below 10 nm. The agreement with the first set of data is good if the split of the VN precipitates in two waves is considered.

8.2.5.3 Annealing (250–600°C: 10^6 h)

During tempering, Laves phase precipitates nucleate and reach a mean radius of about 1 nm in the "as-tempered" condition. The Laves phase population grows, and the phase

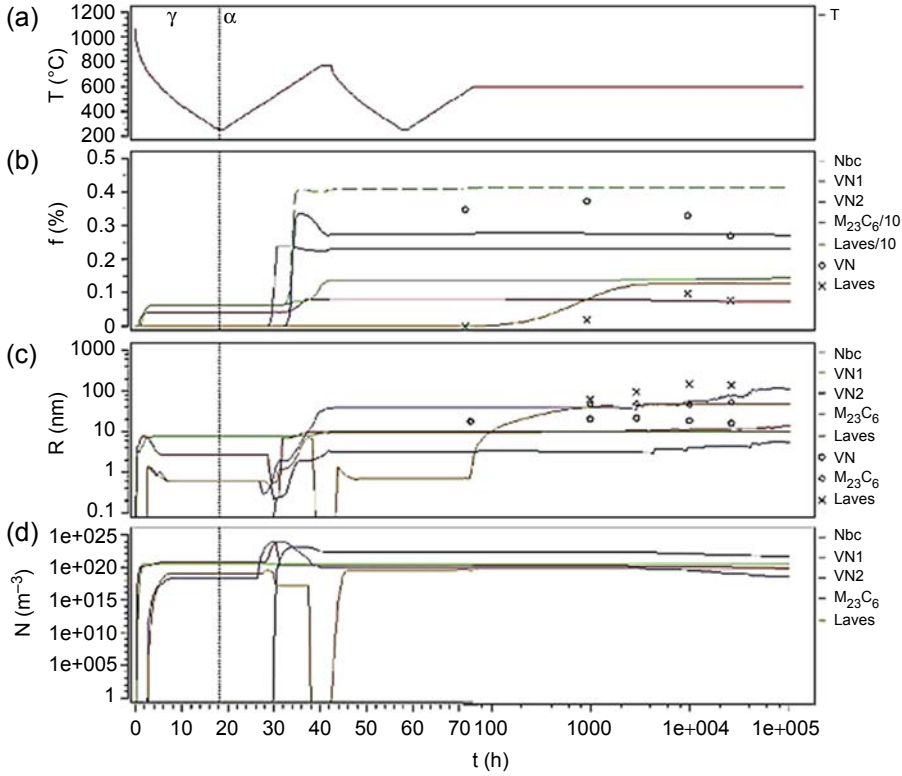


Figure 8.35 Simplified thermal history of P92 type steel [44].

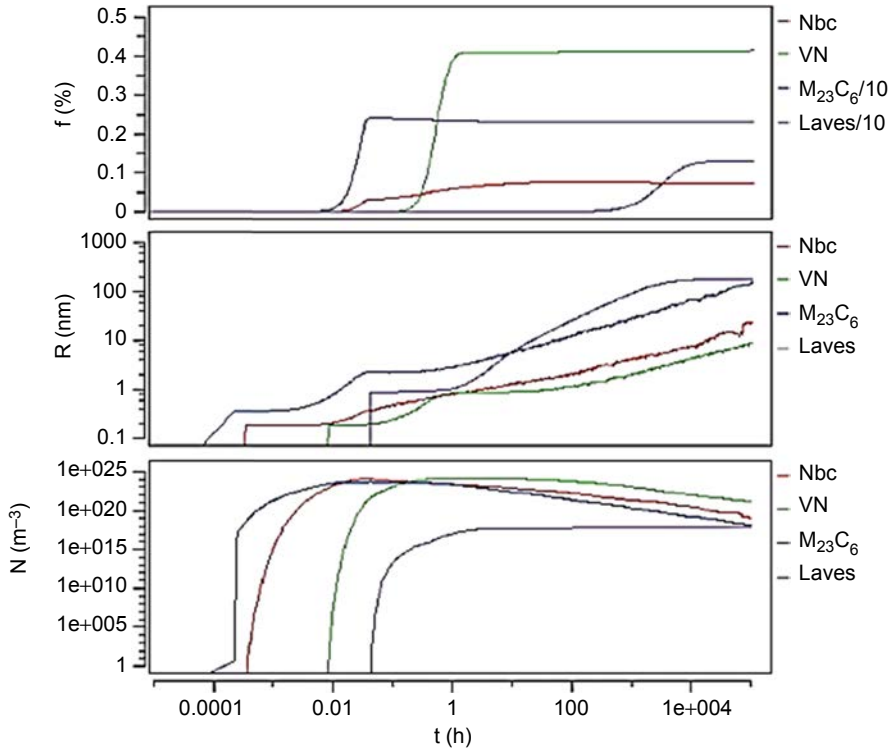


Figure 8.36 Simple isothermal annealing simulation at 600°C of P92 type steel [44].

fraction reaches a noticeable level at about 1000 h simulated annealing time (Fig. 8.36) with a simultaneous matrix depletion of Mo and W. The $M_{23}C_6$ and the VN2 precipitates start to coarsen at about the same time. The VN1 population slightly increases the phase fraction at the expense of the much smaller VN2 precipitates due to the capillarity effect (Gibbs Thomson effect). According to this simulation, no extensive coarsening of VN1 takes place. After about 20,000 h of annealing, the NbC precipitates also start to coarsen.

8.3 Nondestructive testing

Nondestructive testing (**NDT**) is a wide group of analysis techniques used in science and industry to evaluate the properties of a material, component, or system without causing damage. The terms **nondestructive examination** (**NDE**), **nondestructive inspection** (**NDI**), and **nondestructive evaluation** (**NDE**) are also commonly used to describe this technology. Because NDT does not permanently alter the article being inspected, it is a highly valuable technique that can save both money and time in product evaluation, troubleshooting, and research. Common NDT methods include ultrasonic, magnetic particle, liquid penetrant, radiographic, remote visual inspection, eddy-current testing, and low-coherence interferometry. NDT is commonly used in

forensic engineering, mechanical engineering, electrical engineering, civil engineering, systems engineering, aeronautical engineering, medicine, and art.

8.3.1 Dye penetrant

Dye penetrant inspection, also called **liquid penetrant inspection** (**LPI**) or **penetrant testing**, is a widely applied and low-cost inspection method used to locate surface-breaking defects in all nonporous materials (metals, plastics, or ceramics). The penetrant may be applied to all nonferrous materials and ferrous materials, although for ferrous components, magnetic particle inspection is often used instead for its subsurface detection capability. LPI is used to detect casting, forging, and welding surface defects such as hairline cracks, surface porosity, leaks in new products, and fatigue cracks on in-service components.

The operation is schematically shown in Fig. 8.37:

1–2 section of material with a surface-breaking crack that is not visible to the naked eye
3 penetrant is applied to the surface
4 excess penetrant is removed
5–6 developer is applied, rendering the crack visible

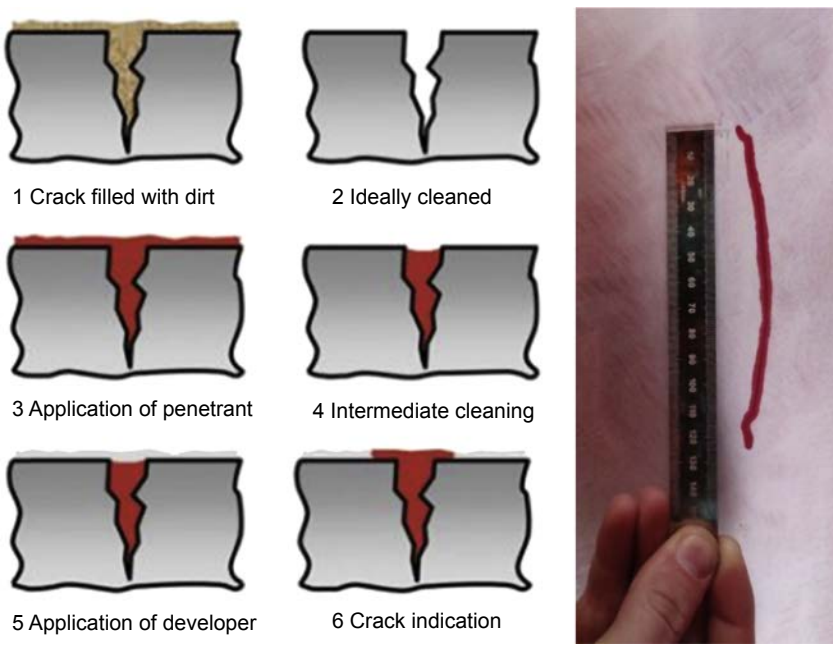


Figure 8.37 Dye penetrant [46].

8.3.2 Acoustic emission

Acoustic emission (AE) is the sound waves produced when a material undergoes stress (internal change) as a result of an external force. AE is a phenomenon occurring

in, for instance, *mechanical loading* generating sources of elastic waves. This occurrence is the result of a small surface displacement of a material produced due to stress waves generated when the energy in a material, or on its surface, is released rapidly. The wave generated by the source is of practical interest in methods used to stimulate and capture AE in a controlled fashion, for study and/or use in inspection, quality control, system feedback, process monitoring, and others (Fig. 8.38).

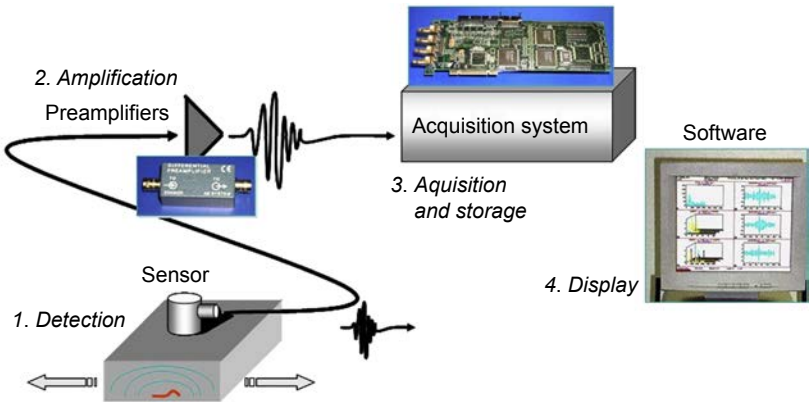


Figure 8.38 Acoustic emission [47].

8.3.3 Eddy-current testing

Eddy-current testing uses electromagnetic induction to detect flaws in conductive materials. There are several limitations: among them, only conductive materials can be tested, the surface of the material must be accessible, the finish of the material may cause bad readings, the depth of penetration into the material is limited by the materials' conductivity, and flaws that lie parallel to the probe may be undetectable.

In a standard eddy-current testing a circular coil carrying current is placed in proximity to the test specimen (which must be electrically conductive) (Fig. 8.39). The alternating current in the coil generates a changing magnetic field that interacts with a test specimen and generates an eddy current. Variations in the phase and magnitude of these eddy currents can be monitored using a second "receiver" coil, or by measuring changes to the current flowing in the primary "excitation" coil. Variations in the electrical conductivity or magnetic permeability of the test object, or the presence of any flaws, will cause a change in eddy current and a corresponding change in the phase and amplitude of the measured current. This is the basis of standard (flat coil) eddy-current inspection, the most widely used eddy-current technique.

However, eddy-current testing can detect very small cracks in or near the surface of the material, the surfaces need minimal preparation, and physically complex geometries can be investigated. It is also useful for making electrical conductivity and coating thickness measurements.

The testing devices are portable, provide immediate feedback, and do not need to contact the item in question. Recently tomographic notion of ECT has been explored.

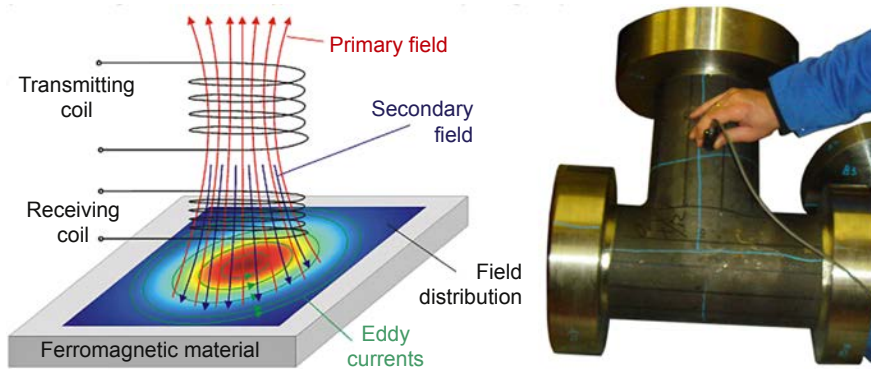


Figure 8.39 Eddy-current testing [48,49].

Another eddy-current testing technique is pulsed eddy-current testing. A major advantage of this type of testing is that there is no need for direct contact with the tested object. The measurement can be performed through coatings, weather sheetings, corrosion products, and insulation materials. This way, even high-temperature inspections are possible. Compared to the conventional eddy-current testing, pulsed eddy-current testing allows multifrequency operation.

8.3.4 Magnetic particle inspection

Magnetic particle inspection (**MPI**) is a NDT process for detecting surface and slightly subsurface discontinuities in ferromagnetic materials such as iron, nickel, cobalt, and some of their alloys. The process puts a magnetic field into the part. The piece can be magnetized by direct or indirect magnetization. Direct magnetization occurs when the electric current is passed through the test object and a magnetic field is formed in the material. Indirect magnetization occurs when no electric current is passed through the test object, but a magnetic field is applied from an outside source. The magnetic lines of force are perpendicular to the direction of the electric current, which may be either alternating current (AC) or some form of direct current (DC) (rectified AC) (Fig. 8.40).

A technician performs MPI on a pipeline to check for stress corrosion cracking using what is known as the "black and white" method. No indications of cracking appear in this picture; the only marks are the "footprints" of the magnetic yoke and drip marks.

A close-up of the surface of a (different) pipeline shows indications of stress corrosion cracking (two clusters of small black lines) revealed by **MPI**. Cracks that would normally have been invisible are detectable due to the magnetic particles clustering at the crack openings. The scale at the bottom is numbered in centimeters.

The presence of a surface or subsurface discontinuity in the material allows the magnetic flux to leak since air cannot support as much magnetic field per unit volume as metals. Ferrous iron particles are then applied to the part. The particles may be dry or in a wet suspension. If an area of flux leakage is present, the particles will be attracted to this area. The particles will build up at the area of leakage and form what

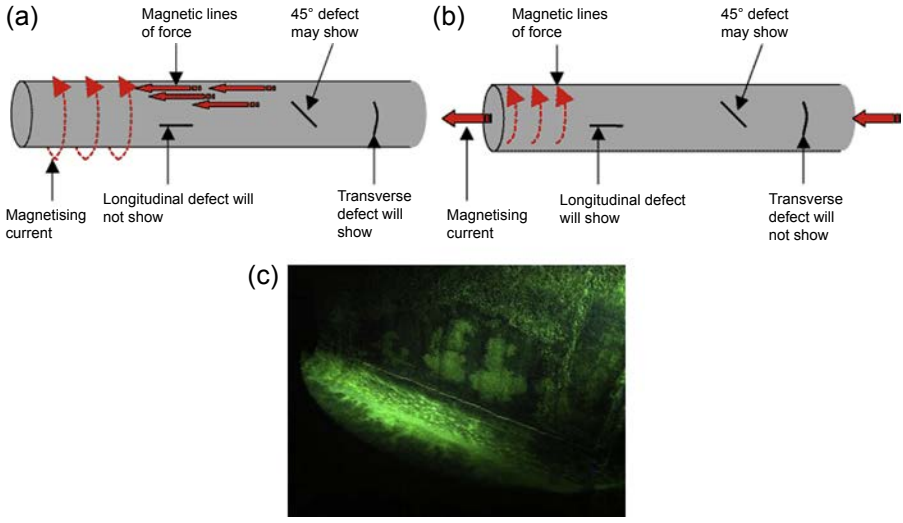


Figure 8.40 Magnaflux inspection [50,51].

is known as an indication. The indication can then be evaluated to determine what it is, what may have caused it, and what action should be taken, if any.

A popular name for MPI is or used to be *magnafluxing*.

8.3.5 Hardness

Hardness is a measure of how resistant solid matter is to various kinds of permanent shape change when a force is applied (Fig. 8.41). Macroscopic hardness is generally characterized by strong intermolecular bonds, but the behavior of solid materials under force is complex; therefore, there are different measurements of hardness: *scratch hardness*, *indentation hardness*, and *rebound hardness*. Hardness is dependent on ductility, elastic stiffness, plasticity, strain, strength, toughness, viscoelasticity, and

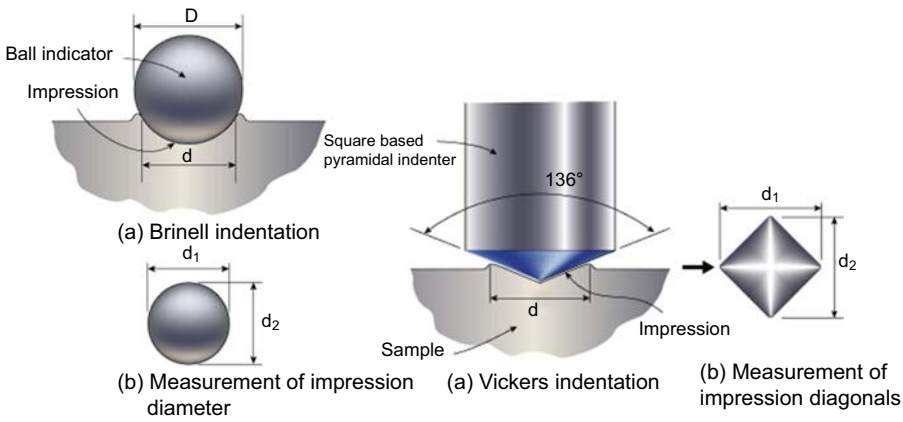


Figure 8.41 Brinnell and Vickers indentation principles [52].

viscosity. Common examples of **hard matter** are ceramics, concrete, certain metals, and super hard materials, which can be contrasted with soft matter.

8.3.6 Holographic interferometry

Holographic interferometry (HI) is a technique that enables static and dynamic displacements of objects with optically rough surfaces to be measured to optical interferometry precision (ie, to fractions of a wavelength of light). These measurements can be applied to stress, strain, and vibration analysis, as well as to nondestructive testing. It can also be used to detect optical path length variations in transparent media, which enables, eg, fluid flow to be visualized and analyzed. It can also be used to generate contours representing the form of the surface.

Holography enables the light field scattered from an object to be recorded and replayed. If this recorded field is superimposed on the "live field" scattered from the object, the two fields will be identical. If, however, a small deformation is applied to the object, the relative phases of the two light fields will alter, and it is possible to observe interference. This technique is known as live HI (Fig. 8.42).

It is also possible to obtain fringes by making two recordings of the light field scattered from the object on the same recording medium. The reconstructed light fields may then interferer to give fringes that map out the displacement of the surface. This is known as "frozen fringe" holography.

The form of the fringe pattern is related to the changes in surface position or air compaction.

Many methods of analyzing such patterns automatically have been developed in recent years.

Infrared and thermal testing is one of many nondestructive testing techniques designated by the American Society for Nondestructive Testing. Infrared thermography is the science of measuring and mapping surface temperatures.

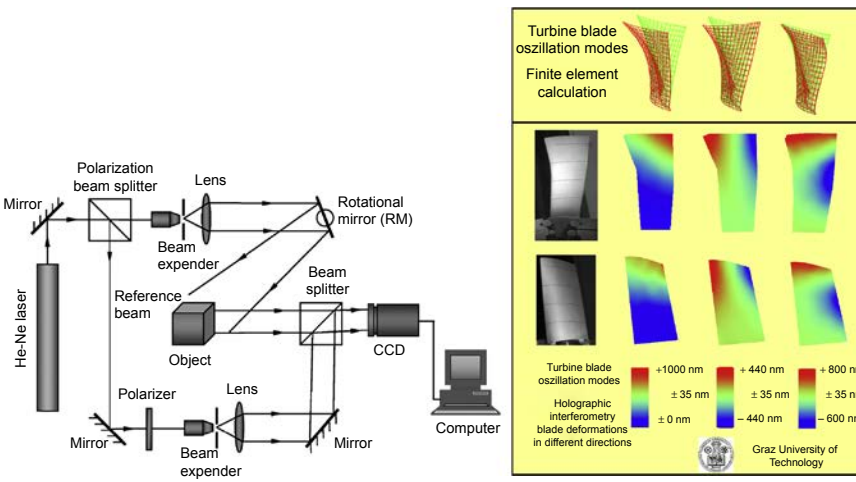


Figure 8.42 Holographic interferometry [52,53].

8.3.7 Infrared thermography

Infrared thermography, a nondestructive, remote sensing technique, has proved to be an effective, convenient, and economical method of testing concrete. It can detect internal voids, delamination, and cracks in concrete structures such as bridge decks, highway pavements, garage floors, parking lot pavements, and building walls. As a testing technique, some of its most important qualities are that it is accurate, repeatable, economical, and not an inconvenience to the public.

An infrared thermographic scanning system can measure and view temperature patterns based upon temperature differences as small as a few hundredths of a degree Celsius. Infrared thermographic testing may be performed during day or night, depending on environmental conditions and the desired results (Fig. 8.43).

All objects emit electromagnetic radiation of a wavelength dependent on the object's temperature. The frequency of the radiation is inversely proportional to the temperature. In infrared thermography, the radiation is detected and measured with infrared imagers (radiometers). The imagers contain an infrared detector that converts the emitting radiation into electrical signals that are displayed on a color or black and white computer display monitor.

A typical application for regularly available IR thermographic equipment is looking for "hot spots" in electrical equipment, which illustrates high-resistance areas in electrical circuits. These "hot spots" are usually measured in the range of 40–150°C (70–270°F) above ambient temperatures. But, when engineers use its patented proprietary systems to locate subsurface targets such as underground storage tanks, pipelines, pipeline leaks, and their plumes, and in this project, hidden tunnels, we are looking for temperature patterns typically in the range of 0.01–1°C above or below ambient temperatures.

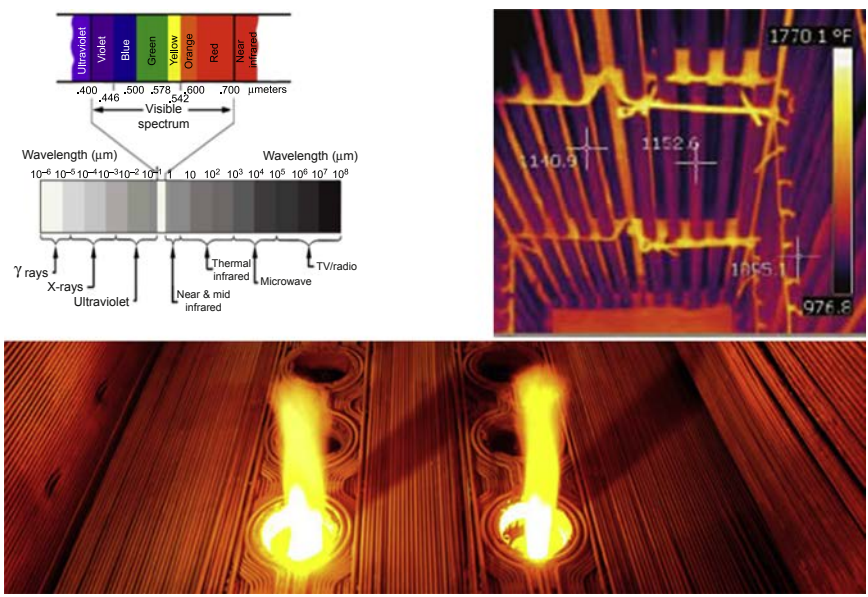


Figure 8.43 Infrared thermography principles and examples [54–56].

After the thermal data is processed, it can be displayed on a monitor in multiple shades of grayscale or color. The colors displayed on the thermogram are arbitrarily set by the thermographer to best illustrate the infrared data being analyzed.

In this roofing investigation application, infrared thermographic data was collected during daytime hours, on both sunny and rainy days. This data collection time allowed for solar heating of the roof and any entrapped water within the roofing system during the daylight hours. IR data was observed until the roof had sufficiently warmed to allow detection of the entrapped wet areas because of their ability to collect and store more heat than the dry insulated areas. The wet areas would also transfer the heat at a faster rate than the dry insulated roof areas. At this point in time, the wet areas showed up as warmer roof surface temperatures than the surrounding dry background areas of the roof. During the rainy day, with minimum solar loading, any entrapped leak plumes would become evident because of their cooler temperature as compared to the dry roof areas.

An infrared thermographic scanning system measures surface temperatures only. But the surface temperatures that are measured on the surface of the ground, above a buried pipeline, are, to a great extent, dependent upon the subsurface conditions.

The subsurface configuration effects are based upon the theory that energy cannot be stopped from flowing from warmer to cooler areas; it can only be slowed down by the insulating effects of the material through which it is flowing. Various types of construction materials have different insulating abilities. In addition, differing types of pipeline defects have different insulating values.

8.3.8 Radiographic testing

Radiographic Testing (RT), or **industrial radiography**, is an NDT method of inspecting materials for hidden flaws by using the ability of short-wavelength electromagnetic radiation (high-energy photons) to penetrate various materials (Fig. 8.44).

Either an X-ray machine or a radioactive source (Ir-192, Co-60, or in rarer cases Cs-137) can be used as a source of photons. Neutron radiographic testing is a variant of radiographic testing that uses neutrons instead of photons to penetrate materials. This can see very different things from X-rays because neutrons can pass with ease through lead and steel but are stopped by plastics, water, and oils.

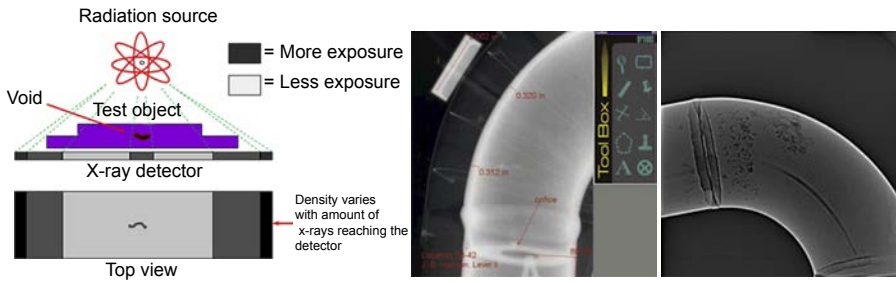


Figure 8.44 Radiography principles and examples of defects [57–59].

Since the amount of radiation emerging from the opposite side of the material can be detected and measured, variations in this amount (or intensity) of radiation are used to determine thickness or composition of material. Penetrating radiations are those restricted to that part of the electromagnetic spectrum of wavelength less than about 10 nm.

8.3.9 Ultrasonic testing

In **ultrasonic testing** (**UT**), very short ultrasonic pulse-waves with center frequencies ranging from 0.1 to 15 MHz and occasionally up to 50 MHz are launched into materials to detect internal flaws or to characterize materials. A common example is ultrasonic thickness measurement, which tests the thickness of the test object, eg, to monitor pipework corrosion.

UT is often performed on steel and other metals and alloys, though it can also be used on concrete, wood and composites, albeit with less resolution. It is a form of nondestructive testing used in many industries including aerospace, automotive, and other transportation sectors.

Fig. 8.45 shows the principle of UT. On the left, a probe sends a sound wave into a test material. There are two indications, one from the initial pulse of the probe, and the second due to the back wall echo. On the right, a defect creates a third indication and simultaneously reduces the amplitude of the back wall indication. The depth of the defect is determined by the ratio D/E_p.

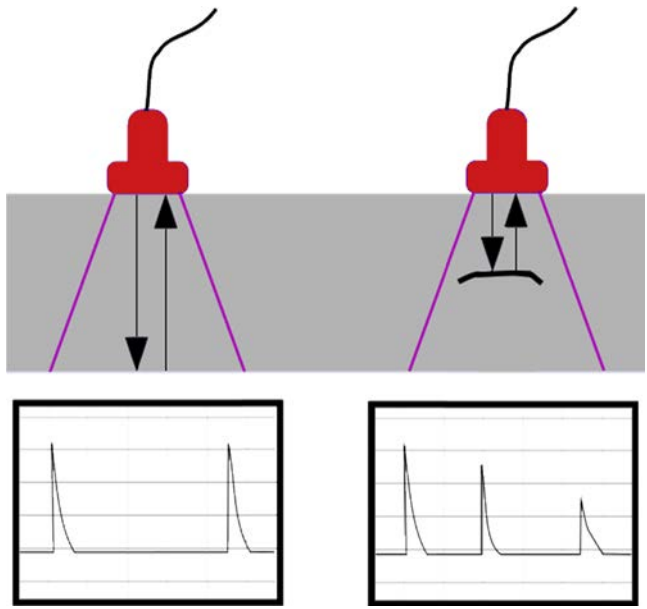


Figure 8.45 Ultrasonic test principles [60].



Figure 8.46 Saarschmiede shaft inspection facility (2007) and six-unit probe holder [61].

Fig. 8.46 shows the equipment for the control of a shaft.

8.3.10 Ultrasonic phased array systems

Ultrasonic phased array systems can potentially be employed in almost any test where conventional ultrasonic flaw detectors have traditionally been used. Weld inspection and crack detection are the most important applications, and these tests are done across a wide range of industries including aerospace, power generation, petrochemical,

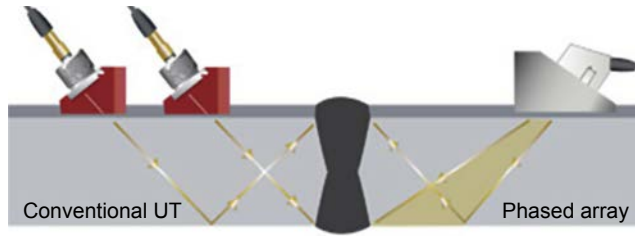


Figure 8.47 Comparison of conventional UT and phased array UT principles [62].

metal billet and tubular goods suppliers, pipeline construction and maintenance, structural metals, and general manufacturing. Phased arrays can also be effectively used to profile remaining wall thickness in corrosion survey applications (Fig. 8.47).

The benefits of phased array technology over conventional UT come from its ability to use multiple elements to steer, focus, and scan beams with a single transducer assembly. Beam steering, commonly referred to sectorial scanning, can be used for mapping components at appropriate angles. This can greatly simplify the inspection of components with complex geometry. The small footprint of the transducer and the ability to sweep the beam without moving the probe also aids inspection of such components in situations where there is limited access for mechanical scanning. Sectorial scanning is also typically used for weld inspection. The ability to test welds with multiple angles from a single probe greatly increases the probability of detection of anomalies. Electronic focusing permits optimizing the beam shape and size at the expected defect location, as well as further optimizing probability of detection. The

ability to focus at multiple depths also improves the ability for sizing critical defects for volumetric inspections. Focusing can significantly improve signal-to-noise ratio in challenging applications, and electronic scanning across many groups of elements allows for C-Scan images to be produced very rapidly.

The potential disadvantages of phased array systems are a somewhat higher cost and a requirement for operator training; however, these costs are frequently offset by their greater flexibility and a reduction in the time required to perform a given inspection.

8.3.11 Linear accelerator

Linear accelerator (LINAC) is a technic used to investigate forged or cast components with very high thickness (Fig. 8.48).

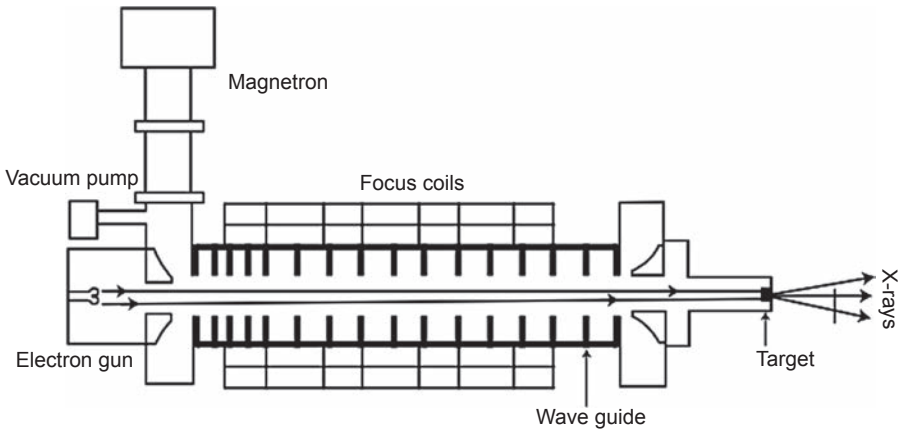


Figure 8.48 Principles of linear electron accelerator (LINAC) [63].

The energy levels mostly used for LINACs are 4 and 8 MeV. LINACs can be constructed for one or two energy levels. In the traveling wave LINAC, the acceleration of electrons from a heated filament to very high energies results from the electrons "riding" a high-frequency (3–10 MHz) electromagnetic wave traveling in a straight line down an acceleration tube (the hollow guide) [63].

The electrons are bunched into pulses at a frequency of a few hundred pulses per second.

The target, which the electrons strike to generate X-radiation, is at the opposite end of the main wave guide of the filament assembly. This is a transmission type target from which the radiation beam passes in a straight line.

The X-ray output from a LINAC is many times higher than from a Bètatron of the same energy. An 8 MeV LINAC with a 2-mm-diameter focal spot can deliver a radiation dose rate of 30 Sv/minute at 1 m distance from the focus. Small, lightweight, portable LINACs of 3 MeV capacity can have outputs of 1.5 Sv/minute at 1 m distance.

The main properties of a LINAC are these:

1. very high output of radiation
2. very small focal spot dimensions (<2 mm)
3. considerable weight (approximately 1200 kg for an 8 MeV stationary installation)

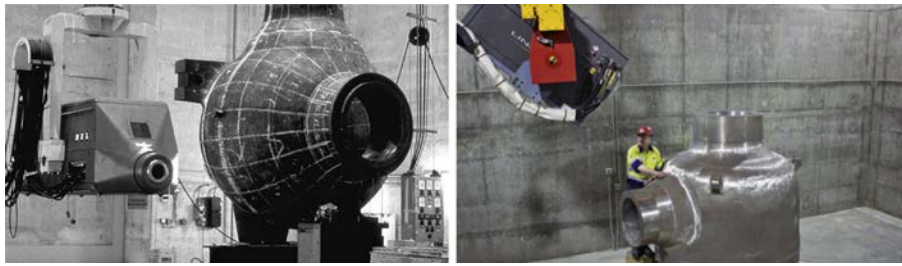


Figure 8.49 LINAC and pump house in a radiation bunker [63,64].

Fig. 8.49 shows an 8 MeV LINAC in a radiation bunker examining a pump housing.

References

[1] http://www.metallographic.com/Lab%20Equip/Equipment.htm.
[2] http://www.microscopyu.com/articles/phasecontrast/phasemicroscopy.html.
[3] T. Shrestha, S. Alsagabi, I. Charit, G. Potirniche, M. Glazoff, Effect of heat treatment on microstructure and hardness of Grade 91 steel, Metals 5 (2015) 131–149, http://dx.doi.org/10.3390/met5010131.
[4] R. Krishna, S.V. Hainsworth, S.P.A. Gill, A. Strang, H.V. Atkinson, Microstructural Evolution in Creep Exposed IN617, 2009. https://lra.le.ac.uk/bitstream/2381/4741/3/DTIprojectECCCpaperassubmittedDec2008.pdf.
[5] https://www.purdue.edu/ehps/rem/rs/sem.htm.
[6] https://nanofabrication.unt.edu/jeol-jsm-7001f-scanning-electron-microscope.
[7] https://www.researchgate.net/figure/277726873_fig5_SEM-micrographs-for-the-as-received-T91-T91-AR-in-a-high-and-b-higher-magnification.
[8] http://preserve.lehigh.edu/cgi/viewcontent.cgi?article=2247&context=etd.
[9] http://www.jeolusa.com/DesktopModules/Bring2mind/DMX/Download.aspx?Command=Core_Download&EntryId=610&language=en-US&PortalId=2&TabId=320.
[10] C. Panait, W. Bendick, A. Fuchsmann, A.F. Gourgues-Lorenzon, J. Besson, Study of the Microstructure of the Grade 91 Steel After More Than 100.000 h of Creep Exposure at 600°C, 2010. https://hal-mines-paristech.archives-ouvertes.fr/hal-00509625/document.
[11] https://www.ifw-dresden.de/de/institute/institut-fuer-komplexe-materialien/abteilungen/mikro-und-nanostrukturen/available-methods/ebsd/.
[12] https://www.deakin.edu.au/research/facilities/electron-microscopy-facility/what-we-do/introduction-to-electron-microscopy.
[13] P. Mayr, Evolution of Microstructure and Mechanical Properties of the Heat Affected Zone in B-containing 9% Chromium Steels (Ph.D. thesis), Institute for Materials Science, Welding and Forming: Graz University of Technology, Austria Graz, July 2007.
[14] L. Li, P. Zhu, G. West, R.C. Thomson, The effect of duration of stress relief heat treatments on microstructural, in: 6th International Conference on Advances in Materials Technology for Fossil Power Plants, Santa Fe, NM, USA, August 31st–September 3rd, 2010.
[15] G. West, R.C. Thomson, Evolution and mechanical properties in Grade 91 and 92 power plant steels, in: A. Strang, W.M. Banks, G.M. McColvin, J.E. Oakey, R.W. Vanstone (Eds.), Proceedings of Parsons 2007-Power Generation in an Era of Climate Change, IOM Communications Ltd, Glasgow, UK, September 2007, p. 521.

[16] http://www.jeol.co.jp/en/products/detail/JEM-3200FS.html.
[17] L. Cipolla, S. Caminada, D. Venditti, H.K. Danielsen, A. Di Gianfrancesco, Microstructural evolution of ASTM P91 after 100,000 hours exposure at 550°C and 600°C, in: 9th Liege Conference on Materials for Advanced Power Engineering, 27th–29th September 2010, Liege, Belgium.
[18] A. Di Gianfrancesco, L. Cipolla, M. Paura, S. Tiberi Vipraio, D. Venditti, S. Neri, M. Calderini, The rule of boron in long term stability of a CrMoCoB (FB2) steel for rotor application, in: 6th International Conference on Advances in Materials Technology for Fossil Power Plants, Santa Fe, NM, USA, August 31st–September 3rd, 2010.
[19] H. Matysiak, et al., Microstructure of Haynes 282 superalloy after vacuum induction melting and investment casting of thin-walled components, Materials 6 (2013) 5016–5037, http://dx.doi.org/10.3390/ma6115016.
[20] http://study.com/academy/lesson/what-is-an-electron-microscope-definition-types-uses.html.
[21] http://www.aimspress.com/article/10.3934/biophy.2015.3.259/pdf.
[22] https://www.lem.kit.edu/english/217.php.
[23] http://www-hrem.msm.cam.ac.uk/research/EFTEM/EFTEM.html.
[24] K. Sawada, H. Kushima, K. Kimura, Microstructural changes of T91 steel during creep under low stress, in: Seminar on 9–12%Cr Heat Resistant Steels 24th September 2010, MINES, ParisTech.
[25] K. Sawada, H. Kushima, M. Tabuchi, K. Kimura, Microstructural degradation of Gr.91 steel during creep under low stress, Materials Science and Engineering A 528 (2011) 5511–5518.
[26] A. Golpayegani, F. Liu, H. Svensson, M. Andersson, H.O. Andren, Microstructure of a creep-resistant 10 Pct chromium steel containing 250 ppm Boron, Metallurgical and Materials Transactions A 42A (April 2011).
[27] L. Lundin, M. Hattestrand, H.-O. Andren, Parsons, Advanced Materials for 21st Century Turbines and Power Plants, The Institute of Materials, London, UK, 2000, pp. 603–617.
[28] O. Dmitrieva, D. Ponge, G. Inden, J. Millán, P. Choi, J. Sietsma, D. Raabe, Chemical gradients across phase boundaries between martensite and austenite in steel studied by atom probe tomography and simulation, Acta Materialia (2011). http://arxiv.org/ftp/arxiv/papers/1402/1402.0232.pdf.
[29] H.-O. Andrén, A. Henjered, L. Karlsson, Stainless Steels 84, The Institute of Metals, Gothenburg, Sweden, 1984, pp. 91–96.
[30] https://rockymountainlaboratory.wordpress.com/.
[31] http://www.glow-discharge.com/.
[32] http://www.nsst.nssmc.com/research_support/bun_gd-oes.html.
[33] http://www.cameca.com/instruments-for-research/sims.aspx.
[34] https://www.phi.com/surface-analysis-techniques/xps-esca.html.
[35] http://cnx.org/contents/uieDnVBC@20.18:UX-PN_YZ@2/Wide-Angle-X-ray-Diffraction-S.
[36] L. Cipolla, Conversion of MX Nitrides in to Modified Z-phase in 9–12%Cr Ferritic Steels (Ph.D. thesis) DCAMM Special Report No. 8116, March 2010.
[37] http://www.thermocalc.com/products-services/software/thermo-calc/.
[38] C. Crozet, A. Devaux, D. Béchet, Microstructure stability: optimisation of 263 Ni-based superalloy: Euro-superalloys, in: 2nd EU Symposium on Superalloys and Their Applications, 12–16 May, 2014, Giens, France, 2014.
[39] http://www.thermocalc.com/products-services/software/dictra/.
[40] http://www.calphad.org/.

[41] http://www.sentesoftware.co.uk/jmatpro.aspx.
[42] http://matcalc.tuwien.ac.at/index.php/about-matcalc/screenshots.
[43] C. Sommitsch, R. Vanstone, T.U. Kern, P. Barnard, P. Mayr, R. Thomson, A. Agüero, CO-ordination of European research in structural materials for power generation equipment, in: J. Lecomte-Beckers, O. Dedry, J. Oakey, B. Kuhn (Eds.), 10th Liege Conference : Materials for Advanced Power Engineering, 2014.
[44] H.J. Rajek, Computer Simulation of Precipitation Kinetics in Solid Metals and Application to the Complex Power Plant Steel CB8 (Ph.D. thesis), Graz University of Technology, Austria, November 2005.
[45] X. Li, N. Saunders, A.P. Miodownik, The coarsening kinetics of γ' particles in nickel-based alloys, Metallurgical and Materials Transactions A 33A (2002) 3367–3373.
[46] http://www.ventureinspection.co.uk/services/dye-penetrant-inspection/.
[47] http://www.epandt.com/us/produits_ea_us.html.
[48] http://www.ndt.net/article/ndtce03/papers/p040/p040.htm.
[49] http://www.ndt-consultants.co.uk/Newwebsite/images/Training/EddyCurrent_Inspection2.jpg.
[50] http://www.twi-global.com/technical-knowledge/faqs/ndt/faq-in-magnetic-particle-inspection-how-do-we-ensure-that-defects-of-all-orientations-are-detected/.
[51] http://steelcityndt.com/magnetic-particle-inspection-mpi/.
[52] http://opticalengineering.spiedigitallibrary.org/article.aspx?articleid=1088594.
[53] http://ttm.tugraz.at/img/research/metrology/gt.gif.
[54] http://web.utk.edu/~jbeard8/IT570/Introduction%20to%20Infrared%20Thermography.pdf.
[55] http://www.flir.com/ogi/display/?id=49564.
[56] http://www.rwe.com/web/cms/en/216628/rwe-technology-international/infrared-thermography/.
[57] http://www.iprt.iastate.edu/assistance/nde/tools/radiographic.
[58] http://www.ndt-training.org/cat_rtcourse.htm.
[59] http://www.ndtservice.net/services/advanced-inspection-services/digital-radiography/.
[60] http://www.wermac.org/others/ndt_ut.html.
[61] A. Zimmer, J. Vrana, J. Meiser, W. Maximini, N. Blaes, Evolution of the ultrasonic inspection o f heavy rotor forgings over the last decades CP1211, Review of Quantitative NDT Evaluation 29 (2010) (American Inst. of Physics).
[62] http://www.olympus-ims.com/en/ndt-tutorials/intro/equipment/.
[63] GE Inspection Technologies, http://www.ge-mcs.com/download/x-ray/GEIT-30158EN_industrial-radiography-image-forming-techniques.pdf.
[64] http://foundrymag.com/print/testingqc/meeting-rising-demand-ndt.

This page intentionally left blank

Welding technologies for ultra-supercritical power plant materials

9

S. Sorrentino
Welding Consumables Research & Development, Air Liquide Welding, Italy

9.1 Introduction: welded fabrication of USC components

Fusion arc welding is the main fabrication technology for components used in ultra-supercritical (USC) power plants. All the most common welding methods are routinely employed in boiler construction, pipework and during manufacturing of cast and forged components, the specific choice depending on the stage of the fabrication, welding position, weld detail type, member diameter and groove thickness. Basically, welding of USC steels (either low-Cr alloyed, high-Cr martensitic or austenitic grades) can be accomplished with the Gas Tungsten Arc-GTA (TIG), Submerged Arc-SA, Shielded Metal Arc-SMA (MMA), Gas Metal Arc-GMA (MIG) and Flux Cored Arc-FCA methods, with other non-arc processes (like Laser Beam and Electron Beam) of very limited industrial usage or even still to emerge from the industrial R&D stage (Friction Stir Welding). Typical productivity figures (ie, weld deposition rate), weldability, robustness, efficiency for in-field plant erection, Weld Metal (WM) aimed chemistry, WM characteristic mechanical properties may preclude or limit the use of high heat input methods or slag-forming processes thus guiding the process selection. A typical large design will use tens of thousands of welds between similar and dissimilar materials. Appropriate welding processes, filler material and heat treatment are crucial for cost-effective manufacturing and safe service over the lifespan of the equipment.

9.1.1 USC plants components, typical metallic materials and associated welding details; in-shop fabrication, plant erection, and repair

High-efficiency fossil coal power plants today are able to operate continuously at high pressure and efficiency (ultimate USC conditions are today around 625°C, 290 bar for the main steam and 580°C, 150 bar for the reheated steam). A typical USC fossil power plant includes a boiler where the water is heated and turned into superheated steam, then delivered to the steam turbine driving the alternate current generator [1].

The pulverized coal is burned in the furnace manufactured with a wall of welded finned tubes known as membrane or water walls. The flames and combustions fumes flow inside and evaporate the water, while the superheater provides the additional heat

Materials for Ultra-Supercritical and Advanced Ultra-Supercritical Power Plants.
http://dx.doi.org/10.1016/B978-0-08-100552-1.00009-9
Copyright © 2017 Elsevier Ltd. All rights reserved.

before delivering to the turbine by the main steam pipes. The steam expanded after the high-pressure section is brought again in the boiler and reheated, then delivered again to the low-pressure section of the steam turbine. The boiler system is a huge welded construction composed of tubes (exposed to the combustion fumes on the external side and water or steam on the inner side) and heavy-walled pipes (headers, manifolds or steam pipes) not exposed on the external side. The dimension of the system is usually very large; this calls for prefabrication of the various subsystems in shop and assembly of the components on site. Difficulties associated with the external fabrication are therefore completely different.

Different areas of the plant experience pressure/load, temperature and corrosion requirements markedly different. Thus, steel grades used for the different sections are properties-tailored for saving cost and technological difficulties (ie, weldability) where service conditions are less demanding. Schematically, a modern generation USC coal power plant makes use of the following steel material classes (in the following, reference is mostly given to relevant ASTM and equivalent ISO/EN product standards) for the different boiler and turbine components (some differences may be due to the industrial tradition of the plant site or for very latest designs; additional minor variations or even more articulate materials placement may be considered by different designers, see also Chapter 18):

- Boiler sections with lowest service conditions: carbon steel, T1 steel (0.5% Mo)
- Boiler lower water wall: T11, T12, T22 low-alloyed bainitic steels (service up to 550°C)
- Boiler upper water wall: T22, T23, T24 low-alloyed bainitic steels (up to 550°C)
- Boiler superheater (SH) outlet header, manifold: P91, P92, E911 high-Cr martensitic steels up to 620°C
- Main steam pipework: P91, P92, E911 high-Cr martensitic steels up to 620°C
- Boiler reheater (RH) outlet header: P91, P92, E911 high-Cr martensitic steels up to 620°C
- RH pipework: P91, P92, E911 high-Cr martensitic steels up to 620°C
- Boiler SH tube assemblies, finish RH: TP304H, TP347H austenitic stainless steels (up to 640°C; ultimate variants TP304HCu* and TP347HFG* are lately used)
- Boiler primary RH tubes, finish RH: TP304H, TP347H austenitic stainless steels (up to 640°C; ultimate variants TP304HCu* and TP347HFG* are lately used)

*Such specific grades are described in Chapter 18.

Materials for valves and turbine casings are most often the cast equivalent or variants of Gr. 11, Gr. 22, Gr. 23, Gr. 91 and Gr. 92 Cr bainitic/martensitic steels:

- G20Mo5, G20Mn5 (½Mo) for parts with service temperature below 500°C
- G17CrMo5-5 (1¼Cr ½Mo) for inner casing, valves, nozzles used up to 530°C
- G17CrMo9-10 or G17CrMoV5-10 (2¼Cr 1Mo-type) for inner casing, valves, and ancillary articles used up to 550 and 560°C, respectively
- ASTM A217M-C12A or G-X12CrMoVNbN 9-1 (9Cr1MoVNb) for valves, flanges, nozzles, inlet piping used up to 600°C
- G-X12CrMoWVNbN 10-1-1 (9Cr1MoWVNbN) for valves, bonnets, piping used up to 625°C
- G-X13CrMoCoVNbNB 9-2-1 (CB2)* for valve casings used up to 625°C

*Such specific grades are described in Chapter 18.

Arc welding is advantageously used to join sub-castings where integral manufacturing is technologically difficult, more costly or impractical and for repairing defective areas after imperfections excavation.

Similarly, mechanized welding is used to join different forged sections of the steam turbine rotor, intended to withstand the various load levels in the low, intermediate and high-pressure stages, respectively. USC steels in this application are ferritic/martensitic grades of the (Ni)CrMoV-type with different alloying contents depending on the temperature experienced in the various sections; grades with 1.5, 2.25, 3.5 and 9–10% Cr (FB2 and X12CrMoWVNbN 10-1-1) respectively, are of most common usage.

It is recognizable that dissimilar metal welding (DMW) between different steel grades is a major task of the welded manufacturing in all areas described.

9.1.2 Welded pipework, manifold and headers fabrication

Bainitic and martensitic steels (also known as creep strength–enhanced ferritic steels, CSEFs) are today the unique choice in USC power plants for this heavy-walled component due to the characteristic lower thermal expansion and higher thermal conductivity. P91, P92, and E911 steel grades are today extensively used for temperatures up to 625°C in most advanced designs with adequate weldability and toughness in the weld area (weld metal, WM and heat affected zone, HAZ). Use of 12% Cr grade (P122), also known as HCM12A, 12Cr-1.5W-Mo-V-Nb-N on thick-walled semifinished products has been discontinued in recent years due to the severe and unexpected creep degradation occurring well before the expected service life (thus, welding of this grade here is not dealt with).

Boiler headers (as depicted in Fig. 9.1) are manufactured by heavy-walled seamless pipes. Welding is extensively used for joining the tubes stubs (using a combination of GTA + manual metal arc (MMA) methods on T-butt joints) and the headers subsections (by SA or NG-GTA girth butt welding). In-shop manufacturing is done whenever possible with the ability of rotating the pipe, thus taking advantage of high-productivity methods like SAW. Post-weld heat treatment (PWHT) can be done in a furnace for optimal control. Latest designs for very large boilers (ie, up to 1 GW electrical power)



Figure 9.1 Headers with their tubing and associated tube stubs prefabbricated in-shop (Vallourec) [2].

can have pipe wall thickness (WT) up to 80–90 mm and outer diameter (OD) up to 400–450 mm (P92 steel) if direct entry stub type is used, even thicker otherwise.

Main steam pipes can be either seamless or longitudinally welded. Joining of the pipe sections has to be done on-site during the plant erection with fixed pipes and positional welding (ie, in the ASME 5G/6G position) with manual processes (mostly GTA for the root pass and MMA for filling and capping). Post-weld heat treatment is given to the joints only locally on the welded area with heated bands. Typical dimension can be 15–25 mm for the WT and 600–700 mm for the OD if the welded pipe is given full normalizing and tempering (N+T) heat treatment after seam welding (in such instance ASME Boiler and Pressure Vessel Code or equivalents may grant a nominal weld strength factor (WSF) = 1).

9.1.3 Fabrication of welded tube assemblies

Tubing is less subjected to thermal fatigue due to the thin walls, so austenitic steel can be used also taking advantage of the intrinsic higher resistance to the fireside corrosion or the steam side oxidation. Welding is used for both joints between homologous and dissimilar grades (ie, for joining with CSEF steel sections).

Traditionally, TP304H and TP347H austenitic stainless steels have been used for this purpose, or even very recently introduced (2014) advanced 12% Cr steels (VM12-SHC) for lower temperature SH and RH sections. Tube bundles are joined in shop as much as possible, and subsystems are then joined together on site. Joint details include butt welds done at either shop or during boiler erection using the GTA (alone or for the root pass) and MMA methods in combination.

9.1.4 Fabrication of membrane walls

Membranes or water walls are very large structures composed of finned tubes joined together to enhance the heat exchange surface (as depicted in Figs. 9.2 and 9.3). Mechanical properties, creep strength requirements in particular, vary between the various sections subjected to different temperatures. In the lower side, usually low-alloyed grades (T/P11, T/P12 and T/P22) are successfully employed. In the upper section, service conditions demand more performant materials. Today, most advanced



Figure 9.2 Water wall panels during welded manufacturing in workshop. Thousands of thin welds are required to join tubes to fins and between tube ends (Vallourec) [2].

designs employ enhanced bainitic low-alloyed steels like T/P23 and T/P24 and even high Cr martensitic T91 tubing for the uppermost sections. Shop fabrication is extensively used, PWHT exhent is limited to critical sections more restrained or solicited. Due to the large areas to be welded, the SA method is extensively used to join the fins to the tubes with fillet welds. Girth butt welding of tubes ends is accomplished by the manual GTA (alone or for the root pass) and MMA methods in combination.



Figure 9.3 High-productivity tube-to-fin panel mechanized multi-welding (Pemamek) and membrane wall subassemblies ready for erection on-site (Seamlimited) [3,4].

9.1.5 Fabrication of welded rotors for steam turbines

Rotors are bulky components subjected to severe thermomechanical load, demanding high metallurgical cleanliness and integrity of the forgings, with local temperature depending on the specific section (HP, IP, LP). Fabricated rotors are made joining the different forged sections either involving similar or DMW in the circumferential joints. Mechanized Narrow Gap-SA or Narrow Gap-GTA methods are mostly used to reduce the volume of the WM needed (Fig. 9.4). Fig. 9.5 shows the welding of IP/LP turbine rotor.

(a)

	Integral forged rotor	Welded rotor	Features of welded rotor
High-, intermediate- to low-pressure rotor	Material: 2-1/4 CrMoV steel	Welded joint Materials High-temp. zone: 12 Cr steel Low-temp. zone: 3.5 NiCrMoVsteel	Use of 12 Cr steel in high-temperature zone and 3.5 NiCrMoV for zone requiring high toughness results in improved high-temperature performance, large capacity and reduced delivery time. Large bore structure allows quick start operation.
High- to intermediate-pressure rotor	Overlay welding Material: 12 Cr steel	Materials High-temp. zone: 12 Cr steel Low-temp. zone: 2-1/4 CrMoV steel	Use of 12 Cr steel only in high-temperature zones results in improved high-temperature performance, increased capacity and reduced delivery time.
Large- size, low-pressure rotor	Material: 3.5 NiCrMoV steel	Material: 3.5 NiCrMoV steel	Use of small-size parts results in reduced delivery time.

(b)

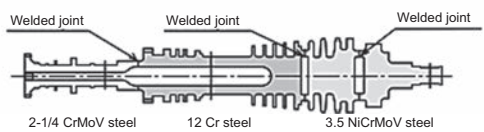


Figure 9.4 (a) Manufacturing of welded fabricated rotors vs. integral rotors [5]. (b) Typical layout of a welded rotor with LP, IP and HP sections.

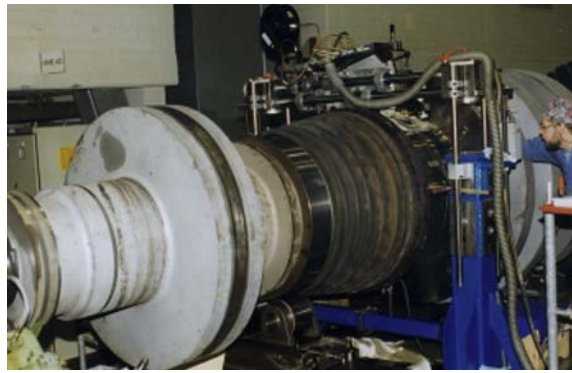


Figure 9.5 IP/LP turbine rotor during welding [6].



Figure 9.6 Post-weld heat treatment of welded rotor with local enclosure [6].

To avoid permanent plastic deformation due to the steel softening at the PWHT temperature and to guarantee constant temperature distribution, the welded rotor assembly is slowly rotated during the entire heat treatment process, as depicted in Fig. 9.6.

9.1.6 Fabrication of casings, valves and other cast components

USC casings are large envelopes subjected to the same pressure and temperature requirements of the boiler section, thus manufactured by casting low-Cr bainitic or high-Cr martensitic steels. It is often convenient to fabricate separately modular subcomponents to limit the mold size and cost, so welding is used to join these subsystems. Welding repair of castings is also used extensively after excavating defects from the surface and inspecting the area with penetrant testing prior the final welding. SMAW (Fig. 9.7) is almost exclusively used. The PWHT is ideally made after any welding operation, including weld repair, has been performed.

9.2 Welding metallurgy of USC materials

Three broad classes of steel are lately used in USC plants to resist the different degree of creep and corrosion/oxidation damage, with the nominal alloying content growing

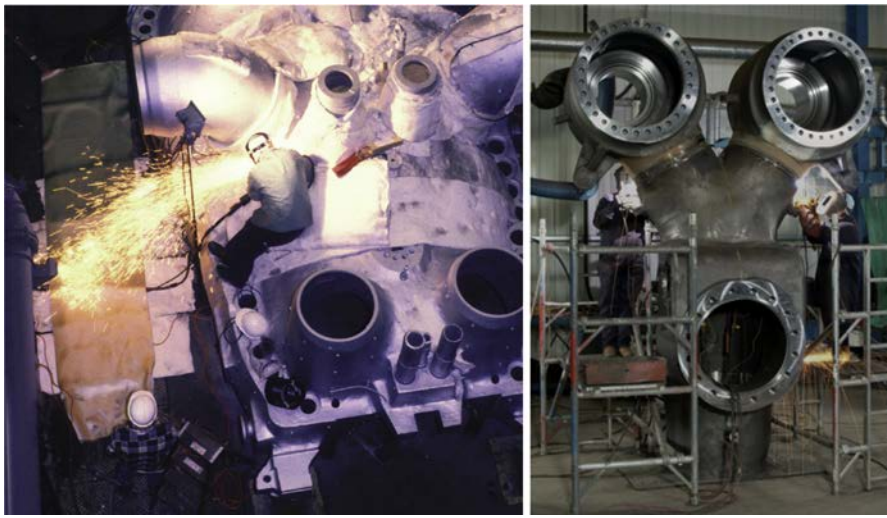


Figure 9.7 Excavation of the defective area by grinding is the first step in repairing defective castings [7]; valve casing welded fabrication with the MMA process (Goodwin Steel Castings Ltd.) [8].

with the service temperature (non-alloyed steels used in sections with low creep load are not included):

- low-Cr bainitic steels (Cr < 3.5% wt.)
- high-Cr martensitic steels (9 < Cr < 12%)
- austenitic Cr-Ni stainless steels (Cr > 18%, Ni > 8%)

Fusion arc welding used for manufacturing USC components greatly affects the behavior of the metallic materials in proximity of the weldments. The effect can be extremely complex due to the local and graded alterations following the weld thermal cycle. Thus, the much optimized BM microstructure of bainitic and martensitic steels will be strongly altered in the HAZ, as exemplarily depicted in Fig. 9.8; the fused zone itself (FZ or WM) will have a different chemistry resulting from the mixture of the deposited weld metal and the bevel parent material dilution. Further complication is added due to the PWHT given to the welded assembly most times to relieve welding and fabrication residual stresses and modify the as-welded microstructure in appropriate manner.

It is useful to study these influences separating the effects in the HAZ and WM, respectively. Moreover, different alloy systems give completely different responses to the thermal cycle and the PWHT. As common behavior, it is useful to recall the fusion welding results in a very steep heating of the metal in the HAZ and WM with peak temperature depending of the exact location with respect of the fusion line (for the HAZ) and the process chosen (for the WM). Upon cooling, the material returns with less severe gradient down to the preheating temperature. Segregation of elements in the solid–liquid transition zone (Fig. 9.9), precipitates dissolution and reformation/coarsening, grain coarsening, grain refining and

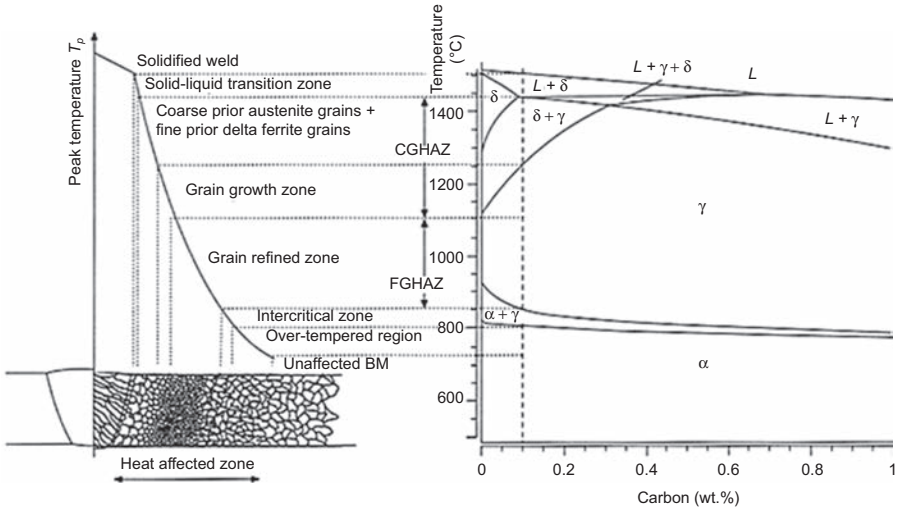


Figure 9.8 Schematic representation of the subzones of the HAZ corresponding to the calculated phase diagram of X10CrMoVNb9-1 with 0.1% C nominal content (Gr. 91) [9]. Heat affected subzones are bounded by the peak temperature experienced during the welding thermal cycle at the relevant location. The SL, CG, GG, FG, IC and OT zones are traditionally described.

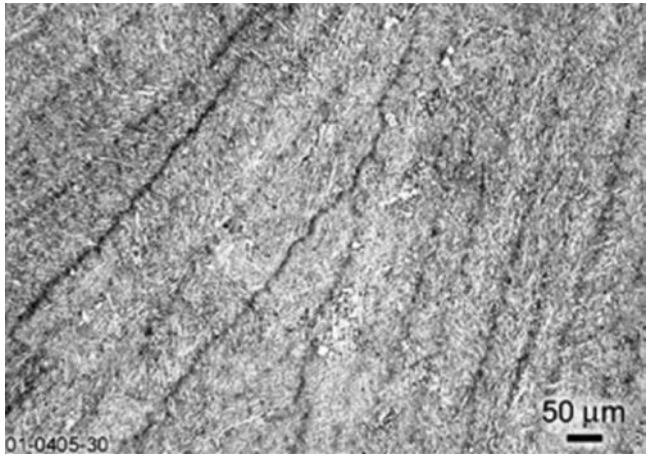


Figure 9.9 Dendritic solidification substructure observed in Grade 91 weld metal after tint etching [10].

over-tempering extent depend on the time spent at high temperature during the weld cycle are all inherent features of ferritic, bainitic, and martensitic steels due to the liquid (L) → delta ferrite (δ) → austenite (γ) → ferrite (α) transformation. Solid-state transformation will result in nonequilibrium microstructures specific of the alloy system and the cooling rate experienced.

A dominant feature of the filler materials used in the different welding methods is to give an undiluted weld deposit with chemistry very close to the relevant USC grade composition; thus, the WM will often match the parent alloy chemistry. This is because it is largely accepted that weldments creep and oxidation/corrosion properties (the crucial needed) are mainly influenced by the chemical composition; the adequate microstructure for proper weld creep strength can be obtained in a wide range of welding heating/cooling rate. The advanced bainitic steels (Gr. 23 and 24) are more delicate on this aspect. Other features (eg, grain size, heating rate, PWHT schedule) play a less important role. Similarly, PWHT will result in comparable behavior for WM and BM with close chemistry (especially if N+T performed after welding).

Solidification of Cr ferritic grades is quite simple to describe, with delta (δ) ferrite as the first solid phase to form, then transforming to austenite (γ). Austenite further decomposes in either martensite (high Cr steels) or bainite (low Cr steels). Segregation of crucial elements (eg, Nb; partition of C and N has been recently discovered, as well) at micro-scale (dendrite size magnitude) or macrosegregation can lead to local phase transformation behavior and thus to the retainement at the room temperature of austenite or delta ferrite. These phases are mostly unwanted as they have poorer mechanical properties at both short (impact toughness) and long term (creep strength). It is worth noting that martensitic steels (or weld consumable fillers) can have actual chemistry such alloyed that the end of martensitic transformation (M_f temperature) is lowered to temperatures well below the preheating schedule. It is of the utmost importance to give the weldments the possibility to cool down to M_f temperature before giving the PWHT, to avoid reformation of hard and brittle hard martensite.

In principle, nonequilibrium transformation for Cr ferritic grades can be studies with CCT diagrams for estimating the behavior of the HAZs of the relevant steel being welded upon cooling from the austenite field. It is a fortunate circumstance that WMs mostly match the BMs composition, so BM CCTs are a good reference to study transformations of weld deposits, as well (In Fig. 9.10 are reported exemplary diagrams for Gr. X20, 91, E911 and 92 high Cr martensitic steels).

Anyway, columnar WM coarser grain size, variation in peak temperature in the austenite field and alloy chemistry modifications made for process technology reasons (eg, deoxidant elements addition in the arc column and weld pool) or better toughness, can shift the phase stability fields and associated critical temperatures (A_{c1}, A_{c3}, B_s, $B_{50\%}$, B_f, M_s, M_f). In that case, accurate measurements can be made with dilatometric studies on WM samples with heating and cooling rates characteristic of welding operations, as shown for example on Fig. 9.11 for CB2-type 9%Cr martensitic steel; see also Fig. 9.12 for application to a P91 WM. As a general trend, CCT curves for WM and HAZ (CG region) are shifted towards longer times and lower temperatures with respect to the BM of the same composition, due to the effect of the coarser austenitic grain size and higher peak temperature.

Empirical formulas or more sophisticated models (often based on neural network data regression) are also available for estimation purpose; they are sufficiently accurate for welding engineering calculations where many factors and procedure variations cannot be easily modeled. The equilibrium A_{c1} temperature based on Mn and Ni content in the WM is also estimated using the following formula (elements by wt%) [12]:

$$A_{c1}(°C) = (854.5 \pm 0.6) - (43.9 \pm 1) \times (Mn + Ni) - (9 \pm 0.4) \times (Mn + Ni)^2$$

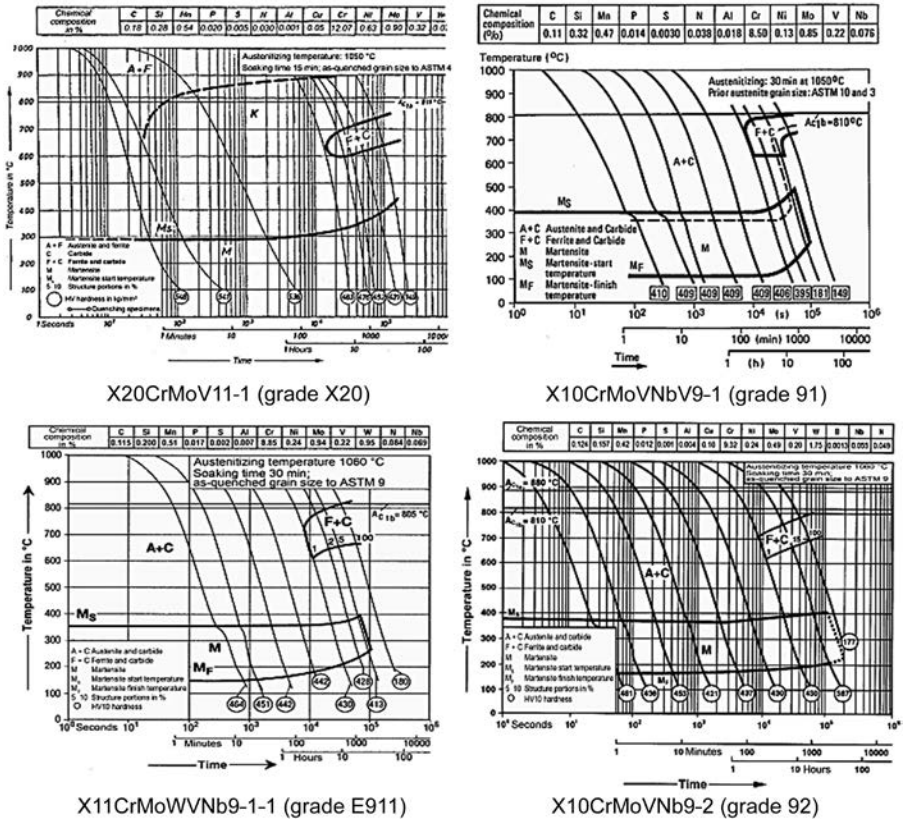


Figure 9.10 CCT diagram for Gr. X20, 91, E911 and 92 high Cr USC martensitic steels [11]. It is recognizable a final fully martensitic microstructure is obtained in a wide range of cooling rates encompassing the entire arc welding characteristic values, with Ms temperature nearly insensitive, as well. In this situation the as-cooled (as-welded) microstructure may have hardness in excess of 400 VHN mainly controlled by the carbon content only.

B_s temperature (empirical) has been given by the classical work of Steven and Haynes and Lee (believed more accurate for Cr bainitic steels), respectively (elements by wt%):

$$B_S(°C) = 830 - 270C - 90Mn - 37Ni - 70Cr - 83Mo$$

$$B_S(°C) = 745 - 110C - 59Mn - 39Ni - 68Cr - 106Mo - 17Mn{\cdot}Ni + Cr^2 + 29Mo^2$$

According to Leslie, $B_{50}(°C) = B_S - 60$

$$B_f(°C) = B_s - 120$$

$$M_S(°C) = 539 - 423C - 30.4Mn - 17.7Ni - 12.1Cr - 7.5Mo + 10Co - 7.5Si$$

(elements by wt%)

Tempering diagrams are also available to study the evolution of the mechanical properties with the time/temperature combination following a PWHT (Fig. 9.13).

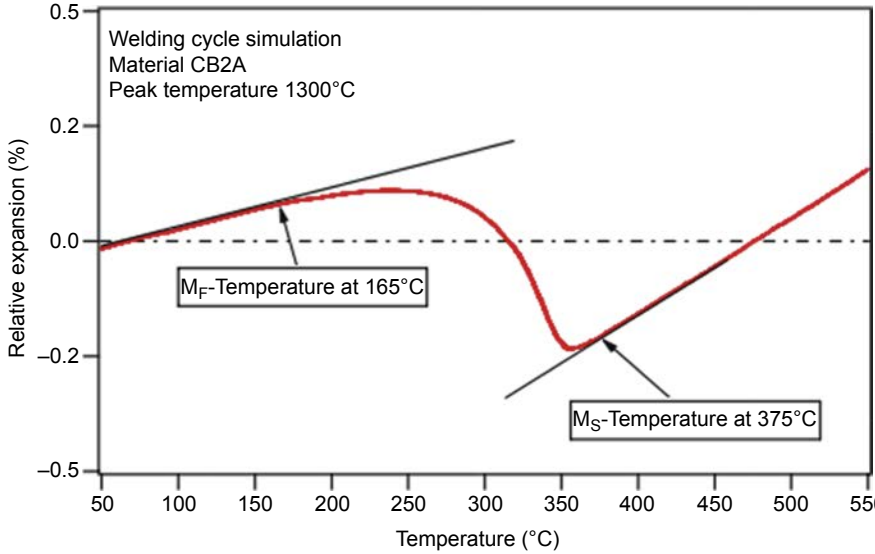


Figure 9.11 Martensitic transformation observed and associated M_f, M_s estimation in CB2A 9%Cr martensitic steel during a simulated single pass weld thermal cycle ($T_{peak} = 1300°C$; $\Delta t_{800\text{-}500\ °C} = 43$ s; this cooling rate is characteristic of the CGHAZ in a 9%Cr steel pipe arc weldment 50 mm thick, made with ~3 kJ/mm heat input and ~275°C interpass temperature) [13]. Steel composition is 0.17C-0.2Si-0.2Mn-8.8Cr-1.5Mo-0.2Ni-0.3V.

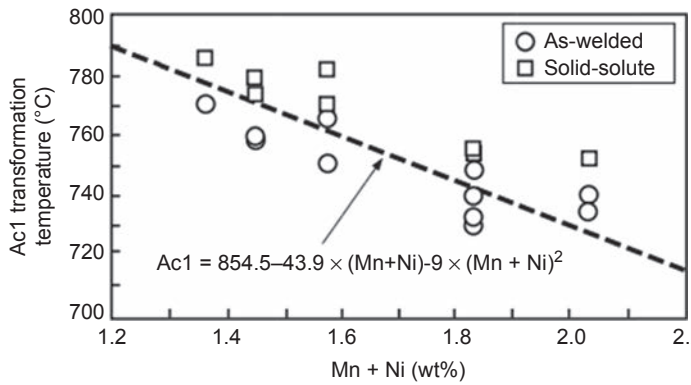


Figure 9.12 A_{c1} transformation temperature vs. Mn+Ni content of 9%Cr ferritic weld metal (Kobelco) [14]. For sufficiently high Ni + Mn contents the WM critical temperature coincides with PWHT temperature appropriate for effective HAZ tempering and stress-relieving.

Stainless austenitic grades used in USC plants feature an FA solidification mode for enhanced resistance to solidification cracking. Upon cooling, no significant microstructural transformation occurs. Thus, weldments properties are much more influenced by the chemical composition alone.

The range of BMs used in a USC is quite ample to match the best cost-effective grade with the local service conditions of the specific component/equipment section. It is not surprising that a relevant part of the welding activity involves DMW.

9.2.1 Low Cr (low alloyed) bainitic steel grades

The low-alloyed steels, grades 11/12/22 and the newer grades 23 and 24, as tubes or pipes, are used in USC boiler components operating at lower temperatures (<570°C), like water walls and economizers. For the tubes used for water walls, the welding of the tubes is performed in the workshop.

For characteristic cooling rates, WM (with composition matching the BM) and HAZ feature an as-welded bainitic microstructure, with portions already tempered due to the overlapping beads of a multilayer weld (Figs. 9.14–9.17) [9,15]. As most of times bainitic weldments are designed not to be given a final PWHT, control of the pass shape, cooling rate, beads proper placement and thickness are of the utmost importance to get compliant mechanical properties. This poses special demand on welders skill and process control. Extent of carbides precipitation upon cooling from peak temperatures characteristic of the welding cycle (up to ~1350°C) is only modest. The bulk of (re)precipitation occurs if the weldment is given a final PWHT.

The hardness has generally to be brought under 350–360 HV_{10} in all weldments areas, according to the most common engineering criteria, to limit the tendency to hydrogen induced (delayed) cracking and and ensure adequate ductility; the area most prone to harden upon cooling is the coarse grain HAZ, where the cooling rate is highest and the prior austenite grain size largest. This proves generally very difficult for standard Gr. 12, 12, or 22 so a PWHT is needed to further temper the microstructure.

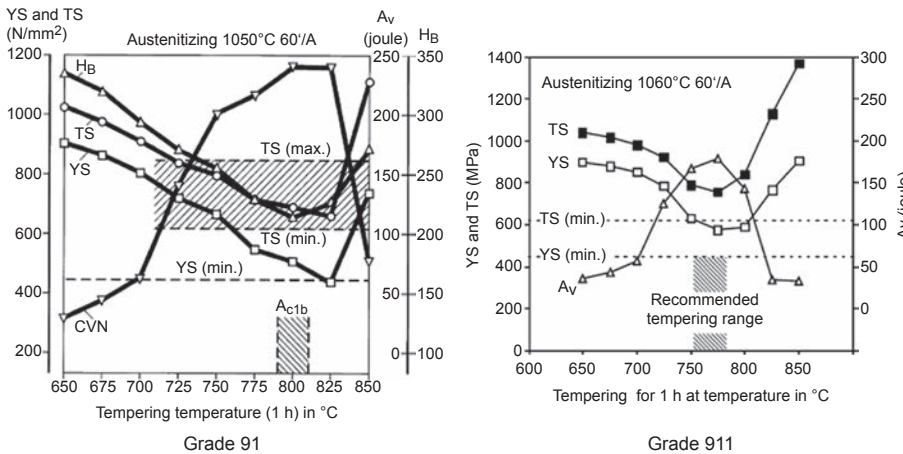


Figure 9.13 Tempering behaviors of martensitic 9%Cr steels (Vallourec) [11].

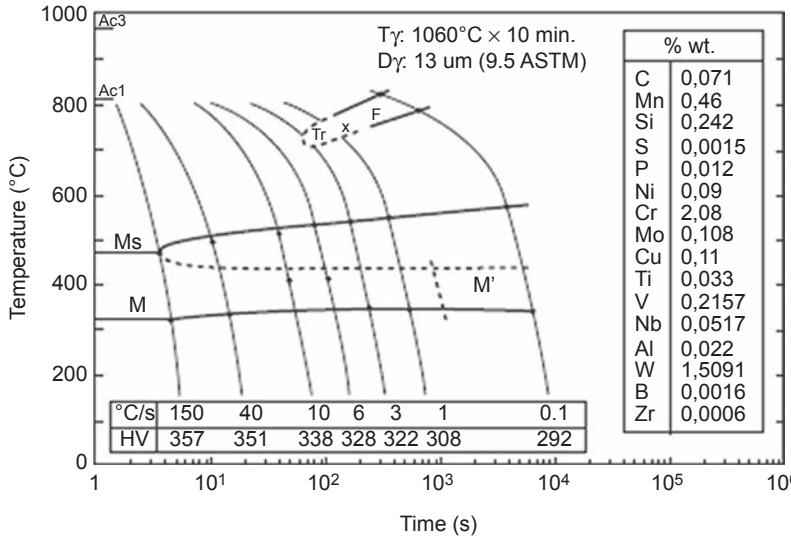


Figure 9.14 Grade 23 CCT diagram [15].

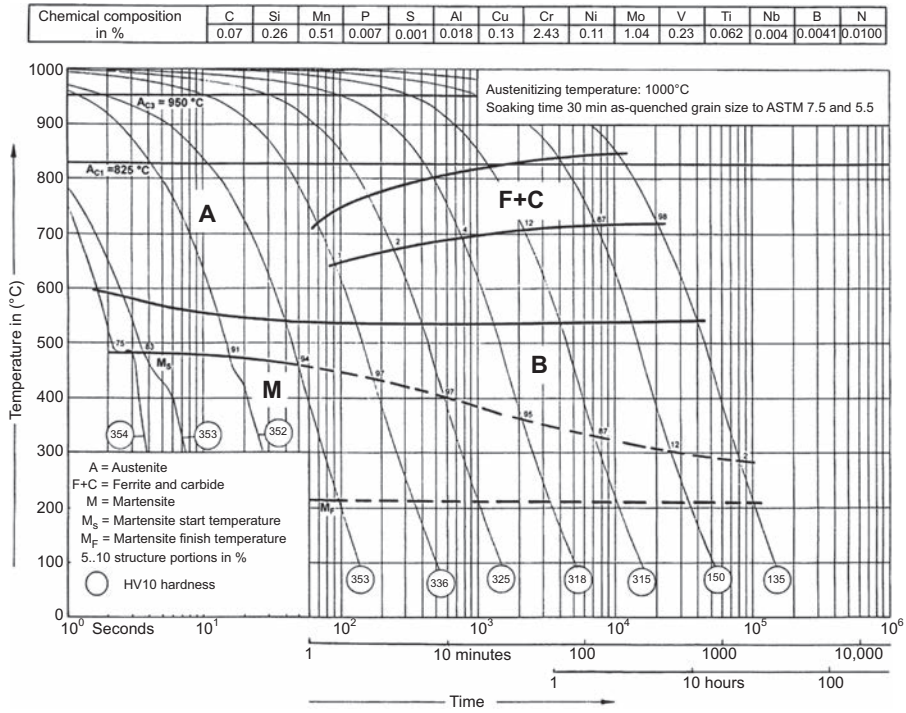


Figure 9.15 Grade 24 CCT diagram (Vallourec).

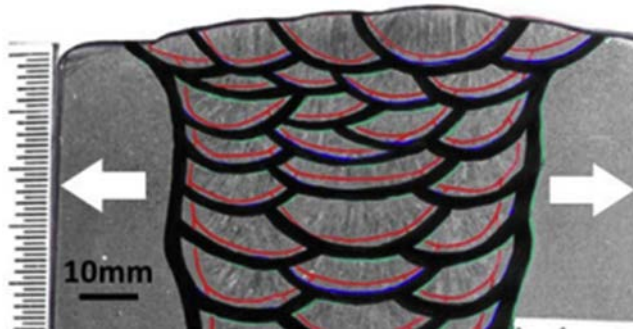
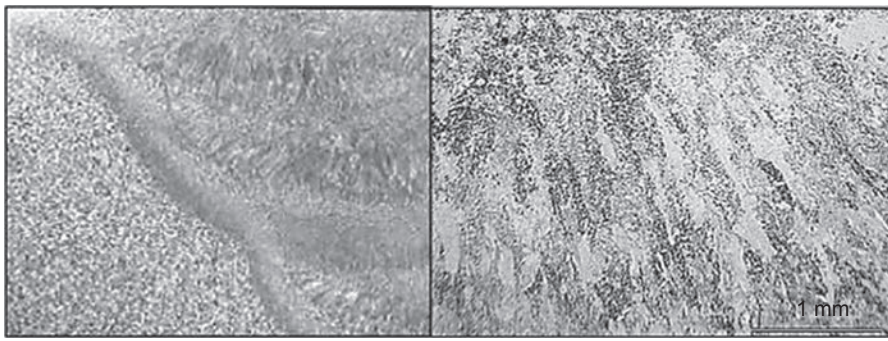
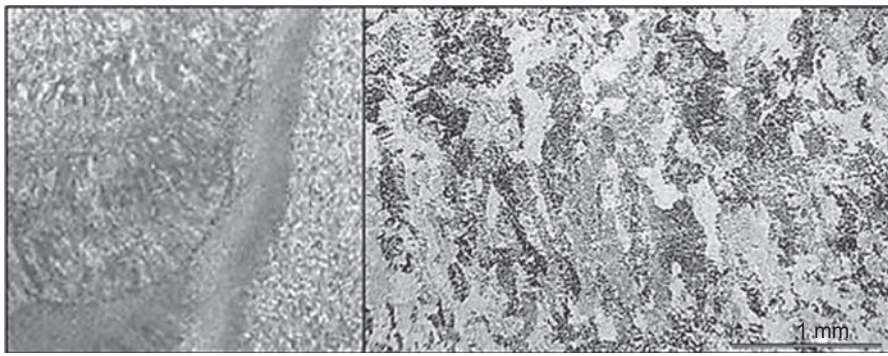


Figure 9.16 Macrostructure of multipass weldment [9].



SMAW (left macro – , right microstructure)



SAW (left macro – , right microstructure)

Figure 9.17 P23 steel (OD 219 mm, WT 31.7 mm) multipass welded joints [15]. It is evident the coarser microstructure associated with the SAW method and its characteristic higher heat input.

Grades 23 and 24 (and associate matching fillers) have been purposely developed with lower carbon content for obtaining as-welded hardness already meeting the figures stated in relevant design codes (thus, hardly exceeding 350 HV_{10} hardness as-welded). Anyway, meeting at the same time the PWHT avoidance, good as-welded hardness, adequate short- (tensile strength, impact toughness) and long-term mechanical properties (creep strength) is challenging, especially for manual on-site welding of thin tubing; welding conditions and heat control have to be very tightly controlled for effective interbead and layer-to-layer tempering and almost no loss of volatile weld consumable alloying elements (like boron, titanium, nitrogen). Nevertheless, sufficient experience has now accumulated with successful homologous and dissimilar weldments made on thin members without PWHT (see as example results in Tables 9.1–9.4 compiled from an extensive optimization and characterization work made on P23 and P24 pipe girth weldments using the SMA and MMA methods. Note that the actual welds properties are influenced by the specific welding procedure adopted.). Thick pipes usually require PHWT to achieve the full range of properties. This final heat treatment is recommended (or mandatory) above 10–16 mm of thickness. T/P23 weldments are tempered at temperatures between 715–740°C, while T/P24 ones at 720–760°C (for comparison, traditional T/P22 steel is given PWHT at 690°).

9.2.2 High alloyed (high Cr) martensitic grades

Nowadays, alloys in this class used for manufacturing USC plants hardware are usually supplied in seamless tubes, pipes, or longitudinally welded pipes. The base material is supplied in the N+T condition, with actual austenitization and tempering parameters depending on the product thickness. Guidance is given in ASTM A335, ASME Boiler and Pressure Vessel Code (BPVC) Sec. 1 or equivalent standards. Those grades exploit the tempered martensite with precipitates microstructure for outstanding creep resistance.

The dominant feature of the martensitic grades is the high alloy content that promotes, upon cooling (eg, in WM and HAZs), the formation of a hard and brittle microstructure due to the martensitic transformation, regardless of the cooling rate resulting from the weld procedure. The base material with normalizing and tempering treatment features a tempered martensitic microstructure with precipitation of $M_{23}C_6$ at the grain boundaries and MX-type precipitates within the matrix [17]. Additional precipitation occurs over time during high temperature service; furthermore, transformation of as-tempered precipitates results in lower ductility and notch toughness. Fig. 9.18 and Table 9.5 list the precipitates commonly classified in martensitic CSEF steels. They can undissolve/reform either during the austenitization or at temperatures at high range of the thermal cycle, the tempering (and PWHT, too) or creep service.

Following the weld+PWHT cycle, starting from the weld metal towards the base material (Fig. 9.19), the markedly graded microstructure can be classified conveniently as follows: weld metal with a tempered martensitic structure (Fig. 9.19(a)), HAZ with tempered martensite structure with possible presence of islands of δ-ferrite (Fig. 9.19(b)), HAZ with fine-grained region (Fig. 9.19(c)), HAZ with intercritical microstructure (Fig. 9.19(d)) and unaffected base material (Fig. 9.19(e)) with the original tempered martensitic structure.

If a microhardness survey is taken across a multilayer weld joint in the same sequence as the above metallographic examination, as depicted in Fig. 9.20, a gradient

Table 9.1 **Chemical composition of welding wires and all-weld metal for low-alloyed steels (homogeneous welds) [16]**

	C	Si	P	S	Mn	Cr	Mo	V	W	Al	B	N	Nb	Ti	Cu
P23–SMAW Thyssen Cr 2 WV[a]	0.06	0.22	0.017	0.007	0.46	2.28	0.067	0.28	1.72	–	0.002	0.017	0.043	0.001	–
P23–3/SMAW All-weld metal	0.06	0.29	0.015	0.007	0.53	2.33	0.073	0.25	1.23	0.001	0.002	–	0.028	0.005	–
P23–SMAW SAF AL CROMO E223[a]	0.05	0.38	0.011	0.007	0.55	2.12	0.08	0.23	1.38	0.002	0.0009		0.015	0.006	–
P23–SAW Thyssen Union S1 Cr 2 WV Flux: UV 430 TTR-W[a]	0.075	0.22	0.017	0.001	0.47	2.19	0.09	0.23	1.88	0.022	0.001	0.009	0.063	0.048	–
P23–5/SAW All-weld metal	0.068	0.44	0.010	0.006	1.32	2.09	0.03	0.19	1.32	0.013	0.001	–	0.015	0.002	–
P23–SAW SAF AL CROMO SF223[a]	0.055	0.27	0.011	0.004	0.56	1.93	0.08	0.23	1.25		<0.0001		0.017		
P23–6/SAW All-weld metal	0.052	0.37	0.010	0.005	0.58	2.18	0.058	0.22	1.23	0.024	0.001	–	0.007	0.004	–
P24–SMAW Thyssen CrMoVTiB[a]	0.06	0.44	0.008	0.005	0.54	2.37	0.96	0.23	–	–	0.002	0.034		0.032	
P24–3/SMAW All weld metal	0.06	0.45	0.011	0.007	0.51	2.30	0.91	0.26	0.021	0.006	0.003	–	0.010	0.023	
P24–SMAW SAF AL CROMO E224[a]	0.075	0.51	0.004	0.003	0.46	2.47	0.97	0.22	<0.005	0.002	0.0024		0.016	0.063	
P24–4/SAW All-weld metal	0.08	0.41	0.008	0.005	0.41	2.41	0.99	0.22	0.016	0.007	0.002	–	0.014	0.055	
P24–SAW Thyssen Union S1 CrMoVTiB[a] Flux: UV430 TTR-W	0.06	0.24	0.004	0.002	0.53	2.39	1.01	0.24	–	–	0.0037	–		0.073	0.14
P24-5/SAW All weld metal	0.05	0.37	0.007	0.004	1.17	2.23	0.92	0.21	0.025	0.017	0.001	–	0.007	0.009	0.19
P24–SAW SAF AL CROMO SF224[a]															
P24–6/SAW All-weld metal	0.07	0.52	0.012	0.006	0.54	2.72	1.06	0.24	0.020	0.038	0.003	–	0.017	0.032	0.05

[a]Data from fabricators.

Table 9.2 Test results on SAW homogeneous P23 pipe welds [16]

SAW girth welds in P23 pipes (OD 219 × 30mm)		
	Weld no. P23-5 Filler: Union S1 Cr2WV Heat input: 9 kJ/cm Preheat 180°C, PWHT 740°C, 2 h	Weld no. P23-6 Filler: Al CROMO SF 223 Heat input: 10–16 kJ/cm Preheat 150°C, PWHT 740°C, 2 h
Transverse tensile testing (EN 895) Required: greater than specified minimum BM (EN 288-3): min. 510 MPa specified in ASTM A335		
Tensile strength BM (MPa)	633–634	
Tensile strength girth welds (MPa)/Fracture location	577/outside weld in base metal 566/outside weld in base metal	563/outside weld in base metal 578/outside weld in base metal
Side bending (EN 910) Required: 120° without cracks of 3 mm in each direction (EN 288-3)		
Side bends	No cracks >3 mm	No cracks >3 mm
Charpy-V impact testing (EN 875) Required: 27 J (34 J/cm^2) in WM at room temperature (PED)		
Impact base metal (J/cm^2)	207–219–233/219	
Impact HAZ (J/cm^2)	215–209–220/215	228–217–221/222
Impact weld metal (J/cm^2)	216–279–182/226	175–218–172/188
Hardness testing (EN 1043-1) Required: max. 350 HV10 (power plant applications) max. 320 HV10 (EN 288-3)		
HV10 base metal	203	
HAZ max. HV10 face HAZ max. HV10 root	256 231	227 221
Weld metal max. HV10 face Weld metal max. HV10 root	236 222	207 227

in the hardness values due to graded microstructure is observed (a minimum in hardness value is attributed to the ICHAZ microstructure, also often referred as softened zone) [19]. While the actual magnitude and spacing of hardness peaks and troughs depend on the specific WM/BM chemistry and weld/PWHT schedule adopted, the curve shape is characteristic of high Cr martensitic weldments.

As consequence of this characteristic graded structure of the welded joints in the CEFSs, the creep properties are different as a function of the joint zones. The classification of service cracking in weldments originally devised by Schueller et al. [20], which describes the location of cracking relative to the weld, is still used today in

Table 9.3 Test results on SMAW homogeneous P24 pipe welds [16]

SMAW girth welds in P24 pipes (OD 370 × 25 mm)		
	Weld no. P24-3 Filler: Union CrMoVTiB Heat input: 8–27 kJ/cm Preheat 150°C, PWHT 740°C, 2 h	Weld no. P24-4 Filler: Al CROMO E 224 Heat input: 25–37 kJ/cm Preheat 200°C, PWHT 740°C, 2 h
Transverse tensile testing (EN 895) Required: greater than specified minimum BM (EN 288-3): min. 585 MPa for T24 specified in ASTM A213		
Tensile strength BM (MPa)	640–654	
Tensile strength girth welds (MPa)/Fracture location	596/outside weld in base metal 600/outside weld in base metal	627/outside weld in base metal 609/outside weld in base metal
Side bending (EN 910) Required: 120° without cracks of 3 mm in each direction (EN 288-3)		
Side bends	Cracks due to porosities	No cracks >3 mm
Charpy-V impact testing (EN 875) Required: 27 J (34 J/cm^2) in WM at room temperature (PED)		
Impact base metal (J/cm^2)	260–246–273/260	
Impact HAZ (J/cm^2)	115–228–129/157	216–114–240/190
Impact weld metal (J/cm^2)	70–175–80/108	42–123–104/90
Hardness testing (EN 1043-1) Required: max. 350 HV10 (power plant applications) max. 320 HV10 (EN 288-3)		
HV10 base metal	212	
HAZ max. HV10 face HAZ max. HV10 root	247 247	243 256
Weld metal max. HV10 face Weld metal max. HV10 root	228 233	231 227

the power generation industry circles and is shown in Fig. 9.21 [21,22]. Types I, II and III are associated with the fabrication of a joint and may be either solidification (hot cracking), hydrogen (cold or delayed cracking), reheat, temper embrittlement, and occasionally long-term creep-related cracks. Type IV cracking forms toward the outer edge of the visible HAZ, beside the parent metal (Fig. 9.22), and it is exclusively a creep cracking mechanism that occurs after prolonged service in the creep temperature regime. While it is well established that Type-IV cracking occurs toward the outer edge of the visible HAZ where overtempering has occurred, the exact location, in terms of micro-structure, has been reported to occur in both the intercritically

Table 9.4 Test results on SAW homogeneous P24 pipe welds [16]

SAW girth welds in P24 pipes (OD 370 × 25 mm)		
	Weld no. P24-3 Filler: Union S1 CrMoVTiB Heat input: 9 kJ/cm Preheat 180°C, PWHT 740°C, 2 h	Weld no. P24-6 Filler: Al CROMO SF 224 Heat input: 10–20 kJ/cm Preheat 150°C, PWHT 740°C, 2 h
Transverse tensile testing (EN 895) Required: greater than specified minimum BM (EN 288-3): min. 585 MPa for T24 specified in ASTM A213		
Tensile strength BM (MPa)	640–654	
Tensile strength girth welds (MPa)/Fracture location	627/outside weld in base metal 632/outside weld in base metal	632/outside weld in base metal 617/outside weld in base metal
Side bending (EN 910) Required: 120° without cracks of 3 mm in each direction (EN 288-3)		
Side bends	No cracks >3 mm	No cracks >3 mm
Charpy-V impact testing (EN 875) Required: 27 J (34 J/cm^2) in WM at room temperature (PED)		
Impact base metal (J/cm^2)	260–246–273/260	
Impact HAZ (J/cm^2)	277–255–109/214	235–242–254/244
Impact weld metal (J/cm^2)	218–36–222/159	89–204–85/126
Hardness testing (EN 1043-1) Required: max. 350 HV10 (power plant applications) max. 320 HV10 (EN 288-3)		
HV10 base metal	212	
HAZ max. HV10 face HAZ max. HV10 root	284 260	258 254
Weld metal max. HV10 face Weld metal max. HV10 root	247 222	239 235

(IC) heated HAZ and the grain-refined or fine-grain (FG) HAZ. Thus, there is not a single HAZ microstructural region associated with type IV cracking, although the softest zone has been mostly associated with the failure location. This behavior has been observed first during service at high temperature, then made the object of a huge amount of studies.

The distinction between the two zones is not simple to be observed in practice. Fig. 9.23 shows the HAZ microstructure of a recently developed boron-containing 9%Cr forging martensitic steel (FB2), and it illustrates the difficulty of distinguishing

Steel	Precipitate	Formula	Remark
12 CrMoV	$M_{23}C_6$	$(Cr,Fe,Mo)_{23}C_6$	Precipitate during tempering
P91	$M_{23}C_6$	$(Cr,Fe,Mo)_{23}C_6$	Precipitate during tempering
	MX	(Nb,V)(N,C)	Undissolved during austenitisation
	MX	(V,Nb)(N,C)	Precipitate during tempering
	Laves phase	$(Fe,Cr)_2Mo$	Precipitate during creep (T<650°C)
P92	$M_{23}C_6$	$(Cr,Fe,Mo,W)_{23}C_6$	Precipitate during tempering
	MX	(Nb,V)(N,C)	Undissolved during austenitisation
	MX	(V,Nb)(N,C)	Precipitate during tempering
	Laves phase	$(Fe,Cr)_2(Mo,W)$	Precipitate during creep (T<720°C)

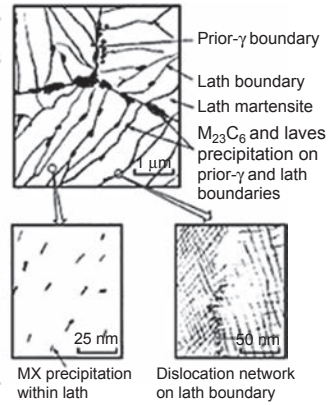


Figure 9.18 Typical precipitates and their distribution in CSEF high Cr steels and their weldments [17].

Table 9.5 Phases, composition, and formation in CSEF steels [17]

Phase	Composition/stechiometry	Precipitates during
$M_{23}C_6$	$Cr_{23}C_6$, $Fe_{21}Mo_2C_6$	Standard heat treatment (N + T for BMs, either N + T or PWHT for weld metals and HAZs)
MX	V(C,N)	
MX_2	ε-Cr_2N	Service temperature (>600°C)
Laves type	$(Fe,Cr)_2(Mo,W)$	
Z	Cr(V,Nb)N	

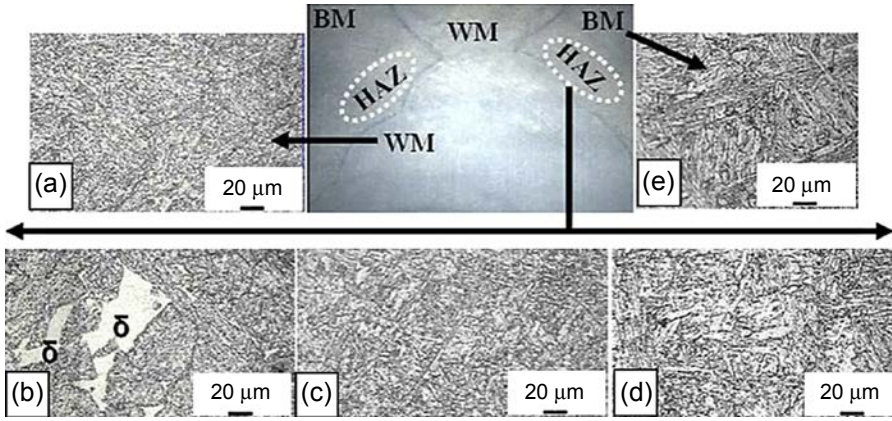
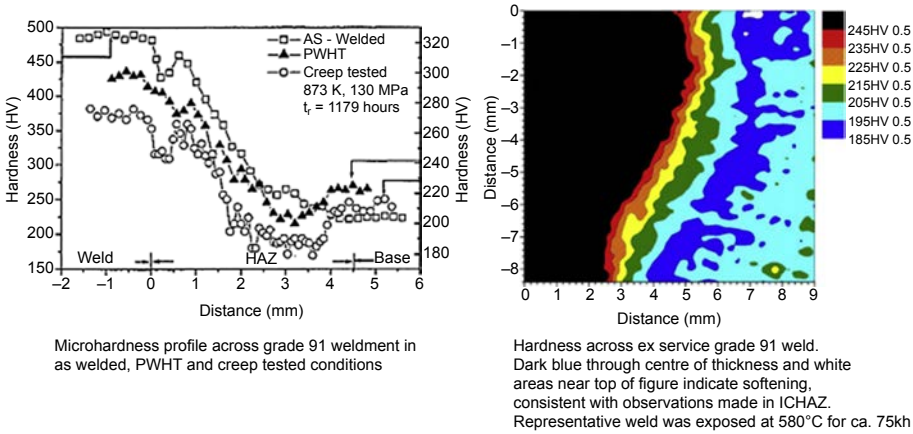


Figure 9.19 Resultant graded microstructure in the Grade 91 steel weld joint due to thermal exposure to different peak temperatures during weld thermal cycles; optical micrographs of different regions of weld joint such as weld metal (a), HAZ coarse grain with δ-ferrite (b), HAZ fine-grained region (c), HAZ intercritical region (d), and base metal (e) [18].



Microhardness profile across grade 91 weldment in as welded, PWHT and creep tested conditions

Hardness across ex service grade 91 weld. Dark blue through centre of thickness and white areas near top of figure indicate softening, consistent with observations made in ICHAZ. Representative weld was exposed at 580°C for ca. 75kh

Figure 9.20 Microhardness variation across a Gr. 91 weldments due to graded microstructure [19].

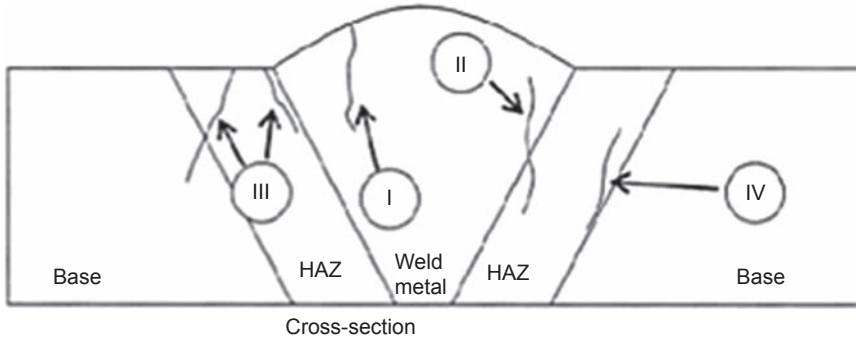


Figure 9.21 Classification of cracking in fusion weldments from Brear and Fleming [21], according to Schueller et al. [22].

the different parts of the HAZ. Different materials, welding thermal cycles, and temperature–stress regimes may bring about differences in the observed failure location, although the failure location in long-term (thus, at low stress) service is most commonly reported to be the fine-grained heat affected zone (FGHAZ), if stresses transverse to the weld are the most significant (like longitudinal joints on tubulars). It is worth noting that, in multilayer welds, the fine-grained and intercritical HAZ regions are essentially almost continuous through thickness, unlike the coarse-grained heat affected zone (CGHAZ), which may exist in disconnected regions beside the fusion boundary. This provides a continuous region that is susceptible to the phenomenon. It should be noted that the number density of cavities is not uniform across the section. The highest density of cavities is expected to occur at midsection, as observed by Yaguchi et al., where the triaxiality is highest [23]. This observation clearly has implications for the use of surface replicas to investigate the extent of creep cavitations

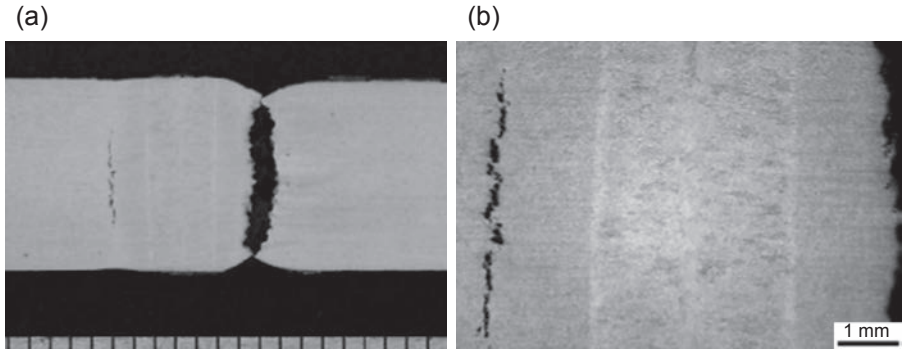


Figure 9.22 Type-IV cracking in electron beam welded 9%Cr-1%Mo steel: (a) macro; (b) micro image; mm scale shown [22]. Cracks have nucleated and progressed on both sides during the creep exposure. Mid thickness is always the location where creep cavities start to form and grow; this behaviour is linked with the higher degree of triaxiality occurring at mid thickness of members.

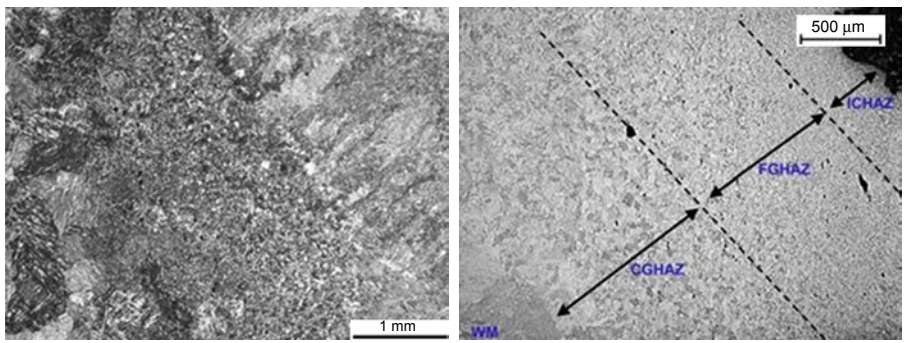


Figure 9.23 Heat affected zone regions of a ruptured creep cross-weld specimen that failed by the type IV mechanism [23].

because the damage is detected at the early stage on the surface, while it has already severely progressed inside the member.

Unwanted service failure times for type IV cracking have been reported to be typically 6–10 years, but much shorter lives have also been reported (as 35,000 h) [23]. On Gr. 91 weldments, while much of the earliest type IV cracking detected occurred in heats with low N/Al ratios (1,5), many examples were found for which cracking was observed after 58,000 h service in heats with much higher N/Al ratios (some >10, at nitrogen levels >0.05%). In principle, N/Al ratio has not been related to similar issues in the WM [24]. This circumstance has backed the specification of N/Al ratio >4 at the very minimum for BM and WM in many procurement specifications or application codes, to avoid most of nitrogen to be combined as AlN instead of forming creep strenghtening carbonitrides.

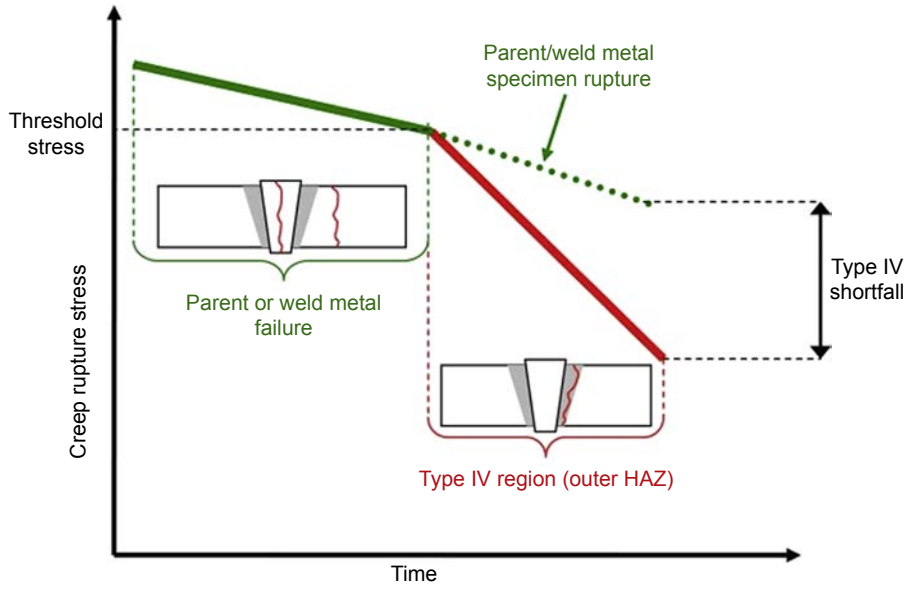


Figure 9.24 Schematic representation of the reduction in creep rupture strength beyond the onset of type-IV cracking for weldments at a fixed temperature [22].

For transverse load, the mechanism is favored at higher temperatures and lower stress levels (thus over longer lifetime). At higher stresses and lower temperatures, failures are more common in the weld metal or parent metal. As the temperature is increased and the stress reduced, at a point type-IV creep cracking becomes the dominant mechanism, as illustrated schematically in Fig. 9.24.

The awareness of the importance of knowledge on creep behavior of welded structures increased continuously within the last decades [25]. The type IV phenomena was firstly evidenced by Schueller as early as 1974 on Gr. 22 welds. It took many years (until late eighties) to fully recognize the issue, accumulate appropriate design data for weldments subjected to creep and find the way in design codes; meanwhile, already in-service weldments were subjected to unexpected HAZ failures, including many on the then recently introduced P91 steel.

More insight on the type-IV cracking in weldments has been gained in the 1990s, after that several failures of welded steam piping systems, some of them in a catastrophic manner, have backed the need for investigations on the creep behavior of welded structures [26]. Weldments of ferritic steels exposed to high-temperature creep loading show very similar behavior in tendency, irrespective of the chemical composition and other parameters like welding procedure, groove preparation, etc. Numerous creep tests of cross-weld samples showed that at lower temperatures there is no big difference between the base metal and cross-weld creep strength [17]. This difference becomes more prominent as the temperature increases and the applied stress level is lowered. The time of deviation of cross-weld creep strength from base metal mean creep strength is varying with creep testing conditions, material grades (the most

prominent influence), stress level, temperature, welding procedure (weak influence), PWHT schedule, etc. Fig. 9.25 compares the creep rupture strength of cross-welds with the mean line of base metal creep rupture strength of 9% Cr steel grade E911.

As a clear example of Type IV cracking as a progressive creep damage phenomena taking place in the weldments HAZs over the service life, microstructure and hardness across a Grade 122 welded joint (Fig. 9.26) shows the distribution of Vickers

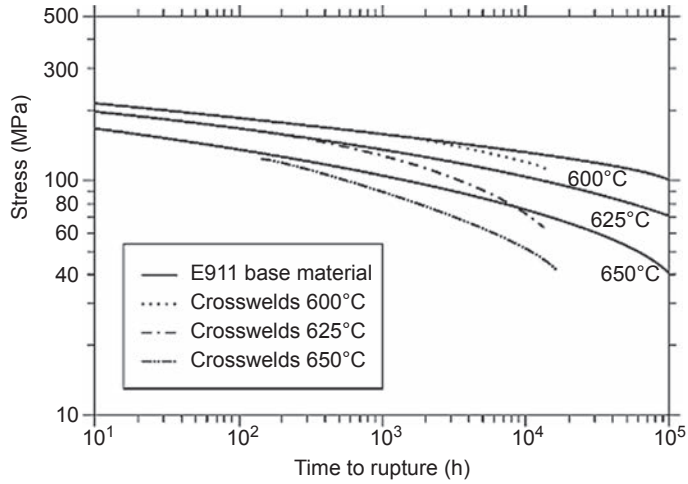


Figure 9.25 Comparison of cross-weld creep rupture strength to mean base material creep rupture strength of E911 high Cr martensitic steel at different temperatures [25]. A similar behaviour is found for any 9–11% Cr CSEF steel.

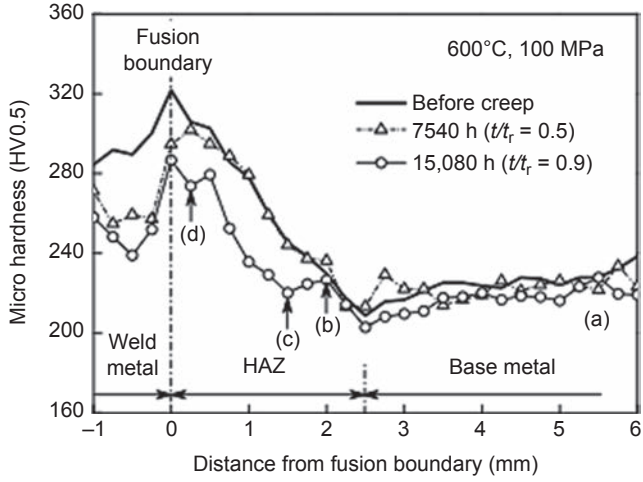


Figure 9.26 Distribution of Vickers microhardness in the HAZ of a Gr. 122 (11%Cr) joint before creep and after creep interruption at 0.5 and 0.9 of life fraction [26].

microhardness ($HV_{0.5}$) in the HAZ of the joint before and after creep at 600°C and 100 MPa for 7540 h (0.5 of life) and 15,080 h (0.9 of life). Fig. 9.27 shows the micrographs for the locations (a)–(d) of the welded joint indicated in Fig. 9.26 after creep for 15,080 h; these correspond to (a) base metal, (b) intercritical HAZ, (c) fine-grained HAZ and (d) coarse-grained HAZ. Softening of the HAZ becomes evident at the last stage of the creep life due to the accumulated microstructural changes. The Type IV rupture is reported brittle because of a small creep deformation at failure. The nucleation and growth of cavities in the FGHAZ/ICHAZ are claimed to be the main damage mechanism behind the intergranular fracture of high Cr welds during creep.

The difficulty in clearly studying the behavior of the HAZ portions has led to the development of studies on homogeneous specimens using thermo-mechanical simulators, in which a small cylindrical sample of few millimeters can experience a thermal cycle resembling those encountered by a specific HAZ location with its characteristic peak temperature and cooling rate. In this way the various effects can be studied separately and more insight gained (Fig. 9.28).

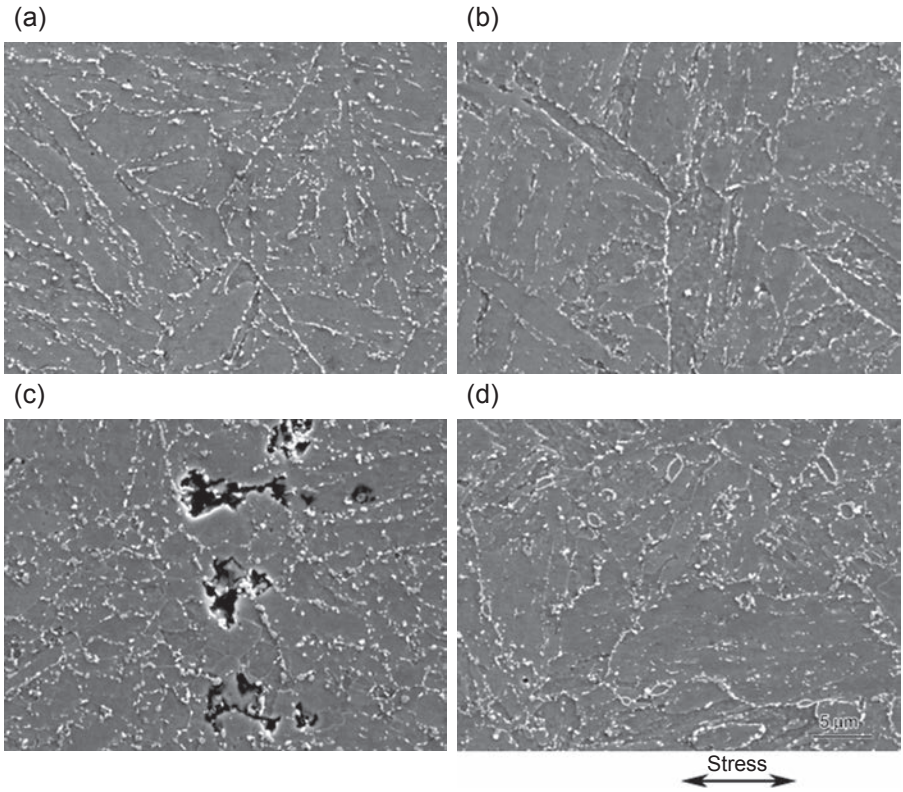


Figure 9.27 SEM micrographs of a Gr. 122 (9%Cr) steel joint after creep at 600°C and 100 MPa for 15,080 h: (a) base metal; (b) 2 mm; (c) 1.5 mm; (d) 0.25 mm from the fusion boundary [26].

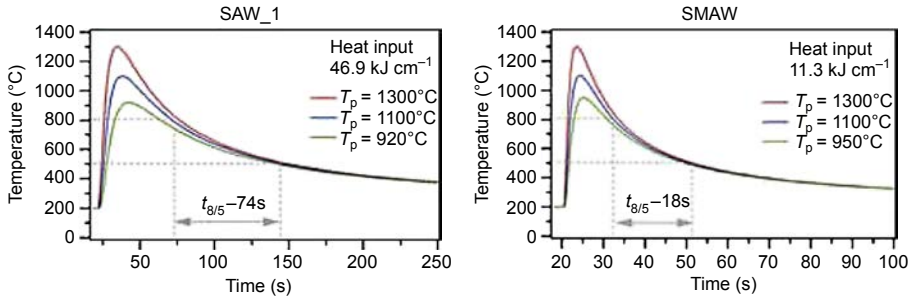


Figure 9.28 Calculated weld time–temperature cycles for Gleeble HAZ simulation of CB2 steel. Heat input ranging from 0.37 to 8.4 kJ/cm resulted in characteristic cooling times (Δt800–500°C) from 5 to 137 s. Peak temperatures are selected to simulate CGHAZ (1300°C), FGHAZ (1100°C), and ICHAZ (960°C, 950°C, 920°C) [27].

One remarkable feature of the 9–12% Cr multilayer WMs is that creep strength closely matches the BM (ie, WM has hardly been associated with a Type IV failure location), even if the WM chemistry is similar to BM (eg, in GTA weldments).

Various explanations for the soft FG(IC)HAZ weaker creep properties have been proposed over time, so far without completely explaining the phenomena on a theoretical ground.

With reference to a 9–11%Cr martensitic steel, it is generally accepted the main effect promoting the damage in the FGHAZ is the altered distribution of the creep-strengthening $M_{23}C_6$ precipitates [29]. In the FGHAZ the altered distribution of $M_{23}C_6$ precipitates (either undissolved or nucleated) is promoted by the thermal cycles, and furthermore, there is evidence to suggest that the fine MX precipitates in the FGHAZ coarsen more quickly during high-temperature service, further reducing the creep resistance of this location. As consequence, there is the coexistence of grain boundaries with coarsened precipitates and newly formed boundaries free of, anticipated to be weak and prone to softening and recovery (Fig. 9.29).

Premature failure is due to the influence of the heterogeneity in the HAZ microstructure, a triaxial stress state in service, and the accumulation of residual stress during welding. In particular, there is a concentration of stress and coarsening of carbide in the ICHAZ and FGHAZ, leading to nucleation and growth of voids characteristic of type IV damage.

A recent study, in particular, tried to advance the understanding of the phenomena with the aid of cutting edge characterization techniques based on advanced electron microscopy associated with grain misorientation measurements. The work was undertaken on P91 pipe welds investigating the outer edge FGHAZ as-welded, after PWHT and after creep testing. It is claimed, as widely recognised, the as-welded FGHAZ consists of martensite laths inside the prior austenite grains. The undissolved, Cr-rich $M_{23}C_6$ carbides are distributed on the prior austenitic grain boundaries (PAGBs) and some lath boundaries together with fine ones nucleated in consequence of the weld thermal cycle. Fine $M_{23}C_6$ carbides nucleate on the PAGBs and internal martensite laths. The high fraction of unrecrystallized grains show a high strain level (Fig. 9.30).

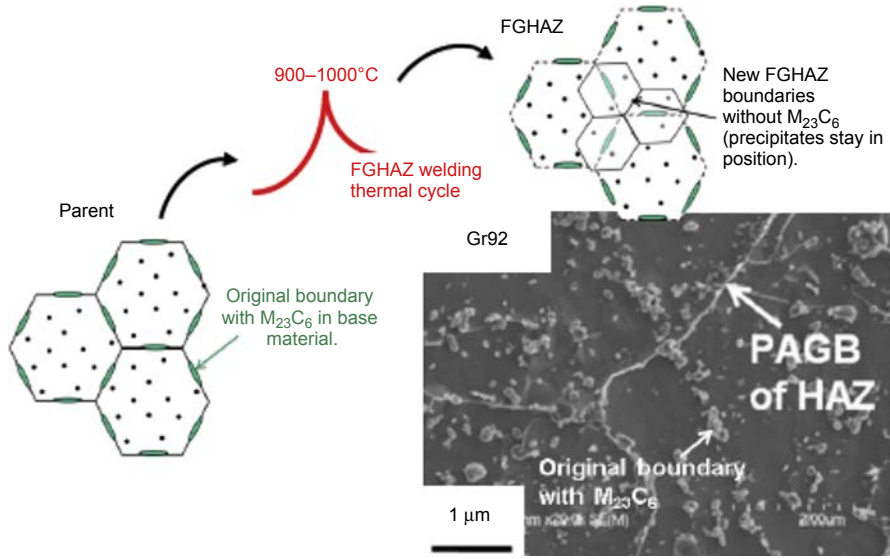


Figure 9.29 Schematic illustrating the development of microstructure in the FGHAZ of typical 9-12%Cr CSEF steels [29].

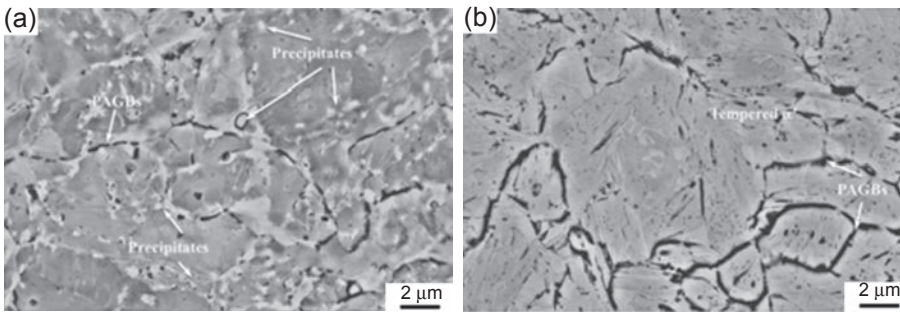


Figure 9.30 (a) Backscattered electron (BSE) images of the as-welded FGHAZ; (b) deep etched with 10% Nital to show the prior austenitic grain boundaries (PAGBs) [28].

PWHT produces fine equiaxed ferrite grains and coarsened precipitates. The creep test further tempers the martensite, and promotes the grain growth of high angle grains. Coarsening and segregation of Cr-rich $M_{23}C_6$ carbides in specific grains causes a higher local strain during creep. MX particles coarsen and stabilize on the high-angle grain boundaries. Other carbide boundary networks on HAGBs weaken the creep strength of GBs. Connected wedge-type cavities on GBs cause the intergranular Type IV rupture with a low entire creep strain and a large local deformation in the transition zone between FGHAZ and ICHAZ.

Low peak temperature in the ICHAZ ($A_{C3} > T_p > A_{C1}$) and outer edge of the FGHAZ ($T_{peak} \approx A_{C3}$) tends to retain the variations in precipitate distribution in the

BM. Recrystallization during PWHT further enhances the nonuniform distribution of carbides. It is proposed that the creep strain mismatch between the unrecrystallized grains with precipitates and fully recrystallized grains precipitate-free promotes the nucleation of initial cavities during creep [28].

Normalization eliminates the HAZ of the weld. As the entire welded member needs to be normalized and then tempered, this can be extremely impractical for large components or on-site. Nevertheless, usage on important applications have been reported alongside valid technical results [28], as for large-diameter longitudinally welded pipework.

Variations have been reported for changes in the welding procedure details. Weld variables reported to make a difference are the bevel preparation [25,26], the width of the HAZ [17,30], the WM creep strength [31] and the PWHT soaking temperature [34]. All those factors seem to affect the deformation constraint on the FGHAZ, which influences the tendency to shear and the formation of creep voids. Anyway, these effects are still the object of basic studies, and no guidance for exploiting the effects on the design side has been given.

9.2.3 Austenitic steel grades

Due to higher Cr content the austenitic steels exhibit higher corrosion resistance than ferritic steels. Furthermore, the proper addition of C, Nb, and N results in an increased elevated temperature strength and creep resistance. Weldability of austenitic grades is by far the most forgiving among the various USC materials classes. USC austenitic steels microstructure consists of a minor content of delta ferrite and carbides in austenite (γ) matrix; the semi-finished products are supplied in the solubilized state. The hardness is very little sensitive to the thermal cycle followed in the HAZ and WM. The matching WMs are usually slightly over-alloyed with respect to the matching BM; this results in weldments generally stronger than the parent metal at room temperature (short term) (Fig. 9.31).

Because of the high susceptibility of austenitic stainless steels to hot cracking, the weld metals are alloyed with higher Mn content than the base metal. Furthermore, intergranular reheat cracking is also a critical issue for the stabilized austenitic steels. After fast cooling from welding temperature, the finely precipitated niobium carbonitrides generate residual stresses in the HAZ and precipitation hardening. Such weldments are not usually given a stress relief prior to enter in service; as consequence, after service exposure to high temperature creep capitation occurs at HAZ grain boundary.

Low heat input together with the interpass temperature below 150°C is necessary to suppress hot cracking. Preheating and heat treatment after the welding process in the fabrication of these steel grades are not mandatory. However, if the material is sensitized after welding, a post-welding treatment (solution treatment) can be done to restore the properties, mainly to increase the wet corrosion resistance.

Regarding the creep properties, unlike CSEF steels, the welded joint austenitic steels do not show appreciable difference compared to BMs. As an example,

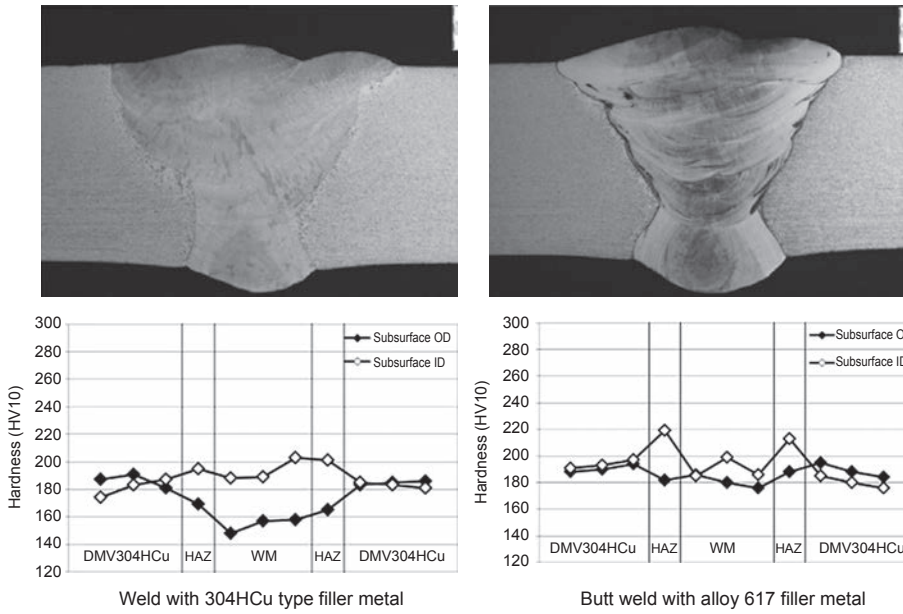


Figure 9.31 Austenitic stainless steel 304HCu butt weld joints and their hardness profiles [32].

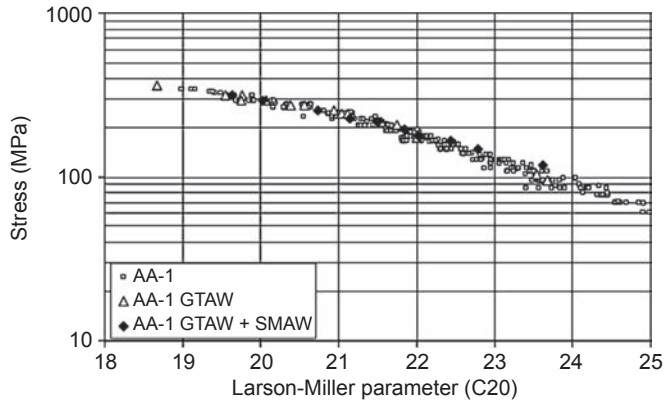


Figure 9.32 TEMPALOY AA-1 austenitic steel: comparison of creep strength of base metal and cross-weld joints [33].

Fig. 9.32 shows the creep tests on similar butt welded joints of TEMPALOY AA-1: tests were conducted to study the effect of the gas tungsten arc welding (GTAW) and GTAW + SMAW welding process on cross-weld creep properties; the filler metal used was a specific similar welding consumables. Creep resistance of welded joints is in line with that of base material in the temperature range 600–800°C [33].

9.2.4 Dissimilar metal welding of USC steels

9.2.4.1 General aspects

The topic of USC steels dissimilar metal welding (DMW) is both ample and complicated due to the many situations faced in different designs and welded details. It is not possible to give here more than an introduction; in the following, the basic principles of good welding engineering practice are given for the broad situations more easily encountered in the USC component welded manufacturing. Some guidance is also given in AWS D10.8 or BS 2633 standards.

When dissimilar joints are made between CSEF steels (ferritic to ferritic), stresses developed at the joint interface are low because their coefficients of thermal expansion are low and their thermal conductivities are high. When exposed to PWHT or service temperatures, such joints undergo significant redistribution of interstitial C and N and modification of the microstructure. The common outcome is an enrichment of C in the higher Cr side, associated with a harder matrix and a higher amount of carbides. A depleted zone is left in the adjacent layer (fusion line) with lower carbide fraction (gone into solution). This softened zone behaves in the long term similar to the FG(IC) HAZ, with unoptimal precipitate distribution, triaxility of stress and accumulation of deformation. As a consequence, premature failure of DMW has been reported under creep service.

Mitigation of carbon migration is approached mostly by using a Ni alloy consumable that with appropriate chemistry is able to dilute the alloying element coming from the sides without forming hard microstructure or detrimental precipitates. Ni matrix effectively reduces the migration, acting as a diffusion barrier. Thermal expansion coefficient is also not much different from ferritic steels. Several choices are possible, with more experience accumulated using Ni alloys 625 and 617. For joining ferritic to austenitic steels, EPRI P87 filler metal has been tested, demonstrating good elevated temperature properties, and it promises an improvement in cross-weld rupture life between CSEF steels and austenitic stainless steels. Little tendency for C migration or detrimental carbide formation has been documented when EPRI P87 filler metal was welded with a 9%Cr CSEF steel and austenitic stainless steel.

Another approach is to use a transition piece made of Ni alloy 800 to be welded on both sides to the dissimilar sides. If the weldments has to be given PWHT, usually the ferritic sides are buttered with suitable filler metal (eg, Ni based) prior PWHT, and then joined to the other.

9.2.4.2 Weldments between low-Cr bainitic grades or between high-Cr martensitic grades

Such joints are recurrent, for example, in the membrane walls transition between sections made out of different low-Cr grades (eg, lower made out of T11 with T22/T23/T24). The filler material mostly matches Gr. 11 steel. Preheating and PWHT schedules are chosen according the more alloyed BM side.

9.2.4.3 Weldments between high-Cr martensitic grades

The newest designs using Gr. 92 steel also use components made of Gr. 91 (or E911, or even cast steels) that are required to be welded together. Considering the affinities, either a 91 or 92-type WM would be a possible choice, with the former most probably less expensive and of better availability. PWHT can be adjusted to meet both sides requirements.

9.2.4.4 Weldments between low-Cr and high-Cr grades

Such joints are common in transition between the membranes and the headers, or between turbine rotor sections. In principle, five options are possible for choosing the WM:

- matching the lower Cr alloy side
- matching the higher Cr alloy side
- using a low-Cr, low-C consumable with strong carbide formers (B23, B24)
- an intermediate Cr composition (5 or 7% Cr)
- a nickel alloy consumable (617, 625)

Generally, the task is accomplished using a filler material of the lower grade involved or an intermediate grade, on the ground that one needs to match the strength of the weaker alloy. Preheating and PWHT choice would be driven from the BM more alloyed, but modification is done to reconcile the different metallurgical behavior. Thus, often the lowest permissible temperature for the more alloyed steel is used with time appropriate for sufficient tempering and stress relief (eg, 720–730°C for Gr. 91, 92 welded with Gr. 22) without overtempering the lower alloyed grade. One common difficulty is to avoid the WM carbon migration toward the high-Cr side during the PWHT and the high temperature service, which has more affinity; the outcome is a C-enriched HAZ and a loss of C in the WM, both possible sources of lack of adequate mechanical properties in the short and long term. One possible solution is the use of Ni-based filler material.

9.2.4.5 Weldments between martensitic and austenitic grades

The situation arises when connecting austenitic reheater tubes to the martensitic headers or main steam pipework. The transition WM sometimes is of the 309H type if the service is capable of tolerating the dilution between the ferritic and austenitic side. Preheating and PWHT are governed by the requirements of the high-Cr martensitic grade (Fig. 9.33). More frequently, a Ni consumable is used with more favorable behavior for metallurgical compatibility, long-term creep strength and ductility. Carbon migration is reduced to a minimum, and PWHT is well tolerated. PWHT can be detrimental to the austenitic side; the martensitic side must be buttered and given the PWHT before filing the groove. Compositions classified under the AWS standard as ENiCrFe-2 (alloy 82) and ENiCrFe-3 (alloy 625) are mostly used (Fig. 9.34), or the EPRI 87 filler material. EPRI P87 is not yet included in the EN codes, thus its usage may be limited in European projects. The decarburated/carburated zone is very narrow (Figs. 9.35 and 9.36).

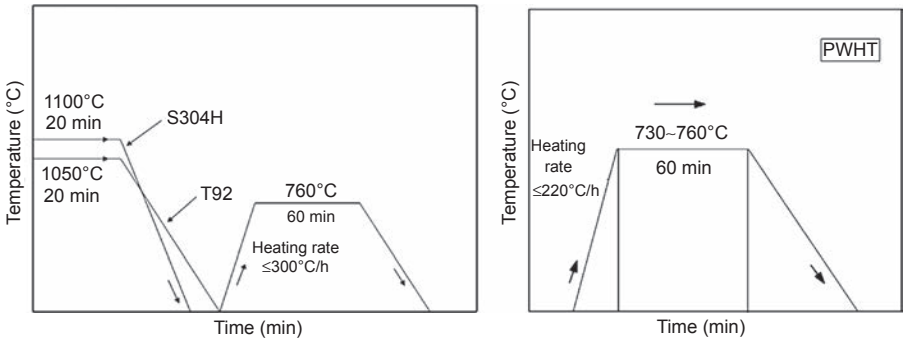


Figure 9.33 Schematic diagram of heat treatment processes of T92 and S304H steels. Schematic diagram of PWHT process of T92/S304H dissimilar materials joints made on tubing [34].

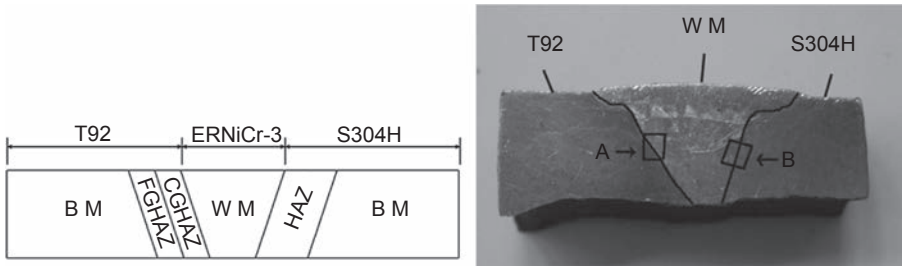


Figure 9.34 Schematic diagram of T92/S304H dissimilar materials joints [34].

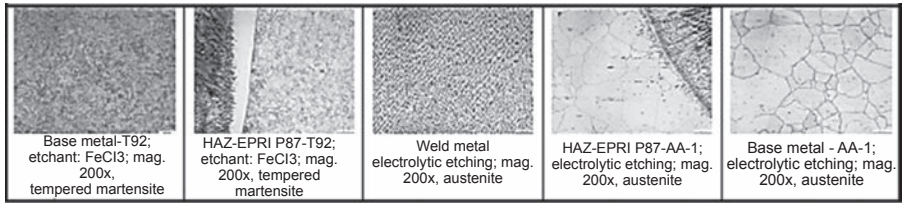


Figure 9.35 Results of macro and microscopic metallographic tests of dissimilar butt joint made of TEMPALOY AA-1 and T92 (EPRI 87 filler material) [35].

9.2.5 Repair welding

This topic has recently gained great attention driven by the demand for alteration of existing designs or repair/life extension. The dominant features of this activity are:

- The difficulty to perform local PWHT when the repair is done in situ and the metallurgical effect on BMs already been exercised.
- The difficult weldability associated with material already degraded after prolonged high-temperature service. Fusion welding always requires a minimum ductility to avoid cracking issues. Unfortunately, metallurgical transformations after long high-temperature service exhausts virgin material ductility (or impairs impact toughness), making the repair approach problematic.

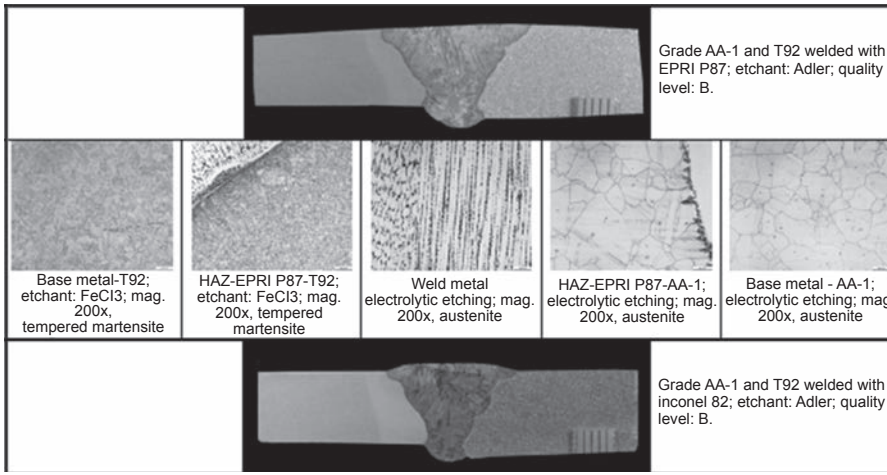


Figure 9.36 Dissimilar welded joint characterization (TEMPALOY AA-1 and T92 with alloy 82 filler metal) [35].

When it is possible to perform PWHT or the weldments are not required to be given (eg, austenitics), the welding procedure does not differ from the first manufacturing practice. Manual welding is mostly used (MMA or GTA). Anyway, even if possible, repeated PWHT thermal cycles (such as in weld repair) may have a negative effect on the life of a given component. When PWHT it is advisable (Cr steels) but impractical, the task is approached with the temper bead technique, in which the HAZ coarse-grain hard and brittle microstructure of the repair layer is tempered by the subsequent layer without having time to develop hydrogen induced cracking. The process has been added for qualification to Section IX of the ASME BPVC.

9.2.6 Principles of weld metal development for creep-resistant USC steels

The basic aspect pertains to the ability to develop mechanical and technological properties matching the relevant base steel being joined. The baseline is a similar alloy system for developing adequate creep strength. Anyway, the WM is not amenable to the same heat treatment of the BM semifinished products, and the molten pool solidification results in coarser dendritic microstructure. Corrections are therefore made to compensate. Basic aspects to be considered are these:

- For any method different from GTA, there is a need for adding deoxidant elements for preventing CO porosity in the WM (Mn, Si, Al, Ti, Zr alone or in combination).
- There is a presence of higher amounts of nitrogen and oxygen, depending on the specific process, due to the contact with the atmosphere of the weld pool. Contents may vary depending of the type of protection (ie, if welding occurs under inert/active gas, or a slag, or both). However, it is anticipated that higher variation is obtainable with respect to the BM processing.

- For martensitic grades, depending on the WM composition, δ-ferrite may form and be present after cooling, resulting in a detrimental effect on toughness and creep resistance. Mn, Co, and Ni are usually added to the consumable for suppressing that tendency (as evaluable with the formula):
  $Cr_{eq} = Cr + 6Si + 4Mo + 1.5W + 11V + 5Nb + 12sol.Al + 8Ti - 40C - 2Mn - 4Ni - 2Co - 30N - Cu\ (mass\ \%) < 9 \div 10\%$
- Ni and Mn additions have a side effect on the WM A_{c1} temperature. This effect is especially problematic with 11% Cr content.
- The carbon content is usually slightly lower than the parent material to control the hardenability of the WM.
- All slag-forming consumables for welding CSEF steels shall be H4 or H5 grade (ie, the lowest) with regard to the diffusible hydrogen content. Seamless cored wires are therefore preferred. SAW agglomerated fluxes are preferred with high basicity index (B.I. = 2.7–3).
- A ferritic WM subjected to PWHT is predicted to have a final lower notch toughness (at the BM same composition; GTA welds possess the most favorable situation compared to slag-forming processes). This behavior is largely attributable to the typical WM inclusions content, higher for SMAW, SAW and FCAW WMs. While an optimized welding procedure is also important for obtaining acceptable properties, consumables are usually over-alloyed to compensate for such behavior by adding Ni. Minimum WM notch toughness is required to be >27 J (average) at the testing temperature for equipment manufactured under by the PE Directive or other corporate specifications. Si, N, B, Ti, and Nb excessive additions are generally recognized to lead to inferior toughness (also because they promote the possible formation of delta ferrite).
- For martensitic grades, the WM must be capable of effective PWHT at temperature lower than BM tempering conditions. On the other side, Mn + Ni additions promote lower A_{c1} temperature; additions must be carefully controlled to avoid a WM A_{c1} temperature close or under the PWHT temperature and the consequent detrimental formation of austenite during the tempering.
- Boron additions are today a preferred option for enhancing creep strength in modified 9–11% Cr steels. Unfortunately, high B content is detrimental for WM toughness and solidification cracking tendency.
- It can be expected that control of the WM nitrogen content (balance absorption/desorption from the arc and weld pool) plays a crucial role where this kind of alloying is exploited.
- To enhance weldability, tramp elements (P, S mainly; also Sb, As, Sn, Bi, Pb, Tin for bainitic steels) are to be kept at the lower range as technically feasible. This is normally achievable in the filler consumables by a vacuum melting practice fabrication for the wires or electrode cores and starting from pure raw materials. Addition of iron powder for enhanced deposition efficiency is therefore discouraged. This aspect is often controlled specifying (10P + 5Sb + 4Sn + As)/100 = X < 15 (mass ppm), Mn:S > 50.
- Where precipitation strengthening is used for creep resistance purpose (as in CSEF steels), WM variations in alloying elements forming or influencing the formation of carbides, carbonitrides, nitrides, precipitates (MX) or other phases (Laves) can lead to a range of all-weld-metal (AWM) creep properties, welding and processing factor being equal. In this regard, content of C, N, Nb, B, V, Ti, Al, and Cu elements should not be allowed to be excessively low in the actual WM composition from the reference. This behavior is also reflected in the scatter band normally recorded when testing AWMs for creep strength.

9.2.7 Damage of weldments subjected to high-temperature service, mechanical properties, creep behavior

The fusion weldments basically experience the same thermal, mechanical and environmental loads of the adjacent base materials. However, the specific resistance of the welded area is seldom equivalent to the parent wall; while higher properties are almost always useless, inferior properties often govern the design and the lifetime of the welded structure. Variation in properties is due to the slightly different chemistry, the thermally affect microstructure, the presence of imperfections, and different thermo-physical behavior (dissimilar welds).

9.2.7.1 Oxidation (fireside/steam side), welding overlay

Usually the resistance to either fireside or steam corrosion is governed by the metal composition at the exposed surfaces subjected to the influence of the combustion fumes (that also contain water steam) or the steam, respectively; in this respect, Cr content has by far the most beneficial influence due to its oxide scale; in particular, above 10–11% Cr, the corrosion rate becomes very low. Thus, it is especially important that the weld surfaces have Cr content not lower than the adjacent base material with the lowest content (>8.5% on tubing, anyway). This usually ensures adequate hot corrosion resistance behavior of the weldments, matching the relevant steel grade being joined, thus avoiding preferential thinning of the WM. It was recently evidenced on 9–12% Cr steels that higher Mn and Si may be also helpful.

Welding overlay of semifinished product is sometime used on boiler members exposed to harsh fumeside corrosion, where the BM composition could not guarantee adequate service life. Ni alloys are mostly used due to the metallurgical compatibility with the underlying base material and high Cr content.

9.2.7.2 Short-term strength behavior

Weldments subjected to high temperature service have reduced mechanical strength compared to room *T*; this effect, of course, is considered at the design stage by adequate rerating of the properties with respect to room temperature figures. From the metallurgical point of view, no correction is made for the HAZ or WM, as the matching compositions and the microstructure evolution following the thermal cycle and the PWHT ensures no additional softening (however, a reduction factor can be introduced depending on the extent of NDT performed on the welded member).

9.2.7.3 Ductility and toughness

The ability of the welded members to withstand deformation accommodations or resist brittle fracture is of the utmost importance (for bainitic and martensitic steels). These behaviors must be possessed in the entire range of the temperature encountered during service, including shut-down operations where the weldments can be stressed at room temperature or even subzero (eg, during hydro-testing of the equipment). For a given WM grade, actual composition, welding method, parameters and

PWHT schedule have a profound influence on these properties. Moreover, the initial properties are usually degraded over time due to the in-service microstructural evolution and precipitates coarsening. The different classes of USC steels are differently affected.

To ensure that the weldments enter in service with a sufficient ductility and notch toughness, most construction codes, material standards and regulator authorities specify minimum values of the elongation-at-fracture recorded during the tensile test and the absorbed energy during the Charpy-V test. Minimum figures often specified for notch toughness are 27, 34, or 47 J (average absorbed energy of three specimens) at room temperature or lower. In this regard, welds of the 9–12% Cr class are the most difficult. Adequate knowledge has developed on this topic:

- Higher PWHT temperatures are beneficial for better toughness, at the expense of the tensile strength and, less markedly, the creep strength.
- Lower WM oxygen content usually leads to better toughness due to lower amount of nonmetallic inclusion, all other factors being equal. In this respect, slagless welding methods are favored (GTA overall) (Fig. 9.37).
- Coarse microstructure, coarse precipitates are detrimental.
- In multilayer weldments, it has been shown the layer thickness influenced the notch toughness; thin layers give higher notch toughness due the higher fraction of refined grain zones. The same holds for the HAZs (Fig. 9.38). For very thick weldments, a difference between notch locations has also been evidenced (Fig. 9.39).

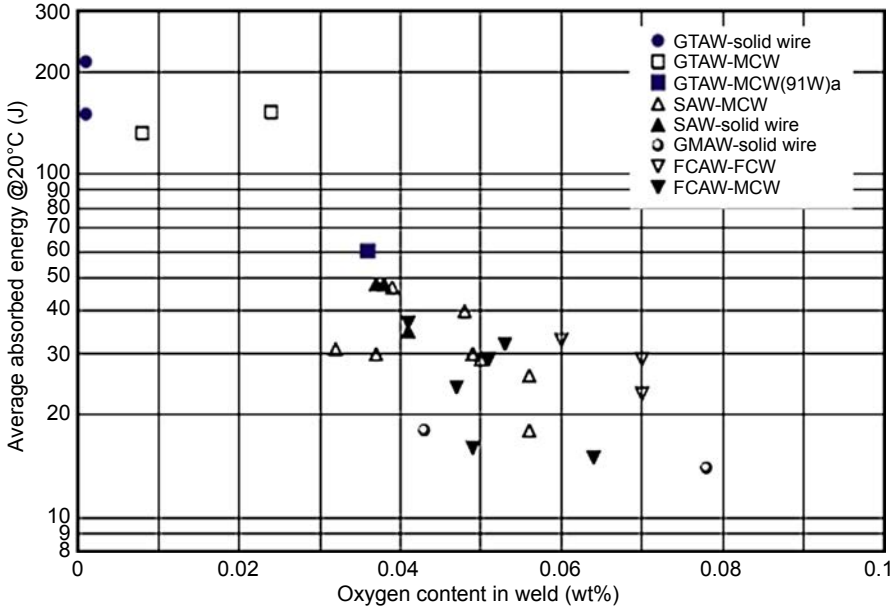


Figure 9.37 Effect of oxygen content on toughness for selected Grade P91 weldments [36].

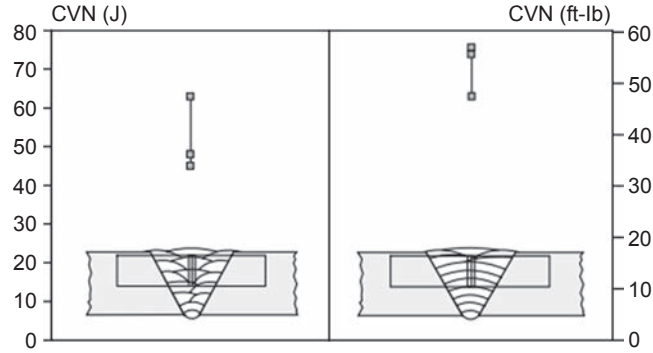


Figure 9.38 Toughness at RT in relation to the welding technique (SMAW All Weld Metal for grade 91) [37].

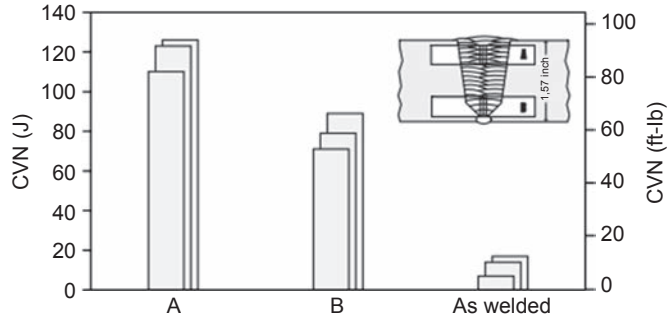


Figure 9.39 Toughness in relation to the specimen location at SAW pipe joint on P91 steel [37].

9.2.7.4 Hydrogen delayed cracking, stress corrosion cracking

High-Cr steels are especially sensitive to the weld diffusible hydrogen. Upon completion of the welding operation, the assembly is left to cool down, allowing complete martensitic transformation. Before the PWHT, hardness in the as-welded area can be as high as 400–450 HV. If the PWHT is not given immediately, it is a safe choice to mildly reheat the assembly at moderate temperature (250–400°C, at which no microstructural transformation occurs) for sufficient time, allowing for hydrogen baking out.

There were instances of P91 piping left in moist air before PWHT in which stress corrosion cracking (SCC) occurred in the weld area. Such a possibility should be avoided by proper management of the manufacturing operations and storing welded members in dry areas of the shop.

Enhanced low-carbon bainitic steels (Gr. 23, 24) have presented in the first installations serious problems of stress corrosion cracking on in-service welded membrane walls that were not given any PWHT (Fig. 9.40), utilities being initially unaware of this possibility. The high hardness of the weld area at root of the joint promoted the

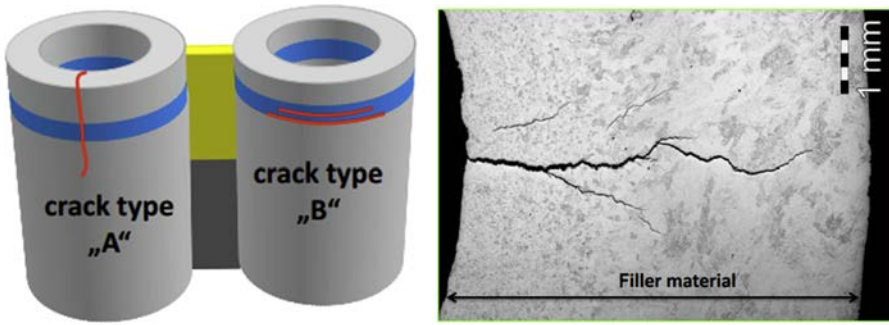


Figure 9.40 Stress corrosion cracking of Grade 24 steel welds for water wall panels [38].

cracking mechanism that has been identified as either induced by hydrogen or anodic condition. Recently, a mild stress relief (eg, 500°C, not affecting the microstructure) has been proposed to ease the issue. Additional requirements on the welding procedure and tighter control of the layer strategy and the heat input are also directed to avoid hard zone at the weld root on tubing welds.

9.2.7.5 Temper embrittlement, stress relief cracking

Weldments of Gr. 22, 23, and 24 are known to be prone to temper embrittlement after PWHT. This issue is controlled by specifying very low level of tramps element in the WM (a convenient index can be the X factor: $(10P + 5Sb + 4Sn + As)/100 = X < 15$ (mass ppm)).

For CSEF bainitic steels, stress relief cracking is recently being considered as a possible failure mechanism during high-temperature exposure (as during PWHT). Influence of the member thickness, HAZ/WM coarse grain size, and bevel angle has been proposed.

9.2.7.6 Thermo-mechanical fatigue

Weldments are most often located at steel member discontinuities acting as stress concentrators, or they can even join materials with markedly different physical properties (eg, thermal expansion in dissimilar welds between ferritic and austenitic grades). As a consequence, thermal fatigue due to repeating thermal load oscillations (low-cycle fatigue) can severely damage the weldments, thick ones being more subjected [46]. This issue is usually addresses at the design stage. Studies evidencing the influence of filler materials chemistry are at the early stage.

9.2.7.7 Creep

The introduction of weldments inside a member subject to high temperature service results in inferior creep life if the weldments are not given a full heat treatment to restore the BM-like microstructure (like shown in Fig. 9.41). Unfortunately, this is by far the most common situation due to the practical difficulty of giving full N+T heat

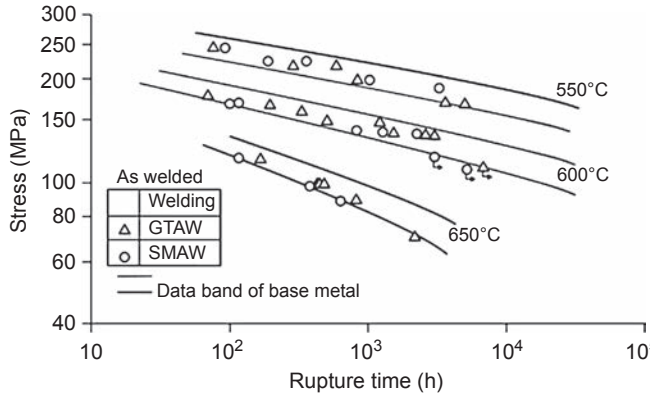


Figure 9.41 Creep rupture data for T23 cross-welds in the as-welded condition [39].

treatment to the welded equipment. Welded semifinished products (eg, tubulars) are usually given full N + T (or solubilization for austenitics).

Similarly to BMs, creep life of weldments is the main design criteria for weldments subject to high-temperature services. Design criteria are given considering the presence of the weld inside the member. Usually, no design credit is given for the following aspects:

- specific welding method (ie, no difference between GTA, SMA, SA)
- actual WM chemistry
- actual BM chemistry
- PWHT schedule
- welding procedure details (preheating/interpass, bevel geometry)

9.3 Weldments design, codes and standards, approvals

In the design of a welded member, the effect of the process on the mechanical properties of the WM and HAZ must be considered. Where it is known that specific weld properties cannot match the BM, behavior-correcting factors are introduced, depending on the alloy system, the PWHT performed (N + T or stress relief/tempering), and the loading direction. Guidance is given in the following codes or national equivalents:

- ASME Boiler Pressure Vessel Code, Sec. I and III
- ASME B31.1 Power Piping Code
- European Pressure Equipment Directive (PED/EN13445 standard)

Dealing with short-term properties, tensile and yield strength of the WM can generally match relevant BM at both room and service temperature. Ductility and elongation are only required to be above a certain level to allow accommodation of plastic strain to the manufacturing operation or to avoid brittle fracture during equipment pressure testing or under residual stress loads.

The ratio of creep resistance of the welded joint to the creep resistance of the base metal is called the Weld Stress Factor (WSF). WSF is the most important information for welds in the material design codes as time-dependent properties. In general, boilers require a WSF of 0.8–0.85 over 100,000 h (11.41 years). Dealing with creep strength, the European Creep Collaborative Committee (ECCC) defined WSF and similarly SRF (stress reduction factor) in their ECCC Recommendations (Volume 2 Part IIb) as follows [40]:

$$\text{SRF (t,T)} = (R_{u/t/T} - R_{u(w)/t/T})/R_{u/t/T};\ \text{WSF}\,(t, T) = \frac{R_{u(w)/t/T}}{R_{u/t/T}}$$

where $R_{u/t/T}$ is the creep rupture strength of base material samples at a time t and temperature T and $R_{u(w)/t/T}$ is the creep rupture strength of cross-weld samples at a time t and temperature T. Lack of long-term creep rupture data makes the determination of accurate WSF very difficult in these creep regions.

Extrapolation of WSF from short-term creep rupture tests leads the risk of overestimation of long-term creep properties and is not recommended. This emphasizes the necessity for long-term creep rupture data of base material and welded joints. Guidance on WSF extrapolation is given in EN 13445-2:2002 standard; for a 200,000 h life service, a 7 years creep testing program is recommended for unwelded BMs, while for welds with HAZ type IV failures no extrapolation is allowed.

In Fig. 9.42, WSFs for several ferritic steel grades with PWHT at different temperatures are shown [41]. A reduction of up to 50% in creep rupture strength of weldments compared to base material creep rupture strength emphasizes the importance of further research in this field and a correct consideration of WSF during design stage of new USC equipments.

It is not surprising that the alloy systems most affected by such derating are those in which the BM is heavily creep-strengthened by precipitates, as for Gr. 23, 24, 91, 92, and 122 (Fig. 9.43); after the welding cycle, the precipitation composition, size distribution, amount and distribution can be significantly altered, leading to poorer

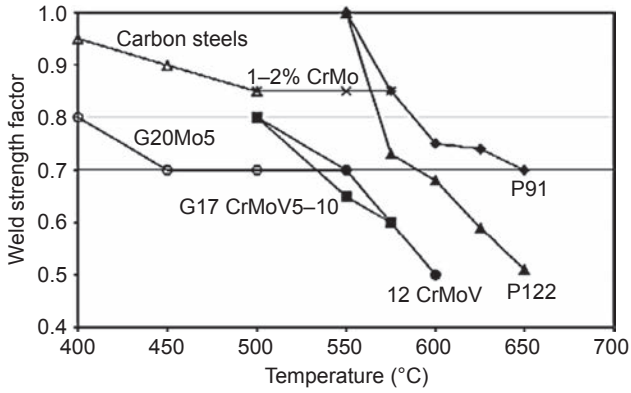


Figure 9.42 Weld strength factors for the 100,000 h creep rupture strength of different ferritic steel grades [41].

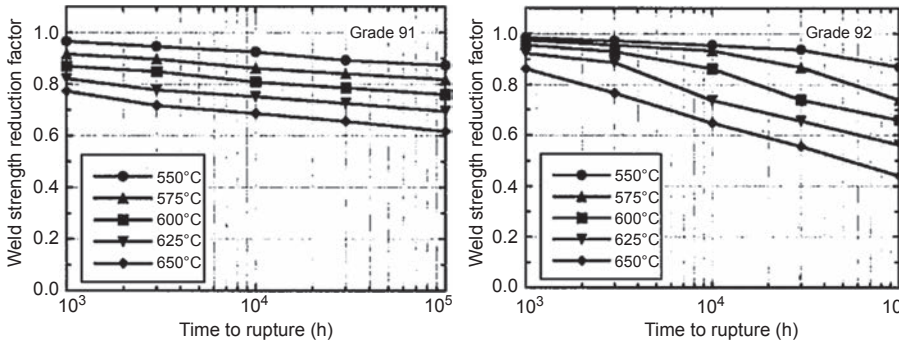


Figure 9.43 Changes in the weld strength reduction factor of Grade 91 and 92 steels with increase in creep rupture life over a range of temperatures from 550°C to 650°C [42].

properties compared to the optimized BM. This has profound implications for any new materials development in this field if the original heat treatment cannot be replicated on the weldments. Materials whose creep resistance is mostly based on solid solution strengthening (as most of austenitic grades) are therefore predicted to have WSFs close to 1.

Tables 9.6 and 9.7 show, respectively, the revisited allowable stress and the WSF for CSEF steels from 100,000 h cross-weld uniaxial creep tests. Some design codes use other tests, such as cross-weld multiaxial creep tests, to define weld properties. However, fatigue damage, and therefore creep-fatigue damage, has not been factored into the design codes for older coal-fired power plants. Revision of WSFs is continuously ongoing as new long-term creep results on weldments become available [41].

9.4 Arc welding technology and consumables for USC materials

9.4.1 General aspects

A variety of stick electrodes, solid or cored wires and fluxes are available from major filler materials manufacturers following AWS, ISO, EN or national specifications for most USC materials, though some have a restricted choice of type and/or size dictated from the specific use on small tubes. For some grades, classifications are available on a commercial basis only, or even by customer specification (similar to "G" or "Z" classification in AWS and ISO/EN standards).

Whenever possible, standards may serve as valid guidance in selecting consistent testing conditions for the production of the coupons necessary to establish WM chemical and mechanical properties of the deposits (specific requirements are given for the welding condition and the passes arrangement). AWS 5.01 "Filler Material Procurement Guideline" or the analog ISO 14344 provide guidelines to specify and purchase adequate welding material (either with classification or user-defined). Specified welding parameters and testing conditions are based on long industrial experience and may

Table 9.6 Revisited allowable tensile stress of the steels regulated in the thermal power standard code METI (Japan) [42]

Material			Allowable stress (MPa)				
Type	**Form**	**Thickness**	**550°C**	**575°C**	**600°C**	**625°C**	**650°C**
91	Plate, pipe, forging	≤76 mm	94	81	63	45	29
		>76 mm	94	81	62	45	29
	Tube		94	83	62	44	29
92	Pipe, forging		107	101	78	56	30
	Tube		107	101	76	55	30
122	Plate, pipe, forging		106	100	68	46	27
	Tube		111	102	66	46	27

Table 9.7 Proposed weld strength reduction factor for various USC grades [42]

Material		Weld strength reduction factor				
Type	**Form**	**550°C**	**575°C**	**600°C**	**625°C**	**650°C**
91	Plate, pipe, forging	1.00	0.87	0.79	0.74	0.70
92	Pipe, forging	1.00	0.80	0.66	0.54	0.50
122	Plate, pipe, forging	1.00	0.73	0.68	0.59	0.51

be used as starting point for the development of the user welding procedure. Minimum mechanical properties stated are nowadays more and more frequently supplemented by proprietary requirements in search of the best efficiency of the welded construction.

It was shown how filler materials for steels (either low alloyed, martensitic, or austenitic) used in USC manufacturing are formulated to give a weld deposit with chemistry much similar to the relevant base materials being joined. This choice aims to promote in the WM comparable creep rupture strength and short-term tensile properties, sufficient low-temperature impact strength (eg, measured by Charpy-V notched bars), and ductility (possibly also after prolonged service at high temperature). Actual heat analysis for solid wires (as used in GTA, GMA and SA processes) is normally sufficient in preparing the welding procedure or for assessing the properties of the weldments. Slag-forming consumables give weld deposits whose mechanical properties are more affected by the slag system used. This is especially true for toughness, so lot-to-lot testing may be necessary, including mechanical properties. On WM deposits, accurate methods for measurements of key aloying elements include the combustion technique (CA) for carbon and nitrogen and either optical emission spectrometry (OES) or X-ray fluorescence analysis (XRF) for non-interstitials (Cr, Mo, Mn, Si, W etc.).

Regardless of the steel grade being considered, the WM will have a relatively coarse microstructure; to get an acceptable ductility and toughness, it will be very often subject to a PWHT. For Cr steels, this implies tempering at a temperature lower than the base material. In general, the higher the fraction of creep-strengthening precipitates, the lower the impact toughness will be, other factors being equal. Thus, WM creep properties and notch toughness are conflicting properties that are balanced through an elaborate chemistry. In general, WM mechanical properties are strongly affected by the undiluted chemistry, while the welding method and the typical welding parameters associated plays a secondary role, also due to the levelling effect of the PWHT. A notable exception concerns the impact toughness, where the characteristic WM oxygen content (promoting higher nonmetallic inclusion amount) and the layer thickness in multipass welding have a significant effect. Non-slag-forming consumables are usually favored when low temperature toughness is required due to the intrinsic lower inclusions potential, with basic slag-forming fillers next.

Whenever alloyed ferritic steels are involved (invariably above 2% Cr), limitation of the diffusible hydrogen is of the outmost importance to prevent delayed cracking and thus matching consumables are always of the low-hydrogen type. This aspect is relaxed dealing with austenitic steels. Alongside, the tendency to solidification or crater cracking is minimized by low residual elements content in the WM.

Care should be taken to see that the weld metal contains very low concentrations of tramp elements such as As, Sn, Sb, Pb, S, and P. If S or P is at a maximum of 0.010%, crater cracking and grain boundary cracking can be avoided.

9.4.2 MMAW (SMAW)

Manual metal arc electrodes (MMA) are available from major consumable manufacturers and classified under several standards, the dominant ones being AWS/SFA A5.5 (low-alloyed steels), AWS/SFA A5.4 (stainless steels) and the European and Japanese equivalents. Most of grades have been recognized since a long time; recently (ed. 2015), products for T/P 92 welding were recognized by ASME/AWS standard under the "B92" designation. Nomenclature follows the relevant base material; classification is based on AWM chemistry and room-temperature minimum mechanical properties (see Tables 9.8 and 9.9). Normal diameters are 2.5, 3.2, 4.0, and 5.0 mm.

In general, chemistries match the relevant base materials with modification on some key alloying elements. However, more original concepts are also promoted, like the use of cobalt to partly replace nickel on 9Cr-class WMs. It is recognized Co does not depress A_{c1} temperature, so the WM is more forgiving in this respect during the PWHT. Ni addition has traditionally been made to enhance the room-temperature notch toughness, but Ni-free formulations also exist; for Gr. 91 WMs, the limit to the Mn + Ni content has been recently lowered to 1.2% in the ASME BPV Code, with some proprietary specifications already demanding Mn + Ni lower than 1.0%. As to the welding position, most of the observations made are on welds produced in the flat (1G) position. A loss of toughness is often observed in shielded metal arc welds

Table 9.8 Classification of SMAW electrodes for welding USC austenitic steels (ASME boiler pressure vessel code–specifications for welding rods, electrodes, and filler metals. SFA-5.4/SFA-5.4M specification for stainless steel electrodes for shielded metal arc welding)

Chemical composition requirements for undiluted weld metal													
AWS classification[c]	UNS number[d]	Weight percent[a,b]											
		C	Cr	Ni	Mo	Nb (Cb) plus Ta	Mn	Si	P	S	N	Cu	Other[e]
E308H-XX	W30810	0.04–0.08	18.0–21.0	9.0–11.0	0.75	–	0.5–2.5	1.00	0.04	0.03	–	0.75	
E308L-XX	W30813	0.04	18.0–21.0	9.0–11.0	0.75	–	0.5–2.5	1.00	0.04	0.03	–	0.75	
E308MO-XX	W30820	0.08	18.0–21.0	9.0–12.0	2.0–3.0	–	0.5–2.5	1.00	0.04	0.03	–	0.75	
E308LMo-XX[f]	W30823	0.04	18.0–21.0	9.0–12.0	2.0–3.0	–	0.5–2.5	1.00	0.04	0.03	–	0.75	
E309-XX	W30910	0.15	22.0–25.0	12.0–14.0	0.75	–	0.5–2.5	1.00	0.04	0.03	–	0.75	
E309H-XX	W30910	0.04–0.15	22.0–25.0	12.0–14.0	0.75	–	0.5–2.5	1.00	0.04	0.03	–	0.75	
E16-8-2-XX	W36810	0.10	14.5–16.5	7.5–9.5	1.0–2.0	–	0.5–2.5	0.60	0.03	0.03	–	0.75	
E347-XX	W34710	0.08	18.0–21.0	9.0–11.0	0.75	8×C, min to 1.00 max	0.5–2.5	1.00	0.04	0.03	–	0.75	

[a]Analysis shall be made for the elements for which specific values are shown in the table. If, however, the presence of other elements is indicated in the course of analysis, further analysis shall be made to determine that the total of these other elements, except iron, is not present in excess of 0.50 percent.
[b]Single values are maximum percentages.
[c]Classification suffix -XX may be -15, -16, -17, or -26. See Clause A8 of Annex A for an explanation.
[d]ASTM DS-56H/SAE HS-1086, Metal & Alloys in the Unified Numbering System.
[e]Analysis for Bi is required to be reported if intentionally added, or if it is known to be present at levels greater than 0.002%.
[f]E308LMo-XX and E309LMo-XX were formerly named E308MoL-XX and E309MoL-XX, respectively.

Table 9.9 Classification of SMAW electrodes for welding USC low-alloyed steels (ASME boiler pressure vessel code–specifications for welding rods, electrodes, and filler metals. SFA-5.5/SFA-5.5M specification for low-alloy steel electrodes for shielded metal arc welding) [i,j]

Chemical composition requirements for undiluted weld metal												
AWS classification[c]		UNS number[d]	Weight percent[a,b]								Additional elements[e,f]	
A5.5	A5.5M		C	Mn	Si	P	S	Ni	Cr	Mo	Type	Amount
E9015-B23 E9016-B23 E9018-B23	E6215-B23 E6216-B23 E6218-B23	K20857	0.04–0.12	1.00	0.60	0.015	0.015	0.50	1.9–2.9	0.30	W V Nb B Al Cu N V Nb	1.50–2.00 0.15–0.30 0.02–0.10 0.006 0.04 0.25 0.05 0.15–0.30 0.02–0.10
E9015-B24 E9016-B24 E9018-B24	E6215-B24 E6216-B24 E6218-B24	K20885	0.04–0.12	1.00	0.60	0.020	0.015	0.50	1.9–2.9	0.80–1.20	Ti B Al Cu N V	0.10 0.006 0.04 0.25 0.07 0.15–0.30
E9015-B91K[h]	E6215-B91K[h]	W50425									Cu	0.25

Table 9.9 Continued

Chemical composition requirements for undiluted weld metal												
AWS classification[c]		UNS number[d]	Weight percent[a,b]								Additional elements[e,f]	
A5.5	A5.5M		C	Mn	Si	P	S	Ni	Cr	Mo	Type	Amount
E9016-B91K[h]	E6216-B91K[h]	W50426	0.08–0.13	1.20	0.30	0.01	0.01	0.80	8.0–10.5	0.85–1.20	Al	0.04
E9018-B91K[h]	E6218-B91T[h]	W50428									Nb	0.02–0.10
											N	0.02–0.07
											W	1.50–2.00
											V	0.15–0.30
E9015-B92[g]	E6215-B92[g]										Nb	0.02–0.08
E9016-B92[g]	E6216-B92[g]	W59016	0.08–0.15	1.20	0.60	0.020	0.015	1.00	8.0–10.0	0.30–0.70	B	0.006
E9018-B92[g]	E6218-B92[g]										Al	0.04
											Cu	0.25
											N	0.03–0.08

[a]Single values are maxima, except where specified otherwise.
[b]Weld metal shall be analyzed for those elements for which specific values are shown. Other elements listed without specified values shall be reported, if intentionally added. The total of these latter unspecified elements and all other elements not intentionally added shall not exceed 0.50%.
[c]The suffixes A1, B3, C3, etc. designate the chemical composition of the electrode classification.
[d]SAE-HS–1086/ASTM DS–56, Metals & Alloys in the Unified Numbering System.
[e]Analysis for boron is required to be reported for any weld metal if it has been intentionally added or is known to be present at levels greater than 0.0010%.
[f]Analysis for cobalt is required to be reported if intentionally added, or if it is known to be present at levels greater than 0.20%.
[g]Mn + Ni shall be 1.40% max.
[h]The E90XX-B91 [E62XX-B91] classifications were formerly classified as E90XX-B9 [E62XX-B9] in AWS A5.5/A5.5M:2006.
[i]The letters "(X)XX" ["XX"] used in the classification designations for all electrodes in this table stand for the various tensile strength levels (70, 80, 90, 100, 110, and 120 ksi [49, 55, 62, 69, 76, and 83 MPa × 10]), of weld metals.
[j]In order to meet the alloy requirements of the "G" group, the undiluted weld metal shall have the minimum of at least one of the elements listed in this table. Additional chemical requirements may be agreed upon between the purchaser and supplier.



Figure 9.44 SMAW and SAW welding on Grade 23 pipe (Air Liquide Welding) [15].

(SMAW) made in vertical (3G) and overhead (4G) positions due to bead control problems and lack of tempering and grain refinement.

Electrodes are most often available for usage with direct polarity (DCEP); however, products that can be used with AC are also available. Products for low-alloyed steels are of basic slag lime type (designation suffixed with "-16"; lime type, suitable for DCEP), while products for austenitic grades can be of the lime type or rutile slag (the latter suffixed with "-17"; titania type, suitable for AC or DCEP). Suitability to weld fixed pipework (ASME 5G/6G position) is crucial for on-site usage (see Fig. 9.44). To prevent hydrogen-induced cracking on ferritic weldments, preheating and interpass temperature must be maintained from beginning of welding until the PWHT. Codes and standards dictate the minimum level of preheating needed, 250°C being a typical figure. Any adsorbed moisture has to be removed by redrying according to the manufacturers recommendations. Products with low moisture adsorption are most preferred (H4R suffix).

As always when the properties are strongly affected by minor elements additions, it is of the utmost importance to ensure elements are properly transferred to the deposit. Arc length can have a pronounced effect on the droplet oxidation and nitrogen absorption/desorption from the weld pool. This is especially critical when welding pipes in fixed position, a typical application of MMA welding. Low-carbon versions are also available for low-Cr steel fillers to enhance ductility of the deposit and reduce preheating requirements.

Electrodes intended for welding high-temperature USC austenitic steels, including dissimilar welding with ferritic grades (E308H, E316H, E347, E16-8-2 and E309H), can have either basic or rutile slag system, the latter more easily usable and with better seam appearance at the expense of slightly lower impact toughness. Most are suitable for positional welding on fixed pipework. Carbon is minimum specified to provide higher tensile and creep strength at the service temperature. Weld metal delta ferrite content has to be precisely controlled to minimum (5-6 FN) consistent with sufficient resistance to solidification cracking to minimize the effect of sigma phase embrittlement in high-temperature service, taking into account the effect of the base material dilution. E16-8-2 WM (with 3-4 FN) is often preferred when higher hot ductility is desired (especially for welding thick TP347 tubes) or to avoid in-service HAZ cracking and low creep fatigue ductility associated with E347 WM, but only for filling the groove or capping. The root pass is deposited by the GTA process using a higher Cr rod wire to avoid wet corrosion problems during the plant shutdown.

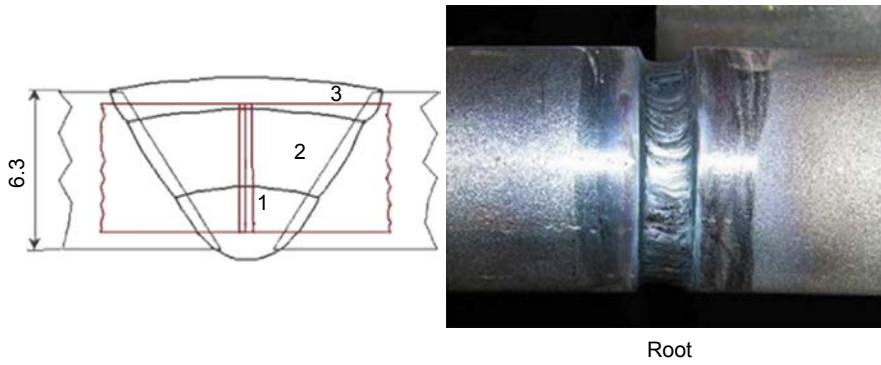


Figure 9.45 GTA welding of T24 boiler tube (38 OD × 6.3 WT mm); the site of the notched test specimen is shown [47]. Three layers with single beads are most often recommended to fill the groove on bainitic steel butt weldments ~6 mm thick.

9.4.3 GTAW (TIG)

This process is widely employed for root welding or small-diameter pipework using DC polarity and argon gas shielding (Fig. 9.45). The composition of the undiluted deposit will be very close to the original wire chemistry, with little or no loss of the intentional alloying elements. Some very minor loss of Si, Mn, and C (about 0.01–0.02%) normally occurs. Most preferred size for manual root welding is 2.4 mm. Gas purge of the backing side is always required (AWS D10.88) for high-Cr steels to protect the root bead from oxidation, until two to three layers are completed. GTAW uses inherently low hydrogen consumable if proper care and cleanliness of the filler product is observed; successful weldments have been performed with reduced preheating temperature compared to slag-forming processes.

The integrity of the GTA deposit can be unparalleled, at the expense of rather low productivity and deposition rate; similarly, AWM short-term properties are the highest among all the methods due to the low oxygen content of the WM (100–200 wt. ppm) and the thin deposited layers. Thus, this method is sometime preferred where very demanding mechanical properties are to be achieved for martensitic steels (eg, 9%Cr steel WM notch toughness even below room temperature).

GTA consumables are always classified based on the steel wire analysis, as given in AWS/SFA A5.28 (low-alloyed steels), AWS/SFA A5.9 (stainless steels) and the European and Japanese equivalents (see Tables 9.10 and 9.11).

9.4.4 GMAW (MIG), FCAW

GMA welding has not gained widespread acceptance in the power industry due to the difficulty in controlling the element transfer across the arc (which is protected with a not inert shielding gas mix). Anyway, it is possible to use the solid wire classified for GTA welding normally made available in spools.

Slag-forming FCA consumables have been more recently introduced for enhanced productivity and ease of use (with rutile slag system), with most interest for fixed

Table 9.10 Classification of solid wires and rods for welding USC austenitic steels (ASME boiler pressure vessel code–specifications for welding rods, electrodes, and filler metals. SFA-5.9/SFA-5.9M specification for bare stainless steel welding electrodes and rods)

Chemical composition requirements													
AWS classification[c]	UNS number[d]	Composition, wt.%[a,b]										Other elements	
		C	Cr	Ni	Mo	Mn	Si[e]	P	S	N	Cu	Element	Amount
ER308H	S30880	0.04–0.08	19.5–22.0	9.0–11.0	0.50	1.0–2.5	0.30–0.65	0.03	0.03	–	0.75	–	–
ER308L	S30883	0.03	19.5–22.0	9.0–11.0	0.75	1.0–2.5	0.30–0.65	0.03	0.03	–	0.75	–	–
ER16-8-2	S16880	0.10	14.5–16.5	7.5–9.5	1.0–2.0	1.0–2.0	0.30–0.65	0.03	0.03		0.75	–	–
ER347	S34780	0.08	19.0–21.5	9.0–11.0	0.75	1.0–2.5	0.30–0.65	0.03	0.03	–	0.75	Nb[f]	10 × C min/1.0 max
ER347Si	S34788	0.08	19.0–21.5	9.0–11.0	0.75	1.0–2.5	0.65–1.00	0.03	0.03	–	0.75	Nb[f]	10 × C min/1.0 max
ER309	S30980	0.12	23.0–25.0	12.0–14.0	0.75	1.0–2.5	0.30–0.65	0.03	0.03	–	0.75	–	–
ER309Si	S30981	0.12	23.0–25.0	12.0–14.0	0.75	1.0–2.5	0.65–1.00	0.03	0.03	–	0.75	–	–

[a]Analysis shall be made for the elements for which specific values are shown in this table. If the presence of other elements is indicated in the course of this work, the amount of those elements shall be determined to ensure that their total, excluding iron, does not exceed 0.50 percent.
[b]Single values shown are maximum percentages.
[c]In the designator for composite, stranded, and strip electrodes, the R shall be deleted. A designator C shall be used for composite and stranded electrodes and a designator Q shall be used for strip electrodes. For example, ERXXX designates a solid wire and EQXXX designates a strip electrode of the same general analysis, and the same UNS number. However, ECXXX designates a composite metal cored or stranded electrode and may not have the same UNS number. Consult SAE HS-1086/ASTM DS-56, Metals & Alloys in the Unified Numbering System for the proper UNS number.
[d]SAE HS-1086/ASTM DS-56, Metals & Alloys in the Unified Numbering System.
[e]For special applications, electrodes and rods may be purchased with less than the specified silicon content.
[f]Nb may be reported as Nb + Ta.

Table 9.11 Classification of solid electrodes and rods for welding USC low-alloyed steels (ASME boiler pressure vessel code–specifications for welding rods, electrodes, and filler metals. SFA-5.28/SFA-5.28M specification for low-alloy steel electrodes and rods for gas shielded arc welding)[j]

Chemical composition requirements for solid electrodes and rods															
AWS classification[b]		UNS number[c]	Weight percent[a]												
A5.28	A5.28M		C	Mn	Si	P	S	Ni	Cr	Mo	V	Ti	Zr	Al	Cu[d]	Other elements total
ER80S-B2	ER80S-B2	K20900	0.07–0.1	0.40–0.70	0.40–0.70	0.025	0.025	0.20	1.20–1.50	0.40–0.65	–	–	–	–	0.35	0.50
ER70S-B2L	ER49S-B2L	K20500	0.05	0.40–0.70	0.40–0.70	0.025	0.025	0.20	1.20–1.50	0.40–0.65	–	–	–	–	0.35	0.50
ER90S-B3	ER62S-B3	K30960	0.07–0.12	0.40–0.70	0.40–0.70	0.025	0.025	0.20	2.30–2.70	0.90–1.20	–	–	–	–	0.35	0.50
ER80S-B3L	ER55S-B3L	K30560	0.05	0.40–0.70	0.40–0.70	0.025	0.025	0.20	2.30–2.70	0.90–1.20	–	–	–	–	0.35	0.50
ER80S-B6[e]	ER80S-B6[e]	S50280	0.10	0.40–0.70	0.50	0.025	0.025	0.60	4.50–6.00	0.45–0.65	–	–	–	–	0.35	0.50
ER80S-B8[f]	ER80S-B_8[f]	S50480	0.10	0.40–0.70	0.50	0.025	0.025	0.50	8.00–10.50	0.80–1.20	–	–	–	–	0.35	0.50
ER90S-B9[g,h,i]	ER80S-B9[g,h,i]	S50482	0.07–0.13	1.20	0.15-0.50	0.010	0.010	0.80	8.00–10.50	0.80–1.20	0.15–0.30	–	–	0.04	0.20	0.50

[a]Single values are maximum.
[b]The suffixes B2, Ni1, etc., designate the chemical composition of the electrode and rod classification.
[c]SAE HS-1086/ASTM DS-56H, Metals and Alloys in the Unified Numbering System.
[d]Copper due to any coating on the electrode or rod plus the copper content of the filler metal itself, shall not exceed the stated 0.50% max.
[e]Similar to former class ER502 in AWS Specification A5.9-93.
[f]Similar to former class ER505 in AWS Specification A5.9-93.
[g]Niobium (Columbium) 0.02–0.10%.
[h]Nitrogen 0.03–0.07%.
[i]The sum of Mn and Ni shall be less than or equal to 1.50% max.
[j]In order to meet the requirements of the "G" classification, the electrode must have a minimum of one or more of the following: 0.50% Nickel, 0.30% Chromium, or 0.20% Molybdenum. The composition shall be reported; the requirements are those agreed to by the purchaser and supplier.

pipework welding of martensitic grades (9Cr). Welding is carried out with an Ar–CO_2 mix and DC+ current; 1.2 mm is the wire diameter mostly used. AWM notch toughness is usually at the lowest range among the various arc welding methods, unless prolonged PWHT is employed, due to the characteristic high oxygen content in the WM (~600 wt. ppm). Formulations result in a WM with a tendency to higher content of Ti and Al than the MMA, SAW or GTA processes. Aluminium is claimed to have a detrimental effect on microstructural stability, and high (~0.03%) levels in parent steels have been reported to induce large Al nitride precipitates, with impaired creep ductility. Titanium is beneficial, as it contributes to the formation of fine MX precipitates, delaying dislocation recovery and thus increasing creep strenght. While deliberate additions of Nb are made to enhance creep strength, increases in Nb in the range 0.1–0.5% have also been shown to have a detrimental effect on the creep strength of 9% Cr parent steels.

The use of a rutile slag system also leads to the associated addition of Nb and V, which are impurities in natural rutile. In previous work on modified 9% Cr weld metals, Nb has been shown to be detrimental to toughness, after a 760°C/8 h PWHT [43].

FCA products are standardized in AWS/SFA A5.29/A5.36 (low-alloyed steels) AWS/SFA A5.22 (stainless steels).

9.4.5 SAW

Where the fabrication is amenable to mechanization (flat position, rotating pipework) SAW method (and its narrow gap variant) it is most often preferred due to the high integrity of the deposit and the good productivity; thus, the usage is mostly oriented to thick pipework made out of high-Cr steels, for tube-to-fin fillet welds on water walls (single bead) or for joining sections of turbine rotors. In these applications an agglomerated basic flux is invariably adopted with wires of limited size (eg, 2.4, 3.2 and 4.0 mm). C, Mn, and Si loss/pickup from the flux with respect to the wire depend mainly on the flux basicity index, with each product having specific behavior. Room-temperature notch toughness is usually inferior to the MMA method, mostly due to the higher layer thickness that results in less tempering of the previously deposited layer. Higher Si in the WM results in lower toughness, other factors being similar. It is worth to note that the SAW is usually employed on CSEF steel thick-walled weldments that are given longer PHWT; this results in short-term tensile properties at the lowest side of the allowable range.

Cored wires were also made recently available for even enhanced productivity in tube-to-fin welding. Cobalt-alloyed combinations are also available to avoid or limit Ni alloying, contributing to the sufficient notch toughness. Influence of alloying elements (notably Ni and Co) and interstitials were studied in great detail for the complicated steel chemistry of the P92 steel welds made by the SAW process. Moreover, Co does not significantly affect the A_{C1} temperature, unlike Ni. Consequently, it gives greater safety for PWHT, avoiding partial re-austenitization if PWHT is performed at too high a temperature. This property can also be used to raise PWHT temperature to improve toughness, providing that the temperature range is narrow enough not to exceed the A_{C1} temperature.

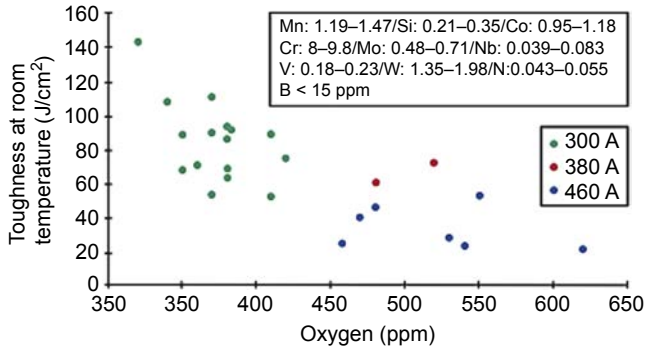


Figure 9.46 Influence of oxygen content on Gr. 92 SA weldments [44].

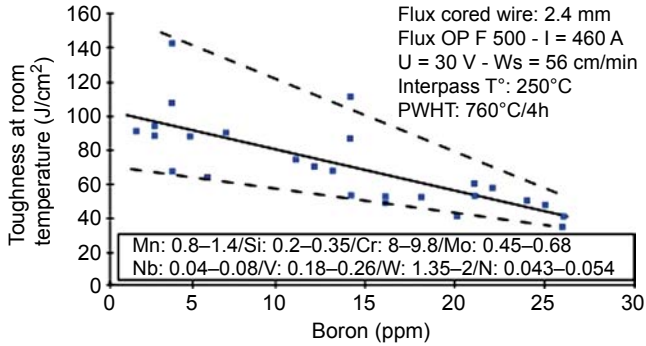


Figure 9.47 Influence of boron content on P92 SA weld metal toughness [44].

This study that also highlighted the effect of O content on toughness in weld metal, confirms that weld metal toughness decreases as O content increases (Fig. 9.46). It is then important to minimize the oxygen content in weld metal through the choice of flux and wire and also a control of welding current [45].

The influence of boron content was also studied, by varying the B content in SAW wire. Fig. 9.47 illustrates the detrimental effect of boron on toughness. However, boron is essential for creep properties, its removal leading to a sharp decrease of creep properties.

The effect of other chemical elements on toughness has been investigated. For this purpose, AWM were generated using a seamless flux-cored wire with SAW, with different levels of C, Cr, W, and N. Variations of W, C, and Cr within the base material range did not significantly affect toughness of the weld metal. However, nitrogen content has a great influence on toughness level, decreasing N content resulting in a toughness improvement.

Furthermore, the detrimental effect of B and Ti on toughness was also confirmed during this study. Despite the adverse effect of nitrogen and boron on toughness,

minimum values have been set in the weld metal to match creep properties of the base material.

Compositions matching P23, P24, and P91 (B23, 24, and B91, respectively) CSEFs have been classified under the AWS/SFA A5.23 standard (Tables 9.12 and 9.13).

9.4.6 Qualification of filler materials for creep service

Qualification of a specific consumable or deposit for service at high temperature is usually made at the early stage to develop a database of creep strength properties for design purpose and obtain approval from regulatory bodies where needed. Thus, some guidance has been developed to endure consistency of the properties based on the original composition developed. As a possible protocol, qualification according to European rules requires that the welded assembly to test the AWM properties has to be made according to the general welding procedure qualification under ISO 15613 or ISO 15614 standards. The qualification of the creep resistant consumables is regulated by EN 14532 standard (Welding Consumables–Test methods and quality requirements) with a particular, creep-related requirement given in EN 14532-2 standard (Welding Consumables–Test methods and quality requirements–Part 2: Supplementary methods and conformity assessment of consumables for steel, nickel and nickel alloys).

Consumables intended for use in the creep regime, defined by a temperature range for ferritic–martensitic, austenitic, and nickel-base materials, shall be qualified for the maximum service temperature by comparison tests with a matching parent material: a stress rupture all-weld material creep test series of at least four tests has to be produced with the longest test not shorter than 10,000 h, one test above 1000 h, and one between 50 and 250 h; tests shorter than 50 h are censored.

The regression line of this test series is then compared with the 20% scatter band around the mean rupture strength lines of the reference parent material, for which EN 14532-2 Appendix E gives the equations based on Manson–Brown regression parameter approaches following the discontinued ISO 6303 Appendix. The source of the coefficients to the equations is the British Guideline PD 6525.

All weld material specimens—according to EN 14532-2—are expected to fall within the scatter band of the matching parent material. If this is not the case, as is likely for longer testing times, detailed warnings about the longer or shorter duration shall be stated on the consumables qualification certificate [47].

9.5 Welding procedures, NDT, quality assurance, weldments testing

Heat-resistant materials require great care during the welding activities to retain the very special microstructure and characteristics. Properties in the short and long term are strongly dependent on the BM and WM chemistry, the heat treatment, and thermal cycles associated with the welded manufacture. It is of the utmost importance to keep the welding procedure under control to ensure consistent results and to test properly the weldments.

Table 9.12 Specification for low-alloy steel electrodes and fluxes for submerged arc welding (ASME boiler pressure vessel code–specifications for welding rods, electrodes, and filler metals. SFA-5.23/SFA-5.23M specification for low-alloy steel electrodes and fluxes for submerged arc welding)

Chemical composition requirements for weld metal[a]											
Weld metal designation[b]	UNS number[c]	Weight percent[d,e,f]									
		C	Mn	Si	S	P	Cr	Ni	Mo	Cu	Other[g]
B23	K20857	0.04–0.12	1.00	0.80	0.015	0.020	1.9–2.9	0.50	0.30	0.25	W: 1.50-2.00 V: 0.15-0.30 Nb: 0.02-0.10 B: 0.006 Al: 0.04 N: 0.07
B24	K20885	0.04–0.12	1.00	0.80	0.015	0.020	1.9–2.9	0.30	0.80–1.20	0.25	V: 0.15-0.30 Nb: 0.02-0.10 Ti: 0.10 B: 0.006 Al: 0.04 N: 0.05
B91	W50442	0.08–0.13	1.20[h]	0.80	0.010	0.010	8.0–10.5	0.80[h]	0.85–1.20	0.25	Nb: 0.02–0.10 N: 0.02-0.01 V: 0.15–0.25 Al: 0.04

[a]These requirements are applicable to both flux–solid electrode and flux–composite electrode combinations.
[b]The weld metal designation for composite electrodes is obtained by placing an "EC" before the appropriate electrode designation.
[c]Refer to ASTM DS-56/SAE HS-1086, Metals & Alloys in the Unified Numbering System.
[d]The weld metal shall be analyzed for the specific elements for which values are shown in this table. If the presence of other elements is indicated in the course of this work, the amount of those elements shall be determined to ensure that their total (excluding iron) does not exceed 0.50%.
[e]Single values are maximum.
[f]As a substitute for the weld pad in Figure 3, the sample for chemical analysis may be taken from the reduced section of the fractured tension test specimen (see 10.2) or from a corresponding location (or any location above it) in the weld metal in the groove weld in Figure 4. In case of dispute, the weld pad shall be the referee method.
[g]Analysis for B is required to be reported if intentionally added, or if it is known to be present at levels greater than 0.0010%.
[h]Mn + Ni = 1.40% maximum (see A7.2.3.1 in Annex A of the relevant standard).

Table 9.13 Specification for low-alloy steel electrodes and fluxes for submerged arc welding (ASME boiler pressure vessel code–specifications for welding rods, electrodes, and filler metals. SFA-5.23/SFA-5.23M specification for low-alloy steel electrodes and fluxes for submerged arc welding)

Chemical composition requirements for solid electrodes											
Electrode AWS classification	UNS number[c]	Weight percent[a,b]									
		C	Mn	Si	S	P	Cr	Ni	Mo	Cu[d]	V	Other[e]
EB23	K20857	0.05–0.12	1.10	0.50	0.015	0.015	1.9–3.0	0.50	0.50	0.10	0.15–0.30	W: 1.50-2.00 Nb: 0.02-0.10 B: 0.006 Al: 0.04 N: 0.05
EB24	K20885	0.04–0.12	1.00	0.50	0.015	0.020	1.9–3.0	0.30	0.80–1.20	0.10	0.15–0.30	Nb: 0.02-0.10 Ti: 0.10 B: 0.006 Al: 0.04 N: 0.07
EB91	S50482	0.07–0.13	1.25[f]	0.50	0.010	0.010	8.50–10.50	1.00[f]	0.85–1.15	0.10	0.15–0.25	Nb: 0.02–0.10 N: 0.03–0.07 Al: 0.04

[a]The electrode shall be analyzed for the specific elements for which values are shown in this table. If the presence of other elements is indicated in the course of this work, the amount of those elements shall be determined to ensure that their total (excluding iron) does not exceed 0.50%.
[b]Single values are maximum.
[c]Refer to ASTM DS-56/SAE HS-1086, Metals & Alloys in the Unified Numbering System.
[d]The copper limit includes any copper coating that may be applied to the electrode.
[e]Analysis for B is required to be reported if intentionally added, or if it is known to be present at levels greater than 0.0010%.
[f]See A7.2.3.1 in Annex A of the relevant standard for a discussion of the B91 alloy and recommendation regarding the Mn + Ni level achieved in the weld deposit. See also Note j of Table 9.12 for limits on the Mn + Ni content of the B91 weld deposit.

9.5.1 Welding methods, weld metal shape

The choice of the welding methods is subjected to the manufacturer's preference. However, broad method combinations can be given:

- Small bore tubes (up to 100 mm OD) or thin members (eg, up to 6–8 mm WT) are usually welded with the GTA (TIG) method for the root and the filling layers; long, straight tube-to-fin welds are welded with the SAW method.
- Intermediate thickness (up to 25 mm) can be welded with the GTA and MMA (SMA) or manual FCAW. Welds done in shop in 1G or 2G positions can be accomplished by SA welding. Specific stick electrodes can weld the root directly.
- Heavy-walled pipe work or rotor forgings are normally done with semiautomatic methods like GTA, SA and their narrow gap or hot wire versions to save time and WM volume.
- Repair welding is usually accomplished using the SMAW or, lately, the FCAW method.

In a multipass weld, the bead shape and the welding position also have a significant effect on the weld properties. When the weld deposit is thin and wide, it allows for some degree of tempering of the previous deposit from the heat of welding and promotes grain refinement in the previously deposited weld metal. Thicker beads limit the degree of grain refinement and lead to loss of toughness in the weld metal. As to the welding position, most of the observations made are on welds produced in the flat (1G) position. A loss of toughness is observed in SMAW made in vertical (3G) and overhead (4G) positions due to bead control problems and lack of tempering and grain refinement.

Where nitrogen is a key element for WM creep strengthening, it also crucial to control adsorption/desorption in various positions of a fixed pipe weldments.

9.5.2 Gas back protection

The weld area on the back side of the joint must be protected from the oxidation of the Cr and consequent loss. Regardless of the Cr content of the grade being welded, a good gas protection will ensure a sound WM smoothly blending with the parent wall. For low-Cr bainitic steels (ie, Cr <3.5%) no back protection is strictly required; for high-Cr martensitic grades and austenitics purging is always required.

Pure argon is exclusively employed, with gas flow maintained till the deposit of two to three layers.

9.5.3 Heating and cooling the assembly, hydrogen control

For welding bainitic and martensitic grades, the management of the thermal cycle allows one to avoid the hydrogen delayed cracking, solidification cracking issues and the proper microstructure formation, avoiding unwanted softer or brittle phases. In the following figures are reported exemplary heat cycles during the welding fabrication for a bainitic steel, a martensitic, and a 9%Cr cast steel (Figs. 9.48–9.50, respectively). Preheating/interpass level is choosen to avoid hydrogen delayed cracking and to control the weld hardness to some extent for bainitic grades; the weldments must be allowed to cool below the M_f temperature to obtain a full martensitic microstructure (this is not necessary for low-Cr bainitic WMs). The PWHT will soften the as-welded microstructure and release the residual stresses, restoring sufficient ductility and notch toughness. This treatment is carried out at a temperature sufficiently below the A_{c1}

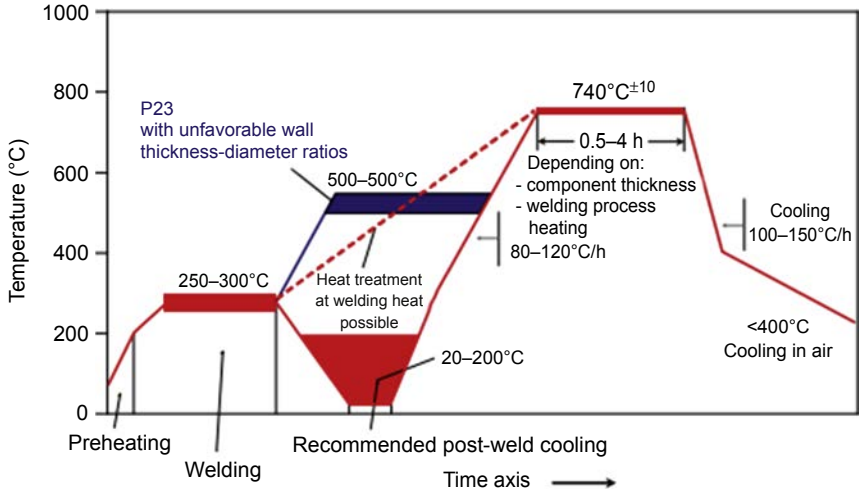


Figure 9.48 Temperature control in welding of T/P23 and T/P24 steels (wall thickness >10 mm) [47].

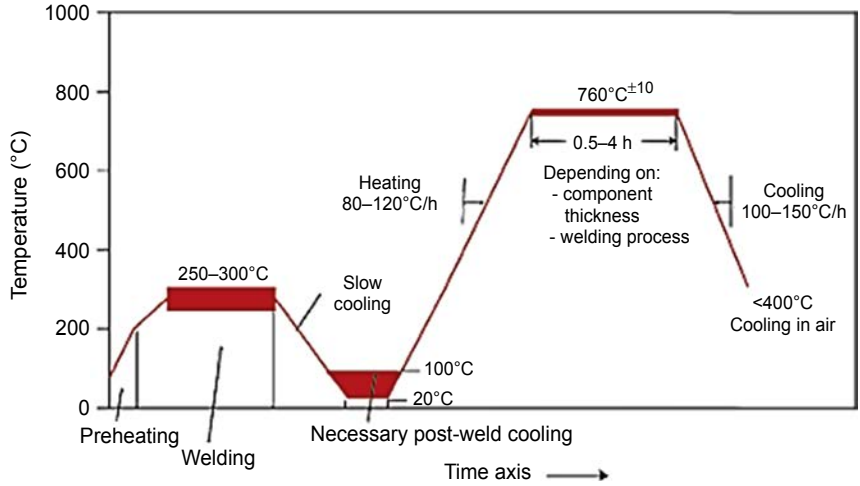


Figure 9.49 Temperature control in welding of E911/P92 steels [47].

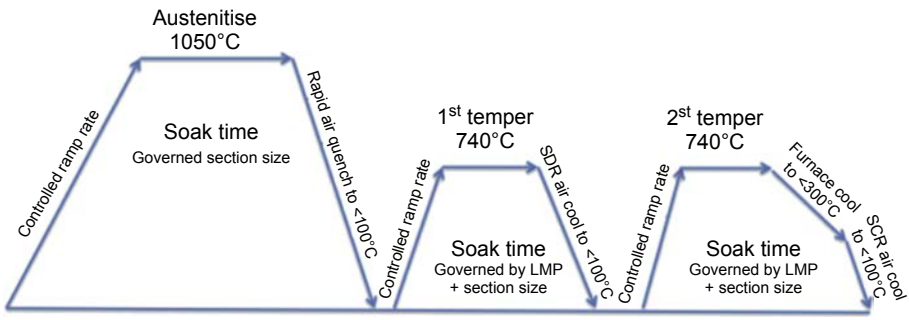


Figure 9.50 Typical heat treatment cycle for 9% Cr steel castings [8].

level. For very thick-walled weldments (as found on castings), it can be necessary to perform a double tempering to affect properly the entire thickness.

9.5.4 Preheating and interpass

The interval between the preheating and interpass manages the transformation of the austenite into bainite and martensite in the CEFS to avoid hydrogen-induced cracking (Fig. 9.51). The level of preheating is chosen according the grade being welded (as shown in Table 9.14); high-Cr martensitic grades are generally welded starting

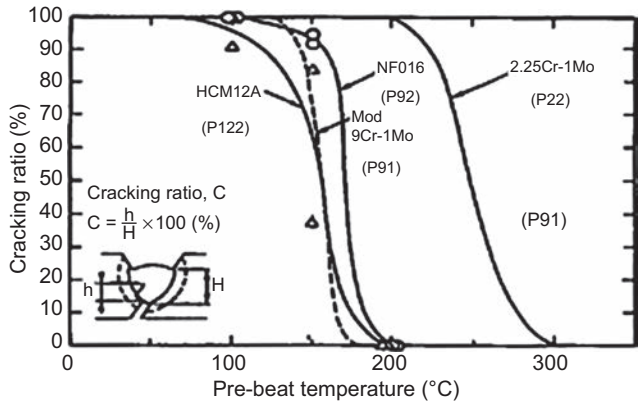


Figure 9.51 Y-groove hydrogen cracking test result of P92 weld metal and comparison with other Cr-Mo steels including P91, P22, and P122 [14].

Table 9.14 Recommended preheat and interpass temperature for common CSEF steels [22]

Alloy	Minimum preheat[a]		Maximum interpass		ASME allowable PWHT range
	°F	°C	°F	°C	°C
T/P23	350–400[b]	175–200	600	315	720–800
T24	400	200	600	315	720–775
T/P91	350–400[c]	175–200	660	350	730–800
T/P92	350–400	175–200	660	350	

[a]The minimum preheat recommendations in this table do not supersede existing code requirements, such as those present in ASME B31.1 for grade 91. Section 131.4.5, which addressed P5A and P5B (some now classified as P15 C/E materials), requires 400°F (200°C) for material that has either a specified minimum tensile strength in excess of 60,000 lb/in.^{2} (413.8 MPa) or has both a specified minimum chromium content >6% and a thickness at the joint in excess of 0·50 in. (13.0 mm); 300°F (150°C) for all other materials having this P number.
[b]If there is concern to have minimal hardness (<350 Hv) without PWHT (to minimize susceptibility to SCC), then a 400°F (204°C) preheat is advised.
[c]Note that welding has been successfully performed using the gas tungsten arc welding (GTAW) process and reduced preheat temperatures.

from 200°C, while thin-walled members, or when non-slag-forming consumables are used, can be welded starting from 150°C. Following these schedules, most of the welding activity will be done with the steel not completely transformed into martensite, preventing hydrogen cracking.

For austenitic grades in similar welding, no preheating is necessary; the maximum interpass temperature ensures limited risk of solidification cracking issues.

9.5.4.1 PWHT: extent and methods

The heat treatment temperature is specific of each grade, with some margin on the Larson-Miller parameter that can be used to favor either the creep strength or the toughness of the weldments. Holding time is most often selected mainly looking at the reference thickness. In any case, the holding temperature should never exceed the lower critical transformation temperature; as this depends on the BM and WM actual chemistry, an accurate analysis is strongly recommended. Most of weld mechanical properties are available for combination of chemistry and duration more frequently reported in product standards, for which test assemblies have uniform thickness ranges (eg, 20 mm) and prescribed preheat and interpass schedules resembling widespread industrial practice. For CSEF steels, they are these (AWS):

- Gr. 23, 24: 740°C × 2 h (Larson-Miller Parameter, C20 = 20.57; preheat and interpass: 180–250°C)
- Gr. 91, 92: 760°C × 2 h (Larson-Miller Parameter, C20 = 20.97; preheat and interpass: 200–315°C)

Other key numbers are reported in Table 9.15.

Control of thermal inhomogeneity is also critical. In a heavy section pipework, due to the method of heating (bands) during PWHT, defective heat treatment may be caused. In such a case, a nonuniform PWHT may result if the outside surface temperature reaches PWHT temperature well before the inside of the component does. Practices such as increasing the size of the heating band, using properly sized heating pads to prevent large gaps, or overlap through the circumference of the tube or pipe and using a control thermocouple under each heating pad are recommended in addition to the guidelines specified by AWS D10.10.

Exceeding the A_{c1} temperature during PWHT of CSEF steel welds results in the formation of detrimental microstructure for the creep properties (ferrite) and toughness (fresh martensite). The products of austenite decomposition in CSEF welds are determined by the level of inhomogeneity in their microstructure. The as-welded microstructure in multilayer CSEF welds consists of fresh martensite and partly tempered martensite. The latter is produced by reheating during the sequential bead deposition in multipass welds. It is expectable that upon exceeding the A_1 temperature the fresh martensite and the partly tempered martensite would transform to austenite that has varying alloying content and homogeneity. During cooling, the austenite containing higher amounts of undissolved precipitates (carbides and carbonitrides) is less stable and would decompose to ferrite, while higher alloyed homogeneous austenite would form fresh martensite.

Table 9.15 Transformation temperature in °C, normalization, and PWHT for CSEF steels [22]

Material	M_S	M_F	B_S	A_1	A_3	Normalization	Tempering/PWHT
T23	~540	~325	~620	800–820	960–990	1040–1080	730–800/720–800 (PWHT)
T24	~460	~260	~550	815	950	980–1020	720–775
P(T)91[a]							
Base (Alex.)	372–393	159–196	N/A	788–813	833–860	1050–1080	730–780/730–770 (PWHT)
Base (V&M)	372–393	159–196	N/A	800–830	890–940	1050–1080	730–780/730–770 (PWHT)
Weld	390–418	200–237	N/A	770–801	832–861	1050–1080	730–780/730–770 (PWHT)
P(T)92[a]							
Base (Alex.)	366–396	135–198	N/A	795–817	854–867	1040–1080	730–800
Base (V&M)	366–396	135–198	N/A	795–835	900–925	1040–1080	730–800
Weld	376–423	185–229	N/A	759–800	832–861	1040–1080	730–800
E911	360	160	N/A	~805	~980	1040–1080	740–780/730–800 (PWHT)
VM12	300	175	N/A	~810–825	~890	1040–1080	750–800

A_1, lower critical transformation temperature; A_3, upper critical transformation temperature; B_s, bainite start temperature; M_F, martensite finish temperature; M_s, martensite start temperature.
[a]*VM*, Vallourec and Mannesmann; *Alex.,* Alexandrov.

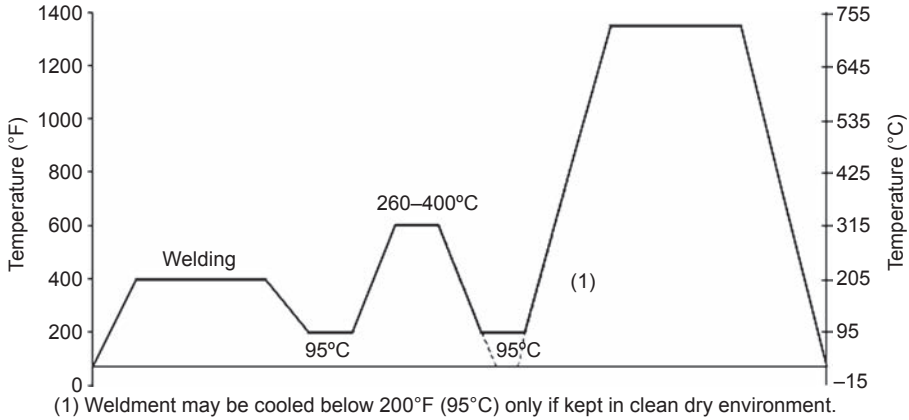


Figure 9.52 Hydrogen bake on 9%Cr weldments with PWHT at a later time [19].

For 9%Cr weldments, where the PWHT cannot be carried out upon weld cooling under M_f temperature, it is not safe to leave the assembly without prior dehydrogenation. This can be accomplished holding the assembly between 250 and 400°C for a time related to the member thickness. Afterward, the assembly can be cooled down even to room temperature (at least below 93°C is recommended in AWS SFA-5.23 for maximizing the WM martensitic transformation), awaiting the final PWHT (Fig. 9.52). Welds on P91 are at risk of SCC in this condition and are not to be stored in a wet environment.

Local PWHT is required when the welded assembly cannot be put in a furnace or for in-field weldments. Heated bands are most often used to precisely monitor and control the thermal cycle. The size of the areas to be heated depends on the thickness and the restraint of the weldments. Recommendations can be found in specific standards and codes. Resistance heating is the preferred method, while flame heating should be discouraged due to the low precision attainable and the risk of localized overheating. PWHT is recognized as the most common cause of issues for Cr creep-resistant steels. Accurate planning, simulation on mock-ups and extensive monitoring are strongly recommended.

9.5.4.2 Weldment testing

The development of a welding procedure with a well-established technique involves small preliminary trial activities. After, a qualification coupon is prepared, it is welded in accordance to the preliminary procedure being qualified and subjected to NDT. ASME BPVC Section IX " *Welding and Brazing Qualifications*" sets the requirements for writing a Welding Procedure Specification (WPS) and testing the WPS through a procedure qualification. Similarly, the EN ISO 15614-1 "*Specification and qualification of welding procedures for metallic materials–Welding procedure test–Part 1: Arc and gas welding of steels and arc welding of nickel and nickel alloys*" document sets the standard according to the European standards. All documents call for a minimum

testing extent, supplemented in case by specific requirements, such those included in the following most recognized application standards:

- EN 13445: pressure vessels
- EN 12952: water tube boilers
- EN 13480: piping
- ASME BPVC Sec. VIII: rules for construction of pressure vessels
- ASME B31.1 power piping

Where applicable, PWHT is included in the procedure specification. For boiler construction, creep-resistant steels are used mostly as tubular products, with welded joints to be produced either in shop (1G and 5G positions) and on the boiler erection site (5G position).

For WPS qualification purposes, butt complete groove joints manufactured out of intended creep-resistant steels, or similar, are required to be subjected to the following tests:

- NDT (Visual, Radiographic, Penetrant testing)
- static transverse tensile testing
- transverse bend testing
- metallographic inspection on weldments section
- hardness testing on metallographic sections taken into the WM, HAZ, and BM

As an example, common requirements for the weld and the affected parent metal (as wholly influenced by the PWHT) are these:

- Minimum hardness limit for P91 components entering service is generally considered to be ~190 HV to 200 HV. According to ASTM standards, the maximum hardness limit for P91 BM is 265 HV.
- P91 weld metal (and coarse-grained HAZ) would be expected to have hardness of ~240–260 HV following PWHT at 750/760°C for 2 h (V&M data book).
- Weld hardness for PWHT at 730°C (minimum allowed by ASME) for 2 h would be ~280–290 HV (V&M data book).
- The limit of acceptability for welds depends upon the difference in hardness between the weld metal/CGHAZ and the weak Type IV region. The relative weakness of the Type IV zone is worse for PWHT at 730°C.

Testing practice can follow either ASTM standards associated with ASME code or European equivalents, with only very minor differences. Measured weldments properties are normally required to equal or exceed minimum BM specified figures. Measurement of welds notch toughness properties (in both WM and HAZ) by Charpy-V specimens is nearly always specified by the mentioned application standards, with minimum average values required (mostly 47 J in PED regulated equipment) at the lowest intended operating temperature (eg, 20°C, the most often specified figure). Through-thickness specimens are used; in case of thick weldments or for studying the passes arrangement effect, Charpy-V specimens sampling can be performed at various joint section heights (eg, close to the root or the top surface). Additionally, hot tensile testing (eg, at the intended maximum service temperature) is often required and the behavior, compared to the BM, reported. AWM tensile testing can also be specified as an additional test to check WM yield strength and ductility by the elongation measurement. Usually, AWM testing is performed at both RT and service temperature also to check properties used at the design stage.

Thus, a possible choice for WPS qualification testing standard is presented in Table 9.16.

More sophisticate fracture toughness testing may be required to be used as material property input for fitness-for-service procedures. R5 Code "Assesment of Structural Integrity at High Temperature" and R6 Code "Assessment of the Integrity of Structures Containing Defects," mantained by former British Energy (now EDF), are examples of such procedures specific for the energy sector. Topics as creep-fatigue or creep data extrapolation are there treated.

In Fig. 9.53 is depicted the sampling practice for creep specimens extracted from a pipe girth weld [28].

9.5.4.3 Nondestructive testing

The integrity of the weldments just after the fabrication, prior to enter the service, and during the plant production must be assessed with great reliability.

The ASME BPVC is a classical reference for weldments inspection requirements and imperfection acceptance levels. NDT methods are covered in Sec. V of the code. As a basis, pertinent surface methods are the visual testing (VT) and the magnetic particle

Table 9.16 WPS qualification tests and associated standards

Test	Testing standard (EN)	Testing standard (ASTM)	Specimen type
Static transverse tensile testing on weldments	EN 895: Destructive tests on welds in metallic materials, transverse tensile test	ASTM A370: Mechanical testing of steel products. ASTM E8 Tension testing of metallic materials	Rectangular section, full thickness
Bend testing on weldments	EN 910: Destructive tests on welds in metallic Materials–Bend tests	ASTM E190: Guided bend test for ductility of welds	Lateral bending, rectangular section, full thickness
Hardness testing on weldments	EN 1043-2: Destructive tests on welds in metallic materials	ASTM E 92: Vickers hardness of metallic materials	–
Notch toughness testing on weldments	EN 875: Destructive tests on welds in metallic materials–impact tests	ASTM E23: standard test methods for notched bar impact testing of metallic materials	Through thickness 10-mm-thick notched bar
All weld metal tensile testing	EN 876: Destructive tests on welds in metallic materials–longitudinal tensile test	ASTM E8: Tension testing of metallic materials	Cylindrical, proportional

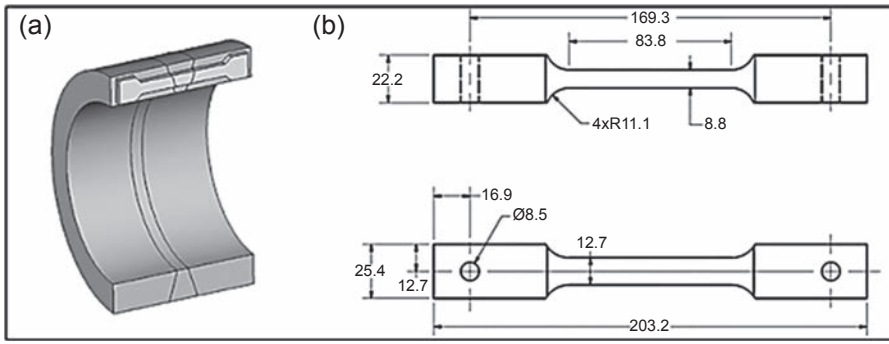


Figure 9.53 (a) Schematic of cross-weld creep test specimen extracted from the welded pipe after PWTH; (b) the dimension of the creep rupture specimen (in mm) [28].

testing (PT). Volumetric methods are radiographic testing (RT) and ultrasonic testing (UT), depending on the actual wall thickness and the joint accessibility and geometry. Complete penetration of circumferential groove joints will be examined (100% extent) with RT prior to the PWHT at temperature below 100°C to ensure complete martensitic transformation; after PWHT, the inspection will be repeated. After PWHT, the same joints are subjected to UT (100% extent) to complement RT in assessing the presence of discontinuities parallel or transverse to the weld direction. Complete penetration angled weldments (eg, T-joints) are controlled by UT (100% extent) as well. All weldments are also subjected to PT on the weldments surfaces (100% extent).

European equivalent standards are also available, with separate documents for each of these:

- type and level of imperfections
- techniques for performing the various NDT methods
- quality levels associated with the relevant NDT method being employed

ASME B31.1 code is often used for steam transferring lines external to the boiler, with similar requirements for groove welds. A general guidance is given in Table 9.17.

After entering in service, boiler weldments (or the BM itself) are at risk of developing creep damage, fatigue cracks and loss of material due to steam oxidation, among other damage modes. A variety of methods are available for service inspection to address these damaging issues (a general guidance is given in Table 9.18). The metallographic replica is the main standard technique for assessing the presence of creep damage at various stages, in the BM or weldments. Unfortunately, Type IV cracking on martensitic steels begins away from surface of the welded member; when it is detectable at surface, usually in the volume the damage is already severe.

Complex and thick welded component can be reliable inspected only by RT. This may require the use of special equipment for thick-walled castings (Fig. 9.54).

Ferritic steel weldments are made mainly with matching consumables (ie, with ferritic matrix), with no difference expected in radiation absorption in the WM. The use of austenitic and Ni-based consumables can complicate the ND investigations.

Table 9.17 Mandatory minimum nondestructive examinations for pressure welds or welds to pressure retaining components [48]

Piping design conditions and nondestructive examination			
Type weld	**Temperatures over 750°F (400°C) and at all pressures**	**Temperatures between 350°F (175°C) and 750°F (400°C) inclusive with all pressures over 1025 psig [7100 kPa (gage)]**	**All others**
Butt welds (girth and longitudinal)[a]	RT or UT for over NPS 2. MT or PT for NPS 2 and less[b]	RT or UT for over NPS 2 with thickness over 3/4 in. (19.0 mm); VT for all sizes with thickness 3/4 in. (19.0 mm) or less	Visual for all sizes and thicknesses
Welded branch connections (size indicated is branch size)[c,d]	RT or UT for over NPS 4. MT or PT for NPS 4 and less[b]	RT or UT for branch over NPS 4 and thickness of branch over 3/4 in. (19.0 mm) MT or PT for branch NPS 4 and less with thickness of branch over 3/4 in. (19 mm) VT for all sizes with branch thickness 3/4 in. (19.0 mm) or less	VT for all sizes and thicknesses
Fillet, socket, attachment, and seal welds	PT or MT for all sizes and thicknesses[e]	VT for all sizes and thicknesses	VT for all sizes and thicknesses

General notes.
(A) All welds shall be given a visual examination in addition to the type of specific nondestructive examination specified.
(B) *NPS*, nominal pipe size.
(C) *MT*, magnetic particle examination; *PT*, liquid penetrant examination; *RT*, radiographic examination; *UT*, ultrasonic examination; *VT*, visual examination.
(D) For nondestructive examinations of the pressure retaining component, refer to the standards listed in Table 126.1 or manufacturing specifications.
(E) Acceptance standards for nondestructive examinations performed are as follows: *MT*, see para. 136.4.3; *PT*, see para. 136.4.4; *RT*, see para. 136.4.5; *UT*, see para. 136.4.6; *VT*, see para 136.4.2.
Notes:
[a]The thickness of butt welds is defined as the thicker of the two abutting ends after end preparation.
[b]RT may be used as an alternative to PT or MT when it is performed in accordance with para. 136.4.5.
[c]RT or UT of branch welds shall be performed before any nonintegral reinforcing material is applied.
[d]In lieu of volumetric examination (RT, UT) of welded branch connections when required, surface examination (PT, MT) is acceptable and, when used, shall be performed at the lesser of one-half of the weld thickness or each 1/2 in. (12.5 mm) of weld thickness and all accessible final weld surfaces.
[e]Fillet welds not exceeding 1/4 in. (6 mm) throat thickness, which are used for the permanent attachment of nonpressure retaining parts, are exempt from the PT or MT requirements of the table.

Table 9.18 Types of imperfections versus NDE method [49]

Table A-110
Imperfection vs Type of NDE Method

	Surface [Note (1)]		Subsurface [Note (2)]		Volumetric [Note (3)]				
	VT	PT	MT	ET	RT	UTA	UTS	AE	UTT
Service-Induced Imperfections									
Abrasive Wear (Localized)	◉	⊙	⊙	...	◉	⊙	⊙	...	⊙
Baffle Wear (Heat Exchangers)	◉	...	...	⊙	...	...	...	...	...
Corrosion-Assisted Fatigue Cracks	◎	⊙	◉	...	◎	◉	...	◉	...
Corrosion									
-Crevice	◉	...	...	...	...	...	...	...	◎
-General / Uniform	...	...	...	◎	⊙	...	⊙	...	◉
-Pitting	◉	◉	◎	...	◉	◎	◎	⊙	◎
-Selective	◉	◉	◎	...	...	...	...	...	◎
Creep (Primary) [Note (4)]	...	...	...	...	...	...	...	...	...
Erosion	◉	...	...	...	◉	◎	⊙	...	⊙
Fatigue Cracks	◎	◉	◉	⊙	⊙	◉	...	◉	...
Fretting (Heat Exchanger Tubing)	⊙	...	...	⊙	...	...	...	...	⊙
Hot Cracking	...	⊙	⊙	...	⊙	◎	...	⊙	
Hydrogen-Induced Cracking	...	⊙	⊙	...	◎	⊙	...	⊙	...
Intergranular Stress-Corrosion Cracks	...	...	...	...	...	◎	...	...	...
Stress-Corrosion Cracks (Transgranular)	◎	⊙	◉	◎	⊙	⊙	...	⊙	...
Welding Imperfections									
Burn Through	◉	...	...	...	◉	⊙	...	...	◎
Cracks	◎	◉	◉	⊙	⊙	◉	◎	◉	...
Excessive/Inadequate Reinforcement	◉	...	...	...	◉	⊙	◎	...	◎
Inclusions (Slag/Tungsten)	...	...	⊙	⊙	◉	⊙	◎	◎	...
Incomplete Fusion	⊙	...	⊙	⊙	⊙	◉	⊙	⊙	...
Incomplete Penetration	⊙	◉	◉	⊙	◉	◉	⊙	⊙	...
Misalignment	◉	...	...	...	◉	⊙	...	...	...
Overlap	⊙	◉	◉	◎	...	◎	...	...	...
Porosity	◉	◉	◎	...	◉	⊙	◎	◎	...
Root Concavity	◉	...	...	...	◉	⊙	◎	◎	◎
Undercut	◉	⊙	⊙	◎	◉	⊙	◎	◎	...
Product Form Imperfections									
Bursts (Forgings)	◎	◉	◉	⊙	⊙	⊙	⊙	◉	...
Cold Shuts (Castings)	◎	◉	◉	◎	◉	⊙	⊙	◎	...
Cracks (All Product Forms)	◎	◉	◉	⊙	⊙	⊙	◎	◉	
Hot Tear (Castings)	◎	◉	◉	⊙	⊙	⊙	◎	◎	...
Inclusions (All Product Forms)	...	...	⊙	⊙	◉	⊙	◎	◎	...
Lamination (Plate, Pipe)	◎	⊙	⊙	...	...	◎	◉	◎	◉
Laps (Forgings)	◎	◉	◉	◎	⊙	...	◎	◎	
Porosity (Castings)	◉	◉	◎	...	◉	◎	◎	◎	...
Seams (Bar, Pipe)	◎	◉	◉	⊙	◎	⊙	⊙	◎	...

Legend:

AE — Acoustic Emission
ET — Electromagnetic (Eddy Current)
MT — Magnetic Particle
PT — Liquid Penetrant
RT — Radiography
UTA — Ultrasonic Angle Beam
UTS — Ultrasonic Straight Beam
UTT — Ultrasonic Thickness Measurements
VT — Visual

◉ — All or most standard techniques will detect this imperfection under all or most conditions.
⊙ — One or more standard technique(s) will detect this imperfection under certain conditions.
◎ — Special techniques, conditions, and/or personnel qualifications are required to detect this imperfection.

GENERAL NOTE: Table A-110 lists imperfections and NDE methods that are capable of detecting them. It must be kept in mind that this table is very general in nature. Many factors influence the detectability of imperfections. This table assumes that only qualified personnel are performing nondestructive examinations and good conditions exist to permit examination (good access, surface conditions, cleanliness, etc.).

NOTES:
(1) Methods capable of detecting imperfections that are open to the surface only.
(2) Methods capable of detecting imperfections that are either open to the surface or slightly subsurface.
(3) Methods capable of detecting imperfections that may be located anywhere within the examined volume.
(4) Various NDE methods are capable of detecting tertiary (3rd stage) creep and some, particularly using special techniques, are capable of detecting secondary (2nd stage) creep. There are various descriptions/definitions for the stages of creep and a particular description/definition will not be applicable to all materials and product forms.



Figure 9.54 Radiography of a 7.5-ton valve casting using an 8.5 MeV linear accelerator at Goodwin's site (Goodwin Steel Castings Ltd.) [8].

Austenitic and DMW with austenitic materials or use of Ni-based consumables can greatly complicate the UT of weld due to the attenuation inherent of the coarse-grain austenitic alloys.

Martensitic Cr steels especially attribute their creep resistance to a well-defined favorable microstructure (tempered martensite with carbide dispersion). Achieving that microstructure is not always straightforward, especially if complex manufacturing operations are involved (eg, intermediate reheating, hydrogen diffusion treatments). Thus, the metallographic investigation is of paramount importance. Again, metallographic replica can assist during the manufacturing stages to assess the favorable microstructure presence. Another common method to assess the effectiveness of the PWHT on large 9% Cr equipment requires the use of a portable instrument to make a survey for the surface WM hardness.

9.6 Future trends

In the field of USC material welding the choice of BMs is well established; moving to higher service temperatures is a major challenge for the fossil power generation to get the desired strong reduction in CO_2 emission and increased efficiency that is achievable only by a new generation of materials (see the A-USC welding Chapter 18 for more details). Attempts to mitigate the Type IV damage in HAZs on existing CSEF steel by welding procedure, PWHT and consumables variations have not resulted in consistent results and adequate robustness for industrial usage.

Repair and life extension of welded components will also play an increased role. Welding established USC steels will thus focus on the raising of productivity,

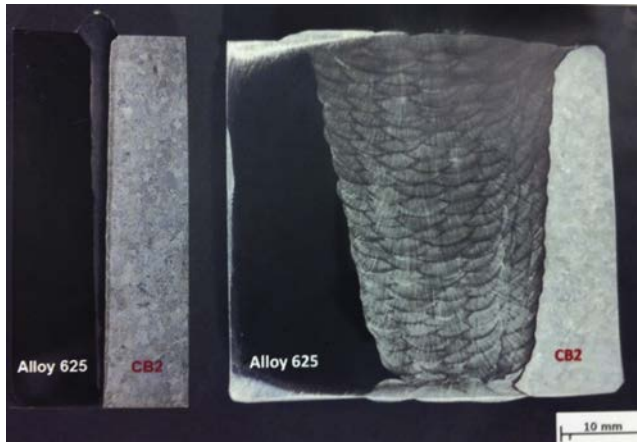


Figure 9.55 Comparison between electron beam and arc fusion dissimilar metal welding of Ni alloy 625 and CB2 martensitic steel (Technical University Graz). The beam alignment with respect to the joint line has been shifted on the Ni side to reduce the CB2 steel dilution into the WM. Proper beam placement with respect to the bevel line, limited WM mixing and poor reparability are always a serious difficult for beam welds [50].

consumable user friendliness and more robust weld metal properties rather than the development of new alloy variations. In this regard, supplying weld metals with more close control of the chemistry will be significant. Resistance to hot cracking using higher interpass temperatures and very fast travel speeds is also being sought by many manufacturers for reducing fabrication cost. Another main driver will be the improvement of the PWHT robustness on 9%Cr steel piping with further reduction of the Mn + Ni in the WM content without impairing the impact toughness.

Welding methods alternative to fusion arc processes have been tested on USC steel materials; however, they have found very little industrial acceptance so far, mainly due to the difficulty in controlling the WM chemistry in deep penetration beam processes (like EBW, LBW, LB-GMAW), or FSW due to the absence of filler materials. Of course, productivity figures could be significantly enhanced (Fig. 9.55). Tight tolerances are also required, making these methods impractical for the members size normally employed. Also repair of defective beam welds on thick members would be very complicated, as the joint is normally completed in one or two opposite passes and the imperfections then discovered only very late in the joint fabrication; excavation by usual methods (grinding, arc gouging) makes the bevel unsuitable to further welding activity with high energy methods.

Ideally, weldments creep damage should be detected at earliest, allowing the decision to repair or replace the affected joint. However, the replica method and the observation at the microscope only give information of the surface condition of the component; an effective method for volumetric evaluation is an object of considerable R&D efforts. Special UT technique has been recently proposed to address the difficulty (Fig. 9.56).

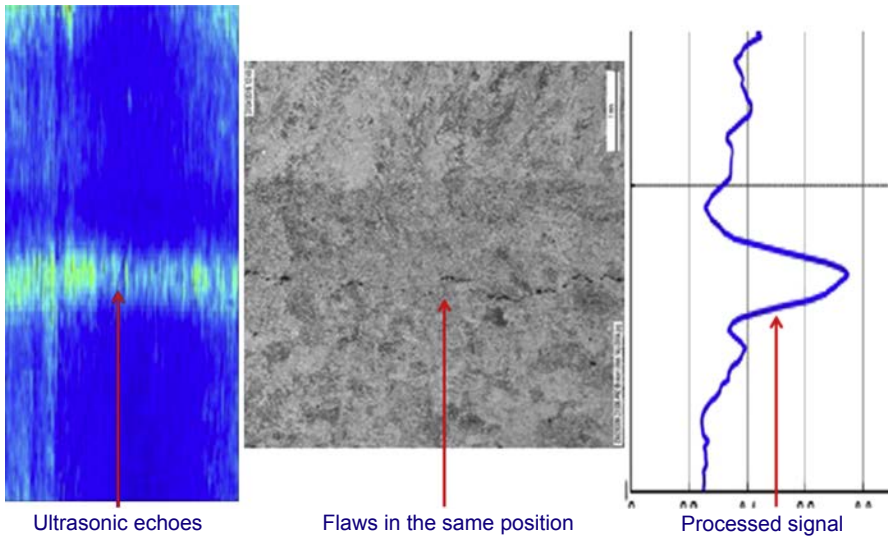


Figure 9.56 Verification of the UT signals against sectioning of specimens with creep damage. This method is aimed to the earliest detection of Type IV cracks (The Welding Institute) [51].

List of acronyms

1G Flat welding position (ASME)
2G Horizontal welding position (ASME)
5G Girth welding (fixed pipe, ASME)
CSEF Creep strength enhanced ferritic (steel)
GMA Gas metal arc
GTA Gas tungsten arc
HP High pressure (turbine stage)
IP Intermediate pressure (turbine stage)
LP Low pressure (turbine stage)
MIG Metal inert gas
MMA Manual metal arc
NG-GTA Narrow gap gas tungsten arc
NG-SA Narrow gap submerged arc
PWHT Post-weld heat treatment
SA Submerged arc
SMA Shielded metal arc
TIG Tungsten inert gas

Acknowledgments

I would like to express my gratitude to my dear colleagues Dr. Bruno Leduey and Dr. Philippe Corroyez of Air Liquide Welding, whose comments and suggestions added considerable value to this chapter.

References

Code and standards

- ASME Boiler Pressure Vessel Code–Specifications for Welding Rods, Electrodes, and Filler Metals. SFA-5.4/SFA-5.4M Specification for Stainless Steel Electrodes for Shielded Metal Arc Welding.
- ASME Boiler Pressure Vessel Code–Specifications for Welding Rods, Electrodes, and Filler Metals. SFA-5.5/SFA-5.5M Specification for Low-Alloy Steel Electrodes for Shielded Metal Arc Welding.
- ASME Boiler Pressure Vessel Code–Specifications for Welding Rods, Electrodes, and Filler Metals. SFA-5.9/SFA-5.9M Specification for Bare Stainless Steel Welding Electrodes and Rods.
- ASME Boiler Pressure Vessel Code–Specifications for Welding Rods, Electrodes, and Filler Metals. SFA-5.23/SFA-5.23M Specification for Low-Alloy Steel Electrodes and Fluxes for Submerged Arc Welding.
- ASME Boiler Pressure Vessel Code–Specifications for Welding Rods, Electrodes, and Filler Metals. SFA-5.28/SFA-5.28M Specification for Low-Alloy Steel Electrodes and Rods for Gas Shielded Arc Welding.
- ASME Boiler Pressure Vessel Code–Specifications for Welding Rods, Electrodes, and Filler Metals. SFA-5.29/SFA-5.29M Specification for Low-Alloy Steel Electrodes for Flux-Cored Arc Welding.
- ASME Boiler Pressure Vessel Code–Specifications for Welding Rods, Electrodes, and Filler Metals. SFA-5.01M/SFA-5.01 Welding Consumables – Procurement of Filler Materials and Fluxes.
- ASME Boiler Pressure Vessel Code–Specifications for Welding Rods, Electrodes, and Filler Metals. SFA-5.02/SFA-5.02M Specification for Filler Metal Standard Sizes, Packaging, and Physical Attributes.
- AWS D10.21:20XX, Guide for Welding Advanced Chromium-Molybdenum Steel Piping and Tubing (under drafting/approval).
- AWS D10.8-96, Recommended Practices for Welding of Chromium-Molybdenum Steel Piping and Tubing.
- BS 2633:1987 Specification for Class I arc welding of ferritic steel pipework for carrying fluids.
- AWS D10.4:1986(R2000) Recommended practices for welding austenitic stainless steel piping and tubing.
- AWS D10.10/D10/10M:1999(R2009) Recommended practices for local heating of welds in piping and tubing.
- EN 14532 Welding Consumables – Test methods and quality requirements.

Broad reference papers, guidelines and proceedings

- D.J. Abson, J.S. Rothwell, Review of type IV cracking of weldments in 9–12% Cr creep strength enhanced ferritic steels, International Materials Reviews 58 (8) (2013) 438–473.
- Advances in Materials Technology for Fossil Power Plants, in: Proceedings from the Fourth International Conference, EPRI, 2005.
- Advances in Materials Technology for Fossil Power Plants, in: R. Viswanathan, D. Gandy, K. Coleman (Eds), Proceedings of the 5th International Conference, EPRI, 2007.
- Advances in Materials Technology for Fossil Power Plants, in: Proceedings from the Sixth International Conference, EPRI, 2010.

- Advances in Materials Technology for Fossil Power Plants, in: D. Gandy, J. Shingledecker, Proceedings from the Seventh International Conference, EPRI, 2013.
- Guidelines and Specifications for High-Reliability Fossil power Plants, 2nd edition, EPRI, 2015, Technical report.
- Creep strength enhanced ferritic (CSEF) steel welding guide, Report no. 1024713, EPRI, Palo Alto, CA, USA, 2011.

Specific references

[1] V. Viswanathan, R. Purgert, P. Rawls, Coal Fired Power Materials; Advanced Materials And Processes, August 2008.

[2] http://www.vallourec.com/fossilpower/EN/Application/Pages/water-wall-panels.aspx.

[3] http://www.pemamek.com/welding-solutions/industrial-boilers/water-wall-panel-lines.

[4] http://www.seamlimited.com/photogallery.php.

[5] T. Shige, R. Magoshi, S. Itou, T. Ichimura, Y. Kondou, Development of large-capacity, highly efficient welded rotor, Mitsubishi Heavy Industries, Ltd. Technical Review 38 (1) (February 2001).

[6] W. Janssen Welding on Rotors for Power Plant Turbo Sets: State of the Art: http://www.energy.siemens.com/br/pool/hq/energy-topics/pdfs/en/steam-turbines-power-plants/2_Welding_on_Rotors.pdf.

[7] https://www.mdaturbines.com/wp-content/uploads/2014/02/Weld-Distortion-Cut-sheet-proof-10-28-13.pdf.

[8] Advanced Material Castings for High Temperature Coal Fired Steam Turbine Applications, Goodwin Steel Casting Ltd. www.goodwinsteelcastings.com/.../gsc-advanced.

[9] P. Mayr, Weldability of Modern 9% Cr Steels for Application in USC Power Plants (Doctoral thesis), Graz University of Technology, 2007.

[10] S.S. Babu, S.A. David, M.L. Santella, J.M. Vitek, E.D. Spect, J.W. Elmer, Proc. Numerical Analysis of Weldability, Verlag der Technischen Universitat, Graz, Austria, 2005, pp. 179–205.

[11] B. Hahn, W. Bendick, Pipe Steels for Modern High-Output Power Plants: Part 1 Metallurgical Principles – Long Term Properties – Recommendations for Use. www.vallourec.com/.../V_B01B0005B-15GB.pdf.

[12] M.L. Santella, R.W. Swindeman, R.W. Reed, J.M. Tanzosh, Martensite Formation in 9 Cr-Mo Steel Weld Metal and Its Effect on Creep Behavior. http://aprs.ornl.gov/~webworks/cppr/y2001/pres/111523.pdf.

[13] P. Mayr, Evolution of Microstructure and Mechanical Properties of the Heat Affected Zone in B-containing 9% Chromium Steels, (Doctor of Technical Sciences) Graz University of Technology, Austria, July 2007.

[14] Kobelco Welding Today, 12 (1), 2009.

[15] A. Poli, S. Caminada, C. Rosellini, A. Bertoni, G. Liberati, Fabrication and weldability of Grade 23 tubing and piping. Proceedings of the Super High Strength Steels Conference, Associazione Italiana Metallurgia, Milan; 2005.

[16] A. Dhooge, J. Vekeman, New generation 2.25 Cr steels T/P23 and T/P 24 weldability and high temperature properties, Welding in the World 49 (2005) n°9–10.

[17] F. Masuyama, M. Matsui, N. Komai, Creep rupture behaviour of advanced 9-12% Cr steel weldment, Key Engineering Materials (171–174) (2000) 99–108.

[18] M.D. Mathew, V. Shankar, R. Sandhya, Creep–fatigue-oxidation interaction in Grade 91 steel weld joints for high temperature applications, Materials Science and Engineering A 528 (2011) 8428–8437.

[19] S.A. David, J.A. Siefert, Z. Feng, Welding and weldability of candidate ferritic alloys for future advanced ultrasupercritical fossil power plants, Science and Technology of Welding and Joining 18 (8) (2013).
[20] H.J. Schüller, L. Haigh, A. Woitscheck, Cracking in the weld region of shaped components in hot steam lines materials investigations, Der Maschinenschaden 47 (1) (1974) 1–13.
[21] J.M. Brear, A. Fleming, Prediction of P91 Life Under Plant Operating Conditions, Proc. ETD Int. Conf. on 'High Temperature Plant Integrity and Life Extension', Cambridge, UK, April 2004 (Robinson College).
[22] D.J. Abson, J.S. Rothwell, Review of Type IV Cracking of Weldments in 9–12% Cr Creep Strength Enhanced Ferritic Steels International Materials Reviews, November 2013, 58 (8), 437–473.
[23] M. Yaguchi, T. Ogata, T. Sakai, Creep strength of high chromium steels welded parts under multi-actual stress conditions, in: I.A. Shibli, S.R. Holdsworth (Eds.), Proc. 2nd ECCC Creep Conf. on 'Creep & Fracture in High Temperature Component – Design & Life Assessment Issues', DEStech Publications, Inc., Zürich, 2009, pp. 215–226.
[24] C.J. Middleton, J.M. Brear, R. Munson, R. Viswanathan, An assessment of the risk of type IV cracking in welds to header, pipework and turbine components constructed from the advanced ferritic 9% and 12% chromium steels, in: R. Viswanathan et al. (Ed.), Proc. 3rd EPRI Conf. on 'Advances in Materials Technology for Fossil Power Plants', Institute of Materials, London, 2001, pp. 69–78.
[25] H. Cerjak, The Role of Welding in the Power Generation Industry – Houdremont Lecture on the Occasion of 61st IIW Annual Assembly, Graz, 2008.
[26] J.F. Henry, F.V. Ellis, C.D. Lundin, The Influence of Flux Composition on the Elevated Temperature Properties of Cr-Mo Submerged Arc Weldments – WRC Bulletin 354, Welding Research Council, New York, 1990.
[27] P. Mayr, Evolution of Microstructure and Mechanical Properties of the Heat Affected Zone in B-Containing 9% Chromium Steels Submitted for the Degree of Doktor der technischen Wissenschaften. https://online.tugraz.at/tug_online/voe_main2.getvolltext?pCurrPk.
[28] Y. Wang, L. Li, Microstructure evolution of fine-grained HAZ in type IV failure of P91 welds, Welding Journal, (January 2016).
[29] P. Mayr, J.S. Rothwell, The cross-weld performance of 9%Cr creep resistant steels and the influence of welding parameters, in: D. Gandy, J. Shingledecker, (Eds.), Advances in Materials Technology for Fossil Power Plants; Proceedings from the Seventh International Conference, EPRI, 2013.
[30] H. Cerjak, P. Mayr, Creep strength of welded joint of ferritic steels, in: F. Abe, T.U. Kern, R. Viswanathan (Eds.), Creep Resistant Steels, Woodhead Publishing, 2008, pp. 472–503.
[31] M. Tabuchi, H. Hongo, Evaluation of microstructure and creep damage in high-Cr ferritic steel welds, Acta Metallurgica Sinica (English Letters) 24 (3) (June 2011) 225–234.
[32] J. Vekeman, S. Huysmans, E. De Bruycker, Weldability assessment and high temperature properties of advanced creep resisting austenitic steel DMV304HCu, Welding in the World 58 (2014) 873–882, http://dx.doi.org/10.1007/s40194-014-0166-3.
[33] S. Caminada, G. Cumino, L. Cipolla, D. Venditti, A. Di Gianfrancesco, Y. Minami, et al., Creep properties and microstructural evolution of austenitic TEMPALOY steels, International Journal of Pressure Vessels and Piping (2010) 1–9.
[34] J. Cao, Y. Gong, K. Zhu, Z. Yang, X. Luo, G. Fu-Ming, Microstructure and mechanical properties of dissimilar materials joints between T92 martensitic and S304H austenitic steels, Materials and Design 32 (2011) 2763–2770.

[35] M. Urzynocok, R. Jachym, K. Kwiecincki, P. Mariani, Y. Minami, Application of EPRI87 in dissimilar welding austenitic-martensitic welded joints of TEMPALOY AA-1 and T92 steel grades: Advanced in Materials Technology for Fossil Fuel Power Plants: Proc. of 7th Int. Conf, October 22–25, 2013 Waikoloa, Hawaii, USA.
[36] P. Goswami, P(T)91 Steel – A Review of Current Code and Fabrication Practices: Sixth International Conference on Advances in Materials Technology for Fossil Power Plants, August 31–September 3, 2010, Santa Fe, New Mexico.
[37] H. Heuser, R. Fuchs, B. Hahn, Properties of matching filler metals for T91/P91. Conference proceedings: EPRI-RRAC Fifth International Conference on Welding and Repair Technology for Power Plants, October 2002, 4-1.
[38] G. Ludenbach, Stress Corrosion Cracking of T24, VGB Congress, Mannheim, 2012.
[39] F. Masuyama, Material Properties and Heat Treatment and Steamside Oxidation, Component Integrity and Life Assessment. Modules of the ETD Training Course 'T23/P23 and T24/P24 – plant experience+Fabrication, Welding, Heat Treatment, Oxidation and Damage Mechanisms' EDT, 2008.
[40] P.F. Morris, "Terms and Terminology for weld creep testing", ECCC Recommendations, 2 (IIb) (2001).
[41] J. Schubert, A. Klenk, K. Maile, Determination of weld strength factors for the creep rupture strength of welded joints, in: Int Conf. Creep and Fracture in High Temperature Components – Design & Life Assessment Issues, DEStech Publications, London, 2005.
[42] K. Kimura, M. Tabuchi, Y. Takahashi, K. Yoshida, K. Yagi, Long-term creep strength and strength reduction factor for welded joints of ASME Grades 91, 92 and 122 type steels, International Journal of Microstructure and Materials Properties (IJMMP) 6 (1/2) (2011).
[43] J. Parker, Factors affecting type IV creep damage in grade 91 steel welds, Materials Science and Engineering A 578 (2013) 430–437.
[44] C. Chovet, E. Galand, B. Leduey, Effect of Various Factors on Toughness in P92 SAW WM. Oerlikon Competence, May 2009.
[45] D. Hueggenberg, A. Klenk, K. Maile, Behaviour of Ferritic/Martensitic Welds in High Temperature Components Operating Under Creep and Creep-Fatigue Conditions. Presented at: Cyclic Operation of Power Plants and CCGTs – Technical, Operational and Cost Issues, Charlotte, NC, USA, 2012, pp. 28–29. November 2012; 29 pp. (2012).
[46] G. Merckling, Specifications for creep-resistant steels, in: F. Abe, T.-U. Kern, R. Viswanathan, (Eds) Creep-Resistant Steels. ISBN:9781845691783.
[47] H. Heuser, C. Jochum. Pipe steels for modern high output power plants – filler metals and their use in welding, Vallourec & VoestAlpine Bohler Welding. http://www.vallourec.com/fossilpower/Lists/Brochures/Attachments/7/V_B01B0005B-15GB.pdf.
[48] ASME B31.1–2010, Power Piping, ASME Code for Pressure Piping. B31.
[49] ASME Boiler Pressure Vessel Code-2015, Section V, Article 1, Table-1, Imperfection vs. type of NDE.
[50] C. Lochbichler, E. Schmidtne, S. Baumgartner, Latest development of cast and welding consumables for coal-fired steam turbine components/Nickel-base alloy 625 and CB2 steel for A-USC technology: pennwell.websds.net/2013/.../T4S2O3-paper.pdf.
[51] CreepTest – Early-Stage Creep Damage Detection. http://www.twi-global.com/news-events/case-studies/creeptest-early-stage-creep-damage-detection-607/.

This page intentionally left blank

Part Two

Advanced ultra-supercritical power plant materials

This page intentionally left blank

New martensitic steels

10

F. Abe
National Institute for Materials Science, Japan

10.1 Introduction

Energy security combined with lower carbon dioxide emissions are increasingly quoted to protect the global environment in the 21st century. Coal provides us abundant, low-cost resources for electric power generation. However, traditional coal-fired power plants have been emitting environmentally damaging gases such as CO_2, NO_x, and SO_x at high levels relative to other electric power generation options. Adoption of ultra-supercritical (USC) power plants with increased steam parameters significantly improves efficiency, which reduces fuel consumption and the emissions of environmentally damaging gases. In Japan, coal-fired steam power plants have already extended to the USC conditions in the 1990s, which are based on materials technology accumulated for high-strength heat-resistant steels [1,2]. This enables the steam temperature to be raised to 610–620°C, as shown in Fig. 10.1.

In addition to enough creep strength, high operational flexibility is another issue for thick-section components in USC power plants. Martensitic steels of 9 to 12% Cr can offer the highest potential to meet the required flexibility because of their smaller thermal expansion and larger thermal conductivity than austenitic steels and Ni-base alloys.

The materials development projects for advanced ultra-supercritical (A-USC) power plants with steam temperature of 700°C or above have been performed to achieve a high efficiency in Europe [3,4], in the United States [5], in Japan [6], China [7], India [8], and so on. These projects involve the replacement of martensitic 9 to 12Cr steels with Ni-base alloys for the components subjected to the highest temperature. To minimize the requirement of expensive Ni-base alloys, martensitic 9 to 12Cr steels can be used for the components subjected to the next-highest temperatures, below 650°C [1]. Critical issues for the development of martensitic 9 to 12Cr steels for 650°C USC boilers are the improvement of oxidation resistance as well as long-term creep strength, including welded joints. In the A-USC project in Japan, the target values of 100,000 h creep rupture strength for candidate ferritic steels for thick-section boiler components are larger than 80 MPa at 650°C and larger than 0.7 of weld strength reduction factor at 650°C and 100,000 h [6].

This chapter comprehensively describes the development history of martensitic 9 to 12Cr steels in coal-fired power plants, the strengthening mechanisms and degradation behavior in creep of martensitic 9 to 12Cr steels, and the key metallurgy for achieving the improvement of long-term creep strength of base metal and welded joints for martensitic 9Cr steel at 650°C by microstructure stabilization near prior austenite grain boundaries (PAGBs). The improvement of oxidation resistance in steam at 650°C is achieved by pre-oxidation treatment in argon gas.

Materials for Ultra-Supercritical and Advanced Ultra-Supercritical Power Plants.
http://dx.doi.org/10.1016/B978-0-08-100552-1.00010-5
Copyright © 2017 Elsevier Ltd. All rights reserved.

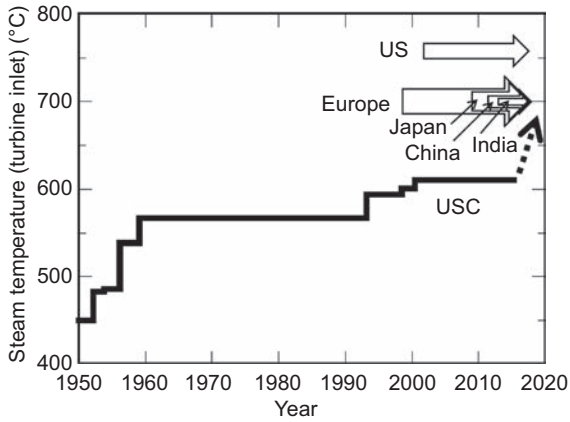


Figure 10.1 Increase in steam temperature of coal-fired power plants in Japan and intended steam temperature in several A-USC projects.

10.2 Development history and utilization of 9 to 12Cr martensitic steels in coal power plants

Fig. 10.2 shows the development progress of martensitic boiler and turbine steels in Japan. The improvement of creep strength of martensitic 9 to 12Cr steels has been achieved by substituting a part or all of Mo with W and also by the addition of Co, Nb, nitrogen, and boron. The total concentration of alloying elements has been gradually increasing to improve the creep strength. The increase in ferrite-forming element W requires higher Co, which is an austenite stabilizing element, for the elimination of δ-ferrite. Three high-strength 9Cr steels of MARBN, Low-C 9Cr, and SAVE12AD are candidates in the A-USC project in Japan for the thick-section boiler components such as main steam pipes and headers operating at 650°C maximum [1,6]. The candidates for the highest temperature boiler components at around 700°C are Ni-base alloys. MARBN is a martensitic steel strengthened by boron and MX nitrides, which was alloy-designed on the base of the stabilization of martensitic microstructure in the vicinity of PAGBs [9]. Low-carbon 9Cr steel was alloy designed to stabilize the martensitic microstructure at elevated temperature, by minimizing impurities Ni and Al as low as possible [10]. The carbon concentration is also reduced to 0.035%, which improves weldability. SAVE12AD contains high boron but low nitrogen, similar to MARBN [11]. Original SAVE12 contained a high Cr concentration of 12%, but in SAVE12AD the Cr concentration is reduced to 9% to achieve long-term stabilization of martensitic microstructure [12].

MTR10A, HR1200, and TOS110 in Fig. 10.2 were developed by fabrication companies in Japan in the late 20th century before starting the A-USC project for application to turbine rotors with steam temperature of 630°C [13]. These rotor steels were originally intended to be used in 650°C-class USC power plants. At present, however, we have no 650°C-class USC power plant. Therefore, the rotor steels are

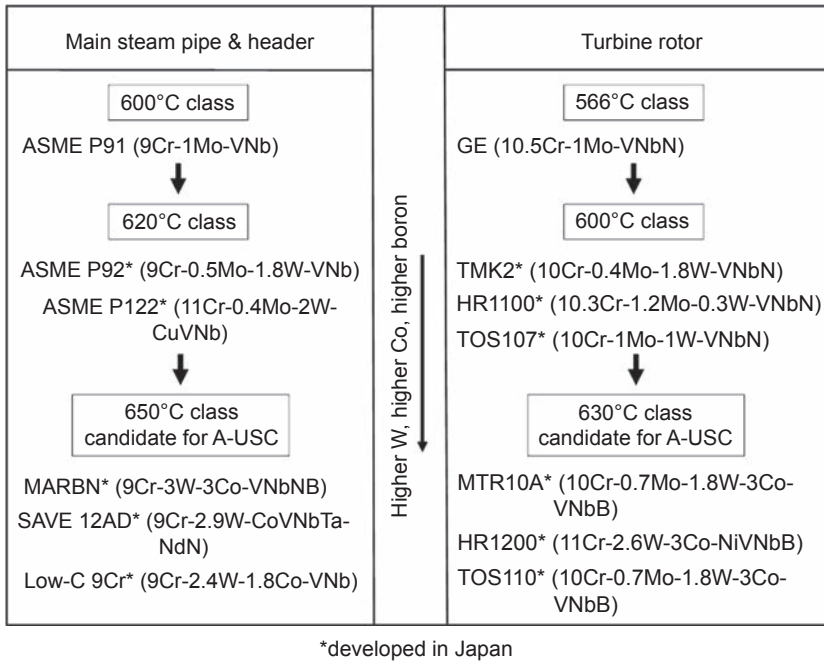


Figure 10.2 Development progress of martensitic boiler and turbine steels in Japan.

now candidates in the A-USC project in Japan for the next-highest temperature rotors, operating at 630°C maximum. MTR10A, HR1200, and TOS110, which were developed as upgrade versions of TMK2, HR1100, and TOS107, respectively, are martensitic 10 to 11Cr steels containing high W, Co, and boron, similar as boiler steels MARBN, Low-C 9Cr and SAVE12AD.

In Europe, the development and evaluation of martensitic 9 to 12Cr steels for boiler and turbine of USC power plants have been continued within the frame of European COST programs, COST 501 (1986–1997), COST 522 (1998–2003), and COST536 (2004–2009), where COST means Cooperation in Science and Technology [14,15]. The target temperature of the steels to be developed was set to be 600, 620, and 650°C in the COST 501, COST 522, and COST 536 programs, respectively. The outcome of COST 522 was the demonstration of the manufacturability of large rotor forgings in the alloy with the highest potential for 620°C application, which is an FB2 steel (9Cr-1Mo-1Co-0.2V-0.07Nb-0.02N-100 ppm boron type). In the COST 536 program, on the base of the promising composition of FB2, the role of Nb and Ta in the long-term creep stability has been investigated using a trial melt FB2-3Ta (8.9Cr-1.49Mo-1.0Co-0.2V-0.003Nb-0.013B-0.009N-0.08Ta) with higher Si for steam oxidation resistance, a changed boron/nitrogen ratio, lowest Ni content, and replacement of a part of Nb by Ta [15]. The results of creep rupture testing at 650°C on a trial melt FB2-3Ta suggest that Ta in the chosen concentration would not be more effective than Nb compared to FB2.

Other strategies in Europe are that the characterization of 9Cr steel having the same chemical compositions as MARBN and the further optimization of MARBN are being conducted in several projects, UK Impact project [16], MACPLUS project [17], Energy Materials Working Group (WG2), and EMEP (engineered micro- and nanostructures for enhanced long-term high-temperature materials performance) [18,19]. Their objectives are to develop advanced MARBN for the long-term safe operation at 650°C.

In China, a martensitic 9Cr steel G115 was developed for pipe applications at 650°C or below and is now a candidate steel in the A-USC project in China [20]. The chemical composition of G115 is 9Cr-3W-3Co-1CuVNbB containing 150 ppm boron and 140 ppm nitrogen, similar to MARBN except for the addition of 1% Cu.

In the United States, there is no program on the development of new martensitic 9 to 12Cr steels in the US DOE/OCDO A-USC project. The strategy in the United States is to use existing martensitic 9 to 12Cr steels.

10.3 Basic methods of strengthening martensitic 9 to 12Cr steels in creep at elevated temperature

The basic methods in which creep-resistant steels can be strengthened are solid solution hardening, precipitation hardening, dislocation hardening, and boundary and sub-boundary hardening [21–23]. It is possible to combine several strengthening mechanisms, but it is often difficult to quantify the contribution of each mechanism to the overall creep strength. It becomes evident that the boundary and sub-boundary hardening is the most important strengthening mechanism in long-term creep of martensitic 9 to 12Cr steels and is enhanced by fine dispersion of precipitates along boundaries for up to long times. In the following, recent topics on the basic methods of strengthening martensitic 9 to 12Cr steels for power plants are described.

10.3.1 Solid solution hardening

Substitutional solute atoms, such as Mo and W, which have much larger atomic sizes than that of solvent iron, have been favored as solid solution hardeners for both ferritic and austenitic creep-resistant steels. The contribution from solid solution hardening due to Mo and W to the overall creep strength of creep-resistant steels is practically superimposed on other strengthening mechanisms, eg, precipitation hardening. The addition of Mo and W sometimes causes the precipitation of $Fe_2(Mo,W)$ Laves phase and enhances fine distributions of $M_{23}C_6$ carbides during exposure at elevated temperature. The M in $M_{23}C_6$ means the metallic elements and C the carbon. European scientists and engineers have favored the addition of Mo for enhancing the solid solution hardening of 9 to 12Cr steels, while Japanese have utilized W.

Fig. 10.3 shows the amount of $Fe_2(Mo,W)$ Laves phase in 0.08C-9Cr-(W/Mo)-0.2V-0.05Nb-0.05N-0.005B steel at 650°C as a function of 1/2W/(1/2W + Mo) and also the creep rupture data for 0.08C-9Cr-(W/Mo)-0.2V-0.05Nb-0.05N-0.005B steel with 3W-0Mo and 0W-1.5Mo at 600–700°C [24]. The amount of $Fe_2(Mo,W)$ Laves

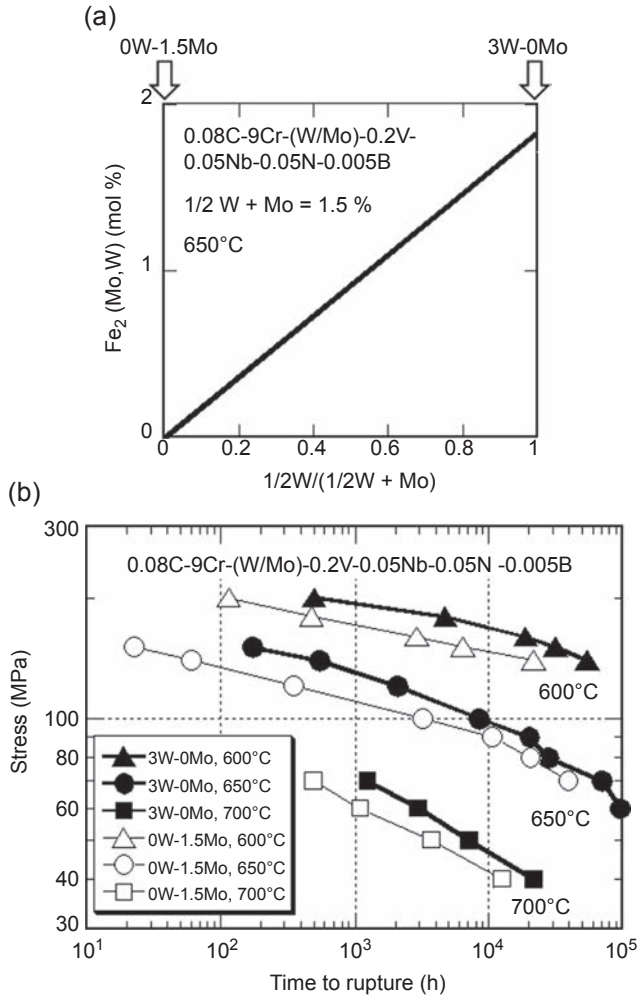


Figure 10.3 (a) Amount of Fe_2(Mo,W) Laves phase at 650°C as a function of 1/2W/(1/2W + Mo) and (b) creep rupture data for 0.08C-9Cr-(W/Mo)-0.2V-0.05Nb-0.05N-0.005B steels with 3W-0Mo and 0W-1.5Mo at 600 to 700°C.

phase was estimated by Thermo-Calc. Because the atomic weight of W is two times of Mo, the atomic concentration of W in the 9Cr steel with 3W-0Mo is the same as that of Mo in the 9Cr steel with 0W–1.5Mo. The increase in the amount of Fe_2(Mo,W) Laves phase with increasing 1/2W/(1/2W + Mo) indicates that the concentration of dissolved W and Mo in the matrix decreases with increasing 1/2W/(1/2W + Mo). The higher creep rupture strength of the 9Cr steel with 3W-0Mo than the 9Cr steel with 0W–1.5Mo shown in Fig. 10.3(b) indicates that the solid solution hardening due to W and Mo is not a main strengthening mechanism for the 9Cr steel. The addition of W stabilizes fine distributions of $M_{23}C_6$ carbides in the 9Cr steel during creep,

enhancing the precipitation hardening due to $M_{23}C_6$ carbides. Although the precipitates of Fe_2(Mo,W) Laves phase are prone to coarsening in 9Cr steels during creep at 600–650°C, the precipitation hardening and boundary hardening enhanced by fine $M_{23}C_6$ carbides are the main strengthening mechanisms for the 9Cr steel.

Regarding the effect of interstitial solute atoms, it is proven that nitrogen is beneficial to the long-term creep strength of ferritic and austenitic creep-resistant steels through its solid solution hardening as well as precipitate hardening by forming fine nitrides.

10.3.2 Precipitation hardening

To achieve enough strengthening by this effect, creep-resistant steels usually contain several kinds of carbides, carbonitrides, intermetallic compounds, and metallic phases in the matrix and at grain boundaries (GBs). The common carbides and carbonitrides in steels are $M_{23}C_6$, M_6C, M_7C_3, MX, and M_2X. The X in MX and M_2X means the carbon and nitrogen. Intermetallic compounds mainly consist of Fe_2(Mo,W) Laves phase, Fe_7W_6-μ phase, χ phase, and so on.

Several mechanisms have been proposed for the threshold stress, which is defined as the stress needed for a dislocation to pass through precipitate particles, such as the Orowan mechanism, local climb mechanism, general climb mechanism, and Srolovitz mechanism [25]. The Orowan stress σ_{or} is given by

$$\sigma_{or} = 0.8\, MGb/\lambda \tag{10.1}$$

where M is the Taylor factor (=3), G the shear modulus, b the magnitude of the Burgers vector, and λ is the mean interparticle spacing [21]. Typical values of the volume fraction, diameter, and spacing of the major particles contained in martensitic 9 to 12Cr steels after tempering are listed in Table 10.1, together with the Orowan stress estimated from the values of interparticle spacing [21].

The coarsening of fine precipitates, such as $M_{23}C_6$, MX, and Fe_2(W,Mo) Laves phase, and the dissolution of fine MX to form massive precipitates of Z phase, which have been observed in 9 to 12Cr steels, increase the λ term in Eq. (10.1) and hence decrease the Orowan stress. This results in a drastic reduction in the resistance to creep and causes a premature creep rupture.

Table 10.1 Volume fraction, diameter and spacing of each kind of precipitates in martensitic 9 to 12Cr steels, together with Orowan stress estimated from the values of interparticle spacing

Particle	Volume fraction V (%)	Diameter d_p (nm)	Spacing λ_p (nm)	Orowan stress σ_{or}(MPa)
Fe_2(W,Mo)	1.5	70	410	95
$M_{23}C_6$	2	50	260	150
MX	0.2	20	320	120

Sawada and coworkers observed that the number density of Z phase gradually increased with time after about 10,000 h in Gr.91 during creep at 600°C, while that of MX decreased substantially after 30,000 h, as shown in Fig. 10.4 [26]. This suggests that the MX particles become dissolved with time in favor of the growth of the thermodynamically more stable Z phase.

10.3.3 Dislocation hardening

For a moving dislocation, other dislocations act as obstacles. This is the most basic definition of dislocation hardening. The dislocation hardening is given by

$$\sigma_\rho = 0.5\, MGb(\rho_f)^{1/2}, \tag{10.2}$$

where ϱ_f is the free dislocation density in the matrix [21]. The dislocation hardening is an important strengthening mechanism in steel at ambient temperature. Martensitic 9 to 12Cr steels usually contain a high density of dislocations even after tempering, in the range of 1 to $10 \times 10^{14}/m^2$ in the matrix.

In contrast, at elevated temperatures, cold working enhances softening by promoting the recovery of excess dislocations and recrystallization of the deformed microstructure, reducing the creep strength. Thus dislocation hardening is not beneficial to the long-term creep strength at elevated temperature where recovery and recrystallization take place.

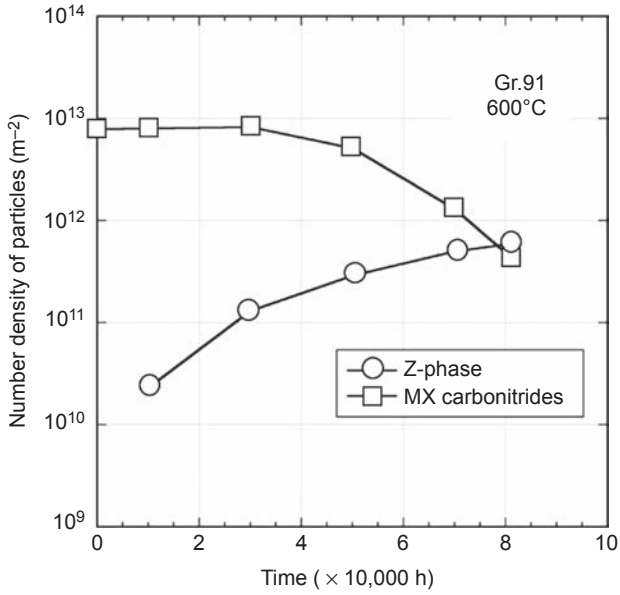


Figure 10.4 Change in number density of MX and Z phase particles in Gr.91 during creep at 600°C and 70 MPa.

10.3.4 Boundary and sub-boundary hardening

The tempered martensitic microstructure of 9 to 12Cr steels consists of laths, blocks, and packets in prior austenite grains after appropriate tempering, as shown schematically in Fig. 10.5. The laths, blocks, and packets have a high dislocation density with fine precipitates of $M_{23}C_6$ mainly along various boundaries as well as fine MX mainly in the matrix. The $M_{23}C_6$ carbides are usually rich in Cr, while the MX carbonitrides are rich in V and Nb. Fig. 10.6 shows the TEM micrograph of Gr.91 (9Cr-1Mo-VNb steel) after normalizing and tempering.

The laths and blocks can be regarded as elongated subgrains. The sub-boundary hardening due to the presence of laths and blocks is given by

$$\sigma_{sg} = 10Gb/\lambda_{sg} \tag{10.3}$$

where λ_{sg} is the short width of elongated subgrains [21].

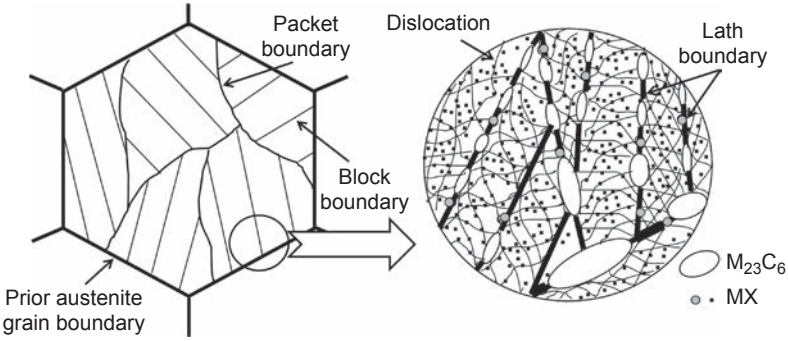


Figure 10.5 Schematic illustration of tempered martensitic microstructure of 9 to 12Cr steels.

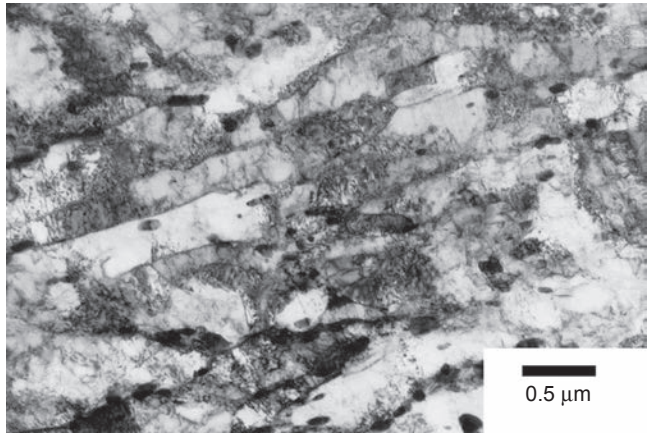


Figure 10.6 TEM micrograph of Gr.91 after normalizing and tempering.

The subgrain width λ_{sg}, corresponding to the width of laths and blocks, in martensitic 9 to 12Cr steels is in the range of 0.3–0.5 μm after tempering. The values of $G = 64$ GPa at 650°C, $b = 0.25$ nm, and $\lambda_{sg} = 0.3$–0.5 μm give the sub-boundary hardening of 530–320 MPa, which is much higher than the Orowan stress given in Table 10.1 for $Fe_2(W, Mo)$, $M_{23}C_6$, and MX. The sub-boundary hardening enhanced by fine distributions of precipitates along boundaries gives the most important strengthening mechanism for creep of tempered martensitic 9 to 12Cr steels.

10.4 Degradation in creep strength at long times

The loss of creep strength at long times has extensively been investigated for a number of martensitic 9 to 12Cr steels [22,23]. The proposed mechanisms for microstructure degradation during creep exposure leading to the loss of creep strength are classified next:

1. precipitation of thermally stable phases and dissolution of fine carbonitrides
2. preferential recovery of microstructure near PAGBs
3. combined coarsening of laths and precipitates
4. recovery of excess dislocations resulting from low-temperature tempering
5. static recovery
6. adverse effect of δ-ferrite
7. loss of creep ductility

It is possible to combine several mechanisms, but it is often difficult to quantify the contribution of each mechanism to the overall creep strength loss. For the development of advanced martensitic steels, which will be described in Section 10.6, we need to take the alloy design for minimization of the degradation into account. In the following, the recent topics on degradation mechanisms are described.

With respect to the effect of precipitation of thermally stable phases and dissolution of existing fine carbo-nitrides, European scientists and engineers have considered that the precipitation of Z phase exhibits the most detrimental effect on the creep strength of martensitic 9 to 12Cr steels. The Z phase is a complex nitride in the form of Cr(Nb,V)N. The precipitation of Z phase takes place after a long time at and above 550°C, and it forms large particles at the expense of previously existing fine vanadium nitrides, consequently leaving a vanadium nitride-free zone around the Z phase [27–29]. This causes a drastic loss of creep strength. 12Cr steels are more susceptible to the precipitation of Z phase than 9Cr steels [30]. Higher concentrations of Ni and nitrogen also accelerate the precipitation of Z phase [31,32]. It should be noted that there are some discrepancies about the experimental results concerning the effect of Z phase on the degradation in creep rupture strength of 9 to 12Cr steels. Sklenicka and coworkers pointed out that the synergetic effect of Z phase precipitation and tungsten depletion in solid solution due to Fe_2W Laves phase formation could be the reason for the sigmoidal shape of creep rupture data of TAF 650 steel (0.1C-0.55Mn-0.07Si-10.84Cr-0.14Mo-2.63W-2.86Co-0.55Ni-0.19V-0.06Nb-0.016N-0.019B) at 650°C [33]. Based on the results shown in Fig. 10.4, Sawada and coworkers concluded that the preferential recovery in the vicinity of PAGBs and the abrupt decrease in number

density of MX particles due to Z phase formation contribute to the premature failure of Gr.91 at 600°C.

Di Gianfrancesco and coworkers investigated the microstructural evolution in P91 after very long-term creep testing, more than 100,000 h at 550, 600, and 650°C [34]. They observed the precipitate particles of Z phase in P91 after aging at 600 and 650°C for more than 100,000 h. Because their creep rupture data showed no degradation for more than 100,000 h, they pointed out that the Z phase could not be listed among the degradation mechanisms of Gr.91. Maruyama and coworkers investigated the microstructure evolution and degradation in creep rupture strength of Gr.91 at 600 to 700°C [35,36]. The creep rupture data exhibit the degradation in creep strength at low stresses and long times above about 10,000 and about 200 h at 650 and 700°C, respectively. Their results on the microstructure observations show no precipitation of Z phase and no disappearance of existing MX. They reported that MX precipitates and Z phase have nothing to do with the breakdown. We need further discussion about the effect of Z phase formation on the degradation in creep rupture strength and also about the main strengthening mechanisms in creep of 9 to 12Cr steels.

Al and Ti form AlN and TiN in creep-resistant steels by consuming nitrogen and fine nitrides during creep exposure because Al and Ti are strong nitride-forming elements. This leads to the degradation in creep strength. Usually, Al is used as a deoxidizing element in melting and casting process of creep-resistant steels, and hence a small amount of Al remains in the steels after casting as an impurity in the form of Al_2O_3 and soluble Al. Soluble Al can form AlN during creep exposure. Fig. 10.7 shows the degradation in creep rupture strength of a high Al heat of tempered martensitic 12Cr-1Mo-1W-0.3V steel for a turbine blade [37,38]. The creep rupture data are substantially the same between the low and high Al heats at short times, while the degradation in creep rupture strength becomes more significant in the high Al heat with increasing test duration at long times above 10,000 h at 550°C. The formation of AlN particles has been observed after long-term creep exposure. Soluble nitrogen and fine

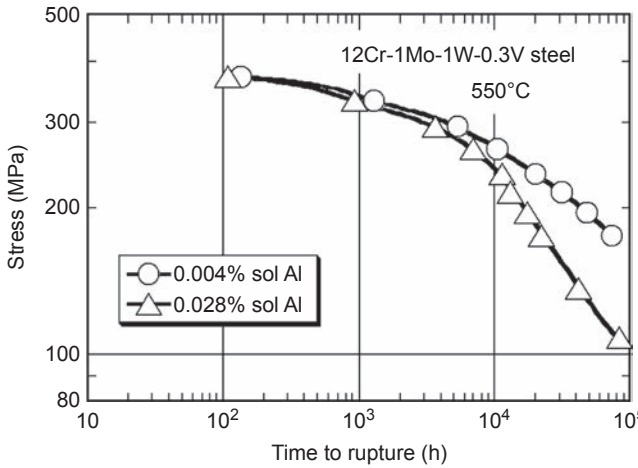


Figure 10.7 Effect of Al on creep rupture data for 12Cr-1Mo-1W-0.3V steel.

nitrides are available for creep strengthening but the formation of AlN and TiN during creep offsets the beneficial effect of nitrogen. Therefore, the available nitrogen concentration N_{av} is defined as the concentration of nitrogen free from AlN and TiN. Assuming the formation of stoichiometric compound of AlN and TiN, the N_{av} is described as

$$N_{av} = \text{Nitrogen} - \text{Al} - \text{Ti} \ (\text{at } \%) \tag{10.4}$$

which corresponds to

$$N_{av} = \text{Nitrogen} - 0.519\ \text{Al} - 0.292\ \text{Ti} \ (\text{mass } \%) \tag{10.5}$$

and

$$N_{av}\ (\text{mass } \%) = 1/4\ N_{av} \ (\text{at } \%) \tag{10.6}$$

The time to rupture of the nine heats of 12Cr-1Mo-1W-0.3V steel in NIMS Creep Data Sheets decreases as the available nitrogen concentration N_{av} decreases at low stresses and long times. In Gr.91, the insufficient initial strength associated with low nitrogen and high Al after tempering heat treatment results in insufficient creep strength at elevated temperature, and a high concentration of Al is more susceptible to forming cracks early in life [39]. Another topic on the effect of impurities is Ni. The results that Ni accelerates the degradation in long-term creep rupture strength of Gr.91 have been reported [40]. The EPRI guideline recommends less than 0.2% Ni for Gr.91, which is lower than the level of 0.4% currently stated in the ASME/ASTM specifications [41].

With respect to the effect of preferential recovery of microstructure near PAGBs and the effect of combined coarsening of laths and precipitates, Fig. 10.8 shows a

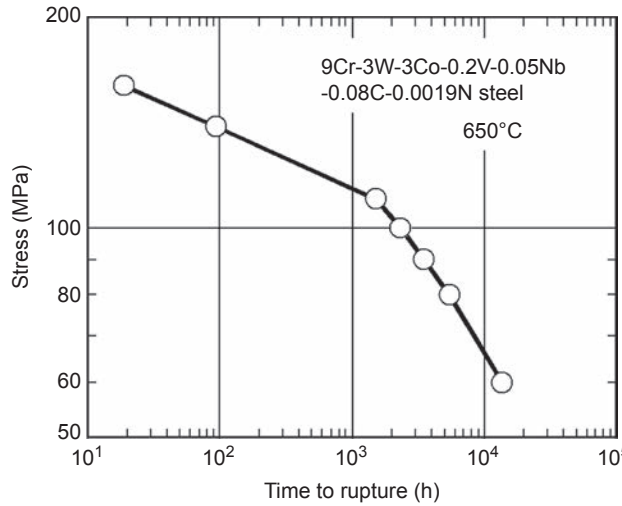


Figure 10.8 Creep rupture data for 9Cr-3W-3Co-VNb steel at 650°C.

loss of creep rupture strength for a 9Cr-3W-3Co-0.2V-0.05Nb steel with 0.08% carbon but no addition of nitrogen at long times above about 1000 h at 650°C [42]. The residual nitrogen concentration of the steel was only 0.0019% (19 ppm), suggesting an extremely low amount of MX carbonitrides and hence an extremely low driving force for Z phase formation during creep. Therefore, the dissolution of fine M_2X and MX carbonitrides and the precipitation of Z phase cannot be responsible for the loss of creep rupture strength. The proposed mechanism for the loss of creep strength in the steel is the coarsening of $M_{23}C_6$ carbides and laths in the vicinity of PAGBs.

Kushima and coworkers observed the preferential recovery of lath martensitic microstructure in the vicinity of PAGBs of Gr.91 after creep rupture testing for 34,141 h at 600°C and 100 MPa [43]. The preferential recovery promotes localized creep deformation in the vicinity of PAGBs, which results in the premature creep rupture.

With respect to the effect of recovery of excess dislocations resulting from low-temperature tempering, excess dislocations resulting from low-temperature tempering (750°C) promote a rapid reduction in creep rupture strength in 12Cr-1Mo-1W-VNb steel at 600 and 650°C over long periods; see Fig. 10.9 [44]. This is because excess dislocations accelerate recovery and recrystallization during creep with the aid of stress, which also accelerates microstructure evolution during creep. The high-temperature tempering (800°C) results in a lower dislocation density, suggesting less driving force is available for microstructural evolution during creep. The tempering is usually carried out at temperatures of about 700°C or lower for 12Cr turbine steels, whereas it is as high as 750–800°C for 9 to 12Cr boiler steels. Therefore, the stabilization of microstructure including excess dislocations is more critical for turbine steels than for boiler steels.

With respect to the effect of static recovery, Maruyama and coworkers recently proposed that the tempered martensitic microstructure in 9 to 12Cr steels remains unchanged during short-term aging, whereas the static recovery of lath martensitic microstructure proceeds during aging when the diffusion distance is sufficiently long, as is the case in the long-term creep [35,36]. Fig. 10.10 shows the creep rupture data and Vickers

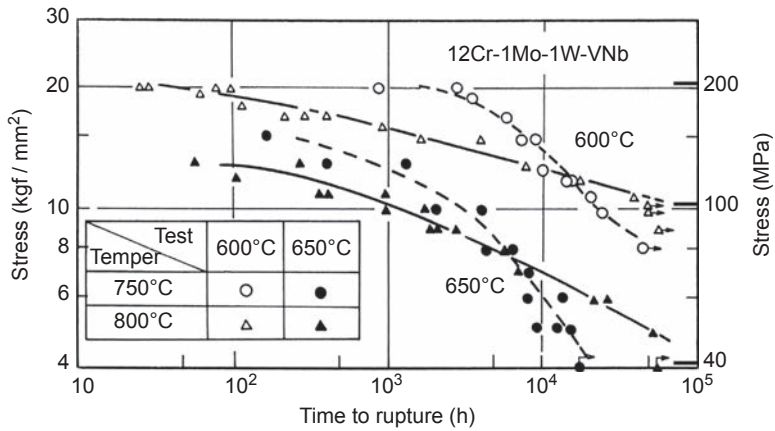


Figure 10.9 Effect of tempering temperature on creep rupture strength of 12Cr-1Mo-1W-VNb steel at 600 and 650°C.

hardness in the grip portion of the creep ruptured specimens of Gr.91. The creep rupture data exhibit the degradation in creep strength at low stresses and long times at 650 and 700°C. The hardness of Gr.91 is kept constant at short times during aging, whereas it decreases at long times due to the static recovery of lath martensitic microstructure at 650 and 700°C. The static recovery means the recovery due to thermal aging under no stress. The drop in hardness accords very well with the degradation in creep strength, suggesting that the static recovery of lath martensite microstructure causes the degradation in creep strength of Gr.91.

The subgrain width is kept constant in the time range shorter than 5000 h at 650°C and 100,000 h at 600°C, and then increases with increasing aging time, Fig. 10.11. The interparticle spacing of MX precipitates does not change at all, even after long-term aging, due to their high thermal stability, while that of $M_{23}C_6$ precipitates is kept constant up to

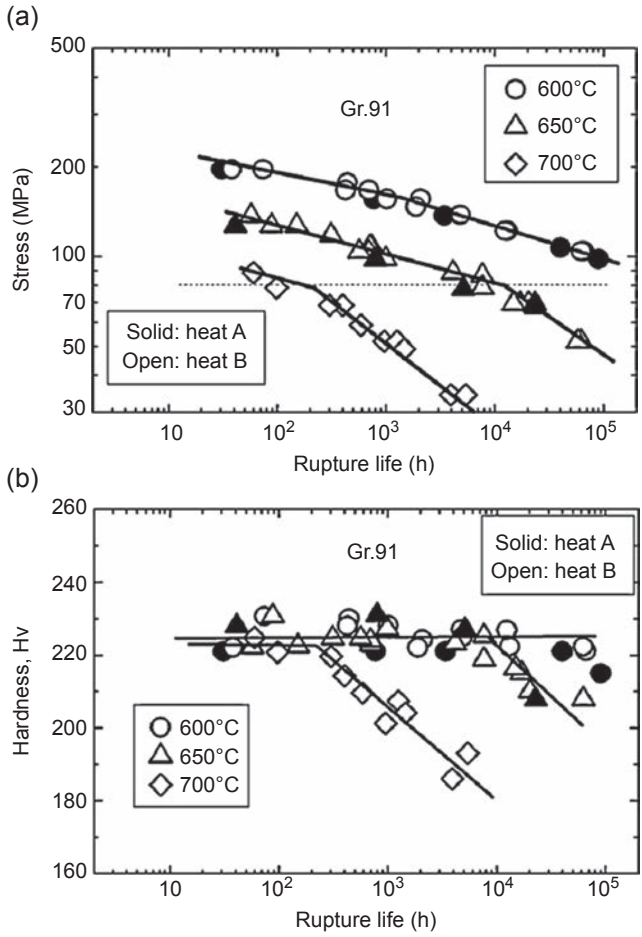


Figure 10.10 (a) Creep rupture data and (b) hardness change in head portion under no stress (thermal aging) of Gr.91.

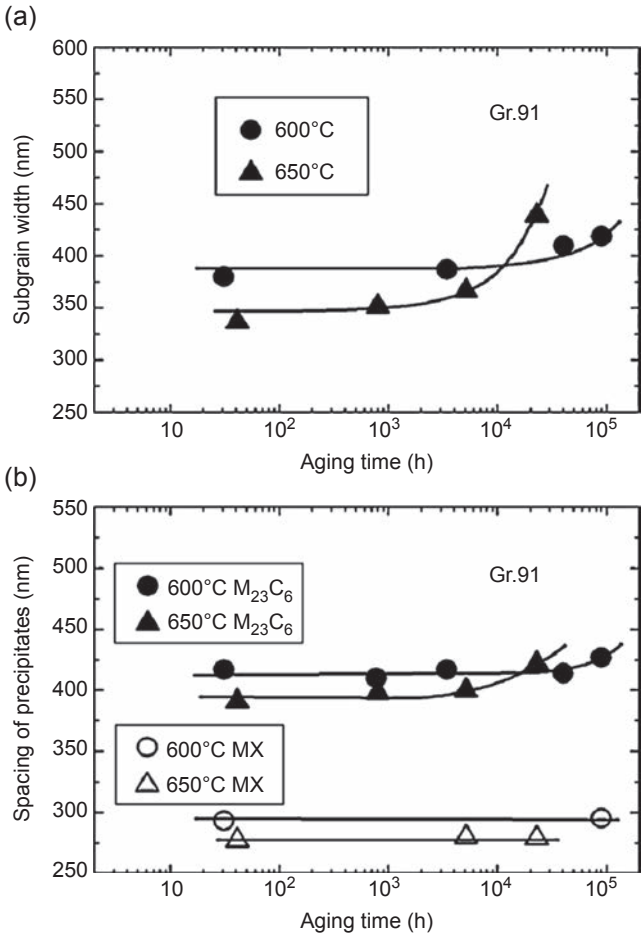


Figure 10.11 (a) Subgrain width and (b) interparticle spacing of $M_{23}C_6$ and MX in Gr.91 during aging.

5000 h at 650°C and 100,000 h at 600°C, and then it increases with increasing aging time. Maruyama and coworkers consider that subgrain boundaries are the major obstacles to dislocation motion in 9 to 12Cr steels, and the creep strength of Gr.91 is determined by subgrain width [21]. There are two types of recovery processes of subgrains that happen in Gr.91 steel during creep exposure: strain-induced recovery and static or thermal recovery. Since the static recovery of subgrains happens during long-term creep, the acceleration of creep deformation and the consequent breakdown of creep strength should take place in this region. The static recovery of subgrains is caused by a loss of pinning force from $M_{23}C_6$ precipitates due to coarsening.

With respect to the adverse effect of δ-ferrite, the degradation in creep strength of dual-phase 12Cr steel (12Cr-0.4Mo-2W-CuVNb steel, specified as KA-SUS410J-3DTB) is explained by this effect [45,46].

With respect to the effect of loss of creep ductility, Maruyama and coworkers pointed out that the loss of ductility is the origin of the loss of creep rupture strength in 11Cr-2W-0.3Mo-CuVNb steel at 650°C [21].

10.5 Fundamental aspects of tempered martensitic microstructure and creep deformation

The tempered martensitic microstructure of creep strength–enhanced ferritic steels, such as Gr.91 (9Cr-1Mo-VNb steel), Gr.92 (9Cr-0.5Mo-1.8W-VNb steel), and Gr.122 (11Cr-0.4Mo-2W-CuVNb steel), consists of laths, blocks, and packets in prior austenite grains. The coarsening rate of $M_{23}C_6$ carbides is much larger in the vicinity of PAGBs than within grain. The stabilization of fine precipitates, especially at and near PAGBs, for up to long times is a key issue for the suppression of creep strength loss, as will be described later.

The creep and creep rate curves consist of the primary or transient creep region, where the creep rate decreases with time, and of the tertiary or acceleration creep region, where the creep rate increases with time after reaching a minimum creep rate, as shown schematically in Fig. 10.12. There is substantially no steady-state region, where the creep rate is constant. In tempered martensitic steels, there is an ever evolving microstructure, and the change in creep rate reflects coupled elementary processes, such as micro-grain growth, change in dislocation density, and change in precipitate volume fraction and size [47,48]. This suggests that there is no dynamic microstructural equilibrium in tempered martensitic steels during creep. During creep, the recovery of excess dislocations and the coarsening of precipitates and laths take place with the aid of stress and strain.

The present author has revealed for tempered martensitic 9Cr steel that the transient creep is basically a consequence of the movement and annihilation of a high density of dislocations produced by martensitic transformation during cooling after normalizing and also produced by plastic deformation upon loading and that the acceleration creep is a consequence of gradual loss of creep strength due to the microstructure evolution [47,48]. He has also suggested that the migration of lath or block boundaries, causing the coarsening of the laths or blocks in the acceleration creep region, is closely correlated with the onset of acceleration creep. The creep life t_r of Gr.91 is correlated with the onset time of acceleration creep, namely, the time to minimum creep rate t_m as [49,50].

$$t_r = g\, t_m. \tag{10.7}$$

$$\begin{aligned} 1/g &= (t_m/t_r) \\ &= 1.10 \times 10^{-1}\, log\, \sigma + 2.90 \times 10^{-3} \quad \text{at 40 to 100 MPa} \\ &= 4.05 \times 10^{-1}\, log\, \sigma - 5.89 \times 10^{-1} \quad \text{at 100 to 260 MPa} \end{aligned} \tag{10.8}$$

The ratio of the time to minimum creep rate to the creep life (t_m/t_r) slightly decreases with decreasing stress: $t_r = 4.5\, t_m$ at 100 MPa. The average value of g over a wide temperature and stress range is evaluated to be 3.7.

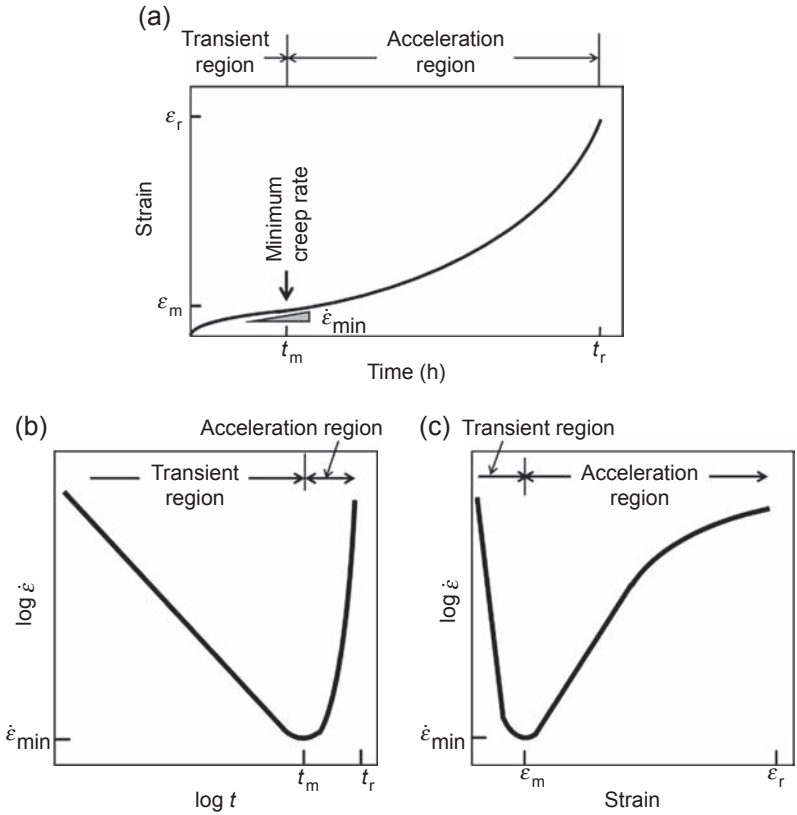


Figure 10.12 (a) Schematic creep curve, (b) creep rate versus time curve and (c) creep rate versus strain curve.

The coarsening rate of precipitates during creep is much larger at and in the vicinity of PAGBs than within grain because of enhanced diffusion along PAGBs. The coarsening of precipitates increases the interparticle distance and reduces the pinning of boundaries for migration. This suggests that the stabilization of fine precipitates, especially at and near PAGBs, for up to long times is a key issue for the suppression of boundary migration, which results in the retardation of onset of acceleration creep.

10.6 New martensitic 9Cr steel

10.6.1 Precipitate design

Bhadeshia pointed out that in a multiphase system such as creep-resistant 9 to 12Cr steels, the coarsening behavior of precipitates is greatly influenced by the presence of other phases [51]. In the following, for simplicity, we will describe what kind of precipitate phases are the most appropriate as coarsening-resistant phases during

exposure at elevated temperature, based on Fe-M-C alloys, where M is alloy element and C is carbon [9]. The volume diffusion controlled Ostwald ripening of M_aC_b carbides in Fe-M-C alloys has been given by the following [52].

$$r^3 - r_0^3 = k_3 t \tag{10.9}$$

$$k_3 = 8\,(a+b)\,\sigma V D_M u_M / 9aRT\,(u_{pM} - u_M)^2 \tag{10.10}$$

where r and r_0 are the average particle radius at the time t and $t=0$, respectively, σ is the interfacial energy of the carbides, V is the molar volume of the carbides, D_M is the volume diffusion coefficient of metal M, u_M and u_{pM} are the concentration of M in matrix and carbides, respectively, R is gas constant, and T is temperature. The main factors affecting the coarsening rate of precipitate particles are diffusion coefficient, solid solubility of participating elements, and interfacial energy. We evaluate the diffusion coefficient and solid solubility of alloying elements in iron. Impurity diffusion coefficients in iron are not so different, less than one order of magnitude, among different elements, such as W, Mo, V, and Nb [53]. On the other hand, the solid solubility of alloying elements, which are equilibrating with their carbides, nitrides, and Fe_2(Mo,W) Laves phase in Fe-M-0.1%C ternary, Fe-M-0.05%N ternary, and Fe-M binary alloys, respectively, is evaluated by using Thermo-calc. This is shown in Fig. 10.13. The solid solubility of V, Nb, and Ti equilibrating with their nitrides in Fe-M-0.05% N alloys is very low. It should be noted that TiN is extremely stable for up to melting temperature because of extremely low solid solubility in iron for up to melting temperature. This indicates that we cannot control a dispersion of fine TiN by appropriate heat treatment, such as solution treatment and subsequent aging or tempering. Thus TiN is excluded from the present precipitate designing. Carbides and nitrides of V and Nb and carbides of Ti are the most appropriate candidates, which show very low coarsening rate during exposure at elevated temperature. However, the addition of carbon to a 9Cr steel causes the formation of a large amount of $M_{23}C_6$ carbides rich in Cr. Wey and co-workers reported that the coarsening rate of Cr carbides in iron was much larger than that of V and Nb carbides at elevated temperature [52]. Therefore, it is crucial for 9Cr steel to reduce carbon concentration to very low amounts, so as to promote the formation of MX nitrides as very fine and thermally stable particles for prolonged periods of exposure at elevated temperatures and also to eliminate unstable Cr-rich carbides $M_{23}C_6$ [54,55].

The Thermo-Calc evaluation of equilibrium phases in a 9Cr-3W-3Co-0.2V-0.05Nb-0.05N steel during tempering at 800°C is shown in Fig. 10.14 as a function of carbon concentration. Three kinds of precipitate phases of $M_{23}C_6$ carbide, MX carbonitride, and Fe_2W Laves phase appear as equilibrium precipitate phases at 800°C. However, Fe_2W Laves phase does not precipitate in the present steel during tempering at 800°C for 1 h, because of short tempering time. Therefore, Fe_2W Laves phase is neglected in Fig. 10.14. The change in amount of $M_{23}C_6$ and MX with carbon concentration at a creep test temperature of 650°C is similar as those at 800°C. The amount of $M_{23}C_6$ carbides rich in Cr decreases with decreasing carbon concentration, while the amount of MX carbonitrides is approximately constant for a wide range of carbon

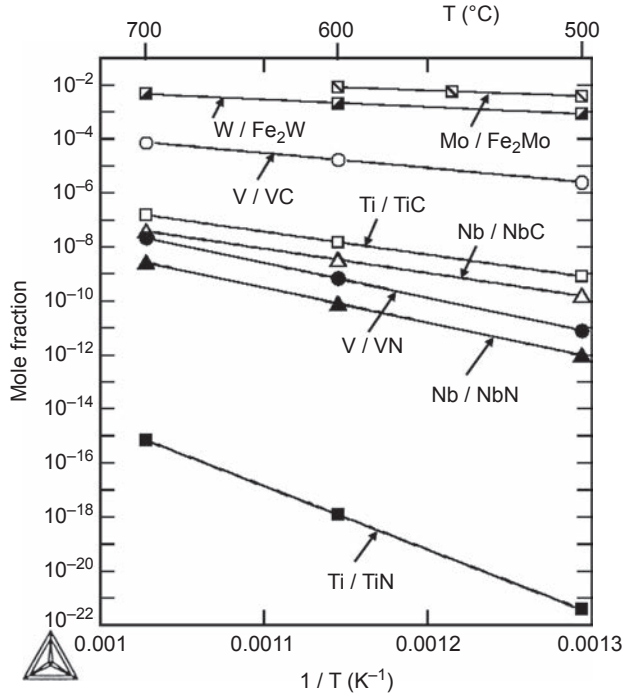


Figure 10.13 Solid solubility of alloying elements, which are in equilibrium with their carbides, nitrides and the $Fe_2(Mo, W)$ Laves phase in iron.

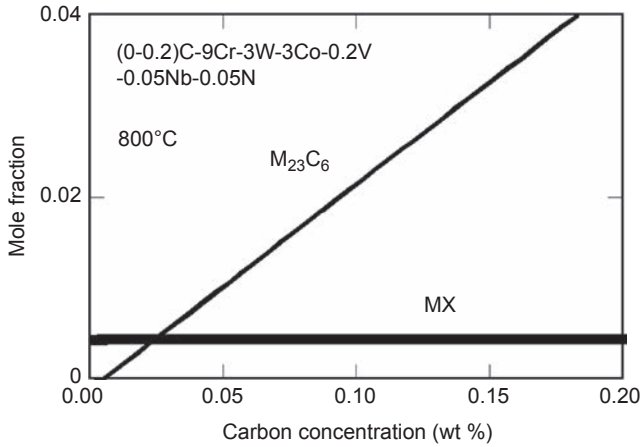


Figure 10.14 Amounts of $M_{23}C_6$ carbides and MX carbonitrides in 9Cr-3W-3Co-0.2V-0.05Nb-0.05N steel at tempering temperature of 800°C as a function of carbon concentration.

concentration from 0% to 0.15%. The amount of MX carbonitrides is larger than that of $M_{23}C_6$ carbides at low-carbon concentrations below 0.02%. The MX carbonitrides consist of mainly vanadium nitrides and of small amount of niobium carbides, suggesting that the MX carbonitrides are substantially vanadium nitrides. This indicates that we can obtain substantially vanadium nitrides alone after tempering by reducing carbon concentration to very low amounts below 0.02%.

In the present research, a fine dispersion of thermally stable precipitates against coarsening and its effect on creep strength have been examined for a tempered martensitic 9Cr steel on the basis of following scenarios:

1. elimination of unstable $M_{23}C_6$ carbides and dispersion of nano-size MX carbonitrides alone by reducing carbon concentration
2. reduction of coarsening rate of $M_{23}C_6$ carbides near PAGBs by using boron
3. combination of coarsening-resistant $M_{23}C_6$ carbides and nano-size MX carbonitrides

10.6.2 Martensitic 9Cr steel strengthened by nanometer-size MX nitrides: MARN

Based on the estimation in Fig. 10.14, elimination of unstable $M_{23}C_6$ carbides and dispersion of nanometer-size MX nitrides were examined using 9Cr-3W-3Co-0.2V-0.05Nb-0.05N steel with different carbon concentrations of 0.002, 0.018, 0.047, 0.078, 0.120, and 0.160% [54,55]. A large number of fine precipitate particles having a size less than 10 nm are distributed along boundaries, such as PAGBs and lath, block, and packet boundaries, and in the matrix of the steel with 0.002% C after tempering, as shown in Fig. 10.15. This is quite different from the microstructure of the steel with 0.078% C, where the large particles of $M_{23}C_6$ carbides of 100–300 nm size are distributed along PAGBs together with the fine particles of MX carbonitrides.

The time to rupture is substantially independent of carbon concentration in the higher carbon region above 0.047%, but it significantly increases in the lower carbon region below 0.018%, as shown in Fig. 10.16, which is also typical for applied stresses within the range of 140–200 MPa. On the other hand, the minimum creep rate significantly decreases in the lower carbon region below 0.018%. It is evident that the creep strength of 9Cr steel significantly improves by the elimination of $M_{23}C_6$ carbides and a dispersion of nanometer-size MX nitrides alone.

Fig. 10.17 compares the creep rate versus time curves between the two representative steels in Fig. 10.16 with 0.002% and 0.078% C at 650°C and 140 MPa [56]. The creep rates in the initial stage are lower in the steel with 0.002% carbon than in the steel with 0.078% carbon. The minimum creep rate of the steel with 0.002% carbon is about 1/10 of that of the steel with 0.078% carbon, while the time to rupture of the steel with 0.002% carbon is about 10 times of the steel with 0.078% carbon. The observed longer creep life by reducing carbon concentration results from a decrease in minimum creep rate. The lower values of the initial creep rates in the steel with 0.002% carbon than in the steel with 0.078% carbon results from larger precipitation hardening after tempering. However, the difference in initial creep rates between the two steels is only slight as shown by 1/3 orders of magnitude, which is much smaller than the difference

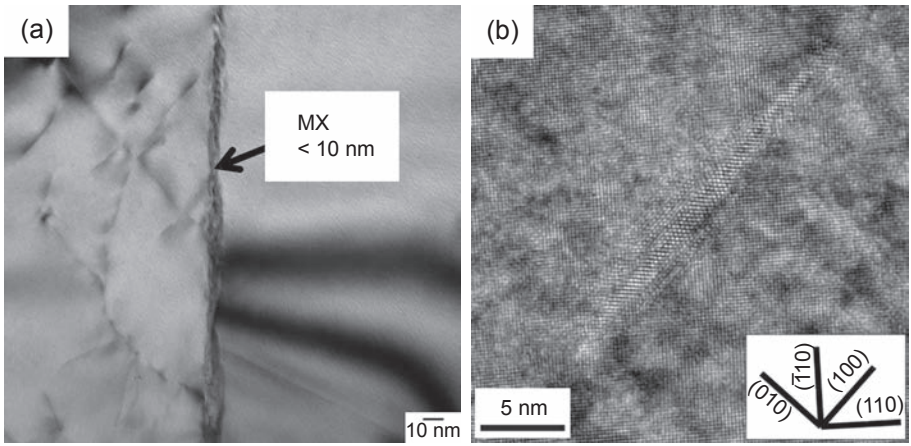


Figure 10.15 MX carbonitrides (a) along boundary and (b) in the matrix of very low-carbon 9Cr-3W-3Co-0.2V-0.05Nb-0.05N-0.007B steel with 0.002% C after tempering.

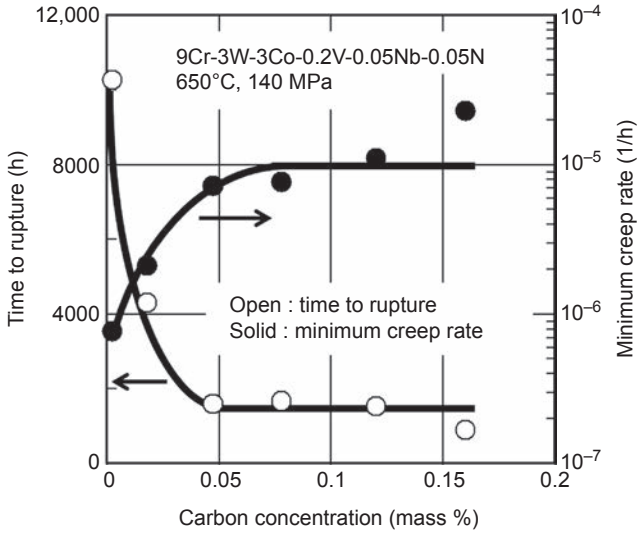


Figure 10.16 Time to rupture and minimum creep arte of 9Cr-3W-3Co-VNb steel at 650°C and 140MPa, as a function of carbon concentration.

in minimum creep rate between the two steels. On the other hand, the onset of acceleration creep is retarded up to longer times in the steel with 0.002% carbon, which further decreases the minimum creep rate. The present very low-carbon 9Cr steel is designated MARN (MARtensitic 9Cr steel strengthened by nano-size MX nitrides).

Whereas the density of precipitates along boundaries is much higher in the steel with 0.002% carbon than in the steel with 0.078% carbon as described earlier, the density of MX carbonitrides in the matrix within laths is lower in the steel with 0.002% carbon than

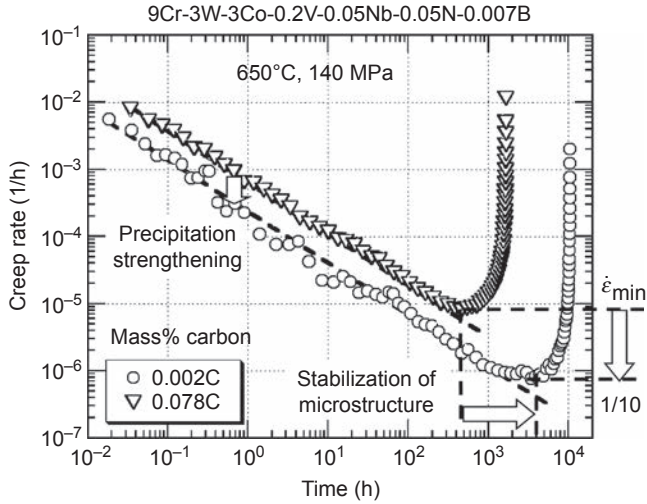


Figure 10.17 Creep rate versus time curves of 9Cr-3W-3Co-0.2V-0.05Nb-0.05N steel with 0.002% and 0.078% C at 650°C and 140 MPa.

in the steel with 0.078% carbon: 5.5×10^{13} and $7.5\times10^{13}/m^2$ for the steels with 0.002% and 0.078% carbon, respectively [55,56]. This is due to the amount of MX carbonitrides along boundaries being much larger in the steel with 0.002% carbon than in the steel with 0.078% carbon because of no $M_{23}C_6$ carbide in the steel with 0.002% carbon. On the other hand, most of MX carbonitrides in the steel with 0.078% carbon are distributed in the matrix, and only a slight amount of MX carbonitrides is distributed along boundaries together with large amount of $M_{23}C_6$ carbides. The fine MX carbonitrides in the matrix act as obstacles for dislocation movement to lath and block boundaries, which reduces the dislocation annihilation and decreases the creep rate, as illustrated in Fig. 10.18. At lath and block boundaries, climbing and redistribution of dislocations in the boundary wall are prohibited when dense distributions of MX and $M_{23}C_6$ in the boundary wall act as obstacles, which reduces the efficiency of dislocation absorption at boundaries. This also reduces dislocation annihilation and decreases the creep rate. Therefore, the creep rate in the transient region is given by the following [9,56]:

$$\dot{\varepsilon} = \rho_f v_g b \eta, \tag{10.11}$$

where ρ_f is the free dislocation density in the matrix within laths, v_g is the velocity of free dislocations in the matrix, b is the magnitude of Burgers vector, and η is the efficiency of dislocation absorption at boundaries. The lower creep rates in the steel with 0.002% carbon than in the steel with 0.078% carbon in the transient region suggest that the lower η in the steel with 0.002% carbon due to fine distribution of MX along boundaries is a main factor for the lower creep rate in the transient region rather than the precipitation hardening due to fine MX in the matrix. The agglomeration and coarsening of precipitates at boundaries during transient creep promote climbing and redistribution of dislocations in the boundary wall, resulting in an increase of the

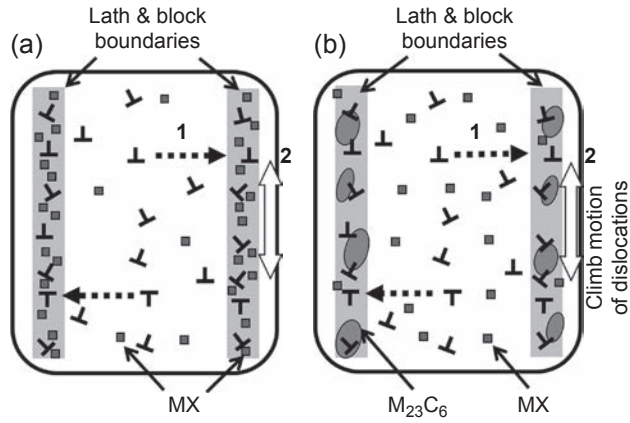


Figure 10.18 Schematics of dislocation movement in lath and block microstructure of 9Cr steel. (a) 0.002% C–0.05% N and (b) 0.078% C–0.05% N.

efficiency of dislocation absorption at boundaries. The absorption of dislocations at boundaries accelerates further agglomeration and coarsening of precipitates and also promotes climbing and redistribution of dislocations in the boundary wall. These chain reactions promote the migration of lath or block boundaries, promoting the onset of acceleration creep. The present results suggest that the boundary and sub-boundary hardening enhanced by fine distributions of precipitates along lath and block boundaries is a main strengthening mechanism for creep of the present 9Cr steel.

10.6.3 Martensitic 9Cr steel strengthened by boron and MX nitrides: MARBN

10.6.3.1 Effect of boron

Fig. 10.19 shows the creep rupture data for 9Cr-3W-3Co-0.2V-0.05Nb steel with different boron concentrations (0, 48, 92, and 139 ppm B) at 650°C. Nitrogen was not added in the steel to avoid the formation of boron nitrides (BN) [57]. The base steel without boron (0 ppm B) exhibits a loss of creep rupture strength at long times above about 1000 h at 650°C. With increasing boron concentration, however, the time to rupture significantly increases at low stress and long time conditions. The long-term creep rupture strength of T/P92 (9Cr-0.5Mo-1.8W-VNb) [58] is roughly the same as the present 9Cr steel with 92 ppm boron, while that of T91 (9Cr-1Mo-VNb) [59] is roughly the same as the present 9Cr steel with 48 ppm boron. The long-term creep rupture strength of P122 (11Cr-0.4Mo-2W-1Cu-VNb) [60] is located at intermediate between that of T91 and T/P92.

The addition of boron also improves the creep rupture ductility at 650°C and long times as shown in Fig. 10.20 for the reduction of area, although the reduction of area is roughly the same among the steels containing 48–139 ppm boron. This suggests that the localization of creep deformation near PAGBs is less pronounced by the addition

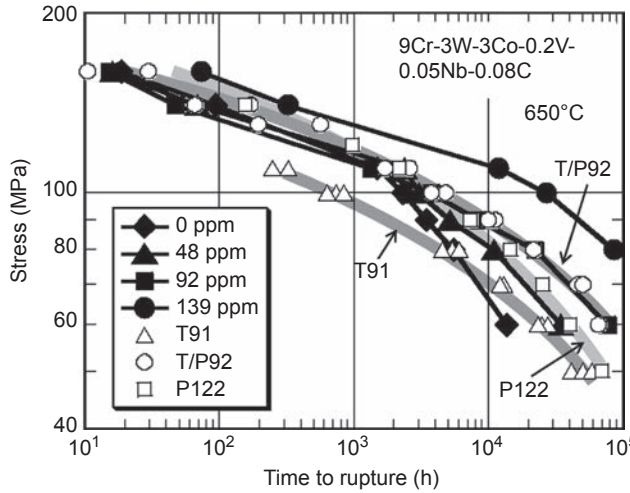


Figure 10.19 Creep rupture data for 9Cr-3W-3Co-0.2V-0.05Nb steel at 650°C, comparing with data for T91, T/P92 and P122.

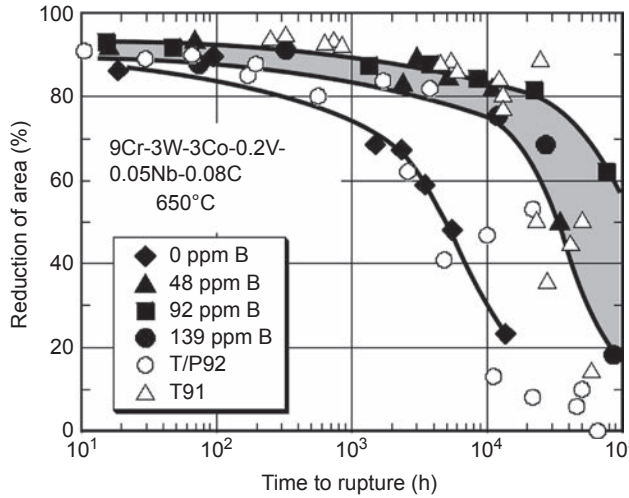


Figure 10.20 Effect of boron on reduction of area of 9Cr-3W-3Co-0.2V-0.05Nb steel at 650°C, together with data for T91 and T/P92.

of boron. The reduction of area after long-term creep rupture testing is on order of 9Cr-boron steel ≥ T91 > T/P92. The improved reduction of area by the addition of boron is advantageous to the creep-fatigue life because the creep-fatigue life is proportional to the reduction of area in creep rupture test, namely, proportional to the creep ductility but not proportional to the creep strength [61].

The fine distribution of $M_{23}C_6$ carbides along PAGBs is maintained in the 9Cr steel with 139 ppm boron during exposure at 650°C, Fig. 10.21 [62]. The analysis

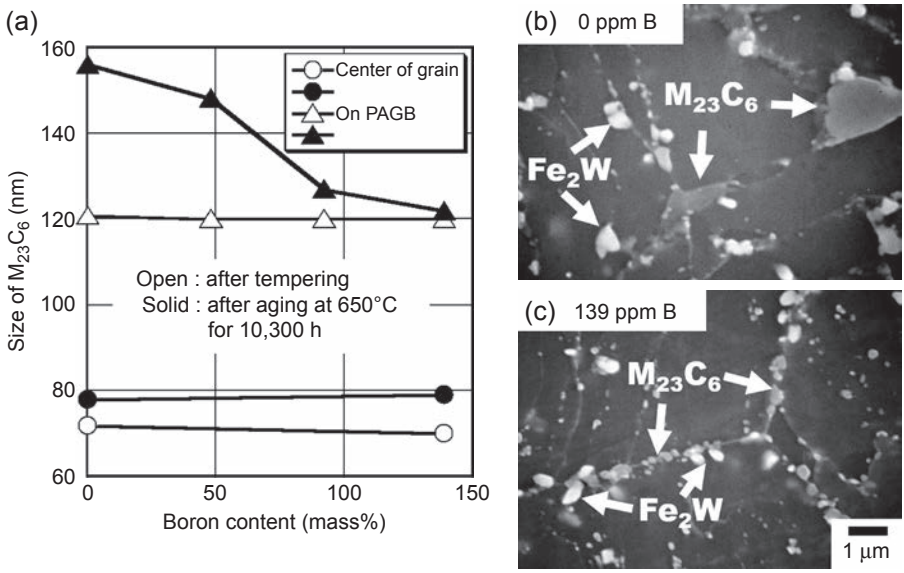


Figure 10.21 (a) Effect of boron on size of $M_{23}C_6$ particles as a function of boron concentration, (b) and (c) SEM micrographs of 9Cr-3W-3Co-VNb steel with 0 and 139 ppm boron after aging at 650°C for 10,300 h.

by means of field emission type auger electron spectroscopy (FE-AES) shows that boron is enriched in $M_{23}C_6$ carbides, which is more significant at and near PAGBs than inside the grains, suggesting GB segregation of boron. This is correlated with the reduction of coarsening rate of $M_{23}C_6$ carbides in the vicinity of PAGBs. In the base steel without boron, a fine distribution of $M_{23}C_6$ carbides is observed after tempering, but extensive coarsening takes place in the vicinity of PAGBs during creep. This indicates that the addition of boron reduces the rate of Ostwald ripening of $M_{23}C_6$ carbides in the vicinity of PAGBs during exposure at 650°C.

The onset of acceleration creep is retarded and the transient creep region continues for up to a longer time with increasing boron concentration, Fig. 10.22. The longer duration of the transient creep region, which corresponds to a lager value of t_m in Eq. (10.7), results in a lower minimum creep rate and a longer time to rupture. The extensive coarsening of $M_{23}C_6$ carbides in the vicinity of PAGBs in the base steel without boron promotes the migration of lath and block boundaries during creep, and hence the onset of acceleration creep takes place at earlier times, resulting in higher minimum creep rate and shorter time to rupture. The boundary and sub-boundary hardening enhanced by the distributions of $M_{23}C_6$ carbides along boundaries is the most important strengthening mechanism for long-term creep.

10.6.3.2 Additive strengthening due to boron and MX nitrides

The nitrogen concentration dependence of the time to rupture and minimum creep rate of 9Cr-3W-3Co-0.2V-0.05Nb steel containing about 140 ppm boron at 650°C and 120 MPa is shown in Fig. 10.23(a) [63]. The peaks of the time to rupture and

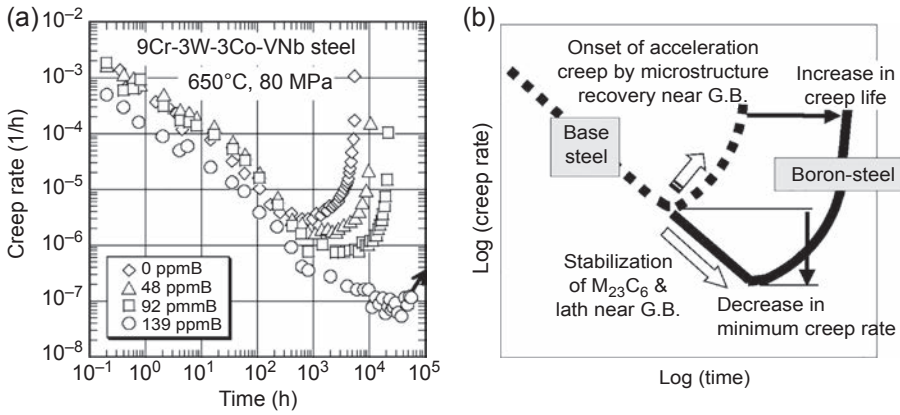


Figure 10.22 (a) Effect of boron on creep rate versus time curves of the steels at 650°C and 80 MPa and (b) mechanisms of boron effect on creep rate versus time curves.

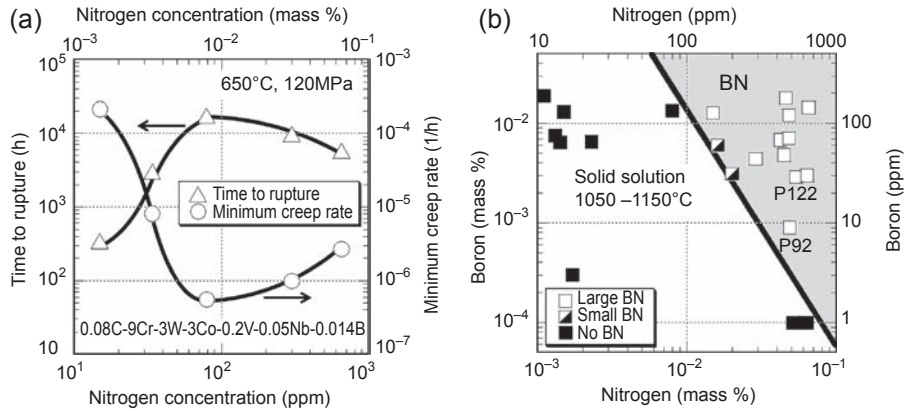


Figure 10.23 (a) Time to rupture and minimum creep rate of 9Cr steel with 140 ppm boron at 650°C and (b) composition diagram of boron and nitrogen at a normalizing temperature of 1050–1150°C.

minimum creep rate are located at about 80 to 100 ppm nitrogen, which corresponds to the maximum solid solubility of nitrogen in equilibrium with BN in the steel containing 140 ppm boron at a normalizing temperature of 1100°C; see Fig. 10.23(b) [64]. This indicates that the addition of nitrogen without the formation of any BN during normalizing significantly improves the creep strength, but excess addition of boron and nitrogen causes the formation of BN during normalizing heat treatment, which consumes soluble boron and nitrogen and degrades the creep strength.

Excess addition of boron and nitrogen also degrades the creep rupture ductility at 650°C and long times, as shown in Fig. 10.24. The degradation in reduction of area is significant in the present steels containing 300 and 650 ppm nitrogen, where a large amount of BN is formed during normalizing. The present results suggest that BN formed during normalizing provides preferential nucleation sites for creep voids. On

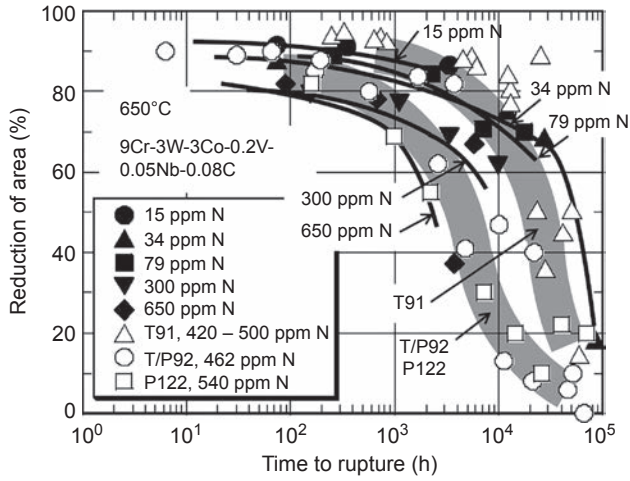


Figure 10.24 Effect of nitrogen concentration on reduction of area of 9Cr-3W-3Co-0.2V-0.05Nb steel containing 140 ppm B after creep rupture testing at 650°C, together with data for T91, T/P92 and P122.

the other hand, the present steel containing nitrogen less than 100 ppm exhibits enough reduction of area, larger than or the same as T91.

Inclusions in 9 to 12Cr steels were examined by SEM observations of ductile fracture surface combined with energy dispersive X-ray spectrometry (EDS) analysis [63]. In ductile fracture of steels, inclusions provide nucleation sites for microvoids, which grow and coalesce as the strain increases, exhibiting a dimple pattern. The SEM observations of ductile fracture surface enable us to characterize inclusions more effectively than the conventional method of optical microscopic observations of polished cross-section. Although the EDS analysis is less sensitive to light elements such as boron than the FE-AES and secondary ion mass spectrometry (SIMS), the EDS analysis can easily characterize BN inclusions because of their large size of several μm or more.

Rod specimens, having a size of 3.6 mm diameter and 50 mm length with a 0.8 mm depth circular notch at the center of rod, were bent and fractured at room temperature. Fig. 10.25 shows an example of the characterization of boron nitride particles in 9Cr-3W-3Co-0.2V-0.05Nb steel with 71 ppm boron and 480 ppm nitrogen in as tempered [65]. A large number of boron nitride inclusions were observed at the bottom of dimples on the ductile fracture surface, together with Al_2O_3 inclusions. Gu and coworkers made analysis of the creep voids formed in P92 steel after creep exposure [66]. Their analysis revealed that the majority of creep voids were associated with hard inclusions. Chemical analysis of these inclusions showed that the vast majority were BN, although some Al_2O_3 and MnS particles were also observed.

Based on the characterization of boron nitride inclusions, the solubility product for boron nitride in 9 to 12Cr steels at a normalizing temperature of 1050–1150°C is given by [65]

$$\log[\%B] = -2.45\log[\%N] - 6.81, \tag{10.12}$$

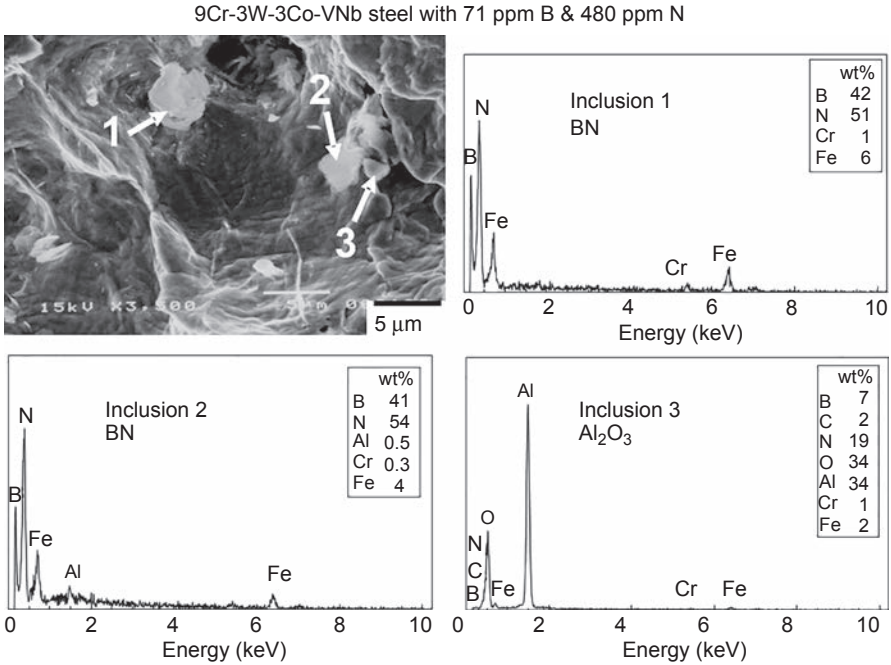


Figure 10.25 SEM micrograph of ductile fracture surface of 9 Cr-3W-3Co-0.2V-0.05Nb steel with 71 ppm B and 480 ppm N and EDS analysis of inclusions.

where [*%B*] and [*%N*] are the concentration of soluble boron and soluble nitrogen in mass %, respectively [14]. This is shown in Fig. 10.23(b). At a boron concentration of 140 ppm in 9Cr steel, only 95 ppm nitrogen can dissolve in the matrix. On the other hand, at a nitrogen concentration of 0.05% (500 ppm), which corresponds to the nitrogen concentration in Gr.91, Gr.92, and Gr.122, the maximum soluble boron concentration is only 3 ppm.

The formation of BN consumes soluble boron. Fig. 10.26 compares the enrichment of boron in $M_{23}C_6$ carbides between 9Cr-3W-3Co-VNb steel with 0.0015 and 0.065N [63]. FE-AES was used for analyzing boron. In the 0.0015N steel, no boron nitride forms during normalizing heat treatment, and hence most of boron can contribute to the GB segregation and to the enrichment in $M_{23}C_6$ carbides near PAGBs. On the other hand, in the 0.065N steel, a large amount of BN forms during normalizing at high temperature. Therefore, most of boron is consumed to form the BN. The present results suggest that a critical issue for the stabilization of martensitic microstructure is to increase soluble boron free from BN but not total boron concentration.

SIMS is another potential technique for analyzing light elements such as boron. Two different types of SIMS equipment were used for analyzing boron: dynamic SIMS with a quadrupole-type mass analyzer and time-of-flight (ToF) type SIMS employing a micro-focused ion beam [67]. 9Cr-3W-3Co-0.2V-0.05Nb steel with 47B-17N, 130B-71N and 150B-300N (ppm) in as tempered were used for the SIMS analysis.

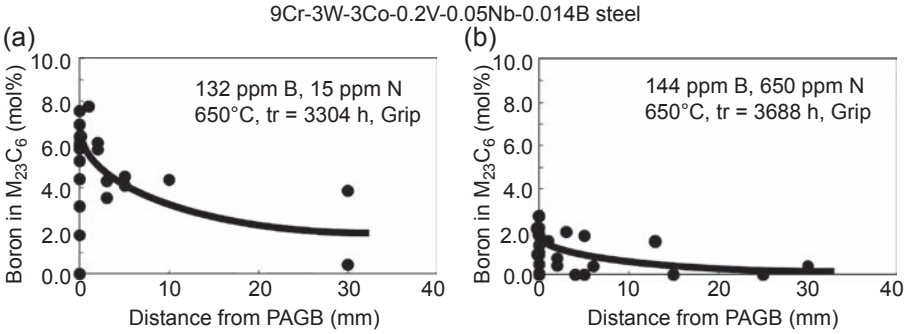


Figure 10.26 Concentration of boron in $M_{23}C_6$ carbides in the steels after creep rupture testing at 650°C for 3000–4000 h, as a function of distance from prior austenite grain boundary.

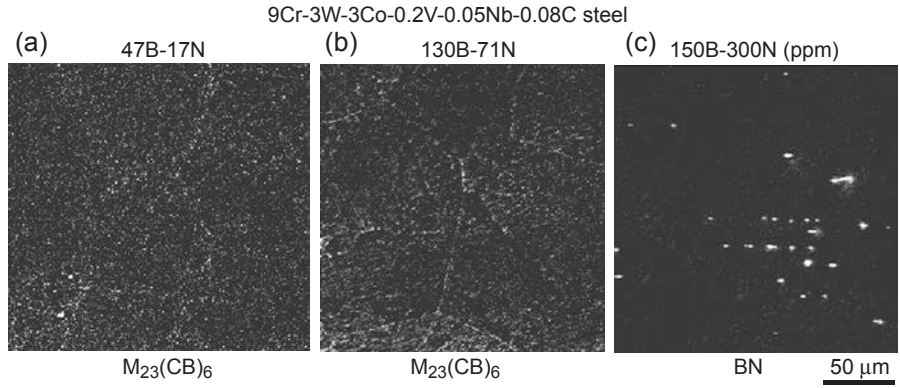


Figure 10.27 Imaging of BO_2^- ions in 9Cr steel with (a) 47B-17N, (b) 130B-71N and (c) 150B-300N (ppm), by ToF-SIMS.

The secondary negative ions of BO_2^- were used to analyze the distribution of boron in the specimen. This is shown in Fig. 10.27. Boron is enriched along PAGBs, at which $M_{23}C_6$ carbides are distributed, in the 9Cr steel with 47B-17N and 130B-71N (ppm), while relatively large particles containing boron form in the matrix but no enrichment of boron along PAGBs in the 9Cr steel with 150B-300N (ppm).

Because the ion images obtained by ToF-SIMS shown in Fig. 10.27 are less quantitative, line scans of the secondary ion counts of BO_2^- were carried out, together with CN^-, CrO_3^-, and FeO_2^- ions. This is shown in Fig. 10.28, which shows the line scan of BO_2^-, CN^-, CrO_3^-, and FeO_2^- ions in 9Cr steel with 47B-17N, 130B-71N, and 150B-300N (ppm) by ToF-SIMS. The correlative distribution of BO_2^- and CrO_3^- ions in the 9Cr steel with 47B-17N and 130B-71N (ppm) suggests the enrichment of boron in $M_{23}C_6$ carbides rich in Cr, which corresponds to the enrichment of boron along PAGBs shown in Fig. 10.27. The correlative distribution of BO_2^- and CN^- ions in the 9Cr steel with 150B-300N (ppm) shows the formation of boron nitride particles, which corresponds to relatively large particles containing boron in Fig. 10.27. It should be noted that the formation of BN consumes most of the boron in the specimen, resulting

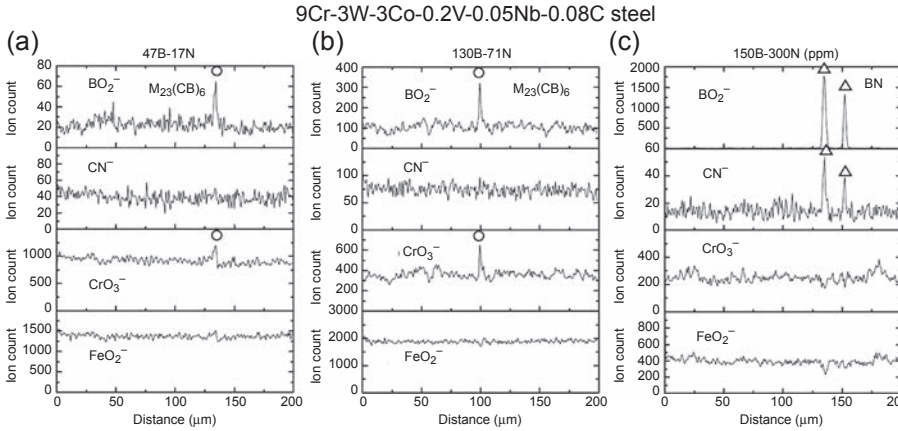


Figure 10.28 Line scan of BO_2^-, CN^-, CrO_3^- and FeO_2^- ions in 9Cr steel with (a) 47B-17N, (b) 130B-71N and (c) 150B-300N (ppm), by ToF-SIMS.

in no enrichment of boron along PAGBs. The results by SIMS are basically the same as those by FE-AES.

Liu and coworkers carried out the analysis of boron in 9 to 12Cr steels by means of atom probe-field ion microscopy (AP-FIM) [68]. Their results show that boron is enriched and evenly distributed inside $M_{23}C_6$ carbides but no segregation at the $M_{23}C_6$ carbide/alloy matrix interface. Their results also indicate that the enrichment of boron in $M_{23}C_6$ carbides is more significant near PAGBs, which is the same as the analysis by FE-AES shown in Fig. 10.26.

10.6.3.3 Suppression of Type IV fracture in HAZ of welded joints

Fig. 10.29 compares the creep rupture data between the base metals and welded joints for 9Cr-boron steel containing different boron and nitrogen concentrations and conventional steels of P92 and P122 at 650°C [42,69]. The addition of boron and nitrogen without any formation of BN during normalizing causes no grain refinement and no Type IV fracture in the heat-affected zone (HAZ) of welded joints, while the formation of BN during normalizing produces the fine-grained microstructure in HAZ and causes the premature rupture in welded joints due to Type IV fracture; see P92 and P122. Soluble boron is essential for the suppression of grain refinement and Type IV fracture.

P91, P92, and P122 contain the nitrogen of 0.05–0.06%. We observed that the addition of 0.05–0.06% nitrogen to 9Cr steel produces the fine-grained microstructure during heating of welding, irrespective of boron concentration in the range of 0–130 ppm [70].

The multiaxial stress condition in the HAZ with lower creep strength, which results from mechanical constraint effect by the surrounding weld metal and base metal with higher creep strength, is essential for the brittle Type IV fracture in the HAZ of welded joints, as shown schematically in Fig. 10.30 [71]. Using simulated HAZ specimens, we have investigated the relationship between the creep strength and microstructure

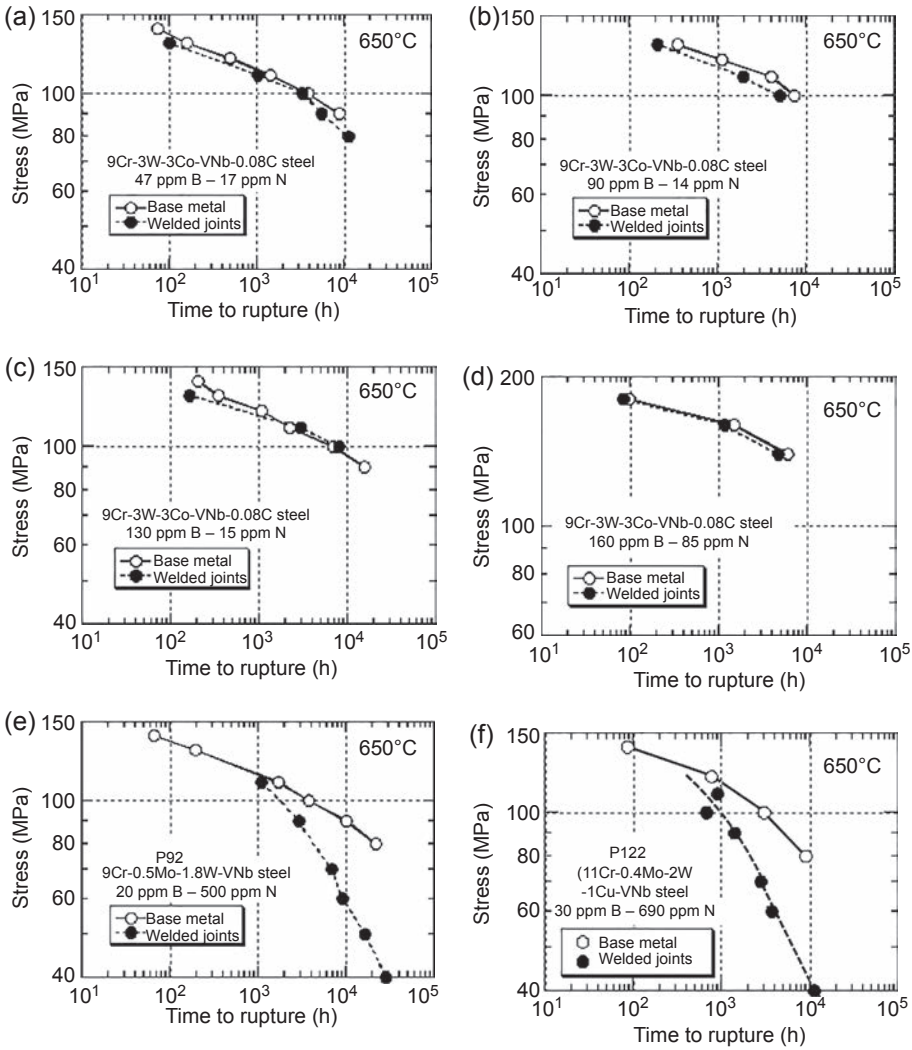


Figure 10.29 Creep rupture data for base metals and welded joints of the steels at 650°C.

of HAZ for Gr.92 and 9Cr-3W-3Co-VNb steel with 90 ppm boron (9Cr-90 ppm B steel) [72]. Fig. 10.31 shows the time to rupture of the simulated HAZ specimens of Gr.92 and the 9Cr-90 ppm B steel at 650°C and 110 MPa, as a function of peak temperature in the thermal cycle. The thermal cycle conditions for the preparation of simulated-HAZ specimens are shown in Fig. 10.32. At a heating rate of 100 K/s, the A_{C1} temperature was found to be 817°C (1090 K) and 841°C (1114 K) for P92 and the 9Cr-90 ppm B steel, respectively, while the A_{C3} temperature was 912°C (1185 K) and 920°C (1193 K) for P92 and the 9Cr-90 ppm B steel, respectively. The specimens were kept for 0.5 s at various peak temperatures between 810 and 1125°C and then cooled

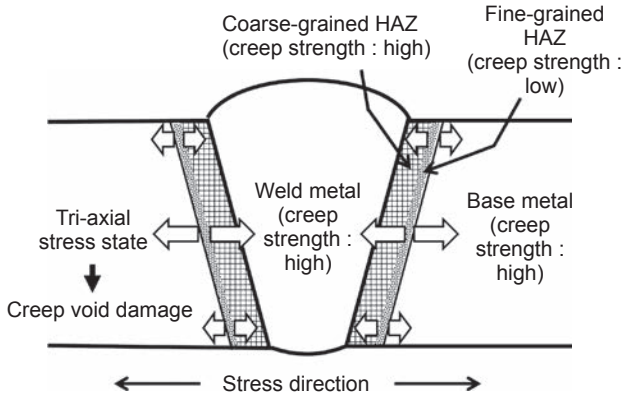


Figure 10.30 Schematics of welded joints of 9 to 12Cr steels.

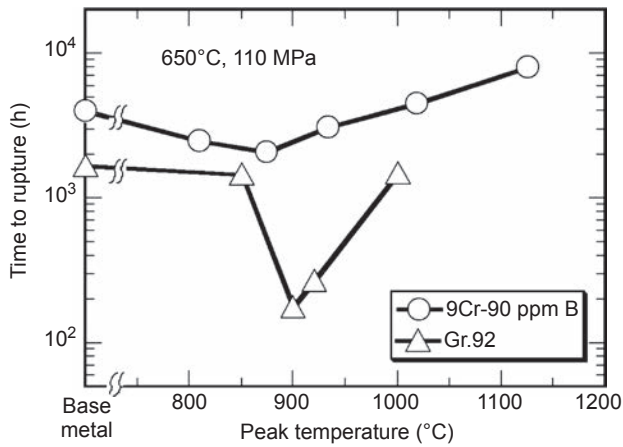


Figure 10.31 Time to rupture of simulated-HAZ specimens of Gr.92 and 9Cr-90 ppm boron steel at 650°C and 110 MPa.

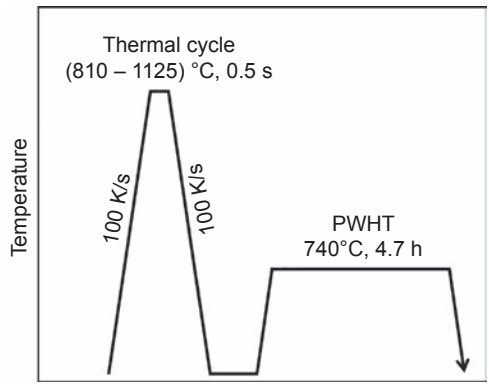


Figure 10.32 Thermal cycle conditions of simulated-HAZ specimens.

to room temperature. Finally, the post-weld heat treatment (PWHT) was carried out for each specimen including the base metal at 740°C for 4.7 h. The heat treatment conditions, grain size, and precipitates at GBs after PWHT in the A_{C3} simulated HAZ specimens are given in Table 10.2.

The degradation in time to rupture in the A_{C3} simulated HAZ specimens of Gr.92 in Fig. 10.31 shows that it is not caused by the grain refinement but that the reduction of boundary and sub-boundary hardening is the most important [72]. The A_{C3} simulated HAZ specimens of Gr.92 exhibit the fine-grained microstructure, where very few $M_{23}C_6$ carbides are formed along PAGBs, as shown in Fig. 10.33. Inside the grains, the A_{C3} simulated HAZ specimens of Gr.92 consisted of equiaxed subgrains with low density of dislocations and sparse distributions of large $M_{23}C_6$ carbides. These observations suggest that the boundary and sub-boundary hardening is significantly reduced in the A_{C3} simulated HAZ specimens of Gr.92 compared with that in the base metal.

Table 10.2 Heat treatment conditions, grain size and precipitates at GBs after PWHT in A_{C3} simulated-HAZ specimens of Gr.92 and 9Cr-90 ppm B steel

	Heat treatment	Grain size after PWHT	Precipitates at GBs after PWHT
Gr.92	Normalizing→Tempering→Thermal cycle→PWHT	fine grains	poor $M_{23}C_6$ at PAGBs
9Cr-90B	Normalizing→Tempering→Thermal cycle→PWHT	Basically coarse grains with fine grains along GBs of coarse grains	Enough $M_{23}C_6$ at PAGBs of coarse grains and Fe_7W_6-μ phase at GBs of fine grains

Thermal cycle: Peak Temp. 950°C, PWHT: 740°C×4.7 h.

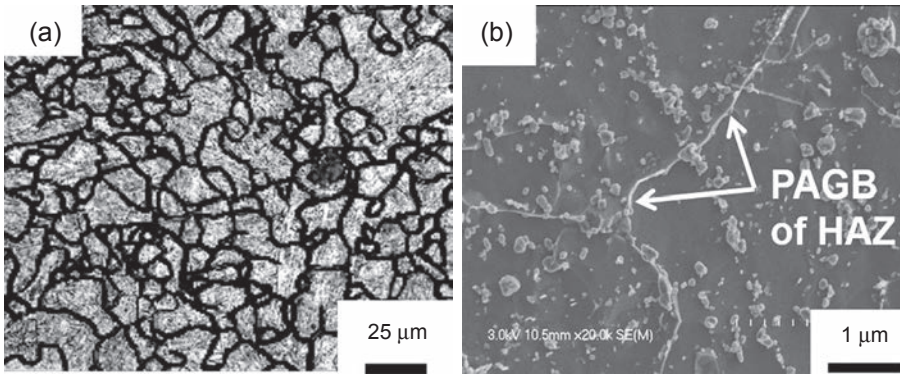


Figure 10.33 (a) Optical and (b) scanning electron micrographs of Gr.92 after thermal cycle to a peak temperature of 950°C followed by PWHT.

The 9Cr-90 ppm B steel basically consists of coarse grains of roughly 200–300 μm after the A_{C3} thermal cycle, which is substantially the same as that of base metal and of fine grains of 10–50 μm at PAGBs of coarse grains as shown in Fig. 10.34 [73,74]. PAGBs of the coarse grains are covered by enough $M_{23}C_6$ carbides even after the A_{C3} thermal cycle followed by PWHT, substantially the same as the base metal. It should be noted that a large number of Fe_7W_6-μ phase forms at GBs of the fine grains during PWHT, Fig. 10.34(c). Inside the grains, the tempered martensitic microstructure substantially consists of blocks, Fig. 10.34(d). Therefore, the boundary and sub-boundary hardening is enough in the 9Cr-90 ppm B steel even after the A_{C3} thermal cycle followed by PWHT, suggesting no reduction of creep strength in the A_{C3}- HAZ. Indeed, the time to rupture of A_{C3} simulated HAZ specimens of 9Cr-90 ppm B steel is substantially the same as that of base metal as shown in Fig. 10.31.

The grain refinement behavior in Gr.92 and no grain refinement behavior in the 9Cr-boron steel during heating are explained as follows [42]. Fig. 10.35 shows schematically the microstructure evolution in these steels during thermal cycle followed by PWHT [75]. In Gr.92, the nucleation of γ phase takes place at PAGBs at temperature above A_{C1} during heating, Fig. 10.35(a). This is an initial stage of diffusive α/γ transformation. The diffusive transformation produces fine-grained microstructure when the peak temperature is not so high, at around A_{C3} temperature, Fig. 10.35(b). In the

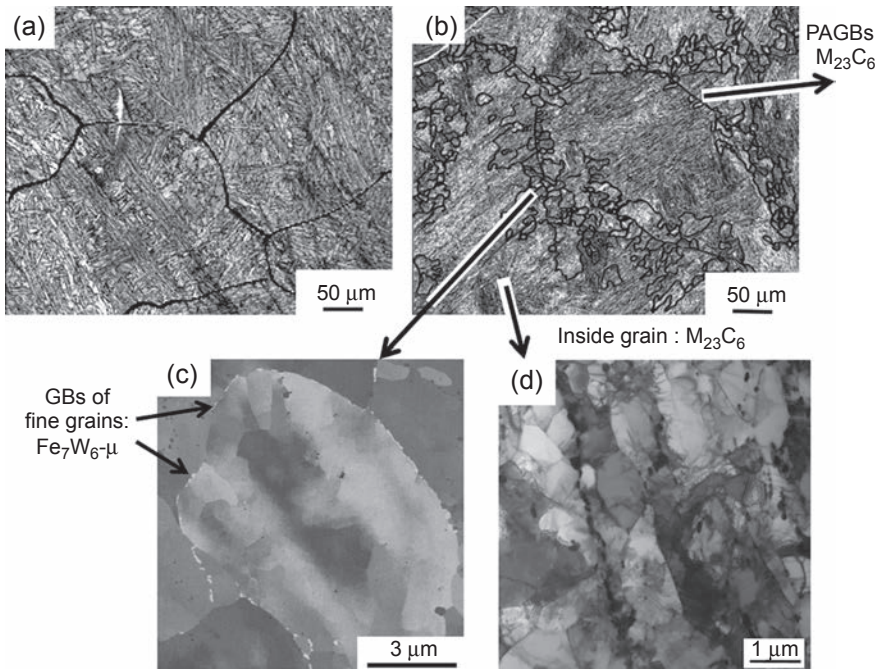


Figure 10.34 Optical micrographs of (a) base metal and (b) simulated-HAZ specimen of 9Cr-3W-3Co-VNb steel with 90 ppm boron after thermal cycle to a peak temperature of 950°C and subsequent PWHT, (c) Fe_7W_6-μ phase precipitates at grain boundaries of fine grains and (d) TEM microstructure inside coarse grain.

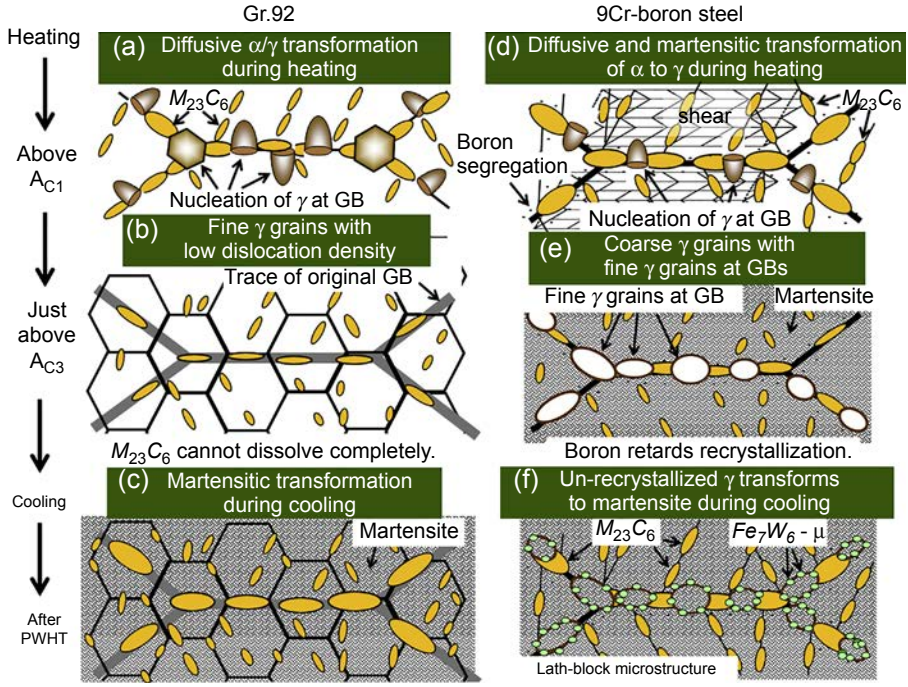


Figure 10.35 Schematics of microstructure evolution in Gr.92 and 9Cr-boron steel during simulated-HAZ thermal cycle.

9Cr-boron steel, on the other hand, the GB segregation of boron reduces GB energy and makes the GBs less effective as heterogeneous nucleation sites for γ phase. This retards diffusive α/γ transformation, and hence martensitic reverse transformation by shear can take place during heating, Fig. 10.35(d). The observed higher A_{C1} temperature of 841°C for the 9Cr-90 ppm B steel at a heating rate of 100 K/s, in comparison with that of 817°C for Gr.92, is correlated with the retardation of α/γ transformation. The nucleation of γ phase by diffusive transformation also take place at part of PAGBs in 9Cr-boron steel during heating, which produces the fine grains at part of PAGBs of coarse grains, Fig. 10.34(b).

Santella and coworkers performed synchrotron diffraction experiments to examine the real-time transformation behavior of the 9Cr-boron steel containing 130 ppm boron and P92 under simulated HAZ thermal cycle [76]. They showed that when heated to peak temperatures near 1100°C both steels rapidly transformed from α to 100% γ, which corresponds to the α/γ transformation during heating of normalizing. When the 9Cr-boron steel and P92 were heated to peak temperature of 911 and 896°C, respectively, about 56% and 15% of the original α never transformed to γ in the 9Cr-boron steel and P92, respectively, as shown in Fig. 10.36. Their results suggest the retardation of α/γ transformation in the 9Cr-boron steel during heating in comparison with P92. Kobayashi and coworkers observed a similar effect using electric resistivity measurements to follow the α to γ transformation in Fe-0.1C steel

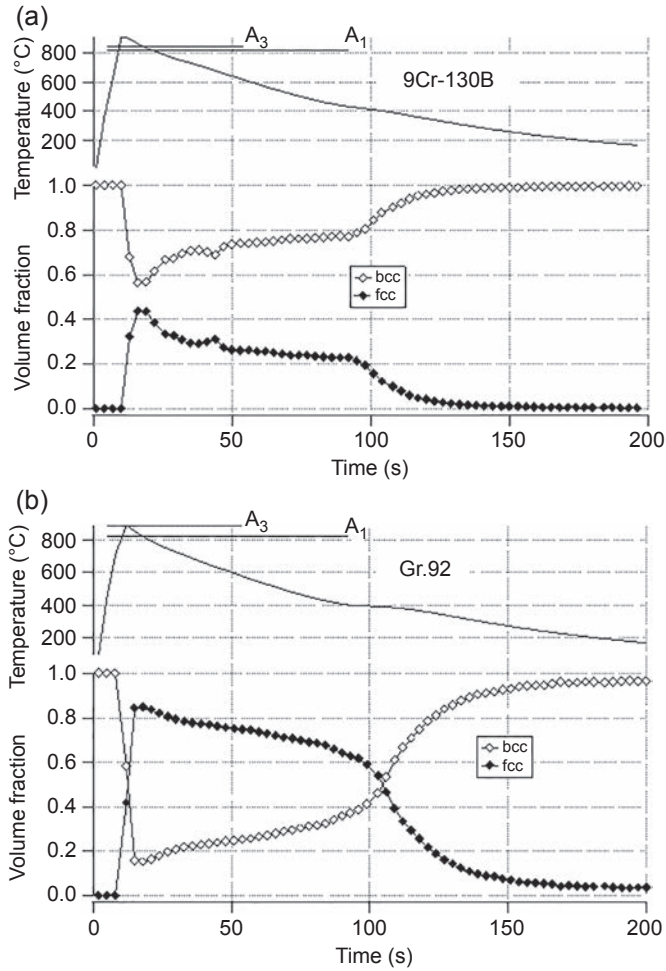


Figure 10.36 Plots of temperature and corresponding bcc and fcc phase fractions with time for (a) 9Cr-3W-3Co-VNb steel with 130 ppm boron, peak temperature of 911°C and (b) Gr.92, peak temperature of 896°C.

with and without 98 ppm boron during continuous heating at a rate of 10°C/min [77]. Their results showed that the boron addition shifted the α to γ transformation to higher temperature. Azuma and coworkers observed metallographically that the addition of 90 ppm boron retarded the transformation in 12Cr turbine steels [78].

The direct or in situ observation of the surface of 9Cr-130 ppm boron steel by using a confocal scanning laser microscope during heating clearly shows a high surface relief at a temperature of 950°C just above A_{C3}, Fig. 10.37, suggesting martensitic or displacive transformation [79]. In Fig. 10.35(b), carbonitrides such as $M_{23}C_6$ also become dissolved during heating but cannot dissolve completely when the peak temperature is not so high, at around A_{C3}. In the 9Cr-boron steel,

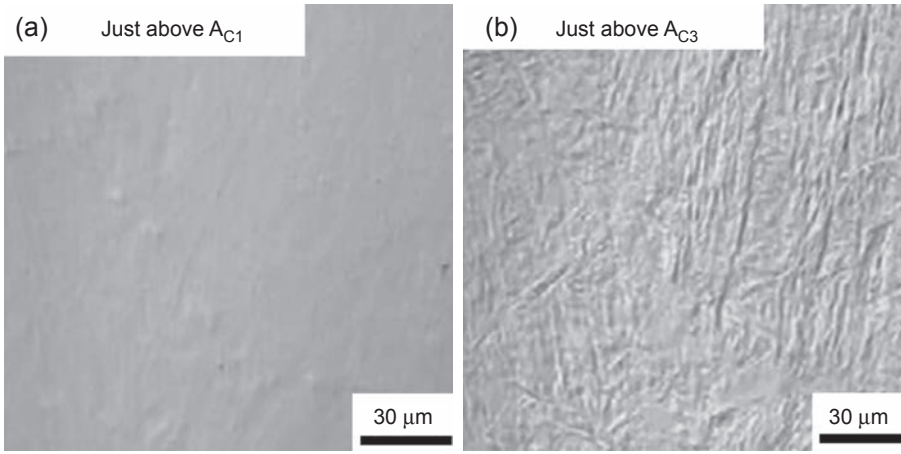


Figure 10.37 Direct observation of 9Cr-boron steel surface during heating. (a) 903°C just above Ac1 and (b) 950°C just above Ac3.

on the other hand, the martensitic transformation introduces a high density of dislocations, but recrystallization cannot take place because boron increases recrystallization temperature, Fig. 10.35(e), indicating no production of new GBs. The resultant microstructure of 9Cr-boron steel after PWHT exhibits enough $M_{23}C_6$ carbides along PAGBs and block boundaries, which is substantially the same as that of the original microstructure, Fig. 10.35(f), although fine grains form at part of PAGBs of coarse grains. The martensitic transformation takes place also in Gr.92 during cooling. During subsequent PWHT, carbonitrides precipitate preferentially at existing carbonitrides and also at new GBs of fine-grained microstructure, Fig. 10.35(c). The resultant microstructure shows that very few precipitates are formed along PAGBs. The production of new GBs and incomplete dissolution of $M_{23}C_6$ carbides are responsible for the very few precipitates along GBs in the fine-grained microstructure after PWHT.

It should be noted that the temperature range for the formation of fine-grained microstructure in Gr.92 is overlapped with that for the very few precipitates along GBs, Fig. 10.38 [42]. This suggests that the observations of fine-grained HAZ provide us an indication of the degradation in creep strength due to Type IV fracture in welded joints, although the reduction of boundary and sub-boundary hardening is more important for the degradation in creep strength than the grain refinement.

10.6.3.4 Mechanisms for boron effect

Fig. 10.39 shows the mechanisms responsible for the effect of GB segregation of boron on the suppression of diffusive α/γ transformation in HAZ of welded joints during heating and on the reduction of coarsening rate of $M_{23}C_6$ carbides in the vicinity of PAGBs during creep at 650°C [42]. The segregation of boron at GBs is estimated to be several percent near the A_{C3} temperature of 950°C and to be more than 10% at the creep test temperature of 650°C, as shown in Fig. 10.40. We estimate the equilibrium

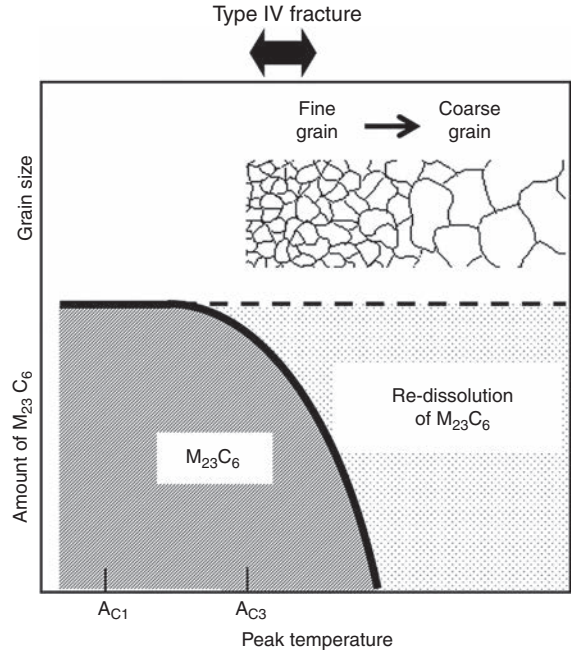


Figure 10.38 Schematics of grain size and amount of $M_{23}C_6$ carbides in Gr.92 during simulation heating.

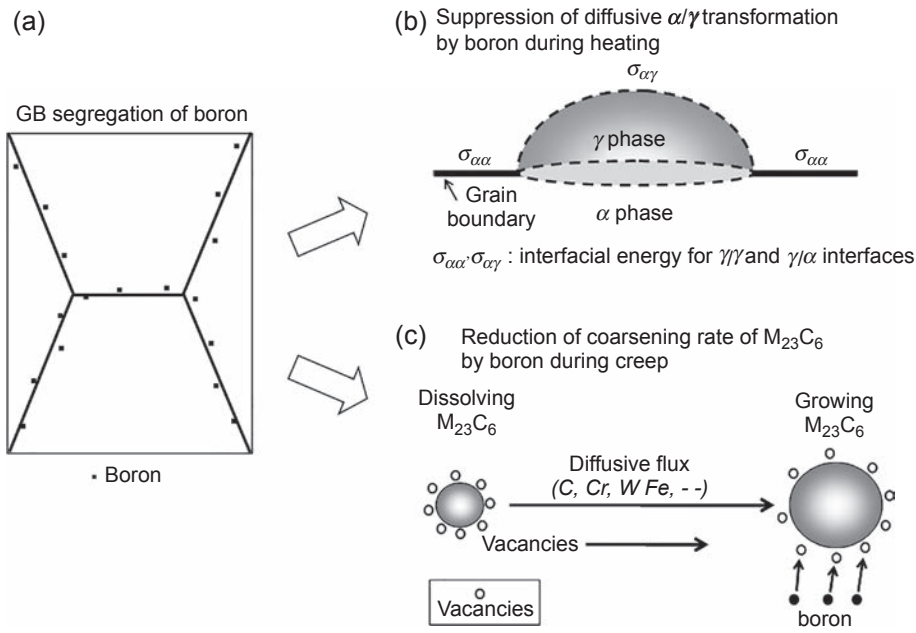


Figure 10.39 Schematics of (a) GB segregation of boron, (b) diffusive α/γ transformation at GB during heating and (c) reduction of coarsening rate of $M_{23}C_6$ carbides by boron during creep.

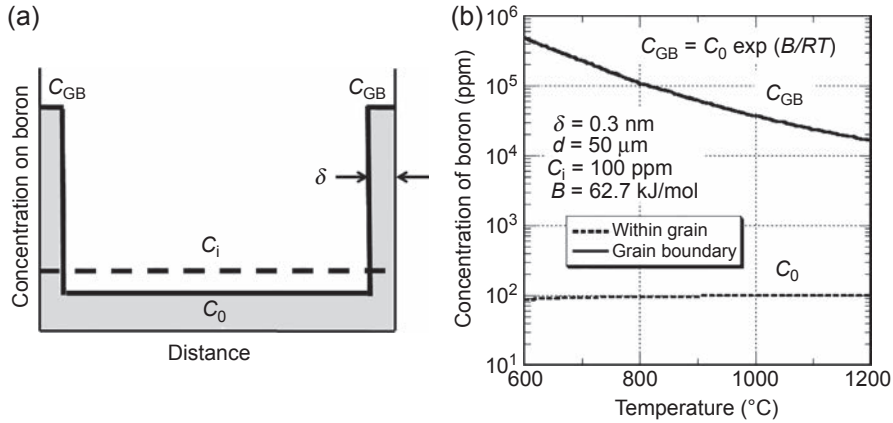


Figure 10.40 (a) Concentration profile of boron and (b) concentration of boron at grain boundaries (C_{GB}) and inside grain (C_0) as a function of temperature.

GB segregation of boron, assuming that initially boron is distributed homogeneously with the concentration C_i as illustrated in Fig. 10.40(a).

After achieving equilibrium GB segregation, the concentration of boron at GBs, C_{GB}, is described as

$$C_{GB} = C_0 \exp(B/RT), \tag{10.13}$$

where C_0 is the concentration of boron within grain, B the binding energy between boron and GB, R the gas constant, and T the absolute temperature. Using a binding energy of $B = 62.7$ kJ/mol [80] reported for type 316 stainless steel, Fig. 10.40(b) shows the concentration of boron at GBs (C_{GB}) and inside grains (C_0) as a function of temperature, where the initial boron concentration C_i and the grain size are assumed to be 100 ppm and 50 μm, respectively. At a temperature of 950°C, segregation of several percent of boron can be achieved at GBs.

The GB segregation of boron reduces the interfacial energy $\sigma_{\alpha\alpha}$ for α/α boundary and makes the α/α boundaries less effective as heterogeneous nucleation sites for γ phase, Fig. 10.39(b). This retards the diffusive α/γ transformation, and hence the martensitic reverse transformation by shear can take place during heating, as already described.

The formation of fine grains at part of PAGBs of coarse grains shown in Fig. 10.34(b) suggests that the nucleation of γ phase by diffusive transformation takes place preferentially at part of PAGBs during heating, but the martensitic transformation also takes place at other part of PAGBs during heating [81]. The formation of fine grains by diffusive transformation is limited only at PAGBs of coarse grains because of the retardation effect by boron due to GB segregation. Inside the grain, only martensitic transformation takes place during heating. The nucleation of γ phase by diffusive transformation is promoted at GBs because strained regions at GBs enable nuclei to be formed with a much smaller free energy. We think that the driving force for

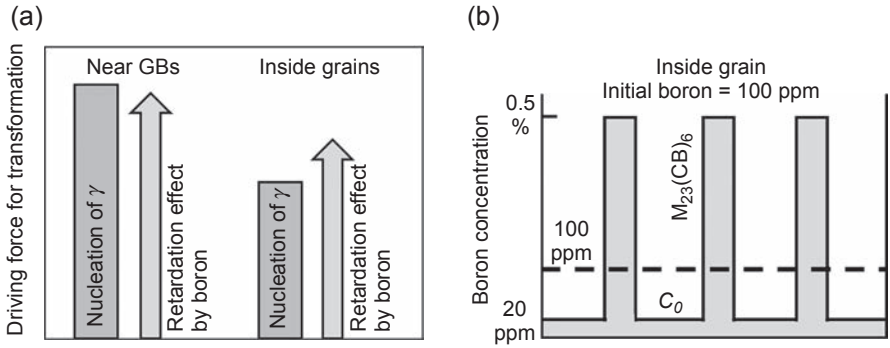


Figure 10.41 (a) Schematic drawing of driving force for α/γ transformation during heating and (b) boron concentration distribution inside grain.

diffusive α/γ transformation at PAGBs during heating is a little bit larger than or the same as the retardation effect by boron near PAGBs, Fig. 10.41(a). The driving force for diffusive α/γ transformation is considered to be much smaller inside the grain than near PAGBs because strained regions are limited near GBs. The retardation effect by boron is also smaller inside the grain than near PAGBs because of no segregation of boron inside the grain. The present results that the martensitic α/γ transformation takes place inside the grain during heating suggest that the retardation effect by boron is larger inside the grain than the driving force for nucleation of γ by diffusive α/γ transformation, Fig. 10.41(a). The concentration of soluble boron in the matrix is estimated to be about 20 ppm, by assuming the initial boron concentration is 100 ppm, the enriched boron concentration in $M_{23}C_6$ carbides inside the grain is 0.5%, and the mole fraction of $M_{23}C_6$ carbides is 0.0016 by Thermo-Calc, Fig. 10.41(b). We think that the soluble boron concentration of 20 ppm in the matrix is enough to retard the diffusive α/γ transformation, and hence the martensitic α/γ transformation takes place inside the grain during heating.

Ostwald ripening of carbides in a solid matrix requires the accommodation of a local volume change around a growing carbide particle because the specific volume of the carbide is larger than that of the alloy matrix [42]. As a small carbide goes into solution, carbon atoms take up interstitial sites in the matrix, and vacancies are created at and near the carbide interface, as shown in Fig. 10.39(c). Then vacancies migrate through the matrix and arrive at a growing carbide interface, which accommodates local volume change. If the enriched boron atoms at PAGBs occupy vacancies around the growing $M_{23}C_6$ carbides, the local volume change cannot be accommodated. This reduces the coarsening rate of $M_{23}C_6$ carbides in the vicinity of PAGB. We think that the main effect due to boron is to occupy vacancies around the growing carbide particles in the vicinity of PAGBs. This makes it difficult to accommodate local volume change.

It is concluded that the enrichment of soluble boron at and near PAGBs by the segregation is essential for the reduction of coarsening rate of $M_{23}C_6$ carbides in the vicinity of PAGBs and for the change in α/γ transformation behavior in HAZ from diffusive to martensitic during heating of welding.

10.6.3.5 *Martensitic 9Cr steel strengthened by boron and MX nitrides: MARBN*

Based on the suppression of Type IV fracture using boron and the improvement of long-term creep strength of base metal by using both boron and MX nitride without any formation of BN during normalizing heat treatment, a 9Cr-3W-3Co-0.2V-0.05Nb steel containing 120–150 ppm boron and 60–90 ppm nitrogen was alloy designed. The steel is denoted MARBN, which means martensitic 9Cr steel strengthened by boron and MX nitrides. Fig. 10.42 shows the creep rupture data for the base metal and welded joints of MARBN at 650°C, together with those for P92 and P122 [57]. MARBN exhibits not only much higher creep rupture strength of base metal than P92 and P122 but also substantially no degradation in creep rupture strength of welded joints compared with base metal, indicating no Type IV fracture. MARBN also exhibits enough creep rupture ductility, larger than or same level as T91, because of low nitrogen concentration below 100 ppm; see Fig. 10.24.

Now let us check the alloy design of MARBN for minimization of the degradation in creep strength at long times described in Section 10.4. The GB segregation of boron reduces the preferential microstructure recovery near PAGBs in MARBN. The addition of boron reduces the coarsening rate of $M_{23}C_6$ carbides, which reduces the static recovery of martensitic microstructure. Maruyama and coworkers reported that 9Cr steels are more stable against the static recovery than 12Cr steels [35,36]. With respect to Z phase precipitation, the combination of 9% Cr and low nitrogen concentration of MARBN reduces the driving force for Z phase formation. With respect to impurity effects due to Al and Ni, Al and Ni were minimized in MARBN. While Al was used as a deoxidizing element in the melting process, the concentration of residual Al was intended to be 10 ppm or below. Although excess dislocations after low-temperature

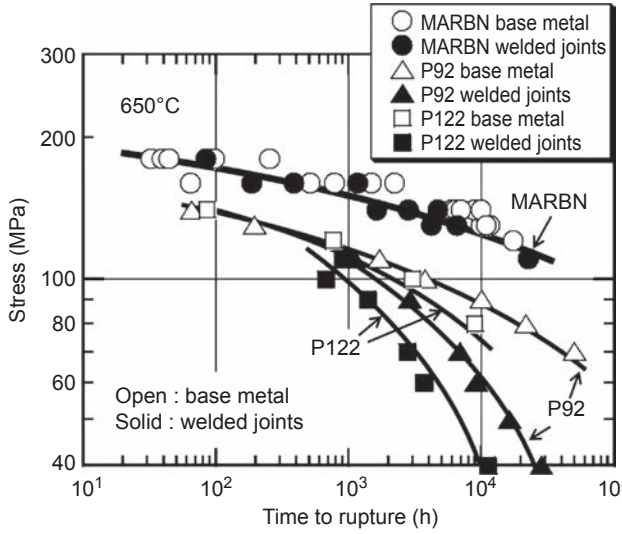


Figure 10.42 Creep rupture data for MARBN, P92 and P122 at 650°C.

tempering at 700°C or below accelerates the microstructure recovery and degrades the creep strength, the tempering temperature of MARBN was as high as 780–800°C. MARBN contains no δ-ferrite. These stabilize the martensitic microstructure of MARBN during exposure at elevated temperature and minimize the degradation.

Tabuchi and coworkers carried out the creep rupture testing for dissimilar welded joints of MARBN and Ni-base alloys, such as MARBN/Alloy 617 and MARBN/Alloy 263 at 650°C for up to about 30,000 h [82]. The creep rupture strength of MARBN/Alloy 617 and MARBN/Alloy 263 dissimilar welded joints was only a little bit lower than that of MARBN base metal. They observed that a creep crack initiated in the fusion boundary at the lower surface of creep specimen and then propagated toward HAZ. Finally, ductile trans-granular fracture with necking took place in the base metal of MARBN. Their results suggest the fracture mode in dissimilar welded joints is not Type IV fracture.

10.6.3.6 Improvement of oxidation resistance by pretreatment

We have revealed that the addition of 3% Pd significantly improves the oxidation resistance of 9Cr steel in steam at 650°C by the formation of thin scale of Cr_2O_3 [83]. This suggests that the formation of protective Cr_2O_3 scale is possible even for 9Cr steel. However, the application of 9Cr steel containing 3% Pd to main steam pipes of A-USC boilers is economically unfeasible because Pd is very expensive. In NIMS, we have also achieved the formation of protective Cr_2O_3-rich scale on the surface of 9Cr steel by the pre-oxidation treatment in argon (Ar) gas [84,85], by the combination of shot-peening of Cr and pre-oxidation treatment in air at 700°C [86], and by the coating of Ni-(20-50)Cr thin layers [87–91]. In the following, the long-term stability of Cr_2O_3-rich scale formed by the pre-oxidation treatment in Ar gas is described. The oxidation behavior of 9Cr steel in steam at 650°C depends on many factors, such as pre-oxidation temperature and time, oxygen concentration in Ar gas, and minor elements, such as Si.

The sheet specimens having a size of 10 × 20 × 2 mm were cut from bulk materials, which were already heat treated, ground on a SiC paper of 320 grit, rinsed in acetone, and then supplied to the oxidation test in steam. The pre-oxidation treatment was carried out in Ar gas at 500–700°C, using the furnace used for the oxidation test. The Ar gas containing 0.3 ppm oxygen was supplied for the pre-oxidation treatment, except for the experiments examining the effect of oxygen concentration in Ar gas on the subsequent oxidation resistance in steam. The oxidation test was carried out in steam at 650°C for up to a long time exceeding 20,000 h.

The effect of oxygen concentration in the Ar gas supplied for the pre-oxidation treatment on the subsequent oxidation resistance in steam at 650°C was examined using Ar gas containing 0.1 ppm, 0.3 ppm, and 1% oxygen [84,85]. The results are shown in Fig. 10.43. The pre-oxidation treatment was carried out in Ar gas at 700°C for 50 h. The effect of oxygen concentration in the Ar gas becomes more significant with decreasing Si concentration in the 9Cr steel. The weight gain of the 9Cr steel containing 0, 0.3, and 0.5% Si decreases with decreasing oxygen concentration in the Ar gas. The X-ray diffraction experiments for the 9Cr steel after the pre-oxidation treatment show that Cr_2O_3 and Fe_3O_4 form on the specimen surface and that the diffraction

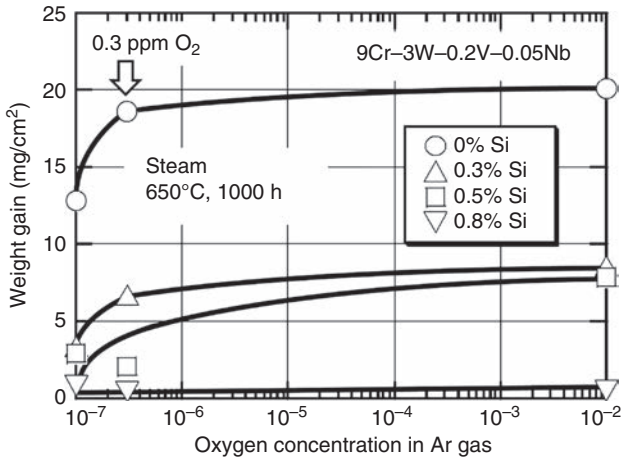


Figure 10.43 Effect of oxygen concentration (partial pressure) in Ar gas for pre-oxidation on weight gain of 9Cr steel in steam at 650°C for 1000 h.

peaks due to Cr_2O_3 become more dominant with decreasing oxygen concentration in the Ar gas. This suggests that the pre-oxidation treatment in Ar gas containing low oxygen concentration enhances the formation of Cr_2O_3 scale.

The weight gain in steam at 650°C decreases with increasing pre-oxidation temperature and time. The long-term stability of Cr_2O_3 scale formed by the pre-oxidation treatment has been examined for the MARB1, MARB2, and MARN steels in steam at 650°C, where MARB1 and MARB2 are 9Cr-3W-3Co-0.2V-0.05Nb steel with 100 and 200 ppm boron, respectively, and MARN is described in Section 6.2. The weight gain curves are shown in Fig. 10.44, where the results after the pre-oxidation treatment in Ar gas at 700°C for 50 h are compared with those without pre-oxidation treatment. For the three steels MARB1, MARB2, and MARN, the oxidation resistance in steam is significantly improved by the pre-oxidation treatment, which produces the thin scale of Cr-rich oxides. No evidence was found for the breakaway in the weight gain curves for the specimens with pre-oxidation treatment. The present results indicate that the thin scale of Cr-rich oxides is stable during oxidation in steam at 650°C for a long time exceeding 20,000 h. Excellent oxidation resistance of the three steels is also confirmed even in the condition of no pre-oxidation by the Task 3 of DOE Vision 21 project [92].

Fig. 10.45 compares the cross-section of the MARB1, MARB2, and MARN specimens with and without the pre-oxidation treatment, after oxidation test in steam at 650°C for 500 h. Without pre-oxidation, the thick scale having a thickness of 50–100 μm forms during oxidation in steam. The major component of the scale is Fe_3O_4. After the pre-oxidation treatment, the thin scale of Cr_2O_3 having a thickness of less than 0.1 μm is stable during oxidation in steam. No evidence was found for the exfoliation and cracking of the Cr_2O_3-rich scale.

The combination of scanning TEM (STEM)-EDS analysis shown in Fig. 10.46(a) and selected area electron diffraction in TEM shown in Fig. 10.46(b) shows that the

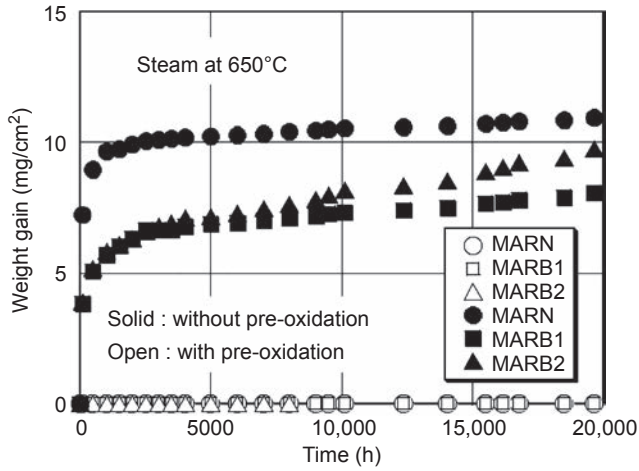


Figure 10.44 Weight gain of 9Cr steel MARN, MARB1 and MARB2 with and without pre-oxidation treatment.

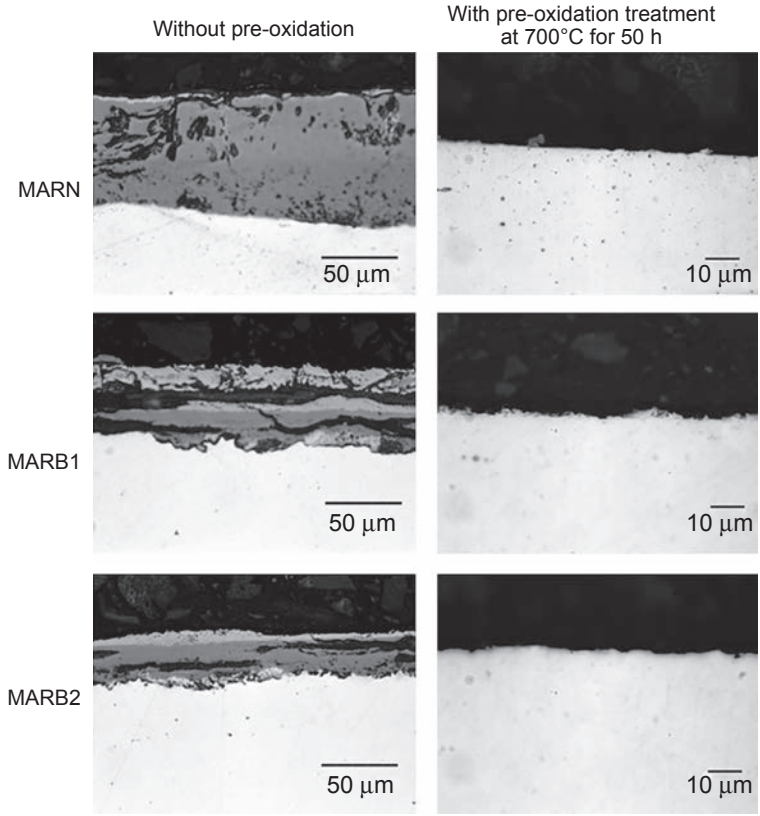


Figure 10.45 Cross-section of the steels after oxidation in steam at 650°C for 500 h.

major component of the thin scale is Cr_2O_3 containing a small amount of Fe [84,85]. The Mn-rich layer, identified as $(Fe, Cr, Mn)_3O_4$, is located close to the scale/steam interface. It should be noted that Si ions are enriched along the interface between the Cr-rich oxide scale and alloy matrix. In Fig. 10.46(a), the particles containing high Si and having a size of about 0.1 μm are the precipitates of Fe_2W Laves phase but not particles containing Si. The characteristic X-ray images from Si and W cannot be distinguished from each other.

Exfoliation of the thin scale of Cr_2O_3-rich oxides formed by the pre-oxidation treatment has been investigated by cyclic oxidation test in steam [86]. No

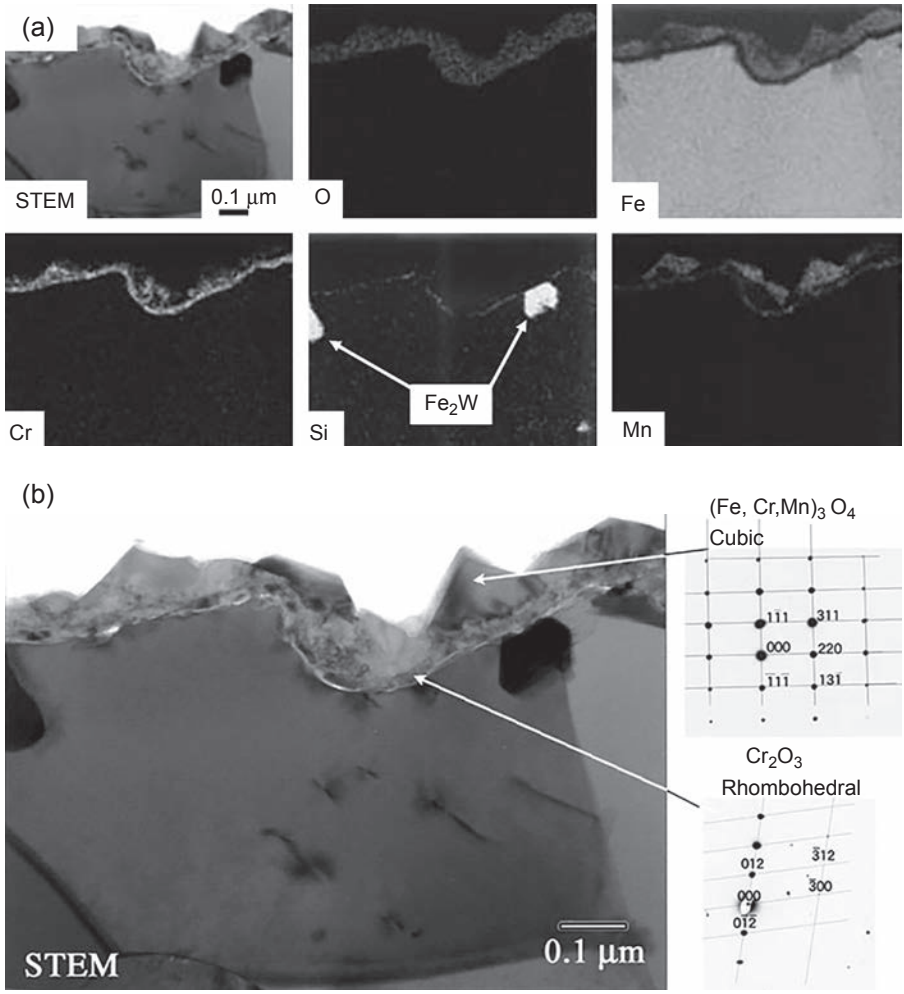


Figure 10.46 (a) STEM-EDS analysis and (b) selected area electron diffraction in TEM of cross-section of 9Cr-3W-VNb steel with 0.8% Si after pre-oxidation treatment in Ar gas at 700°C for 50 h.

evidence has been observed for the exfoliation of thin scale of Cr_2O_3-rich oxides up to 40 cycles of cyclic heating and cooling in steam between 150 and 650°C. No difference is observed in weight gain between cyclic and continuous oxidation tests. Further investigation based on cyclic oxidation test under stress will be necessary.

10.6.3.7 Production of MARBN pipe

The production of a large-diameter and thick-section pipe and subsequent fabrication of circumference welds of the pipe have successfully been performed for MARBN [93]. This is based on the collaboration between NIMS and private companies in Japan. A 3-ton ingot, having a size of 785 mm in diameter and 580 mm in height, was prepared by vacuum melting. The ingot was successfully hot-forged to a pipe, which was heat treated and machined to a size of 470 mm in outer diameter, 65 mm in thickness, and 1300 mm in length. The pipe was normalized at 1100°C for 3 h followed by air cooling and then tempered at 780°C for 4 h followed by air cooling. Fig. 10.47(a) and 47(b) show the appearance of the pipe after machining. Circumference welding of the MARBN pipe has successfully been carried out using gas tungsten-arc welding process and using filler wire of Ni-base AWS ER NICr-3 (Alloy 82). The preheating temperature was kept to be 150°C or more to avoid low-temperature cracking, while the interpass temperature was below 200°C

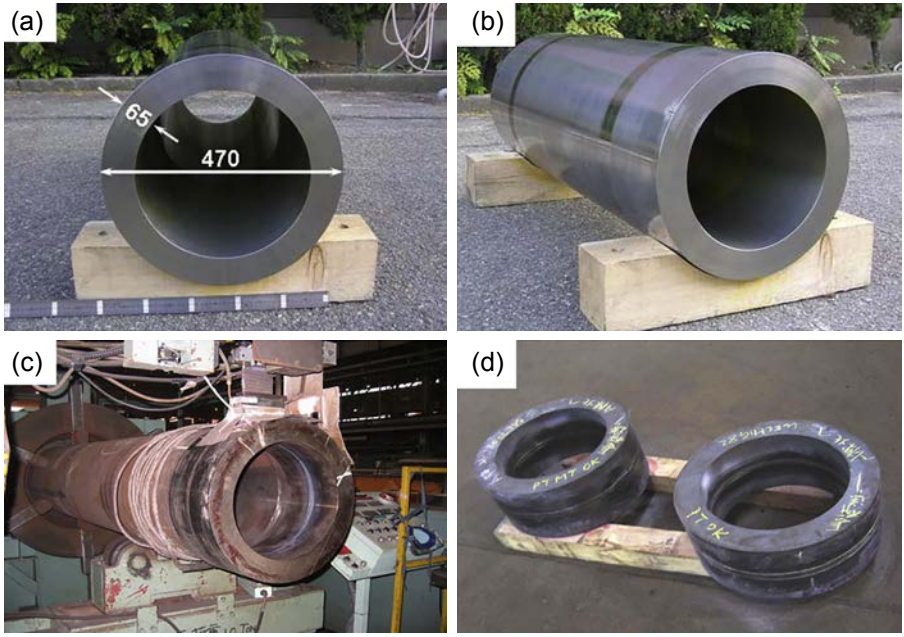


Figure 10.47 (a) and (b) Appearances of MARBN pipe with 470 mm in outer diameter, 65 mm in thickness and 1300 mm in length, and (c), (d) circumference TIG welding of MARBN pipe.

to avoid high-temperature cracking. After welding, the welded joints were subjected to PWHT at 740°C for 4 h. Fig. 10.47(c) and 47(d) show circumference TIG welding of the MARBN pipe and appearance of welded joints after PWHT, respectively. The creep rupture data for the specimens taken from the pipe were identical to those shown in Fig. 10.42.

10.7 Summary

1. Boundary and sub-boundary hardening gives the most important strengthening mechanism for creep of martensitic 9Cr steel and is enhanced by fine dispersion of precipitates along boundaries. Based on the boundary and sub-boundary hardening, a new martensitic 9Cr steel has been alloy designed for application to thick-section boiler components, such as main steam pipes and headers, with steam temperature of 650°C maximum in coal-fired power plants.
2. The addition of boron and nitrogen to 9Cr-3W-3Co-VNb steel without any formation of BN during normalizing heat treatment improves the long-term creep strength of base metal and suppresses the Type IV cracking in HAZ of welded joints at 650°C.
3. The enrichment of soluble boron at and near PAGBs by the segregation is essential for the reduction of coarsening rate of $M_{23}C_6$ carbides near PAGBs, which enhances the boundary hardening, and also for the change in α/γ transformation behavior from diffusive to martensitic in HAZ of welded joints during heating of welding, which produces approximately the same microstructure between HAZ and base metal. The enhancement of boundary and sub-boundary hardening by fine distributions of $M_{23}C_6$ carbides along boundaries retards the onset of acceleration creep, which effectively decreases the minimum creep rate and increases the creep life.
4. The addition of excess nitrogen of 300 and 650 ppm to the 9Cr steel with 140 ppm boron causes the formation of a large amount of BN during normalizing, which significantly reduces the soluble boron concentration and accelerates the degradation in both creep strength and rupture ductility.
5. 9Cr-3W-3Co-0.2V-0.05Nb steel with 120–150 ppm boron and 60–90 ppm nitrogen (MARBN) exhibits not only much higher creep rupture strength of base metal than Gr.91, Gr.92, and Gr.122 but also substantially no degradation in creep strength due to Type IV fracture in HAZ of welded joints at 650°C.
6. The formation of protective Cr_2O_3-rich scale is achieved on the surface of MARBN by pre-oxidation treatment in argon gas. This significantly improves the oxidation resistance of MARBN in steam at 650°C.
7. MARBN is suitable as thick-section boiler components for long-term service at steam temperature of 650°C in coal-fired power plants.

References

[1] F. Abe, Development of creep-resistant steels and alloys for use in power plants, in: A. Shirzadi, S. Jackson (Eds.), Structural Alloys in Power Plants, Woodhead Publishing Limited, Cambridge, UK, 2014, pp. 250–293.

[2] F. Abe, Research and development of heat resistant materials for advanced USC power plants with steam temperature of 700°C and above, Journal of Engineering 1 (2015) 211–224.

[3] K. Metzger, K.H. Czychon, K. Maile, A. Klenk, A. Helmrich, Q. Chen, GKM test rig: investigation of the long term operation behavior of tubes and forgings made of alloys for future high efficient power plants, in: Proc. of 7th International Conference on Advances in Materials Technology for Fossil Power Plants, ASM International, Waikoloa, Hawaii, USA, 2013, pp. 86–95.
[4] A. Di Gianfrancesco, A. Tizzanini, C. Stolzenberger, ENCIO project: an European approach to 700°C power plant, in: Proc. of 7th International Conference on Advances in Materials Technology for Fossil Power Plants, ASM International, Waikoloa, Hawaii, USA, 2013, pp. 19–23.
[5] J. Shingledecker, R. Purgert, P. Rawls, Current status of the U.S. DOE/OCDO A-USC materials technology research and development program, in: Proc. of 7th International Conference on Advances in Materials Technology for Fossil Power Plants, ASM International, Waikoloa, Hawaii, USA, 2013, pp. 41–52.
[6] M. Fukuda, E. Saito, H. Semba, J. Iwasaki, S. Izumi, S. Takano, T. Takahashi, Y. Sumiyoshi, Advanced USC technology development in Japan, in: Proc. of 7th International Conference on Advances in Materials Technology for Fossil Power Plants, ASM International, Waikoloa, Hawaii, USA, 2013, pp. 24–40.
[7] R. Sun, Z. Cui, Y. Tao, Progress of China 700°C USC development program, in: Proc. of 7th International Conference on Advances in Materials Technology for Fossil Power Plants, ASM International, Waikoloa, Hawaii, USA, 2013, pp. 1–8.
[8] A. Mathur, O.P. Bhutani, T. Jayakumar, D.K. Dubey, S.C. Chetal, India's national A-USC mission – plan and progress, in: Proc. of 7th International Conference on Advances in Materials Technology for Fossil Power Plants, ASM International, Waikoloa, Hawaii, USA, 2013, pp. 53–59.
[9] F. Abe, Precipitate design for creep strengthening of 9% Cr tempered martensitic steel for USC power plant, Science and Technology of Advanced Materials 9 (2008) 013002.
[10] T. Sato, K. Tamura, Y. Fukuda, K. Asakura, T. Fujita, Development of low-C 9Cr steel for USC boilers, CAMP-ISIJ 19 (2006) 565 (in Japanese).
[11] K. Metzger, K.H. Czychon, E. Roos, K. Maile, Testing for the investigation of the damage mechanism of high-temperature for the 700°C power plant, in: Proc. of 34th MPA-Seminar, Stuttgart, Germany, 2008. 48.1–48.12.
[12] M. Igarashi, Y. Sawaragi, Development of 0.1C-11Cr-3W-3Co-V-Nb-Ta-Nd-N ferritic steel for USC boilers, in: Proc. of International Conference on Power Engineering-97 (ICOPE-97), Tokyo, Japan, 1997, pp. 107–112.
[13] K.-H. Mayer, F. Masuyama, The development of creep-resistant steels, in: F. Abe, T.-U. Kern, R. Viswanathan (Eds.), Creep-Resistant Steels, Woodhead Publishing Limited, Cambridge, 2008, pp. 15–77.
[14] R. Blum, R.W. Vanstone, Materials development for boilers and steam turbines operating at 700°C, in: Proc. of 6th International Charles Parsons Turbine Conference. Dublin, Ireland, 2003, pp. 498–510.
[15] T.-U. Kern, K.-H. Mayer, B. Donth, G. Zeiler, A. Di Gianfrancesco, The European efforts in development of new high temperature rotor materials – COST536, in: Proc. of 9th Liege Conference on Materials for Advanced Power Engineering, 2010, pp. 29–38. Liege, Belgium.
[16] P. Barnard, P. Moody, Y. Maclachlan, D. Allen, S. Robert, H. Du, R. Thomson, A new MarBN alloy for USC power plant, in: Proc. of 5th Symposium on Heat Resistant Steels and Alloys for High Efficiency USC/A-USC Power Plants 2013, Seoul, Korea, 2013, p. 31.
[17] E. Zanin, E. Coda, P. Kilgallon, S. Lockyer, P. Mayr, C. Schlacher, O. Tassa, R. Vanstone, Component performance-driven solutions for long-term efficiency increase in ultra supercritical power plants Macplus Project, in: Proc. of 10th Liege Conference on Materials for Advanced Power Engineering, 2014, pp. 803–819. Liege, Belgium.

[18] C. Sommitsch, R. Vanstone, T.-U. Kern, P. Barnard, P. Mayr, R. Thomson, A. Agüero, Co-ordination of European research in structural materials for power generation equipment, in: Proc. of 10th Liege Conference on Materials for Advanced Power Engineering, 2014, pp. 3–18. Liege, Belgium.
[19] E. Plesiutschunig, C. Beal, S. Paul, G. Zeiler, S. Mitsche, C. Sommitsch, Microstructure for an optimized creep rupture strength of high Cr steels, in: Proc. of 10th Liege Conference on Materials for Advanced Power Engineering, 2014, pp. 180–188. Liege, Belgium.
[20] Z. Liu, H. Bao, G. Yang, S. Xu, Q. Wang, Y. Yang, Material advancement used for 700°C A-USC-PP in China, in: Proc. of 7th International Conference on Advances in Materials Technology for Fossil Power Plants, ASM International, Waikoloa, Hawaii, USA, 2013, pp. 171–179.
[21] K. Maruyama, K. Sawada, J. Koike, Strengthening mechanisms of creep resistant tempered martensitic steel, ISIJ International 41 (2001) 641–653.
[22] F. Abe, Bainitic and martensitic creep-resistant steels, Current Opinion in Solid State and Materials Science 8 (2004) 305–311.
[23] F. Abe, Strengthening mechanisms in steel for creep and creep rupture, in: F. Abe, T.-U. Kern, R. Viswanathan (Eds.), Creep-Resistant Steels, Woodhead Publishing Limited, Cambridge, 2008, pp. 15–77.
[24] K. Yokokawa, O. Kanemaru, H. Miyazaki, T. Ohba, F. Abe, Effect of W-Mo balance on creep deformation behavior of 9Cr steel, CAMP-ISIJ 12 (1999) 243 (in Japanese).
[25] K. Maruyama, H. Nakashima, Materials Science for High Temperature Strength, Uchida-Rokakuho, Tokyo, 1997 (in Japanese).
[26] K. Sawada, H. Kushima, M. Tabuchi, K. Kimura, Microstructural degradation of Gr.91 steel during creep under low stress, Materials Science and Engineering A 528 (2011) 5511–5518.
[27] H.K. Danielsen, J. Hald, Behaviour of Z phase in 9-12% Cr steels, Energy Materials 1 (2006) 49–57.
[28] A. Strang, V. Vodarek, Z phase formation in martensitic 12CrMoVNb steel, Materials Science and Technology 12 (1996) 552–556.
[29] L. Cipolla, H.K. Danielsen, D. Venditti, P.E.D. Nunzio, J. Hald, M.A.J. Somers, Conversion of MX nitrides to Z-phase in a martensitic 12% Cr steel, Acta Materialia 58 (2010) 669–679.
[30] K. Sawada, H. Kushima, K. Kimura, M. Tabuchi, TTP diagram of Z phase in 9-12% Cr heat-resistant steels, ISIJ International 47 (2007) 733–739.
[31] K. Sawada, M. Taneike, K. Kimura, F. Abe, Effect of nitrogen content on microstructural aspects and Creep behaviour in extremely low carbon 9Cr heat-resistant steel, ISIJ International 44 (2004) 1243–1249.
[32] V. Vodarek, A. Strang, Effect of nickel on the precipitation processes in 12CrMoV steel during creep at 550°C, Scripta Materialia 38 (1998) 101–106.
[33] V. Sklenicka, K. Kucharova, M. Svoboda, L. Kloc, J. Bursik, A. Kroupa, Long-term creep behaviour of 9-12% Cr power plant steels, Materials Characterization 51 (2003) 35–48.
[34] A. Di Gianfrancesco, L. Cipolla, F. Cirilli, G. Cumino, S. Caminada, Microstructural stability and creep data assessment of Tenaris Grades 91 and 911, in: Proc. of 1st International Conference on Super-High Strength Steel, Sheraton Hotel, Rome, Italy, CD-ROM, November 2–4, 2005.
[35] H.G. Armaki, K. Maruyama, M. Yoshizawa, M. Igarashi, Prevention of the overestimation of long-term creep rupture life by multiregion analysis in strength enhanced high Cr ferritic steels, Materials Science and Engineering A 490 (2008) 66–71.

[36] R.P. Chen, H.G. Armaki, K. Maruyama, M. Igarashi, Long-term microstructural degradation and creep strength in Gr.91 steel, Materials Science and Engineering A 528 (2011) 4390–4394.
[37] F. Abe, H. Tanaka, M. Murata, Impurity effects on heat-to-heat variation in creep life for some heat resistant steels, in: Proc. of BALTICA VII International Conference on Life Management and Maintenance for Power Plants, Helsinki, June 12–14, 2007, pp. 171–184.
[38] F. Abe, Heat-to-heat variation in long-term creep strength of some ferritic steels, International Journal of Pressure Vessels and Piping 87 (2010) 310–318.
[39] J. Brett, J.S. Bates, R.C. Thomson, Aluminium nitride precipitation in low strength Grade 91 power plant steels, in: R. Viswanathan, D. Gandy, K. Coleman (Eds.), Proc. of the 4th International Conference on Advances in Materials Technology for Fossil Power Plants, 2012, pp. 1183–1197. October 25–28, 2004, Hilton Head Island, South Carolina, USA.
[40] K. Kimura, Y. Takahashi, Evaluation of long- term creep strength of ASME Grades 91, 92 and 122 type steels, in: Proc. of ASME 2012 Pressure Vessels and Piping Conference, July 15–19, 2012. Toronto, Canada. PVP2012–78323.
[41] J. Parker, K. Coleman, EPRI guidelines for fabrication of components manufactured from Grade 91 steel, in: Proceedings of ASME 2012 Pressure Vessels and Piping Conference, July 15–19, 2012. Toronto, Canada. PVP2012–78226.
[42] F. Abe, M. Tabuchi, S. Tsukamoto, Mechanisms for boron effect on microstructure and creep strength of ferritic power plant steels, Energy Materials 4 (2012) 166–175.
[43] H. Kushima, K. Kimura, F. Abe, Degradation of Mod.9Cr-1Mo steel during long-term creep deformation, Tetsu-to-Hagane 85 (1999) 841–847 (in Japanese).
[44] A. Iseda, H. Teranihsi, F. Masuyama, Effect of chemical compositions and heat treatments on creep rupture strength of 12 wt% Cr heat resistant steels for boiler, Tetsu-to-Hagane 76 (1990) 1076–1083 (in Japanese).
[45] M. Igarashi, M. Yoshizawa, A. Iseda, H. Matsuo, T. Kan, Long-term creep strength degradation in T122/P122 steels for USC power plants, in: Proc. of 8th Liege Conference on Materials for Advanced Power Engineering 2006, Liege, Belgium, 2006, pp. 1095–1104.
[46] K. Kimura, K. Sawada, H. Kushima, Y. Toda, Degradation behaviour and long-term creep strength of 12Cr ferritic creep resistant steels, in: Proc. of 8th Liege Conference on Materials for Advanced Power Engineering 2006, Liege, Belgium, 2006, pp. 1105–1116.
[47] F. Abe, S. Nakazawa, H. Araki, T. Noda, The role of microstructural instability on creep behavior of a low activation martensitic 9Cr-2W steel, Metallurgical Transactions 23A (1992) 469–477.
[48] F. Abe, S. Nakazawa, The effect of tungsten on creep behavior of tempered martensitic 9Cr steels, Metallurgical Transactions 23A (1992) 3025–3034.
[49] F. Abe, Creep modeling and creep life estimation of Gr.91, International Journal of Materials Research 103 (2012) 765–773.
[50] F. Abe, Creep behavior, deformation mechanisms and creep life of Mod. 9Cr-1Mo steel, Metallurgical and Materials Transactions 46A (2015) 5610–5625.
[51] H.K.D.H. Bhadeshia, Design of ferritic creep-resistant steels, ISIJ International 41 (2001) 626–640.
[52] M.Y. Way, T. Sakuma, T. Nishizawa, Growth of alloy carbide particles in austenite, Transactions of the Japan Institute of Metals 22 (1981) 733–742.
[53] H. Oikawa, Review on lattice diffusion of substitutional impurities in iron, Technology Report, Tohoku University 47 (1982) 215–224.

[54] M. Taneike, F. Abe, K. Sawada, Creep-strengthening of steels at high temperatures using nano-sized carbonitride dispersions, Nature 424 (2003) 294–296.
[55] M. Taneike, K. Sawada, F. Abe, Effect of carbon concentration on precipitation behavior of $M_{23}C_6$ carbides and MX carbonitrides in martensitic 9Cr steel during heat treatment, Metallurgical and Materials Transactions A 35A (2004) 1255–1262.
[56] F. Abe, Analysis of creep rates of tempered martensitic 9% Cr steel based on microstructure evolution, Materials Science and Engineering: A 510–511 (2009) 64–69.
[57] F. Abe, M. Tabuchi, S. Tsukamoto, Alloy design of martensitic 9Cr-boron steel for A-USC boiler at 650°C – beyond Grades 91, 92 and 122, in: Proc. of Energy Materials, 4–6 November 2014, Xi'an, China, 2014, pp. 129–136.
[58] NIMS Creep Data Sheets, No.48A, National Institute for Materials Science, Tokyo, Tsukuba, 2012.
[59] NIMS Creep Data Sheets, Atlas of Creep Deformation Property, No. D-1, National Institute for Materials Science, Tokyo, Tsukuba, 2007.
[60] NIMS Creep Data Sheets, No. 51A, National Institute for Materials Science, Tokyo, Tsukuba, 2012.
[61] M. Kimura, K. Kobayashi, K. Yamaguchi, Creep and fatigue properties of newly developed ferritic heat-resisting steels for ultra super critical power plants, Materials Science Research International 9 (2003) 50–54.
[62] T. Horiuchi, M. Igarashi, F. Abe, Improved utilization of added B in 9Cr heat-resistant steels containing W, ISIJ International 42 (2002) S67–S71.
[63] H. Semba, F. Abe, Alloy design and creep strength of advanced 9% Cr USC Boiler steels containing high concentration of boron, Energy Materials 1 (2006) 238–244.
[64] K. Sakuraya, H. Okada, F. Abe, BN type inclusions formed in high Cr ferritic heat resistant steel, Energy Materials 1 (2006) 158–166.
[65] K. Sakuraya, H. Okada, F. Abe, BN type inclusions formed in high Cr ferritic heat resistant steel, Tetsu-to-Hagane 90 (2004) 819–826.
[66] Y. Gu, G.D. West, R.C. Thomson, J. Parker, Investigation of creep damage and cavitation mechanisms in P92 steels, in: Proc. of 7th International Conference on Advances in Materials Technology for Fossil Power Plants, ASM International, Waikoloa, Hawaii, USA, 2013, pp. 596–606.
[67] S. Suzuki, R. Shishido, T. Tanaka, F. Abe, Characterization of the inhomogeneous distribution of light elements in ferritic heat-resistant steels by secondary ion mass Spectrometry, ISIJ International 54 (2014) 885–892.
[68] F. Liu, D.H.R. Fors, A. Golpayegani, H.-O. Andren, G. Wahnstrom, Effect of boron on carbide coarsening at 873 K (600°C) in 9 to 12 pct chromium steels, Metallurgical and Materials Transactions A 43A (2012) 4053–4062.
[69] M. Tabuchi, T. Watanabe, K. Kubo, M. Matsui, J. Kinugawa, F. Abe, Creep crack growth behavior in the HAZ of Weldments of W containing high Cr steel, International Journal of Pressure Vessels and Piping 78 (2001) 779–784.
[70] F. Abe, M. Tabuchi, M. Kondo, H. Okada, Suppression of Type IV fracture in welded joints of advanced ferritic power plant steels – effect of boron and nitrogen, Materials at High Temperatures 23 (2006) 145–154.
[71] F. Abe, M. Tabuchi, Microstructural and creep strength of welds in advanced ferritic power plant steels, Science and Technology of Welding and Joining 9 (2004) 22–30.
[72] Y. Liu, S. Tsukamoto, T. Shirane, F. Abe, Formation mechanism of type IV failure in high Cr ferritic heat-resistant steel-welded joint, Metallurgical and Materials Transactions A 44 (2013) 4626–4633.

[73] Y. Liu, S. Tsukamoto, K. Sawada, F. Abe, Role of boundary strengthening on prevention of type IV failure in high Cr ferritic heat-resistant steels, Metallurgical and Materials Transactions A 45A (2014) 1306–1314.
[74] Y. Liu, S. Tsukamoto, K. Sawada, M. Tabuchi, F. Abe, Precipitation behaviour in the heat affected zone of boron added 9Cr-3W-3Co steel during post weld heat treatment and creep deformation, Metallurgical and Materials Transactions A 46A (2015) 1843–1854.
[75] F. Abe, M. Tabuchi, S. Tsukamoto, T. Shirane, Microstructure evolution in HAZ and suppression of type IV fracture in advanced ferritic power plant steels, International Journal of Pressure Vessels and Piping 87 (2010) 598–604.
[76] M. Santella, E. Specht, J. Shingledecker, F. Abe, A synchrotron diffraction study of transformation behaviour in 9Cr steels using simulated weld heat-affected-zone conditions, in: Proc. of 7th International Charles Parsons Turbine Conference, Glasgow, UK, September 11–13, 2007, pp. 427–438.
[77] S. Kobayashi, K. Toshimori, K. Nakai, Y. Ohmori, H. Asahi, T. Muraki, Effects of boron addition on tempering processes in an Fe-9Cr-0.1C alloy martensite, ISIJ International 42 (2002) S72–S76.
[78] T. Azuma, K. Miki, Y. Tanaka, T. Ishiguro, Effect of B on the behavior of austenite formation and recrystallization in high Cr ferritic heat resistant steel, Tetsu-to-Hagane 86 (2000) 667–673.
[79] T. Shirane, S. Tsukamoto, K. Tsuzaki, Y. Adachi, T. Hanamura, M. Shimizu, F. Abe, Ferrite to austenite reverse transformation process in B containing 9% Cr heat resistant steel HAZ, Science and Technology of Welding and Joining 14 (2009) 698–707.
[80] L. Karlsson, H. Norden, Non-equilibrium grain boundary segregation of boron in austenitic stainless steels-II Fine segregation behavior, Acta Metallurgica 36 (1988) 13–24.
[81] F. Abe, M. Tabuchi, S. Tsukamoto, Alloy design for suppression of Type IV fracture in 9Cr steel welds at 650°C, in: Proc. 10th Liege Conference, September 15–17, 2014, pp. 91–100.
[82] M. Tabuchi, H. Hongo, F. Abe, Creep strength of dissimilar welded joints using High-B-9Cr steel for advanced USC boiler, Metallurgical and Materials Transactions A 45A (2014) 5068–5075.
[83] T. Itagaki, H. Kutsumi, H. Haruyama, M. Igarashi, F. Abe, Steam oxidation of high-chromium ferritic steels containing palladium, Corrosion 61 (2005) 307–316.
[84] H. Kutsumi, T. Itagaki, F. Abe, Improvement of oxidation resistance of 9% Cr steel for A-USC by pre-oxidation treatment, in: J. Lecomte-Beckers, M. Carton, F. Schubert, P.J. Ennis (Eds.), Proc. 7th Liege Conference on Materials for Advanced Power Engineering, 2002, pp. 1629–1638. Liege, Belgium.
[85] H. Okubo, S. Muneki, T. Hara, H. Kutsumi, F. Abe, Improvement of oxidation resistance of 9% Cr steel for A-USC by pre-oxidation treatment, in: Proc. of the 34th MPA-Seminar on “Materials and Components Behaviour in Energy & Plant Technology”, MPA, Stuttgart, October 9 and 10, 2008, pp. 42.1–42.11.
[86] H. Haruyama, H. Kutsumi, S. Kuroda, F. Abe, Effect of shot peening and pre-oxidation treatment in air on steam oxidation resistance of Mod.9Cr-1Mo steel, in: Proc. 4th Int. Conf. on Advances in Materials Technology for Fossil Power Plants, Hilton Head Island, SC, USA, 2004, pp. 412–419.
[87] T. Sundararajan, S. Kuroda, T. Itagaki, F. Abe, Steam oxidation resistance of Ni-Cr thermal spray coatings on 9Cr-1Mo steel. Part 1: 80Ni-20Cr, ISIJ International 43 (2003) 95–103.
[88] T. Sundararajan, S. Kuroda, T. Itagaki, F. Abe, Steam oxidation resistance of Ni-Cr thermal spray coatings on 9Cr-1Mo steel. Part 2: 50Ni-50Cr, ISIJ International 43 (2003) 104–111.

[89] T. Sundararajan, S. Kuroda, K. Nishida, T. Itagaki, F. Abe, Behaviour of Mn and Si in the spray powders during steam oxidation of Ni-Cr thermal spray coatings, ISIJ International 44 (2004) 139–144.

[90] T. Sundararajan, S. Kuroda, F. Abe, Steam oxidation studies on 50Ni-50Cr HVOF coatings on 9Cr-1Mo steel: change in structure and morphology across the coating/substrate interface, Materials Transactions 45 (2004) 1299–1305.

[91] T. Sundararajan, S. Kuroda, F. Abe, Effect of thermal spray on the microstructure and adhesive strength of high-velocity oxy-fuel-sprayed Ni-Cr coatings on 9Cr-1Mo steel, Metallurgical and Materials Transactions A 35A (2004) 3187–3199.

[92] J.M. Sarver, J.M. Tanzosh, An evaluation of the steamside oxidation of candidate USC materials at 650°C and 800°C, in: Proc. 4th Int. Conf. on Advances in Materials Technology for Fossil Power Plants, Hilton Head Island, SC, USA, 2004, pp. 1326–1339.

[93] F. Abe, M. Tabuchi, H. Semba, M. Igarashi, M. Yoshizawa, N. Komai, A. Fujita, Feasibility of MARBN steel for application to thick section biler components in USC power plant at 650°C, in: Proc. of 5th International Conference on Advances in Materials Technology for Fossil Power Plants, USA, CD-ROM, October 3–5, 2007.

New austenitic steels for the advanced USC power plants

11

M. Spiegel[1], *P. Schraven*[2]
[1]Salzgitter Mannesmann Forschung GmbH, Duisburg, Germany; [2]Salzgitter Mannesmann Stainless Tubes, Mülheim an der Ruhr, Germany

11.1 Introduction

The worldwide demand for energy will further increase by about one-third within the next 25 years [1]. As renewable energies will only partly cover this demand, fossil power plants will further play an important role while the emission of climate-damaging CO_2/kWh must be reduced. This is only possible by a reduction of fuel consumption per kWh, ie, a higher efficiency of the steam plants. Many developments of austenitic grades for fossil-fired plants were developed in the past.

Esshete 1250 was developed in England for temperatures from 600–650°C and has a sufficient rupture strength at 600°C. In this temperature range, the material shows a satisfying behavior; however, its steam oxidation resistance is quite low at $T > 650$°C as well as under fireside corrosion conditions.

AC 66 is a development of Mannesmann that was initially created for coal gasification plants and shows an excellent corrosion and oxidation resistance. This alloy may be improved regarding a satisfying rupture strength at 700°C. Other developments are based on steels present in the ASME. Super 304HCu is based on ASME TP 304 and has a 50% higher rupture strength due to precipitation of Nb(C,N) particles. TP347HFG is a further development of TP 347 with a finer grain size, improving oxidation resistance and rupture strength.

The steel HR3C is a development from TP310. The rupture strength was improved by 135%, by alloying Nb and N and by modifying the amounts of C, Si, and Mn.

The steels Tempaloy A-3 and NF 709 are newly developed materials and cheaper than ASME Alloy 800 H, and they show a higher rupture strength. This was achieved by reducing the nickel content and by alloying Mo, Ti, N, and B. The increase in rupture strength was 14–33% compared to Alloy 800H.

SAVE 25 is cheaper and shows a higher rupture strength compared to HR3C. The higher rupture strength is achieved by alloying of W and C.

Currently, there is a focus on the development of power plants with steam temperatures of about 700/720°C and 350 bars with around 50% efficiency [2]. This requires components that are able to withstand very high temperatures and pressure loads caused by flowing steam in the interior of the boiler tubes. Therefore, materials should have good creep strength, high oxidation resistance in the presence of pressurized steam, and a good fireside corrosion resistance, especially with respect to sulfur-related

Materials for Ultra-Supercritical and Advanced Ultra-Supercritical Power Plants.
http://dx.doi.org/10.1016/B978-0-08-100552-1.00011-7
Copyright © 2017 Elsevier Ltd. All rights reserved.

corrosion phenomena like internal sulfidation and Type II hot corrosion, as observed on nickel alloys [3]. The most recent development is Sanicro 25, which was developed by Sandvik [4,5]. Based on Sanicro 25, several concepts are now being developed to expand the application areas of austenitic alloys with respect to the nickel-based materials. Europe has supported various studies for the thermal power plant of the next generation (A-USC) where higher temperature are required for the efficiency and compensate for the necessity of capturing carbon. The new trend toward non-steady power generation in flexible-working and coal-fired power stations or in solar-thermic power plants, where temperature changes are due to changes in sunshine intensity, leads to higher structural strength requirements.

This chapter gives an overview of current important developments, being at different stages of industrialization. Two of these concepts are based on new, intermetallic phase hardening mechanisms, ie, Laves phase and sigma phase hardening. The third concept is the so-called alumina-forming austenite (AFA) concepts, which exploits the potential of corrosion-resistant alumina-forming alloys.

11.2 Future trends

The **Laves phase strengthened** concept was developed and published by Japanese researchers [6–8] and will be classified as one of the most promising intermetallic phase hardening concepts. The base composition is in at.%: Fe-20Cr-30Ni-2Nb, and the material is strengthened by precipitation of intermetallic Fe_2Nb phase in combination with Ni_3Nb. The precipitation of Fe_2Nb within the grain occurs in the so-called Widmannstätten type, ie, in an ordered crystallographic orientation with the austenite matrix. The authors use the so-called "grain boundary precipitation strengthened mechanism" (GBPS) to achieve a 10^5 h strength of 80 MPa at 973 K. The authors show that the creep strength correlates with the area fraction of Laves phase precipitates at the grain boundaries in the sense that a higher area fraction shows a higher creep strength by revealing still a high ductility of 77% even at higher creep strength [6,7]. Addition of 0.03% of boron leads to a four times higher creep life due to a finer dispersed precipitation of Laves phase at the grain boundary compared to the boron-free version. Furthermore, the material was also tested in steam oxidation environments. The authors show that it develops a chromia scale upon oxidation at 1073K. The oxidation kinetic is comparable to that of 316L [8]. However, an internal oxidation zone was found, which depth decreases due to the protective property of the oxide. Combined creep and oxidation tests have shown that the grain boundary Laves phase is also stable under combined creep/oxidation conditions. The authors claimed that sufficient Laves phase at grain boundaries increases the creep rupture strength and suppress intergranular oxidation during creep in steam. In conclusion, the GBPS mechanism is a promising concept for further development of materials for ultra-supercritical thermal power plants running at 700°C.

The **AFA concept** was developed in the United States [9]. The concept is based on the idea to promote the oxidation/corrosion resistance by alloying a certain amount of aluminium to the material with the aim to develop a protective alumina scale at

higher temperatures as oxidation protection. Several alloys were developed and tested, basically on the composition Fe-25Ni-14Cr-3.5Al-2.5Nb-2Mn-2Mo-1W-0.1C-0.01B. So-called AFA high performance and AFA superalloys were also designed with higher chromium contents and higher aluminium contents, respectively. The temperatures of operation were foreseen to be 650°C for the conventional normal AFA alloys and up to 950°C for the high-performance alloys. The creep rupture life is dependent on the composition of the material and scatters around the Super 304 and NF 709 grade in the temperature region between 500°C and 700°C. The alloys show good steam oxidation resistance and are possible candidates for coal-fired boilers $T < 700$°C according to their creep properties. Also under carburizing and sulfidizing conditions the materials show promising behavior. From an industrialization point of view the material was mainly processed for use in heat exchangers and turbine recuperators. Production was successfully done on strip, foil, and tube form by different manufactures. For the thermal power plant application, some modified alloys are developed showing a good combination of creep strength and oxidation resistance. Also centrifugally cast versions are now available.

In conclusion, Sanicro 25, the Laves phase strengthened alloys, and the AFA alloys are promising candidates for future applications in demanding services such as energy production. The most promising future concept is the concept of intermetallic phase hardening by a systematic engineering of particle within the grain and at grain boundaries. Follow this line, the sigma phase concept as developed by Salzgitter Mannesmann Stainless Tubes GmbH and Salzgitter Mannesmann Research GmbH was developed, showing promising creep and corrosion properties. The main task in this development is the use of a potentially harmful phase as a hardening phase and the engineering of the precipitation sequence of $M_{23}C_3$, Nb(C,N), and sigma Phase. In the following, this concept is discussed in detail.

11.3 Sigma phase strengthened concept (Power Austenite) [10]

The aim of the development of Power Austenite was to achieve an excellent hot corrosion behavior in the presence of aggressive flue gases as well as in steam, together with a satisfactory creep resistance of 100 MPa at 700°C. The alloying concept was based on AC 66, which is known to give a high oxidation and corrosion resistance due to its 27 wt% of chromium. The major task was, therefore, to increase the creep strength of AC 66.

11.3.1 Alloying concept and resulting microstructure

Sigma phase is known as a detrimental phase in alloys, leading to embrittlement and early fracture. In most reported cases, sigma phase was observed after long exposure times in austenitic alloys, very often at grain boundaries. The phase appears in the Fe-Cr system, as shown in Fig. 11.1 and is stable up to approx. 800°C in the pure binary system.

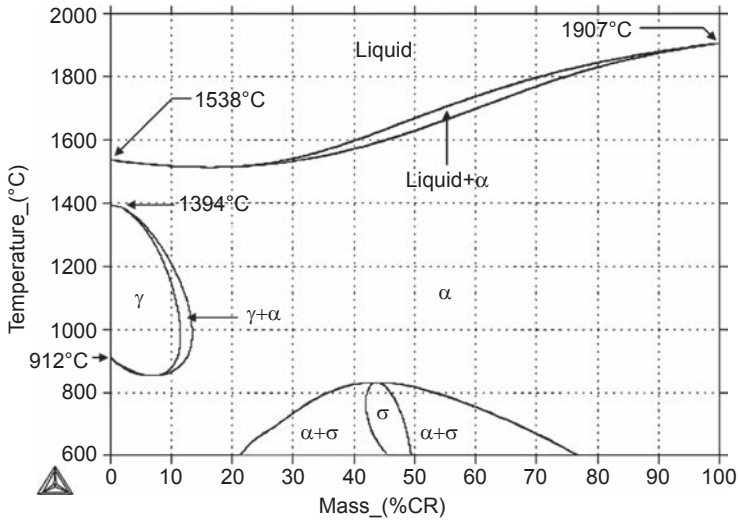


Figure 11.1 Occurrence of sigma phase in the binary Fe-Cr system.

Table 11.1 Composition of sigma phase in common ferritic and austenitic alloys

Type	Fe	Cr	Ni	Mo	Si
17Cr-11Ni-2Mo-0.4 Ti	Bal.	30	4.3	9	0.8
17Cr-11Ni-2Mo-0.4 Ti	bal.	33	4.5	5.4	0.7
316	55	29	5	11	–
20Cr-(25-34Ni)-(6.5–8) Mo	35/37	17/26	15/21	21/28	–
25Cr-20Ni	40	46	9.4	–	3

Sigma stabilizing elements are chromium as well as Mo and Silicon. Table 11.1 summarizes the possible compositions of sigma phase in common ferritic and austenitic stainless steels. It is very clear that the phase consists of chromium, iron, and some nickel as well as molybdenum and silicon.

It is important to note that sigma phase in insoluble for carbon, nitrogen, and boron. These elements strongly retard the formation kinetics with respect to carbides and nitrides, and it is very difficult to nucleate sigma phase directly within the austenite grain as the lattices are incoherent and the diffusion of carbon and nitrogen in austenite is quite slow. It takes several thousands of hours to nucleate sigma phase in austenite. In most cases, sigma phase forms by precipitation from δ-ferrite islands with a reasonably fast kinetics. This transformation is in particular harmful for the material as δ-ferrite films are usually formed also at grain boundaries. In addition, grain boundary sigma phase is formed much easier also without prior δ-ferrite formation due to the energetic preferable nucleation site. Is has been shown in the literature

that the nucleation of sigma phase within austenite grains enhances the creep strength [11]. The authors have shown that at 700°C an increasing volume fraction of sigma phase within the austenite grain enhances the creep strength. With time, however, the formation of grain boundary sigma occurs, and the strength strongly decreases.

The aim of the Power Austenite development was to achieve a sigma phase hardened structure by stabilization of the grain boundaries by precipitation of B-stabilized $M_{23}(C,B)_6$ and secondary Nb(C,N) and grain strengthening by early precipitation of sigma phase and Nb(C,N). The microstructural concept was achieved by the range of chemical composition shown in Table 11.2. Prior to melting, thermodynamic calculations were performed with MatCalc to estimate the stabilities of the different phases. The calculation is shown in Fig. 11.2. It shows that after solidification of the austenite, the precipitation starts with Nb(C,N), followed by $M_{23}C_6$ and sigma phase. The stability range of sigma is starting from approximately 580–1050°C, with a middle alloy composition shown in Table 11.2.

Table 11.2 Composition of Power Austenite: MoW, limits of patent application

	C	Si	Cr	Ni	Mo	Nb	N	B
Min	0.02	0.1	25	22	1	0.4	0.01	10 ppm
Max	0.15	2	33	38	6	1.5	0.2	100 ppm

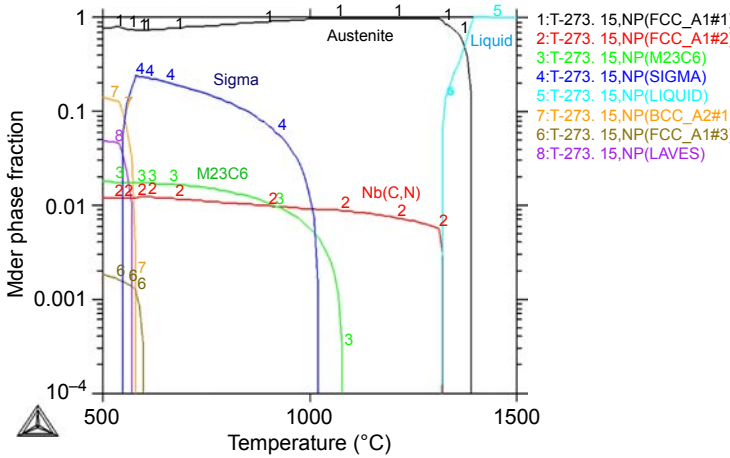


Figure 11.2 Thermo-Calc calculation of phases, stable in Power Austenite, with composition limits as shown in Table 11.2.

Fig. 11.3 shows the microstructure in an SEM image that was achieved on a heating of Power Austenite after annealing at 1150°C followed by 700°C tempering.

Sigma phase, $M_{23}C_6$, and some Nb(C,N) are precipitated in the entire grain. The sigma phase is grown as plates, which appear needle-like in the SEM cross-sectional view. The crystallographic relationship between austenite and sigma phase has been

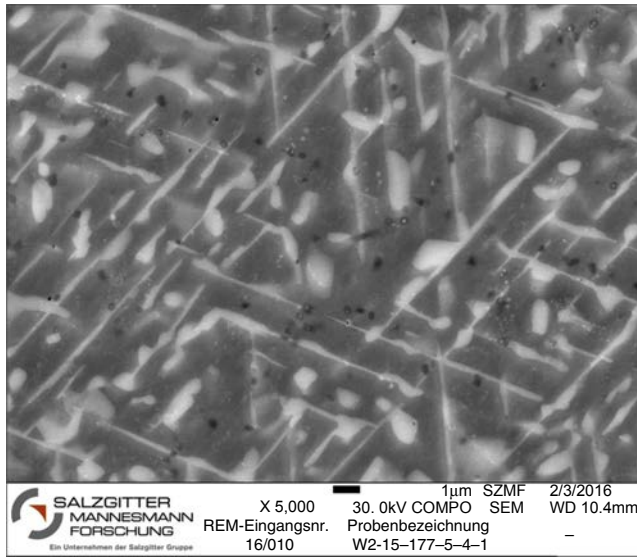


Figure 11.3 Strengthening concept of Power Austenite: SEM picture showing sigma phase and Nb(C,N) precipitated in the grain as well as $M_{23}C_6$. Note the Widmannstätten type of precipitation orientation.

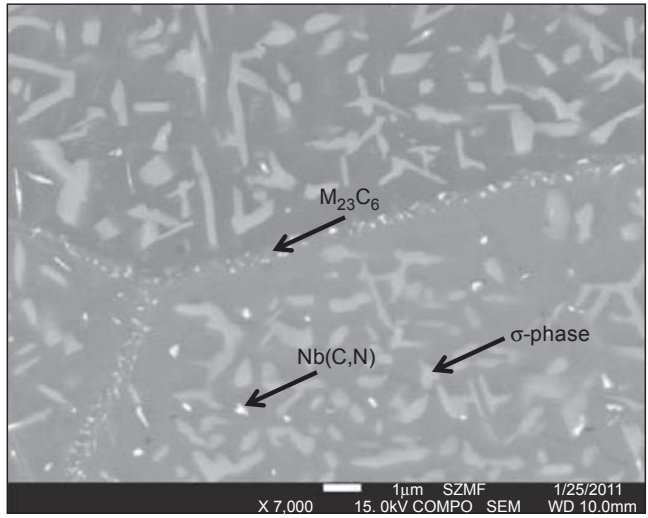


Figure 11.4 Strengthening concept of Power Austenite: SEM picture showing sigma phase and Nb(C,N) precipitated in the grain as well as Nb(C,N) and $M_{23}C_6$ at the grain boundaries, 12.295 h of creep testing.

reported to be (111) γ parallel (001) σ [12], which can be seen very clearly in Fig. 11.3. Adjacent to the plate like σ, some globular precipitates are also formed.

In comparison with Fig. 11.3, Fig. 11.4 shows a SEM picture obtained from a sample broken after 12.295 h of creep testing. The grain boundaries are decorated with $M_{23}C_6$ and Nb(C,N). Globular sigma phase and small Nb(C,N) particles have precipitated in the entire grain.

Fig. 11.5 summarizes the Power Austenite microstructural concept in a schematic, idealized view. The most important point is the stabilization of the grain boundaries by boron-stabilized $M_{23}(C,B)_6$

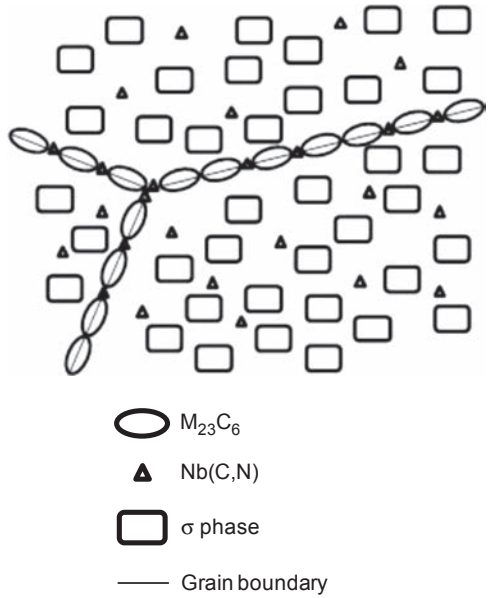


Figure 11.5 Strengthening concept of Power Austenite: schematic view.

11.3.2 Creep strength

To evaluate the creep strength, iso-stress tests were carried out at 120 MPa at 700 and 740°C. The results are shown in Fig. 11.6, compared to other austenitic boiler grades AC 66 and DMV 310 N. In comparison, Alloy 617 is also shown according to the creep evaluation of Spiegel et al. [3]. The creep strength at 740°C is much better than 310 N and AC 66. The rupture time of one melt is approaching DMV Alloy 617 B.

Figs. 11.7 and 11.8 show a creep rupture diagram at 650°C in Fig. 11.7 and the corresponding creep rate in Fig. 11.8. The broken points at 300 and 265 MPa fit very well to the Sanicro 25 middle values, whereas two other samples at 230 and 195 MPa are still running and approaching the middle values. It is very interesting to compare the rupture points with the creep rate shown in Fig. 11.8. First, the creep

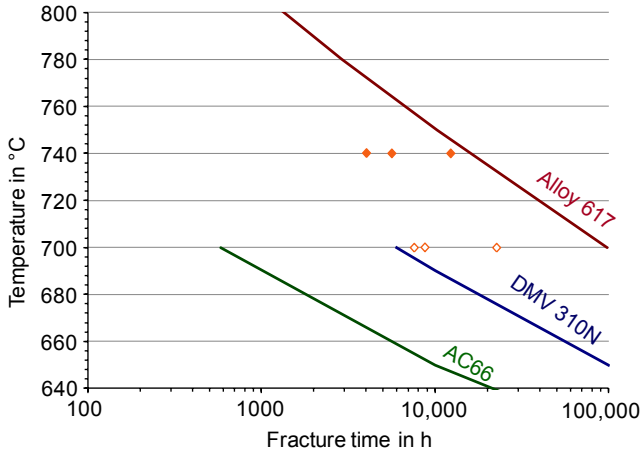


Figure 11.6 Results of iso-stress tests at 120 MPa at 740 and 700°C.

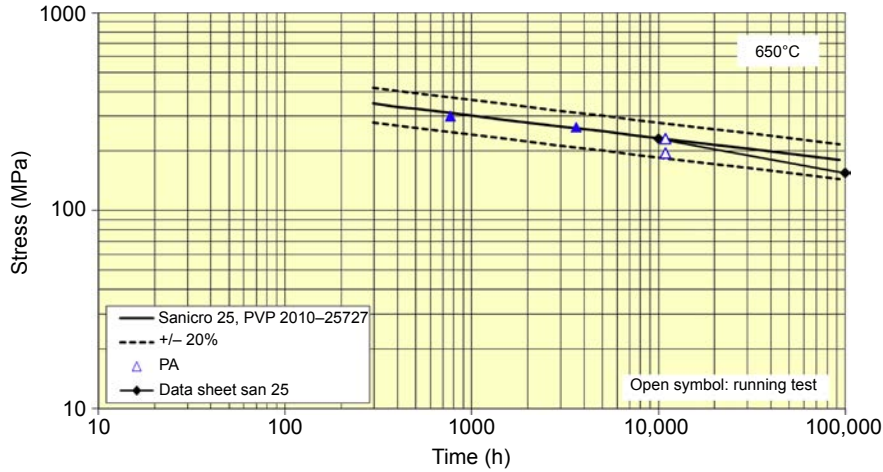


Figure 11.7 Results of creep tests at 650°C with two samples running.

rate decreases; however, after approximately 1000 h, it increases again. This is of high importance, and the alloy precipitates sigma phase, and the creep rate decreases again thereafter before approaching the tertiary creep regime. As lower the stress level, as much more pronounced is the maximum peak. Figs. 11.9 and 11.10 show the creep rupture diagram for 700°C at stress levels of 180, 145, and 120 MPa with rupture points in the lower scatter band of Sanicro 25. One sample at 120 MPa is still running. Comparing the creep rate in Fig. 11.10, the maximum is still pronounced; however, it decreases with decreasing stress level. According to the creep rate, the sample running at 120 MPa is supposed to run at least into the lower scatter band.

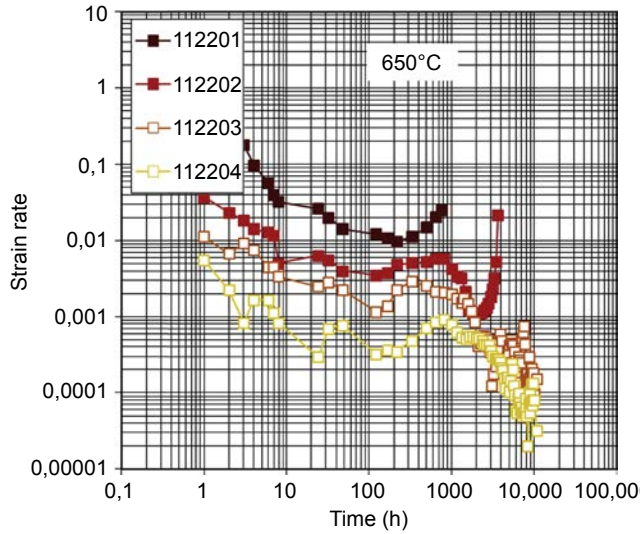


Figure 11.8 Creep rate at 650°C at different stress levels. The maximum creep rate at 1000 h is due to precipitation of sigma phase.

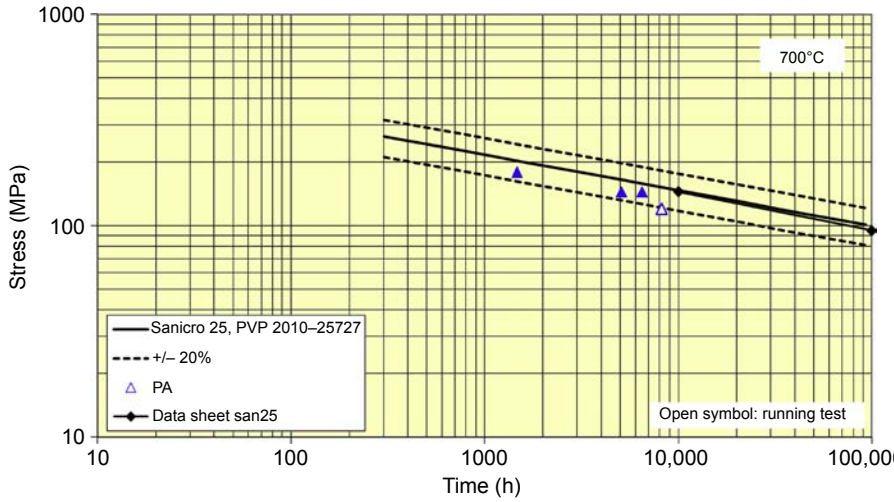


Figure 11.9 Results of creep tests at 700°C with one sample running. Creep values are approaching the Sanicro 25 mid values.

In conclusion, the creep behavior is strongly dependent on the stress-assisted precipitation of sigma phase in the interior grain. This gives some options to optimize the creep properties by adequate heat treatments after solution annealing.

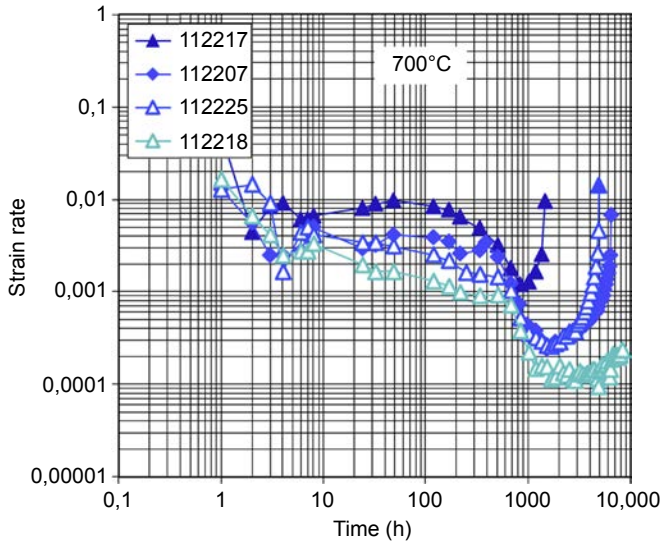


Figure 11.10 Creep rate at 700°C at different stress levels. One sample is running. The maximum creep rate is shifted to lower times and not as pronounced as at 650°C.

11.3.3 Fireside corrosion behavior

The high efficient 700°C technology does not only require materials with low steam oxidation rates and sufficient creep strength. Fireside corrosion issues, especially by sulfur-rich deposits, have to be considered and are expected to occur much more frequently in the future by increasing temperature. Fireside corrosion processes are complex reaction cycles, consisting of reactions of flue gas components (ie, SO_2/SO_3, O_2) with the material, of reactions of alkali-salts (sulfates, chlorides) within the deposits with the material, and reactions of components of the flue gas with components of the deposit. In energy conversion systems, liquid sulfates are usually formed as eutectic mixtures in ashes on superheater tubes. The main constituents of such systems are $CaSO_4$, Na_2SO_4, and K_2SO_4, depending on the chemistry of the coal. Eutectic mixtures usually have lower melting point than the pure substances. This becomes detrimental if metal components start to dissolve in the solid mixture, thereby decreasing the liquidus temperature. This is especially the case if $NiSO_4$ is formed by reaction of the nickel in the alloy with SO_3 in the combustion gas.

The risk of fireside corrosion failures strongly depends on the composition of the fuel, ie, waste, biomass, or coal and its conversion to form corrosive species like HCl, SO_2, and H_2S, as well as alkali-salts (halides and sulfates) within ash deposits. Table 11.3 gives an overview on the composition of commonly used fuels, regarding their content of corrosive species like chlorine, sulfur, alkali elements, and heavy metals. The most corrosive fuel with a high chlorine content is waste, especially in addition with heavy metals and alkali elements. Biomass (wood) also contains potassium as a corrosive species, in combination with chlorine and sulfur. Looking

Table 11.3 Overview on the composition of commonly used fuels. Most relevant for corrosion of superheaters are chlorine and sulfur, mostly bonding to chlorides and sulfates

	Cl (wt%)	S (wt%)	Na_2O (wt%)	K_2O (wt%)	CaO (mg/kg)
Waste	0.5	0.2	1.5	0.3	3.0
Used wood	0.01–0.44	0.02–0.58	0.05	0.7	4.5
Wood	0.005–0.02	0.02–0.1	0.02–0.05	0.2–0.5	0.35–1
Lignite	0.005–0.012	0.1–2	0.01–0.3	0.002–0.1	2–3.5
Char	<0.2	0.5–1.1	0.01–0.1	0.05–0.4	0.05–5.5

at coal, the chlorine content of lignite is in the range of wood; however, its sulfur content is higher. Char may also contain high amounts of chlorine, as well as a high concentration of sulfur.

For the development of a fireside corrosion-resistant material, the temperature dependence of the corrosion rate is an important issue. The corrosion loss generally shows a so-called "bell shaped" behavior, ie, increasing with temperature up to 700°C and then decreasing again. The highest corrosion loss is generally observed at 700°C and decreases with the chromium content. Chromia scales formed on the material are generally stable under fireside corrosion conditions; however, they need to be dense and protective. The most important element to achieve a protective chromia scale is chromium, the amount of which should not be lower than 25 wt%. The fireside corrosion behavior of several austenitic steels and nickel alloys beneath sulfate deposits at 650° is reported in [13], concluding that a chromium content higher than 25 wt% is absolutely necessary to reduce fireside corrosion.

The fireside corrosion behavior of the Power Austenite was tested in 3000 h tests in simulated coal combustion gas containing N_2-4%O_2-15%CO_2-0.25%SO_2 with deposits of Na_2SO_4-K_2SO_4-$CaSO_4$ at 700°C, conditions which are generally agreed to be proper for lab testing. A typical scale on Power Austenite after the experiment is shown in a metallographic cross-section in Fig 11.11(a) and in an SEM micrograph in Fig. 11.11(b). The scale thickness is about 10 μm, showing also some internal sulfidation zone underneath. In the SEM micrograph (11b), the microstructure of the scale is shown in more detail. The more dense part close to the metal surface is chromia, giving the necessary stability of the alloy. The upper part of the scale is composed of Fe_2O_3 and some Cr_2O_3, showing that the chromia scale needs some time to develop, during which sulfur ingress is possible into the alloy.

For the stability of the protective chromia scale, the chromium flux to the surface has to be constant and stable. Especially in the case of Power Austenite, a lot of chromium is fixed to sigma phase and may remain immobile and, therefore, not helpful for the formation of a chromia scale. Fig. 11.12 shows the metal/oxide interface after a 12.295 h creep test at 740°C in air. The sigma phase precipitates are dissolved underneath the scale, and chromium is released to form a chromia scale with self-healing properties.

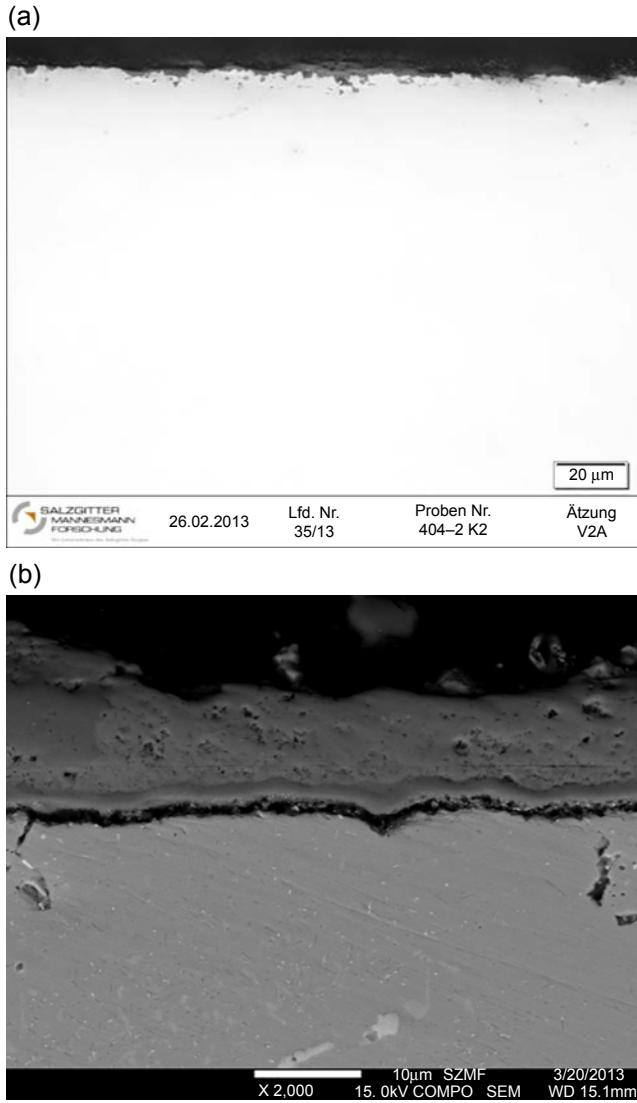


Figure 11.11 Metallographic cross-section after fireside corrosion testing at 700°C for 3000 h (a) light optical microscopy, (b) SEM. The dense part in the right picture is chromia, covered with a scale consisting of Fe_2O_3 and Cr_2O_3.

In a laboratory-scale test to solar-thermic applications for molten salt receivers, the material also shows good corrosion resistance in the presence of a molten nitrate due to its high nickel content.

First production trials have shown that the material can be produced with a common production route for seamless tubes at Salzgitter Mannesmann Stainless workshops.

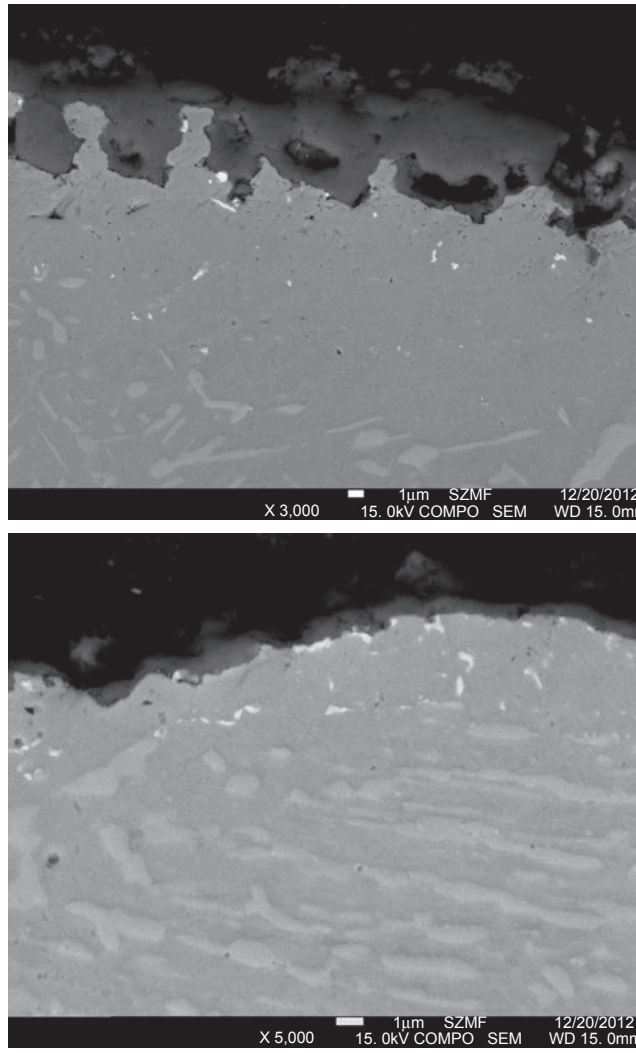


Figure 11.12 Metallographic cross-section after creep testing at 740°C, 120 MPa, and 12.295 h. Sigma phase is dissolved, releasing chromium.

Fig. 11.13 shows one of the first pilgered tubes, with dimensions 89×14 mm. The resulting microstructure after cold pilgering and annealing 1200°C, 30′ is shown in Fig. 11.14.

Fig. 11.14 shows the microstructure in a light optical micrograph from a 89 × 14 mm tube after the first pilger step of Power Austenite after 30 min of solution annealing at 1200°C. The structure is fully austenite, with a grain size of 4 (ASTM E112). Some segregation lines are visible, however, not detrimental.



Figure 11.13 Cold pilgered tube of Power Austenite with dimension 89 × 14 mm.

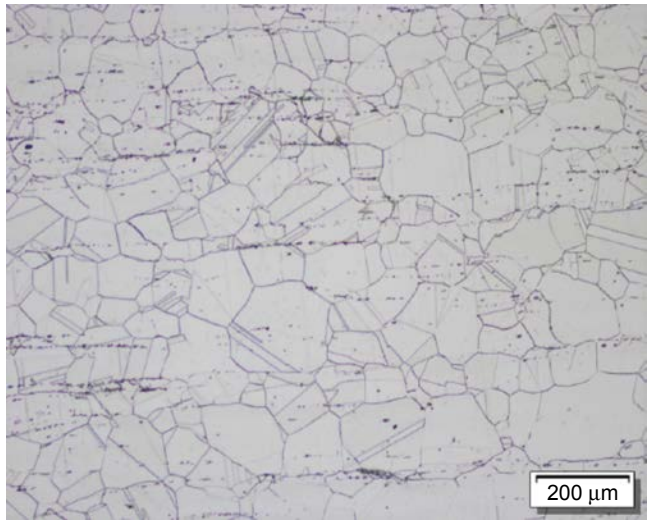


Figure 11.14 Microstructure of cold pilgered Power Austenite tube from Fig. 11.13 after annealing at 1200°C 30′. The material shows some segregation lines, which are not harmful for the creep properties.

11.4 Summary

New material trends in austenitic stainless steels for use in power plants are discussed in this chapter. New materials have to be developed to meet the general trend on the development of power plants with steam temperatures of about 700/720°C and 350 bar with around 50% efficiency. This requires components that are able to withstand very high temperatures and pressure loads caused by flowing steam in the interior of the boiler tubes. Therefore, materials should have good creep strength, high oxidation resistance in the presence of pressurized steam, and a good fireside corrosion resistance, especially with respect to sulfur-related corrosion phenomena. Furthermore,

new technologies like solar-thermic power plants are going to be developed with respect to the molten salt technology, which requires high corrosion resistance and stability against creep/fatigue fractures. Besides conventional developments like Sanicro 25, the concept of intermetallic phase hardening and AFA are two most promising developments.

The Laves phase strengthened concept was developed and published [4–6]. The base composition is in at.%: Fe-20Cr-30Ni-2Nb, and the material is strengthened by precipitation of intermetallic Fe_2Nb phase in combination with Ni_3Nb. The authors use the so-called "grain boundary precipitation strengthened mechanism" (GBPS) to achieve a 10^5 h strength of 80 MPa at 973 K. Furthermore, the material was also tested in steam oxidation environments. The authors show that it develops a chromia scale upon oxidation at 1073 K. The oxidation kinetic is comparable to that of 316 L [6].

The AFA concept was developed in the United States [7]. The concept is based on the idea to promote the oxidation/corrosion resistance by alloying a certain amount of aluminium to the material with the aim to develop a protective alumina scale at higher temperatures as oxidation protection. Several alloys were developed and tested, basically on the composition Fe-25Ni-14Cr-3.5Al-2.5Nb-2Mn-2Mo-1W-0.1C-0.01B. So-called AFA high performance and AFA superalloys were also designed with higher chromium contents and higher aluminium contents, respectively. The temperatures of operation were foreseen to be 650°C for the conventional normal AFA alloys and up to 950°C for the high-performance alloys. The creep rupture life is dependent on the composition of the material and scatters around the Super 304 and NF 709 grade in the temperature region between 500 and 700°C. The alloys show good steam oxidation resistance and are possible candidates for coal-fired boilers $T < 700$°C according to their creep properties. Also under carburizing and sulfidizing conditions, the materials show promising behavior.

The new austenitic material Power Austenite, a sigma phase hardened concept was developed by Salzgitter Mannesmann Stainless Tubes and Salzgitter Mannesmann Forschung GmbH. The microstructure is characterized by grain boundary strengthening with boron-stabilized $M_{23}(C,B)_6$ in combination with sigma phase and Nb(C,N) as the major strengthening mechanism. The creep behavior is strongly dependent on the stress-assisted precipitation of sigma phase in the interior grain. This gives some options to optimize the creep properties by adequate heat treatments after solution annealing. Good creep properties are achieved at 650 and 700°C, almost comparable to Sanicro 25. The material shows a significant fireside corrosion resistance, which makes it to an ideal candidate for 700°C power plants. The material is now in industrial production and will be implemented in German testing power plants projects for 700°C and thermocyclic applications.

In conclusion, Sanicro 25, the Laves phase strengthened alloys, the AFA alloys, and the sigma phase hardening concept (Power Austenite) developed by Salzgitter Mannesmann are promising candidates for future applications in demanding services such as energy production by conventional thermal power plant and solar-thermic application. All concepts, except the Laves phase strengthened materials, have reached

significant stages of industrial production or have been on the market for many years, eg, Sanicro 25. In the end, only industrial experience can show how the different concepts are useful in technical practice and how the economic value develops. However, without any pioneering work and some trust in the market, material prices will not develop toward economic values. From that point of view, it is not only a matter of science and engineering but also of wise political decisions for a reliable energy supply.

References

[1] International Energy Agency, World Energy Outlook, OECD Publishing, 2011.
[2] R. Blum, The European Perspective and Advancements for advanced USC steam power plants, in: Advances in Material Technology for Fossil Power Plants, Proceedings from the Sixth International Conference, 2010.
[3] M. Spiegel, et al., in: Proceedings of Eurocorr 2011, Stockholm, Sweden, 2011.
[4] G. Chai, M. Boström, M. Olaison, U. Forsberg, Creep and LCF behaviors of newly developed advanced heat resistant austenitic stainless steel for a-USC, Procedia Engineering 55 (2013).
[5] J. Högberg, G. Chai, P. Kjellström, M. Boström, U. Forsberg, R. Sandström, Proceedings of the ASME 2010 Pressure Vessel & Piping Conference, Bellevue Washington, USA, 2010.
[6] I. Tarigan, et al., Materials Research Symposium Proceedings 1295 (2011).
[7] I. Tarigan, et al., Proc. of 12th Int. Conf. on Creep and Fracture of Engineering Materials and Structure (JIMIS 11), Kyoto, 2011.
[8] Lyta, et al., Materials Transactions 34 (12) (2013).
[9] M. Brady, et al., ORNL Report, ORNL/TM-2013-479, 2013.
[10] M. Spiegel, et al., Proc. of Liege Conference (USB), Liege, 2014.
[11] D.J. Chastell, P.E. Flewitt, Materials Science and Engineering 38 (1979).
[12] Hsieh and Wu, ISRN Metallurgy (2012).
[13] B.A. Baker, et al., NACE Corrosion (2003).

Sanicro 25: an advanced high-strength, heat-resistant austenitic stainless steel

12

G. Chai[1,2], *U. Forsberg*[1]
[1]Sandvik Material Technology, Sandviken, Sweden; [2]Linköping University, Linköping, Sweden

12.1 Introduction

The demand for electric power has been continuously increasing around the world. Meanwhile, the consciousness of the environmental impact from human action is growing. Although combustion processes generate carbon dioxide, considered a greenhouse gas, it is not realistic to disregard any kind of electric power generation. Coal-fired boilers, for example, will continue to contribute to meet the large part of the electricity demand for many years to come, as coal is available at a competitive price in many different countries and often is the single domestic energy source [1]. This has increased pressure on the coal fired power industry to raise the efficiency of the plants and thereby reduce the emissions. The best way to improve the operating efficiency is to increase the temperature and pressure in the boilers. Today's modern state-of-the-art power plants operate at steam temperature and pressure of around 600°C and 30 MPa, and they have a maximum efficiency 45–47%. The target for the next-generation power plants is higher pressures 30–35 MPa and final steam temperatures of about 700°C. This would increase the efficiency to around 50–55% and reduce the CO_2 emission, with about 45% compared with the world average level and with about 15% when compared with a modern USC power plants [2].

In the early 1990s, an EU-funded project named Thermie AD700 technology was started with the purpose to develop a new type of coal-fired power plant with higher steam pressure and temperature, 35 MPa/700°C and higher, and an efficiency higher than 50% [3]. The operating conditions in these advanced ultra-supercritical (A-USC) coal-fired boilers would require new, more heat-resistant materials than what were available on the market. The requirements were improved high-temperature strength, enhanced creep properties, and satisfying high-temperature corrosion resistance compared with the materials used in contemporary boilers, which operated at maximum temperature around 650°C. One of the initiatives of the AD700 project was to develop a range of new advanced materials that could permit the raising of main and reheat steam temperatures in boilers up to 700°C and beyond [3].

Sandvik AB was within this project asked to develop a new type of austenitic stainless steel for use in superheaters and reheaters. The targeted 100,000 h' creep strength for the "new" material was set to about 100 MPa. For even higher material temperatures

Materials for Ultra-Supercritical and Advanced Ultra-Supercritical Power Plants.
http://dx.doi.org/10.1016/B978-0-08-100552-1.00012-9
Copyright © 2017 Elsevier Ltd. All rights reserved.

in the superheater/reheater and for other vital parts such as evaporator/water walls, headers, steam-pipes, and turbine components, other groups were formed. The works in these groups were concentrated around Ni-based alloys, which were considered to be the only option for these applications.

As said, the austenitic stainless steel grades commercially available today allow a maximum material temperature of about 650°C. Above this temperature the only option is, if not including Sanicro 25, to use nickel-based alloys [4]. Since the Ni-based alloys are considerably more expensive, the Sanicro 25 could greatly reduce the cost of the entire boiler.

The austenitic stainless-steel grade Sandvik Sanicro 25 (UNS S31035) was therefore developed, in collaboration with a number of different industrial partners within the Thermie-AD700 project in Europe [5]. The alloy has thereafter exhibited excellent high-temperature strength, creep properties, and corrosion resistance at material temperatures up to about 700°C. Actually, Sanicro 25 has the highest creep strength among the commercial heat-resistant austenitic stainless steels [5–7]. These properties make it a promising candidate for usage in superheaters and reheaters in advanced ultra-supercritical boilers at material temperatures up to 700°C (1292°F). The material properties have been verified in various laboratory studies and in several different test installations in commercial power boilers in Europe. This chapter will give a review on Sanicro 25 material, properties, and its applications.

12.2 Development of new high-strength austenitic material for high-efficiency coal-fired power plant

Heat-resistant materials are a class of materials developed for usage in applications where the temperatures are high. For the boiler materials in this application, operating at a material temperature of 700°C and a pressure of 35 MPa not only requires a high creep strength, but also satisfactory corrosion and steam oxidation resistance. This at the same time has good fabricability and weldability properties. To achieve these properties, a number of basic alloy design principles were used. First, a good alloy system should be used. Since the material will be used at a metal temperature about 700°C, Fe-Ni-Cr alloy system can be chosen. The second is to choose strengthening mechanisms. Both solid solution strengthening and precipitation hardening can be applied. Actually, precipitation hardening is the main mechanism to reach a very high elevated temperature creep strength. Niobium can be used to stabilize the austenitic structure. The key issue is to attain stable precipitates, such as Laves phase, carbides, MX (M = Nb, Cr or W, X = N or C), or carbonitrides that can lead to an increase of creep strength and consequently suppress the precipitation of other phases [8–10]. Copper is added to form copper-rich nano particles that increase the creep strength [11,12]. The third is to have good corrosion resistance. To achieve a good steam oxidation and hot corrosion resistances, a high Cr content can be used. To obtain good structure stability,

addition of Ni and N can suppress the formation of sigma phase [13] and thereby allow for good fabricability. To ensure a balanced composition consideration and optimized microstructures, a thermodynamic simulation using the Thermo-Calc software [14] was done. Table 12.1 shows the nominal composition of Sanicro 25 material. A high amount of W, N, Co, and Nb are for solid solution hardening, and high Nb, N, Cr, and Cu are for precipitation hardening. A Cr content of approximately 21.5–23.5 wt% is used to obtain good steam oxidation resistance and hot corrosion resistance. Ni content approximately 25.0% together with a relatively high amount of nitrogen are used for structure stability.

Fig. 12.1 shows a thermodynamic calculation showing the precipitates in Sanicro 25 material in the temperature ranged of interest. These phases are those desired as discussed previously.

Table 12.1 Nominal chemical composition of Sanicro 25 (wt%)

C	Si	Mn	P	S	Cr	Ni	N	W	Co	Cu	Nb
0.04 – 0.1	0.4 Max	0.6 Max	0.03 Max	0.015 Max	21.5 – 23.5	23.5 – 26.6	0.15 – 0.30	2.0 – 4.0	1.0 – 2.0	2.0 – 3.5	0.30 – 0.60

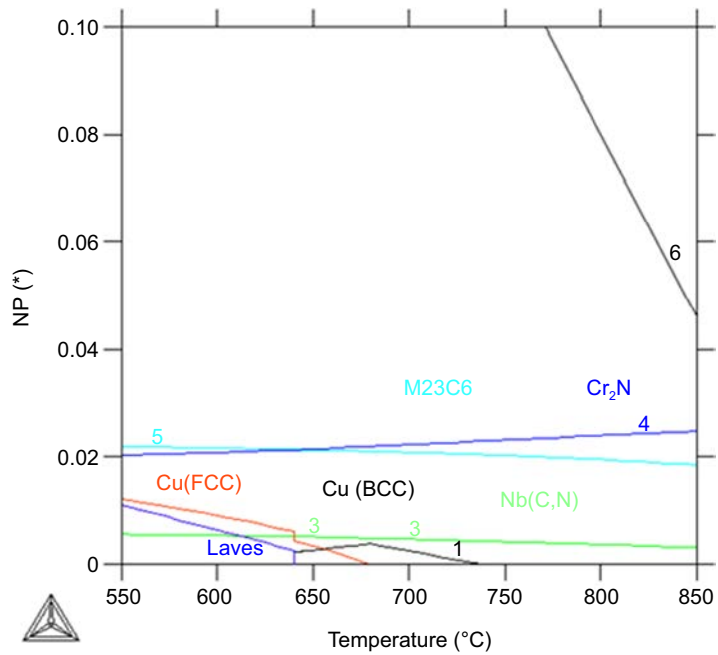


Figure 12.1 Thermodynamic calculation with database TCFE5 showing the precipitates in Sanicro 25 material in the temperature ranged of interest [15].

12.3 Microstructure

12.3.1 Microstructure evolutions

In a solution-treated Sanicro 25 material, a few small NbCrN-nitrides with sizes of some hundred nanometers to a few micrometers can be observed (Fig. 12.2(a)). They are primary particles that have formed during solidification. This is mainly due to high Nb and N in the material. During aging at high temperature, some precipitates will appear. Fig. 12.2(b) shows the microstructure in Sanicro 25 aged at 700°C for 3.000 h. Small, bright precipitates have formed mainly in the grain boundaries, twin boundaries, and NbCrN–nitrides. A small amount of intragranular precipitates is also observed, and these appear to have a more rod-like morphology compared with the grain boundary precipitates that show a more round shape. Analysis of energy-dispersive X-ray spectroscopy (EDS), indicates that the particles contain a high amount of W and Cr, and they are Laves phase identified by TEM analysis. At 10.000 h (Fig. 12.2(c)), the amount and size of the Laves phase have increased both on the grain boundaries and in the grains. Near the grain boundary, $M_{23}C_6$ precipitates appeared. Actually, they can be observed both on the grain boundaries and in the grains. At 30.000 h (Fig. 12.2(d)),

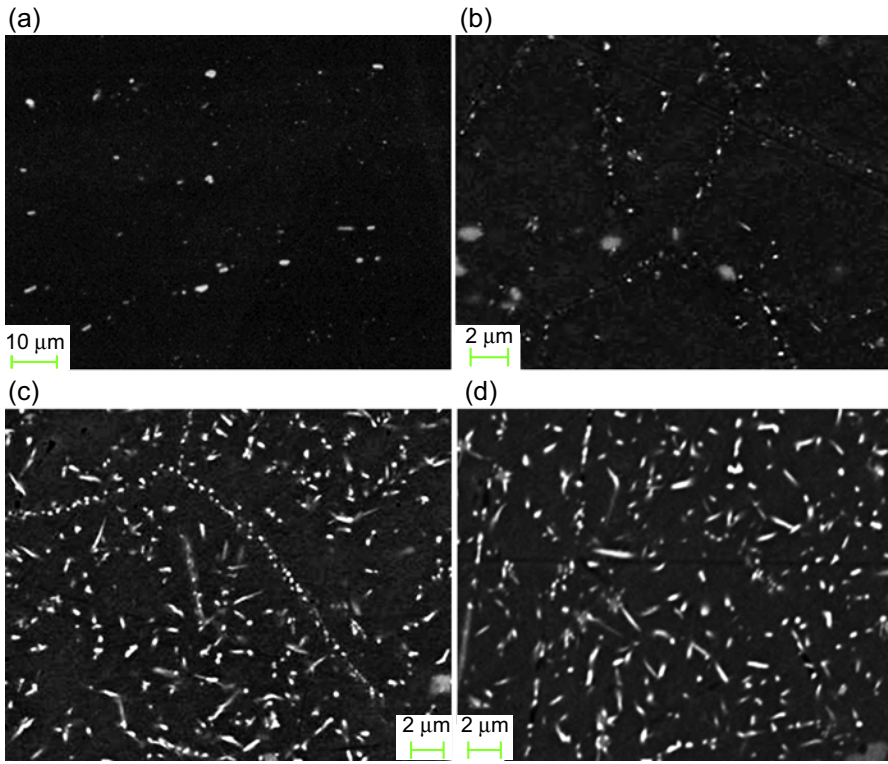


Figure 12.2 Microstructures of Sanicro 25 [15], (a) As received; and statically aged at 700°C for (b) 3.000 h, (c) 10.000 h, (d) 30.000 h [15].

the number density of Laves phase appears not to have changed much from 10.000 h, but the particles seem slightly coarser. Small particles that are darker than the austenite are also detected in the material. EDS indicates that the particles are Cr-rich and could be Cr_2N. Few, small sigma precipitates can also be found. The diffraction patterns from TEM analysis shows that $M_{23}C_6$ carbides have a $<110>_\gamma$//$<110>M_{23}C_6$ coherent relationship to the austenite matrix (Fig. 12.3(a)), and Laves phase has a $<100>_\gamma$//$<100>_{Laves}$ coherent relationship to the austenite matrix (Fig. 12.3(b)).

12.3.2 Microstructure stability

One of the most important aspects to obtain long-term high creep resistance is that the small beneficial precipitates are stable and do not grow or dissolve during service. Fig. 12.4 shows a quantitative analysis for density and mean particle size of $M_{23}C_6$ and Laves phase in Sanicro 25 in the statically aged specimens and in the creep-tested specimens with different rupture times. Due to the limited resolution of BSE-images, the smallest particles cannot be detected. However, a general tendency on the evolution of the particles can be seen.

The particle density seems to be relatively steady with time, indicating fast nucleation. The particle size increases fast in the beginning, and then it continuously increases with time up to 10.000 h but with a lower growth rate. After 15.000 h, the growth of the precipitates is very small. With the limited amount of sample at longer times at 700°C, the coarsening process is still unclear. However, Fig. 12.5 shows the microstructure in the creep-tested sample at 650°C for 70.000 h. The precipitates are still very small compared with those in Fig. 12.2. This indicates that the growth rates of these precipitates during long-term high-temperature aging or creep testing are rather

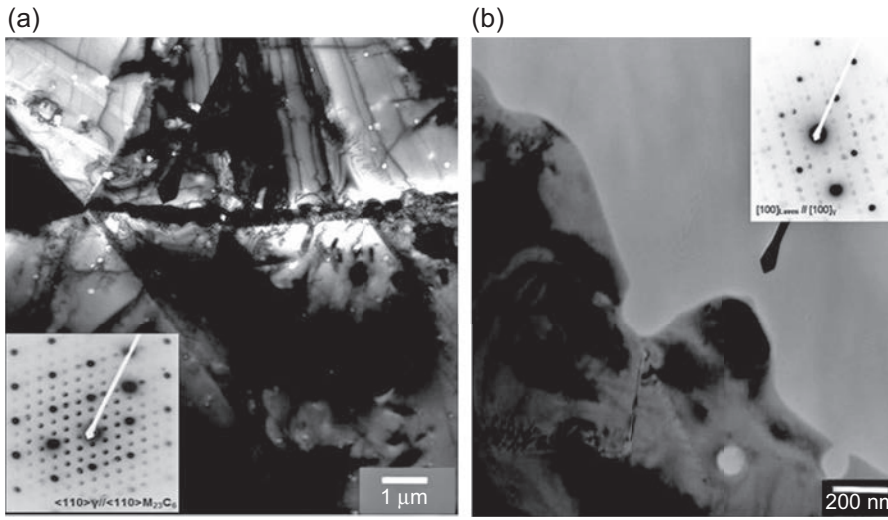


Figure 12.3 Diffraction patterns of the precipitates and the matrix [15]: (a) $M_{23}C_6$ and austenitic phase, (b) Laves phase and austenitic phase.

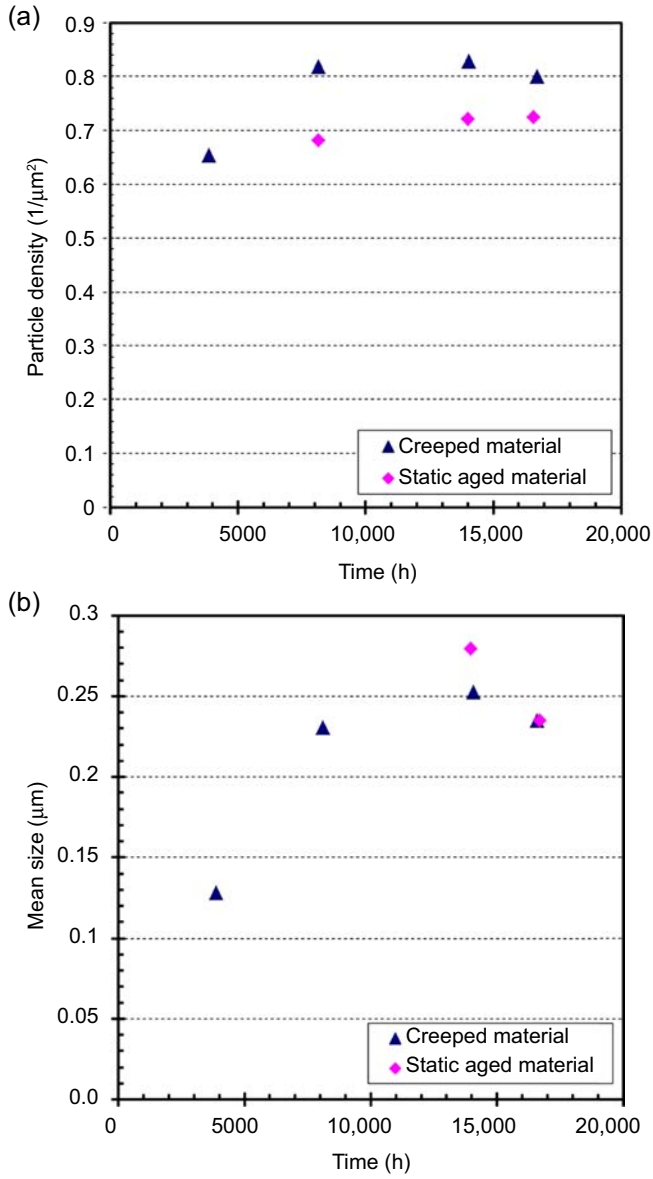


Figure 12.4 Results from the image analysis on creep specimens: (a) mean particle size as a function of time at 700°C; (b) particle number density as a function of time at 700°C [15].

small. Comparing aged and creep-tested materials with each other, it appears that the tendencies of the influence of time on both particle density and size are similar. However, particle density is higher in the creep-tested material than in the aged material. The mean particle size, on the other side, is smaller in the beginning compared with aged material, but it becomes similar for a longer time. This could be that the

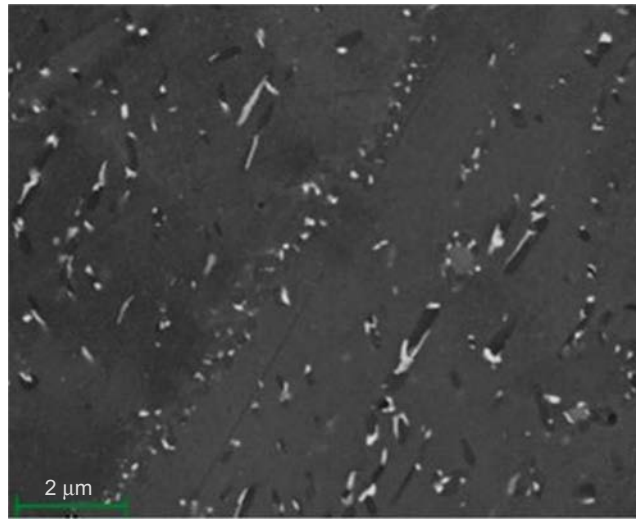


Figure 12.5 Microstructures of Sanicro 25 in the creep-tested material at 650°C for 70.000 h.

dislocations formed during the creep testing function as favorable nucleation sites for the precipitates leading to a higher nucleation rate, and consequently higher particle density. The higher dislocation density in the creep-tested material can also increase the diffusion rate in the material, which could affect the nucleation and growth of the precipitates.

Numbers of precipitates with nano size can be observed in the aged or creep-tested Sanicro 25 material, as shown in Fig. 12.6. They are intra- and intergranular $M_{23}C_6$ and Laves phases (Fig. 12.6(a) and (b)). In the aged material the Laves phase are needle-shaped but rather small. In the creep-tested materials, these particles are fine and isometric. This indicates that Laves precipitates during creep process may contribute more resistance and less damage. Copper-rich nanoparticles can also be observed. They are round with a size up to 50 nm (Fig. 12.6(c)). In this material, a dense distribution of about 10-nm large precipitates was observed (Fig. 12.6(d)). Due to the limitation of the TEM, these particles could not be identified, but they are probably MX carbides or carbonitrides. Similar particles have been identified in other analyses. These particles were rather stable [4]. These nano particles contribute to the creep strength of Sanicro 25.

12.4 Creep and rupture behaviors

12.4.1 Creep strength of Sanicro 25 at elevated temperature

Great numbers of creep tests on Sanicro 25 have been performed. More than 86.000 h have been run, and some of them are still running. Fig. 12.7 shows the applied stress versus rupture time of the creep testing data and the linear regressions in the creep data for Sanicro 25. There are linear slopes for all temperatures, and all are parallel

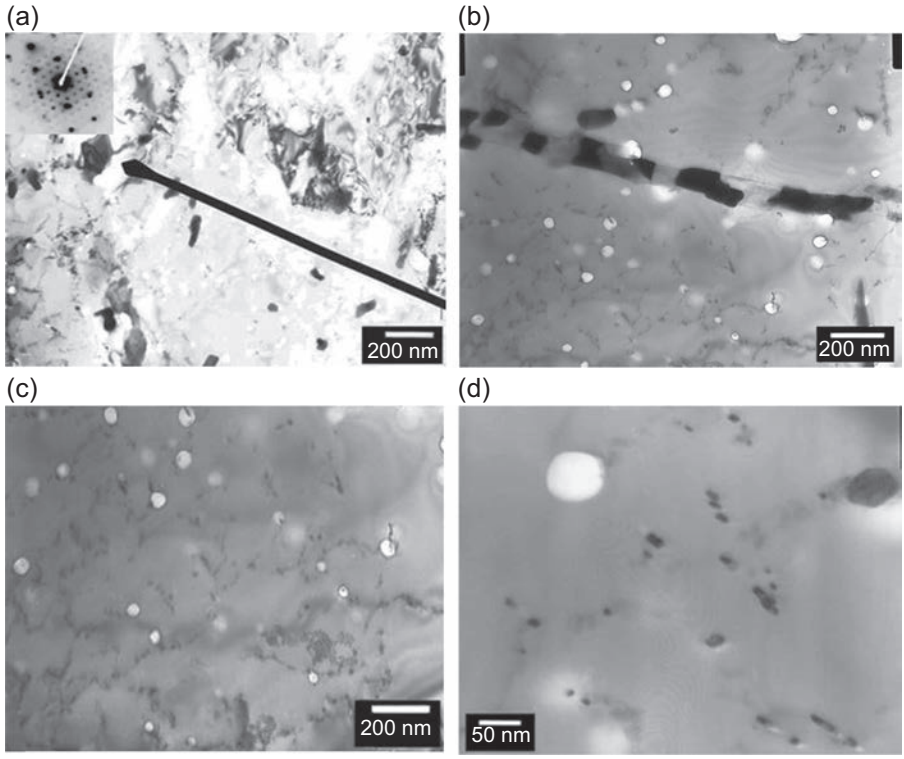


Figure 12.6 Fine precipitates in Sanicro 25 material aged at 700°C for 30.000 h [7]: (a) $M_{23}C_6$, (b) Laves phase, (c) copper-rich phase, (d) nanoparticles.

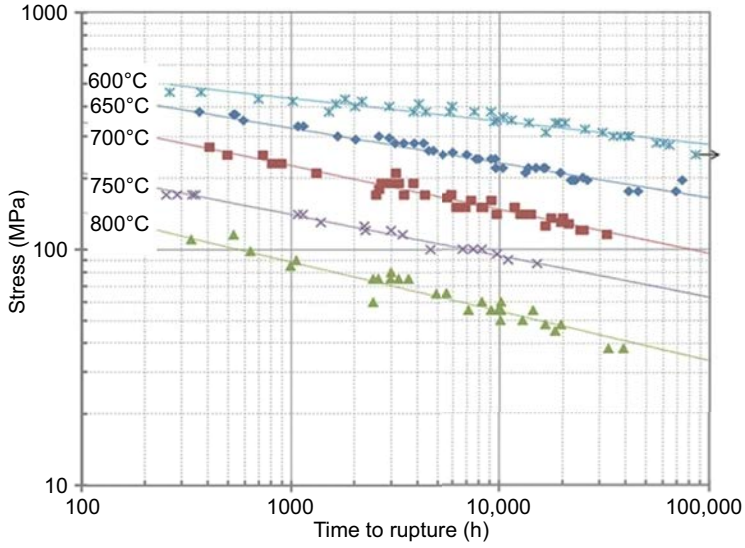


Figure 12.7 Creep strength versus rupture time of Sanicro 25 austenitic stainless steel and the linear regressions in the creep data [7,18].

to each other. No turn point on the slope can be observed. This means two things. One is that no creep mechanism changes with the creep time at a temperature, and the other is that the temperature change from 600°C to 800°C does not change creep mechanism. This can be correlated to the structure stability of the material as discussed in previous chapter.

12.4.2 Creep strength after extrapolation

As known, pressure vessel components are normally designed for a long service time such as 200.000 h. However, such creep data are usually not available for design. The design data are therefore obtained by extrapolation from the creep data of shorter tests. Different models and approaches have been developed. Two methods are used in this work. One is the known Larson–Miller relations as follows. C here used is 20. Fig. 12.8 shows the applied stress and Larson Miller parameter, PLM, for Sanicro 25, which gives creep strength of 104 MPa at 700°C for 100.000 h.

Another proposed procedure for extended extrapolation of creep rupture data is the free temperature model (FTM) that allows for extrapolation by more than a factor of three in time [12]. The procedure is based on a time–temperature parameter (TTP), which has the general mathematical form:

$$P_{\mathrm{TTP}} = v\,(T)\log\,(t_{\mathrm{r}})\, + w\,(T) \tag{12.1}$$

where P_{TTP} is the time–temperature parameter, t_{r} is the time to rupture, and v(T) and w(T) are functions of temperature. The FTM is reported to be well suited for austenitic

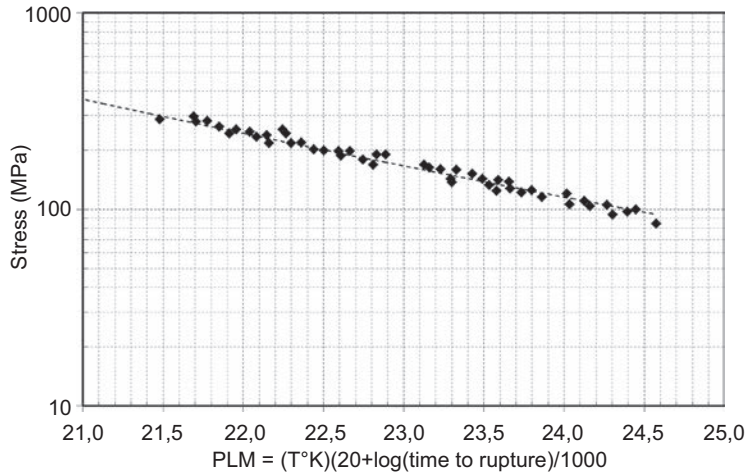


Figure 12.8 Larson–Miller relation with a linear regression in the creep data of Sanicro 25 austenitic stainless steel.

stainless steels [16]. The master curve is expressed by the creep stress as a function of polynomial in the TTP:

$$\log(\sigma) = \sum_{j=0}^{n_P} a_j TTP^j \tag{12.2}$$

The coefficient a_j is fitted to the creep rupture data, and the stress–rupture time relations are derived. The reason for using a polynomial in log (t_r) rather than log (σ), which is the more common approach, is that it has been shown that this improves the accuracy in extended extrapolated values [17]. To extrapolate the creep rupture data, the polynomials in Eq. (12.1) were both set to order three, and the master curve, Eq. (12.2), was set to a second-order polynomial. Fig. 12.9 shows an extrapolation with rupture data up to 40.000 h at different temperatures. The extrapolation was performed three times with rupture data up to 40.000 h where the evaluation satisfies the post-evaluation tests (PATs) and other criteria proposed by the European Collaborative Creep Committee (ECCC) [13]. At 700°C and 100.000 h, the rupture strength from this extrapolation is 99 ± 3 MPa, which is close to that from the linear least squares regression (104 MPa) (Fig. 12.8).

12.4.3 Standard and code cases for Sanicro 25, UNS S31035

The first European approval was obtained in March 2007, in form of a Particular Material Appraisal TÜV file no 3537W137650. The approval was valid for cold pilgered tubing with outside diameter between 25 and 114.3 mm, with wall thicknesses between 3 and 16 mm, and was valid until January 2009. In September 2008 a VdTÜV blatt was issued, WB 555 09.2008 in both a German and English version.

European approvals are based on nominal measured creep data, obtained from actual creep testing in laboratory. The values are then extrapolated to 100.000 h according to different principles. Creep data for Sanicro 25 in the European VdTÜV approval are compared with other high-strength materials as shown in Fig. 12.10(a) (The materials 347HFG, UNSS30432, and TP310HCbN are the grades that are used in today's state-of-the-art boilers, producing steam at 600–620°C). As can be seen in the graph, Sanicro 25 is stronger (same value as Alloy617) than all other alloys for temperatures up to 700°C.

The ASME approval took longer to get. In December 2012, ASME approved Sanicro 25 in Code Case 2753 for Section I, ie, for use in steam power boilers, and in Code Case 2752 for Section VIII Div 1 at the same time for use in Pressure Vessels. The allowable stresses (identical in the two code cases) are calculated using the same formulas and criteria. The allowable stress values published in the code case tables are those that the designers are to use. Fig. 12.10(b) shows a comparison between the maximum allowable stress values for Sanicro 25 and values for five (not including 347HFG) of the six high-temperature alloys that are compared in Fig. 12.10(a) based on European PED data. Fig. 12.11 shows a comparison between the maximum allowable stress values in imperial units. It can be seen that Sanicro 25 is the strongest of all materials besides Alloy 617. An interesting observation is that as the European PED is basing the pressure calculation on average creep value and ASME on maximum

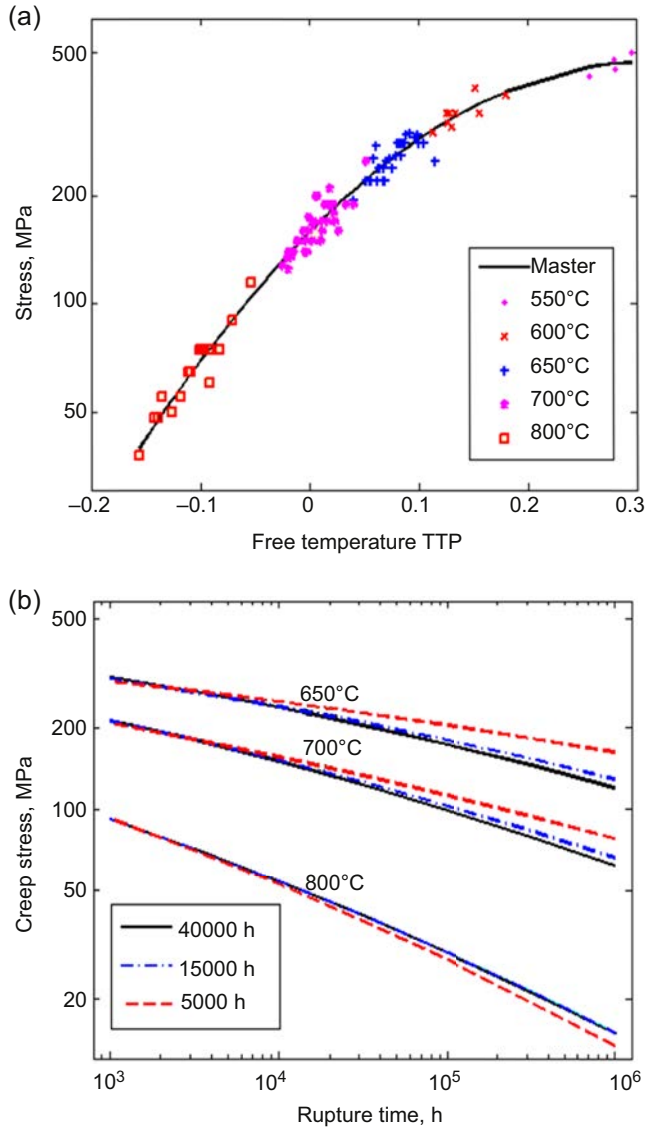


Figure 12.9 Extrapolation with FTM, (a) a master curve for the creep data of Sanicro 25 material, (b) result of the extrapolation with the FTM, performed three times with rupture data up to 5.000 h, 15.000 h and 40.000 h [15].

allowable stress values, derived from the nominal creep values. This means that the actual figures are different in the two codes. According European rules, Sanicro 25 is assigned with creep rupture strength of 95 MPa at 700°C, while the ASME max allowable stress value at 700°C is about 80 MPa. Both values are based on similar laboratory creep data.

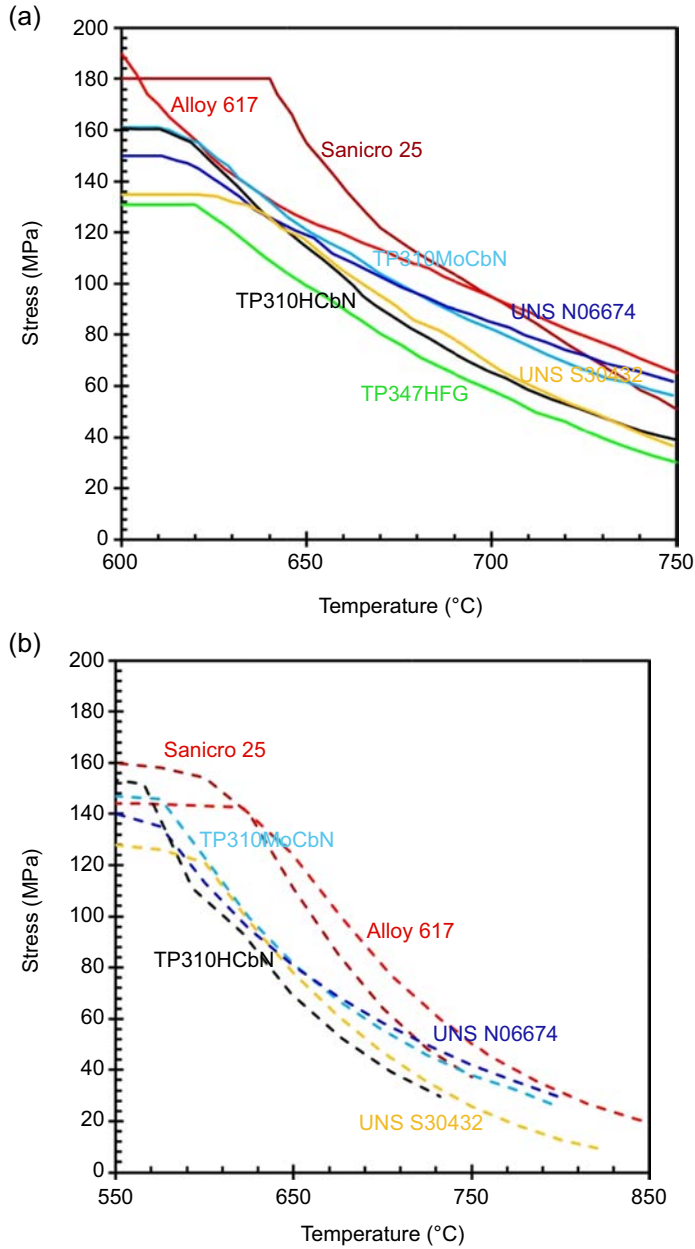


Figure 12.10 Comparisons of the creep strengths of different austenitic stainless and nickel-based alloys, (a) European Pressure Directive (PED), the values have been extrapolated to 100.000 h. Data are from European VdTÜV datasheets; TP347HFG 547; UNS S30432 550; UNS No S31042/TP310HCbN, 546; TP310MoCbN(NF709) 563; UNS N06674 (HR6W) 559; and Alloy 617 485; (b) AMSE, maximum allowable stress values used for design.

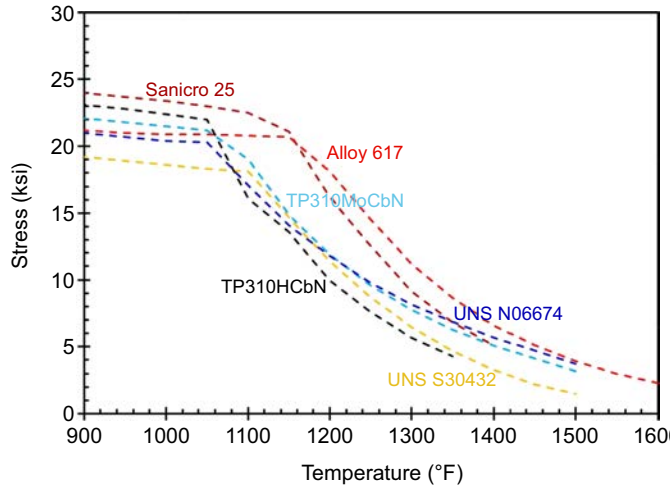


Figure 12.11 Max allowable stress values for different austenitic stainless and nickel-based alloys at different temperatures used for design according to ASME, in imperial units.

The relations between the other shown materials are similar as in the PED case. Note, however, that the UNSN06617 is approved with a higher design value in the ASME boiler and pressure vessel code than in the European PED. For details, see Fig. 12.10, comparing respective values according the two different codes.

12.4.4 Creep ductility

Fig. 12.12 shows the rupture elongation versus creep temperature from 600 to 800°C. Since different stresses at each temperature were applied, this caused large scatter in the elongation due to different creep rupture time. A longer creep rupture time generally leads to a lower elongation. Despite all these factors, the material shows relatively high creep rupture elongation. In this figure, the elongation of a field-tested material that had been installed in a coal-fired power plant for 22.400 h is compared. It is the elongation that the field-tested material was tested at room temperature (RT), which is about 26%. The material is still ductile.

Some results show that Sanicro 25 has a better creep ductility than some other austenitic stainless steel and Ni-based alloys [19]. Addition of Cu, Co, and W was believed to be one of the reasons [19]. Recently, the electron backscatter diffraction technique, EBSD, was reported to be used to investigate the creep deformation behavior of Sanicro 25 material [18,20]. The creep deformation structure and grain orientation were studied. Different from the normal creep deformation structure, amounts of twins in the creep tested can be observed. Fig. 12.10(b) shows an EBSD image of the grain structure in a creep-tested material at 650°C for 75.000 h. It seems that these twins have formed during the creep test. As known, the formation of twins in the metal material can improve the ductility or deformation ability of the material. That can explain that the Sanicro 25 material after a long-term installation (about 24.000 h) in a power plant can still show high elongation [5].

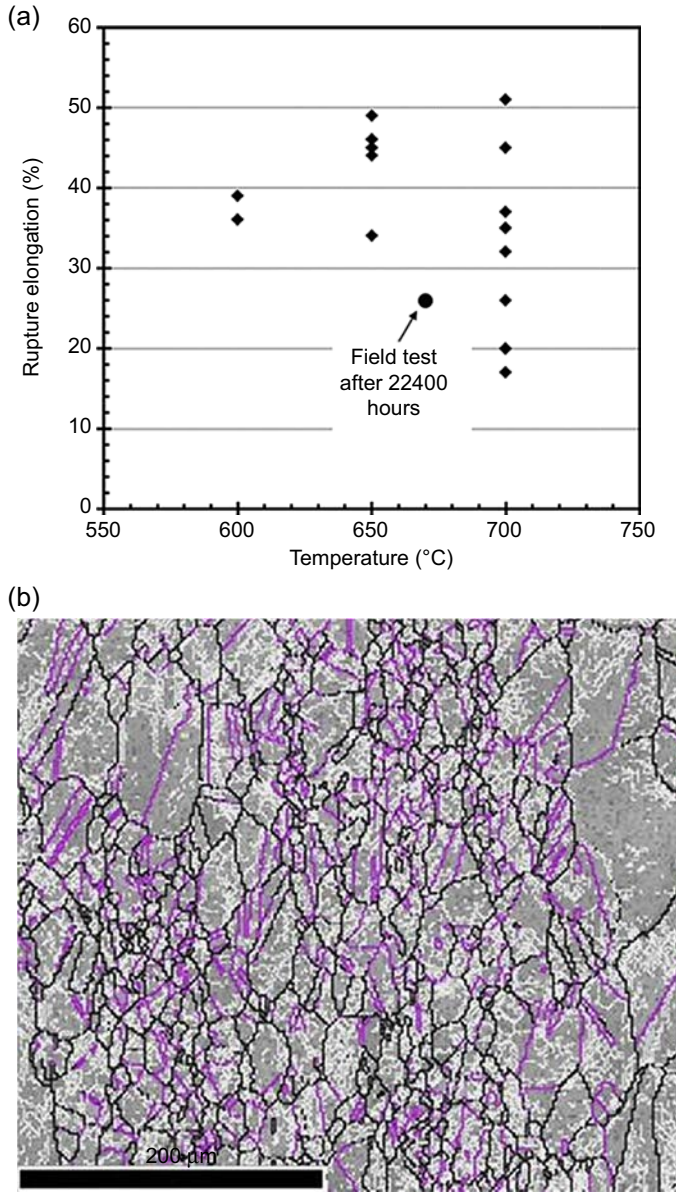


Figure 12.12 Electron backscatter diffraction (EBSD) image shows creep-induced twinning, grain boundary (*black lines*), twin boundary (*violet lines*), and low-angle disorientations–dislocation structure (*white lines or points*) in the creep-tested sample at 650°C for 75.000 h [18].

12.4.5 Creep-strengthening mechanisms

In the temperature range up to 700°C, one of the main creep-strengthening mechanisms is the interaction between dislocations and precipitates. Fig. 12.13 shows some examples how interactions between dislocations and precipitates in a Sanicro 25 creep

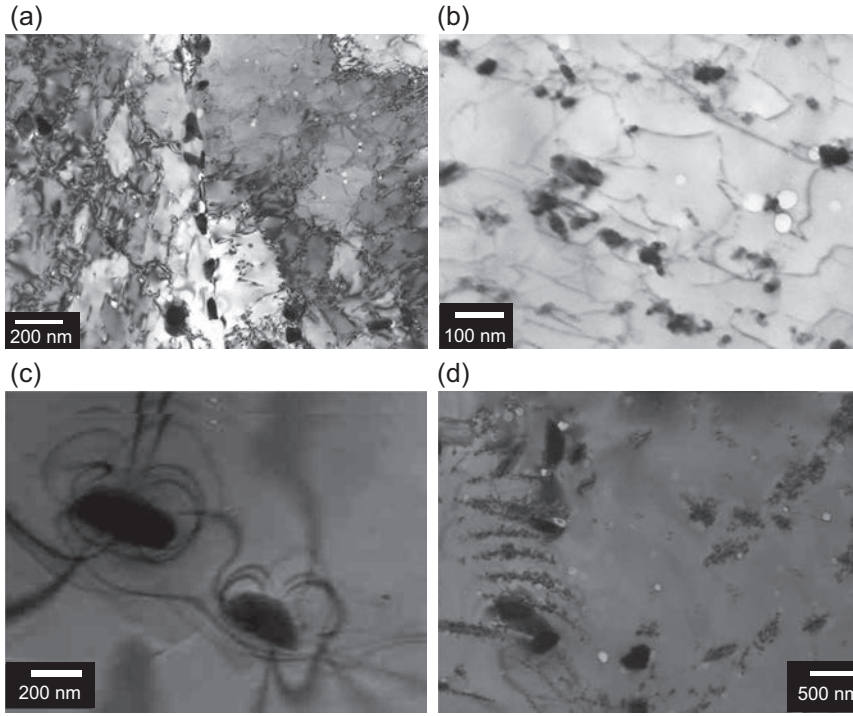


Figure 12.13 Interactions between dislocations and precipitates in a Sandvik Sanicro 25 creep specimen, 210 MPa at 700°C for 3.153 h [7,18].

specimen tested with 210 MPa at 700°C and with a rupture time of 3.153 h. Dislocation subcells (Fig. 12.13(a)) and moving dislocations at the nano-sized particles (Fig. 12.13(b)–(d)) can be seen. Around the intragranular precipitates, the dislocation density is high, which indicates that they function as obstacles for the dislocation movements. This increases the creep strength.

12.5 Low-cycle fatigue properties

Low-cycle fatigue behaviors in Sanicro 25 have been investigated [7,18,21–23]. Fig. 12.14(a) shows a longer low cycle fatigue (LCF), life with total strain amplitude compared to NF709 material. These results are the EU Thermie AD700 project [5]. All solid points are the new results [7,18]. They are comparable to those from the Thermie AD700 project. Fig. 12.14(b) shows the cyclic stress-strain responses of Sanicro 25. At room temperature, the alloy shows a normal cyclic hardening and softening response. At temperatures between 600 and 700°C, only monotonic cyclic hardening can be observed. However, they are not parallel to each other. As expected, the start stress was higher if the temperature is lower. It is interesting to mention that cyclic hardening rate increases with increasing temperature. One explanation is that dynamic strain aging could have already occurred during the cyclic loading at these

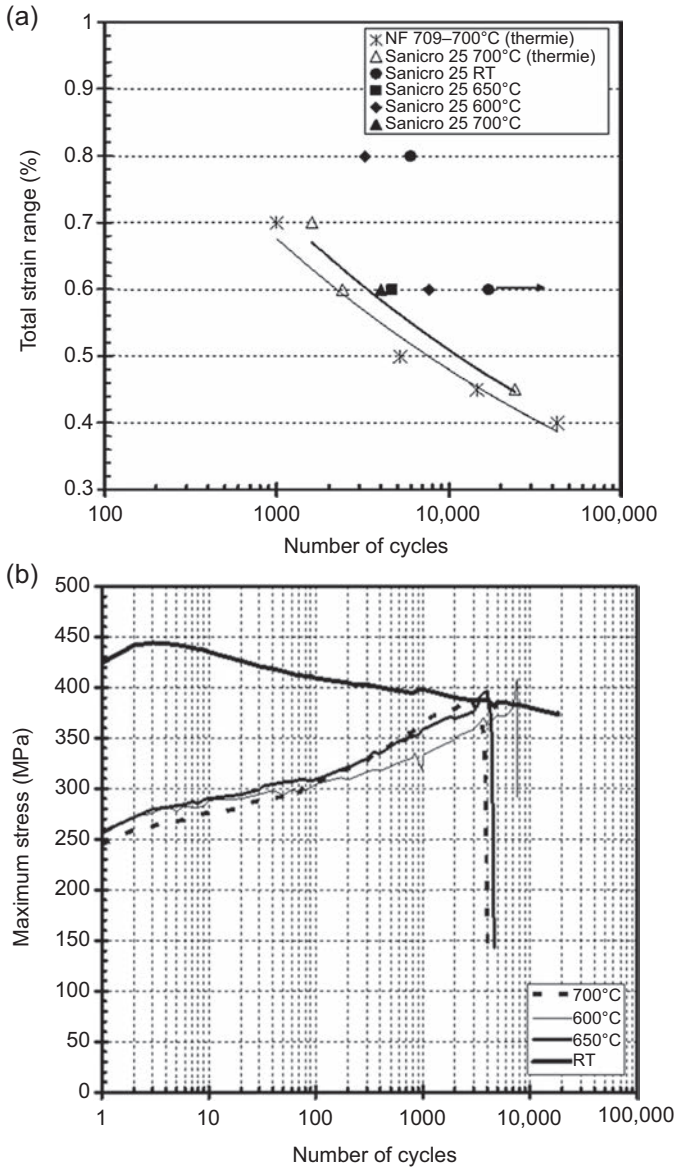


Figure 12.14 Low-cycle fatigue behavior of Sanicro 25. (a) Total strain range versus fatigue life, (b) Cyclic stress response of Sanicro 25 with a total strain range of 0.6% [7,18].

temperatures. The monotonic increase of stress during cyclic loading can be attributed to dynamic strain aging [7,18].

It was found that the damage behaviors in Sanicro 25 during low-cycle fatigue testing at room temperature and high temperature are different. At RT, dense dislocations and deformation bands can be observed. However, the damage or crack initiation is mainly caused by the formation of defects such as slip bands or persistent slip band, twin bands,

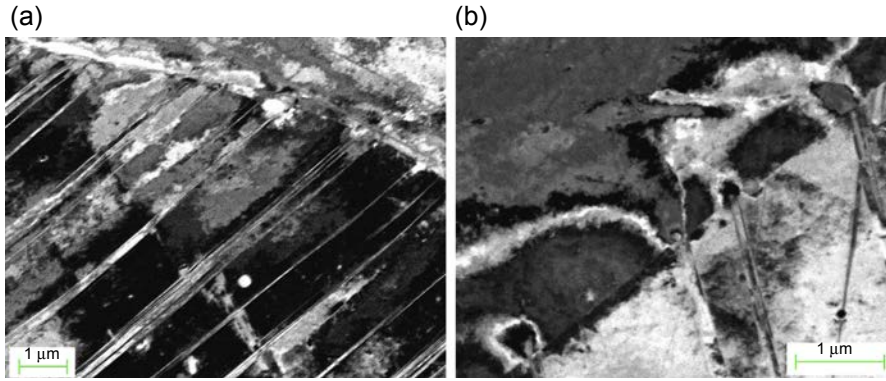


Figure 12.15 Electron channel contrast image of microstructures in low-cycle fatigue tested Sanicro 25 material; (a) at RT, 0.8% strain and 5.948 cycles, (b) at 650°C, 1.2% strain and 1.571 cycles [7].

and stacking faults (Fig. 12.15(a)). The damage at the grain boundary was caused either by the formation of slip bands or stacking faults, or by the interaction of the slip bands at different grains [7]. At high temperature, twin and stacking fault type of defects are less observed. Dislocation or slip bands and planer dislocations can be observed [7]. They form a type of elongated sub-dislocation structure or cells. Interaction between the aforementioned defects or dislocation often occurs. With high strain amplitude, damage at grain boundaries caused by the formation of slip bands can also be observed (Fig. 12.15(b)). With lower strain amplitude, localized deformation can be observed in a low magnification. Planer dislocation structure is a typical one. In this case, the damage occurred both at grain boundary and in grains. A zig-zag form of grain boundaries can also be observed. The width of zig-zag way at the grain boundary is similar to the width of planer dislocation line distance in the grain. This may be attributed to intrusion and extrusion or dislocation slipping process [7]. This discussion shows that the damage of Sanicro 25 material during LCF depends on temperature and also strain amplitudes.

12.6 High-temperature corrosion and steam oxidation behavior

12.6.1 General behaviors

Material corrosion can be a severe problem in a coal-fired power plant. Superheater and reheater tubes may suffer from steam oxidation on the inside and hot corrosion due to deposits on the outside, which can cause even worse corrosion.

12.6.2 Oxidation resistance in steam

Since the interior surface of the superheater and reheater tubes are exposed to high-temperature steam environments, oxide scales are gradually formed on the surface [24]. Metal loss and area reduction of the tubes due to steam oxidation are not

very serious since the steam is a relatively innocuous environment, compared with the severe operating conditions on the fireside of the tubes. The problem is the fact that the oxide scales can start to spall after operating periods in the range of 500 to 50.000 h. The spalled scale particles are shed into the steam circuit and cause bursting due to tube blockages or erosion damage of turbines, and large amounts of scales may accumulate in tube bends causing problems with plugging [25]. Therefore, steam oxidation becomes one of the most important corrosion problems in coal-fired power plants.

Fig. 12.16 shows comparisons of steam oxidation resistances in different austenitic heat-resistant stainless steels. Sanicro 25 has a lower oxidation rate. At 700°C for 1000 h (Fig. 12.16(a)), the steam oxidation rate of Sanicro 25 is about 0.028 mg/cm^2, while the steam oxidation TP 310HCbN is about 0.178 mg/cm^2 although it contains a higher Cr content. The result from the oxidation tests in steam showed low oxidation rate for Sanicro 25 (UNS S31035). The visual examination showed that a very thin oxide layer had formed on the surfaces of Sanicro 25 material. Shot-peening can greatly improve the steam oxidation resistance of super UNS30432 material. These results have been confirmed in other tests at 625°C and 650°C for 10.000 h as shown in Fig. 12.16(b).

As known, Cr content is the most important material parameter that affects steam oxidation behavior. Due to its stability, thin and dense scale and high melting temperature, Cr_2O_3, is generally considered as one of the ideal prospective scales on metals used in an oxidizing environment. For austenitic stainless-steel boiler tube material, a uniform layer of Cr_2O_3 on the surface is necessary to prevent the tubes from steam oxidation. This indicates not only the formation of a continuous uniform layer Cr_2O_3, but also the ability to heal any cracking in the scale whenever it occurs. Generally, the weight loss due to steam oxidation was greatly reduced with the increase in Cr content [28]. For a Fe-Cr-Ni system, a Cr content of above 20% can lead to a satisfactory scaling resistance [29]. Ni addition was believed to affect the growth rate of the oxide scaling [30–32]. An increase in Ni content suppresses internal oxidation and increases the tendency to form a continuous Cr_2O_3 layer. This may be due to that increase in Ni content reduces or retards the Cr depletion [33]. It was found that the critical or optimum Cr content to form a protective layer of Cr_2O_3 decreases with increasing in Fe-Cr-Ni alloys [34]. This may provide an explanation why Sanicro 25 has a higher steam oxidation resistance since it contains enough high-Cr content, but also much higher Ni content (25% vs 20%) comparing with TP 310HCbN.

The steam oxidation mechanisms depend on the temperature and environments. It was found that Cr_2O_3-based surface scales formed during exposure in Ar-50% H_2O at 600–700°C, as shown in Fig. 12.17, whereas more rapidly growing Fe/Cr–rich oxides were found at 750°C [35].

12.6.3 Hot corrosion or flue gas oxidation resistance

The quality of coal is different from different resources. A hot corrosion test for Sanicro 25 material based on some European coal quality was carried out at 700°C for an exposure time of 3.000 h [5]. TP310MoCbN (NF709) was chosen as a reference material because this material is known as one of the best commercially available steels

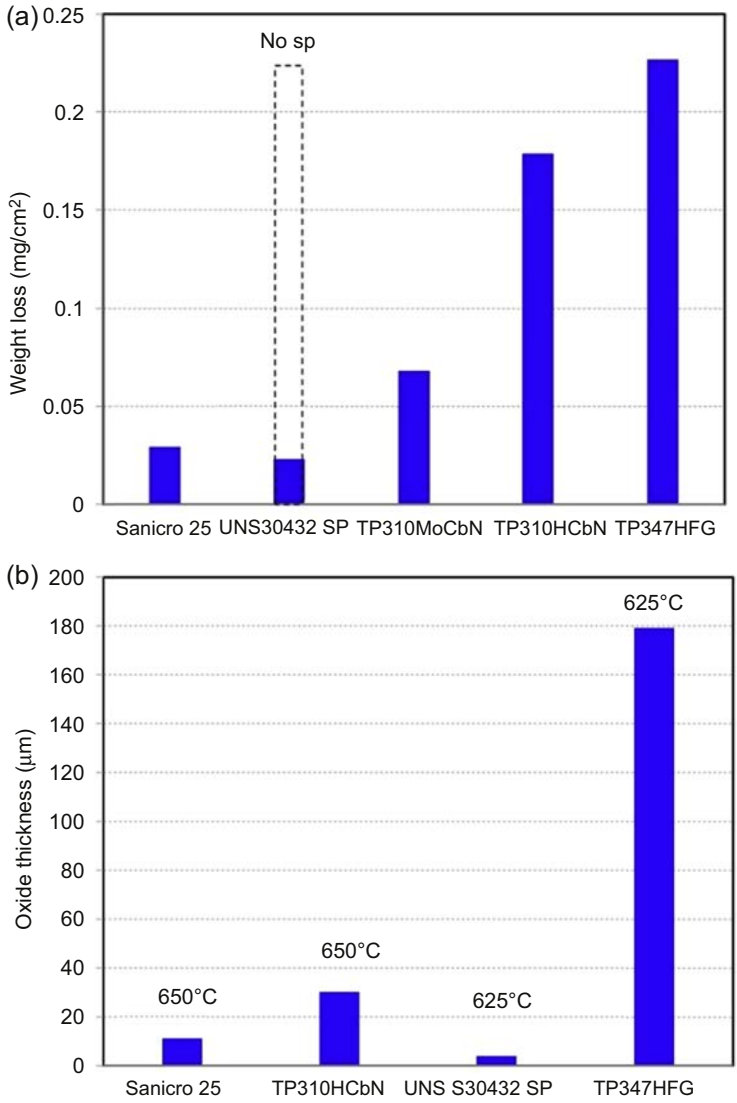


Figure 12.16 Comparison of steam oxidation resistance of austenitic stainless steels, (a) oxidation in steam at 700°C for 1.000 h [26], (b) oxidation in steam at 650°C and 625°C for 10.000 h [27]; *SP*, shot peened.

in this respect. Test specimens of both NF709 and Sanicro 25 were covered with ash and exposed for a gas flow during the test time. The ash composition (wt%) was 5% Na_2SO_4, 5% K_2SO_4, 30% Fe_2O_3, 30% Al_2O_3 and 30% SiO_2, and the gas composition was 0.25% SO_2, 3.5% O_2, 15% CO_2, and balance of N_2. The samples were covered by a definite amount of ashes in an ethyl alcohol suspension. The ashes were renewed every 100 h for the first 500 h of testing and then every 500 h up to the end of the test

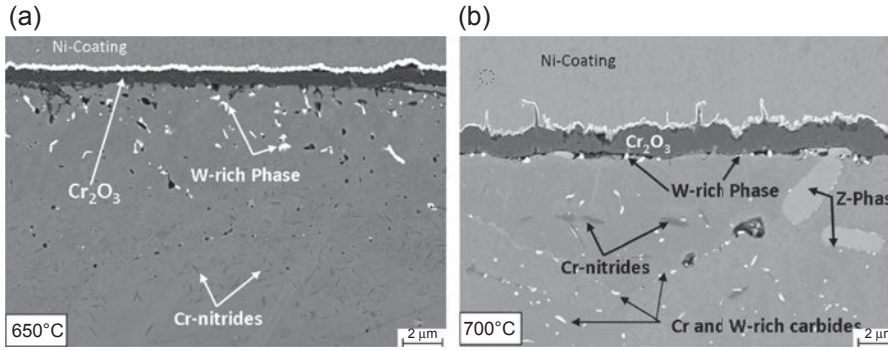


Figure 12.17 SEM images showing steam oxidation behavior of Sanicro 25 in Air–50% H_2O at temperature of (a) 650°C, and (b) 700°C for 3000 hours [35].

(3.000 h). This methodology assures a better exchange between gas environment and metal surface and consequently a better simulation of the material performance in service. After exposition the corroded samples were subjected to a chemical descaling process to determine the mass change for each material as a function of test duration.

Fig. 12.18 shows the results obtained. It is clear that Sanicro 25 has much lower corrosion rate than NF709. A microstructure study also shows that the corrosion morphology differs a lot from one material to the other. Sanicro 25 is characterized by localized corrosion with some deep pits especially after longer exposure time (Fig. 12.19(a)), while NF709 shows a more uniform corrosion front with a great loss of thickness after 3.000 h of exposition (Fig. 12.19(b)).

For flue gas corrosion, a simulated corrosive environment of $N_2 + 10\%\ CO_2 + 0.08\%\ SO_2 + N_2$ was used to study the kinetics of the oxidation of Sanicro 25 and nickel-based alloys at 700°C for 500 h [36]. The results (Fig. 12.20) show that Sanicro 25 has a lower weight loss even comparing with the nickel-based alloys. It was found that a thin layer of oxide was tightly adhered to the surface. They are mainly Cr_2O_3, but also Fe_2O_3 and Fe_3O_4. It is the oxidation kinetics that determines the diffusion of Cr and the formation of Cr_2O_3. With an increase in the concentration of Cr oxide, a pure oxide layer of Cr_2O_3 has also been formed, which increases the corrosion resistance.

12.7 Weldability

12.7.1 Weldability of Sanicro 25

Sandvik Sanicro 25 possesses good weldability. Tables 12.2–12.4 show the welding methods and parameters for welding Sanicro 25 material. The recommended welding method is tungsten inert gas welding (TIG/GTAW/141/141). Preheating and post-weld heat treatment is not normally necessary. In common with all austenitic stainless steels, Sanicro 25 has low thermal conductivity and high thermal expansion. Welding should, therefore, be carefully planned in advance so that distortion of the welded joint can be minimized. The welding of fully austenitic steels usually involves the risk

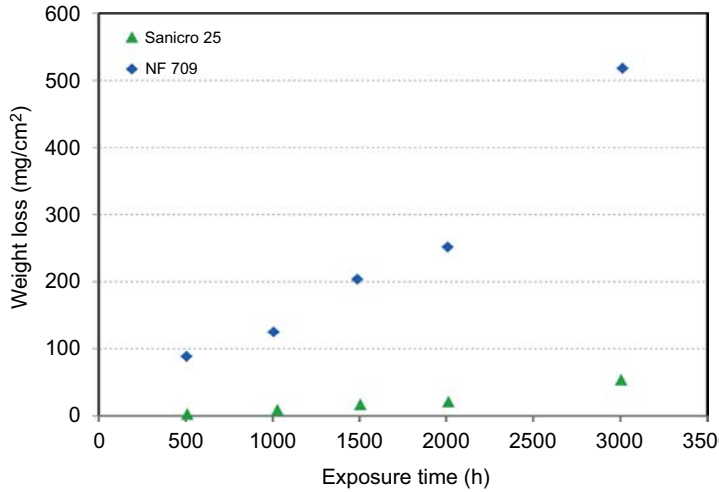


Figure 12.18 Weight change after descaling as function of test duration [5].

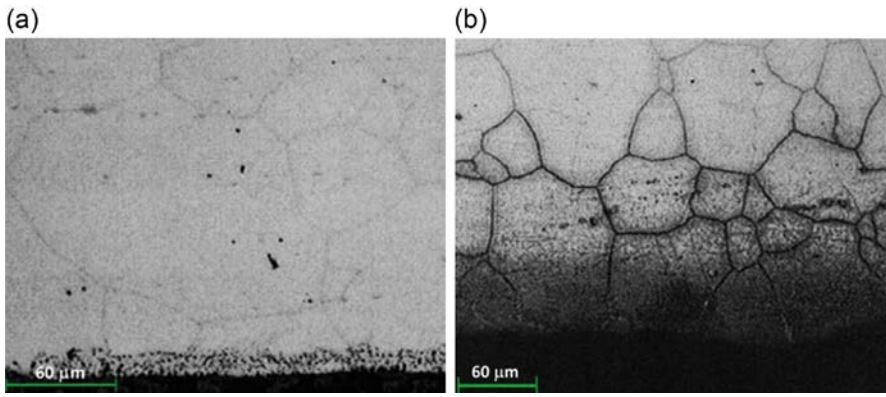


Figure 12.19 Hot corrosion behavior at 700°C for an exposure time of 3.000 h [5], (a) Sanicro 25 material, (b) NF 709 material.

of hot cracking in the weld metal, particularly if the weldment is under constraint. To reduce this risk, the welding should be carried out with a low heat input and an interpass temperature below 100°C.

As filler metal for tungsten inert gas welding, Alloy 617 mod (eg, UTP A 6170 Co mod, DIN EN ISO 18274: SNi6617, NiCr22Co12Mo9) is recommended. Sanicro 25 can also be welded with the regular Alloy 617 (eg, UTP A 6170 Co).

Sanicro 25 has also a good weldability for dissimilar welds. For dissimilar welding to other austenitic stainless steels, the welding processes should be similar to Sanicro 25 itself. No preheating and post-weld heat treatment are necessary from Sanicro 25 itself, but it is possible if required by other austenitic stainless steels. For dissimilar welding to low-alloy steels, the welding process to Sanicro 25 can be applied, but the

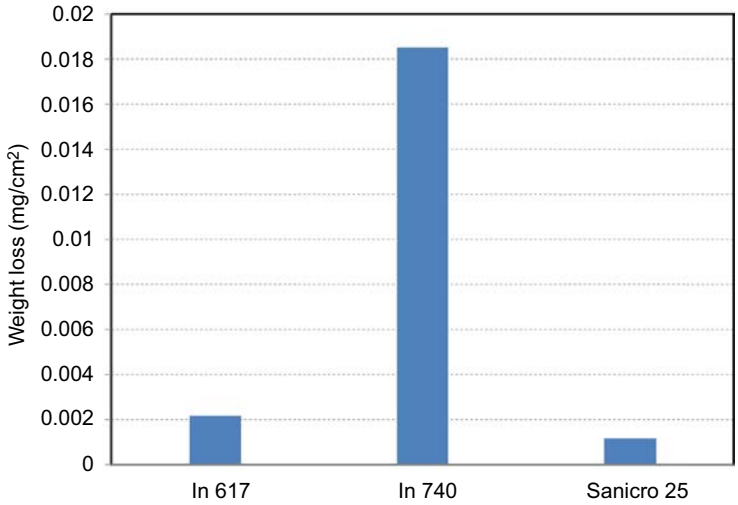


Figure 12.20 Corrosion resistance in the flue gas environment, a comparison of the kinetics of oxidation of Sanicro 25 and nickel-based alloys UNSN06617 andAlloy 740 in the environment 9% O_2+0.2% HCl+0.08% SO_2+N_2 at 700°C for 500 h [36].

Table 12.2 Welding data for TIG/GTAW, manual welding

Rod	Diameter (mm)	Current (A)	Voltage (V)
Alloy 617(mod)	1.6 2.0 2.4	70–140 100–160 170–200	9–12 9–12 12–16

Table 12.3 Welding data for TIG/GTAW. Shielding gas and root gas for filler material Alloy 617 (mod)

Shielding gas	Gas flow (l/min)	Root gas	Root gas flow (l/min)
Ar	8–10	Ar	3–5

Table 12.4 Heat control to avoid hot cracking

Factors	Limit	Remarks
Preheat Interpass temp. Heat input	Not applicable <100°C <1.0 kJ/min	A preheat of 50–70°C can be done if there is a risk for condensed moisture on joint surfaces; preheating with flame shall be avoided.

requirements for the low-alloy steels should be considered. Preheating can be used, but should be kept low. The interpass temperature should also be kept low. Post-weld heat treatment can be used. The welding heat input should also be kept low.

12.7.2 Creep strength of welded Sanicro 25 tube material

Since Alloy 617 has a satisfactory corrosion resistance, tensile properties, and creep strength [37], Alloy 617 and modified Alloy 617 are recommended as filler metals to weld Sanicro 25. Creep testing of butt-welded tubes with these filler metals is still in progress. Some of them have already been running for about 50.000 h. Figure weld one shows the results of the creep test being performed at 650°C and 700°C. The welded Sanicro 25 tube material with filler metal of Alloy 617 has a little lower creep strength compared to the base material. This may be due to the fact that the creep strength of Alloy 617 is lower than Sanicro 25 at temperature below 700°C, as shown in Fig. 12.21 The welded Sanicro 25 tube material with filler metal of modified Alloy 617 shows the similar creep strength as the base material, especially at a longer creep time. This gives a recommendation to use modified Alloy 617 as a filler metal to weld Sanicro 25 tube material, preferably.

12.8 Fabricability

12.8.1 Fabricability of Sanicro 25

Cold deformation and bending of tubes are fabrication processes in the manufacture of boilers in power generation. Sanicro 25 has a good fabricability. Fig. 12.22 shows two different 180° bends and two different 90° bends performed at 20°C [5]. The bending radius ratio were 3.1 (16% strain) and 2.3 (22% strain) for both of the 180° and 90°

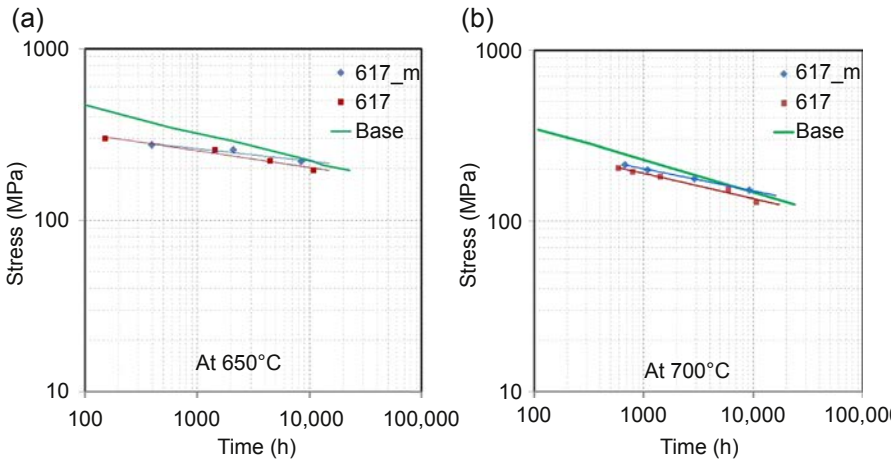


Figure 12.21 Creep behaviors of Sanicro 25 welded material with a filler metal of either normal Alloy 617 (a) or modified Alloy 617_m (b) at 650°C or 700°C.

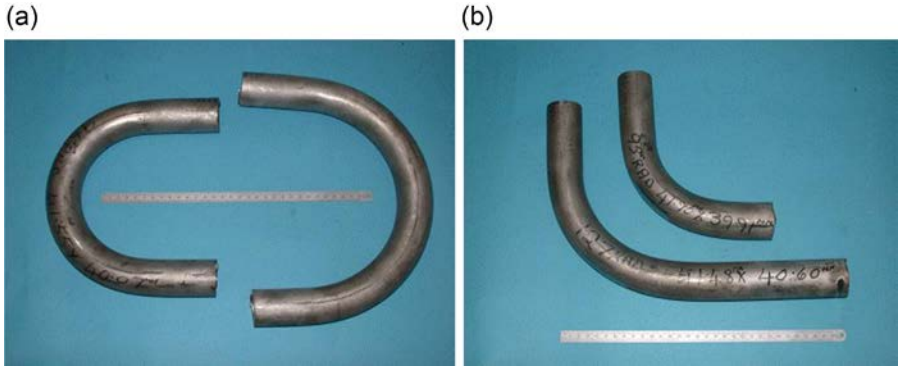


Figure 12.22 Bending test for Sanicro 25 tube; (a) two different 180° bends with bending radius ratios of 3.1 and 2.3, (b) two different 90° bends with bending radius ratios of 3.1 and 2.3 [5].

bends. The bending operation was performed successfully without any cracks in the tube wall and the maximal measured ovality on the tube was 1.6%.

Cold deformation or bending of tube can lead to strain-induced hardening in austenitic stainless steels, and consequently a reduction of ductility. This may result in failure of tube material after a short operation time. Therefore, the pressure vessel design codes usually provide the guidelines for maximum level of allowable strain, depending on materials and type of components. Above this maximum level of strain, a solution treatment is usually required, which can recover the ductility, but it will also increase manufacturing costs.

Fig. 12.23 shows the influence of aging time on the elongation of the cold deformed (15% strain), or cold deformed (15% strain) + solution annealed (SA) austenitic stainless steels at 625°C [38]. 310 HNbN (which is equivalent to TP 310 HCbN, as Niobium = Nb in Europe and Columbium Cb in the United States) in the cold-deformed condition shows very low elongation, only a few percent, and no recovery with increasing time like others. The cold-deformed Sanicro 25 shows an elongation of about 22% at an aging time of 1.800 h and about 30% at 5.500 h. This indicates that this material is ductile during operation at this temperature. The solution annealing will generally recover the elongation, depending on materials. The elongation of the cold deformed 310 HNbN after the solution annealing is about 12% at about 600 h and 23% at about 6.500 h. The elongation of the cold-deformed Sanicro 25 after the solution annealing is about 30% at about 2.100 h and 55% at about 5.500 h. The elongation of the cold-deformed XA 704 after the solution annealing recovers greatly, but decreases again after a longer time. The influence of solution annealing on the elongation of the cold-deformed 304H is relatively small. These results show that except Sanicro 25, the other materials with a strain of 15% may require a solution annealing after straining to ensure the materials to have enough high ductility [38].

12.8.2 Creep strength in cold deformed, not heat treated, material

It is usually concerning if superheater tubes materials in cold-worked state can degrade the long-term creep behavior. Fig. 12.24 shows comparisons of the creep behaviors of

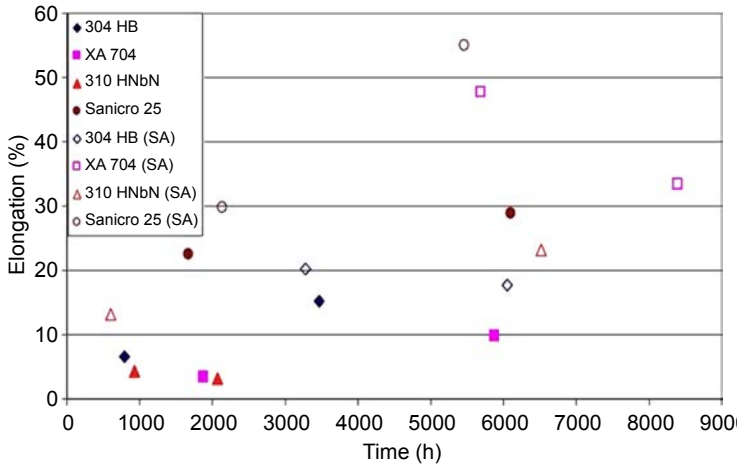


Figure 12.23 Influence of aging time on the elongation of the cold deformed (15% strain), or cold deformed (15% strain) + solution annealed (SA) austenitic stainless steels at 625°C [38].

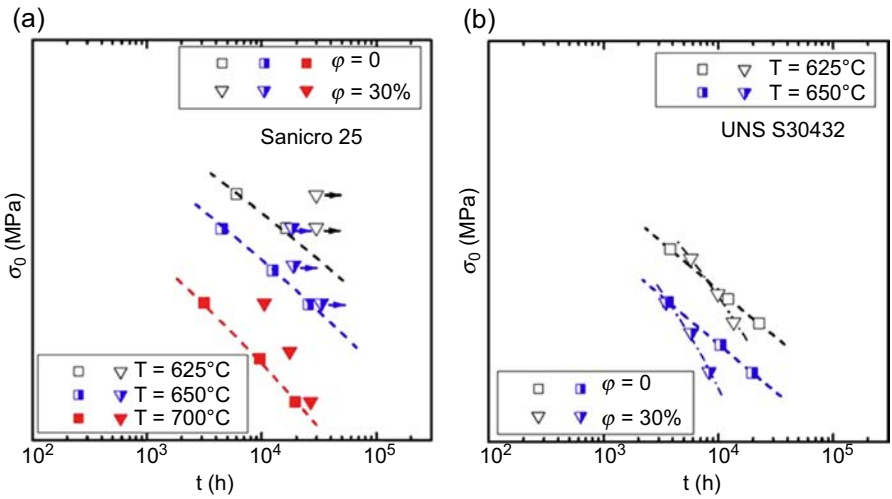


Figure 12.24 Comparison of creep behaviors of the materials in annealed condition and in cold-worked condition for Sanicro 25 (a) and UNS 30,432 (b) [39].

the materials in annealed (0) and 30% cold formed (30%) condition. Data is from a German study set up to suggest max allowed cold deformation that could be allowed without need of a post bend heat treatment. "FV A238, Abschlussbericht des Forschungsvorhabens Untersuchung der zeitabhängigen Festigkeits- und Verformungseigenschaften von Uberhitzerrohrwerkstoffen nach Kaltverformung, 2007-2010" (39). The comprehensive study included creep testing of samples after 15, 25 and 30% cold deformation and tests were ran for more than 30.000 h. Continued creep testing of up to 69600 h (Feb 2016), have reconfirmed the findings for Sanicro 25.

For UNS S30432 (Fig. 12.24 (b) the material with cold deformation show lower creep strength compared to that in annealed (without deformation).

The results lead to a suggestion to increase the max allowed deformation for Sanicro 25 without additional heat treatment from 20 (44) to 30%. In a case when there is no risk for stress corrosion cracking the study indicate that it would be possible to increase the max deformation without need for post bend heat treatment up to 30%. The change has however noy yet been introduced in the VdTUV blatt.

For the height of a (tower design) boiler, it is important to have small heating surfaces with high heat transfer. This means higher allowable cold deformation saves erection cost. One meter saving means a saving of several hundred thousands of Euros. A change from maximum 10% deformation up to max 20% deformation (ie, from bending radius R/D = 5 to R/D 2.5) means that the height of the superheater/reheater can be reduced by 50% (eg, tube size 38 mm, makes height 190 mm with 20% deformation and 380 mm with 10% deformation).

The ASME boiler and pressure vessel code Sect I PG19 limits, however, the max allowed deformation/strain to 15% for alloys containing N and/or Cb for temperatures up to 675°C, and to 10% for operation at higher than 675°C for all materials. This means different rules for boilers to be built according to European versus American codes.

The German study [39], however, opens up for a discussion with independent authorities whether or not it could be possible to take advantage of these good results for Sanicro 25 in the local pressure vessel codes and standards.

The higher allowable maximum strain level makes it possible to build smaller boilers, which can have great economic and environmental effects.

12.9 Field experiences: testing in boilers

Sanicro 25 tubes have been installed for testing in five different boilers in Europe.

Four of the installations have been made in different 700°C test programs. Sanicro 25 and other potentially interesting materials were tested at relevant temperatures. The first installation was in 2004 in a co-fired, coal and wood-pellet power boiler in Denmark [40]. A rig was installed in unit #3 in the Esbjerg Plant. It consisted of a single loop of superheater tubes inserted in the superheater area in the USC unit with steam temperature 560°C and steam pressure 275 bar. The steam was taken from the outlet of superheater 1 (560°C) and superheated to 720°C. The highest metal temperature in the part in which Sanicro 25 was tested was estimated to 657°C.

Another test rig with Sanicro 25 was installed in the lignite-fired plant Weisweiler [41] with material temp around 655°w at 169 bar pressure.

A bigger test was started in 2005 in the COMTES project, EON hard coal unit at Scholven, Germany [42]. The superheater was manufactured using DMV310N, HR3C, Sanicro 25, Alloy 617B, and Alloy 740. Material temperature for the Sanicro 25 test was estimated to 610–630°C. The total testing period was 22.400 h between 2005 and 2009.

Sanicro 25 showed the best oxidation behavior of the high-alloy austenitic steels. However, both Sanicro 25 and Alloy 617B in some cases suffered from local corrosion attacks,

which very likely will lead to lifetimes less than the 200.000 h design life of these materials. The high corrosion rates are believed to be related to the fuel composition and the specific temperature range. All tested superheater materials are considered susceptible to the corrosion mechanism, even though not observed on all materials and samples. Results from another project [40] did not show corrosion rates in the same range. Further studies of corrosion rates at various temperatures and fuel compositions are recommended to optimize superheater materials selection. Alternatives include restrictions in fuel compositions or partial replacements of superheater sections within the unit design lifetime.

The fourth installation was made in 2008 in a reheater in a lignite-fired boiler at Boxberg, operating at 580°C/66 bar. Material temperature was thereby estimated to 610 and 630°C respectively. An evaluation after 26.000 h showed insignificant wall thinning and an inside steam oxide with a thickness below 10 µm. The tubes are still in service (August 2015), but are planned to be taken out in 2016, after 8 years operation.

The latest installation was in 2009 in a superheater test loop [43] in the GKM HWT 725 I project with up to 630°C steam temperature in a bituminous coal-fired boiler at GKW Mannheim operating at 165 bar pressure.

Fig. 12.25 shows the steam oxidation inside (Fig. 12.25(a)) and flue gas corrosion outside (Fig. 12.25(b)) of the tube installed in one of the aforementioned power plants for 32.000 h. The corrosions in both sides are very small.

12.10 Future trends

With a growing supply of electricity from intermittent power generation sources, as solar and wind plants, the demands on flexibility of coal-fired power boilers will increase by more rapid startup and shutdown processes and increasing ability to operate with reduced capacity. The other is more flexibility on fuel selection, eg, using different types of coals and mixing with biomass. This is valid for the existing power fleet but will also have to be considered for new higher efficiency plants.

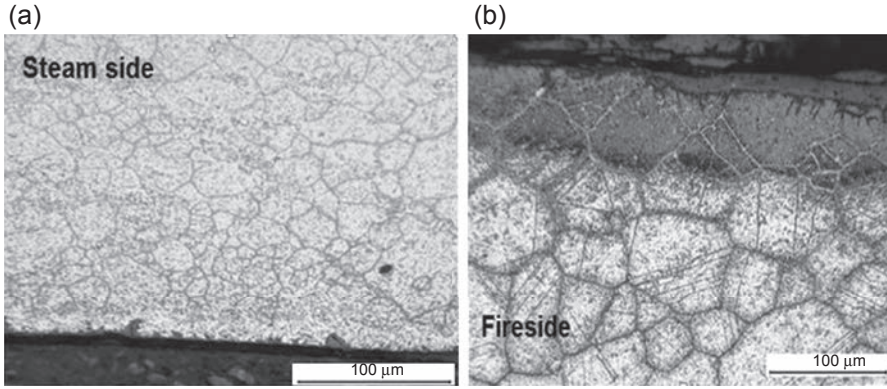


Figure 12.25 (a) Steam oxidation inside, (b) flue gas corrosion outside of the tube installed for 32.000 h.

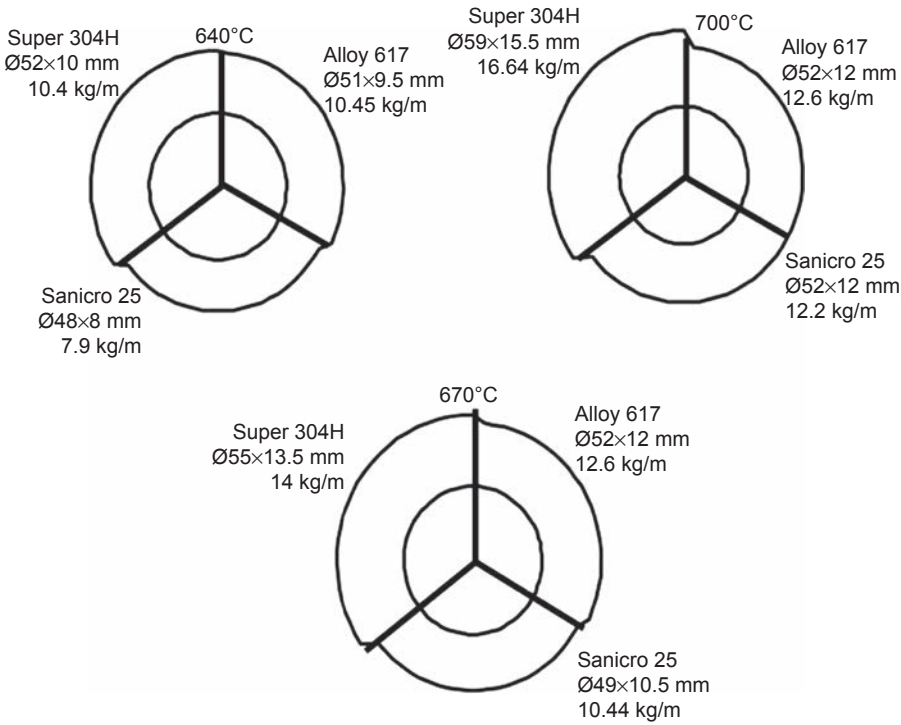


Figure 12.26 Wall thickness calculations for different heat-resistant grades using European VdTÜV data [44].

All these mean that there will be a growing demand for materials with high creep strength combined with good fabricability and aging properties. Material needs to maintain ductility in cyclic conditions. High strength allows thinner wall design, which means less weight. The thinner wall also implies a lower outer metal surface temperature, which if anything is positive for the corrosion resistance of the tubes. Typically, metal loss increases with increasing temperature. Thinner walls also mean lower stresses in the construction. Fig. 12.26 shows comparisons of wall thickness between Sanicro 25, UNS S34042, and Alloy 617 (European VdTÜV value) based on their creep strengths. By combining with a greater allowable deformation (smaller cold bend radii) a smaller space is needed to produce the required steam. This contributes to a smaller boiler, ie, to a lower weight per kW generated electricity.

12.11 Conclusions

A new austenitic stainless steel gradeUNS S31035 (Sandvik Sanicro 25) has been developed for superheater and reheaters in high-efficiency advanced coal ultra-supercritical power plants, A-USC. Extrapolation from creep data with two methods gives

creep strength of around 100 MPa at 700°C for 100.000 h, which is higher than that of other austenitic stainless steels available today.

The alloy has excellent steam oxidation resistance, good hot corrosion resistance, and very good fabricability and weldability properties.

This makes Sanicro 25 a cost-efficient option in high-efficiency coal-fired boilers for superheaters and reheaters operating at metal temperatures up to 700°C. For such temperatures the only other option is to use more costly nickel-based materials.

Currently available materials (TP310HCbN, UNS S34042) allow use at metal temperatures up to around 650°C. Sanicro 25 is therefore an excellent option in steam applications in metal temperatures 650 up to 700°C; the high creep strength makes it an interesting option for use in high-pressure superheaters instead of currently available materials that would result in too heavy wall thicknesses.

Acknowledgments

This paper is published by permission of Sandvik Materials Technology. Supports from Mr. Timo Peltala, Mr. James Shipley, Mr. Pasi Kangas, Dr. Jesper Ederth, Mr. Peter Stenvall, Dr. Magnus Boström, Mr. Johan Hernblom, and Mr. Jan Högberg are greatly acknowledged.

References

[1] IEA, Energy Statistics, 2009. http://www.iea.org/stats (2010.02.25).
[2] R. Blum, R.W. Vanstone, Materials development for boilers and steam turbines operating at 700°C, in: Proceedings to the Fourth International Conference on Advances in Materials Technology for Fossil Power Plants, October 2004, p. 116.
[3] J. Bugge, AD 700-Advanced 700°C PF power plant, http://www.unece.org/fileadmin/DAM/ie/se/pdfs/AD700PFCoal.pdf.
[4] P.J. Maziasz, I.G. Wright, J.P. Shingeldecker, Defining the materials issues and research for ultra-supercritical steam turbines, in: Proceedings to the Fourth International Conference on Advances in Materials Technology for Fossil Power Plants, October 2004.
[5] R. Rautio, S. Bruce, Sandvik Sanicro 25-A new material for ultrasupercritical coal fired boilers, in: Proc. from the Fourth Inter Conf. on Advances in Materials Technology for Fossil Power Plants, October 2004, p. 274.
[6] G. Chai, J.O. Nilsson, M. Boström, J. Högberg, U. Forsberg, Advanced heat resistant austenitic stainless steels, Proc. of ICAS 2011 (2010) 56.
[7] G. Chai, M. Boström, P. Kjellström, U. Forsberg, Procedia Engineering 55 (2013) 232.
[8] Y.U. Kim, S.I. Kwun, J.H. Shim, D.B. Park, Y.W. Cho, Y.H. Chung, W.S. Jung, The Effect of Cooling Conditions After Solution Treatment on the Creep Rupture Strength of Sanicro 25, 2009, 3rd Symposium on Heat Resistant Steels and Alloys for High Efficiency USC Power Plants www.nims.go.jp/hrdg/USC/Proceeding/Proceeding033Jung.pdf.
[9] S. Latha, M.D. Mathew, P. Parameswaran, K.B. Sankara, S.L. Mannan, Thermal creep properties of alloy D9 stainless steel and 316 stainless steel fuel clad tubes, International Journal of Pressure Vessels and Piping 85 (2008) 866.
[10] T. Sourmail, Precipitation in creep resistant austenitic stainless steels, Materials Science and Technology 17 (2001) p.1.

[11] A. Tohyama, Y. Minimi, in: R. Viswanathan, J. Nutting (Eds.), Advanced Heat Resistant Steels for Power Generation, IoM Communications Ltd, London, 1999, p. 494.
[12] A.K. Laha, J. Kyonob, N. Shinya, An advanced creep cavitation resistance Cu-containing 18Cr–12Ni–Nb austenitic stainless steel, Scripta Materialia 56 (2007) p.915.
[13] R.M. Davison, T.R. Laurin, J.D. Redmond, H. Watanabe, M. Semchyshen, A review of worldwide developments in stainless steels, Materials & Design 7 (3) (1986) 111.
[14] http://www.thermocalc.com/start/.
[15] P. Kjellström, Microstructure and Creep Mechanisms in Advanced Heat Resistant Materials (M. Sc. thesis), Royal Institute of Technology, Sweden, 2010.
[16] R. Sandström, A procedure for extended extrapolation of creep rupture data, Journal of Testing and Evaluation 31 (2003) 58.
[17] R. Sandström, L. Lindé, Precision in the extrapolation of creep rupture data, Journal of Testing and Evaluation 27 (3) (1999) 203.
[18] G. Chai, J. Hernblom, K. Hottle, U. Forsberg, T. Peltola, Long term performance of newly developed austenitic heat resistant stainless steel grade UNS S31035, in: Proceedings of the ASME Symposium on Elevated Temperature Application of Materials for Fossil, Nuclear, and Petrochemical Industries, March 25–27, 2014.
[19] P. Moody, Strain induced hardening of advanced austenitic stainless steels, evaluation of creep properties, advances in materials for fossil power plants, in: Proc. from the Eight Inter. Conf. August 31–September 3, 2010, USA.
[20] G. Chai, J. Hernblom, U. Forsberg, T. Peltola, Creep Behavior in a Newly Developed Heat Resistant Austenitic Stainless Steel, 160 (9) (2015) 400–405.
[21] J. Polák, R. Petráša, M. Heczkoa, T. Krumla, G. Chai, Analysis of cyclic plastic response of heat resistant Sanicro 25 steel at ambient and elevated temperatures, Procedia Engineering 74 (2014) 68–73.
[22] J. Polák, R. Petráša, M. Heczko, I. Kuběna, T. Krumla, G. Chai, Low cycle fatigue behavior of Sanicro 25 steel at room and at elevated temperature, Materials Science and Engineering A 615 (10/2014) 175–182.
[23] J. Polák, R. Petráša, M. Heczkoa, T. Krumla, G. Chai, Evolution of the cyclic plastic response of Sanicro 25 steel cycled at ambient and elevated temperatures, Journal of Fatigue 83 (2016) 75.
[24] G. Chai, Oxidation behaviours of austenitic boiler tube stainless steels in high temperature steam environments, Sandvik Steel T9800782 (1998).
[25] J. Armitt, et al., The Spalling of Steam Growth Oxide from Superheater and Reheater Tube Steels, Electric Power Research Institute, EPRI FP-686, 1978.
[26] J. Flyg, P. Viklund, R. Pettersson, Oxidation av rostfria stål i vattenånga, ref. no. 708002, KIMAB, Sweden, 2007, 8.
[27] http://edok01.tib.uni-hannover.de/edoks/e01fb12/721448585.
[28] N.B. Pilling, R.B. Bedworth, Journal of the Institute of Metals 29 (1970) 373.
[29] N. Otsuka, High temperature oxidation of stainless steel boiler tubes in superheated steam, Sumitomo Metal 44 (1992) 30.
[30] F. Eberle, C.H. Anderson, Journal of Engineering and Power Transmission, ASME 84 (1962) 223.
[31] S. Jasson, et al., British Corrosion Journal 4 (1969) 21.
[32] W.E. Ruther, S. Greenberg, The Electrochemical Society 111 (1964) 1116.
[33] J.E. Croll, G.R. Wallwork, Oxidation of Metals 1 (1969) 57.
[34] A. Brasunas, J.T. Gow, O.E. Harder, Proceedings of ASTM 46 (1946) 870.
[35] J. Zurek, S.-M. Yang, D.-Y. Lin, T. Huttel, L. Singheiser and W.J., Quadakkers, Microstructural stability and oxidation behavior of sanicro 25 during long-term steam exposure in the temperature range 600–750°C, Materials and Corrosion 66(4) (2015) 315.

[36] P. Jamrozik, M. Sozanska, Evaluation of the applicability of Sanicro 25 steel in supercritical boilers, Solid State Phenomena 212 (2014) 201–204.
[37] Special metals, Inconel Alloy 617, Data Sheet, www.specialmetals.com.
[38] P. Moody, Strain induced hardening of advanced austenitic stainless steels evaluation of creep properties, in: Proc. of the Sixth Inter. Conf. on Advances in Materials Technology for Fossil Power Plants, New Mexico, 2010, pp. 933–941.
[39] F. Muller, A. Scholz, M. Oechsner, Zulässige kaltverformungsgrade zeitstandbeanspruchter bauteile aus austenitischen stahlen und nickellegierungen, FVW/FVHT, 34, 2011, Vortragsveranstaltung am 25. C:_falk\publik\2011_1N25_vdeh\paper\2 BMI1919a_VV11.doc, pp 1–10.
[40] Esbjerg Test Rig, VGB Research Project 260 http://www.vgb.org/en/research_project260.html.
[41] http://www.hitachi.com/rev/pdf/2010/r2010_03_111.pdf.
[42] Component test facility for a 700°C power plant (COMTES) EUR 25921 EN.
[43] 700C plant vision of high efficiency and clean energy production http://seminar.mpa.uni-stuttgart.de/s-2013/Download.
[44] VdTuV Werkstoffblatt 555, Sanicro 25, 2008.

This page intentionally left blank

New Japanese materials for A-USC power plants

13

A. Di Gianfrancesco
Materials & Technologies Consultant, Rome, Italy

13.1 Introduction

In recent years, boilers for coal-fired power plants have been constructed at a rapid pace in China, India, and other newly industrializing economies. In Japan, too, the importance of boilers for thermal power generation has continued to grow ever since the country's use of nuclear power dropped in the wake of the 2011 Great East Japan Earthquake and tsunami waves. However, in terms of unit of electrical energy generated, coal-fired power generation emits more CO_2 than any other type of power generation. From the standpoint of suppressing global warming, it is extremely important to improve coal-fired power generation efficiency. In the 1990s, Japan was the first country in the world to put into practical use a high-efficiency, ultra-supercritical (USC) boiler (steam temperature: 600°C class) for coal-fired power plants [1]. Recent years have seen the development of advanced ultra-supercritical (A-USC) boiler technology that is aimed at raising steam temperature to 700°C [2,3]. The key to ensuring more favorable steam conditions is the development of new boiler tubes and pipes for use under more severe high-temperature environments.

Nippon Steel & Sumitomo Metal Corporation (NSSM) has developed boiler tubes and pipes that are marketed as SUPER304H, SUS304J1HTB, ASME SA213 Code Case (CC) 2328, and TP347HFG (ASME SA213 TP347HFG), which have become world standard [4], and in this way the company has contributed much to the development of USC boilers. It is also pressing ahead with the development and commercialization of the high-strength Ni-based alloy HR6W (ASME SB167 CC 2684), which is suitable for A-USC boilers [5].

Mitsubishi Hitachi Power Systems (MHPS) has established an alloy design method capable of reducing the time and the cost of development of Ni-based superalloys used in thermal power plants. By using this method, MHPS has developed the FENIX-700, LETS700R, USC141, and USC800 superalloys for application in boiler and turbine in A-USC power plants [6].

Toshiba developed the nickel-based super alloy TOS1X for the 700°C-class A-USC turbine rotor [7].

These companies are working with Japanese manufacturers of boilers, turbines, and valves in a nine-year (FY 2008–FY 2016) project named "Development of Component Technologies for the Practical Application of Advanced USC Thermal Power Generation," which is subsidized by Japan's Ministry of Economy, Trade, and Industry (METI). Project members have been striving to evaluate the long-time properties

Materials for Ultra-Supercritical and Advanced Ultra-Supercritical Power Plants.
http://dx.doi.org/10.1016/B978-0-08-100552-1.00013-0
Copyright © 2017 Elsevier Ltd. All rights reserved.

of the aforementioned newly developed alloys and to establish the application technology. The project members plan to conduct a series of boiler component tests using 700°C and more steam temperature [8,9].

13.2 Development of boiler tubes and pipes for advanced USC power plants: HR6W, HR35

13.2.1 HR6W

13.2.1.1 Alloy design and properties

When developing HR6W for A-USC boiler pipes and tubes, importance was attached to not only its creep rupture strength but also its creep ductility, thermal fatigue resistance, and fabricability into large-diameter, thick-walled pipes. The precipitation strengthening of γ′-phase ($Ni_3(Al,Ti)$) used for conventional high-strength Ni-based alloys was not applied in the design of the new alloy [10].

First, from the standpoint of corrosion resistance and microstructural stability for use in 700°C-class A-USC boilers, the optimum amount of Cr was decided to be 23%. The creep rupture strength and microstructure of Ni-Fe-Mo-W model alloys were studied [11]. When Mo was added singly, σ phase (an embrittlement phase) precipitated in large quantities during more than 10,000 h of creeping at 700–750°C, causing strength, creep ductility, and thermal fatigue resistance to deteriorate markedly. On the other hand, when only W was added, it was possible to restrain the precipitation of σ phase during the many hours of creeping and obtain a stable microstructure with an optimum Ni content of 45%. In addition, from the results of phase diagram calculations and experiments, it was confirmed that a comparatively fine Laves phase of Fe_2W type precipitated during creeping, helping to strengthen the alloy significantly.

The optimum composition of the ultimately developed alloy HR6W was established as 23Cr-45Ni-7W [12–14]. Table 13.1 shows the composition specifications of

Table 13.1 Chemical composition specification of HR6W

WT (%)	C	Si	Mn	Cr	Fe	W	Ti	Nb	B	N	Ni
Min				21,5	20,0	6,0	0.05	0,10	0,0005		
Max	0,1	1.0	1,5	24,5	27,0	8,0	0,20	0,35	0,0060	0,02	Bal.

HR6W registered in the ASME Standard. In addition to W, the alloy is added with C, Ti, Nb, and B to increase alloy strength through the formation of fine carbides.

Fig. 13.1 shows the microstructure of an extracted replica of HR6W aged at 750°C for 3000 h. Even after these many hours of aging, the microstructure reveals a fine Laves phase and $M_{23}C_6$ carbide, and it is free of σ phase precipitation.



Figure 13.1 TEM microstructure of extracted replica of HR6W aged at 750°C for 3000 h [10].

Fig. 13.2 shows the phase fractions of HR6W calculated using Thermo-Calc. Even at 800°C, the Laves phase precipitates stably, indicating that it helps strengthen the alloy in the temperature region in which it would be used for A-USC boilers.

Fig. 13.3 shows that the HR6W thermal expansion coefficient in lower than S304H austenitic steel, but worse than alloy617 and Grade 91. Table 13.2 shows that the mechanical properties of HR6W are lower than Alloy 617.

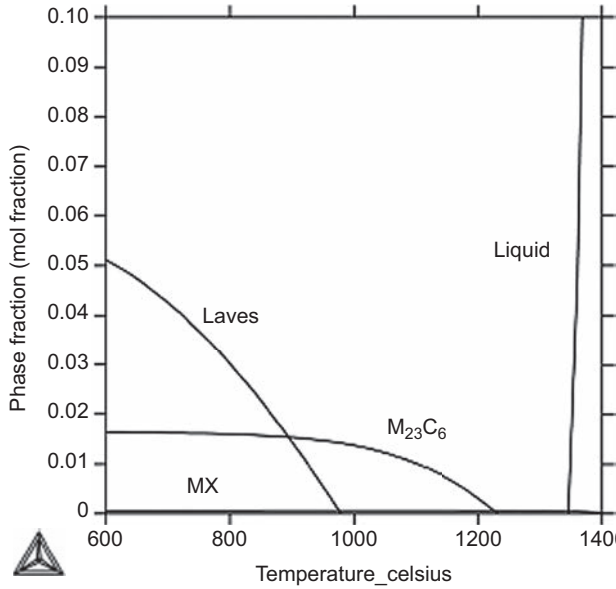


Figure 13.2 Phase fractions of HR6W computed by Thermo-Calc [10].

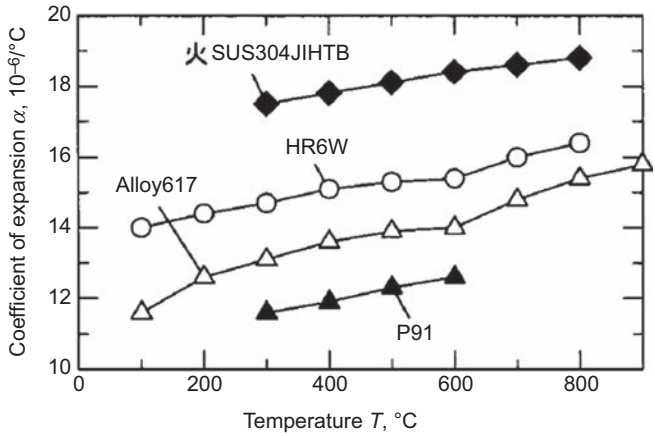


Figure 13.3 Coefficient of expansion of tested alloys [13].

Table 13.2 Mechanical properties of tested alloys [15]

Temperature	Alloy	0.2% proof stress $\sigma_{\alpha 2}$ (MPa)	Tensile strength σ_g (MPa)	Elongation (%)	Reduction of area ϕ_p (%)
RT	HR6W	270	666	57	66
	Alloy617	355	760	72	64
700°C	HR6W	167	459	57	49
	Alloy617	226	494	49	39

13.2.1.2 Creep rupture strength and microstructure evolution

Fig. 13.4 shows the creep rupture strength of HR6W. Including creep rupture data collected over a maximum period of more than 60,000 h, the stress-creep rupture diagrams show a mild gradient, demonstrating that the alloy maintains high creep rupture strength on a stable basis even in a temperature range of 650–800°C. The average creep rupture strength of HR6W for 100,000 h registered in the German Standard TUV (VdTUV559/2) is 118 MPa at 650°C, 85 MPa at 700°C, 62 MPa at 750°C, and 42 MPa at 800°C. It has been confirmed that HR6W also has good creep rupture ductility even on the long-hour side [14].

Fig. 13.5(a) shows an optical micrograph (longitudinal section of specimen) of HR6W ruptured at 700°C, 98 MPa, in 58,798 h. Many precipitates were observed at the grain boundaries and in the grains. Those precipitates were mainly Cr-based carbides (identified later as $M_{23}C_6$ under TEM). Blocky embrittlement phases, such as the σ phase, were not observed at all. The creep rupture elongation of the aforementioned ruptured specimen was 39%, while the microstructure in the neighborhood of the ruptured part revealed markedly deformed grains. Fig. 13.5(b) shows the microstructure of an extracted replica of the ruptured specimen observed under the TEM.

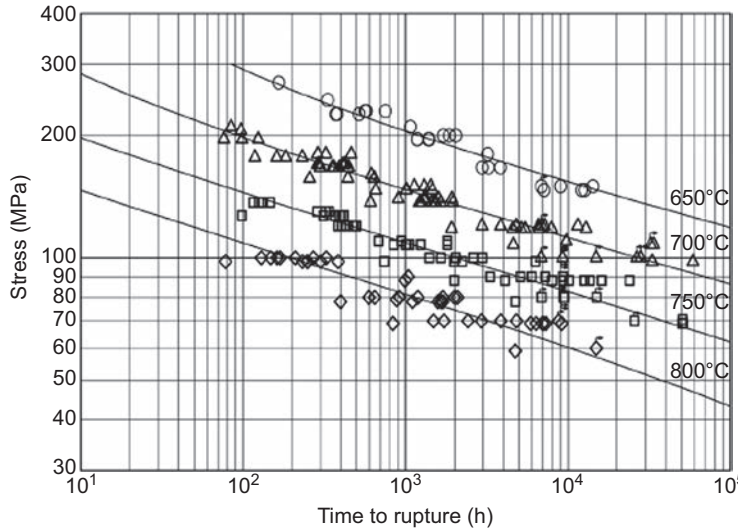


Figure 13.4 Creep rupture strength of HR6W.

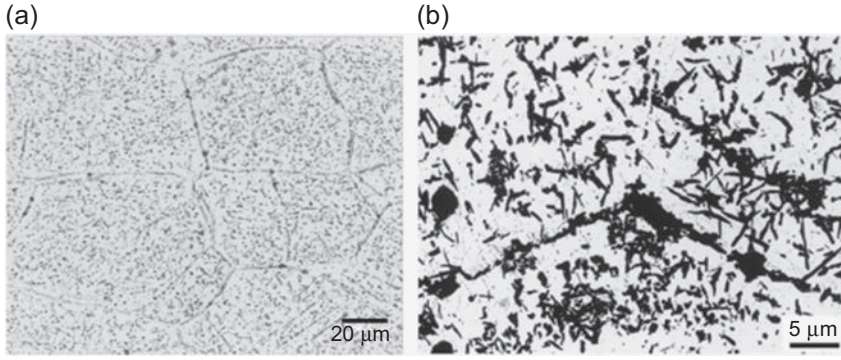


Figure 13.5 Optical and TEM microstructure on extraction replica of HR6W after creep rupture (700°C, 98 MPa, 58.798 h).

The precipitates in grain boundaries were identified as $M_{23}C_6$, while those in grains were identified as Laves phase and $M_{23}C_6$, as shown in Fig. 13.1. Even at 700°C on the long-time side, σ phase was not observed.

Precipitates approximately 1–3 μm observed in large quantities in the grains were identified as Laves phase (see Fig. 13.5(c)). Extreme coarsening of the Laves phase was not observed. The Laves phase containing W (Fe_2W) gradually precipitates finely with the lapse of time, and it takes many hours until precipitation equilibrium is reached. It is estimated that the fine precipitation of the Laves phase over many hours [16] contributes to stable precipitation strengthening of the alloy.

Tungsten is concentrated in Laves phase and the Cr diffuse away from Laves phase to the interphase of Laves/γ matrix. As a result, the concentration of Cr promotes α–Cr

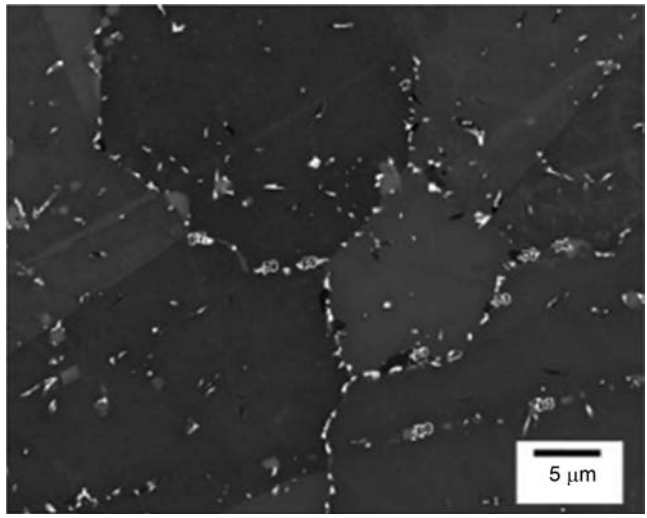


Figure 13.6 The SEM picture of HR6W alloy crept at 700°C/100 MPa, 79,986 h.

formation [17]. Fig. 13.6 shows α–Cr particles with Laves phase at grain boundaries and also in the grains at the vicinity of Laves phase [18].

TEM images (Fig. 13.7) clearly shows the precipitated Laves phase morphology after long-time stress rupture tests at 700°C, 750°C, and 800°C [5]. It can be seen that the growth rate of Laves phase is very sensitive to the test temperature. The dispersive precipitated Laves phase is already grown to a certain size at 750°C after long-time stress rupture test.

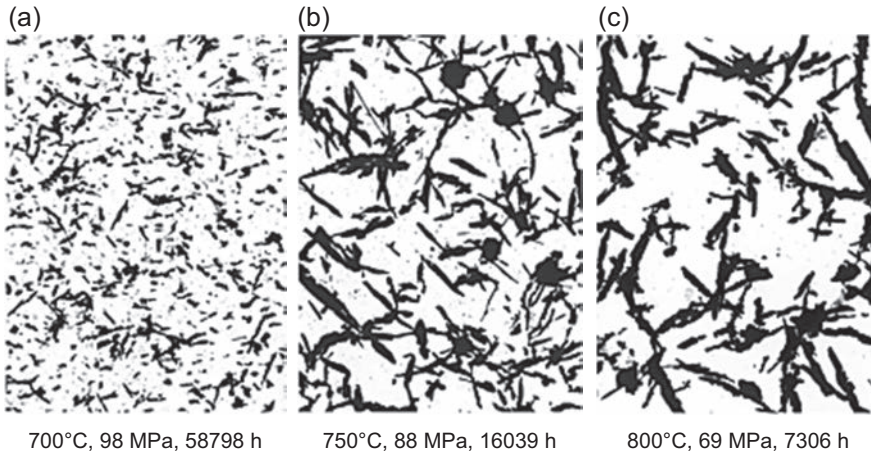


Figure 13.7 The TEM microstructure of HR6W alloy after creep tests.

13.2.1.3 Service performance

Fig. 13.8 compares the creep fatigue strength of HR6W at 700°C with that of Alloy 617 (a general-purpose Ni-based alloy) [19]. With regard to CP waveform (0.01%/s on the low-speed (C) side, 0.8%/s on the high-speed (P) side), the creep fatigue life of HR6W is longer than that of Alloy 617. It is widely known that the creep fatigue life of CP waveform has some correlation with creep rupture ductility [20]. Since HR6W has high creep rupture ductility, it is estimated that the alloy shows good creep fatigue resistance. The figure shows SEM images of the fracture surfaces of the two alloys after a creep fatigue test. While Alloy 617 revealed intergranular fractures over the entire surface, HR6W showed many transgranular fractures. The implication is that the fracture ductility of HR6W is higher than that of Alloy 617, and is therefore superior in creep fatigue resistance.

With high-strength Ni-based alloys of the γ′-phase strengthened type, as represented by Alloy 617, stress relaxation cracking (SR cracking) has become a problem. It occurs in the process of relieving welding residual stress while the alloy is used

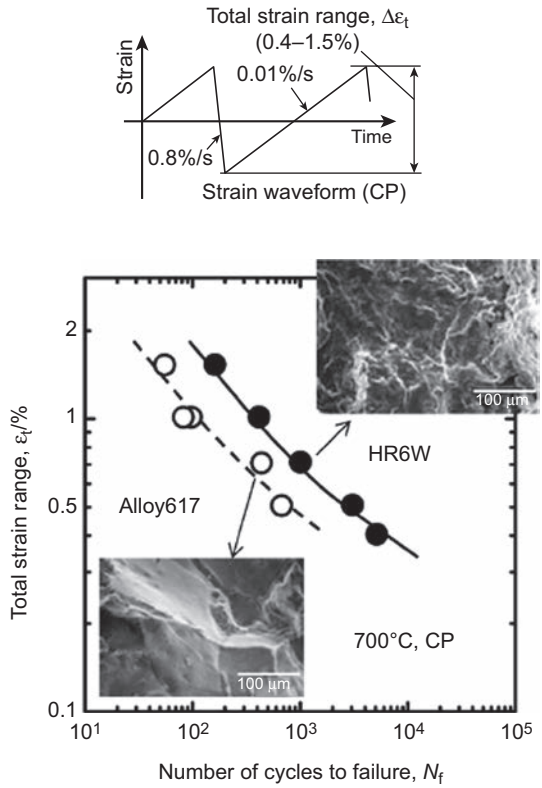


Figure 13.8 Creep fatigue properties of HR6W and alloy 617 [19].

under high temperatures [21]. Sensitivity to SR cracking has much to do with material ductility at high temperatures, when stress relieving occurs easily. In a JIS-compatible hot tensile test (strain rate after yielding: about $1.25 \times 10^{-3}\,s^{-1}$), Alloy 617 showed good ductility comparable to that of HR6W. To simulate the hot deformation at a low strain rate, during which SR cracking occurs, the author and collaborators carried out an extra-low strain-rate tensile test, with the strain rate set at $1.0 \times 10^{-6}\,s^{-1}$, or 1/1000 of the ordinary strain rate.

The test results are shown in Fig. 13.9 [22]. In a temperature range of 700–750°C, with A-USC boiler pipes used, HR6W displays high rupture ductility. Next, to evaluate the sensitivity of HR6W to SR cracking, the author and collaborators welded for restraint

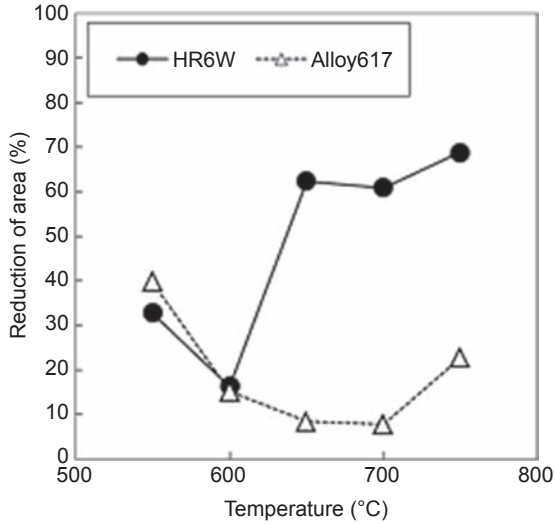


Figure 13.9 Rupture ductility by extra-low strain-rate tensile tests [22].

a small-diameter tube whose grain size was adjusted to the same size as that of a large-diameter, thick-walled pipe, subjected the welded pipe to aging at 700°C for 1000 h, and observed cross-sections near the weld zone under an optical microscope [23]. HR6W revealed no SR cracking. In contrast, Alloy 617 showed marked SR cracking. From these results, it was judged that the alloy ductility, measured during the aforementioned extra-low strain-rate tensile test, had high correlation with alloy sensitivity to SR cracking. Thus, the test demonstrated that HR6W had excellent resistance to SR cracking.

13.2.1.4 Mock-up manufacture and properties

The newly developed HR6W has good hot workability [23]. Fig. 13.10 shows a fabrication step of a large-diameter, thick-walled HR6W pipes of practical sizes already manufactured to verify the fabricability of HR6W pipes (Fig. 13.11) and tubes (Fig. 13.12). The large-diameter, thick-walled HR6W pipe shown was used for amock-up of a reheater header fabricated for the METI project in Japan that was mentioned earlier.



Figure 13.10 fabrication of large-diameter, thick-wall pipe of HR6W (457 mm in diameter with 60 mm thickness) [25].



Figure 13.11 Appearance of HR6W thick-wall pipe [25].



Figure 13.12 HR6W tubes [22].

In the bend processing test of large-diameter pipes (φ 350 mm × t 40 mm), made in MHPS, thick-wall steel pipes of Ni-based alloys (HR6W and Alloy 617) were used. The bending test was conducted using the same method as conventional steel. Specifically, the pipe was heated locally in a circle with a high-frequency induction heater while it was pressed/bent by the roller. Fig. 13.13 is the photograph of bend processing of HR6W large-diameter pipes (bend radius: 4D). After bending, re-solution heat treatment was conducted on the Ni-based alloys (HR6W and Alloy 617) under the same conditions as the original pipe.



Figure 13.13 Induction bend processing of the HR6W large-diameter pipes and final component [24,25].

The material properties were then examined. For each test material, the properties were almost as good as those of the original pipe, thus demonstrating that appropriate post-bending heat treatments can realize properties equivalent to the original pipe.

To verify the developed manufacturing techniques, MHPS also used HR6W to fabricate mock-ups of the superheater outlet header, the reheater outlet header, and the superheater heat transfer tube panel. As components of a 700°C-class A-USC boiler, the outlet header dimensions were determined to be φ 558.8 mm × t 138 mm for the superheater and φ 635 × t 72 mm for the reheater, respectively. The radiation

detection nozzle and the thermometer protection nozzle were also attached to the headers. Fig. 13.14 gives an exterior view of the mock-up of the superheater outlet header and the longitudinal macrostructure of the circumferential welded joint of the central header. There were no welding defects such as cracks in the circumferential weldment with a thickness of 138 mm, indicating the soundness of welded joints. The mock-up fabrication confirmed the practical applicability of the developed welding and bending techniques [29].

Fig. 13.15 compares the creep rupture properties of HR6W large-diameter pipe welded joints with that of the base metal. When also including the data on small-diameter tube joints (which was obtained on occasions other than the national project) in addition to Fig. 13.15, the maximum assessment duration of creep rupture testing

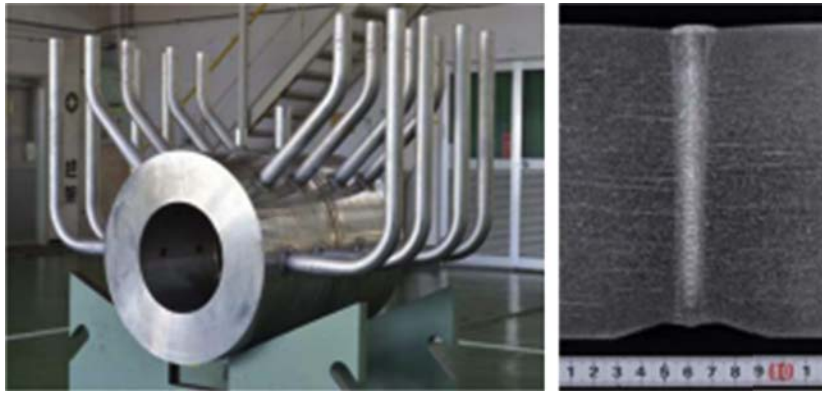


Figure 13.14 Exterior view of the HR6W superheater outlet header mock-up and the longitudinal cross-sectional macrostructure of the circumferential weldment [25].

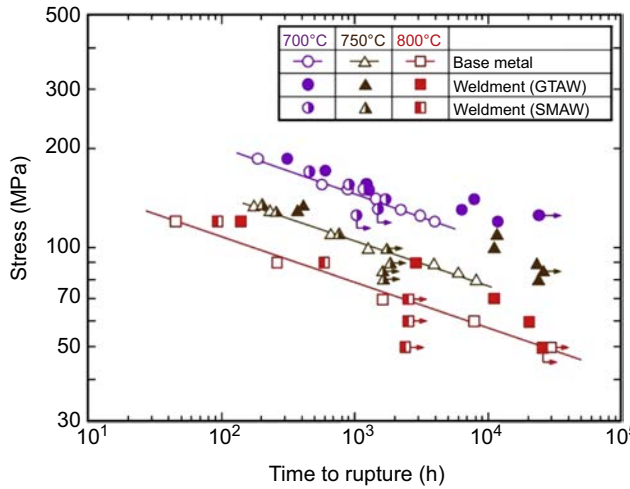


Figure 13.15 Creep rupture properties of the HR6W large-diameter pipe welded joints [25].

reaches 70,000 h [30]. With HR6W, the creep strength of welded joints is as good as or superior to the base metal throughout the temperature range of 700–800°C. According to the extrapolation results of creep rupture data, the 700°C creep rupture strength at 100,000 h is expected to satisfy the target strength of 90 MPa or higher in the national project. The testing is still ongoing to obtain the results of 100,000 h.

13.2.2 HR35

13.2.2.1 Alloy design and properties

The HR35 is a Ni-based alloy (50Ni-30Cr-4W-Ti) that has been developed by NSSM for high-temperature application in boiler of USC and A-USC power plants as thick, large-diameter pipe, like headers, connecting pipe, main and hot reheat steam pipe, or as small-diameter tubes for superheaters/reheaters [26].

In fact, for the main steam pipe of an A-USC boiler, a material superior to HR6W in high-temperature strength is required. To impart to good ductility, thermal fatigue resistance, and formability comparable with those of HR6W for large-diameter, thick-walled boiler pipes, the author and collaborators designed a high-strength Ni-based alloy without applying the precipitation strengthening of the γ′ phase [27].

Fig. 13.16 shows an isothermal section of a Cr-Ni-Fe-7W pseudo-quaternary system at 750°C obtained using Thermo-Calc. When the Cr and Ni content of HR6W

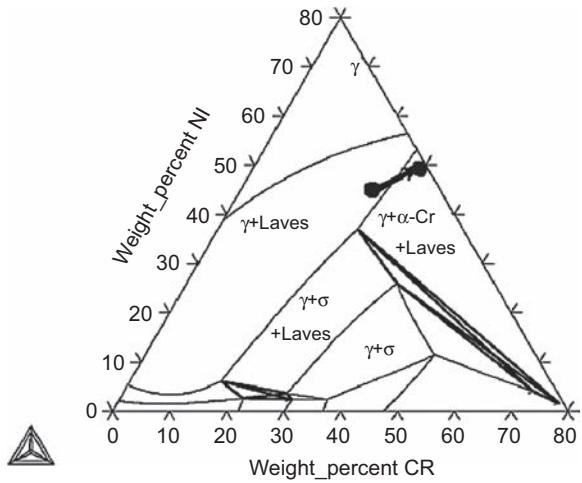


Figure 13.16 Calculated phase diagram of Cr-Ni-Fe-7W system (750°C).

(23Cr-45Ni) are increased further, the α-Cr phase (fine precipitate) stabilizes in addition to the fine Laves phase precipitation. The newly developed HR35 has a base composition of 30Cr-50Ni, and it utilizes the α-Cr phase as the main strengthening phase, which is finely precipitated during creeping. In addition, HR35 is added with 4–6%W and 0.8%Ti to utilize the precipitation strengthening of fine Ni3Ti as well as the α-Cr phase, Laves phase, and $M_{23}C_6$ carbide.

13.2.2.2 *Creep rupture strength, microstructure, and other properties*

Fig. 13.17 shows the microstructure of an extracted replica of an HR35 creep-ruptured grip part (750°C, 127 MPa, 2527 h) observed under a TEM. The rod-shaped precipitates are the α-Cr phase, which has uniformly precipitated finely and densely in the grains. An example of composition analysis using energy dispersive X-ray (EDX) spectroscopy is also shown in the photo. It was found that the α-Cr phase of HR35 contains small amounts of solid solutions of Ni and W.

Fig. 13.18 shows the creep rupture strength of HR35. For HR35, creep rupture data for over a maximum of 20,000 h has already been accumulated, and the results of a long-time test are being evaluated. The average creep rupture strength of Alloy 617 at 700°C (source: ECCC data sheet) is shown by the *dotted line* in the figure.

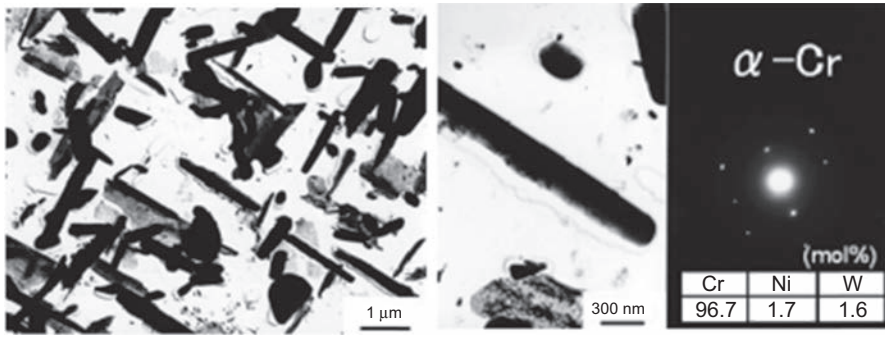


Figure 13.17 TEM microstructures of extracted replica of HR35 after creep rupture (750°C, 127 MPa, 2527 h) [27].

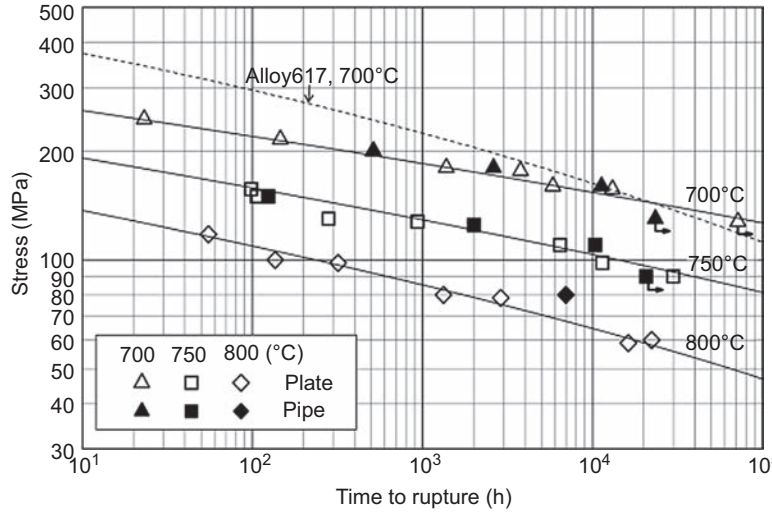


Figure 13.18 Creep rupture strength of HR35 [27].

The 100,000-h average creep rupture strength of HR35 at 700°C is considered to be equal or superior to that of Alloy 617. In addition, the gradient of the stress rupture time curve of HR35 is mild, showing that HR35 has stable creep rupture strength even on the long-time side at 700–800°C. Furthermore, it has been confirmed that the creep rupture ductility of HR35 on the long-time side is quite satisfactory [27].

Fig. 13.19(d) shows an optical micrograph of a long-time creep rupture specimen of HR35 (700°C, 157 MPa, 13,110 h). HR35 showed good microstructural stability without precipitation of the σ-phase and any other embrittlement phase. Fig. 13.19

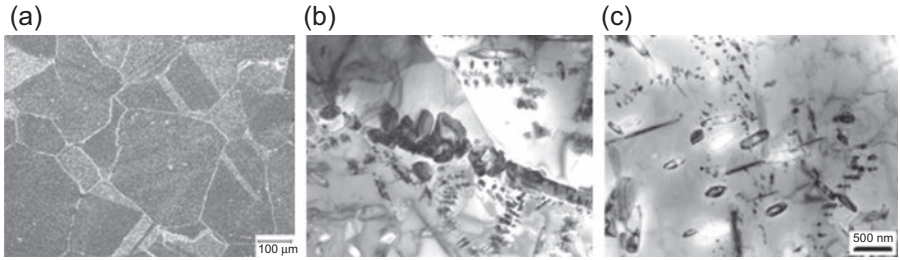


Figure 13.19 Optical and TEM microstructures of HR35 after creep rupture (700°C, 157 MPa, 13,110 h) [27].

contains also thin-film TEM micrographs of a ruptured specimen of HR35: (a) intergranular, (b) transgranular. From these results, and the results of SEM observations, it was found that the grain boundaries were densely covered with precipitates that were mostly identified as $M_{23}C_6$ carbide. Rod-shaped precipitates in the grains were the α-Cr phase, and marked coarsening of the phase was not observed.

Next, to evaluate sensitivity to SR cracking, the author and collaborators carried out an extra-low strain-rate tensile test with the strain rate set at $1.0 \times 10^{-6} s^{-1}$ and evaluated the rupture ductility of HR35. The stress–strain curve at 700°C is shown in Fig. 13.20, while rupture ductility at 600–800°C is shown in Fig. 13.21.

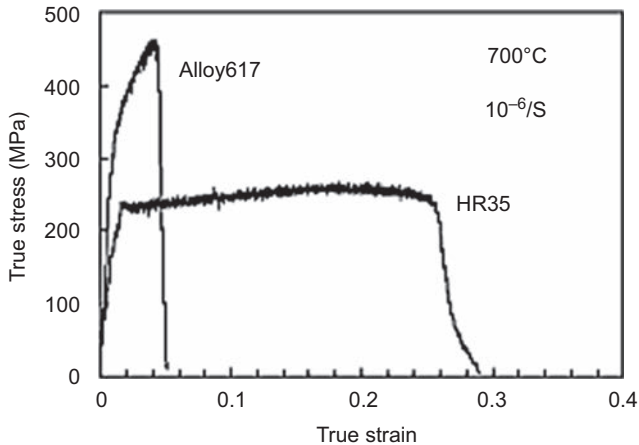


Figure 13.20 S–S curves obtained by extra-low strain-rate tensile tests [27].

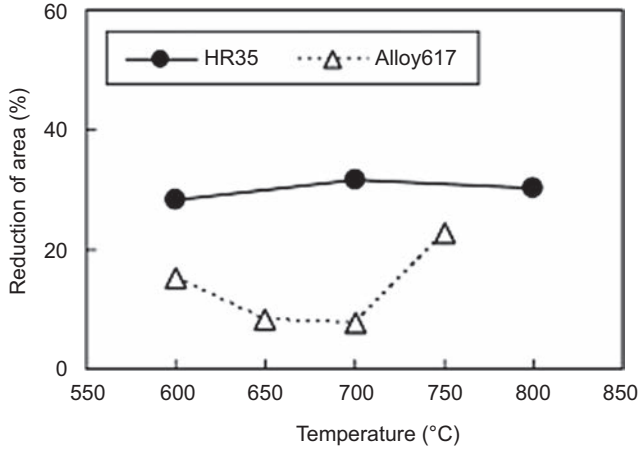


Figure 13.21 Rupture ductility by extra-low strain-rate tensile tests [27].

A marked difference in hot tensile ductility was observed between HR35 and Alloy 617. Compared with Alloy 617, HR35 has much higher ductility, and it is considered to have good resistance to SR cracking.

The hot workability of HR35 is better than that of Alloy 617. A large-diameter, thick-walled HR35 pipe (350 mm in diameter, 40 mm in wall thickness) was successfully manufactured and evaluated (Fig. 13.22), as well as the weldability as shown in the same Fig. 13.22.



Figure 13.22 Appearance of HR35 thick-wall pipe and pipe welding test.
Courtesy of IHI, M. Fukuda, Advanced USC technology development in Japan, in: J. Lecomte-Beckers, Q. Contrepois, T. Beck, B. Kuhn (Eds.), 9th Liege Conference: Materials for Advanced Power Engineering 2010.

It was confirmed that the creep rupture strength of the large-diameter pipe shown in Fig. 13.22 was nearly equal to that of the HR35 plate manufactured in the laboratory. The long-time creep rupture strength of HR35 is being evaluated [10].

13.2.2.3 Creep rupture strength of welded joints

Creep strength should be taken into consideration when designing A-USC boiler piping and headers. In so doing, it is important to examine the creep strength of welded

joints, bends, and welded metals, as well as base metals. Given next are the results of welded joint examinations [26].

With respect to the welded joint of each test material, long-term creep testing is under way to evaluate the creep rupture strength at 100,000 h, which is an indicator of allowable tension stress in boiler materials. As an example, Fig. 13.23 gives the 700°C creep rupture properties of plate welded joints of Ni-based candidate alloys and the

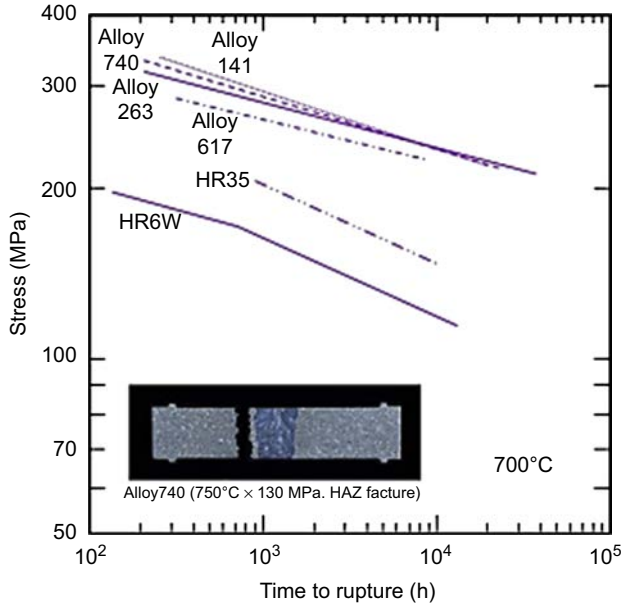


Figure 13.23 Creep rupture properties and the cross-sectional macrostructure of the Ni-based alloy plate welded joints [26].

cross-sectional macrostructure. At 700°C, Alloy 263, Alloy 740, and Alloy 141 are especially superior in creep rupture strength, which are then followed by Alloy 617, HR35, and HR6W in sequence.

When the temperature was further elevated, differences in the strength among the alloys tended to diminish. For Ni-based alloys, there have been no reports about creep strength reduction due to HAZ failure, whose occurrence was reported regarding the welds of high-strength, ferritic, heat-resistant steels. In several types of Ni-based alloys, however, HAZ ruptures occurred in the welds during long-term creep rupture testing, indicating the importance of verification of welded joint strength due to 100,000 h of continuous examination.

13.2.3 Steam and hot corrosion properties

Steam oxidation tests shown that scale is formed on the inner surface of high-temperature heat transfer tubes and piping as a result of the reaction with superheated steam. When heat transfer is prevented by scale formation, the metal temperature increases, accelerating the occurrence of creep damage. The deposition of exfoliated scale may

result in blocked tubes/pipes or steam turbine erosion. When used in A-USC boilers, the Ni-based candidate alloys are supposed to be exposed to temperatures of 700°C or above, which is higher than conventional steel. As these alloys contain more added elements than the currently used austenitic steels, many unclear points of their behavior including the growth rate and properties of scale are still unknown. MHPS therefore examined the steam oxidation properties of Ni-based candidate alloys through laboratory testing in a high-temperature steam environment.

In testing, a test piece was placed in a reaction tube and was exposed to hot steam of a predetermined temperature. An electric furnace was used to produce hot steam by superheating ion-exchanged water in which the dissolved oxygen level is reduced by N_2 gas. The testing was conducted at three different temperatures (700°C, 750°C, and 800°C) with maximum test duration of 10,000 h. After the test completion, the tendency of scale growth was measured as the average cross-sectional thickness of the inner scale layer, whereas scale properties were evaluated by composition analysis. As the steam oxidation properties of the test materials, the average thicknesses of steam oxidation scale (inner layers) after 10,000 h of steam exposure are shown in Fig. 13.24 [31]. In the 700°C or 750°C steam environment, which is similar to that of A-USC boiler components subject to high temperatures, no significant differences were seen in the scale thickness of these Ni-based alloys (approximately 5 μm thick in general), as shown in Fig. 13.25 in comparison with the other competitor materials. When compared with the currently used austenitic steel (25Cr steel or KA-SUS310J1TB), the Ni-based alloys yielded thinner scale and therefore exhibited superior steam oxidation resistance. Although Ni-based alloys (excluding HR6W) yielded slightly thicker

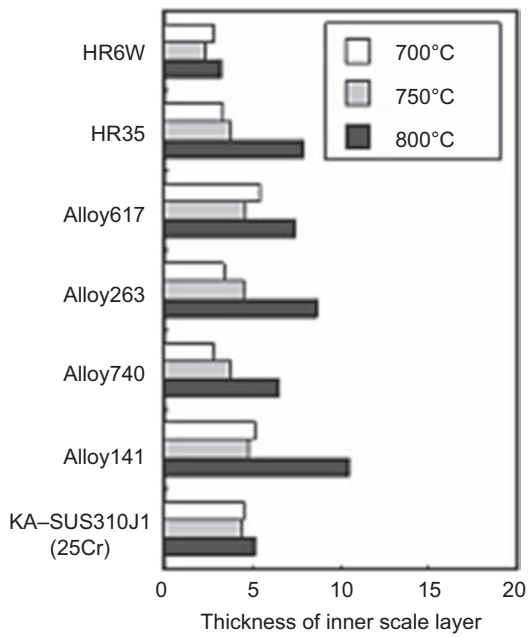


Figure 13.24 Steam oxidation property of HR6W and other superalloys [25].

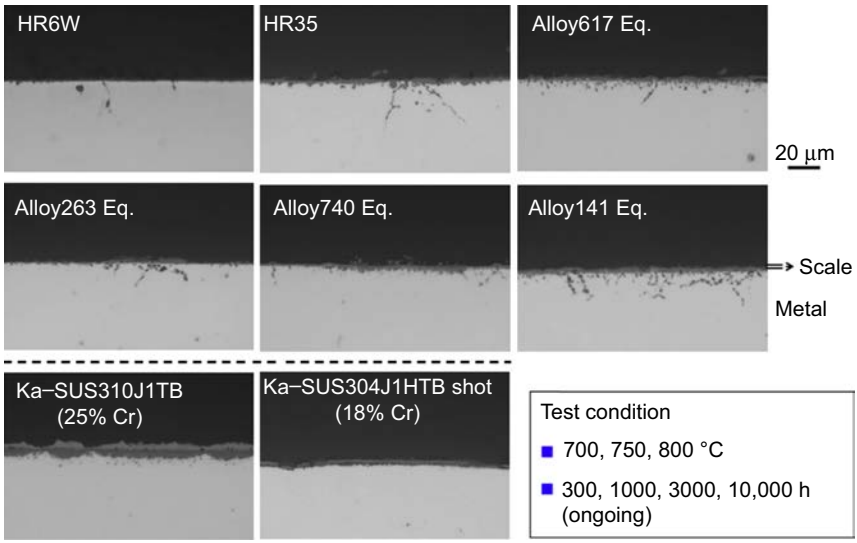


Figure 13.25 HR6W and HR35 steam oxidation tests at 750°C for 3000 h.
Courtesy of Babcock-Hitachi K.K., M. Fukuda, Advanced USC technology development in Japan, in: J. Lecomte-Beckers, Q. Contrepois, T. Beck, B. Kuhn (Eds.), 9th Liege Conference: Materials for Advanced Power Engineering 2010.

scale than 25Cr steel at 800°C for 10,000 h, the thicknesses of the formed layers were approximately 10 μm, which indicates that no practical problems will be caused.

Fig. 13.26 shows the results of a high-temperature (650°C) corrosion test carried out using synthetic coal ash. It can be seen that HR6W is nearly equal in corrosion

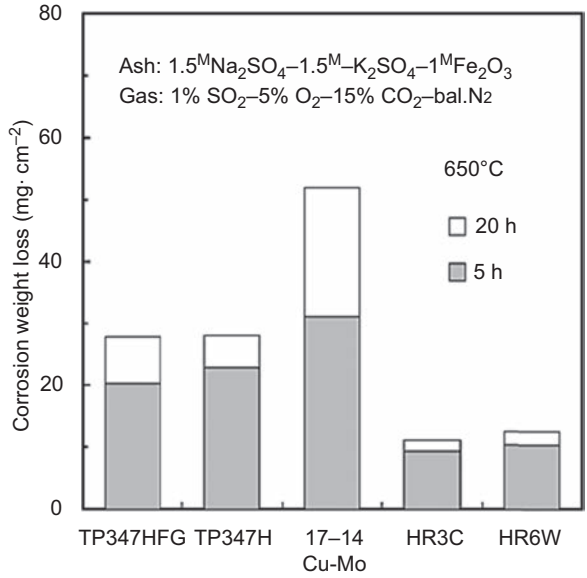


Figure 13.26 Hot corrosion properties of HR6W and other austenitic steels [10].

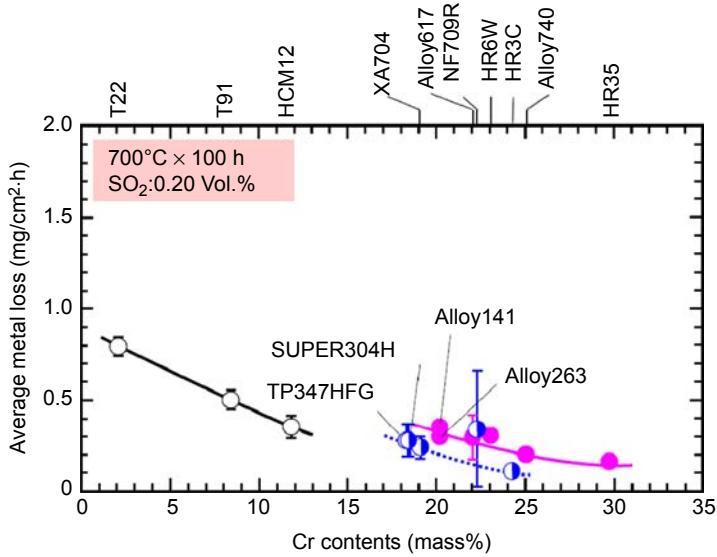


Figure 13.27 Hot corrosion tests on HR6W and HR35.
Courtesy of Mitsubishi Heavy Industries M. Fukuda, Advanced USC technology development in Japan, in: J. Lecomte-Beckers, Q. Contrepois, T. Beck, B. Kuhn (Eds.), 9th Liege Conference: Materials for Advanced Power Engineering 2010.

resistance to HR3C (25Cr-20-Ni-Nb-N), which is widely used for boiler tubes. In Fig. 13.27 a comparison of the results with the competitor materials is presented.

13.2.4 Field testing

To verify the candidate materials and developed manufacturing techniques, we started field testing in May 2015 in cooperation with the Mikawa Power Station of the Sigma Power Ariake in Omuta City, Fukuoka, Japan. In this testing, heat transfer tube panels were attached to the actual boiler. Operation is under way in the 700°C steam environment involving other components such as the header, piping, high-temperature valve, and turbine casing. Inserted into the panels are the A-USC candidate materials (HR6W, HR35, Alloy617, Alloy263, and Alloy740) and the currently used austenitic steels (KA-SUS304J1HTB and KA-SUS310J1TB) for comparison. HR6W is used for the piping test, and the hot bending parts and circumferential welded joints manufactured by our company are also inserted as test materials. The other components included are HR6W high-temperature valves and Alloy 625 turbine casing.

Fig. 13.28 is a photograph of the actual unit with the HR6W pipes inserted. The planned test duration is approximately 10,000 h. After completion, the tubes and pipes will be removed for investigation. The data on corrosion resistance and material properties, which shows the material change with time, will be collected to verify the soundness of A-USC boiler materials.

Along with the field testing, we started developing technologies for creep damage assessment and nondestructive inspection, as maintenance technologies for Ni-based



Figure 13.28 Field testing with the inserted HR6W large-diameter pipes [25].

alloys (candidate materials for use in piping). In the creep damage assessment, the elementary process during the creep of Ni-based alloys and the fracture morphology are examined, and the applicability of existing life assessment methods such as the creep void method and the hardness method is also under examination using materials with creep interrupted. For the nondestructive inspection methodology, on the other hand, we are evaluating the applicability of ultrasonic waves to Ni-based alloys, through which it is difficult for ultrasonic waves to be transmitted. We will keep working on the development of these technologies to make them practically applicable. A new Ni-based alloy with a permissible upper temperature of 800°C (USC800), which exhibits both superior high strength and hot processability, is also under development to make it practically viable [32]. Such development of new materials will give us the capability to satisfy the need for the further elevation of the steam temperature.

HR35 tubes have been also under testing in the HWTI test loop in GKM power plants in Mannheim Germany in two superheaters operating at 635 and 725°C [33].

13.2.5 Conclusion

The nickel-based alloy developed, HR6W (Vd-TÜV559/9, UNS N06674), which is strengthened by Fe_2W-type Laves phase and $M_{23}C_6$, is one of the candidate materials for thick-wall pipe applications.

The stability of long-term creep strength and superior creep rupture ductility have been proven by creep rupture tests of up to 60,000 h at 650–800°C. Various sizes of HR6W thick-wall pipes have been successfully manufactured thanks to good formability. It has also been confirmed that HR6W has a better SR cracking resistance by means of extra-slow strain-rate tensile tests at elevated temperatures. HR6W has been evaluated in the A-USC projects of Europe and Japan as a candidate material for tubes and pipes.

To realize A-USC boilers, which are the key technology for the increased efficiency of coal-firing power generation, we have undertaken research for the practical application of boiler materials. The manufacturing techniques were established, and the properties of long-term creep strength, high-temperature corrosion, and steam oxidation were evaluated. The practical applicability of tested materials has been indicated. With respect to the long-term creep strength, testing will be continued to obtain the creep rupture strength at 100,000 h. Field testing has been carried out since May 2015 to verify the soundness of A-USC boiler materials. MHPS with NSSM will further develop technologies for creep damage assessment and nondestructive inspection for maintenance purposes, aiming to realize the early commercial use of A-USC boilers.

Evaluation of HR6W and HR35 in the METI Project Nippon Steel & Sumitomo Metal has been pressing ahead with research on the practical use of alloy pipes and tubes for A-USC boilers as part of its participation in the project entitled "Development of Component Technologies for Practical Application of Advanced USC Thermal Power Generation," subsidized by Japan's METI. The first five years, from FY 2008 to FY 2012, were devoted to the development of the component technologies. For common test materials, including HR6W and HR35, the company is responsible for the project's focus on the properties of the base metals, while the boiler manufacturers are responsible for its focus on the properties of the joints. For HR6W and HR35, the companies have carried out various evaluation tests for the base metals and welded joints (using the general-purpose welding material for Alloy 617) of plates, large-diameter, thick-walled pipes, and small-diameter tubes.

Both the base metals and the welded joints demonstrate excellent properties for practical uses.

13.3 Superalloys development in MHPS

13.3.1 Alloy design strategy

FENIX700 is an iron-nickel-based alloy with a materials price that is about two-thirds of the typical Ni-based alloys and with an excellent manufacturability for large forged products: therefore a possible material candidate for rotor components.

LTES700R is a Ni-based alloy with a linear expansion coefficient that is at the same range of the high-Cr steel, having an excellent weldability. Therefore it is also a candidate material for forged components, like bolts, blades, and rotors.

USC141 is also a Ni-based alloy having a creep strength for 100,000 h at 700°C estimated about 180 MPa: this material is a candidate for turbine blades, bolts, and superheater tubes.

USC800 is a Ni-based alloy also showing excellent hot forgeability, a creep strength for 100,000 h at 700°C estimated about 270 MPa: this material is a candidate for turbine blades, bolts, and superheater tubes as well as for large piping (header and steam line).

Table 13.3 shows the Ni-based alloys that MHPS plan to use for practical application. It is estimated that these materials will attain the high-temperature creep strength of more than 100 MPa for 100,000 h, which was targeted in the national project

Table 13.3 New Ni-based alloys under development and evaluation

Alloy	C	Ni	Cr	Mo	Co	W	Nb	Al	Ti	Fe
FENIX700	0,01	42	16	–	–	–	2	1,3	1,7	Bal
LTES700R	0,03	Bal.	12	6,2	–	7	–	1,65	1,65	–
USC141	0,03	Bal.	20	10	–	–	–	1,2	1,6	–
USC800	0,04	Bal.	17	6	23	2	–	4	–	–

development [34]. FENIX700 and LTES700R [35] have been used to trial manufacture a 10-ton-class, large forged rotor successfully. In addition, these materials used for the trial manufacture of a roughly Φ1000-mm, large forged rotor resulted in the nondestructive inspection detection dimension of about 2 mm or less. On the other hand, USC141 [37] and USC800 have excellent high-temperature strength and superior hot workability, and they are being verified in many ways for use in blades, bolts, boiler piping, etc.

The long-term creep strength of these materials will be continuously tested to 100,000 h to actually verify the reliability targeted for practical realization.

13.3.2 FENIX700

The FENIX700 has been developed as modification of alloy 706, widely used as material for gas turbine disks [38]. Compared to Alloy 706 (Ni-36Fe-16Cr-3Nb-1.7Ti-0,3Al), FENIX-700 contains less niobium and large amount of aluminum (Table 13.3), and it is strengthened only by γ-prime, without δ and η, as theoretically predicted by Thermo-Calc in Fig. 13.29 [39,40]; it has stability of the microstructure at high temperature and a good manufacturability able to produce large forgings.

Two 10-ton trial forgings were successfully produced by vacuum induction melting (VIM) and ESR remelting and a 14,000-ton hydraulic press. The rotor forgings have been annealed at 980°C followed by two steps aging at 840°C and 730°C. The final products (Fig. 13.30) have ASTM grain size range respectively of 0.5–1.3 and 2–3; the minimum detectable flaw size have been evaluated as 3.7–4.8 and 1.6–1.9 mm. These differences in grain size and detectability are due to the change in forging parameters: the second rotor was finished at 50°C lower than the first one, and also the forging ratio was increased.

The γ-prime particle sizes are quite homogeneous and in the range of 60–90 nm, as shown in Fig. 13.31. Also the tensile, impact, and ductility properties are very similar in the different zones.

Fig. 13.32 shows the results of impact and tensile test of aged samples at 700°C up to 3000 h, compared with the 706 reference alloy.

The creep properties are shown in Fig. 13.33: the difference in the creep behaviors can be attributed to the difference in γ-prime size; it is also possible to observe a good relationship between laboratory- and industrial-forged components. The forecast for stress to have rupture at 700°C in 100,000 h is higher than 100 MPa.

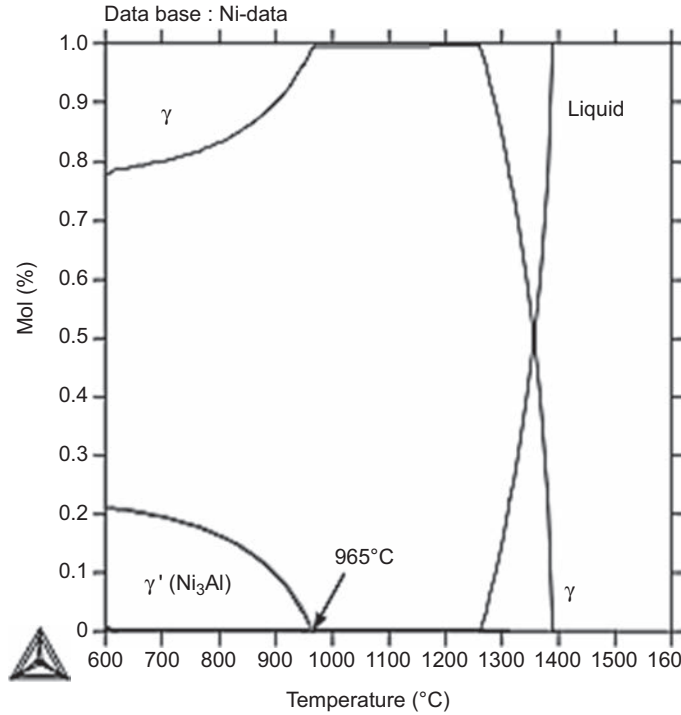


Figure 13.29 Phase fractions of FENIX-700 computed by Thermo-Calc [39,40].

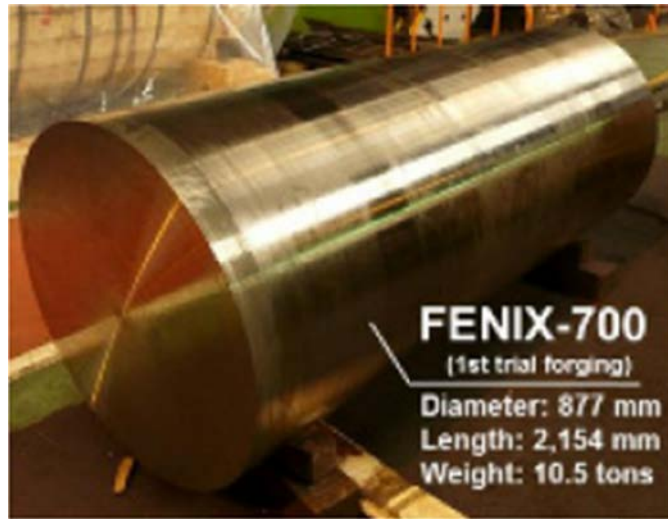


Figure 13.30 FENIX-700 first trial forging [41].

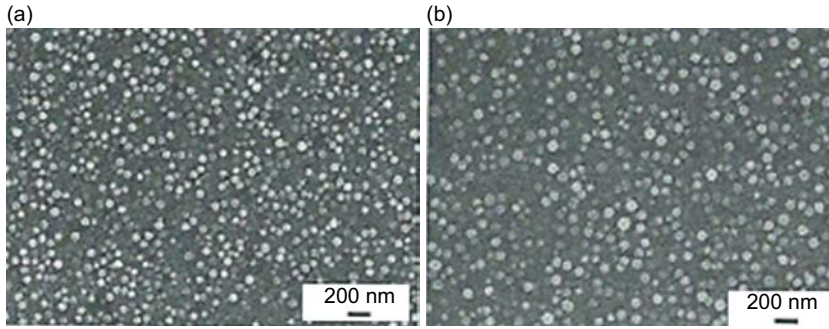


Figure 13.31 FE-SEM micrographs of γ-prime particles in two different positions: (a) 62 nm; (b) 92 nm [38].

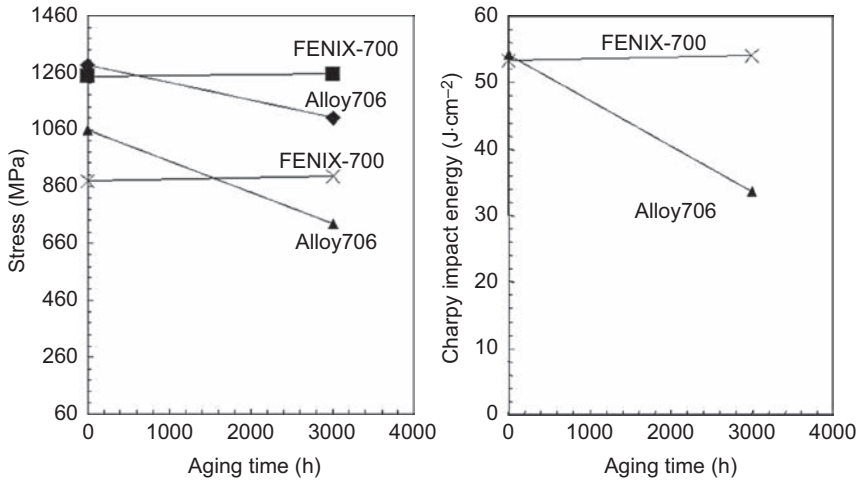


Figure 13.32 Impact and tensile tests results of aged samples at 700°C up to 3000 h [42].

13.3.3 LTES700R

This alloy has been developed for forged components that need a low thermal expansion coefficient (CTE), comparable with 12% Cr steels, and good high-temperature strength. The alloy design was made starting from Refractaloy 26, increasing the Mo and Al contents, to obtain precipitation of γ-prime [Ni_3(Al,Ti)] and to prevent the formation of Laves phase, through the optimization of W and Mo content, as shown in Table 13.3 [35].

The precipitation hardening is obtained in the range 725–775°C (Fig. 13.34), and the hardness is stable up to 120 h (Fig. 13.35). The mean CTE from RT to 800°C is show in Fig. 13.36 and compared with low- and high-Cr steels and Refractaloy 26.

The microstructure after double aging is presented in Fig. 13.37: the optical picture (a) shows blocky precipitates of retained eta carbides, M_6C, undissolved in the

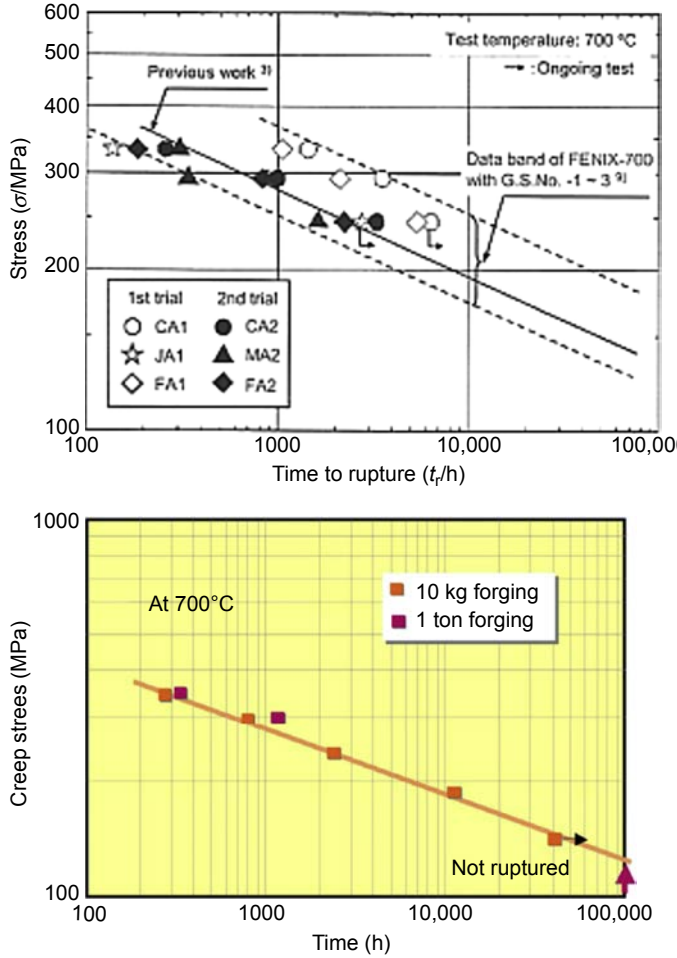


Figure 13.33 Creep stress–time to rupture curve of trial forgings in different positions and the comparison with the laboratory forging [38,39].

solution treatment; the precipitation of alpha-W phase is not confirmed. TEM image shows densely populated γ-prime phases that have spherical shape; the precipitation of Laves phase is not confirmed.

Regarding the mechanical properties, LTES700R alloy has a 0.2% proof strength at RT similar to 12% Cr steel, but higher at tensile strength at high temperature and better ductility.

The creep properties, shown in Fig. 13.38 as a Larson–Miller plot, are about 100°C higher than 12% Cr: with a forecast of above 98 MPa at 700°C, that is the target for the A-USC turbine rotor material.

The new superalloy, LTES700R, with low thermal expansion could be suitable for large components like turbine rotors, especially weld rotors for A-USC turbines, and it is planned to conduct a trial forging to study castability and forgeability. Fig. 13.39 shows the welded trial rotor made by LETS700R alloy.

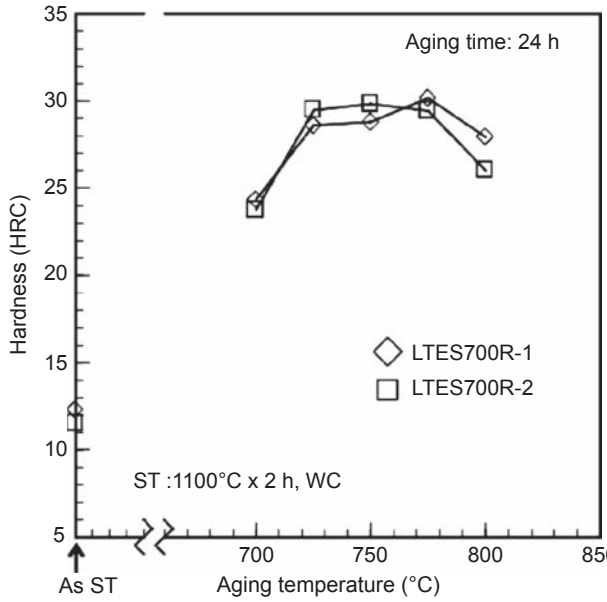


Figure 13.34 The effect of aging temperature on hardness [35].

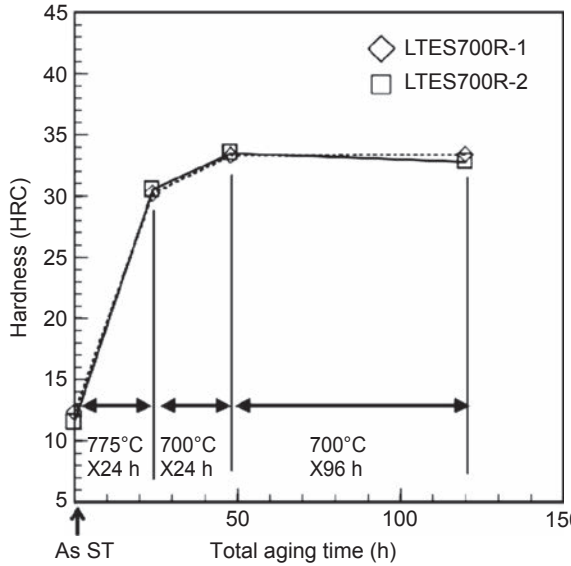


Figure 13.35 The effect of aging time on hardness [35].

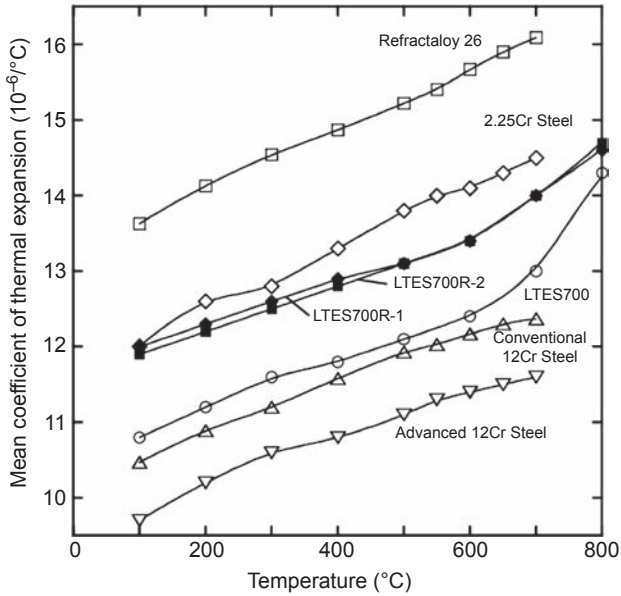


Figure 13.36 Mean CTE of alloy LTE700R and conventional steels and alloys for steam turbines [35].

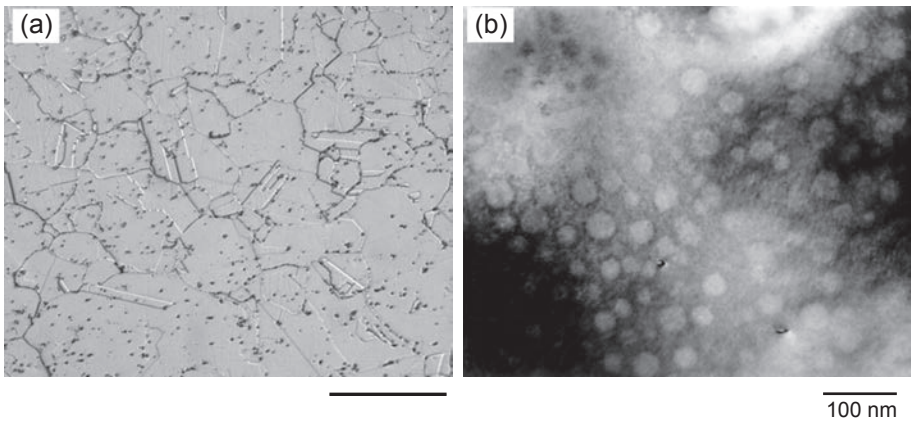


Figure 13.37 Microstructure of double-aged alloy LTES700R: (a) optical microscope and (b) TEM [35].

13.3.4 USC141

The USC141 is a low thermal expansion precipitation strengthening Ni-based superalloy with chemical composition reported in Table 13.3. The alloy design started with the base of Alloy 252 (Ni-9,7Mo-18Cr-10Co-1.1Al-2.7Ti), eliminating the expensive Co and optimizing the Al and Ti contents. The results can be summarized in Fig. 13.40, jointly with USC800: the γ-prime stability is similar to the alloy 263 [44].

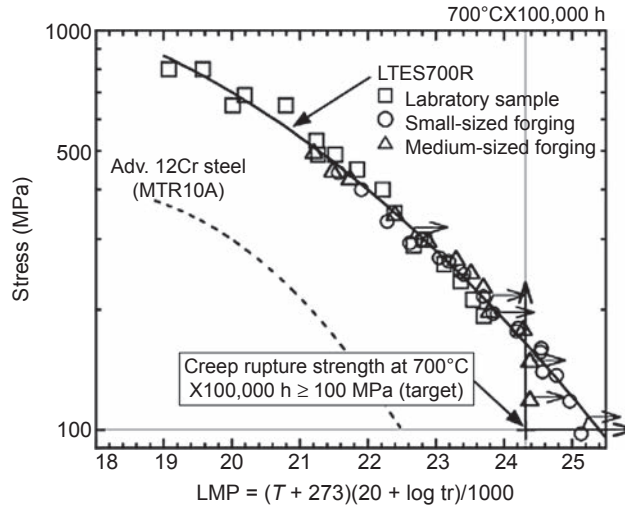


Figure 13.38 Creep rupture strength of alloy LTES700R and advanced 12Cr steel [36].

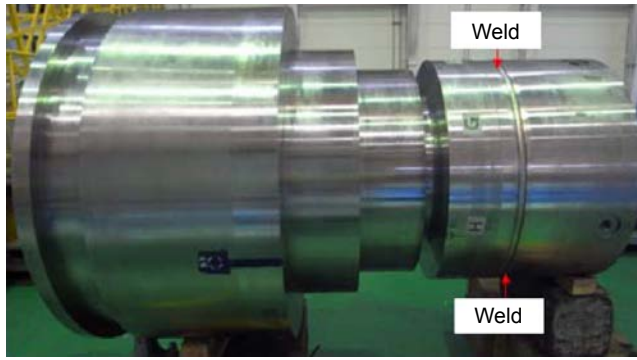


Figure 13.39 LTES700R welded rotor [33].

The USC141 is usually solution treated and then aged to increase high-temperature strength for turbine blades and bolts applications. On the other hand, this alloy seems to be only solution treated, to have low hardness, for application in boiler tubes that usually are joined by welding and bent by cold working.

The microstructure of the initial bar as solution treated at 1066°C for 4 h is shown in Fig. 13.41 by light microscopy and FE-EPMA: the grain size is 5.5 ASTM, without precipitation of carbides and metallic compound along the austenite grain boundaries. Just some undissolved carbides are present and no γ-prime particles. After two-step aging treatment carried out at 850°C for 4 h followed by air cooling and then by second aging at 760°C for 16 h with air cooling up to room temperature, $M_{23}C_6$ carbides are observed along the austenite grain and a large amount of small γ′ in the grain, as shown in Fig. 13.42.

Fig. 13.43(a) shows the results of the creep tests of USC141 bar material in solution-treated condition and after two-step aging (Ag): the results at temperature over

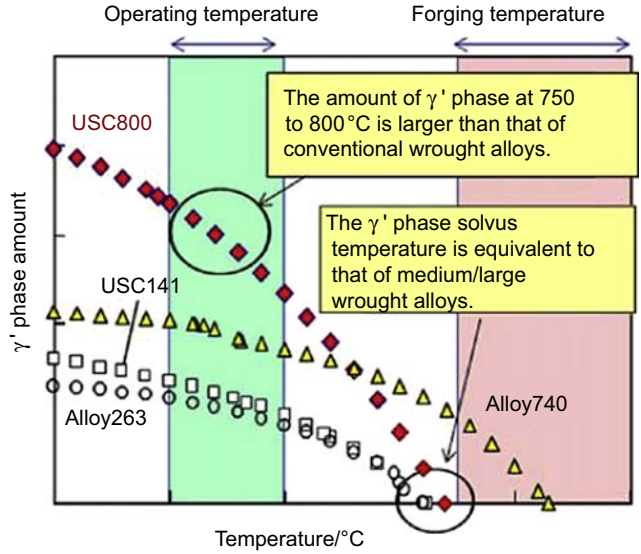


Figure 13.40 Metallurgical feature of USC141 and USC800 [6].

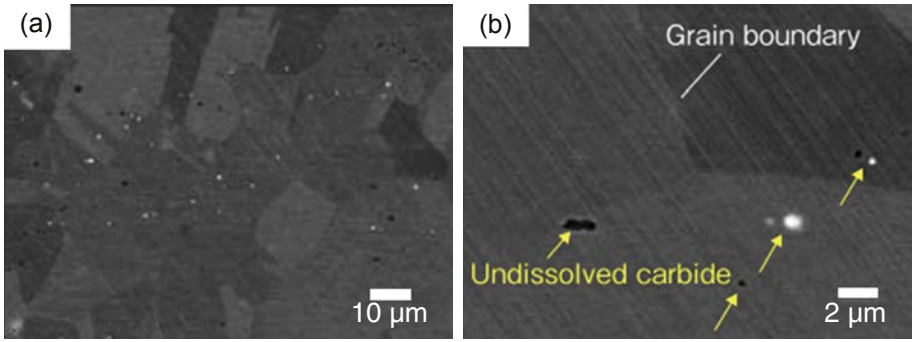


Figure 13.41 FE-EPMA, backscattered electron images in solution treated: (a) low magnification, (b) high magnification [43].

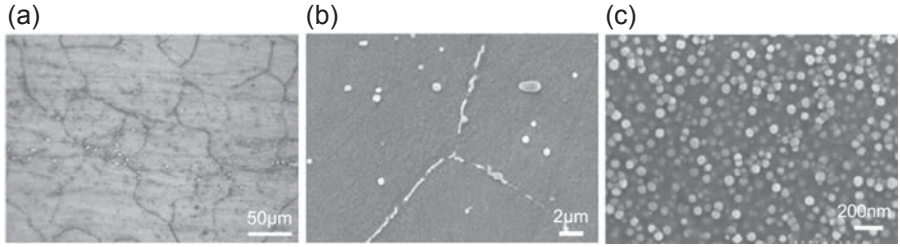


Figure 13.42 Microstructure of USC141 after two-step aging: (a) optical microstructure, (b) SEM image of grain boundary, (c) SEM image of γ′ in the grain [44].

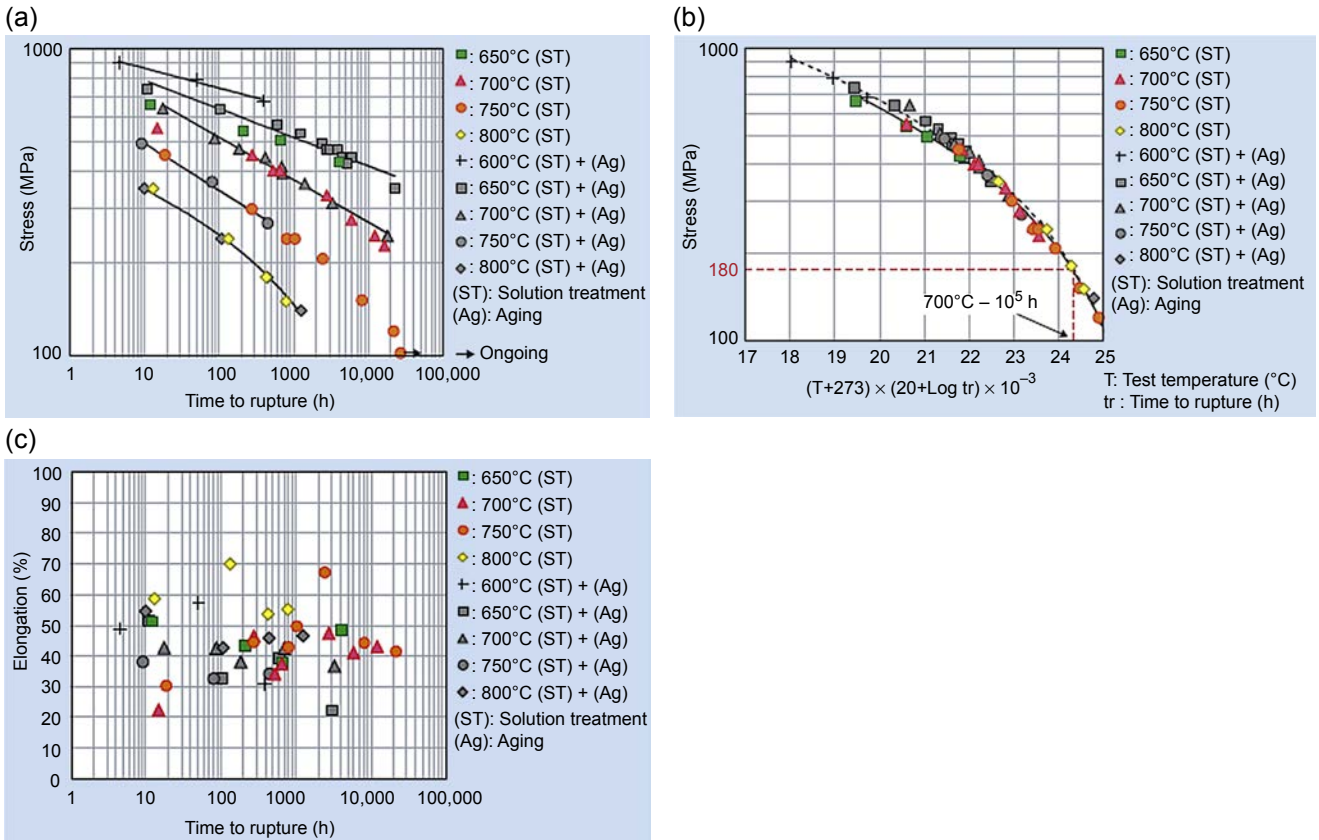


Figure 13.43 Creep rupture strength of USC141 in solution treated and after aging: (a) creep rupture strength as a function of rupture time, (b) creep rupture strength as a function of Larson–Miller parameter, and (c) creep rupture elongation as a function of rupture time [43].

700°C are almost the same due to the precipitation of γ′during the tests. In Fig. 13.43(b), all the data are plotted as a function of Larson–Miller parameter, and the creep strength at 700°C for 100,000 h is estimated as 180 MPa. Fig. 13.43(c) shows a quite good elongation in creep rupture at all the temperatures and treatment conditions.

The evolution of the γ′ precipitates in the austenite grain in USC141 bar material in solution-treated condition is presented in Fig. 13.44 as a function of temperatures and creep test durations. As previously discussed the γ′ phase is not present in as treated condition, and γ′ particles precipitated and grew during tests. The mean radius of γ′ particles was measured by image analyses of SEM micrographs and was plotted in Fig. 13.43(d) as function of the third of the root of the creep rupture time showing with linear relationship. Consequently, it can be seen that the growth of γ′ particles of USC141 bar as solution treated during creep test is in the stage of Ostwald ripening.

Fig. 13.45 shows the SEM microstructure around the austenite grain boundaries after creep rupture tests at 700°C and 750°C of USC141 bar as solution treated. Precipitates particles appear at the austenite grain boundaries: these phases were predicted by JMatPro as shown in Fig. 13.46. The equilibrium phases diagram shows that in the range 700–800°C also $M_{23}C_6$, μ-phase, and M_6C are present in this alloy. Experimental confirmation has been obtained by backscattered electron images and EPMA element map of C, Cr, Mo, Ti, and Al (Fig. 13.47) in a sample after creep rupture at 700°C and 16.385 h. Three phases were observed: white in μ-phase Ni_7Mo_6 enriched in Mo, black is $M_{23}C_6$ reach in C and Cr, and gray phase in the grain is γ′ because of enriched Al and Ti. The white phase has been also observed by TEM analyses (Fig. 13.48) as the electron beam diffraction pattern and the dark field image. The chemical composition analyzed by EDS shows a content of Ni, Cr, and Mo in good agreement with the theoretical value.

The microstructure of the tubular products is shown in Fig. 13.49, and it is similar to the bar material, with a small amount of $M_{23}C_6$ at the grain boundaries and without segregation of undissolved carbides: the ASTM grain size is about 2–3. The creep properties of the tube compared with the bar materials are presented in Fig. 13.50: it is possible to observe that the tube creep behaviors are better than bar material due to the lager grain size. Therefore the estimation of the creep rupture strength at 700°C is increased to 10 MPa. Longer creep tests are still running to confirm the behaviors.

13.3.5 USC800

The USC800 was developed to target the manufacture of A-USC turbine rotors, the weight of which is expected to exceed 10 tons. In fact a lot of high-strength superalloys for aircraft or industrial gas turbines have been developed up to now, but it is difficult to manufacture the large-scale parts due to their poor manufacturability.

This new Ni-base superalloy has been tailored by alloy design procedure using thermodynamic calculation to optimize the chemical composition, reported in Table 13.3, and produced in trial small-scale ingot manufacture to verify the forgeability (Fig. 13.40) over 1000°C, where γ′ is dissolving, and verified as strengthening in the scheduled operating condition (700–800°C).

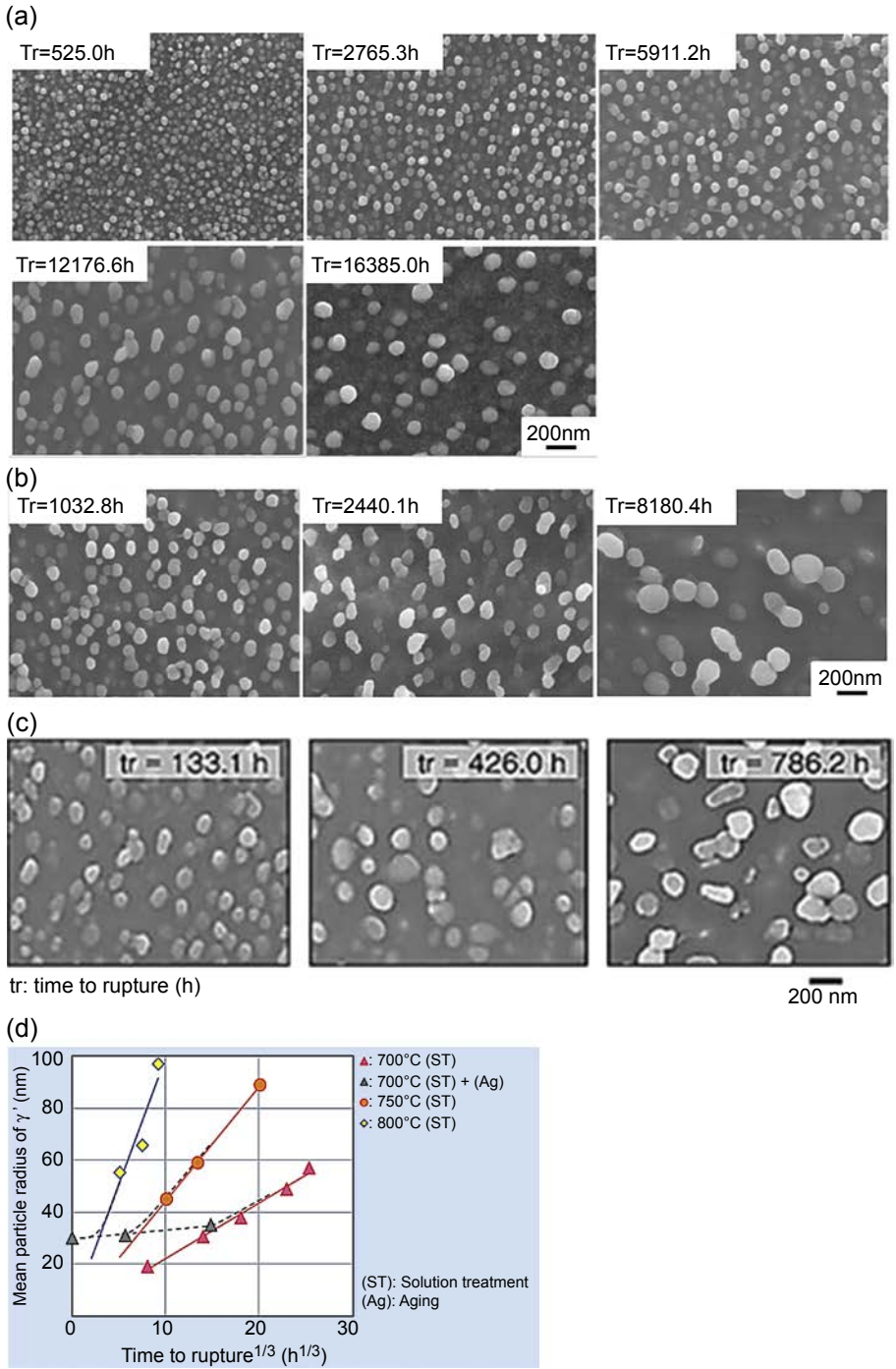


Figure 13.44 SEM images of γ′ particles after creep rupture test in solution-treated test temperature (a) 700°; (b) 750°; (c) 800°; (d) correlation between mean radius of γ′ particles and creep rupture life in solution treated [43,44].

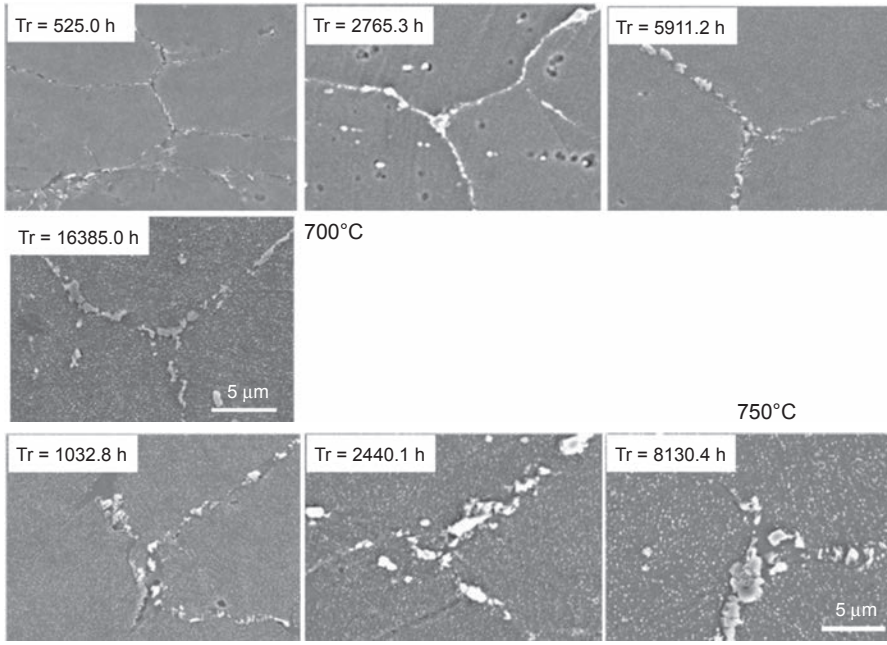


Figure 13.45 SEM images of γ′ particles in austenite grains USC141 bar as solution treated after creep tests at 700°C and 750°C [41].

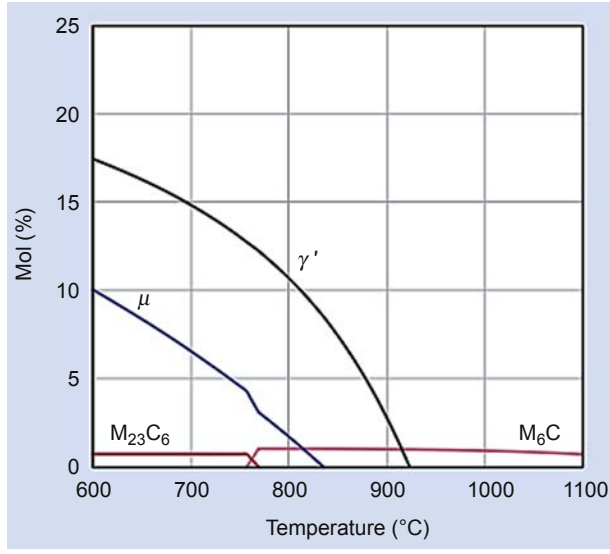


Figure 13.46 Equilibrium calculation of USC141 by JMatPro [43].

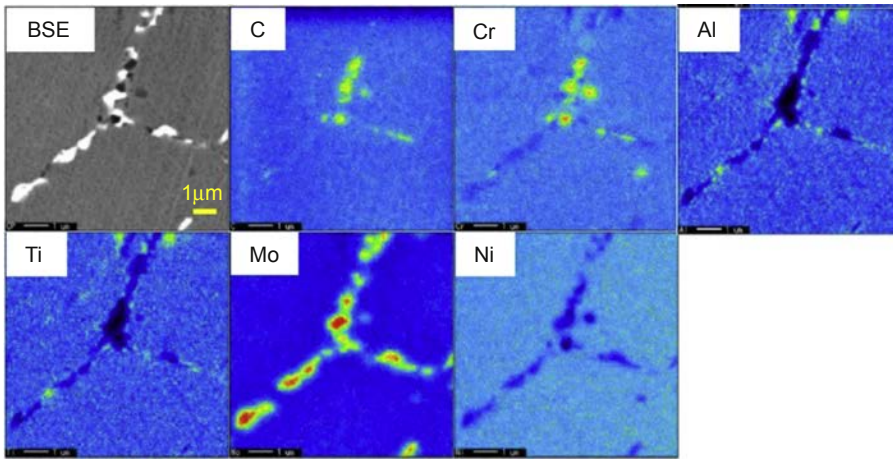
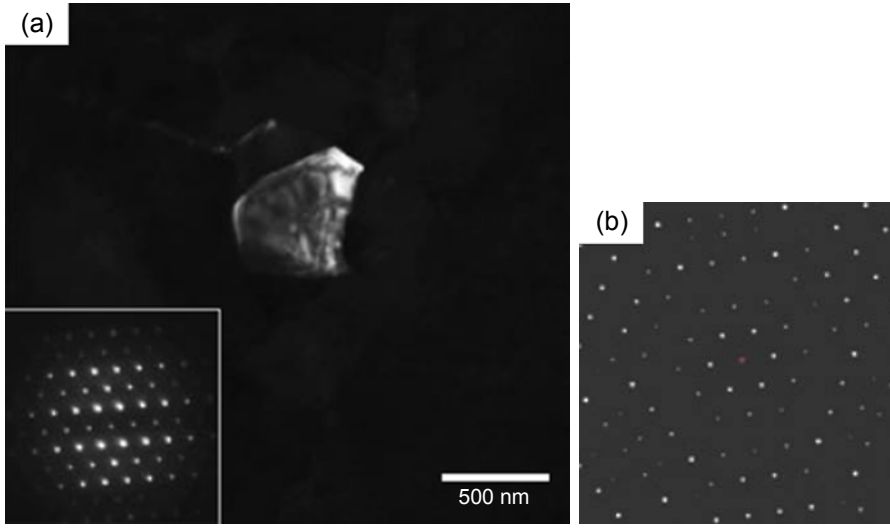


Figure 13.47 FE-EPMA, backscattered electron image and elemental map images after creep rupture test at 700°C in solution treated [43].



(c)

(at%)

Evaluation contents	Ni	Cr	Mo
EDX analysis of Mo compound	34.5	18.0	47.5
Equilibrium calculation of μ phase by JMatPro	29.4	22.9	47.7

Figure 13.48 TEM analysis of Mo compound: (a) dark field image and [001] zone axis SAD pattern; (b) [001] zone axis SAD pattern of μ phase-Fe_7W_6 (simulation), (c) EDX analysis of Mo compound and equilibrium calculation of μ phase by JMatPro [43].

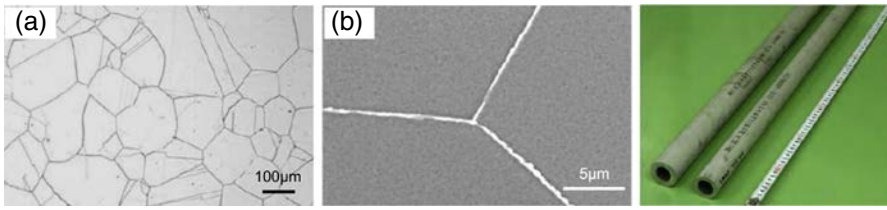


Figure 13.49 Microstructure of USC141 tube (OD44.5×10 mm): (a) optical microstructure, (b) SEM image of grain boundaries [44]; Appearance of USC141 trial tube (OD38.1×8.3 mm) [43].

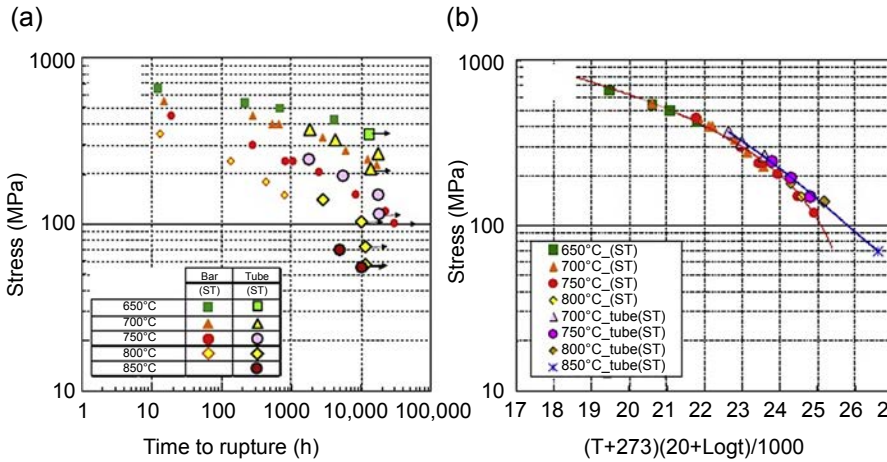


Figure 13.50 Creep rupture strength of USC141 tube compared with bar material as solution treated [41].

Fig. 13.51 shows the optical micrographs of the round bar after forging and heat treatment. The microstructure in part D is coarser than in A. There are some precipitate reach areas (dark contrast) in all the positions of the specimens: these particles in the grains are Cr- and Mo-rich carbides, as shown in Fig. 13.52.

Scaling up to industrial size, the production route was made by primary melting of a 6-ton ingot in VIM, used as an electrode for vacuum arc remelting (VAR). The 800-mm diameter VAR ingot weighing about 6 ton was forged and heat treated at 1100°C/6 h, 900°C/24 h, and 700°C/16 h after forging: Fig. 13.53 shows the ingot before forging and after forging (3 ton) as an octagonal bar with 450 mm diameter and 2.500 mm length. The bar was controlled by US testing, and no defects were detected.

Fig. 13.54 shows the welded cylindrical specimens machined from the bar and the aspect of the tubes produced.

In Fig. 13.55 the results obtained in the creep and low-cycle fatigue tests on USC800 are presented, compared with the USC141 and the 617 and 263 alloys. The USC800 is reaching 100 MPa for rupture at 100,000 h at 800°C and 250 MPa for 700°C: the creep strength is about twice of 617 and 263 alloys. Moreover, it has a low-cycle fatigue life of 5–10 times longer than that of alloy 263 widely used in gas turbines. It is found that

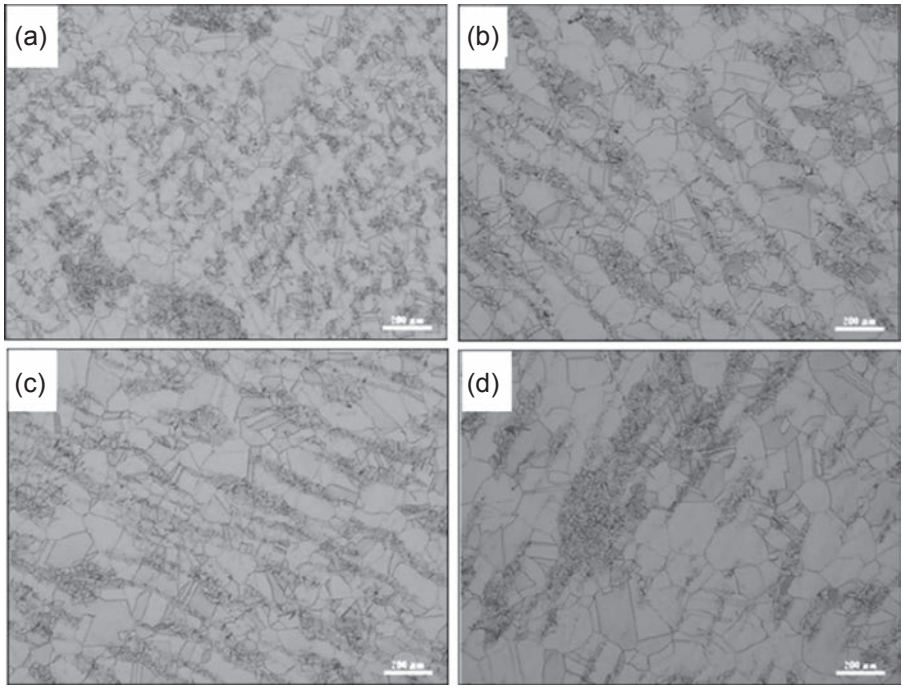


Figure 13.51 Microstructure after forging and heat treatment [32].

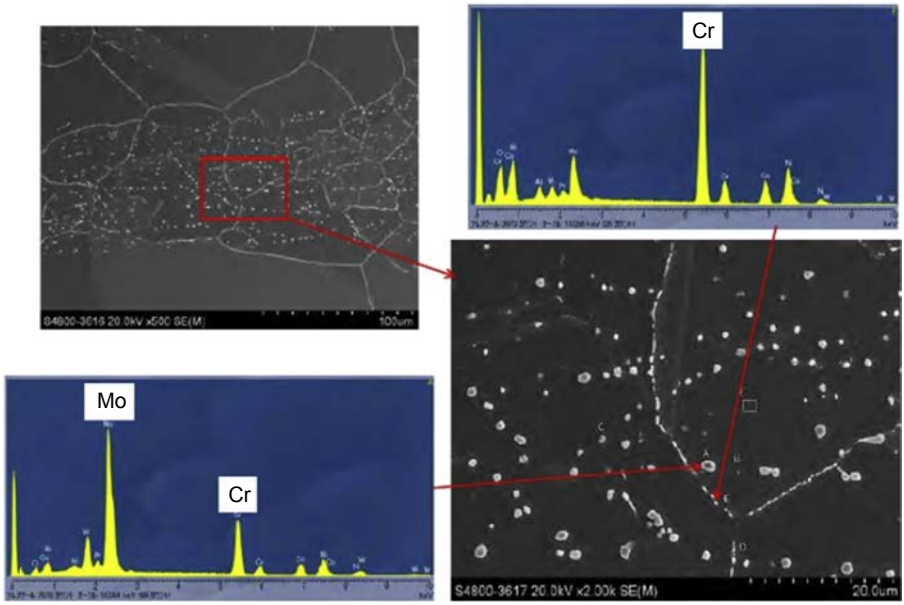


Figure 13.52 SEM micrographs after forging and heat treatment [31].

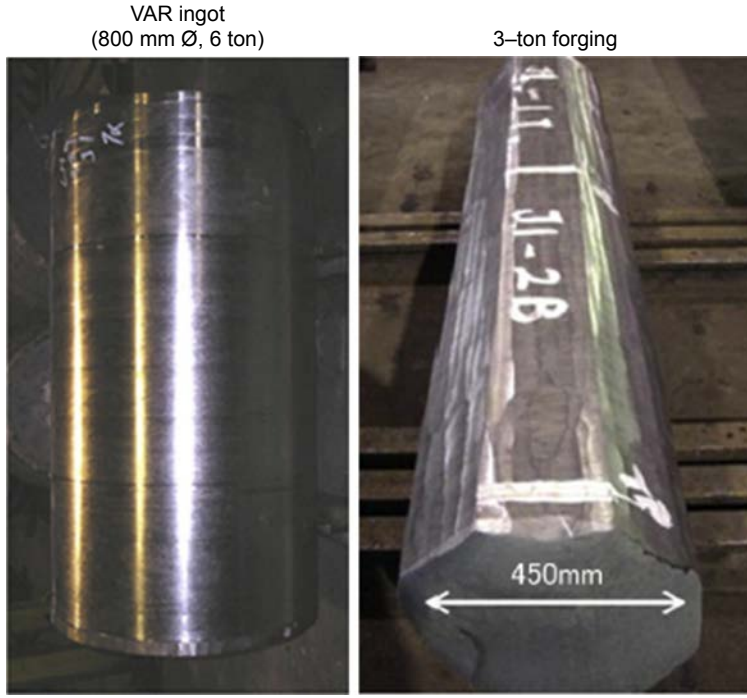


Figure 13.53 Trial manufacturing results of USC800 [6].

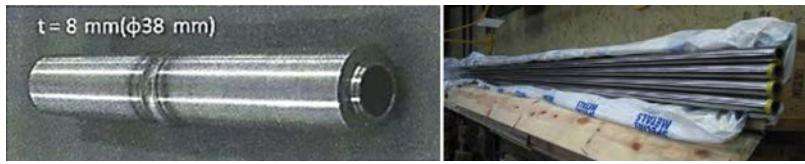


Figure 13.54 38-mm cylindrical machined-welded specimens and 50×8 mm tubes for boiler [31].

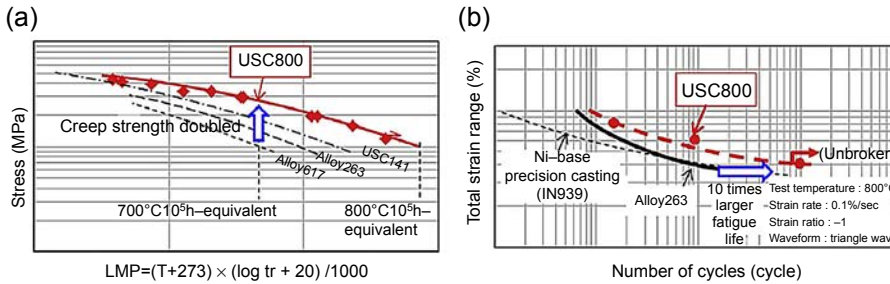


Figure 13.55 Creep and low-cycle fatigue properties of USC800 [6].

die forging, pipes, tubes, bolts, sheets, bars, and wires can be easily formed from the trial manufactured forging, proving the applicability of such forged material not only to steam turbine, but also for various components in the A-USC thermal power plants.

Fig. 13.56 shows outlines of the turbine rotation test facility and the rotor structure. This facility features the capability of simulating a 700°C or higher temperature field using heat radiated from the heater and a driving motor capable of long-term testing at the rated rotation of 3600 rpm in a vacuum. During this test, the highest stress occurs at the turbine blade root, but it will not be exposed to a temperature as high as 700°C in actual operation. Therefore the life evaluation is an acceleration test against actual operation.

As a result, no problems were found in the nondestructive inspection of the materials and welds, and the soundness was verified. In the future, MHPS will manufacture turbine blades that are being developed simultaneously with the welded rotor to complete a

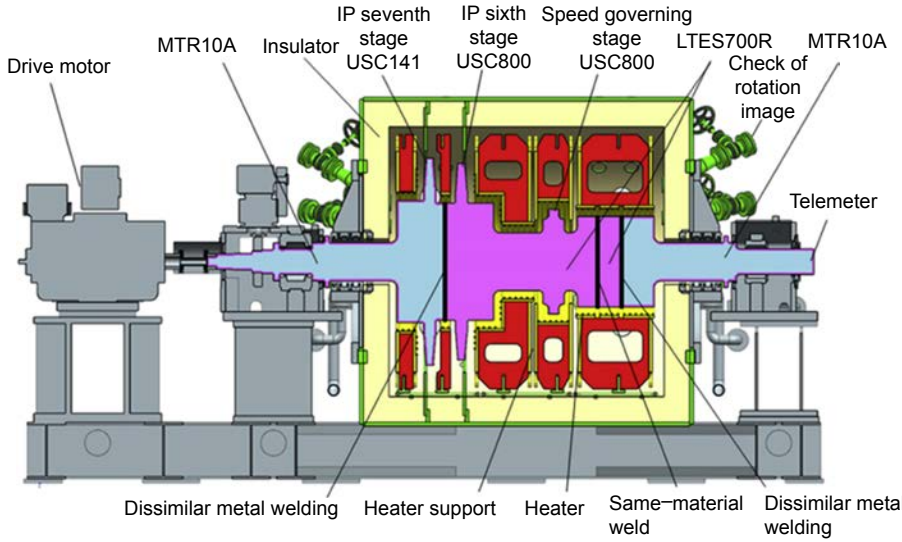


Figure 13.56 Rotor test facility and structure for rotation test [33].

rotation test rotor, and they will implement a verification test in 2016. After the soundness of the material and the welded rotor is verified, MHPS will proceed with the practical application of the A-USC technology.

13.4 TOS1X

13.4.1 Toshiba alloy design strategy

TOS1X is an alloy with improved the creep rupture strength of Alloy 617. Alloy 617 is relatively good candidate for A-USC turbine rotors. This alloy has good weldability and forgeability. But creep rupture strength is not enough for our target [45].

TOS1X is similar to Alloy 617 but contains more Al (1.6%) and Ta and Nb to enhance creep rupture strength.

TOS1X-II is similar to TOS1X but contains less Cr, and Al is decreased from 1.6% to 1.25%, and Ti is increased from 0.3% to 1.35%, adding tantalum (Ta) and niobium (Nb) for enhancing precipitation hardening due to γ' [45,46] formation retarding the precipitation of the undesirable σ phase [47]: the result is a further creep strength improvement and establishing an even stronger alloy with good forgeability and weldability.

The chemical compositions of these alloys are summarized in Table 13.4.

Table 13.4 Chemical composition of TOS1X alloy (wt%) [45]

Alloy	Ni	C	Cr	Al	Ti	Mo	Co	Ta	Nb
617	Bal.	0.05–0.15	20–24	0.8–1.5	<0.6	8–10	10–15	–	–
TOS1X	Bal.	0.05	23	1.6	0.3	9	12.5	0.1	0.3
TOS1X-II	Bal.	0.07	18	1.25	1.35	9	12.5	0.1	0.3

13.4.2 TOS1X

TOS1X was developed from Alloy 617 by Toshiba, targeting a 100,000 h creep rupture strength at 700°C to be around 150 MPa.

A 1000-mm diameter piece of forged material weighing 7 tons has been made successfully. Larger forged material will be made next year. A model rotor with a weight of 7 tons was manufactured using the TOS1X by double-melt process (VIM and ESR) and forging (Fig. 13.57). The model rotor has neither forging crack nor segregation (Fig. 13.58). The yield and tensile strength of the model rotor were the increase of about 10% of Inconel 617. The 700°C/10^5 h creep rupture strength of the model rotor was 160 MPa or more (Fig. 13.59).

The creep behavior of the TOS1X trial and rotor forged materials Fig. 13.60 shows a significant improvement of the creep strength in comparison with the alloy 617 and the rotor steels.

13.4.3 TOS1X-2

TOS1X-2 is a further development of TOS1X with lower content of Cr and a different balance of Al and Ti as shown in Table 13.4. With these modification in the chemistry, it is possible to reduce the presence of σ phase, as shown in Fig. 13.61 presenting the pseudoternary phase diagram of Inconel alloy 617 at 750°C computed by Thermo-Calc. The phase diagrams describe the relation of Al and Ti content and equilibrium phase. In case of 23 mass% Cr content, which is the same level as typical Inconel alloy 617, γ' phase must coexist with σ phase on any composition. On the other hand, it seems to be avoidable of the σ phase precipitation in case of 18 mass% Cr content. The phase diagrams show the decrease of Cr content is effective way for the σ phase inhibition.

Based on these calculations, some experimental heats have been produced and tested to select the optimized chemistry (Table 13.4).

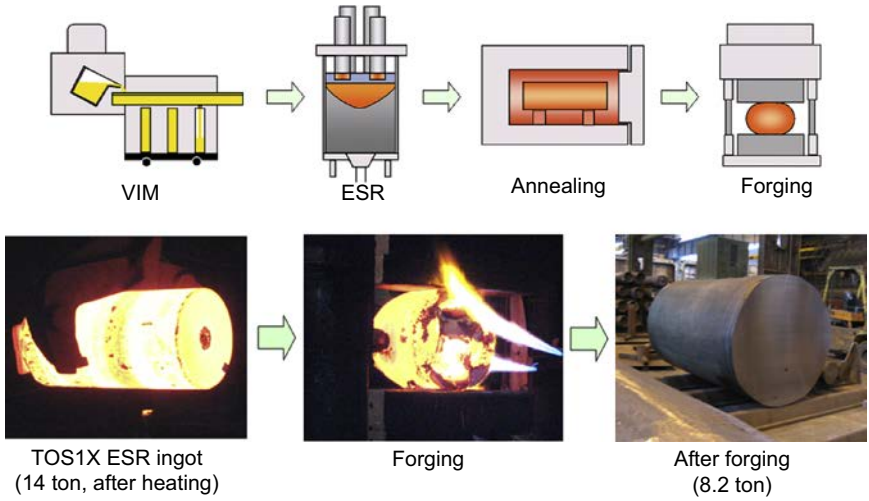


Figure 13.57 TOS1X trial forging (NEDO Project) [49].

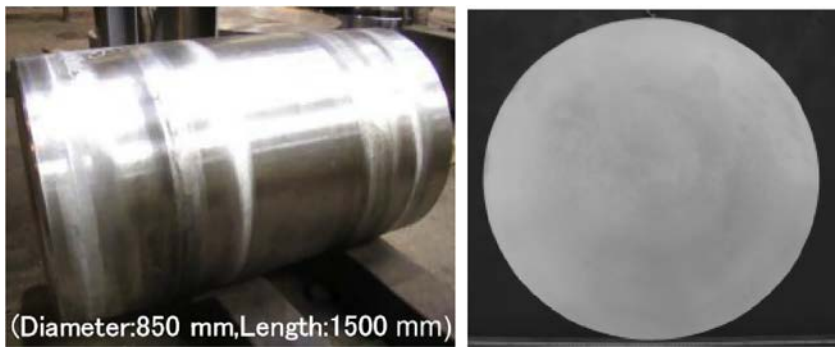


Figure 13.58 TOS1x 7-ton model rotor and cross-sectional macrostructure of "TOS1X" [48].



Figure 13.59 First trial forging for TOS1X was completed [49].

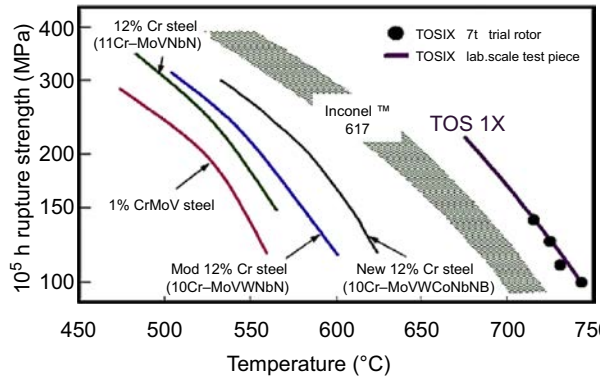


Figure 13.60 Creep rupture strength of TOS1X trial rotor [48].

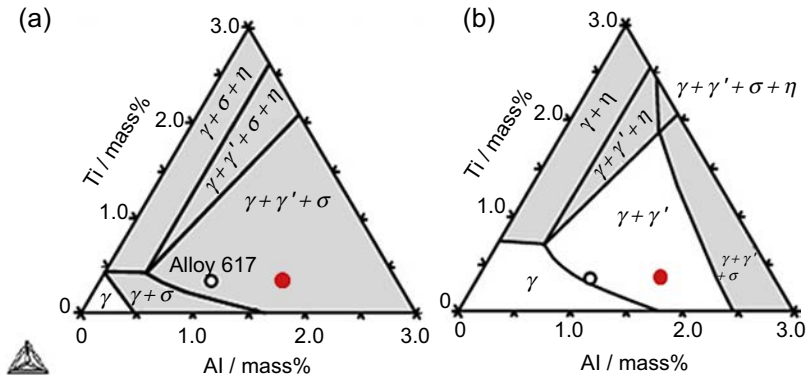


Figure 13.61 Computed pseudoternary phase diagram of Inconel Alloy 617 at 750°C. (a) 23 mass% Cr, (b) 18 mass% Cr [50,52].

In Fig. 13.62 the microstructure of the TOS1X-2 is compared with those of alloy 617, confirming the higher amount of γ′ phase. In the same figure is presented the Time-Temperature-Precipitation diagram in which $M_{23}C_6$, M_6C, and γ′ can be found: the nose seems to be in the range of 750–800°C where remarkable increase of hardness occurs in a short time.

Fig. 13.63 show the microstructure of the trial rotor in different positions: core, 1/2R, and surface.

Fig. 13.64 shows creep tests results of TOS1X-2 50 kg lab-scale material. The longest data of creep rupture test is about 12,000 h; a much longer test is now in progress. Creep strength of TOS1X-2 is much higher than that of Inconel alloy 617 and TOS1X-1. TOS1X-2 is expected to have enough creep strength for 750°C class A-USC turbine rotor material.

After the trial test, Saarschmiede manufactured a trial rotor for Toshiba using TOS1X [2] with VIM/VAR melting route to obtain an ingot of 1300 mm and weight 38.8 tons in 2013. After homogenization treatment, forging was carried out under

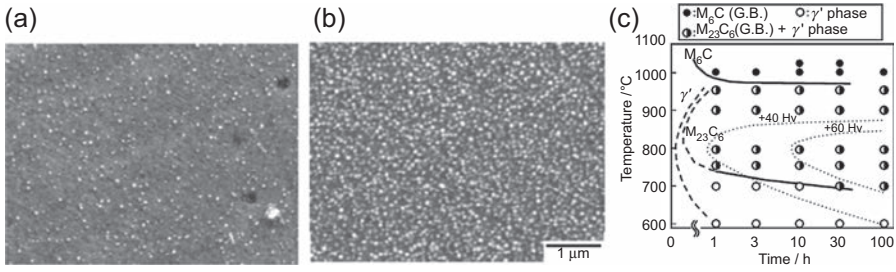


Figure 13.62 Microstructure of TOS1X-2 compared with conventional Alloy 617 and TTP diagram [52].

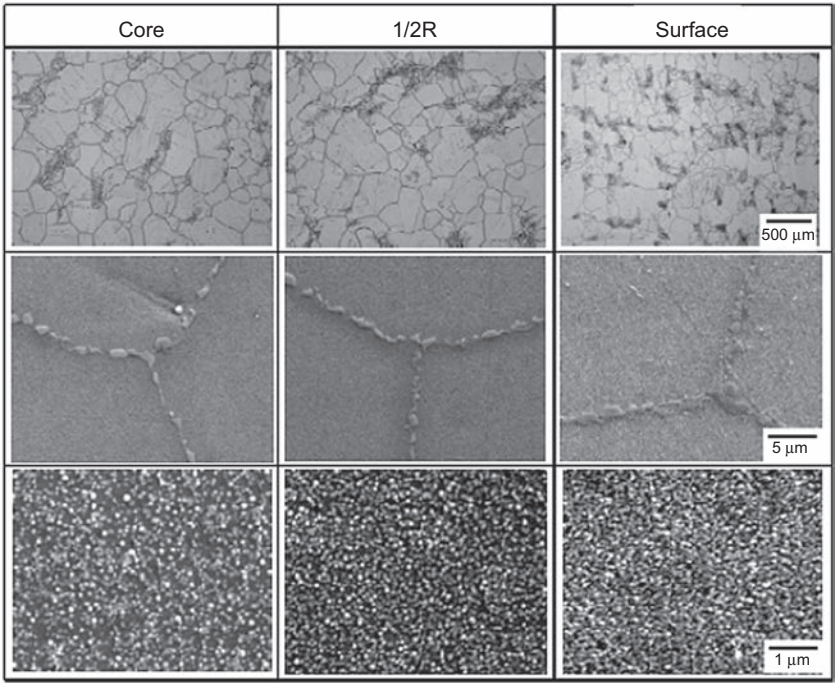


Figure 13.63 Microstructure of the rotor model [45].

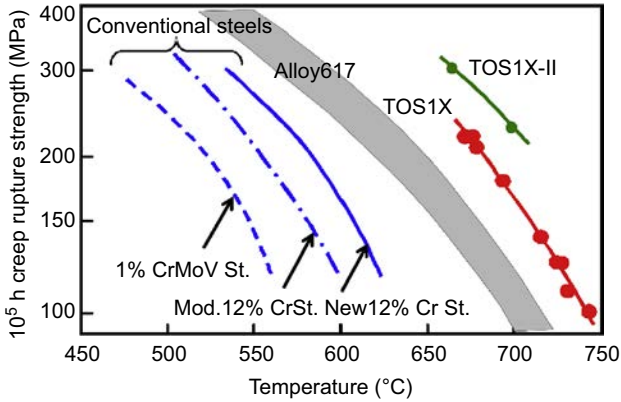


Figure 13.64 10^5 h creep rupture strength of turbine rotor alloys [45].

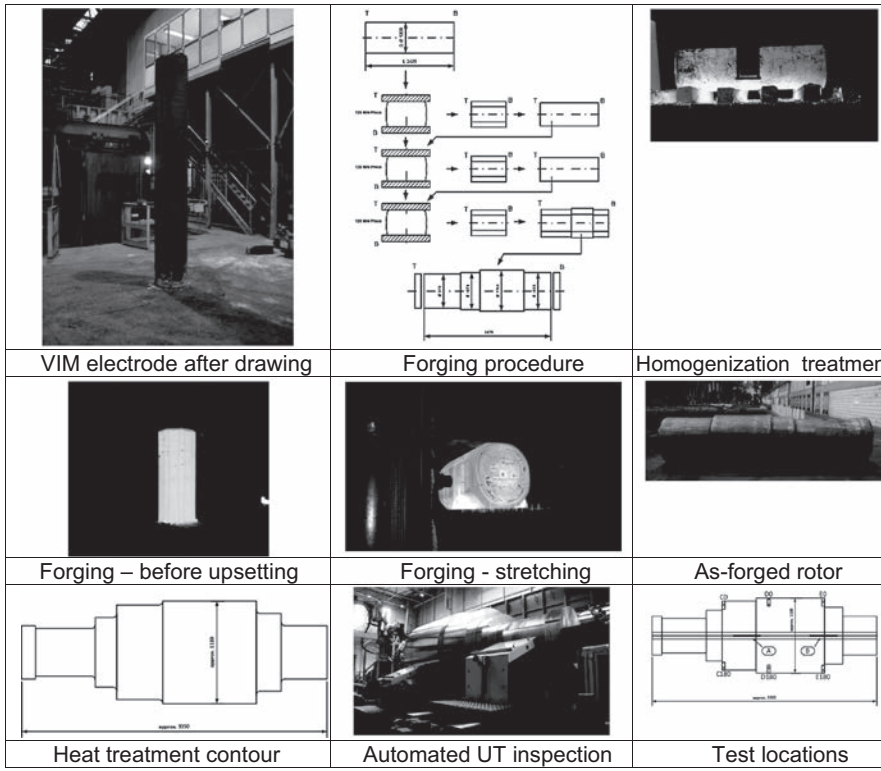


Figure 13.65 Saarschmiede forging steps [51].

an 85 MN press using upsetting operations. Finally, air cooling was carried out for the mechanical processing. The forged component has a diameter 1.100 × 3316 mm. Fig. 13.65 shows the forging steps in the Saarschmiede workshop [51].

It was possible to form an ingot of this size in material TOS1X-2 without any problems. However, it is essential to have a forging press with correspondingly high pressing force and speed. A targeted forging strategy is required to forge a part of such great size with a stepped contour in a nickel-based material. This is the only way to achieve the optimum microstructure that is as uniform as possible along the length and throughout the cross-section of the forging; only a slight influence is to be achieved with subsequent heat treatment. This needs to be taken into account in particular, with regard to the best possible minimum detectable defect size in the US inspection.

For this rotor, the required minimum detectable defect size MDDS was achieved. Further optimization for future manufacturing of a rotor component of comparable size could be achieved whereby the focus should be on further adaptations of the forging steps and of the forging contour.

Consequently, investigations have already commenced into creating a microstructural model for the material TOS1X-2. Future manufacturing should therefore be accompanied by corresponding forming simulations with regard to an optimized forging strategy so that even more uniform, finer microstructures can be achieved [51,53].

References

[1] H. Yamada, Y. Hattori, N. Komai, K. Sato, H. Ohira, T. Yanagisawa, The Thermal & Nuclear Power 52 (10) (2001) 1217.
[2] R. Blum, J. Bugge, in: Proc. of 6th Int. Conf. on Advances in Material Technology for Fossil Power Plants, 2010, p. 1.
[3] M. Fukuda, E. Saito, The Thermal & Nuclear Power 60 (10) (2009) 961.
[4] Y. Sawaragi, Y. Teranishi, A. Iseda, K. Yoshikawa, Sumitomo Metals 42 (4) (1990) 260.
[5] M. Igarashi, H. Semba, M. Yonemura, T. Hamaguchi, H. Okada, M. Yoshizawa, A. Iseda, in: Proc. of 6th Int. Conf. on Advances in Material Technology for Fossil Power Plants, 2010, p. 72.
[6] S. Imano, J. Sato, H. Kamoshida, T. Shibayama, A. Ota, Alloy design and innovative manufacturing technology of high-strength Ni-Base Wrought alloy for efficiency improvement in thermal power plants, Mitsubishi Heavy Industries Review 52 (2) (June 2015).
[7] K. Imai, K. Nemoto, S. Miyashita, Y. Yoshioka, M. Yamada, T. Suga, Development of a Rotor Alloy for Advanced Ultra Super Critical Turbine Power Generation System, 2008. http://ci.nii.ac.jp/naid/110007703934.
[8] M. Fukuda, Journal of the Japan Society of Mechanical Engineers 114 (4) (2011) 244.
[9] M. Fukuda, et al., The Thermal & Nuclear Power 62 (10) (2011) 731.
[10] H. Semba, H. Okada, T. Hamaguchi, S. Ishikawa, M. Yoshizawa, Development of Boiler Tubes and Pipes for Advanced USC Nippon Steel & Sumitomo Metal Technical Report No. 107, February 2015.
[11] Y. Sawaragi, K. Yoshikawa, Study report of 123 committee, Japan Society for the Promotion of Science 27 (3) (1986) 45.
[12] Y. Sawaragi, Y. Hayase, K. Yoshikawa, in: Proc. of Int. Conf. on Stainless Steel, ISIJ, Chiba, 1991, p. 633.
[13] H. Semba, M. Igarashi, Y. Yamadera, A. Iseda, Y. Sawaragi, Study report of the 123 committee, Japan Society for the Promotion of Science 44 (2) (2003) 119.
[14] H. Semba, H. Okada, M. Igarashi, in: Proc. of 5th Int. Conf. on Advances in Material Technology for Fossil Power Plants, 2007.
[15] Y. Noguchi, M. Miyahara, H. Okada, M. Igarashi, K. Ogawa, Creep-fatigue properties of Fe-Ni base alloy HR6W for piping in 700°C USC power plants, Journal of the Society of Materials Science, Japan 57 (6) (June 2008) 569–575.
[16] H. Okada, H. Semba, S. Ishikawa, M. Yoshizawa, CAMP-ISIJ 25 (2012) 1192.
[17] X. Xie, Y. Wu, C. Chi, M. Zhangfor, Advanced Ultra-Super-Critical Fossil Power Plant Application, 2015 (Chapter 3) http://dx.doi.org/10.5772/61139.
[18] J.P. Shingledecker, N.D. Evans, Creep-rupture performance of 0.07 C–23Cr–45Ni–6W–Ti, Nb austenitic alloy (HR6W) tubes, International Journal of Pressure Vessels and Piping 87 (6) (2010) 345–350, http://dx.doi.org/10.1016/j.ijpvp.2010.03.011.
[19] Y. Noguchi, M. Miyahara, K. Okada, M. Igarashi, K. Ogawa, Journal of The Society of Materials Science, Japan 57 (2008) 569.
[20] S.S. Manson, Fatigue at Elevated Temperatures. ASTM STP 520, ASTM, 1973, p. 744.
[21] M. Speicher, et al., in: Proc. of 3rd Symp. on Heat Resistant Steels and Alloys for High Efficiency USC Power Plants, 2009.
[22] H. Okada, H. Hirata, H. Semba, M. Igarashi, in: Proc. of 8th NIMS-MPA-IFW Workshop on Advances in High Temperature Materials for High Efficiency Power Plants, 2010 (Japan).
[23] A. Iseda, H. Okada, H. Semba, M. Igarashi, in: Proc. of Symposium on Heat Resistant Steels and Alloys for USC Power Plants. Korea, 2007, p. 229.

[24] M. Fukuda, E. Saito, H. Semba, J. Iwasaki, T. Takahashi, S. Izumi, S. Takano, Y. Sumiyoshi, Advanced USC technology development: in Japan, in: Proceedings of Seventh International Conference Advances in Materials Technology for Fossil Power Plants, 2014, pp. 24–40.
[25] Sumitomo Metal Industries distinguishing Itself Through Rapid Progress: Stainless Steel World, July/August 2011.
[26] N. Saito, N. Komai, Y. Sumiyoshi, Y. Takei, M. Kitamura, T. Tokairin, Development of materials for use in a-USC boilers, Mitsubishi Heavy Industries Technical Review 52 (4) (December 2015).
[27] H. Semba, H. Okada, M. Igarashi, H. Hirata, M. Yoshizawa, in: Proc. of 9th Liege Conf. on Materials for Advanced Power Engineering, 2010, p. 360.
[28] M. Fukuda, Advanced USC technology development in Japan, in: J. Lecomte-Beckers, Q. Contrepois, T. Beck, B. Kuhn (Eds.), 9th Liege Conference: Materials for Advanced Power Engineering, 2010.
[29] N. Saito, et al., Fabrication trials of Ni-based alloys for advanced USC boiler application, in: Proceedings of Seventh International Conference Advances in Materials Technology for Fossil Power Plants, 2014, pp. 190–201.
[30] T. Tokairin, et al., Metallurgical investigation of orbital narrow gap HST weldment of Ni based alloy pipe, in: Proceedings of 13th International Conference on Creep and Fracture of Engineering Materials and Structures, 2015.
[31] Y. Tanaka, et al., Hot corrosion properties of Ni-based alloys used in an advanced-USC boiler, in: Proceedings of Seventh International Conference Advances in Materials Technology for Fossil Power Plants, 2014, pp. 1422–1431.
[32] S. Imano, et al., Development and trial manufacturing of Ni-base alloys for coal fired power plant with temperature capability 800°C, in: Proceedings of Seventh International Conference Advances in Materials Technology for Fossil Power Plants, 2014, pp. 202–214.
[33] K. Maile, S. Zickler, K. Metzger, Qualification of structural materials for the advanced 700°C fossil fired power plant – experience gained in the GKM field test loops, in: Conf. Proc. Baltica IX: International Conference on Life Management and Maintenance for Power Plants, 2013, pp. 194–203.
[34] E. Saito, N. Matsuno, K. Tanaka, S. Nishimoto, R. Yamamoto, S. Imano, Latest technologies and future prospects for a new steam turbine, Mitsubishi Heavy Industries Technical Review 52 (2) (June 2015).
[35] R. Yamamoto, Y. Kadoya, T. Nakano, S. Kurata, in: Development of Ni-Based Superalloy for Advanced: 700°C-class Steam Turbines Proc. of 5th Inter. Conf. on Advances in Materials Technology for Fossil Power Plants, 2007. EPRI Report No 1016250.
[36] R. Yamamoto, et al., Development and trial manufacturing of Ni-based superalloy "LTES700R" for advanced 700°C class steam turbines, in: D. Gandy, J. Shingledecker (Eds.), Advances in Materials Technology for Fossil Power Plants: Proceedings From the Seventh International Conference, ASM International, Materials Park, OH, 2013, pp. 468–481.
[37] T. Ohno, et al., Development of low thermal expansion nickel base superalloy for steam turbine applications, Energy Materials 2 (4) (2007).
[38] K. Takasawa, T. Takahashi, R. Tanaka, T. Kure, S. Imano, E. Saito, Trial production and evaluation of 10-ton class A-USC turbine rotor of Ni-Fe base superalloy FENIX-700, in: Proceedings of Seventh International Conference Advances in Materials Technology for Fossil Power Plants, 2014, pp. 1283–1290.

[39] M. Fukuda, E. Saito, Y. Tanaka, T. Takahashi, S. Nakamura, J. Iwasaki, S. Takano, S. Izumi, Advanced USC Technology Development in Japan: 6th EPRI Int. Conf. on Advances in Materials Technology for Fossil Power Plants: Santa Fe, NM USA, August 31 – September 3, 2010.
[40] T. Takahashi, S. Ohsaki, K. Kajakawa, T. Kure, S. Imano, J. Sato, E. Saito, H. Doi: Manufacturability of Ni-Fe Base Superalloy FENIX-700 for A-USC Steam Turbine Rotor Large Forgings (2010). http://www.jsw.co.jp/product/technology/uploads/gihuo61/pdf
[41] Y. Ookomori, Recent Trends and Developments in the Heavy Open –Die Forging in Japan: http://www.forgefonderie.org/IMG/pdf/japan.pdf.
[42] S. Imano, H. Doi. K. Kajakawa, T. Takahashi, Modification of Alloy 706 for High Temperature Turbine Rotor Application: Superalloys 718, 625, 706 and Derivatives TMS 2005, pp. 76–86.
[43] C. Aoki, T. Uehara, H. Kamoshida, S. Imano, T. Sato, Application of Ni Based Superalloy USC141 TM for Boiler Tubes of 700°C-Class a-USC Power Plants: https://www.hitachi-metals.co.jp/rad/pdf/2014/vol30.pdf.
[44] T. Uehara, C. Aoki, T. Ohno, P. Schraven, H. Kamoshida, S. Imano, Creep rupture properties of Ni-base superalloy USC141 as solution treated for 700°C class A-USC boiler, in: Proceedings of Seventh International Conference Advances in Materials Technology for Fossil Power Plants, 2014, pp. 1407–1416.
[45] P. Weitzel, J. Tanzosh, B. Boring, N. Okita, T. Takahashi, N. Ishikawa, Advanced Ultra-Supercritical Power Plant (700 to 760°C) Design for Indian Coal: PowerGen ASIA 2012: Bangkok, Thailand, 5 October 2012.
[46] S. Miyashita, M. Yamada, T. Suga, K. Imai, K. Nemoto, Y. Yoshioka, Development of a rotor alloy for advanced ultrasupercritical turbine power generation system, in: Proceedings of the 34th MPA Seminar. Stuttgart, Germany, 2008, pp. 15.1–15.12.
[47] F. Abe, Research and development of heat-resistant materials for advanced USC power plants with steam temperatures of 700°C and above, Engineering 1 (2) (2015) 211–224, http://dx.doi.org/10.15302/J-ENG-2015031.
[48] T. Takahashi, Development of advanced-ultra super critical steam turbine system, in: 8th NIMS-MPA-IFW Workshop on Advances in High Temperature Materials for High Efficiency Power Plants, March 24–26, 2010. NIMS, Tsukuba, Japan.
[49] The NET Power Cycle and the Combustor and Turbine Development, March 2013. www.anlecrd.com.au/LiteratureRetrieve.aspx?ID.
[50] S. Miyashita, Y. Yoshioka, T. Kubo, Development and Evaluation of a Ni-based Superalloy Rotor Material for a-USC Steam Turbines: Creep and Fracture of Engineering Materials and Structures, The Japan Institute of Metals, 2012.
[51] A. Diwo, S. Miyashita, Y. Yoshioka, B. Donth, J. Terhaar, N. Blaes, D. Bokelmann, Manufacture of a Large Steam Turbine Rotor Forging in an Ni-Base Alloy for Use in Advanced USC Power Plants: IFM2014 Japan, September 29 – October 3, 2014.
[52] S. Miyashita, Y. Yoshioka, T. Kubo, Development and Evaluation of large-scale rotor forging for over 700° V-class A-USC steam turbine, in: Proceedings of Seventh International Conference Advances in Materials Technology for Fossil Power Plants, 2014, pp. 436–447.
[53] M. Fukuda, A-USC Development Project in Japan 8th NIMS-MPA-IFW Workshop on Advances in High Temperature Materials for High Efficiency Power Plants, NIMS, Tsukuba, Japan, March 24–26, 2010.

INCONEL alloy 740H

14

J.J. deBarbadillo
Special Metals Corporation, Huntington, WV, United States

14.1 Background/introduction

Nickel-based alloys such as 800HT (N08811) and 617 (N06617) have been used in welded service for containment of fluids and gases in creep-limited applications in the chemical process and power generation industry for many years. These alloys are well-characterized solid-solution plus carbide-strengthened materials. However, under proposed A-USC operating conditions, very heavy-wall tube and pipe with limited steam capacity will be required if these alloys are to be used. Somewhat higher strength is provided by cobalt-based alloys, but the future cost and availability of cobalt are a concern. This material strength gap was recognized at the outset of the European Thermie AD700 program in 1998. That project team then considered the possibility of using stronger, creep-resistant, nickel-based age-hardened alloys of the type commonly called "superalloys" in the aerospace industry [1].

One class of superalloy that contains 10–20 weight percent γ' is used in sheet form for welded and formed aero-engine cases, ducts, and combustors. These alloys have characteristics that make them candidates for use in tube and pipe for power plants. They are relatively soft and formable in the solution-annealed state. In this condition, they can be rolled and drawn to form sheets and tubes. Tubes can be cold formed by bending. Subsequently, the components are again solution treated and aged. By virtue of their high chromium and aluminum contents, these alloys possess inherent resistance to surface degradation in a wide variety of oxidizing environments. Alloys of this type can be welded successfully, although strict protocols must be followed to prevent atmospheric contamination, and not all welding procedures can be used. Concerns about use of nickel-based age-hardened alloys for power plant applications include cost and availability, and material properties such as long time microstructure stability, residual impact toughness, creep ductility, thermal fatigue resistance, over-temperature damage tolerance, and strain-age and stress relaxation cracking of welds.

The mechanical properties of alloy 263 (UNS N07263) most closely met the requirements for boiler tubes. However, because alloy 263 has relatively poor resistance to corrosion when exposed to high-sulfur coal, alloy composition modifications were explored. This work resulted in the definition of alloy 740 (N07740) that was subsequently characterized under a succession of European projects leading to COMTES700 test loop exposures at the Scholven and Esbjerg plants [2]. The US A-USC Consortium chose a higher operating temperature of 760°C that required the use of

Materials for Ultra-Supercritical and Advanced Ultra-Supercritical Power Plants.
http://dx.doi.org/10.1016/B978-0-08-100552-1.00014-2
Copyright © 2017 Elsevier Ltd. All rights reserved.

age-hardened materials for steam transfer pipes as well as boiler tubing. As described later, it was found necessary to modify the alloy 740 composition to improve its phase stability and heavy-section weldability. The redefined alloy, now designated 740H, meets the design requirements for both the European and US A-USC projects. The properties of alloy 740H have been extensively documented [3–5]. The data generated, primarily from the US program, served as the basis for ASME Code Case 2702 [6]. Alloy 740H has been tested at test loop at Niles, Ohio, [7] and Barry, Alabama [8]. In the next few years, it will be further tested in facilities under construction in Japan and China or planned in Europe, the United States, and India. The chapter summarizes the status, recent developments, and continuing evaluations of 740H.

14.2 Composition

Alloy 740 was designed to have 15–20 weight percent γ′ through a balance of aluminum, titanium and niobium contents. Chromium was increased, and molybdenum was decreased from the levels in alloy 263 to improve "fireside" corrosion resistance. The alloy, designated 740, met the operating steam service goals of the Thermie project (700°C, 35 MPa) for boiler tubing. However, the US A-USC project consortium chose a more challenging steam service goal of 760°C and 35 MPa. For this design an age-hardened alloy was considered necessary for heavy-wall steam headers and transfer piping as well as for boiler tubing. The initial heavy-section welding evaluations made using matching composition filler metal showed alloy 740 was prone to liquation cracking in the weld metal and heat-affected zone (HAZ) [9,10]. The alloy was also observed to form lath and intergranular η and globular G phase during long time exposure at 750–800°C [11–13]. The latter author showed that η has minimal effect on creep life. However, very low residual impact toughness was noted after long time exposure at 700–800°C in samples containing a large amount of acicular η [14]. Based on these observations, the alloy composition was modified to destabilize these phases and also narrow the alloy solidification range to eliminate liquation cracking in weldments. The reformulated alloy, designated 740H, was introduced by Baker. The composition changes included increasing the aluminum/titanium ratio and reducing the silicon, niobium, and boron contents. The nominal composition of 740H is shown in Table 14.1. Note that both 740 and 740H fall within the limits of UNS N07740. Following the introduction of 740H, commercial development of 740 was discontinued, but test results from sample material supplied previously continue to be reported, and distinction between the two alloys is not always clearly made by authors.

14.3 Microstructure and phase stability

The microstructure of alloys 740 and 740H has been studied extensively, and the results have been reported by numerous researchers, including [4,5,11,12,15,16]. Representative microstructures of material in the fully heat-treated (solution-annealed and aged)

Table 14.1 Nominal composition of 740 and 740H and composition limits for UNS N07740

Element	Cr	Co	Al	Ti	Nb	Fe	C	Mn	Mo	Si	Cu	P	S	B
Minimum	23.5	15.0	0.2	0.5	0.5		0.005							0.0006
740	24.5	20.0	0.9	1.8	2.0	0.7	0.03	0.3	0.5	0.5	<0.1	<0.002	<0.002	0.002
740H	24.5	20.0	1.35	1.35	1.5	0.7	0.03	0.3	0.5	0.15	<0.1	<0.002	<0.002	0.002
Maximum	25.5	22.0	2.0	2.5	2.5	3.0	0.08	1.0	2.0	1.0	0.5	0.03	0.03	0.006

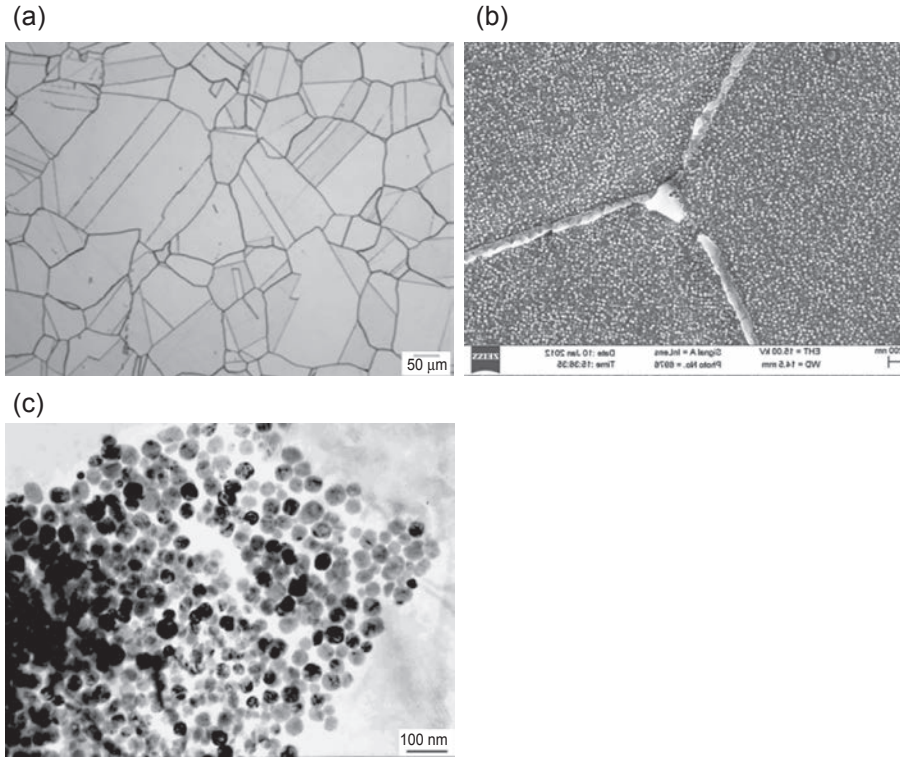


Figure 14.1 Microstructure of solution-annealed and aged 740H: (a) optical, (b) SEM (c) TEM [18].

condition are shown in Fig. 14.1(a) (optical) and Fig. 14.1(b) (SEM). The preferred alloy heat treatment is solution annealing at 1100°C (minimum) and age for at least 4 h at 760–816°C. Water quenching following solution annealing is recommended; however, it is not required. Optical microscopy does not resolve the γ′ phase, so only isolated carbide particles (intragranular MC and grain boundary $M_{23}C_6$) are normally observed. The fine, largely cuboidal γ′ precipitate can be more easily resolved by scanning electron microscopy (SEM) or transmission electron microscopy (TEM). The grain boundaries contain carbide identified as $M_{23}C_6$ and randomly dispersed coarse γ′ particles. Quantitative phase analysis by Xie showed 14.6% γ′, 0.22% MC, and 0.20% $M_{23}C_6$.

Superalloys typically undergo microstructural changes if they are held for long periods of time at elevated temperatures. These changes may include formation of complex carbides, growth of γ′ particles, and the formation of a variety of topological close-packed phases. These phases are brittle and may have undesirable morphologies that reduce ductility and toughness. Their nucleation and growth rate can be accelerated by prior or applied plastic strain or in regions of compositional transition. If superalloys are to be used in the boiler section of power plants, it will be necessary to demonstrate that the microstructure will either, be stable under the service conditions

and design lifetime of the plant or that any phase changes will be benign. An indication of γ′ stability can be obtained through simulation using phase equilibrium software such as Thermo-Calc [17]. A calculated phase stability diagram, shown in Fig. 14.2, predicts a γ′ solvus of 973°C and a maximum weight fraction of about 22%. A region of η stability occurs between 872 and 1040°C. At temperatures below 650°C, σ is predicted to form, although this phase has not been reported in 740H to date.

An estimate of the γ′ weight fraction as a function of aging time is shown in Fig. 14.3. This plot illustrates the relatively rapid rate of formation of the phase and the increasing amount with decreasing temperature. This plot also shows that about 3% additional γ′ will precipitate during service for material given the preferred 800°C aging treatment.

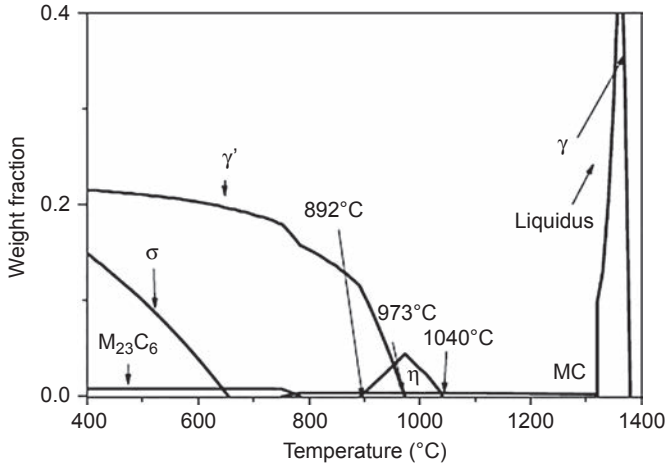


Figure 14.2 Phase stability diagram for nominal 740H composition predicted using Thermo-Calc [18].

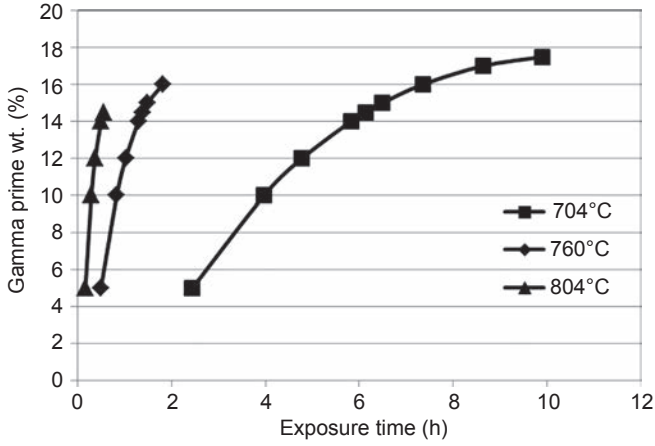


Figure 14.3 Weight fraction of γ′ for 740H, solution annealed, water quenched, and then exposed at various temperatures. Diagram was predicted using JMatPro Software [19].

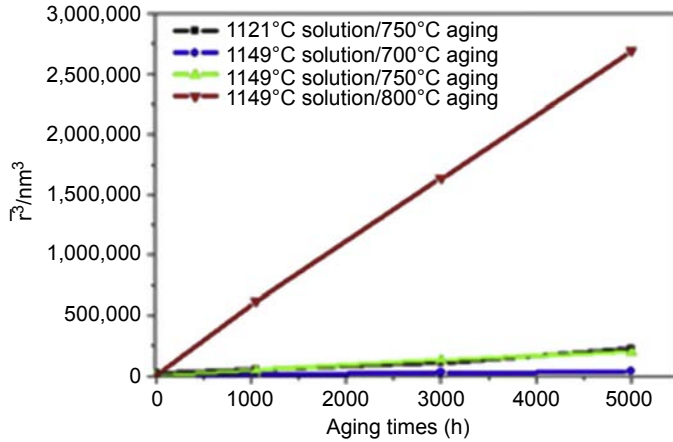


Figure 14.4 Experimentally determined average γ′ particle diameter for solution-annealed and aged 740H exposed isothermally for various temperatures [18].

Xie and coworkers have studied the evolution of γ′ in 740H during isothermal exposure and determined its coarsening rate. His results are summarized in Fig. 14.4 [20]. This data was determined from material that was initially given the standard anneal and age and then exposed for various times up to 5000 h at 700°C, 750°C, and 800°C. Very little γ′ growth occurs at 700°C, while coarsening (overaging) is fairly rapid at 800°C. Alloy 740H γ′ was found to be slightly more stable than that reported in an earlier study of 740. The effect of these microstructural changes on mechanical properties is discussed later in this chapter.

The microstructure of material exposed for 5000 h at 700°C, 750°C, and 800°C is shown in Fig. 14.5(a–c), respectively. Note that the γ′ particles grow significantly, especially at 800°C, but they continue to maintain a generally cubic morphology. Larger, chunky γ′ decorates the grain boundaries. Most of the remaining grain boundary area is covered by $M_{23}C_6$ carbide. Detailed phase identification was performed by Xie and coworkers [18,20]. They found no evidence of η, G, or σ phases in this work.

Creep deformation can accelerate microstructural changes by providing enhanced diffusion and nucleation sites. Fig. 14.6(b) shows the structure near the fracture surface of a specimen tested at 750°C with an initial applied stress of 280 MPa that ruptured in 1087.4 h. The structure is similar to the starting structure, but a chain of grain boundary voids is visible. Test bar fracture occurs by linking of these voids. Although precipitate-free zones do not form adjacent to the grain boundary in material exposed without stress, this feature has been reported to occur as a consequence of creep deformation in both base metal [4] and weld metal [21].

14.4 Mechanical properties

740H is, in principle, a relatively simple alloy with mechanical properties dependent on the volume fraction of γ′ and to a lesser extent grain size and grain boundary

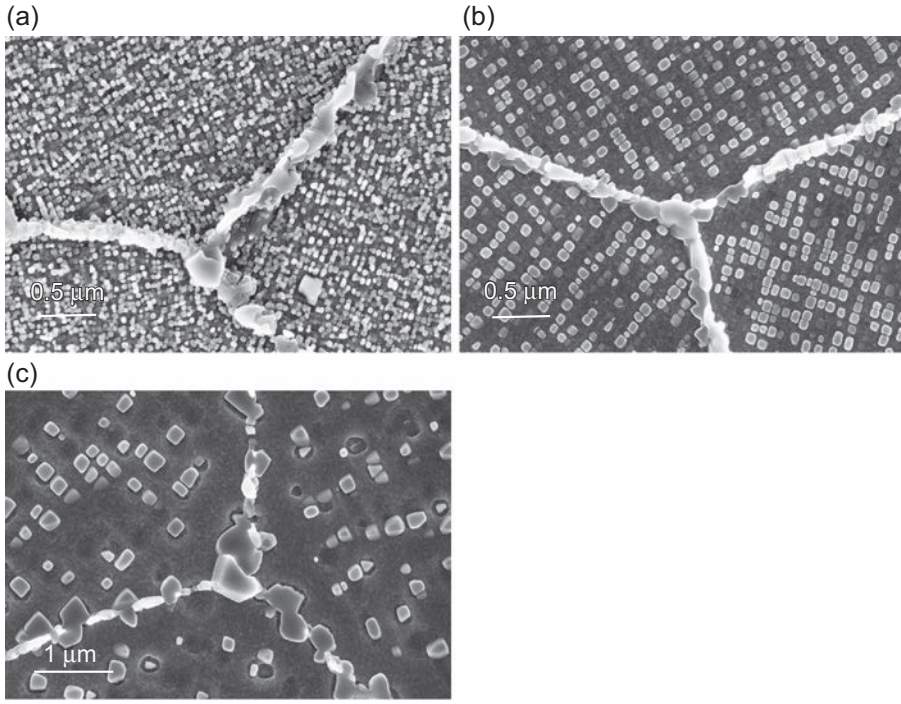


Figure 14.5 SEM micrographs of alloy 740H exposed stress-free for 5000 h at (a) 700°C, (b) 750°C, and (c) 800°C [20].

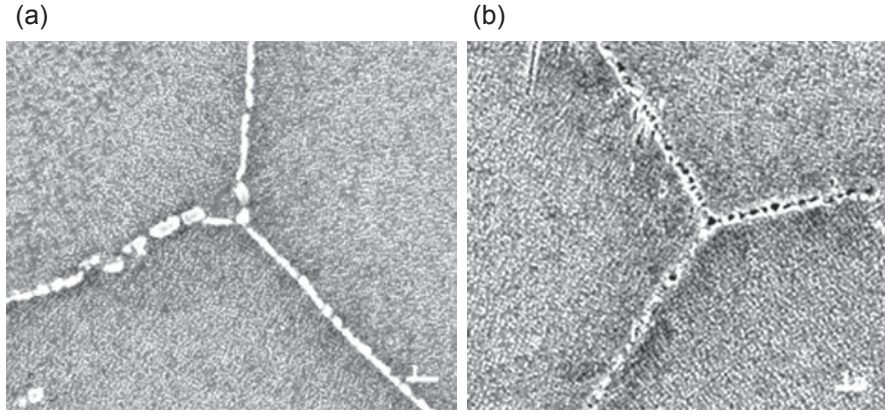


Figure 14.6 Microstructure of broken creep rupture specimen: (a) unstressed region within the specimen grip, (b) near the fracture surface [20].

carbide distribution. However, the properties of manufactured components are often process dependent. Different methods of heat treatment and section size will result in varying annealed grain size, γ′ volume fraction and size distribution, and carbide directionality. These potential variables are discussed in Sections 14.6 and 14.7.

14.4.1 Ambient temperature tensile and impact properties

The ambient temperature tensile and impact properties of alloy 740 and 740H in both the solution-annealed (SA) and solution-annealed and age-hardened (SA + A) conditions are shown in Table 14.2. This data was obtained on a range of tube and pipe dimensions and manufacturing methods as well as on bar and forged parts. The data show that the alloy is capable of meeting ASME code properties using standard mill metal working equipment and heat treatments. Impact toughness in the SA + A condition is uniformly high. Solution annealed properties are of interest for fabricators who need to do cold forming or bending.

14.4.2 High-temperature tensile

Elevated temperature tensile properties for tubes and pipes are shown in Table 14.3. One set of data is plotted as a function of temperature in Fig. 14.7. Tensile strength and fracture elongation decrease with increasing temperature, but yield strength increases in the age hardening range.

14.4.3 Creep and stress rupture

Alloy 740H was optimized to balance creep strength, weldability, and corrosion resistance. The creep rupture properties have been determined on a variety of product forms with a range of composition. The rupture life data generated by Oak Ridge National Laboratory (ORNL) under sponsorship of the US A-USC Consortium from five early heats of 740 and 740H that was used to establish the ASME allowable maximum design stress is shown in Fig. 14.8. The data extend to 50,000 h with some tests continuing that should exceed 100,000 h. The data is reported and analyzed by Shingledecker [13,4] and Tortorelli [22]. It was concluded that the creep strength of 740 and 740H were comparable despite their differences in microstructure. Other conclusions were that within the limited data set there is a modest inverse grain size relationship with minimum creep rate and that the alloy shows notch strengthening at 750°C (only temperature tested). Fig. 14.9 compares the ASME limiting design stress for alloys 617, 740H, and 800HT. Alloy 740H shows a significant strength advantage in the temperature range of interest for A-USC over solid solution–strengthened alloys. At temperatures above 800°C, alloy 740H loses its strength advantage because γ′ coarsens and the volume fraction diminishes. Although the predicted γ′ solvus is 973°C, the γ′ content at 800°C is less than 10% (see Fig. 14.2).

Data generated from newer heats of 740H including extruded pipe and cold-drawn tube is shown in parametric form in Fig. 14.10. The creep rupture life data for mill product forms tend to fall below that of the qualification data, but within the

Table 14.2 Ambient temperature tensile and Charpy V-notch impact properties of mill products and forgings

Form	Size (OD × ID) mm	Heat treatment	No. tests	YS, MPa	TS, MPa	El., %	RA, %	CVN, J/cm^2
ASME min.	All	SA + A		620	1035	20		
Tube	21.3 × 2.78	SA	2	512	943	55.9		
	38.1 × 7	SA	3	394	784	56.3		
	38 × 8.8	SA	24	503	944	51.7		88.3
	50.8 × 8	SA	6	405	824	56.2		113.5
	21.3 × 2.78	SA + A	2	746	1163	42.8		
	38.1 × 7	SA + A	3	769	1118	33.9		
	38 × 8.8	SA + A	21	761	1164	37.0		45.4
	42.2 × 10	SA + A	2	731	1158	36.3		46.6
	42.2 × 11	SA + A	2	736	1153	37.0		43.4
	50 × 10	SA + A	1	747	1172	37.5		
	50.8 × 8	SA + A	6	766	1174	35.8		39.9
Pipe	378 × 88	SA + A	4	728	1094	31.8	32.4	41
	324 × 22.5	SA + A	2	741	1083	33.6	36.2	
	219 × 18	SA + A	1	756	1158	37.6	33.2	73.6
Bar	76.2	SA + A	1	736	1147	36.5		
	343 edge	SA + A	1	758	1110	31.7	29.6	61
	343 center	SA + A	1	681	1060	30.2	25.8	58
Flange	Web	SA + A	2	682	1145	44.3	34.2	142
	Base	SA + A	2	707	1064	46.4	41.8	183
Elbow	203 × 18	SA + A	1	685	1060	41.2	40	

Table 14.3 Elevated temperature tensile properties

Product	Size (OD × wall), mm	Temp.,°C	No. tests	YS, MPa	TS, MPa	El%
Tube	38 × 8.8	650	2	638	985	25.5
		700	1	682	964	23.2
		750	2	621	845	17.4
	50 × 10	650	1	627	978	28.5
		700	1	670	932	18.5
		750	1	649	836	15.0
	50.8 × 8	650	2	610	950	27.0
		700	2	637	906	16.2
		750	2	610	794	12.5
Pipe–740H	378 × 88	650	1	600	924	29.8
		700	1	572	889	15.9
		750	1	573	800	22.5
	323.8 × 22.5	650	2	590	876	30.7
Bar–740	76.2	650	1	596	944	33.0
		700	1	626	982	19.5
		750	1	623	827	28.0

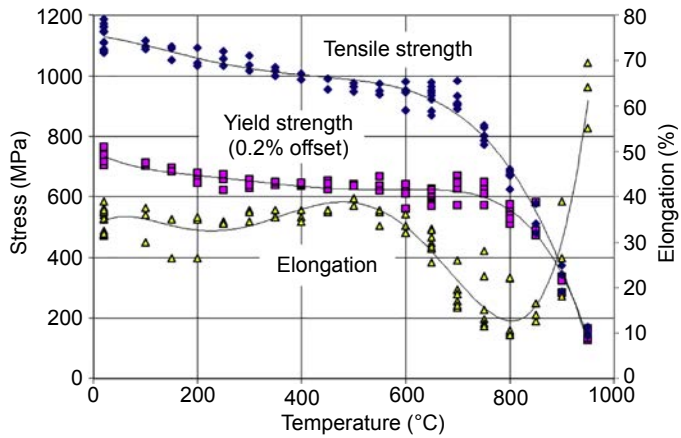


Figure 14.7 Elevated temperature tensile properties, 740 tube samples.

conventional 20% range. It is not clear at this point whether this is a testing issue (different test location, specimen geometry, etc.) or differences in the microstructure of commercial product (grain size γ′ content and size distribution, grain texture, etc.).

Creep rupture elongation for the ORNL and Special Metals tests that include both alloy 740 and 740H is plotted in Fig. 14.11. Although the rupture elongation is quite high at short times and high temperatures, longer time rupture elongation in the 700–760°C range falls between 5% and 10%, and even lower elongation is seen at 650°C. Elongations of this magnitude are seen in a variety of creep-resistant materials

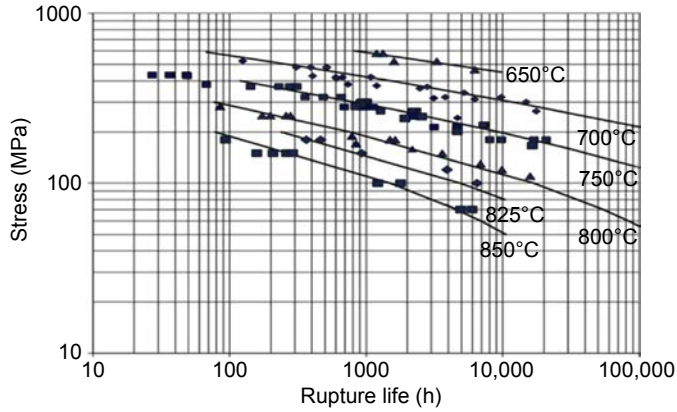


Figure 14.8 Creep rupture properties, ORNL, and Special Metals data [23].

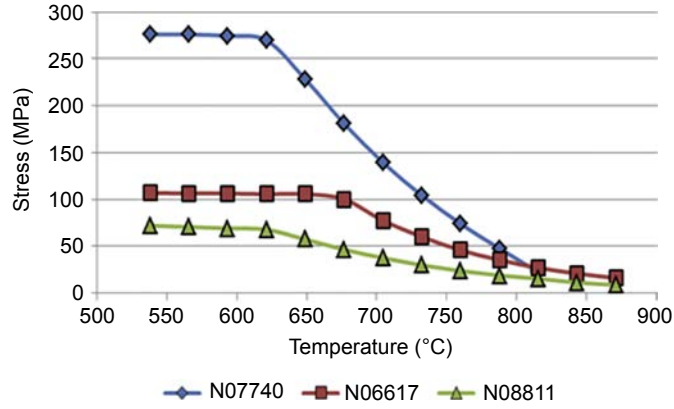


Figure 14.9 Maximum allowable stress values for alloys 800H, 617, and 740H [6].

including ferritic steels. Detailed microstructural analysis has not been done on these specimens to date, but the presence of η in 740 does not seem to be detrimental. Note that η is not stable at 650–700°C in alloy 740 and not stable over the entire range for 740H. Zhang has shown that the rupture mode is predominately intergranular when the rupture elongation is less than 10% [24]. Fig. 14.6(b) shows a typical microstructure with small creep voids that eventually link up to form a crack.

14.4.4 Fatigue

Very little work has been done on fatigue or thermal fatigue of 740 or 740H. In unpublished work, Special Metals conducted rotating beam tests on 740 at 760°C and determined a 10^8 rotation fracture stress of 344 MPa. That is approximately 45% of the tensile stress at that temperature. Strain-controlled fatigue tests, also on 740, were done under the Thermie project at 750°C. Zhang and Takahashi at CRIEPI performed more detailed load-controlled and strain-controlled axial fatigue tests on 740H

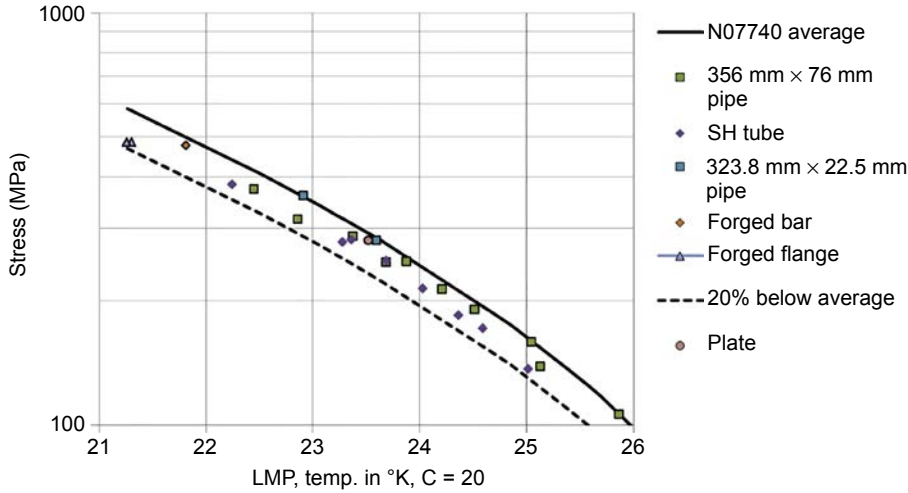


Figure 14.10 Larson-Miller representation of creep rupture data for mill products. *Solid line* represents average of ORNL data for boiler tube [25].

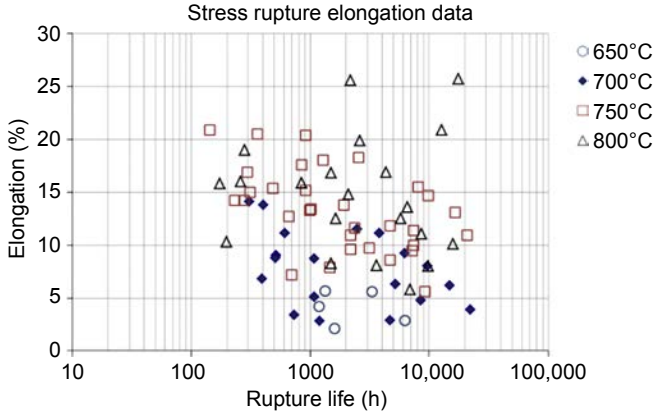


Figure 14.11 Creep rupture elongation for 740H, combination of ORNL, and Special Metals data.

material from 378-mm diameter extruded and heat-treated pipe [24]. The authors reported that the axial fatigue limit was about 50% of the tensile strength. Fig. 14.12 shows strain-controlled data for the Thermie and CRIEPI. A spectrum of fatigue testing of 740H including hold time cycles is underway in the United Kingdom.

14.4.5 Residual properties after long time exposure

To further evaluate the microstructural stability of 740H, material obtained from commercially produced tube and pipe was exposed stress-free for times up to 10,000 h at 700°C, 750°C, and 800°C. Longitudinal Charpy V-notch impact and hardness tests were conducted, and the microstructure of the exposed material was analyzed

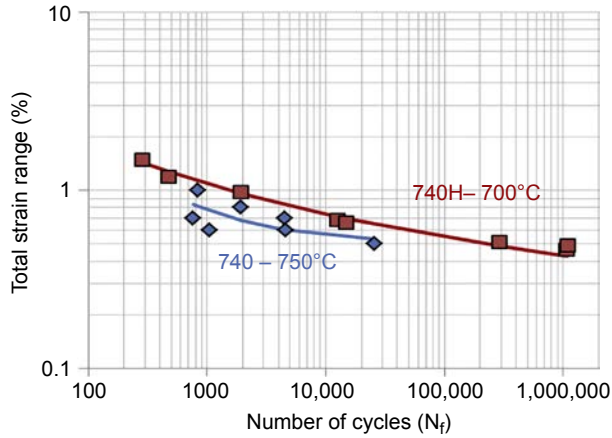


Figure 14.12 Strain-controlled axial fatigue properties, Zhang 700°C, and Thermie 750°C.

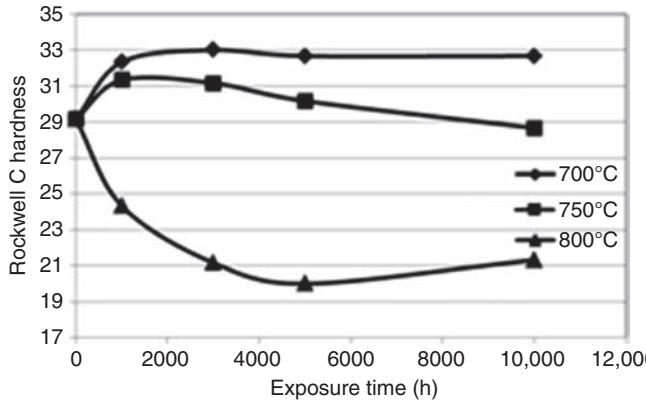


Figure 14.13 Hardness of alloy 740H after nonstress aging.

in detail. The hardness data are shown in Fig. 14.13. Representative microstructures were shown in Fig. 14.5. The impact test data is summarized in Fig. 14.14(a) and (b) [5]. Impact toughness dropped 50% or more at all temperatures during the first 1000 h of exposure, but then it stabilized at a level that is sufficient for the application. It was concluded that the initial loss in impact toughness was due to precipitation of intergranular carbide. This explains why the toughness drops at 800°C despite the drop in hardness due to coarsening of γ′. Xie examined the fracture surfaces and concluded that fracture was entirely intergranular [5].

14.5 Corrosion properties

Alloy 740H was initially designed to be used uncoated as boiler tube. Resistance to hot corrosion in the presence of combustion gas and coal ash deposits on the outside

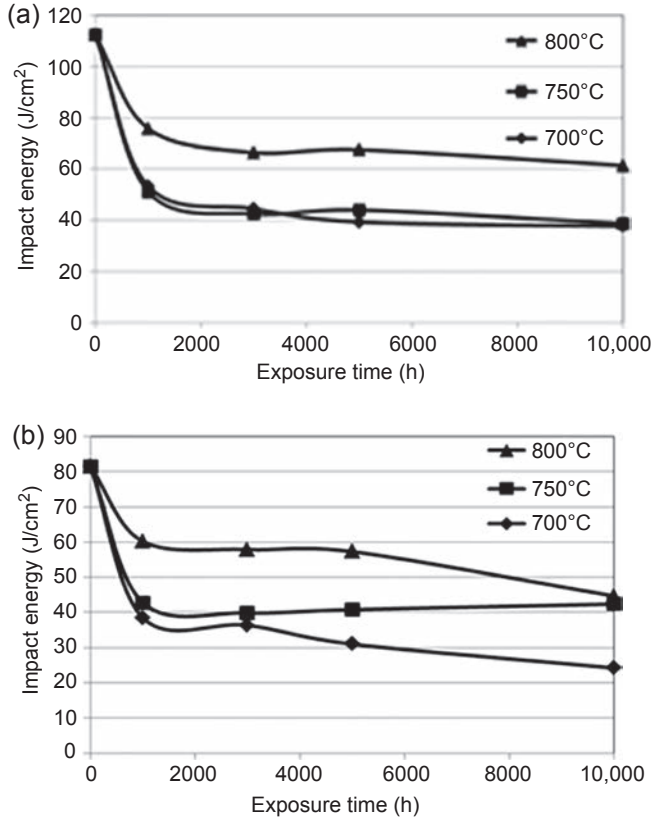


Figure 14.14 Charpy V-notch impact resistance of alloy 740H: (a) tube, (b) pipe.

of the tube and oxidation by supercritical steam on the inside are key requirements. A hot corrosion target of less than 2-mm corrosion attack in 200,000 h at 700°C was established for the Thermie program. Subsequently, the behavior of 740H in both steam and coal ash of various compositions has been extensively characterized in Europe and the United States. Recently, there has been interest in the resistance of 740H to corrosion in supercritical CO_2. Evaluation of 740H in other high-temperature corrosive environments such as molten salt has been less thorough, but by virtue of its 24.5% Cr content, alloy 740H should have substantial resistance to many oxidizing environments.

14.5.1 Oxidation in dry air and steam

Alloy 740H is resistant to scaling in the presence of high-temperature dry air and steam at temperatures of interest to A-USC programs. This has been confirmed by independent studies in the United States and Europe. This work was reported by Smith and later reviewed with new data by Maitra [26,27]. It showed parabolic weight change in the range 650–800°C in tests lasting up to 10,000 h with no observed oxide

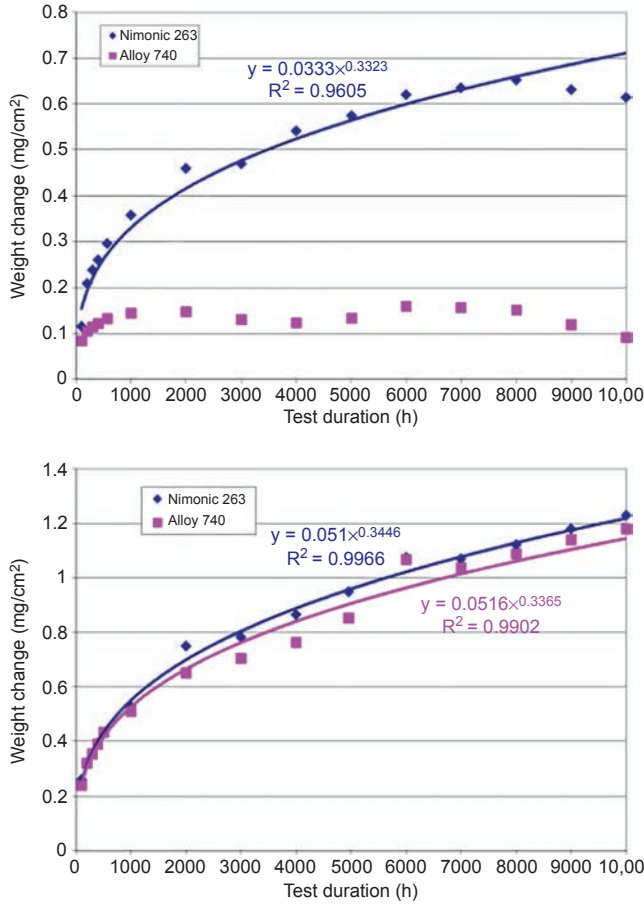


Figure 14.15 Air and steam oxidation data for material exposed at 750°C. Data generated by Ansaldo Ricerche under Thermie/AD 700 [26].

spallation (Fig. 14.15). Optical and scanning electron metallography performed on long time oxidation test samples showed that matrix chromium content is sufficient to replenish the scale and that internal attack is minimal. Similar results were obtained by other investigators [28–30].

Sarver and Tanzosh characterized candidate nickel-based alloys for A-USC service in a program sponsored by the US A-USC Consortium [31]. They developed rate constant data for various candidate A-USC alloys, including 740H, at 650°C, 700°C, and 800°C. The steam oxidation testing was performed using high-purity water with 100–300 ppb of dissolved oxygen and 20–70 ppb of ammonia to produce a pH value of 8.0–8.5 and a pressure of 1.7 MPa. These authors reported the chromium level at the alloy–oxide interface for alloy 740H as 17.4% after 4000 h at 800°C. Chromium depletion extended inward to a depth of 56 μm. Aluminum and silicon enrichment was found just below the Cr_2O_3 scale. Internal grain boundary

penetration after 4000 h appears negligible at 650°C, approximately 20 μm at 700°C and greater than 32 μm at 800°C. In this test, alloy 740H had slightly lower mass gain than alloy 617.

14.5.2 Coal ash corrosion

While resistance to steam oxidation is largely a matter of having sufficient chromium, resistance to coal ash corrosion is more complex. While stainless steels and nickel-based alloys generally have low rates of attack in high-sulfur coals under supercritical operating conditions, they show a greatly accelerated rate in the 700–800°C temperature range where liquid tri-sulfate deposits may be present [32]. Alloying elements such as molybdenum and tungsten promote breakdown of protective chromium oxide films in contact with sulfate and chloride-containing ash deposits, thereby making some common alloys vulnerable to pitting attack. For example, alloy 617 with 9% Mo has a high rate of attack compared with alloy 740H that has only 0.5% Mo [33]. Independent studies of alloy 740H corrosion in a variety of coal ash conditions show similar relationships [34–36]. Smith has published a detailed review of this work [37].

A recent experiment compared welded and base metal samples of alloys 263, 617, and 740H in simulated Shenhua No. 2 coal ash deposit [3]. Testing was performed at 750°C, exposing coupons having a painted-on slurry comprised of a simulated ash containing 6% Fe_2O_3-29% $CaSO_4$-1.9% Na_2SO_4-1.9% K_2SO_4-39% SiO_2-22% Al_2O_3-0.05% KCl-0.05% NaCl. A simulated flue gas comprised of N_2–15% CO_2–3.5% O_2–5% H_2O–0.1% SO_2 flowed over the samples at 500 sccm with a platinum catalyst preceding the samples. Samples of both base metal and weld metal were tested. Gas tungsten arc welds (GTAW) were made on alloy base plates using matching composition welding wire. Alloys were tested in their standard heat-treated condition. Samples were exposed for 1000 h, with the ash coating reapplied at weekly intervals. Cross-sections of tested samples were made and evaluated, yielding corrosion depth results shown in Fig. 14.16 for alloys 740H, 263, and 617. Corrosion depths and corrosion product morphologies of base metal and weld metal were similar despite the

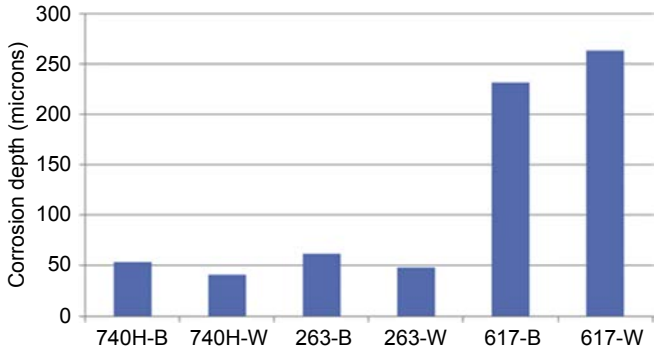


Figure 14.16 Maximum pit depth for base metal and weld metal samples for alloys 740H, 263, and 617 in a simulated Chinese coal ash (750°C, 1000 h) [3].

inhomogeneous nature of the weld metal. External oxide scales were chromium-rich with low levels of titanium present in all cases. Alloy 740H formed a thinner, more compact chromia scale. All alloys developed internal oxides along grain boundaries rich in aluminum and titanium. Chromium sulfides (verified with SEM-EDS and backscatter visualization), evident in the micrographs as medium-gray globular internal precipitates tending to reside on grain boundaries, were much more pronounced in the alloy 617 and 263 samples than in the alloy 740H samples (Fig. 14.17). The alloy 617 samples exhibited significant pitting. Alloy 263 exhibited incipient shallow pits, and alloy 740H had no pits. Natesan has proposed that nickel alloys exhibit an incubation period in this environment, so eventual pitting of 740H is likely [36].

The US Department of Energy has sponsored a comprehensive study of corrosion under ash deposits created by controlled burning of eight commercial grades of coal that represent the spectrum of coal compositions used in the United States. Coals with high moisture, volatiles, sulfur, or chlorine are included. Various boiler alloys were exposed to these ash deposits under an atmosphere defined from boiler gas sampling. The initial 704°C, 1000 h results of these trials showed 740H to have a low corrosion rate; however, sulfate-dominated fluxing occurred in exposure to certain grades of coal where a spinel oxide scale developed [38]. Alloy 740H was the only nickel-based alloy tested. This work highlights the need to thoroughly evaluate the performance of superheater tube alloys in the specific fuel environment.

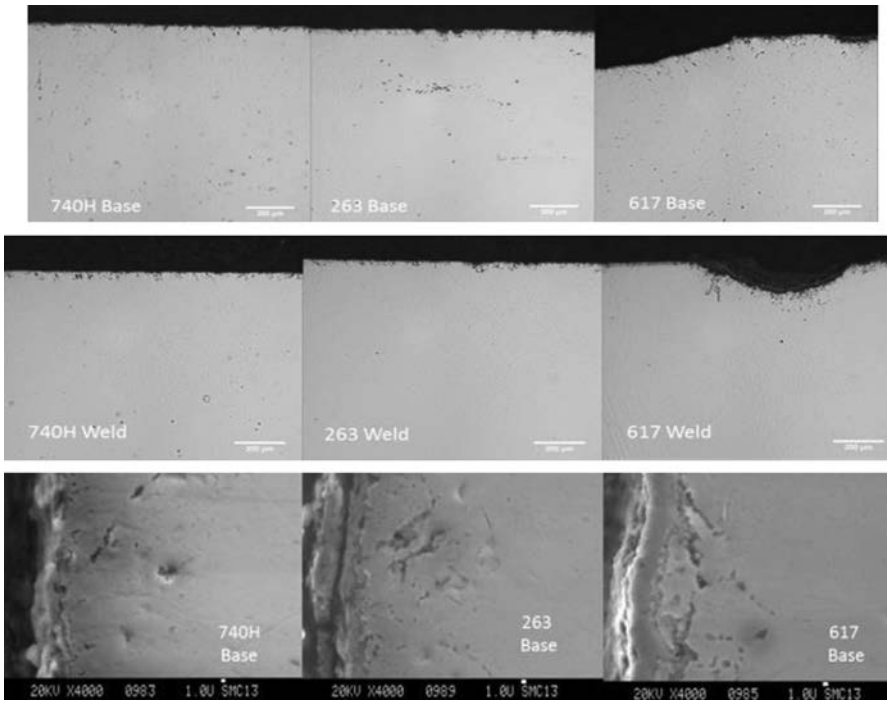


Figure 14.17 Surface profiles for specimens exposed at 750°C for 1000 h. SEM photographs of base metal specimens.

14.5.3 Corrosion in supercritical carbon dioxide

Supercritical carbon dioxide is under consideration for use as a working fluid in various power generation systems, including nuclear, solar, and fossil. This fluid provides a means of achieving high levels of efficiency at moderate temperatures. Little published information is currently available on the corrosion of nickel-based alloys in pure and impure CO_2. The University of Wisconsin has evaluated the corrosion behavior of metal samples in supercritical CO_2 at temperatures up to 650°C [39]. The limited test data indicate that 740H has a very low rate of mass gain at that temperature. Pint and Keiser at Oak Ridge National Lab have reported 500 h exposure data for alloys tested at temperatures of 650–750°C in a similar system at Oak Ridge National Lab [40]. These tests show chromia scale–forming alloys, including 740H, to have a low rate of mass gain at 700°C and 0.1 MPa pressure. Somewhat higher mass gains were observed when the temperature and pressure were increased to 750°C and 20 MPa. More comprehensive long-term corrosion data is expected from these continuing programs.

14.5.4 Stress corrosion cracking

Stress corrosion cracking (SCC) would not be expected to occur under boiler operating conditions; however, during maintenance shutdown, the system may be exposed to condensed impure aqueous fluids containing chlorides and hydroxides. SCC has been observed in stainless steels in operating boilers. Crum and Maitra conducted tests in two environments (ASTM G-36 boiling 45% magnesium chloride and boiling 50% sodium hydroxide) to determine the relative sensitivity of 740H to this mode of failure [41]. The data reported here are extracted from a larger list of materials that were tested. Test materials were cold rolled to a 1.32- to 3.18-mm thick strip. The age-hardened alloys were given their standard annealing and age-hardening heat treatment. The solid solution–strengthened alloys were tested after annealing at standard solution–annealing temperatures. U-bend specimens with applied stress greater than the yield stress were used.

A summary of the boiling 45% magnesium chloride tests is given in Table 14.4. Stainless steel 347 suffered early failure with trans-granular cracking. Alloys 617 did not fail, but one specimen was cracked. 740H exhibited no cracking. The boiling sodium hydroxide tests showed similar results, with 347 showing severe general corrosion and the nickel-base alloys including 740H having some cracking but no failure. Typically resistance to chloride SCC is enhanced by increasing nickel content. The nickel content of all alloys tested was 50–59% except for 347 SS, which had 11% nickel. Based on experience with these alloys in the chemical process industry, it was concluded that neither 617 nor 740H would be subject to SCC in boiler operation.

14.6 Manufacturing of mill product forms

14.6.1 Melting and remelting

In the early stages of the A-USC program, nickel-based superalloys were considered necessary only for superheater tubing. Tube can be manufactured from 500-mm

Table 14.4 Results of U-bend stress corrosion cracking tests in boiling aqueous solution of 45% magnesium chloride [41]

Alloy	Condition	Time to crack, h	Time to fail, h	Max crack depth, mm	Crack morphology	Comments
740H	Aged	<720	NF 720	0	None	
		NC 720	NF 720	0	None	
S17	Annealed	720	NF 720	0.05	Trans	
		NC 720	NF 720	0.02	Trans	
347	Annealed	5	24	2.97	Trans	Crack full thickness
		5	24	2.97	Trans	Crack full thickness



Figure 14.18 Macro-etched head-end ingot slice of 762-mm diameter 740H VIM/VAR ingot.

diameter vacuum induction melt (VIM) and electro-slag remelt ingots of the type for aerospace applications. These ingots typically weigh 5000 kg or less. However, in the US A-USC project, superalloys will be needed for the much larger steam transfer pipes and associated connections. These pipes will require ingots on a size scale never previously made with γ′-strengthened alloys. The first trial 740H pipe extrusion used a 762-mm diameter, 7570-kg ingot. Vacuum arc remelting (VAR) was specified as the remelting step to minimize the risk of solidification segregation. Conservative ingot heating and cooling practices were employed to negate the possibility of thermal stress cracking. A head-end macro-etch plate from the first large ingot is shown in Fig. 14.18. No evidence of solidification segregation was found. Table 14.5 shows the excellent chemistry uniformity. The details for this work have been reported previously [42]. From this work, it was concluded that ingot size would not be a limiting factor in the manufacture of large pipes.

14.6.2 Manufacture of tubing

The first tubes made for the Thermie program used a production route similar to that used in the nickel-based alloy industry for "hard" alloys such as 625. Subsequent production

Table 14.5 Composition of selected locations in head slice

Element	Edge	Mid-radius	Center
C	0.044	0.044	0.043
Cr	24.61	24.63	24.64
Al	1.36	1.36	1.36
Ti	1.34	1.33	1.33
Co	20.12	20.12	20.14
Nb	1.46	1.45	1.44

has used a similar process but tailored to available process equipment and final tube dimensions. The nominal manufacturing method is to forge an ingot to a 300- to 350-mm diameter rod, condition, and cut into billets. The billets are trepanned and machined to form a nose radius. The machined billets are then heated and extruded to a tube shell in a horizontal press. The shells are conditioned and then drawn or pilgered to final size. Depending on size, multiple cold-working, process-annealing, and pickling cycles are required. The tubes are then given the specified anneal and age, followed by nondestructive inspection and mechanical property testing. Both batch and continuous annealing procedures have been used; however, due to the time required, aging must be a batch process. A range of tube diameter/wall sizes ranging from 18 mm/2–50 mm/10.5 mm have been manufactured to date. The properties of mill-produced tube are summarized in Tables 14.2 and 14.3 and Fig. 14.9. While large quantities of boiler tubing may be needed for A-USC plants, supply of tube is not likely to be a constraint because conventional manufacturing equipment that is widely available can be used.

14.6.3 Manufacture of pipe

The first superalloy pipe was extruded from alloy 263 at Wyman-Gordon in Livingston, Scotland in 2002. Although this relatively short pipe was made from a conventional size ingot, it demonstrated the feasibility of manufacturing heavy-wall pipe. In 2011, a larger pipe of alloy 740H was extruded at Wyman-Gordon in Houston TX [43]. This 378 mm OD × 88 mm W × 10.5 mL pipe is shown in Fig. 14.19. Since then, a number of other pipes have been manufactured by a similar process. Mechanical properties are listed in Tables 14.2 and 14.3. It should be noted that average grain size of extruded pipe will be larger than that of cold worked tube due to the high temperatures required to extrude large pipe. Tube grain size is typically ASTM 3–5 whereas pipe is generally 1–3.

The manufacturing method for pipe depends on its size. Pipes smaller than about 300-mm OD can be produced by horizontal extrusion by the process used for tube shells. The pipes are conditioned and heat-treated without additional cold working. For large-diameter or heavy-wall pipes produced at Wyman-Gordon, the manufacturing method involves compaction and piercing an ingot in a closed die press and then machining the billet. This billet is then vertically extruded as shown in Fig. 14.19.

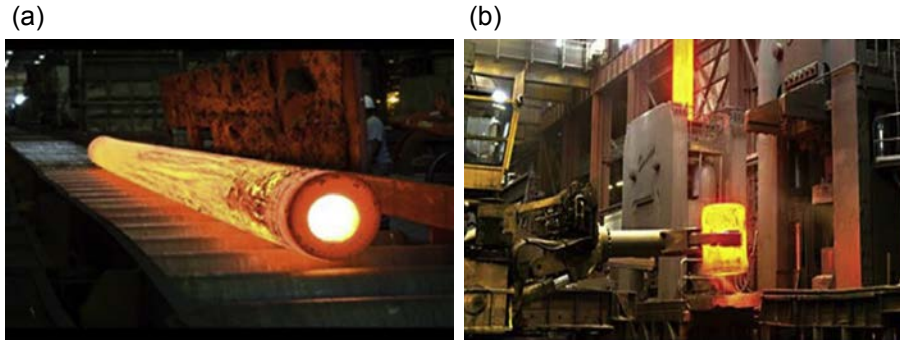


Figure 14.19 (a) As extruded 740H pipe, (b) Vertical piercing and extrusion process used at Wyman-Gordon Houston.

The maximum size pipe that can be produced is limited by the extrusion press load capacity rather than the billet size. Based on the initial extrusion trial, Klingensmith generated a reference table of possible 740H pipe sizes [43]. He projected that a 740H pipe as large as 860 mm OD × 63 mm W × 4.2 mL could be extruded on the Wyman-Gordon presses. With the recent addition of a similar size extrusion press in China, there are three presses capable of producing large superalloy pipes. An alternative method, hot roll piercing, that is commonly used for steel has not been tried on 740H.

Some component designs contemplate using pipe with walls too thin to extrude and too large in diameter to draw. In that case, circumferential cold roll forming on a lubricated mandrel can be used. The feasibility of making pipes by this process was demonstrated at PCC Rollmet in Irvine, California. A 66 mm OD × 15 mm W × 2mL pipe was produced from a trepanned bar. Larger diameter pipes will be produced for a project now underway.

14.6.4 Other mill product forms

Although the primary application for alloy 740H is for tube and pipe, it has been produced in other mill forms. Forged bar is an intermediate step in the manufacture of tubing, wire, and forging stock. Forging billet would be supplied in a mill-annealed condition with a capability heat treatment test to demonstrate fitness for service. In some cases, it may be desirable to machine components directly from mill heat-treated bar. To show capabilijty a 325-mm diameter bar was heat treated and tested. The tensile and impact toughness properties are shown in Table 14.2. This test is discussed in more detail in Section 14.7.6.

Spooled welding wire in standard sizes such as 0.89, 1.14, and 1.57 mm are now commercially available. Plates and sheets have been only made on a pilot scale; however, based on the similarity of 740H to traditional sheet alloys such as 263 and X750, manufacture of these products for applications such as membrane walls and heat exchangers should not be a problem.

14.7 Fabrication of components

14.7.1 Forming characteristics

Alloy 740H was designed to be formed in the annealed condition and then heat treated. Alloy 740H has relatively low hot forming loads compared to other nickel-based alloys with higher refractory metal contents. Fig. 14.20(a) and (b) show the peak compressive flow stress as a function of temperature for alloys 617 and 740H. These results were correlated with actual extrusion loads for same size pipes of the two alloys. Hot tensile ductility as determined by the Gleeble test shows greater than 70% reduction of area between 1025°C and 1175°C. At temperatures below about 925°C, γ′ can form during hot working with an associated increase in forming load and the possibility of surface cracking may be encountered.

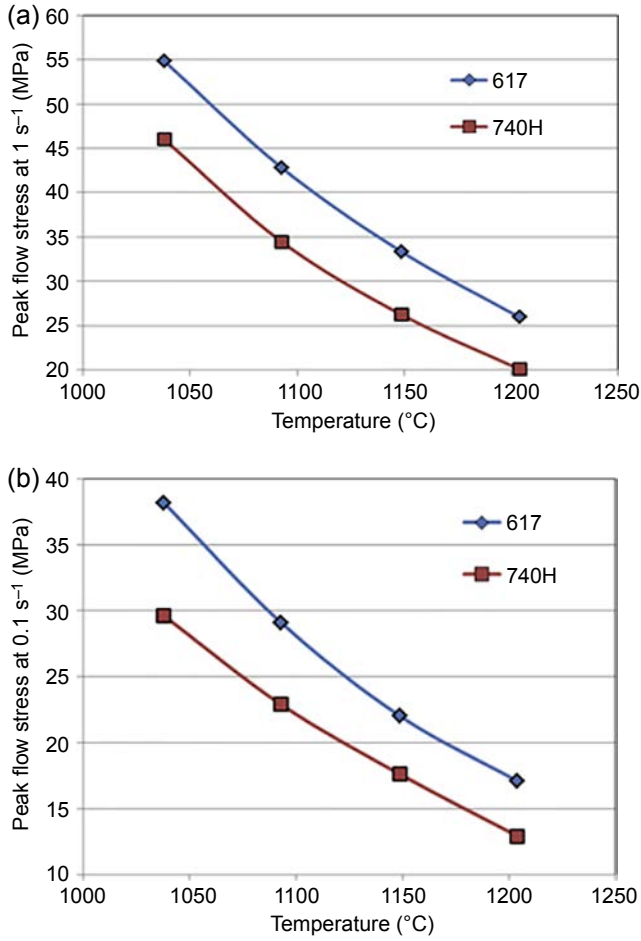


Figure 14.20 Compressive flow stress as a function of temperature for alloys 617 and 740H at $\dot{\varepsilon}$ of (a) 0.1/s and (b) 1.0/s.

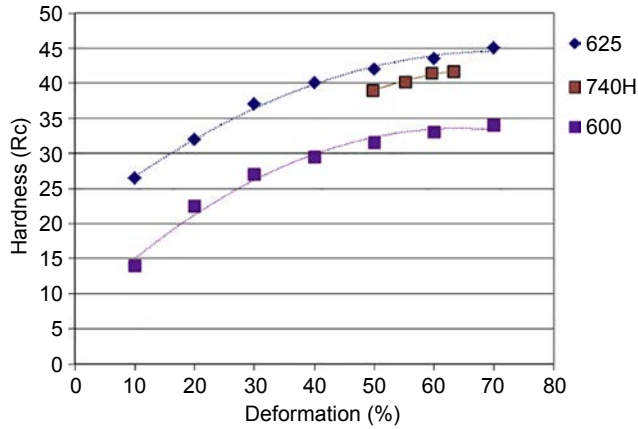


Figure 14.21 Cold work hardening curves for various nickel alloys.

Cold workability is important for the mill manufacture of tube, sheet, and wire as well as for fabricating operations such as bending, flaring, and hydroforming. Alloy 740H can sustain 50% or more cold compressive deformation when in the annealed condition. Work hardening is greater than alloy 600, but not as great as 625. Limited data from simple sheet rolling trials is shown in Fig. 14.21. A consideration for cold-worked alloy 740 is the possibility of strain-age cracking. All age-hardened alloys are subject to this phenomenon, and although 740H with a low level of γ' is relatively insensitive, for complex cold-worked parts, precautions should be taken.

14.7.2 Tube bending

Coal-fired boilers may contain small and large radius tube bends. Normally, bending is done in the shop of the designer/fabricator. Tube bending can be done cold or hot over a mandrel or by hot extrusion. Several fabricators have successfully made bends in alloy 740H tubing. Most of the trials have involved cold bending of solution-annealed material. Tensile properties of solution-annealed tube are shown in Table 14.2. The yield and tensile strength and ductility are similar to that of solution-annealed alloys 617 and 625. Cold bending of aged material is much more difficult due to greater spring back, inconsistent wall dimensional control, lower ductility, and potential for strain-age cracking. Yang et al. reported the unsatisfactory results of one such trial [44]. Accordingly, cold bending of 740H in the aged condition is not recommended.

ASME Code Case 2702 requires a full solution anneal before age hardening if the deformation exceeds 5%. Several independent studies have shown that alloy 740H shows a progressive loss of creep strength when cold tensile strain exceeds about 5% [45,46]. Shingledecker conducted a detailed investigation of the effect of cold work during bending on creep rupture properties of directly aged alloy 740H and compared the results with literature data for other age-hardened nickel-based alloys. He found that the loss of creep strength in tube as determined by an internally pressurized test is proportional to the amount of cold strain. The mechanism of failure is enhanced void

formation in the extrados region of the bend. At approximately 15% cold strain the creep strength falls outside of the scatter band for conventionally heat-treated material. It should be emphasized that full solution anneal and age will restore the original creep strength of cold worked 740H.

Zhou and coworkers have reported that a super-solvus heat treatment to precipitate intergranular $M_{23}C_6$ carbide at 1010°C followed by the conventional 800°C age-hardening treatment restored the creep strength of 740H [47]. This treatment was suggested as a way to avoid a more costly solution-annealing treatment. Additional creep testing will be required to gain code approval for this treatment.

14.7.3 Pipe bending

Large-diameter pipes such as those used for the boiler header cannot be bent cold due to the excessive forces required. A commonly used manufacturing technique is hot induction bending. This process involves passing the pipe incrementally through an induction coil while simultaneously applying a bending moment. This method has been used to bend 740H boiler tubes; however, process detail, microstructure, and properties have not been reported. Hot bending of 740H pipe has only recently been demonstrated. The details of this work which were not available when this manuscript was prepared are reported elsewhere [48].

14.7.4 Small forged components

Small fittings such as flanges, nozzles, saddles, and weldolets are required for power plant construction. If only a few parts are needed, they can be machined from forged bar, but for commercial production, they would be more economically be made by forging. Fig. 14.22 shows an as-forged and a machined prototype weld neck flange produced at Maass Flange Corporation, Houston, Texas, from a 102-kg, 375-mm-long billet cut from 200-mm-diameter bar of 740H. The parts were made by upsetting on a hydraulic press and then hammer forging the web in three sessions, and finally punching out the center. The initial forging temperature was 1176°C with a finishing

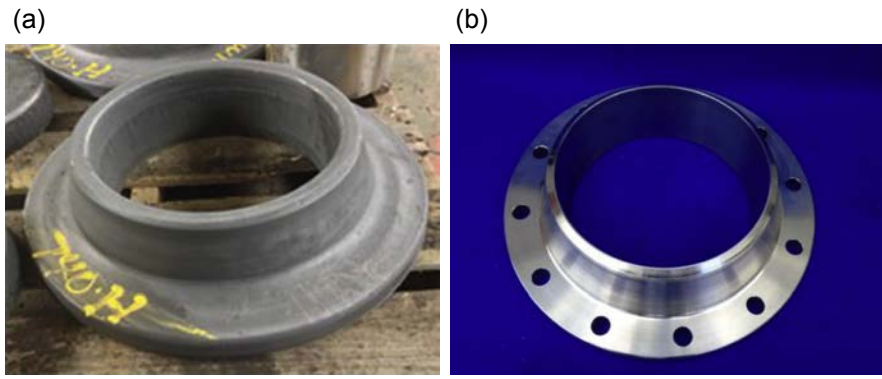


Figure 14.22 (a) As-forged weld neck flange, (b) Fully heat-treated and machined flange.

temperature of 1190°C to fill the corners. Excellent crack-free surface and corner fill was obtained.

The forging was annealed at 1121°C, water quenched, and aged at 800°C prior to sectioning for metallographic examination. A macro-etched cross-section of one segment is shown in Fig. 14.23. The grain size of ASTM –1 to 1 is coarser than that obtained in tube and pipe. A somewhat lower forging temperature would be required to produce an average grain size of 2–3 that would provide the best balance of creep strength and impact toughness. Tensile properties shown in Table 14.6 meet ASME code requirements. Two locations were tested, the horizontal base and the vertical web. Charpy V-notch impact toughness at these locations was very high. Two creep rupture tests have been conducted at 700°C at a stress of 482 MPa. The rupture lives of 71.8 and 80.5 h were relatively short but within the conventional 30% stress range.

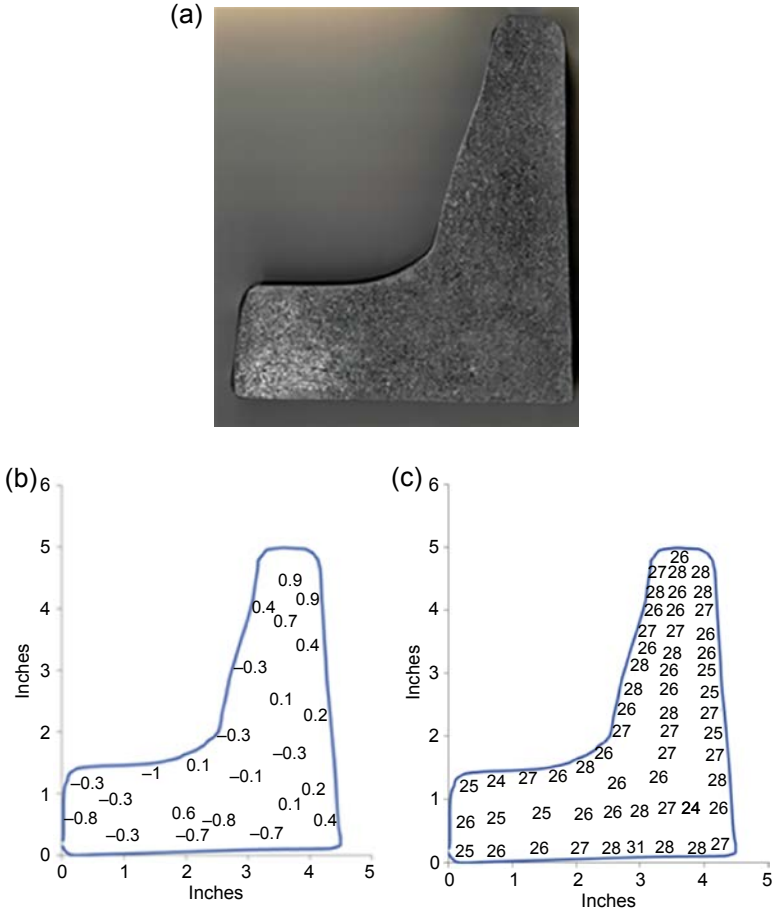


Figure 14.23 (a) Macro-etched cross-section, (b) ASTM grain size, (c) Rockwell C hardness.

Table 14.6 Mechanical properties of heat-treated alloy 740H weld neck flange

Source	Sample	0.2% YS, Mpa	UTS, Mpa	El, %	RA, %	CVN, J/cm^2
ASME 2702	Minimum	620	1035	20		
Web	A	682	1043	44.8	36.1	183
	B	682	1048	43.9	32.3	172
Base	A	699	1064	48.6	42.2	214
	B	716	1064	44.3	41.5	242

14.7.5 Small complex mode forgings

Fittings such as tees, reducers, and elbows involve combinations of compressive and tensile deformation. These parts may be made either hot or cold depending on the size. A prototype tee was made from a solution-annealed 200 mm OD × 18 mm w pipe section by cold hydroforming by CBI-Alloy Piping Products, Inc. in Shreveport, Louisiana. This was a multistep operation involving three successive expansions and process anneals. Photos of the partially formed and finished machined part are shown in Fig. 14.24. No tearing was experienced. Mechanical properties were not determined.

Other components of interest were hot formed from pipe of similar size at CBI APP. These parts include a hot forged elbow and several concentric reducers. The room temperature properties of the heat-treated elbow are shown in Table 14.4. These parts are shown in Fig. 14.25(a) and (b).

14.7.6 Large forged components

Large pipe fittings and valve components must be press forged and will require extensive machining. Whereas small parts such as the flange previously described can be quickly heated and cooled, and given optimum process conditions, should exhibit microstructure and properties similar to pipe and tube, the properties of large forgings will be location and thickness dependent. While no large forged part has yet been made from 740H, the properties of a solution-annealed, water-quenched and aged 343-mm-diameter bar shown in Table 14.2 are informative. Yield strength near the surface is comparable to that of thin wall tube, but yield strength at the bar center, while meeting ASME minimum, is significantly lower. Ductility and toughness were good. A hardness traverse taken on the as quenched bar showed VHN 170 at the surface and VHN 290 at the center. This is indicative of strong auto-aging in the bar center. Because the γ' that forms on slow cooling is relatively coarse, after the final aging treatment, the bar center will have lower strength than the surface. The microstructure and creep strength at the center of the bar has not been evaluated.

A calculated continuous cooling transformation diagram for alloy 740H is shown in Fig. 14.26. This diagram supports the notion that significant γ' hardening will occur

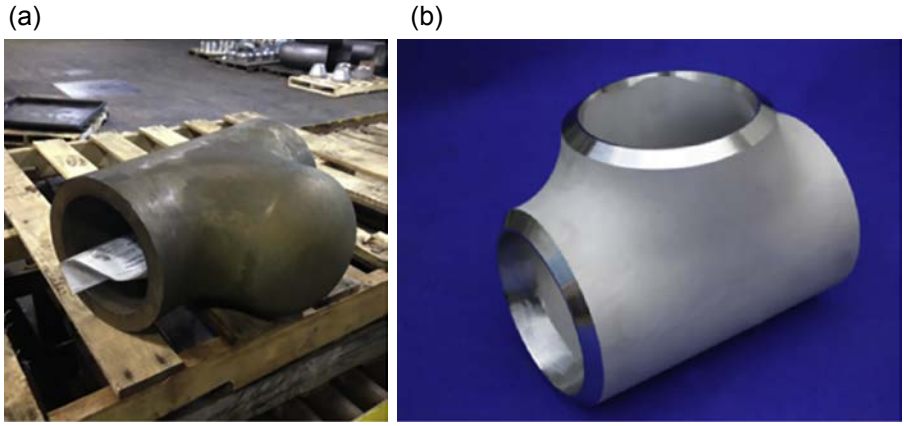


Figure 14.24 (a) As hydro-formed tee, (b) Heat-treated and machined tee.

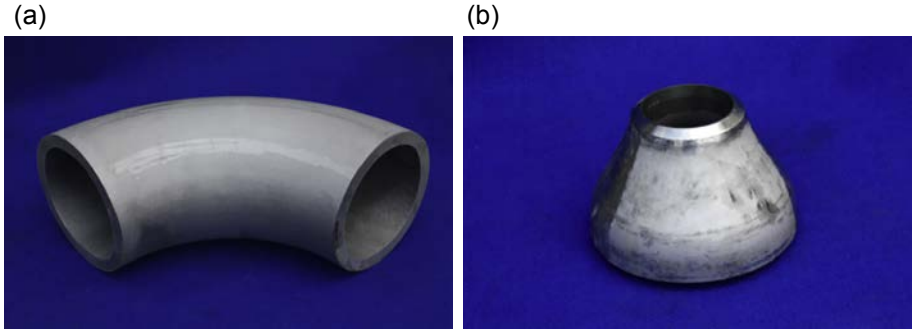


Figure 14.25 (a) Hot-formed elbow, (b) Cold-formed concentric reducer.

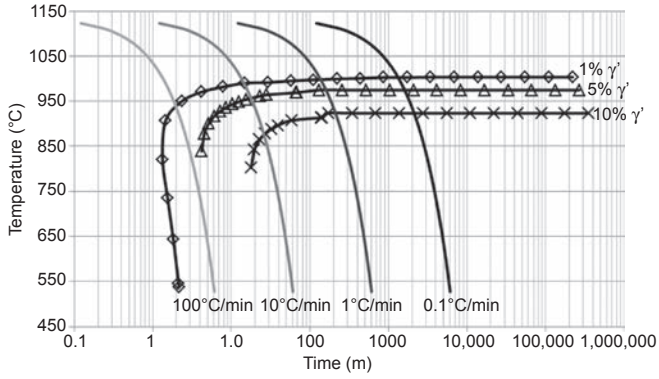


Figure 14.26 Calculated continuous cooling diagram for nominal 740H composition.

even during water quenching of a large forging. A cooling simulation was conducted for the bar heat treatment using DEFORM software [49]. The cooling rate at a depth of 25 mm was 315°C/min and at the bar center was 30°C/min. Based on the calculated CCT diagram, there should be about 10% γ′ in the center and no γ′ at the surface. That is consistent with the experimental results.

For large parts that must be machined, it is recommended that a γ′ coarsening treatment of 24 h at 900°C followed by a furnace cool be applied to reduce the hardness. This can be done either as a hold step on cooling from forging, or as a re-heat treatment. The hardness in this condition is approximately Rc 20 compared to Rc 30–35 when directly water or air cooled after annealing or forging.

14.8 Casting

Alloy 740H was considered in both the European and US A-USC programs for components in valve bodies and turbine casings that are traditionally produced as castings. Although superalloy aero-engine castings are commonly vacuum melted and investment cast, no currently existing foundry can make the largest castings needed for power plants. It has been reported that 740H has been air-induction melted and cast under an argon blanket into sand molds. While acceptable mechanical strength was obtained, ductility was low, and center cracking was noted [50,51]. The cracking was attributed to the presence of eutectic MC carbide networks at grain boundaries. Roberts has suggested a composition modification to suppress the formation of these carbides.

14.9 Welding

14.9.1 Welding procedures and best practices

Fusion welding is an essential joining method for power plant construction. The initial welding studies on precursor alloy 740 showed that it could be readily welded by GTAW and GMAW processes using a matching composition filler metal with good operability and tensile and bend properties [52]. Successful girth welds were made on boiler tubes and tested in the European and US programs. However, extensive micro-fissuring was observed in restrained heavy-section welds [9,10]. The composition changes that led to the redefined alloy 740H were described earlier in this chapter [14]. A reduction in liquidus–solidus temperature range provided greatly improved resistance to liquation cracking while retaining good operability. Extensive welding procedure development work has subsequently been done to support the various A-USC projects. These welding procedures were documented and communicated in industry workshops [53,54]. Table 14.7 shows welding procedures that have been used successfully.

Alloy 740H has generally good operability for a superalloy with good wetting and tie-in such that, under laboratory conditions and recommended procedures, ASME code quality welds with good properties have been consistently made. Shop-floor welding experience has been mixed due to the unfamiliarity of production welders

Table 14.7 Parameters used to produce acceptable welds in 740H using matching composition filler wire

INCONEL alloy 740H welding Parameters	Manual GTAW	Manual *p*-GMAW	Hot-wire GTAW
Power source	Miller Dynasty DX-300	Miller Axcess 350	AMI Model 415
Process	Manual GTAW	Manual P-GMAW	Hot-wire GTAW
Current, amps	180 ± 5	130 ± 5	110–270
Voltage, volts	15.0 ± 0.75	27.0 ± 1	15-Sep
Shielding gas	75 argon/25 helium	75 argon/25 helium	75 argon/25 helium
Flow rate, cfh	30	40	40
Electrode or wire feed speed (ipm)	2% thoriated tungsten 1/8″ dia wire	250 ipm with 0.045″ dia. Wire	100–175 with 0.045″ dia wire
Travel speed (ipm)	~8.0	~10.0	4–12
Heat input (kJ/in)	36	58.5	23.1
Interpass temperature	<350°F	<350°F	<350°F

with nickel-based superalloys. This experience highlights the need for rigorous welder training and qualification programs. Some key requirements for making successful alloy 740H welds are (1) use of pure, inert shielding gas, (2) careful management of heat input and interpass temperature, (3) maintenance of correct bead geometry, and (4) frequent removal of residual surface oxides. At the present time, there is no alloy 740H–coated electrode, although the SMAW process has been used with generic nickel-based welding electrodes to make dissimilar metal welds. The submerged arc welding process is not recommended for this alloy due to the difficulty in retaining the reactive age-hardening elements in the weld metal.

14.9.2 Weldment properties

ASME Code Case 2702 requires that welding of 740H be done with the base metal in the age-hardened condition and that the weldment then be stress relieved using the specified age-hardening treatment. Local solution treatment is not permitted because that would generate a γ' partially solutioned zone with properties that have not been documented. All of the cross-weld properties reported in this section were generated following that procedure. However, alternative procedures would be desirable for fittings and assemblies that could be heat-treated in entirety. Gollihue has welded light- and heavy-section plate in the solution-annealed condition and then applied the standard heat treatment. No problems of operability or stress relief cracking were encountered. Santella initially reported mechanical properties of welded age-hardened boiler tubes that were re-solution treated and aged. The tensile properties were similar to the conventionally prepared welds, and the creep strength was increased but not to the level of the base metal [55,56].

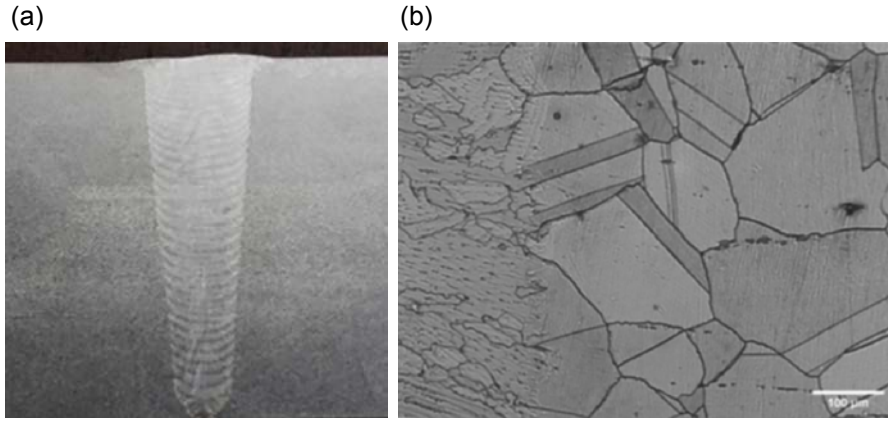


Figure 14.27 (a) Cross-section of multipass HW-GTAW weld in 378 mm OD × 88 mm W pipe, (b) microstructure at the fusion line.

Welds have been made in a plate, tube, and pipe in the course of developing procedures. The following are selected examples to illustrate the material capability. Additional data was reported by [9,53]. Three pairs of segments of the 378 mm OD × 88 mm W pipe described in Section 6.3 were welded at Babcock and Wilcox in Barberton, Ohio. Circumferential welds were made using a hot-wire, narrow-groove GTAW process with a fixed torch and rotating work piece. Argon-25% helium was used as the shielding gas for the matching composition filler wire. Welds were made with 5, 2, and 1° beveled V-grooves with a 1.57-mm land. A cross-section of a weld with a 5° bevel is shown in Fig. 14.27(a). The microstructure at the fusion line is shown in Fig. 14.27(b). One characteristic of welds in 740H is the virtual absence of a coarse-grain heat-affected zone. This unusual behavior may be due to the pinning of grain boundaries by NbC as inferred from the work of Bechetti [57]. The full pipe sections were aged for 5 h at 800°C using a ceramic tile heating blanket. This is a commonly used procedure for post-weld heat treatment of welds at the plant construction site. No fissures, porosity, or cracking were detected with ultrasonic, radiographic, or microscopic examination. The cross-weld tensile properties are listed in Table 14.8 and weld metal impact properties in Table 14.9. Bend test results are shown in Fig. 14.28. Per ASME Code Case 2702, a 4T minimum bend radius is applied. Baker reported additional detail on these procedures [58].

Gas metal arc welding is commonly used in boiler construction. To demonstrate the applicability to 740H, *p*-GMAW welds were made using the parameters listed in Table 14.7 in 50.8-mm-thick plate. As with the GTAW process, operability was excellent. Tensile properties are shown in Table 14.10. Four full-section 2T side bends passed ASME Section IX requirements.

14.9.2.1 Creep rupture properties

Oak Ridge National Lab has conducted extensive creep rupture testing of GTAW-welded boiler tubes using cross-weld specimens [55,56]. Creep fracture was primarily

Table 14.8 Tensile properties of HW-GTAW pipe weld

Sample location	YS, MPa	UTS, MPa	El, %	RA, %	Fracture location
OD	815	1135	21.3	22.8	Weld
OD	803	1122	21.2	24.9	Weld
Mid-wall	762	1098	24.6	22.3	Base
Mid-wall	758	1089	20.6	21	Base
ID	750	1081	21.4	22.9	Base
ID	756	1087	24.4	24.5	Base
ASME min		1035			

Table 14.9 Charpy V-notch ambient temperature impact tests. Heat treatment I standard SA = A, heat treatment II, SA + A + A

Heat treatment	Location	Base/weld	Orientation	J/cm^2
I	Pipe Ctr	Base	L	81
II	Pipe Ctr	WC	T	82
II	Pipe Ctr	HAZ	T	67
II	Outside pad	Base	L	73
II	Adjacent to weld	Base	L	54



Figure 14.28 Cross-weld ambient temperature tensile test and full-section 4T side bend test.

in the weld metal with a shorter rupture life than the base metal average. Failure was reported to be by creep cavitation at vertical dendrite boundaries. No heat-affected damage was observed. A detailed analysis of the microstructure and fracture location of these samples has been conducted by Bechetti at Lehigh University. The results of

Table 14.10 Tensile properties of *p*-GMAW weld in 50.8-mm-thick plate

Test	0.2% YS	UTS	El, %	R of A%	Failure
1	722.6	1052.2	21.2	22.3	Weld
2	766.7	1057	18.4	18	Weld
3	749.5	1054.2	19.6	22.6	Weld
4	776.4	1066.7	21.7	23.3	Weld
ASME		1035			

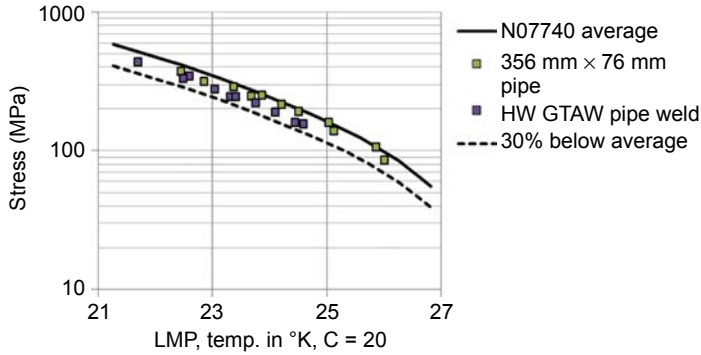


Figure 14.29 Creep rupture properties on cross-weld specimens.

this study will be published in 2016. Based on analysis of these creep rupture results, a creep strength reduction factor (WSF) of 0.7 was assigned in the ASME Code Case. Fig. 14.29 shows cross-weld creep test results obtained by Special Metals on tube and pipe welds. These tests also failed in the weld metal; however, the strength reduction of about 20% was less than the base metal average. This is attributed to use of a slightly stronger filler metal composition.

The metallurgical cause of the loss of weld metal creep strength has been investigated in projects at Ohio State and Lehigh Universities [21,59]. These studies show that the large degree of interdendritic segregation during weld metal solidification is the root cause. In power plant construction, full homogenization of welds, a process that would require heating for an extended time at a temperature just below the alloy solidus, is impractical. Consequently, the weld behaves as a composite with composition modulation. The SEM micrograph in Fig. 14.30(a) illustrates this dendritic structure in 740H weld metal. In this case the lighter areas are regions of high γ' content (22.8%) and the darker regions of lower γ' content (9.8%). This disparity is primarily due to the partitioning of titanium and niobium during solidification. As a result of this segregation, during creep strain, grain boundary migration and directional coarsening of γ' particles induces the formation of low-strength precipitate-free zones. Cavitation and final creep fracture are initiated in these zones. This is illustrated in Fig. 14.30(b). Various avenues to mitigate these effects are being explored.

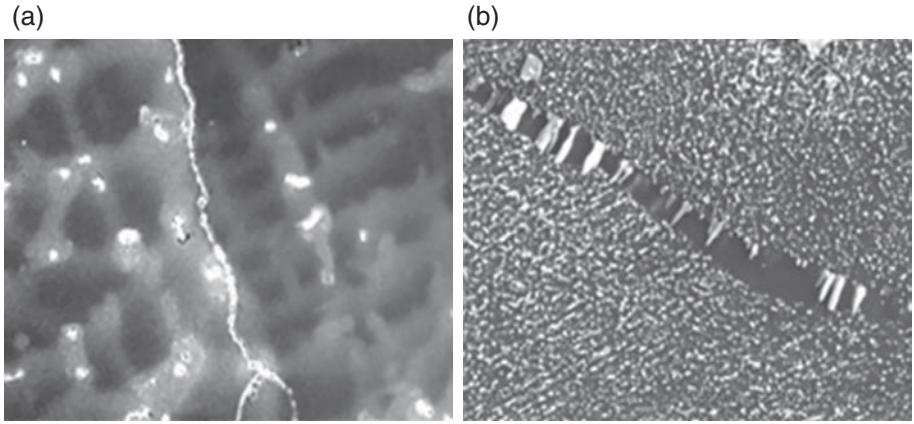


Figure 14.30 (a) SEM micrograph showing dendrite structure with modulated γ′ density [59], (b) SEM micrograph showing γ′ with a directional growth habit and precipitate-free zone [21].

ASME currently applies WSF only to longitudinal seam welds that are unlikely to be used in A-USC power plant design. There are several strategies that can be applied if a higher strength weldment is required. Baker has reported a WSF of 0.80 for one experimental heat of filler wire indicating that the strength of the aged weld metal is composition sensitive. Hence an optimum creep strength filler wire composition within UNS N07740 may be possible. The US consortium has explored other filler metals in their experimental program at ORNL. In this work a WSF of 0.82 for alloy 263 and 0.85 for Haynes alloy 282 was reported [56]. A third alternative is to solution treat the weld before aging. This approach yielded a WSF of 0.88. Solution treatment may be difficult to apply for field fabricated piping, but it could be useful for welding fittings in the fab shop.

14.9.2.2 Long time aged properties

The effect of high-temperature exposure time on 740H base metal was discussed in Section 14.4.5. A similar study was conducted on a 740H plate welded by GTAW using matching composition filler metal. The weld was aged at 800°C for 4 h prior to stress-free exposure at various temperatures for up to 10,000 h. Cross-weld Charpy V-notch impact tests were conducted with the notch located in the weld metal. The results of this study are shown in Fig. 14.31. Note that the impact values are higher than that of the base metal and that they do not drop off as quickly. This is attributed to the effect of the composite weld metal structure with higher ductility (lower γ′ content) dendrite cores. SEM micrographs are shown in Fig. 14.32. The microstructure of the weld metal is stable to at least 10,000 h with no indication of η or precipitate-free zones.

14.9.3 Fabricated components

A simulated boiler header was fabricated using the preferred process parameters. Circumferential welds were made on 378 mm OD × 88 mm W extruded,

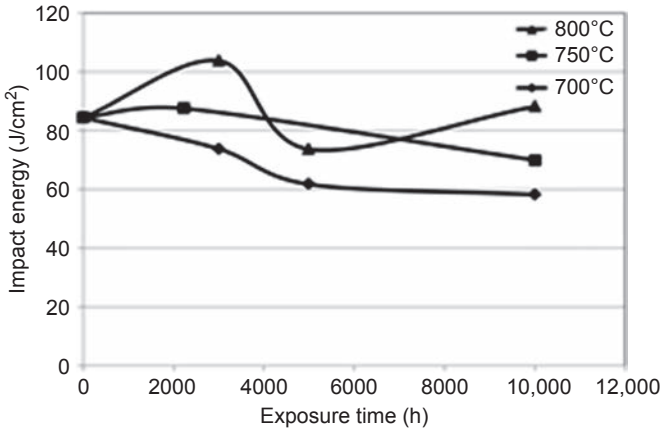


Figure 14.31 CVN impact properties of weld metal exposed stress-free at 700°C, 750°C, and 800°C.

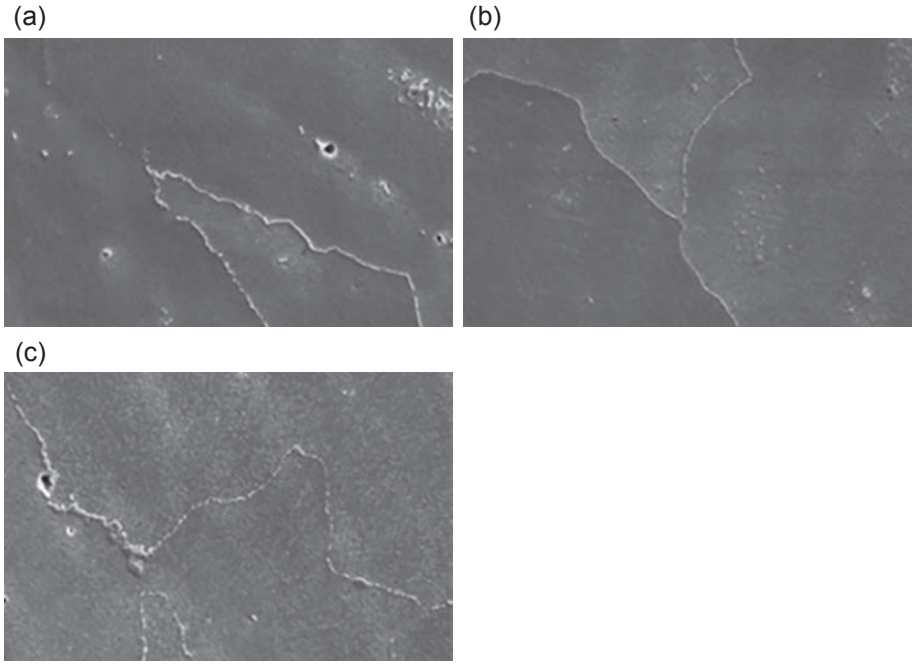


Figure 14.32 SEM microstructures for specimens aged 10,000 h at (a) 700°C, (b) 750°C, and (c) 800°C.

solution-annealed and aged pipe. These welds were made using the hot-wire, narrow-groove GTAW process described previously [58]. For this simulated header, the nipples were inserted in predrilled holes and GTAW welded internally with a special rotary torch. The external welds were made manually by GTAW. This prototype header section is shown in Fig. 14.33.

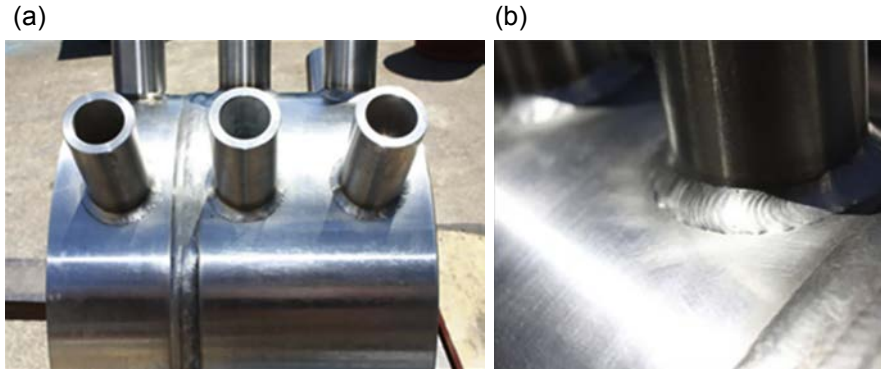


Figure 14.33 (a) Simulated header, (b) detail of nipple weld.

14.9.4 Dissimilar metal welding

Due to their high cost relative to steel, nickel alloys will only be used in sections of the A-USC boiler and turbine where they are absolutely essential. Consequently, they will need to be joined to other materials such as ferritic and austenitic stainless steels. Several fabricators have evaluated dissimilar metal welds incorporating alloy 740H. Baker has presented the results of welds to 316 and P92 steels [60]. Restrained, V-groove plate welds were made using GTAW: FM 82 (ERNiCr-3), P87 (ERNiFeCr-4 draft), and 617 (ERNiCrCoMo-1) and SMAW: WE 182 (ENiCrFe-3) and P87 (ENiFeCr-4 draft). The alloy 740H base metal was in the aged condition, and welds were stress relieved for 4 h at 760°C. This temperature was chosen as the best compromise for stress relieving the different base materials. A representative pair of micrographs is shown in Fig. 14.34. All combinations produced sound welds, and all except SMAW with WE P87 passed ASME tensile and bend qualification requirements with failure in the steel base metal. All creep specimens fractured in the steel member. This work demonstrated the feasibility of welding alloy 740H directly to steel, but more extensive procedure development will be needed to make this a robust process for field welding.

Parameter	740H/316 w FM82		740H/P92 w FM82		740H/P92 w WE182	
	GTAW		GTAW		SMAW	
0.2% YS, MPa	367	365	418	419	409	497
UTS, MPa	642	666	672	677	677	681
El, %	21.9	31.8	23.3	22.5	23.6	21.2
RA, %	41.4	72	64.4	64.3	63.2	63.3
Fracture location	82/316	316	P92	P92	P92	P92
ASME min UTS	517		620		620	
2-T side bend	Passed		Passed		Passed	

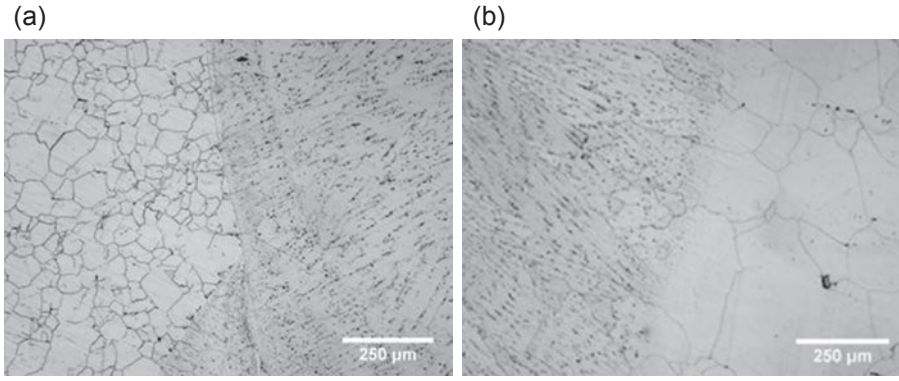


Figure 14.34 Photomicrographs of polished and etched cross-sections from 316-FM82-740H GTAW joint (316/weld fusion line at left; weld/740H fusion line at right).

14.9.5 Stress relief and stress relaxation cracking

Stress relief cracking is a well-documented problem in some γ′ strengthened nickel-based alloys such as Waspaloy. Consequently, there has been considerable interest in how alloys such as 740H, albeit with a lower volume fraction of γ′, will perform. Ramirez used Gleeble tests to simulate the effect of various heating cycles that might be applied during the stress relief/aging cycle on the heat-affected zone in 740. He concluded that it is relatively resistant to HAZ cracking (similar to alloy 718) [61]. To date, many alloy 740H weldments in 10- to 75-mm-thick section, some with restraint, have been made and stress relieved with no reported weld metal or HAZ cracking. However, these short time tests cannot fully predict the sensitivity to cracking of highly restrained weldments in service. Special Metals has studied the stress relaxation cracking issue by using a circular patch test that has been employed for evaluating stainless steel [62,63]. In this test a circular 19-mm-deep U-groove was machined in a 37.5-mm-thick annealed and aged 740H plate. A nine-pass GTAW weld was made with the final cap pass at the outside to accentuate the stress in that area. The welded plate was stress relieved for 4 h at 800°C and then exposed at 700°C for a total time of 10,000 h. The plate was removed from the furnace and examined with ultrasonic and radiographic methods at 1000 h intervals. No cracking was observed. The appearance of the plate at the end of the test is shown in Fig. 14.35.

The weld cross-section after completion of the test is shown in Fig. 14.36(a). Examination of other planes revealed isolated porosity and lack of fusion voids. There was no evidence that these cavities enlarged during the test. The microstructure in the HAZ and weld metal is shown in Fig. 14.36(b). No creep voids were seen. The grain size of both the base metal and HAZ was ASTM 2.5–3. The lack of a coarse grain zone is typical for GTAW welds in alloy 740H weldments. The test evaluation including residual mechanical properties is continuing. Additional details will be published in the future.

Additional projects to investigate stress relaxation cracking in 740H and other nickel-based alloys are under way at the Center for Integrative Materials Joining Science for Energy Applications at Ohio State [64] and Lehigh Universities, as well as several boiler manufacturers.

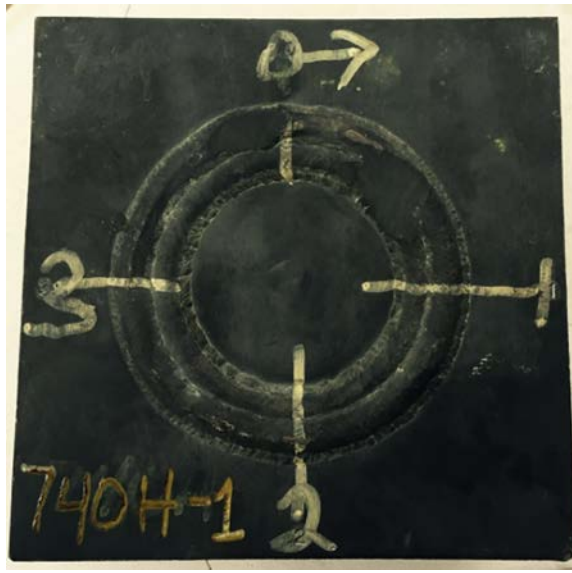


Figure 14.35 Borland test specimen after 10,000 h interrupted exposure at 700°C.

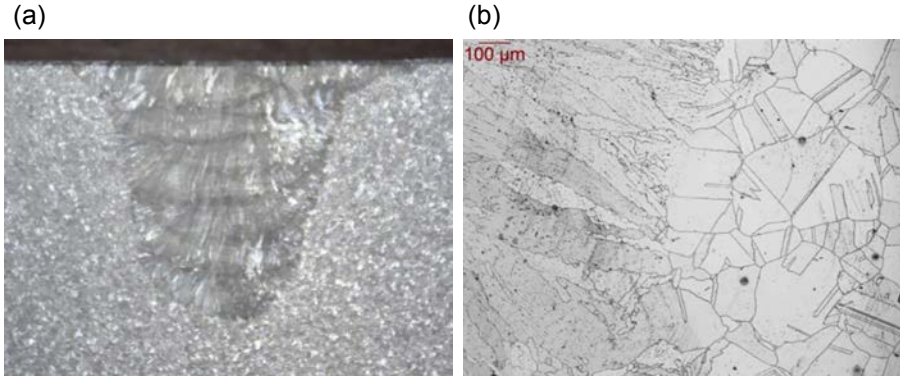


Figure 14.36 (a) Cross-section of weld after 10,000 h exposure at 700°C, (b) microstructure at fusion line in highest residual stress area at the top of the weld.

14.10 Summary

A large amount of work has been done in laboratories and plants in the United States, Europe, and Asia to characterize the structure and properties of alloy 740H. This chapter provided an overview of published information. There is also a reserve of unpublished information that has been generated by power plant designers and fabricators. Taken as a whole, this information supports the belief that alloy 740H has material properties and fabricability suitable for use for welded pressure-containing components for power plants operating in the 650–800°C temperature range. However, actual operating experience is very limited. Test loops containing 740H boiler tubing have been

built and operated and the material evaluated as mentioned previously. Additional test loops and pilot plants that include tube, pipe, and fittings are in the material procurement or construction stage. These include exposure to supercritical CO_2 as well as supercritical steam. One full-scale plant application for 740H pipe is in final installation. Clearly the installation, service, and repair experience will provide important information for improving the technology of 740H and other age-hardened alloys.

Several areas of technology need further development. Creep fatigue and thermal fatigue need to be more thoroughly examined. A more comprehensive understanding of stress relaxation cracking in complex restrained structures is also needed. Since this kind of cracking may take thousands of hours to become evident, a full characterization will take some time. Experience under plant conditions is the real test. Other welding issues include (1) increasing weld creep strength, (2) developing a coated electrode for SMAW, (3) more thorough characterization of dissimilar metal welds, and (4) characterization of welds made in solution-annealed base metal.

References

[1] K. Nicol, Status of Advanced Ultra-supercritical Coal-fired Power Plant, IEA Clean Coal Centre, London, UK, 2013.

[2] G. Schmidt, et al., Component Test Facility for a 700°C Power Plant (Comtes 700), Final Report to the European Commission, Directorate General for Research and Innovation, Luxembourg, 2013, EUR 2591.

[3] B.A. Baker, R.D. Gollihue, J.J. deBarbadillo, S.J. Patel, D. Maitra, Manufacturing demonstration of INCONEL alloy 740H for AUSC boilers, in: Proceedings: Seventh International Conference on Advances in Materials Technology for Fossil Power Plants, EPRI, ASM International, Waikaloa, HA, USA, October 22–25, 2013, pp. 215–229.

[4] J.P. Shingledecker, N.D. Evans, G.M. Pharr, Influences of composition and grain size on creep rupture behavior of INCONEL alloy 740, Materials Science and Engineering 578 (August 2013) 277–286.

[5] J.J. deBarbadillo, B.A. Baker, X. Xie, Microstructure stability of alloy 740H and its effect on material properties, in: Proceedings: ASME Symposium on Elevated Temperature Application of Materials for Fossil, Nuclear and Petrochemical Industries, ASME, Seattle, WA, USA, March 25–27, 2014.

[6] ASME, Case 2702 Seamless Ni-25Cr-20Co material, Section 1, cases of the ASME boiler and pressure Vessel code, BPV-Supp. 7, American Society of Mechanical Engineers, 2011.

[7] D.K. McDonald, E.S. Robitz, Coal ash corrosion resistant materials testing program, in: Proceedings: 19th Annual Conference on Fossil Energy Materials, NETL, Knoxville, TN, USA, May 2005.

[8] J.L. Marion, S. Sen, State of the art ultra-supercritical (USC) and readiness for advanced ultra-supercritical (A-USC) steam power plants, in: Global Energy Technology Summit 2014, Nov. 7–9, 2014, New Delhi, India, CD, 2014.

[9] J.M. Sanders, B.A. Baker, J.A. Siefert, R. Gollihue, Elimination of fissures in thick section Inconel alloy 740 welds, in: Proceedings: 34th Annual International Technical Conference on Clean Coal and Fuel Systems, Coal Technology Association, Clearwater, FL, USA, May 2009.

[10] J.E. Ramirez, Susceptibility of IN740 to HAZ liquation cracking and ductility dip cracking, Welding Journal 91 (April 2012) 122s–131s.
[11] S. Zhao, J. Dong, X. Xie, G.D. Smith, S. Patel, Thermal stability study on a New Ni-Cr-Co-Mo-Nb-Ti-al superalloy, in: Proceedings: Superalloys, TMS, Seven Springs, PA, USA, 2004, pp. 63–72.
[12] Q. Wu, Microstructural Evolution in Advanced Boiler Materials for Ultra-supercritical Coal Power Plants (Ph.D. dissertation), University of Cincinnati, 2006.
[13] J.P. Shingledecker, H. Hendrix, J. Siefert, J. Phillips, R. Purgert, P. Rawls, U.S. Program on advanced supercritical power plant materials – the economy of using advanced alloys, in: IEA Clean Coal Centre Workshop: Advanced Ultrasupercritical Coal-fired Power Plants, Vienna, Austria, September 19–20, 2012.
[14] B.A. Baker, R.D. Gollihue, Optimization of Inconel alloy 740 for advanced ultra supercritical boilers, in: Proceedings: Sixth International Conference on Advances in Materials Technology for Fossil Power Plants, EPRI, ASM International, Santa Fe, NM, USA, August 31–September 3, 2010, pp. 96–109.
[15] N.D. Evans, P.J. Masiasz, R.W. Swindeman, G.D. Smith, Microstructure and phase stability in INCONEL alloy 740 during creep, Scripta Materiala 51 (2004) 503–507.
[16] C. Chi, S. Zhao, F. Lin, X. Xie, Structure stability study on Inconel 740/740H Ni-base superalloy for 700°C AUSC power plant application, in: The 5th Symposium on Heat Resistant Steels and Alloys for High Efficiency USC/AUSC Power Plants, Seoul, Korea, May 26–29, 2013.
[17] Thermo-Calc Software Inc, 4160 Washington Road, Suite 230, McMurray, PA, USA, 15317.
[18] X. Xie, et al., An investigation on structure stability of advanced heat resisting steels and Ni-base superalloys for 600–700°C AUSC power plant application, in: Proceedings: Seventh International Conference on Advances in Materials Technology for Fossil Power Plants, EPRI, Waikoloa, HA, USA, 2013, pp. 98–119.
[19] JMatPro version 6.2, Sente Software Ltd., Surrey Technology Centre, 40 Occam Road, Surrey, UK GU2 7YG.
[20] S. Zhao, F. Lin, R. Fu, C. Chi, X. Xie, Microstructure evolution and precipitates stability in INCONEL alloy 740H during creep, in: Proceedings: Seventh International Conference on Materials Technology for Fossil Power Plants, EPRI, ASM International, Waikaloa, HA, USA, 2013, pp. 265–275.
[21] D.H. Bechetti, J.N. DuPont, J.J. deBarbadillo, B.A. Baker, M. Watanabe, Microstructural evolution of INCONEL alloy 740H fusion welds during creep, Metallurgical and Materials Transactions A, TMS/ASM 46A (2015) 739–755.
[22] P.F. Tortorelli, K.A. Unocic, H. Wang, M. Santella, J.P. Shingledecker, Creep-rupture behavior of precipitation strengthened Ni-base alloys under advanced ultra-supercritical steam conditions, in: Proceedings: Seventh International Conference on Advances in Materials Technology for Fossil Power Plants, ASM International, Waikaloa, HA, USA, 2013, pp. 131–142.
[23] J.J. deBarbadillo, B.A. Baker, R.D. Gollihue, Nickel-base superalloys for advanced power systems – an alloy producer's perspective, in: The 4th International Symposium – Supercritical CO_2 Power Cycles, Pittsburgh, PA, USA, September 9–10, 2014.
[24] S. Zhang, Y. Takahashi, Evaluation of high temperature strength of a Ni-Base alloy 740H for advanced ultra-supercritical power plant, in: Proceedings: Seventh International Conference on Materials Technology for Fossil Power Plants, EPRI, Waikaloa, HA, USA, ASM International, 2013, pp. 242–253.
[25] J.J. deBarbadillo, B.A. Baker, R.D. Gollihue, S.J. Patel, Alloy 740H component manufacturing development, in: Proceedings: Energy Materials Conference, CSM and TMS, Wiley Press, Xi'an China, 2014, pp. 203–210 (CD).

[26] R.J. Smith, B.A. Baker, G.D. Smith, Nickel alloys for the next generation of advanced steam boilers, in: VGB Materials and Quality Assurance Conference, Dortmund, Germany, March 2004.
[27] D. Maitra, B.A. Baker, G.D. Smith, Oxidation behavior of candidate alloys for advanced-ultra super critical boiler application, NACE Corrosion (2013) Paper No 2280.
[28] S. Osgerby, A. Fry, Assessment of steam oxidation behavior of high temperature plant materials, in: Proceedings: Fourth International Conference on Advances in Materials Technology for Fossil Power Plants, EPRI, Hilton Head Island, SC, USA, October 2004.
[29] G.R. Holcomb, S.D. Cramer, B.S. Covino, S.J. Bullard, M. Ziomek-Moroz, D.E. Altman, Oxidation of Alloys for Advanced Steam Turbines, Report No. DOE/ARC-2005-067, January 1, 2005. [OSTI ID No. 895402], 2005.
[30] G. Holcomb, High pressure steam oxidation of Ni-Base superalloys in advanced ultra-supercritical steam boilers and turbines, in: Proceedings of: 8th International Symposium on Superalloy Derivitives, TMS, September 28–October 1, 2014, pp. 613–627(CD).
[31] J.M. Sarver, J. Tanzosh, Characterization 718 and of steam-formed oxides on candidate materials for USC boilers, in: Proceedings: Sixth International Conference on Advances in Materials Technology for Fossil Power Plants, August 31–September 3, 2010. Santa Fe, NM, USA.
[32] M. Tamura, N. Yamanouchi, M. Tanimura, S. Murase, Promising alloys for the heat exchangers of advanced coal fired boilers, in: Proceedings: Exposition and Symposium on Industrial Heat Exchanger Technology, ASM, Materials Park, OH, 1985, p. 273.
[33] B.A. Baker, G.D. Smith, Corrosion resistance of alloy 740 as superheater tubing in coal-fired ultra-supercritical boilers, NACE Corrosion 2004 (2004) Paper No. 04526.
[34] P. Castello, V. Guttman, N. Farr, G.D. Smith, Laboratory simulated fuel-ash corrosion of superheater tubes in coal fired ultra supercritical boilers, in: Proceedings of the EUROMAT Conference, Wiley-VCH Verlag – ORA/PRO 60750, Munich, September 1999.
[35] M.S. Gagliano, H. Hack, G. Stanko, Fireside corrosion resistance of proposed USC superheater and reheater materials, in: Proceedings: 34th International Technical Conference on Clean Coal and Fuel Systems, Coal Technology Association, Clearwater, FL, USA, May 2009 (CD).
[36] K. Natesan, Z. Zeng, D.L. Rink, Materials performance of structural alloys in simulated Oxy-fuel environments, in: Proceedings: 24th Annual Conference on Fossil Energy Materials, NETL, Pittsburgh, PA, USA, May 2010.
[37] G.D. Smith, B.A. Baker, S.J. Patel, J.J. deBarbadillo, Assessment of the coal ash corrosion resistance of nickel-base alloys in advanced ultra-supercritical boiler environments, in: Proceedings: 37th International Technical Conference on Clean Coal and Fuel Systems, Sarasota FL, USA, 2012(CD).
[38] S.C. Kung, High-temperature corrosion mechanisms for selected Iron and nickel-based alloys exposed to sulfur and chlorine-containing environments, Corrosion 71 (4) (April 2015) 483–501.
[39] K. Sridharan, Corrosion in Supercritical Carbon Dioxide: Materials, Environmental Purity, Surface Treatments and Flow Issues, U. S. DOE Report 10-872, December 10, 2013, 205, 2013.
[40] B.A. Pint, J.R. Keiser, The effect of temperature on the sCO_2 compatibility of conventional structural alloys, The 4th International Symposium on Supercritical CO_2 Power Cycles, September 9–10, 2014, pp. 1–13.

[41] J.R. Crum, D. Maitra, Stress corrosion cracking resistance of candidate AUSC alloys, NACE Corrosion (2014) Paper No. 3981.
[42] J.J. deBarbadillo, B.A. Baker, R.D. Gollihue, Age-hardened nickel-base alloys for advanced energy applications, in: 8th International Symposium on Superalloy 718 and Derivatives, TMS, Pittsburgh PA, September 28–October 1, 2014, pp. 681–696 (CD).
[43] L. Klingensmith, Development of extruded heavy-wall large diameter nickel-base alloy piping for AUSC power plants, in: Global Advanced Fossil Gen Summit 2011, Asian Coalition for Climate and Energy, Shanghai, China, December 6–7, 2011, pp. 272–298.
[44] H.-C. Yang, et al., Discussion of delivered condition specified in ASME code case 2702 on INCONEL 740H used for a-USC boiler, in: Proceedings: Seventh International Conference on Advances in Materials Technology for Fossil Power Plants, EPRI, Waikoloa, HA, USA, 2013, pp. 276–280. ASM International.
[45] J.P. Shingledecker, G.M. Pharr, Testing and analysis of full-scale creep-rupture experiments on INCONEL alloy 740 cold-formed tubing, Journal of Materials Engineering and Performance 22 (2) (2013) 454–462.
[46] K. Kubishiro, K. Nomura, S. Takahashi, M. Takahashi, H. Nakagawa, Effect of pre-strain on creep properties of alloy 740, in: Proceedings: Sixth International Conference on Advances in Materials Technology for Fossil Power Plants, EPRI, ASM International, Santa Fe, NM, USA, 2010, pp. 164–170.
[47] R. Zhou, L. Tang, B. Wang, S. Hou, Y. Guo, Effect of heat treatment on the microstructure and properties of cold worked Inconel 740H boiler tubes, in: Energy Materials 2014, CSM/TMS, Xian China, 2014, pp. 279–285 (CD).
[48] J.J. deBarbadillo, B.A. Baker, S.A. McCoy, Alloy 740H—Development of fittings capability for AUSC applications, in: Proceedings: Eighth International Conference on Advances in Materials Technology for Fossil Power Plants, Algarve, Portugal, ASM International, October 2016, to be published.
[49] DEFORM, Scientific Forming Technologies Corporation, 2545 Farmers Drive – Suite 200, Columbus, OH, USA.
[50] P.D. Jablonski, J.A. Hawk, INCONEL alloy 740: potential for use in A-USC Castings, in: Proceedings: 8th International Symposium on Superalloy 718 and Derivitives, TMS, 2014, pp. 809–822(CD).
[51] S. Roberts, R. Lease, Advances in large nickel alloy turbine casting for 700°C operation, in: Energy Materials 2014, CSM and TMS, Xi'an China, 2014, pp. 211–218.
[52] J.M. Sanders, J.E. Ramirez, B.A. Baker, Weldability investigation of INCONEL alloy 740 for ultra supercritical boiler applications, in: Proceedings: Fifth International Conference on Advances in Materials Technology for Fossil Power Plants, ASM International, March 2008, pp. 818–829.
[53] J.A. Siefert, J.M. Tanzosh, J.E. Ramirez, Weldability of INCONEL alloy 740H, in: Proceedings: Sixth International Conference on Advances in Materials Technology for Fossil Power Plants, Santa Fe, NM, USA, August 31 – September 3, 2010, pp. 1045–1066.
[54] R.D. Gollihue, B.A. Baker, J.E. Dierksheide, J.M. Tanzosh, Practical guide to welding INCONEL alloy 740H, in: Proceedings: Seventh International Conference on Advances in Materials Technology for Fossil Power Plants, EPRI, Waikaloa, HA, USA, 2013, pp. 1025–1038.
[55] M. Santella, J.P. Shingledecker, R. Swindeman, Materials for advanced ultra-supercritical steam boilers, in: Proceedings: 24th Annual Conference on Fossil Energy Materials, Pittsburgh, PA, USA, May 26, 2010.

[56] J.P. Shingledecker, Creep-rupture performance of INCONEL alloy 740 and welds, in: Proceedings: Seventh International Conference on Advances in Material Technology for Fossil Power Plants, EPRI, ASM International, Waikaloa, HA, USA, 2013, pp. 230–241.
[57] D.H. Bechetti, J.N. DuPont, J.J. deBarbadillo, B.A. Baker, Homogenization and dissolution kinetics of fusion welds in Inconel alloy 740H, Metallurgical and Material Transactions A, TMS/ASM 45A (2014) 3051–3063.
[58] B.A. Baker, R.D. Gollihue, J.J. deBarbadillo, Fabrication and heat treatment of weld joints in Inconel alloy 740H superalloy steam header pipe and superheater tubing, in: Proceedings: Welding and Repair Technology for Power Plants, Tenth International EPRI Conference, Marco Island, FL, USA, June 26–29, 2012(CD).
[59] D.C. Tung, J.C. Lippold, Weld solidification behavior of Ni-Base superalloys for use in advanced supercritical coal-fired power plants, in: E.S. Huron et al. (Ed.), Superalloys, TMS, 2012, pp. 563–567.
[60] B.A. Baker, R.D. Gollihue, J.J. deBarbadillo, Dissimilar metal welding of alloy 740H, in: Welding and Repair Technology for Power Plants, Eleventh International EPRI Conference, EPRI, Naples, FL, June 2014.
[61] J.E. Ramirez, Evaluation of susceptibility of alloy IN740 to HAZ stress-relaxation cracking, Welding Journal 92 (April 2013) 89s–100s.
[62] J.C. Borland, Cracking tests for assessing weldability, British Welding Journal 7 (1960) 508–512.
[63] M.W. Spindler, The use of Borland specimens of reproduce reheat cracking in type 316H, in: International Conference on High Temperature Plant Integrity and Life Extension, Robinson College, Cambridge University, UK, April 14–16, 2004.
[64] D.C. Tung, J.C. Lippold, Modeling stress relaxation test for advanced ultra supercritical alloys, in: Proceedings: Seventh International Conference on Advances in Materials Technology for Fossil Power Plants, ASM International, Waikaloa, HA, USA, 2013, pp. 1038–1046.

HAYNES 282 alloy

15

K.L. Kruger
Haynes International, Inc., Kokomo, IN, United States

15.1 Introduction

Precipitation-hardened alloys fill a unique niche of providing strengths and properties that cannot be matched by solid solution alloys. While the precipitation heat treatments inherently create complications for manufacturing, age hardenable, γ′-strengthened alloys often provide creep strengths more than double that of solid solution alloys at select temperature ranges. One of these, HAYNES 282 Alloy (Ni-19Cr-10Co-8.5Mo-1.5Al-2.1Ti), brings a new level of weldability and fabricability that is unmatched in wrought alloys of similar creep strength, like Waspaloy and René-41 [1–4]. In spite of its γ′ content and high strength at temperatures up to 900°C (1650°F), 282 alloy has excellent formability, fabricability, and forgeability, and it is remarkably easier to weld than other γ′ alloys of similar strength due to its greater resistance to strain-age cracking. This surprising combination of properties has created great interest for advanced ultra-supercritical steam applications, both for turbines and other components. However, 282 alloy is more than a niche alloy for A-USC applications alone, having already been adopted for hot section parts in gas turbines for aircraft and power generation, and creating a base for improved product availability in the future. In this chapter, the basic metallurgy and properties of HAYNES 282 alloy are provided, together with information about environmental resistance, weldability, and casting of the alloy.

15.1.1 Composition, basic metallurgy, and physical properties

15.1.1.1 Composition of HAYNES 282 alloy in comparison to other wrought γ′ alloys

The compositions of HAYNES 282 alloy and other wrought γ′-strengthened alloys of the same family are shown in Table 15.1. All of the five alloys listed are nickel-based and contain similar alloying additions, although they exhibit some substantial differences in properties and manufacturability. Reasons for the composition designed by Lee Pike are described in detail in his 2008 paper [5], but they are summarized next.

The Ni content of all of these alloys provides a relatively noble face-centered cubic (γ) base with excellent solubility for many alloying elements that bring useful metallurgical properties. All of these alloys are chromia-formers, with 19–25 wt% Cr to provide resistance to both oxidation and hot corrosion. At 20% Cr, 282 alloy has adequate Cr content balanced for operating at temperatures below the γ′-solvus temperature of 997°C (1827°F). The judicious addition of 10% Co helps to control the γ′

Materials for Ultra-Supercritical and Advanced Ultra-Supercritical Power Plants.
http://dx.doi.org/10.1016/B978-0-08-100552-1.00015-4
Copyright © 2017 Elsevier Ltd. All rights reserved.

Table 15.1 Nominal composition of several wrought gamma-prime alloys (wt%)

Alloy	Ni	Cr	Co	Mo	Ti	Al	Fe	Mn	Si	C	B	Other
282	57[a]	20	10	8.5	2.1	1.5	<1.5	<0.3	<0.15	0.06	0.005	–
Waspaloy	58[a]	19	13.5	4.3	3	1.5	<2	<0.1	<0.15	0.08	0.006	Zr-0.05
R-41	52[a]	19	11	10	3.1	1.5	<5	<0.1	<0.5	0.09	0.006	–
263	52[a]	20	20	6	<2.4	<0.6	<0.7	0.4	0.2	0.06	0.005	Cu <0.2
740H	52[a]	25	20	0.5	1.8	<0.9	0.7	0.3	<0.5	0.03	0.005	Nb 2

"HAYNES" and "282" are registered trademarks of Haynes International, Inc., Kokomo, Indiana, USA [1].
740H is an INCONEL alloy produced by Special Metals Corporation, Huntington, West Virginia, USA [6].
[a]As balance.

solvus, and is on the low end of the range for other alloys in this class since Co is a relatively costly element. The elements Al and Ti form the potent strengthening phase, gamma-prime (γ′), an ordered fcc Ni_3(Al,Ti) precipitate that is the basis for the entire family of precipitation-strengthened alloys of this type. Since relatively small changes in the amount of these two elements have strong effects on the properties and fabricability of these alloys, 282 alloy was designed to carefully balance the best combination of these traits. At a combined Al + Ti content of 3.6 wt%, 282 alloy achieves about 19 vol% γ′ phase in the fully aged condition. Since this volume fraction is about 5–6% less than similar γ′ alloys like Waspaloy and R-41, the impact of lower volume fraction is offset by additions of molybdenum. Mo is an important solid solution strengthening element for providing excellent creep strength, especially in exposures near the higher end of the expected temperature range. Mo is present in the similar alloys in contents between 0.5 and 10 wt% (see Table 15.1). As discussed later, Mo does not appear to have an adverse impact on environmental resistance to steam at 700°C, but it may reduce resistance at 800°C and above. Minor alloying additions that provide enhanced mechanical properties are C and B. Finally, no intentional additions of Mn and Si are made for 282 alloy (similar to R-41 and Waspaloy alloys), which contribute to favorable thermal stability (as both are potent Nv value contributors). In contrast, Mn and Si are specified additions to 263 alloy, presumably for improved oxidation resistance and/or castability [7]. In spite of these differences, controlled studies by Pike and Srivastava have shown remarkable similarities in the oxidation resistance of all of these alloys, except alloy 740, which was not included in the study [8].

15.1.1.2 Metallurgical phases in HAYNES 282 alloy

All of the alloys listed in Table 15.1 are multiphase materials, with fcc (γ) matrices containing distributed carbides (mainly MC, M_6C, and/or $M_{23}C_6$ types) and, in the aged condition, γ′ precipitates and some other minor phases. Like other alloys in that family, HAYNES 282 alloy achieves maximum cold formability in the mill-annealed condition. Solution-annealing treatments to maximize formability are performed in the range of 1121–1149°C (2050–2100°F), followed by water quenching for optimum ductility. This treatment results in grain sizes in the range of ASTM 3–5, of which a typical microstructure is shown in Fig. 15.1. With its excellent hot forging characteristics, bar and billet product can be forged and annealed to achieve targeted grain sizes that range from ASTM 4–9 (or even finer), depending on the application and property needs. However, final processing and annealing should target grain sizes that achieve the desired balance of properties (eg, for optimum creep strength, the desirable grain size is on the coarser end of that range—ASTM 3–5). Like plate and sheet, process piping and similar creep-limited applications would benefit from these moderate grain sizes. For disk materials that have a high-cycle fatigue component to the loading, finer grain sizes may be desired.

As Fig. 15.1 shows, the microstructure is comprised of a relatively equiaxed γ matrix that is generally free of secondary precipitation, but it shows indications of annealing twins and some large, blocky primary MC carbides phases. Since the solution-annealing temperature is above the solvus of the $M_{23}C_6$ carbides, the grain boundaries are

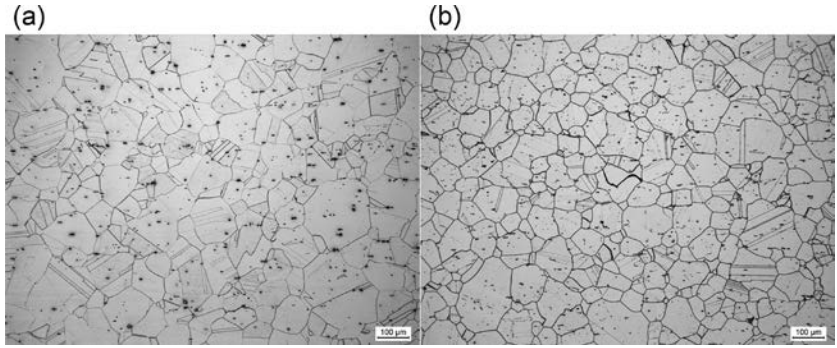


Figure 15.1 Typical microstructures of (a) as-mill annealed and (b) aged HAYNES 282 alloy.

generally clean like the grain interiors. The blocky carbides are titanium-rich, and may be dispersed as stringers during deformation processing. The compositional design and control of 282 alloy favors an early lag in γ′ precipitation, so water quenching (and similar rapid cooling) results in very little γ′ phase. As such, solution-annealed 282 alloy exhibits good ductility (>55% elongation) and fairly low hardness values (92–96 HR_B).

After fabrication, solution annealing is recommended in the same 1121–1149°C (2050–2100°F) temperature range, with as rapid cooling as possible being preferred. Since most fabricated parts can only be annealed in vacuum or inert gas furnaces, quench rates are generally more limited. If possible, a targeted cooling rate of 111–278°C (200–500°F)/minute would be desirable until the metal temperature is below 538°C (1000°F). Failure to reach this cooling rate will not likely have a major negative impact on strengths, but it may limit formability in subsequent fabrication steps.

To achieve full strength, 282 alloy is age hardened via either a one-step or a two-step heat treatment. In most cases, a two-step treatment of 1010°C (1850°F)/2 h/Air Cool (AC) + 788°C (1450°F)/8 h/AC is preferred to obtain the greatest creep strength and high-temperature ductility at the upper ranges of the operating temperature. Examples of typical two-step aged microstructures for 282 alloy are shown in Fig. 15.2 [9]. The first step of the two-step heat treatment targets in the formation of chromium-rich $M_{23}C_6$ carbides at the grain boundaries in an optimized morphology for the best combination of mechanical properties. This effect is achieved as carbides precipitate in grain boundaries in a closely stacked configuration appearing like a blocky "stone wall" (as revealed by preferential etching in the SEM micrograph in Fig. 15.2(a)). Additionally, some secondary carbides do precipitate intragranularly. Since this step of the heat treatment is above the γ′ solvus temperature of 997°C (1827°F), no γ′ phase precipitates (and the strength does not increase dramatically from this part of the heat treatment). Air cooling at each step aids in achieving improved consistency of properties.

In situations where the components cannot easily fit into a furnace, an alternative single-step treatment of 800°C (1475°F)/6–8 h/AC can provide similar creep properties up to about 750°C (1382°F), but that does not quite match the full strength from the two-step age process at the highest temperatures (ie, 750–900°C (1382–1652°F)). The impact on mechanical properties is more fully discussed in Section 15.1.2. The single-step age, like the second step of the two-step treatment, results in the precipitation

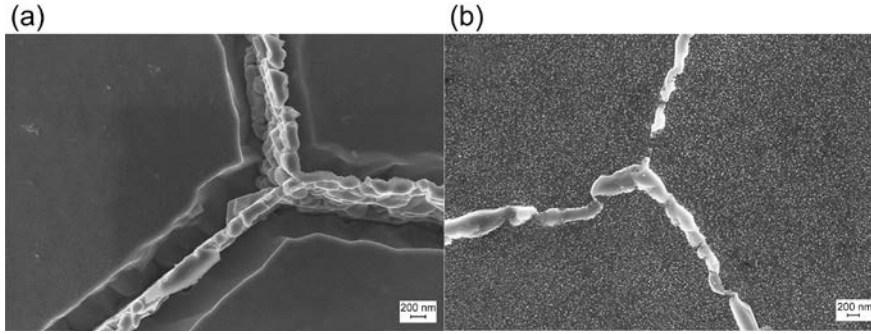


Figure 15.2 Microstructures of two-step aged HAYNES 282 alloy, (a) preferentially etched to highlight the morphology of grain boundary carbides precipitated during the first step of the heat treat cycle, and (b) etched to highlight the uniform distribution of ultra-fine γ′ particles precipitated by second step of the cycle.
After S. Srivastava, J. Caron, L. Pike, Recent developments in the characteristics of HAYNES 282 alloy for use in A-USC applications, in: Proceedings From the 7th International Conference on Advances in Materials Technology for Fossil Power Plants October 22–25, 2013, Waikoloa, Hawaii, Electric Power Research Institute, 2014, pp. 120–130.

of very fine γ′ precipitates. As shown in Fig. 15.2(b), these precipitates are roughly spherical in shape and approximately 20 nm in average diameter. In general, the distribution of the γ′ particles is fairly uniform, while the size distribution is monomodal.

For A-USC applications, it is presumed that the single-step aging would be required, and ASME Code Case data are being collected using this treatment in a program that began in 2015. Completion of testing and development of the Code Case is expected to take a number of years.

15.1.1.3 Thermal stability (secondary phases and γ′ coarsening)

Metallurgical thermal stability is a critical property of alloys intended for long-term, elevated temperature service. For γ′-strengthened alloys in particular, loss of ductility and/or loss of strength are the two key issues stemming from microstructural instabilities. Loss of ductility is often the most severe impact of poor metallurgical stability. Although all alloys exhibit microstructural changes from exposures in the intermediate temperature ranges (ie, 538–1000°C (1000–1832°F)), precipitation of deleterious secondary phases (like TCP-type sigma or Laves phases) is one of the key causes of embrittlement. While deleterious phases precipitate at elevated temperatures, the embrittlement at those temperatures is often less apparent than its impact on room temperature ductility. As such, embrittlement behavior can often be easily assessed as remnant ductility from room temperature tensile tests after exposures. In addition to loss of ductility, secondary phase precipitation can also contribute to loss of strength issues due to element partitioning, in which precipitation of TCP-type phases can thermodynamically lock up critical elements (such as Mo) and deprive the matrix of solid solution–strengthening contributions. However, the most common contributor to loss of strength in the γ′ alloys stems from metallurgical changes that occur in the γ′ phase

itself over time, including coarsening and/or dissolution. These changes are a function of the stability of γ′ over the entire temperature range up to the γ′ solvus temperature. The following review details the available information on secondary phase formation and γ′ stability in 282 alloy and similar materials.

Secondary phase formation

Thermal stability was one of the key features targeted during the development of 282 alloy [10]. The result of the proper balance of elements in 282 alloy is an excellent blend of hot- and cold-workability, superior weldability relative to other alloys in its class, and excellent stability during long-term thermal exposure. As a result, 282 alloy is not prone to severe embrittlement as are certain other alloys in its class. In a recent study by Ennis et al., microstructures of 282 alloy exposed at 700°C for 3000 h revealed "little change from the as-received condition" [11]. They further completed phase stability calculations using Thermo-Calc and concluded that only very little variations could be expected in the dominant phase fractions, which included γ′, mu (μ) phase, and $M_{23}C_6$ carbides. However, they did predict the potential for sigma (σ) phase if melted with all alloying elements at maximum concentrations. They conceded that σ-phase has never been detected in the alloy, but they suggested follow-on experiments to look at local variations in alloy composition like interdendritic regions and at dendrite core areas.

Longer exposures were reported in a 2010 study by Pike, in which properties and microstructures of 282 alloy after thermal exposures up to 16,000 h were compared to other alloys in its class [12]. These studies focused exclusively on samples in the fully wrought condition, which was most relevant to the majority of product sold. To date, phases observed in as-welded microstructures and castings have not received as much scrutiny of phase stability, although some discussion is included here in later sections. Optical micrographs from the 2010 study on wrought products after 1000 h at 760°C (1400°F) exposure are shown in Fig. 15.3(a)–(d) for samples of 282, R-41, Waspaloy, and 263 alloys.

Of the four alloys studied, R-41 alloy (Fig. 15.3(b)) exhibited significant intragranular precipitation, consistent with previous reports of mu (μ) and sigma (σ) phase precipitation at these temperatures [13–14], and likely a substantial contributing factor in the alloy's known low ductility at elevated temperatures. The remaining alloys all showed very little or light secondary phase precipitation. At all temperatures reported in the study, both 282 alloy (Fig. 15.3(a)) and Waspaloy (Fig. 15.3(c)) showed no evidence of deleterious phases at any of the temperatures after 1000 h, and 263 alloy (Fig. 15.3(d)) only revealed deleterious phase formation at the 871°C/1600°F exposure. In that case, the plate-like precipitates were identified as likely being hexagonal eta (η) phase (Ni_3Ti), which had been previously reported [15–16]. In spite of the apparent lack of deleterious phases in the micrographs, ductility of Waspaloy alloy at intermediate temperatures is substantially lower than that of the other alloys, except R-41 alloy. The ductility of 282 alloy remains at 20% elongation or above throughout the temperature range. Other phases observed in all four alloys included primary TiN and MC phases, and secondary $M_{23}C_6$ carbides, predominantly along grain boundaries. Further, 282 alloy exhibited some secondary M_6C carbides. In R-41 alloy, M_6C phase was also identified (albeit as a primary precipitate), and at the mid-range temperatures, large intragranular phases (mu and possibly sigma) were observed. In 263 alloy,

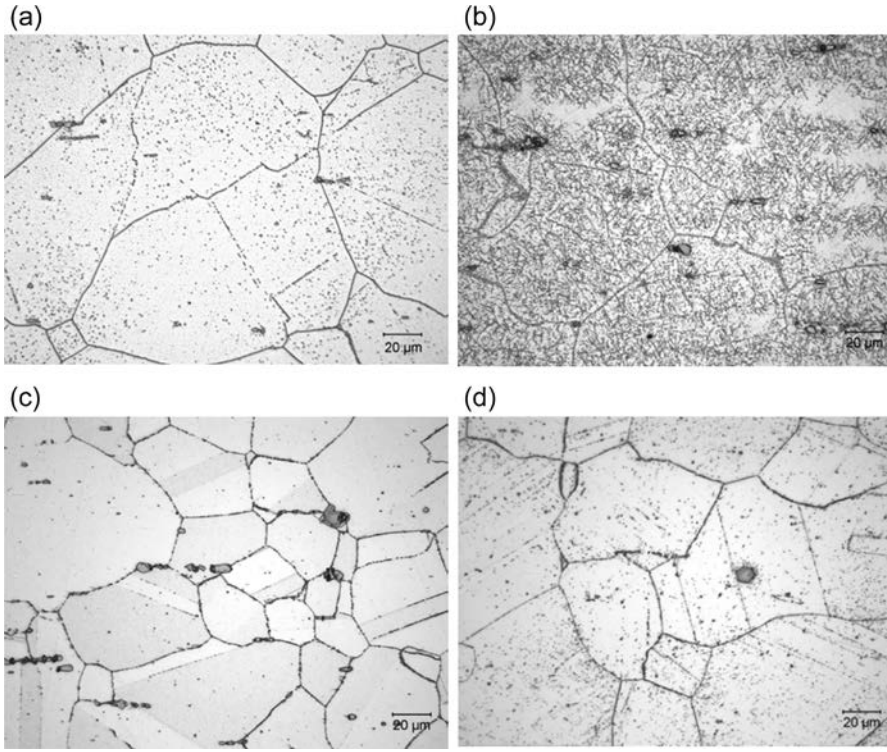


Figure 15.3 Microstructures after 1000 h thermal exposures at 760°C (1400°F) for (a) 282 alloy; (b) R-41 alloy; (c) Waspaloy alloy, and (d) 263 alloy.
Reproduced from L. Pike, Long term thermal exposure of HAYNES 282 alloy, in: 7th International Symposium on Superalloy 718 and Derivatives, TMS (The Minerals, Metals & Materials Society), 2010, pp. 645–660.

a small amount of eta (η) phase was observed, especially at 816°C/1500°F. For 282 alloy and Waspaloy alloy, no additional phases were observed for any of the exposure temperatures within the 1000-h period. Of all alloys studied, the predominant phases observed were γ′ and secondary grain boundary carbides.

The remaining alloy from Table 15.1 not included in the study, alloy 740, exhibited long-term precipitation of hexagonal eta (η) and G-phases, as reported in the literature [17]. These were largely resolved by compositional changes from 740 to the 740H version of the alloy, and elevated ductility values taken from published brochure data show high values similar to 263 alloy. More recent studies suggest that eta (η) phase should still be thermodynamically stable at higher temperatures and longer times, but not at concentrations that would affect the structural stability in use [18].

Stability and coarsening behavior of γ′ phase

At the low end of the temperature range (ie, 649°C/1200°F) of the same thermal stability study by Pike, the γ′ size distribution did not increase much compared to the as-aged

condition [12]. Consistent with the difference in the initial heat treatments, 282 and 263 alloys had smaller initial γ′ precipitates relative to R-41 and Waspaloy alloys, which persisted after the 649°C/1200°F exposure for 1000 h. After the 760°C/1400°F exposure, the γ′ particles in 282 alloy coarsened somewhat, as well as trending toward a more cuboidal shape. However, the distribution remained as homogeneous as the initial and 1200°F-exposed samples.

ORNL (Oak Ridge National Laboratory, USA) has conducted similar research in the 700–800°C temperature range since γ′ phase stability is the basis for 282 alloy's excellent creep strength for A-USC application [19]. Comparing 282 alloy to alloy 740, the calculated γ/γ′ lattice mismatch was greater for alloy 740. Higher mismatch implies higher interfacial energy, which typically creates as a larger driving force for coarsening and tends to favor a cuboidal γ′ morphology. However, the rate of coarsening of the γ′ phase appeared higher in 282 alloy than in alloy 740, even though the γ′ remained spherical in 282 alloy and was cuboidal in alloy 740. Plots that revealed a higher coarsening rate for 282 alloy did have error bands that overlapped with the alloy 740 rate. Long-term coarsening rates will obviously need to be a topic of further study for 282 alloy to ensure adequate reliability for life predictions.

If temperatures exceed the expected ranges of A-USC operation, it is anticipated that additional and/or accelerated γ′ coarsening would occur. The γ′ was observed to coarsen for all four alloys in the study by Pike at 816°C/1500°F, with the homogeneity of the distribution unaffected for all but 263 alloy [12]. At that temperature in 263 alloy, the γ′ appeared to align along preferred directions. At the highest 871°C/1600°F exposure, all four alloys exhibited considerable coarsening with more obvious trends toward cuboidal shapes for all, except the R-41 alloy that remained spherical. In 263 alloy, the volume fraction of the gamma-prime phase was considerably lower after the 871°C/1600°F exposure than for the other exposure temperatures.

Although the work evaluating the γ′ growth kinetics in 282 alloy has been enlightening and adequate for initial modeling efforts as reported by Schwant et al. [20], very long-term studies will likely need to be pursued. Room temperature tensile measurements of long-term thermally exposed materials have revealed very little degradation of yield strengths or ductility, even after 16,000 h. These results at the very least imply sufficiently modest coarsening kinetics to expect a reasonable service life for 282 components at the highest operating temperatures in A-USC applications. In fact, after creep testing and microstructural analyses of the thermal stability and time-dependent deformation behavior of both Inconel alloy 740 and Haynes 282 alloy, Tortorelli et al. concluded that "both alloys meet A-USC goal with single-step heat treatments" [19]. Their work is the most advanced found in the literature to date toward understanding the microstructural evolution of γ′ phase for A-USC conditions.

15.1.1.4 Physical properties (density, melting points, CTE, thermal conductivity, Cp, ϱ, etc.)

No discussion is included here regarding physical properties for 282 alloy, but tabulated values of relevant properties are summarized in Appendix A for reference.

15.1.2 Mechanical properties of HAYNES 282 alloy

15.1.2.1 Tensile properties

In Fig. 15.4, room and elevated temperature tensile properties for HAYNES 282 alloy are compared to the alloys listed in Table 15.1, together with the data for HAYNES 230 and 617 alloys, the two leading solid solution nickel alloy candidates for A-USC applications

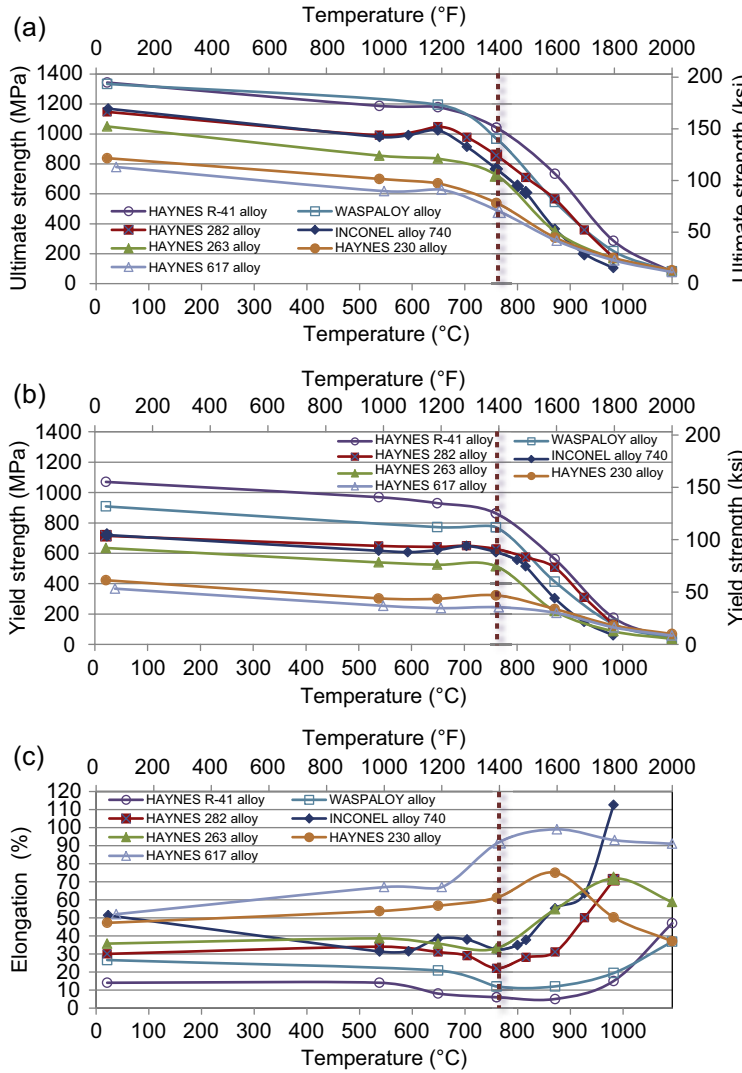


Figure 15.4 (a) Ultimate tensile strength, (b) 0.2% offset yield strength, and (c) % elongation as a function of temperature for HAYNES 282 alloy and comparative age-hardened and solid solution alloys based on published brochure properties, with *vertical dashed line* at 760°C. (See Table 15.2 for references.)

Table 15.2 Solution annealing temperatures and precipitation heat treatment conditions associated with properties for all alloys in Fig. 15.4

Alloy	Solution annealing	Aging (precipitation) heat treatment
HAYNES R-41 alloy	1975°F (1080°C)/WQ,	1950°F (1066°C)/30min/AC; 1400°F (760°C)/16 h/AC
HAYNES Waspaloy alloy	1975°F (1080°C)/WQ	1825°F (995°C)/2 h/AC; 1550°F (845°C)/4 h/AC; and 1400°F (760°C)/16 h/AC
HAYNES 282 alloy	2075°F (1135°C)/WQ	1850°F (1010°C)/2 h/AC and 1450°F (788°C)/8 h/AC
INCONEL alloy 740	2100°F (1149°C)/WQ	1470°F (799°C)/16 h/AC
HAYNES 263 alloy	2100°F (1149°C)/WQ	1472°F (800°C)/8 h/AC
HAYNES 230 alloy	2250°F (1232°C)/WQ	None
HAYNES 617 alloy	2150°F (1177°C)/RAC	None

AC, air cool; *WQ*, water quench.
With data taken from published brochures from Haynes International, Inc., HAYNES® 282® Alloy. Kokomo, Indiana (Brochure H-3173A). Available from: http://www.haynesintl.com, Haynes International, Inc., HAYNES® Waspaloy Alloy. Kokomo, Indiana (Brochure H-3128C), 2008. Available from: http://www.haynesintl.com, Haynes International, Inc., HAYNES® R-41 Alloy. Kokomo, Indiana (Brochure H-3056A), 2002. Available from: http://www.haynesintl.com, Haynes International, Inc., HAYNES® 263 Alloy. Kokomo, Indiana (Brochure H-3047D), 2000. Available from: http://www.haynesintl.com, Haynes International, Inc., HAYNES® 230® Alloy. Kokomo, Indiana (Brochure H-3000H), 2004. Available from: http://www.haynesintl.com, and Haynes International, Inc., HAYNES® 617 Alloy. Alloy At-a glance. Kokomo, Indiana (Brochure H-3171B), 2008. Available from: http://www.haynesintl.com, and Special Metals Corporation Special Metals Corporation., INCONEL® Alloy 740. Huntington, West Virginia (Publication Number SMC-090), 2004. Available from: http://www.specialmetals.com.

[21,22]. The heat treating conditions for all items in Fig. 15.4 are summarized in Table 15.2. The substantial benefit of age-hardening is immediately apparent, especially in comparisons to ultimate and yield strengths in Fig. 15.4(a) and (b), for which 282 alloy shows over 60–70% greater yield strength than either solid solution material.

In this same figure, alloy 740 and 282 alloy have remarkably similar ultimate strengths up to 650°C (1200°F) and similar yield strengths up to 800°C (1472°F). On both curves, 282 alloy distinguishes itself to higher temperatures than alloy 740, likely benefitting from the solid solution elements that contribute to stability for an additional 100°C for equivalent strength levels. The other feature of note for 282 alloy is that the yield curve is quite flat and uniform from room temperature up to approximately 850–875°C, where the yield strength begins to show the common decline associated with γ′ coarsening near the solvus temperature. For 282 alloy, the γ′ solvus temperature is 997°C (1827°F), but the good solid solution alloying content of this material allows it to hold similar good strengths in the same category as the solid solution alloys at the higher temperatures.

The γ′ alloys share common trends in ductility behaviors that tend to differ from the solid solution alloys. All of the γ′ alloys show a ductility dip around 760°C in Fig. 15.4(c), while both solid solution alloys show increasing ductility trends in the same temperature range. Similarly, the solid solution alloys exhibit trends of increasing ductility from room temperature to about 538°C (1000°F), which 282 and 263 alloy share. In contrast, the other γ′ alloys show flat to declining ductility, especially alloy 740, which shows an approximately 20% decline in ductility over this lower temperature range, with 538°C representing its minimum ductility. Both 740 and 282 alloys show a ductility trough at 760°C, which is the minimum for 282 alloy at 22%, or about 10% lower than the minimum for alloy 740. Within 60°C (~100°F) of that temperature in either direction, the elongation for 282 alloy returns to levels closer to 30%.

Tensile properties for longer term exposures at temperatures for A-USC applications in Fig. 15.5 have been reported by Pike, showing HAYNES 282 alloy 760°C/1400°F yield strengths increasing modestly for the first 1000 h before gradually trending downward out to 16,000 h to levels just below the original age-hardened properties [12]. Simultaneously, 282 alloy showed an increase in ductility, with elongations climbing from around 20% to over 32%. Both properties show tendencies toward flattening trends, suggesting some stable long-term level, but very long-term data (eg, 50,000 h or greater) have not been found in the literature. No comparative information was available for the performance of alloy 740 in this type of test.

Since A-USC components may require field heat treatments, the capability to perform the first 1010°C (1850°F) step of the two-step treatment for HAYNES 282 alloy has been questioned. As such, studies have been conducted to evaluate properties with an alternative single-step 802°C (1475°F) heat treatment for 4–8 h. All results discussed earlier are based on two-step age treatments. Initial results reported by Tortorelli et al. as early as 2013 indicated that a single-step treatment at 800°C for 4 h could be sufficient to generate an adequate γ′ precipitate size to effectively strengthen the alloy [23]. Results generated by Haynes International, shown in Table 15.3, reveal the benefit of the first aging step on the high-temperature ductility, but this is somewhat offset by higher general yield strengths in the single-step aged condition. Based on these and other promising results, a single-step aging treatment is being pursued for ASME Code Case development.

15.1.2.2 Creep and rupture properties

As illustrated in Fig. 15.6, perhaps the most significant attribute of HAYNES 282 alloy that has generated ongoing testing and interest for A-USC applications is the excellent creep strength of the material [24]. Studies have been conducted by ORNL, EPRI, NETL, and a number of other organizations, and as succinctly stated by Tortorelli et al.: “Inconel alloy 740 and Haynes 282 would have creep lifetimes exceeding the US. A-USC boiler tubing lifetime goal of 100,000 hours at 750°C and 100 MPa” [18]. Of the two alloys, their analysis showed “a clear advantage of Haynes 282 to Inconel 740/740H in creep strength for temperatures below 800°C, with equivalence between the two alloys at 800°C,” (based on currently available data). This conclusion makes 282 alloy the strongest commercially available alloy for creep resistance, which becomes even more attractive when other properties are considered (eg, weldability and thermal stability).

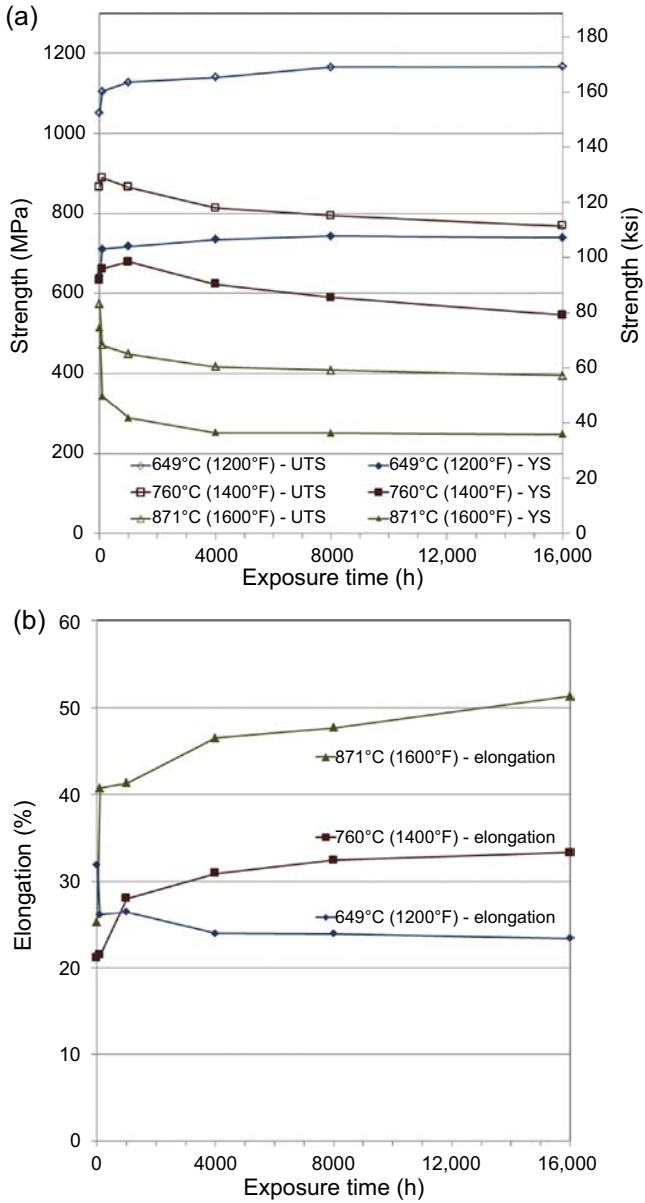


Figure 15.5 Tensile results versus time showing (a) yield and ultimate strengths and (b) elongation in 282 alloy for up to 16,000 h exposures.
After L. Pike, Long term thermal exposure of HAYNES 282 alloy, in: 7th International Symposium on Superalloy 718 and Derivatives, TMS (The Minerals, Metals & Materials Society), 2010, pp. 645–660.

Table 15.3 Comparison of single-step aged tensile properties for HAYNES 282 alloy with two-step aged values

Test temperature	Age-hardening treatment	0.2% YS MPa (ksi)	UTS MPa (ksi)	Elong %	R.A. %
Room temperature	Two-step age	706 (102.3)	1152 (167.1)	29.9	33.1
	Single-step age	741 (107.4)	1183 (171.5)	31.3	35.4
760°C (1400°F)	Two-step age	632 (91.7)	866 (125.6)	21.1	22.6
	Single-step age	658 (95.4)	857 (124.2)	18.3	18.3

Two-step age = 1010°C (1850°F)/2 h/Air Cool (AC) + 788°C (1450°F)/8 h/AC; Single-step age = 800°C (1475°F)/8 h/AC. After S. Srivastava, J. Caron, L. Pike, Recent developments in the characteristics of HAYNES 282 alloy for use in A-USC applications, in: Proceedings From the 7th International Conference on Advances in Materials Technology for Fossil Power Plants October 22–25, 2013, Waikoloa, Hawaii, Electric Power Research Institute, 2014, pp. 120–130.

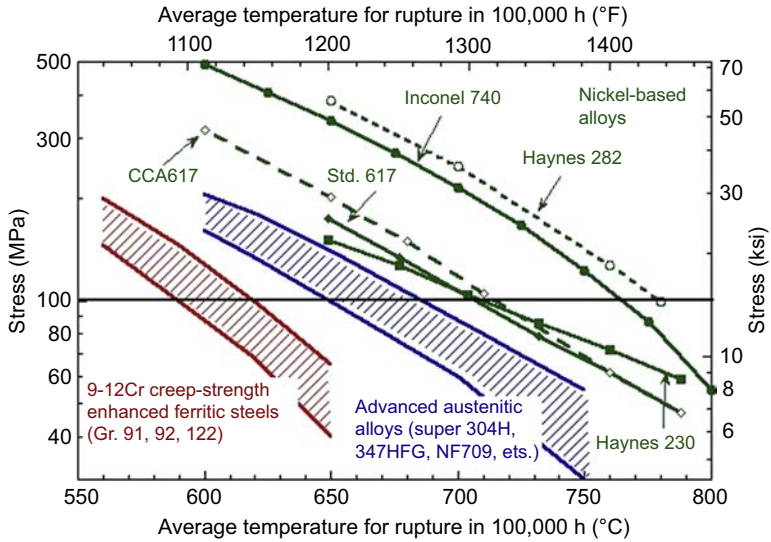


Figure 15.6 100,000 h creep rupture strength as a function of temperature for alloy/alloy class showing superior rupture strength of HAYNES 282 alloy based on two-step aged data. Courtesy of J. Shingledecker, R. Purgert, P. Rawls, Current status of the U.S. DOE/OCDO A-USC materials technology research and development program, in: Advances in Materials Technology for Fossil Power Plants. Proceedings from the Seventh International Conference, October 22–25, 2013, Waikoloa, Hawaii, USA, ASM International. EPRI Report Number 3002002375, 2014, pp. 41–52.

To quantify the differences, Tortorelli et al. performed an analysis following a Wilshire approach in an attempt to improve the accuracy of creep life predictions versus the standard Larson–Miller parameter (LMP) curve fitting [25]. In this more conservative analysis, 282 alloy showed 18–22% higher 100,000-h creep rupture strength than alloy 740H, although the general trends were similar to the LMP analysis. Like the LMP analysis, both alloys were projected to have capability to meet the US A-USC boiler tubing 100,000-h lifetime

goal at 750°C and 100 MPa. It was noted that this analysis did not take any microstructural effects into account, and it identified that issue as a need for further research.

The same group conducted detailed metallography and SEM work of alloy 740H and 282 alloy, with additional information published [26]. One of the interesting conclusions from that report is the strong similarity in 100,000-h creep rupture life for 282 alloy in the single-step versus two-step aged condition at the temperatures of A-USC interest, which is shown in Fig. 15.7.

Similar testing has been conducted by Srivastava et al. to compare the impact of single-step aging to two-step aging on creep rupture life from 650 to 816°C [10]. Their results shown in Fig. 15.8 reveal similar strong correlations at the lower temperatures, regardless of the aging treatment, but a small debit in rupture life as temperatures increase. This was attributed somewhat to increased coarseness of γ′ due to the higher aging temperature, but it may also have a contribution from the decreased boundary strength from the optimized first step of the two-step treatment. As such, components that are sufficiently sized for a practical two-step aging treatment should likely use the two-step treatment preferentially. Efforts may be necessary to allow the ASME Code Case to include both aging treatments as options.

15.1.2.3 Fatigue resistance

Since HAYNES 282 alloy is under consideration for turbine rotor and blade applications, data are required for both low-cycle, hold-time, and thermal fatigue resistance

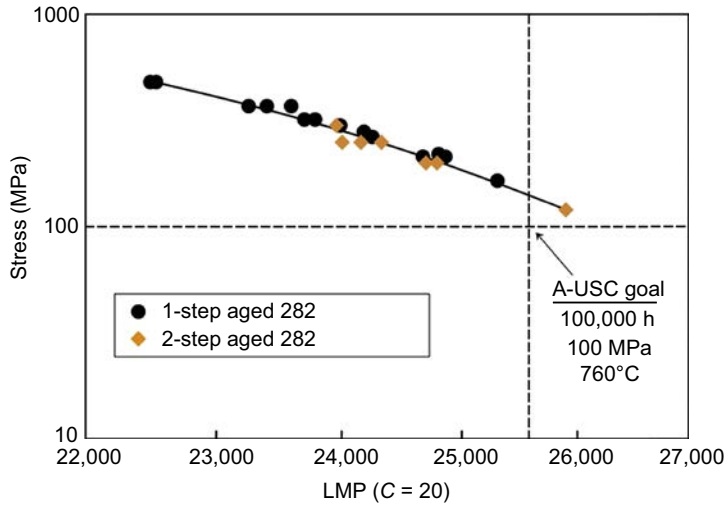


Figure 15.7 Comparison of single-step and two-step aged creep rupture curves for HAYNES 282 alloy showing little difference in lifetimes.
After P. Tortorelli, K. Unocic, H. Wang, M. Santella, J. Shingledecker, Ni-based alloys for advanced Ultrasupercritical steam boilers, in: Fossil Energy Crosscutting Research Program Review, April 25, 2015, Pittsburgh, Pennsylvania, 2015. http://www.netl.doe.gov/File%20Library/Events/2015/crosscutting/Crosscutting_20150429_0900A_ORNL.pdf.

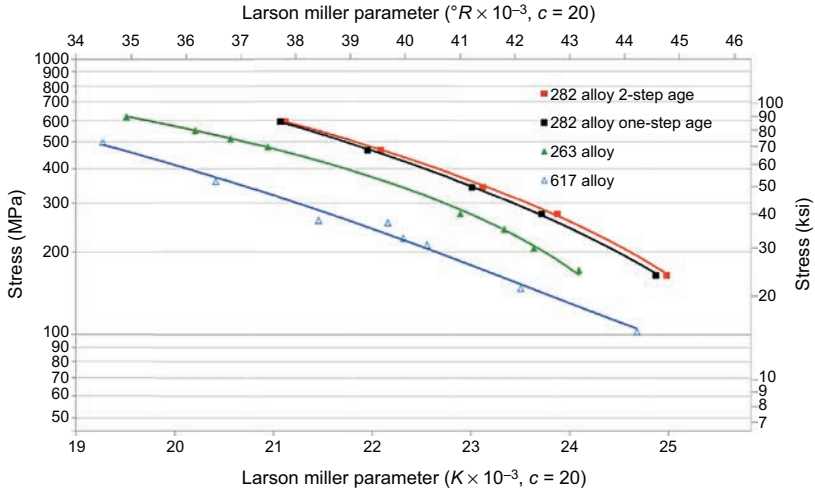


Figure 15.8 Comparison of single-step and two-step aged creep rupture curves for HAYNES 282 alloy over 650 to 816°C temperature range.
After S. Srivastava, J. Caron, L. Pike, Recent developments in the characteristics of HAYNES 282 alloy for use in A-USC applications, in: Proceedings From the 7th International Conference on Advances in Materials Technology for Fossil Power Plants October 22–25, 2013, Waikoloa, Hawaii, Electric Power Research Institute, 2014, pp. 120–130.

for heavy section parts, and high-cycle fatigue resistance for airfoil materials. A number of studies have been conducted on both low and high cycles, which will only briefly be mentioned here.

Low-cycle fatigue behavior

In the earliest reported study by Pike, 282 alloy fatigue life was found to increase with decreasing temperature and strain range [27]. The S–N curves dropped gradually with increasing temperature for tests in the 649–816°C (1200–1500°F) temperature range, but they showed more pronounced decreases above that range (up to the maximum tested temperature of 871°C (1600°F)). At lower strain ranges, fractography revealed extensive short intergranular cracks that seemed to initiate along oxidized grain boundaries. At the highest total strain range tested (1.0%), extensive trans-granular cracking was observed perpendicular to the axial direction.

Similar to Pike's results, Buckson and Ojo reported relatively short periods of initial cyclic hardening, followed by cyclic softening to specimen failure at all the strain amplitudes tested (ie, 0.5–1.0%) [28]. They concluded that 282 alloy showed a "strong fatigue deformation resistance." Brommesson and Ekh conducted experiments reported in 2012 for LCF properties of 282 alloy at RT and 650°C with a specific goal of fitting the data for modeling [29]. They reportedly found success with the RT data, but the 650°C data did not correlate well with their model.

In one of the most extensive fatigue studies, a Ph.D. dissertation by Rozman for Oregon State University summarized an evaluation of fatigue crack growth rates of

282 alloy for A-USC rotor applications [30]. Using ASTM methodologies at temperatures of 550, 650, and 750°C, and loading frequencies from 0.25 to 25 Hz, 282 alloy exhibited similar behavior to previous studies for lower frequencies, but it deviated at the higher frequencies. These differences were attributed to variations in microstructures. In his conclusions, 282 alloy had lower fatigue crack growth rates than Waspaloy, but they were similar to Udimet 720 at high loading frequency (ie, above ~5 Hz). At frequencies below about 0.33 Hz, 282 alloy exhibited fatigue crack growth rates slightly higher than 718 alloy, but lower than those of Waspaloy and Udimet 720. These were noted to be significant given the higher creep strength temperature capability for 282 alloy relative to these materials. However, Rozman's study raised issues of potential isolated indications of intergranular crack propagation within the crack growth region at 750°C. To correlate these crack indications with microstructures, he proposed "more detailed post-test analysis of the crack growth region, including visual identification and chemical analyses of affected and unaffected grain boundaries that showed indications of intergranular crack propagation."

Finally, as part of a detailed study by Shen et al. from GE, 282 alloy was evaluated to determine fatigue performance in steam and air environments [31]. Experimental work included hold-time fatigue tests and microstructural analyses of crack tip characteristics. From these, models were developed to correlate LCF and crack growth rates for 282 alloy at A-USC conditions. In addition, long-term microstructural stability and defect interactions were studied. While limited data are available publically, it is clear the significant progress has been made to characterize and model properties for the alloy for steam rotor applications.

High-cycle fatigue behavior

Turbine materials in A-USC conditions present some very substantial materials challenges, including need for high creep strength, oxidation resistance, and good high cycle fatigue (HCF) performance. Given the excellent creep strength of 282 alloy, a limited number of investigations of HCF behavior have been reported to date. Additional results are expected from the triple-melted disk specimen produced under license to GE by Special Metals Corporation. Results by Maziasz and Shyam suggests that the triple-melted material is much finer grained and has a lower twin density than double-melted 282 alloy [32]. Results of preliminary 800°C (1472°F) HCF testing of wrought 282 alloy in both steam and air have not revealed any adverse effects of steam in testing to date [33]. Microstructural effects within the fracture sites seem to have the greatest effect on fatigue. Shyam et al. conducted high-cycle fatigue testing of 282 alloy in a 100% steam environment at 800°C [34]. Under the conditions investigated, the fatigue lifetime was found not to be strongly influenced by the loading environment, but rather it showed significant correlation with crystallographic orientations within the microstructures. First, crystallographic crack initiation was observed, with subsequent trans-granular propagation from the crack initiation region. The size of this flat trans-granular surface crack initiation region was larger than the subsurface crack initiation region. By characterizing relative grain misorientations in the regions of crack initiation, they found a correlation with large grain clusters having less than 20° misorientation, which corresponded to a cluster size range of 200–300 μm. Since

the fracture surface analysis indicated that the crack initiation regions were also in the size range of 200–300 μm (almost an order of magnitude larger than the average grain size), they suggested that these regions "collectively form microstructural neighborhoods that could nucleate fatigue cracks." The authors plan to incorporate these findings into a probabilistic model for fatigue crack initiation that accounts for the morphology of the fracture surface and the active deformation mechanisms.

15.1.3 Environmental resistance properties

15.1.3.1 Static oxidation behavior in air

Oxidation resistance evaluations were an early emphasis for HAYNES 282 alloy testing. Pike and Srivastava conducted static oxidation and dynamic burner rig experiments on four of the γ′-strengthened alloys listed in Table 15.1, including 282, 263, Waspaloy, and R-41 alloys [8]. After 1008 h at 871, 927, and 982°C (1600, 1700, and 1800°F) in slow-flowing air (sufficient to ensure adequate oxygen to the surfaces), samples were analyzed for metallographic and weight changes. To determine metal loss, all samples were given a descale treatment at the conclusion of the test to remove the surface oxide scale. The difference from the descaled weights relative to the preexposed weights were attributed to oxidation, and recorded as the actual metal loss. The metal loss values are combined with average and maximum oxide penetration measurements taken via optical microscopy to provide a reasonably quantitative measure of differences. Their results are summarized in Table 15.4.

Table 15.4 Summary of results of static oxidation tests

		Metal loss		Average metal affected		Maximum metal affected	
Exposure temp	**Alloy**	**μm**	**mils**	**μm**	**mils**	**μm**	**mils**
871°C (1600°F)	282 alloy	5	0.2	35	1.4	41	1.6
	R-41 alloy	5	0.2	35	1.4	41	1.6
	Waspaloy alloy	8	0.3	44	1.7	48	1.9
	263 alloy	3	0.1	46	1.8	54	2.1
927°C (1700°F)	282 alloy	3	0.1	46	1.8	54	2.1
	R-41 alloy	5	0.2	46	1.8	56	2.2
	Waspaloy alloy	8	0.3	97	3.8	107	4.2
	263 alloy	5	0.2	79	3.1	96	3.8
982°C (1800°F)	282 alloy	5	0.2	58	2.3	71	2.8
	R-41 alloy	5	0.2	84	3.3	96	3.8
	Waspaloy alloy	23	0.9	147	5.8	155	6.1
	263 alloy	28	1.1	150	5.9	180	7.1

Metal affected = metal loss + internal penetration; 1 mil = 0.001 inch = 25.4 μm.
After L. Pike, S. Srivastava, Oxidation behavior of wrought gamma-prime strengthened alloys, Materials Science Forum 595–598 (2008) 661–671.

As a consistent trend, both average and maximum affected metal measurements show that 282 and R-41 alloys provided the greatest static oxidation resistance. These trends do not always match the initial metal loss results, especially at the lower temperatures. At 871°C (1600°F), a slight, but consistent weight gain observed in all four alloys was attributed to the formation of protective chromia scales. Differences started to appear at 927°C (1700°F) with Waspaloy showing a slightly greater weight gain than 282 and R-41 alloys (which were similar), but 263 alloy continued a gradual weight loss after approximately 400 h. At 982°C, the weight loss in 263 alloy began earlier and was substantial (and was attributed to scale spallation), while R-41 alloy also exhibited an early weight loss that stabilized later in the test and did not have a significantly detrimental impact on the affected metal results. Waspaloy and 282 alloys both exhibited weight gain throughout the test.

The study concluded that 282 alloy showed good static oxidation resistance at all temperatures tested, and it was as good or better in performance than the other three γ′-strengthened alloys in this study [8]. The metallography of the static oxidation samples at 871°C showed internal oxidation in all four alloys that consisted of aluminum and titanium-rich oxides, while nitridation was also observed in the 263 alloy. At the higher 927 and 982°C (1700 and 1800°F) temperatures in flowing air, the oxidation resistance of both 282 and R41 alloys was clearly superior to Waspaloy or 263 alloys, both of which also displayed nitridation attack. The study also concluded that 282 alloy performed similarly well in the burner rig tests, with all alloys showing nitridation in the severely cyclic tests.

15.1.3.2 Oxidation behavior in water vapor and steam atmospheres

The addition of water vapor in a thermal environment generally intensifies the rate of corrosion in most metallic materials. The high temperatures and pressures of an A-USC environment are expected to present even greater challenges from the threat of erosion, oxide spallation, and thinning from chromia volatilization. While it is clear that a number of researchers have evaluated 282 alloy in this context and have published some valuable technical information, very long-term studies are not readily found. Some of the more relevant studies will be briefly reviewed.

For lower water vapor fractions from 5% to 20%, Deodeshmukh reviewed the performance of 282 alloy, although in foil forms that are somewhat less meaningful to A-USC applications [35–36]. As others have also shown, a $CrO_2(OH)_2$ (g) species can form in the presence of water vapor, and it has a higher vapor pressure than the CrO_3 (g). This reaction can cause vaporization losses at temperatures as low as 650°C (1200°F). The stated concern triggering Deodeshmukh's study was the potential for chromia vaporization to change the oxidation kinetics from parabolic to linear, which would be followed by catastrophic breakaway oxidation. Further, the parabolic scale growth and linear scale vaporization can occur simultaneously in water vapor environments. In his study, 282 alloy did not exhibit breakaway oxidation at 760°C (1400°F) after a year-long exposure, but breakaway oxidation was observed at 871°C (1600°F) over the same time period.

Holcomb and Hsu developed a methodology for calculating an expected chromia evaporation rate as a function of temperature and experimentally validating the vaporization [37]. By linking the Cr diffusion profile with the chromia evaporation rates within a cylindrical geometry specimen, they created a prediction for breakaway oxidation times, accounting for expected upstream saturation of $CrO_2(OH)_2$ (g) along the steam path. Their paper detailed the methodology for HAYNES 230 alloy, but it did not detail the results for 282 alloy.

Further work by Holcomb et al. with 760°C steam exposure of wrought and cast versions of 282 alloy, 263 alloy, and Nimonic alloy 105 are converted from tabular results into a graphical presentation in Fig. 15.9 [38]. In this figure, 282 alloy and alloy 105 have the lowest internal oxidation attack after 1000 h. After 2000 h, the wrought alloy 105 continued to show the lowest oxidation rates, while all other specimens,

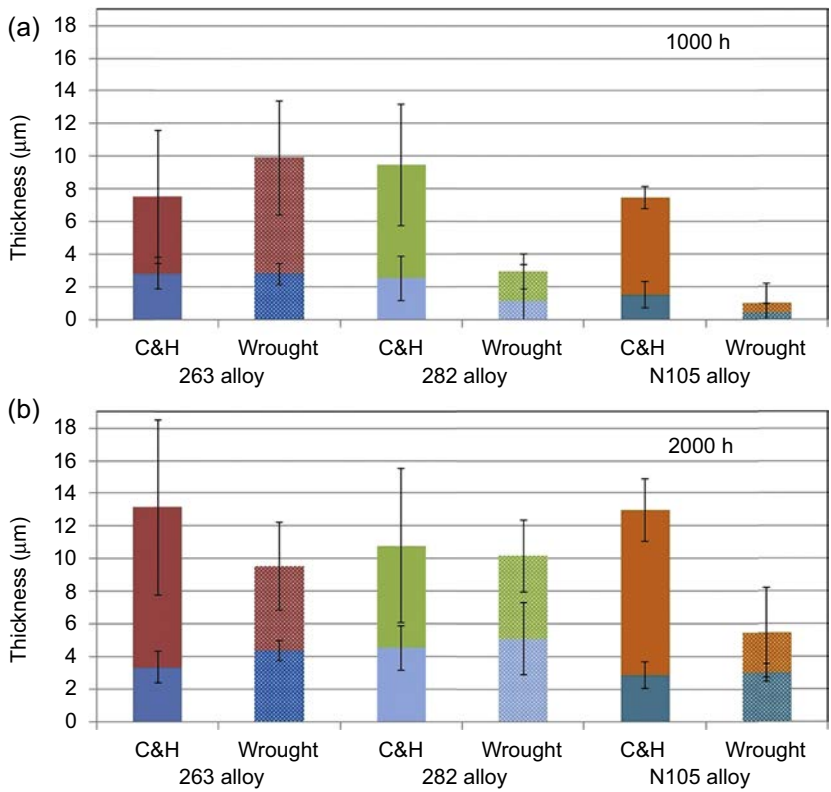


Figure 15.9 Comparison of scaling behavior at 760°C for (a) 1000 h and (b) 2000 h exposures of 263, 282, and N105 alloys in wrought and "cast and homogenized" conditions, where lower *bar* represents external scale thickness and upper *bar* represents internal oxidation.
After G. Holcomb, P. Wang, P. Jablonski, J. Hawk, Materials performance in USC steam, in: Proceedings of the 24th Annual Conference on Fossil Energy Materials, Pittsburgh, PA, May 25–27, 2010. FY10.MSE.1610222.682 (Online) 2010, p. 24. http://www.osti.gov/scitech/servlets/purl/1011514.

including 282 alloy showed relatively similar performance. Since the higher 1000-h results did not increase substantially at 2000 h and the lowest rates increased to approximately similar levels across the board, it may be concluded that insufficient data are available to determine if the rates have a long-term parabolic behavior.

A similar study by Essuman et al. found similar results to Holcomb's after 5000 h of exposure in laboratory air and 17-bar steam at 800°C using cast and homogenized (C&H) versions of several alloys, including 282 alloy [39]. They concluded that: "in general, all of these Ni base alloys showed protective behaviour after 5000 h in both environments with relatively low mass gains and thin oxides."

To obtain real-world results about the performance of various nickel-based alloys at A-USC conditions, Alstom cooperated with Southern Company affiliate Alabama Power to construct a test loop at Plant Barry in Bucks, Alabama, USA. This is the site of the first test loop in the world to operate at 760°C steam-cooled condition, and it performed for over 17,000 h between 2011 and 2014. Although results have not been published to date, Alstom acknowledged this accomplishment with a press release stating that all 94 specimens made from eight different superalloys and three different surface coatings "…appeared in good condition and retained their original mechanical integrity." [40].

In addition to the real-world exposures, the US A-USC consortium continues to sponsor research at the US national labs to expand the database of nickel alloys under consideration. Pint et al. have conducted studies to identify the compositional basis for the observed positive steam-side oxidation results of commercially produced 282 and 740H alloys by comparing "model alloys" of a similar compositional basis [41]. Minor variations in the model alloys were then compared to the commercial results, but no conclusions were able to be drawn. However, basic steam exposure results generated at 800°C for 282 alloy are shown in Fig. 15.10.

Pint et al. also microstructurally examined the internal attack after exposures to 17 bar/800°C steam for up to 5000 h, the results of which are shown in Fig. 15.11 [41]. All of the micrographs show surface scale growth over time with internal oxidation, with strong similarities to other reported materials in this class.

15.1.3.3 Fireside corrosion resistance

While fireside corrosion testing has been performed for many years on a wide range of potential A-USC materials, the number of studies reported in the literature for fireside corrosion behavior of HAYNES 282 alloy is remarkably low. One of those studies was by Pint, who modeled alloys using a binary Ni-Cr base with Al + Ti additions to assess whether γ' precipitates were detrimental to corrosion resistance in simulated coal ash and oxy-fired conditions [42]. At 700°C, the Al + Ti additions were shown to reduce the metal loss rates, and both 282 and 740 alloys exhibited rather low metal loss numbers (although 282 alloy had the higher rate). At 800°C, Pint observed an unexpectedly dramatic difference between 282 and 740 alloys, with the 282 alloy specimen reportedly consumed in testing after 500 h. The results were attributed to beneficial effects of the higher Cr content of 740H alloy, with some additional positive impact from Ti contents in the scale.

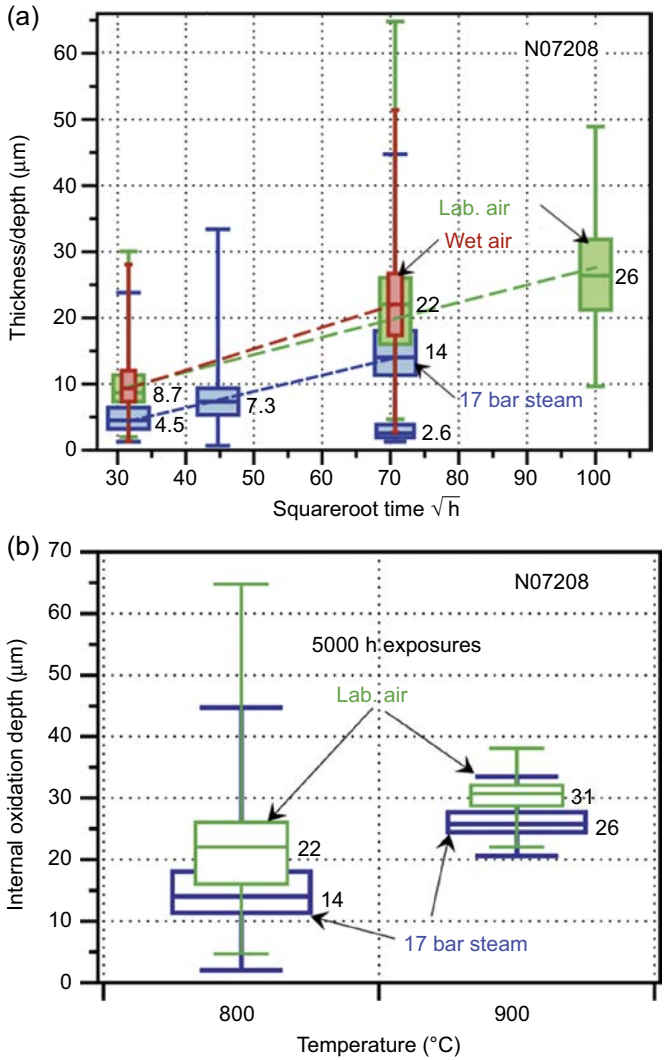


Figure 15.10 *Box* and whisker *plots* for HAYNES 282 alloy showing (a) internal oxidation depth as a function of exposure time at 800°C, and (b) internal oxidation depth at 800° and 900°C after 5000 h exposures in laboratory air and 17 bar steam. The median values are noted in each case. After B. Pint, B. Thiesing, Effect of environment on the oxidation behavior of Commercial and Model Ni-Base Alloys – NACE Paper C2015-5919, Houston, TX, in: Presented at NACE Corrosion 2015, Dallas, Texas, USA, March 2015.

Further comparisons of behavior showed that 282 and 617 shared poor corrosion behavior in the oxy-fired synthetic ash environment. Since both alloys have over 8% Mo, Pint created a second set of Ni-Cr model alloys with 20% Cr, 0–20% Co, and 0–8% Mo, from which he drew a number of conclusions based on 500 h exposures. First, at 700°C, the Mo was not necessarily detrimental, and it even appeared to have

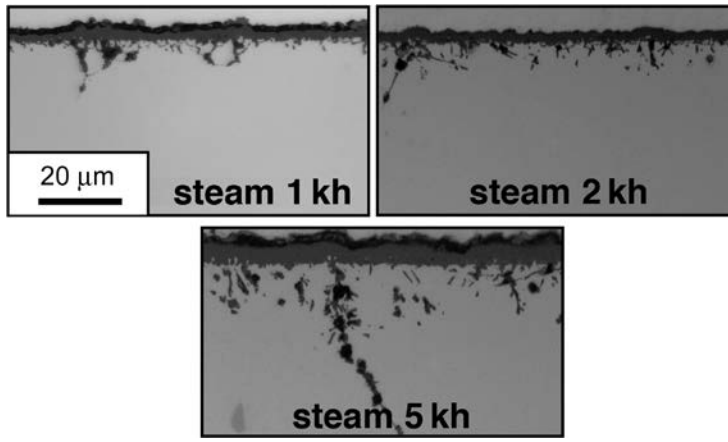


Figure 15.11 Microstructures of HAYNES 282 alloy showing internal oxidation attack after exposure to 17 bar steam at 800°C [41].
After B. Pint, B. Thiesing, Effect of environment on the oxidation behavior of Commercial and Model Ni-Base Alloys – NACE Paper C2015-5919, Houston, TX, in: Presented at NACE Corrosion 2015, Dallas, Texas, USA, March 2015.

a somewhat positive impact. This trend changed at 800°C, with higher Mo contents showing higher metal loss rates. Changes in Co content did not appear to have a major impact at either temperature, and little could be conclusively deduced about strategies to improve fireside corrosion resistance. Regardless of this result, it appeared that 282 alloy was not well suited to fireside exposure without other mitigation strategies commonly applied to current classes of materials (eg, weld overlay, coatings, etc.). However, given the limited scope of data, further and longer term studies may be warranted.

15.1.4 Welding and weldability

Since HAYNES 282 alloy was originally developed to target gas turbine combustion path applications, weldability was a critical requirement from the beginning of development. As detailed by Caron, high-strength γ' alloys in these applications often suffer from three different forms of weld cracking: weld solidification cracking, heat-affected zone (HAZ) liquation cracking, and strain-age cracking [43]. Each of these must be understood to evaluate the weldability of alloys.

15.1.4.1 Strain-age cracking susceptibility

Strain-age cracking is typically attributed to residual stresses in the material that are induced by solidification shrinkage coupled with formation of γ' during heat treatment. Since the cracking typically strikes during heat up in the first post-weld heat treatment (eg, post-weld solution anneal), detection of the problems is not immediate, which adds cost and creates delays. Alloys with very rapid γ' precipitation

kinetics are usually much more susceptible, and 282 alloy was designed to avoid these issues [5].

Some of the earliest evaluations of strain-age cracking in 282 alloy focused on the use of controlled heating rate tests (CHRT) as an effective method of distinguishing its propensity compared to other γ′ alloys [44]. To better use CHRT methods, Metzler modified specimen geometry and chose single temperatures, heating rates, and extension rates to show that Gleeble-based CHRT methods could reliably distinguish even minor differences in strain-age cracking susceptibility in different alloys [45]. As verification of the validity of the method, he also showed the CHRT resulted in ductile rupture in non-γ′ alloys, while the strain-age sensitive (γ′/γ″) alloys consistently exhibited signs of intergranular fracture in post-test fractography. The ranking of 282 alloy in the CHRT is compared to three other alloys in Fig. 15.12. Based on extensive positive feedback from many fabricators to date, the CHRT value of 15% minimum confirms the good strain-age cracking resistance of 282 alloy.

15.1.4.2 Weld solidification cracking

The Variable Restraint, or "Varestraint," weldability test is an extensively used test for evaluating weld solidification cracking susceptibility [43]. In a Varestraint test, an autogenous GTAW weld bead is applied to a sample while a bending strain induces cracking in the partially solidified metal at the trailing edge of the weld pool. Residual

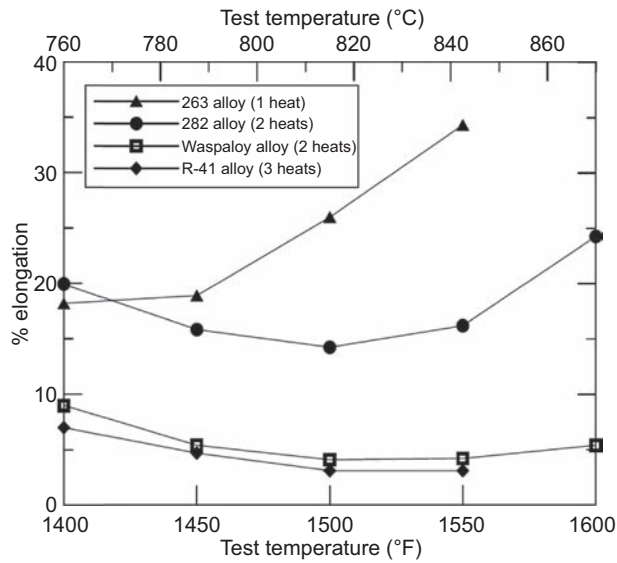


Figure 15.12 CHRT ductility results suggesting that 282 alloy has much lower susceptibility to strain-age cracking than Waspaloy or R-41 alloys, while 263 alloy with very low susceptibility shows even higher ductility [5].
Used with permission; L. Pike, HAYNES® 282™ alloy – a new wrought superalloy designed for improved creep strength and fabricability, in: Proceedings of GT2006 ASME Turbo Expo 2006: Power for Land, Sea and Air, May 8–11, 2006. Barcelona, Spain, 2006 (Paper 91204).

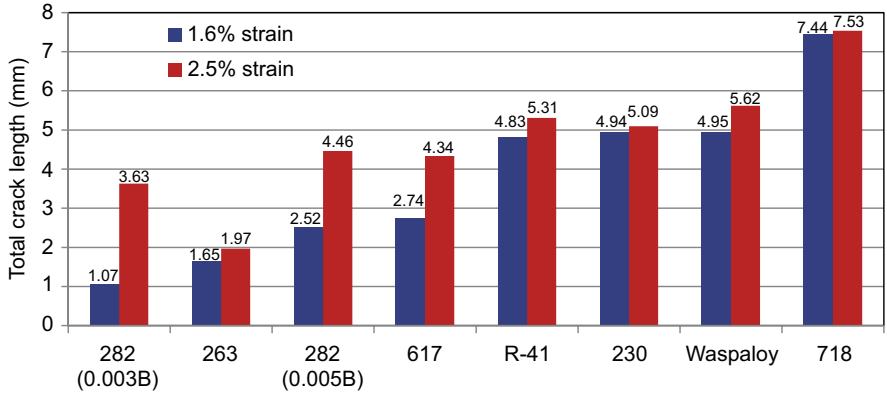


Figure 15.13 Total crack length results from subscale longitudinal Varestraint testing in various alloys.
After J. Caron, Weldability and welding metallurgy of HAYNES 282 alloy, in: 8th International Symposium on Superalloy 718 and Derivatives, John Wiley & Sons, 2014, p. 273–286.

cracks are optically measured (at 20–50X) to generate total crack length and/or maximum crack length (MCL) data, which are then correlated to susceptibility. Bending strains are varied in the fixture to allow for distinctions to be made in comparative susceptibility between alloys.

In research by Caron, 282 alloy with two levels of boron were evaluated in Varestraint testing [43]. The results shown in Fig. 15.13 demonstrate that 282 alloy exhibited excellent solidification cracking resistance in both heats, regardless of boron content. Similar results were obtained for both total and MCL measurements. Although values for both 282 heats were good, the heat with the low (0.003 wt%) levels of boron produced the best Varestraint results, and standard quality controls have been implemented to ensure production welding products are produced with boron below a 0.005% maximum. When crack lengths at the two different levels of strain were compared, results indicated that 282 alloy may be more sensitive than the other alloys to cracking in conditions of high weld restraints. However, the results of this particular study showed that 282 alloy exhibited better solidification cracking resistance than even 718 alloy, a well-known and frequently welded material.

15.1.4.3 Heat-affected zone liquation cracking

In addition to research by Caron, anther research project by Andersson also focused on hot ductility testing as a means of evaluating HAZ liquation cracking propensities in 282 alloy [43,46]. In the 2010 paper, J. Andersson et al. used a Gleeble to experimentally determine what they termed the “brittle temperature range” (BTR), which they defined as the difference between the nil strength temperature (NST) caused by liquation on heating and ductility recovery temperature, defined as the temperature on cooling where solidification has sufficiently occurred to measure a bulk ductility. They correlated the BTR ranges to predictions of susceptibility for hot cracking

during welding. With a BTR of 110–125°C, 282 alloy was found to exhibit good hot ductility. Similarly, Caron also explored NST evaluations via Gleeble experiments to assess HAZ liquation cracking in 282 alloy, calling the "BTR" range the "liquation cracking temperature range" (LCTR) [43]. His LCTR range for 282 alloy in the age-hardened condition was estimated at ~90°C, in reasonable agreement with findings of Andersson et al. This was based on an NST of 1321°C (from an average of three samples), together with recovery of a small amount of ductility (ie, ~3%RA) at 1232°C. Since ductility increased to 28%RA on cooling to 1218°C, the DTR was estimated at ~1230°C. He reported comparable data from the literature tested in a similar manner for Waspaloy (209°C) and 718 (103°C). As such, 282 alloy appears to have better HAZ liquation cracking resistance than these alloys.

Finally, although no experimental work was done to verify, Andersson et al. concluded that an observed Vickers hardness increase of 103 units during a cool-down cycle from the 1121°C indicated a risk for age cracking during post-weld heat treatments of large welded structures [46]. However, strain-age cracking usually occurs during the post-weld heat up during the transition to the solution anneal temperature, before residual stresses can be relaxed. As such, these expected problems should have appeared during CHRT testing, for which 282 alloy performed well. Further, initial results of heavy section weldments of castings by Maziasz and Shyam have shown "good weldability, and preliminary creep rupture properties of the weldment that are equivalent to the base-metal at 750–800°C with proper post-weld heat-treatment" [32]. This suggests that the concern of Andersson et al. may have been overstated, since the cast segments were substantial in cross-section.

15.1.4.4 Weld repairs after long-term thermal exposures

Since weld repair issues have created many problems in A-USC component test programs, studies have been performed on HAYNES 282 alloy to assess weldability in the long-term thermally exposed condition. In a promising study by Caron and Pike, samples exposed at 760°C for 4000 h were successfully welded without cracking or other defects [47]. The obvious conclusion is that no pre-weld solution anneal is necessary prior to repair welding 282 alloy after field exposures. While evidence of liquation in the HAZ nearest to the weld metal was observed, no evidence was found of associated cracking. As previously discussed, the dominant secondary phases observed after long-term thermal exposure, ie, intergranular $M_{23}C_6$ and intragranular γ' were resolutioned upon post-weld solution annealing and age hardening, effectively rejuvenating the microstructure. Some shifts in fracture location for tensile tests performed on these rejuvenated weldments were observed, with failure consistently occurring at the base-metal/HAZ interface. Some reductions were also observed in strength of the weldments, which was attributed to a large HAZ grain size. As a final part of the study, hot ductility testing similar to the aforementioned results showed that long-term exposed 282 alloy displayed excellent ductility recovery, with little difference from on-heating and on-cooling tests. That suggests that 282 alloy possesses excellent resistance to HAZ liquation cracking even in the long-term exposed condition.

15.1.4.5 Dissimilar welding capabilities

While few results have been formally published, extensive work on dissimilar welding has been done and presented in a number of conferences (eg, Shingledecker and Purgert [48] or Tortorelli et al. [49]). For A-USC applications, work by EPRI involved the evaluation of a welded rotor configuration produced by joining HAYNES 282 alloy to Udimet alloy 720Li. By all indications, the work was quite successful with nondestructive evaluation of the joint verified, and heat treatment studies confirming no observable signs of strain-age cracking [48]. To date, the dissimilar weld joint area is in need of further evaluation, especially in regard to long-term thermal stability of dissimilar weld joints at relevant intermediate temperatures.

15.1.4.6 Heavy section weldments

Similar to the limited work on dissimilar welds, heavy section welds are important requirements in boilers and piping. While there have not been extensive evaluations of welding thick sections of 282 alloy, during a recent trial some 3.5″-thick 282 segments were successfully welded at the Babcock & Wilcox Research Center via the hot wire gas tungsten arc welding (HW-GTAW) process. Based on initial test results and weld characterization at the time of writing, 282 alloy appears to offer good thick-section weldability.

The exciting part of these reports is that most studies overall have continued to describe positive findings for all weldability evaluations, suggesting that 282 alloy's unique combination of material properties and weldability offer true solutions for the materials challenges of A-USC applications.

15.1.5 Castings and castability

A-USC applications are somewhat unique in their demand for very large castings for turbine casings, valve bodies, and similar components. Given the positive feedback about wrought HAYNES 282 alloy and its favorable weldability behavior, strong interest in castings and castability is not surprising. The Energy Industries of Ohio (EIO) has been spearheading the casting research on 282 alloy. They lead both the consortia for US boiler and steam turbine manufacturers, with the EPRI acting in partnership as the technical lead for A-USC materials development. NETL has created a substantial body of casting materials research, and it has worked extensively on 282 alloy. EIO has also worked in cooperation with the Foundry Research Institute in Kraków, Poland to similarly developed models and technology toward the practical development of cast 282 parts.

In US DOE (Department of Energy)-supported research for A-USC power plants, Jablonski et al. of NETL (National Energy Technology Laboratory) cast components in 263, Haynes 282, and Nimonic 105 alloys, and they assessed microstructures and mechanical properties with different heat treatments [50]. Since large castings typically have appreciable nonuniform solidification patterns, homogenizing heat treatments were evaluated and discussed. Input from this research was used to continue development of full-scale, thick-section castings for steam turbine components.

One of the Polish Institute's earliest papers explored the susceptibility of 282 alloy to the formation of shrinkage cavities and contractions by studying stepped and

spiral-fluidity castability tests [51]. These studies employed air induction melting with argon shield gases, with and without deoxidizing additions. N. Sobczak and others found rather strong susceptibility to casting contractions (and the consequent formation of shrinkage cavities), and they emphasized the importance of low superheating values for best results. They concluded that thin-wall castings, which require a high level of superheat, represented substantial challenges. However, large and heavy section castings, like those needed in A-USC turbine housings, etc., can be poured with low superheat, leading to a reasonable expectation of controllable shrinkage (on the order of 2%) and components of good cast quality. Their results also showed that using deoxidizers (eg, NiMg alloy) was effective at reducing oxygen content in the final castings by a factor of three.

As a continuation of this research, Matysiak and others evaluated microstructures in thin-walled, investment-cast 282 alloy components [52]. They found that these high superheat, 282 alloy castings exhibited rather complex dendritic microstructures that included more than the commonly observed: γ, γ′, and primary MC carbide phases. They reported observations of uniformly distributed primary nitrides (MN), along with other previously unreported phases: carbosulfides (M_2SC), globular σ phase, and a lamellar eutectoid phase, all three found in the final interdendritic regions. It must be noted that the components were evaluated in the as-cast condition with no post-cast heat treatment or homogenization. In contrast, Yang et al. conducted a study of as-cast 282 alloy to assess microstructural changes over time [53]. In their paper, two types of primary phases were found in the as-cast condition, including TiN and (Ti,Mo)C, together with $M_{23}C_6$ and M_6C carbides on and near grain boundaries. In addition, somewhat coarser γ′ was observed (with a "star morphology"), but no reports were made of any appearance of σ phase. Further, thermodynamic analyses and Scheil predictions did not indicate that other such phases would be stable.

While this thin-walled geometry was expected to represent the greatest challenges, the researchers did report that "…FPI and X-ray inspections revealed no critical defects in the castings such as; missruns, hot tears, porosity, dross or non-metallic inclusions" [52]. This suggests that even challenging castings might be successfully poured, although higher casting temperatures than typically used in common industrial practices might be required.

One of the greatest obstacles to developing models that would assist with improved casting trials was the scarcity of thermophysical data for 282 properties above 1000°C (1832°F). To address this need, J. Sobczak et al. conducted spiral-fluidity tests and performed numerical analyses on the solidification patterns that allowed them to back-calculate the thermophysical properties in both the semisolid and liquid states [54]. To verify the data, they input the data into virtual casting models and compared the results with actual castings. They concluded that the consistency was satisfactory, and particularly good for prediction of the porosity distribution and occurrence of surface defects.

One of the more recent reports involved investigation of the intensity of reactions of molten 282 alloy with three common foundry refractories [55]. The project evaluated alumina, zirconia+silica, and zirconium silicate ceramics in contact with the molten metal, focusing on the impact of the relatively large amount of highly reactive alloying elements (aluminum, titanium) in the alloy. The study made conclusions about the resistance and

suggested that ceramics based on zirconium compounds might minimize reactions at the liquid metal/ceramic material interface. Further, absolute minimization of contact times was recommended together with minimization of overheating as much as possible.

To take the previous research closer to casting larger and more practical components, Pirowski recently published results of thermal analyses of a 282 alloy step block casting (ie, mold with progressively increasing wall thicknesses) [56]. From these measurements taken during solidification, a relationship was derived to predict dendrite arm spacing (DAS) in castings as a function of wall thickness. Jumping from a 10-mm wall thickness to 44 mm increased solidification times by a factor of approximately 7, and it doubled the DAS value.

The research done by the Foundry Research Institute, ORNL, and NETL has helped to bridge the challenges of casting in air with the high reactivity of the Ti and Al. NETL reported that their extensive program suggested that alloys like 263 and 282 alloy could be cast successfully, while the Foundry Research Institute indicated that large components necessary for A-USC applications may be the most technologically viable parts (requiring the lowest superheat during pouring). EIO has pushed ahead with scale-ups at two different commercial casting vendors, who have made static sand cast test blocks, step blocks of about 450 kg (1000 lb) finished weight, and centrifugal castings [57]. Based on positive results, a larger, 6000-lb valve body was cast by Flowserve (Dayton, Ohio), as shown in Fig. 15.14. In parallel with characterization of this practical casting, work is continuing toward development of the necessary data for modeling and improvements of this process.



Figure 15.14 ~2700 kg (6000 lb) finished weight valve body cast from Haynes 282 alloy by Flowserve in Dayton, Ohio.
Photo courtesy of Energy Industries of Ohio. After R. Purgert, J. Shingledecker, Update on U.S. DOE/OCDO Advanced Ultra-Supercritical (A-USC) Steam Boiler and Turbine Consortium, in: Presentation to: 2015 DOE-FE Cross-Cutting Review Meeting April 29, 2015, Pittsburgh, PA USA. 2014. [Online] Available from: http://www.netl.doe.gov/File%20Library/Events/2015/crosscutting/Crosscutting_20150429_0830A_EIO.pdf.

15.2 Conclusions

In reviewing material characteristics most necessary to support A-USC applications, HAYNES 282 alloy appears to be one of a select few alloys that offer a balance of long-term creep strength, thermal stability, oxidation resistance, weldability, manufacturability, and repairability suitable for these uses. Indeed, no other wrought alloy appears to match the creep strength capability of 282 alloy, which offers potential cost savings from reduced material usage. The weakest link for A-USC applications appears to be fireside corrosion resistance of 282 alloy, for which mitigation strategies have been identified. While significant work remains to complete all material database development items, the alloy is deserving of the time and effort.

15.3 Future trends

Since HAYNES 282 alloy has shown a number of positive attributes that could resolve materials challenges for A-USC applications, further development efforts are required to realize this promise. The most pressing development trend is the creation of an ASME Code Case to allow the alloy to be used in A-USC designs. The full scope of testing has been identified, and creep and tensile tests have already begun at ORNL. The data collection effort will take time to gather some of the long-term creep points necessary to support the statistics, so the Code Case may not be available for another 2–3 years.

Based on excellent hot workability and stability of the composition, a rather extensive data development program is underway by the US A-USC Consortium to consider forged 282 alloy for steam rotors, for which a road map of planned work is shown by Shen et al. [31]. Other forms requiring hot work include capability to produce large diameter pipe. While few facilities have the press tonnage needed for these large forms, trials should be conducted to assess the capability of producing 282 alloy tubes in sizes needed for these applications, since strengths should allow for thinner walls.

Finally, additional product development work with HAYNES 282 powder for additive manufacturing and powder consolidation applications is being conducted. Powder has been produced for trials, and it is available in limited mesh ranges from Haynes International. Initial consolidation trials have been conducted, with trials still in early stages [33]. Details of the performance will take some time for information to be reported.

Acknowledgments

Since this text draws from and summarizes the research of others, the author would like to express appreciation to key people for allowing permissions to share data and figures, especially Lee Pike, John Shingledecker, Bob Purgert, Bruce Pint, Pete Tortorelli, and others.

References

[1] Haynes International, Inc., HAYNES® 282® Alloy. Kokomo, Indiana (Brochure H-3173A) 2008. Available from: http://www.haynesintl.com.
[2] Haynes International, Inc., HAYNES® Waspaloy Alloy. Kokomo, Indiana (Brochure H-3128C) 2008. Available from: http://www.haynesintl.com.
[3] Haynes International, Inc., HAYNES® R-41 Alloy. Kokomo, Indiana (Brochure H-3056A) 2002. Available from: http://www.haynesintl.com.
[4] Haynes International, Inc., HAYNES® 263 Alloy. Kokomo, Indiana (Brochure H-3047D) 2000. Available from: http://www.haynesintl.com.
[5] L. Pike, Development of a fabricable gamma-prime (γ′) strengthened superalloy, in: R. Reed et al. (Ed.), Superalloys 2008, TMS, 2008, pp. 191–200.
[6] Special Metals Corporation, INCONEL® Alloy 740. Huntington, West Virginia (Publication Number SMC-090) 2004. Available from: http://www.specialmetals.com.
[7] United States Patent and Trademark Office, Ni-Cr-Co Alloy for Advanced Gas Turbine Engines. Washington, DC, 2011 (U.S. Patent No. 8,066,938).
[8] L. Pike, S. Srivastava, Oxidation behavior of wrought gamma-prime strengthened alloys, Materials Science Forum 595–598 (2008) 661–671.
[9] L. Pike, HAYNES® 282™ alloy – a new wrought superalloy designed for improved creep strength and fabricability, in: Proceedings of GT2006 ASME Turbo Expo 2006: Power for Land, Sea and Air, May 8–11, 2006, Barcelona, Spain, 2006 (Paper 91204).
[10] S. Srivastava, J. Caron, L. Pike, Recent developments in the characteristics of HAYNES 282 alloy for use in A-USC applications. in: Proceedings From the 7th International Conference on Advances in Materials Technology for Fossil Power Plants October 22–25, 2013, Waikoloa, Hawaii, Electric Power Research Institute, 2014, pp. 120–130.
[11] P. Ennis, A. Strang, S. Gill, G. Mccolvin, H. Atkinson, Microstructural stability of nickel based alloys for advanced power plant applications, Energy Materials 4 (4) (2012) 184–188, http://dx.doi.org/10.1179/174892312X13269692038978, © 2012 Institute of Materials, Minerals and Mining and W. S. Maney & Son Ltd. Received September 1, 2011; accepted January 12, 2012.
[12] L. Pike, Long term thermal exposure of HAYNES 282 alloy, in: 7th International Symposium on Superalloy 718 and Derivatives, TMS (The Minerals, Metals & Materials Society), 2010, pp. 645–660.
[13] H. Beattie, W. Hagel, Intergranular precipitation of intermetallic compounds in complex austenitic alloys, Transactions of the AIME 221 (1961) 28–34.
[14] H. Collins, Relative long-time stability of carbide and intermetallic phases in nickel-base superalloys, Transactions of the ASM 62 (1969) 82–104.
[15] W. Betteridge, J. Heslop (Eds.), The Nimonic Alloys, Crane, Russak & Company, Inc., New York, NY, 1974, pp. 86–87.
[16] J.-C. Zhao, V. Ravikumar, A. Beltran, Phase precipitation and phase stability in nimonic 263, Metallurgical and Materials Transactions A 32A (2001) 1271–1282.
[17] X. Xie, S. Zhao, J. Dong, G. Smith, B. Baker, S. Patel, A new improvement of Inconel alloy 740 for USC power plants, in: Advances in Materials Technology for Fossil Power Plants: Proceedings From the Fifth International conference 2007, ASM International, 2008.
[18] P. Tortorelli, H. Wang, K. Unocic, M. Santella, J. Shingledecker, V. Cedro III, Long-term creep-rupture behavior of INCONEL® 740 and HAYNES® 282, in: Proceedings of the ASME Symposium on Elevated Temperature Application of Materials for Fossil, Nuclear, and Petrochemical Industries, March 25–27, 2014, 2014.

[19] P. Tortorelli, K. Unocic, H. Wang, M. Santella, J. Shingledecker, Ni-Based alloys for advanced ultrasupercritical steam boilers, in: Fossil Energy Crosscutting Research Program Review, April 25, 2015, Pittsburgh, Pennsylvania, 2015. http://www.netl.doe.gov/File%20Library/Events/2015/crosscutting/Crosscutting_20150429_0900A_ORNL.pdf.
[20] R. Schwant, C. Shen, M. Soare, New materials enable unprecedented improvement in turbine performance, Advanced Materials & Processes (2013) 18–22 ASM International.
[21] Haynes International, Inc., HAYNES® 230® Alloy. Kokomo, Indiana(Brochure H-3000H) 2004. Available from: http://www.haynesintl.com.
[22] Haynes International, Inc, HAYNES® 617 Alloy. Alloy At-a glance. Kokomo, Indiana (Brochure H-3171B) 2008. Available from: http://www.haynesintl.com.
[23] P. Tortorelli, K. Unocic, H. Wang, J. Moser, C. Stevens, Determination of go-forth single-step aging treatment for Haynes alloy 282, in: A-USC Steering Committee Meeting Open Session March 13, 2013, Chicago, Illinois, 2013.
[24] J. Shingledecker, R. Purgert, P. Rawls, Current Status of the U.S. DOE/OCDO A-USC materials technology research and development program, in: Advances in Materials Technology for Fossil Power Plants. Proceedings from the Seventh International Conference, October 22–25, 2013, Waikoloa, Hawaii, USA, ASM International. EPRI Report Number 3002002375, 2014, pp. 41–52.
[25] P. Tortorelli, K. Unocic, H. Wang, M. Santella, J. Shingledecker, Ni-Based alloys for advanced ultrasupercritical steam boilers, in: Fossil Energy Crosscutting Research Program Review, May 22, 2014, Pittsburgh, Pennsylvania, 2014. http://www.netl.doe.gov/File%20Library/Events/2014/crosscutting/Crosscutting_20140522_1600B_ORNL.pdf.
[26] P. Tortorelli, et al., Creep-rupture behavior of precipitation-strengthened Ni-Based alloys under advanced ultrasupercritical steam conditions, in: Proceedings from the 7th International Conference on Advances in Materials Technology for Fossil Power Plants October 22–25, 2013, Electric Power Research Institute, Waikoloa, Hawaii, 2014, pp. 131–142.
[27] L. Pike, Low-cycle fatigue behavior of HAYNES® 282® alloy and other wrought gamma-prime strengthened alloys, in: Proceedings of ASME Turbo Expo 2007: Power for Land, Sea and Air, May 14–17, 2007, Montreal, Canada. Paper No. GT2007-28267, 2007, pp. 161–169. http://dx.doi.org/10.1115/GT2007-28267.
[28] R. Buckson, O. Ojo, Cyclic deformation characteristics and fatigue crack growth behaviour of a newly developed aerospace superalloy Haynes 282, Materials Science and Engineering A (2010). http://dx.doi.org/10.1016/j.msea.2012.06.034.
[29] R. Brommesson, M. Ekh, Experiments and modelling of the cyclic behaviour of Haynes 282, Technische Mechanik 32 (2–5) (2012) 130–145.
[30] K. Rozman, Characterization of High Temperature Fatigue Mechanisms in Haynes 282 Nickel Based Superalloy (Dissertation for the degree of Doctor of Philosophy in Materials Science), Oregon State University, Corvallis, Oregon, USA, 2014.
[31] C. Shen, T. Hanlon, S. Ismonov, A. Loghin, M. Soare, N. Zhou, J. Li, Modeling Creep-Fatigue-Environment Interactions in Steam Turbine Rotor Materials for Advanced Ultrasupercritical Coal Power Plants, 2012, [Online] https://www.netl.doe.gov/File%20Library/Events/2012/26th%20Annual%20Conference%20on%20Fossil%20Energy%20Materials/Shen–2012-FE-v3.pdf.
[32] P. Maziasz, A. Shyam, Ni-Based alloys for advanced ultrasupercritical steam boilers, in: Fossil Energy Crosscutting Research Program Review, April 25, 2015, Pittsburgh, Pennsylvania, 2015. http://www.netl.doe.gov/File%20Library/Events/2014/crosscutting/Crosscutting_20140522_1630B_ORNL.pdf.

[33] P. Maziasz, et al., Ni-Based alloys for advanced ultrasupercritical steam boilers, in: Fossil Energy Crosscutting Research Program Review, April 25, 2015, Pittsburgh, Pennsylvania, 2015. http://www.netl.doe.gov/File%20Library/Events/2015/crosscutting/Crosscutting_20150429_1030A_ORNL.pdf.

[34] A. Shyam, S. Hawkins, S. Roy, S. Dryepondt, D. Erdman, P. Maziasz, The effect of steam on the elevated temperature high cycle fatigue life of alloy 282, in: J. Lecomte-Beckers, O. Dedry, J. Oakey, B. Kuhn (Eds.), 10th Liege Conference: Materials for Advanced Power Engineering 2014, 2014.

[35] V. Deodeshmukh, Long-term performance of high-temperature foil alloys in water vapor containing environment. Part I: oxidation behavior, Oxidation Metals 79 (5–6) (2013) 567–578. Springer-Verlag. http://dx.doi.org/10.1007/s11085-012-9343-1.

[36] V. Deodeshmukh, Long-term performance of high-temperature foil alloys in water vapor containing environment. Part II: chromia vaporization behavior, Oxidation Metals 79 (5–6) (2013) 579–588. Springer-Verlag. http://dx.doi.org/10.1007/s11085-012-9344-0.

[37] G. Holcomb, D. Hsu, Steam turbine materials and corrosion, in: Proceedings of the 21st Annual Conference on Fossil Energy Materials, Knoxville, TN, April 30–May 1, 2007, U.S. Department of Energy, Office of Fossil Energy, Advanced Research Materials, 2007.

[38] G. Holcomb, P. Wang, P. Jablonski, J. Hawk, Materials performance in USC steam, in: Proceedings of the 24th Annual Conference on Fossil Energy Materials, Pittsburgh, PA, May 25–27, 2010, 2010. FY10.MSE.1610222.682 (Online). http://www.osti.gov/scitech/servlets/purl/1011514.

[39] E. Essuman, L. Walker, P. Maziasz, B. Pint, Oxidation behaviour of cast Ni–Cr alloys in steam at 800°C, Materials Science and Technology 29 (7) (2013) 822–827. http://dx.doi.org/10.1179/1743284712Y.0000000103. Institute of Materials, Minerals and Mining.

[40] S. Patel, Alstom reports major boost for advanced ultrasupercritical technology, Power Magazine (2015). [Online] http://www.powermag.com/alstom-reports-major-boost-for-advanced-ultrasupercritical-technology/.

[41] B. Pint, B. Thiesing, Effect of environment on the oxidation behavior of commercial and model Ni-Base alloys – NACE paper C2015-5919, Houston, TX, in: Presented at NACE Corrosion 2015, Dallas, Texas, USA, March 2015.

[42] B. Pint, Effect of alloy composition on fireside corrosion rates in air- and oxy-fired systems, in: Proceedings from the 7th International Conference on Advances in Materials Technology for Fossil Power Plants October 22–25, 2013, Electric Power Research Institute, Waikoloa, Hawaii, 2014, pp. 892–902.

[43] J. Caron, Weldability and welding metallurgy of HAYNES 282 alloy, in: 8th International Symposium on Superalloy 718 and Derivatives, John Wiley & Sons, 2014, pp. 273–286.

[44] M. Rowe, Ranking the resistance of wrought superalloys to strain-age cracking, Supplement to the Welding Journal 85 (2) (2006) 7s–34s.

[45] D. Metzler, A Gleeble®-based method for ranking the strain-age cracking susceptibility of Ni-Based superalloys, Supplement to the Welding Journal 87 (2008) 249s–256s.

[46] J. Andersson, G. Sjöberg, M. Chaturvedi, Hot ductility study of HAYNES® 282® superalloy, in: 7th International Symposium on Superalloy 718 and Derivatives, TMS, 2010, pp. 539–554.

[47] J. Caron, L. Pike, Weldability of HAYNES 282 superalloy after long-term thermal exposure, [Online] in: MATEC Web of Conferences, vol. 14, 13003, 2014. Available from: http://www.matec-conferences.org, http://dx.doi.org/10.1051/matecconf/20141413003.

[48] J. Shingledecker, R. Purgert, Steam turbine materials for advanced ultrasupercritical (AUSC) coal power plants. Presentation to: 2014 NETL Crosscutting Research Review Meeting May 22, 2014: Pittsburg, PA, USA, 2014, [Online] Available from: http://www.netl.doe.gov/File%20Library/Events/2014/crosscutting/Crosscutting_20140522_1030B_EPRI.pdf.

[49] P. Tortorelli, Y. Yamamoto, P. Maziasz, J. Moser, C. Stevens, M. Santella, et al., Materials for Advanced Ultra-Supercritical (A-USC) Steam Boilers, 2012, [Online] http://web.ornl.gov/sci/fossil/pdf/Materials/FEM%20Conf%202012%20Tortorelli%20USC%20Boiler.pdf.

[50] P. Jablonski, J. Hawk, C. Cowen, P. Maziasz, Processing of advanced cast alloys for A-USC steam turbine applications, JOM 64 (2) (2012) 271–279. http://dx.doi.org/10.1007/s11837-012-0241-4.

[51] N. Sobczak, et al., Castability of HAYNES 282 alloy, in: Proceedings of Advanced Ultra-supercritical Coal-Fired Power Plants Workshop, EVN Forum Maria Enzersdorf, Vienna, Austria, September 19–20, 2012, 2012. Available from: http://ausc.coalconferences.org/ibis/ausc.coalconferences/home.

[52] H. Matysiak, et al., Microstructure of Haynes® 282® superalloy after vacuum induction melting and investment casting of thin-walled components, Materials 6 (2013) 5016–5037. Available from: http://www.mdpi.com/journal/materials.

[53] Y. Yang, R. Thomson, R. Leese, S. Roberts, Microstructural evolution in cast HAYNES 282 for application in advanced power plants, in: Proceedings From the 7th International Conference on Advances in Materials Technology for Fossil Power Plants October 22–25, 2013, Electric Power Research Institute, Waikoloa, Hawaii, 2014, pp. 143–154.

[54] J. Sobczak, et al., Numerical analysis of the casting process of Haynes® 282® alloy, in: Proceedings of the 71st World Foundry Congress Advanced Sustainable Foundry Workshop, Palacio Euskalduna, Bilbao, Spain, May 19–21, 2014, 2014.

[55] Z. Pirowski, Evaluation of high-temperature physico-chemical interactions between the H282 alloy melt and ceramic material of the crucible, Archives of Foundry Engineering 14 (4) (2014) 83–90.

[56] Z. Pirowski, Thermal analysis in the technological "step" test of H282 nickel alloy, Archives of Foundry Engineering 15 (1) (2015) 87–92.

[57] R. Purgert, J. Shingledecker, Update on U.S. DOE/OCDO Advanced Ultrasupercritical (A-USC) Steam Boiler and Turbine Consortium, in: Presentation to: 2015 DOE-FE Cross-Cutting Review Meeting April 29, 2015: Pittsburgh, PA, USA, 2014. [Online] Available from: http://www.netl.doe.gov/File%20Library/Events/2015/crosscutting/Crosscutting_20150429_0830A_EIO.pdf.

Appendix A: Physical properties (English and Metric units)

Physical properties of HAYNES® 282® Alloy* – British units

Temperature (°F)	Specific heat (Btu/lb °F)	Thermal conductivity (Btu in/h ft² °F)	Thermal diffusivity (ft²/h)	Electrical resistivity (μohm in)	Mean coefficient of thermal expansion (μin/in °F)	Dynamic modulus of elasticity (Young's modulus) (msi)	Dynamic ehear modulus (msi)	Poisson's ratio
RT	0.104	72	0.112	49.7	–	31.5	11.9	0.319
200	0.110	82	0.121	50.3	6.7	31.0	11.7	0.325
300	0.114	90	0.128	50.7	6.8	30.6	11.5	0.330
400	0.118	99	0.135	51.2	6.9	30.2	11.3	0.335
500	0.122	107	0.143	51.6	7.0	29.7	11.1	0.335
600	0.125	116	0.150	52.0	7.1	29.2	10.9	0.335
700	0.128	124	0.156	52.3	7.2	28.7	10.7	0.337
800	0.131	132	0.163	52.7	7.3	28.2	10.6	0.338
900	0.134	140	0.170	53.0	7.5	27.7	10.4	0.340
1000	0.136	148	0.176	53.5	7.5	27.2	10.1	0.342
1100	0.138	156	0.183	53.7	7.6	26.6	9.9	0.346
1200	0.140	164	0.190	53.4	7.8	26.0	9.7	0.350
1300	0.142	173	0.197	53.3	7.9	25.4	9.4	0.353
1400	0.150	177	0.192	53.1	8.1	24.7	9.1	0.355
1500	0.156	182	0.190	52.9	8.4	23.8	8.8	0.355
1600	0.158	187	0.192	52.5	8.7	22.9	8.4	0.355
1700	0.160	192	0.195	51.9	9.0	21.7	8.0	0.359
1800	0.161	199	0.200	51.3	9.3	20.6	7.6	0.363

*Age-hardened at 1850°F/2 h/AC + 1450°F/8 h/AC.

Physical properties of HAYNES® 282® Alloy* – Metric units

Temperature (°C)	Specific heat (J/kg K)	Thermal conductivity (W/m K)	Thermal diffusivity (cm^2/s)	Electrical resistivity (μohm cm)	Mean coefficient of thermal expansion (μm/m K)	Dynamic modulus of elasticity (Young's modulus) (GPa)	Dynamic shear modulus (GPa)	Poisson's ratio
RT	436	10.3	0.0288	126.1	–	217	82	0.319
100	463	12.0	0.0315	127.8	12.1	213	80	0.326
200	494	14.1	0.0348	129.9	12.4	209	78	0.335
300	522	16.3	0.0381	131.8	12.8	202	76	0.335
400	544	18.5	0.0413	133.4	13.1	196	73	0.337
500	563	20.5	0.0444	135.0	13.5	190	71	0.341
600	581	22.6	0.0473	136.2	13.7	183	68	0.346
700	594	24.8	0.0509	135.5	14.2	175	65	0.352
800	650	26.1	0.0488	134.5	14.9	166	61	0.355
900	668	27.3	0.0498	132.6	15.9	154	57	0.357
1000	676	28.9	0.0521	129.9	16.9	140	51	0.363

*Age-hardened at 1010°C/2 h/AC + 788°C/8 h/AC.

This page intentionally left blank

Alloy 617 and derivatives

16

J. Klöwer
VDM Metals GmbH, Werdohl, Germany

16.1 Introduction

The history of Alloy 617 dates back to the 1970s when Eiselstein at al. [1] developed Alloy 617 and applied for a patent for a nickel-chromium-cobalt-molybdenum alloy characterized by "good strength up to 2000°F, by excellent resistance to cyclic oxidation, by structural stability and by excellent workability" [1]. Alloy 617 was specifically designed for high-temperature applications up to 1200°C; it derives its high creep strength through both solid solution hardening and carbide precipitation. Since then, Alloy 617 has found wide application in industrial gas turbines (rings and combustion chambers), industrial furnaces, and components in petrochemical plants. Typical application temperatures were 800°C and above.

In the 1980s, Alloy 617 was selected as a suitable alloy for the German high-temperature Reactor (HTR) projects [2–6]. Within the framework of the "PnP" (Prototype Nuclear Process Heat) program, Alloy 617 has been thoroughly investigated. Research work was composed of extensive creep testing, corrosion testing (high-temperature corrosion in air, in helium, and in carbon-containing gases), welding, and fabrication of large components. The general result of these projects was that Alloy 617 is suitable for application in high-temperature reactors. More recently, Alloy 617 was investigated in the US HTR program [7].

About 15 years ago, nickel Alloy 617 (UNS N06617) was selected as a candidate material for the first boilers in the European USC 700°C Boiler projects [8,9] due to its combination of high creep resistance, good workability, and weldability. It also played a role that Alloy 617 was approved for pressure vessel application by VdTÜV [10] and ASME [11]. However, when designing the first USC boilers (700°C boilers) in Germany, it became clear that the maximum allowed 100,000 h creep rupture strength of 95 MPa was not sufficient. To further increase its creep strength and, at the same time, increase the ductility in the temperature range 650–750°C, a modified version of Alloy 617 with narrowly tolerated alloying elements and additions of boron was designed. This alloy is labeled Alloy 617B. It was approved by VdTÜV in the framework of the German activities (MARCKO DE) to qualify materials for the 700°C USC boilers in a single appraisal [12] in 2003 and has been covered by a VdTÜV data sheet since 2013 [13].

Materials for Ultra-Supercritical and Advanced Ultra-Supercritical Power Plants.
http://dx.doi.org/10.1016/B978-0-08-100552-1.00016-6
Copyright © 2017 Elsevier Ltd. All rights reserved.

16.2 Metallurgy of Alloy 617

Alloy 617 is an austenitic nickel alloy with about 55% nickel. Like most nickel-based high-temperature alloys, it derives its creep strength at intermediate and high temperatures from three mechanisms:

1. solid solution strengthening
2. carbide formation (mostly $M_{23}C_6$, some M_6C and Ti(C,N))
3. to a certain degree, also from the formation of ordered, intermetallic phase Ni_3(Al,Ti), which is also called γ′-phase

The strengthening mechanisms and their underlying physical principles (inhibition of dislocation movement and reduction of grain boundary and lattice diffusion) are well understood, and from the extensive literature available on the topic of high-temperature plasticity, only a small selection can be quoted here [14–18]. Likewise the evolution of microstructure in Alloy 617 and its effect on mechanical properties, mainly on creep resistance, has been studied by many investigators, eg, Mankins et al. [19], Kihara et al. [20], Schepp [4], Kirchhöfer [21], Wolf [22], Wu [23,24], and Krishna [25]. More recently, the interaction between precipitation microstructure and the cyclic thermomechanical properties of Alloy 617B, whose knowledge is essential for new-generation flexible power plants, has been extensively investigated by Maier et al. [26–28].

The chemical composition of Alloy 617 according to ASME SB 168 and VdTÜV data sheet 485 is shown in Table 16.1. The alloy contains 22% chromium to provide sufficient oxidation resistance and to form carbides, which strengthen the alloy and prevent abnormal grain growth. Furthermore, chromium is, like molybdenum and cobalt, a strong solid solution–strengthening element.

Aluminum and titanium are added to form γ′-precipitates. While solid solution strengthening and carbide strengthening are predominant at high temperatures, γ′- formation is an important strengthening factor at intermediate temperatures. It can be seen from the time-temperature-precipitation diagram shown in Fig. 16.1 that γ′ dissolves at temperatures above 1000°C. Consequently, it has no strengthening effect above that temperature. Some authors have also reported evidence of other intermetallic phases (eg, CrMo, Ni_2CrMo, μ-phase) [19,24,25]. Their findings are partly contradictory. It seems that, depending on the exact alloy composition and heat treatment, the microstructure of Alloy 617 varies. This stresses the necessity of a small scatter of alloying elements and fixed production routes.

Based on these considerations, a modified version of Alloy 617, labeled Alloy 617B, was developed [29,30]. The composition of Alloy 617B (also named 617mod) is shown in Table 16.1. Compared to standard Alloy 617, it is characterized by a narrower scatter of alloying elements. The lower limits of the solid solution–strengthening elements (Cr, Co) and the precipitation-strengthening elements (Al, Ti) were increased. Also the permitted amount of potentially detrimental or softening elements like Fe, Si, and Mn was decreased.

The main effect of the controlled chemistry lies in the reduction of the scatter of creep strength data. Creep rupture data can indeed exhibit a considerable scatter, as

Table 16.1 **Nominal alloy composition of Alloy 617 (DIN 2.4663) and Alloy 617B (DIN 2.4673)**

	Alloy 617 ASME SB 168	Alloy 617 [10] VdTÜV data sheet 485	Alloy 617B [13] VdTÜV data sheet 573
UNS	N06617	–	N06617
DIN-No	–	2.4663	2.4673
Ni	≥44.5	Balance	Balance
Cr	20.0–24.0	20.0–23.0	21–23
Co	10.0–15.0	10.0–13.0	11–13
Mo	8.0–10.0	8.0–10.0	8–10
Ti	≤0.6	0.20–0.50	0.25–0.5
Al	0.8–1.5	0.60–1.50	0.8–1.3
B	≤0.006	–	0.001–0.005
Fe	≤3	≤2.00	≤1.5
Mn	≤1.0	≤0.70	<0.5
Si	≤1.0	≤0.70	<0.3
C	0.05–0.15	0.050–0.100	0.05–0.08
P	–	≤0.012	<0.012
Cu	≤0.5		–
S	≤0.015	≤0.008	<0.008
V	–	–	≤0.6
Nb	–	–	≤0.6
As	–	≤0.010	–
Bi	–	≤0.010	–

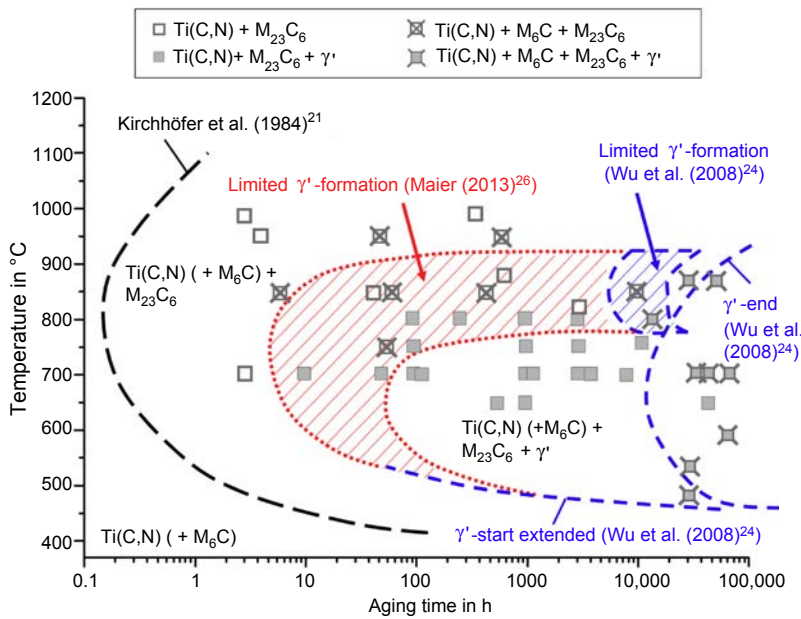


Figure 16.1 Time-temperature-precipitation diagram of Alloy 617 [26].

shown in Fig. 16.2 [31]. There are several causes for the broad scatter: differences in heat treatment, grains sizes, particle distribution, and chemical composition. By narrowing the scatter of alloy composition and increasing the lower limits of the strengthening alloys, the creep rupture data are shifted to the upper limits of the scatter band.

The micrographs of Alloy 617B do not differ from those of Alloy 617. Fig. 16.3 shows typical light-microscope pictures of Alloy 617B in solution-annealed and in a stress relief–annealed condition. A typical grain size lies between 100 and 200 µm. Smaller grains provide generally higher fatigue resistance but lower creep resistance. Some carbide bands and carbonitrides may be visible. After additional stress relief annealing at 980°C (see Section 16.4.3), a larger amount of secondary carbide precipitates is visible along grain boundaries and within the grains. Transmission electron microscopy (TEM) shows that the carbides found at grain boundaries and within the

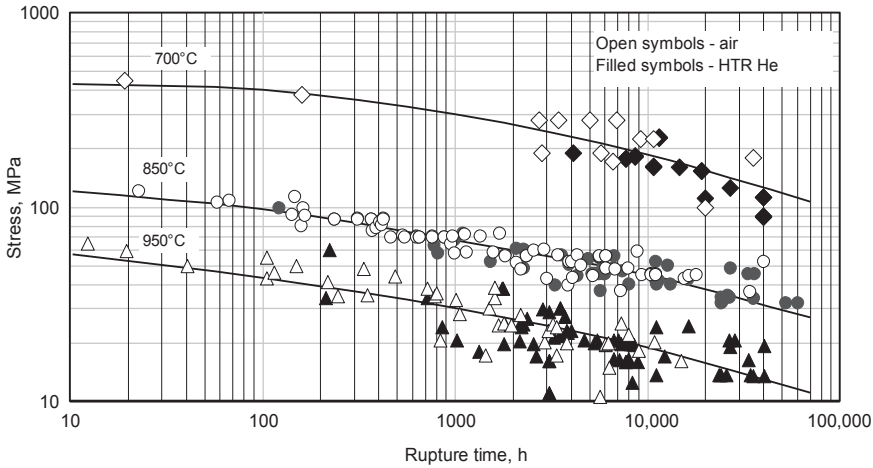


Figure 16.2 Creep rupture strength of Alloy 617 as a function of rupture time showing the scatter of creep data [31].

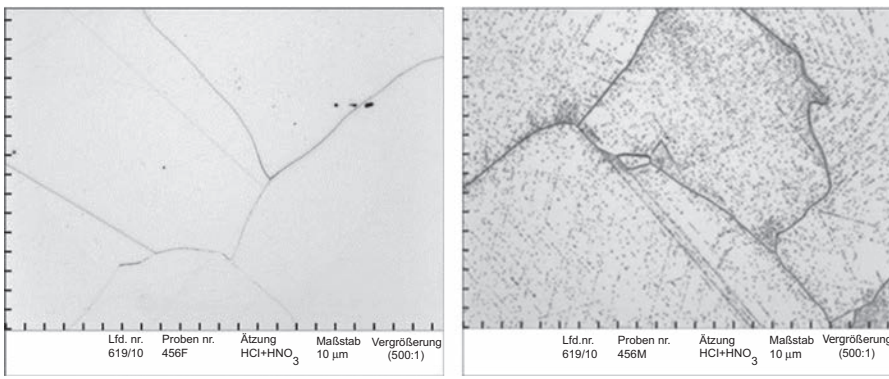


Figure 16.3 Typical micrographs of Alloy 617B after solution annealing (1160°C/20 min, left side) and in stress relief–annealed condition (1160°C + 980°C/3 h, right side).

grains are mainly secondary carbides of the type $Cr_{23}C_6$. To a much lesser degree, primary molybdenum-rich M_6C carbides may also be present. After standard heat treatment (solution annealing followed by stress relief annealing), γ′-precipitates are not detectable. This was confirmed by TEM investigations [26,27].

It could be shown that boron has a strong effect on both strength [32] and ductility [29,32] of Alloy 617. The mechanisms are not fully understood; however, it is known from nickel superalloys that boron segregates at grain boundaries [33]. Recent atom probe analysis in Alloy 617B has shown that boron segregates also at the matrix/carbide interfaces [34] (Fig. 16.4).

Alloy 617B may also contain additions of vanadium and/or niobium to form fine carbides. It was found that such carbides further enhance the ductility of Alloy 617B by preventing the formation of carbide banding and that they reduce the susceptibility to so-called relaxation cracking (see Section 16.4.3). Alloy 617B with additions of niobium and/or vanadium is labeled Alloy 617occ (optimized chemical composition) [29,35].

16.3 Properties of Alloy 617 and derivatives

16.3.1 Mechanical properties

Table 16.2 shows typical mechanical properties of Alloy 617. The material shows high strength and good ductility over the entire temperature range. No significant difference between Alloy 617 and its derivatives 617B, 617 mod, and 617occ can be found.

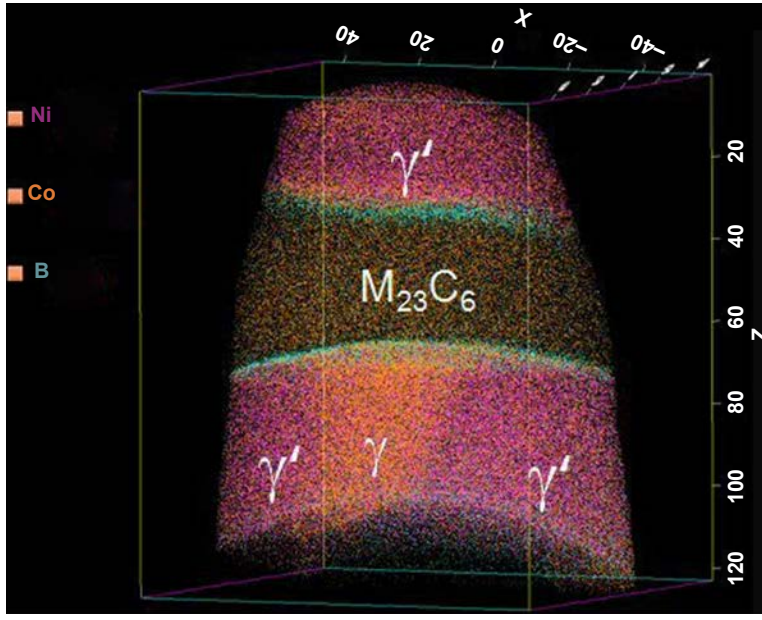


Figure 16.4 Atom probe picture of Alloy 617B, showing boron enrichment at the phase boundaries between carbides, γ′, and fcc matrix [34].
Courtesy D. Raabe, Max-Planck Institut für Eisenforschung, Düsseldorf.

Table 16.2 Typical mechanical properties of Alloy 617B condition: stress relief annealed; after refs [10,13,36,37]

Temperature	Yield strength (YS)	Ultimate tensile strength (UTS)	Fracture elongation (El)*	Reduction of area (RoA)	Young's modulus €
°C	MPa	MPa	%	%	GPa
20	300	680–950	30*/35**	43	212
100	270	650			206
200	230	620			200
300	220	600			194
400	210	570	49	44	188
500	200	540			181
600	190	510	67	47	173
650	187	460	96	55	
700	185	400	113	69	166
750	180	340	111	82	
800			136	88	157
900				92	149
1000					139
1100					129

*Transverse, **longitudinal direction.

Typical Charpy V-notch values are above 100 J/cm [2] in transversal and above 150 J/cm [2] in longitudinal direction.

After 1-year exposure at 700°C, yield strength and tensile strength are considerably increased, as can be seen from Table 16.3, while fracture elongation and reduction of area are not affected. The strengthening effect can easily be explained by the formation of small γ′ particles. This mechanism is known from other nickel-based superalloys, and it is confirmed by TEM investigations. Fig. 16.5 shows a TEM bright field micrograph after 1-year exposure at 700°C, revealing beside $M_{23}C_6$ (carbides along grain boundaries and within the grain) particles of $Ni_3(Al,Ti)$ (γ′) with an average size of 50 nm.

16.3.2 Thermophysical and electrical properties

Typical thermophysical and electrical properties are summarized in Table 16.4. Thermophysical and electrical properties fall well within the range that is typical for austenitic stainless steels and nickel alloys. Both thermal conductivity and coefficient of thermal expansion are lower than the corresponding values in ferritic boiler steels.

The same thermophysical data apply for Alloy 617 and 617B. However, since the alloy composition of Alloy 617B is more narrowly tolerated, the scatter of thermophysical properties in Alloy 617B can be expected to be lower.

The melting range of Alloy 617 is 1330–1380°C; its density is 8.4 g/cm^3.

Table 16.3 Mechanical properties after 1-year exposure (measured values) [26,38]

Temperature	Yield strength (YS)	Tensile strength (UTS)	Fracture elongation (El)A	Fracture toughness (RoA)
°C	MPa	MPa	%	%
20	439	902	36.0	33.0
400	377	765	41.4	40.4
600	362	768	42.4	35.5
650	357	701	62.8	50.2
700	348	585	67.3	59.5
750	333	463	65.5	74.5
800	250	317	117	84.7
900	151	159	105.9	92.0

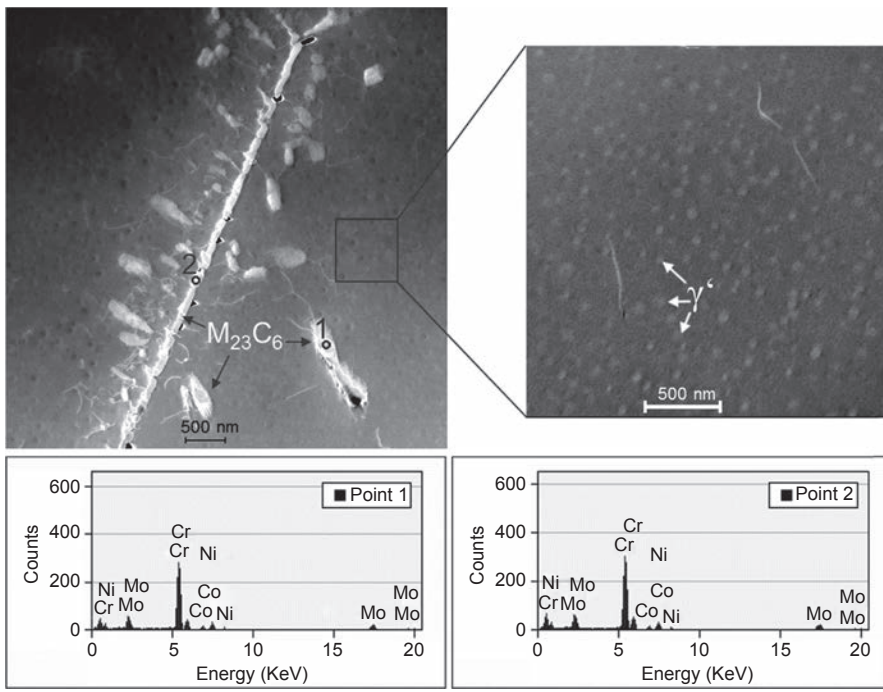


Figure 16.5 STEM-HAADF (high-angle angular dark field picture) of the microstructure after 1-year exposure [26]. Left side: chromium carbides ($M_{23}C_6$) along grain boundaries; right side: γ′ particles.

Table 16.4 Typical thermophysical properties of Alloy 617B: thermal conductivity, specific heat, coefficient of thermal expansion, and electrical resistance of Alloy 617B as a function of temperature [36,37]

Temperature	Thermal conductivity	Specific heat	Coefficient of thermal expansion between 20°C and *T*	Electrical resistance
°C	W/m K	J/kg K	10^{-6}/K	μΩ cm
20	11.7	–	–	122
100	13.1	474	12.55	125
200	14.9	494	13.13	126
300	16.7	511	13.43	127
400	18.7	528	13.72	128
500	20.7	544	14.09	129
600	23.5	584	14.62	131
700	27.7	663	15.33	133
800	27.0	658	16.02	134
900	27.2	662	16.60	135
1000	28.5	664	17.09	138
1100	30.7	681	17.64	141
1200	32.3	701	18.22	141

16.3.3 Creep data

The creep behavior of Alloy 617 and derivatives was investigated in a couple of studies [39–43]. The latest assessment of the creep rupture behavior of standard Alloy 617 has been made in 2005 by the European Creep Collaborative Committee (ECCC) [39] and in 2010 by Schubert et al. [40]. The creep rupture behavior of the new Alloy 617B was assessed during the Marcko-DE2 project in 2004, revealing a 100,000 h creep rupture strength of 100 MPa and leading to the VdTÜV single appraisal [12]. The 100,000 h 1% creep strain limits (Rp_1) and the creep rupture strengths (Rm) as calculated for Alloy 617 and Alloy 617B are listed in Table 16.5. The results clearly show that the creep rupture strength of Alloy 617B is superior to that of the classical Alloy 617 as listed in VdTÜV data sheet and ECCC data sheet [43].

More recent creep data assessments were carried out by Krein et al. [41] and Knezevic et al. [44]. Krein's evaluation was based on creep test results from 10 heats and several product forms (sheet, tube, pipe, bar). The results are included in Fig. 16.6. At 700°C, the 100,000 h creep rupture strength of Alloy 617B is 130 MPa (compared to 119 MPa listed in the Alloy 617B VdTÜV data sheet and 95 MPa listed in the 617 VdTÜV data sheet). At temperatures above 750°C, the beneficial effect of the controlled chemistry is negligible, as can be seen in Fig. 16.6.

The intersection point between the curves 0.2 yield strength and 100,000 h creep rupture strength as a function of temperature is at about 670°C [36]. Therefore, at a design temperature above 670°C, time-dependent mechanisms (creep) become the relevant deformation mechanism [36].

Table 16.5 100,000 h creep data at 700°C of Alloy 617 (UNS N06617) and Alloy 617B [10,13,42]

Temperature	Alloy 617	Alloy 617 (2.4663)	Alloy 617 (2.4663)	Alloy 617B (2.4673)
°C	Allowable stress according ASME Part II–D in MPa	1% creep strain limit (10^5 h) VdTÜV data sheet 485 in MPa	10^5 h creep rupture strength VdTÜV data sheet 485 in MPa	10^5 h creep rupture strength VdTÜV data sheet 573 in MPa
600			190	265
650		97	125	187
700	81	66	95	119
750	50.4	44	65	69
800	31.3	28	43	*43*
850	19.4	18	27	*27*
900	12.3	10	16	*16*
950		4	8.5	*8.5*
1000		1	(4.5)	*(4.5)*

For Alloy 617B at temperatures above 750°C, the values for Alloy 617 apply.

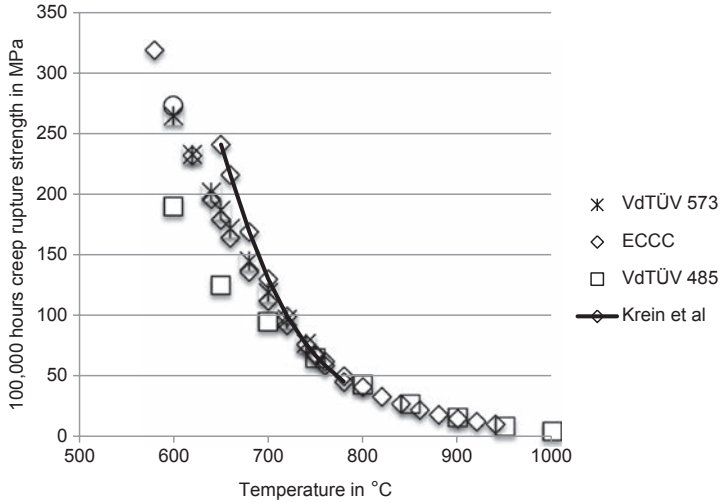


Figure 16.6 Creep rupture strength of Alloy 617B in the temperature range from 580 to 900°C [10,13,41,44].

16.3.4 Fatigue

The fatigue behavior of Alloy 617B was extensively tested by Maier et al. [26–28, 45–48]. They investigated Alloy 617B in solution-annealed condition (1175°C), in stress relief–annealed condition (1175 + 980°C/3 h), and in an aged condition (1175 + 980°C/3 h + 700°C/1 year) and compared their results to data from literature. Tests included complex low-cycle fatigue tests (CLCF tests) at test temperatures between room temperature and 900°C as well as creep fatigue and thermomechanical fatigue tests (TMF tests). Their results show that the lifetime of Alloy 617B at 700°C is not affected either by stress relief annealing at 980°C nor by 1-year exposure at 700°C [26].

Fig. 16.7 shows the damage parameter $d_n D_{TMF}$ as a function of the number of cycles to failure Nf for all tests with solution-annealed, stress relief–annealed, and aged condition [26]. All but one experiment can be described within a scatter band of factor two. Thus, the $d_n D_{TMF}$ parameter is well suitable for lifetime assessment of (power plant) components under thermocyclic loading conditions.

Maier could also show that a larger amount of very large grains (500 µm and above) results in reduced resistance to low-cycle fatigue [38].

16.3.5 High-temperature corrosion

Environmental degradation of materials through corrosive gases, ashes, and salts is an important issue in coal-fired power plants. As a general rule, nickel alloys are more resistant to high-temperature corrosion than ferritic and stainless steels.

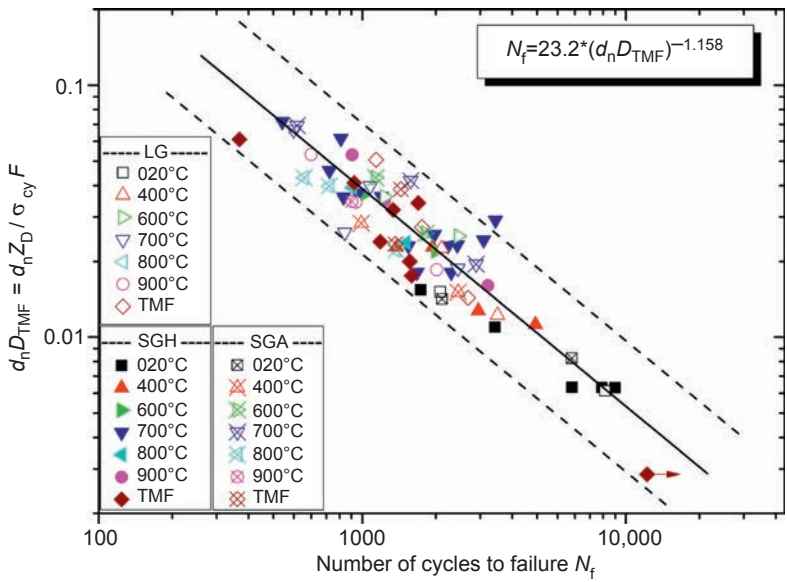


Figure 16.7 Fatigue diagram: damage parameter $d_n D_{TMF}$ as a function of the number of cycles Nf to failure for tests with solution-annealed (LG), stress relief–annealed (980°C, 3 h: SGH), and aged Alloy 617B (700°C, 1 year: SGA) [26].

The simplest case of high-temperature corrosion is high-temperature oxidation in air or steam. Here, the corrosion attack is determined solely by the growth rate and the adherence of the oxide layer. Alloy 617 is resistant in air up to at least 1100°C; it derives its resistance to oxidation and high-temperature corrosion from the formation of a dense, stable chromium oxide layer (Cr_2O_3), which protects the subjacent material against oxygen pickup and internal oxidation. Above 1100°C, evaporation of chromium oxide will become important. At boiler temperatures up to 800°C, no significant oxidation is to be expected [49].

Protective oxide scales are also impervious to carbon. However, if the oxygen partial pressure of the environment is below the value needed for chromium oxide formation, carbon pickup will occur. How much carbon penetrates into the material depends on the temperature, the gas composition, and the alloy composition. Alloy 617 has, compared to other nickel high-temperature alloys, a very high resistance to carbon pickup [50,51].

Unlike in carbon-bearing environments, an oxide layer does not give complete protection in the presence of sulfur [52]. However, in oxidizing/sulfidizing environments, Alloy 617 shows good resistance to SO_2-containing gases.

A specific corrosion attack is corrosion under sulfate-containing deposits in coal-fired power plants and waste incineration plants. This so-called "hot corrosion" was investigated in particular with reference to industrial gas turbines, and all nickel alloys, cobalt alloys, and steels are prone to it [53]. Corrosion starts with the decomposition of sulfate into basic Na_2O and acidic SO_3. As a following step, basic or acidic dissolution of the metal surface occurs according to the equations:

$$Cr_2O_3 + 2SO_3 \Leftrightarrow 2CrSO_4 + \tfrac{1}{2}O_2 \quad \text{(acidic dissolution) or}$$

$$Cr_2O_3 + Na_2O \Leftrightarrow 2CrO_2^- + 2Na^+ \quad \text{(basic dissolution).}$$

In pure sulfate, acidic dissolution dominates at temperatures below 800°C.

The aggressivity of corrosion attack depends sensitively on the temperature, the composition of the deposit, and the oxygen and chlorine partial pressure of the environment. As a general rule, a high chromium concentration is beneficial; high molybdenum concentrations may increase the corrosion rate [53–56]. The corrosion rate is difficult to predict, and in most cases, only field tests can provide reliable information about the actual behavior under service conditions. Under very severe conditions (high sulfate concentrations), cladding with a high-chromium alloy (NiCr 50, Alloy 33) [57] may be an option.

16.4 Fabrication, heat treatment, and welding of Alloy 617 and derivatives

16.4.1 Fabrication

Alloy 617/617B is typically produced by open melting in an electric arc furnace or an induction furnace. This is followed by vacuum treatment using a vacuum oxygen

decarburization followed by electro-slag remelting or vacuum arc remelting. Melting, casting, and remelting procedures are those typical for nickel superalloys [14,58]. For very high requirements concerning homogeneity and cleanliness of the material, melting in a vacuum induction furnace is an option. For boiler applications, vacuum induction melting is typically specified.

Hot working of the ingots is done by forging or hot rolling in the temperature range of 950–1200°C. Because of the high strength of Alloy 617/617B even at very high temperatures, high press and rolling forces are needed. Depending on the following production steps (hot or cold working), the hot-working ratio should be between two and four. If the final product is a hot-worked product, the hot-working ratio should at least be three to ensure a homogeneous microstructure over the entire cross-section.

Alloy 617 can easily be cold worked using standard cold-working processes, eg, cold rolling, wire drawing, bar drawing, or pilgering. Again, here, high cold-working forces are required, and intermediate annealing may be necessary. If the cold-working ratio is more than 10%, a final solution annealing is recommended.

16.4.2 Component manufacturing

In the framework of the various European research projects on materials for 700°C power plants, all relevant components have been produced. Generally, component production routes are similar to those for manufacturing components in stainless steel. However, the high flow stresses and the small hot-working temperature range of Alloy 617 have to be taken into account, limiting the number of potential component manufacturers to those with experiences in nickel alloys.

Fig. 16.8 shows some typical components: a superheater part, a header, and a forged component. Thin-walled tubes for membrane walls, superheaters, and reheaters with typical dimensions (eg, $\varnothing_A$ 38 mm × WT 8.8 mm, $\varnothing_A$ 33.7 mm × WT 5 mm, $\varnothing_A$ 60.3 mm × WT 10 mm, $\varnothing_A$ 114.3 mm × WT 20 mm, whereas $\varnothing_A$ is the outer diameter and WT is the tube wall thickness) were produced by Salzgitter Mannesmann Stainless Tubes using hot extrusion followed by cold pilgering [59,60].

Finned tubes in Alloy 617/617B have not yet been produced. Boiler membrane walls can be made by longitudinally welding seamless boiler to strips lying in between two boiler tubes.

For the manufacturing of pipes and thick-walled components in 700°C power plants, several production methods were tested. Pipes with an outer diameter of 420 mm and a wall thickness of 35 mm, an outer diameter of 400 mm and a wall thickness of 50 mm, an outer diameter of 460 mm and a wall thickness of 80 mm, and an outer diameter of 500 mm and a wall thickness of 30 mm were produced by a combined piercing/drawing ("Ehrhardt") process. Pipes with outer diameters up to 350 mm and a wall thickness up to 72.5 mm were produced by piercing and hot pilgering for the tests loops HWT II (Mannheim, Germany) and ENCIO (Venice, Italy). All pipes, produced by Vallourec, Germany, fulfilled the requirements for pressure vessel approval [61–63].

Valves and extremely thick-walled components were made from forgings followed by deep-hole boring. Also, plates in Alloy 617B with thicknesses from 5 to 25 mm were produced for the structural steelwork in a 700° power plant.

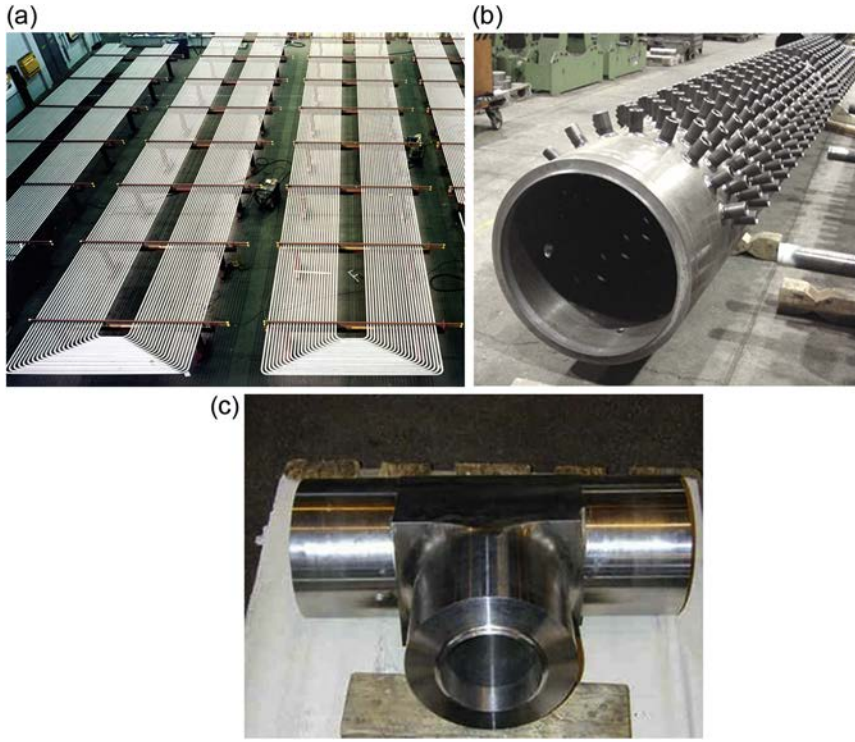


Figure 16.8 Typical components in Alloy 617B: (a) superheater tubes, (b) header, and (c) forged component.

In a Joint Industry Project headed by the German FDBR (Fachverband Dampfkessel, Behälter, und Rohrleitungsbau e.V.), a longitudinally welded pipe in Alloy 617 was produced [64]. The tube with a final outer diameter of 542 mm and a wall thickness of 31.5 mm and a length of 4500 mm was produced by bending and subsequent GTAW (gas tungsten arc welding) welding under protective gas (95% argon, 5%H_2) using 617B filler metal. The welding procedure is described in Ref. [64]. Mechanical tests including fracture mechanics and creep test carried out on the welded joint show that the determined mechanical properties correspond to the mechanical properties of the base metal.

16.4.3 Heat treatment

Solution annealing may be carried out in the temperature range 1140–1200°C. However, high solution-annealing temperatures above 1180°C should be avoided because of the risk of grain coarsening.

A stress relief annealing for large, welded components in Alloy 617 at 980°C for 3 h is highly recommended. Like most high-strength alloys, Alloy 617 is susceptible to so-called "stress relaxation cracking" at operating temperatures between 650 and 750°C. This phenomenon has been largely investigated on Alloy 800H (UNS N08810) [65].

While the mechanism is still not clear, it could be shown for many alloys that stress relief annealing (also called "relaxation annealing" or "soft annealing") prevents cracking.

This phenomenon was investigated thoroughly in the frame of the German 700°C power plant programs, when cracks were detected in the injection cooler in the test circuit in Scholven power plant after relatively short service times [66]. To investigate the sensitivity to this type of cracking, tensile tests at a constant and slow strain rate of 10^{-5} to $10^{-6}\,s^{-1}$ (slow strain rate tensile test (SSRT) or constant strain rate tests (CSR)) were found to be representative.

In a recent study, SSRT tests with a strain rate of $10^{-6}\,s^{-1}$ in comparison to standard tensile tests at 700°C were carried out for a variety of heats in solution-annealed and stress relief–annealed condition [67,68]. The aim was to investigate the effect of boron and heat treatment on the susceptibility of Alloy 617B to "stress relaxation cracking" Fig. 16.9 shows the effect of boron and heat treatment on the yield strength of Alloy

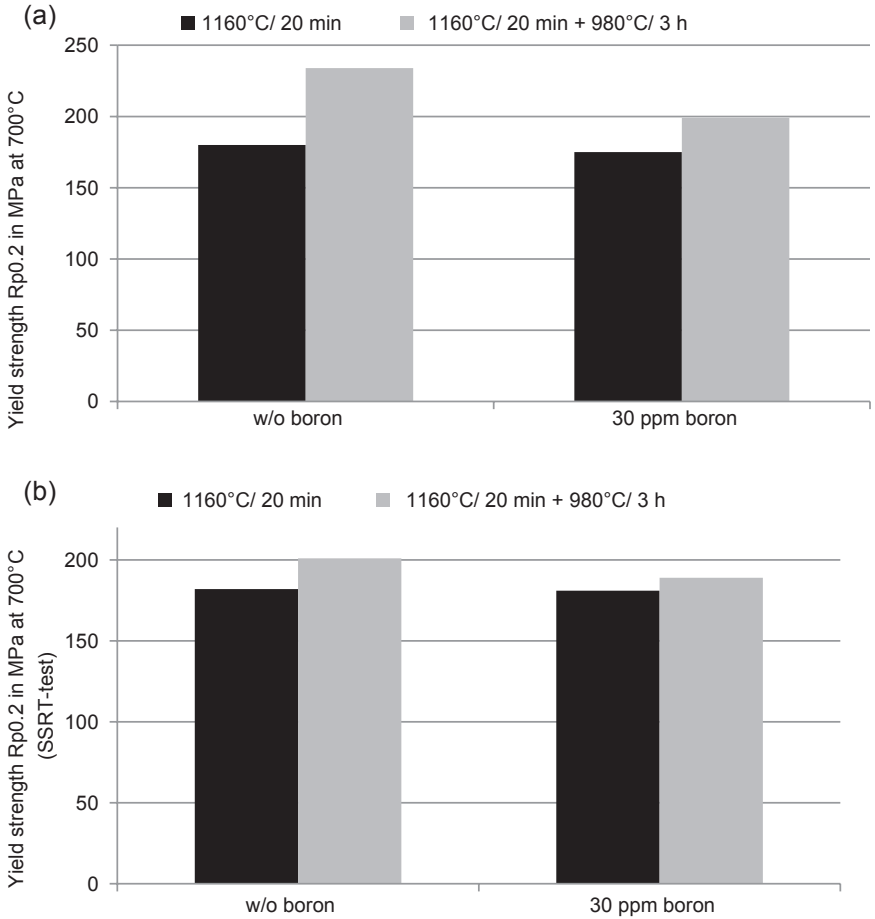


Figure 16.9 Effect of alloy composition and heat treatment on the yield strength of Alloy 617 modifications at 700°C: (a) standard tensile test at 700°C, (b) slow strain rate tensile test (SSRT test) at $10^{-6}\,s^{-1}$.

617 at 700°C measured in a standard tensile test (Fig. 16.9(a)) and a SSRT at $10^{-6}\,s^{-1}$ (Fig. 16.9(b)). It can be seen that the effect of boron on the yield strength in the standard tensile as well as in the SSRT test at 700°C is small.

Fig. 16.10 shows the effect of boron and heat treatment on the reduction of area at 700°C measured in a standard tensile test (Fig. 16.10(a)) and a SSRT at $10^{-6}\,s^{-1}$ (Fig. 16.10(b)). While the impact of stress relief annealing on the reduction of area in a standard tensile test is insignificant, stress relief annealing at 980°C had a tremendous effect on the ductility under creep conditions (relaxation behavior), as can be seen in Fig. 16.10(b). The beneficial effect of stress relief annealing is more pronounced in the boron-alloyed modification; in boron-free Alloy 617, the reduction of area is increased from a value as low as 10% to more than 30%; in the boron-alloyed modifications, it is increased from about 20% to more than 50%.

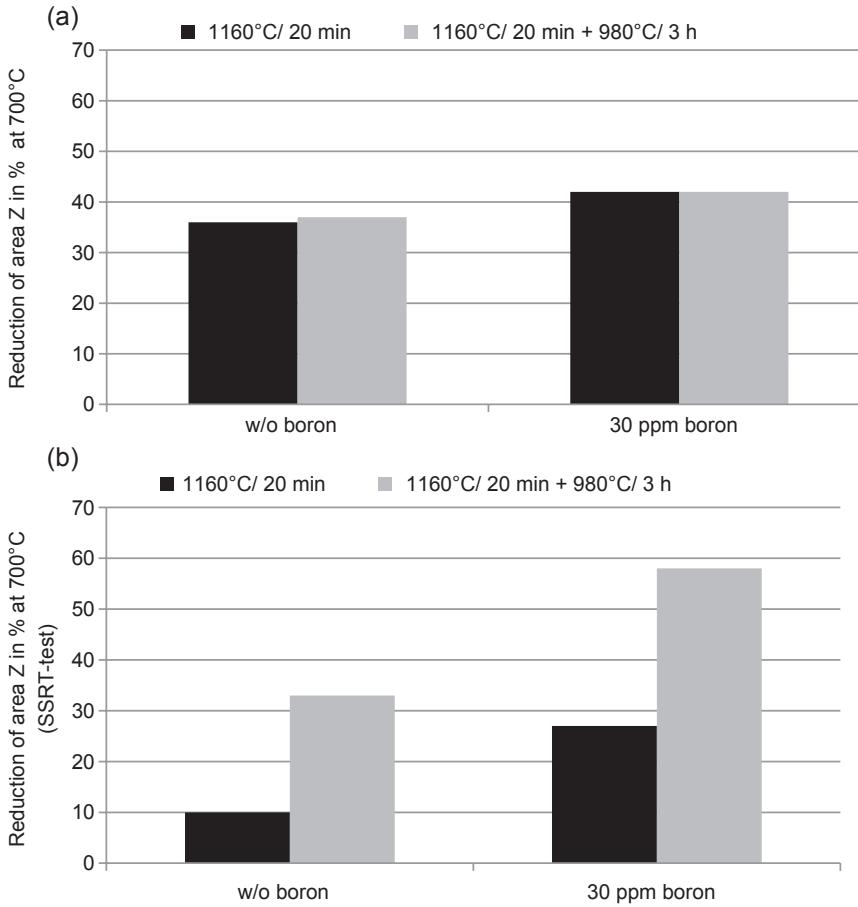


Figure 16.10 Effect of alloy composition and heat treatment on the reduction of area of Alloy 617 modifications at 700°C: (a) standard tensile test at 700°C, (b) slow strain rate tensile test (SSRT test) at $10^{-6}\,s^{-1}$.

At the same time, the fracture mode changes from brittle intercrystalline fracture in boron-free Alloy 617 to ductile transgranular fracture in boron-alloyed 617B. Fig. 16.11 shows typical SEM pictures of fractures after SSRT testing at 700°C.

This beneficial effect of stress relief annealing is in agreement with the results of van Wortel, who found that the ductility in a three-point bending test increased when an additional heat treatment at 980°C was applied [69]. It is assumed, that the major effect of the heat treatment is relief of residual stresses resulting from cold work, welding, or other treatments that induce residual stresses [28,67,68,70]. A second effect of the 980°C heat treatment may be the development of a favorable carbide distribution [26]. Stress corrosion cracking (so-called SAGBO: stress-assisted grain boundary oxidation) does not play any role, as an earlier comparison of SSRT tests in vacuum and in air has demonstrated [29].

Internal stresses caused by carbide precipitates may play an additional role. Maile et al. [70] could show that the precipitations in Alloy 617 are correlated with a contraction of volume, which leads to additional internal stresses. By carrying out a stress relief annealing at 980°C, the volume contraction is prevented since most carbides will be precipitated prior to service [70]. Indeed, both light microscopy and TEM investigations show an increased number of carbides after annealing at 980°C (see Fig. 16.3). In the case of thick components, slow cooling from solution-annealing temperature to room temperature through the intermediate temperature range has a similar effect as the stress relief annealing [67,68].

Boron clearly has a beneficial effect on the ductility. Boron-alloyed Alloy 617B is much less prone to stress relaxation cracking. Following is the assessment given in the literature [71,72]:

1. reduction of area: $Z < 5\%$ = extremely sensitive
2. reduction of area: Z of 5–10% = strongly sensitive
3. reduction of area: Z of 10–20% = slightly sensitive
4. reduction of area: $Z > 20\%$ = not significantly sensitive

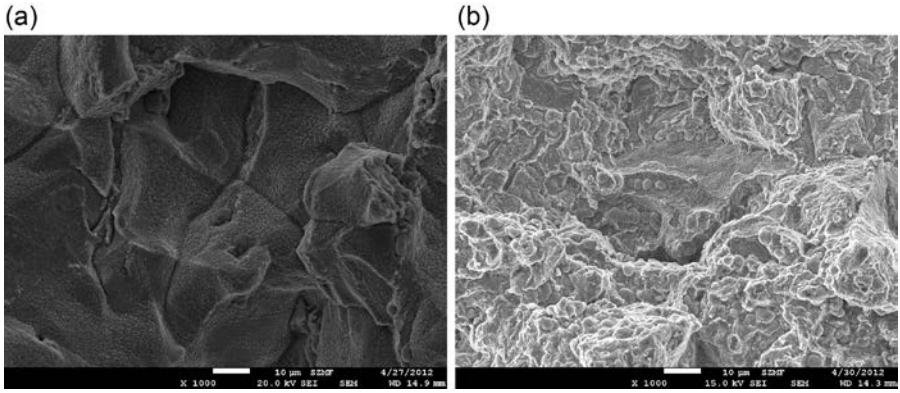


Figure 16.11 SEM micrographs showing the fracture mode of Alloy 617/617B after slow strain rate tensile tests ($10^{-6}\,s^{-1}$) at 700°C: (a) brittle intergranular fracture of Alloy 617 without boron, annealed 1160°C, water quenched; (b) ductile transgranular fracture of Alloy 617B with boron, annealed 1160°C, furnace cooled.

Boron-alloyed 617B is not sensitive to “stress relaxation cracking.e However, it should be noted that after cold-working, welding, or surface treatment, the susceptibility to stress relaxation cracking may become important again. Under such conditions, the necessity of a stress relief annealing must be carefully evaluated.

Stress relief annealing prior to service does not affect the creep behavior of Alloy 617B, as can be seen from Fig. 16.12. All samples of the stress-relieved components (tube, pipe, forgings) fall well within the scatter band of Alloy 617B creep data.

16.4.4 Welding

Generally, Alloy 617/617B can be welded by all standard welding methods; GTAW or plasma arc welding are advantageous to gas metal arc welding. The filler metal should be matching filler metal. For thicker components and high safety requirements, the best results are achieved by using narrow-gap GTAW [37,64,73,74]. SAW (submerged-arc welding) is not recommended. This is because of the risk of aluminum evaporation in the weldment, which may lead to compositional changes and a decrease of creep rupture strength. For the post-welding heat treatment, the reader is referred to Section 16.4.3.

Like all high-temperature nickel alloys, Alloy 617/617B is prone to hot cracking if improperly welded [75–77]. Basically, there are three types of hot cracking:

Type A: solidification cracks in the weldment
Type B: liquation cracks in the heat-affected zone close to the weldment
Type C: ductility dip cracks (DDC) in the heat-affected zone

The differentiation between type B and type C can be difficult; however, most authors agree that cracks in Alloy 617 and 617B are Type C cracks (DDCs). To avoid hot cracking, the energy input should not exceed 7.5 kJ/cm, and the interpass temperature should not exceed 120°C. If properly welded, Alloy 617 does not show hot cracking. However, small fissures (grain boundary separations) in the heat-affected zone may be found. These do not have a negative impact on mechanical properties [76].

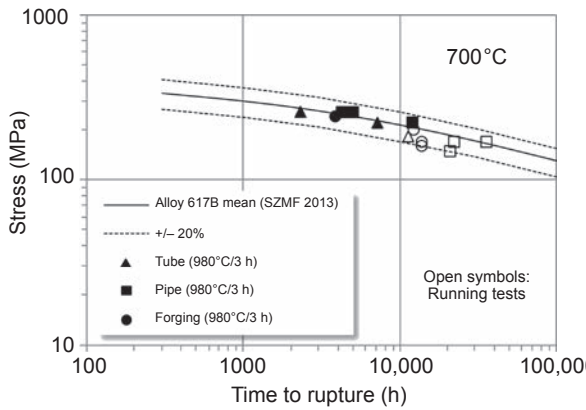


Figure 16.12 Effect of stress relief annealing on the creep behavior of Alloy 617B [39].

The effect of alloy composition and heat treatment on the susceptibility of Alloy 617 to hot cracking was investigated by Zinke et al. [67,68,77]. They used the method of so-called PVR testing. The deformation crack test (PVR test) is one out of three test methods listed in the ISO/TR 17641-3:2005. In this test a flat tensile specimen is welded while a linearly increasing tension with a maximum tension speed of v_{max} is applied. The point on the PVR specimen where the initial hot crack occurs corresponds to the critical tension speed v_{cr}, which can be used as a criterion for hot cracking resistance. The higher the critical speed, the higher the resistance to hot cracking. After welding, all specimens showed liquation cracks and/or DDC; solidification cracks in the weldment were not observed.

A comparison of the heat treatment conditions showed that the solution-annealed specimens exhibited a greater resistance to hot cracks than the stress relief–annealed samples.

A negative effect of used boron concentrations on the hot crack resistance was not found, as long as the boron concentration did not exceed 50 ppm.

16.5 Experiences from field testing

Alloy 617B has been tested in a variety of laboratory and field tests since 1990 [9,66,78–92]. Projects comprised such focusing on the selection of materials (Marcko DE) and/or on investigation and qualification (COORETEC) [9,83], leading to the selection of Alloy 617B for the 700°C technology.

More than 100 tons of Alloy 617B were tested in a 700°C loop in the coal-fired power plant in Scholven, Gelsenkirchen, [66] within the research program COMTES 700 (2004–2011). The tested components included membrane walls, injection coolers, turbine valves, and high-pressure pipes. After one up to three years after test start, the larger components (turbine, valves, injection coolers, and high-pressure pipes) showed cracks in the heat-affected zone. In all cases the "leakage before fracture" criterion was fulfilled. The cracks were found to be caused by so-called "relaxation cracking" due to high residual stresses in the heat-affected zone. The lessons learned from this project was that a stress relief annealing after welding of large components is inevitable (see Section 16.4.3). During this project, methods to repair cracked components were also developed.

Several other test rigs have been constructed in Europe since 2004; the most recent is that of Grosskraftwerk Mannheim, Germany [85–92] (Project HWT II: Hochtemperatur-Werkstoff-Teststrecke II–high-temperature materials test rig II). The components of the test rig were exposed to cyclic loading to simulate the conditions typical for a power plant after the German energy transition "Energiewende." In this test rig the target of 2500 cycles (approximately 9900 h at temperatures above 700°C) was achieved, before a shutdown was necessary due to damage in a bypass valve. The damage was considered to be a consequence of the extreme cyclic loading conditions. The findings of HWT II will allow the construction of safer and more reliable future 700°C power plants. A third test loop, HWT III, is currently in projection. Test rigs using Alloy 617B are also in planning or in construction in India, China, Korea, and Japan.

For further reading about the European USC projects the reader is referred to the corresponding chapters in this book.

16.6 Conclusions/outlook

A modified Alloy 617B (DIN 2.4673) has been tailored for application in 700°C USC boilers. Compared to Alloy 617, it has a 25% higher creep strength at 700°C and higher ductility under creep conditions.

Results from slow strain rate tests simulating creep conditions show that the susceptibility to cracking can be reduced significantly by a heat treatment at 980°C for 3 h after welding and cold working. Boron increases the beneficial effect of this stress relief annealing.

If the peculiarities of this alloy are respected, components for 700°C boilers can easily be produced from modified UNS N06617 (DIN 2.4673) and used for 700°C boilers in USC power plants.

For even higher requirements concerning creep strength, Alloy C-263 may be an option. This alloy will be described in Chapter 17.

Acknowledgments

Many persons have contributed to the work described in this chapter. The author wishes to thank especially Dr. Juliane Mentz and Dr. Michael Spiegel from Salzgitter Mannesmann Research Institute, Dr. Martin Wolf and Dr. Nicole de Boer from VDM Metals, Dr. Manuela Zinke from the University of Magdeburg, Dr. Gerhard Maier from Fraunhofer Institute for Mechanics of Materials, Freiburg, Patrik Schraven from Salzgitter Mannesmann Stainless Tubes, and Vida Knezevic from Vallourec for their contribution to this work. Special thanks are also due to Mr. Ralf-Udo Husemann (Hitachi Power Europe), Dr. Mirko Bader and Mr. Helmut Tschaffon (EON), Dr. Ralf Mohrmann (RWE), Mr. K. Metzger (Großkraftwerk Mannheim), and Dr. T. Gräb (Bilfinger) for many fruitful discussions on Alloy 617 and 617B.

References

[1] U.S. Patent 3,859,060.
[2] H. Kirchhofer, J. Rottmann, F. Schubert, H. Nickel, Berichte der KFA Jülich No. 1903, 1989.
[3] Y. Pan, K.H. Lang, D. Löhe, E. Macherauch, Cyclic deformation and precipitation behaviour of NiCr22Co12Mo9 during thermal fatigue, Physica Status Solidi (A) 138 (1993) 133–145.
[4] G.P.P. Schepp, Mikrostruktur und Kriechverhalten der Nickelbasislegierung Inconel 617 im Temperaturbereich zwischen 850°C und 950°C unter Berücksichtigung aufgekohlter Gefügezustände (Ph.D. thesis), 1983, Erlangen.
[5] G. Merckling, K.H. Lang, E. Macherauch, Das Ermüdungsverhalten der nickelbasis-superlegierung NiCr22Co12Mo9 im temperaturbereich 295K – 1473K, Zeitschrift für Metallkunde 84 (1993) 844–853.

[6] F. Schubert, H.J. Penkalla, G. Ullrich, in: Proc. Conf. High Temperature Metallic Materials for Application in Gas-Cooled Reactors, Wien, 1981.
[7] T.C. Totemeier, H. Tian, Creep-fatigue-environment interactions in Inconel 617, Materials Science and Engineering: A 468–470 (2007) 81–87.
[8] Final report, Project No. A130, AVIF, Contract No. 0327062, BMWA (MARCKO-DE2), 2005.
[9] R. Blum, R.W. Vanstone, Materials development for boilers and steam turbines operating at 700°C, in Materials for Advanced Power Engineering, in: Proceedings of the 8th Liege Conference, 2006, pp. 41–60.
[10] VdTÜV-Werkstoffblatt (VdTÜV Material Data Sheet) 485 Hochwarmfeste Nickelbasislegierung NiCr23Co12Mo, ed. 06/2013.
[11] ASME International: Standard Specifications B-166/B-168, ed. 2010.
[12] T.Ü.V. Rheinland, TÜV Einzelgutachten (Single Material Appraisal) from 08.07.2003.
[13] VdT.Ü.V. Werkstoffblatt (VdTÜV Material Data Sheet) 583: Creep Resistant Nickel Alloy NiCr 23Co12Mo, ed. 09/2013.
[14] N.S. Stoloff, Fundamentals of strengthening, in: C.T. Sims, W.C. Hagel (Eds.), Superalloys II, John Wiley & Sons, New York, 1972, pp. 79–117.
[15] B. Ilschner, Hochtemperaturplastizität, Springer Verlag, Heidelberg, 1973.
[16] H.J. Frost, M.F. Ashby, Deformation Mechanism Maps, Pergamon Verlag, Oxford, 1982.
[17] H. Riedel, Fracture at High Temperatures, Springer Verlag, Berlin, 1987.
[18] R.W. Cahn, P. Haasen, E.J. Kramer (Eds.), Material Science and technology, H. Mughrabi (Ed.), Plastic Deformation and Fracture, vol. 6, VCH, Weinheim, 1993.
[19] W.L. Mankins, J.C. Hosier, T.H. Bassford, Microstructure and phase stability of Inconel alloy 617, Metallurgical and Materials Transactions A 5 (1974) 2579–2590.
[20] S. Kihara, J.B. Newkirk, A. Ohtomo, Y. Saiga, Morphological changes of carbides during creep, Metallurgical and Materials Transactions A 11 (1980) 1019–1031.
[21] H. Kirchhöfer, F. Schubert, H. Nickel, Precipitation behaviour of Ni-Cr-22Fe-18Mo (Hastelloy X) and Ni-Cr-22 Co-12 Mo (Inconel 617) after isothermal aging, Nuclear Technology 66 (July 1984) 139–148.
[22] H. Wolf, Kriechen der Legierungen NiCr22Co12Mo und 10CrMo 9 10 bei konstanter und zyklischer Beanspruchung (Ph.D. thesis), University of Erlangen, Erlangen, 1990.
[23] Q. Wu, Microstructural Evolution in Advanced Boiler Materials for Ultra Supercritical Coal Power Plants (Ph.D. thesis), University of Cincinnati, July 2006.
[24] Q. Wu, H. Song, R.W. Swindemann, J.P. Shingldecker, V.K. Vasudevan, Microstructure of long-term aged IN 617 Ni base superalloy, Metallurgical and Materials Transactions A 39 (2008) 2569–2585.
[25] R. Krishna, Microstructural Investigations of Alloys Used for Power Generation Industries (Ph.D. thesis), University of Leicester, Leister, 2010.
[26] G. Maier, Mikrostruktur, Verformung und Lebensdauer der Legierung Alloy 617B – Experimente, Modelle und Bauteilvorhersagen (Ph.D. thesis), Karlsruher Institut für Technologie, Shaker Verlag GmbH, Germany, 2013.
[27] G. Maier, C. Somsen, J. Klöwer, R. Mohrmann, Wechselwirkung zwischen Mikrostruktur und Verformung der legierung Alloy 617B – Experimente und Modelle, in: 36. Vortragsveranstaltung der AG Warmfeste Stähle und Hochtemperaturwerkstoffe, Stahlinstitut Vdeh, Düsseldorf, November 2013.
[28] G. Maier, M. Schlesinger, H. Oesterlin, Microstructure, deformation and lifetime of alloy 617B – experiences from different heat treatments and heats, in: Proceedings of the 39th MPA-seminar, Stuttgart, 8–9 October 2013.

[29] J. Klöwer, R.U. Husemann, M. Bader, Development of alloy 617 for boilers in 700°C power plants, in: Paper Presented at 4th Symposium on Heat Resistant Steels and Alloys Used for High Efficiency USC Power Plants, 11–13 April 2011, Beijing, China.
[30] R.U. Husemann, M. Bader, J. Klöwer, Metallurgical aspects during manufacturing of nickel alloy 617B, in: 9th International NIMS-MPA-IFW Workshop for Advances in High Temperature Materials for High Efficiency Power Plants, NIMS, Tsukuba, Japan, 24–26 March 2010.
[31] P.J. Ennis, W.J. Quadakkers, Mechanical properties and high temperature corrosion resistance of alloy 617 at 700–1000°C, in: Proceedings of the Conference Parsons 2007, 7th International Charles Parson Turbine Conference 11–13 September 2007, Glasgow, UK, 2007.
[32] M. Spiegel, M. Bader, J. Klöwer, K.H. Tak, H. Tschaffon, U. Zeislmair, Der Einfluss von Bor in Alloy 617, in: Paper Presented at: Langzeitverhalten Warmfester Stähle, vol. 34, Vortragsveranstaltung, Düsseldorf, November 2011.
[33] T. Alam, et al., Metallurgical and Materials Transactions A 43 (2012) 2183.
[34] D. Tytko, P.P. Choi, J. Klöwer, A. Kostka, G. Inden, D. Raabe, Microstructural evolution of a Ni-based superalloy (617B) at 700°C studied by electron microscopy and atom probe tomography, Acta Materialia 60 (4) (2012) 1731–1740.
[35] R.U. Husemann, J. Klöwer, unpublished results.
[36] M. Spiegel, et al., Alloy 617 B: Metallurgy, Properties, Fabrication and Welding, 2013, unpublished report, Duisburg.
[37] Alloy 617 – Material Data Sheet der VDM Metals GmbH, ed. 2014.
[38] G. Maier, Unpublished Report of the Fraunhofer Institute for Mechanics of Materials, 2013, Freiburg.
[39] S. Chandra, R. Cotgrove, S.R. Holdsworth, M. Schwienherr, M.W. Spindler, Creep rupture data assessment of alloy 617, in: Proceedings of ECCC Conference: Conf. Creep and Fracture in High Temperature Components, London, 2005, pp. 178–188.
[40] F. Schubert, Neuauswertung des Zeitstandverhaltens von lösungsgeglühtem Alloy 617 samt seiner Schweißverbindung im Temperaturbereich 550–1000°C, in: Proceedings of the Conference Langzeitverhalten Warmfester Stähle und Hochtemperaturwerkstoffe, Düsseldorf, 2010.
[41] R. Krein, J. Klöwer, P. Schraven, V. Knesevic, Assessment of creep rupture data of the nickel alloy 617B Creep behaviour of alloy 617B, VGB PowerTech 93 (2013) 88–93.
[42] ASME Boiler and Pressure Vessel Code II, Part D: “Properties”, ASME International, New York, July 2011, p. 214.
[43] ECCC Data Sheet Alloy 617, 2005.
[44] V. Knesevic, A. Schneider, C. Landier, Creep behaviour of thick-wall Alloy 617 seamless pipes for 700°C power plant technology, Procedia Engineering 55 (2013) 240–245.
[45] G. Maier, H. Riedel, T. Seifert, J. Klöwer, R. Mohrmann, Time and temperature dependent cyclic plasticity and fatigue crack growth of the nickel-base Alloy617B – experiments and models, Advanced Materials Research 278 (2011) 369–374.
[46] G. Maier, H. Riedel, B. Nieweg, C. Somsen, G. Eggeler, J. Klöwer, R. Mohrmann, Cyclic deformation and lifetime of Alloy 617B during thermomechanical fatigue, Materials at High Temperatures 30 (1) (2013) 27–35.
[47] G. Maier, H. Riedel, C. Somsen, Cyclic deformation and lifetime of Alloy 617B during isothermal low cycle fatigue, International Journal of Fatigue 55 (2013) 126–135.
[48] G. Maier, M. Möser, H. Riedel, T. Seifert, D. Siegele, J. Klöwer, R. Mohrmann, High temperature plasticity and damage mechanisms of the nickel alloy 617B, in: Proceedings of the 36th MPA-seminar, Stuttgart, 7–8 October 2010.

[49] R. Krein, M. Spiegel, J. Konrad, Erfordernisse der Zeitstandfestigkeit und Hochtemperaturkorrosionsbeständigkeit für moderne Dampferzeugersysteme, in: VDI Conference, Werkstoffe in der Kraftwerkstechnik, Karlsruhe, 2013.
[50] J. Klöwer, in: U. Heubner, J. Klöwer (Eds.), Nickel Alloys and High Alloyed Special Stainless Steels, fourth ed., Expert Verlag, Esslingen, 2012, p. 112.
[51] J. Klöwer, U. Heubner, Carburisation of nickel-base alloys and its effect on the mechanical properties, Materials and Corrosion 49 (1998) 237–245.
[52] H.J. Grabke, in: A. Rahmel (Hrsg.) (Ed.), Aufbau von Oxidschichten auf Hochtemperaturwerkstoffen und ihre Technische Bedeutung, DGM, Frankfurt, 1983, p. 89.
[53] R.A. Rapp, et al., High temperature corrosion in energy systems, Materials Science and Engineering 50 (1981) 1–17.
[54] P. Kofstad, High Temperature Corrosion, Elsevier Applied Science, London, New York, 1988.
[55] M. Spiegel, Molten salt-induced corrosion of metals, in: in: A. Bard, M. Stratmann, G. Frankel (Eds.), Encyclopedia of Electrochemistry, vol. 4, 2007.
[56] F. Lüttschwager, Rauchgasseitige Korrosion von Nickellegierungen für zukünftige 700°C-DampfkraftKraftwerke (dissertation), RWTH Aachen, Aachen, 2011.
[57] L. Paul, et al., Performance of Weld Overlay Materials in Simulated Coal Fired Combustion Environment, NACE International, Houston, TX, 2004, Paper No. 04523, Corrosion 2004.
[58] M. Donachie, S. Donachie, Superalloys – a Technical Guide, ASM International, Materials Park, Ohio, 2003.
[59] N. de Boer, K. Klenke, B. Donth, V. Knezevic, J. Paal, P. Schraven, F. Grimm, Herstellung und Verarbeitung der Nickellegierungen für die Teststrecke HWT II im Grosskraftwerk Mannheim, VGB PowerTech 8 (2015) 35–43.
[60] P. Schraven, Qualification and Experience on A 617 and C-263 boiler tubes, in: Paper Presented at 7th International Conference on Advances in Materials Technology for Fossil Power Plants, Waikoloa, USA, 22–25 October 2013.
[61] K. Metzger, V. Baumhoff, H.C. Schröder, K. Maile, S. Zickler, Commissioning of the thick walled pipe test rig for 725°C power plants, in: Proceedings of the 39th MPA-Seminar, 8th and 9th October 2013.
[62] V. Knezevic, N. de Boer, F. Müller, B. Koschlig, M. Jarrar, Heavy wall Ni-based alloys seamless pipes – performance and challenges, in: VGB Workshop Materials and Quality Assurance, Linkebeek, Belgium 29–30 April 2015.
[63] V. Knezevic, A. Schneider, B. Koschlig, H. Bröker, Vallourec and Mannesmann activities on Nickel-based materials for advanced ultra super critical power plant application, in: Vortragsveranstaltung der AG Warmfeste Stähle und Hochtemperaturwerkstoffe, vol. 34, Stahlinstitut VdEH, Düsseldorf, November 2010.
[64] M. Bockelmann, J. Böllinger, J. Heinemann, M. Wolf, Längsnahtgeschweißte Rohre aus alloy 617B für die neue Kraftwerksgeneration, to be published.
[65] H. van Wortel, Control of Relaxation Cracking in Austenitic High Temperature Components, CORROSION 2007, Paper No. 07423, NACE International, Houston, TX, 2007.
[66] C.G. Stolzenberger, 700°C-Technologie: Stand der Entwicklung der 700°C-Technologie, in: Proceedings of the Conference, 36. VDI Jahrestagung Schadensanalyse in Kraftwerken, Würzburg, Germany, 13/14 October 2010.
[67] J. Klöwer, J. Mentz, M. Zinke, Development of crack-resistant alloy 617B for components in 700°C power plants, Paper No. C-2013–0002284, in: Corrosion 2013, NACE International, Orlando, Florida, 2013.
[68] J. Klöwer, M. Zinke, J. Mentz, J. Konrad, Correlation of microstructure and properties of Alloy 617, in: Presentation at the 2nd International Conference on Materials for Energy (EnMat II), Karlsruhe, Germany, May 2013.

[69] J.C. van Wortel, Chemical applications and operational experiences, in: FDBR Workshop, Düsseldorf, 24–25 February 2005.
[70] K. Maile, R. Scheck, Beurteilung einer Rissbildung in einer Schweißverbindung aus Alloy 617, in: 38. VDI Jahrestagung Schadensanalyse in Kraftwerken, Würzburg, Germany, 23–24 October 2012.
[71] A. Dhooge, J. Vekeman, New generation 2 ¼ Cr steels T/P 23 and T/P 24 weldability and high temperature properties, Welding in the World 49 (2005) 75–93.
[72] J.G. Nawrocki, J.N. DuPont, C.V. Robino, A.R. Marder, Welding Journal 80 (2001) 18–24 Welding Research Supplement.
[73] M. Wolf, Recent developments in welding of nickel alloys for new power plant technology, in: Paper Presented at Journaux Materiaux haute temperature, Institut de Soudure, Paris, 7–8 December 2010.
[74] T. Gräb, Erfahrungen mit dem Schweißen von Alloy 617 und Alloy C-263, in: Proceedings of the Conference, Hochlegierte Stähle und Nickellegierungen für Industrieanlagen und Energietechnik, Dresden, 09–10 October 2013.
[75] A. Neidel, S. Riesenbeck, B. Fischer, E. Caglyan, T. Gädicke, Heissrisse in der WEZ schmelzschweißtechnisch gefügter Nickelbasis-Bleche – was denn nun? Praktische Metallographie Sonderband 43 (2011) 159.
[76] A. Klenk, to be published.
[77] C. Fink, D. Keil, M. Zinke, Evaluation of hot cracking susceptibility of nickel base alloys by the PVR-test, Welding in the World 56 (2012) 37–43.
[78] K. Maile, Qualification of Ni-Based alloys for advanced ultra supercritical plants, in: Proceedings of the 6th International Conference on Creep, Fatigue Creep-Fatigue Interaction, Procedia Engineering, vol. 55, 2013, pp. 214–220.
[79] R. Uerlings, in: Proceedings of the Conference, 35. VDI Jahrestagung Schadensanalyse in Kraftwerken, Würzburg, Germany, 14/15 October 2008.
[80] H. Tschaffon, 700°C power plant technology – status and challenge, in: J. Lecomte-Beckers et al. (Ed.), Proceedings of the 9th Liege Conference on Materials for Advanced Power Engineering 2010, Schriftenreihe des Forschungszentrums Jülich, vol. 94, 2010, p. 18.
[81] H. Tschaffon, M. Bader, Ergebnisse der Test- und Entwicklungsphase der 700°C-Kraftwerkstechnologie, 4. FDBR Werkstofftagung, Düsseldorf, November 2010.
[82] G. Gierschner, H. Penner, Auf dem Weg zum 700°C Kraftwerk, in: Proceedings of the Conference, 36. VDI Jahrestagung Schadensanalyse in Kraftwerken, Würzburg, Germany, 13/14 October 2010.
[83] C. Ullrich, G. Gierschner, C. Stolzenberger, H. Tschaffon, Erfahrungen beim Testbetrieb von Komponenten für das 700°C – Kraftwerk, in: Proceedings of the 10th VDI Conference, "Feuerung Kessel", Kessel, Germany, 2011.
[84] A. Di Gianfrancesco, A. Tizzanini, M. Jedamzik, C. Stolzenberger, Encio project: an European approach to 700°C power plant, in: Proceedings of the 7th International Conference on Advances in Materials Technology for Fossil Power Plants, Waikoloa, USA, 22–25 October 2013, pp. 9–23.
[85] A. Klenk, K. Maile, Investigations on nickel-based alloys and welds for a-USC applications, in: Proceedings of the 7th International Conference on Advances in Materials Technology for Fossil Power Plants, Waikoloa, USA, 22–25 October 2013, pp. 155–166.
[86] K. Metzger, K.H. Czychon, K. Maile, A. Klenk, A. Helmrich, Q. Chen, GKM test rig: investigation on the long term operation behavior of tubes and forgings made of Alloys for future high efficient power plants, in: 6th International EPRI Conference on Advances in Materials Technology for Fossil Power Plants, Santa Fe, 31 August–03 September 2007.

[87] K. Metzger, S. Zickler, K. Maile, Experience with the operation of a test-rig for 700°C power plant, in: 6th International Conference on Creep, Fatigue and Creep-fatigue Interaction, Chennai, India, 22–24 January 2012.
[88] S. Zickler, S. Wagner, K. Maile, K. Metzger, K.H. Czychon, High-temperature materials for future high-efficient power plants, in: 38th MPA Seminar, Stuttgart, 7–8 October 2013.
[89] K. Maile, S. Zickler, K. Metzger, Qualification of structural materials for the advanced 700°C Fossil fired power plant – experience gained in the GKM field test loops, in: BALTICA IX International Conference on Life Management and Maintenance for Power Plants, Helsinki-Stockholm, 11–13 June 2013.
[90] D. Hüggenberg, M. Speicher, A. Klenk, S. Zickler, M. Schwienheer, Y. Wang, H. Oesterlin, G. Maier, Hochtemperatur-Werkstofftestst recke HWT II – Begleitende experimentelle und numerische Untersuchungen an Werkstoffen und Komponenten, VGB PowerTech 08 (2015) 52–62.
[91] O. Birkle, et al., Konstruktion, Herstellung und Betrieb von Armaturen in der 725°C HWT II Teststrecke, VGB PowerTech 08 (2015) 27–34.
[92] K. Metzger, R. Stork, J. Bareiß, K. Maile, Auslegung, Einrichtung und Betrieb der Hochtemperatur-Werkstofftestst recke HWT II im Großkraftwerk Mannheim, VGB PowerTech.

Alloy 263

17

A. Di Gianfrancesco
Materials & Technologies Consultant, Rome, Italy

17.1 Introduction

Alloy 263 (UNS N07263/W.Nr. 2.4650/AMS5886), usually called also Nimonic 263, is a quite old superalloy developed by Rolls-Royce Ltd in 1971 to provide a material in different shapes, like sheet and bar, which could be readily fabricated and would offer improved ductility in welded assemblies to replace the Nimonic alloy 80A.

It was designed as sheet material to meet specific design criteria in terms of proof stress and creep strength. It is now available in all standard forms. The welding techniques for this alloy are similar to those in common use for other age-hardenable nickel-base alloys. During salvage welding operations, a pre-weld heat treatment is not necessary on age-hardened assemblies, but a subsequent age-hardening treatment is desirable after all salvage welding is completed. Material will age in service if temperatures are above 750°C [1].

Alloy 263 is widely used in aircraft engines in several components, ie, blades operating at temperature >900°C with stress of 35 bar and short time, but in the case of the A-USC power plants the operation conditions are in the range on 750°C with applied stress of 350 bar (350 kg/cm^2) for a very long time. Therefore the properties in such conditions have to be verified.

17.2 Physical metallurgy

Alloy 263 is an age-hardenable Ni-Co-Cr-Mo-Ti-Al alloy that combines very good high-temperature strength with excellent ductility, formability, and weldability. The chemical composition of the alloy 263 is summarized in Table 17.1. It has to be noted that a strict control of impurities in trace elements has to be done during the melting.

Alloy 263 is normally given a two-stage heat treatment, that is, solution treatment and age hardening prior to service. This heat treatment is normally carried out in air. Material is usually supplied in the solution-treated condition and aged by the customer as part of the fabrication process. Material can, however, be supplied to any requested heat treatment condition.

Cooling for hot-rolled sheet from solution treatment temperature may be by water quenching (WQ) or by air cooling (AC); the former is recommended. For cold-worked products, especially sheet, fluidized bed quenching (FBQ) produces less distortion

Materials for Ultra-Supercritical and Advanced Ultra-Supercritical Power Plants.
http://dx.doi.org/10.1016/B978-0-08-100552-1.00017-8
Copyright © 2017 Elsevier Ltd. All rights reserved.

than WQ without any appreciable change of properties. The solution treatment temperature of 1150°C yields a compromise between tensile and creep strengths, coupled with good ductility values in both cases.

Inter-stage annealing to remove residual cold-work is normally applied during manipulation operations. The treatment recommended for sheet is 15 min/1050–1100°C/WQ or AC.

Welding operations should be carried out with the material in the solution-treated condition. An 8h/800°/AC aging treatment can be applied to the welded component [1].

17.3 Physical properties

The physical properties of the alloy 263 are summarized in Table 17.2.

17.4 Hot working

Alloy 263 may be hot worked in the temperature range 950–1150°C.

Annealing: alloy 263 bar or heavy section is usually softened by a heat treatment of 2 h/1150°C/WQ, namely the first stage of the recommended two-stage heat treatment for bar.

Annealing of alloy 263 sheet, required during manipulatory operations, should be by heating for 15 min in the temperature range 1050–1100°C followed by rapid cooling (WQ for heavier sheet and AC for thin-section sheet). FBQ may also be used [1].

Table 17.1 Chemical composition (%WT) of alloy 263 [1]

C	**Si**	**Mn**	**S**	**Ag**	**Al**	**B**	**Bi**	**Co**
0.04–0.08	<0.40	<0.60	<0.007	<0.0005	<0.60	<0.005	<0.0001	19.0–21.0
Cr	**Cu**	**Fe**	**Mo**	**Pb**	**Ti**	**Al + Ti**		**Ni**
19.0–21.0	<0.20	<0.7	5.6–6.1	<0.0020	1.9–2.4	2.4–2.8		Balance

Table 17.2 Physical properties of the alloy 263 [1,2]

Density	g/cm^3 8.36
Melting range	Liquidus temperature, °C 1355 Solidus temperature, °C 1300
Specific heat, in the range 20–100°C	461 J/kg, °C
Electrical resistivity at RT	115 µohm-cm
Thermal conductivity at RT	11.7 W/m-K
Main coefficient of thermal expansion 25–1000°C	18.1 µm/m-°C

17.5 Heat treatment

The alloy 263 has been developed for several applications in the gas turbine manufacture component, and therefore different heat treatments have been tailored for the different products as follow [3]:

- extruded bar: solution treatment of 1150°C for 1.5–2.5 h + water quench aging treatment of 800°C for 8 h + air cool (as per BS HR10/AMS 5886)
- hot-rolled sheet: solution treatment of 1150°C for 0.5 h + water quench; or air cool aging treatment of 800°C for 8 h + air cool (as per BS HR206/AMS 5872)
- cold-rolled sheet: solution treatment of 1150°C for 3–10 mins + water quench; or FBQ aging treatment of 800°C for 8 h + air cool (as per BS HR206/AMS 5872)

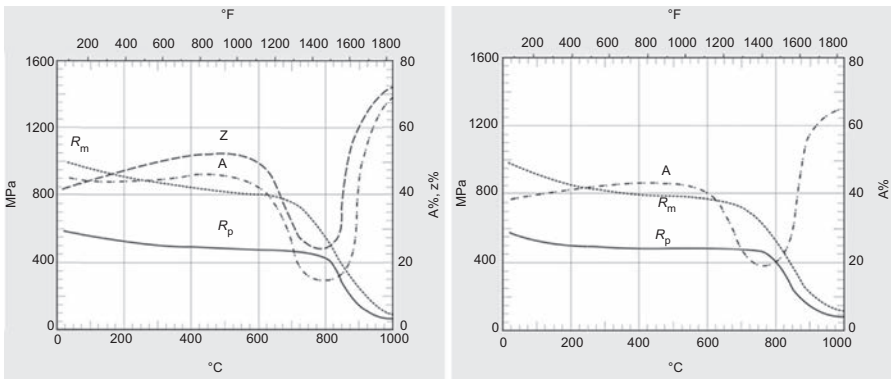
17.6 Mechanical properties

Tensile properties: the data given in Fig. 17.1 are presented, on the left for extruded section and forged and on the right for cold-rolled sheet 0.7–1.2 mm.

Impact data: the room temperature Charpy impact strength of extruded and forged section given the recommended heat treatment of 2 h/1150°C/WQ + 8 h/800°C/AC is in the region of 111 J. Long-term embrittlement has been investigated by room and elevated temperature Charpy impact testing of extruded and forged section given the recommended heat treatment. The data given in Table 17.3 represent the findings of these investigations and in general show the results of duplicate tests.

17.7 Microstructural analyses

Alloy 263 has an FCC austenitic (γ) matrix with the following phases reported to be present: gamma prime (γ') eta (η), MX, $M_{23}C_6$, M_6C, and mu (μ) [4,5]. Precipitation of MX, $M_{23}C_6$, and γ' occur during the standard precipitation heat treatment. The



Extruded bar: heat treatment 2 h/1150°C/WQ + 8 h/800°C/AC

Cold rolled sheet: heat treatment 3–10 min/1150°C/FBQ or WQ + 8 h/800°C/AC

Figure 17.1 Tensile properties of extruded bar and cold-rolled sheet. [1]. (*A*, elongation; R_m, tensile strength; R_p, 0.2% proof stress; *Z*, reduction of area).

Table 17.3 Impact values for A263 [1]

Soaking time h	Soaking temperature, °C				
	600	700	750	800	900
30	111:103	73:75	68:80	98:98	190:176
100	88:92	54:58	65:56	87:79	160:165
300	87:100	34:30	41:43	58:52	108:119
1000	71:71	27:33	24:22	62:57	56:60
3000	98:81	12:14	24:35	39:35	46:53
10,000	27:26	9:11	26:22	34:33	45:45

Soaking time h	Soaking and test temperature, °C			
	600	750	800	900
30	157:150	100:100	125:114	172:174
100	146:130	96:92	114:100	180:160
300	160:156	81:85	91:104	141:145
1000	108:114	71:69	87:79	123:119
3000	152:114	73:52	79:83	111:106
10,000	65:64	42:39	72:71	110:107

precipitated γ' that forms is meta-stable and is replaced over time by the more stable η phase [6,7].

The alloy has two main strengthening mechanisms: solid solution strengthening and precipitation hardening. Solution-strengthening elements such as molybdenum provide high-temperature strengthening through lattice distortion due to its atomic size difference from the matrix. Boron and zirconium also improve creep rupture properties. Some of the benefits of solid solution strengthening include reduced diffusion and lower overall stacking fault energy. Precipitation hardening is the principal strengthening mechanism in Nimonic 263 and occurs due to the precipitation of γ' during the precipitation hardening heat treatment (typically a few hours at 800°C). Initial precipitation creates a distribution of very fine spherical gamma prime particles. Fig. 17.2 shows the microstructure of the alloy 263 billet after solution heat treated for 2 h at 1150°C with a water quench, followed by an aging heat treatment of 4 h at 800°C.

Fig. 17.3(a) shows the fine distribution of γ' precipitate (23 ± 4 nm) at 750°C, 50 h aging [9]. These fine γ' particles distributed coagulate to a larger size (68 ± 20 nm) at 850°C for 50 h aging as shown in Fig. 17.3(b). The TTT diagram of alloy 263 is clearly shown in Fig. 17.3(c). It can be learned from this diagram that the basic structure for alloy 263 is mainly fine γ' precipitation in Ni-Cr-Co-Mo γ-matrix and carbide $M_{23}C_6$ distributed at grain boundaries. It can be seen also from this TTT diagram that the Ni_3Ti type η phase can be formed at high-temperature long-time aging. The Ti-rich

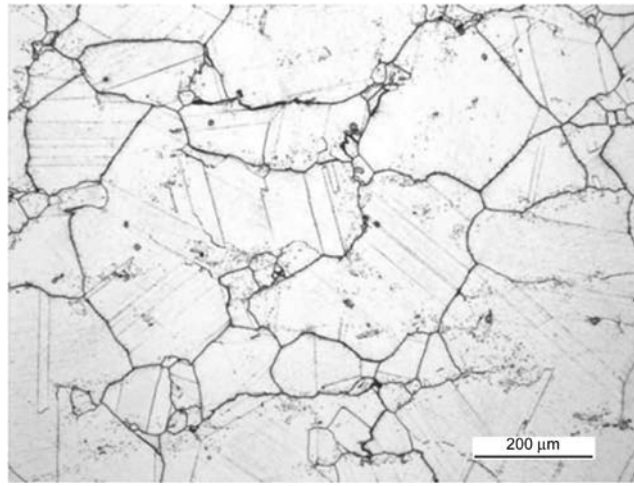


Figure 17.2 Typical A623 microstructure by light microscopy after heat treatment [8].

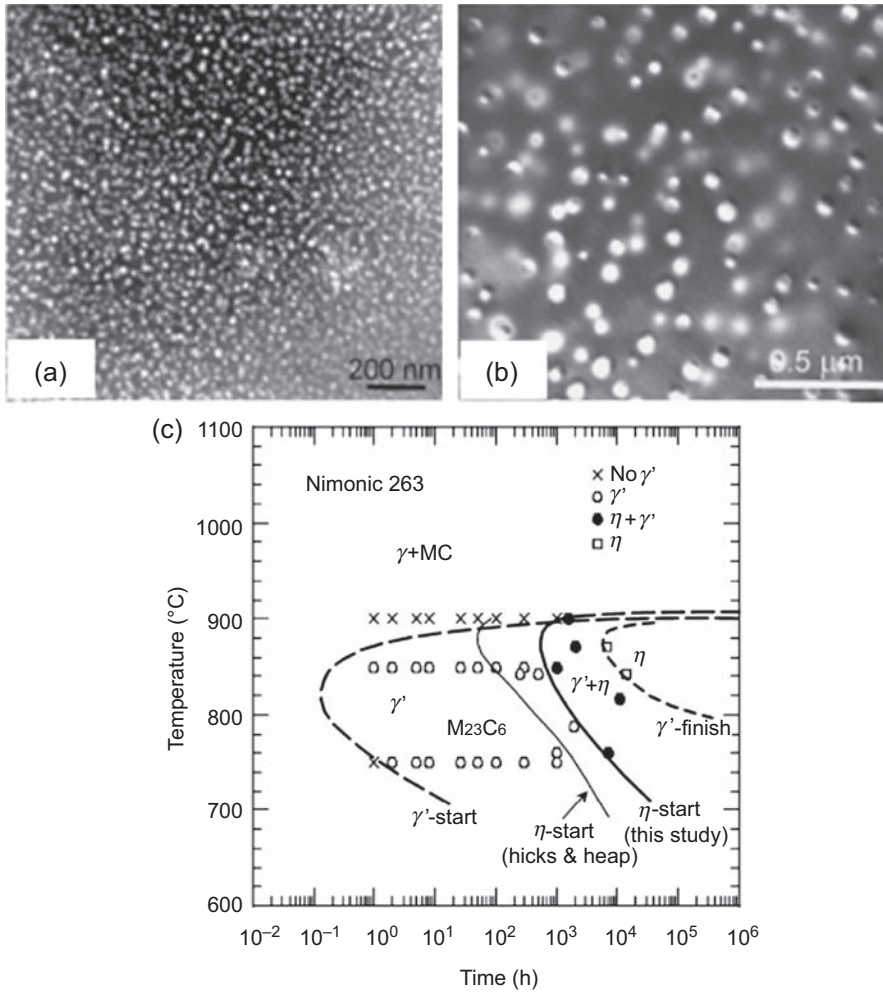


Figure 17.3 TEM dark field images of alloy 263 aged at 750°C (a) and 850°C (b) for 50 h and TTT curve (c) [5,9].

γ'- $Ni_3(Al,Ti)$ in alloy 263 is a meta-stable precipitated phase for good strengthening effect. However, the meta-stable Ti-rich type γ' phase will transform to a stable Ni_3Ti type η phase for long-time aging at high temperature [5,10].

Fig. 17.4 shows the very large, plate-like η phase formation in alloy 263 after long-time aging at high temperature [5].

Phase diagram calculation by Thermo-Calc can help us to understand the phase stability in the different temperature ranges. The equilibrium phase diagram of alloy 263 (Fig. 17.5) shows that the η, σ, and μ phase can be formed in different temperature ranges [11].

It is clearly seen that except γ', η and μ phase can be formed in a wide range of high temperatures. Fig. 17.6 is an example of a big amount of large plate-like Ni_3Ti type η phase formed after stress rupture test at 775°C, 115 MPa for 12,601 h [11]. It is clear that the strengthening effect of γ' is decreased dramatically by the transformation from γ' to η.

It means that the structure stability of alloy 263 should be improved for 700°C A-USC boiler superheater and reheater tubing components at very long time service.

Below the γ' solvus temperature, the precipitate exists, and the separation of pinning events is likely to be determined by the precipitate spacing. Fig. 17.7, taken from Zhang and Knowles [12], shows a photomicrograph of alloy 263 that has been crept at 800°C, and 160 MPa, in which the dislocation pinning action of the γ' particles, causing bowing, can be seen.

Precipitate coarsening for C263 as a function of exposure time and temperature, after standard heat treatment, was measured experimentally by Betteridge and Heslop [13], and by Zhang and Knowles [12] at 800°C, as shown in Fig. 17.8(a). Zhang and

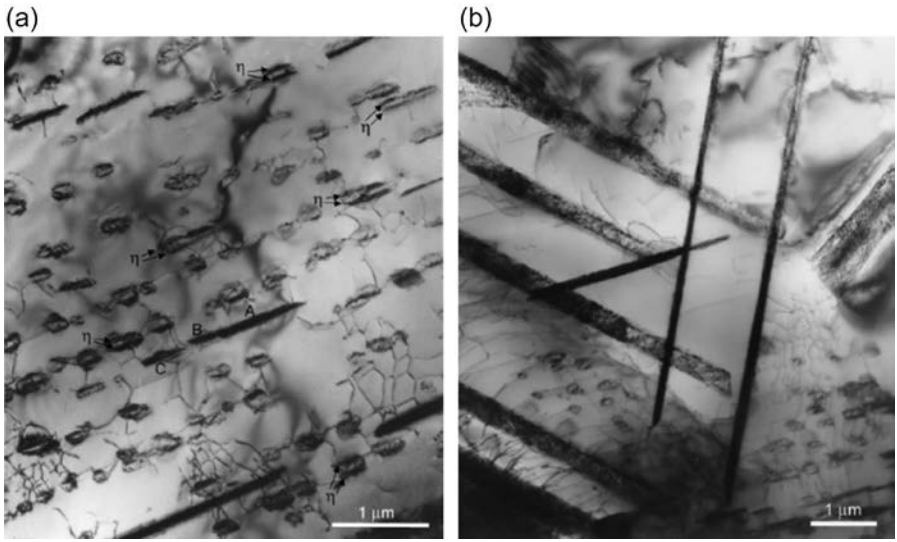


Figure 17.4 The TEM images of arranged γ' phase transformed to η phase after heat treatment at 800°C for 8 h then aged at 900°C for 1250 h (a) and dislocations distribution at η/γ' boundaries (b) [9].

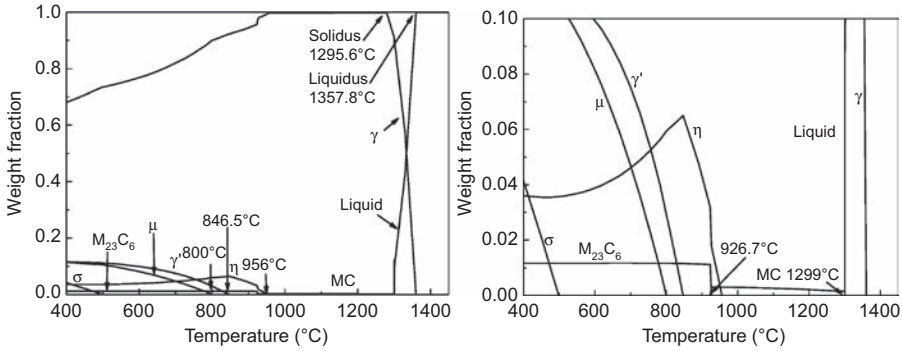


Figure 17.5 Phase diagram of alloy 263 calculated by Thermo-Calc [9].

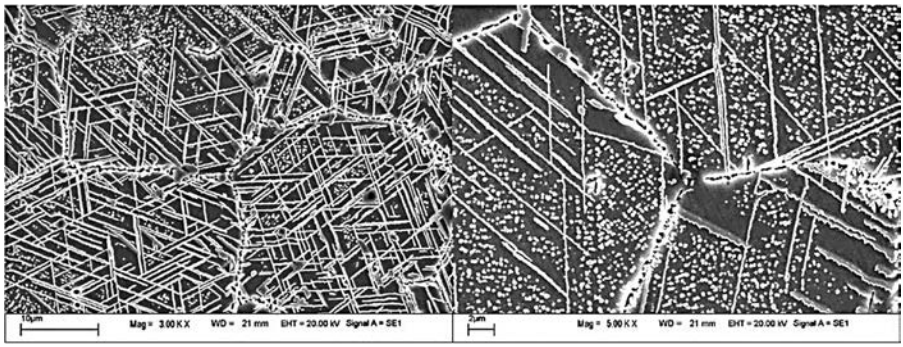


Figure 17.6 Microstructure instability of alloy 263 after the stress rupture test at 775°C, 115 MPa of 12,601 h [9].

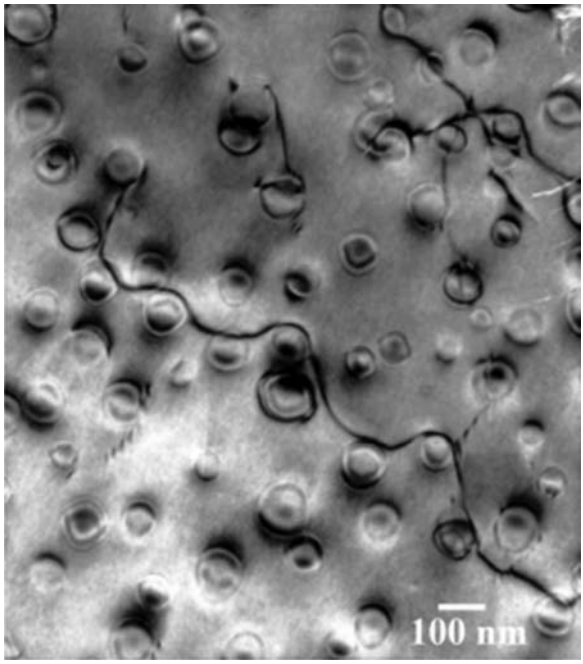


Figure 17.7 TEM photograph showing dislocation bowing at γ precipitates in a crept specimen at 800°C,160 MPa [12].

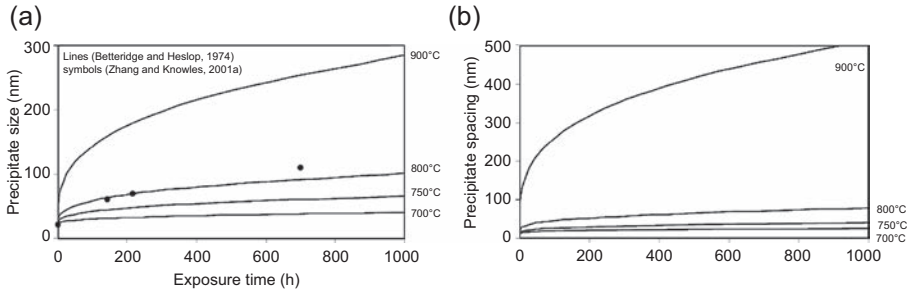


Figure 17.8 Graphs showing the evolution of precipitate size and spacing [12].

Knowles also determined the dependence of steady-state volume fraction of γ' as a function of temperature. The results are shown in Fig. 17.8(b).

17.8 Weldability

Alloy 263 is readily welded by automatic and manual T.I.G. processes and by M.I.G. processes. The choice of process depends on the joint configuration and on material thickness. For simple butt joints, automatic T.I.G. welding can be used, with or without filler metal additions, depending on thickness. Material thinner than 1.6 mm can be welded without filler metal, but above this thickness, filler metal must be added. The limiting thickness for automatic T.I.G. welding is around 3.25 mm.

For more complicated joints, or for thicker material, manual T.I.G. welding can be employed. This process can be used on all section thicknesses, but the much faster M.I.G. processes are normally used for material above 4.8 mm thick, particularly if a lot of welding is involved. As alloy 263 does not suffer from heat-affected zone cracking, both "spray" and "dip" transfer conditions can be used when M.I.G. welding, although "dip" transfer is preferred.

The filler metal to be used for all argon-shielded welding processes is NIMONIC filler metal 263, of matching composition to the base alloy. It is available in 914-mm straight lengths at 3.3, 2.6, 2.0, 1.6, and 1.2 mm diameter for manual welding and on reels at 1.6, 1.1, and 0.9 mm diameter for automatic T.I.G. and M.I.G. welding.

The shielding gas should be either pure argon or argon plus 5% hydrogen, if the latter is preferred. On no account should argon–oxygen mixtures or carbon dioxide be used [1].

The welding parameters should be adjusted to low interpass temperature (maximum 150°C) and low heat input to restrict formation of hot cracks. Moreover, it is difficult to set corresponding composition of the welds, especially for alloy 263 with higher Ti content, using existing filler metals. Therefore, the so-called "duplex electrode" concept was applied in case of these alloys. In this approach, critical alloying elements were transferred gradually into the arc to avoid burn out of Al and Ti as well as to limit transfer of Si. The determined chemical composition of welds corresponded to the respective base material analysis, as shown in

Table 17.4 Chemical compositions of weld metals for Inconel 617 mod. and Alloy 263 [14]

Alloy	Filler metal1	C	Si	Mn	Cr	Co	Mo	Ti	Al	Fe
Inconel 617mod.	Thermanit 617 D	0.06	0.6	<0.3	21.0	11.0	9.0	0.3	1.2	1.0
Alloy 263	Thermanit 263	0.06	0.7	<0.2	20.0	20.0	6.0	2.0	0.3	0.5

the example in Table 17.4. The Si content in the welds arose from additives used in electrodes cover, but no negative effect on joint properties was observed. After welding, a heat treatment of 3 h at 980°C/4 h at 810°C should be carried out for alloy 617 mod/alloy 263, which prevents relaxation cracking under service conditions [14].

17.9 Examples of trial components manufacturing

17.9.1 Pipe for ENCIO project

For the ENCIO R&D project activities, thick A263 pipe has been produced by VDM Metals forged billets obtained by VIM + ESR/VAR remelting; Vallourec produced pipe with the process route summarized in Fig. 17.9. In Fig. 17.10 a final pipe is shown with the dimension of the pipe realized by A263 and A617, both scheduled for ENCIO project [15].

17.9.2 Forged rotor for NextGenPower project

For the NextGenPower program the main goal was the manufacture of a full-scale rotor with diameter of 1000 mm, to be joined with advanced 9–12% Cr martensitic steels to demonstrate the manufacture of welded IP rotor, as shown in Fig. 17.11.

A VIM/ESR/VAR ingot was produced by Saarschmiede (Fig. 17.12) and then forged, heat treated, and machined as shown in Fig. 17.13. From forged material, two slices were cut after forging process at both ends of the forging for structural analyses, to control these:

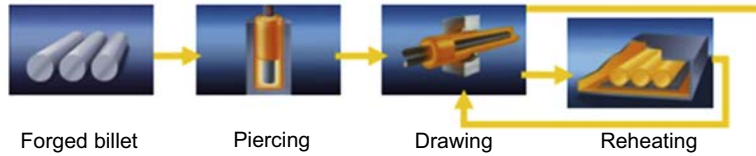
- segregations, microstructure, and chemical composition were investigated,
- Grain size was measured at several distances from the core to the surface (Fig. 17.14),
- UT inspection with MDDS 2.8–4.9 mm: no indicated defects.

The mechanical properties of the trial rotor have been evaluated in different position of the trial rotor: the results are summarized in Table 17.5.

17.9.3 Rotor welding for NextGenPower project

With a live steam temperature of 750°C and an IP turbine outlet steam temperature of c. 350°C, part of the rotor has to be manufactured of Ni-alloy, but the other part can be made of less expensive 9–12% Cr martensitic steel. In NextGenPower, the martensite

- VDM metals: Forget billets (VIM and ESR/VAR)
- Vallourec:
  - Piercing & drawing (Ehrhardt process) – Vallourec Reisholz



  - Hot pilgering (Mannesmann process) – Vallourec Rath

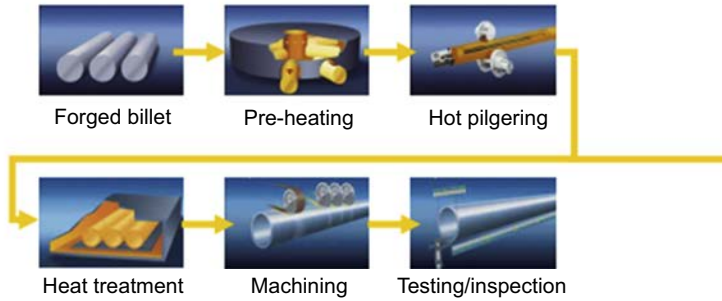
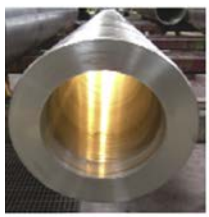


Figure 17.9 Manufacturing routes for heavy-wall Ni-based alloys seamless pipes [15]



	Press and drawing process	Pilger process
Alloy 617		
Dimension range	OD 400 – 500 mm WT 30 – 80 mm	OD 340 – 350 mm WT 72.5 – 85 mm
Alloy C 263		
Dimension	OD 380 mm WT 60 mm	OD 350 mm WT 72.5 mm

Figure 17.10 Dimensions of heavy-wall Ni-based alloys seamless pipes produced by Vallourec [15]

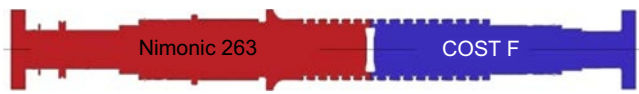


Figure 17.11 Dissimilar weld joint alloy 263 + COST F applicable for IP turbine of A-USC power plant [16].

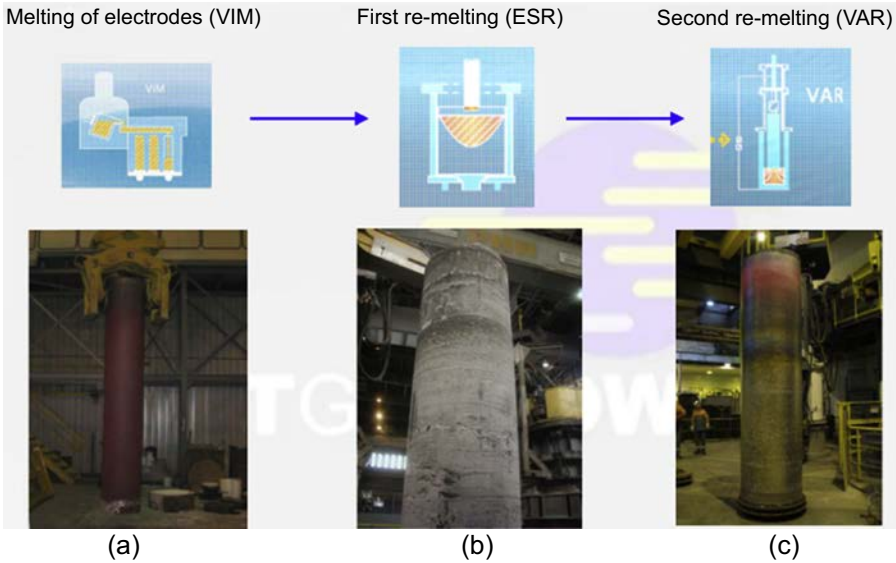


Figure 17.12 Ingot after VIM (a), after ESR (b), after VAR (c) [16].

COST F (X14CrMoVNbN10-1) was selected for its very good creep properties up to 600°C. For a similar metal weld joint, ie, an A263-A263 weld with A263 filler material, the rotor is weld with A263 in solution-treated condition, and precipitation hardening takes place at 800°C (8 h) afterward. However, with a dissimilar metal joint, ie, A263 welded to COST F, the temperature of precipitation hardening of 800°C is above the COST F tempering temperature of c. 700°C. Hence, A263 has to weld in the precipitation hardened condition. Welding is performed using a T.I.G. hot-wire narrow gap welding [16].

17.9.3.1 Homogenous welding

Properties of similar weld joint A263 + A263 (Fig. 17.15) have been investigated at first as a background for final heterogeneous weld joint A263 + COST F. A263 was welded in precipitation hardened condition. Three different PWHT were applied and compared with a not-heat-treated weld joint. All three PWHTs were carried out with the same temperature but different duration, where time1 < time2 < time3. Temperature of PWHT was chosen with respect to typical tempering temperatures of COST F steel used in heterogeneous combination of A263 + COST F. Cap, filler, and root of the weld joint were analyzed. All the samples were broken in the filler metal. Longer PWHT leads to increase of tensile strength. This phenomenon is most likely attributed to carbide formation and precipitation of gamma prime phase in filler metal.

For optimal PWHT T(°C)/time2, hot tensile test at 700 and 750°C was carried out and compared to results measured at room temperature, Fig. 17.16. Cap, filler, and root

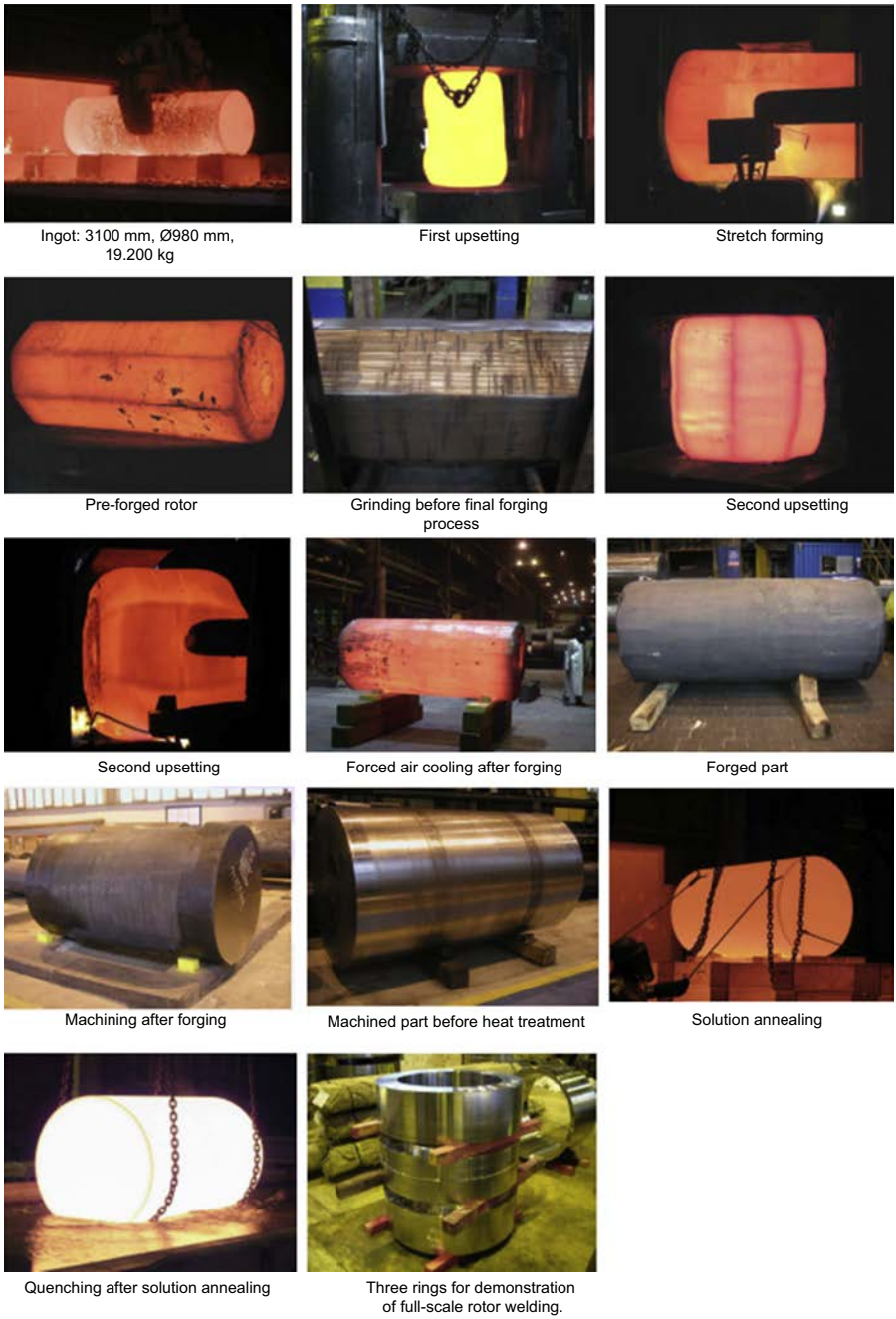


Figure 17.13 Process steps for the production of the trial 1000-mm rotor [16].

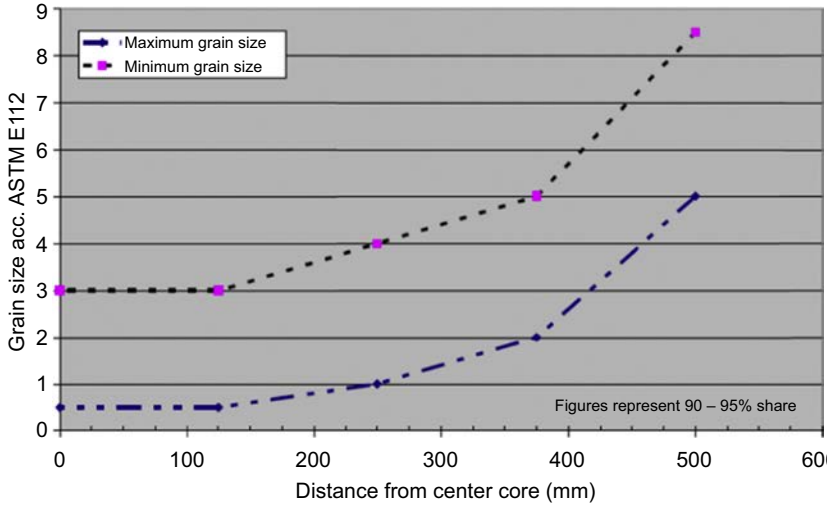


Figure 17.14 Grain size as function of the distance from core in the A263 trial rotor [16].

Table 17.5 Mechanical properties of A263 trial rotor in different positions [16]

Sample location		Temperature (°C)	$R_{p0.2}$ (MPa)	R_m (MPa)	Elongation (%)	RA (%)	Impact energy (J)
Top	Rim	25	642	993	27.0	24.0	48, 45, 43
	Transition	25	675	943	22.3	21.2	43, 41, 42
	Core	25	671	946	23.4	22.0	42, 43, 42
	Rim	750	482	692	32.3	41.3	
	Transition	750	514	675	39.3	41.5	
	Core	750	521	673	31.0	41.7	
Bottom	Rim	25	646	986	29.0	24.7	57, 59, 60
	Transition	25	640	965	26.7	23.9	50, 49, 53
	Core	25	637	962	27.8	25.7	52, 50, 50
	Rim	750	518	695	41.9	47.7	
	Transition	750	488	644	39.7	44.3	
	Core	750	490	652	46.4	48.9	

of the weld joint were analyzed. Elevated temperatures of tensile test led to decrease of tensile strength from 1000 to 700 MPa. All the samples were broken in filler metal.

Test samples (Ø160 mm) from alloy A263 were welded in test laboratories of Polysoude (FRA).

- T.I.G. hot-wire narrow gap welding applied,
- nickel-based welding wire used,
- base material in solution-annealed or precipitation-hardened condition investigated,
- various PWHT applied on the weld joints.

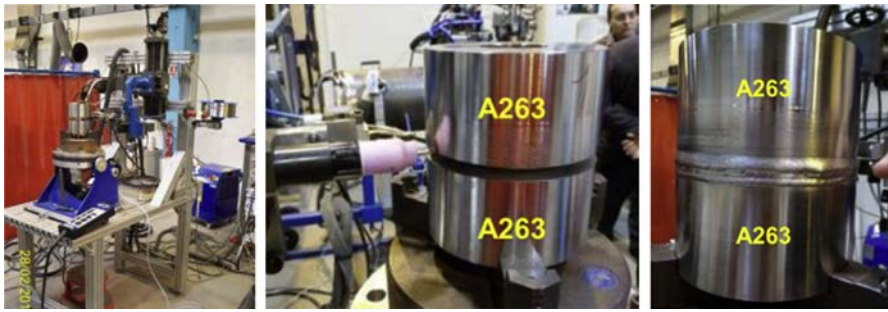


Figure 17.15 A263 Homogeneous welding trial [16].

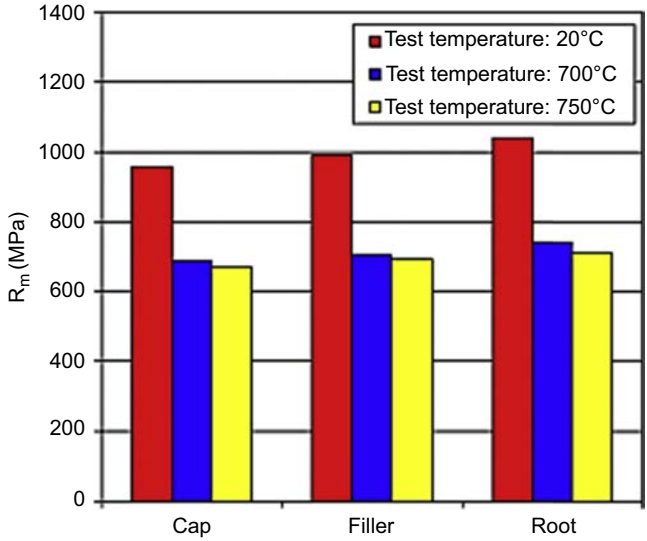


Figure 17.16 Tensile strength at elevated temperatures measured for homogeneous weld joint A263 + A263 treated with optimal PWHT T(°C)/time2. Tensile properties were analyzed for cap, filler, and root area of the weld joints [17].

The main goal was to demonstrate weldability of A263 in precipitation hardened condition.

17.9.3.2 Heterogeneous welding

The heterogeneous welding trial manufacture steps between A263 and COST F are shown in Fig. 17.17. Macrostructure of heterogeneous weld joint A263 + COST with/without cladding of COST F is shown on Fig. 17.18. Cross-sections taken from three different locations were analyzed for both variants. No defects or cracks were indicated on all analyzed cross-sections. Both weld joints meet requirements of quality degree B (the highest quality) given by EN ISO 5817.

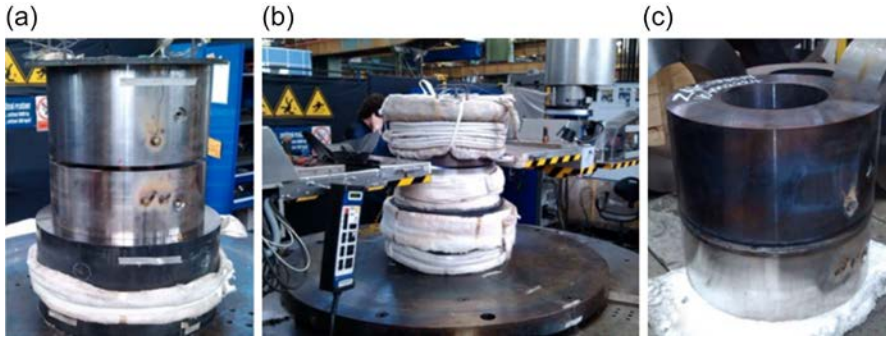


Figure 17.17 Welding of A263 + COST F Ø500 mm. Two counterpieces before welding (a), welding process (b), finished weld joint (c) [17].

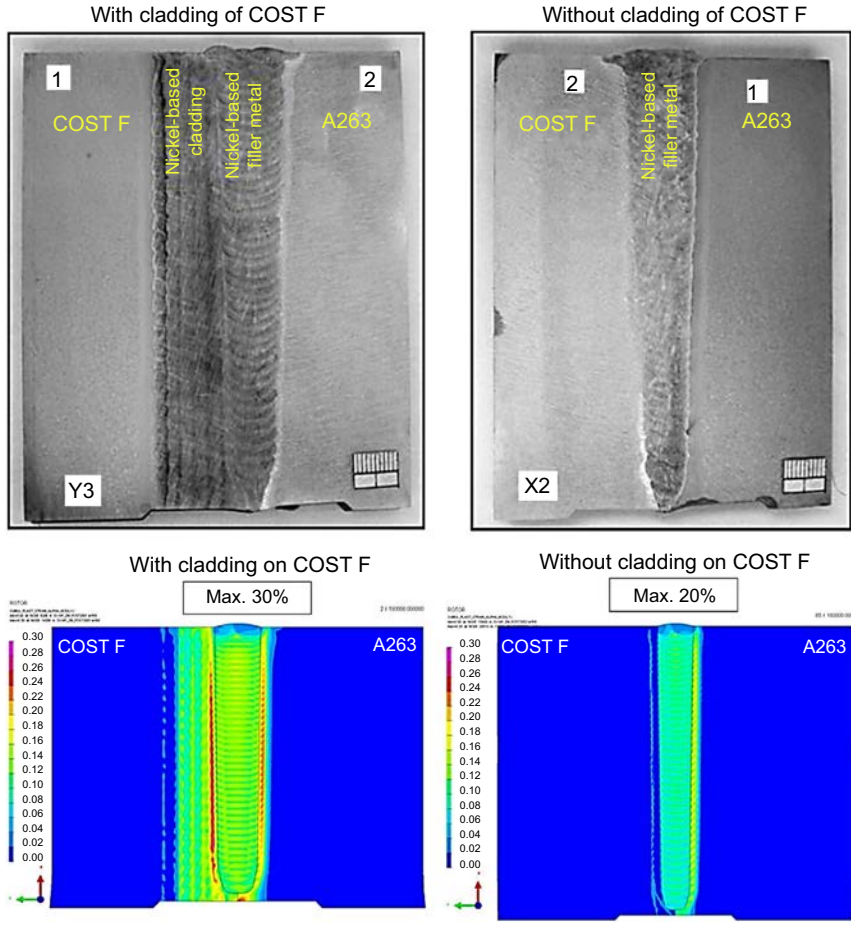


Figure 17.18 Macrostructure of dissimilar weld joint A263 + COST F taken for both variants with/without cladding of COST F and numerical simulation of plastic strains after welding and PWHT of both variants with/without cladding on COST F [17].

Numerical simulation of distribution of plastic strains across the weld joint was carried out for both variants (with/without cladding of COST F) of A263 + COST F Ø500 mm weld joint. PWHT was also taken into account in the simulation. Weld joint processed without cladding exhibited lower values of plastic deformations, Fig. 17.18. The highest values of plastic strains were found especially at transition between cladding of COST F and filler metal.

17.9.3.3 Demonstration of full-scale rotor welding A263 + COST F Ø1000 mm

Based on previous results achieved for experimental weld joints, full-scale rotor welding was demonstrated [16]:

- Two identical weld joints A263 + COST F Ø1000 mm were manufactured (Fig. 17.19).
- Welding depth was 120 mm.
- Optimal PWHT was applied on both weld joints.
- Both weld joints were inspected by UT testing with no indications.
- Mechanical testing started in 09/2014 (tensile test and hot tensile test, Charpy impact test, HCF, fatigue crack growth, long-term creep tests).

17.10 Long-term properties

The creep properties for the A263 are quite well known for the aircraft applications: very high temperature and quite short time and mainly for sheet products. Data for the creep behavior at A-USC service temperature in the range 650–800°C are practically unavailable, as well as the assessment for long-term predictions. Fig. 17.20 shows the creep behavior obtained in the ENCIO project on the pipe shown in Fig. 17.10. The only comparison, available in literature, is reported in Fig. 17.21, where the A263 curve (*green dashed line*) is just a little down from IN740.

17.11 Chemistry optimization

Long-term creep strength is also required for A-USC applications, and unfortunately Alloy C-263 shows η-phase (an intermetallic phase: Ni_3Ti) precipitation after long-time exposure between 700°C and 900°C, which is detrimental for long-term creep properties. In the frame on NextGenPower project, the composition of Alloy C-263 was thus optimized to overcome the formation of η-phase. Trial tests were made to study the effect of hardening contribution elements on microstructural and mechanical properties. Then, a 500-mm-diameter forged rotor was made from optimized 263 alloy and shows promising properties.

As the phase is formed at the expense of the hardening gamma prime phase and the η precipitates are large platelets extending across grains, the η phase generally has an effect on long-term creep behavior in superalloys, as just shown in Figs. 17.6 and



Figure 17.19 Trial manufacture of dissimilar welded rotor A263 + COST F Ø1000 mm [17].

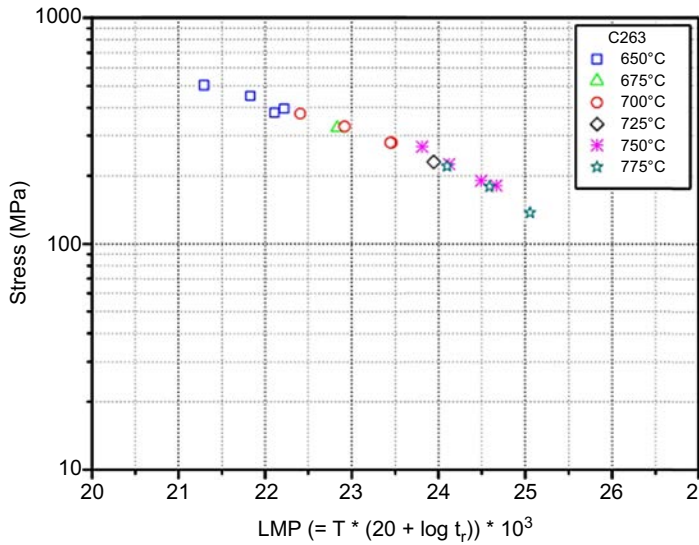


Figure 17.20 Stress–temperature–rupture time correlation: C-263 [15].

17.8. In this context, Aubert & Duval has focused its research on development of a new alloy based on A263 composition with higher microstructure stability at 750°C while keeping the processing properties of A263 [18].

Three conditions were defined to optimize the Alloy C-263 composition. The first condition was defined to improve microstructure stability at 750°C and so to remove η phase formation. Then, the second and third conditions concern process properties (workability, weldability, etc.), which were expected to be as good as those of Nimonic C-263. To satisfy these conditions, γ' solvus and γ' content at 750°C have to be similar to those of Nimonic C-263. As we know, formation of η and γ' phases are linked to Ti and Al contents. Consequently, Thermo-Calc software with the database TCNI5 was used to define Ti-Al couples that satisfy

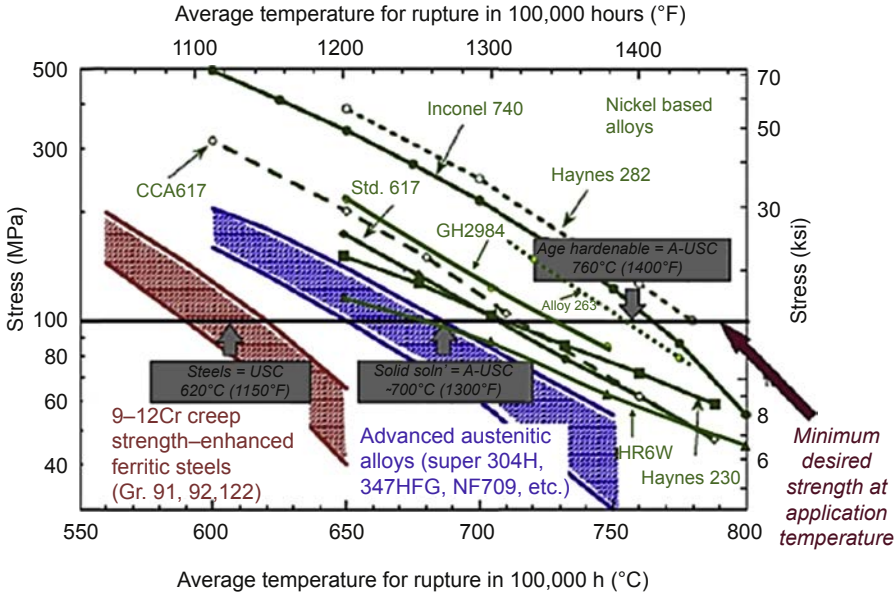


Figure 17.21 Creep strength comparison among some candidate materials [11].

the previous conditions. The stability window of η phase for Nimonic C-263 composition as a function of Ti and Al contents was determined, and the boundary of the domain is plotted on Fig. 17.22 (*dash line*). The Ti-Al couple for Nimonic C-263 is also reported on Fig. 17.22, and it appears that Nimonic C-263 lies in the stability window for η phase. Nimonic C-263 γ' solvus calculated by Thermo-Calc was found to be equal to 900°C. Simulations were then made to determine all Ti-Al couples, which allow 900°C as γ' solvus, and the results were plotted on Fig. 17.22 (*solid line*). Nimonic C-263 γ' content was calculated to be equal to 10 at% at 750°C.

As for γ' solvus, Ti-Al couples that allow 10 at% of γ' content at 750°C were determined and plotted on Fig. 17.22 (*dash line*). Simulations were also performed for 9 at% and 11 at% γ' content at 750°C to surround the 10 at% line.

The best compromise was then chosen for the optimized composition: composition in the area without η formation, with a γ' solvus of 900°C and a γ' content at 750°C of near 10 at%. Ti-Al contents were then defined as %Al of 0.83 +/–0.05 and % Ti of 1.53 +/–0.05 (cross on Fig. 17.22).

Table 17.6 summarizes the variation in the chemistry for A263 optimized composition respect to the original formulation.

The main goal was the improvement of creep properties of standard A263 true to the improvement of the microstructural stability. Fig. 17.23 shows that the microstructure of the new version is finer than the original, with a population of γ' with dimension in the range of 22 nm (Fig. 17.24). After aging at 750°C for 3000 h, only γ' phase is present, without η formation (Fig. 17.25).

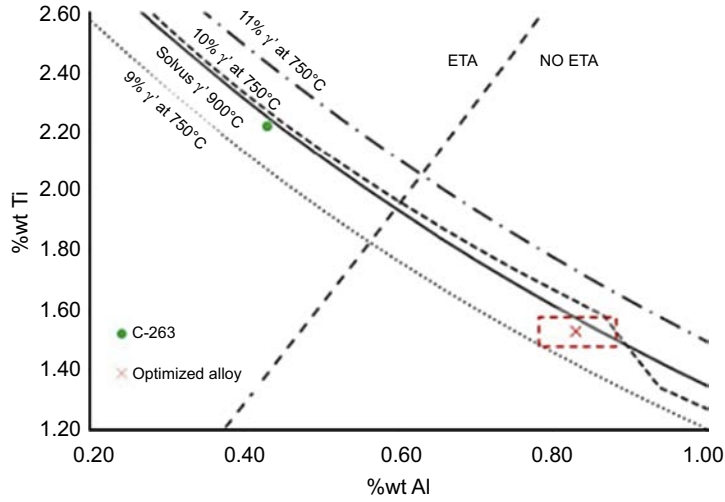


Figure 17.22 Thermo-Calc simulations to define stability window of η phase, γ' solvus, and γ' content at 750°C [18].

Table 17.6 Experimental compositions of tested alloys (weight percent) [18]

	Ni	Cr	Co	Mo	Ti	Al	C
C-263	Bal	19.7	20	5.8	2.2	0.42	0.05
Optimized alloy	Bal	19.7	20	5.9	1.53	0.79	0.05
Industrial cast	Bal	19.8	20	6.1	1.51	0.78	0.05

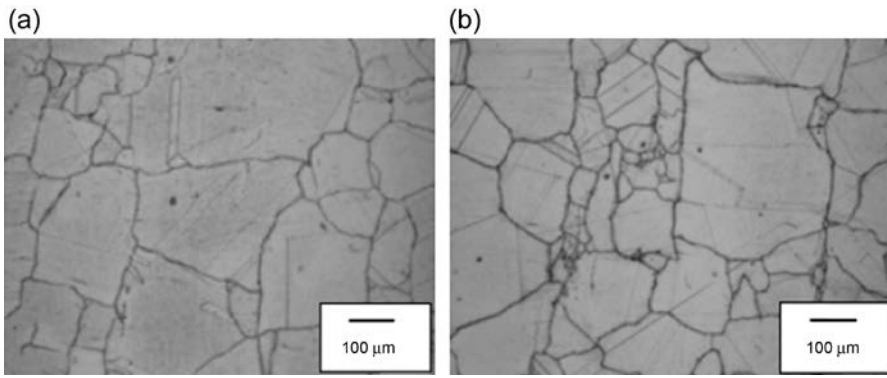


Figure 17.23 Optical micrographs of experimental alloys. (a) alloy 263; (b) optimized alloy [18].

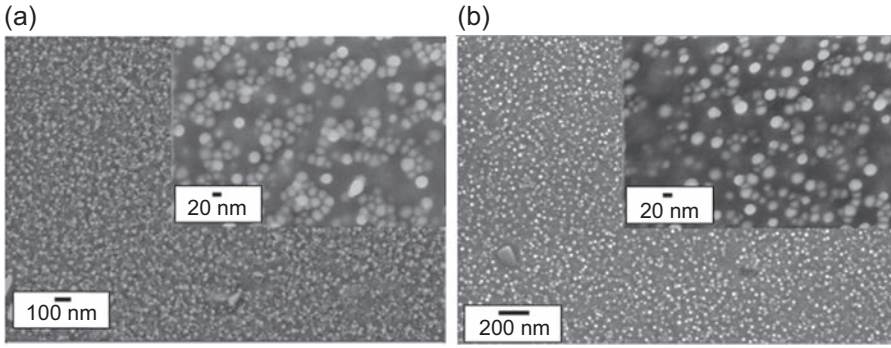


Figure 17.24 FEG-SEM micrographs after heat treatment: secondary γ' precipitates (around 22 nm) [19].

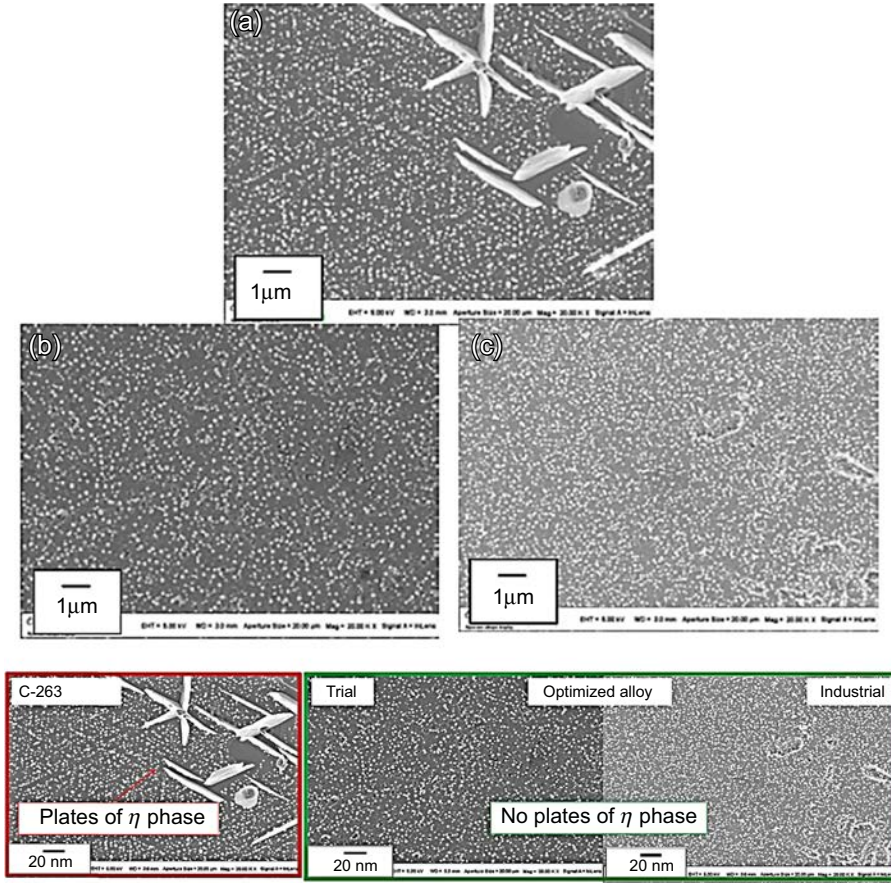


Figure 17.25 FEG-SEM micrographs after 3000 h/750°C [19].

Mechanical and creep properties are summarized in Fig. 17.26:

- Charpy impact tests and creep tests 750°C/250 MPa were performed on over-aged samples 50°C/3000 h.
- Results were compared with results obtained on not-over-aged samples.
- For optimized alloy, long-term aging at 750°C has no effect on impact strength, whereas it is highly decreased for standard A263.
- Higher influence of long-term aging on creep rupture life of standard A263 than for Optimized alloy was observed.
- Decrease of mechanical properties of standard A263 is mainly caused by η phase precipitation.

Table 17.6 shows also the results obtained in the 6-ton industrial cast produced by VIM + VAR Melting – ingot Ø640 (VIM + VAR) as shown in Fig. 17.27:

- Bar with diameter of 500 mm was forged.
- Four discs for welding trials were cut off and heat treated.
- Remaining material was reforged to Ø300 mm and heat treated.
- Mechanical properties will be compared with rotor with the same diameter but forged from standard A263 in Saarschmiede.

17.11.1 Conclusions

Aubert & Duval has optimized C-263 grade based on these points:

- higher microstructure stability regarding η phase
- similar workability and properties as C-263
  - similar γ' solvus temperature
  - similar γ' content at 750°C

Trial and industrial tests were performed and demonstrated that chosen composition of optimized alloy satisfies the three criteria of material design.

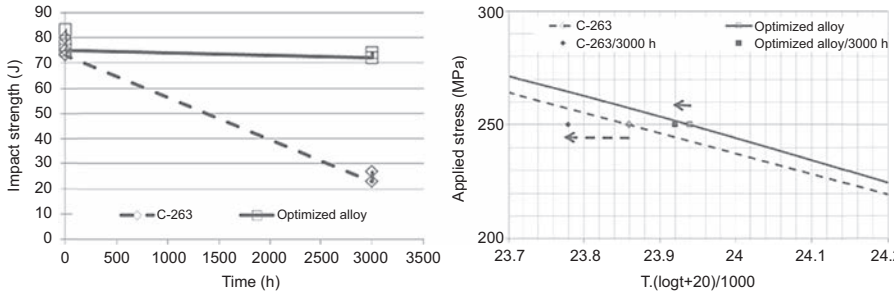


Figure 17.26 : Impact strengths and creep results on C-263 and optimized alloy without and with over-aging at 750°C/3000 h [18].

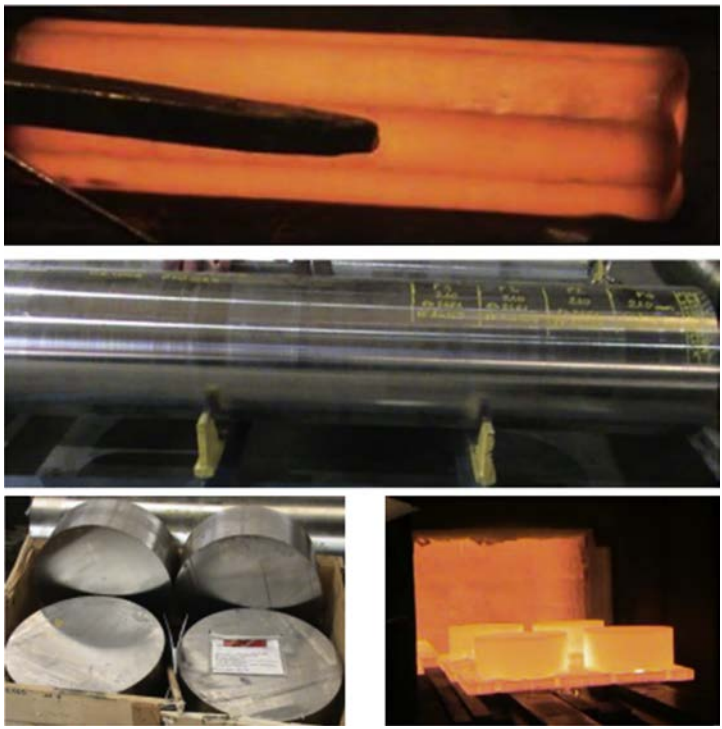


Figure 17.27 Industrial cast production steps [17].

17.11.2 Optimized alloy versus C-263

Microstructure:

- after standard heat treatment: similar grain size and same population of secondary γ' precipitates,
- after long-term aging: no η-phase precipitation after long-term aging.

Mechanical properties:

- after standard heat treatment: similar properties; tensile properties could be improved with a better arrangement of Ti and Al contents,
- after long-term aging: no decrease of impact strength and creep rupture life for optimized alloy.

The new composition seems promising for a new superalloy with high potential for applications at high temperature and long time in future A-USC steam turbines.

17.12 Corrosion and oxidation

17.12.1 Fireside corrosion

INCONEL alloy 740H, alloy N06230, NIMONIC alloy 263, and INCONEL alloy 617 test specimens (base metal samples denoted with "B" and matching all-weld metal

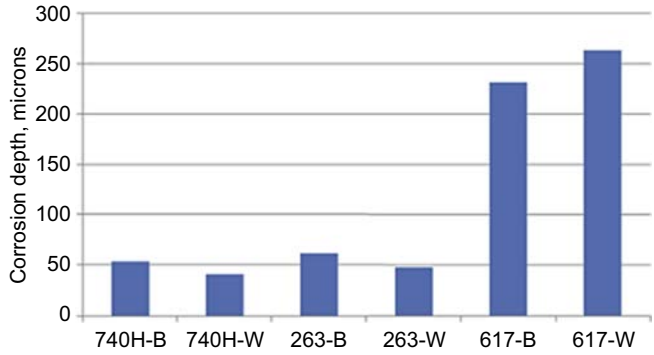


Figure 17.28 Attack depth after simulated coal ash corrosion exposure at 750°C (1382°F) for 1000 h. Base metal, "B"; all-weld metal, "W" [20].

samples denoted with "W") were exposed at Special Metals Corporation at 750°C (1292°F) for times to 1000 h in a synthetic flue gas composition of 15 Vol. % CO_2 + 5.0% Vol. % H_2O – 3.5 Vol. % O_2 + 0.1 Vol. % SO_2 + Bal. N_2 and a specimen coating of synthetic coal ash consisting of 6% Fe_2O_3 – 29% $CaSO_4$ – 1.9% Na_2SO_4 – 1.9% K_2SO_4 – 39% SiO_2 – 22% Al_2O_3 – 0.05% KCl – 0.05% NaCl. Samples were cycled to room temperature at weekly intervals and re-coated. Fig. 17.28 shows corrosion depth measurements with reference to the original sample surface after 1000 h of testing. Photomicrographs of sample cross-sections are shown in Fig. 17.29. Significant pitting corrosion is evident in the alloy 617 sample; incipient pit formation was noted in the alloy 263 sample as well [20].

17.12.2 Steam oxidation

The steam oxidation resistance of candidate alloys for an A-USC is a further consideration in selecting an alloy for the boiler, superheater, and reheater tubing, and the header and transfer piping. The concern is that steam-side oxidation could potentially lead to wall loss, compromising structural integrity as well as act as an insulating barrier to heat transfer. Loose scale can also lead to clogging of the tubes.

Fig. 17.30 shows oxidation depth results from exposure of coupons of alloy INCONEL 740H and NIMONIC alloy 263 in air + 10% water vapor at 800°C (1470°F) for 3077 h. Samples were cycled to room temperature once per week [20].

Other two steam oxidation tests were conducted, one at high pressure and one at atmospheric pressure. The atmospheric pressure test was designed to mimic the time and temperatures of the high-pressure test. In this case, six alloys (230, 263, 282, 617, 625, 740) were examined and results compared [21].

Triplicate samples were exposed in the high-pressure test. One specimen of each alloy was exposed in the atmospheric pressure test.

The total time at 670°C was 293 h, with a pressure of 267 ± 17 bar. For most of the test, water was injected into the autoclave at a rate of 4.5 g/min. The density of water under these test conditions was 0.0675 g/cm^3, with a resulting water velocity at test conditions of 2.1 mm/min.

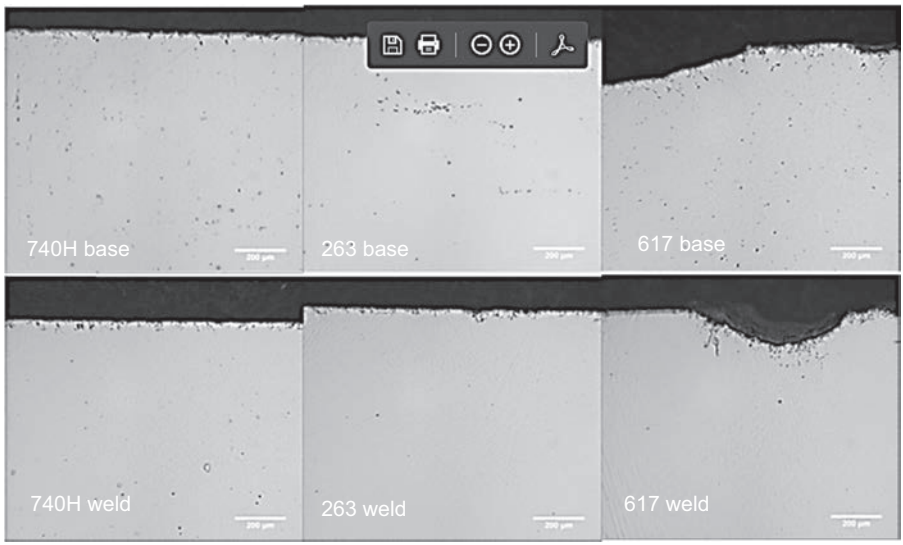


Figure 17.29 Photomicrographs of cross-sections from samples of alloys 740H, 263, and 617 after simulated coal ash corrosion exposure at 750°C (1382°F) for 1000 h [20] (Marker line = 200 μm).

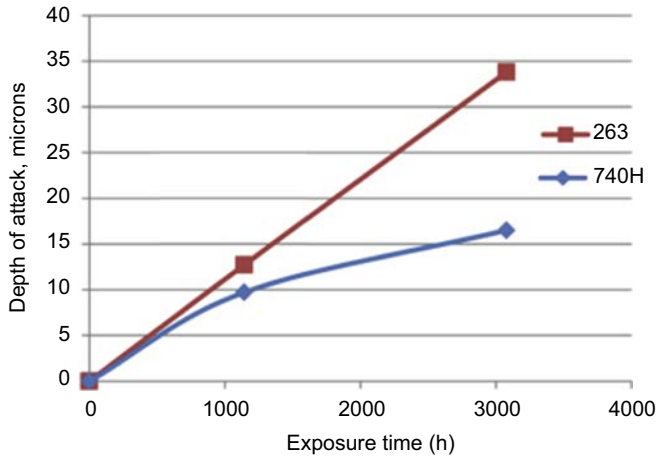


Figure 17.30 Depth of oxidation results for alloys 263 and 740H after 3077 h of exposure in air + 10% water vapor at 800°C (1470°F) [20].

The atmospheric pressure test was programmed to mimic the time and temperature profile of the high-pressure test. The test medium was steam with 10% Ar, flowing at a rate of 25 cm/min (at temperature). The Ar carrier gas helped to prevent backflow of air from the water condensing exit line during temperature fluctuations in the furnace.

Data collected included mass change measurements, scanning electron microscopy (SEM) of the surfaces, cross-sections of exposed samples using back-scattered electrons (BSE), and microanalysis using wavelength dispersive spectroscopy.

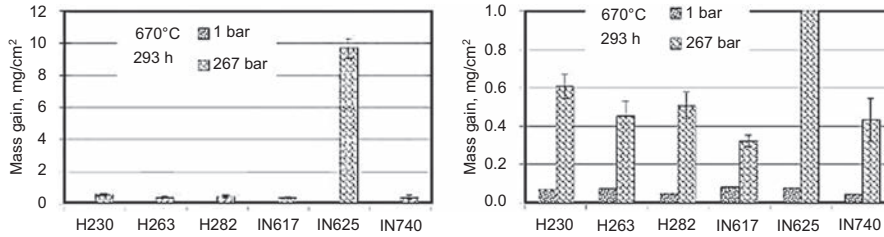


Figure 17.31 Mass gain results after 293 h at 670°C for high-pressure and atmospheric pressure steam oxidation exposures. The plot on the right shows the same data as on the left but with an expanded scale [21].

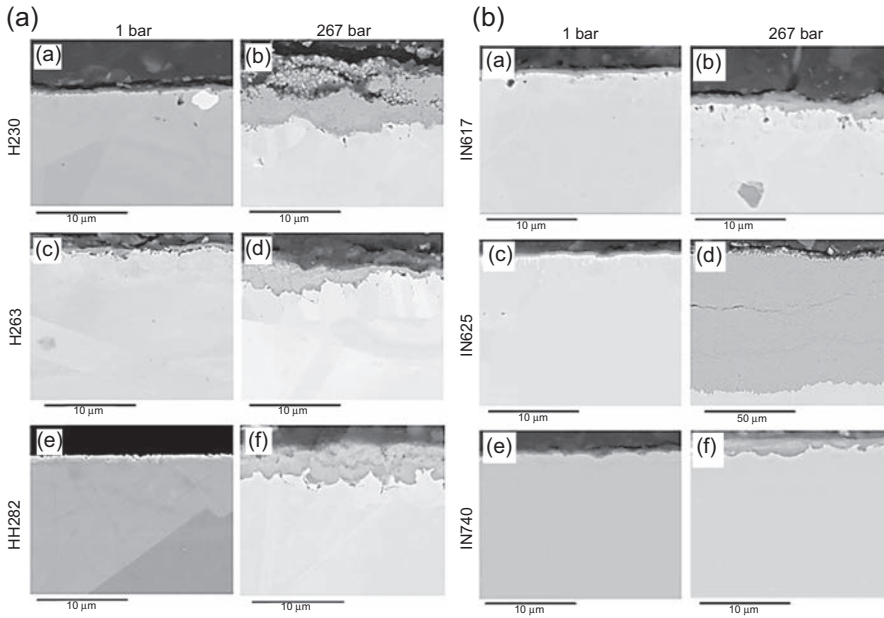


Figure 17.32 BSE cross-section images of all the alloys after 293 h exposure at 670°C in steam [21].

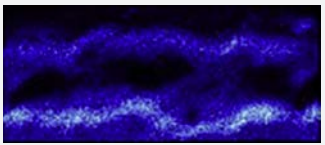
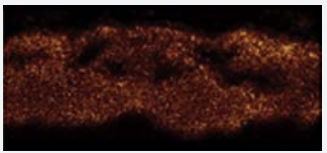
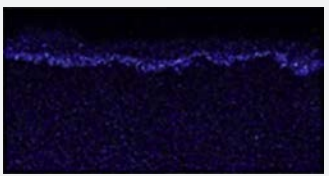
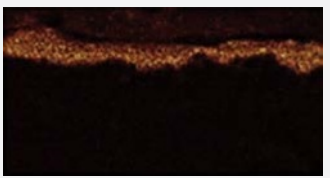
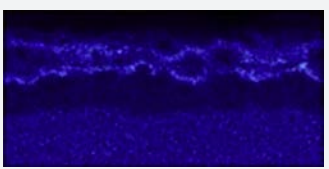
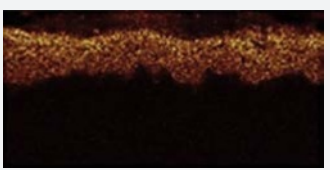
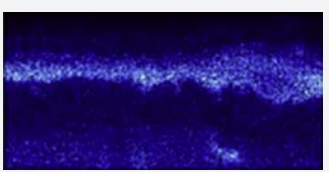
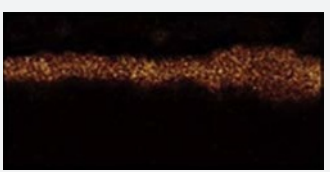
Mass change data for the high-pressure and atmospheric pressure tests are shown in Fig. 17.31. The error bars on the high pressure data show the standard deviation from triplicate samples. In all cases the high pressure mass gains were higher than at atmospheric pressure.

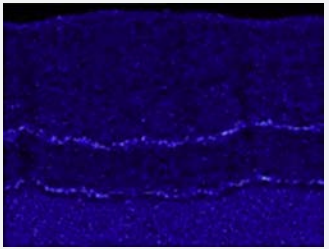
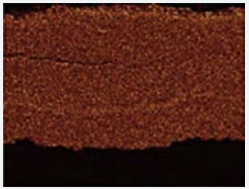
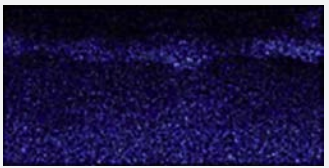
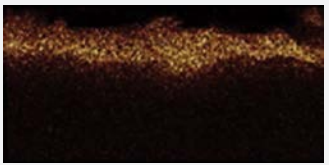
Cross-sections are shown in Fig. 17.32. All six of the 1-bar cross-sections show a thin, dense, and compact scale that is presumably chromia, but too thin for accurate SEM microanalysis.

The oxide scales at 267 bar are thicker, and much thicker in the case of IN625.

Table 17.7 shows elemental maps of Cr and O for 267 bar exposures. Alloys 230 and 282 have thin ribbons of high Cr oxide within the scale. Alloys 263 and IN740 have a layer of high Cr oxide near the metal–scale interface, and alloy IN617 has high

Table 17.7 **Scale morphologies and maps of Cr and O after 293 h exposure at 670°C and 267 bar in steam [21]**

Alloy	Brief description	Cr map	O map
H230	High Cr ribbons		
H263	Variable thickness, thin sections have high Cr oxide near the alloy interface		
H282	High Cr ribbons		
IN617	High Cr oxide throughout		

IN625	Very thick oxide scale with overall metal ratios similar to that of the alloy. Some high Cr ribbons		
IN740	High Cr oxide near the alloy interface		

Cr oxide throughout. The oxide scale for IN625 has overall metal ratios close to that of the alloy. There are ribbons of higher Cr content similar to those found in the much thinner scales on H230 and H282. The thicker scales for these alloys, as compared to the 1-bar exposure, correspond to the mass gain behavior shown in Fig. 17.32.

References

[1] N. Alloy 263. www.specialmetals.com.
[2] H.263 Alloy. www.haynesinternational.com.
[3] http://www.aircraftmaterials.com/data/nickel/C263.html.
[4] S.A. Smith, G.D. West, K. Chi, W. Gamble, R.C. Thomson, Microstructural Evolution in Nimonic 263 for High Temperature Power Plant. https://dspace.lboro.ac.uk/2134/15338.
[5] J.C. Zhao, V. Ravikumar, A.M. Beltran, Phase precipitation and phase stability in Nimonic 263, Metallurgical and Materials Transactions A-Physical Metallurgy and Materials Science 32 (6) (2001) 1271–1282, http://dx.doi.org/10.1007/s11661-001-0217-4.
[6] G.V.S. Murthy, K. Anish, G. Sridhar, T. Jayakumar, R.N. Ghosh, Characterization of precipitation behavior in Nimonic 263 by Ultrasonic velocity measurements, Review of Progress in Quantitative Nondestructive Evaluation, Vols 28a and 28b 1096 (2009) 1252–1258.
[7] C.T. Sims, N.S. Stoloff, W.C. Hagel, Superalloys II High-temperature Materials for Aerospace and Industrial Power, first ed., John Wiley & Sons, United States of America, 1987.
[8] R. Pohja, A. Nurmela, S. Holmström, P. Moilanen, Creep-Fatigue Properties of Nickel-Base Superalloy 263: Baltica, 2013.
[9] X. Xie, Y. Wu, C. Chi, M. Zhang, Superalloys for Advanced Ultra-Super-Critical Fossil Power Plant Application. http://dx.doi.org/10.5772/61139.
[10] B. Hicks, M. Heap, Report No, B48749, Lucas Gas Turbine Equipment Ltd., Materials Laboratory, Burnley, September 25, 1968.
[11] X.S. Xie, J.X. Dong, J. Wang, Structure Stability Analyses on Nimonic 263 After Long Time Stress Rupture Tests (internal report), High Temperature Materials Research Laboratories, University of Science & Technology, Beijing, 2011.
[12] Y.-H. Zhang, D. Knowles, Micromechanisms of Creep Deformation of C263 Superalloy, Interim Report 2/AT29, UTC, Department of Materials Science and Metallurgy, Cambridge University, UK, 2001.
[13] W. Betteridge, J. Heslop, The Nimonic Alloys, Edward Arnold, UK, 1974.
[14] M. Schmitz-Niederau, O. Trunova, State of the art of welding of high temperature materials for modern power plants, in: J. Lecomte-Beckers, O. Dedry, J. Oakey, B. Kuhn (Eds.), 10th Liege Conference: Materials for Advanced Power Engineering 2014, September 14–17, 2014.
[15] V. Knezevic, N. de Boer, A. Di Gianfrancesco, A. Schneider, J. Klöwer, Creep behaviour of heavy wall Alloy 617occ and C263 seamless pipes for 700°C power plants technology, in: 13th Int. Conf. on Creep and Fracture of Engineering Materials and Structures, 31.05.2015–04.06.2015. Toulouse, France.
[16] S. Hřeben, C. Crozet, B. Donth, Rotor forgings and welding, invited lecture, in: J. Lecomte-Beckers, O. Dedry, J. Oakey, B. Kuhn (Eds.), 10th Liege Conference: Materials for Advanced Power Engineering 2014, September 14–17, 2014.
[17] S. Hreben, P. VitekV. Polivka, , Demonstration of heterogeneous welding of nickel-based alloys in manufacture of full-scale welded rotor for A–USC turbine, in: J. Lecomte-Beckers, O. Dedry, J. Oakey, B. Kuhn (Eds.), 10th Liege Conference: Materials for Advanced Power Engineering 2014, September 14–17, 2014.

[18] C. Crozet, A. Devaux, D. Bechet: Microstructure stability: optimisation of 263 Ni-based superalloy. http://dx.doi.org/10.1051/matecconf/20141417006.
[19] C. Crozet, A. Devaux, D. Bechet, Microstructure stability: optimisation of 263 Ni-based superalloy, EuroSuperalloys 2014 (May 2014) 12–14 (Gience, France).
[20] INCONEL® ALLOY 740H® A Superalloy Specifically Designed For Advanced Ultra Supercritical Power Generation. www.specialmetals.com/…/PCC%20EG%20740H%.
[21] R. Gordon, Holcomb: High Pressure Steam Oxidation of ni-base Superalloys in Advanced Ultra-Supercritical Steam Boilers and Turbines. www.osti.gov/servlets/purl/1178148/.

This page intentionally left blank

Welding technologies for advanced ultra-supercritical power plants materials

18

S. Sorrentino
Welding Consumables Research & Development, Air Liquide Welding, Italy

18.1 Introduction

Materials for next-generation A-USC fossil-fired power plants are going to be used in welded constructions similarly to current USC steels, with design of members and equipments resembling broad established concepts. As a consequence, the range of semifinished products is not going to vary compared to the current one, the expected higher creep strength and corrosion resistance of the A-USC base materials (BMs) mainly influencing the size and thickness.

Thus, fusion arc welding will continue to be the key fabrication technology as well. R&D in this sector has been intense in the last decade, with demonstrative welded articles or full-scale mock-ups used to validate the developed concepts, including service in test loops. As of today, welding technology and associated filler materials are sufficiently mature, at least for some specific grades and a limited choice of arc welding methods, for undertaking such kind of manufacturing. Difficulties still exist mainly for ferritic steels because promising BM candidates emerged only very recently, and nickel-based alloys due to delicate weldability; unlike, most A-USC austenitic grades are considered of good weldability and fabricability, and their use has been already introduced in state-of-art USC designs. Also, dissimilar metal welding (DMW) is an area of great complexity and concern, with qualification of the various solutions currently being undertaken. Anyway, no welding solution has been used straightly on large-scale A-USC manufacturing so far.

It is also important to recognize that in any A-USC alloy system (ferritic, austenitic steels, and nickel alloys), there are numerous candidates to enter the market for the same application or plant section; these alloys are often either proprietary or derived from publicly funded large R&D programs worldwide, also according to the industrial tradition of the relevant geographical area [1–5]. This, of course, is enlarging the efforts for the development of matching welding consumables. Moreover, the metallurgical behavior of some A-USC alloys can strongly limit or make extremely difficult the usage of high heat input methods or slag-forming filler metals. Anyway, most of the common welding methods routinely employed in boiler construction, pipework and during manufacturing of cast and forged components can be successfully employed for manufacturing A-USC equipment. Due to the difficult fabricability of sound large semifinished products of Ni or Fe-Ni alloys, welding of subcomponents will play a larger role in cost-effective A-USC metal manufacturing.

Materials for Ultra-Supercritical and Advanced Ultra-Supercritical Power Plants.
http://dx.doi.org/10.1016/B978-0-08-100552-1.00018-X
Copyright © 2017 Elsevier Ltd. All rights reserved.

In general, at least for A-USC ferritic steels and nickel grades, improved properties are obtained due to precise minor alloying additions. Weld metal (WM) compositional ranges and cleanliness requirements are often very tight and not easy to be consistently achieved during field welding; this is to say welding technologies for A-USC power plants require the highest care in the process and the selection of adequate filler material, which have to be carefully coordinated to the BMs as well as to the operation conditions. There is obviously the need for accumulating experience in large fabrication and long-time service at high temperature.

This chapter aims to introduce the broad topic, addressing the most recurrent behavior and difficulties. Additional details can be also found in the specific chapters dealing with the different A-USC BMs.

18.2 Experience accumulated in other industrial fields

It is well apparent the development of filler materials and the welding technology for A-USC austenitic steels and nickel alloys has taken advantage from the experience accumulated in other industrial applications, especially the process industry and aero-engine manufacturing. Some candidate BMs themselves are evolution of grades that have been using for decades in these industries. It is anticipated that previous use of some specific grades in other industrial applications has shortened the development of the matching filler materials, if not even of the very same BMs. This typically has been the case of austenitic steels and nickel alloys.

A typical example is the use of wrought 617 (UNS N06617) nickel alloy (and its various "nuances", the 617B/CCA (ASME Code Case 1956) or 617 Mod. being the most prominent) for thick boiler components like headers and heavy walled pipework [6]. Close filler metals matching compositions have existed for a long time for joining in the process industry under the designation E/ER NiCrCoMo-1 (AWS A5.11). Another notable application is the use of nickel alloy 625 (UNS N06625) for cast components or steam turbine casings [7]. Matching consumables for joining thick-walled sub-castings or repair (now needed) are closely related to those have been used in the process industry for joining or cladding. Also austenitic steel candidates for A-USC application have their close equivalent in the process industry like the well known AISI 304H or 310H grades.

Additions to the original formulations were made to enhance the creep strength, allowing usage beyond 650–700°C. This has usually brought additional weldability problems aside to the expectable behavior. Additionally, use outside the fossil power generation has been limited to thin-wall members or cladding.

18.3 Weldability and welding metallurgy (ferritic, austenitic steels and nickel alloys)

18.3.1 Welding of A-USC ferritic steels

The current 9–12% Cr martensitic steels will continue to be used also in the A-USC power plants, but only for the components having 600–620°C as maximum service temperature. The ferritic matrix is very desirable due to the low thermal expansion coefficient and the good thermal transfer.

This class of A-USC materials is populated by many candidates for thick-walled pipework, with intense R&D efforts on BM itself still underway compared to austenitic steels and nickel alloys. No single grade has emerged with distinct advantages over the existing best-in-class Grade 92 steel martensitic steel or its equivalent FB2/CB2 forged and cast grades, when one comes to the entire spectrum of mechanical, corrosion, or technological properties the next-generation alloy must possess. Basic weldability, short-term or long-term fusion weldment mechanical properties have played a significant role in frustrating the development efforts so far.

Direction of development on the welding fabrication side has been the avoiding of non-ferritic WMs for joining A-USC ferritic grades, the improvement of the creep weld strength factors (WSF), and avoiding or reducing the type IV cracking tendency during creep exposure, all retaining short-term room or high-temperature properties close to the existing ones or above the minimum codes requirements. The availability of an 11%Cr weldable grade for thick headers or pipework is especially sought for adequate oxidation resistance at higher temperature, especially after that the P122 steel (also known as HCM12A, 12Cr-1.5W-Mo-V-Nb-N) usage in welded members has been discontinued due to the lack of long term microstructural stability.

This class of A-USC steels considered for welding is currently loosely based on the 9–11% Cr steel alloy system with martensitic microstructure after normalizing and tempering (N + T) heat treatment or precipitation strengthening from complex phases. Most of them are in early stage of R&D programs, in which weldability, matching WM development, heat affected zone (HAZ) behavior and effect of PWHT have not been completely evaluated. Alloy concepts being exploited to go beyond the grade 92 (9Cr0.5Mo1.5WVBNbN) systems include many grades with 11% nominal Cr content for enhanced corrosion strength, as summarized below:

- Strengthening with Co, W, B, Nd, and N additions (9%Cr MARtensitic steel strengthened by Boron and Nitrides (MARBN)), also allegedly promoting the avoidance of type IV cracking in HAZs. Control of the B and N content, together with increased normalizing temperatures are required to generate the optimum microstructure without coarse boron nitrides precipitates. The most notable feature is the apparent lack of an fine grain heat affected zone (FGHAZ) in the new MARBN-type steel originally developed at the National Institute for Materials Science in Japan. They contain nominally 9% Cr, 3% Co, and 3% W; hence, the designation 9Cr3W3CoVNbBN is commonly used to describe the family [8].
- Similar compositions to MARBN steels, known under the name SAVE12AD (9Cr2.9 WCoVNbTaNdN steel) where Nd and Ta are claimed to improve the creep strength of

welded joints. Filler material studied were alloy 82 alongside the gas tungsten arc (GTA) method [9].

- Exploiting the intentional formation of the Z-phase (Z steels) with limited addition of Ta or similar elements, to get a fine initial Z-phase distribution, replacing the strengthening effect given by MX precipitates in conventional steels [10].
- Avoiding the precipitation of the detrimental Z-phase in the long term for 11% Cr steels (as occurring in thick P122 members) by removing altogether Nb alloying, thus obtaining a long-term stable MX precipitation [10].
- Avoiding the precipitation of the detrimental Z-phase in the long term for 10% Cr steels by removing nitrogen alloying, thus preventing the formation of (V,Nb) nitrides and ultimately the Z-phase [11].

On a theoretical ground, as for USC steels, WMs have in principle to match BM compositions for comparable creep strength and corrosion resistance.

Basically, the class of MARBN steels have seen more efforts so far, seemingly solving all the issues only very recently, as demonstrated from the inclusion (ed. 2015) of the grade 9Cr2.9WCoVNbTaNdN (designation 9Cr-3W-3Co-Nd-N) in the ASME Boiler and Pressure Vessel Code under the Case 2839 for tubes, pipes, and forgings in the N + T condition. Use of this material is allowed by the code up to 649°C; welding qualification has to be performed according to the Sec. IX, under the P-No. 15E, Group 1. PWHT is mandatory with temperature in the range 730–790°C. The concept was proposed claiming that the controlled addition of B and N could suppress the type IV cracking in the HAZs, potentially removing the main limiting factor for full exploitation of the BM excellent creep properties. This behavior has been much studied using simulated HAZ specimens obtained by Gleeble thermo-mechanical simulator. It has been widely reported that fusion weldment HAZs apparently lack the fine-grain zone, thus eliminating the weak portion normally subjected to the degradation and eventual failure during creep exposure [12–14].

Weldability issues are similar to the existing CSEF grades, the control of which requires preheating and control of the thermal cycle including managing the critical temperatures and need of PWHT for reducing hardness peaks and restoring ductility and room-temperature notch toughness. This latter property has especially proved extremely difficult to achieve consistently for HAZs and matching WMs, preventing the application on code-governed constructions [15]. Testing of MARBN fusion arc weldments for creep in the very long term ($>10^4$ hours) has also not been demonstrated extensively [15]. In the mid-term, extrapolated creep results on PWHT weldments have demonstrated WSF is close to 1, a behavior current martensitic steels welds approach only after complete N+T treatment. Evaluation of the WSF is especially complicated, because so far no matching WM has been developed with the adequate creep strength. As cross weld creep tests were mainly made on weldments with either Ni-based WM, lower creep strength fillers (like P92-type) or even using non-arc methods, the MARBN HAZ behaviour has not been extensively tested with the constrain associated to a typical fusion weld. Thus, claimed WSF figures could be subjected to revision as new data become available. Fig. 18.1 shows the creep behavior of early MARBN steel weldments.

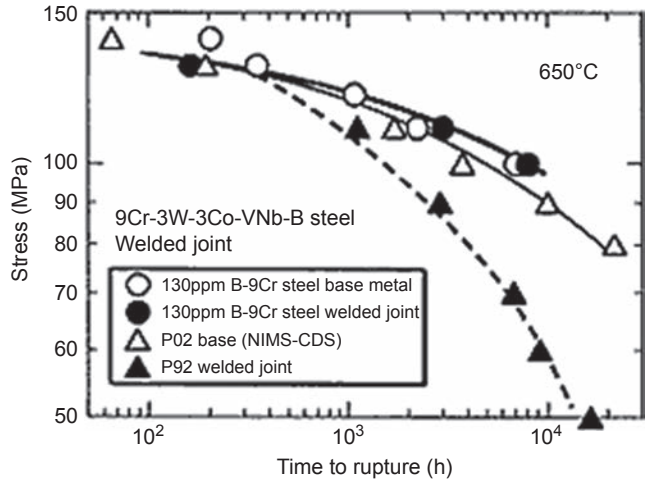
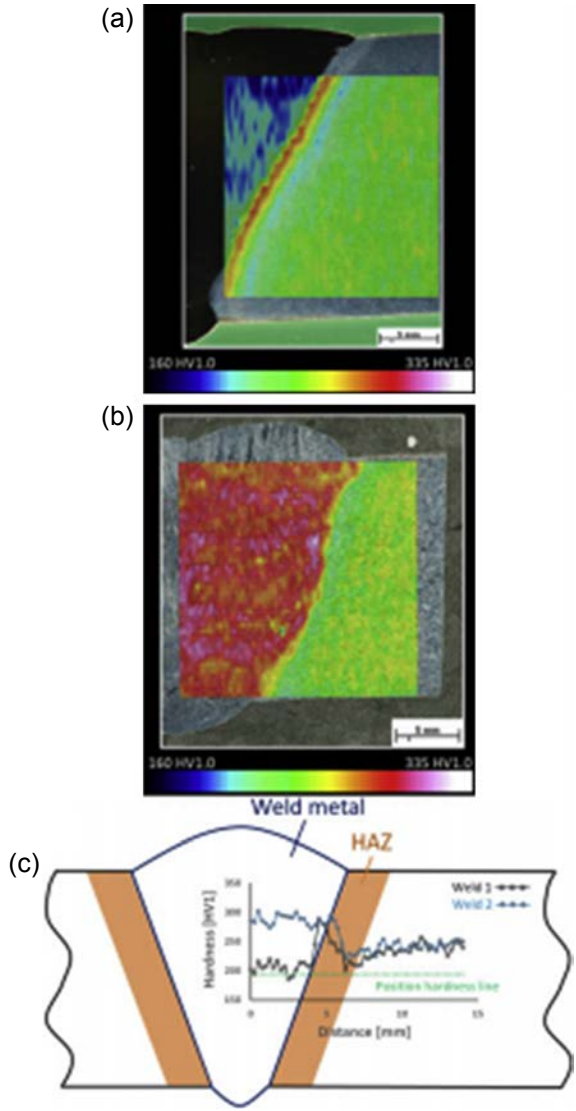


Figure 18.1 Creep rupture data of NIMS (Japan) for parent steel and cross-weld specimens of 92 grade and a boron-containing steel tested at 650°C [12].

Solidification cracking of boron-containing WMs, difficulty in obtaining sufficient notch toughness at room temperature and the control of the nitrogen to boron ratio has led to the use of Ni-based consumables (Fig. 18.2) for welding MARBN semifinished products, with composition of the Inconel 625 or Inconel 182 type [16]. If such alloys are used, of course, any creep failure is moved away from the WM, and notch toughness requirements that can be easily met in the WM.

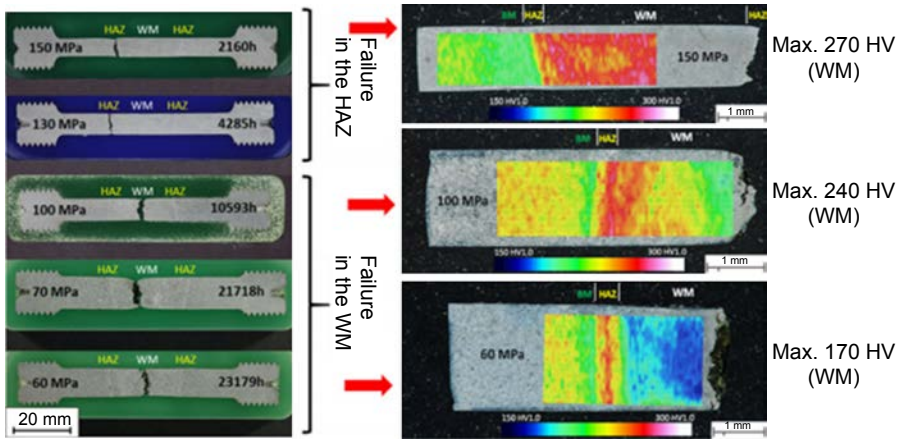
The development of matching fillers for MARBN grades has been approached in the most straightforward way with the GTA method and solid wires with similar chemistry. Success has been reported at least in obtaining sound multilayer weldments. Virtually no result for full qualification of a MARBN weld has been reported, including evaluation of AWM properties, HAZ notch toughness and ductility. Creep failure in the WM has been reported with a PWHT of 4 h at 740°C (see Fig. 18.3). The precise ratio between B and N has to be maintained also in the WM; this is a serious difficulty even when using the GTA method due to the nitrogen adsorption/desorption from the weld pool (Table 18.1) [15,16].

For tubing applications up to 10 mm thickness, a 12%Cr grade (12Cr1.5W1.5CoB) has been recently approved for usage up to 620°C in welded construction (VM12-SHC, ASME Code case 2781). Welding has been proved feasible and matching consumables made available for the GTA and SMA methods. Notch toughness is very close to the limit allowed for ferritic welds (27J) after a PWHT of 770°C, despite the Ni alloying of the WM. Co alloying prevents the formation of delta ferrite without suppressing the Ac_1 temperature (see Table 18.2). Temperature control during welding has to be tight for sufficient weldments mechanical properties (Fig. 18.4) [17].



a weld 1 - GTAW process using NBAS 70V20 filer metal: *b* weld 2 - GTAW process using matching 9Cr filer metal:
c comparison of hardness distribution across fusion line of weld 1 and weld 2

Figure 18.2 Hardness maps of MARBN weldments with both a Ni consumable and matching composition [13].



Hardness maps including weld metal (WM), HAZ and base material (BM) of failed crosswelds (weld 2) at 150, 100 and 80 MPa

Figure 18.3 Failure modes and associated hardness maps for the MARBN test weldments [15].

Table 18.1 Filler material (as rods and solid wire, respectively) compositions used in the study on MARBN weldments (elements concentration in wt.%, Fe remainder) [15]

Analysis	C	Si	Mn	Cr	Ni	W	V	Nb	Co	Fe	B	N
Ni-based filler (Weld 1), GTA multilayer welding	0.02	0.1	3.1	20.5	bal.	…	…	2.9	…	<1.0	…	…
9Cr MARBN-type filler (Weld 2), GMA multilayer welding	0.090	0.20	0.4	9.4	…	2.9	0.2	0.05	2.9	bal.	0.01	0.014

No undiluted all-weld-metal composition has been reported.

18.3.2 Austenitic grades (304HCu, TP347HFG, 310N(HR3C), Tempaloy AA-1, Sanicro25, HR6W, HR35 steels)

Most mature candidates with Fe austenitic matrix in the A-USC class include grades to be used mainly in next-generation superheater/reheater tubes (304HCu, 310N (HR3C), Sanicro25, Tempaloy AA-1) and in seamless thick-walled components (HR6W, HR35, Fe-45Ni alloys). Cr content ranges between 18% and 30%, with complex additions of Cu, W, B, Ti, and Nb depending on the specific grade (see details in the relevant BMs chapters). Maturity of such BMs is excellent for

Table 18.2 Mechanical properties of VM12-SHC tube weldments [17]

Chemical composition of pure deposited metal in % (Fe remainder)												
	C	Si	Mn	Cr	Ni	Mo	V	W	Nb	N	Co	B
GTAW	0.17	0.2	0.43	11.6	0.40	0.3	0.22	1.44	0.06	0.04	1.64	0.003
SMAW Ø 4.0 mm	0.13	0.33	0.66	11.2	0.79	0.33	0.24	1.48	0.06	0.05	1.59	0.003

Mechanical properties: (a) Pure deposited metal at RT						
Welding process	Heat treatment soaking temperature and time (°C/h)	Yield strength (MPa)	Tensile strength (MPa)	A_s (%)	CVN (ISO-V) (J)	Hardness HV10
GTAW	770/2	684	822	18.5	33/38/43/47/50	297
SMAW Ø 4.0 mm	770/2	689	832	17.2	40/41/42/48/49	281

(b) Welded joint, pipe Ø 140 mm; wall thickness 10 mm					
Welding process	Heat treatment soaking temperature and time (°C/h)	Tensile strength (MPa)	Fracture location	CVN (ISO-V)(J)	Hardness HV10
GTAW	770/0.5	745	Base metal	37/38/40	Max. 351
SMAW Ø 4.0 mm	770/2	728	Base metal	47/51/51	Max. 297

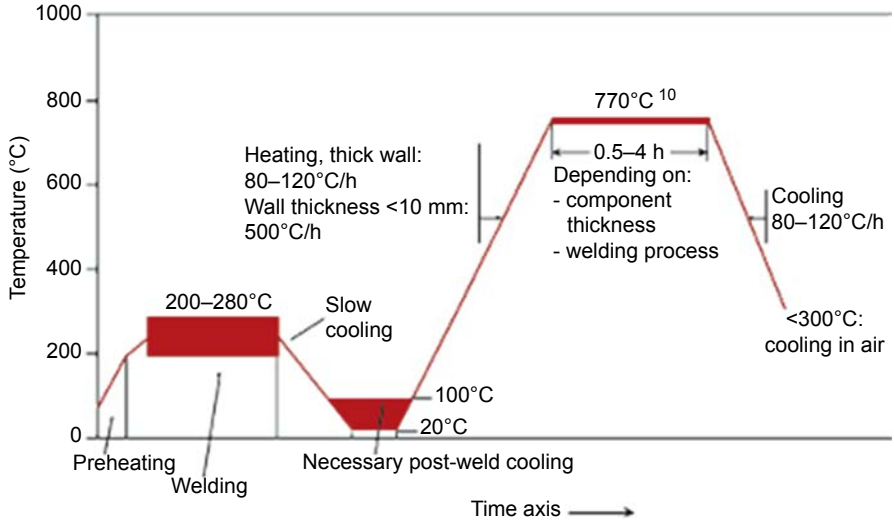


Figure 18.4 Temperature management during welding of VM12-SHC tubing [17].

tubing alloys (they are already approved in codes for USC manufacturing), while high-Ni alloy candidates for thick-walled components are emerging from the R&D stage. All these grades are, in principle, intended for use in the as-welded condition, with WMs mostly not matching the relevant BM. BMs are supplied in the solution annealed condition.

Weldability of austenitic grades is widely regarded as the most favorable between the various A-USC BMs classes; consumables are available for tubing materials for the tungsten inert gas (TIG) method and often as coated electrodes for the shielded metal arc welding (SMAW) method. Both types are very suitable for site erection and positional welding on thin weldments. So far, welding of 40–45% Ni steels has been accomplished using the GTA method with a Ni-based (matching alloy 617 composition) solid wire consumable [18].

When using Ni-based WMs, extreme cleanness of the welding environment is very important. For welding the 304HCu grade, nearly matching consumables are available with no delta-ferrite and Ni much higher than the BM, thus minimizing the risk of solidification cracking achieved by significant Mn alloying and very low impurities level [19]. All other grades have austenitic (γ) microstructure at all temperatures with no phase transformation. Thermal cycles associated with arc welding are sufficiently rapid to avoid any embrittlement in the HAZs with highest Cr content (25% nominal for 310N) after welding (this may not be the case after prolonged high temperature service).

When using Ni-based WMs, the creep damage is obviously moved to the HAZs.

18.3.3 Nickel alloys (617, 625, 740H, 263, 282)

Candidates of this class of A-USC grades are today a handful of alloys all required to be satisfactorily welded or repaired in shop. Their usage is to be exploited for thick-walled pipework (main steam pipe), boiler headers, or thin superheater tubing. The different candidates have not reached homogenous maturity. It is advised that large R&D programs worldwide have or could be developing their own “nuances” of the same mother alloy concept. Nevertheless, standard codifications also exist, eg, in the ASME BPV Code.

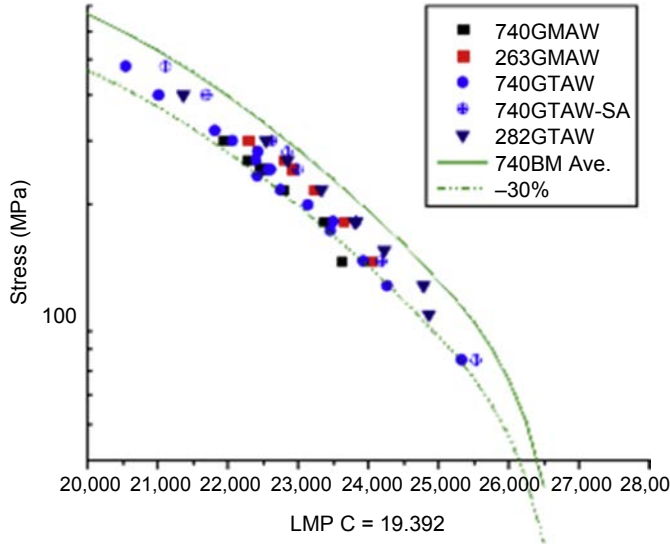
Alloy 617B is possibly the most mature and most frozen industrial candidate due to the longer engineering experience and a large amount of data generated, though not the most performing in its class. It is a Ni-Cr-Mo-Co solution strenghtened alloy with sufficient weldability, with austenitic microstructure at all temperatures. Controlled additions consist mainly in C, Al, Ti, and B. It is delivered in the solution annealed condition. A WSF of about 0.80 was found to describe the rupture behavior of a welded seam subjected to transversal creep stress [20].

Alloy C263 is another promising candidate with higher creep strength, in an earlier stage of industrial development for power plant applications. It is a precipitation strenghtened alloy subjected to artificial aging once manufactured [21].

Alloy 740H (UNS N07740) is claimed to have the highest strength and limit temperature capabilities of any other A-USC candidate Ni alloy, allowing the use

Table 18.3 **Evaluated compositions of alloy 740H (elements concentration in wt. %) [22]**

Heat	FM1	FM2	BM1	BM2	BM3	BM4	BM5	BM6	BM7	BM8
C	0.031	0.046	0.033	0.042	0.039	0.046	0.039	0.060	0.035	0.030
Mn	0.370	0.302	0.295	0.293	0.300	0.300	0.298	0.305	0.358	0.260
Fe	0.550	1.054	1.051	1.056	1.037	1.073	1.050	1.107	1.198	0.460
Si	0.190	0.220	0.219	0.497	0.243	0.223	0.503	0.269	0.201	0.510
Cu	0.0610	0.0050	0.0039	0.0039	0.0049	0.0059	0.0060	0.0270	0.0356	0.0200
Ni	Bal.	Bal.	Bal.	Bal.	Bal.	Bal.	Bal.	Bal.	Bal.	Bal.
Cr	24.13	24.34	24.25	24.48	24.46	24.60	24.27	25.38	24.27	24.34
Al	1.260	1.300	1.440	1460	1.460	1.280	1.380	1.080	1.230	0.970
Ti	1.310	1.497	1.420	1.417	1.430	1.148	1.696	1.483	1.373	1.780
Co	19.76	19.87	20.75	20.04	20.00	20.05	19.84	20.23	19.51	19.80
Mo	0.5800	0.5280	0.5347	0.5301	0.5420	0.5443	0.5369	0	0.5515	0.5000
Nb	0.930	1.585	1.050	1.048	1.308	1.557	1.569	1.617	1.516	1.990
P	0.0040	0.0032	0.0032	0.0030	0.0033	0.0033	0.0035	0	0	<0.005
B	0.0010	0.0008	0.0009	0.0007	0.0008	0.0009	0.0008	0.0003	0.0004	0.0037
V	0.0050	0.0075	0.0069	0.0074	0.0069	0.0079	0.0090	0.0024	0.0049	0
W	0.0020	0.0030	0.0024	0.0019	0.0029	0.0019	0.0040	0.0409	0.0426	0
Zr	0.0030	0.0244	0.0141	0.0128	0.0112	0.0123	0.0130	0.0246	0.0220	0.0250
N	<0.001	0.0030	0.0059	0.0075	0.0061	0.0047	0.0135	0	0.0119	0



ID	WSF
740GMAW	0.71
263GMAW	0.82
740GTAW	0.74
740GTAW-SA	0.88
282GTAW	0.85

Figure 18.5 Creep rupture behavior of alloy 740H weldments compared to the 740H BM [23].

up to 760°C (examples of compositions used in a systematic study are given in Table 18.3). It is a precipitation strenghtened grade featuring the Ni-Cr-Co-Mo-Nb-Al-Ti alloy system, subject to artificial aging once the component is manufactured. It features an austenitic microstructure (γ) with γ′ reinforcing precipitates, $M_{23}C_6$, G-phase, and ε−phase. It is proposed for utilization in the solubilized and aged condition. After welding, a PWHT is advised, similar to the original aging treatment (eg, 4 h at 800°C). Alternatively, the welded component can be subjected to the full annealing (1 h at 1120°C) plus aging. Thick, demonstrative multilayer weldments have been fabricated within a large R&D program with the hot wire GTAW process using a closely matching filler wire. Such weldments were claimed able to pass full procedure qualification as per ASME BPVC Sec. IX, being free from micro-fissuring or hot cracking in both WM and HAZ [22].

In Fig. 18.5, the creep rupture results for 740H weldments with a variety of WM and heat treatment conditions are between the average strength line of the base metal, shown by the *solid line*, and the −30% strength line of the base metal, shown by the *dotted line*. The 30% reduction in stress is equivalent to a WSF of 0.70. The

740GMAW and 740GTAW specimens exhibit a WSF slightly greater than 0.70, but the application of solution-annealing heat treatment after welding and prior to aging improves this to close to 0.90. The use of alternative filler metals, Alloy 263 and Alloy 282, was found to improve the WSF to 0.82 and 0.85, respectively. Rupture always occurs in the WM for aged weldments.

At room temperature, short-term tensile strength matched the BM; in the creep service condition, a WSF of 0.70 has been validated up to 10,000 h for matching WM after weldments aging, which can improve to match BM creep rupture strength for full annealing + aging.

Ni alloys can find successful use in the turbine side, either as material for casings or cast components or to manufacture rotors sections. Traditionally, alloy 625 has been proposed, and industrial use in welded construction has been demonstrated [24]. This alloy features a Ni-Cr-Mo-Nb alloy system, supplied in the annealed condition. Ni-based, thick semifinished products are more subject to alloy elements macrosegregation. This behavior is usually controlled by Vacuum Arc Remelting practice and homogenization heat treatments; thus, it is not usually a concern for weldability.

Weldability of nickel alloys has specific difficulties that have to be managed properly for a successful fabrication in thick members [25]. The dominant feature (ie, common to all grades to a various extent) is the susceptibility to hot cracking in the WM. The traditional methods to control the issue are to work with filler material of extreme cleanness for tramp elements, use no preheating, and limit the heat input and the interpass temperature to below 250°C (and the preheat in dissimilar metal welding with ferritic grades). It is also of the utmost importance to prepare the bevel edges by removing any trace of foreign matter. Weldability testing can be useful to assess the tendency of the specific grade/heat being welded; Transvarestraint testing has been traditionally used for this purpose [26]. Mo, Ti, Si, Nb, C, and B are elements all predicted (using computational thermodynamic calculations) to partition to the liquid phase upon solidification ($k<1$), thus enlarging the liquidus–solidus range and ultimately leading to increased tendency to hot cracking (Fig. 18.6) [27].

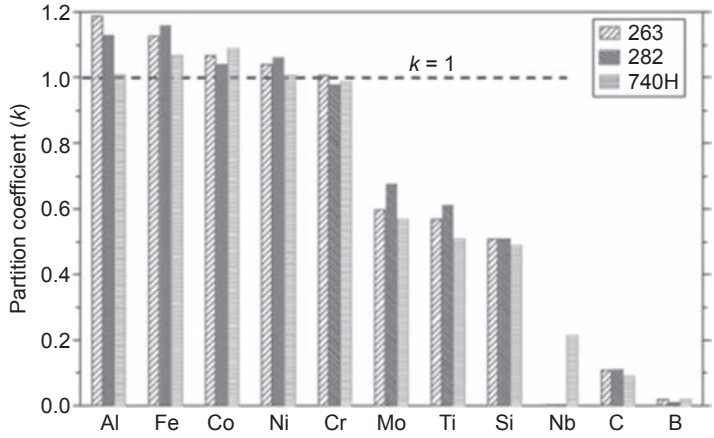


Figure 18.6 Partition of key elements during solidification for various Ni-base alloys [27].

Additionally, reheat cracking (also known as relaxation cracking) in the WM (or HAZs) affects to a various extent the alloys containing Al and Ti due to the formation of the strengthening γ′ precipitate at the grain boundary. The stress relaxation occurring in high-temperature service promotes the phenomena, especially in thick and restrained weldments. This difficulty is mostly avoided if the weldment has a lower fraction of γ′ precipitates, as in the C263 and 740H grades. Alloy 617B weldments are known to be sensitive to the issue; a PWHT of such welds has been proposed before entering in service to avoid this matter. Specific testing on WMs or simulated HAZs has been proposed to assess the specific tendency, as slow strain rate tensile testing at high temperature (eg, the intended service temperature). Evaluation is done on the reduction-of-area at fracture. It is important to remark that as soon the weldments are put in service at high temperature, the γ′ precipitates fraction will slowly increase over time; thus, stress relaxation cannot be completely ruled out in the longer term. This aspect still needs R&D effort, which is currently underway.

HAZs and WM hardening with respect to the BM were observed in Al + Ti-containing Ni alloys; this can be attributed to the strain hardening effect in heavily restrained weldments or precipitation hardening due to the weld thermal cycles. Solid solution alloys usually see the WM on a similar hardness level. This behavior holds also at high temperature [28].

Dealing with filler consumables, in Ni-base alloys the high-temperature strength is reached by two strengthening mechanisms: solid solution or/and precipitation hardening. Alloy 617 is a typical solid solution–hardened Ni-base alloy. Standard Ni-base alloy was modified to fulfil higher creep rupture properties at 700°C. In Alloy 617 Mod. the content of C, Si, Mn, and Fe is reduced, whereas the minimal contents of Cr, Co, Al, and Ti are slightly increased compared to Alloy 617. The higher amount of Ti in combination with Co addition in Alloy 263 results in the formation of Ni_3(Al,Ti) precipitates and thus in precipitation strengthening of the alloy. The chemical compositions of Inconel 617 Mod. and Alloy 263 WMs are given in Table 18.4. Their use is widespread for welding additional non-matching A-USC nickel alloys.

Alloy 617 Mod. can be welded in the same way as alloy 617, but the risk of hot cracking remains very high. The welding parameters should be adjusted to low interpass temperature (max. 150°C) and low heat input to restrict formation of hot cracks.

Table 18.4 Chemical compositions of weld metals for Inconel 617 Mod. and Alloy 263 (elements concentration in wt.%, Ni remainder) [29]

Alloy	Filler metal	C	Si	Mn	Cr	Co	Mo	Ti	Al	Fe
Inconel 617 Mod	Thermanit 617 D	0.06	0.6	<0.3	21.0	11.0	9.0	0.3	1.2	1.0
Alloy 263	Thermanit 263	0.06	0.7	<0.2	20.0	20.0	6.0	2.0	0.3	0.5

Moreover, it is difficult to set matching composition of the welds, especially for alloy 263 with higher Ti content, using existing filler metals.

Critical alloying elements have to be transferred gradually into the arc to avoid burn out of Al and Ti as well as to limit transfer of Si. After welding, a heat treatment of 3 h at 980°C or 4 h at 810°C should be carried out for alloy 617 Mod./alloy 263, which should prevent relaxation cracking under service conditions [30].

Further knowledge on A-USC material weldments is mandatory, also due to the comparatively higher raw material cost. Common areas of R&D research involve these aspects:

- Reduce the creep strength derating for longitudinal seams, allowing more profitable usage of large fabricated headers
- Avoid as much as possible Ni-based consumables on similar welding of martensitic and austenitic A-USC steels, thus developing matching compositions where still lacking
- Development of slag-forming consumables with ultra-low residuals; extend their usage of higher productivity methods (manual metal arc (MMA), submerged arc welding (SAW))
- More understating of the behavior of DMWs; study of the weldments behavior under creep-fatigue service
- Repair/alteration welding onto service-aged material

18.4 Arc welding consumables development, specific aspects of the welding procedures

All the three classes of A-USC alloys have specific metallurgical behaviors; when one comes to the development of matching filler materials, common difficulties are encountered, as summarized in Table 18.5.

Most of the Ni-based BM grades are produced by Vacuum Inert Melting/Vacuum Arc Remelting for the utmost purity and homogeneity, a practice not easy to be replicated for welding fillers.

Approaching the weldability studies has always started with the GTA method and a closely matching filler wire. To enhance productivity, the NG (narrow gap) variant has also been satisfactory employed. As of today, GTA remains the most mature and straightforward way to weld or weld repair the A-USC materials because, in principle, the inert shielding and precise control of the filler addition allows the following:

- to minimize the loss of crucial oxidable elements (eg, B, Ta, Al, Ti). Many Ni alloys have a relevant content of Al and Ti that cannot be transferred across the arc using welding methods other than inert gas shielding
- to control the nitrogen amount in the WM (where pertinent)
- to limit the BM dilution

Slag-forming consumables exist for selected solid solution Ni alloys; MMA and SAW fillers for welding alloy 625 are classified under the E/ER NiCrMo-3 type and for welding 617 alloy under the E/ER NiCrCoMo-1 classification. The latter alloy

Table 18.5 Specific development behaviors for A-USC matching filler metals

	Control of WM nitrogen alloying/weld pool loss	Control of oxidable elements (B, Ta)	Transfer of Al, Ti across the arc	Large fraction of precipitates	Stress relaxation	WM solidification cracking
Martensitic 9–11% Cr steels	Y	Y	NR	Y	NR	Y (boron-containing steels)
Austenitic steels, Fe-Ni alloys (eg, HR6W)	Y	NR	NR	NR	NR	Y (thus, on Fe-Ni alloys matching consumables are mostly avoided)
Solidification-strengthened Ni alloys	NR	NR	NR	NR	Y	Y (major issue)
Precipitation-strengthened Ni alloys	NR	NR	Y	Y	Y	Y (major issue)

Y, key aspect; *NR*, aspect not relevant for the material and the application being considered.

Table 18.6 AWS composition ranges for alloys 82, 617, and 625 (ASME boiler pressure vessel code – specifications for welding rods, electrodes, and filler metals. SFA-5.14/SFA-5.14M specification for nickel and nickel-alloy bare welding electrodes and rods)

	Weight percent[a,b]																	
AWS classification[f]	**UNS number[c]**	**C**	**Mn**	**Fe**	**P**	**S**	**Si**	**Cu**	**Ni[d]**	**Co**	**Al**	**Ti**	**Cr**	**Nb(Cb) plus Ta**	**Mo**	**V**	**W**	**Other elements, Total**
ERNi-CrCoMo-1	N06617	0.05 to 0.15	1.0	3.0	0.03	0.015	1.0	0.50	Rem	10.0 to 15.0	0.8 to 1.5	0.60	20.0 to 24.0	–	8.0 to 10.0	–	–	0.50
ERNiCrMo-3	N06625	0.10	0.50	5.0	0.02	0.015	0.50	0.50	58.0 min.	–	0.40	0.40	20.0 to 23.0	3.15 to 4.15	8.0 to 10.0	–	–	0.50
ERNiCrMo-3	N06082	0.10	2.5 to 3.5	3.0	0.03	0.015	0.50	0.50	67.0 min	(e)	–	0.75	18.0 to 22.0	2.0 to 3.0	–	–	–	0.50

[a]The weld metal shall be analyzed for the specific elements for which values are shown in this table. If the presence of other elements is indicated in the course of the work, the amount of those elements shall be determined to ensure that their total does not exceed the limit specified for "Other Elements, Total" in the last column of the table.
[b]Single values are maximum, except where otherwise specified. Rem = remainder.
[c]ASTM DS-56H/SAE HS-1086, Metals & Alloys in the Unified Numbering System.
[d]Includes incidental cobalt.
[e]Co is 0.12 maximum when specified by the purchaser.
[f]For strip, the classification designator "R" shall be replaced with "Q."

is also used for welding of any A-USC austenitic steels (except the 304HCu) or DMW between austenitics and Ni alloys. E/ER NiCrMo-3 consumables are most often used for joining alloy 625 to other Ni alloys or ferritic grades in DMW. Limitation of heat input makes the use of large-diameter consumables unlikely. Optimization of TIG compositions also included the narrowing of the liquidus–solidus temperature range.

Standard filler materials for Ni alloys amenable to homologous and dissimilar weldments are presented in Table 18.6. Alloys 82(182), 625, and 617 have their standard equivalent for wire product amenable to fabrication with GTA (or NG-GTA) or used in more productive SAW combinations (where possible due to the limitation of heat input).

No AWS (or equivalent) standard exist for wire used in joining alloy 263 and 740H. Reference has to be made to the BMs classifications (UNS N07263 and N07740, respectively) or to SAE/AMS 5966 standard for alloy 263 wire.

18.5 Dissimilar metal welding, repair welding

Basically, current USC material satisfactory used up to 620°C-class power plants will still be used on future A-USC boiler in sections where temperatures are below this limit. Therefore, the joining between USC and A-USC grades is a matter of great importance and concern. Just like USC DMV, it is not possible here to give more than an overview on the topic, anticipating that considerable R&D effort is still underway.

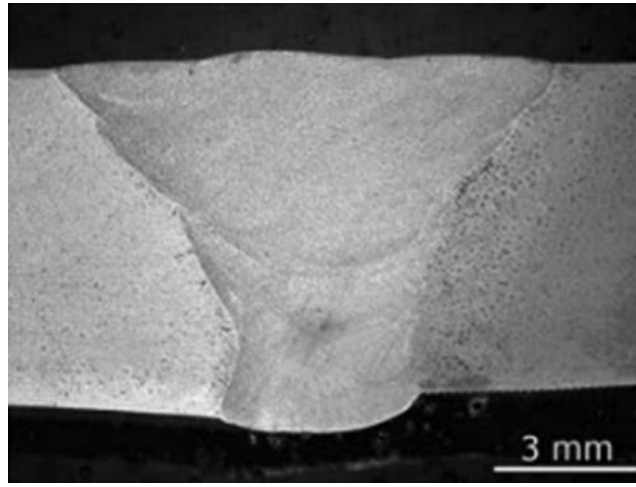
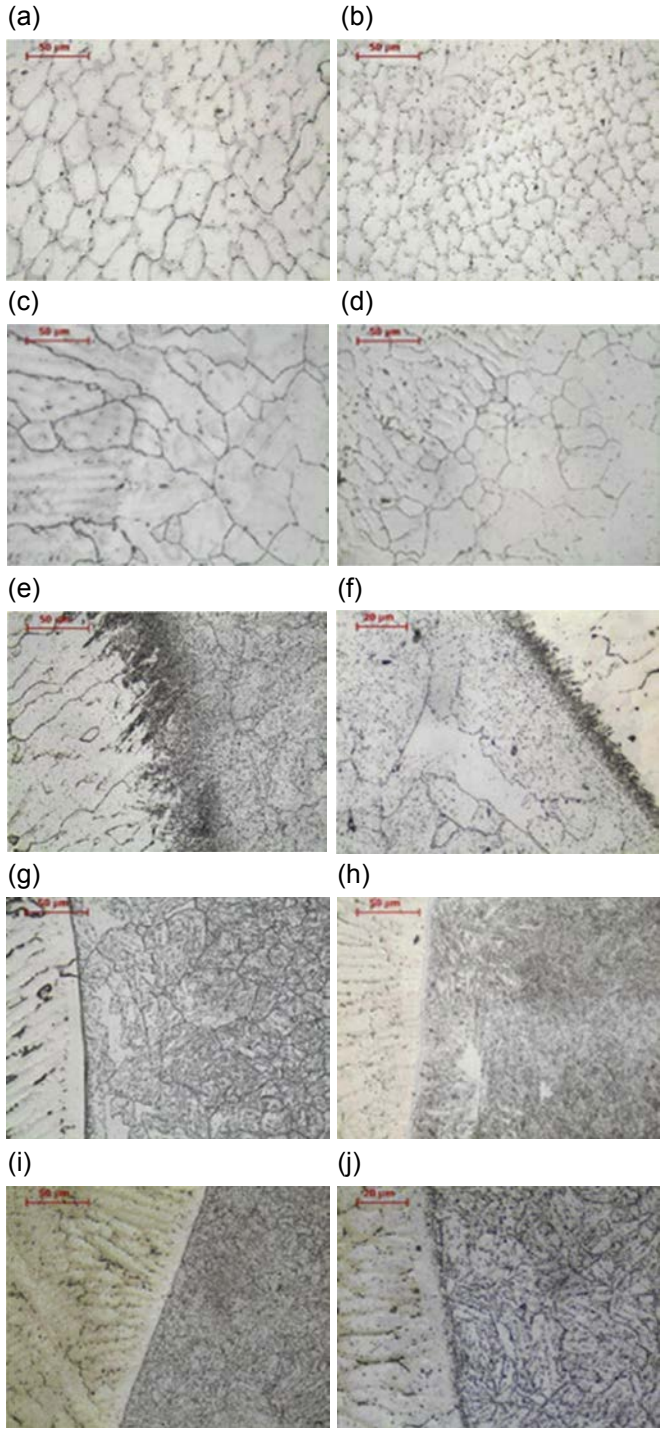


Figure 18.7 P92-304HCu steels welded with 304HCu matching WM [19]. A typical all-weld-metal analysis for matching 304HCu GTA consumable is 0.1C-0.4Si-3.2Mn-18Cr-16Ni-0.4Nb-0.8Mo-3Cu-0.2N (Böhler). EPRI P87 WM features a composition like 0.1C-0.3Si-1.5Mn-9Cr-bal.Ni-1Nb-2Mo-38Fe (EPRI).


(a)
(b)
(c)
(d)
(e)
(f)
(g)
(h)
(i)
(j)

With respect of USC steels, DMW of A-USC materials includes nickel alloys also on one BM side.

18.5.1 Weldments between USC martensitic steels and A-USC austenitic steels

This type of weldment has already been demonstrated, allowing usage of advanced austenitic tubing on USC-class designs. Examples include joining of the most performing CSEF steels (either T/P 91 or 92) with an advanced austenitic steel among Tempaloy AA-1, 304HCu, TP347HFG, and HR3C [19,31]. The task can be accomplished using an austenitic filler material matching the 304HCu (if this alloy is on one side) or Ni-based consumables (alloy 617, EPRI P87). Weldability and difficulties in performing the PWHT aimed to temper and stress relief the Gr.91/92 side are similar to those described for DMW between USC steels. In particular, use of a Ni-based consumable results in a much lower carbon migration between members with different C and Cr contents (Figs. 18.7 and 18.8).

18.5.2 Weldments between martensitic steels and nickel alloys

Examples of this class of welded details include joints between Gr.92 or CB2 CSEF steel and a Ni alloy of the type 617, 625, 263, and 740H as tubes, pipes or forgings.

DMW of solid solution Ni alloys (617B and 625) is relatively straightforward, and a matching consumable has been available for many years for the GTA, MMA and SAW methods. The Ni alloying is sufficient to dilute the Fe from the ferritic side without detrimental effects.

By utilizing the SMAW and GTAW processes, code quality weldments were produced by joining alloy 740H to P92 steel using either Ni alloy 82 (GTA) or 182 (MMA) as filler materials [32]. Table 18.7 shows the room temperature mechanical properties of both

Figure 18.8 P92-304HCu steels DMW. Weld microstructures for WMs and HAZs with 304HCu-type and EPRI 87 filler materials [19]: (a) weld microstructure (304HCu WM); (b) weld microstructure (EPRI P87 WM); (c) fusion line between the 304HCu BM and the 304HCu WM, visible presence of epitaxial crystallization; (d) fusion line between the 304HCu BM and the EPRI P87 WM, visible presence of epitaxial crystallization; (e) fusion line between the P92 steel and the 304HCu WM after heat treatment 760°C/24 h, visible zone of carbon diffusion from the steel to the weld; (f) fusion line between the P92 steel and the 304HCu WM after heat treatment 760°C/2 h, visible zone of carbon diffusion from the steel to the weld and presence of ferrite δ in the HAZ coarse-grained area; (g) fusion line between the P92 steel and the 304HCu WM after heat treatment 760°C/8 h, visible presence of ferrite δ in the HAZ coarse-grained area; (h) fusion line between the P92 steel and the EPRI P87 WM, visible presence of ferrite δ in the HAZ coarse-grained area; (i) fusion line between the P92 steel and the EPRI P87 WM after heat treatment 760°C/8 h, no traces of carbon diffusion; (j) fusion line between the P92 steel and the EPRI P87 WM after heat treatment 760°C/24 h, no traces of carbon diffusion.

Table 18.7 Room-temperature tensile properties for 1-inch (25.4 mm)-thick alloy 740H to P92 steel dissimilar GTAW and SMAW weldments [32]

0.2% Yield strength (for information only)		Ultimate tensile strength		Elongation at fracture (for information only) [%]	Reduction of area [%]	Failure location
Ksi	MPa	Ksi	MPa			
GTAW						
60.6	417.8	97.4	671.5	23.3	64.4	P92
60.7	418.5	98.2	677	22.5	64.3	P92
SMAW						
59.4	409.5	98.2	677	23.6	63.2	P92
72.1	497.1	98.8	681.2	21.2	63.3	P92

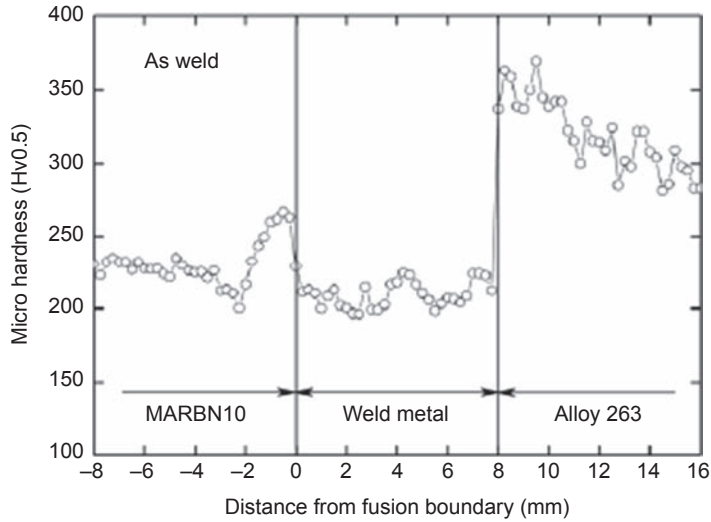


Figure 18.9 Hardness survey in DMW between MARBN and 263 alloys after PWHT [33].

the SMA and GTA dissimilar weldments. Each weldment was given a post-weld aging treatment of 1400°F/4 h/AC (760°C) to satisfy requirements of both alloy 740H and P92. Transverse side bends were sectioned from each dissimilar weldment and tested in accordance with ASME BPV Code Sec. IX and AWS B4.0.

Welding of MARBN steels with either alloy 617 or 263 alloy has also been studied using the GTA method and Ni alloy 82 as filler material (Figs. 18.9–18.11 and Table 18.8) [33].

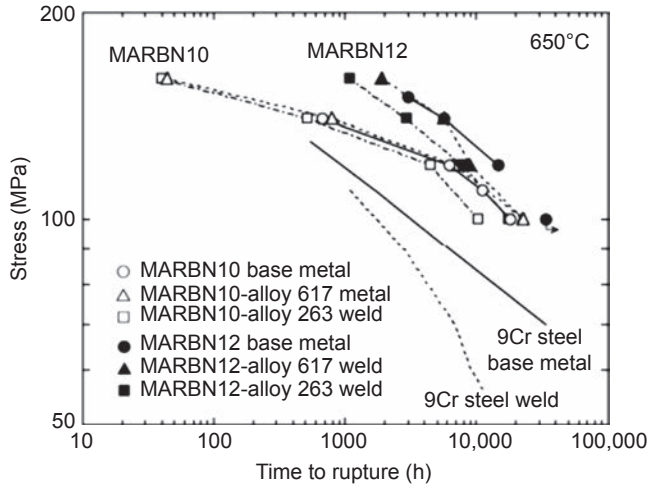


Figure 18.10 Creep rupture properties of weld between MARBN and Ni alloys at 650°C [33].

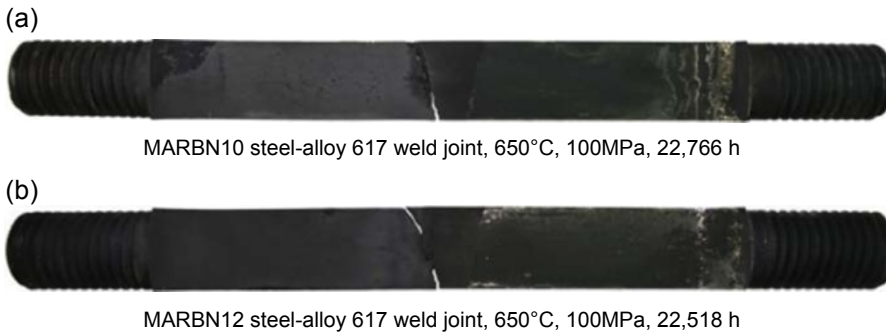


Figure 18.11 Fractured specimens (on the MARBN side) after creep testing of welds between MARBN and Ni alloy 617 at 650°C [33].

Of course, the creep damage of the studied weldments has accumulated to the MARBN side close to the fusion line; no detrimental influence of the presence of the Ni WM has been reported with respect to the expected creep life.

18.6 Welding of A-USC valves, casings and cast components

This application is quite mature, and complex, large welded assemblies have already been successfully manufactured out of the CB2 (GX13CrMoCoVNb9 2 1) martensitic steel or Alloy 625 [34]; examples of such components include inner turbine

Table 18.8 MARBN steels used in DMW with alloy 263 and 617 (elements concentration in wt.%, Fe remainder) [33]

	C	Si	Mn	P	S	Cr	W	Mo	Co	Ni	V	Nb	N	O	B	Sol. Al
MARBN10	0.078	0.29	0.54	0.003	0.001	9.11	3.13	<0.01	3.03	<0.01	0.21	0.052	0.0030	0.003	0.010	0.001
MARBN12	0.081	0.30	0.53	0.001	0.001	9.09	2.62	<0.01	3.02	<0.01	0.21	0.052	0.0072	0.003	0.011	0.001

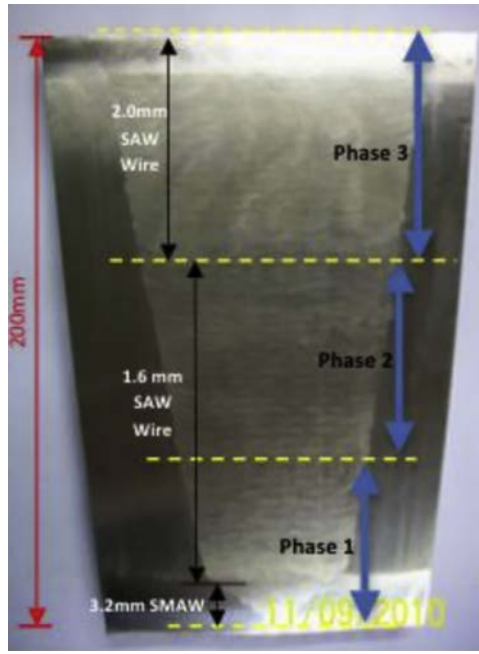


Figure 18.12 Heavy-walled welded cast alloy 625 using a combination of SMAW and SAW methods (Goodwin Steel Casting Ltd).

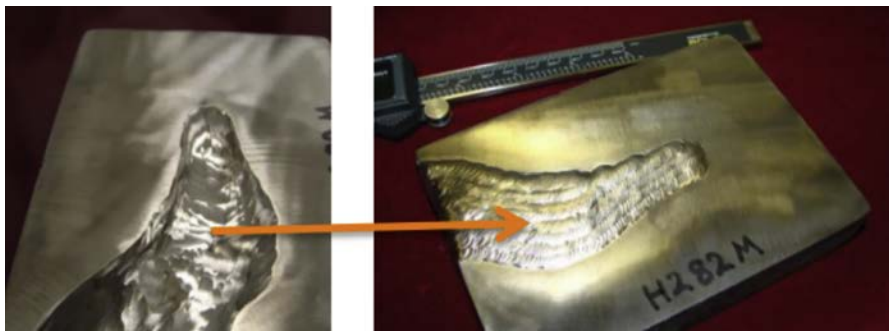


Figure 18.13 Repair study on 282 Ni cast alloy [35].

casings, steam valves, and nozzles (Fig. 18.12). Alloy 617 has also received attention for the same kind of components and even higher service temperature. In this industry, fusion welding is crucial for joining subassemblies and repair of large castings after excavation of the defective area. The SMAW process is mostly used, with filler materials capable of being used in out-of-position welding. Products are commercially available from manufacturers under the most common standards: AWS A5.5 E9015-G and A5.29 E91T1-GM for CB2-like compositions, and A5.11 ENiCrCoMo-1 and ENiCrFe-3 for alloys 617 and 625, respectively. Diameter available

Table 18.9 CB2 SMA weld metal composition [36]

Elements		CB2 weld metal typical
C	%	0.11
Mn	%	0.5
Si	%	0.2
Cr	%	9.5
Mo	%	1.5
V	%	0.19
Nb	%	0.045
Co	%	0.95
Ni	%	0.7
B	ppm	65
N	ppm	170

Table 18.10 Mechanical properties of CB2 SMAW (all weld metal) [36]

		Kv + 20°C (J/cm^2)	Rm (MPa)	Rp0.2 (MPa)	A (%)
PWHT	**Electrode diameter (mm)**	**>35 req.**	**–**	**min. 547 req.**	**–**
760°C/2 h	Ø 3.2	43	788	650	18.5
	Ø 4.0	43	818	683	18.9
	Ø 5.0	50	767	626	18.9
760°C/4 h	Ø 3.2	58	757	607	22.6
	Ø 4.0	66	763	614	19.5
	Ø 5.0	55	739	595	19.9
730°C/24 h	Ø 3.2	60	781	641	18.5
	Ø 4.0	54	890	770	15.6
	Ø 5.0	49	761	623	19.4
750°C/10 h	Ø 4.0	33-36-44 (39)	798	660	19.1
	Ø 4.0	–	427*	407*	12.1*

*Values obtained at 600°C (all the other characterizations were performed at room temperature).

is usually limited to 3.2 mm to limit the heat input and the consequent tendency to solidification cracking. Assemblies welded out of the CB2 steels are given a PWHT with potentially very long soaking time to adequately temper the steel throghout the heavy wall thickness.

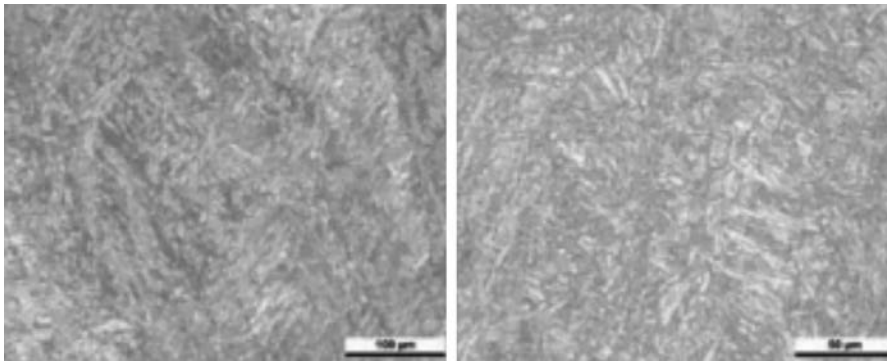


Figure 18.14 Martensitic microstructure of CB2 deposit [36].

Precipitation-strengthened nickel alloys (Alloy 282, 263) were also investigated for even higher creep strength and possibilities of higher service temperature (Fig. 18.13). Welding of heavy section age-hardened cast alloys is still poorly known, and they are likely to be much more difficult due to the high strength of the material and relatively low ductility at room temperature. Casting (and therefore fusion welding) of these alloys is extremely difficult due to the high reactivity of Al and Ti in air. As part of the R&D efforts, welding repair studies were undertaken with the GTA method and matching solid wires as filler materials [35].

It is worth noting that any welded assembly will put expensive nickel alloys only in the upper temperature section; in practice, DMW with martensitic grades (the next performing materials class) will be always necessary, eg, between Alloy 625/617 and CB2/9Cr martensitic steels at the inlet steam pipe.

Within the European COST funded R&D program, a consumable chemical composition called WB2, suitable to weld matching CB2 steel was established years ago [36]. Then, it was developed a range of diameters for a SMAW electrode according to WB2 specification. The toughness specification was 27 J absorbed energy at room temperature after PWHT. All-weld-metal coupons were deposited for different diameters with a preheat of 200°C and an interpass temperature of 250°C. Welding parameters are as follows: (1) Ø 3.2 mm: 116 Amps, 22 V, heat input 8 kJ/cm, (2) Ø 4.0 mm: 160 Amps, 24 V, heat input 12 kJ/cm, and (3) Ø 5.0 mm: 206 Amps, 26 V, heat input 13 kJ/cm. Different types of PWHT were performed: 760°C/2 h, 760°C/4 h, 750°C/10 h, and 730°C/24 h with a heating and cooling rate of 50°C/h. The typical chemical composition of WM is presented in Table 18.9. The mechanical properties obtained with the different diameters and PWHT are presented in Table 18.10, showing results that conform to requirements both in terms of tensile properties and toughness. A micrograph of the martensitic type of microstructure is presented in Fig. 18.14. The A_{c1} transformation temperature of the WM has been determined to be 830°C.

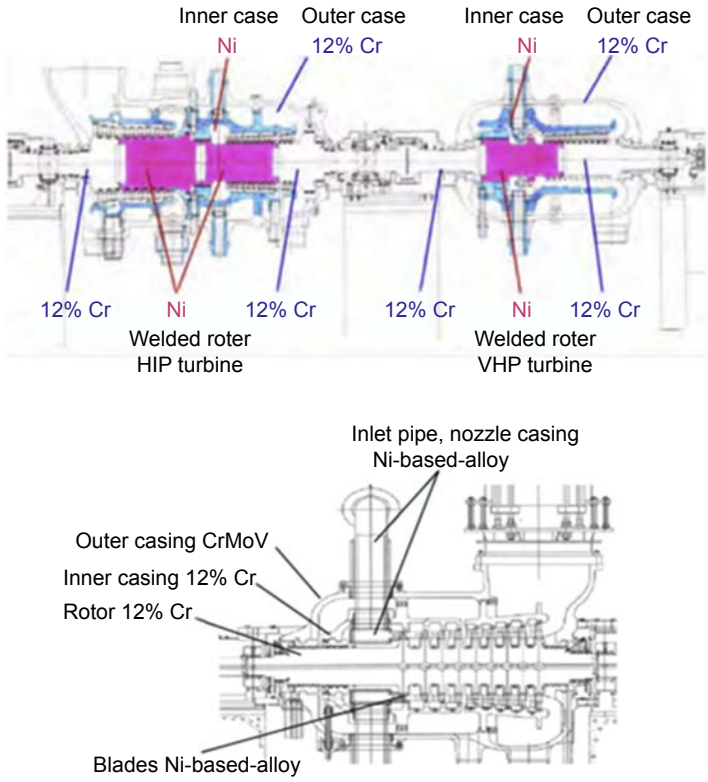


Figure 18.15 Steam turbine rotors welded constructions concepts [37,38].

Common nondestructive testing techniques for heavy-walled castings have been magnetic particle inspection (MT) and ultrasonic inspection (UT). These techniques have been used for assessing the quality of the original steel castings during manufacture and in-line inspection during service. Unfortunately, neither of these inspection techniques are acceptable for Ni alloy casting due to the attenuation seen in Ni alloys volumetric inspection using ultrasonics and its poor magnetic permeability, preventing MT from being a feasible technique for surface crack detection. The standard techniques for defect detection in Ni alloys are radiography (volumetric) and dye penetrant (surface). Radiography inspection, due to grain size and density of Ni alloy material, is performed using a linear accelerator for heavy sections castings.

18.7 Welding of rotors; technologies, fabrication issues, non destructive testing

Similarly to welded manufacturing of USC steam turbine rotors, the possibility of placing expensive and difficult to fabricate Ni alloy as described in Fig. 18.15 is of great interest for A-USC constructions. Welding of 12%Cr to Ni forgings is currently investigated for a variety of versions aimed to match the ferritic matrix thermal

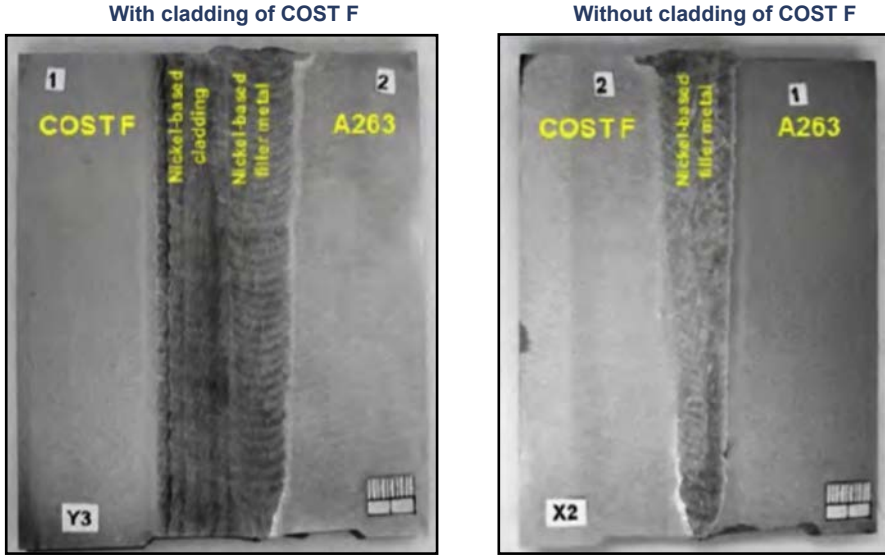


Figure 18.16 DMW between alloy 263 and COST F Cr steel forgings. Preliminar buttering of the ferritic side with a Ni consumable was considered.

expansion and with improved forgeability. Further than alloy 617 and 263, which are also promising candidates, newer compositions were studied in Japan for both the ferritic and the Ni sides [37,38]:

- MTR10A (10Cr-0.7Mo-1.8W-3Co-VNbB) steel
- HR1200 (11Cr- 2.6W-3Co-NiVNbB) steel
- TOS110 (10Cr-0.7Mo-1.8W-3Co- VNbB) steel
- FENIX 700 (16Cr-42Ni-2Nb-1.3Al-1.7Ti-Fe bal.)Fe-Ni alloy with improved forgeability and lower raw material cost
- LTES700R (0.03C-12Cr-6.2Mo-7W-1.65Al-0.65Ti-Ni bal.) weldable Ni alloy with thermal expansion coefficient matching 10%Cr steel

Material name	C	Ni	Cr	Mo	Co	W	Nb	Al	Ti	Fe
FENIX700	0.01	42	16	–	–	–	2	1.3	1.7	Bal.
	Iron-nickel-based alloy with a material price that is about two-thirds of that of typical Ni-based alloys. Excellent manufacturability for large forged products. Candidate material for the rotor.									
LTES700R	0.03	Bal.	12	6.2	–	7	–	1.65	0.65	–
	Ni-based alloy with a linear expansion coefficient that is suppress to approximately the same level as high Cr steel**.** Excellent weldability. Candidate material for the rotor.									

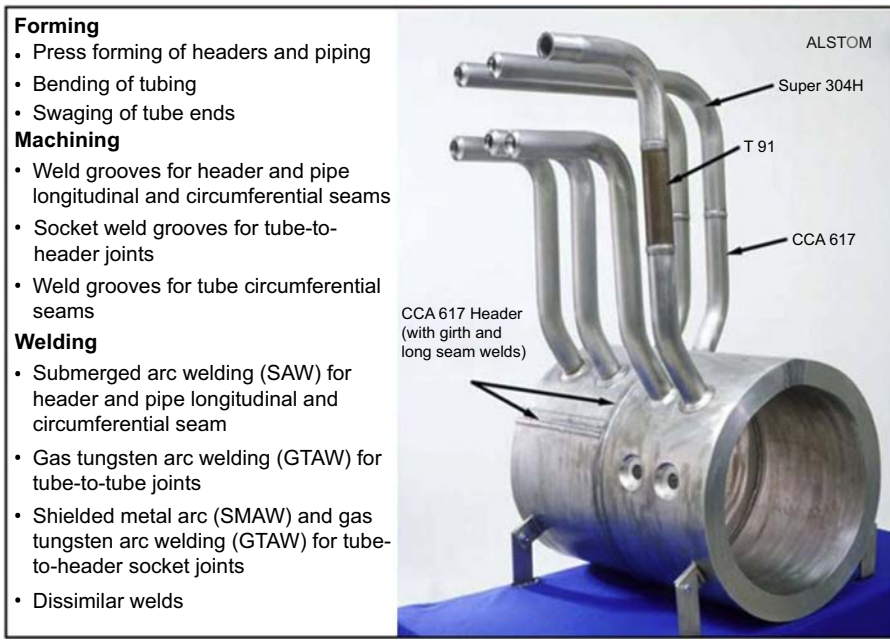


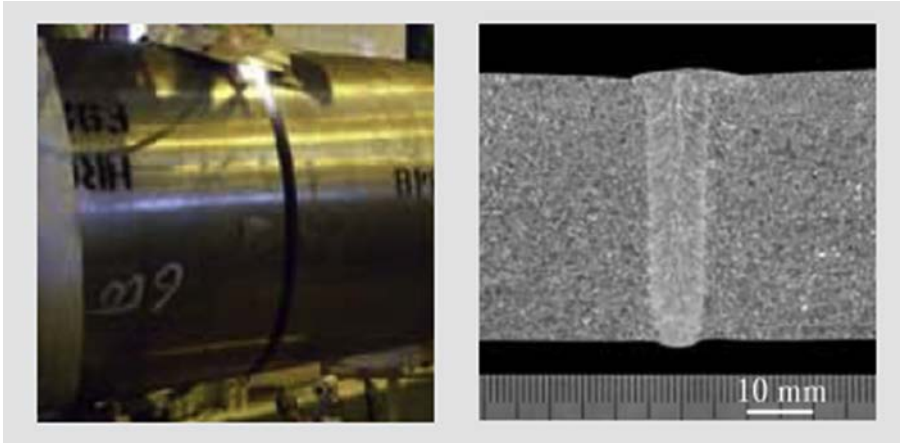
Figure 18.17 A-USC welded header mock-up with tubing (Alstom Boiler, now GE Power).

Almost no detailed information has been given on the weldability and welding methods.

Welding of precipitation-strengthened alloys (like 263) to Cr steel is especially complicated because the aging heat treatment is not compatible with Cr steel tempering Large Ni forgings share the same NDT issues illustrated for Ni castings. Welding in the precipitated strengthened condition has been demonstrated (Fig. 18.16) using the NG-GTA method and alloy 263 filler wire, including buttering of the Cr side. On DMW, it is difficult to find a compromise for the preheat/interpass schedule and the needed PWHT, as the Ni side would be better welded with low interpass and high temperature PWHT (the opposite is beneficial for the COST Cr steel). PWHT schedule strongly affects the weldments mechanical properties.

18.8 Welding of boiler systems

Welded boiler manufacturing, involving homologous and DMW has already been demonstrated on full-size mock-up (Fig. 18.17 shows an heavy-walled header and associated tubing out of early A-USC alloys). A variety of methods is available according the kind of alloy, member thickness, welding position, and weldability constraint; GTA and NG-GTA dominate these applications, with a limited choice of stick electrodes (for alloys 304HCu, 617B, 740H) and SAW combinations (well established for 617B alloy only). The candidate BMs for boiler systems will have significantly



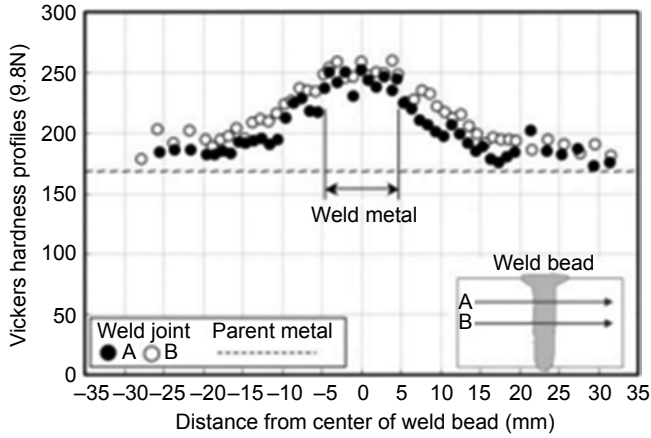


Figure 18.18 Testing involving narrow-groove HST [hotwire switching TIG (tungsten inert gas)] welding of HR6W Ni alloy has demonstrated the integrity of the welds [39]. Filler material for HR6W alloy is usually a non-matching Ni-based material for avoiding solifification cracking issues.

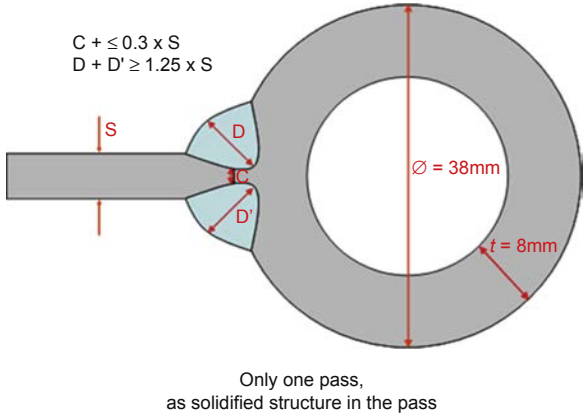


Figure 18.19 Schematic view of the SA welded joint for the waterwall application.

higher cost per kilogram compared to the current USC steels; the use of low productivity methods is not seen as a limiting factor so far compared to the raw material cost.

Most of the welding procedures for thick-walled joints on Ni alloys have reported the use of limited heat input for avoiding solidification cracking issues, generally under 1.5 kJ/mm. Where modest improved productivity is sought while keeping low figures for the arc energy, the NG-GTA is the most usual choice; unparalleled weld joint integrity has already been demonstrated in many years of successful

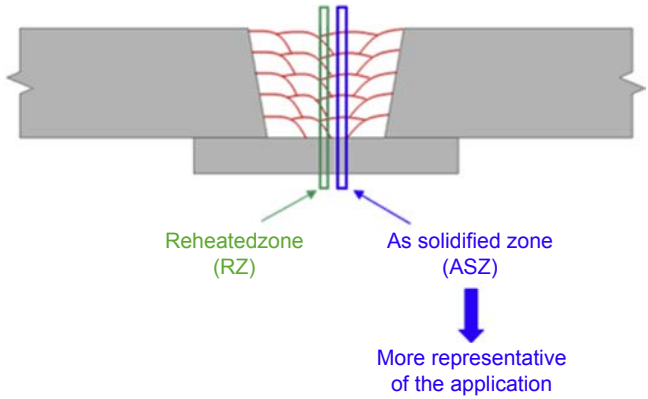


Figure 18.20 Welding configuration and Charpy-V impact bars notch location.

application in the nuclear and power generation industry. An example of hot wire NG multilayer welded joint on HR6W austenitic alloy thick-wall pipe is reported in Fig. 18.18.

As of today, no candidate for an 11%Cr-class martensitic steel has emerged for industrial validation for thick-walled pipework, as the avoiding of the detrimental Z-phase proved extremely difficult to overcome. Within Europe, two Research Fund for Coal and Steel funded large R&D programs ("CRESTA") aimed to develop new 11%Cr martensitic steels included weldability studies [10,11]. Two baseline WMs were investigated to exploit the avoiding of the Z-phase by the elimination of the Nb alloying altogether ("Nb-free" steel concept) or, alternatively, promoting the immediate precipitation of the same phase in a stable and strengthening amount and size ("Z" steel concept). Both thick-walled pipes and tubing welding were to be studied. Avoiding the use of Ni-based filler materials has been pursued as much as possible, as well as delta-ferrite presence on matching martensitic WMs.

A consumable matching version of Z-steel was characterized after use for water-wall application with the productive SAW method. Fig. 18.19 shows the schematic view of the welded joint for the water wall application.

The developed filler material for the named Z5 steel was tested on all-weld-metal deposit, prepared with the following parameters:

- welding configuration according to Fig. 18.20, 30 mm thickness
- pass sequence: four runs per layer
- Heat Input = 1.5 kJ/mm
- interpass temperature = 230–250°C

Chemical composition of all-weld-metal is presented in Table 18.11. Table 18.12 shows the PWHT conditions applied and the results of the KCV impact and hardness tests. The impact test notch is located in an as-solidified zone (see Fig. 18.20). This location has been selected because it is the most representative of the real joint in the water wall. It can be seen that Ta content could not be reached (poor transfer efficiency across the arc) at the same level as Z5 BM plate (0.6%).

Toughness was unexpectedly better in the as weld conditions than with PWTH. The hardness in all the PWTH conditions was still very high and over the usual values of Grades 91–92 welds after PWHT. The higher values of the hardness obtained after 12 h at 740°C is to be associated with the completion of the precipitation of Z-phase.

Table 18.11 Chemical composition of the SAW flux cored filler metal (elements concentration in wt.%, Fe remainder)

	Z5 steel target		SAW 009 experimental wire electrode
%	Min	Max	
C	0.02	0.04	0.033
Si	0.20	0.40	0.33
Mn	0.40	0.60	0.55
P		0.015	0.008
S		0.012	0.01
Cr	11.50	12.5	11.7
Mo		0.10	0.013
W	2.80	3.20	3.05
Al		0.05	0.012
Cu		0.10	0.027
Ti			0.007
Ta			0.13
Ni	0.80	1.20	1.08
Co	5.50	6.50	6.39
Nb		0.01	0.005
V		0.01	0.02
N	0.03	0.04	0.0453
O			0.0577
B	0.005	0.009	0.0096

Table 18.12 Results of the hardness and impact test in the as-welded condition and with different PWHT schedules

SAW 009 weldments	
Kv +20°C in As Solidified Zone (ASZ)	HV 10
As-welded	
22-14-11 (16)	
After 740°C/12 h	
9-9-7 (8)	390
After 720°C/12 h	
7-7-7 (7)	348
After 700°C/12 h	
11-11-14 (12)	334
After 680°C/12 h	
8-16-10 (11)	341

Table 18.13 Chemical composition of Cresta 19 weld metal using the SA welding (Air Liquide Welding)

[Wt %]	**C**	**Si**	**Mn**	**Mo**	**Cr**	**W**	**Co**	**V**	**N**	**B**	**Ni**	**Cu**
Cresta 19 SA weld metal	0.11	0.34	0.43	0.16	**10.2**	2.53	2.84	0.22	0.0317	**0.001**	0.40	0.37

[ppm]	**P**	**S**	**Ti**	**Al**	**O**	**Nb**
Cresta 19 SA weld metal	120	80	10	150	513	2

The values in bold indicate the elements that are out of the aimed range.

A parallel welding study concerned the version of Nb-free martensitic steel for both thick-walled and thin-member fabrication. Welding tests according the requirements of EN 15614 standard for thick-walled components, with reference to header/piping application, and simulated thin-walled components, with reference to boiler tube dimensions for membrane walls, have been made. Subsequent post-weld heat treatment has been performed in accordance with requirements of grade P92. In addition, the plate butt weld test has also been performed without PWHT.

The following welding parameters have been applied:

RFCS CRESTA Nb-free steel pipe butt weld (flat position)	
• dimension of base material:	ø219.1 × 25 mm
• welding process:	Manual GTA
• filler:	Cresta 19 cored TIG rod (ø2.4 and 3.2 mm)
• weld preparation:	U-groove

Table 18.14 Mechanical properties of Nb-free welds made with the Cresta 19 SA flux cored wire (Air Liquide Welding)

Temperature (°C)	Tensile strength (MPa)	Location of fracture
RT (20)	728	BM
RT (20)	730	BM
RT (20)	727	BM
RT (20)	734	BM, very close to HAZ
550	385	BM
600	316	BM
650	244	BM

Temperature (°C)	KV (J)	Shear aspect (%)	Lateral expansion (mm)	Sampling
RT (20)	34	30	0.53	Weld metal
RT (20)	23	30	0.48	Weld metal
RT (20)	18	30	0.41	Weld metal

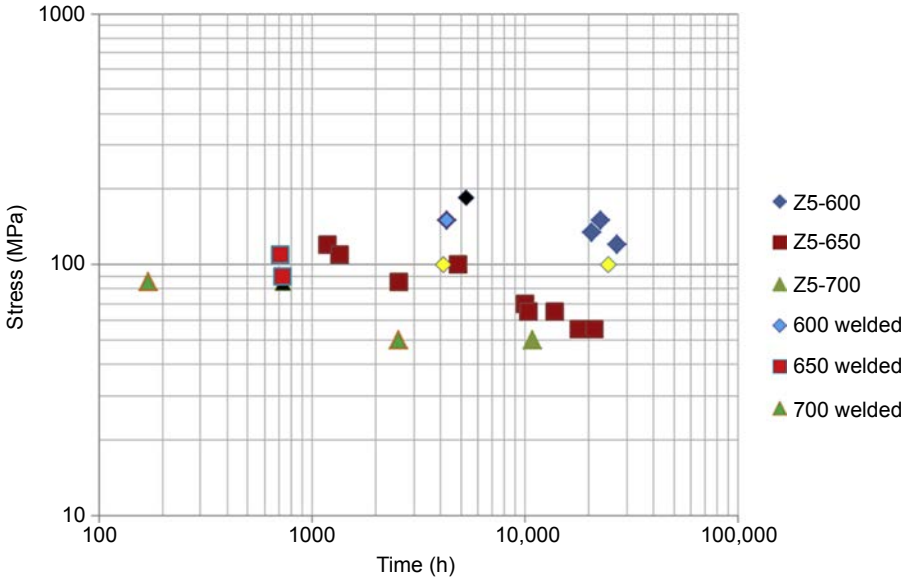


Figure 18.21 Creep resistance comparison between Z5 base metal its welded joints with IN625-type consumable.

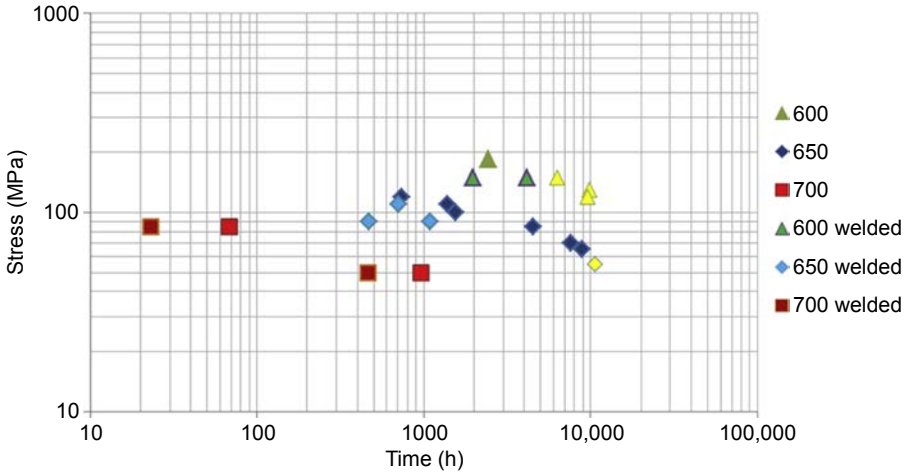


Figure 18.22 Creep resistance comparison between Nb-free base metal and its welded joints with the experimental matching filler.

• welding positions:	Flat
• preheating:	200 ÷ 250°C
• interpass temperature:	≤250°C
• intermediate cooling:	RT
• PWHT:	760 ± 10°C/75′
RFCS CRESTA Nb-free steel plate butt weld (flat position)	
• dimension of base material:	7.1(thickness) × 400 mm
• welding process:	SAW
• filler:	Cresta 19 flux cored wire (ø2.4 and 3.2 mm)
• weld preparation:	V-groove
• welding positions:	Flat
• preheating:	200 ÷ 250°C
• interpass temperature:	≤250°C
• intermediate cooling:	RT
• PWHT:	760 ± 10°C/30′ + alternative without PWHT

A matching flux core wire electrode with diameters 2.4 and 3.2 mm has been developed after systematic study of the influence of boron, oxygen and cobalt on the impact toughness and delta ferrite avoidance. After welding the chemical composition of both prototype WMs was verified, as shown in Table 18.13 for the SA weld. In Table 18.14 are reported the results of the weldments short-term mechanical properties; good agreement with the aimed chemistry was found. Substantial boron loss was evidenced, a common difficult with those classes of consumables. Weldments short term tensile properties were found promising, with WM impact toughness still needing more consistency. Hardness testing of both the welds after post-weld heat treatment showed average values in the range of 247295 HV10, which is in compliance with EN ISO 12952.

A limited number of cross-weld specimens has been subject to creep testing at 600, 650, and 700°C for both type of steels. A reduction in creep life has been shown, resembling conventional 9–11%Cr martensitic steels (Figs. 18.21 and 18.22).

As of 2016, the R&D program is continuing with new steel compositions and accompanying weldability studies aimed to waterwall applications with no PWHT and WM/HAZ hardness below 350 HV.

List of acronyms

1G	Flat welding position (ASME)
2G	Horizontal welding position (ASME)
5G	Girth welding (fixed pipe ASME)
CSEF	Creep strength enhanced ferritic steel
DMV	Dissimilar metal welding
GMA	Gas metal arc

GTA	Gas tungsten arc
HP	High pressure
HW-TIG	Hot wire tungsten inert gas
IP	Intermediate pressure
LP	Low pressure
MIG	Metal inert gas
MMA	Manual metal arc
NG-GTA	Narrow gap gas tungsten arc
NG-SA	Narrow gap submerged arc
PWHT	Post-weld heat treatment
SA+A	Solution annealed and aged
SA	Submerged arc
SMA	Shielded metal arc
TIG	Tungsten inert gas

Acknowledgments

I would like to express my gratitude to my dear colleagues Dr. Bruno Leduey and Dr. Philippe Corroyez of Air Liquide Welding, whose comments and suggestions added considerable value to this chapter.

References

Code and standards

- ASME Boiler Pressure Vessel Code – Specifications for Welding Rods, Electrodes, and Filler Metals. SFA-5.11/SFA-5.11M Specification for Nickel and Nickel-Alloy Welding Electrodes for Shielded Metal Arc Welding.
- ASME Boiler Pressure Vessel Code – Specifications for Welding Rods, Electrodes, and Filler Metals. SFA-5.14/SFA-5.14M Specification for Nickel and nickel-Alloy Bare Welding Electrodes and Rods.
- ASME Boiler Pressure Vessel Code – Specifications for Welding Rods, Electrodes, and Filler Metals. SFA-5.01M/SFA-5.01 Welding Consumables – Procurement of Filler Materials and Fluxes.
- ASME Boiler Pressure Vessel Code – Specifications for Welding Rods, Electrodes, and Filler Metals. SFA-5.02/SFA-5.02M Specification for Filler Metal Standard Sizes, Packaging, and Physical Attributes.
- ASME Boiler Pressure Vessel Code – Specifications for Welding Rods, Electrodes, and Filler Metals SFA-5.34/SFA-5.34M Specification for Nickel-Alloy Electrodes for Flux Cored Arc Welding.
- ISO 18274:2010 Welding Consumables – Solid Wire Electrodes, Solid Strip Electrodes, Solid Wires and Solid Rods for Fusion Welding of Nickel and Nickel Alloys – Classification.
- ISO 14172:2015 Welding Consumables – Covered Electrodes for Manual Metal Arc Welding of Nickel and Nickel Alloys – Classification.
- ISO 12153:2011 Welding Consumables – Tubular Cored Electrodes for Gas Shielded and Non-gas Shielded Metal Arc Welding of Nickel and Nickel Alloys – Classification.

Broad references

- Advances in Materials Technology for Fossil Power Plants: Proceedings from the Fourth International Conference.
- Advances in Materials Technology for Fossil Power Plants; Proceedings of the 5th International Conference EPRI by ASM International (Author), R. Viswanathan, D. Gandy, and K. Coleman (Eds.).
- Advances in Materials Technology for Fossil Power Plants: Proceedings from the Sixth International Conference.
- Advances in Materials Technology for Fossil Power Plants: Proceedings from the Seventh International Conference (EPRI 2013) by D. Gandy (Author), J. Shingledecker (Author) (Eds.).
- F. Abe. Research and Development of Heat-Resistant Materials for Advanced USC Power Plants With Steam Temperatures of 700°C and Above. Engineering 1(2) (2015) 211–224.
- Welding Metallurgy and Weldability of Nickel-Base Alloys, J.C. Lippold, S.D. Kiser, J.N. DuPont isbn:978-0-470-08714-5.

Specific references

[1] Progress of China 700°C USC development program, in: R. Sun, Z. Cui, Y. Tao (Eds.), Advances in Materials Technology for Fossil Power Plants; Proceedings from the Seventh International Conference, October 22–25, 2013. Waikoloa, Hawaii, USA.

[2] ENCIO Project: An European Approach to 700°C power plant, in: A. Di Gianfrancesco, A. Tizzanini, M. Jedamzik, C. Stolzenberger (Eds.), Advances in Materials Technology for Fossil Power Plants; Proceedings from the Seventh International Conference, October 22–25, 2013. Waikoloa, Hawaii, USA.

[3] Advanced USC Technology Development in Japan, in: M. Fukuda, E. Saito, H. Semba, J. Iwasaki, S. Izumi, S. Takano, T. Takahashi, Y. Sumiyoshi (Eds.), Advances in Materials Technology for Fossil Power Plants; Proceedings from the Seventh International Conference, October 22–25, 2013. Waikoloa, Hawaii, USA.

[4] Current Status of the U.S. DOE/OCDO A-USC materials technology research and development program, in: J. Shingledecker, R. Purgert, P. Rawls (Eds.), Advances in Materials Technology for Fossil Power Plants; Proceedings from the Seventh International Conference, October 22–25, 2013. Waikoloa, Hawaii, USA.

[5] India's National A-USC mission – plan and progress, in: A. Mathur, O.P. Bhutani, T. Jayakumar, D.K. Dubey, S.C. Chetal (Eds.), Advances in Materials Technology for Fossil Power Plants; Proceedings from the Seventh International Conference, October 22–25, 2013. Waikoloa, Hawaii, USA.

[6] Status of advanced ultra-supercritical pulverised coal technology Kyle Nicol CCC/229, December 2013, ISBN:978-92-9029-549-5 . copyright © IEA Clean Coal Centre.

[7] Advanced Material Castings for High Temperature Coal Fired Steam Turbine Applications, Goodwin Steel Casting Limited, UK. http://www.goodwinsteelcastings.com/downloads/gsc-advanced-material-castings.pdf.

[8] F. Abe, M. Tabuchi, S. Tsukamoto, T. Shirane, Microstructure evolution in HAZ and supression of Type IV fracture in advanced ferritic power plant steels, International Journal of Pressure Vessels and Piping 87 (2010) 598–604.

[9] A. Iseda, M. Yoshizaw, H. Okada, T. Hamaguch, H. Hirata, K. Joutoku, T. Ono, K. Tanaka, Development of 9Cr ferritic steel tube and pipe SAVE12AD for advanced power boilers, The Thermal and Nuclear Power Generation Convention 12 (2016) 49–55. http://doi.org/10.14942/tenpes.12.49.

[10] A. Di Gianfrancesco, S. Matera, J. Hald, B. Beal, C. Sommith, C. Chovet, G. Herhart, C. Turconi, A. Helmrich, S. Pillot, H. Danielsen, New Creep Resistant Stable Steel for USC Power (CRESTA) Final Report, 2014, ISBN:978-92-79-35039-9, ISSN:1831-9424, http://dx.doi.org/10.2777/59550.
[11] O. Tassa, S. Matera, J. Hald, S. Pillot, S. Sorrentino, K. Matocha, Z. Kubon, V. Kurka, M. Vindys, B. Gsellmann, D. Halici, T. Steck, A. Helmrich, A. Kopp, S. Neri, S. Mengaroni, New Creep Resistant Stable Steel for USC Power II (CRESTA II) Midterm Report, 2016.
[12] F. Abe, M. Tabuchi, Microstructure and creep strength of welds in advanced ferritic power plant steels, Science and Technology of Welding 9 (1) (2004) 22–30.
[13] C. Schlacher, C. Béal, C. Sommitsch, S. Mitsche, P. Mayr, Creep and damage investigation of advanced martensitic chromium steel weldments for high temperature applications in thermal power plants, Science and Technology of Welding and Joining 20 (1) (2015) 82–90, http://dx.doi.org/10.1179/1362171814Y.0000000259.
[14] Feasibility of MARBN steel for application to thick section boiler components in USC power plant at 650°C, in: F. Abe, M. Tabuchi, H. Semba, M. Igarashi, M. Yoshizawa, N. Komai, A. Fujita (Eds.), Advances in Materials Technology for Fossil Power Plants; Proceedings from the Fifth International Conference. October 3–5, 2007. Electric Power Research Institute, Marco Island, FL, USA.
[15] EU FP7 Component Performance-driven Solutions for Long-Term Efficiency Increase in Ultra Supercritical Power Plants - MACPLUS, Project Work Package 2 Final Report (S. Sorrentino, P. Mayr, C. Schlacher et al., in preparation).
[16] C. Schlacher, C. Sommitsch, P. Mayr, C. Gupta, H. Toda, K. Usegi, Y. Suzuki. Creep and damage investigation of improved 9%Cr steel welded joints, in: Trends in Welding Research 2012: Proceedings of the 9th International Conference (ASM International).
[17] Pipe steel for modern high output power plants, Vallourec. http://www.vallourec.com/fossilpower/Lists/Brochures/Attachments/7/V_B01B0005B-15GB.pdf.
[18] N. Komai, N. Saito, Y. Takey, Evaluation of creep rupture strength in Ni-based alloy weldments for an advanced USC Boiler, in: Advances in Materials Technology for Fossil Power Plants; Proceeding from the Seventh International Conference, October 22–25, 2013. Hilton Waikoloa Village, Waikoloa, Hawaii.
[19] K. Pańcikiewicz, A. Ziewiec, P. Zbroja, P. Kajda, E. Tasak, Microstructure and Properties of Dissimilar Welded Joints Made of Steels Used in the Power Industry, Bulletin of the The Institute of Welding (Biuletyn Instytutu Spawalnictwa), Poland 58 (5) (2014).
[20] J.K. Wright, L.J. Carroll, R.N. Wright, Creep and Creep-fatigue of Alloy 617 Weldments, INL/EXT-14–32966, August 2014.
[21] A.F. Stam, Demonstration and Component Fabrication of Nickel Alloys and Protective Coatings for Steam Temperatures of 750°C, in: Advances in Materials Technology for Fossil Power Plants; Proceeding from the Seventh International Conference, October 22–25, 2013. Hilton Waikoloa Village, Waikoloa, Hawaii.
[22] J.M. Sanders, B.A. Baker, Elimination of Fissures in Thick Section INCONEL Alloy 740 Welds, in: Proceedings of the 34th International Technical Conference on Clean Coal & Fuel Systems, May 31–June 4, 2009. Clearwater, FL, USA.
[23] J.P. Shingledecker, Creep-Rupture Performance of Inconel Alloy 740 and Welds, in: Advances in Materials Technology for Fossil Power Plants; Proceeding from the Seventh International Conference, October 22–25, 2013. Hilton Waikoloa Village, Waikoloa, Hawaii.
[24] Y. Hirakawa, Y. Kadoya, S. Nishimoto, Y. Tanaka, Trial Production of Alloy 625 and Alloy 617 Casting Component for Advanced 700°C Class Steam Turbines, in: Advances in Materials Technology for Fossil Power Plants; Proceeding from the Seventh International Conference, October 22–25, 2013. Hilton Waikoloa Village, Waikoloa, Hawaii.

[25] J.C. Lippold, J.N. DuPont, S.D. Kiser, Welding Metallurgy and Weldability of Nickel-Base Alloys, 2009, ISBN: 978-0-470-08714-5.
[26] Fabrication trials of Ni-based alloys for advanced USC boiler application, in: N. Saito, N. Komai, Y. Takei (Eds.), Advances in Materials Technology for Fossil Power Plants; Proceedings from the Seventh International Conference, October 22–25, 2013. Waikoloa, Hawaii, USA.
[27] J.N. DuPONT, Welding of Nickel-Based Alloys for Energy Applications, Welding Research Supplement of the Welding Journal (February 2014) s31.
[28] VDM® Alloy 617 B Data Sheet No. 4061, February 2016. http://www.vdm-metals.com/fileadmin/user_upload/Downloads/Data_Sheets/Data_Sheet_VDM_Alloy_617_B.pdf.
[29] Filler Metals for Thermal Power Generation - voestalpine böhler welding. http://www.voestalpine.com/welding/content/download/5213/110732/file/Productlist_ThermalPower_EN.PDF.
[30] D.C. Tung, J.C. Lippold, Testing approaches for stress relaxation cracking in gamma-prime strengthened Ni-base alloys, in: T. Boellinghaus, J.C. Lippold, C.E. Cross (Eds.), Cracking Phenomena in Welds IV, 2016, ISBN: 978-3-319-28432-3.
[31] M. Urzynicok, K. Kwieciński, P. Mariani, Y. Minami, Application of EPRI P87 in dissimilar austenitic-martensitic welded joints of tempaloy AA-1 and T92 steel grades, in: Advances in Materials Technology for Fossil Power Plants; Proceedings from the Seventh International Conference, October 22–25, 2013. Waikoloa, Hawaii, USA.
[32] INCONEL® ALLOY 740H ® A Superalloy Specifically Designed For Advanced Ultra Supercritical Power Generation, Special Metals – a PCC Company. http://www.specialmetals.com/files/PCC%20EG%20740H%20White%20Paper.pdf.
[33] M. Tabuchi, H. Hongo, F. Abe, Creep strength of dissimilar welds for advanced USC boiler materials, in: 13th International Conference on Fracture, June 16–21, 2013. Beijing, China.
[34] Advances in Ni alloy casting production for +700°C applications, in: S. Birks, S. Roberts, R. Leese (Eds.), Proceeding from the Seventh International Conference, October 22–25, 2013. Hilton Waikoloa Village, Waikoloa, Hawaii.
[35] J. Shingledecker, R. Purgert, Steam Turbine Materials for Advanced Ultrasupercritical (AUSC) Coal Power Plants. NETL Crosscutting Research Review Meeting, May 22, 2014, Pittsburg, PA USA.
[36] Welding Consumables for Grade P92 for Power Generation Applications; Oerlikon Competence n.5, November 2010.
[37] S. Hreben, P. Vitek, V. Zednik, L. Prchlik, Similar and Dissimilar Welding of Nickel-based Superalloys for A-USC Steam Turbine Rotors in Nextgenpower Project, in: Advances in Materials Technology for Fossil Power Plants; Proceeding from the Seventh International Conference, October 22–25, 2013. Hilton Waikoloa Village, Waikoloa, Hawaii.
[38] E. Saito, N. Matsuno, K. Tanaka, S. Nishimoto, R. Yamamoto, S. Imano, Latest Technologies and Future Prospects for a New Steam, Turbine, Mitsubishi Heavy Industries Technical Review 52 (2) (June 2015) 39.
[39] Long term creep rupture strength of weldments of candidate Ni and Fe-Ni Materials for tube and pipe of A-USC boilers, in: G. Bao, T. Sato, Y. Marumoto (Eds.), Advances in Materials Technology for Fossil Power Plants: Proceedings from the Sixth International Conference, August 31–September 3, 2010. Electric Power Research Institute, Santa Fe, New Mexico, USA.

This page intentionally left blank

Part Three

Materials' development programs worldwide

This page intentionally left blank

Worldwide overview and trend for clean and efficient use of coal

19

A. Di Gianfrancesco
Materials & Technologies Consultant, Rome, Italy

19.1 Introduction

Coal is a fossil fuel: it is the altered remains of prehistoric vegetation that originally accumulated in swamps and peat bogs. It is a combustible, sedimentary, organic rock that is composed mainly of carbon, hydrogen, and oxygen. It is formed from vegetation that has been consolidated between other rock strata and altered by the combined effects of pressure and heat over millions of years to form coal seams.

The build-up of silt and other sediments, together with movements in the earth's crust (known as tectonic movements) buried these swamps and peat bogs, often to great depths. With burial, the plant material was subjected to high temperatures and pressures. This caused physical and chemical changes in the vegetation, transforming it into peat and then into coal.

Coal formation began during the Carboniferous Period—known as the first coal age—which spanned 360 million to 290 million years ago.

The quality of each coal deposit is determined by temperature and pressure and by the length of time in formation, which is referred to as its "organic maturity." Initially the peat is converted into lignite or "brown coal": these are coal types with low organic maturity. In comparison to other coals, lignite is quite soft, and its color can range from dark black to various shades of brown.

Over many more millions of years, the continuing effects of temperature and pressure produced further change in the lignite, progressively increasing its organic maturity and transforming it into the range known as "subbituminous" coals.

Further chemical and physical changes occur until these coals became harder and blacker, forming the "bituminous" or "hard coals." Under the right conditions, the progressive increase in the organic maturity can continue, finally forming anthracite.

Coal, the second source of primary energy (roughly 30%), is mostly used for power generation (over 40% of worldwide electricity is produced from coal). In addition, coal is used to produce virtually all non-recycled iron. Coal is abundant, affordable, easy to transport, store and use, and it is free of geopolitical tensions; all these attributes make it very popular. On the other hand, pulverized coal plants are the most carbon intensive source of power generation, and this is a real issue, as CO_2 emissions need to be dramatically and urgently reduced. Whereas more efficient plants are built across the world, the transition from subcritical to supercritical (and ultra-supercritical) technology is very slow. And even worse news is that the dramatic reduction of

Materials for Ultra-Supercritical and Advanced Ultra-Supercritical Power Plants.
http://dx.doi.org/10.1016/B978-0-08-100552-1.00019-1
Copyright © 2017 Elsevier Ltd. All rights reserved.

CO_2 emissions that our climate targets require is possible only through development of carbon capture and storage (CCS) technologies. Progress on CCS is very disappointing [1].

19.1.1 Types of coal

The degree of change undergone by a coal as it matures from peat to anthracite—known as coalification—has an important bearing on its physical and chemical properties and is referred to as the "rank" of the coal. Low-rank coals, such as lignite and subbituminous coals are typically softer, friable materials with a dull, earthy appearance. They are characterized by high moisture levels and low-carbon content, and therefore a low energy content.

Higher rank coals are generally harder and stronger and often have a black, vitreous luster. They contain more carbon, have lower moisture content, and produce more energy. Anthracite is at the top of the rank scale and has a correspondingly higher carbon and energy content and a lower level of moisture (see Fig. 19.1). Fig. 19.2 shows an example of the coal appearance.

19.1.2 How coal works

Many people think coal represents a bygone way of life and that the world has moved on to safer and cleaner energy sources [3]. On the contrary, coal provides roughly 40% of the world's electricity—far more than any other source of power—and coal use has nearly tripled since 1960. Coal use will continue to expand if the power industry succeeds in building the many power plants it has proposed for construction, especially in the emerging countries.

Coal's proponents claim coal power is cheap. While the direct price of electricity from the nation's aging fleet of coal plants may be low, it does not reflect the staggering and lasting costs of coal-related air and water pollution, mining accidents, permanently altered landscapes, and most importantly, climate change. Even the newest proposed plants—which would cost far more than existing plants—would have major impacts on air and water quality, and almost the same mining and climate impacts as existing plants.

Technology is evolving that has the potential to substantially reduce coal's contribution to global warming by capturing carbon emissions before they are emitted. This technology could become an important part of the battle against global warming, but it remains to be seen whether it will work at a commercial scale and at what cost.

Meanwhile, a 2009 Union of Concerned Scientists study found that world can dramatically reduce the coal use—and all the environmental and social costs associated with it—while saving energy consumers money with policies that aggressively promote energy efficiency and renewable power.

19.1.3 Coal formation

Coal was formed when dead plant matter submerged in swamp environments was subjected to geological forces of heat and pressure over hundreds of millions of years

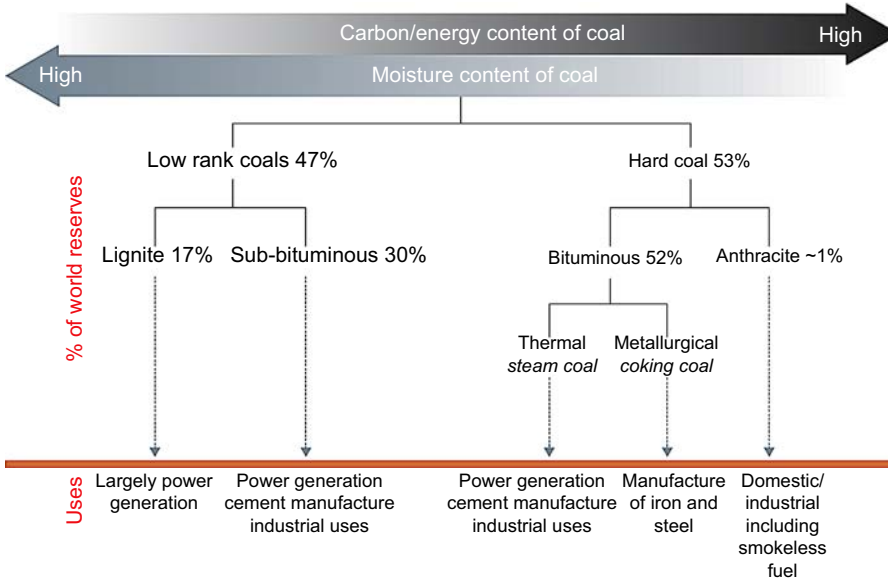


Figure 19.1 Coal classification, world reserves, and use [2].



Figure 19.2 Examples of coal [2].

(Fig. 19.3). As time went by, the plant matter evolved from moist and low-carbon peat, to coal, which is much higher in energy and carbon content. Coal itself has a wide variation in properties, so it is categorized into four ranks—lignite, subbituminous, bituminous, and anthracite—in order of increasing carbon and energy content. Most of the coal burned in the world power plants is of the bituminous, subbituminous, and lignite variety.

Coal of all types can vary widely in the amount of sulfur contained. These differences are determined by the conditions under which the coal formed. Low-sulfur coal deposits formed in a freshwater environment, while those containing higher proportions of sulfur developed in brackish swamps or marine-influenced environments [4].

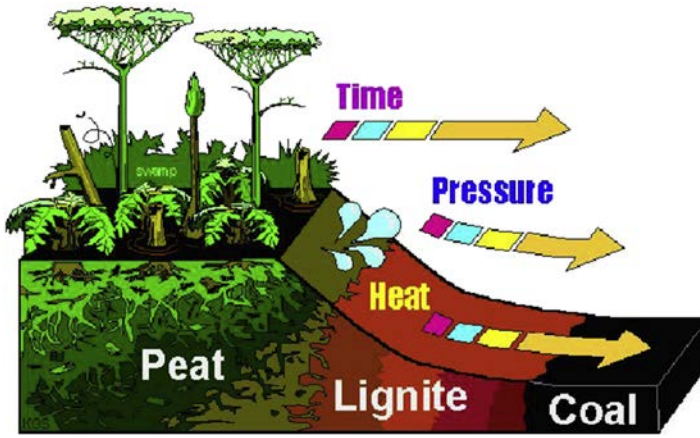


Figure 19.3 The process of coal formation [3].

19.1.4 Coal mining

In 2007, the United States burned roughly one billion tons of coal, enough to fill a railroad car every 3 s. The electricity sector accounted for over 90% of all coal used, with the rest being burned mostly in industrial and commercial settings, like primary steel production [5]. Getting such vast quantities of coal to power plants for burning relies on a vast network of mines, where companies excel at extracting it from the earth at prolific rates.

Removing coal is simple in principle: just expose it, break it up, and cart it off to be burned. In practice, coal mining is an energy-intensive, labor-intensive, and money-intensive undertaking. Underground mining remains one of the most hazardous of occupations, killing and injuring many in accidents, and causing chronic health problems.

Due to a variety of influences, the coal mining industry has undergone dramatic change over the past few decades. More productive, but also more environmentally damaging, surface mining methods have overtaken underground mining as the predominant way of extracting coal. The worst manifestation of this trend has been the rise in prevalence of mountaintop removal mining, in which tops of whole mountains are blasted away to get to the coal seams underneath. The amount of coal produced per worker has also risen dramatically, resulting in overall employment in mining being roughly cut in half between the 1980s and the 2000s. Even the portion of coal still mined underground is extracted with the help of extremely power, efficient machines, and many fewer humans. Overall, coal mining in the United States today looks much different than it did even a few decades ago and currently the employers are about 100,000 respect to the 700,000 one century ago.

This is not the situation of China where a large use of coal is made for power generation and where the extractive industry increase a lot in the last 2 decades and several employers dead in large number of accidents.

19.1.4.1 Underground mining

Two dominant methods together account for the vast majority of underground coal mining: "room and pillar" and "longwall" mining. In room and pillar mining, seams of coal are mined partially, leaving large pillars of coal intact to support the overlying layers of rock. Mining by this method creates a network of alternating open spaces and large pillars of coal (Fig. 19.4(a)). When mining in one part of the coal seam has been finished, miners practice "retreat" mining, extracting as much as possible of the coal in the remaining pillars on the way out, while the roof of the seam begins to collapse behind them.

Longwall mining involves cutting long tunnels into a coal seam and removing the extracted coal by conveyor belt (Fig. 19.4(b)). As the miners and the machinery move along the seam, a hydraulic support system temporarily holds the ceiling of overlying rock in place.

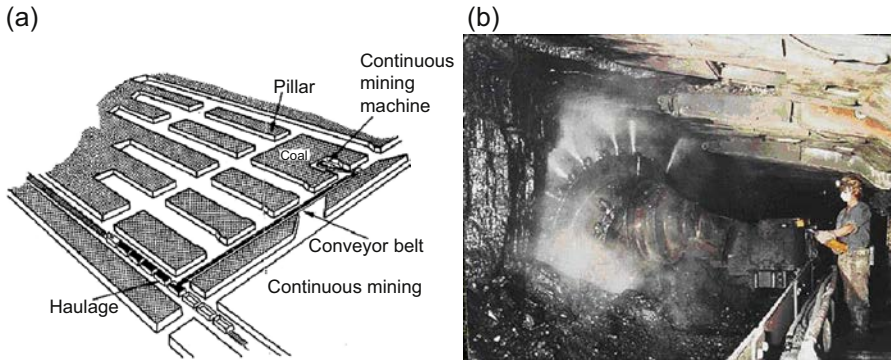


Figure 19.4 Mining: (a) room and pillar (b) longwall.

Both room and pillar and longwall mining are mostly now performed with very powerful mining machines, which rapidly cut coal from the face of coal seams. These machines are phasing out the use of less productive and more dangerous traditional methods, which require intermittently drilling the coal seam and blasting it with explosives.

19.1.4.2 Surface mining

Surface mining is employed when the coal seam is located much closer to the surface (Fig. 19.5). It requires many fewer workers per unit of coal produced and uses very large machinery. Extracting the coal first requires clearing the vegetation and soil from the immediate surface. Then the large intermediate layer of sediment and rock, referred to by the industry as "overburden," must be blasted and removed, either by a process called "draglining" or in large truckloads. With the underlying coal seam finally exposed, it is removed in strips and moved by conveyor belt or truck to its final destination. After mining of the coalbed is completed, the law requires that the



Figure 19.5 Strip mining.

contours of the land be restored and replanted with vegetation, though to date the acres of surface mines that have been successfully reclaimed is relatively low compared with acres of newly mined land [6].

19.1.4.3 Mountaintop removal mining

While coal mining has long caused environmental damage, the most destructive mining method by far is a relatively new type of surface mining called mountaintop removal (Fig. 19.6). For instance, currently practiced in southern West Virginia and Eastern Kentucky (USA), this method requires stripping all trees from the mountaintop and then blasting away the top several hundred feet with explosives. The resulting debris is dumped into an adjacent valley, burying the streams and destroying everything that once grew there. The practice leaves behind a flattened area with soils so poor they can only support exotic grasses, a profound change from a once diverse and heavily forested ecosystem. The damages from MTR include great loss and fragmentation of ecosystems, higher risk of local flooding and runoff, contamination of local groundwater resources, and occasional deadly accidents.

19.1.4.4 Coal transport and process

Coal predominantly gets around the world by train (ie, almost 70% of the coal transported around the United States in 2007 arriving to its destination via railroad), barges, trucks, pipelines, and in some cases coal is transported great distances mainly by boots (see Fig. 19.7).

A common way of avoiding the transportation costs associated with coal is by burning it in “mine mouth” coal plants. As soon as it is mined the coal is immediately put on a conveyor belt that runs directly into the power plant. The growing presence of mine mouth plants has been facilitated by expanding use of long-distance electricity transmission.

Before coal is shipped long distances, it undergoes a process of preparation to lower shipping costs and facilitate use in power plants. Preparation generally includes crushing the coal and removing heavy, extraneous, non-coal materials. If coal is high in sulfur or other impurities, it is washed with a water or chemical bath, removing up to 40% of inorganic sulfur in the coal. Unfortunately, the contaminants and non-coal



Figure 19.6 Mountaintop removal mining.
Ohio Valley Environmental Coalition.



Figure 19.7 Coal transportation systems.

material removed during washing have to go somewhere, and normally they are deposited in large waste reservoirs.

19.1.5 Countries with the biggest coal reserves

It has been estimated that there are over 984 billion tons of proven coal reserves worldwide (2014). This means that there is enough coal to last us over 190 years. Coal is located worldwide: it can be found on every continent in over 70 countries, with the biggest reserves in the United States, Russia, China, and India (Fig. 19.8). Africa and South America have very little coal.

If we look at the proved coal reserve distribution in 2013 by WEC (Fig. 19.9), it is possible to observe that in these are decreased for about 10.

Looking in deeper detail, more than 80% of the world's total proved coal reserves are located in just 10 countries. The United States tops the list with more than a quarter of the proven coal reserves, while China, which ranks third, is the biggest producer and consumer of coal [9].

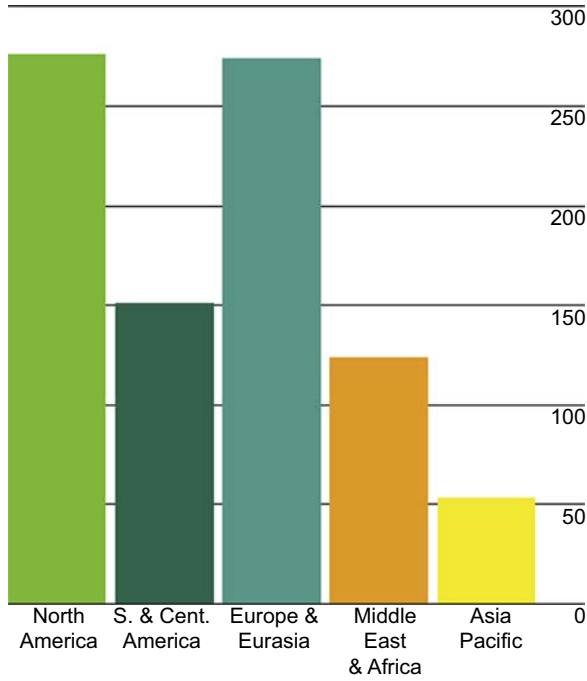


Figure 19.8 Reserves to production (R/P) ratios: Years (2014 by region) [7].

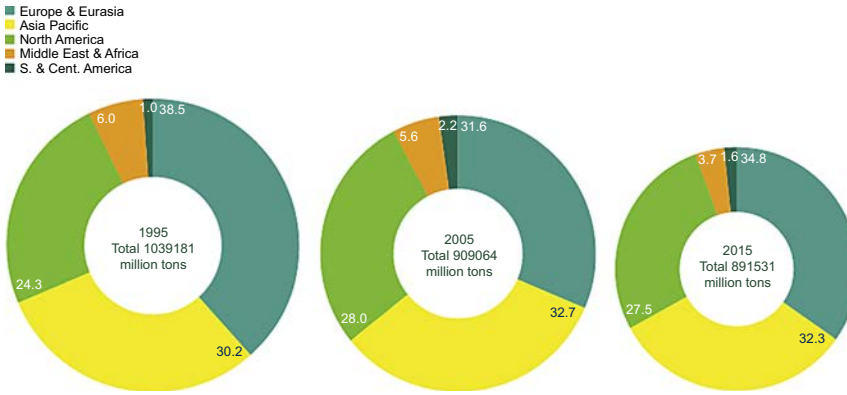


Figure 19.9 Distribution of coal proved reserves in 1994, 2004, and 2014. WEC, bp-statistical-review-of-world-energy-2015-coal-section.

Table 19.1 shows the producers of coal and lignite in the world and the shear of the evaluated reserves. In 2014 there was the first decrease at the world level mainly due to the contraction of production in China.

Nevertheless, in 2014 the total energy demand increased 0.5%, as well as the demand of electricity, but the consumption of coal has reduced despite the increase of oil and gas, as shown in Table 19.2. These could be an effect of the global stagnation,

Table 19.1 Countries with the largest share of proved coal reserves worldwide in 2014 [5] and the coal production in 2014 [10]

Countries	Share of world total reserve	Coal production (Mtons)
United States	26.6%	914
Russian Federation	17.6%	355
China	12.8%	3474
Australia	8.6%	480
India	6.8%	654
Germany	4.5%	188
Ukraine	3.8%	n.a.
Kazakhstan	3.8%	114
South Africa	3.4%	265
Indonesia	3.1%	472
Poland	n.a.	137

Table 19.2 2014 key figures [11]

Oil	+0.4%
Coal	–0.7%
Gas	+0.4%
Electricity	+1.2%
CO_2 (energy)	–0.1%

of the low price of oil, and of the increase of consumption of gas in United States due to the production of shale gas.

19.1.6 Electricity production and CO_2 emission

The main producers of electricity in the world are countries that are G20 members, representing around 85% of global gross domestic product, over 75% of global trade, and two-thirds of the world's population [12].

The members of the G20 are Argentina, Australia, Brazil, Canada, China, France, Germany, India, Indonesia, Italy, Japan, Republic of Korea, Mexico, Russia, Saudi Arabia, South Africa, Turkey, United Kingdom, the United States, and the European Union. Only Iran and Saudi Arabia are also included in the big producers.

Table 19.3 shows in detail the 2014 produced energy of the top 10 countries, and it is possible to note that the first two producers, China and the United States, generate about 61% of the top 10 in total, followed by India and Russia.

In 2014 there was a little slowdown of the world electricity production, mainly induced by the deceleration in China.

Table 19.3 Top 10 electricity producers in 2014

Country	Electricity production (TWh)
China	5583
United States	4330
India	1296
Russia	1064
Japan	996
Canada	640
Germany	616
Brazil	584
France	562
South Korea	540

Table 19.4 Top 10 and lowest nine countries in efficiency of coal-fired power plants

Country	Top 10 Value (%)	Country	Lowest nine (%)
Austria	42.9	Russia	23.9
Japan	41.9	Slovakia	26.7
Ireland	41.6	Bulgaria	27.9
Netherlands	41.1	Czech Republic	29.5
Belgium	40.9	Romania	29.7
France	40.2	Estonia	29.9
Denmark	39.5	Ukraine	30.0
Chile	39.4	Kazakhstan	30.3
Israel	39.3	Greece	31.7
Taiwan	39.2		

Regarding the efficiency of the coal-fired power plants, it is possible to observe that the situation is not similar to the production capability. In fact, in Table 19.4 are reported the top 10 and the lowest nine countries in efficiency. It is possible to note that, with the exception of Japan and France, all the other countries are practically small, but high technology and GPD, countries. Vice versa the lower efficiency power plants are mainly in Russia and other former Russian and East Europe countries. Russian coal-fired plant efficiency is only 23.9%, compared to Austria that has 42.9%: this means, respectively, mainly old subcritical and USC power plants.

South Asian countries, such as China and other emerging countries, like India, South Africa, Chile, and Indonesia, have had in the last decade a relevant increase of

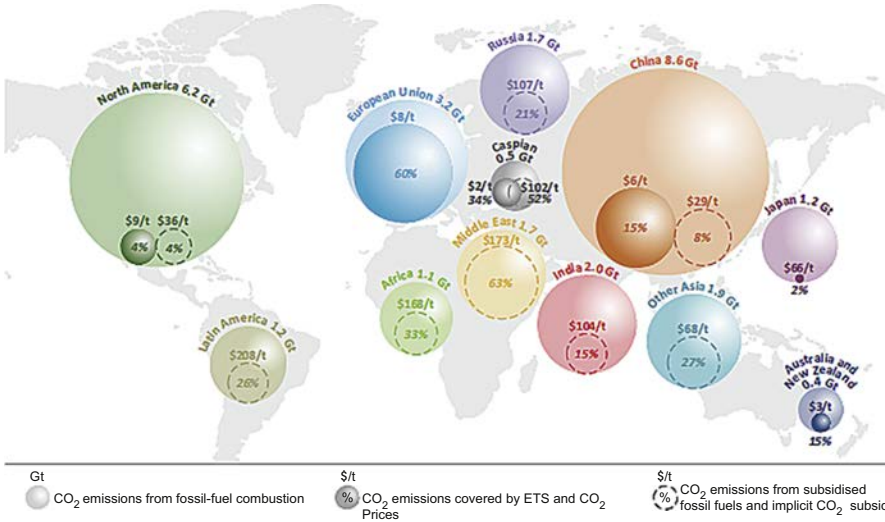


Figure 19.10 CO_2 emissions from fuel combustion [13].

GPD and have increased the efficiency with the construction of supercritical or USC plants, and therefore they are in the range of 35%.

As quite a direct consequence of the electricity production, the CO_2 emission production is distributed almost in the same countries, as shown in Fig. 19.10, but in the top 10 emission countries there is the entrance of Iran and Saudi Arabia (Table 19.5).

Also in this analysis the two bigger producers of CO_2, the United States and China, are emitting in 2014 about 63% of the total top 10.

Table 19.5 Top 10 CO_2 emission producer countries

Country	CO_2 emission ($MtonsCO_2$)
China	8337
United States	5312
India	2187
Russia	1676
Japan	1141
Germany	716
South Korea	589
Iran	586
Canada	518
Saudi Arabia	510

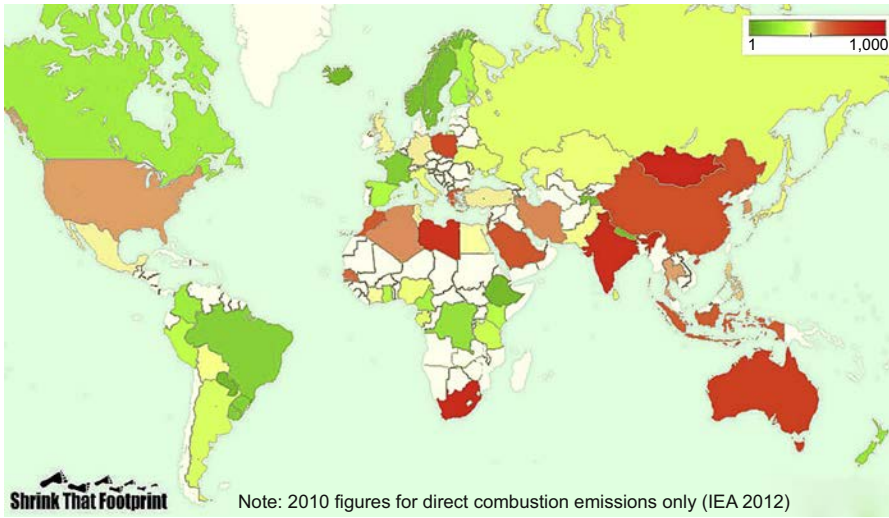


Figure 19.11 Carbon intensity of electricity: g CO_2/kWh (2012) [14].

19.1.7 The carbon intensity of electricity

Electricity emissions are a function of two things: how much electricity is used and how carbon intensive that electricity is. The carbon intensity of electricity varies greatly depending on fuel source. As a rough guide, coal has a carbon intensity of about 1000 g CO_2/kWh, oil is 800 g CO_2/kWh, natural gas is around 500 g CO_2/kWh, and nuclear, hydro, wind, and solar are all less than 50 g CO_2/kWh [12].

The carbon intensity of grid electricity is determined by the fuel mix used in generation. Using data from the International Energy Agency (IEA), a map has been produced to show just how different the carbon intensity of electricity is around the world.

In Fig. 19.11 the countries colored *dark green* like Norway, Iceland, Ethiopia and Paraguay have direct emissions from electricity generation less than 20 g CO_2/kWh because of the dominance of hydroelectricity, some geothermal in Iceland, and a large amount of nuclear in France. In India, Libya, Mongolia, and South Africa, the *dark red coloring* indicates electricity emissions of more than 900 g CO_2/kWh, due to oil, gas, and/or coal's dominance. Most other countries use a mix of generation sources, so they are somewhere in between.

19.1.8 Residential electricity use

The second component of electricity emissions is the amount of electricity used. For this example, residential electricity demand has been used, compared with the emissions caused by household electricity use that accounts for roughly a third of total electricity demand and varies considerably from country to country.

Norway has the biggest usage at almost 8000 kWh per person. Americans, Finns, Canadian, and Swedes all use more than 4000 kWh each, while places like Cameroon, India, and Tanzania use as little as 100 kWh per person.

19.1.9 Electricity emissions around the world

Now that we have data for the carbon intensity of electricity and how much people use in their homes, it is possible to compare residential electricity emissions. Taking in account also the emissions caused by grid losses used but not the upstream emissions from things like fuel production, processing, or equipment manufacturing, the results are revealing.

The largest footprints are from those countries that both use a lot of electricity and have quite carbon-intensive electricity. Of the 60 or so countries [12], Saudi Arabia, the United States, and Australia had by far the largest emissions at more than 2500 kg per person (see Fig. 19.12).

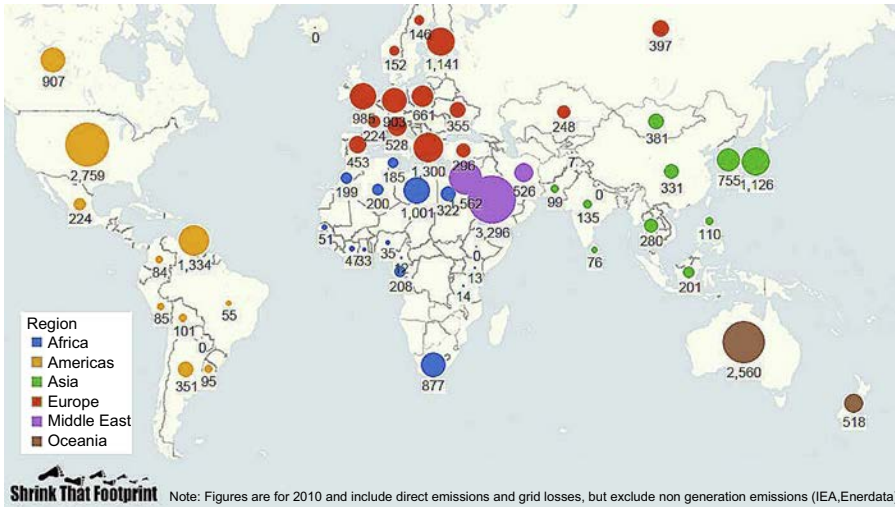


Figure 19.12 Residential electricity emissions: kg CO_2/capita (2010) [14].

In stark contrast, Iceland, Paraguay, and Ethiopia each registered 0 kg due to their incredibly low-carbon power. Notably, Norway, which uses almost double the residential electricity per capita as the United States, has emissions of just 152 kg per person. In contrast, India has more carbon-intensive electricity than the United States, but it emits just 135 kg per person due to such limited electricity use.

It is also interesting that Chinese emissions are just 331 kg per person despite their high coal use. This highlights just how small the residential share of electricity use is in China. A quick look at IEA stats shows that Chinese residents use just 18% of generated electricity; in the United States that figure is 38%.

19.1.10 World coal production and consumption

World coal production declined by 0.7% in 2014, while consumption grew by 0.4%. India (+6.4%) recorded the largest production increment, while China contributed the biggest decline (−2.6%). India accounted for the largest increment to consumption (+11.1%) and Ukraine for the largest decline (−20.2%) (Fig. 19.13).

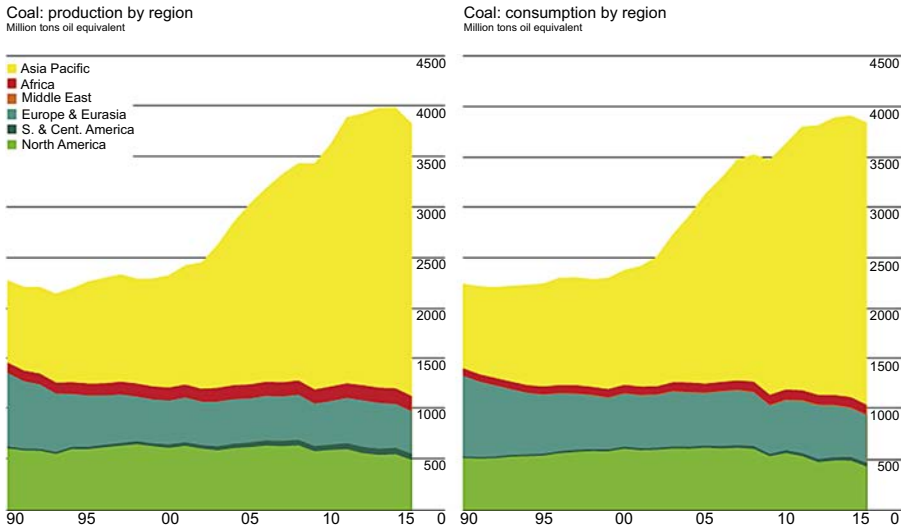


Figure 19.13 Coal production/consumption by region million tons oil equivalent [15].

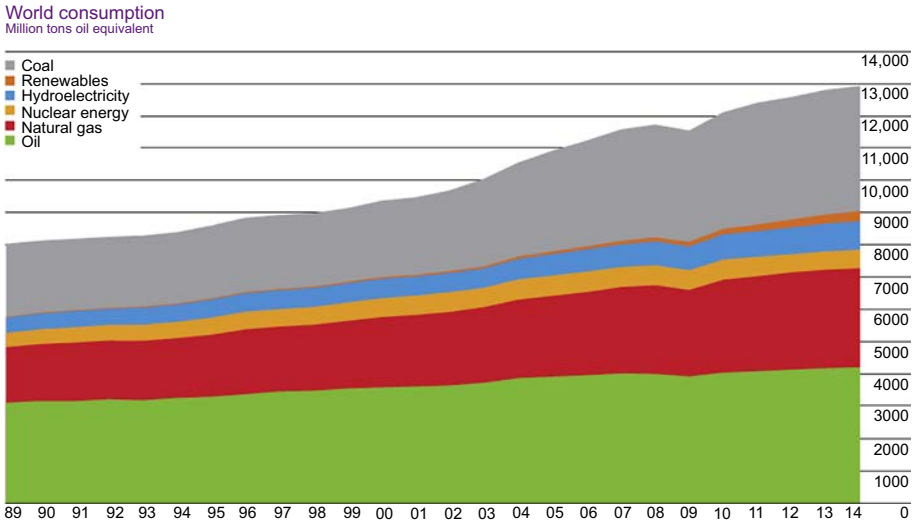


Figure 19.14 Primary energy world consumption (1989–2014) million tons oil equivalent [15].

World primary energy consumption grew by a below-average 0.9% in 2014 (see Fig. 19.14), the slowest rate of growth since 1998 other than the decline in the aftermath of the financial crisis. Growth was below average in all regions except North America and Africa. All fuels except nuclear grew at below-average rates. Oil remains the world's dominant fuel. Hydroelectric and other renewables in power generation both reached record shares of global primary energy consumption (6.8% and 2.5%, respectively).

The Asia Pacific region once again accounted for the largest increment to global primary energy consumption and continues to account for the largest share (41.3% of the global total). The region accounted for over 71% of global coal consumption for the first time in 2014 (Fig. 19.15), and coal remains the region's dominant fuel. Gas is the dominant fuel in Europe, Eurasia, and the Middle East, while oil is the largest source of energy in the Americas and Africa.

Coal prices in 2014 declined in all regions for the third consecutive year, as shown in Fig. 19.16. The price level remained the lowest in North America and highest in Japan. The steam coal price differential between Asia and North America dropped from $20/t in 2013 to $9/t, and the spread between Northwest Europe and North America narrowed from $10/t to $6/t.

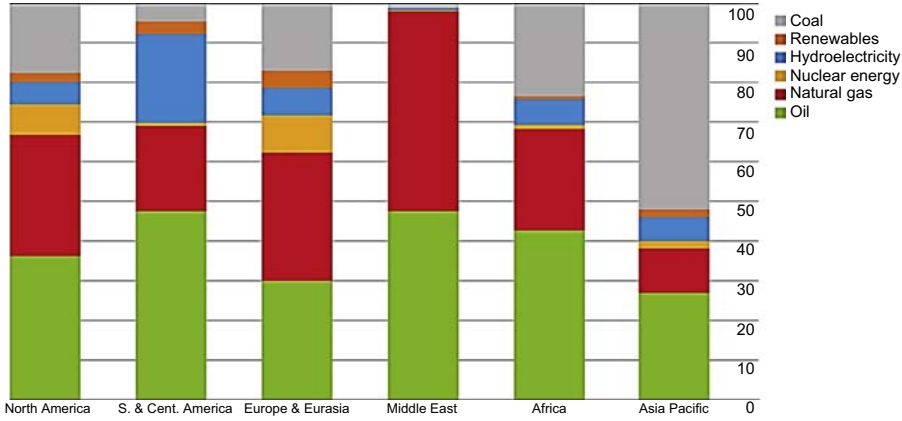


Figure 19.15 Primary energy regional consumption pattern 2014 percentage [15].

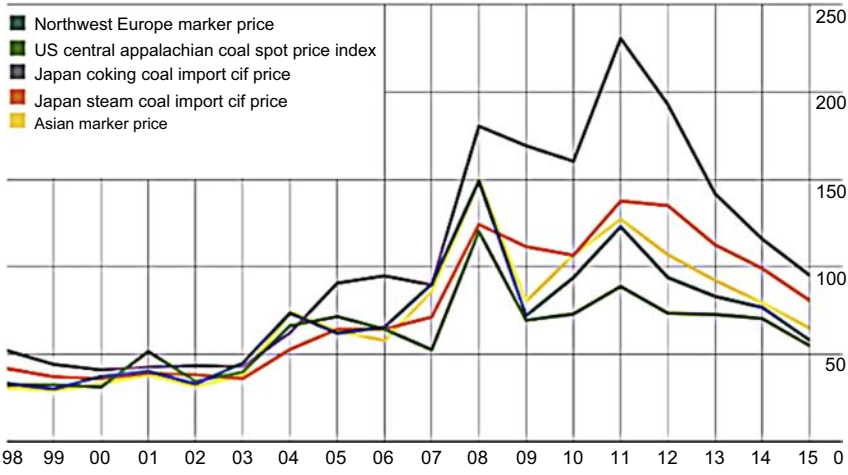


Figure 19.16 Coal price 1990–2014 [16].

19.2 The role of coal in future global energy needs

19.2.1 World coal markets are in transition

While many countries are commencing efforts to phase out coal due to concerns about its contribution to climate change, many other developing nations see coal as one of the cheapest fuels, offering a much needed solution to rapidly growing electricity demand.

Furthermore, coal is not just a cheap fuel: in parts of the world such as India, Indonesia, Pakistan, and China, coal offers employment opportunities where other alternative occupations are often not available. Coal also often subsidizes the cost of other freight, making it possible for cargos of other commodities to get to market, which might not occur in the absence of a dynamic logistical railroad.

19.2.2 Yet coal is not without its disadvantages

It is not only a major emitter of hazardous pollutants including fly ash and particulates, but it is also a significant contributor to the principal greenhouse gas, carbon dioxide. Finally, mining conditions in some countries are insufficient, causing negative effects on the health and safety of employees as well as the local environment [17].

Remarking on the huge and unpredictable change in the energy marked since the beginning of the 21st century, Dr Robert Romanosky from NETL (National Energy Technology Laboratory, USA) at the fourth international conference on advanced materials technology for fossil power plants (EPRI) in 2004 in discussing about the US coal-fired plants said that there were many old plants in operation and there was a proposal (Fig. 19.17) for the construction of 94 new plants for about 64 GW.

Eleven years later (2015), the United States planned the retirement of about 200 coal plants nationwide, which represents the phase-out of nearly 40% of the 523 US coal plants that were in operation just 5 years ago (2010) [19].

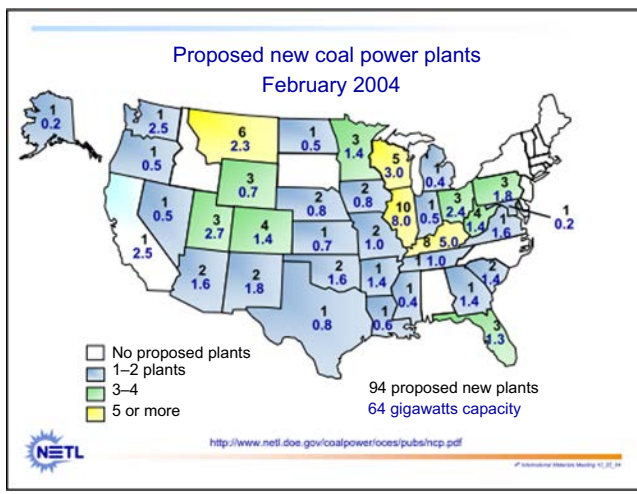


Figure 19.17 Proposed new coal power plants in United States (February 2004) [18].

In year 2015, before and after COP21 conference, some countries announced the phase out of coal in at least the old and low-efficiency coal-fired power plants. These announcements have been made by Canada, the United States, the United Kingdom, Germany, and also by Austria, who we saw has the best efficiency in the world.

The decision of these countries to phase out the dirtiest coal-fired power plants in the next 5–10 years has to be taken positively. An additional positive decision is the increase of biomass co-firing in the existing coal-fired plants.

Co-firing of coal with wood pellets can reduce GHG emissions by 91% compared to burning coal alone, according to a recent Ontario study [20]. Today, more than 100 European power plants co-fire.

On the other side, Southeast Asia is a cornerstone of the global steam coal market, a role the region is set to continue to play in the coming decades. At the end of 2013, Southeast Asia had 28 billion tons of proven coal reserves, about 3% of the world total, with the vast majority (80%) located in Indonesia and most of the remainder in Vietnam. The region has a considerably larger resource base that could be converted to reserves as production expands.

The lower price relative to other fuels and the need to provide electricity to the 120 million people in the region that still lack access all contribute to coal's expanding role in the fuel mix, especially in Indonesia, Malaysia, Philippines, Thailand, and Vietnam. Southeast Asia is one of the few regions in the world where coal's share of the energy mix is projected to increase: by 2020, coal's share of primary energy demand rises to 21%, overtaking natural gas. By 2040, coal just surpasses oil to become the most consumed fuel, accounting for 29% of the mix (Fig. 19.18).

The provision of electricity is critical to India's energy and economic outlook and is a major area of uncertainty for the future. The country's electricity demand in 2013 was 897 TWh, up from 376 TWh in 2000, having risen over this period at an average annual rate of 6.9%.

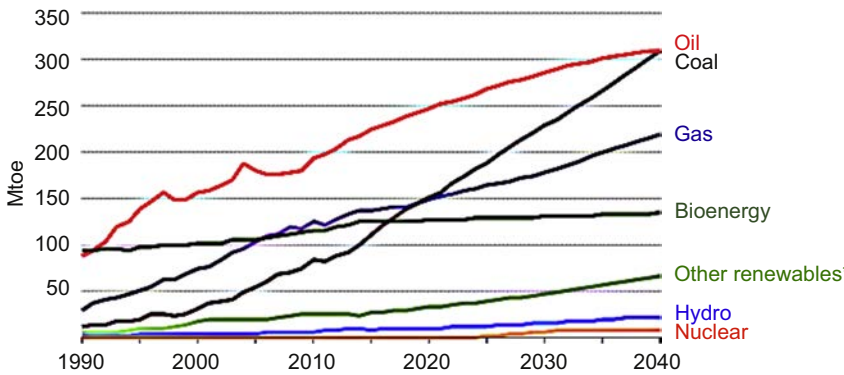


Figure 19.18 Primary energy demand by fuel in Southeast Asia 1990–2040 [21].

On the supply side, India has some 290 GW of power generation capacity, of which coal (60%) makes up by far the largest share, followed by hydropower (15%) and natural gas (8%). The mix has become gradually more diverse: since 2000, almost 40% of the change in installed capacity was non-coal. This is reflected also in the figures for generation, which show how renewables are playing an increasingly important role (Fig. 19.19). But, despite the increase in generation, India faces a structural shortage of power.

Indian coal consumption of 1300 million tons of coal equivalent (Mtce) in 2040 is 50% more than the combined demand of all OECD countries and second only to China in global terms. The projected increase in coal use is split between power generation (to feed an additional 265 GW of coal-fired plants) and industry (primarily for iron, steel, and cement industries). This makes India, by a distance, the largest source of additional global coal demand (Fig. 19.20).

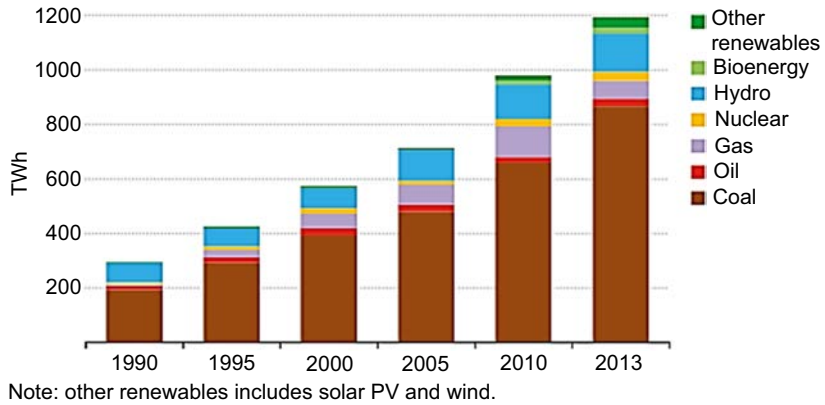


Figure 19.19 Total electricity generation in India by fuel [22].

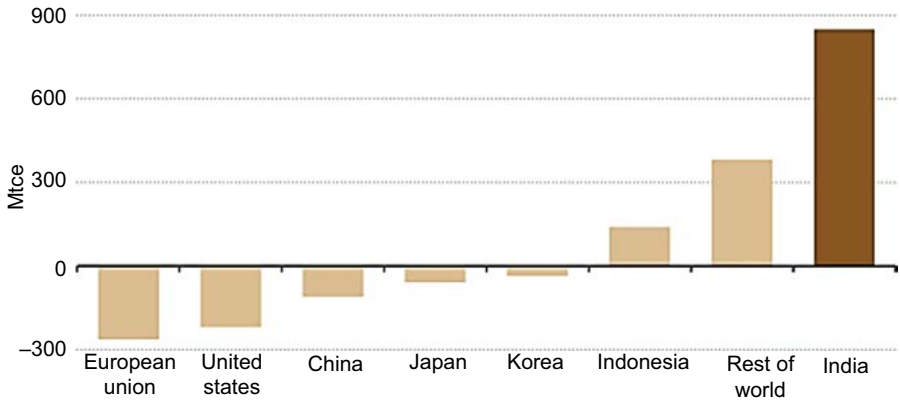


Figure 19.20 Change in coal demand by selected countries and regions in the IEA New Policies Scenario, 2013–2040 [22].

19.3 Advantages and disadvantages of coal-fired for power plant boilers

Fossil fuels are indeed the top fuels used all over the world for generating power and electricity. Among the fossil fuels, coal is the most widely used fuel in power plants. Coal-fired power plant boilers use different kinds of machinery that convert heat energy produced from combustion into mechanical energy.

Coal, gas, and oil are the fossil fuels responsible for most of the world's electricity and energy demands. Coal, which is readily available in most of the developing and developed world, has been used as a major source of fuel even in ancient human civilizations. It also found its use in historic steam engines at the dawn of the industrial revolution.

19.3.1 Advantages of coal as power plant fuel

Today, advances in technology have allowed coal to improve living conditions with its current role in meeting man's fuel needs. Coal has been used extensively in power generation where better technology is employed to ensure that there is a balance between ecology and economics in producing sustainable and affordable energy.

But, is coal really the answer to affordable and sustainable energy?

To find answers for this question, it is best to learn about the advantages and disadvantages of coal-fired plants. Some of its advantages include reliability, affordability, abundance, known technologies, safety, and efficiency.

1. **Reliability.** One of the greatest advantages of coal-fired power plant boilers is reliability. Coal's ability to supply power during peak power demand either as base power or as off-peak power is greatly valued as a power plant fuel. It is with this fact that advanced pulverized coal-fired power plants are designed to support the grid system in avoiding blackouts.
2. **Affordability.** Energy produced from coal-fired plants is cheaper and more affordable than other energy sources. Since coal is abundant, it is definitely cheap to produce power using this fuel. Moreover, it is not expensive to extract and mine from coal deposits. Consequently, its price remains low compared to other fuel and energy sources.
3. **Abundance.** There are approximately over 300 years of economic coal deposits still accessible. With this great amount of coal available for use, coal-fired plants can be continuously fueled in many years to come.
4. **Known technologies.** The production and use of coal as a fuel are well understood, and the technology required in producing it is constantly advancing. Moreover, coal mining techniques are continuously enhanced to ensure that there is a constant supply of coal for the production of power and energy.
5. **Safety.** Generally, coal-fired plants are considered safer than nuclear power plants. A coal power plant's failure is certainly not likely to cause catastrophic events such as a nuclear meltdown would. Additionally, the welfare and productivity of coal industry employees has greatly improved over the years. In fact, injuries, time lost, and fatalities have decreased significantly in the past years.

19.3.2 Disadvantages of coal-fired power plants

On the other hand, there are also some significant disadvantages of coal-fired plants including greenhouse gas (GHG) emissions, mining destruction, generation of millions of tons of waste, and emission of harmful substances.

1. **Greenhouse gas emissions.** It cannot be denied that coal leaves behind harmful by-products upon combustion. These by-products cause a lot of pollution and contribute to global warming. The increased carbon emissions brought about by coal-fired plants have led to further global warming that results in climate changes.
2. **Mining destruction.** Mining of coal not only results in the destruction of habitat and scenery, but it also displaces humans as well. In many countries where coal is actively mined, many people are displaced in huge numbers due to the pitting of the earth brought about by underground mining. Places near coal mines are unsafe for human habitation as the land could cave in at any time.
3. **Generation of millions of tons of waste.** Millions of tons of waste products that can no longer be reused are generated from coal-fired plants. Aside from the fact that these waste products contribute to waste disposal problems; these also contain harmful substances.
4. **Emission of harmful substances.** Thermal plants like coal-fired plants emit harmful substances to the environment. These include mercury, sulfur dioxide, carbon monoxide, mercury, selenium, and arsenic. These harmful substances not only cause acid rain but also are very harmful to humans as well.

19.3.3 The first way forward for clean coal technology

Coal is a precious energy source that should be consumed conservatively.

Despite the shortcoming, coal-fired power plant boilers are still important for the power generation; the traditional fuel combustion technology will be improved with a better performance to deal with the contradiction between industry development and environment.

In fact, coal can still ensure energy security and economic competitiveness. There are environmental challenges, but technologies are available to deal with these. In this chapter the materials under development to help the new technologies for the next advanced ultra-supercritical power plants will be deeply discussed. The future development of coal-fired power plants has to be focused on technologies to reduce both GHG (CO_2) and non-GHG (NOx, SO_2, PM) emissions, as schematically summarized in Fig. 19.21.

For these reasons, R&D programs to increase the efficiency of the coal-fired power plants are running in the world: these will be discussed in detail in the third part of this book and are summarized in Table 19.6. If the problems still open in the materials and components design development will be solved these new advanced ultra-supercritical power plants equipped with CO_2 capture and stored facilities are in fact able to reduce drastically the CO_2 emission, as shown in Fig. 19.22, in agreement with the COP21 directive.

Other type of coal power plants for production of energy that are currently under development and at level of demonstration plants could also give an effort for the reduction of CO_2 emission. These are the IGCC (integrated gasification combined cycle), CFBC (circulating fluidized bed combustion), and oxyfuel power plants.

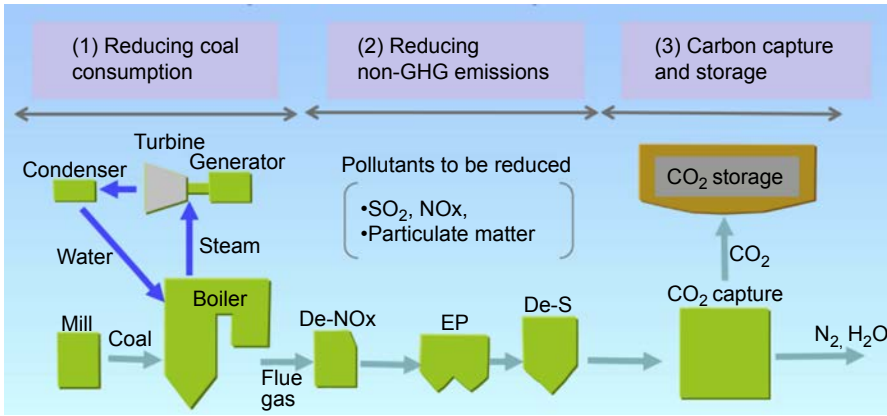


Figure 19.21 Technologies for cleaner coal generation [23].

Table 19.6 Toward >50% cycle efficiency with advanced USC technology plants [23]

National program	Steam temperature	Efficiency (LHV, net)	Program start date	Demonstration plant operational by (size)	Also includes
EU	700°C	>50%	1998	2021 (500MWe)	Coatings, biomass co-firing, cycling
USA	760°C	45–47% (HHV, net)	2000	2021 (600MWe)	Oxyfuel, coatings, high sulfur coal
Japan	700°C	>50%	2008	2021 (600MWe)	Biomass co-firing
China	700°C	46–50%	2011	2021 (660MWe)	
India	700°C	>50%	2011	2017 (800MWe)	

Table 19.7 summarizes the current status of the technologies, the future development, and introduction to the market.

By all these ways the coal-fired power plants are still able to guarantee a sustainable energy for the next generations in the 21st century (Fig. 19.23).

Low-carbon electricity is a wonderful thing, and it will be a central part of tackling climate change [25], but as simply summarized in Fig. 19.24, the coal is responsible, in 2010, only for 13 Gt of greenhouse gas emissions, or a little bit more than a quarter of all emissions. The rest came from industry, transport, buildings, agriculture, forestry, and waste.

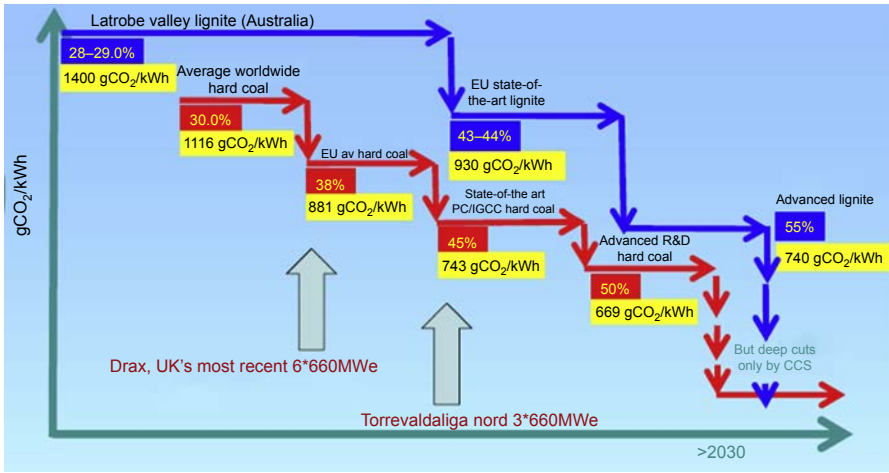


Figure 19.22 CO_2 emission reduction by key coal utilization technologies [23].

The thing that is exciting about electricity from a climate standpoint is that we actually or in the near future have technology that can slash its emissions. To help provide some clarity and context as to the relative importance of low-carbon electricity, these following considerations test a simple idea.

What would global electricity generation emissions look like if the world used just one generation technology?

In 2010 the world generated 21,400 TWh of electricity, which resulted in emissions of 13 Gt CO_2e (the beige balloon) given the current fuel mix. Using the central estimates from the IPCC's (Intergovernmental Panel on Climate Change) excellent meta-study of electricity generation life cycle assessments, we can estimate what these emissions would look like using just one technology [26].

The results are stark

Using coal 21,400 TWh would result in 21 Gt CO_2e, for oil it is 18 Gt, and for natural gas it is 10 Gt. In contrast, geothermal and solar PV are 1 Gt, solar CSP is 0.5, biopower and nuclear 0.4, wind 0.3, ocean 0.2, and hydro 0.1 Gt.

The gap between fossil fuels and the rest is a chasm

These numbers deserve some global context. To have a decent chance of keeping climate change to 2°C, we need to cut global emissions to something like 20 Gt CO_2e by 2050, and down toward zero by the end of the century. That is down from 50 Gt in 2010.

If we clicked our fingers tomorrow and switched all the coal, gas, and oil electricity generation in the world to low-carbon sources, we would still be at 37 Gt: a long way from a stable climate.

But the 13 Gt we currently emit is not where the abatement potential of low-carbon electricity ends.

Table 19.7 Date ranges for technical developments (draft) [24]

Technology	2012–2020	2021–2025	2026–2030	2031–2050
PCC-bituminous coals	Commercial SC and USC plants; oxyfuel demos; R&D on A-USC	Commercial USC plants; commercial-scale A-USC demo with CCS; oxyfuel A-USC pilot/demo	A-USC commercial plants; oxyfuel A-USC demo	A-USC with full CCS commercial available, including oxyfuel
PCC-lignite	Commercial SC and USC plants; lignite drying: 100% dry feed boiler demo and first commercial order; oxyfuel demo; R&D on A-USC	Commercial USC plants with 100% fuel drying; A-USC lignite plant demos with lignite drying; oxyfuel A-USC pilot/demo	Commercial A-USC plants with 100% fuel drying; oxyfuel A-USC demo	Lignite A-USC incorp drying fully commercially available with full CCS, including oxyfuel
CFBC Circulating fluidized bed combustion	Sales of commercial supercritical then USC CFBC boilers	Commercial USC CFBC	A-USC CFBC commercial demo; A-USC oxyfuel demo; first A-USC commercial orders	-USC CFBC with full CCS commercially available, including oxyfuel
IGCC integrated gasification combined cycle	Commercial plants with 1400–1500°C turbines; R&D on availability, low grade coals; pilot dry gas cleaning, non-cryogenic oxygen	Commercial plants with 1600°C turbines for high hydrogen fuel for CCS capability; dry syngas cleaning; some non-cryogenic oxygen; supporting R&D	Commercial plants with 1700°C turbines for high hydrogen fuel for CCS capability; some non-cryogenic oxygen; supporting R&D	Commercial plants with 1700°C + turbine for high hydrogen fuel with full CCS; non-cryogenic oxygen option

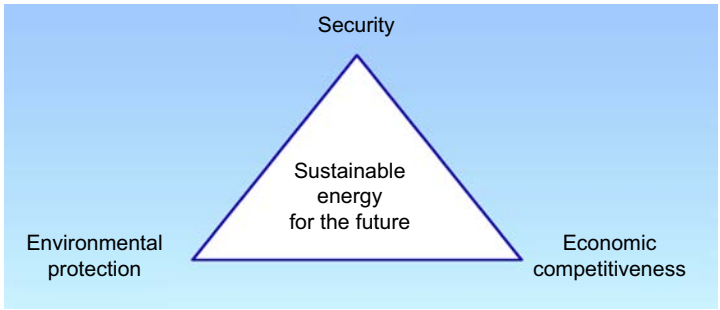


Figure 19.23 Sustainable energy for future [23].

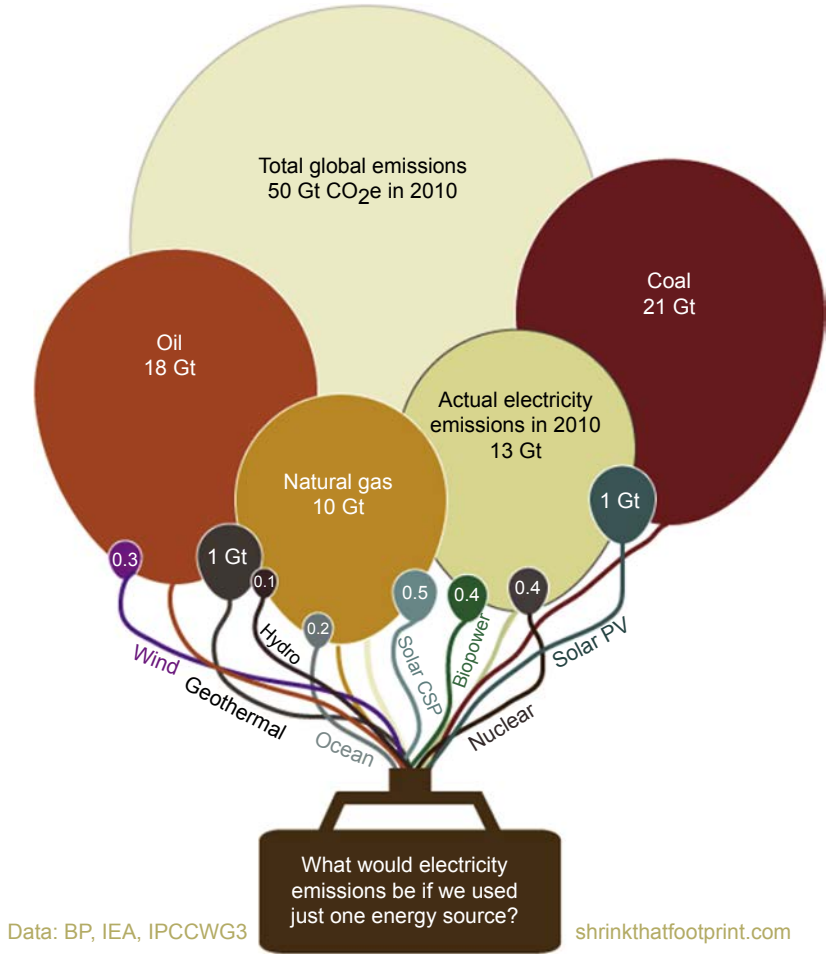


Figure 19.24 Total CO_2 emission and shear of fossil fuels.

A further 20 Gt of current emissions result from transport, industry, and buildings, large swathes of which have the potential to be electrified and benefit from low-carbon electricity.

The remaining emissions from deforestation, agriculture, and waste need their own solutions. And when you consider that energy demand is likely to increase by 50–100% by 2050, we could really do with some negative emission technologies too.

You see, low-carbon electricity really is a wonderful thing.

19.4 Carbon capture, use, and storage

19.4.1 What is CCS?

CCS is a technology that can capture up to 90% of the carbon dioxide emissions produced from the use of fossil fuels in electricity generation and industrial processes, preventing the carbon dioxide from entering the atmosphere [27].

Furthermore, the use of CCS with renewable biomass is one of the few carbon abatement technologies that can be used in a "carbon-negative" mode actually taking carbon dioxide out of the atmosphere.

The CCS chain consists of three parts (Fig. 19.25):

- capturing and separation of the carbon dioxide
- compression and transporting the carbon dioxide
- securely storing the carbon dioxide emissions underground in depleted oil and gas fields or deep saline aquifer formations

First, capture technologies allow the separation of carbon dioxide from gases produced in electricity generation and industrial processes by one of three methods (Fig. 19.26):

- pre-combustion capture
- post-combustion capture
- oxyfuel combustion

Carbon dioxide is then transported by pipeline or by ship for safe storage. Millions of tons of carbon dioxide are already transported annually for commercial purposes by road tanker, ship, and pipelines. Many countries have decades of experience of transporting carbon dioxide by pipeline for enhanced oil recovery projects (Fig. 19.27).

The carbon dioxide is then stored in carefully selected geological rock formations that are typically located several kilometers below the earth's surface.

At every point in the CCS chain, from production to storage, industry has at its disposal a number of process technologies that are well understood and have excellent health and safety records. The commercial deployment of CCS will involve the widespread adoption of these CCS techniques, combined with robust monitoring techniques and government regulation.

19.4.1.1 Pre-combustion capture

A pre-combustion system involves first converting solid, liquid, or gaseous fuel into a mixture of hydrogen and carbon dioxide using one of a number of processes such as "gasification" or "reforming."

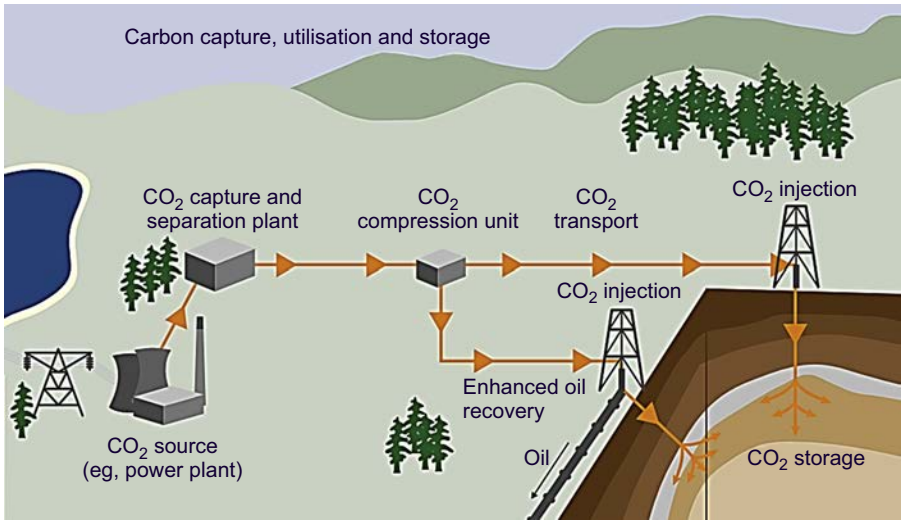


Figure 19.25 Example of CCS flowchart.

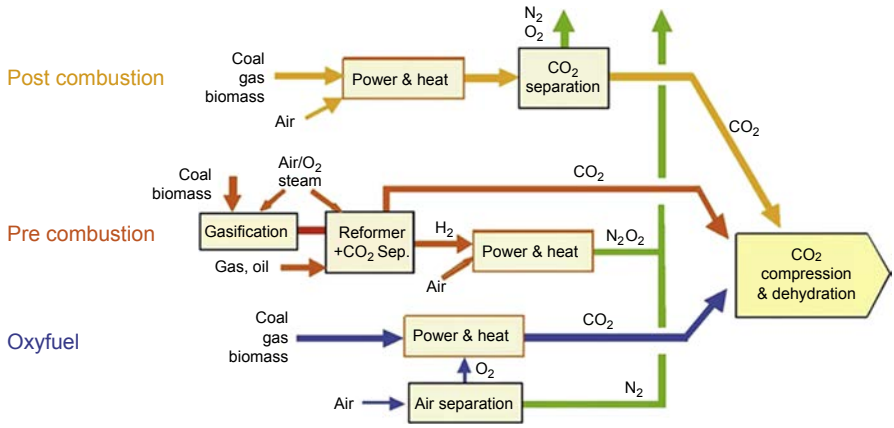


Figure 19.26 Post-combustion, pre-combustion, and oxyfuel flow chart [28].

Reforming of gas is well-established and already used at scale at refineries and chemical plants around the world. Gasification is widely practiced around the world and is similar in some respects to that used for many years to make town gas.

The hydrogen produced by these processes may be used not only to fuel our electricity production but also in the future to power our cars and heat our homes with near zero emissions.

The process layout is summarized in Fig. 19.28.

19.4.1.2 Post-combustion capture

CO_2 can be captured from the exhaust of a combustion process by absorbing it in a suitable solvent. This is called post-combustion capture. The absorbed CO_2 is liberated

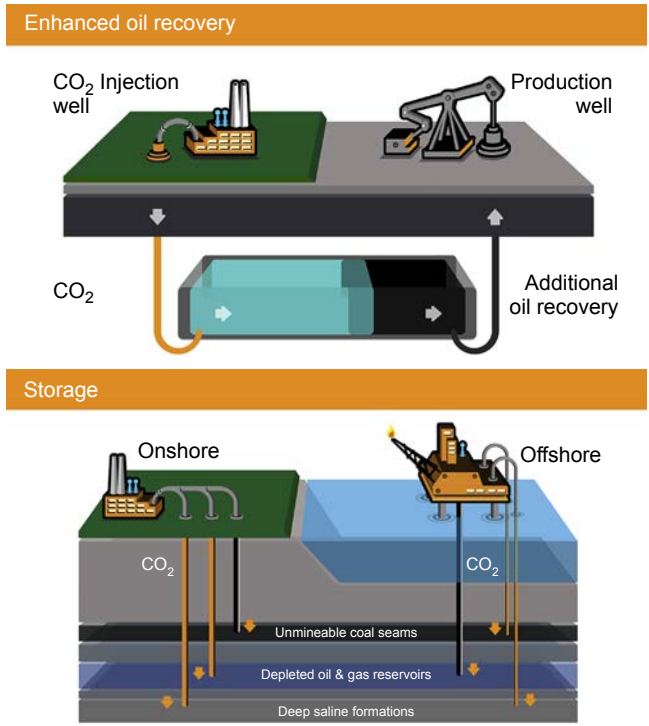


Figure 19.27 Enhanced oil recovery and storage layout [29].

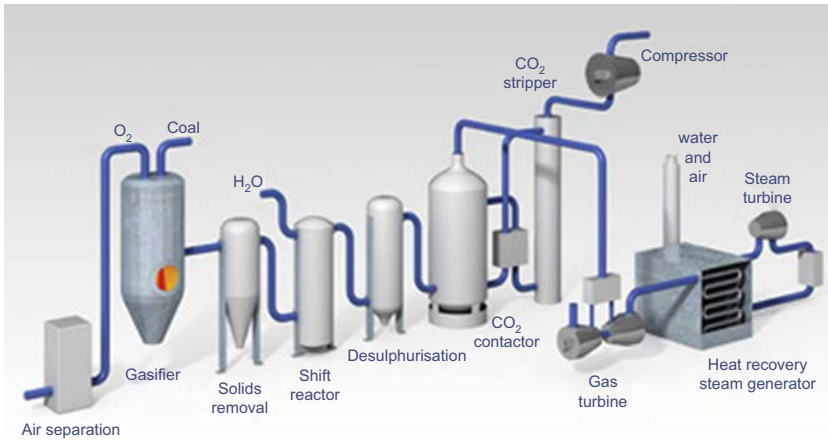


Figure 19.28 A pre-combustion capture system.
Courtesy of Costain.

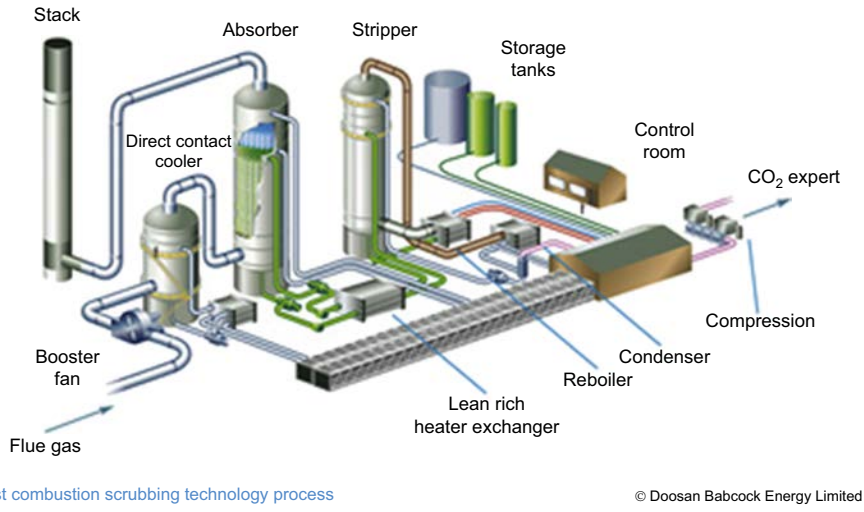


Figure 19.29 Post-combustion scrubbing technology.
© Doosan Babcock Energy Limited.

from the solvent and is compressed for transportation and storage. Other methods for separating CO_2 include high-pressure membrane filtration, adsorption/desorption processes, and cryogenic separation.

The process layout is summarized in Fig. 19.29.

19.4.1.3 Oxyfuel combustion systems

In the process of oxyfuel combustion the oxygen required is separated from air prior to combustion, and the fuel is combusted in oxygen diluted with recycled flue-gas rather than by air.

This oxygen-rich, nitrogen-free atmosphere results in final flue-gases consisting mainly of CO_2 and H_2O (water), so producing a more concentrated CO_2 stream for easier purification. The plant layout is shown in Fig. 19.30 and in Fig. 19.31 is presented an oxyfuel test unit.

19.4.2 Transport

Once captured, carbon dioxide must then be transported by pipeline or ship for storage at a suitable site. The technologies involved in pipeline transportation are the same as those used extensively for transporting natural gas, oil, and many other fluids around the world; CO_2 can also be transported by truck or ship, but in this case, it is carried in liquid form at a pressure of 15 bar and a temperature of −30°C (Fig. 19.32). This last technique is quite similar to the transport of LNG.

In some cases, it may be possible to reuse existing but redundant pipelines. Carbon dioxide is currently transported for commercial purposes by road tanker, ship, and

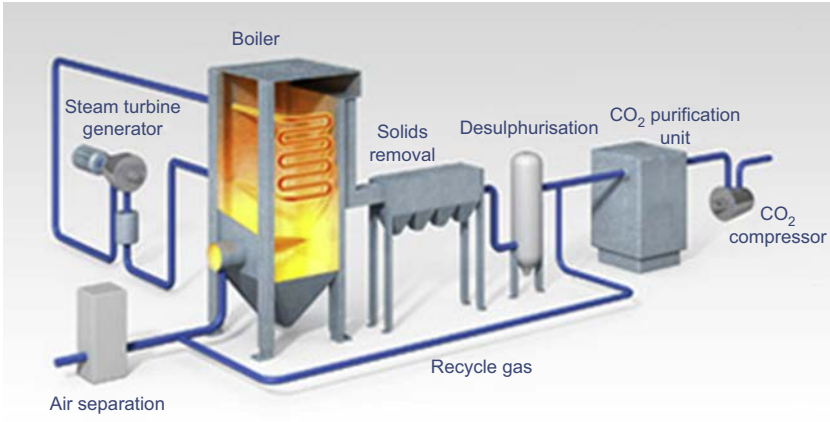


Figure 19.30 An example of an oxyfuel system.
Courtesy of Costain.



Figure 19.31 An oxycoal test unit.
Courtesy of Doosan Babcock.

pipeline. Each CCS project would choose the most appropriate method for transporting carbon dioxide and be subject to planning and health and safety regulation. Large commercial networks of carbon dioxide pipelines have been in operation for more than 30 years with excellent safety and reliability records.

There is significant potential for the development of local and regional CCS pipeline infrastructure, leading to CCS "clusters" where CO_2-intensive industries could locate. Developing clusters, where infrastructure can be shared by a number of industrial sources of carbon dioxide emissions, will result in the most cost-effective way to deliver CCS infrastructure development and ultimately lower costs to consumers.



Figure 19.32 Offshore laying of the CO_2 pipeline at Snøhvit (image courtesy of Statoil), onshore pipeline [30], and shipping by boat [31].

19.4.3 Storage

Once the carbon dioxide has been transported, it is stored in porous geological formations that are typically located several kilometers under the earth's surface, with pressure and temperatures such that carbon dioxide will be in the liquid or "supercritical phase." Suitable storage sites include former gas and oil fields, deep saline formations (porous rocks filled with very salty water), or depleting oil fields where the injected carbon dioxide may increase the amount of oil recovered. Depleted oil and gas reservoirs are more likely to be used for early projects as extensive information from geological and hydrodynamic assessments is already available. Deep saline aquifers represent the largest potential carbon dioxide storage capacity in the long term, but they are currently less well understood [31]. Fig. 19.33 shows two examples of carbon dioxide storage.

At the storage site the carbon dioxide is injected under pressure into the geological formation. Once injected, the carbon dioxide moves up through the storage site until it reaches an impermeable layer of rock (which cannot be penetrated by carbon dioxide) overlaying the storage site; this layer is known as the cap rock and traps the carbon dioxide in the storage formation. This storage mechanism is called "structural storage."

Structural storage is the primary storage mechanism in CCS and is the same process that has kept oil and natural gas securely trapped under the ground for millions of years providing confidence that carbon dioxide can be safely stored indefinitely. As the injected carbon dioxide moves up through the geological storage site toward the cap rock, some of it is left behind in the microscopic pore spaces of the rock. This carbon dioxide is tightly trapped in the pore spaces by a mechanism known as "residual storage."

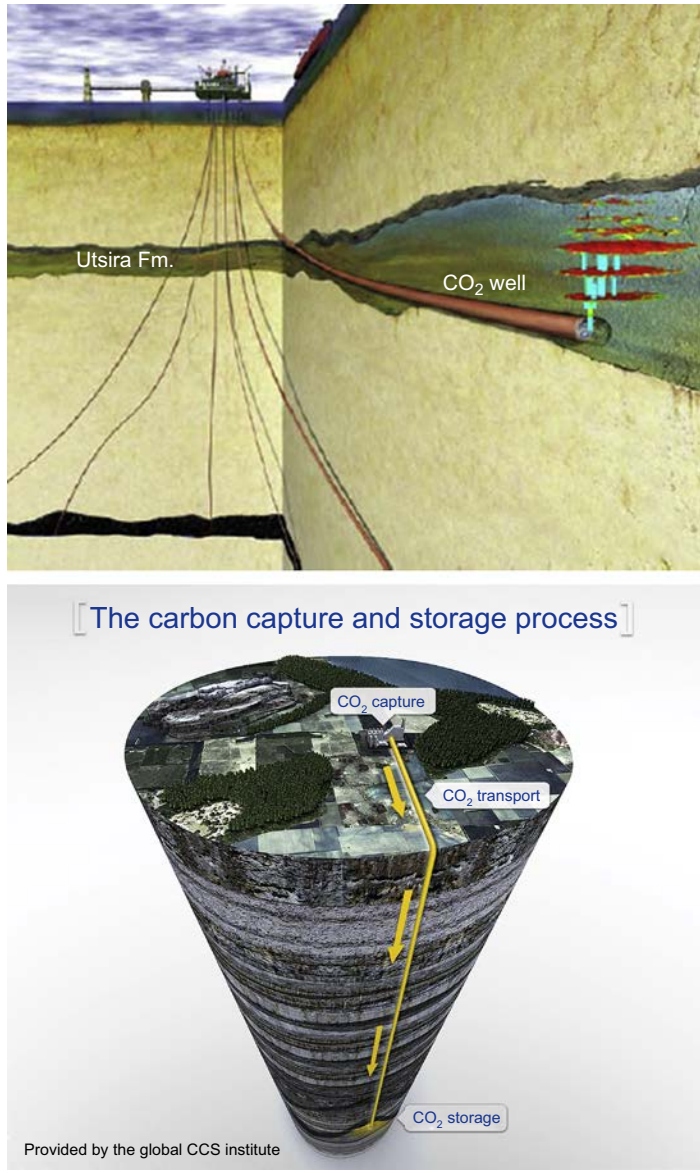


Figure 19.33 Diagram showing how CO_2 is stored underground [32].
Image courtesy of Statoil and Global CCS Institute. https://www.globalccsinstitute.com/sites/www.globalccsinstitute.com/files/pages/92241/3-carbon-capture-and-storage-process.jpg.

Over time the carbon dioxide stored in a geological formation will begin to dissolve into the surrounding salty water. This makes the salty water denser, and it begins to sink down to the bottom of the storage site. This is known as "dissolution storage." Finally, "mineral storage" occurs when the carbon dioxide held within the storage site binds chemically and irreversibly to the surrounding rock.

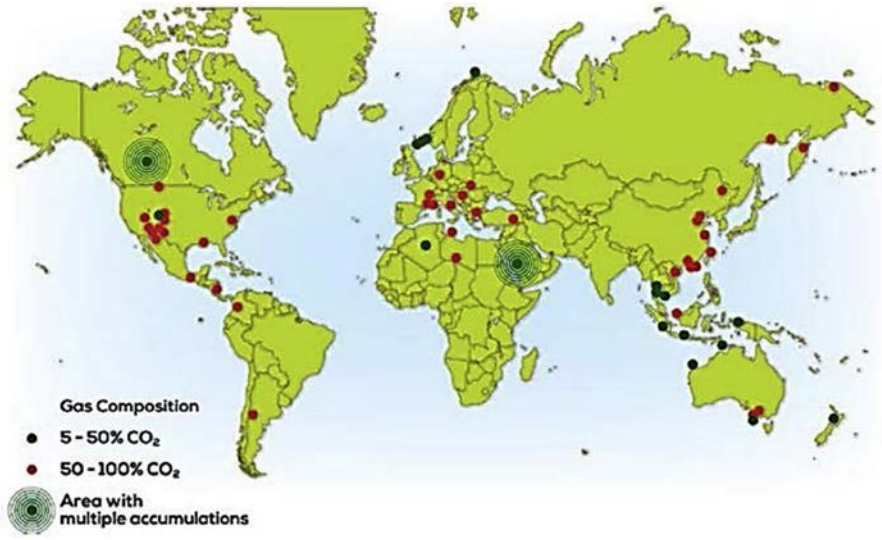


Figure 19.34 Examples of natural accumulations of CO_2 around the world [33].

As the storage mechanisms change over time from structural to residual, dissolution and then mineral storage, the carbon dioxide becomes less and less mobile. Therefore the longer carbon dioxide is stored the lower the risk of any leakage.

In a special report on CCS, the IPCC concluded that in storage sites that have been carefully selected and managed, the fraction of carbon dioxide retained is likely to exceed 99% over 1000 years (Fig. 19.34). This estimate of the risk that carbon dioxide may be released and contribute to climate change was made based on observations and analysis of current carbon dioxide storage sites, natural systems, engineering systems, and models. The IPCC noted that similar fractions retained are likely for even longer periods of time given the evolving roles of different trapping mechanisms further reducing risks of leakage.

Fig. 19.35 shows clearly the main storage sites in the world are practically the same as the fossil fuel reserve locations.

19.5 Why CCS

CCS is a key technology for tackling climate change in an affordable way, delivering economic growth and regional prosperity, and industry already has the skills and experience to safely deliver CCS.

CCS is one of a suite of technologies that will all be required to combat climate change, including renewables, nuclear, and energy efficiency. The importance of CCS as one of the tools against global warming is highlighted in a report by the IEA, which found that CCS could contribute to a 19% reduction in global CO_2 emissions by 2050, and that fighting climate change could cost over 70% more without CCS (Fig. 19.36).

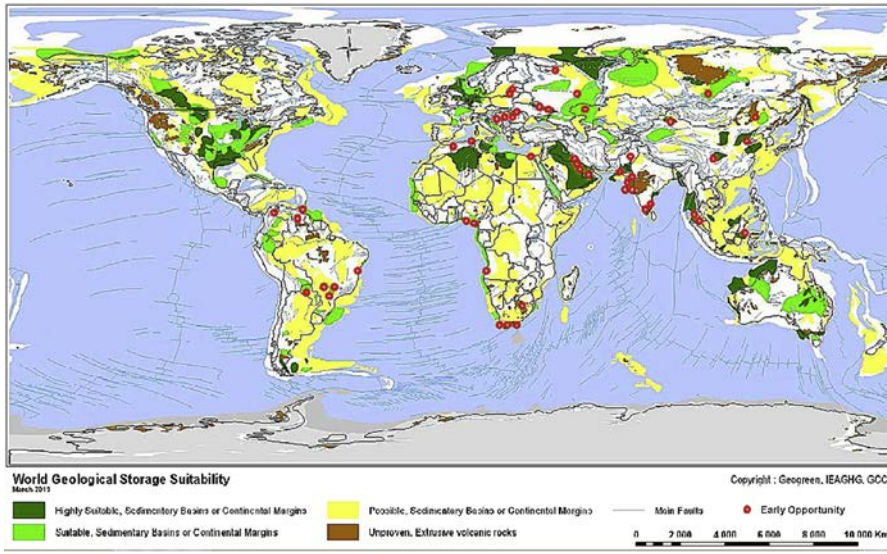


Figure 19.35 Global CO_2 disposal sites [34].

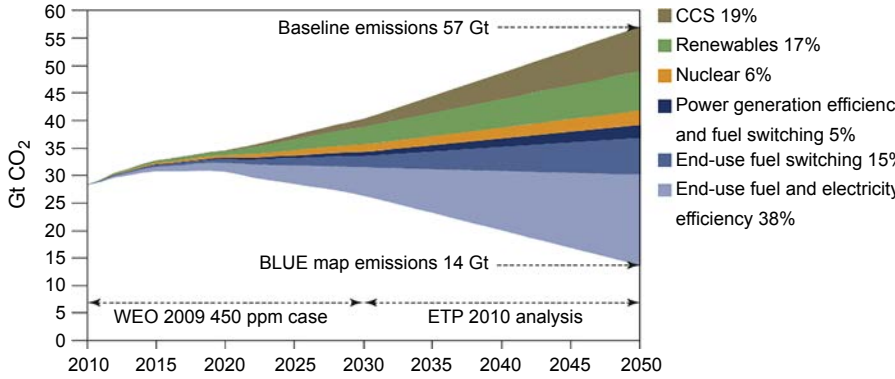


Figure 19.36 Key technologies for reduction of CO_2 emission under Blue Map Scenario [35].

CCS can be applied to fossil fuel-fueled electricity generating plants, such as coal- or gas-fired power stations. Fossil fuel plants with CCS have a key role to play in providing a balanced energy supply, which can cope with rapid changes in demand and intermittency of supply, which nuclear and renewables cannot. CCS will play a key role in the UK to provide secure, affordable, low-carbon electricity in the transition to a low-carbon economy.

CCS can also significantly reduce emissions from industry such as cement, steel, and chemical industries, and in many instances, it is the only currently viable technology to do so. CCS when combined with biomass can result in negative CO_2 emissions. As plants grow, they absorb CO_2 from the atmosphere. When they are burned

to produce power, if the CO_2 is captured and stored there is a net reduction in CO_2 in the atmosphere.

"CCS has a key part to play in ensuring that we can keep the lights on at the same time as fighting climate change. The International Energy Agency has estimated that globally 3400 CCS plants will be needed by 2050 if we are to meet our critical target of 2°C above pre-industrial levels. The UK has the skills and opportunity to lead the world in this technology, which is why in the spending review we committed to investing up to a billion pounds in CCS."

19.6 Tackling climate change

The overwhelming majority of the world's climate scientists and governments agree that climate change is occurring, and the main cause is human use of fossil fuels. Storing carbon dioxide is much safer than the current option of emitting it into the atmosphere. CCS will allow us to continue using fossil fuels while also substantially reducing emissions of greenhouse gas emissions to the atmosphere.

Rapidly developing countries will continue to be reliant on fossil fuels to provide energy for continued growth and development. To maintain secure, low-carbon electricity, developing countries will need to harness the flexibility of fossil fuel electricity generation as more intermittent renewables and inflexible nuclear come onto the grid.

While renewables, nuclear power, and improvements in energy efficiency will play an increasing role in moving the world toward a low-carbon economy, they cannot be the complete answer. CCS gives us the flexibility to deploy other low-carbon technologies making our energy supplies more secure and reliable. To keep the lights on, we will need fossil-derived electricity.

The IEA estimates that energy demand could increase by as much as 45% by 2030. Much of this will be met by fossil fuels, for example, in the developing world; around two new coal-fired power stations are opened every week. CCS will decarbonize energy, generating low-carbon power to help meet increasing energy demand.

CCS is not applicable only to fossil fuel power plants, but it can also be applied to any large industrial sources of carbon dioxide, such as cement, steel, and chemical industries. In some sectors, CCS represents the sole option for reducing carbon dioxide emissions at the scale necessary.

CCS combined with burning biomass for energy could result in negative carbon dioxide emissions. As plants grow, they absorb carbon dioxide from the atmosphere. If they are then burned and the carbon dioxide captured and stored, there is a net reduction in carbon dioxide in the atmosphere.

The IPCC found that to have a reasonable chance that global average temperature increases do not exceed preindustrial levels by more than 2°C, the global carbon dioxide emissions must be reduced by between 50–85% by 2050. To achieve this will require the application of all available low-carbon technologies at a scale and rate far greater than current efforts.

19.7 Industry experience

Industry has decades of experience capturing, transporting, and piping carbon dioxide deep underground, as well as experience in understanding and monitoring the behavior of stored carbon dioxide. Storage sites are very carefully selected in areas where the rock formations will safely absorb carbon dioxide deep below the seabed. There is a strong legal framework, under the European CCS Directive, to ensure the safe geological storage of carbon dioxide. The industry is covered by strict national and international regulations to ensure health and safety and environmental protection, and international standards for CCS are being developed by the International Organization for Standardization (ISO).

Carbon dioxide is a naturally occurring gas, and millions of tons of carbon dioxide are safely transported each year around the world, for example, in the soft drinks industry. The United States has several decades experience of transporting and injecting carbon dioxide for enhanced oil recovery: the first carbon dioxide pipeline was commissioned in 1972, and there are now over 6000 km of carbon dioxide pipelines in the United States.

All the key processes of CCS have been proven over a number of years, and there are currently four industrial-scale CCS projects operating worldwide storing around five million tons of carbon dioxide each year. In March 2012 the Global CCS Institute had identified 75 large-scale integrated projects globally, including 15 projects in operation or under construction that are expected to capture 35.4 million tons/year. What needs to happen now is to integrate CCS into projects at commercial power stations and at other major carbon dioxide-emitting processes to drive the really deep emissions reductions that are needed.

The North Europe countries, like the United Kingdom, Norway, and the Netherlands, benefit from experience with North Sea oil and gas operations, meaning they already have many of the skills that are needed to deploy CCS projects. Furthermore, the first CCS demonstration competition in the United Kingdom provided invaluable knowledge through the Front End Engineering Design studies produced by E.ON and the Scottish Power Consortium.

19.8 Economic importance

The importance of CCS should not be understated. CCS is applicable to both the power sector and the industrial sectors, and it will therefore play a vital role in the move to a low-carbon economy. In the power sector, fossil fuel power with CCS is one of the options that has been identified by the governments as a major part of the low-carbon energy mix alongside nuclear and renewables. CCS will be an increasingly important and necessary option for many industrial sectors, such as steel, cement, chemicals, and ammonia. Many of these sectors do not have any alternatives for reducing their emissions aside from CCS, as their carbon dioxide

is generated in the process (as well as the fuel they use). The ability of CCS to be developed in these sectors will therefore help maintain many of these vital industries in the world, making a significant contribution to local prosperity and retaining a large number of jobs.

Countries that develop CCS early will benefit from the export of skills and technology internationally. The huge contribution that CCS will make to global emissions reductions will result in the development of an enormous new industrial sector potentially worth trillions of dollars annually. Countries blessed with suitable storage capacity, as well as those that take the early steps to develop CCS, will have a unique opportunity to benefit from this emerging sector.

19.9 Affordability

CCS is a cost-effective and affordable way to help secure low-carbon energy supplies. The cost of reducing carbon dioxide emissions will be dramatically higher without CCS, up to 70% higher internationally (according to the IEA).

The cost of individual CCS projects can vary substantially depending on the source of the carbon dioxide to be captured, the distance to the storage site, and the characteristics of the storage site. The cost of capturing the carbon dioxide is typically the greatest cost of a CCS project. Recent studies conclude that the first CCS projects in the power sector are likely to cost between €60–90 per ton of carbon dioxide abated, although these costs are expected to decline significantly reaching €35–50 in the early 2020s primarily as a result of cost reductions for carbon dioxide capture.

Deploying CCS in coal-fired power plants is already cost-competitive (per ton of carbon dioxide emission abated) with other forms of low-carbon energy. Our next step should be to build commercial-scale power plants with CCS to optimize operations and so realize future cost reductions.

Low-cost CCS projects can be developed where carbon dioxide is already separated as part of an existing industrial process, resulting in a pure carbon dioxide stream with very low capture costs. Where these pure carbon dioxide streams are located close to suitable geological storage sites, the complete CCS project chain can be developed at a relatively low cost. Natural gas processing and ammonia plants are examples of industrial activities that separate carbon dioxide as part of standard industrial activity and may be suitable for developing low-cost CCS projects.

As with other forms of low-carbon generation, first of a kind CCS projects will be subject to higher costs and somewhat greater technical uncertainties. They will therefore need additional incentives; with the exception of some of the low-cost CCS opportunities, they cannot be developed based on current carbon prices. CCS should be treated similar to other low-carbon technologies; it needs only a long-term support structure equivalent to that which has been given to other low-carbon technologies in recent years.

19.10 CCS project proposals

Countries that have just started demonstration plants or commercial plants are these:

- United Kingdom: in different places
- Norway: Snøhvit, Sleipner by Statoil
- Algeria: In Salah, BP, Sonatrach and Statoil
- Canada: Weyburn

19.11 Things about CCS

- Tackling climate change without CCS will be more expansive,
- CCS is applicable to industrial sources of carbon dioxide (CO_2), not just to fossil fueled power plants,
- Biomass and CCS will result in negative carbon dioxide emission,
- CCS is already happening!
- Carbon dioxide has been safely captured, stored, and transported for decades,
- Fossil fuel power stations work even when it is not windy or sunny, so low-carbon fossil fuel power stations with CCS are complementary to the intermittent renewables and inflexible nuclear energy,
- Disused oil and gas pipelines can be reused to transport carbon dioxide,
- All the countries (World Committee on Climate Change) see CCS as a key technology,
- Hydrogen produced in the "pre-combustion capture" installation can be used to power vehicles.

19.12 Carbon dioxide reuse

CCS studies suggest that the global warming potential (GWP) from power plants can be reduced by 63–82% with the greatest reduction achieved by oxyfuel combustion in pulverized coal and IGCC plants and the lowest by post-combustion capture in combined cycle (CCGT) plants. However, other environmental impacts such as acidification and human toxicity are higher with than without CCS. For carbon capture and utilization (CCU), the GWP varies widely depending on the utilization option: Fig. 19.37 summarizes the possible utilization of the CO_2.

Mineral carbonation can reduce the GWP by 4–8% compared with no CCU. Utilization of CO_2 for production of chemicals, specifically deimethycarbonate (DMC), reduces the GWP by 4.3 times and ozone layer depletion by 13 times compared to discharging CO_2 to the atmosphere, but acidification is three times higher.

Capturing CO_2 by microalgae to produce biodiesel has 2.5 times higher GWP than fossil diesel with other environmental impacts also significantly higher: Fig. 19.38 shows the flow chart of the biodiesel production process.

On average, the GWP of CCS is significantly lower than the CCU options, However, its other environmental impacts are higher compared to CCU except for DMC production, which is the worst CCU option overall [36].

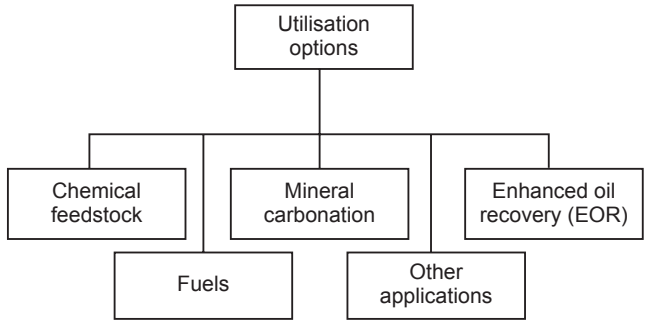


Figure 19.37 Flow chart of possible CO_2 utilizations [36].

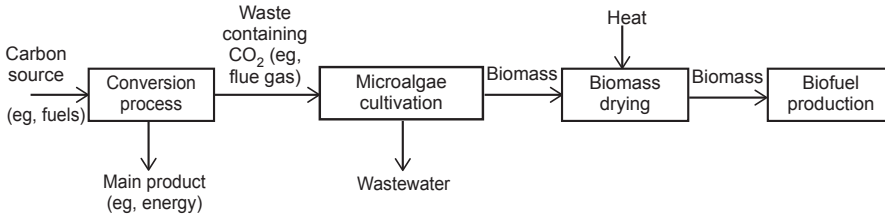


Figure 19.38 Layout of process for utilization of CO_2 to produce biofuels from microalgae [36].

Fig. 19.39 shows an overview of all the possible reuse of CO_2 in the different field of application: from industry to food.

In conclusion, even though both CCS and CCU technologies seek to mitigate climate change, they can only be regarded as temporary solutions, particularly those options that merely delay the emissions of CO_2 rather than eliminate them permanently. Although from an economic perspective CCU would appear to be better option than CCS as the latter is an unprofitable activity, the cost-effectiveness as well as the environmental impacts of CCU have to be evaluated carefully on a life cycle basis to ensure a positive economic and environmental balance. The latter in particular may not always to be the case. Moreover, the potential of CCU is still limited as the current global demand to sink enough CO_2 emissions to contribute significantly to meeting the carbon reduction targets. A further significant issue for CCU is that the "storage" time of CO_2 is limited by short lifespans of the chemicals and fuel produced. Therefore, future research should focus on the development of materials and products with longer lifetimes to enable long-term storage, and there is a risk of CO_2 leakage that could potentially cause more damage than if dilute emissions were to continue unabated. Equally significant is the fact that deployment of large-scale CCS is not expected until well into 2020s by which time it may be too late to reverse the impacts of climate change.

Nevertheless, if these concerns can be addressed, both CCS and CCU could play a role in mitigating climate change, together with the options such as energy demand reduction, renewables, and other low-carbon technologies.

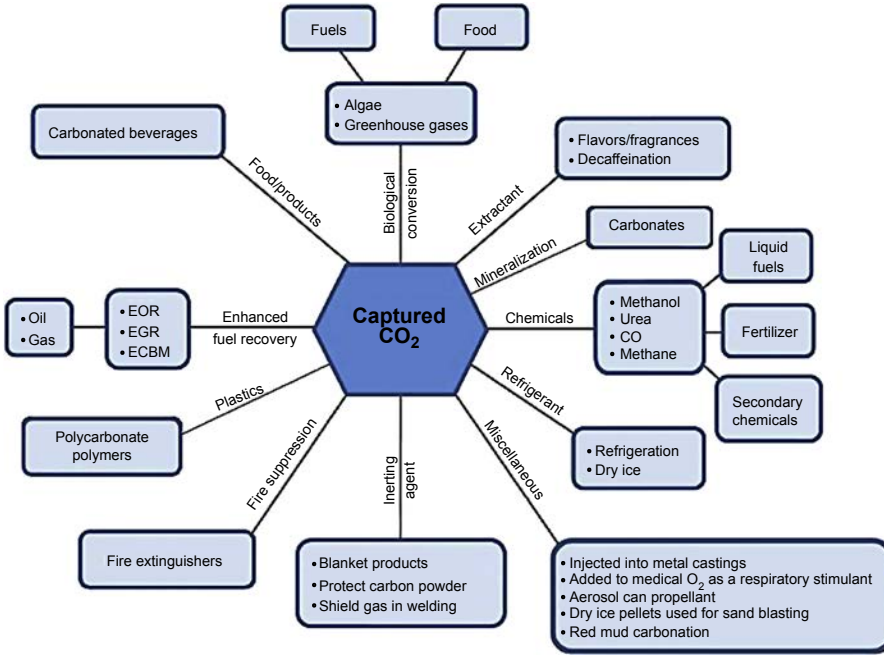


Figure 19.39 Carbon dioxide can be a resource rather than a waste product [37].

19.13 Key points of COP21: long-term goal

The measures in the agreement included these:

- to peak greenhouse gas emissions as soon as possible and achieve a balance between sources and sinks of greenhouse gases in the second half of this century,
- to limit the amount of greenhouse gases emitted by human activity to the same levels that trees, soil, and oceans can absorb naturally, beginning at some point between 2050 and 2100: *the "emissions neutrality"*
- to keep global temperature increase "well below" 2°C (3.6°F) and to pursue efforts to limit it to 1.5°C,
- to review each country's contribution to cutting emissions every 5 years so they scale up to the challenge
- for rich countries to help poorer nations by providing "climate finance" to adapt to climate change and switch to renewable energy; one hundred billion dollars a year in climate finance for developing countries by 2020, with a commitment to further finance in the future.

For the energy world, the year 2015 was a year full of big interrogative points:

- Oil prices could remain at low levels for longer than expected?
- What should happen so that this hypothesis is occurring and what implications this would have for the safety and for the energy transition?
- India will know a period of rapid and sustained growth in demand for energy: how could this dynamic redefine the global energy scenario?

- How can we reconcile the new commitments on climate with the continuous increase in the world's energy needs?
- What are the consequences of the growing adoption of policies in support of energy efficiency and the increasing competitiveness of renewables?
- The revolution of unconventional gas will assume global dimensions, or it is destined to remain a phenomenon confined to North America?

19.14 Will coal be on the dole after COP21?

For coal, COP21 is meant to be the start of the long goodbye.

This is the conference that is supposed to consign the black stuff to the ash heap of history [38].

The world will finally tilt definitively toward windmills and a future filled with sunbeams and smiles. *Perhaps not.*

Coal has certainly been on the back foot.

A recent report from the IEA showed that in 2014 renewables accounted for half of the world's new power generation capacity, and they have already become the second largest source of electricity after coal.

The United Kingdom, the home of the coal-fired industrial revolution, recently announced that power generation from unabated coal would end within 10 years.

"Let me be clear: this is not the future," said Energy Secretary Amber Rudd.

Well, it is not the future, unless you live in India or a host of other emerging economies around the world.

Global energy demand is growing rapidly, which according to the IEA is expected to increase by a third by 2040, with the main demand coming from China, India, Africa, the Middle East, and Southeast Asia.

Look at India, the world's third largest economy, which only accounts for 6% of global energy use. Some 240 million people still lack access to electricity. The country is determined to address this, and they are going on a coal binge to do it.

By 2020, India will be the world's second-largest producer of coal, overtaking the United States. And it will be the world's largest importer.

They are not alone.

The Philippines is set to establish 23 new coal-fired plants by 2020. In fact 40% of the 400 GW of generation capacity to be added in Southeast Asia by 2040 will be coal-fired.

And while coal use will decline in the developed economies of the European Union and the United States, the whiff of sulfur will be rising in Japan, where coal's share of the energy mix by 2030 will increase to 30%.

According to Benjamin Sporton from the World Coal Association, a bit more honesty about coal's role in the future is needed at COP21.

"I think that we need to recognize that there is a role for coal going forward," he said.

"Many countries are using coal and are going to use it for decades to come so we ought to be talking about how the outcome of Paris can support countries to use the best coal technology. And ultimately we need to be talking about CCS as well."

Tim Gore from Oxfam acknowledges that it will not be easy to wean emerging economies away from cheap coal. For the many developing countries that have not yet built electricity grids, leapfrogging to renewables makes a lot more sense. But if COP21 is serious about lightening the lignite, significant amounts of cash will have to be found to fund the move toward greener sources.

"I think it's right that developing countries are clear just how big a transformation is required to move away from fossil fuels," he said.

"This is not a light undertaking. I think that sometimes the issue of a global transformation is presented as inevitable, but actually from most developing country perspectives it does not look like that."

In Paris you will have rich countries that are moving away from carbon rich fuel, telling the rest of the world who are moving toward coal that they must stop doing that by an agreed date in the future.

"It's problematic for us to make that commitment at this point in time. It's certainly a stumbling block," Ajay Mathur, a senior member of India's negotiating team told news agencies.

"The entire prosperity of the world has been built on cheap energy. And suddenly we are being forced into higher cost energy. That's grossly unfair," he said.

19.14.1 How will negotiators square this circle?

If we look to Fig. 19.40, we can see clearly which are the countries responsibilities for the past CO_2 emission and which will be the future of the emission due to the increasing economies.

If an agreement in Paris pushes greater investment into renewables, the costs will fall further, and that may encourage developing governments to go greener quicker. If fossil fuel subsidies are tackled, this will also help, and an effective price or tax on carbon would certainly speed up the deployment of solar and wind.

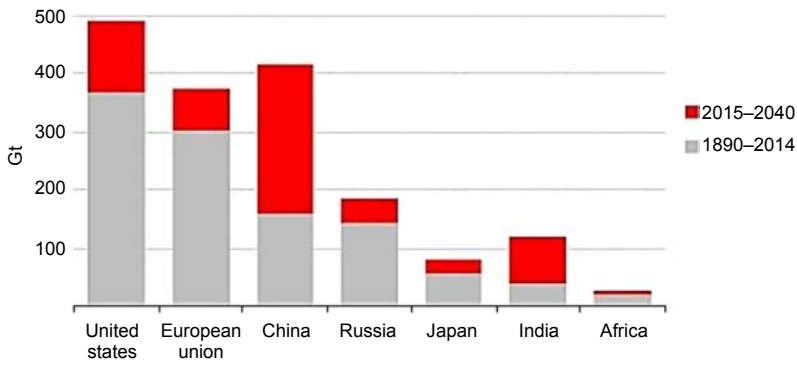


Figure 19.40 Cumulative energy-related CO_2 emissions by region [39].

19.15 Future energy: the electricity system now and decarbonized

Key points:

- A portfolio of low-carbon technologies is needed to reach the 2DS; some solutions will be broadly applicable, while others need to target specific sectors (Fig. 19.41).
- Interactions across the entire innovation system will enable actors to develop necessary incremental improvements and breakthroughs in the technologies needed to meet the climate goals (Fig. 19.42).
- Different national circumstances, including availability of resources, will require tailor-made solutions and pathways for deep decarbonization by 2050 that initially leverage available solutions before developing home-grown solutions (Fig. 19.43).

Energy Technology Perspectives 2014 (*ETP 2014*), released on May 12, 2014, sits at the heart of the IEA's work on energy technology and policy. It offers a comprehensive, long-term analysis of trends in the energy sector and of the technologies that are essential to achieving an affordable, secure, and low-carbon energy system.

With electricity set to be an increasingly important component of energy systems of the future, *ETP 2014* examines in depth what must be done to provide sustainable options for generation, distribution and end-use consumption. In Figs. 19.44 and 19.45, *ETP 2014* shows how the integrated and intelligent electricity system of the

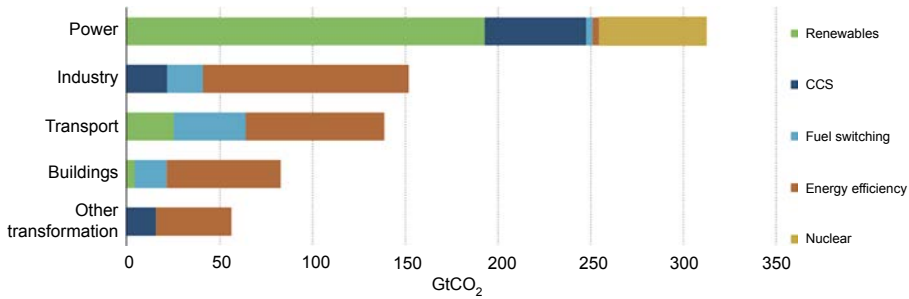


Figure 19.41 Cumulative CO_2 reductions by sector and technology in the 2DS to 2050 [40].

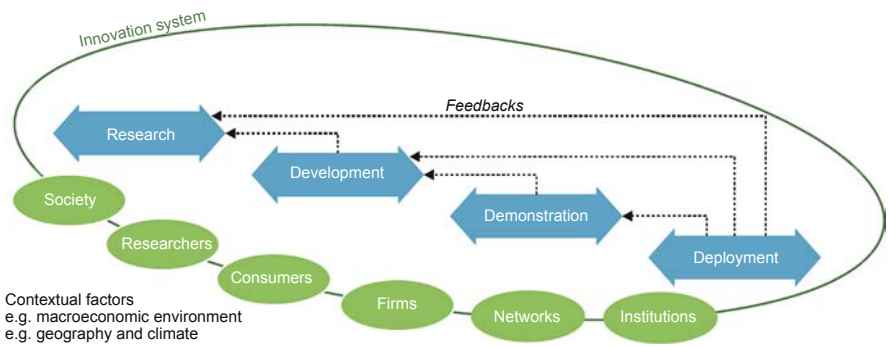


Figure 19.42 Systems-based interactive innovation [40].

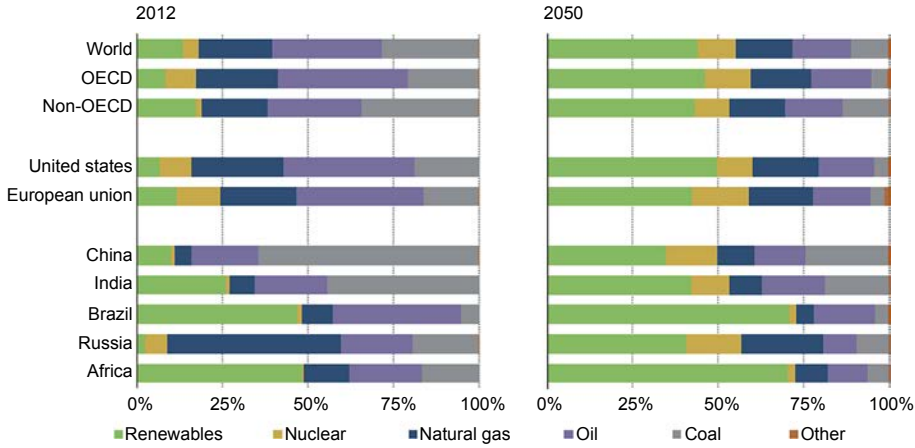


Figure 19.43 Regional primary energy demand profiles in 2DS [40].

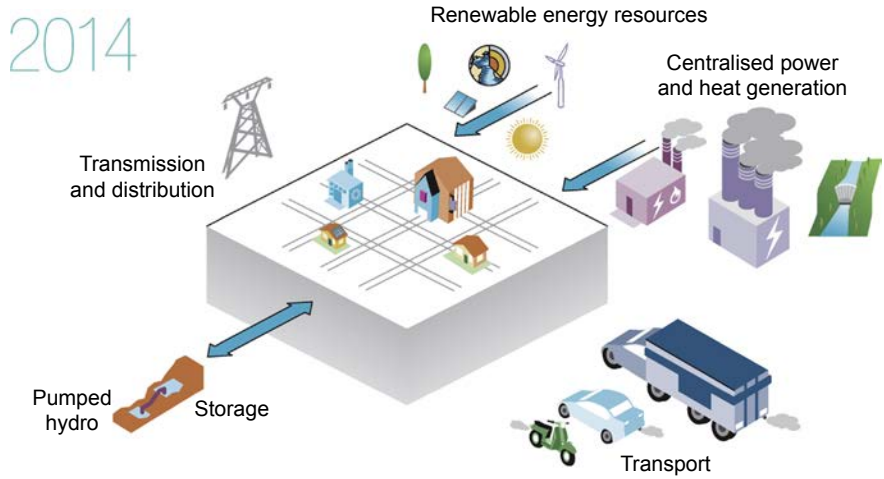


Figure 19.44 The current situation of the electricity systems [41].

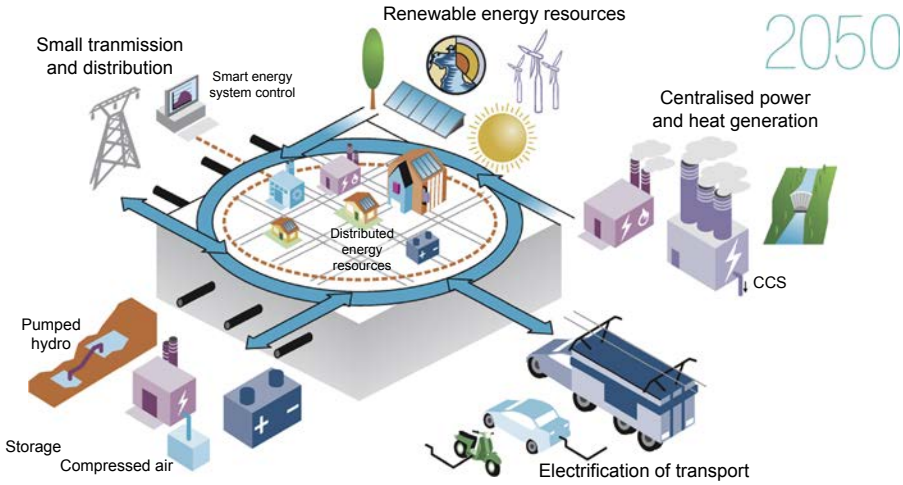


Figure 19.45 The integrated and intelligent electricity system of the future [41].

future differs from today's in the choice of technologies and their placement along the steps of generation, transmission, and distribution. It shows today's situation, where there are very few interactions of the electricity systems between the production and the accumulation and storage of the energy.

To better integrate all elements of electricity systems will increase complexity but improve operations, efficiency, and resilience while optimizing energy resources and investments.

References

[1] About coal, http://www.iea.org/topics/coal/.
[2] World Coal Institute, The Coal Resource: A Comprehensive Overview of Coal. http://www.worldcoal.org/file_validate.php?file=coal_resource_overview_of_coal_report(03_06_2009).pdf.
[3] http://www.ucsusa.org/clean_energy/our-energy-choices/coal-and-other-fossil-fuels/how-coal-works.html#.VpUis-_SlMs.
[4] B. Kennedy, Surface Mining, SME, 1990, p. 68.
[5] EIA, U.S. Coal Consumption by End-use Sector, 2007.
[6] K. Ward, Twice as many acres mined as reclaimed, report says, West Virginia Gazette (March 14, 1999).
[7] Coal Reserves, http://www.bp.com/en/global/corporate/energy-economics/statistical-review-of-world-energy/coal-review-by-energy-type/coal-reserves.html.
[8] bp-statistical-review-of-world-energy-2015-coal-section. https://www.bp.com/content/dam/bp/pdf/energy-economics/statistical-review-2015/bp-statistical-review-of-world-energy-2015-full-report.pdf.
[9] Countries with the Biggest Coal Reserves, November 21, 2013. http://www.mining-technology.com/features/feature-the-worlds-biggest-coal-reserves-by-country/.
[10] http://www.statista.com/statistics/273771/countries-with-the-largest-share-of-global-coal-reserves/.
[11] https://www.worldenergy.org/data/efficiency-indicators/.
[12] http://www.b20coalition.org/about-g20.php.
[13] https://yearbook.enerdata.net/#coal-and-lignite-world-consumption.html.
[14] http://shrinkthatfootprint.com/electricity-emissions-around-the-world.
[15] BP Statistical Review of World Energy, June 2015.
[16] http://www.bp.com/en/global/corporate/energy-economics/statistical-review-of-world-energy/coal-review-by-energy-type/coal-prices.html.
[17] T. Boersma, C.K. Ebinger, March 19, 2015. http://www.brookings.edu/blogs/planetpolicy/posts/2015/03/19-coal-future-global-ene.
[18] R. Romanosky, US/DOE Perspective on USC Steam Power Plants; 4th International Conference on Advances in Materials Technology for Fossil Power Plants, 25–28 October, 2004 (Hilton Head, South Caroline).
[19] Iowa Home to 200th Coal Plant Phase Out, July 2015. http://sierraclub.org/iowa/iowa-home-200th-coal-plant-phase-out.
[20] Phasing out Coal. http://www.pellet.org/wpac-news/phasing-out-coal.
[21] World Energy Outlook Special Report: Southeast Energy Asia Outlook, 2015.
[22] India Outlook Energy World Energy Outlook Special Report OECD/IEA, 2015.

[23] A. Minchener, High Efficiency Low Emissions: The First Way Forward for Clean Coal Technology. https://www.usea.org/sites/default/files/event-/Minchener_USEA_ESF_2014.pdf.
[24] J. Topper, Future Coal Demand: Roadmap for Coal-Fired Power Plant Efficiency and Interaction with CCS, IEA Clean Coal Centre, Washington, DC, March 15, 2012.
[25] http://shrinkthatfootprint.com/why-the-world-needs-low-carbon-electricity#RuEGDaY-74wwcfGys.99.
[26] http://srren.ipcc-wg3.de/report/IPCC_SRREN_Annex_II.pdf.
[27] http://www.ccsassociation.org/what-is-ccs/.
[28] http://www.technip.com/en/our-business/onshore/renewable-energies.
[29] https://www.worldcoal.org/reducing-co2-emissions/carbon-capture-use-storage.
[30] http://www.materialsperformance.com/articles/material-selection-design/2015/08/pipeline-corrosion-issues-related-to-carbon-capture-transportation-and-storage.
[31] http://www.total.com/en/society-environment/environment/climate-and-carbon/carbon-capture-and-storage/how-it-works/carbon.
[32] https://www.globalccsinstitute.com/sites/www.globalccsinstitute.com/files/pages/92241/3-carbon-capture-and-storage-process.jpg.
[33] https://hub.globalccsinstitute.com/publications/what-happens-when-co2-stored-underground-qa-ieaghg-weyburn-midale-co2-monitoring-and-storage-project/20-does-co2-occur-naturally-underground-water-oil-and-gas.
[34] http://stoppingclimatechange.com/michigan's_electricity_crisis.htm.
[35] IEA Energy Technology Perspectives, 2010 © OECD/IEA, 2010, p. 47(Figure ES.1).
[36] R.M. Cuéllar-Franca, A. Azapagic, Carbon capture, storage and utilisation technologies: a critical analysis and comparison of their life cycle environmental impacts, Journal of CO_2 Utilization 9 (2015) 82–102.
[37] http://www.theenergycollective.com/ed-dodge/341971/carbon-dioxide-resource-not-waste-product.
[38] M. McGrath: http://www.bbc.com/news/science-environment-34904127.
[39] Energy and Climate Change, IEA, London, June 15, 2015.
[40] https://www.iea.org/bookshop/710-Energy_Technology_Perspectives_2015.
[41] https://www.iea.org/newsroomandevents/graphics/future-energy-the-electricity-system-now-and-decarbonised.html.

This page intentionally left blank

The US DOE/OCDO A-USC materials technology R&D program

20

J.P. Shingledecker
Electric Power Research Institute, Charlotte, NC, United States

20.1 Introduction

The United States Department of Energy (US DOE) Office of Fossil Energy and the Ohio Coal Development Office (OCDO) were the primary supporters of a US effort to develop the materials technology necessary to build and operate an advanced ultra-supercritical (A-USC) steam boiler and turbine with steam temperatures up to 760°C (1400°F). From 2001 to 2015, the project took the ambitious temperature goal and worked on all facets of materials technology needed to enable A-USC conditions including the development of long-term mechanical test data, enhanced understanding of microstructural development, studies on oxidation and exfoliation, in-plant testing to assess fireside corrosion, numerous welding and weld performance studies, fabrication trials resulting in mock-ups, forging simulations and tests to evaluate rotor capability, casting development, and coatings evaluations. This chapter provides an introduction to the program goals and structure, a discussion on materials selection, highlights of major advancements for both A-USC boilers and turbines, and a prognosis for the future.

20.2 US A-USC materials consortium

In 2010, coal provided 48% of the electric generation in the United States [1] and 40.6% of the electric generation in the world [2]. Coal is abundant, with some studies estimating 150 years of worldwide reserve at current consumption rates [3]. Despite its use as major source of electricity, coal faces strong regulatory and economic challenges as the world adopts policies for reducing carbon consumption. As worldwide demand for electricity grows, it is clear that a robust portfolio of power generation options is needed to ensure reliable and environmentally responsible electricity. To meet the challenges of the 21st century, advancements in coal technology are needed. The Coal Utilization Research Council (CURC)-EPRI Coal Technology Combustion roadmap, Fig. 20.1, identifies key technologies needed to ensure that coal remains an option for power generation in the future. A key aspect of this roadmap is the

Materials for Ultra-Supercritical and Advanced Ultra-Supercritical Power Plants.
http://dx.doi.org/10.1016/B978-0-08-100552-1.00020-8
Copyright © 2017 Elsevier Ltd. All rights reserved.

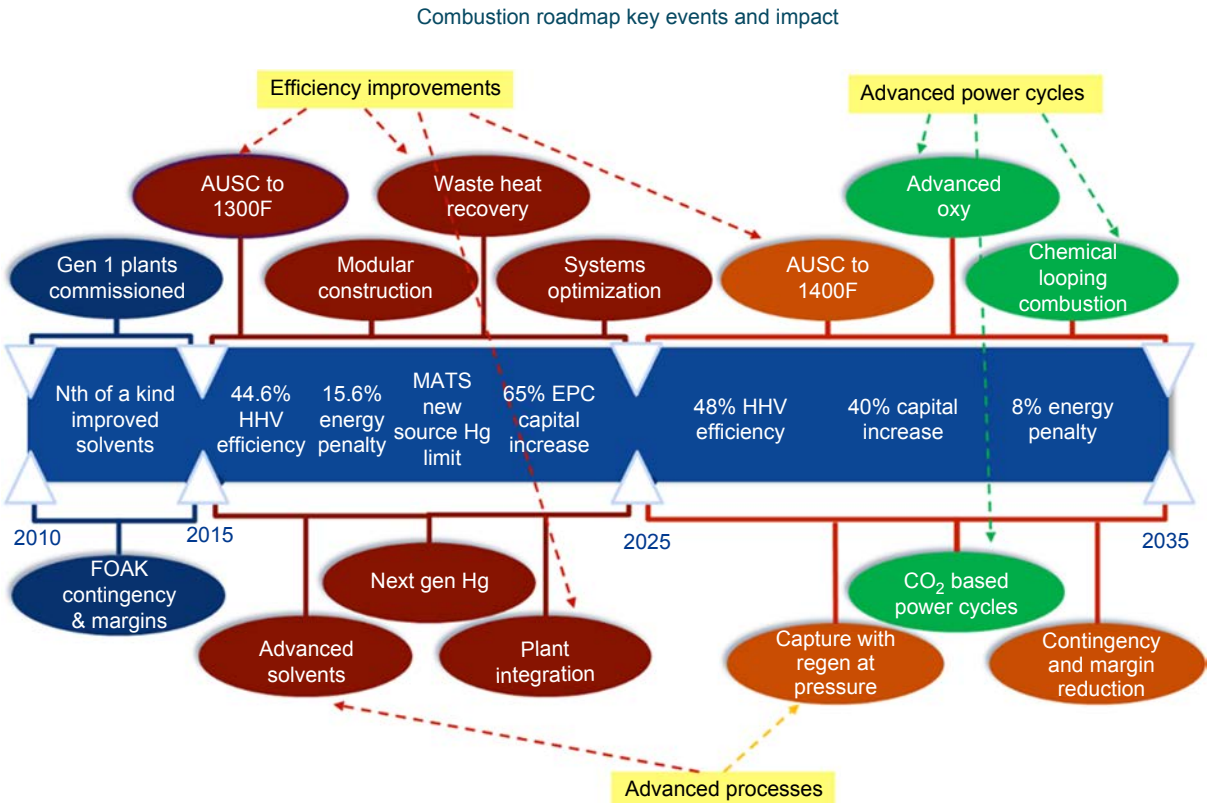


Figure 20.1 CURC-EPRI roadmap combustion timeline and impact. Courtesy of EPRI.

deployment of higher efficiency pulverized coal combustion using advanced ultra-supercritical (A-USC) technology. For the world, the International Energy Agency (IEA) has proposed, in its high-efficiency, low-emission roadmap for coal technology that coal generation from inefficient subcritical plants be replaced by higher efficiency USC and A-USC plants as a first step to carbon reduction, prior to commercial deployment of carbon capture and storage (CCS) technologies [4]. Thus, there are strong environmental and economic drivers for the development and deployment of A-USC technology in the United States and worldwide.

The worldwide development of A-USC technology aimed at steam temperatures of 700°C (1300°F) and greater started initially around 1998 with a variety of European Projects [5]. In 2001, the US Department of Energy, in conjunction with the Ohio Coal Development Office (OCDO) and cost share from all the major US boiler and turbine original equipment manufacturers (Alstom, B&W, Foster Wheel, Riley Power, GE, Siemens), the Energy Industries of Ohio (EIO), and the Electric Power Research Institute (EPRI) with support from Oak Ridge National Laboratory (ORNL) and the National Energy Technology Laboratory (NETL) Albany Research Center (ARC) and managed for DOE by NETL, began an ambitious precompetitive research and development project that would lead to higher efficiency coal-fired power plants with reduced CO_2 emissions [6,7]. Achieving major increases in coal-fired power plant efficiency requires an increase in steam conditions (temperature and pressure) and therefore demands the utilization of new materials and technologies to implement these new materials. Hence, the R&D program's goal was to develop the materials technology necessary to achieve advanced ultra-supercritical steam (A-USC) power plant steam conditions up to temperatures and pressures of 760°C (1400°F) and 35 MPa (5000 psi), respectively, which can reduce all emissions, including CO_2, by 20% or greater compared to today's US fleet [8,9]. Beyond Europe and the United States, national programs now exist in Japan (initiated in 2008), China (2011), and India (2012) with announced plans for demonstration in both China and India around 2020 [10–12]. Fig. 20.2 is a summary of plant efficiency (HHV) and emissions reduction as a function of steam temperature for various US-based modeling studies [13–17] (*solid symbols*) with some current reported plant efficiency data (*open symbols*). There is considerable variation due to local conditions (cooling water temperature, fuel type, specific design considerations such as size and utilization of waste heat, etc.); however, when compared to the US fleet averages of 32.3–32.5% HHV, A-USC conditions are expected to raise efficiency up to 12.5HHV%, which corresponds to a 35% reduction in CO_2 emissions. Even when compared to today's state-of-the-art USC unit operating at 600°C (for US conditions), A-USC offers a CO_2 reduction of ~13%.

The general structure of the consortium was to have task leads from each of the respective manufacturers with EPRI having overall technical oversight and coordination and EIO serving as the principal contractor and project manager. The boiler and turbine activities were separated, but joint quarterly meetings were held for the duration of both projects. The boiler project started in 2001 and was completed in 2015, and the tasks that were conducted were these:

- task 1. conceptual design and economic analysis
- task 2. mechanical properties of advanced alloys

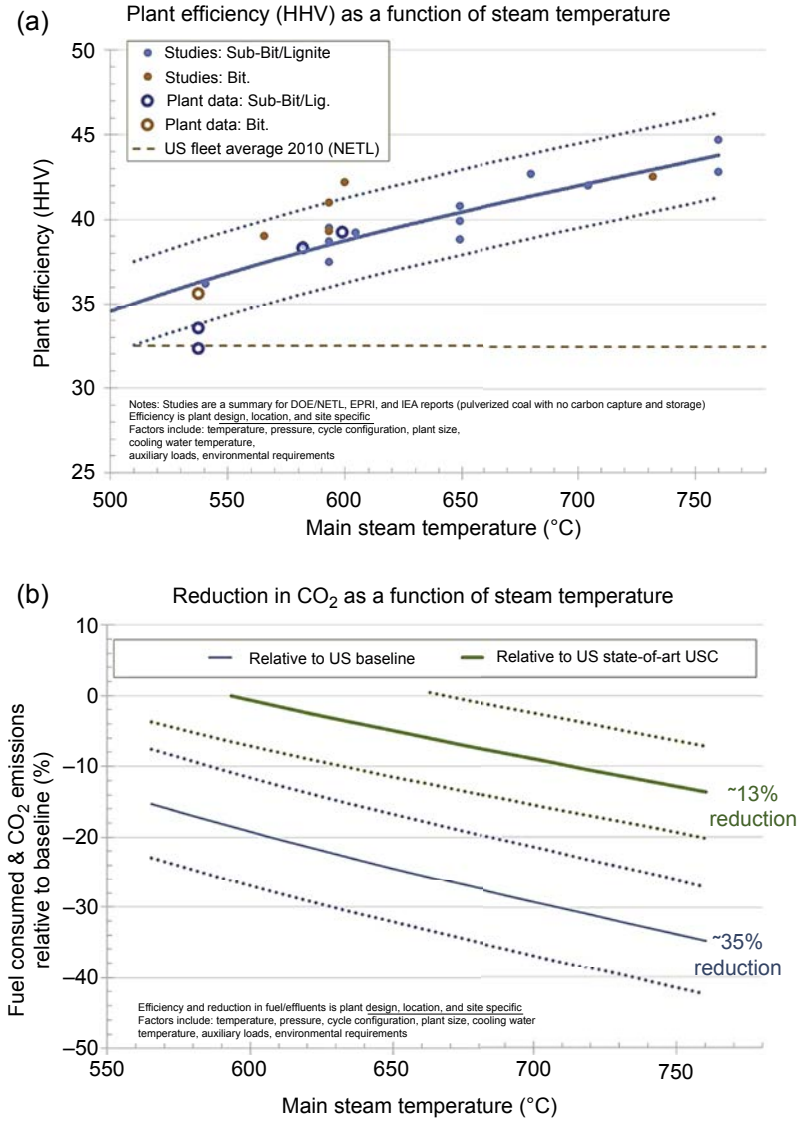


Figure 20.2 Plant efficiency (a) and corresponding reduction in CO_2 emissions (b) due to less coal burned as a function of steam temperature for various studies from the US DOE, EPRI, and the IEA.

- task 3. steam-side oxidation and resistance
- task 4. fireside corrosion resistance
- task 5. weldability
- task 6. fabricability
- task 7. coatings
- task 8. design data and rules

The turbine program was conducted in two phases. In phase I from 2005 to 2009, the following tasks were undertaken:

- design and economic studies
- materials for non-welded rotors
- materials for welded rotors
- castings
- oxidation and solid-particle erosion

After phase I, Alstom and Siemens discontinued participation, so the work scope from 2010 to 2015 was directed toward a bolted rotor construction being developed by GE [18], focusing on the materials of most promise from phase I. The Phase II tasks were these:

- rotor/disc testing (full-size forging development and demonstration)
- bucket (blade) and bolting long-term testing
- casting scale-up for turbine casing and valve bodies
- casing to pipe welding and casting repair

The project structure was very unique, but by developing a consortium based on precompetitive research, the overall benefit to the electricity supply industry and materials research community was highly leveraged in terms of funding and timeliness of research results.

20.3 Materials selection

The consortium first defined the conditions required for the materials to operate at A-USC conditions up to 760°C (1400°F). Based on these preliminary design studies, nickel-based alloys were selected for detailed evaluation because only these alloys had the requisite strength required to operate at A-USC conditions. Current USC boilers operate at temperatures up to approximately 610°C, which is the limit of the most advanced creep strength–enhanced ferritic (CSEF) steels, but for temperatures above 700°C (1300°F), nickel-based alloys are clearly required. Fig. 20.3 shows the temperature required to produce creep rupture in 100,000 h for various alloys. With the aim of 760°C (1400°F), age-hardenable alloys (Inconel Alloy 740/740H and Haynes 282) were considered beyond solution-strengthened alloys such as 617. Using the criteria of 100,000 h strength at 100 MPa (14.5 ksi), these temperature limits can be observed from the plot. Although strength is an important consideration, a number of other critical material properties must be considered for materials operating at A-USC conditions. Much of the work highlighted in the following sections is related to the other important properties needed for boilers and turbines, including fabricability, weldability, weld performance, tensile and fatigue properties, notch sensitivity, steam-side oxidation, and fireside corrosion resistance. Table 20.1 provides a list of some alloys that were studied initially by the consortium and eliminated from future testing. Table 20.2 provides

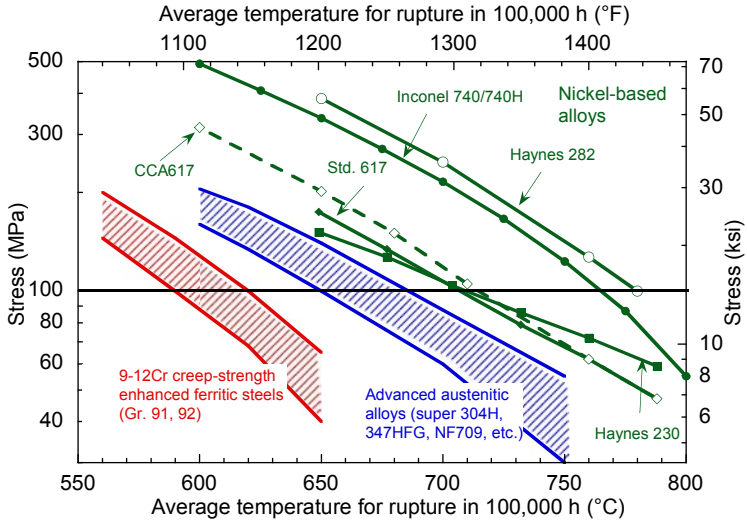


Figure 20.3 100,000 h creep-rupture strength as a function of temperature for alloy/alloy class. After J. Shingledecker, R. Purgert, P. Rawls. Current status of the U.S. DOE/OCDO a-USC materials technology research and development program, in: Advances in Materials Technology for Fossil Power Plants. Proceedings from the Seventh International Conference, October 22–25, 2013, Waikoloa, Hawaii, USA. Published by ASM International © 2014. EPRI Report Number 3002002375, 41–52.

Table 20.1 Ferritic and iron-based austenitic alloys selected for early evaluation and some important findings (status)

Alloy	Component	Comments
SAVE12	Pipe	Unstable microstructure, welding was challenging [20] **(eliminated from testing)**
Super 304H (CC2328)	SH/RH	Met strength projections, may need coatings in some environments and shot-peening for oxidation resistance [21] **(only for tubing)**
HR6W	SH/RH, pipe	Did not meet strength projections [22,23] **(stopped research, new chemistry now available)**

SH/RH: superheater and reheater tubing.

a partial list of the key nickel-based alloys selected by the consortia for study along with comments on their applicability and limitations. Table 20.3 provides the nominal compositions for the nickel-based alloys studied by the consortium.

Table 20.2 Nickel-based alloys evaluated

Alloy	Component	Comments
Haynes 230	SH/RH, pipe	Successful welding trials, maximum size limitations for pipe may limit applicability
CCA617	SH/RH, pipe	Higher strength than 617 but not enough data to change ASME code stress values, not suitable for high sulfur coals, only successful SMAW welds in nickel-based alloys, strain-age cracking concerns, low-yield strength limits applicability for turbine rotor
Alloy 263	Castings	Back-up cast alloy to 282, good castability and weldability, lower strength but good ductility
Inconel 740/740H (ASME Code Case 2702)	SH/RH, pipe	Highest strength alloy in ASME B&PV code to enable A-USC up to 760°C (1400°F), excellent fireside corrosion resistance, successful fabrication and welding, prime candidate for boiler components, cannot be air cast for valves and shells
Haynes 282	Castings, rotor	Higher creep strength than 740H, relatively insensitive to starting microstructural condition, good forging "window" for rotor, can be cast for valves and casings
Waspalloy	Rotor, bolts, blades	Back-up alloy with good turbine history, cannot be welded reliability, poor ductility
Nimonic 105	Bolts, blades	Highest creep strength alloy, only considered for bolting and blading (non-welded components)

Table 20.3 Nominal alloy compositions[a] for A-USC research

Family	Alloy	Code case (if applicable)	C	Ni	Fe	Cr	Mn	Si	Mo	Co	Al	Ti	B	Others
Solid solution	HR6W	2684	0.07	45	Bal.	23	1.0	0.2				0.10	0.003	W: 7.0 Nb: 0.20
	Alloy 617	N06617	0.07	Bal.	0.5	22	0.3	0.3	9	12.5	1.0	0.40		
	CCA617	N/A	0.06	Bal.	0.3	22	0.1	0.1	9	12	1.2	0.40	0.003	
	Haynes[b] 230	N066230	0.10	Bal.	1.5	22	0.5	0.4	2	0.3	0.3		0.004	W: 14.0 La: 0.02
Gamma prime	NIMONIC[c] 263	N/A	0.06	Bal.	0.1	20	0.1	0.1	6	20	0.45	2.2	0.004	
	INCONEL[c] alloy 740H[c]	2702	0.03	Bal.	1	24.5	0.3	0.15	0.1	20	1.35	1.35	0.001	Nb + Ta: 1.5
	Haynes[b] 282[b]	N/A	0.06	Bal.	0.2	20	0.05	0.1	8.5	10	1.5	2.1	0.005	

[a]Sulfur and phosphorous limits omitted from table.
[b]Haynes, 230, and 282 are registered trademarks of Haynes International.
[c]INCONEL, NIMONIC, and 740H are registered trademarks of the Special Metals Corporation, a PCC Company.

20.4 Boiler materials

20.4.1 Inconel 740/740H development

Inconel Alloy 740/740H is an age-hardenable, nickel-based alloy developed by Special Metals Corporation (Huntington, West Virginia, USA) for use as superheater and reheater tubing in A-USC power plants [24]. Due to its excellent high-temperature (creep) strength (see Fig. 20.3) and corrosion resistance, the consortium also evaluated its use for thicker components such as boiler piping and headers. This involved numerous welding and fabrication trials combined with long-term testing. Initial challenges were encountered when welding the alloy in sections up to 75 mm (3″) in thickness. The consortium worked closely with the alloy designers and other research institutions to refine the alloy and weld metal composition. Revolutionary progress was made, and the refined alloy composition, Inconel 740H, is now considered weldable, as shown in Fig. 20.4 with numerous successful welded joints produced [25,26].

Materials used in the construction of fired pressure vessels must be designed to ASME B&PV Code Section I. While there are some materials that are allowed for Section I construction at 760°C (1400°F), they do not have the requisite strength (allowable stresses) needed to design and build an A-USC boiler. Thus, the consortium developed a comprehensive data package that included test data on multiple material heats and product forms containing long-term data [27]. Babcock & Wilcox championed the case with supporting data from the other project members. ORNL conducted the long-term testing, and EPRI conducted the stress analysis. The approved Section I code case, Code Case 2702, contains fabrication rules, welding specifications (including weld strength reduction factors), stress allowables, and other key requirements. Users can now design and specify the alloy for use in Section I construction to a maximum use temperature of 800°C (1472°F). The alloy has also been adopted by ASME Section B31.1 for power piping. Creep rupture testing has surpassed 45,000 h with no drop-off in rupture strength or ductility. Research has included studies on notch sensitivity and microstructural development that suggest the alloy is suitable for long-term service at A-USC conditions [28,29]. Research on the original 740 composition showed the tendency to form eta phase platelets



Figure 20.4 75-mm (3″) weldment in Inconel 740H Pipe (left) and header mock-up (right) [26].

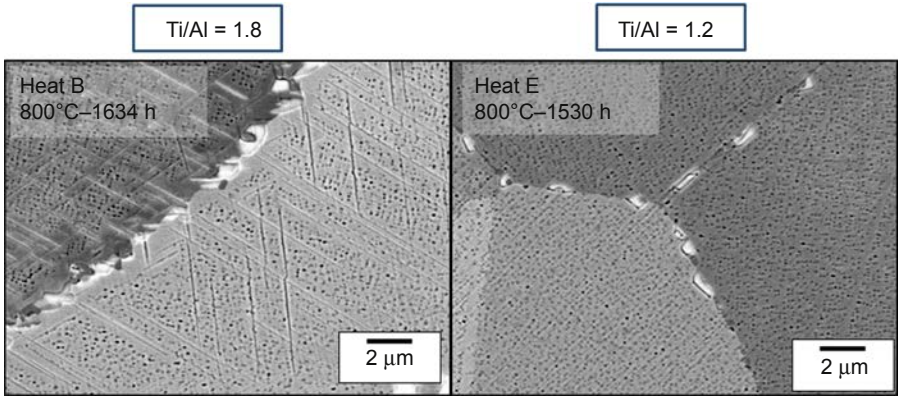


Figure 20.5 Comparison of the microstructures between 740 original composition (Heat B) and the refined 740H composition (Heat E) after creep testing at 800°C [31]. The original 740 composition with a Ti/Al ratio of 1.8 shows eta phase precipitation, but the 740H composition with the optimized Ti/Al ratio of 1.2 does not.

after long-term service [30], which some researchers have suggested is a concern for long-term microstructural stability despite the data suggesting there is no concern over creep strength and ductility due to eta phase formation [28]. Fig. 20.5 compares the microstructures of 740 and 740H after accelerated creep testing at 800°C. The minor modification of the Ti/Al ratio in 740H results in the elimination of eta phase precipitation at A-USC application temperatures [31].

20.4.2 Long-term creep in HR6W, Haynes 230, and CCA617

Long-term creep testing and microstructural analysis were conducted on the Ni-Cr-Fe alloy HR6W and nickel-based alloys Haynes 230 and CCA617 by the consortium. The HR6W alloy tested by the consortium did not meet the intended creep strength projections [22], and the alloy developers have since reevaluated the composition to increase the amount of tungsten (W) in the alloy from nominally 6% (which was tested by the consortium) to 7% [32]. Testing of the Haynes 230 alloy showed no surprises with the alloy meeting the values in the ASME Boiler and Pressure Vessel Code, and the microstructure showed good stability [33]. Long-term creep testing of a controlled composition alloy 617 (CCA617) was conducted by the consortium [34]. Based on an assessment of the data, the alloy was found to be stronger at temperatures up to ~700°C than standard alloy 617 (see Fig. 20.2), but at temperatures approaching the A-USC goal of 760°C, there was no difference in creep strength. Microstructural analysis showed the alloy formed a limited amount of gamma prime at the lower temperatures, which contributed to the increased strength, but this effect went away at higher temperatures [35]. Fig. 20.6 contains transmission electron micrographs of CCA617 after aging for 3000 h at 700–800°C. While fine gamma prime precipitates are observed at 700°C, the precipitates coarsen rapidly at 750–800°C, resulting in the loss of the creep strength advantage of the controlled composition.

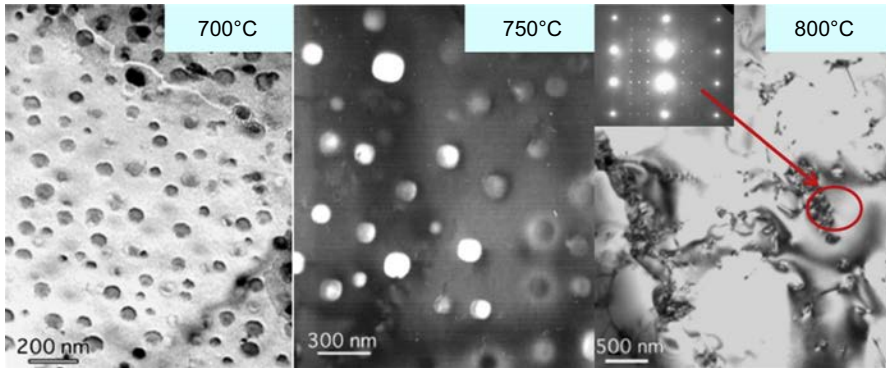


Figure 20.6 Transmission electron micrographs of CCA617 showing gamma prime distribution after 3000 h of thermal aging at 700, 750, and 800°C. At 750°C, the gamma prime coarsens rapidly, and long-term creep strength is reduced to standard 617 behavior.

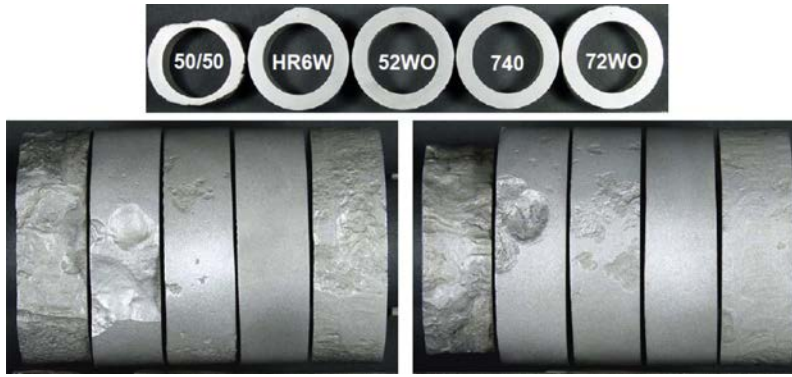


Figure 20.7 Cleaned surface of ring samples (identification at the top) from an air-cooled probes after 16,000 h operation in a utility boiler. Note alloy 740 shows virtually no corrosion wastage with similar performance to high-chromium weld overlays (52 and 72WO). Other alloys, including HR6W, show moderate attack.

20.4.3 Steam-side oxidation, exfoliation, and fireside corrosion

Concerns with fireside corrosion at A-USC temperatures and the wide variety of coals burned in the United States necessitated the consortium to do detailed evaluation of the fireside corrosion resistance of all the alloys. The aim was to determine the suitability of the alloys over the range of temperatures expected in superheaters and reheaters (SH/RH) in an A-USC plant and determine if higher chromium claddings or coatings would be required. Extensive laboratory tests have been conducted on a wide range of alloys, overlays, and coatings with varying sulfur contents [36], air-cooled probes have been fabricated and testing for up to 16,000 h in actual boiler environments [37], a steam-cooled corrosion test loop was operated in a high-sulfur coal environment [38], and the world's first 760°C (1400°F) steam-cooled loop was operated in a US boiler. Fig. 20.7 shows some results from one of the air-cooled probes. In this test,

Inconel 740 performed as well as some of the high-chromium weld overlays. Fig. 20.8 shows the A-USC program's steam loop, which operated with a steam outlet of 760°C (1400°F) for 33 months and contained a variety of materials and overlays. The purpose of this test was to evaluate both fireside corrosion and steam oxidation at A-USC conditions. Results confirmed laboratory studies that, for a relatively low sulfur coal, showed the fireside corrosion rates and steam oxidation rates (see Fig. 20.9) were within acceptable limits for long-term A-USC design of SH/RH components [39].



Figure 20.8 Steam-cooled A-USC corrosion test loop after installation.
Courtesy Alstom, Southern Company, and EPRI, 2015; B. Bordenet, et al., Steam oxidation and fireside corrosion testing of several advanced alloys in a steam loop at a-USC design temperatures, in: Proceedings: EPRI International Conference on Corrosion in Power Plants, 2015, EPRI, Palo Alto, CA, 3002006972.

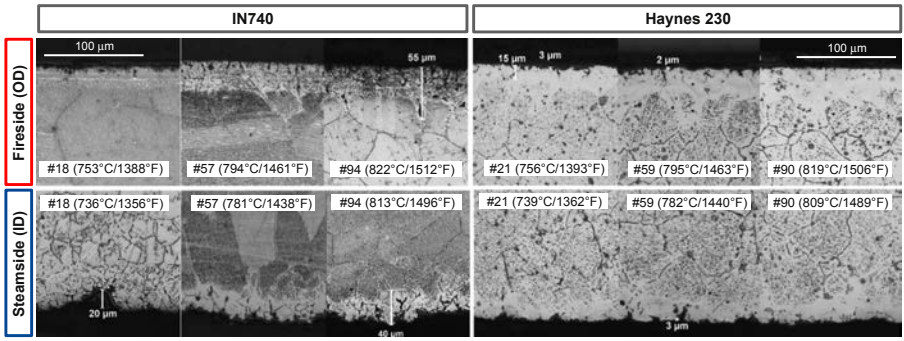


Figure 20.9 Fireside corrosion and steam-side oxidation for alloys 740 and 230 after 33-month exposure in an A-USC steam test loop.
Courtesy of Consortium and EPRI, 2015; B. Bordenet, et al., Steam oxidation and fireside corrosion testing of several advanced alloys in a steam loop at a-USC design temperatures, in: Proceedings: EPRI International Conference on Corrosion in Power Plants, 2015, EPRI, Palo Alto, CA, 3002006972.

The steam-cooled corrosion loops provide limited information on steam-side oxidation and exfoliation. As such, an extensive laboratory test program has also been completed by the consortium studying steam oxidation resistance for all A-USC alloys including the use of shot-peening on stainless steels. Parabolic rate constants, effect of pressure, weld oxidation, exfoliation, and long-term (10,000 h) exposures have been examined in a comprehensive test program involving multiple laboratories, and the results show that steam-side exfoliation blockage is not a concern for the nickel-based alloys, but stainless steels will require careful attention and the use of shot-peening [21,40].

20.4.4 Boiler fabrication trials and heavy-section welding

Extensive boiler fabrication studies have been completed that show it is possible to use typical boiler fabrication processes to construct an A-USC boiler using nickel-based alloys [41–43], as shown in Fig. 20.10. Cold-bending can effect creep strength in some alloys, so the consortium did full-scale testing of tube bends [23,29] to establish the cold-work limits now found in the ASME Section I table PG-19. Few limitations were found for boiler fabrication, but machining time is increased, and the amount of deformation for some swaged components will be limited in comparison to boiler steels.

The consortium qualified over 20 combinations of materials and filler metals for welding. In some cases, flux processes were not possible for use in heavy-section nickel-based piping, and gas tungsten arc (GTAW) and gas metal arc (GMAW) welding



Figure 20.10 A-USC boiler demonstration articles showing fabrication processes for nickel-based materials.
Courtesy of US Consortium and EPRI; J. Shingledecker, R. Purgert, P. Rawls, Current status of the U.S. DOE/OCDO a-USC materials technology research and development program, in: Advances in Materials Technology for Fossil Power Plants. Proceedings from the Seventh International Conference, October 22–25, 2013, Waikoloa, Hawaii, USA. Published by ASM International © 2014. EPRI Report Number 3002002375, 41–52.

were the only processes to be successfully qualified. Hot wire GTAW (also known as hot wire TIG) to enable higher deposition rates has been successfully demonstrated on alloys including Inconel 740H in section thickness up to 75 mm (3″) including narrow groove configurations to improve productivity (see Fig. 20.4). Long-term weldment creep tests [44] have been conducted to establish weld strength reduction factors (WSRFs). Based on an analysis of the consortium data (shown for alloy 617 in Fig. 20.11), WSRFs were instituted in the ASME Boiler and Pressure Vessel Code in Code Case 2805 in 2014 and have since been incorporated into Section I as shown in Table 20.4. Fig. 20.10 shows demonstration articles, which include forming, bending, welding (pipe and tube), machining, application of overlays, and dissimilar metal welding applied to A-USC alloys.

20.5 Turbine materials

20.5.1 Castings for casings and valve bodies

Steam turbine casing and valve bodies are traditionally made via casting. While previous European efforts had some success with casting solid solution–strengthened nickel-based alloys, the use of higher strength precipitation-hardened alloys with high Ti and Al contents (which are very reactive in air) needed to be explored to see if conventional air/protective atmosphere sand casting techniques could be used. A research team from NETL-ARC and ORNL cast a large number of trial alloys and subjected them to destructive evaluation and testing [45]. Based on successful results, scale-up of the most promising alloys, Haynes 282 and Nimonic 263, was started with multiple vendors. These alloys were selected because the small-scale lab trials (~7 kg) showed

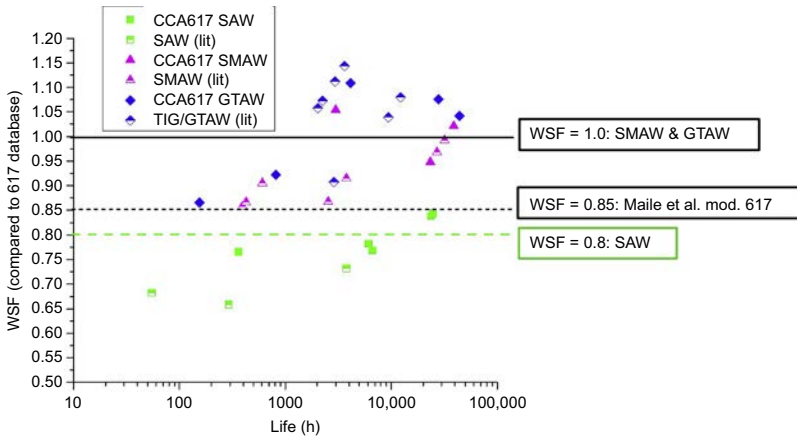


Figure 20.11 Example of consortium alloy CCA617 cross-weld data analysis (*WSF*, weld strength factor) for submerged arc welding (SAW), shielded metal arc welding (SMAW), and gas tungsten arc welding (GTAW) based on alloy 617 base metal and compared to literature (*lit*) data.

Table 20.4 Weld strength reduction factors for A-USC Nickel-Based Alloys Institute by ASME Boiler and Pressure Vessel Code based on assessment of long-term creep data produced by the A-USC Consortium

Temperature		Alloy 230 [N06230]	Alloy 617 [N06617] (except SAW) [a]	Alloy 617 [N06617] (SAW) [b]	Alloy 740/740H [ASME CC2702, ASTM N07740]
°F	°C				
1000	538	1.00			
1050	566	0.95			
1100	593	0.91	1.00	1.00	1.00
1150	621	0.86	1.00	0.80	0.70
1200	649	0.82	1.00	0.80	0.70
1250	677	0.80	1.00	0.80	0.70
1300	704	0.80	1.00	0.80	0.70
1350	732	0.80	1.00	0.80	0.70
1400	760	0.80	1.00	0.80	0.70
1450	788	0.80	1.00	0.80	0.70
1500	816	0.80	1.00	0.80	0.70
1550	843	0.80	1.00	0.80	NP
1600	871	0.80	1.00	0.80	NP
1650	899	0.80	1.00	0.80	NP

[a]Includes SMAW, GTAW, and GMAW filler metal welds.
[b]SAW filler metal welds.

the alloys to have good creep strength and creep ductility similar to their wrought counterparts.

A casting scale-up project was completed using static sand-cast test blocks, step blocks, and centrifugal castings with finished weights of 135–450 kg (300–1000 lbs) and having section thicknesses and cooling rates similar to large valve bodies and steam turbine casings. Three different foundries were engaged with this work. Due to the capabilities of each foundry's heat-treatment furnaces, thermodynamic/diffusion modeling was used develop appropriate homogenization heat-treatment cycles [46]. The resultant properties (tensile, fracture toughness, impact toughness, and creep) of all casting was excellent in part due to the chemical homogeneity, even in thick sections, achieved with the computationally designed heat-treatments. Additional modeling work was used to develop casting simulations for pouring larger casing geometries. Fig. 20.12 shows a ~450-kg (1000 lb) finished weight step casting of cast Haynes 282. In November of 2014, the world's largest pour weight protective atmosphere sand casting of Haynes 282 was completed. About 8000 kg (17,500 lb) of Haynes 282 was poured resulting in a ~2700-kg (6000 lb) 1/2 valve body geometry. The consortium designed the mold gating and risers for a full valve body to evaluate the casting models and foundry capabilities. Surface examination and X-ray examination showed no defects requiring weld



Figure 20.12 About 450-kg (1000 lb) finished weight step casting of Haynes 282. Courtesy of US Consortium and EPRI; J. Shingledecker, R. Purgert, P. Rawls, Current status of the U.S. DOE/OCDO a-USC materials technology research and development program, in: Advances in Materials Technology for Fossil Power Plants. Proceedings from the Seventh International Conference, October 22–25, 2013, Waikoloa, Hawaii, USA. Published by ASM International © 2014. EPRI Report Number 3002002375, 41–52.

repair, which is very impressive for a first-of-a-kind casting [47]. Additional studies have been completed to develop weld repair procedures for the castings and to develop welding procedures to weld a Haynes 282 casting to a 740H pipe. For the casing to pipe weld, hot wire GTAW welding with both 740H and Haynes 282 filler metal have been successful.

20.5.2 Rotors: Haynes 282 triple melt

Scoping studies by the A-USC Turbine Consortium identified Haynes 282 as the most promising turbine rotor/disc alloy. The studies showed that creep behavior of Haynes 282 was relatively insensitive to starting microstructural condition (see Fig. 20.13) and had adequate tensile and fatigue behavior for a 760°C (1400°F) rotor [48]. The current HP and IP A-USC turbine design being considered calls for a bolted rotor similar to an industrial gas turbine [18]. In such a design, the highest temperature component is a forged disk. Haynes 282 is traditionally made via a double melt process, which can leave "stringers" in the microstructure. For rotating equipment where fatigue can be a critical material performance parameter, minimizing microstructural defects such as stringers is important. Thus the consortium developed the processing and procedures to produce clean ingots of Haynes 282, Fig. 20.14, via triple melting, VIM/ESR/VAR (vacuum induction melting/electro-slag remelting/vacuum arc remelting), processing. A first ingot was cast with a weight of ~4500 kg (10,000 lbs) and sectioned to evaluate defects and effects of processing variations. A similarly sized second ingot was also cast and was forged into a ~1100-mm-diameter (44 in.) rotor disc for full property evaluation. Extensive mechanical property studies were conducted that showed the rotor had improved fatigue and creep-fatigue (through hold-time fatigue tests) in comparison to the data produced on standard wrought plate and bar product.

20.5.3 Coatings and oxidation [49]

Initial concerns over steam oxidation and solid-particle erosion (SPE) led the consortium to conduct long-term exposures of alloys for times up to 10,000 h in steam

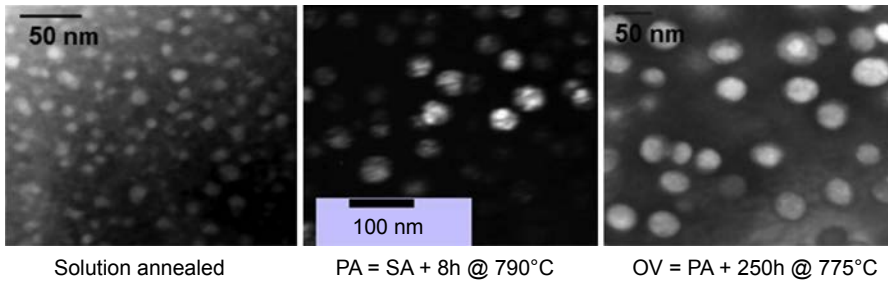


Figure 20.13 Gamma prime distribution and size in three different starting conditions for Haynes 282: solution annealed, peak aged (*PA*), and over aged (*OV*). Despite the differences in size and distribution of gamma prime, all three conditions showed excellent creep-rupture strength meeting the initial criteria for an A-USC turbine rotor [48].

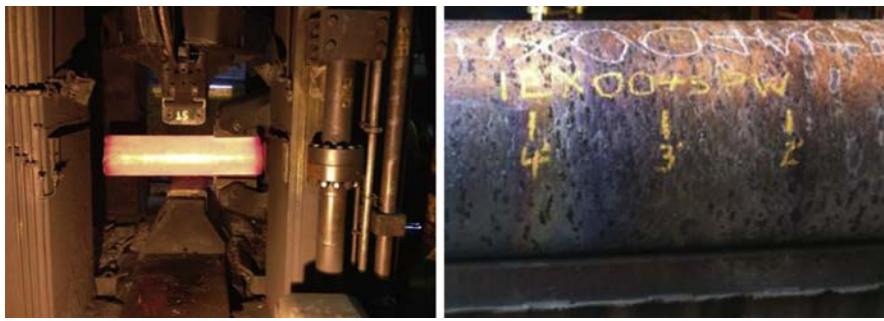


Figure 20.14 Upset and draw operation (left) and world's first Haynes 282 triple melt ingot (right).

at atmospheric pressure and temperatures of 700, 760, and 800°C. Candidate SPE coatings (Table 20.5) were selected and subjected to SPE wear testing. Because the coatings were not available until later in the project, steam exposures of only 1000 h were completed on the candidate SPE coatings. All candidate nickel-based USC alloys showed a low rate of oxidation in long-term testing at 700, 760, and 800°C. No spallation of external scales was observed as shown in Fig. 20.15, suggesting these A-USC alloys considered would perform as well or better, relative to steam oxidation, than current steels and stainless steels in state-of-the-art USC applications.

Candidate SPE-resistant coatings that showed the best steam oxidation resistance were Stellite 6B, Tribaloy T-400C, Metco 45, and CrC-NiCr. Of these four alloys, only the Tribaloy T-400C showed acceptable erosion rates in high-temperature erosion screening studies by the consortium. The extent of oxidation for these coatings after 1000 h exposure was comparable to that of the nickel-based alloys. The SHS 7170, SHS 9172, and MoB-CoCr coatings suffered from extensive internal oxidation or oxidation along coating cracks, and they are not considered suitable for application in a USC steam turbine environment.

Table 20.5 Coatings evaluated by A-USC Turbine Consortium in phase I work scope

Coating	Nominal composition (wt%)	Thickness (μm)	Application method	Substrate	Vendor
Stellite 6B	Co-30Cr-4.5 W-2Si-1.5 Mo-1.1C	N/A	Wrought form	None	Deloro Stellite
Tribaloy T-400C	Co-27Mo-14 Cr-2.6Si	920	Alloy Fusion[a]	Type 304 SS	Deloro Stellite
Tribaloy T-800	Co-28Mo-18 Cr-2.4Si	960	Alloy Fusion[a]	Type 304 SS	Deloro Stellite
Metco 45	Co-25.5 Cr-10.5 Ni-7.5 W-0.5C	250	HVOF	Hastelloy X	BASF
SHS 7170	Fe-Cr-W-B-Mn-Mo-C-Si	250	HVOF	Hastelloy X	Kermetico
SHS 9172	Fe-Cr-W-Nb-Mo-B-C-Mn-Si	250	HVOF	Hastelloy X	Kermetico
MB-42 (MoB-CoCr)	MoB–40% (Co-33Cr) composite	250	HVOF	Hastelloy X; 25 μm CoNi-CrAlY bond layer	Kermetico
CRC-25 (CrC-NiCr)	Cr_3C_2–25% (Ni-20Cr) composite	210	HVOF	Hastelloy X	Kermetico

[a]Alloy Fusion is a proprietary coating application method developed by Deloro Stellite; details are not available.

20.6 The future

20.6.1 Economy of high-strength US A-USC alloy developments

The US program's temperature aim of 760°C (1400°F) steam is greater than the other programs worldwide focused on A-USC at 700°C (1300°F). This has led to the extensive study of alloys Inconel 740H and Haynes 282. A critical advantage of these alloys is that they can be used more cost effectively than solid solution–strengthened nickel-based alloys at 700°C (1300°F) due to their higher strength at lower temperatures with similar alloy cost. One specific study [50] compared alloy 617 to 740H for a prototypical A-USC main steam and hot-reheat piping system and showed that by using 740H in lieu of 617, the number of pipes required would decrease, the length of each individual extruded pipe section would increase, the number of welds for the piping system would decrease, the pipe thickness would decrease, and the amount of

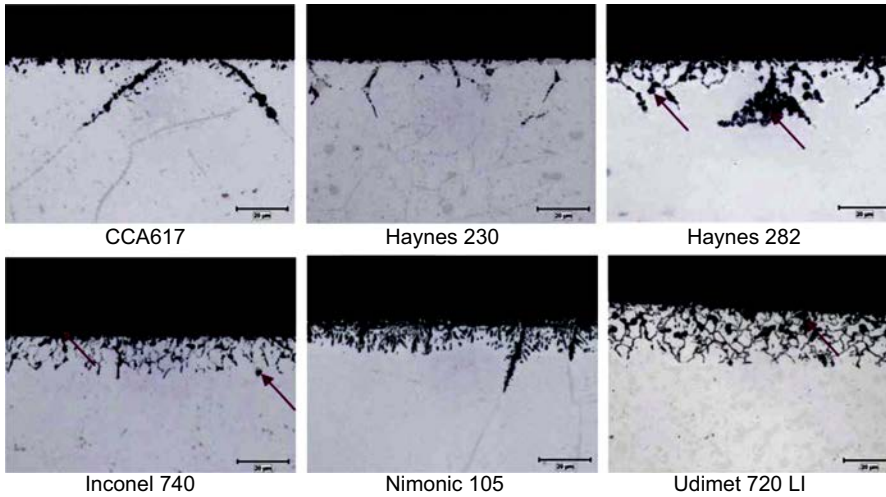


Figure 20.15 Typical oxide scales observed after 8000 h exposure at 760°C for A-USC turbine alloys. Thin protective chromia scales have formed with small internal oxidation (*arrows*) present in some alloys.
Courtesy of A-USC Consortium and EPRI; T. Totemeier, S. Goodstine. Oxidation of candidate alloys and coatings for a-USC steam turbine applications, in: Proceedings to the 6th International Conference on Advances in Materials Technology for Fossil Power Plants, Santa Fe, New Mexico, Distributed by ASM International, August 30–September 4, 2010, EPRI, March 2011, 1022300.

welding (both filler material and welding time) would decrease. The combined effect of these results demonstrated that the utilization of 740H over 617 would result in a significant cost savings with regard to both construction and life management of an A-USC piping system at 700°C (1300°F). Fig. 20.16 is a comparison of the piping system in that study. Of interest is that for the main steam pipe, two 617 pipes were required because the wall thickness of the 617 in a single pipe arrangement exceeded typical boiler fabrication sizes (thickness was greater than 100 mm). Additionally, the processing characteristics for extrusion (the basis of this study) showed 740H could be extruded in large diameter; thus only one reheat pipe was needed compared to two for the 617 system. Depending on alloy cost, the materials savings alone for using 740H in lieu of 617 was 5–20 million USD.

20.6.2 Component test facility

In late 2015, Consortium members B&W, Alstom, GE, and EPRI began pursuing the pre-engineering work on a US-based component test facility. The purpose of the facility will be to test heavy-section components at 760°C in an actual power plant. This facility will run 60°C (100°F) hotter than any other test facility in the world, will evaluate cyclic operation of welds and valves, and will include the world's first A-USC turbine test [51]. The project has four main goals. First, it will evaluate the advanced

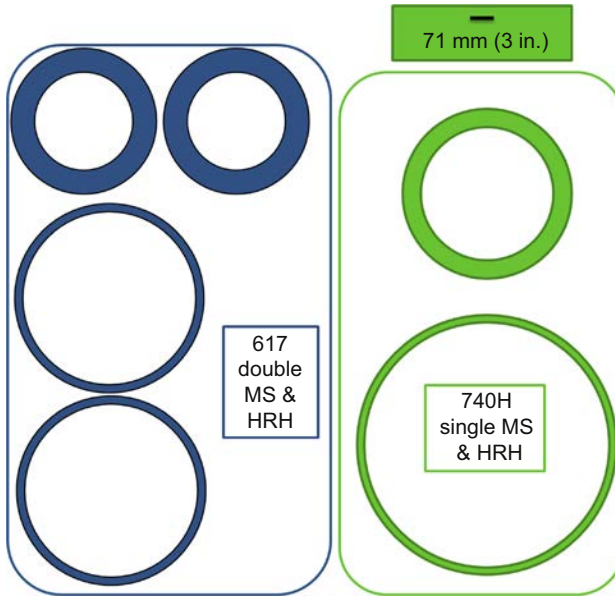


Figure 20.16 Comparison of a 617 and 740H piping system for a 700°C (1300°F) steam plant. The 617 system requires two main steam and two hot-reheat pipes to avoid wall thickness in excess of 75 mm and to allow for extrusion. In contrast, only one main steam pipe and one reheat pipe is needed for the 740H system due to its excellent strength and good fabrication characteristics (after [50]).

materials and components under A-USC conditions. The second goal is to minimize risk for a utility desiring to implement A-USC technology. The principal risks identified by utilities are boiler reliability and safety of thick section piping, valve, and membrane walls as well as turbine operation. Third, there is a goal to understand manufacturing, cost, and supply chain constraints, which for current economic models do not have a firm technical basis since no large-scale engineering project has been built with these materials. Finally, there is a goal for validation of the field fabrication techniques and the ability to construct, install, and repair the advanced materials and components with on-site labor.

20.6.3 A-USC materials technology future

With increasing concerns over the release of CO_2 to the atmosphere, numerous studies have shown efficiency is always the lowest cost approach to reducing emissions. Recent EPRI work shows that in a future where coal-fired power plants require CCS, A-USC technology is the clear economic choice for the coal plant of the future [52]. However, the study clearly showed that in the absence of CCS, the increased cost of the plant due to the use of nickel-based alloys will not be offset by the reduced fuel cost and other associated reductions in cost that come with higher efficiency.

One main driver for this cost is the cost of the main steam and reheat piping system. Alternative technologies have been proposed to address this challenge to make A-USC more economically attractive worldwide including inverted boiler designs [53] or split turbine arrangements. In addition to new power plants, there is the possibility of using A-USC materials technology to improve the efficiency of current plants through the use of a "topping cycle" where a new reheat steam cycle at much higher temperature is integrated into the boiler. Preliminary studies suggest this is a viable option [54], but more site specific work is required to determine the economic and regulatory impacts of this option. Beyond coal-fired generation, the power generation community has been researching alternatives to steam Rankine cycles. One such cycle is a Brayton cycle with supercritical CO_2 as the working fluid. These cycles promise high efficiency and small footprints, but they require high temperatures, beyond 700°C, to enable their performance. For these cycles, A-USC materials technology developed by this consortium will be required [55].

20.7 Conclusions

Revolutionary progress has been made in advancing the materials technology to enable a 760°C (1400°F) A-USC power plant. These successes have only been made possible through a unique, cost-sharing US Consortium of manufacturers and research organizations dedicated achieving to the aggressive goals set forth by the US DOE. The US DOE/OCDO A-USC Consortium has had many successes, including demonstration of welding and fabrication of nickel-based alloys for an A-USC plant, extensive successful fireside corrosion testing including in-plant operation of the world's first 760°C (1400°F) steam-cooled corrosion test loop, development of casting techniques for high-alloy age-hardenable alloys, new materials for rotor forgings, and code acceptance of Inconel 740H, which gives manufacturers, for the first time, an alloy with the requisite strength for a 760°C (1400°F) plant. Based on this successful 14-year effort, a new project to build a 760°C (1400°F) component test facility is now underway. Furthermore, the future for A-USC materials looks bright with new boiler design and alternative power cycles looking to take advantage of these developments.

Acknowledgments

The author based this work on publically available information and did not use government funds in the writing of the chapter. However, the author is extremely indebted to all the members of the A-USC Consortium, the US DOE Office of Fossil Energy, and the Ohio Coal Development Office, who have worked tirelessly toward the development of A-USC materials technology in the United States. Special thanks is given to Bob Purgert, Energy Industries of Ohio, who has been the biggest champion for this work over the entire 14 years.

References

[1] Update, The CURC-EPRI Coal Technology Roadmap, July 2015. Available at: www.coal.org.
[2] International Energy Agency © OECD/IEA, (2012). Available at: www.iea.org.
[3] B. Diczfalusy, Hele coal technology roadmap, in: IEA Clean Coal Centre Workshop: On Advanced Ultrasupercritical Coal-Fired Power Plants, Vienna, Austria, September 12–20, 2012.
[4] K. Burnard, O. Ito, Hele coal technology roadmap, in: IEA Clean Coal Centre Workshop: On Advanced Ultrasupercritical Coal-fired Power Plants, Vienna, Austria, September 12–20, 2012.
[5] R. Blum, R. Vanstone, Materials development for boilers and steam turbines operating at 700°C, in: Proceedings to the 6th International Charles Parsons Materials Conference, Dublin, Ireland, 2003.
[6] R. Viswanathan, R. Purgert, U. Rao, Materials for advanced power engineering 2002, in: Proceedings Part II, Forschungszentrum Julich GmbH, 2002, pp. 1109–1129.
[7] U.S. Department of Energy and Ohio Coal Development Office, Advanced Ultra-Supercritical Materials Project for Boiler and Steam Turbines, EPRI, Palo Alto, CA, March 2011, p. 1022770. Available: http://my.epri.com/portal/server.pt?Abstract_id=000000000001022770.
[8] R. Viswananthan, J.F. Henry, J. Tanzosh, G. Stanko, J. Shingledecker, B. Vitalis, R. Purgert, U.S. program on materials technology for ultra-supercritical coal power plants, Journal of Materials Engineering and Performance 14 (3) (June 2005) 281–292.
[9] J.P. Shingledecker, I.G. Wright, Evaluation of the materials technology required for a 760°C power steam boiler, in: Proceedings to the 8th Liege Conference on Materials for Advanced Power Engineering, Forschungszentrum Jülich GmbH, 2006, pp. 107–120.
[10] F. Masuyama, R&D program for a-USC material development with creep strength/degradation assessment studies, in: Proceedings to the 6th International Conference on Advances in Materials Technology for Fossil Power Plants, Santa Fe, New Mexico, August 30–September 4, 2010, EPRI, March 2011, p. 1022300. Distributed by ASM International. 11–29.
[11] R. Sun, Development of 700C USC coal-fired power generation technology in China, in: IEA Clean Coal Centre Workshop: On Advanced Ultrasupercritical Coal-fired Power Plants, Vienna Austria, September 12–20, 2012.
[12] A. Mathur, O.P. Bhutani, Personal Communication, BHEL, February 2013.
[13] World Energy Outlook. Inernational Energy Agency (2014). ISBN:978-92-64-20804-9. Available: www.iea.org.
[14] Cost and Performance Baseline for Fossil Energy Plants – Volume 3b: Low Rank Coal to Electricity: Combusion Cases. DOE/NETL-2011/1463. Available www.netl.doe.gov.
[15] Engineering and Economic Evaluation of 1300F Series Ultra-Supercritical Pulverized Coal Power Plants: Phase 1, EPRI, Palo Alto, CA, 2008, p. 1015699.
[16] Cost and Performance Baseline for Fossil Energy Plants – Volume 1: Bituminous Coal and Natural Gas to Electricity. DOE/NETL-2010/1397. Available www.netl.doe.gov.
[17] Advanced Ultra-Supercritical Steam Cycle Optimization, EPRI, Palo Alto, CA, 2014, p. 3002001788.
[18] R. Schwant, C. Shen, M. Soare, New Materials Enable Unprecedented Improvement in Turbine Performance, Advanced Materials & Processes, © ASM International, January 2013, pp. 18–22.

[19] J. Shingledecker, R. Purgert, P. Rawls, Current status of the U.S. DOE/OCDO a-USC materials technology research and development program, in: Advances in Materials Technology for Fossil Power Plants. Proceedings from the Seventh International Conference. October 22–25, 2013, Waikoloa, Hawaii, USA, Published by ASM International ©, 2014, pp. 41–52. EPRI Report Number 3002002375.
[20] M. Santella, et al., Weld development for heavy-section SAVE12, in: Presentation at the 5th International Conference on Advances in Materials Technology for Fossil Power Plants, Marco Island, FL, USA, October 3–5, 2007.
[21] R. Viswanathan, J. Sarver, J. Tanzosh, Boiler materials for ultra-supercrtical coal power plants – steamside oxidation, Journal of Materials Engineering and Performance 15 (3) (June 2006) 255–274.
[22] J.P. Shingledecker, N.D. Evans, Creep-rupture performance of 0.07C-23Cr-45Ni-6W-Ti, Nb austenitic alloy (HR6W) tubes, International Journal of Pressure Vessels and Piping 87 (6) (June 2010) 345–350.
[23] J.P. Shingledecker, Creep rupture behaviour and recrystallisation in HR6W and Haynes alloy 230 cold bent boiler tubing for ultrasupercritical steam boiler applications, Energy Materials 2 (4) (2008) 235–240.
[24] G.D. Smith, H.W. Sizek, Introduction of an Advanced Superheater Alloy for Coal-Fired Boilers, Corrosion 2000. Paper 00256 ©, NACE International, TX, 2000.
[25] B.A. Baker, et al., Welding and repair technology for power plants, in: Tenth International EPRI Conference, June 26–29, 2012. Marco Island, FL, USA.
[26] J.A. Siefert, J.M. Tanzosh, J.E. Ramirez, in: Proceedings to the 6th International Conference on Advances in Materials Technology for Fossil Power Plants, Santa Fe, New Mexico, August 30–September 4, 2010. EPRI, Distributed by ASM International, March 2011, p. 1022300. 1045–1066.
[27] J.P. Shingledecker, N.D. Evans, G.M. Pharr, Influences of composition and grain size on creep-rupture behavior of Inconel® alloy 740, Materials Science and Engineering A 578 (2013) 277–286, http://dx.doi.org/10.1016/j.msea.2013.04.087.
[28] J.P. Shingledecker, G.M. Pharr, The role of eta phase formation on the creep strength and ductility of INCONEL alloy 740 at 1023 K (750°C), Metallurgical and Materials Transactions A 43 (6) (2012) 1902–1910, http://dx.doi.org/10.1007/s11661-011-1013-4.
[29] J.P. Shingledecker, G.M. Pharr, Testing and analysis of full-scale creep-rupture experiments on Inconel alloy 740 cold-formed tubing, Journal of Materials Engineering and Performance 22 (2) (2013) 454–462, http://dx.doi.org/10.1007/s11665-012-0274-4.
[30] K.A. Unocic, J.P. Shingledecker, P.F. Tortorelli, Microstructural changes in Inconel ® 740 after long-term aging in the presence and absence of stress, JOM 66 (12) (2014) 2535–2542, http://dx.doi.org/10.1007/s11837-014-1208-4 © 2014 The Minerals, Metals & Materials Society.
[31] J.P. Shingledecker, Metallurgical Effects on Long-Term Creep-Rupture in a New Nickel-Based Alloy (Ph.D. dissertation), University of Tennessee, Knoxville, May 2012.
[32] H. Semba, H. Okada, M. Igarashi, Creep properties and strengthening mechanisms in 23Cr-45Ni-7W (HR6W) alloy and Ni-base superalloy for 700C a-USC boilers, in: Proceedings from the EPRI Fifth International Conference on Advances in Materials Technology for Fossil Power Plants. Copyright © 2008 EPRI, Distributed by ASM International ®, 2008, pp. 168–184.
[33] Q. Wu, V.K. Vasudevan, J.P. Shingledecker, R.W. Swindeman, Microstructural characterization of advanced boiler materials for ultra supercritical coal power plants, in: Proceedings to the Fourth International Conference on Advances in Materials Technology for Fossil Power Plants (Hilton Head, SC, October 25–28, 2004), ASM-International, Materials Park, OH, 2005, pp. 748–761.

[34] J.P. Shingledecker, R.W. Swindeman, Q. Wu, V.K. Vasudevan, Creep strength of high-temperature alloys for ultrasupercritical steam boilers, in: Proceedings to the Fourth International Conference on Advances in Materials Technology for Fossil Power Plants (Hilton Head, SC, October 25–28, 2004), ASM-International, Materials Park, OH, 2005, pp. 1198–1212.

[35] Q. Wu, H.-J. Song, R.W. Swindeman, J.P. Shingledecker, V.K. Vasudevan, Microstructure of long-term aged IN617 Ni-base superalloy, Metallurgical and Materials Transactions 39A (2008) 2569–2585.

[36] H. Hack, G.S. Stanko, Update on fireside corrosion resistance of advanced materials for ultra-supercritical coal-fired power plants, in: The 31st International Technical Conference on Coal Utilization & Fuel Systems, May 21–25, 2006. Clearwater, Florida, USA, .

[37] M. Gagliano, H. Hack, G. Stanko, Update on the fireside corrosion resistance of proposed advanced ultrasupercritical superheater and reheater materials: laboratory and field test results, in: The 2009 Clearwater Coal Conference, 34th International Technical Conference on Coal Utilization & Fuel Systems. Clearwater, FL, May 31–June 4, 2009.

[38] E. Robitz, J. Tanzosh, In situ corrosion testing of ultrasupercritical tube and weld overlay materials, in: Proceedings to the 6th International Conference on Advances in Materials Technology for Fossil Power Plants, Santa Fe, New Mexico, August 30–September 4, 2010. EPRI, Distributed by ASM International, March 2011, p. 1022300. 288–302.

[39] B. Bordenet, et al., Steam oxidation and fireside corrosion testing of several advanced alloys in a steam loop at a-USC design temperatures, in: Proceedings: EPRI International Conference on Corrosion in Power Plants, EPRI, Palo Alto, CA, 2015, p. 3002006972.

[40] J.M. Sarver, C.B. Krichbaum, Influence of materials and operational parameters on steam-side exfoliation, in: Proceedings: EPRI International Conference on Corrosion in Power Plants, EPRI, Palo Alto, CA, 2015, p. 3002006972.

[41] W.R. Mohn, J.M. Tanzosh, Considerations in fabricating USC boiler components from advanced high temperature materials, in: Proceedings to the Fourth International Conference on Advances in Materials Technology for Fossil Power Plants (Hilton Head, SC, October 25–28, 2004), ASM-International, Materials Park, OH, 2005, pp. 165–176.

[42] B.A. Baker, R.D. Gollihue, in: Proceedings to the 6th International Conference on Advances in Materials Technology for Fossil Power Plants, Santa Fe, New Mexico, August 30–September 4, 2010. EPRI, Distributed by ASM International, March 2011, p. 1022300. 96–109.

[43] M. Borden, Weldability of materials for ultrasupercritical boiler applications, in: Proceedings to the Fourth International Conference on Advances in Materials Technology for Fossil Power Plants (Hilton Head, SC, October 25–28, 2004), ASM-International, Materials Park, OH, 2005, pp. 837–854.

[44] J.A. Siefert, J.P. Shingledecker, J.N. Dupont, S.A. David, Weldability and weld performance of candidate nickel base superalloys for advanced ultrasupercritical fossil power plants part II: weldability and cross-weld creep performance, Science and Technology of Welding and Joining (October 2015). Available online http://dx.doi.org/10.1179/1362171 85y.0000000094.

[45] P.J. Maziasz, et al., High temperature mechanical properties and microstructure of cast Ni-Based superalloys for steam turbine casting applications, in: 6th International Conference on Advances in Materials Technology for Fossil Power Plants, Santa Fe, New Mexico, August 30–September 4, 2010.

[46] P.D. Jablonski, C.J. Cowen, Homogenizing a nickel-based superalloy: thermodynamic and kinetic simulation and experimental results, Metallurgical and Materials Transactions B 40B (2) (April 2009) 182–186.

[47] B. Purgert, J. Shingledecker, Update on U.S. DOE/OCDO Advanced ultrasupercritical (A-USC) steam boiler and turbine consortium, in: Presentation at DOE-FE Cross-Cutting Review Meeting, April 29, 2015. Pittsburg, PA, USA. Available at: https://www.netl.doe.gov/File%20Library/Events/2015/crosscutting/Crosscutting_20150429_0830A_EIO.pdf.

[48] R. Viswanathan, J. Shingledecker, J. Hawk, S. Goodstine, Effect of creep in advanced materials for use in ultrasupercritical power plants, in: Proceedings: Creep & Fracture in High Temperature Components, 2nd ECCC Creep Conference, April 21–23, 2009, Zurich, Switzerland, © DEStech Publications, Inc., 2009, pp. 31–43.

[49] T. Totemeier, S. Goodstine, Oxidation of candidate alloys and coatings for a-USC steam turbine applications, in: Proceedings to the 6th International Conference on Advances in Materials Technology for Fossil Power Plants, Santa Fe, New Mexico, August 30–September 4, 2010. EPRI, Distributed by ASM International, March 2011, p. 1022300.

[50] J. Shingledecker, et al., U.S. Program on advanced ultrasupercritical power plant materials – the economy of using advanced alloys, in: Proceedings to the IEA Clean Coal Centre Workshop: Advanced Ultrasupercritical Coal-fired Power Plants. Vienna, Austria, September 19–20, 2012.

[51] P.S. Weitzel, ASME: ComTest Facility Phase 1 Engineering for 760C A-USC Steam Generator Development, Energy-Tech Magazine, March 1, 2016.

[52] H.L. Hendrix, "Advantages of a-UC for CO_2 capture in pulverized coal units" advances in materials technology for fossil power plants, in: Proceedings from the Seventh International Conference. October 22–25, 2013, Waikoloa, Hawaii, USA, Published by ASM International ©, 2014, pp. 60–73. EPRI Report Number 3002002375.

[53] P.S. Weitzel, A steam generator for 700C to 760C advanced ultrasupercritical design and plant arrangement: what stays the same and what needs to change, in: Advances in Materials Technology for Fossil Power Plants. Proceedings from the Seventh International Conference. October 22–25, 2013, Waikoloa, Hawaii, USA, Published by ASM International ©, 2014, pp. 86–97. EPRI Report Number 3002002375.

[54] The Applicability of Supercritical Topping Cycles for Repowering Subcritical Steam-electric Power Plants, EPRI, Palo Alto, CA, 2010, p. 1019676.

[55] I.G. Wright, B.A. Pint, J.P. Shingledecker, D. Thimsen, Materials considerations for supercritical CO_2 turbine cycles, in: Proceedings of ASME Turbo Expo 2013: Turbine Technical Conference and Exposition. GT2013, June 3–7, 2013. San Antonio, TX, USA. GT2013-94941 © ASME.

This page intentionally left blank

The Chinese 700°C A-USC development program

21

Z. Liu[1], *X. Xie*[2]
[1]China Iron and Steel Research Institute Group Co., Ltd, Beijing, China;
[2]University of Science & Technology Beijing, Beijing, China

21.1 Introduction

The higher the steam parameters of coal-fired power plant, the higher is the efficiency of the plant and the lower is the coal consumption of the plant, as well as fewer emissions of the plant. As shown in Fig. 21.1 shows the historic evolution of steam parameters of Chinese coal-fired power plants in the past seven decades [1]. China started to build a 600°C USC coal-fired plant in the year 2003, and all required T23, T/P91, T/P92, S30432, and S31042 boiler tubes and pipes were imported from either Europe or Japan, which led to a very high construction cost. Under such a situation, China Iron & Steel Research Institute Group (CISRI), BaoSteel, Haerbin Boiler maker, and others started to collaboratively investigate and develop aforementioned boiler tubes and pipes under the support of the Ministry of Sciences and Technology of China. After more than 10 years of hard work, by the end of the year of 2013, all critical boiler steel tubes and pipes used for 600°C USC power plants (including T/P91, T/P92, S30432, and S31042) have been widely manufactured by Chinese steel makers. Further, the domestically made boiler steel tubes and pipes realized the bulk exports to overseas, including exports to Japan,

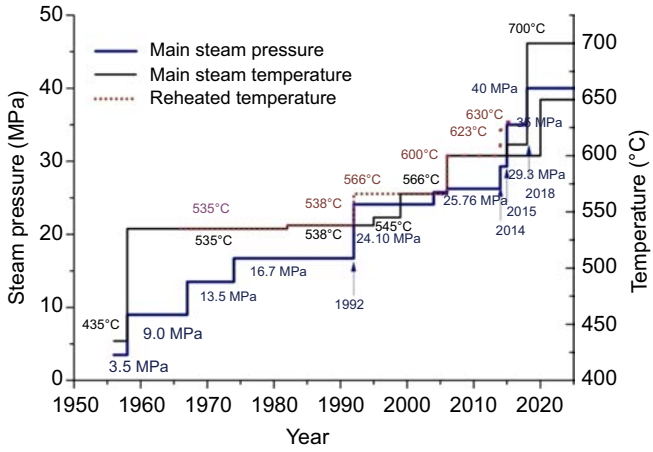


Figure 21.1 Steam parameter evolution of Chinese fossil-fired power plants.

Materials for Ultra-Supercritical and Advanced Ultra-Supercritical Power Plants.
http://dx.doi.org/10.1016/B978-0-08-100552-1.00021-X
Copyright © 2017 Elsevier Ltd. All rights reserved.

Germany, and the United States. The world boiler steel tube and pipe market situation has been completely overturned in the past years. During the period of 2006–2013, the installed 600°C USC power capacity reached to 122.4 GW, accounting for more than 80% of all available 600°C USC power capacity in the world. However, the installed capacity only takes about 14.2% of the currently existing fossil-fired power capacity in China.

According to the data of Organisation for Economic Co-operation and Development (OECD), the CO_2 emission from steel industries only takes 6.15%; however, the CO_2 emission from fossil-fired power plants takes 41%. It was calculated that the CO_2 emission of Chinese fossil-fired power plants will decrease 7.5 million tons annually if the coal consumption decreases 1 g/kWh. In China, the fossil-fired power accounts for about 75% of all electric power, and its actual contribution to the gross power output is about 82%. Therefore, to develop higher steam parameters and bigger capacity fossil-fired power plants is the national energy and environmental protection strategy in China.

Based on currently available heat-resistant steels, Haerbin Boiler Maker designed and built a 660-MW high-efficiency USC coal-fired power plant at ChangXing of Zhejiang province with steam pressure of 29.3 MPa and the steam temperature of 600/623°C. The unit was put into commercial operation on December 17, 2014. The thermal efficiency of the unit is 46%, and coal consumption of the unit is 278 g/kWh. Compared to normal 600°C USC power plants, the unit is of about 2% higher thermal efficiency and reduces the coal consumption up to 9 g/kWh, which will save about 30,000 tons of coal annually and reduce about 0.1 million ton of CO_2 emission annually. In fact, China has entered the batch construction phase to build a high-efficiency USC coal-fired power plant with the reheat steam temperature of 620°C.

In April 2015, Shenhua Guohua Electric Power Company planned to design and build a much higher efficiency USC coal-fired power plant with steam pressure of 35 MPa and the steam temperature of 610/630/630°C. The steam parameters refreshed the operational temperature limit again for commercial higher efficiency USC coal-fired power plants.

21.2 The foundation of China's 700°C A-USC coal-fired power generation technology innovation consortium

To improve the technical level of coal-fired power plants and form independent intellectual property rights from materials research to complete power plant technology, on July 23, 2010, the National Energy Administration set up the National innovative consortium for 700°C A-USC coal-fired power technology at the Great Hall of the People. The members of the national consortium include China Power Engineering Consulting Group Corporation, CISRI, Xi'an Thermal Power Research Institute, Shanghai Power Equipment Research Institute, Institute of Metal Research (IMR) of Chinese Academy of Sciences, five power providing groups, three electrical equipment manufacturing groups, China First Heavy Industries, China Second Heavy Industries, BaoSteel, and Dongbei Special Steel (Group) Company.

The original overall research and development proposals of the Chinese consortium are listed in Table 21.1 [2]. Due to the unavailability of heat-resistant alloys, the timing milestone of the proposed schedule has been postponed backward for a few years. Through the innovation of 700°C A-USC coal-fired power technology, the aim of the consortium is to integrate resources effectively, to solve technical problems together, and to realize the research and development of 700°C A-USC coal-fired power generators independently in the near future, promoting the development of relevant industries and opening up a new path for energy conservation and emission reduction in the power industry.

21.3 The fundamental consideration of China's 700°C A-USC coal-fired demo plant

The major technical difficulty to develop a 700°C A-USC coal-fired plant is the research and development of heat-resistant materials used to manufacture high-temperature parts of boilers and steam turbines, including superheaters, reheaters, main steam pipes, and other high-temperature heavy, thick parts for boiler and high-temperature rotors, casings, blades, and valves for steam turbines. Although superalloys have been used for the making of air engines and gas turbines for many years, the heat-resistant alloys used for 700°C A-USC coal-fired plant are completely different compared to those superalloys used for air engines and gas turbines. The superalloys used for air engines and gas turbines are relatively smaller parts for very high temperature but shorter service time, and the heat-resistant alloys used for 700°C A-USC coal-fired plants are relatively larger parts for medium high temperature but a much longer service time. This is the reason that we termed the alloys used for 700°C A-USC coal-fired plant to be heat-resistant alloys. At present, there are no available and mature heat-resistant alloys used for the construction of 700°C A-USC coal-fired plants worldwide. According to public information, the 700°C A-USC coal-fired plant research and development plans of Europe, the United States, Japan, and China are listed in Table 21.2, from which it is clearly seen that the research and development of heat-resistant materials is always the first priority and the key issue. The capacity of the Chinese demo plant is 660 MW, and steam parameters are 35 MPa and 700°C/720°C/720°C. Since the year of 2010, the preliminary design of boiler and steam turbine of 700°C A-USC demo plant has been carried out and completed under the leadership of the National Innovative Consortium for 700°C A-USC Coal-Fired Power Technology. Since the year of 2012, CISRI, Baosteel, Fushun Special Steel, Inner Mongolia Heavy Industries, IMR, and others have been collaboratively developing heat-resistant materials and their tubes/pipes used for 700°C A-USC coal-fired plants under the financial support of the Ministry of Sciences and Technology of China. Since the year of 2014, CISRI, Fushun Special Steel, Baosteel, China First Heavy Industries, China Second Heavy Industries, IMR, and others have been collaboratively developing heat-resistant materials and their parts used for 700°C A-USC coal-fired plant under the financial support of the Ministry of Sciences and Technology of China and the National Energy Administration. If the research on

Table 21.1 Overall R&D proposal for the Chinese consortium

No.	Content	11	12	13	14	15	16	17	18	19	20	21
1	Overall program design											
2	Filtering, developing, optimizing and assessing of high temperature materials											
3	Key components of main equipments and high temperature pipes											
	1) Boiler's tubes											
	2) Boiler's key components											
	3) Turbine’s forgings											
	4) Turbine’s key components											
	5) High temperature pipes and fittings											
	6) High temperature and high pressure valves											
4	Test platform construction and test											
	1) Design and construction of test platform											
	2) Test of boiler's key components and valves											
5	Demonstration projects											
	1) Preparation											
	2) Construction of the project											
	3) Operation and summary											

Table 21.2 The 700°C A-USC power plant research and development plans worldwide

	Europe	United States	Japan	China
Unit capacity	550 MW	750 MW	650 MW	660 MW
Steam pressure	37.5 MPa	37.9 MPa	35 MPa	35 MPa
Steam temperature	705/720°C	732/760°C	700/720°C	700/720/720°C
Unit efficiency	50%	45–47%	46–48%	48–50%
Development stage 1	1998–2004 materials development	2001–2006 materials development	2008–2016 materials and parts develop-ment and evaluation	2010, startup and unit design
Development stage 2	2002–2005 materials evaluation	2007 materials evaluation		2012–2015 boiler materials development
Development stage 3	2004–2017 Parts evaluation			2014–2018 tur-bine materials development
Demo plant				–2025

heat-resistant materials goes smoothly, China will begin to build a demo 700°C A-USC coal-fired power generator around the year 2025.

21.4 Boiler materials for China's 700°C A-USC coal-fired demo plant

Coal-fired power plants include mainly boilers and turbines. The boiler pipes/tubes and heat-resistant components in the turbine are the bottleneck for the making of fossil power plants. Whether they can be successfully developed is mainly attributed to the heat-resistant materials and equipment manufacturing capacity. The process of developing heat-resistant materials mainly includes composition design, processing property, component manufacturing, and evaluation of component performance. After lengthy, careful discussions, the technical committee of National Innovative Consortium of 700°C A-USC Coal-Fired Power Technology has determined the preliminary scheme on 700°C USC boiler pipes/tubes candidate materials, which was shown in Fig. 21.2 [3]. The typical chemistry of some candidate materials was listed in Table 21.3. The mechanical properties at room temperature and elevated temperature of those candidate materials will be published elsewhere very soon.

21.4.1 Water cooling wall materials

T23 steel is used as water cooling wall material in 600°C USC coal-fired power generators. The reason why T23 steel was chosen can be attributed to that the tubes

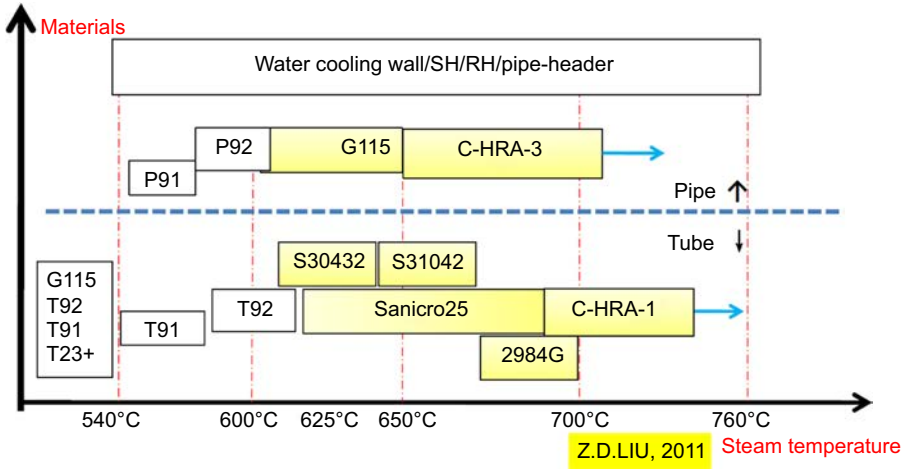


Figure 21.2 Heat-resistant candidate materials for boilers of 700°C power plants in China.

do not need to be heat treated before or after welding. However, from the industrial experiences, there are many problems with the water cooling walls made by T23 steel without pre-weld or post-weld heat treatments. Since the temperature of water cooling walls in 700°C USC coal-fired power generators can reach around 500°C, it is necessary to choose a new kind of material with higher heat resistance. Currently, T23, T91, and G115T are candidate materials for water cooling walls according to the operating temperature from low to high. One of the advantages of this choice is that the diameter and thickness of water cooling wall tubes at different positions can be nearly the same, ensuring excellent heat transfer performance as well as easier and better weldability.

21.4.2 Materials for superheaters and reheaters

S30432 and S31042, two kinds of austenitic tubes in small diameter, are mainly used in superheaters (SHs) and reheaters (RHs) in 600°C USC coal-fired power generators. But the temperature range of SHs and RHs in 700°C A-USC coal-fired power generators is from 600°C to 700°C; therefore, a series of tubes are needed to match the requirement of SHs and RHs at different temperature regions. Considering the cost of power plant construction, the maximum operating temperature of advanced austenitic heat-resistant steels should be expanded, and the use of expensive nickel-based heat-resistant alloys should be lowered. With increasing steam temperature from 600°C to 700°C, the candidate materials are Sanicro25, GH2984G, and Alloy C-HRA-1 according to the operating temperature. The key issue is to increase the comprehensive performance of these three candidate materials by optimizing the compositions and the processing, finally, to satisfy the requirement of a 700°C demo power plant in China.

Table 21.3 **Typical chemistry of candidate materials used for 700°C A-USC power plants**

Alloy	C	Cr	Mo	W	Co	Nb	V	Al	Ti	B	Cu	Ni	Others
G115	0.08	9		3.0	3.0	0.05	0.20			0.015	1.0		Others
Sanicro25	0.08	22.5		3.6	1.5	0.50					3.0	25	Others
2984G	0.06	19	2.0			1.00		0.4	1.0			43	33Fe
C-HRA-3	0.06	22	9.0		12			1.0	0.4	0.003		55	Others
C-HRA-1	0.02	25	0.5		20	1.50		1.47	1.36	0.005	0.02Zr	Bal	Others

21.4.3 Material for boiler pipes and headers

P92 and P122 ferritic pipes are candidate materials for boiler pipes and headers in 600°C USC power plants. The maximum operating temperature of P92 steel is around 600°C. P122 steel has been eliminated since its allowable stress at 600°C was sharply lowered in recent years. With increasing steam temperature from 600°C to 700°C, the candidate materials are P92, G115P, and C-HRA-3 according to the operating temperature. The welding issues between ferritic pipes and nickel-based pipes should also be carefully considered.

21.4.4 The development of materials for 700°C USC boilers in China

21.4.4.1 The development of G115 pipe

G115 ferritic heat-resistant steel developed by CISRI for 650°C USC power plants has undergone trial-manufacturing three times at BaoSteel. The manufactured boiler pipe in large section is under comprehensive property evaluation. The size of the second trial-manufactured boiler pipe by hot extrusion was Φ254 × 25 × 3500 mm. The creep rupture property and corrosion resistance property of manufactured G115 pipes are shown in Fig. 21.3. So far, G115 possesses the best combination of creep rupture strength and corrosion resistance among all the candidate materials for 650°C USC pipes. If the currently used P92 pipes for 600–620°C USC power plants are replaced by G115 pipes, the thickness of the pipes can be largely reduced, thereby reducing the weight as well as the difficulty in welding (Fig. 21.4).

21.4.4.2 The manufacturing of C-HRA-3 pipe

C-HRA-3 is one of the main candidate materials for 700°C A-USC pipes. The smelting of C-HRA-3 alloy with the weight of 6 tons has been successfully finished with the combined efforts of CISRI and Fushun Special Steel Company from January to April in 2013, as shown in Fig. 21.5. The first 6-ton hot extrusion of nickel-base superalloy pipe with the dimension of Φ460 × 80 × 4000 mm was successfully conducted by CISRI and Inner Mongolia North Heavy Industries Group Corp. Ltd. in October 2013 in China, as shown in Fig. 21.6.

21.4.4.3 The manufacturing of C-HRA-1 tube

Inconel 740H is one of the main candidate materials for superheater and reheater (tubes) of 700°C USC power plants. Heat-resistant alloy C-HRA-1 was developed by CISRI and Baosteel with independent property rights. C-HRA-1 tube with the size of Φ51 × 8 mm was successfully manufactured in the production line of a 4.5-ton special smelting and 6000-ton extrusion in BaoSteel Special Metals (Fig. 21.7). C-HRA-1 heat-resistant alloy has equal comprehensive properties with Inconel 740H, but simpler chemical composition and superior microstructure stability.

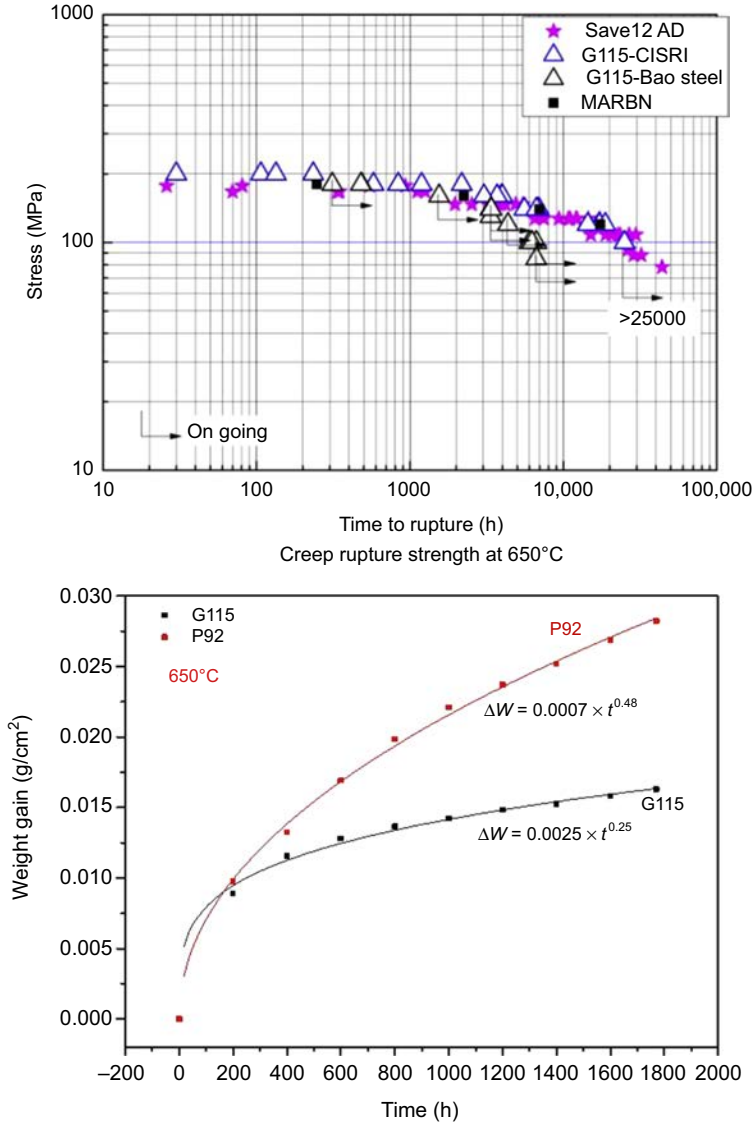


Figure 21.3 The properties of industrially made G115 pipes.

21.4.4.4 The manufacturing of GH2984G tubes

Much effort has been made in the chemical modification of alloy GH2984G developed by IMR. By adding B and P, the creep rupture life and high-temperature ductility of the alloy were been significantly improved. The formation of detrimental σ phase was prohibited by adjusting the contents of Fe and Ni. By modifying the Ti/Al ratio, the formation of needle-like η phase was prohibited, overcoming the problem of detrimental η phase precipitation as early as 500 h at 750°C. Seamless tube was

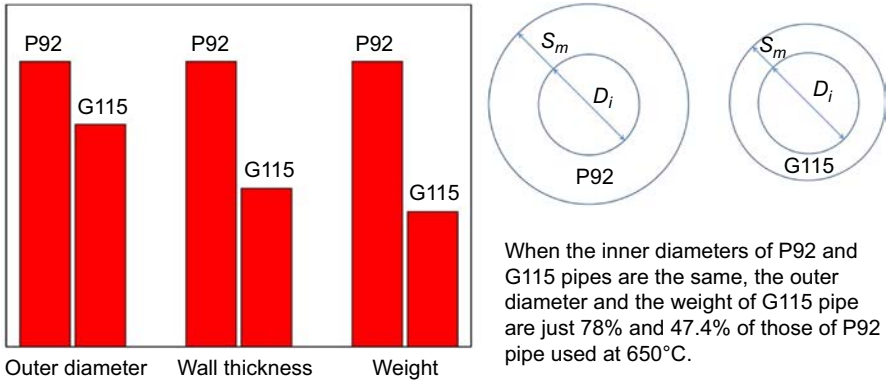


Figure 21.4 Comparison between G115 and P92 pipes.



Figure 21.5 Six-ton C-HRA-3 ingot made by FuShun Special Steel Company (VIM + VAR, Ingot size Φ660 × 1940 mm).

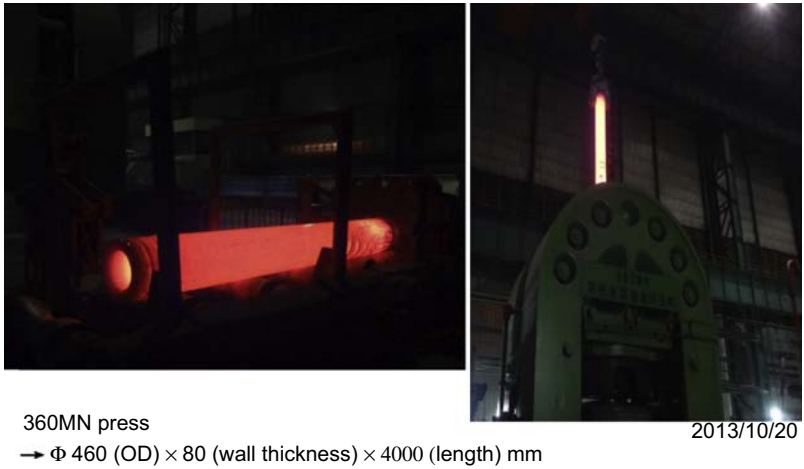


Figure 21.6 Hot extrusion of C-HRA-3 pipe at Inner Mongolia North Heavy Industries Group.

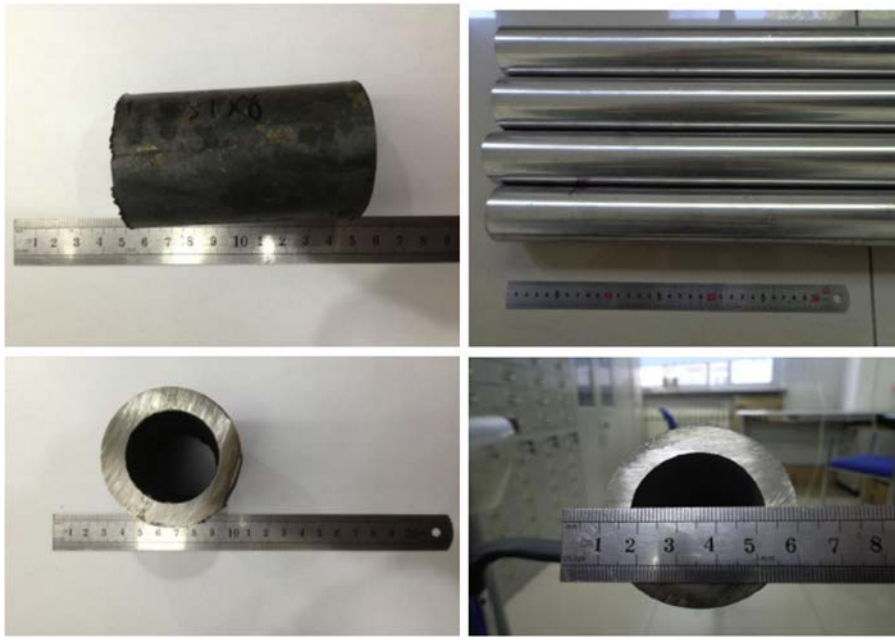


Figure 21.7 C-HRA-1 alloy tubes industrially made by BaoSteel and CISRI.

successfully manufactured by IMR of Chinese Academy of Sciences and BaoSteel's Special Steel Company in 2013.

21.5 Steam turbine materials for China's 700°C A-USC coal-fired demo plant

The major technical challenges for the development of high-temperature rotors, casings, blades, and bolts used for 700°C A-USC turbines are summarized in the following: (1) the chemistry and property optimization of candidate heat-resistant materials; (2) the vacuum melting techniques and stability control of 10-ton-scale nickel-based heat-resistant alloys; (3) the hot deformation technology of 10-ton-scale nickel-based heat-resistant alloys; and (4) the high-temperature casing casting technology for larger than 10-ton (up to 30-ton scale) nickel-based heat-resistant alloys. These technical challenges restrict the development of a 700°C A-USC demo power plant.

Through the close cooperation in the past decades, European and US material R&D facilities and manufacturing enterprises have successfully made 10-ton-scale nickel-based heat-resistant alloy parts used for 700°C A-USC turbines, and the comprehensive properties of these parts are under evaluation. Although the Japanese government launched its national program for a 700°C A-USC power plant in the year 2008, Japanese manufacturing enterprises, such as Mitsubishi, Toshiba, and Hitachi,

have carried out the research and development of key parts used for 700°C A-USC turbines for many years, and they have achieved considerable technical progress.

Considering the current tonnage limitation of smelting and forging for heat-resistant alloys, most turbine rotors for the advanced USC coal-fired power plants are designed and manufactured by dissimilar welding. 12% Cr heat-resistant steels were used for the lower temperature regime, and nickel-based heat-resistant alloys were used for the upper temperature regime. To meet the design and manufacturing demands of turbine rotors for 700°C A-USC power plants, the current research in China is focused on the development of solid solution strengthening C700-R1 (higher than CCA617) and C700-R2 (much higher than CCA617) heat-resistant alloys of 10 tons without macro-segregation, which also show good weldability with 12% heat-resistant steels. The details of chemical compositions and mechanical properties of C700-R1 and C700-R2 alloys cannot be published now because the CR700-R1 and CR700-R2 alloys are under patenting. Inconel 625 is the main candidate material for turbine casing. At present, the difficulty lies in the equipment of vacuum smelting and casting with large tonnage for the cylinder, which can hardly be met by the current smelting and casting equipment in China. The same problem is also faced in Europe and Japan. There are two solutions to this dilemma. The first is to design and build smelting and casting equipment with larger tonnage. The second is to manufacturing Inconel 625 castings with large tonnage following the routine of EAF + AOD/LF/VD + ESR. The National Energy Administration launched scientific research projects on the development of heavy mock-ups of heat-resistant alloys used for 700°C A-USC turbine manufacturing as of June of 2014. In the next few years, there will be a breakthrough in this respect in China.

21.6 Pilot testing rig for China's 700°C A-USC coal-fired demo plant

To qualify and verify the feasibility and maturity of available heat-resistant materials in China and overseas, the National Energy Administration of China decided to design and build an industrial pilot testing rig with the steam temperature up to 700°C. The pilot rig is capable of testing the performance of water wall tubing, superheaters, headers, pipes and associated valves in a near-industrial environment. The designing steam temperature is 700°C, and the steam fluid capacity is 10 ton/h.

Through field investigation and theoretical calculation, Unit #2 of Hua-Neng Nanjing Power Plant was selected to be the host unit. The designed testing rig includes one main steam loop and one bypass steam loop. For the main steam loop, the testing rig extracts steam from the intake header of the superheater of the host unit. The steam parameters are 26.8 MPa and 486°C. The obtained steam first enters the fireside tubing, which is installed inside the boiler furnace, and then the steam is heated to 610°C and further up to 725°C. The fully heated steam flows in an orderly fashion through the safety valve, control valve, stop valve, and heavy pipes to fulfill the qualification and verification of these key parts. The discharged steam is cooled down to the same temperature of the host unit, by a water-spray cooling system, and

is sent back to the steam loop. The purpose of the bypass steam loop is to verify the performance of the bypass valve, the valve's design theory, and its starting characteristics. The testing rig is under construction now, and it is expected to formally be put into use in 2016.

21.7 Structure stability of Inconel 740/740H [4–6]

Evaluation of foreign and domestic high-temperature materials will be both conducted in a 700°C A-USC pilot testing rig. The highest temperature part in China's 700°C coal-fired power plant project should be superheater/reheater tubing components. The fire side temperature of superheater/reheater components can reach 750–760°C and even higher. As we indicated, Inconel 740/740H is one of the main candidate materials for superheater and reheater tubing components of 700°C A-USC programs. Structure stability is one of the most important factors for fossil power plant long-time service. In consideration of that, the candidate material Inconel 740/740H has been chosen for structure stability study.

Inconel 740, a Ni-Cr-Co-Mo-Nb-Ti-Al superalloy developed by Special Metals Corp. (SMC, Huntington), USA, for the European THERMIE AD700 Project, characterized with the highest stress rupture strength and corrosion/oxidation resistance at temperature 750–760°C, is among today's available candidate materials, such as Haynes 230, HR6W, Inconel 617B, and Nimonic263. Inconel 740 contains about 13% γ′ for precipitation strengthening in γ-matrix, about 0.12% $M_{23}C_6$ distributed at grain boundaries, and about 0.2% MC carbide randomly distributed in γ matrix. However, there is also a small amount (about 0.05%) of high-silicon-containing G-phase at grain boundaries.

It can be recognized that the structure stability is good for Inconel 740 at long-time aging at the temperatures under 725°C. The instability of Inconel 740 at 760°C has been confirmed by three important factors: high coarsening rate of γ′ phase in grains, plate-like η phase, and high Si-containing brittle G-phase formation at grain boundaries (see Fig. 21.8). It will clearly develop degradation of both strength and ductility. Just for these reasons the structure stability improvement and modification of Inconel 740 for developing Inconel 740H should be done to fulfill the superheater/reheater requirements at the temperature 750°C and above.

Typical microstructure of Inconel 740H after standard heat treatment is very similar to the structure of Inconel 740. The main strengthening phase γ′(14.5%) homogeneously distributes in Ni-Cr-Co γ-matrix, $M_{23}C_6$ carbide(~0.2%), and also MC-(Nb,Ti)C carbide(~0.2%) formed at solidification process randomly distributes in this alloy. However, the comparison of structure stability of Inconel 740H and Inconel 740 at 750°C long-time aging is quite different (see Fig. 21.9). Inconel 740H keeps stable γ′ strengthening in Ni-Cr-Co γ-matrix and $M_{23}C_6$ carbide at grain boundaries. However, plate-like η-phase formation and high Si-containing G-phase precipitation obviously happen in Inconel 740. Moreover, the γ′ growth rate comparison between Inconel 740H and Inconel 740 (see Fig. 21.10) clearly shows that Inconel 740H characterizes very good structure stability at 750°C long-time aging.

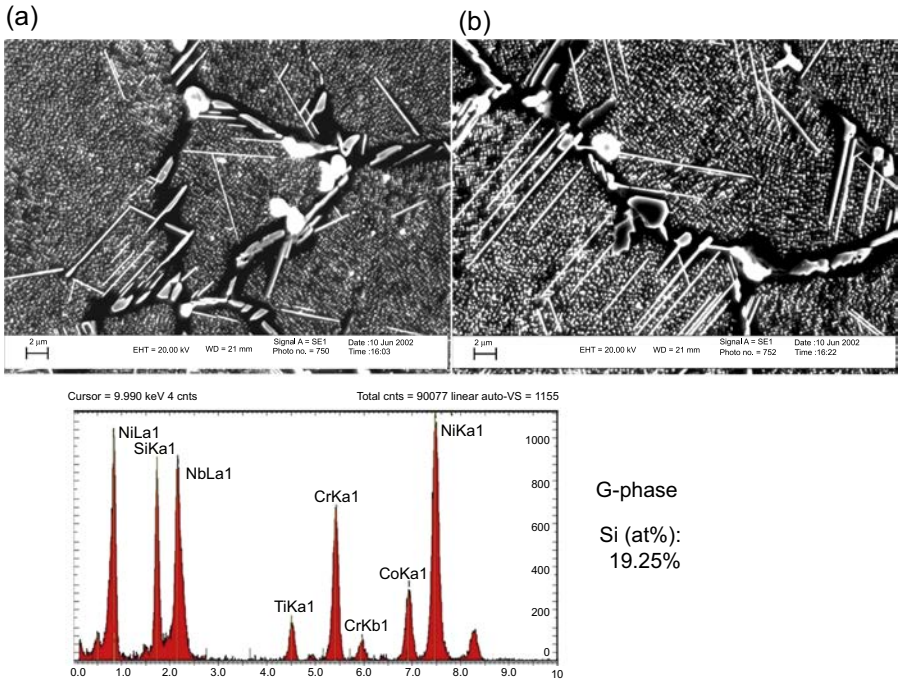


Figure 21.8 The large amount of η phase and G phase in Inconel 740 after 760°C long-time aging for 1000 h (a) and 2000 h (b).

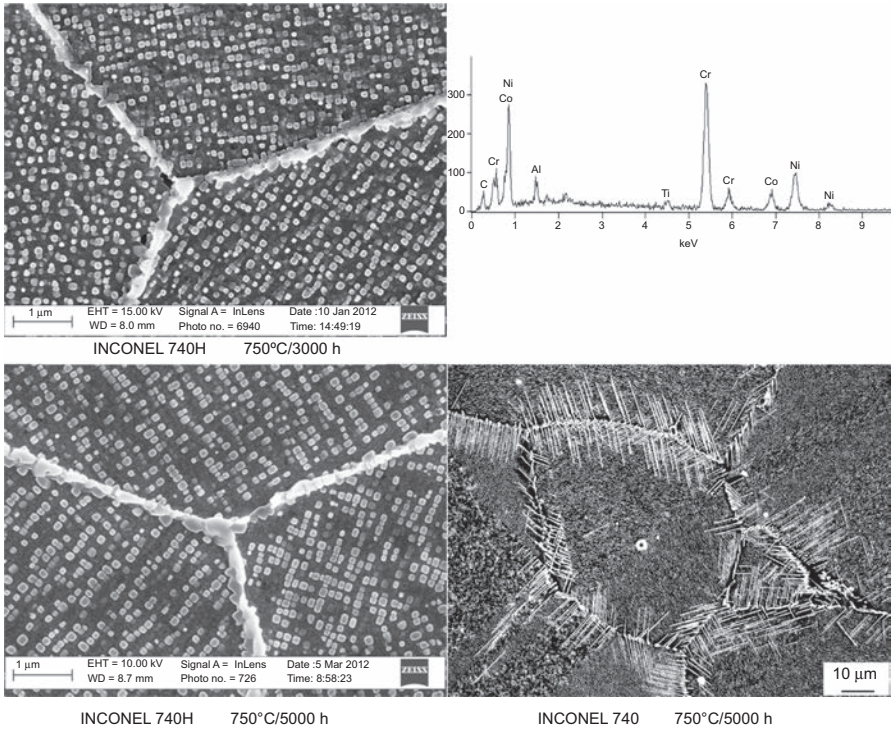


Figure 21.9 Long-time structure stability comparison between Inconel 740H and Inconel 740 at 750°C aging.

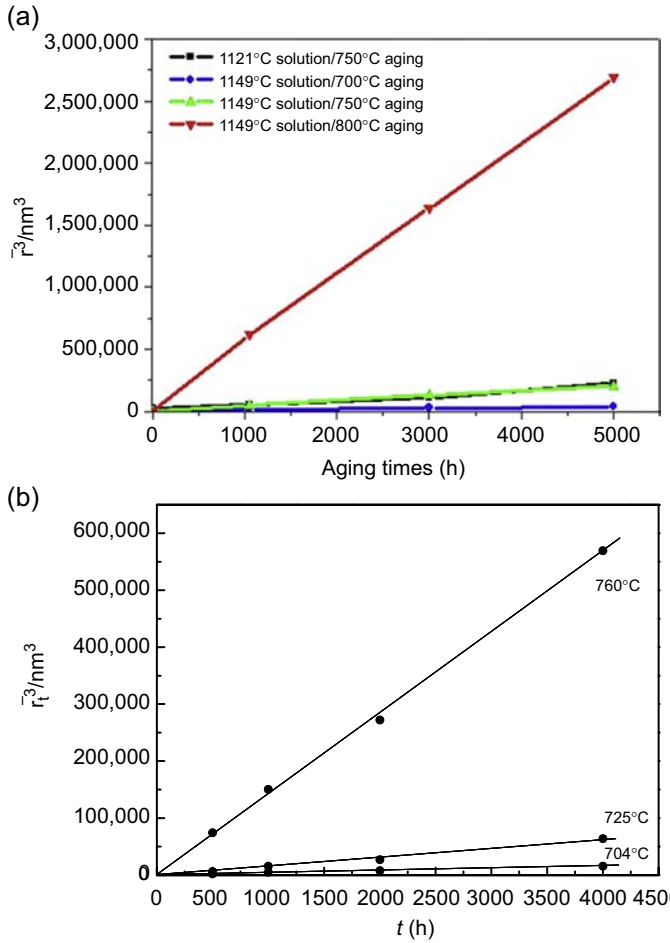


Figure 21.10 γ′ growth rate comparison between Inconel 740H (a) and 740 (b) at high temperatures.

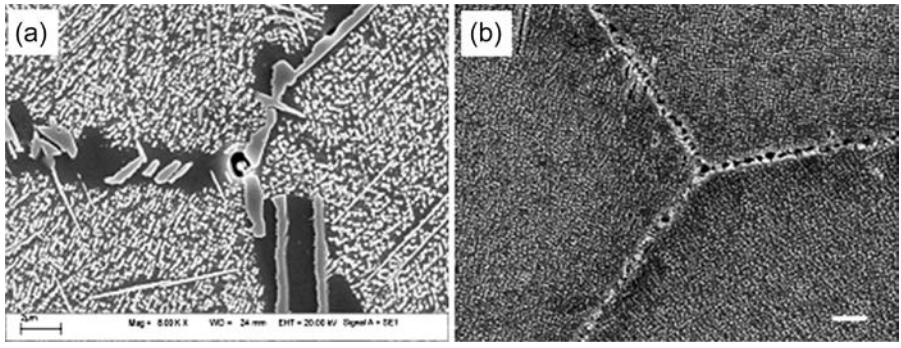


Figure 21.11 Microstructure comparison of Inconel 740 (a) and Inconel 740H (b) stress rupture tested samples.

Table 21.4 Impact toughness comparison of Inconel 740H and Inconel 740 after aging

Alloy	Exposure	CVN (J/cm^2)
740	0 h	45
	750°C/2000 h	13.6
740H	0 h	90.6
	750°C/3000 h	29.8
	750°C/5000 h	23.8

The structure stability study has been also conducted after high-temperature stress rupture tests. The structure of Inconel 740 sample tested at 775°C, 170 MPa, after 2779 h shows a large amount of η phase near grain boundaries and G-phase formation at grain boundaries (see Fig. 21.11(a)). However, the structure of Inconel 740H sample tested at 750°C, 280 MPa, after 1087 h still keeps stable γ′ precipitation in γ matrix and $M_{23}C_6$ carbide distributed at grain boundaries, and there is no existence of plate-like η phase and brittle G phase at grain boundaries (see Fig. 21.11(b)). The impact toughness of Inconel 740H after high-temperature long-time aging is much higher than Inconel 740, as shown in Table 21.4.

21.8 Conclusions

Under the organization and coordination of the National innovative consortium for 700°C A-USC coal-fired power technology, China has determined the capacity and steam parameters of 700°C A-USC demo unit, carried out the boiler and steam turbine preliminary design for the demo unit, investigated and selected the full set of boiler heat-resistant materials, and completed the laboratory investigation and industrial trials of the aforementioned set of boiler tubes and pipes. The required heat-resistant materials for the steam turbine of the demo unit are under investigation now in China. The pilot testing rig for the China 700°C A-USC coal-fired demo plant is under construction as it was planned. If the research and development of the heat-resistant materials and their parts goes smoothly, China may start to build its very first 700°C A-USC coal-fired demo plant in the year 2025.

Acknowledgments

One of the authors, Z.D.Liu, is very grateful to the National Energy Administration and the Ministry of Sciences and Technology of China for the permission to publish the current document and the financial support for the research.

References

[1] Z.D. Liu, The research and development of heat resistant steels and alloys used for 700°C A-USC-PP in China, in: Advanced Ultra-Super-Critical Coal-Fired Power Plants, IEA-Vienna Workshop-2012, Vienna, Austria, September 19–20, 2012.

[2] Z.D. Liu, H.S. Bao, G. Yang, S.Q. Xu, Q.J. Wang, Material advancement used for 700°C A-USC-PP in china, in: Seventh International Conference on Advances in Materials Technology for Fossil Power Plants, October 22–25, 2013, Hilton Waikoloa Village, Hawaii, USA, 2013.

[3] R. Sun, Z.D. Cui, Y. Tao, Development of 700°C USC coal-fired power generation technology in China, in: Advanced Ultra-Super-Critical Coal-Fired Power Plants, IEA-Vienna Workshop-2012, Vienna, Austria, September 19–20, 2012.

[4] X.S. Xie, S.Q. Zhao, J.X. Dong, et al., An investigation of structure stability and its improvement on new developed Ni-Cr-Co-Mo-Nb-Ti-Al superalloy, Materials Science Forum 475 (2004) 613–616.

[5] X.S. Xie, S.Q. Zhao, J.X. Dong, et al., A new improvement of Inconel 740 for USC power plants, in: Proceedings of Advances in Materials Technology for Fossil Power Plants, ASM, 2008, pp. 220–224.

[6] X.S. Xie, C.Y. Chi, J.X. Dong, et al., An investigation on structure stability of advanced austenitic heat-resistant steels and Ni-base superalloys for 600–700°C A-USC power plant application, in: Proceedings of the Seventh International Conference on Advances in Materials Technology for Fossil Power Plants, October 22–25, 2013, Hilton Waikoloa Village, Hawaii, USA, ASM, 2014, pp. 98–119.

This page intentionally left blank

Advanced USC technology development in Japan

22

M. Fukuda
Research Institute for Advanced Thermal Power Systems, Shinagawa, Tokyo, Japan

22.1 Introduction

Since the "oil shock" during the 1970s many coal power plants have been built in Japan to establish a more secure energy supply system. Fig. 22.1 shows the history of the capacity of pulverised coal (PC) power plants. The capacity rose to 35 GW in 2004 and one-fourth of the electricity in Japan today is produced by coal. However, the climate change brought about by CO_2 emissions is a well-known problem. The pressure on PC power plants to reduce CO_2 emissions is much larger than before. The most current plants have a 600°C-class steam temperature, and the net thermal efficiency is approximately 42% (HHV). This means that the CO_2 emission of the most current plants is 10% less than those of the plants from the 1970s. It is believed that future coal power plants will reduce CO_2 emissions even further. Because of the relatively high cost of imported coal and the dense population in Japan, highly efficient and clean technology has been preferred historically to reduce fuel consumption and environmental stress. The improvement in the efficiency of the coal-fired power plants has been mainly achieved by raising steam conditions. As shown in Fig. 22.2, the steam temperature was raised from 538 to 566°C at the end of the 1950s, and it remained at this temperature until 1993. Steam power plants that have

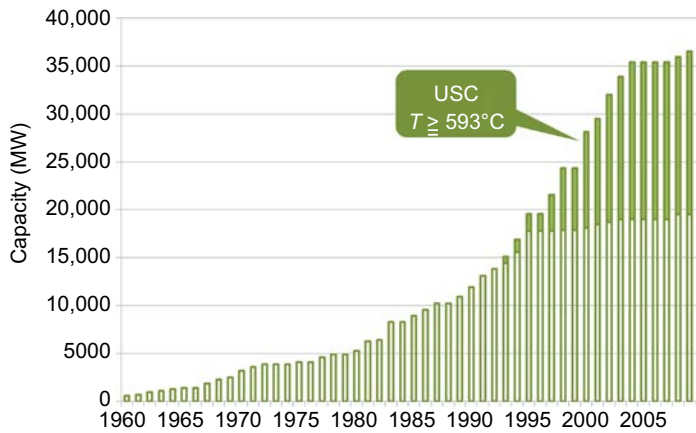


Figure 22.1 History of the capacity of PC power plants in Japan.

Materials for Ultra-Supercritical and Advanced Ultra-Supercritical Power Plants.
http://dx.doi.org/10.1016/B978-0-08-100552-1.00022-1
Copyright © 2017 Elsevier Ltd. All rights reserved.

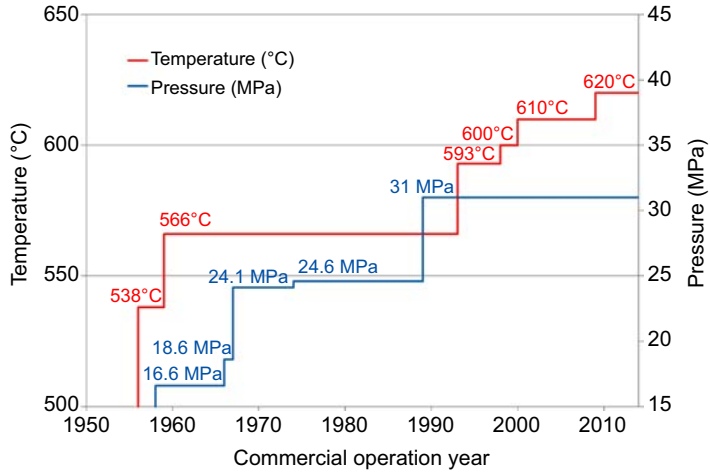


Figure 22.2 History of steam temperature and pressure in Japan.

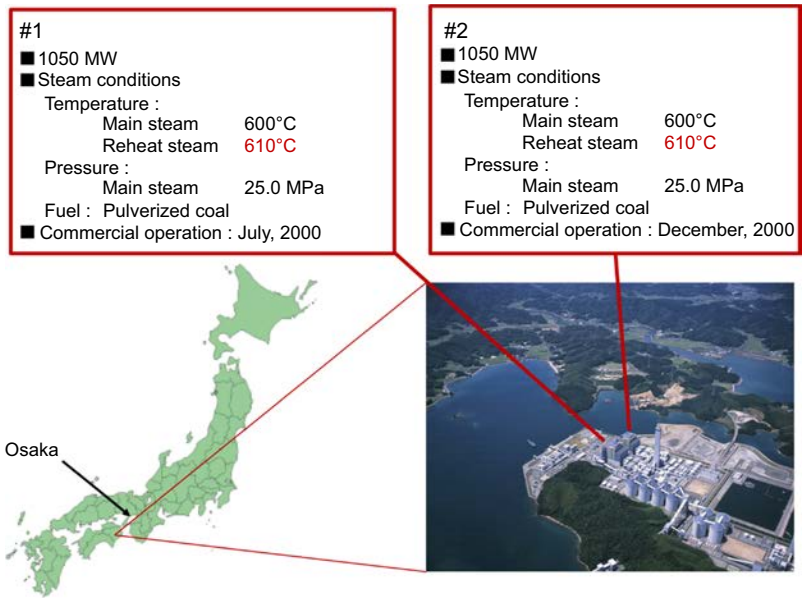


Figure 22.3 Tachibanawan power station [1].

been built recently usually have a steam temperature of around 600°C and a steam pressure of 25 MPa, which we usually call USC.

Fig. 22.3 shows J-Power's Tachibanawan power station. Tachibanawan #1 and #2 both have 1050-MW power output. These are the largest coal power units in Japan. The temperatures of the main steam and reheat steam are 600 and 610°C [1].

Fig. 22.4 shows J-Power's Isogo power station, which is located in the Tokyo metropolitan area. Isogo #2 is the newest coal-fired power plant in Japan. The temperatures of the main steam and reheat steam are 600 and 620°C [1].

Fig. 22.5 shows the number of the existing coal-fired power plants in Japan [3]. There are many older coal-fired power plants, built in the 1970s and early 1980s, which will reach the point where they will need to be retrofitted or replaced in the near future. Almost all Japanese coal power plants already have environmental protection

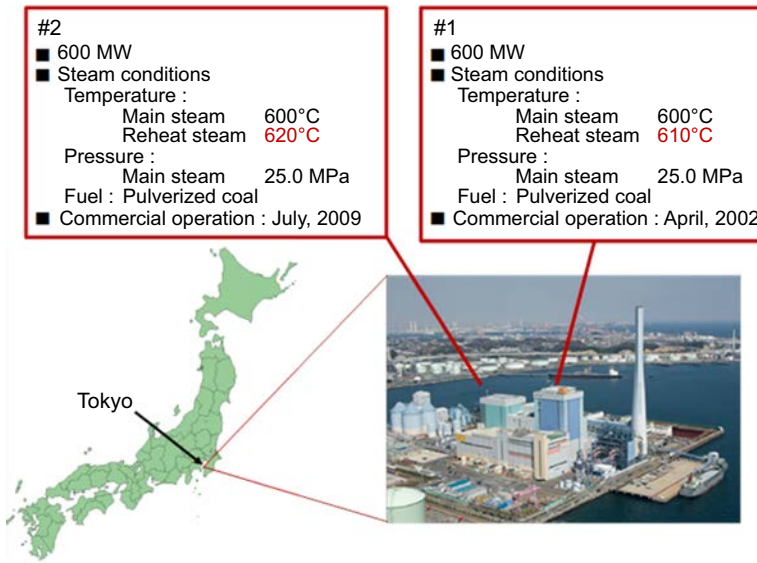


Figure 22.4 Isogo power station [1].

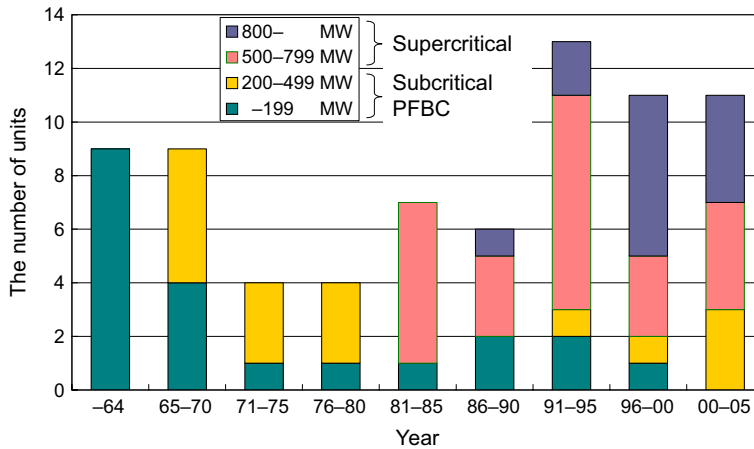


Figure 22.5 The number of existing plants and steam condition [3].

equipment like DeNOx, DeSOx, and EP that make up a large part of the plants. If we can retrofit the old plants with the higher steam temperature technology, it is possible to reduce CO_2 at a much lower cost than if we used the other technologies because we can reuse the expensive environmental protection equipment and some other cold parts from the existing plants.

The earthquake in 2011 struck northern Japan and caused a devastating tsunami. Fukushima #1 nuclear power plant was severely damaged by the tsunami. Almost all nuclear power plants have been shut down since then. In 2015, the Sendai nuclear power plant restarted after a very severe examination by Japanese government. This was the first case restarted after the earthquake. On the other hand, natural gas, oil, and coal-fired power plants are working fully to satisfy the market's demand, as shown in Fig. 22.6 [4]. Natural gas dominates almost half of the power generation, and old oil power plants have returned to the market. Consequently, the cost of fuel, which is imported from abroad, increased significantly and turned the country's international trade surplus into a deficit.

Coal is expected to become the more favorable choice for the newly built power plants because of its price and availability. In this situation, the reduction of CO_2 emission from coal-fired power plants is a crucial issue for the country.

The 700°C class advanced USC (A-USC) technology is being developed based on today's latest 600°C class USC technology by raising the steam temperature 100°C. The target net thermal efficiency for the higher heating value base is 46–48%. This is more than 10% higher than that of the 600°C class USC. That results in a more than 10% drop in CO_2 emissions.

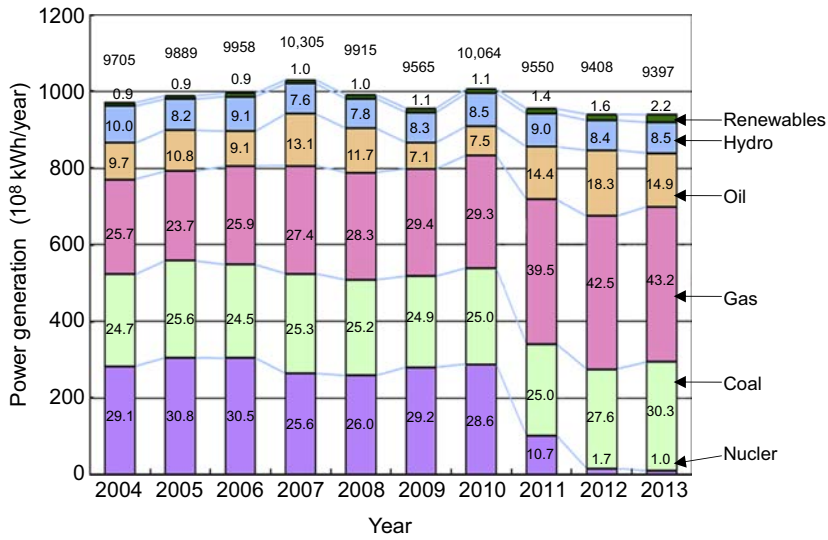
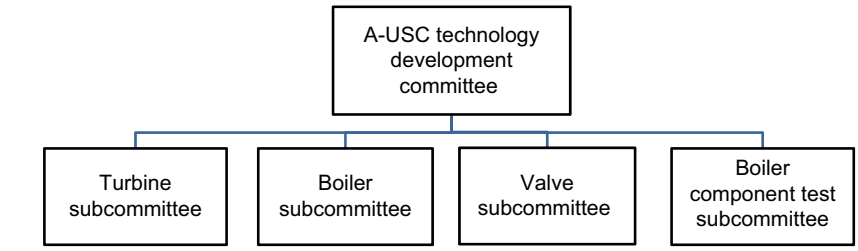


Figure 22.6 Annual power generation in Japan.

22.2 Technology development of A-USC in Japan

Following the USC technology development program, and stimulated by European projects, Japanese boiler, turbine, and valve manufacturers, institutes, universities and utility companies have been cooperating to develop 700°C class advanced USC technology since 2008 with the support of the Japanese government. Fig. 22.7 shows the project structure.

The target of the A-USC project is to develop 700°C-class material and component technology, based on today's latest 600°C-class USC technology, to achieve an HHV base net thermal efficiency of 46–48% for coal-fired power generation (Fig. 22.8) [2].



Members
ABB bailey japan
Central research institute of electric power industry (CRIEPI)
Chubu electric power company
Fuji electric
IHI
J-power
Mitsubishi heavy industries
Mitsubishi hitachi power systems
National institute for materials science (NIMS)
Nippon steel & sumitomo metal
Okano valve Mfg.
Research institute for advanced thermal power systems
Toa valve engineering
Toshiba

Observers
Ministry of economy, trade and industry
Universities
Japan steel works

Figure 22.7 Project structure.

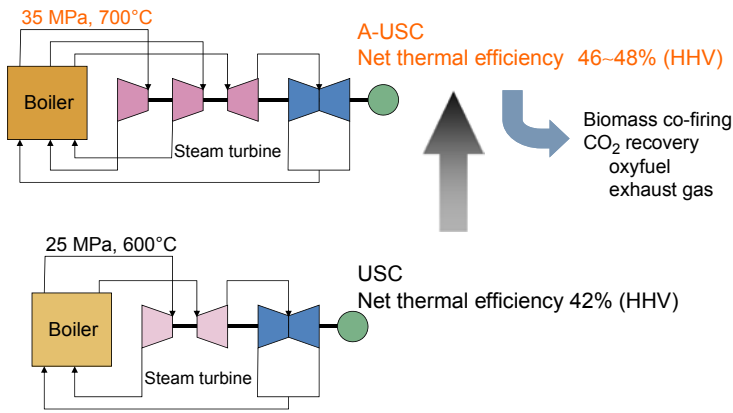


Figure 22.8 700°C-class advanced USC (A-USC) [2].

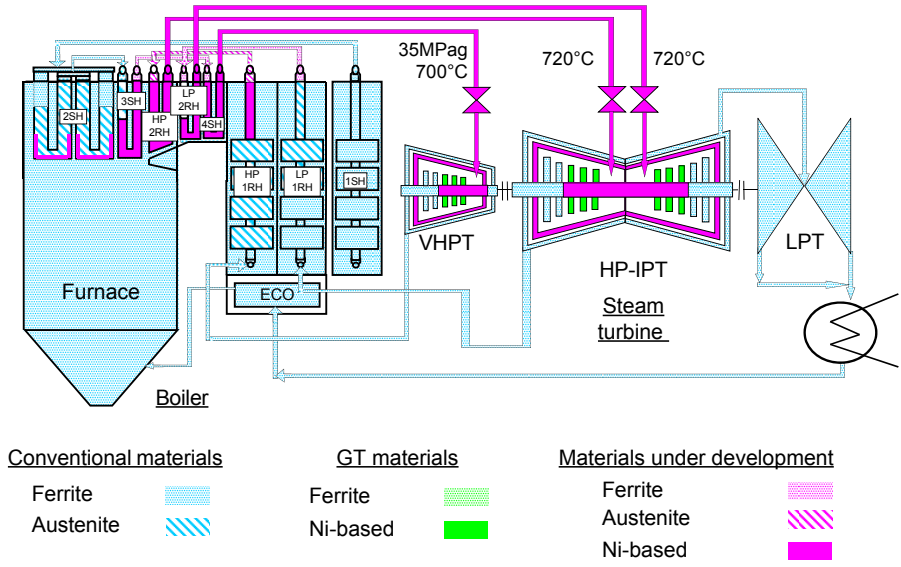


Figure 22.9 Selected materials [2].

The materials newly selected for A-USC are mainly Ni-based alloys and advanced 9Cr steels. Fig. 22.9 shows an example of material selection. The *blue* color represents conventional materials; *green* means gas turbine materials, *pink* means materials under development, and *solid dark pink* means Ni-based alloys under development. Ni-based alloys, which have not been used for USC, were chosen for part of the superheaters and reheaters, the large steam pipes and the valves going from the boiler to the turbines, and a part of the turbine rotors and casings. The turbine rotors consist of Ni-based alloy and 12Cr steel, which are welded together. The turbine nozzles and blades for the high-temperature stages use Ni-based materials that are being used for gas turbines [2].

Fig. 22.10 shows the master schedule of the project. Basic technologies of material and manufacturing for boiler, turbine, and valve are developed and verified by 2012. Long-term material tests are conducted through 2020. In the second half, boiler components and small turbine tests are carried out to verify component level reliability [2].

Once we decide to develop and use a new material, it is necessary to thoroughly develop related technologies such as maintenance, fabrication, component, and system design technology. Fig. 22.11 shows the technologies to be developed [2]. Long-term reliability, high-temperature corrosion resistance, steam oxidation resistance, and fatigue resistance are crucial characteristics for the materials. Life assessment and welding technology for aged materials are necessary to repair used components. Welding, bending, and NDT technologies must be developed to fabricate components. Valves, superheaters, and headers are essential to build a boiler system. In addition to the hardware technologies, system design technologies, such as piping design, structural design, and thermal analysis, are the key to the successful construction and operation of the boiler system.

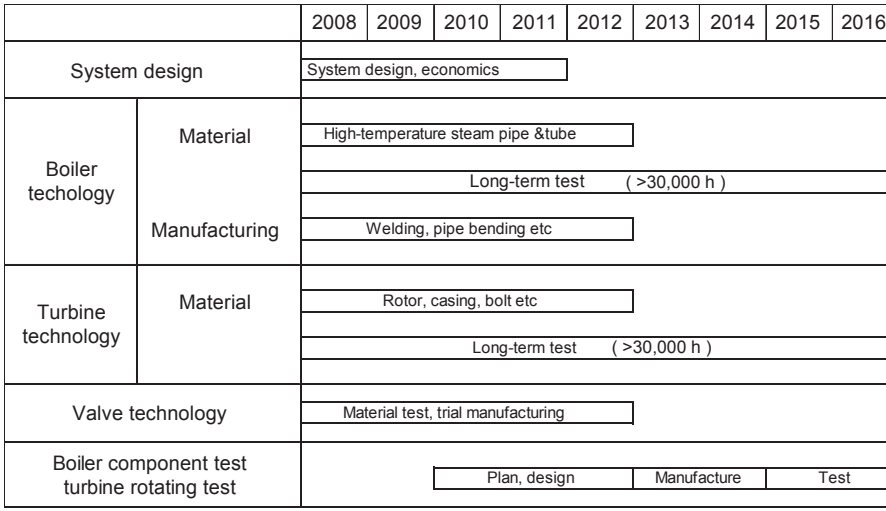


Figure 22.10 Master schedule [2].

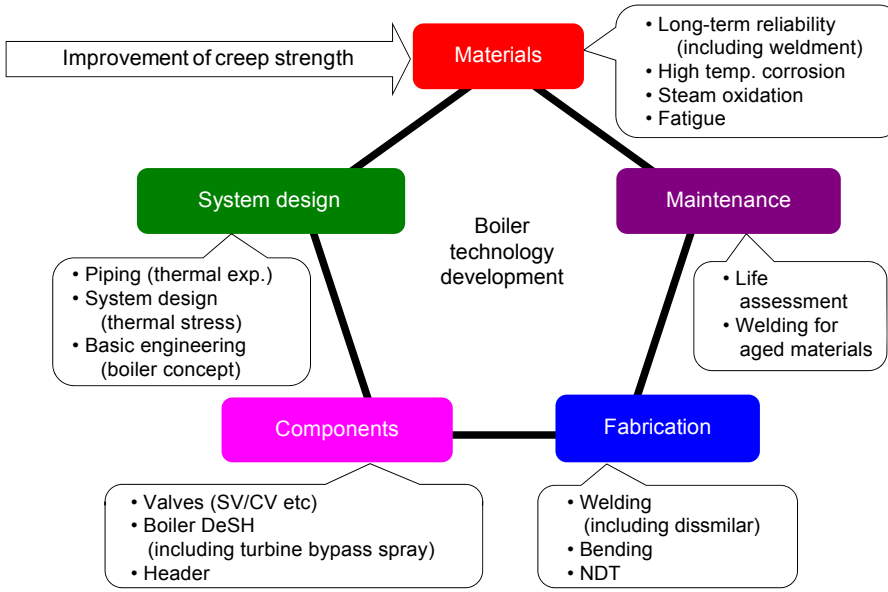


Figure 22.11 Boiler technology development [2].

Fig. 22.12 shows the schematics of the boiler technology development activities in the project. We did a preliminary study on the 700°C system before starting the project, as this is the first attempt to try such a high temperature. Some basic system configurations were studied, and some candidate materials were listed. In the first year of the project, we prepared some plates that were made of the candidate materials. The plates were used for preliminary welding tests and some material tests such as

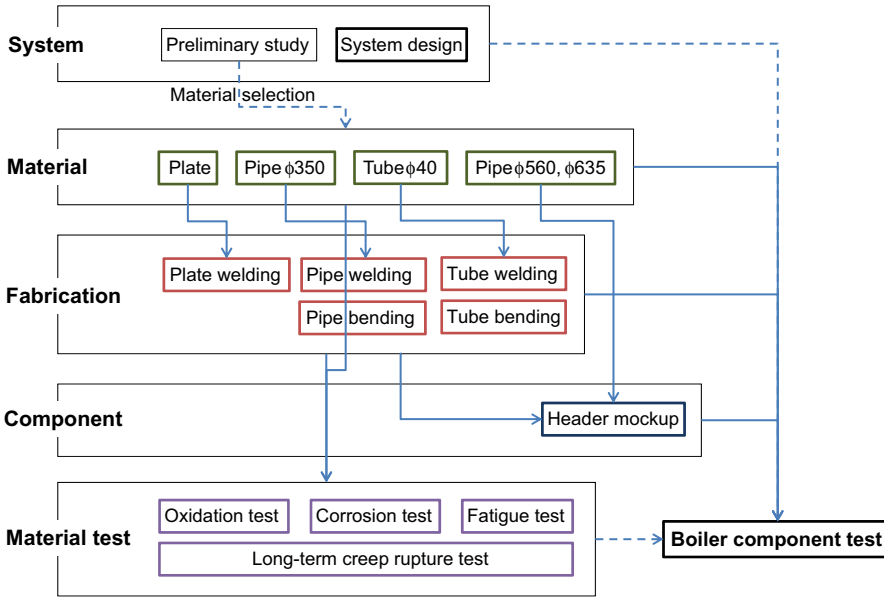


Figure 22.12 Boiler technology development activities [1].

Table 22.1 Candidate materials

HR6W	Ni-based	45Ni-23Cr-7W
HR35	Ni-based	50Ni-30Cr-4W-Ti
Alloy 617	Ni-based	Ni-22Cr-12Co-9Mo-Ti-AI
Alloy 263	Ni-based	Ni-20Cr-20Co-6Mo-Ti-AI
Alloy 740	Ni-based	Ni-25Cr-20Co-2Nb-Ti-AI
Alloy 141	Ni-based	Ni-20Cr-10Mo-Ti-AI
High-B-9Cr steel	Ferritic steel	9Cr-3W-3Co-Nb-V-B
Low-C-9Cr steel	Ferritic steel	0.035C-9Cr-2.4W-1.8Co-Nb-V
SAVE12AD	Ferritic steel	9Cr-3W-2.6Co-Nb-V-B

oxidation tests, corrosion tests, fatigue tests, and long-term creep rupture tests. Some large pipes, which were 350 mm in diameter, were made after the plates. They were used for welding tests, bending tests, and creep rupture tests. 40-mm-diameter tubes were made. They were also used for welding tests, bending tests, and creep rupture tests. A very large pipe, which was 635 mm in diameter, was made to make header mock-ups. A comprehensive boiler component test that includes the technologies that were developed in the first half of the project was conducted [1].

Six Ni-based materials (HR6W, HR35, Alloy 617, 263, 740, and 141) and three advanced 9Cr steels (high-boron 9Cr steel, low-carbon 9Cr steel, and SAVE 12AD) were chosen as the candidate materials (Table 22.1). Fig. 22.13 shows the plates made of the candidate materials [2].



Figure 22.13 Plates made of candidate materials.
Courtesy of Nippon Steel & Sumitomo Metal.

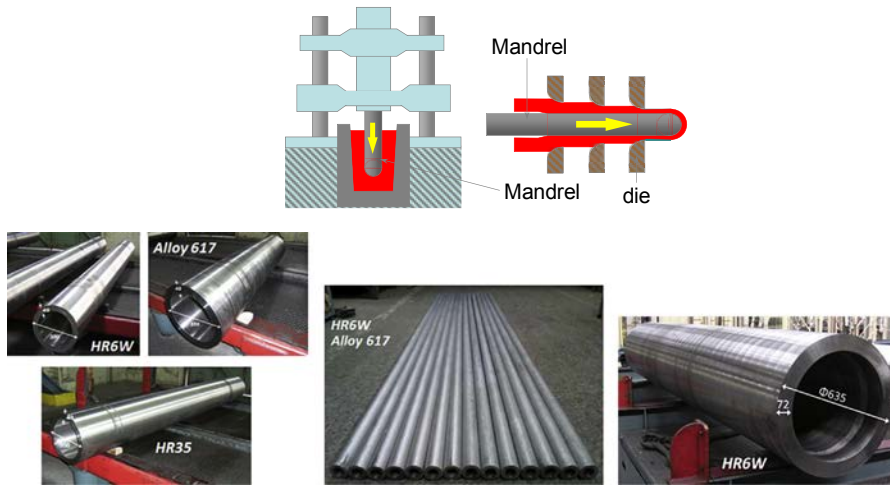


Figure 22.14 Boiler pipes and tubes.
Courtesy of Nippon Steel & Sumitomo Metal.

Fig. 22.14 shows pipes and tubes made of the candidate materials. In 2009, we made pipes with the Ehrhardt push bench method out of HR6W, HR35, and Alloy617. The largest pipe was 635 mm in diameter, and the wall thickness was 72 mm [1].

Fig. 22.15 shows an example of the creep rupture strength that was derived from HR6W creep rupture tests. HR6W was developed by Nippon Steel & Sumitomo Metal

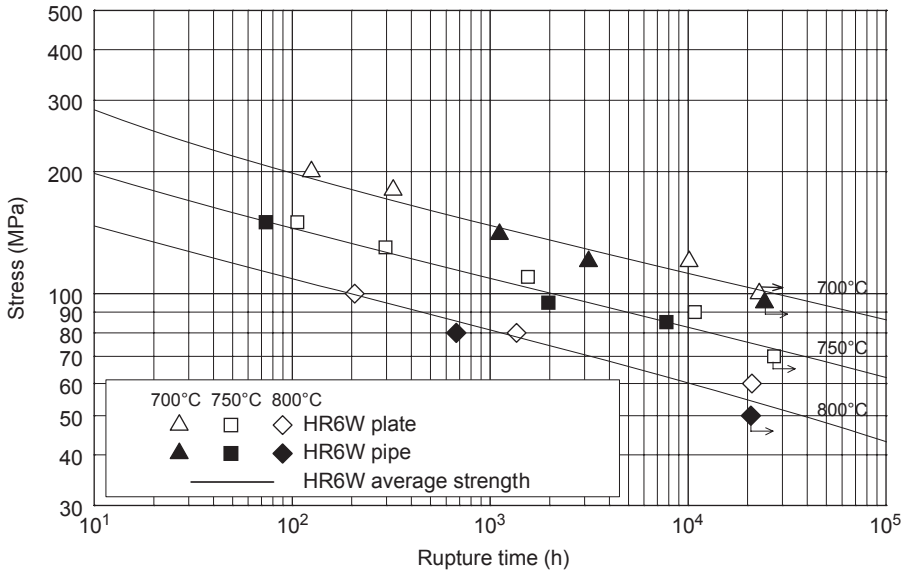


Figure 22.15 HR6W creep rupture strength.
Courtesy of Nippon Steel & Sumitomo Metal.

for pipes and tubes in the A-USC system and designed to have good corrosion resistance to combustion gas in the boiler and good creep strength for pressurized pipes and tubes at 700°C. The 100,000-h creep rupture stress at 700°C is expected to be about 90 MPa, which is the target for large steam pipe materials.

The hot corrosion tests on all candidate materials were carried out. Fig. 22.16 shows the average metal loss after the 100-h exposure test. All candidate materials were coated with compound ash and then exposed to a gas containing sulfur dioxide, 0.2% by volume. The average metal loss decreases with the higher chromium content in the alloys. It was confirmed that the candidate materials and austenitic steels have good hot corrosion resistance because of their high chromium content.

Fig. 22.17. shows the sections of the materials that have been exposed to 750°C steam for 3000 h. The thickness of the oxidized scale on the Ni-based alloys is considerably smaller than the oxidized scale on the 25Cr steel, Ka-SUS310J1TB(HR3C).

We did some welding tests on the candidate pipe materials. The left photo in Fig. 22.18 shows a welded HR35 pipe. The right figure shows the section of the weld. We did not find any flaws in these samples. In a few cases, with another material, we found some small cracks in the heat-affected zone. Therefore, we made another pipe with slightly different amounts of each component. The welding of the improved pipe was successfully done. Some dissimilar welding tests were conducted for tubes as we need to connect different tube materials in boiler superheater and reheater panels. The right photo shows the welding of Alloy 617 and Alloy 263 [1].

The creep rupture strength of the HR6W weld joints is shown in Fig. 22.19. Creep tensile specimens that contain welded portions were cut out from welded HR6W

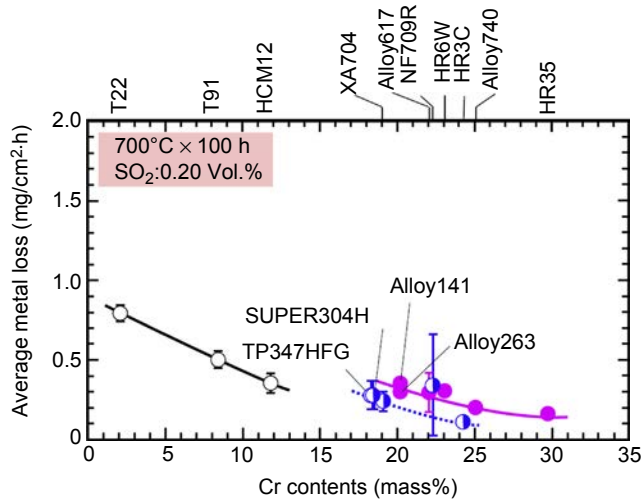


Figure 22.16 Hot corrosion test.
Courtesy of Mitsubishi Heavy Industries.

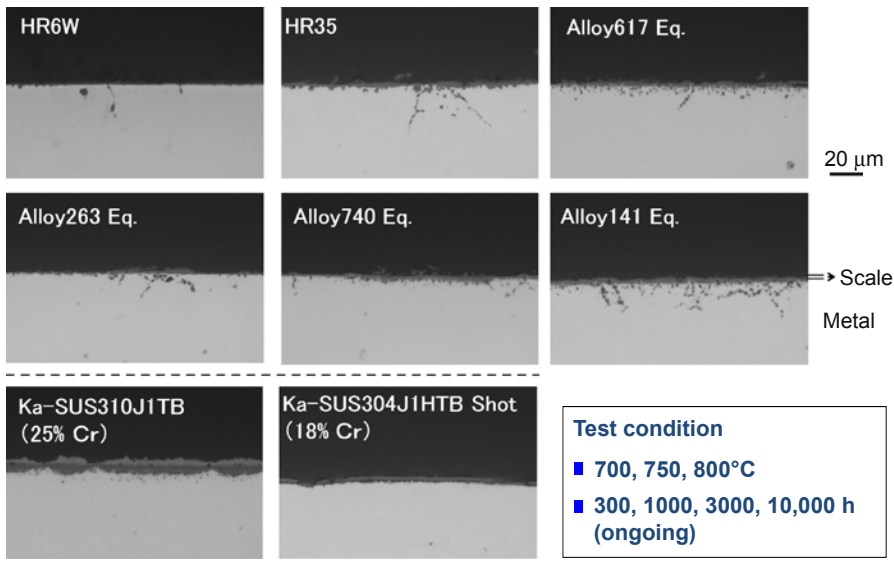


Figure 22.17 Steam oxidation test.
Courtesy of Mitsubishi Hitachi Power Systems.

plates. The weld material was Alloy 617. When tested, all specimens broke at the base material. We can see that the strength of the welded material is equivalent to that of HR6W without a weld joint.

Fig. 22.20 shows bended pipes that are made of Alloy 617 and HR6W. These pipes were cut into pieces to check the shape of the cross-section and to make test specimens.

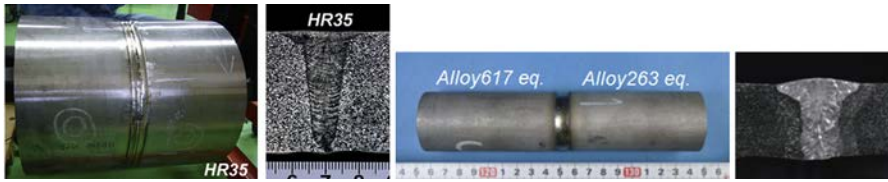


Figure 22.18 Pipes and tube welding.
Courtesy of IHI and Mitsubishi Hitachi Power Systems.

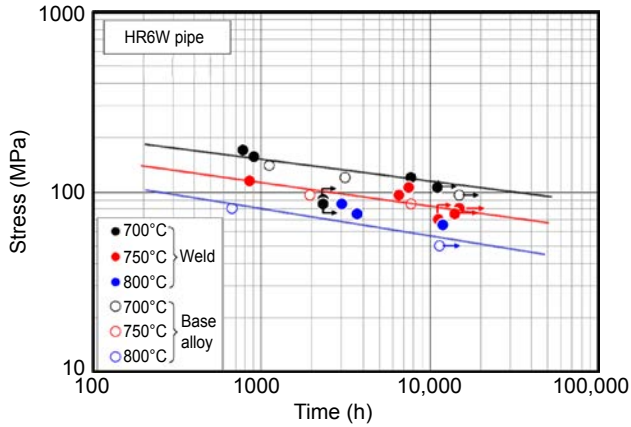


Figure 22.19 Creep rupture strength of HR6W weld.
Courtesy of IHI, Mitsubishi Heavy Industries, Mitsubishi Hitachi Power Systems.

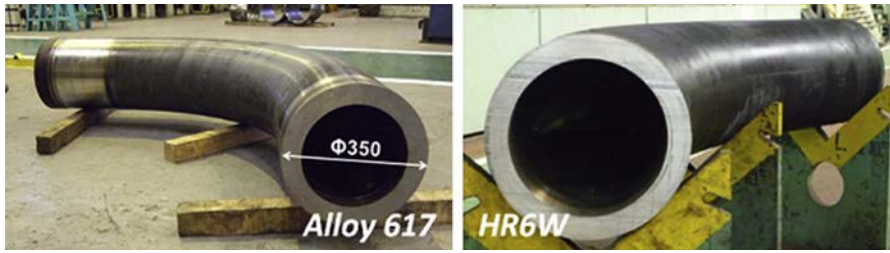


Figure 22.20 Bent pipes.
Courtesy of Mitsubishi Hitachi Power Systems.

As one of the comprehensive tests of the developed technologies, some header mock-ups were made to check the manufacturability of actual parts of the A-USC boiler. Fig. 22.21 shows a reheater and a superheater header mock-up. The pipe used for the reheater header mock-up is shown in Fig. 22.14 [1].

In 2015 and 2016, boiler components such as superheaters, pipes, valves, and a turbine casing were tested using an actual boiler (Fig. 22.22) [1].



Figure 22.21 Header mock-ups.
Courtesy of Mitsubishi Hitachi Power Systems and IHI.

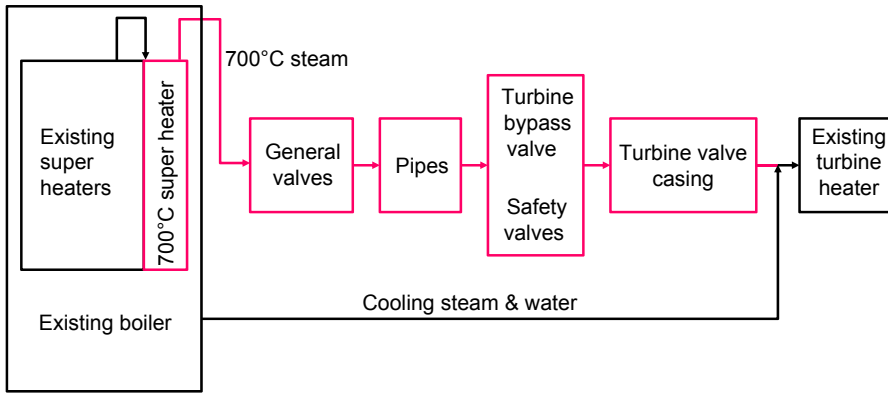


Figure 22.22 Boiler component test [1].

Fig. 22.23 shows the overview of the boiler component test facility. The *blue* colored parts are newly installed high-temperature parts. The 700°C steam flows down from the upper side of the facility to the bottom through the test parts. Fig. 22.24 shows the 700°C superheater during operation.

Ni-based alloys were considered for the 700°C-class turbine rotors. It is necessary to use Ni-based wrought material for rotors of 700°C-class steam turbines unless advanced cooling technology is used. However, it is difficult to make large Ni-based wrought parts, and it is assumed that the largest possible size of a part is around 10 tons. Turbine rotors for large capacity power stations usually weigh 30–40 tons. The "welded rotor" concept was proposed to make large rotors by welding Ni-based wrought material and steel. Fig. 22.25 shows a typical welded rotor.

Fig. 22.26 shows the schematics of the turbine technology development activities in the project. Similar to the boiler technology development, some candidate materials for rotors and casings based on the preliminary study of the 700°C system were selected before starting the project. At first, small specimens were made to check the fundamental characteristics of the candidate materials for rotors. Then 2- to 7-ton rotor materials were forged to check manufacturability of the rotor, followed by 10-ton-class large rotor materials. These rotor materials were used for welding tests including dissimilar welding between Ni-based alloys and steels. Machinability of

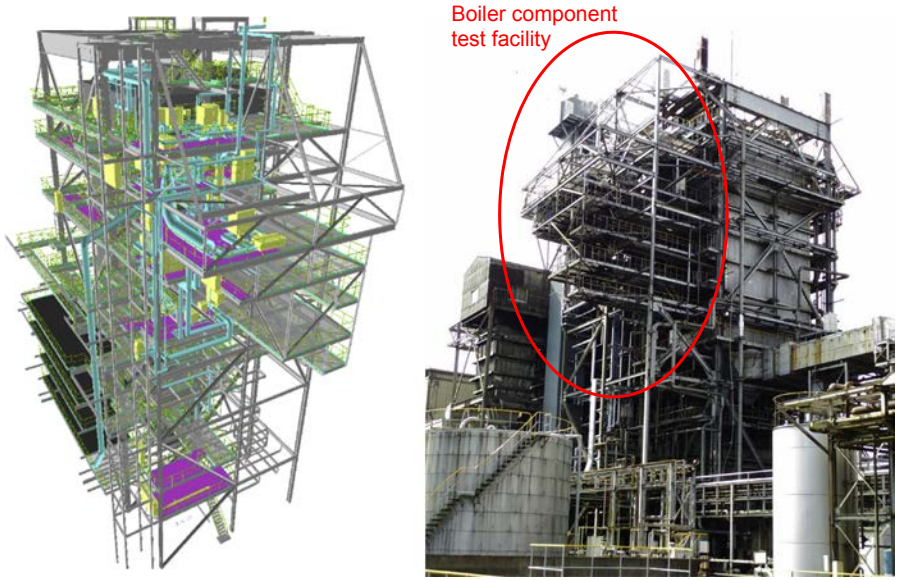


Figure 22.23 Overview of boiler component test facility.
Courtesy of Mitsubishi Hitachi Power Systems and IHI.

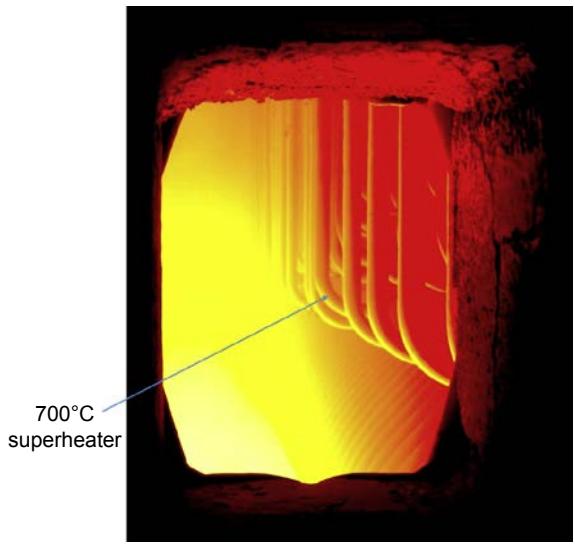


Figure 22.24 700°C superheater.

Ni-based alloys was checked as well. Three candidate materials for castings were chosen. Medium-size step blocks, which were 1–2 tons, were made to check the castability of each material. Unfortunately, one of the candidates was dropped from the list. Then, we casted a full-size valve casing, an inner casing, and nozzle boxes.

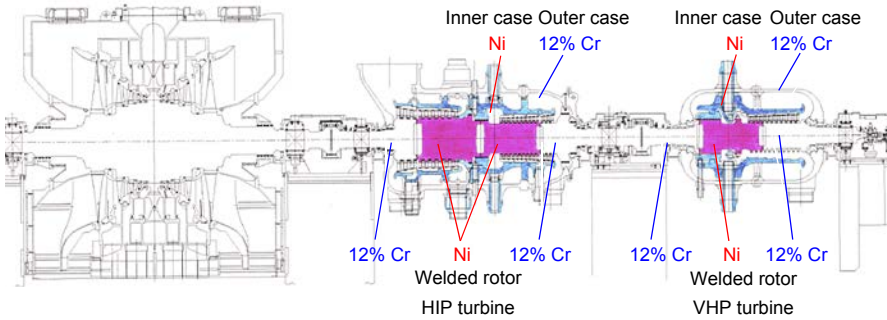


Figure 22.25 Welded rotor.
Courtesy of Mitsubishi Heavy Industries.

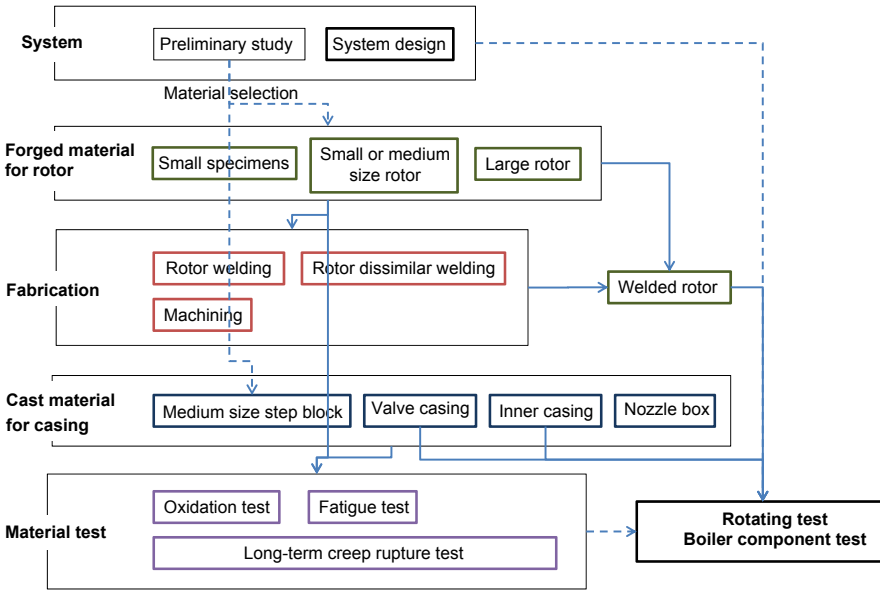


Figure 22.26 Turbine technology development activities [1].

Forged and cast materials were cut into pieces to make material for 700°C superheater test specimens. Welded rotors were made for the rotating test. A medium-size valve casing and a model of an inner casing was installed at the boiler component test facility [1].

There are three candidate materials for steam turbine rotors (Table 22.2). Ni-based alloys, FENIX-700, LTES, and TOS1X, are developed and tested for use at temperatures higher than 700°C. The aim of the development of FENIX-700 is to build a rotor heavier than 10 tons without segregation in the material. The purpose of LTES and TOS1X is to target a weight of around 10 tons, which will be welded to steel parts to make a 30- to 40-ton rotor.

Table 22.2 Candidate materials for steam turbine rotors

Materials	Temperature level	Size	Development target	Chemical composition
FENIX-700	700°C	>10 tons	Ni-based material heavier than 10 tons without segregation	42Ni-16Cr-2Nb-1.2 Al-1.7Ti-Fe
LTES700R	>700°C	30–40 tons ↑ Ni:10 tons welding steel: 20–30 tons	10-ton Ni-based material with low thermal expansion coefficient and good weldability to 12Cr steel	Ni-12Cr-6.2Mo-7 W-1.5Al-0.9 Ti-0.03C
TOS1X	>720°C		10-ton Ni-based material with good weldability to steel	Ni-18Cr-12.5 Co-9Mo-1.25 Al-1.35Ti-0.1 Ta-0.3Nb-0.07C

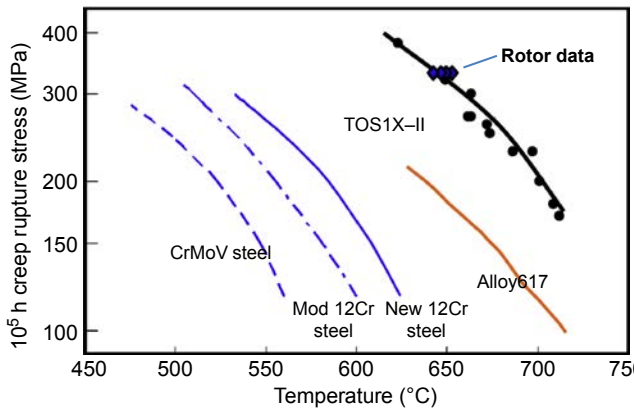


Figure 22.27 Creep rupture strength of TOS1X.
Courtesy of Toshiba.

FENIX-700, which has superior long-term stability at 700°C, was developed from Alloy 706 by reducing Nb content and increasing Ti and Al content. The 100,000-h creep rupture strength at 700°C is expected to be higher than 100 MPa.

TOS1X was developed from Alloy 617. The earlier version of TOS1X, which is now called TOS1X-I, is expected to have around 200 MPa of 100,000-h creep rupture strength at 700°C (Fig. 22.27). A piece of forged material, 1000 mm in diameter and weighing 7 tons, has been made successfully using TOS1X. ITOS1X-II and was

developed from TOS1X-I by increasing the Al and Ti content. TOS1X-II is expected to have around 200 MPa of 100,000-h creep rupture strength at 700°C. A 13-ton piece of forged TOS1X-II has been made successfully (Fig. 22.28).

LTES700R is a Ni-based alloy that has been developed by MHI. This alloy was developed to have a thermal expansion coefficient similar to 12Cr steel, so it conforms well to conventional steels (Fig. 22.29). In addition, the creep rupture strength of LTES700R is higher than the target for 700°C-class rotor materials (Fig. 22.30). Originally, LTES700 was developed for small parts, such as casing bolts. LTES700R was developed from LTES700 for large steam turbine rotors. Fig. 22.31 shows a large piece of LTES700R. Welding technology is crucial for this material. Welding tests including the welding of dissimilar materials were carried out. Fig. 22.32 shows a similar and a dissimilar welding of LTES700R.

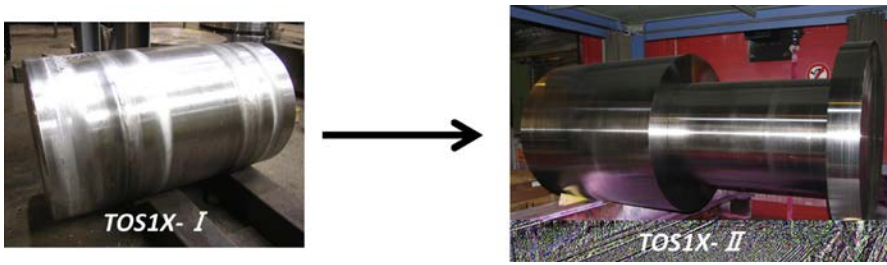


Figure 22.28 Turbine rotor material.
Courtesy of Toshiba.

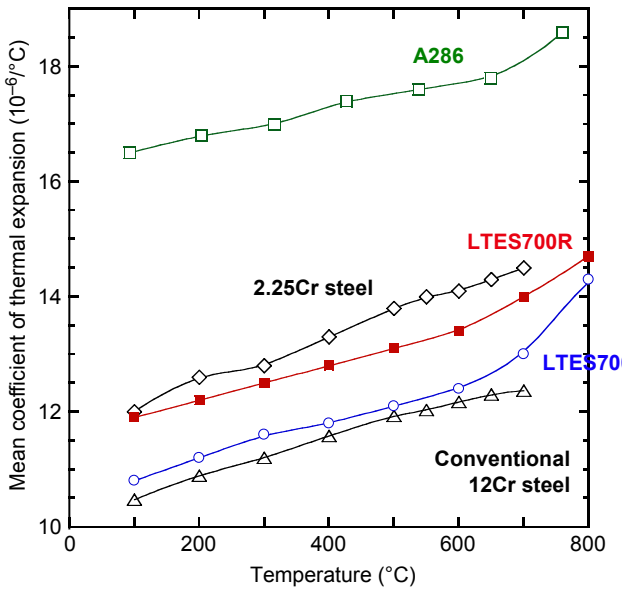


Figure 22.29 Coefficient of thermal expansion of LTES700R.
Courtesy of Mitsubishi Heavy Industries.

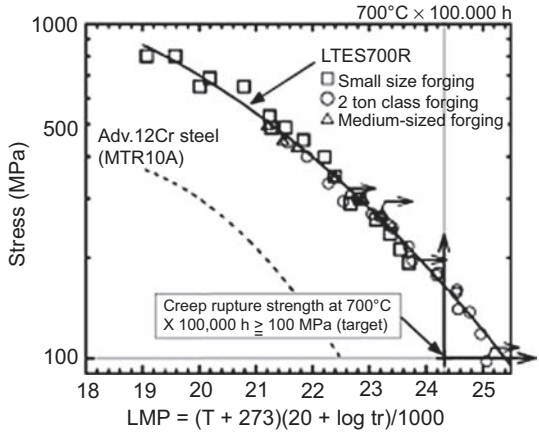


Figure 22.30 Creep rupture strength of LTES700R.
Courtesy of Mitsubishi Hitachi Power Systems.



Figure 22.31 Large LTES700R material.
Courtesy of Mitsubishi Hitachi Power Systems.

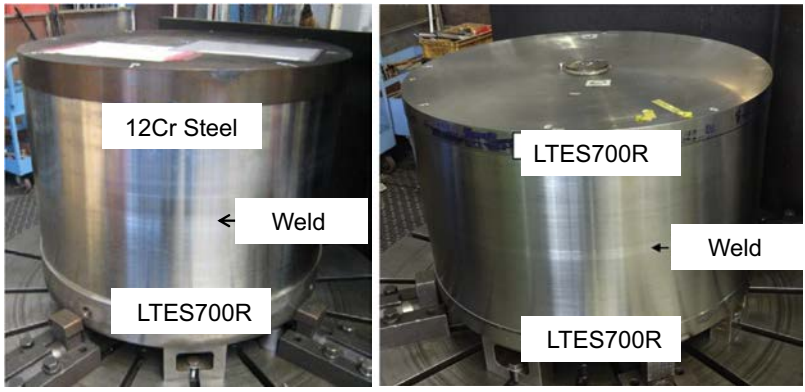


Figure 22.32 Turbine rotor welding.
Courtesy of Mitsubishi Hitachi Power Systems.

At the beginning of the project, three alloys (Alloy 740, Alloy 625, and Alloy 617) were cast into step blocks (Fig. 22.33). The thickness of the casting varies like steps. The maximum thickness resembles the thickness of the flanges of steam turbine casings. They were cut into pieces to make specimens for material tests, such as the tensile test, creep test, and macro- and micro-observation. In 2012, castings of an inner casing, valve, and nozzle boxes were made to check the castability of actual parts. These were also cut into specimens and tested [1].

The concept of 1000-MW-class steam turbine is shown in Fig. 22.34. Five turbine casings and rotors are aligned in tandem. From the left, there is a very high-pressure turbine (VHPT), a high-pressure turbine (HPT), an intermediate-pressure turbine (IPT), and two low-pressure turbines. Part of the rotors of VHPT, HPT, and IPT consists of a newly developed Ni-based material.

The turbine rotor test is conducted in 2016. Rotors made of the candidate rotor materials are tested in a 700°C atmosphere and at actual speed. The rotors are heated by electric heaters in a vacuum chamber and driven by an electric motor (Fig. 22.35) [1].

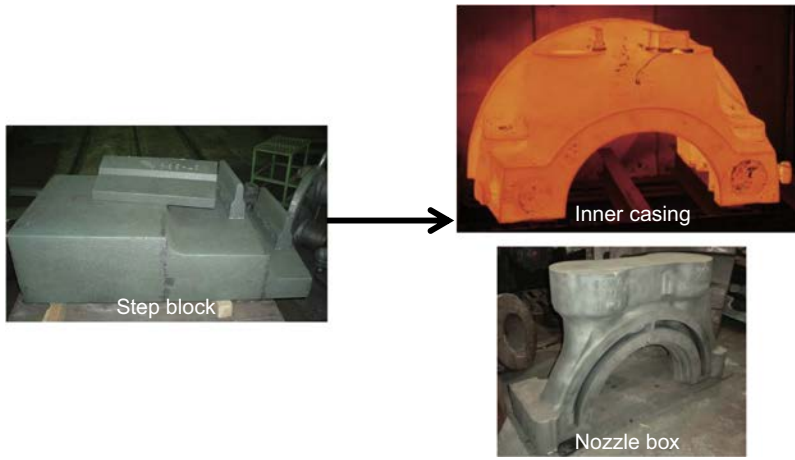


Figure 22.33 Casted materials.
Courtesy of Toshiba and Mitsubishi Hitachi Power Systems.

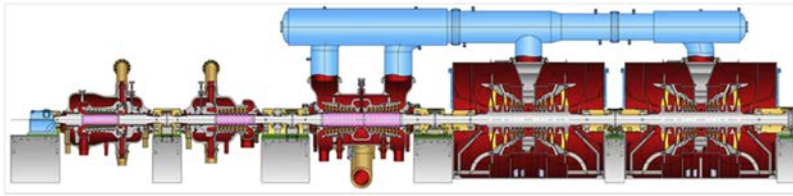


Figure 22.34 Concept of 1000-MW-class steam turbine.
Courtesy of Toshiba.

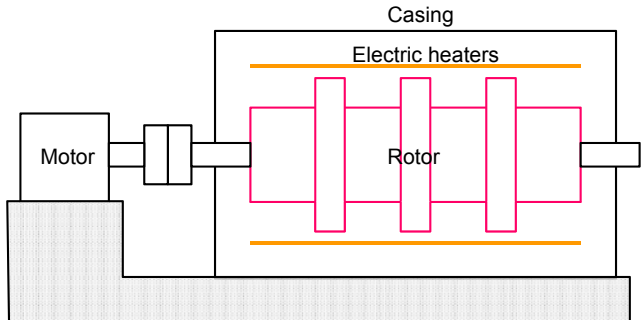


Figure 22.35 Turbine rotor test facility [1].

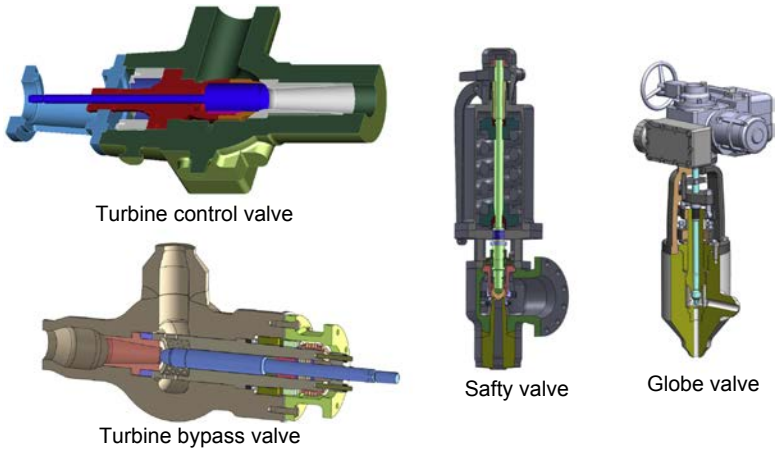


Figure 22.36 High-temperature valves [1].
Courtesy of ABB Bailey Japan, Okano Valve MFG, and Toa Valve Engineering.

It is necessary to develop high-temperature valves which control the flow of the 700°C steam. Fig. 22.36 shows the typical valves [1]. The reliability of them is very important for the stable and safe operation of power plants. Valve materials, which rub against each other in 700°C steam, were tested to find the optimum combination of stem and bushing materials. Fig. 22.37 shows the apparatus used to test the materials [2]. The test material plate is pressed against the test material disc, which rotates at 300 rpm. The materials tested here were Ni-based materials, Stellites, coating materials, etc. In addition to this test, oxidation testing was carried out with the same materials. Packing and gaskets for the valves, which seal the 700°C steam, were tested as well.

If these materials and parts are successfully developed, a material and a parts list to build the system shown in Fig. 22.9 will be described. In addition, as Fig. 22.38 shows, in the future, we can select other system configurations to satisfy various user needs, such as flexible operation and lower initial costs [2].

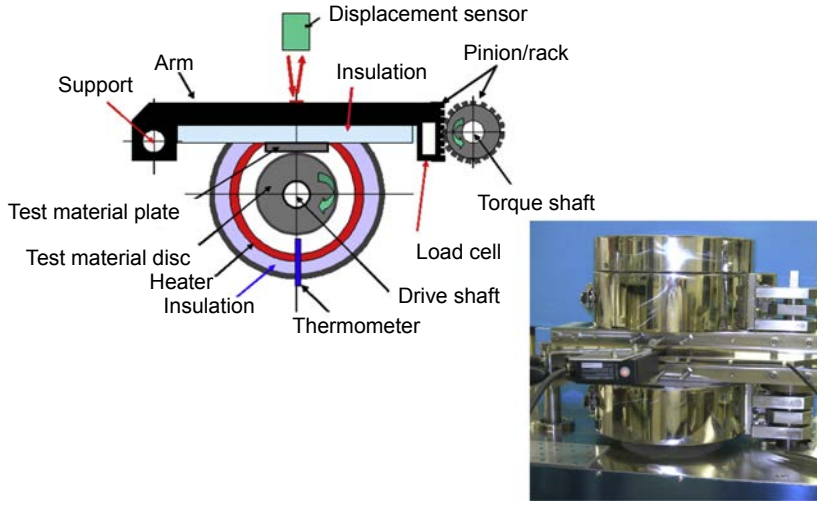


Figure 2.37 Rubbing test apparatus [2].
Courtesy of Fuji Electric.

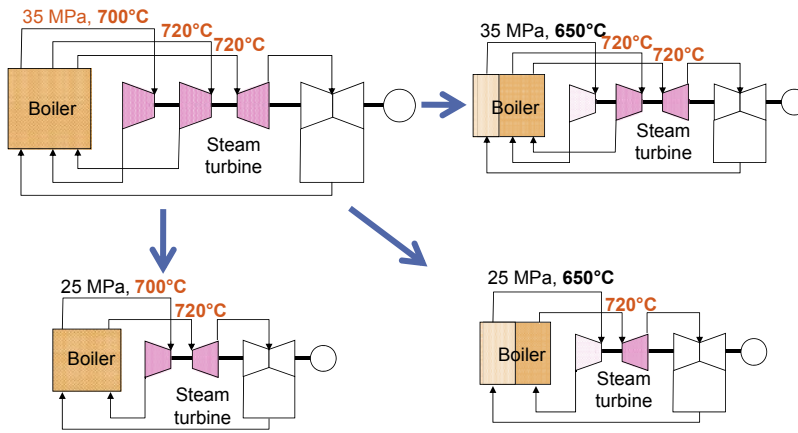


Figure 22.38 Variety of system configurations [2].

22.3 Summary and conclusion

Considering the future needs for coal power plants, Japanese boiler, turbine, and valve manufacturers, institutes, and utility companies have been cooperating to develop 700°C-class A-USC technology with support from the Japanese government since 2008. The key areas of technology development are high-temperature materials such as Ni-based alloys and advanced 9Cr steels and their application to actual power plants. Fundamental material and manufacturing technologies were developed during the first half of the project. For comprehensive verification tests, the boiler components test is completed by the end of 2016, and the turbine rotating test is conducted in 2016.

References

[1] M. Fukuda, The on-going and planned activities of the A-USC project in Japan, in: 39th MPA Seminar, 2013.
[2] M. Fukuda, Advanced USC technology development in Japan, in: 9th Liege Conference-materials for Advanced Power Engineering, 2010.
[3] M. Fukuda, et al., Advanced USC technology development in Japan, in: 7th International Conference on Advances in Materials Technology for Fossil Power Plant, 2013.
[4] http://www.fepc.or.jp/library/pamphlet/zumenshu/pdf/all01.pdf.

A-USC R&D programs in other countries

23

A. Di Gianfrancesco
Materials & Technologies Consultant, Rome, Italy

23.1 Introduction

In addition to the programs for the development of advanced ultra-supercritical power plants just discussed in the previous chapters, there are other emerging countries like Brazil, Russia, India, China (just discussed in Chapter 21), and South Africa (known as the BRICS) with increasing GPD that have few, old, and low-efficiency power plants, mainly subcritical. Therefore there is a need to build new power station: such is the case of India, Russia, Turkey, or South Africa. These countries have also their own coal resources.

Brazil has been not taken into account because it has large hydroelectric capabilities.

South Korea in not in the same condition of the aforementioned countries because they have several new supercritical plants, but they are mentioned because they have industrial companies involved in A-USC programs.

For these countries, it was more difficult to find reference persons and sources, but we try to give an idea of the current and the future situation.

23.2 Indian A-USC program

As just observed in the chapter on coal, India is one of the biggest countries that will require a lot of electricity in the next future. India is the world's fourth largest economy as well as the fourth largest energy consumer, after the United States, China, and Russia, with a real GDP growth rate of 8.7% in the last 5 years and 7.5% over the last 10 years.

India imports a substantial portion of its energy: 80% of its oil, 18% of its gas, and now even 23% of its coal. As the Indian economy continues to grow, so will its energy consumption, especially as the growth of its manufacturing sector catches up with services and agriculture. With domestic resource production facing various challenges, the general expectation has been that Indian energy imports will continue to grow, and energy security concerns will intensify [1]. Many parts of rural India are still deprived of electricity. Need for electrification of all the areas, improvement in lifestyle and increasing industrialization are raising the electricity demand in India steadily and it is expected to increase more sharply in future. India's current installed power generating capacity is about 225,000 MW, of which about 59% is coal based [2]. Fig. 23.1 provides the total installed capacity for different fuel sources in 2013. Coal accounted for nearly 69% of the total electricity generation in 2011 and 59% of the installed capacity in 2013 [3].

Materials for Ultra-Supercritical and Advanced Ultra-Supercritical Power Plants.
http://dx.doi.org/10.1016/B978-0-08-100552-1.00023-3
Copyright © 2017 Elsevier Ltd. All rights reserved.

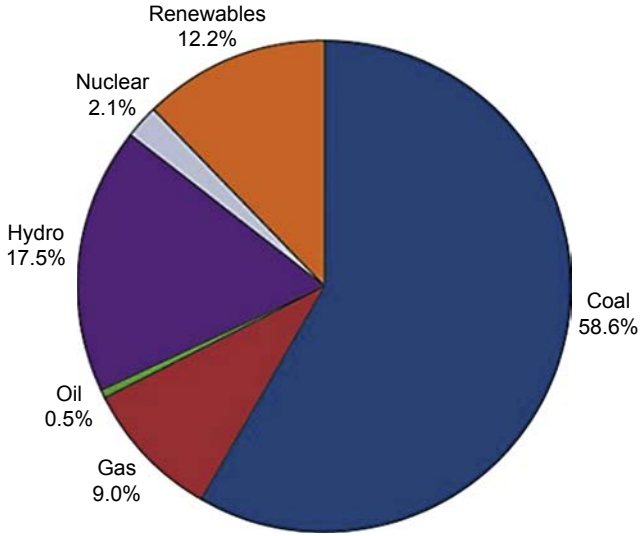


Figure 23.1 Indian installed power generation capacity in 2013.

Therefore coal plays a crucial role in meeting its energy needs: it is the primary source of energy, followed by petroleum and biomass. India is the world's third largest coal consumer and producer [4].

The outlook and options for Indian energy independence therefore become important topics. A 2030 outlook is particularly relevant since it is difficult to significantly change energy policy in 5 or 10 years, but almost any boundary conditions can be changed over a 15-year period. Moreover, there have been few, if any, in-depth perspectives on this topic for 2030.

To overcome the power shortage gap, the Government of India had planned to provide "power for all" by the end of 2012 by creating additional capacity of at least 100,000 MW by 2012 [5].

In fact, in 2012, almost 400 million Indians lacked access to electricity, and the per-capita electricity consumption of India is a measly 600 kWh compared to over 12,000 for the United States. Providing clean and cheap energy access is a major challenge, especially in the developing countries like India [6].

The Ministry of Power, in association with the Central Electricity Authority (CEA) and Power Finance Corporation Ltd, launched an initiative for developing coal-based supercritical (SC) ultra-mega power projects (UMPPs) of nominally 4000 MW each. The SC technology was selected to achieve higher levels of fuel efficiency, resulting in lower CO_2 emissions. As of November 2010, 16 UMPPs were planned in various Indian states [7].

The first 660-MW SC unit was commissioned in December 2010 at Adani Power Limited's Mudra Power Plant [8].

The installed in 2013 capacity is 225 GW and coal-fired thermal shear is 59% (130 GW), with current thermal capacity of mainly subcritical 600/500/250/210/

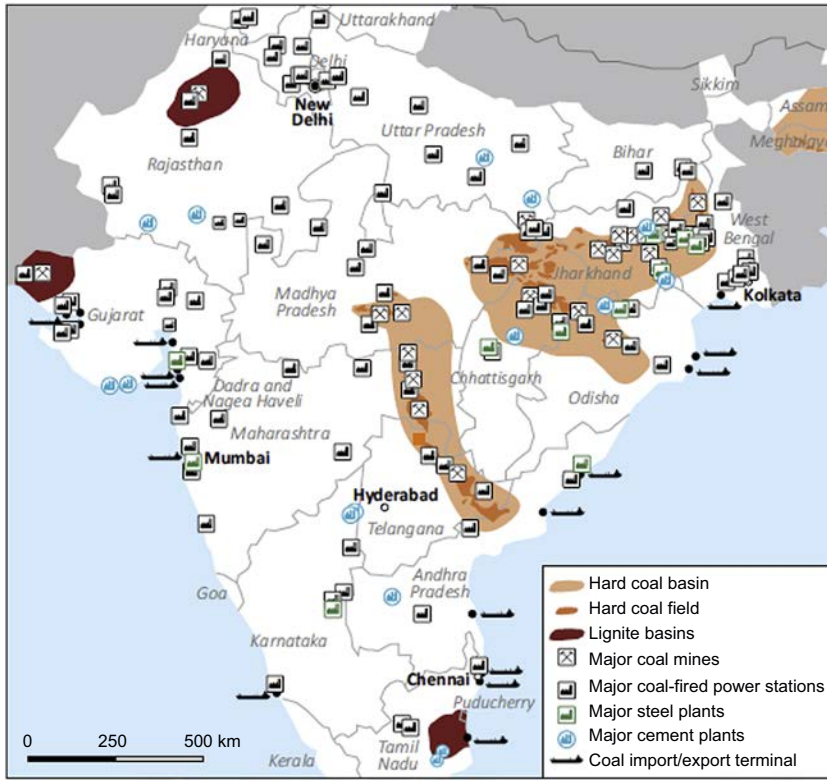


Figure 23.2 Main coal-mining areas and coal infrastructure in India [9].

200MW and some supercritical plants of 660/800 MW set up with steam parameters of 247 kg/cm^2, 565/593°C. India seems to have standardized to two unit sizes, 660 and 800 MW, so each UMPP will have either six 660-MW units or five 800-MW units. Fig. 23.2 shows the location of the coal mine, of infrastructures and of the major thermal power plants in India.

India's National Action Plan on Climate Change (NAPCC) emphasizes the use of clean coal technologies, including SC and USC (250 bar [25 MPa]/600°C/610°C) and integrated gasification combined cycle (IGCC).

The national mission for development of clean coal technologies under NAPCC envisages development of A-USC (300 bar [30 MPa]/700°/700°C) and IGCC. According to the CEA projections, the 11th Five-Year Plan (2007–12) will add 14 SC units (totalling 9520 MW [twelve 660-MW units and two 800-MW units]) out of a total 52,850 MW units. This puts the share of SC units at 18% of the total thermal MW additions in the 11th Five-Year Plan. In the 12th Five-Year Plan (2012–17), an additional 58 SC units (25,660-MW units and 33,800-MW units) will bring the share of SC units to 70% of additional capacity. In the 13th Five-Year Plan, an additional 72 SC units (36,660 and 36,800-MW units) will further increase the SC share of additional capacity to 93% [10].

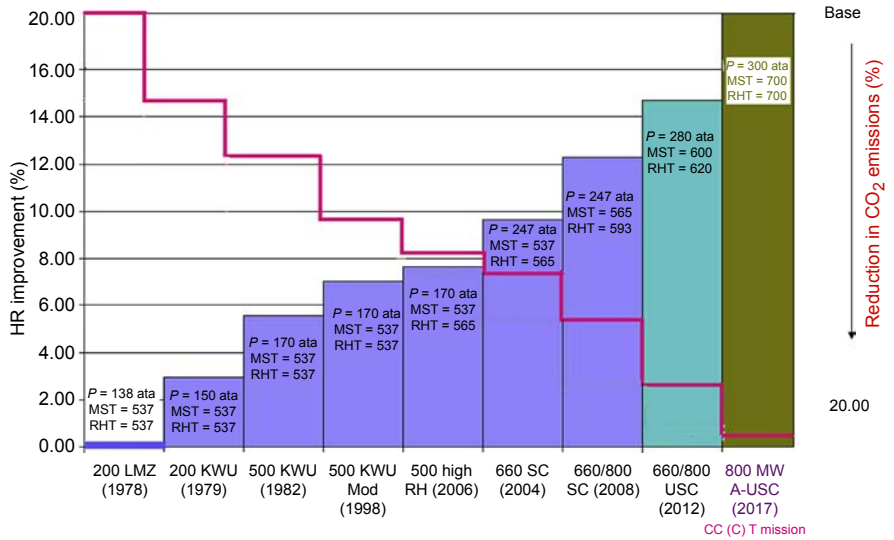


Figure 23.3 History of efficiencies of Indian power plants [6].

Fig. 23.3 shows the trend in efficiency of the Indian Power plants and Fig. 23.4 the forecast for the coal installed capacity and coal consumption.

In 2011, India's first 800-MW coal-fired A-USC power plant was officially targeted to be operational by 2017. It is based on a comprehensive 7-year program covering development and construction phases. Given that the final approval and funding are still pending from the central government, it does not appear that this target will be met. *Currently there is no evidence that this timetable has been maintained; probably some delay will be necessary.*

India has adopted a NAPCC [1] having several missions to reduce the CO_2 emission, and one of these is the clean coal (carbon) technologies [11].

The Indian Government has a forecast that requires 800-GW capacity by 2032 (Integrated Energy Policy) that will be supplied mainly by coal-fired supercritical or ultra-supercritical plants (>600°C) also on the anvil. Table 23.1 summarizes the Indian program.

The technology is being developed through a joint collaboration between Indira Gandhi Center for Atomic Corporation and National Thermal Power Corporation (NTPC). A memorandum of understanding between Indira Gandhi Centre for Atomic Research (IGCAR), Bharat Heavy Electricals Limited (BHEL), and NTPC was signed in August 2010 [12]. The plant will be built at a cost of $1.5 billion.

India has taken up a national mission for the development of A-USC technology under the NAPCC. Like the 52 USC coal power plants other A-USC programs, the Indian program includes building of a test loop.

The test loop is intended to verify corrosion characteristics of the intended materials under the combustion environment with Indian coals for up to 2 years. The test loop

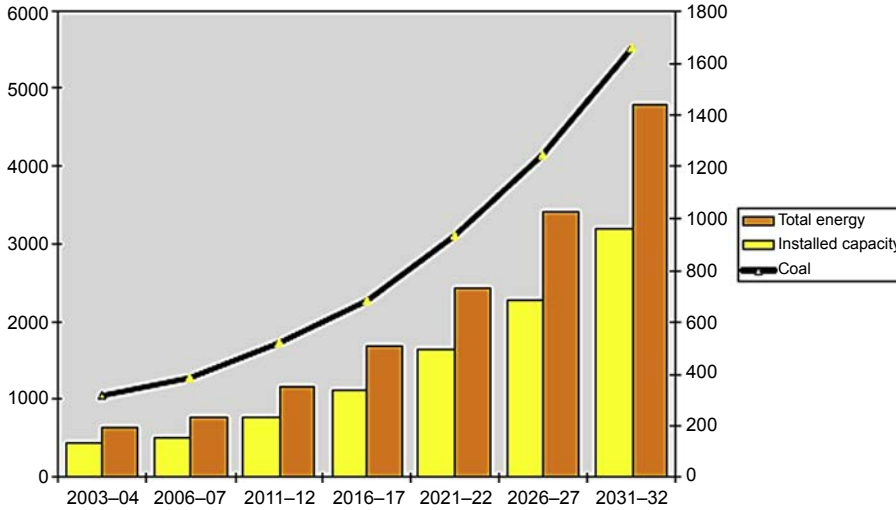


Figure 23.4 Coal production and consumption trend in India [6].

Table 23.1 Power capacity addition

	Subcritical (MWe)	Supercritical (MWe)	Total coal based (MWe)
11th plan (2007–12)	35,814	6080	41,894
12th plan (2012–17)	44,360	24,920	69,280
13th plan (2017–22)	–	A major proportion will be supercritical	63,400
14th plan (2022–27)		A major proportion can be with Adv-USC parameters	

is expected to become operational in 2013 at an existing NTPC coal-fired plant. Only superheater tubes made of Alloy 617, Super 304H, and T91 will be tested.

The selected steam parameters of the Indian A-USC program are 310 bar/710°C/720°C [2]. A617M is the lead candidate material for the boiler as well as the turbine, because this alloy has undergone extensive testing under the European program and has a more developed global supply chain. For thicker headers, IN740 may also be considered. The future plans also include a comprehensive 3-year development program for all major components and processes associated with the manufacturing, installation, and operation of an 800 MW commercial-size A-USC demonstration power plant [13]. The Objectives of National A-USC Mission are the development of all the technologies and equipment for an A-USC power plant with steam parameters of 310 bar/710ºC/720ºC. It was established to realize an 800 MW A-USC Demonstration Power Plant (two pass, spiral waterwall design) in a time frame of 7 years

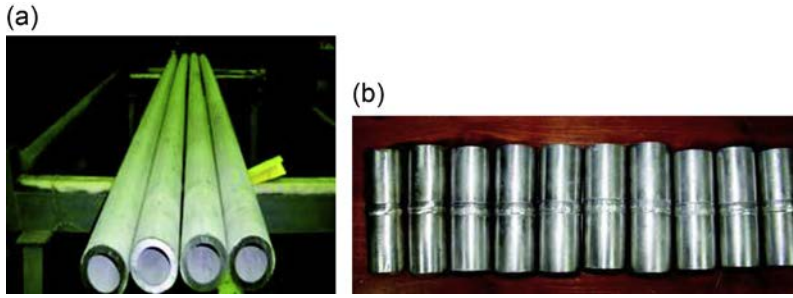


Figure 23.5 (a) Indigenously manufactured SS304HCu boiler tubes (6–7 m length) and (b) welded joints [14].

(2½ years for development and 4½ years for construction), with support of the funding mainly from India Government, with contributions from participating companies. Core development team is made by: BHEL, NTPC, and Indira Gandhi Centre for Atomic Research (IGCAR) with collaborative work with national/international institutions with specialized competencies. The main Major Work Areas are dedicated to the selection and development of new materials true the characterisation and testing for various properties, the development of manufacturing processes for casting, forging, tubes, pipes, and their welding technologies, as well as, by the selection of steam parameters and optimization of thermal cycle, the design and development of equipment such as steam generator, steam turbine, auxiliaries, control systems. For the boiler section, in high temperature zones over 650°C A617M was selected and for the lower temperatures zones, other materials such as SS304HCu, T91/92, T/P23 have been taken in account. A617M has been also selected as material for the turbine components welded rotors for HP and IP and blades. Therefore, program for materials process development are running to produce forged ingots of A617M and SS304HCu on pilot scale and to manufacture A617M and SS304HCu boiler tubes (Fig. 23.5) [14].

For these materials a long term materials characterization program was instituted for creep testing on base materials and welded joints, and hot corrosion tests under simulated flue gas environment.

Main objective of the Corrosion Test Loop is to test for corrosion under Indian coal firing conditions and steam side oxidation: it has been in 2015 at a Power Plant of NTPC for duration of 2 years: A617M, SSS304HCu, T91 are under testing.

23.2.1 Conclusion

- National mission for A-USC technology for power plants initiated by Government of India
- core team of BHEL, NTPC, and IGCAR
- to establish 800-MW demonstration power plant in a time frame of 7 years
- comprehensive plan of action prepared
- pro-active initiatives taken to gain a head start accelerated pace of work
- focus on self-reliance
- low-cost manufacturing through indigenization

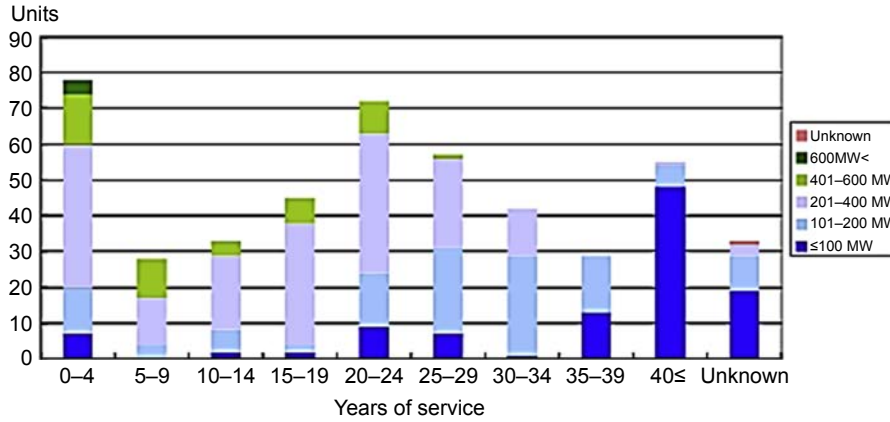


Figure 23.6 The status of the coal-fired thermal power plants in India [16].

As coal will be a principal source of energy for India for the foreseeable future, I believe improvements in coal resource assessment, production, and utilization is necessary. In fact, as possible to note in Fig. 23.6, most of the power plants in India are quite old and as a consequence are operating with low efficiency because they are subcritical.

To meet the national goals for development, access to electricity, and energy security, India will need to continue to rely on coal for its electricity sector during the next 25 years. It is important that supporting investments in technology development and R&D are made in coal extraction, coal conversion, and coal-based power technologies to improve the efficiency and performance of coal-based electricity generation [3].

The year 2016 has started on a bright note for the state of Uttar Pradesh with the commissioning of the 660-MW supercritical unit of Lalitpur Super Thermal Power Project by BHEL. Significantly, this is the second 660-MW unit commissioned by BHEL in Uttar Pradesh within a fortnight [15].

Fig. 23.7 shows that the USC technology with temperature up to 600°C/600°C will be introduced in North Karanpura Project in 2018 [16] and later in 2020 is planned the first A-USC plant.

Fig. 23.8 shows the forecast by IEA for the Indian power plants scenario and the average efficiency up to 2040.

23.3 Other countries

Despite to India and the other countries that just planned R&D A-USC power plants programs, for Russia, South Africa, Turkey there are not information about the development of the A-USC technologies. For South Korea the situation is in my opinion different because there are big Korean companies like Doosan that are very active, through subsidiaries in the European Union, in R&D programs.

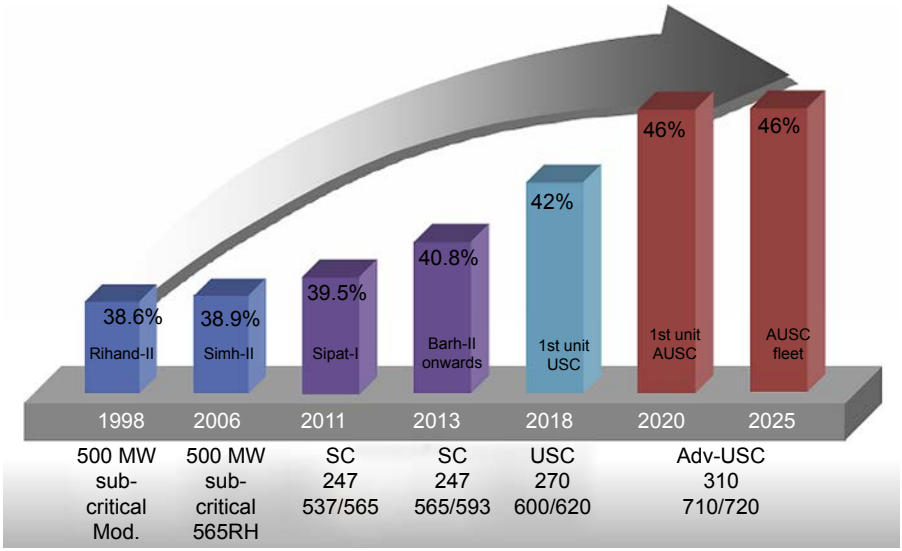


Figure 23.7 National Thermal Power Corporation (NTCP) target program [16].

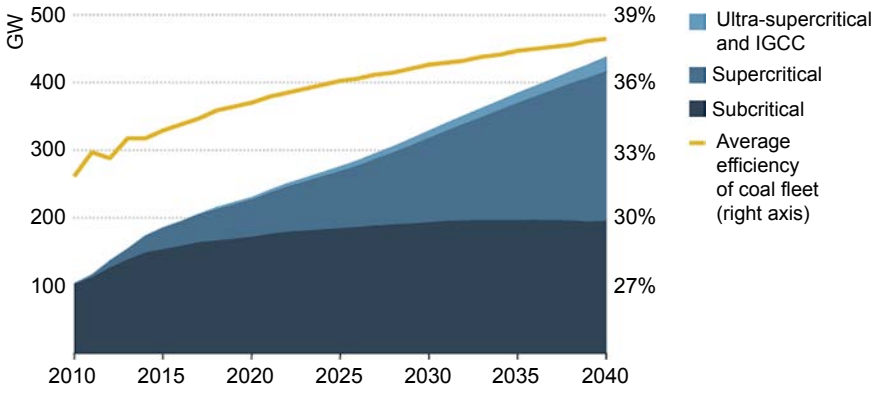


Figure 23.8 Coal-fired power plant capacity by technology and average efficiency in India in the New Policies Scenario [17].

23.3.1 Russia

Russia (an early adopter of SC technology) and former Eastern Bloc countries accounted for as much as 40% of the world's total installed capacity of SC technology in 2004. While Russia continues to build more coal-fired SC plants, its generation mix seems to be focused on gas-fired combined cycle plants using advanced Western gas turbine technology.

In Russia, President Putin has declared a goal to increase coal output by 30% by 2030. With the second largest proven reserves, minimal environmental interference, and an insatiable demand from Asia, this goal seems obtainable [18].



Figure 23.9 Kashirskaya thermal power plant [20].

Some new supercritical power plants are planned to be built [19]:

- Berezovskya, 2011, 800 MWe
- Novocherkasskaya, 2012, 330 MWe, circulating fluidized bed combustion (CFBC)
- Petrovskaya, 2012–14, 3 × 800 MWe

The author is not aware of Russia's plan for A-USC technology.

Russia has experience in development, construction, and service of equipment with ultra-supercritical steam parameters [20]:

- Pilot boiler on testing site of JSC VTI with steam operating temperature up to 650°C and pressure up to 30.0 MPa worked more than 200,000 h. Currently, it has an operable state and could be used for researches.
- Commercial power-generating unit SKR-100 (Kashirskaya TTP, Fig. 23.9) with boiler steam capacity of 100 MW and steam parameters of 650°C and 30 MPa has been operated since 1969 (~100,000 h).

Developing Thermal power plants (TTP) for temperatures 650–680ºC using the advanced austenitic and martensitic steels is crucial for the improving performance of advanced ultra-supercritical thermal power plants.

For that purpose, new types of steels, 0.1C-9Cr-3Co-2W-VNb and 15Cr-16Ni-2Mo-Ti-B, were developed. Steels have shown a high level of service properties and fabricability in manufacturing of parts of TTP equipment (headers, reheaters, steam pipes, etc.).

Therefore it seems that R&D activities are focused on martensitic and austenitic steels, and as consequence, A-USC program, based on Nickel superalloys, is not planned. It has also to be taken in account that historically the R&D activities in superalloys in Russia were focused on cobalt superalloys.

23.3.2 South Korea

South Korea is forced to import 97% of its primary energy demand due to minimal natural energy reserves and a slow-starting renewable energy industry [21].

South Korea is planning to increase the rate of nuclear power and renewable energy as a main policy to decrease CO_2, but it is supposed to construct 15 coal-fired thermal power plants. Although the generation rate of coal-fired thermal power will lower in the future, the generation amount itself is estimated to increase, so it is clear that coal is the main fuel for generation. Especially, the ultra-supercritical pressure technology is necessary in the future to increase consumption of low calorific value coals and keep a low power generation cost. It is also symbolized by pressing ahead with the research and development of the high-efficiency coal-fired thermal power generation technology as the government project. Therefore, it can be thought that Korea has no politic barriers in spreading the technology [22].

In relation to installed capacity, coal plants consist of about 24.5 GW, or about 30% of total capacity. In the new electricity plan released in 2013, South Korea laid out plans to raise coal capacity to 44.9 GW by 2027, and by the end of 2017, the government plans to install 15 more coal-fired facilities with 12.5 GW of capacity [20]. Fig. 23.10 shows the trend in Korean coal capacity versus efficiency and CO_2 emissions.

As part of the planning, Hitachi realized for Korea Western Power Co., Ltd. (KOWEPO) 2 × 1050 MW-class ultra-supercritical* (USC) coal-fired plants (593°C/24.1 MPa) at the Taean Thermal Power Plant (Fig. 23.11): the No. 9 unit is scheduled to begin commercial operations in June 2016, followed by the No. 10 unit in December 2016.

Fig. 23.12 shows the regional changes of installed capacity of power plants of South Korea for coal power plants for the period 2010–27. The left side of each figure shows regional distribution of current power plants in 2010, while the right side shows the projection of power plants by the sixth BPE in 2027 (unit: MW).

Regarding the A-USC, Doosan Group is involved with its subsidiary in the European Union in some R&D program, and therefore it is expected that a national program will be also launched in the next future.

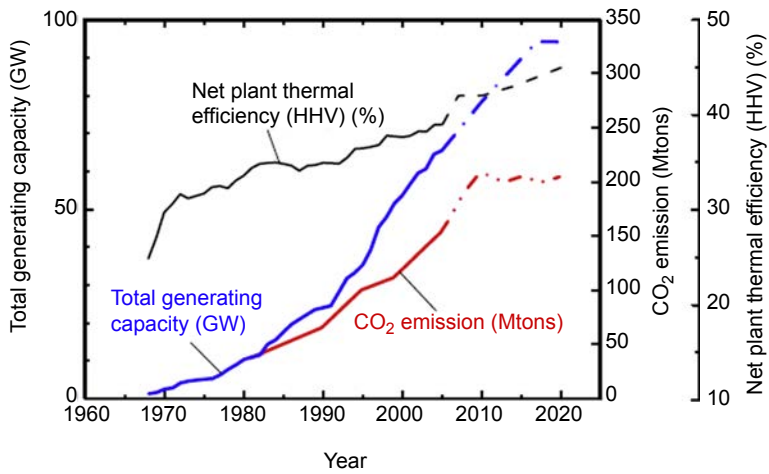


Figure 23.10 Korean trend of CF power plants.
Ryu, Doosan, USC 2007 Symposium, K.-T. Hong, R&D Status & Future Direction of Heat Resistant Materials for Efficient Power Plants, NIST, USA, 23 June 2009.



Figure 23.11 Installation plan at the Taean thermal power plant [23].

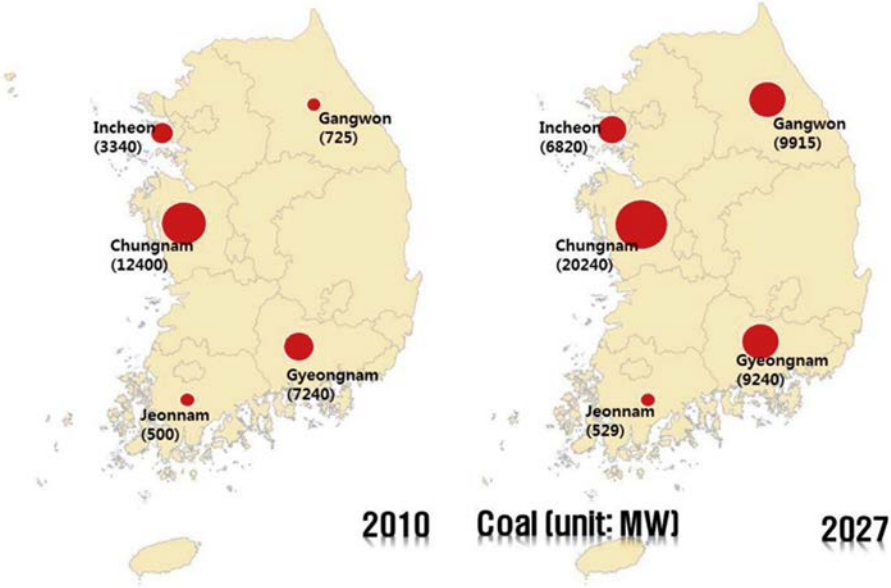


Figure 23.12 The regional changes of installed capacity of coal power plants of South Korea [24].

23.3.3 South Africa

Internationally, coal is currently the most widely used primary fuel, accounting for approximately 36% of the world's electricity production. This situation is likely to remain until at least 2020. Coal has traditionally dominated the energy supply sector in South Africa, from as early as 1880 when coal from the Vereeniging area was supplied to the Kimberly diamond fields.

Presently, about 95% of South Africa's primary energy needs are provided by coal and operated by Eskom, with 13 power stations for a total of 44 GW. This is unlikely to change significantly in the next decade, due to the relative lack of suitable alternatives to coal as an energy source [25]. Table 23.2 shows the Eskom mix of energy sources.

South Africa (SA) produces an average of 224 million tons of marketable coal annually, making it the fifth largest coal producing country in the world. Twenty-five percent of SA production is exported internationally, making South Africa the third largest coal exporting country. The remainder of South Africa's coal production feeds the various local industries, with 53% used for electricity generation. The key role played by our coal reserves in the economy is illustrated by the fact that Eskom is the seventh largest electricity generator in the world, and Sasol is the largest coal-to-chemicals producer.

South Africa's coal reserves are estimated at 53 billion tons, and with our present production rate, there should be almost 200 years of coal supply left. Producing electricity from coal starts when the coal is pulverized in huge mills into a fine powder before it is blown into huge kettles, called boilers. Due to the heat in the boiler, the coal particles combust and burn to generate heat to turn water into steam. The steam from the boilers is used to turn the blades of a giant fan or propeller, called a turbine. The turbine turns a coil made of copper wire (the rotor) inside a magnet (the stator). Together they make up the generator. The generator produces an electric current, which is sent to the homes and factories of consumers via power lines [27].

South Africa, beset by electricity shortage problems, has opened its first coal-fired power plant since 1996. President Jacob Zuma opened the $7.89 bn six-unit, 4764-MW Medupi plant near Lephalale, about 350 km north of Johannesburg, as the

Table 23.2 Eskom power plant mix (2013)

Type	Stations	Capacity (MW)	Percentage
Coal-fired	13	37,780	85.57
Gas	4	2426	5.50
Hydroelectric	2	600	1.36
Pumped storage	2	1400	3.17
Nuclear	1	1940	4.39
Wind energy	1	3	0.01
Total	23	44,149	100.0

Adapted from Eskom, 2014, http://www.eskom.co.za/AboutElectricity/ElectricityTechnologies/Pages/Coal_Power; J.A. Bohlmann, H.R. Bohlmann, R. Inglesi-Lotz, An Economy-wide Evaluation of New Power Generation in South Africa: The Case of Kusile and Medupi, University of Pretoria, Working Paper: 2015-40, June 2015.

country bids to deal with the shortfalls in power that has plagued its economy [28]. The facility was started in 2007, but the first 794-MW unit only came online this week after delays due to strikes, technical issues, and cost overruns.

According to some estimates, the demand in terms of power should double by 2030 to about 66 GW [26,29]. South Africa is currently not involved in any A-USC international program. Just Eskom has cooperated with COMTES700.

23.3.4 Energy trends for Africa

Africa's energy demand is also high, with a further 7000 MW of electricity needed each year to keep up with the continent's growth rate, with 30% of that demand coming from the mining sector. But Africa's fast growing markets have significant deficits in their electricity supply, a gap which is necessary to fuel its economic growth.

South Africa accounts for 42% of this power generation in Africa, with 77% of total power generation made up by coal. Coal production on the continent is set to grow to 501 Mt by 2040. "Coal will still be the biggest source of electricity generation in the next 30 years and Eskom will need 4000 Mt of additional coal," McDonald reveals.

For this reason, coal exploration in African countries has been ongoing, says SRK Consulting SA principal coal geologist Lesley Jeffrey. "The projects served by our Johannesburg office have been mainly in Southern Africa, particularly in South Africa, Botswana, Zambia, and Mozambique."

While Mozambique and Botswana are emerging as new suppliers, South Africa still accounts for 98% of Africa's coal production and exports about 26% of its coal production. "South Africa is strategically located between Atlantic and Pacific coal markets, but its pace of development will depend on political stability, policy support, bureaucratic delays, and allocation of mineral rights." [30].

23.3.5 Turkey

Turkey is another big country having a growing of GPD and large fossil fuel resources. Although per-capita energy use in Turkey is still comparatively low, energy demand is expected to grow rapidly due to the demographics of a very young population and a rapidly growing economy [31]. Fig. 23.13 shows the location of the lignite and hard coal mines. The reserves are estimated in 15 Btons, mainly lignite (90%). At present, only a small power station (300 MW) is fed with domestic hard coal from the Zonguldak basin, while the larger İskenderun power plant (1.200 MW) and Zonguldak Eren Enerji Çatalağzı power plant (1.360 MW) use imported hard coal. Other power plants use lignite, and the power capacity supply in 2012 by coal and lignite is about 12 GW [31].

In 2012, total primary energy supply comprised mainly fossil fuels (90%), with gas accounting for 32%, coal for 30%, and oil for 27%: gas and oil are imported, primarily from Iran and Russia. Renewable energy sources accounted for the remaining 10%, with hydroelectricity (4%) and biofuels (3%) being the primary sources [32,33].

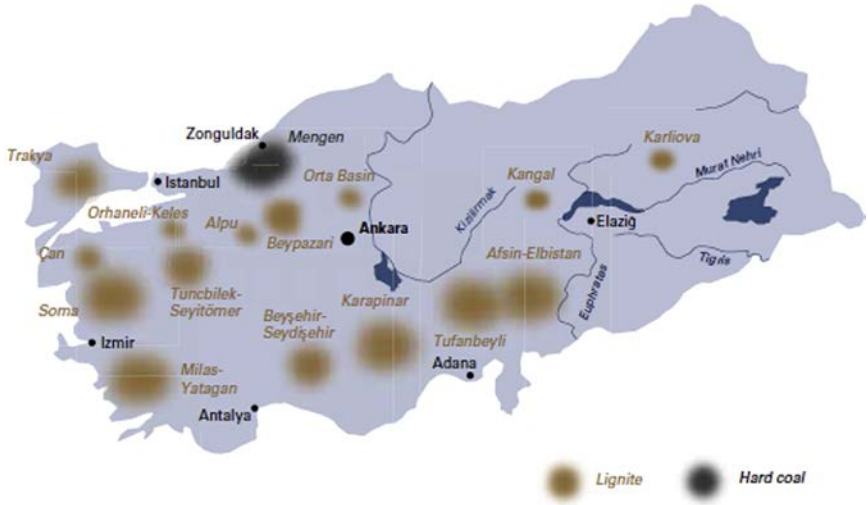


Figure 23.13 Location of Turkish coal mines [31].

Taking in account that the gas is coming mainly from Russia and oil from Iran, coal power plants will be more attractive in the future.

In fact, the Turkish government is planning to double its coal power capacity over the next 4 years, making it the country with the world's third largest investment in the fossil fuel, according to a Turkish energy consulting group. Plans for 80 new plants will quadruple the number of coal-fired power plants from the 22 currently online [34,35].

By 2030, total electricity generation is expected to increase from 240TWh to over 600TWh. The share of coal will grow from approximately 27% to around 32% of total generation: given the increase in total generation, this seemingly modest percentage rise represents a threefold increase in coal-fired generation, to almost 200TWh (see Fig. 23.14). This increase in generation will be met by a threefold increase in installed capacity to almost 35 GW, comprising both lignite and hard coal-fired plants. Of this, approximately 35% will be met by hard coal capacity and the remaining 65% by lignite capacity, given Turkey's limited reserves; it is likely that the majority of hard coal will need to be imported, and thus reliance on overseas sources of supply will not be entirely cut.

The Turkish government has emphasized the importance of energy security in its strategy for the sector. Coal, renewable energy, and to some extent nuclear power are prioritized with the aim of reducing reliance on imports of natural gas and oil. However, the ambitions for renewable energy remain limited in comparison with the ambitions for coal; while the strategy is strongly focused on exploiting domestic reserves of coal, the ambitions for renewable resources are more limited. Most notably, the role of solar and of geothermal energy sources is expected to be far below the technical potential implied by the resource available.

Uncertainties related to natural gas power plants and unexpected delays in lignite projects lead investors to hard coal as a relatively more eligible and cheaper

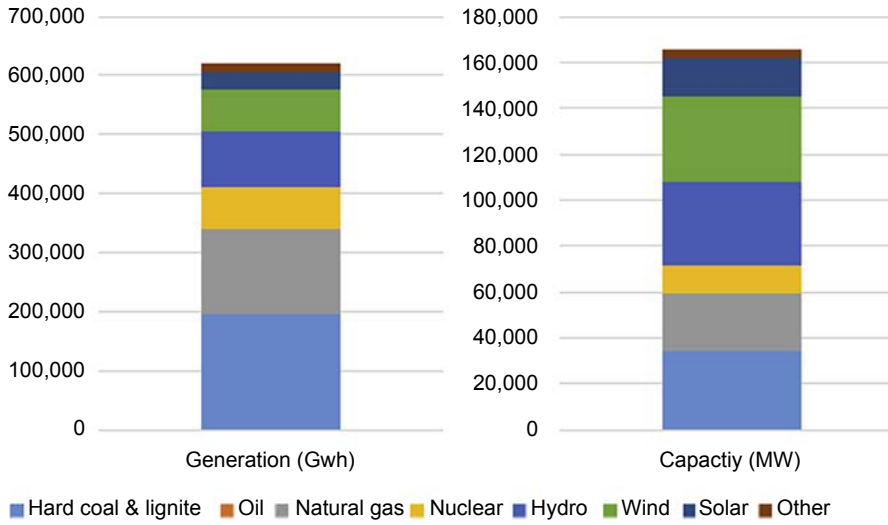


Figure 23.14 Turkey installed capacity and electricity generation by source, 2030.

energy source, and as a result, a great number of projects showed up. In addition, imported coal power plants connected to the grid and projects under either evaluation or licensing process are expected to take an important role to satisfy increasing electricity demand in the future. As of end of 2013, 7 imported coal power plants are connected to the grid, whereas there are 20 projects under evaluation, 10 power plants under construction, and three power plants in the pre-licensing process. In total, current and upcoming imported coal power plants accumulate to 30 GW of installed capacity.

Since the fuel supply of imported coal power plants are transported by sea freight, power plant projects are preferred to be located in regions that have easy access to international ports. In this respect, the majority of the power plant projects are located near to the İskenderun gulf, whereas İzmir, Zonguldak, and Çanakkale come into prominence as other suitable locations for imported coal power plant investments. Kahramanmaraş and Elazığ are the only cities where there are no port connections, yet these three power plant projects have installed capacity of 231 MW (Fig. 23.15).

When geographical distribution of power plants is analyzed, it would not be wrong to say that there is great interest for imported coal power plants in every region of Turkey.

In its first-ever climate pledge realized in September 2015 ahead on the Paris climate talks, Turkey agrees to cut its GHG emission by 21% by 2030, compared to the business-as-usual scenario, by making use of carbon credits from international market mechanisms. The country also plans to increase its solar and wind power capacity to 10 and 16 GW, respectively, and to boost primary energy efficiency by 20% by 2023. In addition to a range of financial and legislative measures to support low-carbon technologies, Turkey has for years been talking about developing a national emissions trading system but so far with no real progress [37].

Turkey is currently not involved in any A-USC international program.

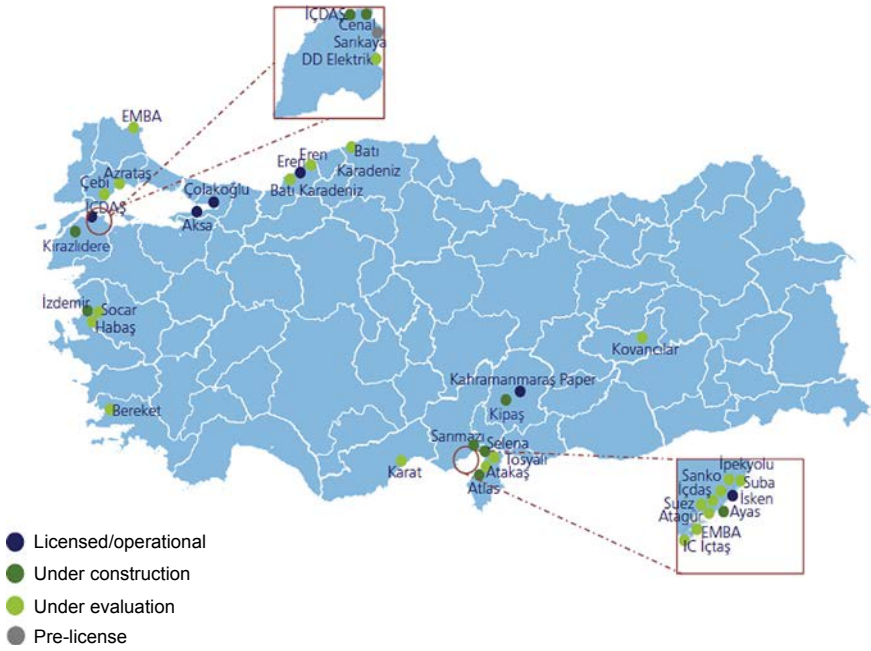


Figure 23.15 Planned coal power plants in Turkey.
EMRA, Deloitte Analysis, as of end of 2013, High Calorific Value Coal, Turkish and Global Outlook. www.deloitte.com/, October 2014.

References

[1] India: Towards Energy Independence 2030, January 2014.
[2] N.C. Bhatt, M. Batrani, J. Mohan, V. Gopalakrishnan, M.K. Verma. Indian AUSC steam turbine program – current status and future program, International Journal of Engineering Research & Technology 4 (3) (March 2015).
[3] R. Banerjee, Coal-based Electricity Generation in India, http://cornerstonemag.net/coal-based-electricity-generation-in-india/.
[4] A.M. Carpenter, R&D Programmes for Clean Coal Technologies; © IEA Clean Coal Centre, October 2014.
[5] D. Zhang (Ed.), Ultra-supercritical Coal Power Plants: Materials, Technologies and Optimisation, FTSE © Woodhead Publishing Limited, 2013, pp. 50–52.
[6] H. Banerj, Clean Coal Technology, the Indian Perspective: Challenges and Road Map, Presented at TREC-step: Tiruchirapalli on 25th January 2012.
[7] P. Ghosh, U. Bhaskar, Conditional Green Waiver for Orissa UMPP Likely, 25 November 2010 (ePaper) livemint.comhttp://www.livemint.com/2010/11/25231550/conditional-green-waiver-for-O.html.
[8] J. Pathak, Adani Power Synchronises India's First 660 MW Supercritical Unit at Mundra, 23 December 2010, Gujarat Money (ePaper) http://gujaratmoney.com/2010/12/23/adani-power-synchronises-indias-first-660-mw-supercritical-unit-at-mundra/.
[9] India Energy Outlook, International Energy Agency: OECD/IEA, 2015.

[10] Bharat Heavy Electricals Limited, in: 'Challenges in Development of Ultra Supercritical Technology', Presented at Indo Australian Workshop on Energy Efficiency, 11 April 2011.
[11] A. Mathur, O.P. Bhutani, T. Jayakumar, D.K. Dubey, S.C. Chetal, in: India's National A-USC Mission – Plan and Progress 7th International Conference on Advanced Materials for Fossil Power Plants 22 October 2013, Hawaii.
[12] India to have its first coal-fired AUSC plant by 2017, The Economic Times – India, 24 January 2011 (e-Paper) http://articles.economictimes.indiatimes.com/2011-01-24/news/28429235_1_ultra-super-critical-boilers-thermal-plants-power-plant.
[13] BHEL Presentation at US A-USC Program Meeting, 6 September 2012. Chicago, Illinois, USA.
[14] S.C. Chetal, T. Jayakumar, A.K. Bhaduri, Materials research and opportunities in thermal (coal-based) power sector including advanced ultra super critical power plants, Proceedings of the Indian National Science Academy 81 (4) (September 2015) 739–754. Published Online on 13 October 2015.
[15] Bharat Heavy Electricals Limited, Press Release, 18 January 2016.
[16] D.K. Dubey, NTPC Plan for Improvement of Power Plant Efficiency: Advanced Technologies and Best Practices for SC TPPs; New Delhi, 21 November 2013, NTPC_plan_for_imp_of_PP_eff_DKD_2013-11-20_r1-0.
[17] India Energy Outlook, World Energy Outlook Special Report: © OECD/IEA, International Energy Agency, 2015.
[18] C. Pedersen, New Financing Options for Coal Power Plants Through the BRICS 'New Development Bank', http://breakingenergy.com/2014/07/31/new-financing-options-for-coal-power-plants-t.
[19] Power Generation from Coal, Ongoing Developments and Outlook: © OECD/IEA, 2011.
[20] V. Skorobogatykh, Martensitic and Austenitic Steels for Application in A-USC Thermal Power Plants; 2nd IEA CCC Workshop on Advanced Ultra-supercritical Coal-fired Power Plants; Rome, Italy 14–15 October 2014.
[21] Spotlight on South Korea – Energy Security Through Diversity, 9 June 2014. http://www.power-technology.com/features/featurespotlight-on-south-korea-energy-s.
[22] S.H. Ryu, J.T. Kim, Korean efforts to develop heat resistant materials for USC steam turbine – an overview, in: Symposium on Heat Resistant Steels and Alloys for USC Power Plants 2007, KIST, Seoul, Korea, July 4–6, 2007.
[23] Hitachi Wins Order for Two 1,050MW Ultra-supercritical Coal-fired Thermal Power PlantsNIST, USA, Hitachi, Ltd., South Korea, Tokyo, 28 February 2012 (NYSE: HIT/TSE:6501).
[24] C. Shim, J. Hong, Impact of a national plan for future electricity supply on ambient air quality in South Korea, Energy Policy ScienceDirect 88 (2016) 278–288.
[25] South Africa looks to relieve power shortages as new coal plant prepares for operations.
[26] J.A. Bohlmann, H.R. Bohlmann, R. Inglesi-Lotz, An Economy-wide Evaluation of New Power Generation in South Africa: The Case of Kusile and Medupi, University of Pretoria, June 2015. Working Paper: 2015-40.
[27] Eskom, 2014. http://www.eskom.co.za/AboutElectricity/ElectricityTechnologies/Pages/Coal_Power.
[28] D. Williams, South Africa Opens First Coal-fired Power Plant in Two Decades, 31 August 2015. http://www.powerengineeringint.com/articles/2015/08/south-africa-opens-first-coal-fi.
[29] South Africa's Coal-fired Power Plant Advances: Voice of Africa, 09 June 2012.
[30] Coal Power Stations Are Still the Energy of the Future – Globally, http://www.sbpr.co.za/coal-power-stations-are-still-the-energy-of-the-future-globally/.

[31] Turkey and coal: SourceWatch, http://www.sourcewatch.org/index.php/Turkey_and_coal.
[32] http://euracoal.eu/info/country-profiles/turkey/.
[33] Z. Oktay, Investigation of Coal-fired Power Plants in Turkey and a Case Study: Can Plant, http://www.sciencedirect.com/science/article/pii/S1359431108001580.
[34] S. Acar, L. Kitson, R. Bridle, Subsidies to Coal and Renewable Energy, The International Institute for Sustainable Development, Turkey, March 2015.
[35] L. Friedman, Turkey: Can a Country Planning 80 Coal-fired Power Plants Get Serious About Climate Change?.
[36] Turkey Plans 80 Coal-Fired Power Plants – What About Climate Change? http://www.sej.org/print/headlines/turkey-plans-80-coal-fired-power-plants-what-about-climate-change.
[37] High Calorific Value Coal, Turkish and Global Outlook, October 2014. www.deloitte.com/.
[38] On the Road to Paris 2015: National Contributions to Global Climate Deal: Turkey, Autumn 2015.

A-USC programs in the European Union

24

A. Di Gianfrancesco[1], *R. Blum*[2]
[1]Materials & Technologies Consultant, Rome, Italy; [2]Consultant (former Dong Energy), Denmark

24.1 History of R&D programs on materials for USC and A-USC power plants

The research programs in the field of steels development have been supported since 1950 by the European Coal and Steel Community (ECSC) that was established, after the World War II, in 1952 by the Treaty of Paris (1951) and signed by Belgium, France, West Germany, Italy, the Netherlands, and Luxemburg. **The ECSC was the first brick of the founding of the European Union.** In a formal sense, the ECSC existed from July 1952 to July 2002, and the rules it laid down for European coal and steel were in force throughout that period. In 2002, as a successor of ECSC, the Research Fund for Coal and Steel (RFCS) was created to fund annually innovative projects to enhance the safety, efficiency, and competitive edge of the EU coal and steel industries [1,2].

In 1983, the first ECSC action started to coordinate programs in West Germany, the United Kingdom, and Italy, with industrial partners like Mannessmann, British Steel, and Dalmine, for the development in Europe of the steel Grade 91; the first European heat was realized in Italy at Cogne Plant. These programs were the first step for the design of the USC (ultra-supercritical) power plant in Europe.

During the last 30 years, the European Union also sponsored several large R&D projects for materials and technologies development founded in the frame of BRITE-EURAM, Joule-Thermie, Marie Skłodowska-Curie Actions, Frame Work P1-7, and COST (European Cooperation in Science and Technology).

For ultra-supercritical and advanced ultra-supercritical materials developments in European Union, the two basic long-term projects were respectively the COST programs and the Joule-Thermie AD700, which will be discussed in the next paragraphs.

During the last decades, the European Union has deregulated the power market, introduced tight emission standards, introduced a carbon dioxide tax to minimize the use of fossil fuel, and stimulated renewable energy by substantial subsidies. Consequently, new hard coal power plant projects are no longer part of the future energy system in Europe. Present natural gas sources and the potential extraction of gas from shale formations together with renewable energy like biomass, wind, and solar energy will be the dominating energy sources for the nearest future in the European Union. For these reasons, electricity from renewable sources and gas has increased, and new build pulverized coal combustion (PCC) plants in Europe are only required with the closure

Materials for Ultra-Supercritical and Advanced Ultra-Supercritical Power Plants.
http://dx.doi.org/10.1016/B978-0-08-100552-1.00024-5
Copyright © 2017 Elsevier Ltd. All rights reserved.

of old PCC plants or nuclear power. Historically, however, Europe has been at the forefront of coal technology and still operates some of the most efficient and environmentally clean PCC plants globally [3]. As this technology widely can be used in new highly efficient biomass-fueled power plants as well as support optimization of these plants, a continuation in further research and development makes a perfect match.

High-temperature materials used in state-of the-art USC PCC plants have been developed and exploited largely in Europe, and research continues.

Fig. 24.1 is a schematic overview and chronology of the high-temperature material research programs in Europe accurate to 2015 and gives an overview of the materials R&D projects organized in three categories: those who are mainly related to advanced 9–12% Cr steels, those who are related to the targeted action AD700, and those that have been established as a national German project supporting both 9–12% Cr steel development and AD700.

It is possible to put in evidence the program focused on development of these:

- **Steels for USC** targeting $T = 650°C$ in *green box*: The main steels research program was COST, which ended in 2008; now these activities are still running in the KMM-VIN WP2 Energy. Other programs were focused on Grade 91 and 23 and later of new ideas to develop the Z-phase strengthened steels (CRESTA I/II) in the frame of RFCS or FP7 (Z-ULTRA).
- **Superalloys for A-USC** targeting $T > 700°C$ in *pink*, *light blue*, and *light purple*. The first high-temperature materials research program in the world was the "AD700," which began in 1998 by an idea of Elsam in Denmark and was continued by COMTES program, finished in

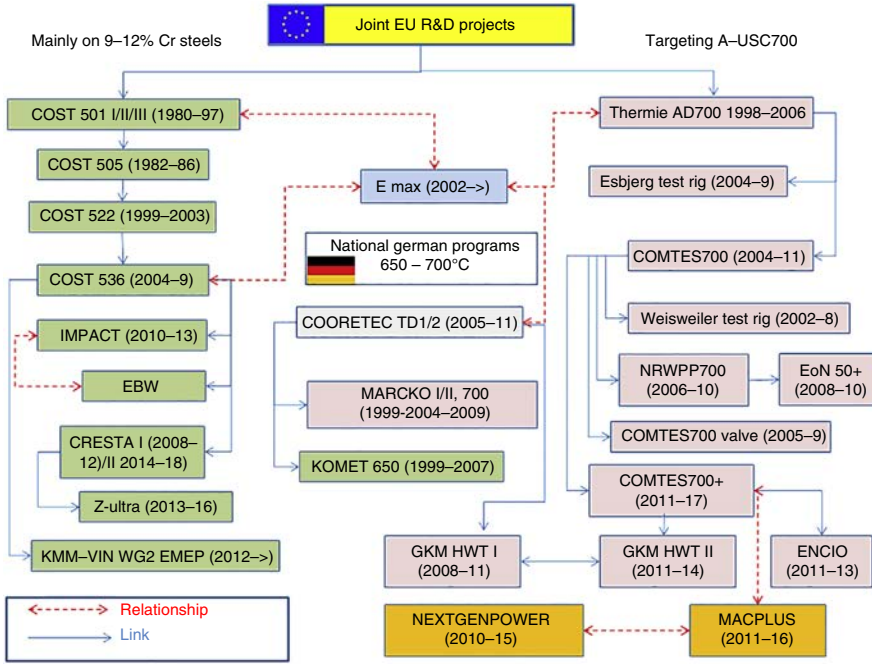


Figure 24.1 Schematic overview and chronology of materials R&D project in relation to target: *green*, steel; *pink*, superalloys; *orange*, multi-materials.

2011 and further under COMTES+ (HWT II and European Network for Component Integration and Optimization (ENCIO)). NextGenPower and MACPLUS are other two programs completed in 2016. Smaller projects, mostly based in Germany and the United Kingdom, with national founding, are also finished or running.

The following sections of this chapter will first explain the coordination and funding initiatives and then expand on the material research programs and projects.

24.2 EU steel development research programs for ultra-supercritical plants

24.2.1 COST programs: 50, 501 (I/II/III), 505, 522, 536

The European Concerted Action Research Programs began in 1971. The first action in the field of HT materials was the program 50 for the gas turbine materials development. After this, the first project for power generation plant was the 501 "Advanced materials for power engineering components, High Efficiency, Low Emission Systems" (1980–97, round I-II-III), which concentrates on materials problems in gas turbines, coal combustion and gasification, and diesel engines. The program COST 501 and COST 505 Materials for steam turbines (1982–86), focused on studying high-temperature crack growth, welding, stress corrosion, and corrosion fatigue cracking of rotor materials (initially 2% CrMoNiWV and later 9–12% Cr HP/IP) and blading materials, provide a good illustration of what can be achieved in long-term collaborative research with realistic technical targets that are periodically defined by the industries involved.

As a result of newly developed steels like grades 91 and 911 for boiler and turbine components and the long-term qualification of laboratory and industrial products, the COST 501 actions made possible in the 1980s to increase the operating conditions (pressure and temperature) of the supercritical plants.

Both COST 522 "Power generation in the 21st century: ultra-efficient, low-emission plant" (1999–2003) and the last part of COST 536 "Alloy development for critical components of environmentally friendly power plant" (ACCEPT) (2004–09) research activities were focusing on the development of 9–12% Cr steels with higher mechanical strength at temperatures above 600°C than Grade 91-911. Several experimental materials have been produced, and materials, like FB2/CB2 for forged and cast components, have been qualified and are now in operation. With these developments, it could be possible to reach improved USC steam conditions: that means temperatures in the range of 600°C and pressure up to 275 bar in the best performing thermal power plants built at the beginning of 21st century in the European Union. This corresponds to an increase in thermal efficiency of around 10% with respect to the best performing European coal-fired power plant in the 1980s.

Whereas the approach in COST 501 was largely empirical and that in COST 522 has been semiempirical, based on physical observations, the COST 536 action was significantly supported by computer-aided alloy design programs like Thermo-Calc, modeling of microstructural stability like DICTRA and MatCalc and prediction of creep resistance of specific microstructures and also on analysis of data using neural networks.

Parallel with these research activities focusing on coal-fired power plants, the introduction of directionally solidified columnar and single-crystal Ni-based superalloys for large gas turbine blades including advanced cooling made it possible to increase operating temperatures of gas turbine power plants significantly and resulted in a thermal efficiency increase of around 10%. Optimized combustion, reduced combustion airflow, enabled a cleaner combustion of natural gas reducing NOx levels down to about 10 ppm, giving in total an efficiency improvement by a factor of five during the last decade, accompanying a substantial reduction in CO_2 emissions.

24.2.1.1 Main results

The main result of the COST programs was the establishment of long-lasting well-functioning cooperation between all the most important European players (steelmakers, forgemasters, plant designers, utilities, universities, R&D centers) involved in the steam power plant technology development. The number of participants and countries increased over the years and generated an unbelievable exchange of experiences and knowledge that have been essential for the development of materials, testing procedures, and investigation methodologies. Last, but not the least, the relationship between participants has been an important issue as well. The different testing programs of the materials, like creep, fatigue, corrosion, oxidation, etc., were also excellent examples of round robin between the different laboratories involved. The long-term creep testing programs, targeting durations over 100 kh, were one of the best examples of this cooperation, and the several long-term aged specimens were used for microstructural investigations that formed the basis and background for new prediction tools, like MATCALC.

24.2.1.2 Boiler materials

After the development and qualification of the grades 91, 911, and 92 for tubes and pipes, these grades have for more than 15 years been the commercial products for the main EU steelmakers as tubular, forged, and cast products. These materials are now used worldwide for superheaters/reheaters components in supercritical plants up to 580°C and for header and steam line USC plants up to 600–620°C.

The martensitic creep-resistant 9 Cr steels, grades 91 and 92 for steam pipework, and FB2 and CB2 for large forgings and castings are all demonstrating improved creep strength of these alloys as compared to earlier martensitic grades such as 9 CrMo and 12 CrMoV. This is due to precipitation hardening by fine MN nitrides based on V and Nb and the stabilization of the martensitic microstructure by additions of W and B [3].

Many attempts in the 522/536 program have been made to develop even stronger martensitic 12% Cr creep resistant steels, to minimize steam oxidation, with the aim to increase the steam temperature up to 650°C. Several trial melts have been produced at laboratory scale, but after 10–30 kh at temperature, the creep strength dropped down to the level of the 9% Cr steels or below.

These attempts have mainly been based on precipitation strengthening by MN nitrides similar to the mentioned 9 Cr steels. However, the fine MN nitrides were transformed to coarse CrMN Z-phase nitrides after long-time exposure at temperatures

above 600°C. This transformation, fine MN nitrides to coarse Z-phase particles, causes a severe loss of long-term creep strength [3,4].

In these programs, a huge effort was made to understand the mechanics and the driving forces of these microstructural changes. Tools like Thermo-Calc, DICTRA, or MATCALC, were available at that time. The microstructure of the early broken creep samples of the new 11–12% Cr steel were compared with the micro structure of crept specimens from the long-term qualification of 9% Cr grades, for more than 100 kh in the temperature range of 550–650°C. These thorough examinations did not only explain the reason for the premature creep rupture in the new 11–12% Cr steels but generated a lot of the basic know-how that favored the evolution of the investigations technics and methodology (ie, EFTEM, APFIM, SEM-FIB) as well as the computational equipment and tools.

The first observations of Z-phase precipitation in martensitic steels were made in 1987 by Schnabel and coworkers that found Z-phase in 11% Cr martensitic steel (X19 CrMoVNbN 11 1) [5]; later in 1996, Vodarek and Strang discovered that modified Z-phase may dissolve MX and cause breakdown in strength [4].

Deeper investigations on Z-phase have been made since year 2000 by Hald [6] and Danielsen [7], who found an explanation for the loss in rupture strength and set up calculation programs that could forecast tendency to this Z-phase formation in 9–12% Cr steels strengthened with V and Nb nitrites. They discovered that high temperatures and increasing Cr content strongly accelerate precipitation of Z-phase and breakdown in strength. This is the main reason for lack of success to develop strong and stable 11–12% Cr steel, and on the contrary, 9% Cr steels are largely unaffected up to long times at 600°C.

This development was backed up by other EU researcher groups like Chalmers University (SE), CSM (IT), TU Graz (AT), Centre des Matériaux de Paris (FR), AGH University Science and Technology Krakow (PL) with the sponsorship of the industrial producers of tube, pipe, cast and forged components, as well as boiler and turbine makers.

These coordinated works, jointly with the activities carried out in Japan, gave a relevant effort to identify the mechanisms of formation and growth, as well as the most critical elements.

Z-phase formation at longer exposure times >50 kh at temperatures above 600°C seems to be an inherent, today well understood phase transformation, metallurgical mechanism in all 9–12% Cr steel strength optimized with Nb and N. Up to now *no attempt* to avoid this transformation in *any* of the many proposed and tested steels with different Nb, N, and Cr content have shown long-time microstructural development with no Z-phase transformation and no decrease in creep rupture strength.

Even the most promising candidate the HB9Cr-steel developed by Fujita and Babcock-Hitachi did not pass the 100,000 h at 650°C before severe Z-phase formation and consequently a major drop in creep rupture strength was documented.

If formation of fine, dispersed, stable Z-phase can be established in 12%-Cr steels by changing chemical composition and defining an optimal final heat treatment, this might be a possibility to develop a microstructure stable martensitic oxidation and creep-resistant steels able to operate at temperatures above 600°C. (See Chapter 3.)

24.2.1.3 Forged and cast

In these programs, new ferritic steels for forging and casting were developed and characterized to increase the operating steam temperatures; the qualifications of these materials are still ongoing after the end of COST 536 program (2004–09), into the KMM-VIN, WG2 EMEP (engineered micro- and nanostructures for enhanced long-term high-temperature materials performance) [8].

The consortium proposed the simulation of manufacturing processes for large components to ensure optimal properties during scale-up from laboratory samples to industrial use.

Currently, our Energy Materials group is composed of 41 research centers/universities and 22 companies, in 16 EU countries and is still growing.

In COST 501, forged and cast 9 to 10% Cr steels were developed with additions of 1.5% Mo (type E) or a combination of 1% Mo and 1% W. They showed much improved creep strength, resistance to embrittlement in operation, and weldability [9–12]. In addition, samples from production components were subjected to low-cycle fatigue and long-term creep testing permitting a statistical evaluation of the results.

Within COST 501 a series of advanced steels for forgings, castings, and pipe/tube application as given in Table 24.1 was qualified, and currently the type E composition is utilized for rotor manufacture.

They are currently in use at temperatures up to 580–600°C. The trend to even higher steam conditions was the subject of the COST 522 program, which explored the possibilities of stabilizing the tempered martensitic microstructure through addition of small quantities of boron. These are the steels (forged steel FB2 and cast steel CB2) now being employed in orders currently being executed in Germany, China, South Korea, and the United States.

After the good results obtained in the COST 501 on composition E, F, and B, a new modified steel called “FB2” was produced as a trial melt. Furthermore, after the promising properties of the trial melt, at the beginning of the new COST 522, it was decided to scale-up FB2 steel to industrial heat to manufacture a trial forged rotor, produced by Boehler (AT), Società delle Fucine (IT), and Saarschmiede (DE) with different process routes and steel refining/re-melting [13–15].

These products were fully qualified, and now also this composition is used for the most recent USC turbine rotor and casing. In Fig. 24.2 are summarized the creep behaviors of forged and cast products.

24.2.2 IMPACT

Based in the United Kingdom, the Innovative Materials Design and Monitoring of Power Plant to Accommodate Carbon Capture (IMPACT) project is a joint venture between E.ON New Build & Technology (plant user), Doosan Power Systems (boiler and welding), Alstom (turbine and components), Goodwin Steel Castings (cast component supplier), National Physical Laboratory (monitoring technology), and

Table 24.1 **Compositions of improved ferritic steels developed in COST 501 and operating temperature for 100 MPa/100,000 h [16]**

COST	Forged steels	C	Cr	Mo	V	Ni	Co	Nb	N	B	100 MPa 100,000 h	Status
	1 CrMoV	0.25	1.0	1.0	0.25						550°C	Long-term operating
	12 CrMoV	0.23	11.5	1.0	0.25						570°C	Long-term operating
501	Type F	0.1	10	1.0	0.2	0.7		0.05	0.05		597°C	Operating in plant
501	Type E	0.1	10	1.5	0.2	0.6		0.05	0.05		597°C	Operating in plant
501	Type B	0.2	9.0	1.5	0.2	0.1		0.05	0.02	0.01	620°C	Operating in plant
522	Type FB2	0.12–0.15	9.0–9.0	1.4–1.6	0.18–0.22	<0.2	0.9–1.4	0.04–0.06	<0.025	0.008–0.01	620°C	Recently operating in plant

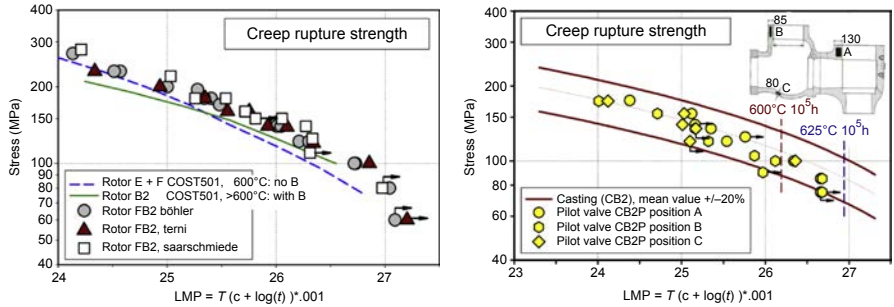


Figure 24.2 Creep behaviors of forged and cast materials developed in COST programs [16].

Loughborough University (microstructural characterization and modeling). The total budget is £1.8 million, partly government funded through the Technology Strategy Board, and run from 2010 to 2013 [17].

The key goal of IMPACT is to improve the efficiency of future steel-based coal-fired power plants, and hence reduce carbon emissions, by the following:

1. improved high-temperature capability of welded thick-section high-alloy steel components in steam plants (boiler, pipework, turbine) by development of innovative materials and processes, including upscaling from laboratory development, a pilot commercial scale "MARBN" steel cast, and a demonstration welded boiler tubing product;
2. better understood, monitored, and controlled performance of these welded components to maximize efficiency while avoiding premature weld type IV cracking as found in current high-alloy steel plants;
3. novel advanced in-service monitoring techniques to enable a plant to operate at highest temperatures and challenging design conditions without prejudice to safety: creep strain monitoring to warn against plant failure risk, semi-nondestructive miniature disc sampling, and testing to identify materials at risk;
4. improved component design capabilities linked to whole-life plant condition monitoring.

The proportion of boron in steels has been previously altered with inconsistent results. Fujio Abe of National Institute for Materials Science of Japan found that alloying boron with nitrogen in certain amounts achieves high creep rupture resistance; MARBN steel (martensite plus boron plus nitrogen) was discovered. The IMPACT project has optimized the composition of MARBN steel, and short-term tests have shown that MARBN has 20–40% higher creep rupture resistance than P92 at temperatures up to 675°C (Fig. 24.3). Heat treatment at 1200°C further increases the creep rupture resistance by 10–15%. Potentially, MARBN has 55% higher creep rupture resistance than P92, but only verified by short-term testing.

However, MARBN steel shows a substantial weld strength reduction and is susceptible to cracking in the heat affected zone (HAZ). The proportions of the alloying elements in MARBN need not be exact: a wide range is acceptable for similar properties. In May 2012, Goodwin Steel Castings (UK) produced an 8-ton melt of MARBN, from which ingots and castings were fabricated and welded (Fig. 24.4). These components are now in long-term tests [18,19].

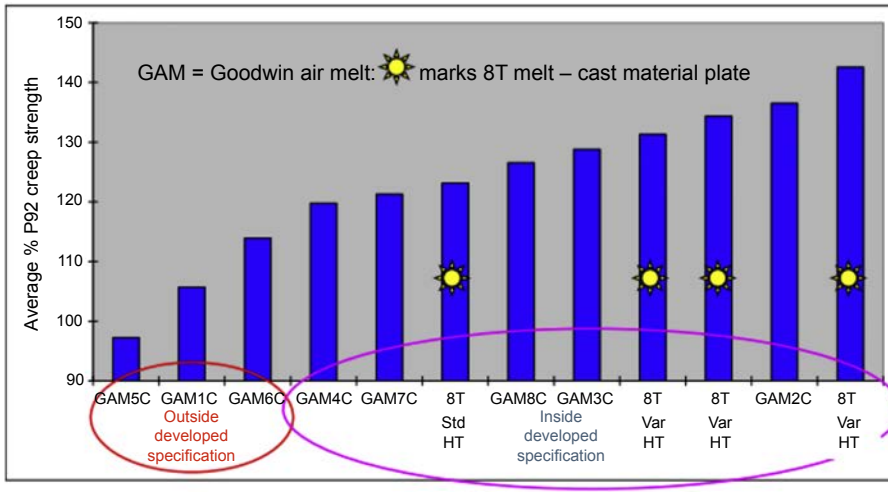


Figure 24.3 IMPACT creep data on MARBN variants [17].



Figure 24.4 Impact 8-ton melt production, May 2012 [17].

24.2.3 CRESTA

24.2.3.1 CRESTA 1

CRESTA "New Creep Resistant Stable Steel for USC Power" (2008–12): this program, sponsored by EU Commission (Grant Agreement RFSR-CT-2008-00024) targeted the development of new stable 10–12% Cr martensitic steel that is able to operate at higher temperatures and in more aggressive environments in steam power plants [20].

The partnership was Centro Sviluppo Materiali (coordinator) (IT), Dong Energy (DK), TU Graz (AT), Air Liquide Welding (FR), DALMINE (IT), Alstom Power Boiler (DE), INDUSTEEL Creusot (FR), and TU Denmark (DK).

Two ways were followed: steel without/reduced elements forming Z-phase or steel forming the Z-phase after the quality heat treatment. The main results obtained are as follows:

- The current available thermodynamic tools give the wrong results in predicting transformation temperatures and thermodynamic stability.
- Fundamental investigations need to improve databases, tools optimization, and calibration.
- The Z-phase steel is still not optimized: it is too brittle, and the Z-phase is not stable.
- A more conventional steel without Nb has been developed; tests are promising, but due to late manufacturing the creep tests are currently still ongoing (now in CRESTA 2) (no longer than 15,000 h).
- Fabricability and weldability of the Nb-free steel has been demonstrated: semi-industrial heat manufactured, thick pipe produced and steam line welded prototype realized, as shown in Fig. 24.5. The target to avoid post weld heat treatment (PWHT) for thin weld has not been reached.

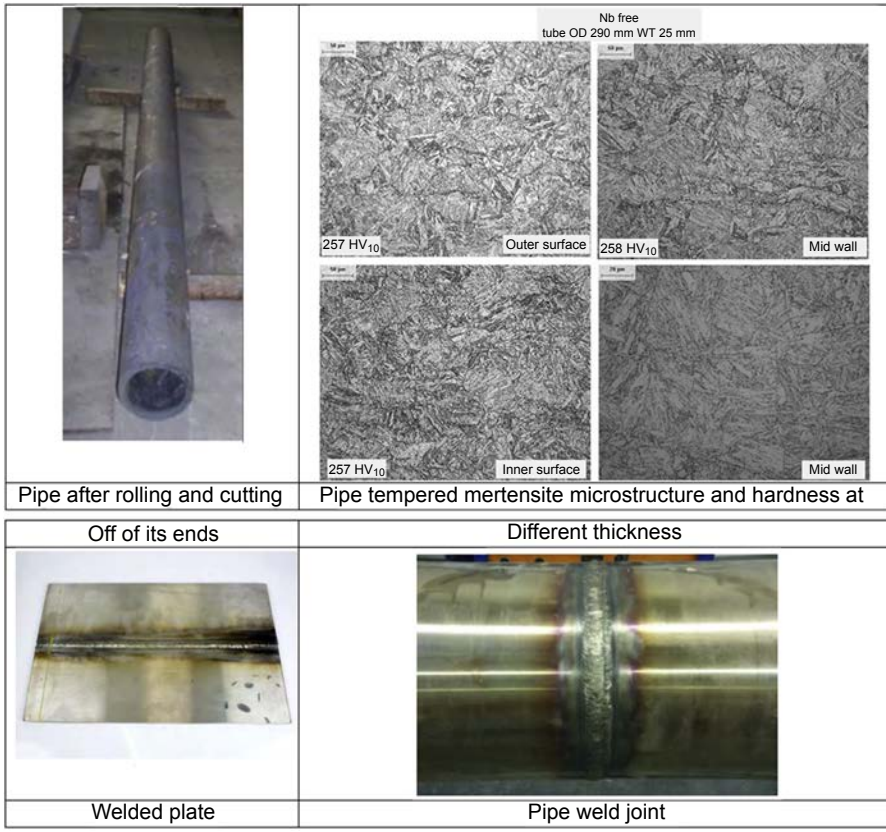


Figure 24.5 CRESTA results.

In spite of the worldwide economic crisis, the consortium partnership decided to complete the program to obtain the most available results and to increase the knowledge for further development of high-temperature steel applications.

The 700°C steam technology concept for the next-generation power plant, nickel-based superalloys is still not consolidated, and advancement in available steel technology base could generate, shortly, additional efficiency increases in coal consumption and in the reduction of CO_2 generation.

24.2.3.2 CRESTA 2

Following CRESTA project end, the consortium decided to present a new proposal to EU RFCS found. The new project (RFSR-CT-2014-00032) July 2014–June 2018 has the following partnership from the previous project: Centro Sviluppo Materiali (IT) (Coordinator), TU Graz (AT), ArcelorMittal INDUSTEEL Creusot (FR), TU Denmark, Air Liquide Welding (FR), ALSTOM Boiler (DE). Two of the partners (Tenaris and Dong Energy) have left the project, mainly due to change in company market strategy, and they have been replaced with new partners from Czech Republic (Materiallovy a Metallurgicky Vyzkum, MMV), who successfully produced the pipe in the CRESTA project, and Italy (Società delle Fucine).

This project targets the consolidation of know-how acquired in the CRESTA project. This will be done through extensive investigations of long-term aged and crept specimens of the developed compositions and prototype tubular and welded components, as well as improvements of the chemical composition of both steels. The consortium would like to reach results targeting the EU standard requirements for approval to industrial applications especially in A-USC power plants with steam operating temperature in the range of 650–700°C.

From the CRESTA project, two 11–12% Cr breakthrough steels emerged that showed very promising results:

- *Z-phase strengthened:* a steel based upon Tantalum Z-phases, CrTaN, as a strengthening agent, instead of MX nitrides, which were unstable in high Cr steels. This steel showed very high creep strength up to 20,000 h, where instabilities in the creep curves have been observed.
- *Nb-free:* a steel with MX (VN) particles as strengthening agent, but without any niobium, which is known to destabilize vanadium-based MX precipitates. In spite of not containing Nb, medium-term tests, currently in the range of 20,000 h, showed creep strength slightly similar to P92 steel. Longer term creep tests planned in CRESTA project are still running. Creep tests from produced pipe are also running, and a program from pipe welded joint is started.

There is a need for further investigations, without interruption of current activities still running, to consolidate knowledge gained so far. Besides, slight changes in compositions are necessary in both steels to improve fabricability (particularly for large-scale industrial applications) or to reduce the cobalt addition for steel cost reduction, boron and nitrogen calibration to improve the properties of the welded joint (reduction of type IV cracking susceptibility), and finely tune heat treatment and PWHT technologies to get mechanical properties able to perfectly fulfil Pressure Equipment Directory and the TÜV/EN

standard requirements. Particularly, the case of welding has also to be taken more deeply into consideration, through development of (almost) matching filler materials.

These steels are to be used mostly in welded constructions. To take advantage of the improved properties, welded joints must retain as much as possible the BM creep strength and good oxidation resistance. Weldability and the development of matching filler materials (ferritic) are therefore taken into careful consideration.

If either of the approaches listed is successful, it will allow the combination of high Cr content for oxidation resistance and long-term creep strength. These are crucial to increase A-USC power plant steam parameters and hereby efficiency in future coal-fired power plants, both in consideration of the following possible development ways:

- Upgraded USC power plant targeting 650°C temperature and 325 MPa pressure for steam conditions: this means a power plant made fully by ferritic, martensitic, and austenitic steels, without use of very expensive Ni-base superalloys that have limited production inside the European Union.
- New advanced USC power plants operating over 700°C requiring superalloys for the hottest components will need better martensitic steel than currently available on the market to reduce the use of the very expensive superalloys in the components scheduled to be operate in the range of 600–650°C.
- Refurbishment of the old SC plant replacing Grade 91 or X20 steels for superheaters bundles.
- Reducing the superalloys overlay for the waste-burning boiler.

If the material can be qualified for these applications, the steam conditions or even double-reheat steam cycles can be applied, which allows a further increase of 1–3% in the power plant efficiency, as well as the improvement in the efficiency of the older plants after refurbishment.

24.2.4 Z-phase strengthened steels for ultra-supercritical power plants

Z-Ultra is a medium-scale European consortium that has received funding from the European Union's Seventh Framework Program for research, technological development, and demonstration under NMP.2012.2.2-3 and under grant agreement no. 309916. The Z-Ultra project is running from 2013 to 2016.

The aim is to develop heat-resistant steel that allows increasing the thermal efficiency of fossil power plants to over 50%, which is 30% higher than the present standard in most existing power plants.

The consortium combines the expertise of a steelmaker, a utility company, an engineering consultant company from Ukraine, and eight research organizations and universities from EU and Eastern partnership countries. The consortium is coordinated by Fraunhofer Inst. Mechanics of Materials IWM (DE), Saarschmiede (DE), Engineering Academy of Armenia, RWE Power AG (DE), TU Denmark, Ustav Fyziky Materialu, Akademie Ved (CZ), Paton Electric Welding Institute (UA), Georgian Technical University, TH Chalmers (SE), TU Graz (AT), and IPP Centre LLC (UA) [21].

The idea is to exploit the Z phase as a thermodynamically stable strengthening agent in martensitic creep-resistant steels. Previously the Z phase has been considered as detrimental, since the coarse Z-phase particles that develop during long-time service in high-chromium steels hardly contribute to the strength while growing at the

expense of the fine, strengthening nitride particles. However, high-chromium contents around 12% are needed since the current 9% chromium steels do not provide sufficient oxidation resistance at 650°C. Hence the challenge is to control the precipitation of the Z phase in 12% Cr steels such that fine Z particles are formed, which are stable for long times. An important aspect is that the beneficial microstructure should be established also by the post-weld heat treatment.

24.2.5 KMM-VIN EMEP

A new framework for coordination of this effort was launched in 2012. KMM-VIN (Knowledge-based Multifunctional Materials Virtual Institute) is a legal entity established in 2007 with membership of mainly academic institutes and aims to foster the creation of a powerful platform for research and development and industrial application of advanced materials. In 2012, it experienced significant expansion as around 40 participants, including many industrial companies from the power generation industry and its supply chain, with a long history of working together within the COST actions, joined the organization.

An Energy Materials Working Group (WG2) has been formed and has adopted a work program for the further improvement of steels for power generation plants. KMM-VIN WG2 is made up of 72 research establishments and 25 companies across Europe. It is an unfunded collaboration, and individual projects are funded by private sources, national governments, or the EC. The A-USC technology projects facilitated by KMM-VIN WG2 coordination effort are detailed subsequently [22].

One of the main goals for EMEP program (engineered micro- and nanostructures for enhanced long-term high-temperature materials performance) is the industrial-scale demonstration of components using the advanced MARBN steel concept with potential to allow increase of operating temperatures from 600–620–650°C.

In the same way that the COST concerted actions provided a framework for collaboration between projects funded by many different agencies, G2 has already fostered collaboration between projects funded by the European Commission Framework Program, eg, MACPLUS and POEMA, projects funded by national governments, eg, the UK IMPACT project, projects funded by academic funding agencies, eg, EPSRC [23], and projects funded privately by WG2 industrial partners.

The planned added value of this KMM-VIN WG2 Materials for Energy network is a reduction of the CO_2 emission of around 8% by the increase of the steam parameters of the nowadays level of 275 bar/600°C to 325 bar/650°C of coal-fired steam power plants at limited investment costs. Continued use of coal will also improve the security and affordable steady electricity supply due to widespread low-cost, long-lasting (150+ years) global coal reserves. It is estimated that replacement of old, inefficient power plants and implementation of state-of-the-art technology in all newly built plants could lead to annual global savings up to 1.7 Gt CO_2, equivalent to 5.5% of the global emissions (IEA 2008).

The targeted improvement in the process efficiency is 20%, in comparison with the current average efficiency level in Europe and the rest of the world (maximum steam temperatures of 580–610°C in new plants), with a corresponding reduction of CO_2

and other emissions. If we want to reach higher temperatures, we need to develop new iron-based materials with coating to facilitate operation at steam temperature of 650°C and to verify the required temperature capability of the new steels to serve as critical components, in particular headers, steam lines, and turbines. This research program exhibits broad alloying concepts, developing these through modeling of the micro/nanostructure development during processing leading to the prediction of the properties of interest [24].

Key objectives to meet are these:

- identification of innovative alloying concepts, promising steel compositions, and surface engineering solutions for elevated temperature service
- identification of coating systems capable of withstanding long-term steam oxidation resistance at 650°C
- evaluation of the most promising surface engineering solutions
- production of small-scale melts (<100 kg) to be selected for satisfactory properties in fabrication (welding, casting, forming, heat treatment, nondestructive inspection, coating, etc.) and improved performance under service conditions (mechanical and environmental resistance)
- characterization of material (coatings and materials) microstructures down to a nanoscale; tailoring materials micro/nanostructure for desired properties; optimization of the processing route, if necessary
- production of the best alloys and protective solutions in the scale of prototype components (approximately 10 tons)
- development and qualification of welding consumables and joining strategies for new alloys
- testing and verification of the new materials systems in terms of the life-limiting long-term performance (creep, fatigue, oxidation, etc.) toward acceptance for new plant design

In recent years, the steel and power generation industries have suffered from a perception that they are in decline and unadventurous, dirty, and lackluster. Consequently, there have been noticeable difficulties in attracting fresh graduates with the inevitable result that there is now both an aging workforce and a gender imbalance within the industry. To address this, EMEP has a set of secondary objectives:

- to attract fresh, bright graduates in the research on challenging new materials for future power generation
- to improve the image of the steel and power generation industries highlighting the challenges and rewards from careers in these industries
- to promote the competitive research, micro/nanostructure characterization, and modeling methods and expertise for materials development activities within the scientific partnership network including the collaborating universities and research institutes
- to develop solutions withstanding higher temperatures than any earlier alternatives, which advance competiveness of European companies providing materials, components, equipment, design, and systems

The programs highlight will be these:

- Microstructural investigations (XRD, LM, SEM, FIB, TEM, EFTEM, 3D APFIM, etc.) of specimens of virgin condition and after long-term creep testing of base material and welds identified precipitation strengthening as the key mechanism to stabilize the tempered martensitic structure against creep.

- Microstructure and creep modeling based on thermodynamic equilibrium and multicomponent diffusion modeling using software such as Thermo-Calc, DICTRA, and MatCalc have supported the understanding of microstructure–property relationships of this class of steels.
- Development of new steel with improved creep strength: one approach is to use the more stable Z-phase itself as a strengthening phase and steel promote a finely dispersed precipitation of Z-phase. Other strengthening phases like intermetallic phases or yttrium dispersoids in ODS alloys will be also investigated.
- New methods of surface engineering to modify the surfaces of candidate structural materials by microstructure and coatings. Microstructure modification can be achieved through heat treatment, mechanical treatment, alloying, etc. Better understanding and control of the effect of microstructure modification is needed. EMEP aims to conduct fundamental investigations on the oxidation resistance and oxidation mechanisms of different ferritic-martensitic steels after selected surface treatments have been performed. This will include the microanalysis of the internal stresses present in the surface layers as a function of the depth, investigation of the microstructure at the surface, and in the near surface area (by cross-sectional scanning electron microscopy (SEM) and focused ion beam–transmission electron microscopy (FIB-TEM) as well as the surface topography by atomic force microscopy (AFM) as this will affect the diffusion paths and consequently the oxidation rate.
- New coating systems will be applied based on a multistep process for the new steels, including deposition techniques such as electrolyzes, hot-dipping, thermal spray, slurry application anodic oxidation, etc. Fig. 24.6 shows the steam oxidation behavior at 650°C of an aluminide coating developed during the previous COST action. The effect of higher temperatures, nonisothermal and thermal transient conditions will be a subject for fundamental, mechanistic, and laboratory development. EMEP will support modeling activities and will contribute to validate any produced models.
- Understanding the degradation of coatings, application method, and tailoring the coating composition and microstructure is vital to the success of coating technology.
- Surface preparation prior to application of the coating, optimization of the diffusion treatment (temperature and time steps) when required, and developing models to predict the performance of the coating in service.

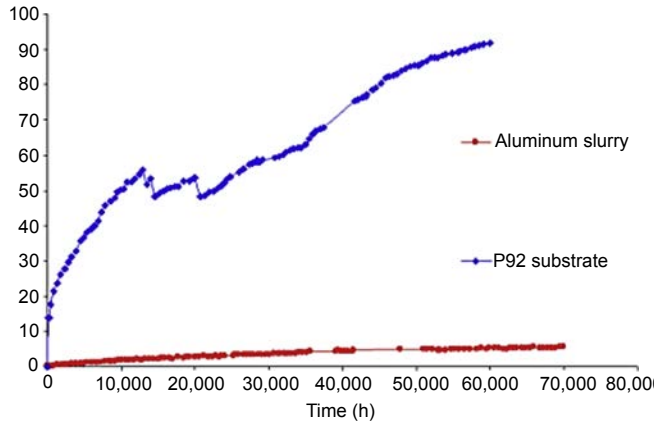


Figure 24.6 Mass change of a slurry aluminide coating deposited on P92 when exposed to flowing steam at 650°C in the laboratory [24].



Figure 24.7 Forging of MARBN trial billets [24].

- Definition of new steam oxidation testing parameters that better reflect real operation conditions. Most laboratories have been testing under atmospheric flowing steam or steam/Ar mixtures isothermally, but recent results have shown that the laboratory observed spallation behavior of uncoated substrates is significantly different from that in a steam turbine at 150 bar.
- The synergy between steam oxidation, wear, and/or erosion of coatings and new materials will be studied specifically for valve seats.
- Steelmakers, forgemasters, and foundries will manufacture trial melts of 50–100 kg size with optimized compositions and heat treatment resulting from the microstructure characterization and modeling exercises.
- Mechanical and oxidation testing including long-term tests will be made at partner laboratories to validate the properties of the developed materials.
- Welding of pipes and other components is known to lead to a loss in creep strength of the HAZ, which has an adverse effect on components lifetime in power plants. New welding consumables will be developed and tested along with the materials solutions for base materials.
- Manufacture of large components weighing up to 30 tons by casting or forging. Forgemasters and foundries will supply components for validation of simulation tools to predict effects of solidification and forging processes on segregation and residual stresses in large components; forging of trial samples are shown in Fig. 24.7.
- Industrial partners will manufacture full-size demonstration components of steam pipes, cast valves, and full-size trial rotors from successful trial melt compositions. Fig. 24.8 shows MARBN tubes for insertion in power plants for long-term testing. These components will be thoroughly tested to validate their properties for plant application prior to installation in commercial operating plants.

An example of the collaboration fostered within the KMM-VIN/EMEP framework is the development of MARBN castings. A casting (Fig. 24.9) was manufactured by Goodwin Steel Castings Ltd. IMPACT project.



Figure 24.8 MARBN tubes samples ready for insertion in power plant for long-term testing [24].



Figure 24.9 MARBN cast bonnet manufactured by Goodwin Steel Castings Ltd [24].

24.3 EU superalloys development research programs for advanced ultra-supercritical power plants

The development of the A-USC technology and materials in Europe started with the AD700 project 1998–2006 that was the first program of this nature in the world [25–27].

All the succeeding projects have been based on the knowledge and experiences made in this program. In Fig. 24.1 has been just presented the summary of all the EU projects and their scheduled timetable that will now be described in this paragraph.

24.3.1 AD700 R&D program

The **AD700** technology initiative began in the early 1990s with the idea of developing a range of advanced materials that would permit the raising of main and reheat steam temperatures in pulverized fuel boilers up to 700°C (1292°F) and consequently to increase the efficiency over 50% [28–34].

Fig. 24.10 shows the relationship between power plant efficiency and carbon dioxide emissions. As efficiency increases, specific carbon dioxide emissions decrease from 1100 g/kWh at 30% net plant efficiency to 650 g/kWh at 50% efficiency. This equates to a reduction in carbon dioxide emissions of 41%. Coal consumption is similarly reduced and clearly illustrates the benefits of efficiency increase with regard to potential environmental protection.

It has to be taken in to account that the AD700 program was planned before any prevision for carbon capture and storage.

A major research and development program was established comprising six phases of effort that started with a conceptual feasibility study at the beginning of 1998. Table 24.2 shows a breakdown of the original scheduled six phases [35,36].

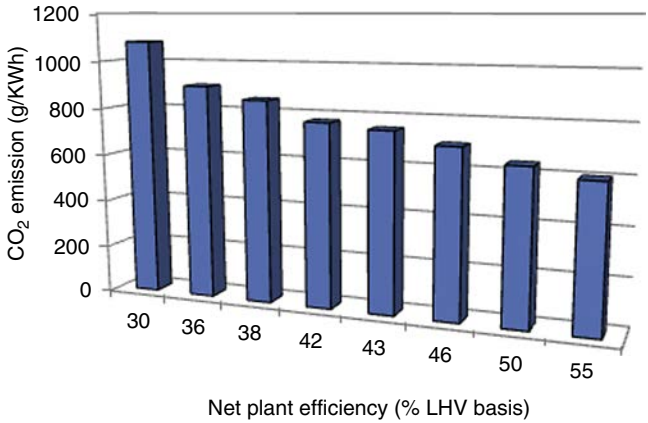


Figure 24.10 Reduction of CO_2 emission as a function of plant efficiency.

Table 24.2 Original timetable of AD700 project

Phase	Description	Time scale
1A	Conceptual feasibility	1998–2000
1B	Materials property	1998–2004
2A	Basic design for Phase 3	2002–2004
2B	Materials properties demonstration	2002–2005
3	COMTES700 (CTF, ETR)	2004–2008
4	Full-scale demonstration plant	2006–2011
5	Operation of FSDP	2012–2014
6	Feedback to partners	2012–2013

It was recognized that high-temperature materials were the key to the successful development of AD700 technology. Due to the extended timescales required for materials testing, validation, and qualification the program was launched with Phase 1 comprising a conceptual feasibility study (Phase 1A) and an investigation of materials property requirements (Phase 1B).

Phase 1 of the program attracted 40 participants from 10 European like power generators, manufactures of power plant equipment, material suppliers, and research centers. The program was industry-focused and funded in part by the European Commission.

Following near-completion of Phase 1A, Phase 2 was initiated in 2001 with 34 participants from across Europe. Phase 2A focused on taking forward a number of boiler design concepts, while Phase 2B continued the laboratory testing and evaluation of new high-temperature materials. By 2004, the third phase, entitled COMTES700, was progressing with the aim of pilot-scale testing of key power plant components at a commercial scale.

The Phase 4 pre-engineering study for a full-scale demonstration plant was scheduled for autumn 2006, but it was initially postponed and further cancelled with the following actions.

24.3.1.1 Materials group

The materials programs were organized in three subgroups: ferritic, austenitic, and superalloys. The aims were the selection of candidate materials available on the market and/or the development of new steels/alloys able to reach the creep rupture strength established target of the following:

- 100 MPa for 100 kh at 650°C for ferritic steels
- 100 MPa for 100 kh at 700°C for austenitic steels
- 100 MPa for 100 kh at 750°C for nickel superalloys

24.3.1.2 Boiler materials subgroup

Some new ferritic steels compositions with Cr content in the range of 12% were produced at laboratory scale, but all showed a drop in creep after 10–20 kh for the microstructural instability.

The high cost of nickel, however, prohibits its extensive use in tubes, and so the boiler materials program also set out to develop a high-temperature austenitic steel with average stress rupture properties of 100 MPa following 100,000 h operation at 700°C. The development of new austenitic material started from NF709 take as reference alloy for this good compromise between creep and corrosion behaviors. About eight new formulations were produced in the laboratory, and after the first characterizations, one composition was selected as a promising new steel. The composition was called Sanicro 25 and has been successfully produced in commercial quantities by Sandvik (see Chapter 12) and has undergone extensive testing as part of the AD700 Phase 3 program.

In parallel with an ongoing R&D program aimed at the development of a high-temperature, solid-solution nickel alloy (A617) for application to pipework and superheater tubes, the AD700 program investigated precipitation hardening nickel alloys (A263 and IN740).

Collectively, this group of three alloys offers a range of new possibilities to the boiler designer. Alloy 617 was at the time considered to be the easiest to fabricate as it does not require a precipitation hardening heat treatment but only with moderate mechanical strength, while the precipitation hardening alloys 263 and 740 offer superior creep and corrosion resistance, respectively.

24.3.1.3 Turbine materials subgroup

As with the boiler materials group, the aims of the steam turbine materials group were these:

- to identify suitable high-temperature alloys
- to demonstrate prototype manufacture and welding
- to define properties and allowable stresses

Most of the alloys investigated had previously been used in other industry sectors such as aerospace and gas turbines, but they required further development of AD700 technology application as size and environment in a steam turbine would but very different from a gas turbine. Nickel-based alloys 617 and 625 were the main candidates for many turbine components, but also other alloys like IN718 and Waspaloy have been used in the preliminary characterization and selection. Their characterization in terms of creep, creep/fatigue crack growth, low-cycle fatigue for castings, forgings, and welds were successfully completed.

Candidate alloy test specimens for material testing were produced by Goodwin Steel Castings Ltd in alloys 263, 617 (Fig. 24.11), 625, and 155.

Due to difficulties experienced with the castability of A617, most of the effort has been focused on the casting of A625. Two full-scale demonstration valves were produced.



Figure 24.11 Alloy 617 full-scale demonstration valve, courtesy of Goodwin Steel Castings Ltd (UK).

Both A617 and A625 have been successfully forged and considered suitable for high-pressure (HP) and intermediate pressure (IP) rotor forgings. For the difficulty of production of large remelted ESR/VAR ingots over 6–8 tons, due to currently unsolved segregation problems, the welded rotor manufacture is a key feature of AD700 turbine technology. Prototype joints have been manufactured successfully by welding 10% chrome steel to the nickel-based alloy.

Moving and stationary turbine blade production has been explored both by the machining and investment casting manufacturing methods.

Bolting materials have been identified and characterized. Solid particle erosion is a known potential problem for turbine blades, and the application of a protective coating has also been demonstrated.

24.3.1.4 Boiler design group

Within the boiler design activities, potential cost savings were identified by considering shortening the main and reheat steam lines using two novel arrangements. First, a twin tower or inverse two-pass boiler design was considered, in which firing takes place in a first tower, with the hot combustion gases moving down and across to a second tower. The final superheater and reheater are arranged at the bottom of the second tower with outlet headers located close to the turbine. The arrangement minimizes the thermal expansion between boiler and steam lines and provide a significant reduction in the length of steam piping to 25 and 30 m (less than half the length of a normal steam pipe arrangement) for each string of 400-MW reference plants. As an alternative arrangement, a horizontal boiler concept, designed with the outlet headers on top of the boiler, was considered. The low-height boiler design arrangement resulted in a similar shortening of the steam lines to around 35–40 m for each string of a 400-MW reference plant.

In total, 10 boiler concepts with different boiler arrangements (tower type, two-pass, inverse twin tower, and horizontal furnace), different power outputs (400 MWe net, 1000 MWe gross), different process cycles (single reheat, double reheat), and different firing systems (tangential firing, opposed wall firing) have been investigated. Turbine designs are based on relatively conventional turbine architectures to ensure high levels of reliability. To minimize the use of nickel alloy components, reduce cost, and accommodate the limited supply capacity, new turbine designs will incorporate welded rotors and castings, with nickel alloys restricted to the highest temperature regions only.

An additional outcome from Phase 1 was proposals for optimizing the layout of "conventional" ultra-supercritical power plants. One result was the "compact design" Fig. 24.12, and the in-line arrangement of boiler and steam turbine, Fig. 24.13. The steam line design for Dong Energy's planned 2 × 800 MW Greifswald power plant (Fig. 24.14) will be based on these design principles (and this plant design also incorporates a low mass flux vertical tube Benson boiler) [31].

Another consideration (particularly with the prospect of more renewables on the grid) has been increased flexibility, with the following goals: minimum load, presently 20%, target 10%; lowest Benson operation load, presently 30%, target 20%; and load following capability, presently 4%/min, target 5%/min.

24.3.1.5 Turbine design group

As for the boiler, also the turbine group design was called to think of a different solution for the manufacture of rotor and casing components due to the use of superalloys for the hottest parts.

The rotor components in USC turbines are usually monoblock forged components or welded between two steels with different grades for the different zones. The

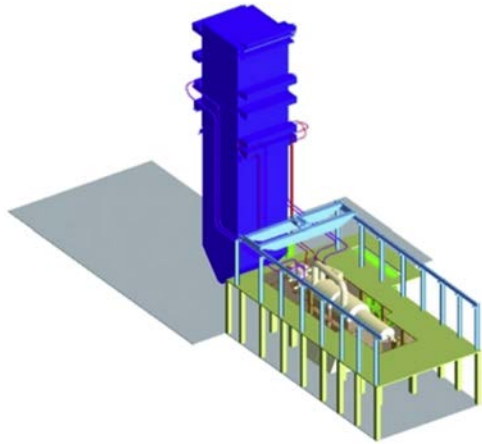


Figure 24.12 Compact design.

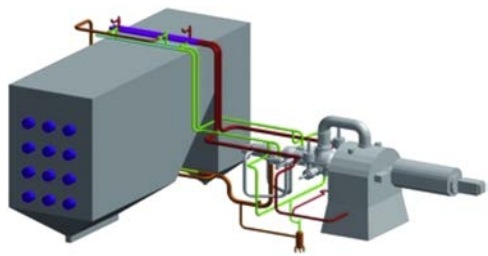


Figure 24.13 The in-line arrangement of boiler and steam turbine.

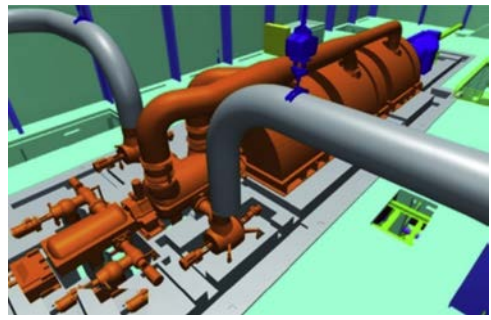


Figure 24.14 Steam line design for Dong Energy's planned 2 × 800 MW Greifswald power plant.

monoblock solution is an unbelievable solution due to the smaller ingots available for the superalloys. Therefore the welded or joined by bolts solution have to be adopted.

The turbine designers in the AD700 program were Alstom and Siemens, and two possible alternatives have been proposed.

Fig. 24.15 shows the Siemens approach for an HP turbine having the following characteristics:

- proven basic concept (Siemens barrel-type)
- solid rotor shaft
- welded rotor and inner casing, both made in superalloys for the hottest zone and 10% Cr steel for the lower temperature zone
- cooled outer casing with full pressure load, inner casing with low-pressure load at inlet and flanged valve attachment

Fig. 24.15 shows also a detail of the possible welded rotor design for the IP turbine [35].

The design philosophy of Alstom's A-USC steam turbine is to remain within the architecture and design practices of the existing SC and USC turbine modules. This means that extensive references are available to demonstrate the robustness of the design approach, and no significant changes or adaptations are required in the design and engineering processes. Fundamentally, this means that the A-USC modules take advantage of the fact that there are no requirements for cooling. Fig. 24.16 shows a typical design schematic of a single reheat arrangement for a 500-MW, 50-Hz generator. To improve the cycle efficiency, an HP heater extraction is located toward the end of the HP expansion. Other power classes and speeds follow analogously. Fig. 24.16 shows a typical design for an A-USC HP turbine. The key design feature,

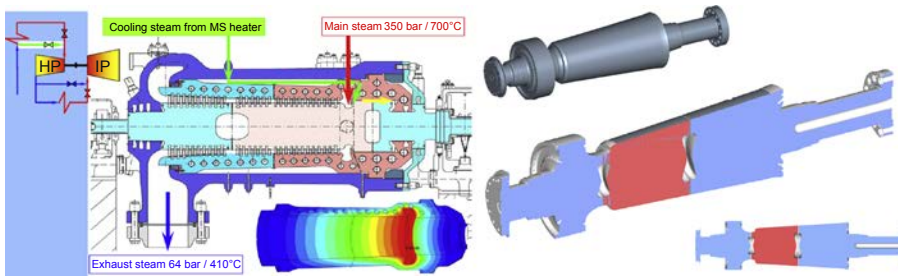


Figure 24.15 Steam turbine design for AD700 power plants.

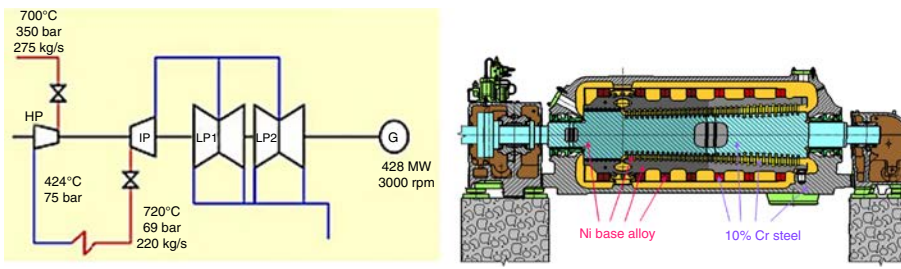


Figure 24.16 500-MW single RH A-USC steam turbine arrangement and HP module design.

which is common to all the Alstom HP turbines, at all steam conditions, is the use of shrink rings to close the upper and the lower casing valves. Shrink ring technology was introduced in the 1960s, and it has been used successfully ever since [36].

Also for Alstom the rotor and casing parts operating at higher temperature are design to be made by superalloys and the lower temperature parts by 10% Cr steels.

24.3.1.6 Conclusion

The phases 1 and 2 of the AD700 project defined the basis for the approach to the development of a 700°C steam power plant able to operate on coal in combination with biomass to enable a reduction of CO_2 emission of around 40% compared with the most advanced USC power plants operating today.

These projects have been the basis for all the further projects proposed in Europe

The technical realization of a 700°C steam power plant depends on a successful development and qualification of advanced ferritic, austenitic, and Ni-based alloys. With respect to austenitic and Ni-based alloys, promising results have been achieved. The economic criterion for the realization of a 700°C steam power plant is a realistic budget price. The consumption of large quantities of expensive Ni-based alloys has significant influence on the investment costs; therefore a successful development of an improved ferritic steel to be used at temperatures up to 650°C would improve the situation by cutting the tonnage of expensive Ni-based alloys.

24.3.2 E MAX

Major European utilities have set up the "E MAX initiative," started in 2002, which is coordinated by VGB. The E MAX initiative aims to develop advanced PCC plants with optimized efficiency, economy, and environmental sustainability. Members of this consortium are EDF (FR), Electrabel (BE), Elsam (DK), EnBW (DE), PPC (GR), RWE (DE), and Vattenfall (SE/DE) [37].

The E MAX initiative organizes and directs high-temperature material research programs, such as COST, AD700, and COORETEC, which will be explained subsequently. Each project consists of a consortium of participants, including component manufacturers, major utilities, and research establishments across Europe. The participants are carefully selected to meet the needs of the program in terms of competencies and knowledge of one or more aspects of the supply chain. Most projects are in part funded by the European Commission.

24.3.3 AD700-3: Esbjerg Test Rig

The Esbjerg Test Rig constituted a part of Phase 3 of the Advanced 700°C PF Power Plant project (AD 700) (2004–10), the aim of which was to develop a coal-fired power plant with efficiencies up to 55% by increasing the steam temperature to 700°C [38].

The Esbjerg Test Rig consisted of a single loop of superheater tubes inserted in the superheater area in the boiler of Esbjerg Unit 3, a USC unit with steam temperature

560°C and steam pressure 275 bar. The steam was taken from the outlet of superheater 1 and superheated to 720°C. It was then cooled in a mixing piece down to 560°C. The test rig has been manufactured by Alstom Power Boilers, Stuttgart, and was installed during the 2004 summer revision and operated for 4 years. The test rig was the sixth in a series of test rigs where materials have been tested in the Unit 3 boiler with exposure times between 7000 and >50,000 h.

It was mainly the flue gas side corrosion and the steam side oxidation behavior that were tested, but also the manufacturing experience was valuable.

The following materials have been tested in the test rig: TP347HFG, S304HCu, TP310N, HR3C, HR6W, Sanicro 25, and IN740, the last two developed in AD 700 Phase 1.

The Esbjerg Test Rig was 100% financed by generators from the Emax-group. The companies responsible for the realization of the test rig and the subsequent evaluation were Alstom Power Boiler, Hitachi Power Europe, VGB Power Tech e. V. (representing the generators), and Elsam Engineering (coordinator). Elsam Kraft was responsible for the operation.

The other and major part of Phase 3 was the COMTES700-Component Test Facility to be installed in the E.ON power plant Scholven Unit F.

24.3.4 Concept study for a European 700°C power plant with ultra-supercritical steam parameters burning low-calorific lignite

The research project, started in 2006, was dealing with the feasibility of design, planning, construction, and operation of a 700°C power plant for low-calorific lignite [39].

Due to the very low-calorific rate, project data from similar concepts like lignite-fired power plants with optimized plant technology and upstream dehydration facility (BoA-Plus) cannot be transferred. The dehydration process for low-calorific lignite with a very high humidity rate requires high energy expenditure, considerably decreasing the overall electric net efficiency. Thus for such fuels, detailed investigation of the dehydration process and its integration into the steam cycle is of utmost importance.

To date, it has not been possible on a European level to get sufficient public financing for various R&D lignite projects (except for the DRYCOAL project), as for hard coal with, eg, AD700, COMTES700, NRW Reference Power Plant. Within the framework of this study, analysis regarding the content is to be combined with a review of the financial options.

The program comprises the following items:

1. analyses of the actual findings of the R&D projects focusing on the 700°C technology,
2. concept and design of a 700°C lignite-fired power plant under the aspects: balance of plant, efficiency, generation costs, and basic conditions,
3. fuel conditioning systems: introduction of lignite dehydration (eg, heat dehydration plant) and integration into the steam cycle,
4. analysis of the public financing options for support of these special technologies,
5. comparison with the EU research priorities.

24.3.5 AD700 Phase 3: COMTES700

COMTES700 was a demonstration project aiming at 700°C live steam temperatures that generally utilized available design codes and design practice, and selected materials identified within the preceding THERMIE/AD700 "Advanced 700°d PF Power Plant" project. Development of new materials was not in the scope of COMTES700.

The main driving power for the development of the COMTES700 project was a group of major European power generators named "Emax Power Plant Initiative." From this group a consortium was formed ready to support the project with a substantial financial contribution. To underline the necessity of an EU support of coal-based energy research, the group decided to apply for additional funding within the Research Program of the European Research Fund for Coal and Steel (RFCS), which positively evaluated the proposal (RFCP-CT-2004-00003).

The project was carried out from July 1, 2004, to December 31, 2011, by Alstom Power Boiler, Hitachi Power Europe, Burmeister & Wain Energy, Siemens, Elsam Engineering, and VGB PowerTech e. V. The total budget is amounting to 15.2 MEuro. Fifty-seven percent thereof is funded by the generators' consortium, 40% by the RFCS, and 3% by the suppliers involved. The project was steered by the COMTES700 partners consortium and coordinated by VGB.

The objective was to design, manufacture, erect, and operate a component test facility (CTF) to test high-temperature durable new materials needed to realize a coal-based power plant with efficiencies above 50% [40,41].

The host plant of the CTF was the German power plant Scholven F owned by E.ON (Fig. 24.17). It is a coal-fired power plant with steam conditions of 535°C and maximum 230 bar, a maximum output of 740 MW, and an average operation time of more than 5000 h a year.

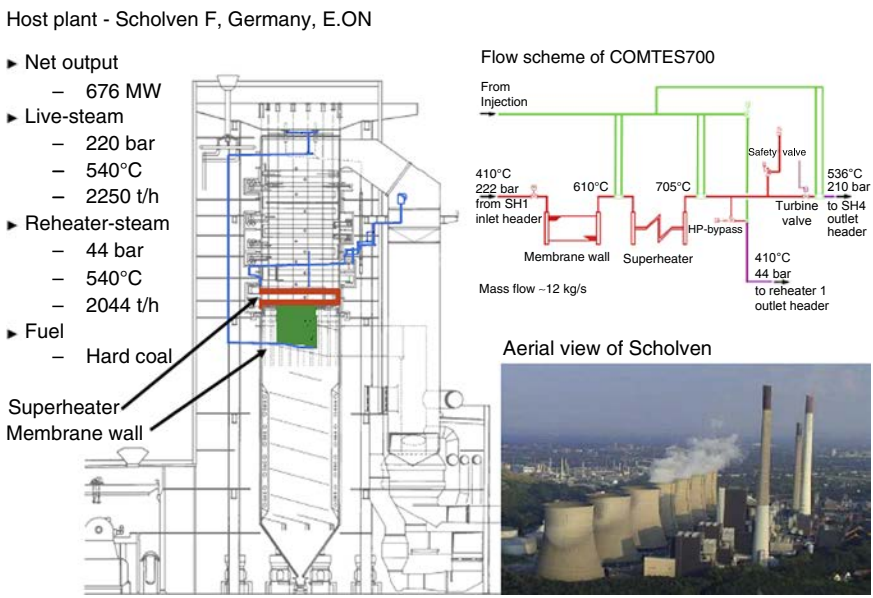


Figure 24.17 Schematic design of the test facility [42].

These are the general conditions of a testing period of approximately 20,000 h of operation with the following focuses:

- manufacturing, bending and welding, also dissimilar, of the materials used
- long-term creep behavior linked with real plant dimensions and other design features
- in-plant monitoring
- determination and evaluation of residual service life
- in-service inspections
- operational testing of Ni-based alloys for tubes, pipes, and valves
- gaining information on magnetite layer on the ribs of internal ribbed tubes
- operational behavior of all components
- flue gas corrosion and steam oxidation behavior of the materials
- erosion effects due soot blowing

The results of the CTF flow back into engineering and design of components to optimize them for the next phase of a 700°C power plant, the erection, and operation of a demonstration plant power plant in Europe.

The project is divided into eight work packages and covers the following parts: engineering (WP 1), material and manufacturing (WP 2), valves and measuring devices (WP 3), control and instrumentation (WP 4), erection (WP 5), operation (WP 6), evaluation (WP 7), and coordination (WP 8).

The COMTES700 test facility was designed and manufactured according to the European harmonized standards. Design practice for the design of the test facility was generally corresponding to the practice used for USC power plants, with the necessary adaptations to integrate the test facility to the host unit.

Fig. 24.17 shows the implementation of the hosting plant and Fig. 24.18 some examples of the installed components.

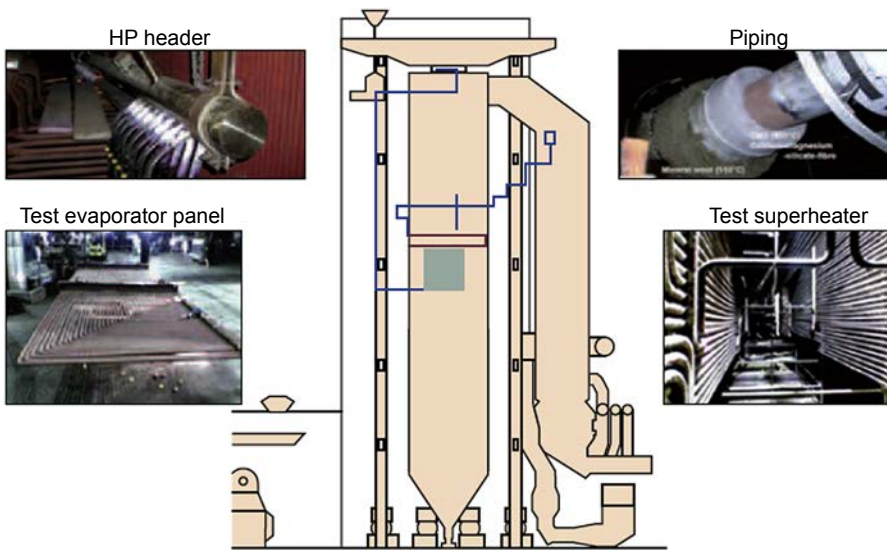


Figure 24.18 Boiler components in the CTF (Scholven Unit) [36].

24.3.5.1 Main results

The integration required relative high attemperator cooling capacity and necessity of horizontal spray attemperators, which in combination with an insufficient draining system caused some operational challenges.

Materials for membrane walls

Even though all membrane wall materials tested in COMTES700 (T24, HCM12, A617B) generally performed well, some reservations regarding all three materials were stated.

T24 has become one of the most widely used materials for membrane walls in USC boilers that are under fabrication or commissioning in Europe. Damages have occurred at the welds in these boilers. Investigations of causes for these damages and measures to avoid them are still ongoing [43].

Evaluations of creep rupture strength for HCM12 issued after the COMTES700 engineering and manufacturing have resulted in a reduction of the allowable design stress in several national standards. The reductions are mainly caused by a microstructural instability, Z-phase formation, during high-temperature service. The alternatives are to strictly limit the maximum metal temperature for this material or to replace it with a different steel-based material grade or with nickel-based alloys. If a nickel alloy is chosen an increased proportion of nickel alloys for the boiler design is foreseen, and thereby increased investment costs. Introduction of a different steel-based grade would likely include the use of T91 and T92 with the challenges of mandatory post-weld heat treatment of all welds on that part of the membrane wall, and 9% steels do not offer optimal steam oxidation resistance for the membrane tubes.

Equipment and procedures for post-weld heat treatment of site welds during the erection of martensitic membrane walls are considered to be the largest challenge. There are currently no known manufacturing and operation experience with 9–12 Cr membrane walls (other than HCM12), and reduction of risks may require further testing and demonstration. Lack of steam oxidation resistance may cause frequent boiler cleaning to keep the oxide formation and thereby the tube wall temperature at a safe level.

Results from another project with simulated service loads have shown that tube-fin welds in membrane walls of A617B can fail [44].

Based on these results, it has been questioned whether the membrane wall tests in COMTES700 have fully demonstrated the ability to operate an A617B membrane wall for a 700°C boiler. Further investigations and testing of A617B membrane wall samples have been initiated. These investigations may result in improvements of material selection, fabrication procedures, and membrane wall design [45].

Materials for superheaters

Results have shown that the tested superheater materials (HR3C, DMV310N, Sanicro 25, A617B, IN740, A263) generally performed well with limited oxidation and corrosion, but Sanicro 25 and A617B did suffer from high corrosion rates in some positions. The high corrosion rates are believed to be related to the fuel composition

and the specific temperature range, and all tested superheater materials are considered susceptible to the corrosion mechanism, even though not observed on all materials and samples. Results from another project [38] did not show corrosion rates in the same range. Further studies of corrosion rates at various temperatures and fuel compositions are recommended to optimize superheater materials selection. Alternatives include restrictions in fuel compositions or partial replacements of superheater sections within the unit design lifetime.

Concern was raised regarding the microstructural stability of the tested version of IN740. Structural stability improvement of IN740 is claimed to include increased Al/Ti ratio and reduced Si content, which may have an effect on the corrosion properties. Testing of the modified material would be recommended.

Alloy 263 was introduced late in the project as an additional candidate material for superheaters. The operational time with this material was, however, too short to conclude on the feasibility. Further testing would be recommended.

Header and piping components

The steepest learning curve in this project was realized with the operational and repair experiences with the thick-walled components in A617B. It was recognized that post-weld heat treatment must be applied to reduce the susceptibility to stress relaxation cracking. Nondestructive examination is crucial for the inspection of fabrication quality. An integrity assessment of service exposed components as well as the necessity of a workable and verified weld repair concept due to the aging effects with A617B including long-term creep rupture testing is needed before A617B can be fully qualified.

Mechanized ultrasonic testing was successfully qualified and verified in COMTES700 for the relevant component thicknesses, but realization of an advanced USC power plant will require larger component thicknesses, and further qualification and verification would thus be required. Design guidelines for nickel-based components should include appropriate acceptance levels.

Extensive work on weld repair concepts is ongoing, and the outcome of the concept development and verification are very important for the overall feasibility of thick-walled components in A617B.

Finally, it should be considered to introduce A263 as material for header and piping, as it would contribute with higher design stress than 617B and consequently lower consumption of expensive nickel alloy. Introduction of A263 would require extensive investigations, including materials qualification, studies of stress relaxation cracking susceptibility, verification of repair concepts, and demonstration in general. Major activities have already been initiated within the ENCIO project [44].

Valves

Generally valves operated without major problems. Thick-walled valves, eg, HP bypass valves, showed crack formation starting on the inside of the valve bodies. Since the cracks were undetectable by NDT in the in-service state, it is questionable if the tested valves could be operated safely for long periods. Therefore, to reduce the risk of both fatigue and creep cracking, it is vital to test available improved designs

where local stress concentrations due to thickness changes are reduced, and reduce temperature differences across the wall thickness during load changes (including start and stop sequences). Furthermore, the design solutions should allow an adequate level of NDT capability. This was planned in ENCIO and HWT II.

Turbine components

A cast A625 turbine control valve was included in the steam cycle of COMTES700, as an activity in a separate project (COMTES700 Turbine Valve [46]). Additional demonstration of cast thick-walled A625 including welds is necessary and was scheduled by the ENCIO project.

24.3.5.2 Conclusions

Key components of an advanced USC power plant have been successfully designed, manufactured, erected, and operated for about 22,400 h to demonstrate if the necessary technical solutions to realize a 700°C demonstration power plant are available. The project did not succeed in demonstrating that all necessary materials and designs can currently be operated without technical and economic risks. Much new knowledge has been gained, but critical issues still need to be solved to reduce risks for the implementation of a large-scale demonstration plant.

COMTES700 impacted a number of followup projects on research and on demonstration levels. Several projects directly related to COMTES700 results or materials are ongoing, monitored by a followup group. Accompanying research has been started on national level, eg, within the framework of the German COORETEC initiative [47,48].

Most important projects for the further development of 700°C technologies are the European demonstration project ENCIO and the German demonstration project HWT II.

All these projects are scheduled to be completed by 2018 allowing a final conclusion on the risks of a 700°C power plant.

The following brief summary indicates which issues should be avoided or to proceed with:

- explore and test alternative candidate materials for membrane wall materials
- improve corrosion properties for superheater materials
- apply PWHT for thick-walled A617B components
- verify weld repair concepts for thick-walled A617B components
- verify a stronger candidate material like A263 for a major reduction of plant cost
- further development of NDT methods and acceptance levels
- minimize thermal stresses in component and process design
- improved valve design
- reduce manufacturing costs

24.3.5.3 Potential for use of the results

An engineering study carried out in parallel to COMTES700 determined the specific investment costs of a commercial power plant with a gross capacity of 1100 MW, which is based on COMTES700's technology, at 2000 €/kW [49]. These costs are

definitely above the costs of state of the-art coal-fired power plants and have to be significantly reduced before achieving commercial viability. Cost reductions are to be expected from optimizations of the design concept, but main drivers would be increased creep strength of alternative materials and optimization of manufacturing methods.

Introduction of a stronger nickel-based material compared with A617B [50], like A263, IN740, A282, or USC800 is still a possible option, but currently in 2016, no successful development of a new generation of martensitic steels with higher creep strength properties than P92 at temperatures above 600°C has been obtained. Therefore a positive impact on plant investment costs has not been obtained. Some additional European research projects are underway to try to find a possible solution.

Since it was the first time that power plant components from Ni-based raw materials were to be manufactured, manufacturing in COMTES700 was basically carried out according to the state of the art. This proved to be very time-consuming and prohibitive. Manufacturing methods for components made from Ni-based materials were standing at the beginning of the learning curve in 2004, which implies a huge potential for clear reductions of investment costs. Demonstration projects like HWT II and ENCIO now include promising new approaches of manufacturing and will provide practical experience with these (forging, hot isostatic pressing, welding procedures, heat treatment, etc.).

The economic potential of advanced USC power plants is to be read against the background of an increasing global demand for coal. Reduction of CO_2 emissions from the use of coal as well as savings in coal is of high importance for emerging economies owning huge own coal resources like India and China. In consequence of the Fukushima accident, not only Japan is looking for a sustainable use of coal in Asia. No wonder that these countries are interested in 700°C power plant technology and are aiming at starting research projects comparable to COMTES700.

Also in Europe, 700°C power plant technology offers potential for CO_2 avoidance by modernizing the coal-fired power plant fleet. In 2011, a study came to the conclusion that increasing renewables installation will not be sufficient to realize the 2020 CO_2 reduction targets of the European Union. Replacement of less efficient by advanced thermal power plants with highest efficiencies could to contribute to the reduction targets [51], which will be the case even beyond 2020, with addition of CCS technologies.

If the European Union sticks to the aim to realize carbon capture and storage, 700°C power plant technology remains an indispensable prerequisite for a sustainable implementation of this technique. Efficiency losses of 7–12% in consequence of carbon capture and storage require highest efficiency power plants to minimize inevitable energy losses.

In some European countries where national incentive schemes, in addition to the European Union Emission Trading System, have spurred rapid growth of renewables installed capacity, balancing of fluctuating energy supply from variable sources like wind and solar is a very big challenge. If other options like grid optimization, storage facilities, or energy demand management are limited, thermal power plants will face the need for flexible operation (part-load operation, frequent startup/shutdown).

Depending on the specific national energy mix, coal-fired power plants might be used as backup capacity. In particular, components made from Ni-based alloys could be also applied in USC power plants at reduced wall thickness according to improved material properties. Investigations on this option have been commenced [52]. But the same rapid growth of renewables, which requires backup capacity, might kick advanced coal-fired power plants off the market, if its utilization is reduced beyond profitability.

Disregarding of the fact that cost reductions are to be expected as a result of the technically focused followup test programs, the commercial viability of the 700°C technology is dependent on electricity prices, CO_2 emission prices, fuel costs/availability, and political priorities resulting in different regulatory frameworks and public approach. These conditions differ significantly subject to the reference framework. The Asian viewpoint might remain different from Europe, and national priorities may differ in Europe as well.

Last but not least, coal is competing with the advantages of renewable energy, which on the other hand include risks related to the fact that these are still evolving technologies.

The technology of a coal-fired power plant with live steam temperatures of 700°C provides an important option for sustainable energy generation with regard to climate protection only with CCS and preservation of resources. Its final marketability depends on the development of rapidly changing global energy markets.

24.3.6 COMTES700 valve

A full-scale turbine control valve was selected for COMTES700 as a steam turbine test component [48]. It is integrated into the CTF for the exposure to steam conditions of 212 bar and 705°a at 12 kg/s. The COMTES700 Turbine Valve is a separate R&D project and is financed by a group of European power generators and the suppliers Siemens and Alstom without public sponsorship.

The main steam control valve was selected because it is one of the most critical components of a 700°C turbo set. It has both high safety relevance and high loading due to internal working pressure at a high metal temperature that is close to the main steam temperature (Fig. 24.19).

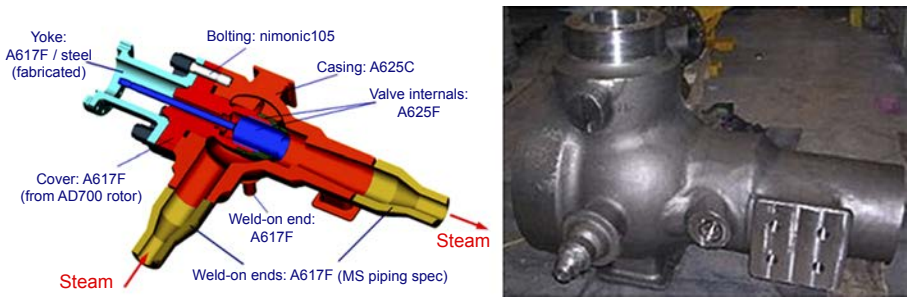


Figure 24.19 Turbine inlet valve [55], fully machined Alloy 625 turbine inlet valve casting produced.
Courtesy of Goodwin Steel Castings Ltd, UK.

Due to the fact that the heat transfer at supercritical steam pressure in the CTF is nearly independent from steam velocity and mass flow, the stationary and transient metal temperatures of the COMTES700 Turbine Valve will be the same as for full-load conditions. Thus, the thermomechanical loads for valve casing and internals will be representative for those of other 700°C steam turbine components.

The valve has a weight of 4 tons and is positioned lying flat on its side. It is a proven design that would be used in turbosets up to 600 MW. The material selection for the valve was made by both suppliers cooperatively. Further, Siemens and Alstom cooperate in manufacturing and testing.

In the interest of optimal quality assurance, E.ON Engineering as well as the RW TÜV and MPA Stuttgart have been involved in material evaluation, mechanical design, and component inspections. A material test program that has been started in advance will evaluate long-term properties parallel to the component test.

During its planned test operation from July 2005 to June 2009, the measurement of metal temperatures, deformations, and strains were carried out. In agreement between host plant and the suppliers, shutdowns of the block will be used for inspections. After the test phase the valve components will be destructively tested.

24.3.7 AD700-4

Between 1998 and 2008, the European Commission invested approximately one billion Euro into A-USC technology. AD700 phases 1, 2, and 3 demonstrated material properties, component design manufacturing capability for A-USC technology.

The next phase was to pre-engineer the full-scale demonstration plant (FSDP) to assess economic and technical viability of A-USC technology, from which the utilities would make a decision whether to go ahead with the build. The first three phases produced a notable research spin-off technology called the Master Cycle; this is a modification of the regenerative feed water preheating system, adding an extra 1.5% points to the net efficiency.

24.3.7.1 Pre-engineering study "NRW power plant 700°C"

The pre-engineering study NRWPP (project for a high-efficiency power plant with a live steam temperature of 700°C, Power Plant 700) directly builds on lessons learned in the COMTES700 project and represents the first stage for the construction of a low-emission power plant, which is to be erected once its technical and economic feasibility has been confirmed [49].

The project has been conceived as a cross-border transnational project. To date, 10 European energy utilities have joined together with the aim of developing this sustainable European concept for generating power on the basis of fossil fuels. These are Dong Energy Generation (DK), E.ON Energie (DE), Electrabel (BE), Electricité de France, EnBW Kraftwerke (DE), EVN (AT), RWE Power (DE), STEAG (DE), and Vattenfall (DK/DE).

In the context of the study, the European energy utilities involved have determine viable technical and economic decision-making principles for power plants

with a live steam condition of 700°C. The project is thus directly linked to the COMTES700.

The pre-engineering study, called the North Rhine-Westphalia Power Plant at 700°C (NRWPP700), began in October 2006 and ended in 2008. The consortium included a group of 20 operators, manufacturers, and suppliers involved in the AD700 program; the project coordinator was VGB.

Over 70% of the funding came from the partners and the rest from regional funds from Brussels via the government of North Rhine-Westphalia. NRWPP700 was completed in three stages, as follows.

Stage 1: Demonstration plant planning (500 MW, bituminous coal): This study determined the technical and economic feasibility of a demonstration unit fired by bituminous coal. On the boiler side, three tower boiler concepts from Alstom, HPE, and Burmeister, and Wain Energy were assessed.

It was decided to opt for an HP boiler with steam parameters of 705/720/36.5 reaching over electrical efficiency (net, LHV (lower heating value)). The steam turbine examined generated a total of 550 MWe at the shaft or 500 MWe net taking into account auxiliary load. A smaller unit size was chosen as it minimizes risk to investors. In 2012, the capital cost for this demonstration unit fired by bituminous coal was €1.7 billion (>3000 €/kW).

The candidate alloys are shown in Table 24.3. It is important to note that A263, IN740, and Sanicro 25 are not more in the development stage. The membrane wall is superheater 1 in this design.

Table 24.3 Candidate materials for the European first stage demonstration plants

Components		Candidate materials
Header inlet	SH 1/2/3/4	P92, A617, A617m
	RH1.1/1.2	13 CrMo4-5, A617m
Header outlet	SH 1/2/3/4	P92, A617, A617m, A263
	RH 1.1/1.2	A617m
Pipes	SH 1	T92
	SH 2	A617m, Sanicro 25
	SH 3	A617m, Sanicro 25, HR3C
	SH 4	IN740
	RH 1.1	A617m, HR3C, S304, T91 10 CrMo9.10
	RH 1.2	A617m
Casing	Outer casing	Cast 9–10% Cr steels
	Inner casing	A625 cast welded with 9–10% Cr steels
Valves	Casing	A625 cast
	Weld-on ends	A617m
Rotor	HP–IP	A617 welded with 2–10% Cr steels
Blades	HP–IP	Martensitic steels, Nimonic 80, Waspaloy

HP, high pressure; *IP*, intermediate pressure; *RH*, reheater; *SH*, superheater.

The following additional research projects were carried out in the scope of NRWPP700:

- production of a casing fabricated from A617m for an HP bypass valve
- processing and relaxation of new nickel alloys under modified cyclic load
- investigation of development possibilities for high-temperature sensors
- components designed for high temperatures
- nondestructive investigations of different welds to produce steam turbine rotors fabricated from nickel alloys
- manufacture of an HP pipe extruded A617 in the extrusion process
- qualification of IN740 for the steam generator superheater
- qualification of A617m for thick-section superheater pipes
- increased thermodynamic investigations regarding the Master Cycle

Stage 2: Commercial plant planning (1000 MWe, bituminous coal): This stage transferred the technical and economic findings of stage 1 to a commercial 1000-MWe unit to test for economic feasibility against a 1000-MWe USC state-of art plant. It was proved technically possible to scale up the boiler and steam turbine. Additionally, the economics for such a unit were calculated. For this study a conventional configuration was chosen, consisting of a single flow HP turbine, a double flow IP turbine, and two double flow low pressure (LP) turbines. To calculate the maximum efficiency of 1100-MW unit, all parameters and components have been pushed to their physical, practical, and economical limits. Using an inland state-of-the-art USC plant (600/610/28) with 45% efficiency (normal operating conditions including startup and shutdown losses) as a starting point, the following efficiency improvements have been estimated for a new A-USC PCC plant:

- +2.2% points were added for steam temperature increase to 705/720°C
- +0.8% for main superheater steam increase to 35 MPa
- +0.2% for increase of boiler inlet temperature
- +0.7% for sea water cooling
- +1.2% for decreasing flue gases in stack to 65°C (+0.4% on new boiler, +0.4% for low temperature heat displacement, +0.4% for high-temperature heat displacement)
- +0.1% for other incremental improvements

The total increase is +5.2% points, resulting in 50.2% efficiency, of which 3.2% points is gained from the increase to A-USC steam parameters. The NRWPP700 concept is CCS ready; it is estimated that the addition of CCS will reduce net efficiency by 8–12% points. Economies of upscaling reduce the specific capital cost to 2000 €/kW for this A-USC 1100-MW commercial unit **compared with the 3000 €/kW for the 500-MW unit.** In comparison, a modern supercritical PCC plant built in 2012 in the developed world would cost <1200 €/kW.

More detailed planning work and substantial reduction of fabrication costs must be demonstrated to lower capital expenditure significant. Stage 2 identified the need for the following additional research projects:

- short-term and long-term properties of nickel alloys; to ensure the long-term reliability of these materials
- further qualifying works on austenitic material Sanicro 25; for a better long-term assessment of this superheater tube material

- production and manufacturing of nickel alloys; to obtain more reliable and cost efficient processes
- developing an improved version of P92; to lower the amount of nickel alloy used and cut investment cost

Stage 3: Commercial plant planning (1000 MWe, lignite coal with pre-drying): This stage transferred the technical and economic findings of stage 2 to a commercial lignite-fired 1000-MWe unit test for economic feasibility against a 1000-MWe USC plant. A lignite-fired PCC plant running at 650°C, 675°C, and 705°C with lignite pre-drying was assessed reaching efficiencies of 51.6%, 52.06%, and 52.63%, respectively (net, LHV). Work from stage 2 was used for this assessment. However, differences in temperatures, pressures, and dimensions required some redesigning (VGB, 2012b; 2013b; Modern Power Systems, 2008).

The reverse approach would have been to pre-engineer a commercial (1000 MWe) unit and subsequently downscale to a demonstration size unit (500 MWe). However, the reverse approach was rejected as no detailed findings of the demonstration plant size would be available for submission in time for funding from EC though FP7.

24.3.8 COORETEC

COORETEC is an initiative by the Federal Ministry of Economics and Technology (BMWi) for the development of a power plant fired by fossil fuels with prospects for the future. The abbreviation COORETEC stands for CO_2 reduction technologies for fossil-fired power plants. Under this heading, two strategic approaches are taken in joint projects involving industry and research:

- technologies for improving power plant efficiency
- technologies for the separation and transport of CO_2 with the aim of safe long-term storage in geological formations

With this focus, COORETEC is integrated into the German Federal Government fifth Energy Research Program on Innovation and New Energy Technologies. The aim is to promote the transition to a reliable, economic, and environmentally safe energy supply. COORETEC thus makes a significant contribution toward implementing the Federal Government energy and climate policies. COORETEC is currently providing funding for A-USC technology in Working Group 2: Coal-fired steam power plants with maximum efficiencies [54].

24.3.8.1 COORETEC, TD-1: testability of thick-walled components made from nickel-based alloys and welded connections using nondestructive testing methods

The application of new technologies to increasing efficiency in high-performance power plants primarily consists in significantly increasing the steam parameters for pressure and temperature. The materials previously used are only conditionally suitable under such loading conditions, and nickel-based alloys must thus increasing be used [47].

In addition to the improved characteristics of the materials themselves, the adequate detectability of defects in thick-walled components made from nickel-based alloys is of critical significance for their manufacture, safe commissioning, and reliable operation.

To guarantee this, work on the examination and development of suitable nondestructive ultrasound testing methods is being carried out in the COORETEC project TD-1 "Testability of thick-walled components made from nickel-based alloys and welded connections using nondestructive testing methods." The creation of a scientific database of process limits should also allow reliable decisions to be made regarding the applicability, reliability, and confidence limits both of the conventional techniques and of the improved testing techniques in their application to welded components made from nickel-based alloys.

According to our current understanding, the same problems are to be expected in ultrasonic testing as for austenitic weld seams, probably in more severe form when inspecting wall thicknesses of 80–100 mm. The main problem lies in the acoustic anisotropy of the weld seams, which often interferes with the way in which the ultrasound waves spread, thus making them unpredictable. Backscattering, reflections, refractions, and wave-splitting thus not only occur at the grain boundaries but also in the area of the fusion line.

The inspection and analysis techniques developed for austenitic materials and welded connections (eg, antenna arrays, synthetic aperture focusing technique) should therefore be tested and developed within the framework of the project for use on these thick-walled nickel-based alloys and their welded connections.

The project was carried out in the period from September 2006 to October 2009 by the IZFP Fraunhofer Institute for Non-destructive Testing, the BAM (Federal Institute for Materials Research and Testing), and the MPA Stuttgart.

The research institutes are jointly examining existing processes with the aid of defined test objects. The IZFP and BAM are working on the development and improvement of the processes and are carrying out the examinations by determining the process limits. The MPA Stuttgart is coordinating the provision and distribution of test objects and is implementing the results in fault tolerance and evaluation by fracture mechanics methods, in addition to verification of the nondestructive testing results.

The participating manufacturing companies, Alstom Power Boiler and Power Generation, Hitachi Power Europe, Essener-Hochdruck-Rohrleitungsbau, MAN TURBO, and Siemens supply the industrial know-how regarding the tests that have to be carried out during manufacturing and acceptance of components and are participating in the manufacture of the test objects.

The participating power plant operators E.ON Energie, EnBW Kraftwerke, Grosskraftwerk Mannheim, RWE Power, STEAG, and Vattenfall Europe Generation define the requirements, contribute their practical experience in the use of nondestructive testing over many years of operation, and are participating in the examination of the processes.

The partners from industry are accompanying the project in a steering committee coordinated by VGB and are evaluating the results established.

Within the framework of the COORETEC research program, 50% of the research project is financed with funds from the German Ministry of Economics; 80% of the industrial funding comes from the participating power plant operators, and 20% comes from the participating manufacturers.

24.3.8.2 COORETEC TD-2: base test (round robin test) for the planned project "nondestructive examination methods for cast nickel-based alloys"

To increase efficiency in conventional-fired power plants, it is necessary to enhance steam temperature and pressure. For these conditions, austenitic steels and nickel-based alloys are needed. For cast thick-walled components out of nickel-based alloys, it is very important to have a possibility to detect defects coming from manufacturing or operation [47].

In this base test, nondestructive examinations (ultrasonic) with at the moment available mobile equipment were carried out at two cast thick-walled components out of Alloy 625. The reason is to find out the state of the art for the followup project COORETEC TD-2 "Nondestructive examination methods for cast nickel-based alloys." It is the aim to determine the possibility to detect material defects by using a reference block and a staged test block for validation. The foreseen examinations deliver the base to develop a procedure for quality assurance for cast thick-walled components out of nickel-based alloys.

VGB coordinates the base test. Participants are the research institutes, generators, and manufacturers, who are also interested in the planned R&D project COORETEC TD-2. In principle, there is also the possibility for other interested companies to take part.

The examinations are carried out from the following research institutes: IZFP and BAM, intelligeNDT System & Services, MPA Stuttgart, Müller und Medenbach, and TÜV Rheinland.

The following manufacturers are attending the project: Siemens, Alstom (CH), BHR Hochdruck-Rohrleitungsbau, and SCHMOLZ+BICKENBACH GUSS. The following generators are participating in the project: EnBW, E.ON New Build & Technology, RWE Power, STEAG, and Vattenfall Europe Generation.

The development of the methods to improve the detectability, the inspection of the improved procedures, and the integration in quality assurance concepts are part of the followup project. The results can also be used to prepare an application for public funding within COORETEC.

24.3.9 E.oN 50+

Building an FSDP involved procurement (site, components, and contractors), construction of components, plant erection, and finally, plant commissioning. The first task of pre-engineering was NRWPP700, described in Section 25.3.7.1, after which E.ON were to take over the FSDP build in a project called E.ON 50+. In 2008, it was decided that a 500-MW FSDP would be built at Wilhelmshaven (Germany). The electricity produced from a demonstration unit is likely to be more expensive than the projected market value, as the unit is smaller, and it is a prototype. Commercial A-USC PCC units are likely to be built in the 1000–1100 MW range, to utilize economies of scale. *In 2010, the FSDP was postponed due to technical problems (such as cracking of thick-section components).* However, research continues to solve

these technical problems, and knowledge from all former and current projects will be consolidated in the FSDP, which was planned to be built from 2017 to 2021 and operated from 2021 to 2026 [55].

Currently it is rather unlikely that this project will be revitalized.

24.4 New materials for steam generators with efficiencies above 50% (MARCKO DE 2) 1999–2004

The aim of the project was to qualify the material NiCr23Co12Mo (Alloy 617) for outlet manifolds and superheater tubes in the steam generators of fossil-fueled power plants; this material, in fact, had been used in the past to line the combustion chamber of stationary gas turbines. The aim was to achieve 100,000 operating hour creep strength of approximately 100 MPa necessary for the purpose of designing steam power plants with net efficiencies of more than 50%. For tube walls exposed to hot flue gases on the combustion chamber side, the material temperatures are another 30–40 K higher than those of the main steam. They are also exposed to corrosive attack [47,48].

Important aspects for process (high-temperature thermomechanical treatment, weldability, bending properties) are still unknown.

The project ran from April 1999 until March 2003 and was assisted and managed on behalf of the VGB by the VGB Technical Committee "Materials and Quality Supervision." The project relates to others promoted by VGB in connection with "New Materials for Power Plants" (NWK). These concern materials for steam turbines, steam generators, and stationary gas turbines. The present project is being promoted as part of the materials program. "Materials of a Low CO_2 Power Plant" (MARCKO), organized by the German Federal Ministry for Economy (project no. 0327062). It is additionally funded by the Research Association of the Working Group of the Iron- and Metal-processing Industry e.V. (AVIF, project no. 130).

The series of MARCKO projects continued with the project called "Material Qualification for the 700/720°C Power Plant" (MARCKO 700). MARCKO 700 started in August 2004 and ended in June 2008. The project was executed Stuttgart Materials Testing Institute; MARCKO 700 helped qualify materials T24, 12 CrCoMo, and Alloy 617 for use in tubes and components, and T91, T92, and VM12 for use in membrane walls. MARCKO 700 started long-term creep rupture tests of components and welds.

24.4.1 Material qualification for the 700/720°C power plant (MARCKO 700) 2004–09

In the area of the steam generator, the main and key components are the thin-walled membrane wall and superheater tubes, as well as the thick-walled components header and pipe. For the membrane wall, the basic dates for the German material 7 CrMoVTiB10-10 are already on hand. This material is to cover the temperature window between 490 and 535°C material temperature. For temperatures above some

535°C, materials from the COST522-and MARCKO-DE2 program (12 CrCoMo and Alloy 617) are applied [55–57].

These materials have an increasing degree of complexity, ie, with regard to chemical composition and heat treatment, resulting from demands for time, and temperature-related strength/ductility.

While in the range up to 550°C, mainly low-alloy steels were applied, the long-term characteristics (strength, forming and creep) of which were well researched; this basis is available only deficiently for the martensitic steels, and for the nickel-based materials, it is fragmentary. Besides the mere codes, this relates mainly to the large-scale processing of the new materials.

The unacceptable economic as well as legal responsibility risk for the manufacturer, which is due to the high net product potential, ie, of a large boiler, can only be borne within the framework of a public support joint project.

The experimental investigations (creep and component tests) to be realized within the framework of this project will create the basis for the scientific evaluation of the long-term characteristics of the materials 7 CrMoVTiB 10-10, 12 CrCoMo, and Alloy 617 under operating conditions and thus for their licensing as construction materials in pressure vessel construction as per the European guideline for pressure vessels.

The project results were enabling planning of material-adapted recurring testing. Further, possibilities emerged to make use of modern methods for "Design by Analysis," which in contrast to standard design makes possible complete exploration of the material potential.

The project was executed MPA Stuttgart, from August 2004 to June 2008.

24.5 Electron beam welding (EBW)

TU Graz and Voest-alpine Giesserei Traisen are researching dissimilar metal welding (DMW) using EBW. EBW has no filler material, shorter welding time, less machining time for joint preparation, and smaller fusion zone. Nickel Alloy 625 has been welded to 9% chromium steel CB2 using EBW; no defects have been found, and testing has shown good mechanical properties. Creep rupture tests are planned.

Working with the IMPACT project, Technical University of Graz and Technical University of Chemnitz are characterizing MARBN steel and the corresponding welding process.

24.6 KOMET 650

KOMET 650, also known as "Power station options: developments in materials and measurement techniques and tests under operating parameters at 650°C," was a wholly German joint research program that started the research on using steels in PCC plant with higher steam temperatures of 650°C and a correlating efficiency of >47%. KOMET650 ran from 1999 to 2008, and there were 15 individual projects in the areas of materials, measurement techniques, and modeling [58].

Small-scale tests were undertaken in the laboratory. Large-scale test were conducted at four steam loops placed in Westfalen PCC plant. Each steam loop tested 10 different materials at temperatures up to 650°C and pressures up to 19 MPa. The total cost of the project was 10 MEuro, which was funded through COORETEC. KOMET650 was made up of 12 companies that published four reports; the findings are summarized in the following sections.

Investigations of the operational behavior of boiler materials and their welded joints at temperatures up to 650°C: This report details the findings from the four steam loops that were placed in Westfalen PCC plant. The steam loops tested numerous materials for use in superheaters.

The investigations found the following practical material limits with respect to steam temperature:

- <550°C for martensitic grades E911 and NF 616
- <570°C for austenitic grades 1.4910, 1.4941, Esshête 1250, and Super 304 H
- <600°C for austenitic Grade TP347HFG
- <620°C for austenitic Grade NF709
- <630°C for austenitic Grade AC66
- >630°C for nickel alloy A617

Findings on the operational behavior of the pipe materials used, and assessment of the overall design in the light of the current regulations: The object was to determine material and component behavior at elbows in various heat-resistant materials and their welded joints, and then to examine the design and measurement principles under realistic operating conditions for steam pipes in the temperature range to 650°C. A steam pipe was fabricated from a selection of martensitic and nickel alloys, with elbow, DMW, and similar welds. The pipe was installed in the Westfalen PCC plant and tested for 8 years (22,170 h). This study concluded that it is still relevant to test the creep deformation for the 9% chromium steels using the "replication method" surface microstructure testing.

Realistic estimates of pipeline life can be obtained only on the basis of pipeline monitoring. A pipeline monitoring process should at least ensure that the average relaxation level can be estimated and that the mounting components, such as hangers and springs, can be checked.

Investigation of materials for use in steam turbines at temperatures up to 650°C: A bypass of steam taken from the test pipe section installed in Westfalen PCC plant was directed onto test pieces installed in two modules: one at 620°C and the other at 650°C. After a year of operation the test pieces were removed and examined using metallographic and scanning electron microscope. The study concluded that steels, especially ferritic and martensitic steels, have a linear growth rate of oxidation and subsequent spallation. As the temperature rises, the oxide layer becomes too thick for operation; this is known as the practical limit. The practical limit for 9–12% chromium martensitic steels is <600°C and for austenitic steels is <620°C. However, initial results have shown that surface treatments, such as coatings, could possibly increase the practical limit of steels.

Operational experience with control valves in the high-temperature range: This project investigated whether the tried and tested materials and fabrication methods

for valves operating at 610°C could be used at 650°C. Thermal shock is a problem for valves as they are made up of components that vary in design, fabrication method, and material: the valve body is a large thick-section component. Two valves were installed in parallel on a bypass of the testing loop of Westfalen PCC plant. Numerous experimental and mathematical investigations into the long-term resilience and operating safety of control valves showed that reliable and safe valves can be produced for steam parameters of 650°C and 18 MPa using material 1.4905 for the valve spindle and material 2.8877 for the piston rings, control, and throttle elements.

KOMET650 concluded that, of the materials tested, steels have a practical limit of 630°C, whereas nickel alloys are suitable for temperatures above 630°C. KOMET650 provided information that will facilitate the development and operation of A-USC technology.

24.7 HWT I

The project HWT I (Hochtemperatur Werkstoff Teststrecke) or high-temperature material tests track is titled "Investigation of the long-term service behavior of tubes for the future high-efficiency power plant." HWT I has installed four test loops in a commercial boiler, unit 6 at GKM PCC plant near Mannheim (Germany). This boiler has a peak temperature of 1260°C, and the test loop will produce steam at 725°C and 16 MPa at a flow rate of 0.32 kg/s. Forty-three different alloys are used; there are three martensitic steels and nine austenitic steels in the first loop; 11 austenitic and three nickel alloys in the second loop; three austenitic and seven nickel in the third loop; and finally seven nickel alloys in the last loop. All aspects of fireside corrosion, steam-side oxidation, DMW, and similar welds with various fabrication methods and designs are planned to be assessed.

Additionally, there are two external loops undergoing creep rupture tests with live steam at 630°C and 725°C testing 10 austenitic steels and nickel alloys. HWT I started in 2008 and with scheduled conclusion in 2015.

Information gathered from the privately funded HWT I project will be used to qualify new superheater materials. Organizations involved include MPA University of Stuttgart, eight manufacturers, two inspection authorities, and four utility companies [61,62].

24.8 Post AD700

Collectively, the AD700 program and the KOMET and MARCKO projects have successfully demonstrated manufacturability of critical components from nickel alloys and assessed their behavior at higher steam parameters with some excellent results. However, the cracking of thick-section nickel alloys must be overcome, manufacturing costs reduced, fireside corrosion under biomass and waste co-firing assessed, performance under static operation to severe cyclic operation guaranteed, and 650°C steels developed to significantly improve the economics of A-USC technology.

The issues are being tackled in AD700 that continues under the names of COMTES+ (ENCIO and HWTII), NextGenPower, and MACPLUS.

24.9 COMTES+

After completion in 2011, COMTES700 has evolved into COMTES700+, set up by VGB, to further qualify candidate A-USC materials in two projects called ENCIO and HWT I-II. COMTES+ will reuse components from COMTES700. Results from COMTES+ are expected by 2017 and should generate all the knowledge necessary to design, build, and operate an FSDP. Together these projects have a budget of approximately 70 MEuro, partly funded by the EC under FP7 [61,63].

24.9.1 Examination of operational and failure behavior of thick-walled components for high-efficiency power plants (HWT II)

HWT II primarily investigates the operation and failure behavior of thick-section components under base load and cyclic operation. The work was completed in a test loop at GKM PCC plant (Germany). HWT II started in January 2011 and was planned to end by December 2014. There are 28 European partners, and it is funded by industry (generating companies, equipment and material suppliers, and inspection authorities involved) and the German government through COORETEC with a budget of 17.6 MEuro.

Steam extracted from Unit 6 at 530°C is heated to 725°C in superheaters fabricated from materials P92, DMV310, A263, IN740, and A617B. The superheater pipes IN740 and A617B are welded to a header fabricated from A617B and A263, respectively. A bypass valve is installed after the header to release steam out of the test loop in case of an emergency. To avoid cracking of the HP bypass valve, the valve has been redesigned and PWHT is used. The valve is of "flow to open design," and the valve body is forged from A617B and weighs 2.6 tons and allows 2.75 kg/s of steam flow. The bypass piping includes a pressure reducing and de-superheating system, which is a process where the temperature of the superheated steam temperature is reduced, using valves and water injection. From the bypass valve, the steam at 725°C passes through a bent pipe extruded from A617B or A263 with an outside diameter of 200 mm and a wall thickness of 50 mm.

Fig. 24.20 shows some components realized and installed in the GKM test loop.

The steam can then be cooled by water injection and a steam cooler to at least 307°C and 2 MPa, to simulate startup and shutdown procedures and definitive cycling conditions. Two steam control valves from Bopp & Reuter and Welland & Tuxhorn will be used to do this. The steam then passes through a straight pipe extruded from A617B or A263 with an outside diameter of 219.1 mm and a wall thickness of 50 mm. After the pipe the steam is passed through two control valves. Finally, the steam at less than 400°C then goes into the reheater tubing. Operation of the test loop started in October 2012 [60,61,64,65].

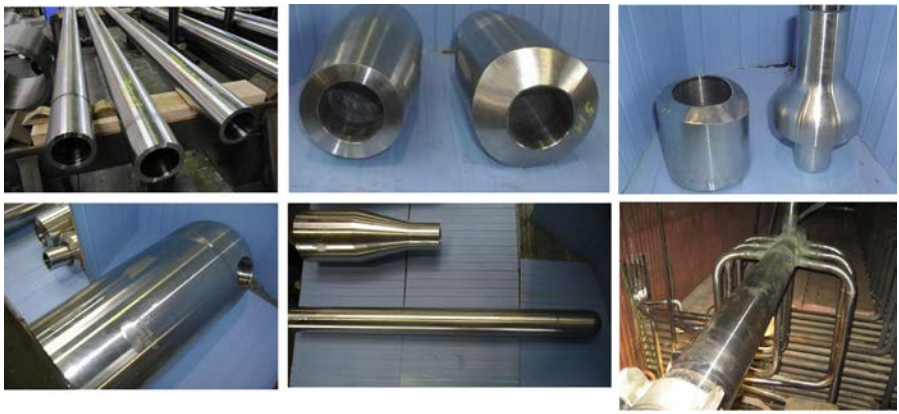


Figure 24.20 Tubes, fittings, nozzle, reducer, transverse nozzle, transition piece, and hemisphere-shape piece [59].

The key goal of HWT II is to concentrate together with the ENCIO project all scientific and technological efforts to make 700°C technologies ready for deployment in coal-fired power plants. HWT II is an important step before the erection of a 700°C power plant can start.

This step consists of the installation of a test facility at the GKM power plant in Mannheim (Germany). The project is focused on scientific investigations, aiming at modeling the material and component behavior and the validation of these results by means of specific designed component tests. Cyclic startup and shutdown loading cause thermomechanical creep-fatigue in the material and thus delivers results about the failure behavior of components in a flexibly operated power plant [66].

The technical concept of the test facility is as follows:

- Steam from Unit 6 (530°C, 167.5 bar) will be heated up in the steam generator up to 725°C. In the test facility, the temperature can be controlled by water injection to reach a temperature range between 400 and 725°C (definitive cycling conditions). Before going back to the reheater of the unit, the steam will be cooled down with injection water and a steam cooler to at least 307°C. The pressure will be released down to 22 bar.
- In the bypass of the test facility a very big bypass valve from Hora will be installed. Besides the function of the valve to release the steam in a case of emergency, the main focus is to verify the production process of such a valve.
- Dependent on the temperatures, the superheater tubes are out of martensitic steel (P92), austenitic steel (DMV310), and nickel-based alloys (A263, A617B). The thick-walled pipes have an outer diameter of 200 mm and a wall thickness of 50 mm and are out of A617B and A263. A header (A263 and A617B) with tubes (IN740 and A617B) is integrated in this pipe. In the rear part of the test facility, a transient load (cycling temperature between 400 and 725°C) is foreseen.

The project is financed by the industry and the German Ministry of Economics and Technology. The industrial fund consists of contributions of generating companies, equipment and material suppliers, and inspection authorities involved in the project. GKM is contractor to the BMWi.

Full partners are research institutes, equipment and material suppliers, and the companies BASF, EnBW, ENT, GKM, MVV, and VGB, representing the following generators: CEZ, EDF, ENEL, Eskom, Evonik, EVN, GDF Suez, RWE, and Vattenfall.

Other partners are ABB, BBS, BGH, BHR, Bopp & Reuther, Böhler, EagleBurgmann, IfW, IWM, KAM, KSB, Lisega, MPA Stuttgart, RWTH Aachen, Saarschmiede, SLV, SMST, TÜV, ThyssenKrupp VDM, V&M, Wrede & Niedecken, and Welland & Tuxhorn.

The project has started in January 2011 and the operation in September 2012. The overall project duration is 4 years (48 months).

A two-day workshop was organized in February 2013 at SLV/GKM in Mannheim to present the result mainly regarding the manufacture of the components and relative installation in the loop.

24.9.1.1 Results of the test loop

The test loop (HWT II) with thick-walled boiler components was operated successfully to yield experience on the material behavior and the functionality of the components in the commercial power plant GKM in Mannheim (Fig. 24.21) [67].

The test rig was aimed toward the material behavior of thick-walled pipes under cyclic loading conditions with additional superimposed secondary stresses. By injection of cooling steam and water, 14 thermal load cycles between 400 and 725°C per day were achieved.

The test rig reached the allotted number of load cycles and was taken out of operation in spring 2014. The operation time of 9900 h at temperatures (>700°C) and 2638 thermal cycles were reached in total. Before operation of the test loop, the qualification of manufacturing processes for all of the components used in the test rig were performed. In the case of the bending process (Fig. 24.22(a)), an optimization of the procedures avoided the creation of surface defects during bending, and systematic

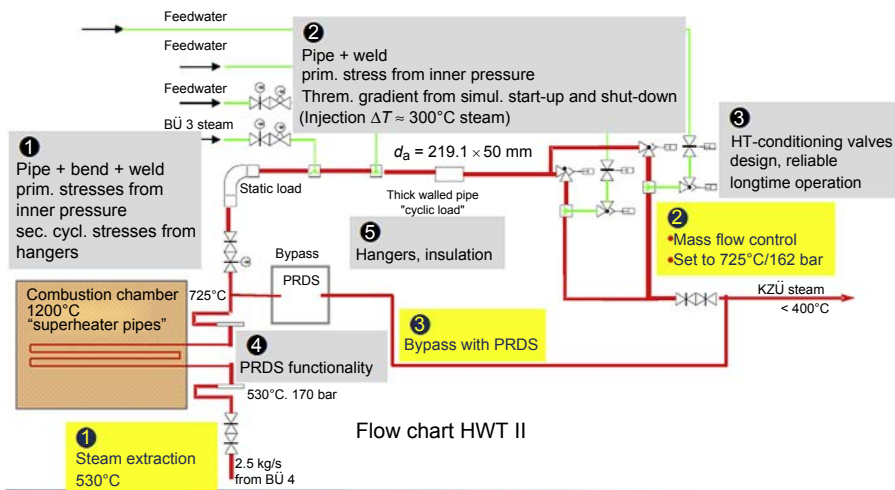


Figure 24.21 Flow chart of HWT II test loop with thick-walled pipes, bends, T-piece, valves, and header made from Alloy 617 modified and Alloy 263 [68].

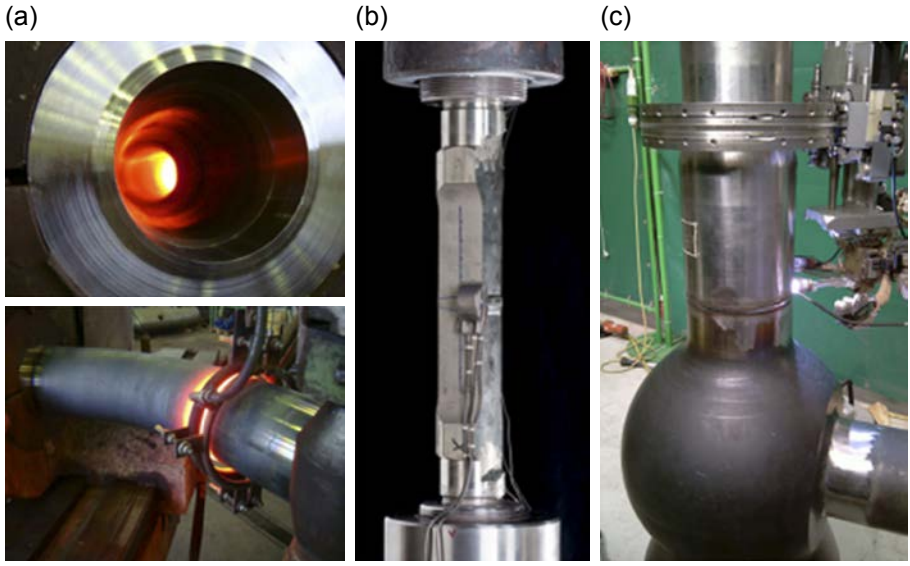


Figure 24.22 (a) Pipe made of Alloy 617 modified (mod.) during inductive bending (Kraftanlagen Mínchen GmbH); (b) large sample tests of test rig welds; (c) high-pressure (HP) steam bypass valve (provided by E.ON) made of Alloy 617 mod. [69].

adjustment of the process parameters resulted in the evaluation of sensitivity of the process. In addition, nondestructive testing (NDT) methods (eg, ultrasonic testing, UT) was performed and adapted. To evaluate the welding process, large-scale samples including the complete weld were prepared using the same welding parameters, materials, and heat treatments as with the welds in the field test (Fig. 24.22(b)). These welds were tested prior to the test rig operation to prevent premature failure. This was particularly important because, in the test loop, many components must be joined together by welding processes, such as the valve shown in Fig. 24.22(c).

Due to the optimization of the welding processes (eg, tungsten inert gas welding or manual metal arc welding), it was possible to avoid specific welding defects, increase the effectiveness of the welding procedures, and improve process security. The key components in the test loop were thick-walled pipes, bends, a T-piece, different types of valves, and a header (Figs. 24.23 and 24.24(a)). Due to the instrumentation of the selected components by the application of more than 70 thermocouples for temperature recording and 16 strain gauges for deformation measurement, online monitoring during the total operation duration was ensured.

Using the constitutive equations established, numerical simulations of the components were performed to determine the distributions of the stresses and strains as the basis for the lifetime assessment of the components. The validation of material models was performed by the comparison of the field measurement with the simulation results. Using the example of sample header (Fig. 24.24), the validations of the numerical models were performed. The header was manufactured from thick-walled pipes made of A617m and A263 with dimensions of OD = 220 mm × WT = 50 mm. The pipes

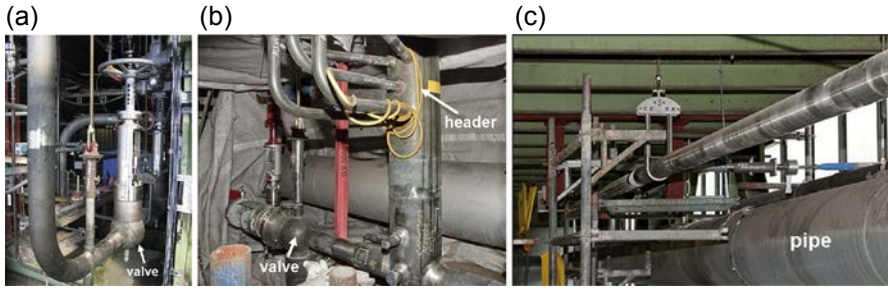


Figure 24.23 (a) Stop valve (provided by KSB AG); (b) control valve (provided by Welland & Tuxhorn AG) and header (provided by Alstom); (c) thick-walled pipe with support construction [67].

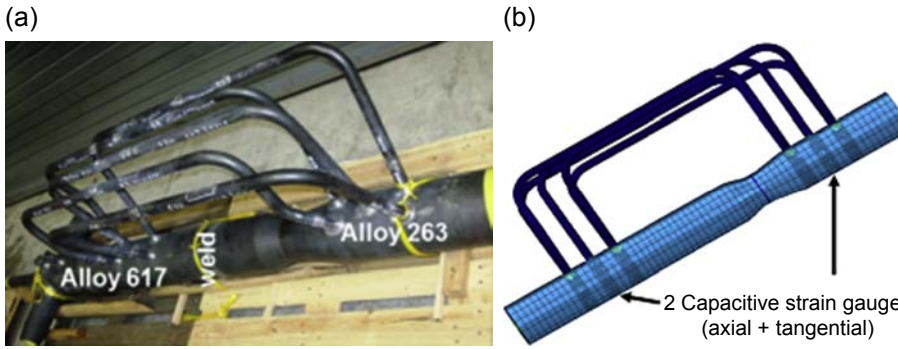


Figure 24.24 (a) Header included in the part of the test loop made of Alloy 617 modified and Alloy 263 before operation [67]; (b) FE model of the header [69].

were forged, hollow-bored, and welded to each other [69]. As shown in Fig. 24.27, a relatively good agreement of the strain development (tangential direction) from the measurement (Fig. 24.24(b)) and from the simulation was achieved. The temperature development from the simulation corresponds also well with the measured values.

Further improvement of the simulation results are expected with ongoing calculations by using a constitutive equation with kinematic hardening. Using the material data and numerical tools developed, it is possible to perform the analysis assessment of the components. The validation of material models was performed by the comparison of the field measurement with the simulation results. Using the example of sample header (Fig. 24.24(a)), the validations of the numerical models were performed. The header was manufactured from thick-walled pipes made of A617m and A263 with dimensions of OD = 220 mm × WT = 50 mm. The pipes were forged, hollow-bored, and welded to each other [69].

As shown in Fig. 24.25, a relatively good agreement of the strain development (tangential direction) from the measurement (Fig. 24.24(b)) and from the simulation was achieved. The temperature development from the simulation corresponds also well with the measured values. Further improvement of the simulation results are expected with ongoing

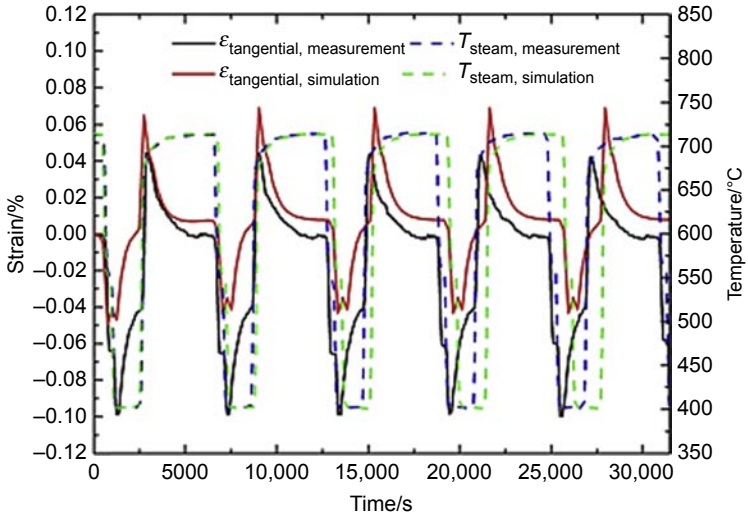


Figure 24.25 Development of the strain and the steam temperature, as well as a comparison of the simulation using viscoplastic model and the measurement on the header from the test loop [69].

calculations by using a constitutive equation with kinematic hardening. Using the material data and numerical tools developed, it is possible to perform the analysis to estimate the lifetime of the component. An example from the test loop is shown in Fig. 24.26(a). After the modeling of the components, the critical areas can be identified (Fig. 24.26(b)).

Depending on the approaches used (stress- or strain-based methods as such as ASME, RCC-MR, or the recommendations of R5 and DIN EN12952-3/4 for the assessment of components under creep-fatigue loading), the stresses or strains were identified at the critical areas in the component and assessed for comparison with the material data. If for example, a strain-based approach is used, the allowable cycles can be determined using design fatigue curves (Fig. 24.27).

24.9.1.2 Conclusions

Investigations aimed to provide data and tools to aid in the design and lifetime assessments of components of an A-USC plant made from nickel-based alloys have been carried out. After testing within the framework of a few different projects, a reasonable database to characterize the materials under investigation was established. This database comprises pedigree data, creep data, information on cyclic behavior and failure, as well as fracture mechanics data. Constitutive equations for the simulation of static creep and thermal cyclic load were established, and the parameters were approximated. A test loop using thick-walled boiler components was operated successfully to yield information on the material behavior in the plant and the functionality of components. Using the constitutive equations that were established, numerical simulations have been performed with the aim to predict lifetime of the components. As a conclusion, valuable data and tools have been established for the assessment of components made of nickel alloys, as particularly relevant for use in high-efficiency power plants.

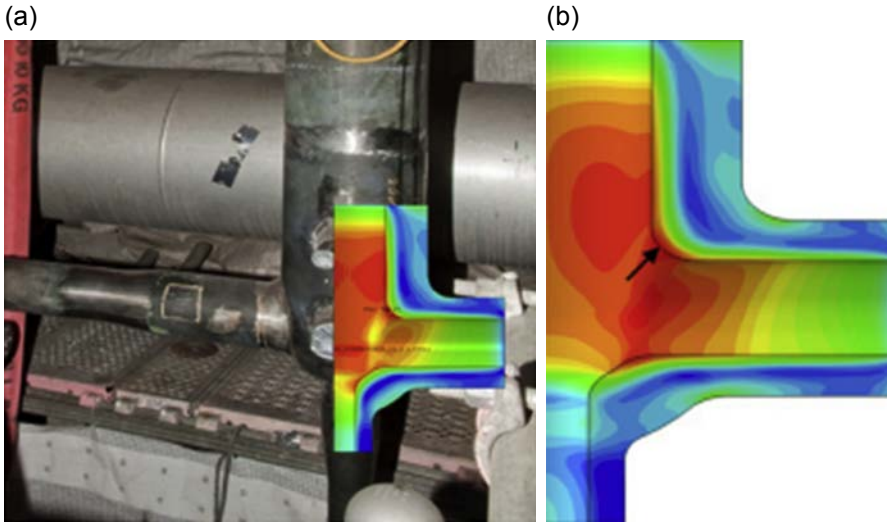


Figure 24.26 (a) Ball-shaped forging made of Alloy 617 modified and (b) contour plot of equivalent von Mises stress in a ball-shaped forging [69].

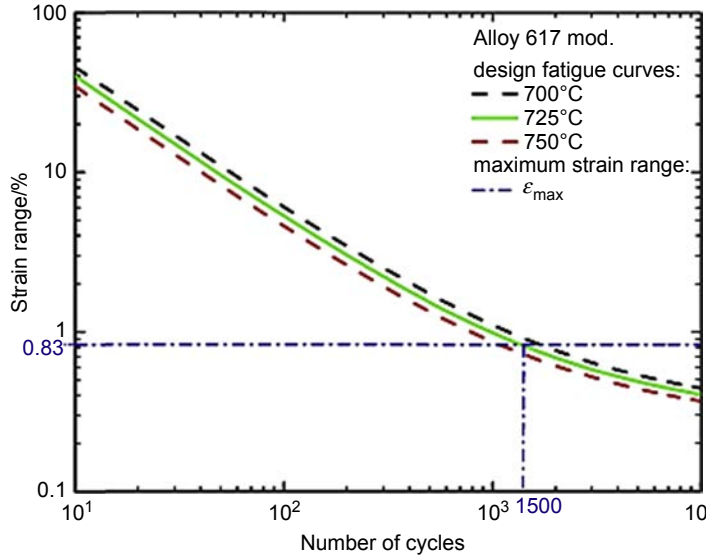


Figure 24.27 Number of allowable cycles according to Manson-Coffin evaluation [67].

24.9.2 ENCIO

In the ENCIO project, scientific and technological efforts aim to the successful deployment of 700°C technology in coal-fired power plants. The key elements of ENCIO were the installation and operation of a test facility in Fusina, at an ENEL power plant in Italy. The project focus was on applied research seeking improved agility, weldability, serviceability, and durability of thick-walled parts, and studies of

materials subjected to static and cyclical (start/stop) loads, and on practical investigations, aiming at proving manufacturing, welding, repair, and lifetime concepts for up to 140 mm thick-section nickel alloy components for a long lifetime. The ultimate goal was transitioning from experimental technology to a trial plant as the final step toward a 700°C power plan [70]. The work was completed using test loops in a new test facility operating at 700°C, 17.7 MPa, and 5 kg/s flow rate of steam.

The ENCIO project started in 2011 and is expected to finish in 2017: 6 years allowing enough operating hours, as well as related data collection, investigations, and evaluation of results.

The program was interrupted in December 2013.

24.9.2.1 Motivation

Europe is still in the global lead for the 700°C technology in the field of fossil fuel–based power generation. To continue with this successful technology development, ENCIO was an important step to deploy this technology and to remain competitive. Therefore a group, representing the leading European power generators and equipment suppliers, has increased its efforts to speed up the evaluation and assessment process out of COMTES700. The 700°C technology is a key factor:

- increasing efficiency of coal-fired power plants
- improving environmental and economic sustainability of coal-fired power plants
- achieving successful deployment of carbon capture technologies

The strategic importance of these R&D activities is evident for the electricity sector. The integration of the renewables is one of the top priorities of European policy. The consequence for the electricity supply system is that an appropriate balance between intermitting and dispatchable generation is absolutely necessary. The fossil fuel–based power generation provides the backup power and grid control function that are necessary to ensure that the targeted contribution of renewable resources to the electricity generation portfolio can be achieved.

It is expected that the price of electricity will increase further as soon as the RES share, the demand for reliable backup power, as well as the global demand for coal will increase. Different investigations in forecasting the evolution of the electricity sector, in Europe and worldwide, show that beyond 2025 the commercial viability will be given that would fit into the time line of the technical maturity of both 700°C technology and carbon capture and storage technologies.

24.9.2.2 Objectives

The experimental, demonstrational, and investigational activities of ENCIO pursue the following targets:

- provide proof of design and material behavior of thick-walled components under real operating conditions,
- close main technical open items derived out of the comprehensive analysis of COMTES700,
- test new developed materials and manufacturing options (eg, post-weld heat treatments) to improve the reliability of weldments made out of Ni-based alloys,

- develop a lifetime monitoring concept for pipes made out of Ni-based alloys,
- explore materials and manufacturing options having the potential to reduce the investment cost of 700°C technology and improve the load change behavior,
- verify the technical conditions for achieving high efficiency and better environmental figures (lower emissions).

24.9.2.3 Host plant

The ENCIO test facility was planned to be installed in the "Andrea Palladio" Power Station, which is owned and operated by ENEL, located in Fusina, very close to Venice (Italy). Unit 4 was selected for the installation of the test facility.



This unit has the following characteristics:

- boiler type: two-pass boiler
- burner configuration: tangential
- steam capacity: 1050 t/h
- production capacity: 320 MWe
- fuel: hard coal + refuse derived fuel
- superheater steam temperature: 540°C
- superheater steam pressure: 177 bar

24.9.2.4 Technical concept diagram

Fig. 24.28 shows the flow chart of the loops.

The overall process design ensured that individual test loops do not affect the overall reliability of the system. Test loops were expected to be installed in parallel to the main steam process, and they can be running independently of each other. This made it possible to exclude one test loop, independently to the others, in case of problems or failures of tested components. This reliable process design seeks for getting a reduced impact on main boiler operations, while it also allows to keep running other test loops if one of them was to be stopped due to failures.

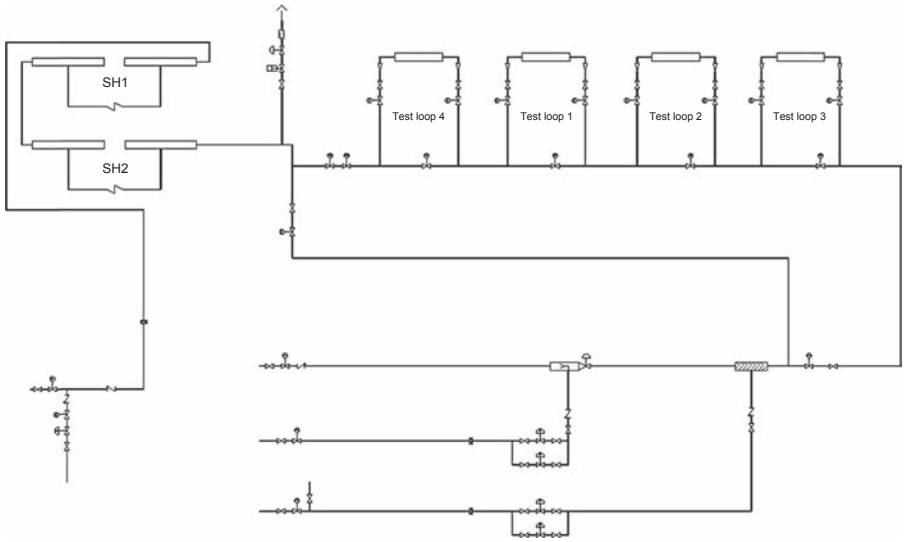


Figure 24.28 Schematic process flow diagram of the ENCIO test facility.

The technical targets of the test loops were these:

- Test loop 1: Development of pipe repair concept; this loop simulated a pipe repair situation. This task involves basic investigations to characterize the aged materials followed by repair welds that were used to optimize welding procedure specifications (tungsten inert gas (TIG) welding with PWHT).
- Test loop 2: Test of hot isostatic pressing (HIP) parts and weldments as well as lifetime monitoring; this loop is used for online monitoring and measuring the creep behavior of Alloy 617B to develop a monitoring concept for nickel alloy pipes. This loop is used to test components, such as T-pieces, valve bodies, and turbine components that have been fabricated using HIP, which is a commercial manufacturing process where materials are placed in an inert atmosphere in a pressure containment vessel for a certain amount of time. The material undergoes plastic deformation, creep, and diffusion bonding, which eliminate internal voids and micro-porosity, and this increase the density of material, which improves the materials properties, such as workability and fatigue resistance.
- Test loop 3: New materials for thick-section components test of different Ni-based alloys and weldments; this loop explored possible improvements in weldability of Alloy 617 by means of improved melting processes to reduce the amount of impurities within the ingot.
- Test loop 4: Testing of turbine cast components and welds; this loop aimed to prove full-scale welds between thick-section Alloy 617 OCC and Alloy 625 cast (this weld is found in the steam turbine).

24.9.2.5 Organization and funding

The ENCIO project was financed by industrial and public funds. The project received funding from the European Community's RFCS under grant agreement no. RFCPCT-2011-00003.

The industrial fund consisted of contributions of generating companies and of equipment and materials suppliers. The generating companies were CEZ, EDF, EnBW

Kraftwerke, ENEL, E.ON New Building & Technology, Eskom Generation Business Engineering, Evonik Energy Services, EVN, GDF Suez, GKM, RWE Power, and Vattenfall Europe Generation (SE/DE).

The equipment and material suppliers were Böhler Schweißtechnik, Holter Regelarmaturen & Co. KG, Sandvik, Sempell, Siemens, Sumitomo, ThyssenKrupp VDM, V&M Vallourec & Mannesmann Tubes, and Voestalpine Giessen Traisen.

The leading partners, who executed the activities in the ENCIO project, are VGB PowerTech as coordinator, Centro Sviluppo Materiali, ENEL Ingegneria e Innovazione, ENEL Produzione, and Hitachi Power Europe.

The total budget of ENCIO was 24 MEuro: this includes 10 MEuro provided from the RFCS and 14 MEuro of industrial funds.

24.9.2.6 Results

The general objective of ENCIO was to test Ni-based components to make 700°C power plant technology ready for deployment. Some technical problems in new materials and/or manufacturing methods generated delay, and the start of test facility operation would be in 2014, 1 year later than scheduled. An additional manufacturing of tubes for the superheaters was raised to question to be successful, and also further technical problems could not be excluded. The project was thus terminated by the COMTES700+ community on December 2013 before the commissioning of the test facility (TF) [71–73].

The following results have been obtained before the major part of the project was closed in December 2013:

- Qualified welding methods (WPQR) were performed for service exposed Alloy 617 B, and monolithic valve bodies were manufactured to reduce weld failure.
- HIP pipes of A617 LCC, leak before rupture behavior is expected during operation.
- Superheater tubes can be manufactured, cold bended, and welded for a demonstration power plant in dimensions, with a corrosion margin for a lifetime of 200,000 h.
- Pipes made from A617 occ (optimized chemical composition) and A263 can be produced by hot pilgering.
- The qualification processes of Ni-based components are established. Volumetric inspection methods like linear accelerator or ultrasonic test (LINAC or UT) are sensitive in the detection of discontinuities, but the minimum detectable and critical flaw size still has to be determined.
- Turbine casing material A625C has to be enhanced with regard to ductility and porosity.
- Test loop components from the A617 family (A617mod, A617B, A617occ, and HIP A617LCC) passed the European and Nationals regulations and would be only installed.

24.9.3 Study on the long-term operating behavior of alloy pipes and forgings for future high-efficiency power plants

In this project (2008–15), a test facility will be constructed especially suited to assess fatigue of safety- and operation-relevant components. Moreover, to determine the failure safety margin, current and future findings from parallel research projects (COORETEC, MARCKO700) on damage development as well as related characteristic values and material laws are to be validated by field trial [74].

The test facility, which has been designed for installation in a power plant of GKM Mannheim, comprises a **superheater test section** that is located within the

boiler and has a temperature of up to 725°C as well as components of two **turbine and creep test sections** that are located outside the boiler and have a temperature of 630 and 725°C, respectively. The study focuses on a temperature of 725°C. However, the 630°C sections can also make an important contribution as a better understanding of steel behavior at 630°C will help to minimize the use of expensive nickel-based materials:

- The **superheater test section** is used to measure the metal temperature of the materials used to assess their influence on the corrosion and oxidation behavior on the steam side. The section is designed for 200,000 h. At the end of the project period, samples are to be taken.
- The **creep test sections** have pipe sections installed that are subjected to internal pressure so as to result in failure after 50,000 h. The wall strength is adapted to this objective. Adequate tools and calculations ensure that the pipe sections will be removed before failure. Operation is accompanied by parallel or running ahead creep tests. At the end of the project, samples are taken and subjected to a metallographic test.
- The **turbine test sections** consist of one pipe each of a major diameter in which small plates made of turbine and boiler materials are exposed to the steam flow. This is to investigate the oxidation strength of the steam turbine materials. It is planned to change sample materials during operation.

The range of materials used (including coatings) extends from ferritic materials through to nickel-based alloys (T24, T92, VM12, TEMPALOY AA1 SB, NF709, NF709R, HR3C, DMV310N, TEMPALOY A3, Sanicro25, Mod. HR6W, S304H SB, DMV304HCU SB, A617mod, IN740, XA704 Mod. SAVE12, Sumitomo New 18/8 Stainless Steel, Sumitomo New Ni Alloy, P92, FB2, CB2, St17/13W, and coatings on 9% Cr steels and Ni-base alloys).

Moreover, in terms of availability, valves and fittings are tested for internal and external tightness as well as operability of components. With regard to the HP bypass system with a steam velocity higher than in a conventional bypass system, it is of special interest to determine the erosion behavior of the Alloy 617.

Within the framework of the project, maintenance and testing strategies are to be developed for the 700°C power plant.

The project started in January 2008 and finished at the end of 2015. Four partners were responsible for project management: GKM Mannheim; MPA Stuttgart; Alstom Power Systems; and EnBW Kraftwerke.

Other companies involved in project work were ABB, Bopp & Reuther Sicherheits und Regelarmaturen, Burgmann Industries & Co KG, BHR Hochdruck-Rohrleitungsbau, KSB, Schweißtechnische Lehr und Versuchsanstalt Mannheim, TÜV SÜD Industrie Service, and Welland & Tuxhorn.

The project is co-financed by the German Federal Ministry of Economics to a considerable extent (grant no. 0327799). Industry mainly contributes its own work and services. GKM, EnBW, MVV, Kraftanlagen München, and VGB participate in the financing.

With the Chairman of the VGB Technical Committee Materials and Quality Supervision being one of the four project managers, a close link between the project work and the VGB is ensured.

24.10 NextGenPower

NextGenPower (SP0) is a project that aims to demonstrate the fabrication and utilization of nickel alloys and material coatings for use in boiler, pipework, and steam turbines in A-USC PCC plants. The NextGenPower project began in May 2010, and it was planned to end in 2014.

24.10.1 Project details

- budget: 10.3 MEuro with EU contribution of 6 MEuro
- funding scheme: collaborative project, large-scale integrating project
- topic: energy.2009.6.1.1 efficiency increases in existing and new build pulverized coal-fired power plants with a view to CCS
- contract no: ENER/FP7EN/249745/"NEXTGENPOWER"

Partners of NextGenPower include VTT (FL), DNV KEMA, E.ON Benelux, Doosan Power Systems, Monitor Coatings, Goodwin Steel Castings, Cranfield University, Aubert & Duval, Saarschmiede, Technical University Darmstadt, Skoda, and VUZ welding repair institute [75].

NextGenPower is managed and coordinated by DNV KEMA.

The schematic overview and partnership of the project and the project organization are shown in Fig. 24.29 [75].

The following bullet points explain how the project is divided:

- **SP1 boiler and pipework** (leader Doosan and Babcock): Using coated steels in the boiler and heat exchangers could be a cheaper alternative than using nickel alloys. This project will assess the application method, welding compatibility (thus ability to be repaired or replaced), and performance of steel coatings in fireside and steam-side corrosion. Mechanical tests are proposed to quantify the life expectancy of coated steels. These tests include creep, low-cycle fatigue, low-cycle fatigue with dwell, notched relaxation, cyclic notched tests, slow strain rate tensile tests, fracture toughness, and hardness. Tests will be conducted selectively upon parent metal, weld metal, cross weld, longitudinal weld, and service simulated material.

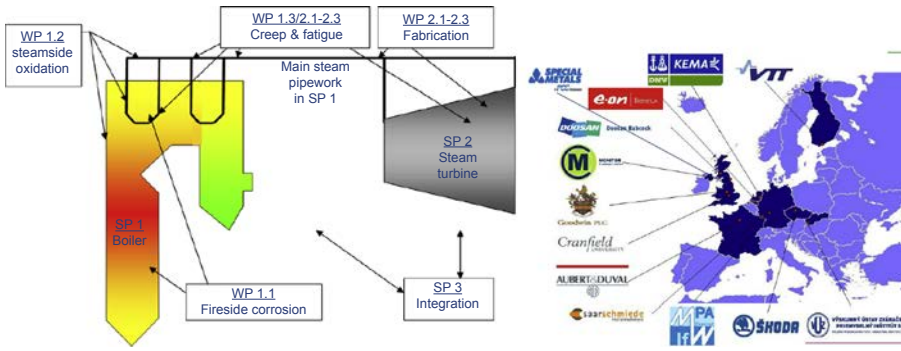


Figure 24.29 Schematic overview and partnership of the project.

Projects include WP1.1 fireside corrosion of membrane walls and superheaters (DNV KEMA), WP1.2 steam-side oxidation in boiler (Cranfield Univ.), and WP1.3 creep and fatigue of tubes, pipework, and steam turbine (Doosan and Babcock).

- **SP2 Steam turbine** (leader Skoda): The project aim is to demonstrate the capability to cast, forge, and weld nickel alloys for rotors, casings, and valve chests. A program of mechanical tests is scheduled to be carried out to verify component properties. Nondestructive inspection techniques will be optimized and qualified. For nickel alloys, steam-side oxidation is negligible, and the mechanical properties can be modeled on the basis of the material composition.

Projects include WP2.1 casting (Goodwin Casting), WP2.2 rotor welding (Skoda); and WP2.3 forging (Saarschmiede).

- **SP3 Integration** (DNV KEMA): The main objective of SP3 is to integrate the work done in SP1 and SP2 and to make sure that at a later stage results can be integrated into the power plant.

Projects include WP3.1 operating conditions and environments (DNV KEMA), WP3.2 integration in power plants (DNV KEMA), and WP3.3 modeling and case studies (Cranfield Univ.).

- **SP4 Dissemination** (DNV KEMA).

24.10.2 Material choice: boiler

The target components were the main steam pipework and superheater outlet headers. These thick-section components are subject to creep, fatigue, and creep-fatigue interaction. The A263, having 30% higher creep strength of similarly priced A617 (Fig. 24.30), was considered a better solution than A617 that is prone to relaxation cracking. IN740 was selected having improved corrosion resistance over A263 for heat exchange applications, and at 750°C, IN740 is stronger than A263 in thin sections. However, IN740 exhibited liquation cracking in the COMTES project and

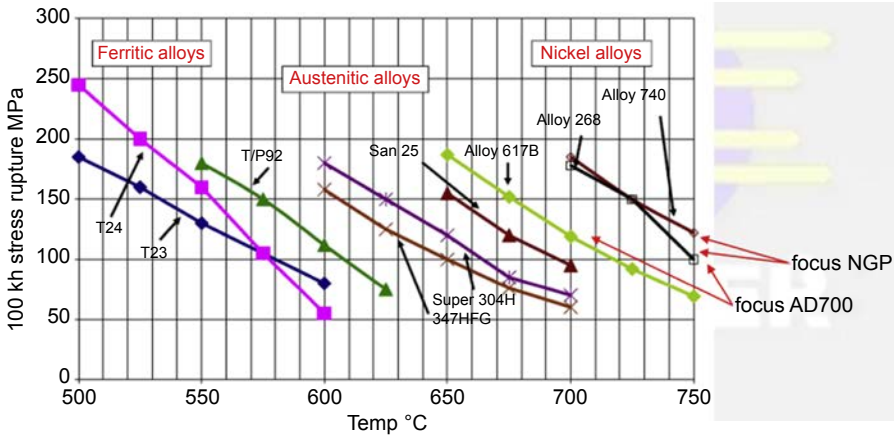


Figure 24.30 Creep properties of various materials [75].

therefore was found to be not suitable for thick-section steam pipes with welding. Based on aforementioned reasons, it was judged that A263 was the more reliable choice for use in thick-section components. Subsequently during this project, Special Metals have developed an upgraded version, IN740H, which they claim overcomes the problems of IN740 (see Chapter 14).

24.10.3 Fireside corrosion

The nickel superalloys are prone to sulfur attach–forming nickel sulfides: liquid eutectic above 635°C (compare iron and iron sulfide eutectic at 985°C). Nickel alloys are also subject to reaction with S and O at grain boundaries.

Nickel alloys are also affected by "hot corrosion": depositing elements (Na, K, S, Cl, Pb, Zn, Fe, Ca) can form low-melting eutectics well below 680°C. Its deposition depends on feedstock and operating conditions. The use of biomass (co-)firing may increase this effect.

24.10.4 Steam-side oxidation: background

The steam at high-temperature oxidizes internally the tube materials. The spallation of oxide flakes may cause blockage leading to overheating and/or erosion in the steam turbine. Ferritic and austenitic steels form Fe- and Cr-containing oxides that become less protective >600°C. Al additions to the alloy form alumina that is more stable than chromia above 700°C. Diffusion aluminide coatings are among the best performers and offer an economic benefit. While the use of Ni alloys will perform better than their ferritic and austenitic counterparts in steam, the long-term steam oxidation resistance has to be verified.

24.10.5 Mechanical issues

Relaxation cracking appears when residual stresses relax during PWHT or service. This problem generates low ductility with cracking within 3 years of operation. This issue was found previously with A617. Precipitates hinder relaxation and generate preferential relaxation in small precipitate-free zones along the grain boundaries with consequent intercrystalline cracking and brittle rupture.

Gas phase embrittlement is generated when hardening precipitates, eg, NbC, may oxidize and form CO_2 gas bubbles, forming intergranular cavities and generating cracking on grain boundaries leading to brittle failure. This issue is found with A718.

Negative creep has been recognized due to an ordering effect causing lattice contractions that can cause failure of bolts and fasteners. This effect was reported for various superalloys: Sanicro71, IN690, and Nimonic 80A.

24.10.6 Creep, fatigue, and creep/fatigue interaction/ background

In the 750°C temperature region, creep is an important failure mechanism, but now it is not the only failure mechanism to be taken in account. The renewables sources

are intermittent in nature and get priority; this forces coal plants to operate flexibly rather than at base load, as in the past. With flexible operation, ie, operation with changing load, fatigue is also becoming a more important failure mechanism; the interaction between creep and fatigue was investigated therefore as well as creep-fatigue that possibly leads to reduced component life. It was also shown in literature that creep-fatigue interaction on the welds can be much more severe than on the parent material.

24.10.7 Material selection (rotor forging and welding)

The main parameters for materials selection are the creep strength, the ability to fabricate full-scale forgings (eg, segregation sensitivity, forgeability, large-scale ingot manufacture), and the weldability. Initially selected materials on basis of creep strength were H230, A263, H282, IN625, IN706, IN718, Nimonic 901, IN740, IN740H, Waspaloy, and Nimonic 105.

Nimonic 105 dropped out due to low toughness; the weldability of IN740 and Waspalloy was considered problematic. Due to its commercial availability, low sensitivity for segregation, experience of the partners with the material, and ability to weld the material to 10 Cr steels, A263 was selected as the best option.

24.10.8 Rotor forging: alloy optimization

Eta (η) phase (intermetallic Ni_3Ti) precipitates arise in A263 after long-time aging. The η precipitates form at the expense of the hardening γ′ phase as large platelets extending across grains and have an effect on long-term creep behavior in superalloys. Aubert and Duval have optimized the composition of A263 to remove the η phase. More details of this work are presented in Chapter 17 [76].

24.10.9 Rotor: issues with forging precipitation hardening Ni alloys

The large-scale ingot manufacture is one of the main problems: a challenge in production of the full-size A263 rotor forging was the manufacturing of a large ingot without or at least marginal segregations during re-melting of the ingot by VAR and ESR.

24.10.10 Casting

The precipitation hardening materials are the most difficult materials to cast, due to the much higher shrinkage of Ni alloys then steels. It has taken more than 15 years to master the process of casting heavy-section material for solid-solution strengthening materials.

24.10.11 Highlights of results

In Fig. 24.31 are presented the prototype-produced components. A263 and IN740H showed good fireside corrosion resistance and steam-side oxidation resistance at



Figure 24.31 Mock-up components realized in the NextGenPower Program.

750°C, and creep, fatigue, and C-F properties of A263 at 750°C are so far satisfactory. The new A263 variant has been produced without detrimental eta phase and the largest forgings ever were produced in the world of precipitation hardening Ni alloy: 0.5-m diameter (A263 mod) and 1.0-m diameter (A263).

Welding of up to 1.0-m-diameter rotor A263 COST F with A263 in precipitation hardened condition has been realized.

A castable Ni-base precipitation hardened superalloy has been developed (G130) and is the largest casting (390 × 321 mm) of precipitation hardening Ni alloy ever produced in the world.

24.10.12 NextGenPower spin-off

- **Current use**
  - IN617, T92, T24 use in current state-of-the-art boilers that are under testing in this project
  - biomass (co-)firing fireside protection
  - exporting of components to China for test loops
- **Future use**
  - although much more renewable generation will be integrated in the grid, the use of coal is inevitable in the future power generation mix
  - generation has to be as efficient and flexible as possible
  - CCS is considered as non-attractive option
  - only solution if efficiency increases (by temperature increasing, thus stronger materials) and flexibility increases (by materials withstanding fatigue and C–F interaction)

24.11 MACPLUS

MACPLUS is an acronym for *ma*terial *c*omponent *p*erformance-driven solutions for *l*ong-term efficiency increase in *u*ltra-*s*upercritical power plants. MACPLUS will assess six aspects of A-USC technology via laboratory testing, industrial-scale test loops, and computer models.

MACPLUS started in January 2011 and was completed in June 2016. MACPLUS is carried out by a consortium of 24 partners and seven subcontractors from 10 European countries**:** Centro Sviluppo Materiali (IT) Coordinator; RWE Power (DE), EON

New Build & Technology (UK), Doosan Babcock (UK), Foster Wheeler Energia (FL), Tubacex (SP), TÜV Rheinland (DE), Cogne Acciai Speciali (IT), Flame Spray Hungary (H), TU Graz (AT), Welding Research Institute (SK), National Physical Laboratories (UK), Royal Technical University (SE), Loughborough University (UK), Fraunhofer Institute Freiburg (DE), Research Centre Juelich (DE), Endesa (SP), TU Denmark, Imperial College (UK), VTT (FL), Alstom (UK), Goodwin Steel Castings (UK), and MPA Stuttgart (DE).

The total budget is €18.2 million, of which €10.7 million is provided from the EC under seventh Framework Programme in the Energy area.

MACPLUS is split into the following work package [77,78]:

- WP1 (Foster Wheeler Energia) to investigate new refractory materials. Two possible solutions have been identified:
  - *functionally graded materials*
  - *modified refractory surface* (melting, cladding, and alloying) to reduce the surface porosity, by laser treatment
- WP2 (TTU Graz) to investigate new ferritic and martensitic steels (MARBN and FB2 mod) for use in headers and pipework to avoid premature type IV cracking of welds.
- WP3 (Centro Sviluppo Materiali) aims to understand the operational behavior of austenitic steels and nickel alloys in superheaters using laboratory specimens and materials from previous test loops, such as the AD700-3. Material modifications via fabrication and composition were assessed along with long-term behavior extrapolation via modeling. A superheater tube and welded joints of thick-section pipes fabricated from modified nickel alloy was fabricated and tested to demonstrate improved performance. Fig. 24.32 shows the trial production of austenitic tubes and laboratory Alloy 263 cast ingots. Tubes have been installed in RWE Power AG test rig [79].
- WP4 (Doosan Power Systems) to assess fabrication and application processes of multilayer and multi-material boiler tubes for application in aggressive fireside conditions. Tubes samples with different coating materials and technologies have been realized and exposed.
- WP5 (Alstom) to assess high-temperature components in a steam turbine using latest generation high-alloy steels for use at 620–670°C, like FB2/CB2, and nickel alloys at



Figure 24.32 Mock-up components realized in MACPLUS program.

670–720°C, like alloy 282. This will be completed via metallurgical-thermo-mechanical modeling and manufacturing. Fig. 24.33 shows the Alloy 282 forging and Fig. 24.34 the trial CB2 cast.

- WP6 (E.ON New Build & Technology) aims to develop advanced design and testing criteria for high-temperature components development, integration, and standardization into A-USC PCC plant. This work is planned to build on existing testing methods to identify future development needs.
- WP7 (Centro Sviluppo Materiali) for the coordination and dissemination of projects WP1–6.

24.11.1 MACPLUS-COMTES700/ETR/TV-cooperation

In the test rigs COMTES700 and Esbjerg Test Rig (ETR) as well as the Turbine Valve project within COMTES700 (TV), different high-temperature resistant materials were tested at temperatures up to 700°C for up to 22,400 h.

The aim of the MACPLUS cooperation is to carry out additional examinations of the material and use the results to develop a verified modeling for the precipitates over the lifetime. The results out of the examinations and modeling will be handed out to the COMTES700, ETR, and TV project partner [80].

The cooperation was started in 2012 and scheduled to be finished with the end of the MACPLUS project in 2016.

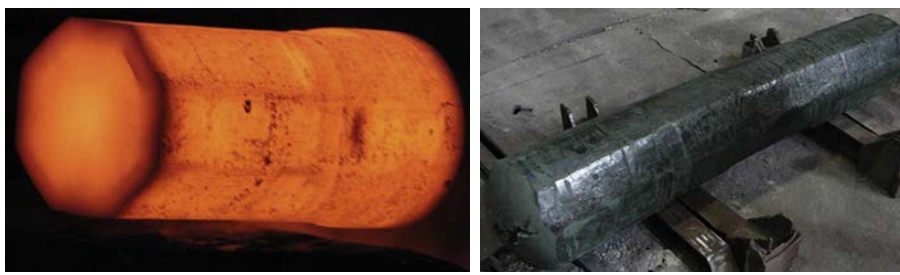


Figure 24.33 Alloy 282 mock-up forging manufacture [79].

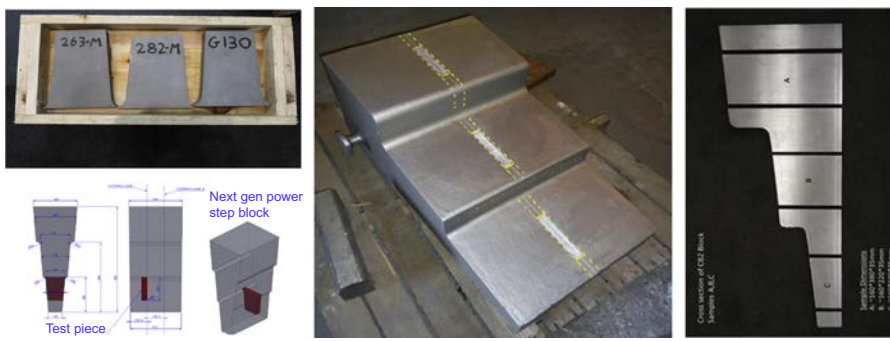


Figure 24.34 CB2 step block [79].

24.12 POEMA: production of coatings for new efficient and clean coal power plant materials

The overall objective of POEMA project is the development of new coatings to protect materials from the corrosion in supercritical steam power plants to increase efficient and clean coal utilization through higher temperature and pressure service, to reduce the emissions. From the mechanical properties perspective, ferritic steels can be used at temperatures up to 650°C, and for higher temperatures (700–750°C), austenitic steels and Ni-based alloys are being considered. Higher temperatures create steam oxidation and steam-grown oxide scales on the inside of tubing. Fireside corrosion is a synergistic effect among metal alloy materials, flue gas, and deposits. It is the leading cause of failure in coal-burning furnaces [81].

The project started in January 2016, and the end is scheduled for December 2016: the partnership is the following: University Complutense De Madrid (SP) (coordinator), TU Georgian, Fraunhofer Gesellschaft Zur Forderung Der Angewandten Forschung Ev (DE), University De La Rochelle (FR), Bundesanstalt Fuer Materialforschung Und Pruefung (DE), TU Chemnitz (DE), Heffield Hallam University (UK), Institute Nacional De Tecnica Aeroespacial (SP), Turbocoating (IT), "G.V. Kurdyumov Institute For Metal Physics, National Academy Of Sciences" (Ukraine), Steinbeis Advanced Risk Technologies (DE), Institute Engineering Thermophysics Nat. Academy Of Sciences Of Ukraine, O.O. Chuiko Institute of Surface Chemistry of Nas of Ukraine, and Alma Consulting Group Espana Sl (SP).

A novel coal-burning process that is the topic of global research could increase the likelihood of corrosion. Oxy-fuel coal combustion, in which coal is burned in an almost pure stream of oxygen, is a more efficient process that uses less fuel. In addition, it produces flue gases consisting mainly of water and carbon dioxide (CO_2). The concentrated CO_2 stream is easier to purify in carbon capture and sequestration schemes designed to reduce CO_2 release into the atmosphere.

Scientists evaluated nano-structured and micro-structured coatings in both air and oxy-fuel combustion. During the first 18 months of the project, work progressed from selection of substrates and coatings for screening, to application and characterization, to the beginnings of life-cycle assessment.

Metal alloy substrates consisting of ferritic steel (P92), an austenitic (HR3C), and two alternative nickel-based alloys are being utilized. From the original 31 coatings, scientists have chosen six coatings to be optimized for the steam oxidation application and five for fireside oxidation protection. To date, all coatings have been applied to the ferritic substrate, and both uncoated and coated samples have been characterized. Lifetime models of some of the coated systems are under development.

Increasing the efficiency of coal-fired power plants will enable significant reductions in CO_2 emissions. Corrosion-protection coatings being developed by POEMA scientists promise to enable long-term operation under the required operating conditions with important environmental benefits.

24.13 "Partner steam power plant" for the regenerative power generation

The research project "Partner Steam Power Plant" (2013–15) will clearly improve the appropriate integration of power generation from fluctuating energy sources. Therefore, existing power plants shall handle fluctuations of power generation from wind or photovoltaic even better to guarantee the energy supply [82].

In Germany and throughout the world the development of renewables makes progress, while the installation of high-capacity electrical storage lags behind. For this transitional period, power plants must perform important grid regulation tasks. Thus, steam power plants are essential partners for renewable energies.

However, existing power plants are only restrictedly suitable for the high-flexible operation to compensate the fluctuating supply from renewables. In part-load operation the efficiency of the plant as well as the materials of the single components are susceptible. Furthermore, in many power plants the stability during fast operation modes is not satisfied.

Thus, existing power plants have to be improved in such a way that they meet these new requirements. That is why different technical points of view are discussed and analyzed in the VGB research project "Partner Steam Power Plants." The involved power plant operators (E.ON; RWE, Steag, and Vattenfall) record the new requirements in a set of specifications. In addition, the Institute of Energy Economics at the University of Cologne (EWI) examines different energy market scenarios using a European electricity market model with high shares of renewable energy sources. The University of Duisburg/Essen and the power plant operators draw up calculations and dynamical simulations of the entire power plant during flexible operation. Critical components and processes of power plants can be identified and improved by these results. These works are carried out by the power plant component manufacturers (Mitsubishi Hitachi, Siemens). In addition, the scientific body DLR analyses the investigations regarding different possibilities of the integration of thermal storage into the power plant process. The project finished in February 2015 and was supported by the German Federal Economics Ministry within COORETEC's research program.

24.14 The European Creep Collaborative Committee (ECCC)

The ECCC, established in 1991 [83], operated successfully until 2005 as a European Thematic Network.

Its achievements included these:

- creep data collection
- all the information on the product to check their analyses
- heat treatment in term of respect to the standards
- the creation of a series of post-assessment tests to improve reliability in creep data assessment
- the production of a series of high-temperature materials data sheets supported by technical recommendations

However, EC funding ceased in 2005, and while ECCC continued on a voluntary basis, some momentum was lost.

Since 2011, ECCC has seen a rebirth and revival, with the creation of a "Joint Industrial Programme" (JIP) to support a central administrative Secretariat operated by Centro Sviluppo Materiali (Rome, Italy), alongside technical management of testing, assessment, and data collation by manufacturers, end users, and materials institutions throughout Europe. The JIP has brought ECCC back to full operating strength and is now delivering new insights into high-temperature materials performance [84].

The ECCC represents a unique European institution. In fact, its members participate both on a national basis and as individual organizations. They contribute through creep testing at a national level, technical input at an organization level, and financial input to a central Secretariat [85]. The rules defined in the memorandum of understanding are able to provide an equitable balance between potentially conflicting interests and meet industrial needs in supporting the safe design and operation of high-temperature plant. After the first 3 years (2011–14) ECCC agreed to renew the JIP for a second 3-year period (2014–17).

During its life, ECCC organized three conferences: Prague (2005), Zurich (2008), and the last in Rome (2014), attended by over 150 worldwide delegates also attests to the effective revival of ECCC.

Despite the EU decision that "European Collaboration in Science and Technology" for high-temperature power plant no longer merits continuity of government support, the activities of ECCC JIP are still ongoing and in strict relationship with the KMM-VIN WG2 program on Materials for Energy, which follows on from COST 536. In fact, it is very useful to share the experiences and views on how best to cope without consistent support from Europe and on whether Europe has the right policies for future industrial development.

24.14.1 The partnership 2015

- Austria: TU Graz
- Belgium: Laborelec
- Denmark: DTU
- Finland: VTT
- France: EDF
- Germany: MPA Stuttgart, Vallourec & Mannesmann, Saltzgitter Mannesmann Forschung Institute, Fraunhofer IWM Freiburg, MPA Darmstadt, VDEH, FZ-Juelich, Böhler Edelsthal, and Siemens
- Italy: Centro Sviluppo Materiali (secretariat), Istituto Italiano della Saldatura, Tenaris Dalmine, Concert, INAIL, Franchini Acciai, RTM Breda, and Ansaldo Energia
- Portugal: ISQ
- Sweden: KTH, Sandvik
- United Kingdom: Eon Engineering, EDF UK, Alstom Power, Doosan Babcock, TWI, and GDF SUEZ Energy International

24.14.2 The Joint Industrial Programme – JIP 1

Some European nations that have considerable facilities and expertise in high-temperature technology but do not have active National Creep Groups have found participation difficult.

ECCC "JIP 1" has developed an agreement of a new series of creep testing programs on its conventional 4-year cycle within each of the WG3.x working groups, many of which are now well under way. There has also been a very encouraging level of interest in new technical work programs, both to reevaluate previous assessments of well-known materials in the light of new data and insights, and to develop and extend assessment technologies into new and innovative areas. Finally, the nine-volume ECCC Recommendations on Creep Data Validation and Assessment Procedures have been substantially revised and updated.

24.14.3 WG3A: ferritic steels

WG3A has long been ECCC's most active WG3.x group, no doubt encouraged by the relatively open commercial environment in high-temperature boiler technology and the overriding importance of creep in thick-section component design and performance. Past highlights have included the compilation and assessment of very large creep rupture databases on the leading steels P91, E911, and P92, which have done much to put early performance claims into proper perspective and will shortly be updated to include the most recent long-term test results.

One, new test program includes a systematic exploration of performance in P92 materials and welds. In the context of adverse plant experience with welds in P91 and P122, this will help clarify whether P92 welds might be at similar risk. Parallel programs include, for example, programs on dissimilar welding austenitic steel to P92, which is giving interesting pointers as to the optimum filler metal choice.

There has recently been an upsurge of interest in using large ECCC datasets to analyze the influence on creep behavior of secondary experimental variables such as chemical composition and heat treatment, and to look at relationships between creep strength and ductility. Nardone [86] and Spindler [87] have each developed modified rupture strength predictions for P91 that take account of individual cast chemical composition. A parallel analysis of the ECCC data set, concentrating specifically on the deleterious influence of nickel, has shown that this varies with time and temperature in a complex way and becomes much more significant in the long term [87]. This analysis confirms Japanese results on a different data set [88] and aligns with microstructural evidence that nickel promotes the long-term precipitation of Z phase and dissolution of the strengthening MX precipitates [89].

These developments clearly offer opportunities for exploitation in life assessment and design with current materials. Further, a better understanding of how compositional factors affect the performance of well-tested materials such as P91 and P92 could also play a role in the development of improved materials [90]. Thus, for example, long-term test data and modeling on P91 and P92 could offer vital pointers toward minimizing long-term Z-phase formation in future martensitic steels.

ECCC is not a materials development organization. The expensive long-term testing and assessment that ECCC undertakes is intended to support proven materials in practical operation, and it should not be wasted on experimental variants, most of which will be discarded. However, the potential for learning from older materials data how best to develop newer materials should not be overlooked. Additionally, it may sometimes be judged that a novel material, albeit not yet in commercial operation, is

sufficiently well established in preferred composition and/or promising in properties to merit inclusion in ECCC's program.

Hence, MARBN steel is now the subject of a new WG3A test program. Further, collaborative interchange between ECCC and materials development programs such as KMM-VIN is to be welcomed and promoted. As ECCC overcomes the remaining difficulties in assessing today's leading materials, the case for tackling tomorrow's materials may strengthen.

24.14.4 WG3B: austenitic steels

WG3B has historically been a smaller working group, dealing as it must with a plethora of competing candidate materials for boiler thin-section applications where creep is only one of the important materials selection criteria. Nevertheless, an extensive range of alloys has been assessed.

There is considerable interest in testing and data collation on the leading material Sanicro 25 (see Chapter 12), which we expect to commence shortly under JIP 2.

Work is also ongoing in a number of areas including HR120, 316H modeling, and 347H weld metals.

24.14.5 WG3C: nickel-based alloys

WG3C probably has the most diverse remit of the WG3.x groups. Activities in steam plant materials overlap with WG3B, while activities on gas turbine alloys tend to involve different organizations and operate in a more commercially restrictive environment. How ECCC should react to that is a matter of debate.

WG3C has had to consider the value of generating a small data set, largely on its own, and then attempting to undertake a reasonably reliable assessment. The major 10-year WG3C program on GTD111, reported at the ECCC conference [91], shows both the merits and the difficulties of such an endeavor. After iterated assessments on a sparse but valuable data set, significant advances in understanding were eventually achieved, including insights into the differing behavior of directionally solidified and equiaxed materials, which are of general relevance to a wider class of blading alloys.

A more conventional assessment has also been carried out on the larger data set available on Alloy 617B, a variant of Alloy 617 designed for enhanced creep properties [92].

WG3C is also supporting a parallel materials modeling project, in partnership with the German Creep Group, to clarify the differences in precipitation sequence between 617B and 617, which may correspond to differences in creep behavior. A collaborative testing program is also being initiated on Alloy 718+, a newly introduced gas turbine material variant offering potentially improved creep strength.

24.14.6 WG1: creep data generation and assessment procedures

WG1 is nowadays the busiest working group, with active subgroups also pushing the boundaries of assessment technology into new fields. The core interest continues to be in creep rupture data and the extent to which ECCC's recommendations and post assessment tests (PATs) ensure a high quality assessment.

Spindler led an illuminating exercise in which he generated an artificial "ideal data set" IDS1, based on a simple mean rupture strength equation, combined with a randomization procedure to generate pseudo "data points" with a typical range of scatter. Round robin trial volunteers from WG1 were invited to carry out their own assessments on IDS1 and to apply the PATs. A wide range of models was produced, some but not all in close conformity with the original generating equation. In some cases, "predictions" in long-term extrapolation showed substantial over-optimism, including predictions based on rigorous mathematical data fitting procedures that passed the conventional PATs.

24.14.7 WG1 subgroups

The subgroup on stress relaxation has reported its first project results [93]. In outline, a model data set was used in a round robin assessment trial, the main focus of which was to test whether predictions based on a culled data set out to 10 h could successfully be extrapolated to describe behavior of the full data set extending to 3000 h. The results were sobering. This has implications for stress relaxation and creep-fatigue testing, where common practice is to employ dwell periods of an hour or less, whereas the periods between transients on operating plant are often in thousands of hours. Flexible plant operation, alongside the growing use of intermittent renewable energy sources, is of course a major current concern in our industries. The view presently taken within ECCC is that we will develop our expertise in creep behavior as our remit to engage with these issues.

Thus, topics such as relaxation process modeling and creep ductility exhaustion fall within our technical scope, whereas the parallel analysis of fatigue phenomena and plant transient modeling should be addressed outside ECCC.

The subgroup on small-scale testing seeks to produce ECCC guidelines on this type of testing and to maximize comparability between these semi-nondestructive tests for plant condition monitoring and conventional uniaxial testing [94].

The newest WG1 subgroup addresses materials modeling, with the ultimate aim of supplanting empirically based creep assessment techniques with microstructurally based mechanistic models. ECCC conference papers such as reference [95] illustrate both the promise and the difficulties encountered in this approach. If the ultimate goal still seems distant, there is no doubt that qualitative identification of key microstructural factors, and quantitative modeling of phase transformations and precipitation behavior, are rapidly advancing to the benefit of high-temperature technology. Quantitative modeling of the resulting mechanical behavior, and its integration into practically viable assessment methodologies, remain as challenges for the future.

24.15 Horizon 2020

Horizon 2020 is an €80 billion research and innovation funding program planned by the European Commission lasting from 2014 until 2020. Roughly €5.8 billion would be for secure, clean, and efficient energy. It will follow on and extend from FP7 [96].

Mastering the design, research, and development of new and improved materials will remain key for achieving the goals of the European Innovation Policy, in agreement with the European Strategy for a smart, sustainable, and inclusive growth EUROPE 2020. Research should respond to people's needs and concerns with integrated solutions that tie energy, natural resources, and human health.

Materials can enable industrial and commercial success for both existing and not yet existing products and processes: they may introduce new functionalities and improved properties adding value to existing products and process, thus representing an invisible revolution; at the same time, the engineered production of materials by design might allow the development of products and processes under a really sustainable systemic approach.

Materials research can be presented starting from the materials themselves (eg, biomaterials, metals, polymers) or the industrial sector (eg, metallurgy, chemistry) or their applications (eg, energy, health, transport), as well through other approaches. Materials profit from a wide range of scientific disciplines, such as chemistry, physics, biology, and engineering, as well as from all available technologies and multidisciplinary approaches, like nanotechnology and biotechnology. This is why several European funding initiatives support materials research within the structure of the EU 7th Framework Programme (eg, research on materials for specific applications in energy can be also funded under Theme 4 Energy, according to the public call for proposals) as well as with other EU funding schemes.

24.16 European future

In this chapter, a short overview of the steels programs for materials and technology development done in Europe and the results obtained have been presented. The results obtained are now applied in the USC power plants targeting net efficiency in the range of 44–46% with 620°C steam temperature, which are currently the best available technology.

In the meantime, Europe countries were the first in the world thinking to the 700°C steam parameters to give an additional improvement to the efficiency and a relevant reduction of the CO_2 emission.

The EU industries developed the materials and the design technologies for such advanced USC power plants, but the financial crisis and the strong effort to the development and application of solar and wind power plants changed a lot the market situation in EU countries.

In fact, currently there are plans in Europe to build an FSDP (500 MW at 705/720/35) only in 2017–21 with operation and feedback in 2021–26, respect to the original EoN50+ scheduled to be in operation since 2014. The numerous high-temperature material research programs and projects in Europe have produced notable research spin-offs for use in USC plants, such as improved steels, boilers, and steam cycle designs.

In the current situation, several EU steelmaker, tubemakers, forgemaster, component producers, and boiler and turbine makers have merged into worldwide groups (ie, Doosan, Mitsubishi Hitachi, General Electric, Westinghouse) or have made commercial agreements with companies in China, India, and other emergent countries where the needs of more energy and therefore of new power plants is requested.

Moreover, in Europe, community countries are at present private enterprises and state enterprises and are there overlapping levels of national and supranational government for the support research programs and industrial developments, which are often seen as conflicting political ideals.

Only in Europe is R&D treated as a primarily short-term endeavor, in which competitive funding is valued above long-term collaboration and construction. Only in Europe is the role of the R&D funding agency so dominated by the need to balance national interests and promote geographic integration. Only in Europe is the development agenda so clearly determined by an internal political agenda.

Does it work? It would be wrong to give a one-sided answer. The EU has led the global response to climate change. Political governance deserves credit for that. Europe also led at the outset in promoting the concept of superalloy-based steam power plant through its AD700 program, which answered the EU call for blue-skies innovation in R&D.

Does Europe still lead in that field?

Recently, the IEA carried out a comparative review [97], pointing out the need for a consistent, coordinated program of research, development, demonstration, and validation over a timescale of the order of two decades.

The IEA concluded that, although significant programs in Japan, China, and India had begun at least a decade later than in Europe and the United States, there is every prospect that these countries will catch up or overtake.

In fact, currently in the European Union, the construction of A-USC demo plants is not planned, and the results of the R&D program and the developed processes for component manufacturing will be usable for the other demo plant projects.

24.17 Conclusions about the EU R&D activities

The following simple sentences summarize the current situation in the European Union:

- EU R&D activities generated new materials like FB2/CB2 for USC and Sanicro25 for USC and A-USC plants. Lot of works have been made to generate data (creep, fatigue, microstructural evolution, etc.) for assessment and tools for micro structural modeling.
- EU materials and components producers have successfully demonstrated fabrication trails of tube, pipe, cast, forged, filler metal, and welded components. Lots of important knowledge on how to handle these materials has been obtained.
- EU will not be the first to realize the A-USC plants, but the results obtained over several years of R&D programs can give relevant input to the A-USC programs running in countries outside Europe.
- Not all the technological matters related to A-USC plants have been completely solved.
- Without CCS the A-USC will not be of any interest with respect to future the GHG emission control. But with CCS and with a major cost reduction for an A-USC plant, such a solution may match alternative clean production methods.
- The European Union is spending a lot of money to increase the renewable sources.
- Many of the findings from the A-USC development can be utilized for advanced high-efficiency biomass-fired plants.

References

[1] Home Page – Research & Innovation - European Commission, http://ec.europa.eu/research/index.cfm.
[2] http://ec.europa.eu/research/industrial_technologies/pdf/rfcs/rfcs-activities_en.pdf.
[3] J. Hald, in: J. Lecompte-Beckers et al. (Ed.), Proceedings of the 9th Liége Conference. Materials for Advanced Power Engineering, Forschungszentrum Jülich, 2010, pp. 55–66.
[4] A. Strang, V. Vodarek, Microstructural Development and Stability in High Chromium Ferritic Power Plant Mater, vol. 12, Sci Tech, 1996, p. 552.
[5] E. Schnabel, et al., Stahl und Eisen 107 (1987) 691–696.
[6] J. Hald, Creep strength and ductility of 9 to 12% chromium steels, Materials at High Temperatures 21 (1) (2004) 41–46.
[7] H.K. Danielsen, Z-phase in 9–12% Cr Steels (Ph.D. thesis), Department of Manufacturing, Engineering and Management of Technical University of Denmark, Lyngby, 2006.
[8] http://www.kmm-vin.info/#!/cihc.
[9] T.U. Kern, K. Wieghardt, H. Kirchner, Material and design solutions for advanced steam power plants, in: EPRI Fourth International Conference on Advanced in Materials Technology for Fossil Power Plants, Hilton Head Island, South Carolina, USA, 25–28 October 2004.
[10] B. Scarlin, R. Vanstone, R. Gerdes, Materials developments for ultrasupercritical steam turbines, ibidem.
[11] B. Scarlin, T-U. Kern, M. Staubli, The European Efforts in Material Development for 650°C USC Power Plants – Cost522, ibidem.
[12] R.W. Vanstone, Alloy design and microstructural control for improved 9–12% Cr power plant steels, in: Annex A, Cost 522 Steam Power Plant, Final Report, 1998–2003.
[13] G. Zeiler, W. Meyer, K. Spiradek, J. Wosik, Experiences in Manufacturing and Long-term Mechanical & Microstructural Testing on 9–12% Chromium Steel Forgings for Power Generation Plants, as reference [1].
[14] N. Blaes, B. Donth, K.H. Schönfeld, D. Bokelmann, High Temperature Steel Forgings for Power Generation, ibidem.
[15] A. Di Gianfrancesco, S. Budano, P. Lombardi, M. Paura, S. Neri, M. Calderini, N. Longari, Experience in manufacture of high chromium forged rotor steels, in: 7th International Conference on Advances in Materials Technology for Fossil Power Plants, Village, The Big Island, Hawaii, 22–25 October.
[16] T.-U. Kern, K.H. Mayer, B. Donth, G. Zeiler, A. Di Gianfrancesco, The European efforts in development of new high temperature rotor materials – COST536, in: 9th Liège Conference on Materials, for Advanced Power Engineering, Liège Belgium, 27th–29th September 2010.
[17] IMPACT – Innovative Materials Design and Monitoring of Power Plant to Accommodate Carbon Capture, http://gtr.rcuk.ac.uk/projects?ref=100819.
[18] D. Allen, Steel in high temperature power plant, in: METEC & 2nd ESTAD: European Steel Technology and Application Days, Düsseldorf, 16 June 2015.
[19] D. Allen, H. Du, R. Vanstone, P. Moody, P. Barnard, S. Roberts, R. Maclachlan, R. Thomson, The 'IMPACT' project – development of 'MARBN' steel for next generation steam plant, in: II Workshop on Upgrading and Efficiency Improvements in Coal-fired Power Plant, Nottingham, UK, 19–20 March 2013, pp. 25.
[20] A. Di Gianfrancesco, S. Matera, J. Hald, B. Beal, C. Sommith, C. Chovet, G. Herhart, C. Turconi, A. Helmrich, S. Pillot, H. Danielsen, New Creep Resistant Stable Steel for USC Power (CRESTA) Final Report: EUR 26415 EN, ISBN:978-92-79-35039-9.
[21] http://www.z-ultra.eu/.

[22] KMM-VIN, Newsletters, 2013, Available at: www.kmm-vin.eu/node/83.
[23] https://www.epsrc.ac.uk/.
[24] C. Sommitsch, R. Vanstone, T.U. Kern, P. Barnard, P. Mayr, R. Thomson, et al., Co-ordination of European research,, in: J. Lecomte-Beckers, O. Dedry, J. Oakey, B. Kuhn (Eds.), Structural Materials for Power Generation Equipment: 10th Liege Conference: Materials for Advanced Power Engineering, 2014, pp. 3–18.
[25] J. Bugge, Advanced 700°C PF Power Plant, http://www.unece.org/fileadmin/DAM/ie/se/pdfs/AD700PFCoal.pdf.
[26] J. Bugge, S. Kjær, R. Blum, High-efficiency coal-fired power plants development and perspectives, Energy 31 (10) (2006) 1437–1445.
[27] R. Blum, S. Kjaer, J. Bugge, Development of a PF Fired High Efficiency Power Plant (AD700), https://www.etde.org/etdeweb/details_open.jsp?osti_id=20903043.
[28] AD700 – Advanced (700°) PF Power Plant: Clean Coal Technology.
[29] Advanced 700 °C PF Power Plant (AD700–2), http://www.vgb.org/en/research_project220.html.
[30] http://www.dongenergy.com/SiteCollectionDocuments/NEW%20Corporate/PDF/Engineering/45.pdf.
[31] http://www.modernpowersystems.com/features/featuread700-innovations-pave-the-way-for-53-per-cent-efficiency/.
[32] R. Blum, R.W. Vanstone, C. Messelier-Gouze, Materials development for boilers and steam turbines operating at 700°, Document Download, Product code: ZCP2004EPRI0116.
[33] S. Kjaer, R. Blum, F. Klauke, R. Vanstone, A. Zeijseink, G. Weissinger, P. Kristensen, J. Meier, K. Wieghardt, The advanced supercritical 700 C Pulverized coal-fired power plant, in: Power-Gen Europe 2001, Brussels, Belgium, 29–31 May 2001.
[34] R. Blum, J. Bugge, S. Kjaer, AD700 innovations pave the way for 53 percent efficiency, Modern Power Systems 28 (11) (2008) 15–19.
[35] K. Wieghardt, Siemens Steam Turbine Design for AD700 Power Plants, in: AD700 Conference, Milan, http://cartechcapstone.wikispaces.com/file/view/Siemans+AD700+Turbine.pdf.
[36] J. Marion, F. Kluger, M. Sell, A. Skea, Advanced USC steam power plants, in: Power-Gen Asia 2014 KLCC, Kuala Lumpur, Malaysia, 10–12 September 2014.
[37] Strategy Study for the Realisation of a Fossil-fired Power Plant With High Efficiency, https://www.vgb.org/en/research_project232.html.
[38] Esbjerg Test Rig, https://www.vgb.org/en/research_project260.html.
[39] European Lignite-fired 700 °C Power Plant Concept Study for a European 700 °C Power Plant With Ultra-supercritical Steam Parameters Burning Low-calorific Lignite, https://www.vgb.org/en/research_project282.html.
[40] Component Test Facility for a 700 °C Power Plant, https://www.vgb.org/en/research_project261.html.
[41] Component Test Facility for a 700 °C Power Plant (Comtes700), Final Report, Research Fund for Coal and Steel EUR 25921 EN, 2013.
[42] H. Urban: Status of VGB High Temperature Projects, http://www.energy.gov.za/files/4thEU-SouthAfricaCleanCoalWorkingGroup/VGB%20%20700C%20projectsHUfinal.pdf.
[43] Optimization of the Heat Treatment of the Material T24, https://www.vgb.org/en/research_project371.html.
[44] European Network of Component Integration and Optimisation (ENCIO), https://www.vgb.org/en/research_project355.html.
[45] Examination of Operational and Failure Behaviour of Thick-Walled Components for High Efficient Power Plants (HWT II), https://www.vgb.org/en/research_project354.html.

[46] COMTES700-Turbine Valve, https://www.vgb.org/en/research_project268.html.
[47] Testability of Thick-walled Components Made From Nickel-based Alloys and Welded Connections Using Non-destructive Testing Methods (COORETEC, TD-1), https://www.vgb.org/en/research_project296.html.
[48] Base Test (Round Robin Test) for the Planned Project, "Non Destructive Examination Methods for Casted Nickel Based Alloys" (COORETEC TD-2), https://www.vgb.org/en/research_project351.html.
[49] Pre-Engineering Study "NRW Power Plant 700 °C", https://www.vgb.org/en/research_project297.html.
[50] Design of a New Generation of 12% Chromium Steels, VGB Research Project 348, http://www.vgb.org/en/research_project348.html.
[51] Calculation of CO_2 -Avoidance Potential by Modernizing Coal-fired Power Plant in the EU Until 2020, VGB Research Project 307, http://www.vgb.org/en/research_project307.html.
[52] R. Jeschke, et al., Flexibility Through Highly Efficient Technology, VGB PowerTech, May 2012, p. 66.
[53] C. Stolzenberger, Steps Towards 700°C power plant, in: User Forum of the Power Plant Technology, 21–25 April 2008.
[54] https://www.cooretec.de/index.php?index=21.
[55] T.B. Gibbons, Recent advances in steels for coal fired power plant: a review, Transactions of the Indian Institute of Metals (1–10, 2013).
[56] Material Qualification for the 700/720°C Power Plant (MARCKO 700), https://www.vgb.org/en/research_project281.html.
[57] MARCKO DE2, https://www.vgb.org/en/research_project198.html.
[58] Follow-up Project "Materials Testing Under Operating Conditions" From the Joint Research Programme KOMET 650, https://www.vgb.org/en/research_project251.html.
[59] B. Bals, F. Hippenstiel, K. Klenke, K. Metzger, Production of thick-walled components made from optimized material Alloy 617 B for highly efficient power plants at operating temperatures of 700°C - HWT II, in: (Clean goal Centre) 2nd Workshop "Advanced Ultra-supercritical Coal-fired Power Plants" Rome, Italy, 14–15 October 2014.
[60] G. Gierschner, C. Ullrich, H. Tschaffon, Latest developments for the flexible high efficient power plant of the future, in: Paper Presented at: Advanced Ultrasupercritical Coal-fired Power Plants, Vienna, Austria, 19–20 September 2012, 2012. Available from: http://ausc.coalconferences.org/ibis/ausc.coalconferences/home, pp. 21.
[61] K. Maile, K. Metzger, GKM test rig – HWT I, HWT II: qualification of materials for 700°C power plant, in: Paper Presented at: 1st International VDI Conference on Alloys in Power Plant Technology, Berlin, Germany, 15–16 June 2012, 2012, pp. 12.
[62] J. Jiang, Component test facility project in China, in: Paper Presented at: Advanced Ultrasupercritical Coal-fired Power Plants, Vienna, Austria, 19–20 September 2012, 2012. Available from: http://ausc.coalconferences.org/ibis/ausc.coalconferences/home, pp. 21.
[63] N. Rogalev, A. Golodnitskiy, A. Tumanovskiy, A. Rogalev, A survey of state-of-the-art development of coal-fired steam turbine power plant based on advanced ultrasupercritical steam technology, Contemporary Engineering Sciences 7 (34) (2014) 1807–1825. Hikari Ltd www.m-hikari.comhttp://dx.doi.org/10.12988/ces.2014.410191.
[64] VGB, Power Plant Technologies, April 2013, Available from: www.vgb.org/en/research_fossil.
[65] T. Grab, F. Stahl, Welding of heavy wall pipes made from high temperature alloys, special requirements and welding procedures, in: Paper Presented at: 1st International VDI Conference on Alloys in Power Plant Technology, Berlin, Germany, 15–16 June 2012, 2012, pp. 12.

[66] 725 High-temperature Material Tests gkm (725 hwt gkm) Study on the Long-term Operating Behaviour of Alloy Pipes and Forgings for Future High-Efficiency Power Plants, https://www.vgb.org/en/research_project321.html.
[67] M. Speicher, D. Hueggenberg, A. Klenk, S. Zickler, K. Metzger, Materials for advanced ultra-supercritical fossil-fuel power plants: materials properties, microstructure, and component behaviour, Energy Technology (2015)http://dx.doi.org/10.1002/ente.201500311.
[68] 700°C Plant Vision of High Efficiency and Clean Energy Production Mpa – Gkm Expertise on Materials and Components; Status of Advanced Ultra Super Critical Power Plant Designed for Operation at 700°C in Germany.
[69] D. Hîggenberg, M. Speicher, A. Klenk, S. Zickler, M. Schwienheer, Y. Wang, et al., Vgb PowerTech, 8, 2015, pp. 52–62.
[70] http://www.encio.eu/index.html.
[71] M. Gazzino, Encio project: overview, status up-date and planned fireside corrosion tests, in: Paper Presented at: Advanced Ultrasupercritical Coal-fired Power Plants, Vienna, Austria, 19–20 September 2012, 2012. Available from: http://ausc.coalconferences.org/ibis/ausc.coalconferences/home, pp. 16.
[72] M.D. Jedamzik, 700C steam generator technology – HPE activities and scope of work in R&D projects, in: Paper Presented at: Advanced Ultrasupercritical Coal-fired Power Plants, Vienna, Austria, 19–20 September 2012, 2012. Available from: http://ausc.coalconferences.org/ibis/ausc.coalconferences/home, pp. 32.
[73] M. Wilde, European Union research activities and new approach on international cooperation, in: Paper Presented at: Advanced Ultrasupercritical Coal-fired Power Plants, Vienna, Austria, 19–20 September 2012, 2012. Available from: http://ausc.coalconferences.org/ibis/ausc.coalconferences/home, pp. 11.
[74] Study on the Long-term Operating Behaviour of Alloy Pipes and Forgings for Future High-efficiency Power Plants, https://www.vgb.org/en/research_project321.html.
[75] http://www.nextgenpower.eu/.
[76] C. Crozet, A. Devaux, D. Béchet, Microstructure stability: optimization of 263 Ni-based superalloy: Eurosuperalloys, in: 2nd European Symposium on Superalloys and Their Applications, 2014.
[77] http://macplusproject.eu/.
[78] E. Zanin, Material-component performance-driven solutions for long-term efficiency increase in ultra supercritical power plants, in: Paper Presented at: Second Workshop on Upgrading and Efficiency Improvements in Coal-fired Power Plant, Nottingham, UK, 19–20 March 2013, pp. 29.
[79] E. Zanin, MACPLUS Project, in: 2nd IEA CCC Workshop on Advanced Ultra-supercritical Coal-fired Power Plants, Rome, 14–15 October 2014.
[80] MACPLUS-COMTES700/ETR/TV-Cooperation, https://www.vgb.org/en/research_project367.html.
[81] POEMA Project, http://cordis.europa.eu/project/rcn/106505_en.html.
[82] Partner Steam Power Plant for the Regenerative Power Generation, https://www.vgb.org/en/research_project375.html.
[83] D.V. Thornton, The activities of the European creep collaborative committee, in: Proceedings of the Conference on "Life Assessment of Industrial Components and Structures", ERA/Value, Churchill College, Cambridge, October 1993.
[84] D.J. Allen, The European Creep Collaborative Committee (ECCC) – rebirth and revival, in: J. Lecomte-Beckers, O. Dedry, J. Oakey, B. Kuhn (Eds.), 10th Liege Conference: Materials for Advanced Power Engineering, 2014, pp. 589–604.

[85] G. Merckling, A. Di Gianfrancesco, S.R. Holdsworth, D.J. Allen, E. Zanin, T.-U. Kern, et al., Joint Industrial Program Proposal for ECCC, February 2011, See "JIP Description" at: http://www.c-s-m.it/en/business_sectors/energy_and_environment/eccc_joint_industrial_project.html.
[86] S. Nardone, Prediction of T/P91 (X10CrMoVNb9-1) creep strength based on materials test certificate data, in: Presentation to ECCC WG3A, Rome, 5–7 September 2013.
[87] M.W. Spindler, Summary of results for models describing meta data factors affecting creep failure in Grade 91, in: Presentation Prepared for ECCC WG3A, Rome, 5–7 September 2013.
[88] D. Allen, Analysis of ECCC creep rupture data on Grade 91 steel – the influence of nickel, in: 3rd International ECCC Creep & Fracture Conference, Rome, Italy, Paper 16, 5–7 May 2014.
[89] K. Kimura, K. Sawada, H. Kushima, Long-term creep strength property of advanced ferritic creep resistant steels, in: Proceedings of the Sixth International Conference on Advances in Materials Technology for Fossil Power Plants, EPRI, Santa Fe, New Mexico, Paper S3A 02_59, August–September 2010.
[90] K. Sawada, H. Kushima, T. Hara, M. Tabuchi, K. Kimura, Heat-to-heat variation of creep strength and long-term stability of microstructure in Grade 91 steels, Materials Science and Engineering: A 597 (2014) 164–170.
[91] D. Allen, E. de Bruycker, J. Keustermans, S. Holmström, M. Gomes, H. Kolkman, C. Messelier-Gouze, E. Vacchieri, ECCC test programme and data assessment on GTD111 creep rupture, strain and ductility, in: 3rd International ECCC Creep & Fracture Conference, Rome, Italy, Paper 14, 5–7 May 2014.
[92] R. Krein, A. Di Gianfrancesco, A. Gotti, P. Lombardi, W. Gamble, P. Barnard, "ECCC assessment of creep rupture strength for the new nickel alloy 617B", the influence of nickel, in: 3rd International ECCC Creep & Fracture Conference, Rome, Italy, Paper 69.
[93] S. Holmström, V. Friedmann, A. Klenk, G. Merckling, M. Norman, R. Pohja, A. Riva, R. Sandström, M.W. Spindler, "Long term stress relaxation modelling", the influence of nickel, in: 3rd International ECCC Creep & Fracture Conference, Rome, Italy, Paper 72.
[94] S. Brett, "The application of small scale sampling and impression creep testing to power plant", the influence of nickel, in: 3rd International ECCC Creep & Fracture Conference, Rome, Italy, Paper 70.
[95] R. Sandström, "Creep strength in austenitic stainless steels", the influence of nickel, in: 3rd International ECCC Creep & Fracture Conference, Rome, Italy, Paper 142.
[96] Horizon 2020, http://ec.europa.eu/research/industrial_technologies/materials_en.html.
[97] K. Nicol, Status of Advanced Ultra-Supercritical Pulverised Coal Technology, IEA Clean Coal Centre Report CCC/229, December 2013.

Index

'*Note:* Page numbers followed by "f" indicate figures, "t" indicate tables.'

A

A-USC technology. *See* Advanced ultra-supercritical technology (A-USC technology)
AC. *See* Air cooling (AC); Alternating current (AC)
AC 66, 375, 377, 381
ACCEPT. *See* Alloy development for critical components of environmentally friendly power plant (ACCEPT)
Acoustic emission (AE), 233–234, 234f
AD700 technology, 790
  AD700 Phase 3, 798–804
    advanced USC power plant, 802
    boiler components in CTF, 799f
    test facility, 798f
  AD700–3, 796–797
  AD700–4, 805–808
    pre-engineering study "NRW power plant 700°C", 805–808
  R&D program, 790–796
    boiler design group, 793
    boiler materials subgroup, 791–792
    in Europe, 796
    materials group, 791
    phases 1 and, 796
    steam turbine design for, 795f
    turbine design group, 794–796
    turbine materials subgroup, 792–793
Advanced ultra-supercritical technology (A-USC technology), 113, 323, 391, 689–691, 736. *See also* Boiler technology development; Ultra-supercritical power plants (USC power plants)
  boiler technology, 423
  cast materials, 134–139, 135t–136t
  development in Japan, 737–752
  linear accelerator X-ray facility, 138f
  master schedule, 738, 739f
  materials, 738
  nickel alloy A625 HP, 136f
  nickel-based superalloys as candidate materials, 189–192, 190t, 191f
  nondestructive testing options, 137t
  nozzle box casting, 137f
  PC, 8
  power plants, 773
  PP, 10, 11f
  programs in European Union
    COMTES+, 815–826
    EBW, 812
    ECCC, 835–839
    EU steel development research programs for USC, 775–788
    EU superalloys development research programs for A-USC, 789–811
    European future, 840–841
    Horizon 2020, 839–840
    HWT I project, 814
    KOMET 650, 812–814
    MACPLUS, 831–833
    MARCKO 700, 811–812
    new materials for steam generators, 811–812
    NextGenPower project, 827–831
    "Partner Steam Power Plant", 835
    POEMA project, 834
    Post AD700 project, 814–815
  project structure, 737, 737f
  R&D programs
    Energy trends for Africa, 767
    Indian A-USC program, 755–761
    on materials, 773–775
    Russia, 762–763
    South Africa, 766–767
    South Korea, 763–764
    Turkey, 767–769
  700°C-class, 736, 737f
  steam turbine blades, 193

AE. *See* Acoustic emission (AE)
AES. *See* Auger electron spectroscopy (AES)
AFA. *See* Alumina-forming austenite (AFA)
Age hardening, 511, 519–520
Air cooling (AC), 571–572
Air liquide test, 632t
Airfoil, 175
Albany Research Center (ARC), 691
All weld metal (AWM), 280
Alloy 263, 469–470, 571
  chemical composition, 572t
  chemistry optimization, 586–592
  corrosion and oxidation, 592–598
  heat treatment, 573
  hot working, 572
  impact values for, 574t
  long-term properties, 586
  mechanical properties, 573, 583t
  microstructural analyses, 573–578
  physical metallurgy, 571–572
  physical properties, 572, 572t
  scale morphologies and maps of Cr and O, 596t–597t
  TEM dark field images, 575f
  trial components manufacturing, 579–586
  weldability, 578–579
Alloy 617, 381, 400–401, 413, 547, 613, 759–760
  Alloy 617B, 609
    atom probe picture, 551f
    components in, 559f
    creep rupture strength, 555f
    mechanical properties, 552t
    thermophysical properties, 554t
  Alloy 617occ, 551
  creep rupture strength, 550f
  and derivatives
    component manufacturing, 558–559
    creep data, 554
    fabrication, 557–558
    fatigue, 556
    heat treatment, 559–563
    high-temperature corrosion, 556–557
    mechanical properties, 551–552
    thermophysical and electrical properties, 552
    welding, 563–564
  European USC 700°C Boiler projects, 547
  experiences from field testing, 564–565
  metallurgy, 548–551
  nominal alloy composition, 549t
  time-temperature-precipitation diagram, 549f
Alloy 740, 469–470
  Alloy 740H, 469–470, 609
    evaluated compositions, 610t
Alloy C263, 609
Alloy development for critical components of environmentally friendly power plant (ACCEPT), 775
Alloying, 377–381
  Power Austenite, 379t
  sigma phase in binary Fe-Cr system, 378f, 378t
  strengthening concept of Power Austenite, 380f
  thermo-calc calculation of phases, 379f
Alloys, 187, 188t
  heat-resistant alloys, 184–187
  optimization, 830
  stainless steels, 178–183
  titanium alloys, 183–184
Alstom test, 633t
Alternating current (AC), 235
Alumina-forming austenite (AFA), 376–377
Aluminum, 548
Ambient temperature tensile and impact properties, 476
“Andrea Palladio” Power Station, 823
Annealing, 104–105, 231–232, 232f, 572
Anthracite, 17, 644
AOD. *See* Argon oxygen decarburization (AOD)
AP-FIM. *See* Atom probe-field ion microscopy (AP-FIM)
APFIM, 217–219, 218f
Ar-protected atmosphere (PESR), 186
ARC. *See* Albany Research Center (ARC)
Arc welding, 249
  alloyed ferritic steels, 289
  consumables development, 614
  FCAW, 294–297
  filler materials, 288
  GMAW, 294–297
  GTAW, 294, 294f
  MMAW, 289–293

qualification of filler materials for creep service, 299
SAW, 297–299
steel grade, 289
Argon gas (Ar gas), 363
Argon oxygen decarburization (AOD), 130, 163
ASME, 79, 476, 501
B31.1 code, 310
BPVC, 290t–292t, 295t–296t, 309–310
Code Case 2702, 491–492, 497
Atom probe-field ion microscopy (AP-FIM), 351
Atom probes, 217
Attemperator, 44, 44f
Auger effect, 219–220
Auger electron spectroscopy (AES), 219–220, 219f
Austenitic grades, 605–609
weldments between, 277, 278f
Austenitic stainless-steel grade, 392
Sandvik Sanicro 25, 392
Austenitic steels, 99–100, 838
for A-USC power plants
AFA, 376
Esshete 1250, 375
future trends, 376–377
sigma phase strengthened concept, 377–387
grades, 274–275, 275f
DMWs, 113–116
SCC, 109–111, 111f
secondary hardening, 112–113
sensitization, 103–105, 104f–105f
sigma-phase precipitation, 108–109, 110f
strain-induced precipitation hardening, 105–108
stress relief cracking, 111–112
thermal fatigue, 102, 102t, 103f
Austenitizing, 230
AWM. *See* All weld metal (AWM)

B

B-stabilized $M_{23}(C,B)_6$, 379
Back pressure turbines, 38
Backscatter Kikuchi diffraction. *See* Electron backscatter diffraction (EBSD)
Backscattered electrons (BE), 204, 594
Bainite, 60–62
Bainitic steels, 249, 283–284
CSEF, 284
Base test, 810
Baseload power plants, 5
BE. *See* Backscattered electrons (BE)
Beam steering, 241–242
“Bell shaped” behavior, 385
Bending of tubes, 413–414
“Benson Low Mass Flux” design, 28–29
BEST. *See* Bohler electro slag toping (BEST)
Bharat Heavy Electricals Limited (BHEL), 758, 761
Bimodal forging, 184
Biogenic processes, 18–19
Biomass-fueled power plants, 3, 3f
Bituminous coal, 17–18
Black coal. *See* Bituminous coal
Blades, 175
BN. *See* Boron nitrides (BN)
Bohler electro slag toping (BEST), 149–151
Boiler, 24–38
drums, 30, 31f
header, 33, 35f
SH and RH, 31–33, 34f
steam line, 33, 36f
steam valves, 33–38, 36f–38f
testing, 416–417
tubes and pipes development for A-USC power plants
base metals, 443
evaluation of HR6W and HR35, 443
field testing, 441–442
HR35, 434–438
HR6W, 424–434
nickel-based alloy development, 442
steam and hot corrosion properties, 438–441
water wall, 25–30
Boiler, and Pressure Vessel Code (BPVC), 261
Boiler component test, 744–745, 745f–746f
Boiler fabrication trials, 701–702
Boiler headers, 249–250

Boiler materials. *See also* Turbine materials
A-USC boiler demonstration articles, 701f
AD700 R&D program, 791–792
boiler fabrication trials, 701–702
for China's 700°C A-USC coal-fired demo plant, 719–725
development of materials for, 722–725
material for boiler pipes and headers, 722
materials for superheaters and reheaters, 720
water cooling wall materials, 719–720
COST programs, 776–777
heavy-section welding, 701–702
Inconel 740/740H development, 697–698
long-term creep in HR6W, Haynes 230, and CCA617, 698
steam-side oxidation, exfoliation, and fireside corrosion, 699–701
Boiler pipes and headers, material for, 722
Boiler system, 247–248
chemical composition
of Cresta 19 filler, 632t–633t
of flux core filler metal, 631t
Nb-free base metal and welded joint comparison, 634f
welding, 627–632
A-USC header mock-up, 628f
narrow-groove HST, 629f
notch location, 630f
welded joint for water wall application, 629f
Boiler technology development, 738, 739f–740f. *See also* Advanced ultra-supercritical technology (A-USC technology)
1000-MW-class steam turbine, 751, 751f
700°C superheater, 745, 746f
bent pipes, 743, 744f
boiler component test, 744, 745f
facility, 745, 746f
boiler pipes and tubes, 741, 741f
candidate materials, 738f, 740, 740t, 741f
for steam turbine rotors, 747, 748t
TOS1X creep rupture strength, 748–749, 748f
casted materials, 751, 751f
header mock-ups, 744, 745f
high-temperature valves, 752, 752f
hot corrosion tests, 742, 743f
HR6W creep rupture strength, 741–743, 742f, 744f
pipes and tube welding, 742–743, 744f
rubbing test apparatus, 752, 753f
steam oxidation test, 742, 743f
turbine rotor
material, 748–749, 749f
test facility, 751, 752f
welding, 749, 750f
turbine technology development activities, 745, 747f
variety of system configurations, 752, 753f
welded rotor, 745, 747f
Boron, 562
concentration, 350f
mechanisms for boron effect, 358–361, 359f–361f
Boron nitrides (BN), 166–167, 344
Boundary hardening, 330–331, 330f
BPVC. *See* Boiler, and Pressure Vessel Code (BPVC)
Brazil, Russia, India, China and South Africa (BRICS), 755
Brittle temperature range (BTR), 534–535
Brown coal, 18, 643
BSE. *See* Backscattered electrons (BE)
BTR. *See* Brittle temperature range (BTR)

C

C-HRA-1 tube manufacturing, 722
C700-R1 alloy, 726
C700-R2 alloy, 726
CALculation of PHAse Diagrams (CALPHAD), 228–229
Cap rock and traps, 672
Carbon capture and storage technologies (CCS technologies), 4, 13, 643–644, 667, 668f, 689–691
affordability, 678
climate change without, 679
economic importance, 677–678
industry experience, 677
International Energy Agency, 676
oil recovery and storage, 669f
oxyfuel combustion systems, 670, 671f
oxyfuel flow chart, 668f

post-combustion, 668f
capture, 668–670
scrubbing technology, 670f
pre-combustion capture, 667–668, 668f–669f
project proposals, 679
reducing emissions from industry, 675–676
storage, 672–674, 673f
for tackling climate change, 674
transport, 670–671
Carbon capture and utilization (CCU), 679
Carbon dioxide, 667, 677
producing biofuels, 680f
resource, 681f
reuse, 679–680
Carbon intensity of electricity, 654, 654f
Carboniferous Period, 643
Carbonitrides, 126–128, 357–358
Castability, 536–538
Casting, 121–122, 124f–125f, 496, 536–538, 778
for casings and valve bodies, 702–704
Doosan G-series 4-casings turbine, 41f
scale-up project, 703–704
steam turbine, 39–40
for ultra-supercritical applications
9% Cr steels, 126–128
casting materials grades, 126, 127t
modified 9% Cr steel, 128
welding, 619–625
CC. *See* Code Case (CC)
CCA617, long-term creep in, 698
CCA617. *See* Controlled composition alloy 617 (CCA617)
CCD. *See* Charge-coupled device (CCD)
CCPP. *See* Combined cycle power plants (CCPP)
CCS technologies. *See* Carbon capture and storage technologies (CCS technologies)
CCU. *See* Carbon capture and utilization (CCU)
CEA. *See* Central Electricity Authority (CEA)
Central Electricity Authority (CEA), 756
Ceramic refractory running system, 123–124
CFBC. *See* Circulating fluidized bed combustion (CFBC)
CGHAZ. *See* Coarse-grained heat affected zone (CGHAZ)
Charge-coupled device (CCD), 201–202
Chemical analyses, 197. *See also* Surface analysis
on bulk, 198–199, 198t–199t
modeling tools, 224–232
Chemistry optimization, 586–592
China Iron & Steel Research Institute Group (CISRI), 715–716
Chinese 700°C A-USC development program. *See also* Indian A-USC program; US DOE/OCDO A-USC materials technology R&D program
coal-fired demo plant, 717–719
boiler materials for, 719–725
pilot testing rig for, 726–727
steam turbine materials for, 725–726
coal-fired power generation technology innovation consortium, 716–717
coal-fired power plant, 715–716
OECD, 716
R&D proposal for Chinese consortium, 718t
steam parameter evolution of Chinese fossil-fired power plants, 715f
structure stability of Inconel 740/740H, 727–730
Chrome molybdenum steels (Cr-Mo steels), 121
1.25Cr-0. 5Mo steel, 73–74
2.25Cr-1Mo steel, 53–54, 57–60, 62f, 65f, 67f, 73–74
9Cr-1Mo steel, 73–74
Chrome molybdenum vanadium steels (Cr-Mo-V steels), 121
1CrMoV steels, 128
2.5Cr-1MoVBTi steel, 54
Chromium (Cr), 126, 408
18Cr-8Ni steels, 54–57
12% Cr steels, 147, 178–180, 179t, 180f
2.25Cr-1. 6WVNb steel, 54, 63f, 65f–66f
creep rupture properties, 68f–69f, 71f
9 to 12 Cr martensitic steels in coal power plants, 324–326, 325f
9% Cr steels, 126–128, 130t, 134f
modified, 126–128
9–12% Cr steels, 88–89, 180–183, 182t, 183f

Chromium (*Continued*)
chemical optimizations, 189, 190t
9Cr-90 ppm B steel, 355, 356f
9Cr-boron steel, 356–357, 358f
chromium-depleted zone, 102–103
Cr(V,Nb)N Z-phase nitrides, 90
Cr_2O_3, 408
oxide scale, 99
CrTaN Z-phases, 93, 95f
sulfides, 484–485
CHRT. *See* Controlled heating rate tests (CHRT)
Circulating fluidized bed combustion (CFBC), 662
Circumferential welds, 498
CISRI. *See* China Iron & Steel Research Institute Group (CISRI)
CLCF tests. *See* Complex low-cycle fatigue tests (CLCF tests)
Clean coal technology, 662–667, 663f. *See also* Coal
CO_2 emission, 664f
date ranges for technical developments, 665t
fossil fuels, 664–667
results, 664
sustainable energy for future, 666f
total CO_2 emission and shear of fossil fuels, 666f
transport and process, 648–649, 649f
Climate change, tackling, 676. *See also* Carbon capture and storage technologies (CCS technologies)
Co element, 511–513
CO_2 emissions, 13, 14f, 17f, 46f, 651–653, 653f, 733–734
Coal, 408–410, 643, 689–691, 736. *See also* Carbon capture and storage technologies (CCS technologies)
ash corrosion, 484–485
brown coal, 18, 643
carbon intensity of electricity, 654, 654f
classification, world reserves, and use, 645f
coal-burning process, 834
coal-fired boilers, 391
dust. *See* Pulverized coal
electricity
emissions, 655
production, 651–653
system, 684–686
formation, 644–645, 646f
in future global energy needs, 658–660
mining, 646–649
reserves, 649–651
residential electricity use, 654
systems-based interactive innovation, 684f
transport and process, 648–649, 649f
types, 644
working process, 644
world coal production and consumption, 655–657
Coal Utilization Research Council (CURC), 689–691
Coal-fired power plant, 715–716
boilers, 661–667
advantages, 661
clean coal technology, 662–667
disadvantages, 662
generation plants, 6–10, 6f
materials used in SC, USC, and A-USC boiler, 11f
maximum operating temperature and pressure, 10f
subcritical to A-USC power plants, 9f
water equilibrium diagram, 9f
power station, 1, 2f
Coal-fired steam power plants, 323
Coal-fired thermal power station, 6
Coalification, 644
Coarse-grained heat affected zone (CGHAZ), 265–268
Coatings, 704–705
innovative TBCs and erosion-resistant coatings, 193
leading edge protection, 193–195, 194f
Code Case (CC), 423
Cold
bending, 69–70
cold-bending, 701
cold-worked products, 571–572
deformation, 413–414
workability, 491
Columbium (Cb), 414
Combined creep and oxidation tests, 376
Combined cycle power plants (CCPP), 145
“Combined cycle”, 1
Complex geometry components, 126
Complex low-cycle fatigue tests (CLCF tests), 556

Component test facility (CTF), 798
boiler components, 799f
Composition, 79, 80f, 81t, 91f
of alloy 740H, 470
filler material, 607t
fuels, 385t
of HAYNES 282 alloy, 511–513
for Inconel 617 and alloy 263, 613t
INCONEL alloy 740H, 470
nominal alloy, 696t
of steel FB2, 151f
of superalloys for blades, 185t
of welding wires, 262t
COMTES project, 416
COMTES 700 project, 798–804
advanced USC power plant, 802
boiler components in CTF, 799f
results, 800–804
test facility, 798f
COMTES 700 Turbine Valve, 804–805
COMTES+, 815–826
ENCIO project, 821–825
long-term operating behavior of alloy pipes and forgings, 825–826
operational and failure behavior of thick-walled components, 815–820
A-USC plant, 820
results of test loop, 817–820
Condenser, 44, 45f
condensing turbines, 38
Constant strain rate tests (CSR), 560
Controlled composition alloy 617 (CCA617), 698
Controlled heating rate tests (CHRT), 533
Conventional ferritic steels, 128
Conventional low-alloyed steels, 53–54, 59t
comparison of allowable stresses, 61f
COORETEC initiative, 808–810
COORETEC, TD-1, 808–809
COORETEC TD-2, 810
COP21, 681–683
Copper, 392–393
Corrosion
fireside corrosion, 592–593
properties of Alloy 740H, 481–486
coal ash corrosion, 484–485
corrosion in supercritical carbon dioxide, 486
oxidation in dry air and steam, 482–484
SCC, 486
COST programs, 775–778
boiler materials, 776–777
COST E and COST F rotor forgings, 155–162
Bohler electro slag topping, 156f
COST F steel, 161f
data and mechanical properties, 160f
FEM model, 158f
HP rotor, 162f
protective gas electro slag remelting, 157f
quality HT cycle, 159f
shaft component, 161f
COST FB2, 162–168, 162f
boron and nitrogen, 167f
flaw sizes, 166f
flow chart of FB2 rotor, 164f
mechanical properties of FB2 rotor forging, 166f
quality HT cycle, 165f
short-term creep testing, 167f
USC power plants, 163f
forging and casting, 778
Cr-Mo steels. *See* Chrome molybdenum steels (Cr-Mo steels)
Cr-Mo-V steels. *See* Chrome molybdenum vanadium steels (Cr-Mo-V steels)
Creep, 284–285, 285f
creep-strengthened low-alloyed steels, 53–54
data, 554
generation and assessment procedures, 838–839
deformation, 474
degradation, 70–71, 72f
ductility, 403
fatigue, and creep/fatigue interaction, 829–830
filler material qualification for creep service, 299
limit stress, 77–78
methods of strengthening martensitic 9 to 12Cr steels in, 326–331
rate in transient region, 342–343
resistance, 547–548
10% Cr steels, 158
9 to 12Cr steels, 338–339

chromium steels, 155
creep-resistant USC steels, weld metal development principles for, 279–280
and rupture behaviors, 397–405
creep-strengthening mechanisms, 404–405
standard and code cases for Sanicro 25, 400–403
rupture properties, 498–501
of HAYNES 282 alloy, 521–524
and stress rupture, 476–479
test sections, 826
Creep rupture strength
of HR35, 435–437
HR6W, 426–428, 427f, 741–743, 742f, 744f
LTES700R, 750f
TOS1X, 748–749, 748f
of welded joints, 437–438
Creep strength, 77–78, 80, 83, 99, 105, 381–383
in cold-deformed material, 414–416
creep rate, 383f–384f
creep test results, 382f–383f
degradation, 331–337, 335f–336f
effect of Al on creep rupture data, 332f
creep rupture data, 333f
tempering temperature, 334f
after extrapolation, 399–400
iso-stress tests results, 382f
of Sanicro 25, 397–399
Creep strength–enhanced ferritic steels (CSEFs), 70–73, 249, 693–694
Creep strength–enhanced low-alloyed steels, 54–57
alloy development concept of T23, 57f
comparison of allowable stresses, 61f
ferritic boiler steels, 55f
Creep strength–enhanced martensitic steels, 79
CRESTA program
CRESTA 1, 781–783
CRESTA 2, 783–784
results, 782f
Cross-weld Charpy V-notch impact tests, 501
Crude oil, 19
CSEFs. *See* Creep strength–enhanced ferritic steels (CSEFs)
CSR. *See* Constant strain rate tests (CSR)
CTE. *See* Thermal expansion coefficient (CTE)
CTF. *See* Component test facility (CTF)
CURC. *See* Coal Utilization Research Council (CURC)
Current Policies Scenario, 12

D

DC. *See* Direct current (DC)
DEFORM software, 494–496
Deimethycarbonate (DMC), 679
DICTRA software, 199, 227–228, 227f
Direct current (DC), 235
Dislocation hardening, 329
Dissimilar metal welding (DMW), 100, 102, 113–116, 249, 276, 503, 617–619, 812
dilution on predicted equilibrium phase, 114f
mises stress prediction, 115f
weldments between
martensitic steels and nickel alloys, 619
USC martensitic steels and A-USC austenitic steels, 617
Dissimilar welded joint, 279f
Dissimilar welding capabilities, 536
Dissolution storage, 673
DMC. *See* Deimethycarbonate (DMC)
DMW. *See* Dissimilar metal welding (DMW)
DOE. *See* US Department of Energy (DOE)
“Draglining” process, 647–648
Drums, boiler, 30, 31f
2DS. *See* 2°C Scenario (2DS)
4DS. *See* 4°C Scenario (4DS)
6DS. *See* 6°C Scenario (6DS)
Ductility, 176–177
recovery temperature, 534–535
and toughness, 281–282, 282f
Duplex electrode concept, 578–579, 613
Dye penetrant, 233, 233f
Dye penetrant inspection, 233

E

E MAX initiative, 796. *See also* AD700 R&D program
E. ON 50+ project, 810–811

EAF. *See* Electric arc furnace (EAF)
EBSD. *See* Electron backscatter diffraction (EBSD)
EBSDP. *See* Electron backscatter diffraction pattern (EBSDP)
EBW. *See* Electron beam welding (EBW)
ECCC. *See* European Creep Collaborative Committee (ECCC)
Economizer, 41–43, 43f
ECSC. *See* European Coal and Steel Community (ECSC)
Eddy-current testing, 234–235, 235f
EDS. *See* Energy-dispersive X-ray spectroscopy (EDS)
EDX. *See* Energy-dispersive X-ray spectroscopy (EDS)
EEL. *See* Electron energy loss (EEL)
EELS. *See* Electron energy loss spectroscopy (EELS)
EFTEM. *See* Energy-filtered transmission electron microscopy (EFTEM)
"Ehrhardt" process, 558
EIO. *See* Energy Industries of Ohio (EIO)
Electric arc furnace (EAF), 163
Electric Power Research Institute (EPRI), 128, 691
  Coal Technology Combustion roadmap, 689–691
Electricity
  emissions, 655
  production from coal, 651–653
  system, 684–686
Electro slag hot topping (ESHT), 157
Electro slag remelting (ESR), 149–151, 197
Electrodes, 293
Electron backscatter diffraction (EBSD), 205–207, 206f–207f, 403, 404f
Electron backscatter diffraction pattern (EBSDP), 206
Electron beam welding (EBW), 812
Electron energy loss (EEL), 212
Electron energy loss spectroscopy (EELS), 211
  to EFTEM, 212
Electron micro probe analyzer (EMPA). *See* Electron microprobe (EMP)
Electron microprobe (EMP), 220–221, 221f
Electron probe microanalyzer (EPMA). *See* Electron microprobe (EMP)
Electron spectroscopy for chemical analysis (ESCA). *See* X-ray photoelectron spectroscopy (XPS)
Electron(s), 202
  detectors, 204
  microscopy, 200–201
"Emax Power Plant Initiative", 798
EMEP. *See* Energy Materials Working Group (EMEP); Engineered micro-and nanostructures for enhanced long-term high-temperature materials performance (EMEP)
EMP. *See* Electron microprobe (EMP)
ENCIO project. *See* European Network for Component Integration and Optimization project (ENCIO project)
Energy, 143
Energy Industries of Ohio (EIO), 536, 691
Energy Materials Working Group (EMEP), 785
Energy Technology Perspectives 2014 (*ETP* 2014), 684
Energy-dispersive X-ray spectroscopy (EDS), 202–203, 211, 348, 435
  EDS detectors, 204
Energy-filtered transmission electron microscopy (EFTEM), 212–217, 213f–217f
Engineered micro-and nanostructures for enhanced long-term high-temperature materials performance (EMEP), 326, 778, 785
Enthalpy-entropy diagram (h-s diagram), 24, 24f
Entropy, 112
Environmental resistance properties of HAYNES 282 alloy, 527–532
  fireside corrosion resistance, 530–532
  oxidation behavior
    in steam atmospheres, 528–530
    in water vapor, 528–530
  static oxidation behavior in air, 527–528
EPRI. *See* Electric Power Research Institute (EPRI)
Erosion-resistant coatings, 193
Esbjerg Test Rig, 796–797
ESHT. *See* Electro slag hot topping (ESHT)

ESR. *See* Electro slag remelting (ESR)
Esshete 1250, 375
ETP 2014. *See* Energy Technology Perspectives 2014 (*ETP* 2014)
European Coal and Steel Community (ECSC), 773
European Creep Collaborative Committee (ECCC), 80–82, 82f, 286, 554, 835–839
  JIP 1, 836–837
  partnership 2015, 836
  WG1, 838–839
  WG3A, 837–838
  WG3B, 838
  WG3C, 838
European Network for Component Integration and Optimization project (ENCIO project), 774–775, 821–825
  host plant, 823
  motivation, 822
  organization and funding, 824–825
  pipe for, 579
  results, 825
  technical concept diagram, 823–824
  test facility, 824f
European Research Fund for Coal and Steel (RFCS), 798
European Union (EU)
  European 700°C power plant, concept study for, 797
  European Thermie AD700 program, 469
  European THERMIE AD700 Project, 727
  European USC 700°C Boiler projects, 547
  steel development research programs for USC
    COST programs, 775–778
    CRESTA program, 781–784
    IMPACT project, 778–780
    KMM-VIN EMEP, 785–788
    Z-phase strengthened steels for USC power plants, 784–785
  superalloys development research programs for A-USC, 789–811
    AD700 Phase 3, 798–804
    AD700 R&D program, 790–796
    AD700–3, 796–797
    AD700–4, 805–808
    COMTES 700 Turbine Valve, 804–805
    Concept study for European 700°C power plant, 797
    COORETEC initiative, 808–810
    E MAX initiative, 796
    E. ON 50+ project, 810–811
Exfoliation, 699–701
Extracting type turbines, 38

F

Fabricability, 413–416
  creep strength in cold-deformed material, 414–416
  of Sanicro 25, 413–414
    bending test for Sanicro 25 tube, 414f
    influence of aging time, 415f
Fabrication, 557–558
  casings, valves, and cast components, 252, 253f
  components, 490–496, 501–502
    forming characteristics, 490–491
    large forged components, 494–496
    pipe bending, 492
    small complex mode forgings, 494
    small forged components, 492–493
    tube bending, 491–492
  membrane walls, 250–251, 250f–251f
  operations, 491
  and properties, 155–168
    chemical composition, 79, 80f
    COST E and COST F rotor forgings, 155–162
    COST FB2, 162–168
    long-term mechanical properties, 80–82
    physical properties, 80, 82f
    weldability and weld procedures, 85–89
  welding, 125
    welded rotors for steam turbines, 251–252, 251f–252f
    welded tube assemblies, 250
Fachverband Dampfkessel, Behälter, und Rohrleitungsbau e. V. (FDBR), 559
Fatigue, 479–480, 556
  resistance, 524–527
    HCF behavior, 526–527
    LCF behavior, 525–526
$FATT_{50}$. *See* Fracture appearance transition temperatures ($FATT_{50}$)
FB2 steel, 149, 162, 778
  chemical compositions, 151f

creep behavior, 151
FB2–2 LN steel creep curves, 169f
microstructure, 154f
FBQ. *See* Fluidized bed quenching (FBQ)
FCAW. *See* Flux cored arc welding (FCAW)
FDBR. *See* Fachverband Dampfkessel, Behälter, und Rohrleitungsbau e. V. (FDBR)
Fe-Cr phase diagram, 85, 86f
FEA. *See* Finite element analysis (FEA)
FEG-SEM. *See* Field-emission gun scanning electron microscope (FEG-SEM)
FENIX700 alloy, 443–444
δ-Ferrite, 85–86
effect, 336
Ferritic
material, 113–114
steels, 837–838
FGHAZ. *See* Fine-grained heat affected zone (FGHAZ)
FIB. *See* Focused ion beam (FIB)
FIBSEM. *See* Field-emission gun scanning electron microscope and ion beam system (FIBSEM)
Field-emission gun scanning electron microscope (FEG-SEM), 204, 204f–205f
Field-emission gun scanning electron microscope and ion beam system (FIBSEM), 208–209, 209f
"Field-emission" gun, 204
Filler materials qualification for creep service, 299
Fine-grained heat affected zone (FGHAZ), 263–268
Finite element analysis (FEA), 116
Fireside corrosion, 592–593, 699–701, 829
behavior, 384–387
cold pilgered tube of Power Austenite, 388f
composition of fuels, 385t
metallographic cross-section, 386f–387f
microstructure of cold pilgered Power Austenite tube, 388f
resistance, 530–532
"Fireside" corrosion resistance, 470
Fittings, 494
Flue gas oxidation resistance, 408–410
corrosion resistance in flue gas environment, 412f
hot corrosion behavior, 411f
weight change, 411f
Fluid-modeling element, 124–125
Fluidized bed quenching (FBQ), 571–572
Flux cored arc welding (FCAW), 139, 294–297
Focused ion beam (FIB), 207–208, 208f
Forged bar, 489
Forged rotor for NextGenPower project, 579
Forging, 493, 778
of MARBN trial billets, 788f
γ′-Formation, 548
Forming
characteristics, 490–491
and properties of formed metal, 68–70
Fossil fuels, 143, 661
anthracite, 17
bituminous coal, 17–18
fossil power plants, 375
lignite, 18
natural gas, 18–19
petroleum, 19
power plants technology
coal-fired power generation plants, 6–10, 6f
fossil fuels classification, 17–19
power generation trend, 10–17
thermal power plant, 19, 20f
thermal power station types, 1–6
power stations, 1
subbituminous coal, 18
450 Scenario, 12
4°C Scenario (4DS), 12
Fracture appearance transition temperatures ($FATT_{50}$), 181
Frequent shutdown, 6
Frequent startup, 6
"Frozen fringe" holography, 237
Full-scale demonstration plant (FSDP), 805
Full-scale rotor welding A263 + COST F Ø1000 mm, 586
Fused zone (FZ), 253
Fusion welding, 496
arc welding, 247, 253
FZ. *See* Fused zone (FZ)

G

G115 pipe development, 722
Gamma prime (γ′), 138, 511–513
Gas metal arc welding (GMAW), 294–297, 498, 701–702
Gas phase embrittlement, 829
Gas tungsten arc (GTA), 603
Gas tungsten arc welding (GTAW)), 66–67, 139, 274–275, 294, 294f, 295t–296t, 701–702
Gasification, 668
  phase, 4, 5f
GBPS. *See* Grain boundary precipitation strengthened mechanism (GBPS)
GBs. *See* Grain boundaries (GBs)
Geothermal power plants, 1, 3f
GH2984G tubes manufacturing, 723–725
GHG emissions. *See* Greenhouse gas emissions (GHG emissions)
Gleeble-based CHRT methods, 533
Global warming potential (GWP), 679
Glow discharge optical emission spectroscopy, 220, 220f
GMAW. *See* Gas metal arc welding (GMAW)
Grain boundaries (GBs), 328
Grain boundary precipitation strengthened mechanism (GBPS), 376
Greenhouse gas emissions (GHG emissions), 11–12, 662
GTA. *See* Gas tungsten arc (GTA)
GTAW. *See* Gas tungsten arc welding (GTAW)
GTD450 turbine blades, 181–183
GWP. *See* Global warming potential (GWP)
GX-12CrMoVNbN9–1, 128, 129f
GX-13CrMoCoVNbNB9, 132–133
GX12CrMoVNbN10–1-1, 128, 132f

H

h-s diagram. *See* Enthalpy-entropy diagram (h-s diagram)
HAADF. *See* High annular angular dark field (HAADF)
“Hard” alloys, 487–488
Hardening, 392–393
Hardness, 236–237, 236f
Haynes 230, long-term creep in, 698
HAYNES 282 alloy, 192, 501, 511. *See also* INCONEL alloy 740H; TOS1X alloy
  castings and castability, 536–538
  composition of, 511–513
  environmental resistance properties of, 527–532
  Haynes 282 triple melt, 704
  mechanical properties of, 519–527
  metallurgical phases in, 513–515
  physical properties, 518
  thermal stability, 515–518
  welding and weldability, 532–536
HAZ. *See* Heat-affected zone (HAZ)
HCF. *See* High cycle fatigue (HCF)
HCM12, 54–57
HCM9M, 54–57
304HCu steels, 605–609
Heat
  heat-resistant
    austenitic stainless steels, 392
    materials, 392–393
  recovery steam generation, 1, 2f
  source, 1–4
  treatment, 60–63, 129, 130f, 559–563, 573
    of alloys, 79
Heat-affected zone (HAZ), 83, 111, 249, 351, 470, 780
  liquation cracking, 534–535
Heat-resistant alloys, 184–187. *See also* Titanium alloys
  alloys, 187, 188t
  chemical composition of superalloys for blades, 185t
  Inconel X-750, 186–187
  Nimonic 80A, 184–186, 186f
  Udimet 520, 187
Heavy section
  welding, 701–702
  weldments, 536
Heavy-wall martensitic 9% Cr steel castings production, 128–131
  chemistry, 129
  heat treatment, 129, 130f
  melting techniques, 130
  microstructural control, 129
  secondary refinement, 130
  weld repair, 130–131

HELE. *See* High-efficiency, low-emissions (HELE)
Heterogeneous welding, 584–586
HHV. *See* Higher heating value (HHV)
HI. *See* Holographic interferometry (HI)
HIC. *See* Hydrogen-induced cracking (HIC)
High annular angular dark field (HAADF), 212–213
High cycle fatigue (HCF), 146
  behavior, 526–527
High pressure (HP), 39, 39f
High-alloyed martensitic grades, 261–274, 266f. *See also* Low-alloyed steel grades
  creep rupture strength, 269f–270f
  CSEF steels, 266t
  graded microstructure, 266f
  heat affected zone, 268f
  history, 77–79
  martensitic steels, 77–79
  microhardness variation, 267f
  microstructure in FGHAZ, 273f
  SEM micrographs, 271f
  steel grades for boilers
    metallurgy and long-term microstructure stability, 85–89
    microstructure instability, 89–92
    nitride-free steel, 93–95
    properties and fabrication, 79–84
    service experiences, 84–85
  type IV cracking, 268f
  Vickers microhardness, 270f
High-Cr grades, weldments between, 277
High-Cr martensitic grades, 261–274, 266f. *See also* Low-alloyed steel grades
  creep rupture strength, 269f–270f
  CSEF steels, 266t
  graded microstructure, 266f
  heat affected zone, 268f
  microhardness variation, 267f
  microstructure in FGHAZ, 273f
  SEM micrographs, 271f
  type IV cracking, 268f
  Vickers microhardness, 270f
  weldments between, 276–277
High-Cr steel rotor forgings, 157
High-cycle fatigue, 181–183
High-efficiency, low-emissions (HELE), 14–15, 15f
High-pressure (HP), 145, 178, 793
  turbine, 146f
High-pressure turbine (HPT), 751
High-strength austenitic material development, 392–393
High-strength Ni-based alloy HR6W, 423
High-temperature corrosion, 556–557
  and steam oxidation behavior, 407–410
    behaviors, 407
    hot corrosion or flue gas oxidation resistance, 408–410
    oxidation resistance in steam, 407–408
High-temperature reactor projects (HTR projects), 547
High-temperature tensile, 476
Higher heating value (HHV), 14–15
HIP. *See* Hot isostatic pressing (HIP)
Hochtemperatur Werkstoff Teststrecke (HWTI), 814
  flow chart of HWT II test loop, 817f
  HWT I project, 814
  HWT II, 815
Holographic interferometry (HI), 237, 237f
Homogenous welding, 581–584, 584f
Hot corrosion, 408–410, 557
  corrosion resistance in flue gas environment, 412f
  hot corrosion behavior, 411f
  properties, 438–441
  tests, 742, 743f
  weight change, 411f
Hot induction bending, 492
Hot isostatic pressing (HIP), 824
Hot wire gas tungsten arc welding process (HW-GTAW process), 536
Hot wire GTAW, 701–702
Hot wire TIG. *See* Hot wire GTAW
Hot working, 572
HP. *See* High pressure (HP); High-pressure (HP)
HPT. *See* High-pressure turbine (HPT)
HR35 alloy, 434–438. *See also* HR6W alloy
  creep rupture strength
    microstructure, and other properties, 435–437
    of welded joints, 437–438
  design and properties, 434
  steels, 605–609

HR6W alloy, 424–434. *See also* HR35 alloy
creep rupture strength and microstructure evolution, 426–428
design and properties, 424–425
long-term creep, 698
mock-up manufacture and properties, 430–434
service performance, 429–430
steels, 605–609
HSC. *See* Hyper-supercritical (HSC)
HTR projects. *See* High-temperature reactor projects (HTR projects)
Hua-Neng Nanjing Power Plant, 726–727
HW-GTAW process. *See* Hot wire gas tungsten arc welding process (HW-GTAW process)
HWTI. *See* Hochtemperatur Werkstoff Teststrecke (HWTI)
Hydrocarbon gas, 18
Hydrogen delayed cracking, 283–284, 284f
Hydrogen-induced cracking (HIC), 111
Hyper-supercritical (HSC), 113

I

IC heated HAZ. *See* Intercritically heated HAZ (IC heated HAZ)
IEA. *See* International Energy Agency (IEA)
IEA New Policy Scenario, 13, 13f
IGCAR. *See* Indira Gandhi Centre for Atomic Research (IGCAR)
IGCC technology. *See* Integrated gasification combined cycle technology (IGCC technology)
IMPACT project. *See* Innovative Materials Design and Monitoring of Power Plant to Accommodate Carbon Capture project (IMPACT project)
IMR. *See* Institute of Metal Research (IMR)
In-shop fabrication, 247–249
Inconel 740/740H
development, 697–698
impact toughness comparison, 730t
structure stability, 727–730
INCONEL alloy 740H. *See also* HAYNES 282 alloy; TOS1X alloy
alloy 263, 469–470
casting, 496
composition, 470
corrosion properties, 481–486
fabrication of components, 490–496
mechanical properties, 474–481
microstructure and phase stability, 470–474
mill product forms, manufacturing of, 486
nickel-based alloys, 469
welding, 496–504
Inconel X-750, 186–187
Indian A-USC program, 755–761. *See also* Chinese 700°C A-USC development program; US DOE/OCDO A-USC materials technology R&D program
coal production and consumption trend, 759f
coal-fired power plant capacity, 762f
conclusion, 760–761
efficiencies of Indian power plants, 758f
Indian installed power generation capacity, 756f
map of thermal power plants, 757f
materials
NTPC target program, 762f
power capacity addition, 759t
status of coal-fired thermal power plants, 761f
Indira Gandhi Centre for Atomic Research (IGCAR), 758
Induction turbines, 38
Industrial radiography. *See* Radiographic testing (RT)
Infrared
and thermal testing, 237
thermography, 237–239, 238f
Innovative Materials Design and Monitoring of Power Plant to Accommodate Carbon Capture project (IMPACT project), 778–780
Institute of Metal Research (IMR), 716
Integrated gasification combined cycle technology (IGCC technology), 4, 662
Intercritically heated HAZ (IC heated HAZ), 263–265
Intergovernmental Panel on Climate Change (IPCC), 664
Intermediate load plants, 5
Intermediate pressure (IP), 39, 39f, 145, 180–181
steam, 32

Intermediate-pressure turbine (IPT), 751
International Energy Agency (IEA), 13, 654, 676, 689–691
International Organization for Standardization (ISO), 677
IP. *See* Intermediate pressure (IP)
IPCC. *See* Intergovernmental Panel on Climate Change (IPCC)
IPT. *See* Intermediate-pressure turbine (IPT)
ISO. *See* International Organization for Standardization (ISO)
Iso-Mar heat treatment, 169
Isogo power station, 735, 735f
ITOS1X-II, 748–749

J

Japan
  annual power generation, 736, 736f
  existing plants and steam condition, 735–736, 735f
  Isogo power station, 735, 735f
  Japanese materials for A-USC power plants, 423
    boiler tubes and pipes, evelopment of, 424–443
    superalloys development in MHPS, 443–460
    TOS1X alloy, 460–465
  METI, 423–424
  PC power plants of capacity in, 733f
  steam temperature and pressure, 734f
  Tachibanawan power station, 734, 734f
JIP. *See* Joint Industrial Programme (JIP)
JMatPro simulation software, 229
Joint Industrial Programme (JIP), 836
  JIP 1, 836–837
Joint Industry Project, 559

K

Knowledge-based Multifunctional Materials Virtual Institute (KMM-VIN), 785
  EMEP, 785–788
KOMET 650, 812–814

L

Ladle furnace (LF), 163
Large forged components, 494–496
Larson–Miller parameter (LMP), 131, 523–524
Latest alloy developments
  CB2 type 9% Cr steel, 132–133
  MarBN steels, 133, 134f
Laves phase, 88–89, 89f
  strengthened concept, 376
LCF. *See* Low cycle fatigue (LCF); Low-cycle fatigue (LCF)
LCTR. *See* Liquation cracking temperature range (LCTR)
Leading edge protection, 193–195, 194f
LF. *See* Ladle furnace (LF)
LHV. *See* Lower heating value (LHV)
Light microscope, 201f
Light optical microscopy, 201–202
Lignite, 18
Linear accelerator (LINAC), 242–243, 242f–243f
Liquation cracking temperature range (LCTR), 534–535
Liquid penetrant inspection (LPI). *See* Dye penetrant inspection
Liquid shrinkage, 124
LMP. *See* Larson–Miller parameter (LMP)
Long time aged properties, 501
Long-term creep
  in HR6W, Haynes 230, and CCA617, 698
  testing, 77–78
Long-term high creep resistance, 395
Long-term microstructure stability, 85–89
  microstructure stability, 87–88
  precipitate stability, 88–89
Long-term properties, alloy 263, 586
Long-term weldment creep tests, 701–702
“Longwall” mining, 647
Low cycle fatigue (LCF), 146
Low-alloy ferritic steels, 83
Low-alloyed steam pipe steels, 84
Low-alloyed steel development
  chemical requirements for, 58t
  conventional low-alloyed steels, 53–54
  creep strength–enhanced low-alloyed steels, 54–57
  material designations of UNS number, 59t
Low-alloyed steel grades, 258–261, 259f–260f. *See also* High-alloyed martensitic grades

Low-alloyed steel grades (*Continued*)
chemical composition of welding wires, 262t
development of low-alloyed steels, 53–57
forming and properties of formed metal, 68–70
properties and metallurgy, 57–63
SAW homogeneous, 263t, 265t
service degradation, 70–74
SMAW homogeneous, 264t
welding and properties of welds, 63–68
Low-carbon
9Cr steel, 324
electricity, 663
martensitic steels, 169
Low-Cr bainitic grades, weldments between, 276
Low-Cr grades, weldments between, 277
Low-Cr steel grades, 258–261, 259f–260f. *See also* High-alloyed martensitic grades
chemical composition of welding wires, 262t
SAW homogeneous, 263t, 265t
SMAW homogeneous, 264t
Low-cycle fatigue (LCF), 180–181
behavior, 525–526
electron channel contrast image of microstructures, 407f
properties, 405–407, 406f
Low-pressure (LP), 145, 175–176
turbine, 6–7
Low-rank coals, 644
Lower heating value (LHV), 14–15
LP. *See* Low-pressure (LP)
LTES700 alloy, 748–749
LTES700R alloy, 443, 446–447, 749, 750f
coefficient of thermal expansion, 749f
creep rupture strength, 750f

M

M.I.G. processes, 578
$M_{23}C_6$ carbides, 326, 330
coarsening rate, 337
distribution, 345–346
elimination, 341
enrichment of boron, 349
MACPLUS, 831–833
MACPLUS-COMTES700/ETR/TV-cooperation, 833
Magnetic particle inspection (MPI), 235–236, 236f, 625
Manual metal arc (MMA), 66–67, 249–250, 289, 614
Manual metal arc welding (MMAW), 289–293, 290t–292t
MARBN. *See* Martensitic 9Cr steel strengthened by boron and MX nitrides (MARBN)
MARCKO. *See* Materials of Low CO_2 Power Plant (MARCKO)
MARCKO 700. *See* Material Qualification for 700/720°C Power Plant (MARCKO 700)
MARN. *See* MARtensitic 9Cr steel strengthened by nano-size MX nitrides (MARN)
Martensite finish temperature (MF temperature), 129
Martensitic 9–12% Cr steels, 77, 83f, 323
in creep, methods of strengthening, 326–331
boundary hardening, 330–331, 330f
dislocation hardening, 329
precipitation hardening, 328–329, 328t, 329f
solid solution hardening, 326–328, 327f
sub-boundary hardening, 330–331, 330f
rotor steels for USC application, 147–155
chemical compositions of steel FB2, 151f
COST developed 10–12% Cr steels, 149f
COST FB2 trial rotor forgings, 152f
creep rupture strength, 154f
data and mechanical properties, 153f
materials for USCs, 155f
mechanical properties of trial rotor FB2, 151f
microstructure of FB2, 154f
10–12% Cr steam turbine rotor steels, 148f
10–12% Cr steels, 147f
Martensitic 9Cr steel
MARBN, 344–368
MARN, 341–344, 342f
precipitate design, 338–341, 340f
Martensitic 9Cr steel strengthened by boron and MX nitrides (MARBN), 133, 134f, 344, 362–363

additive strengthening, 346–351, 347f
effect of boron, 344–346, 345f–346f
creep rupture data, 362f
filler material composition, 607t
hardness maps of MARBN weldments, 606f
mechanisms for boron effect, 358–361
oxidation resistance improvement by pretreatment, 363–367
pipe production, 367–368, 367f
steels, 169, 604, 780
suppression of Type IV fracture, 351–358
MARtensitic 9Cr steel strengthened by nano-size MX nitrides (MARN), 341–344, 342f–344f
Martensitic grades, Weldments between, 277, 278f
Martensitic PH grades, 181
Martensitic stainless steels, 178
Martensitic steels, 79, 249
for cast components
bigger, hotter, higher pressure, 132
cast materials for A-USC, 134–139
casting materials for USC applications, 126–128
heavy-wall martensitic 9% Cr steel castings production, 128–131
latest alloy developments, 132–133
material requirements for USC application, 121
state-of-the-art technology, 132–133
steam turbine applications, 121–126
degradation in creep strength, 331–337
methods of strengthening martensitic 9 to 12Cr steels in creep, 326–331
new martensitic 9Cr steel, 338–368
9 to 12Cr martensitic steels in coal power plants, 324–326
for rotors
international R&D projects, 144f
martensitic 9–12% Cr rotor steels for USC application, 147–155
material development for application temperatures, 168–170
materials for steam turbine rotors in Europe, 155–168
rotor material requirements, 144–147, 145f
steam temperature of coal-fired power plants, 324f
tempered martensitic microstructure and creep deformation, 337–338
weldments between nickel alloys and, 619
Master Cycle, 805
MATCALC project, 229–232, 230f
annealing, 231–232, 232f
austenitizing, 230
tempering, 231, 231f
MatCalc software, 199
Material corrosion, 407
Material Qualification for 700/720°C Power Plant (MARCKO 700), 811–812
Materials of Low CO_2 Power Plant (MARCKO), 811
Materials selection, 693–694
creep-rupture strength, 694f
ferritic and iron-based austenitic alloys, 694t
nickel-based alloys, 695t
nominal alloy compositions, 696t
Maximum crack length data (MCL data), 533–534
MDDS. *See* Minimum detectable defect size (MDDS)
Mechanical preparation method, 199
Mechanical properties
alloy 263, 573, 583t
VM12-SHC tube weldments, 608t
Mechanized ultrasonic testing, 801
Melting, 486–487
techniques, 130
Membrane walls
fabrication, 250–251, 250f–251f
materials for, 800
Metal chemical analysis, 198
Metal inert gas (MIG), 66–67, 294–297
Metallic atom and non-metallic atom particles (MX particles), 108, 133
MX carbonitrides, 342f
Metallic materials, 247–249
Metallography, 199–200, 200f
metallographic specimens, 200
Metallurgical phases in HAYNES 282 alloy, 511–513
Metallurgically stable material, 87
Metallurgy, 85–89
Alloy 617, 548–551
heat treatment and, 60–63
microstructure stability, 87–88
precipitate stability, 88–89

Metallurgy (*Continued*)
properties and, 57–63
steel grades in code and mechanical properties, 57–60
METI. *See* Ministry of Economy, Trade, and Industry (METI)
MF temperature. *See* Martensite finish temperature (MF temperature)
MHI. *See* Mitsubishi Heavy Industries (MHI)
MHPS. *See* Mitsubishi Hitachi Power Systems (MHPS)
Microscopy, 200–219
APFIM, 217–219, 218f
EBSD, 205–207, 206f–207f
EFTEM, 212–217, 213f–216f
FEG-SEM, 204, 204f–205f
FIB, 207–208, 208f
FIBSEM, 208–209, 209f
light optical, 201–202
SEM, 202–203, 203f
STEM, 211, 212f
TEM, 209–210, 210f–211f
Microstructural/microstructure
alloy 740H, 470–474
analyses, 197, 698. *See also* Surface analysis
alloy 263, 573–578
modeling tools, 224–232
control, 129
evolution
HR35, 435–437
HR6W, 426–428, 428f
evolutions, 394–395
instability, 89–92
microstructural
investigations, 199
microstructural-crystallographic technique, 205
stability, 99
sigma, 377–381
Power Austenite, 379t
sigma phase in binary Fe-Cr system, 378f, 378t
strengthening concept of Power Austenite, 380f–381f
thermo-calc calculation of phases, 379f
stability, 87–88, 89t, 395–397, 469
MIG. *See* Metal inert gas (MIG)
Mill product forms, manufacturing of, 486
melting and remelting, 486–487
other mill product forms, 489
pipe manufacturing, 488–489
tubing manufacturing, 487–488
Millions of tons of waste products, 662
Mineral storage, 673
Minimum detectable defect size (MDDS), 152f, 163–164
Mining
coal, 646–649
coal transport and process, 648–649, 649f
mountaintop removal mining, 648, 649f
surface mining, 647–648
underground mining, 647
destruction, 662
Ministry of Economy, Trade, and Industry (METI), 423–424
Minor alloying additions, 511–513
Mitigation of carbon migration, 276
Mitsubishi Heavy Industries (MHI), 137
Mitsubishi Hitachi Power Systems (MHPS), 423
superalloys development in, 443–460
MMA. *See* Manual metal arc (MMA)
MMAW. *See* Manual metal arc welding (MMAW)
Modeling tools
CALPHAD, 228–229
DICTRA software, 227–228, 227f
JMatPro simulation software, 229
MATCALC project, 229–232, 230f
thermo-Calc software, 224–226, 225f–226f
Modified 9% Cr steels, 126–128
Mold cavity, 122–123, 123f
Molding process, 122, 123f
Mollier diagram. *See* Enthalpy-entropy diagram (h-s diagram)
Molten metal, 123
Molybdenum (Mo), 53–54, 133, 511–513
Mountain-top removal, 648
Mountaintop removal mining, 648, 649f
MPI. *See* Magnetic particle inspection (MPI)
MT. *See* Magnetic particle inspection (MPI)
MX particles. *See* Metallic atom and non-metallic atom particles (MX particles)

N

310N(HR3C) steels, 605–609
Nanomaterials, 204
NAPCC. *See* National Action Plan on Climate Change (NAPCC)
Narrow gap (NG), 614
Narrow gap gas tungsten arc (NG-GTA), 614, 627–628
National Action Plan on Climate Change (NAPCC), 757–758
National Energy Technology Laboratory (NETL), 536, 658, 691
National Thermal Power Corporation (NTPC), 758
  target program, 762f
Natural gas, 1, 18–19
"Nb-free" steel, 628
NDE. *See* Nondestructive evaluation (NDE); Nondestructive examination (NDE)
NDI. *See* Nondestructive inspection (NDI)
NDT. *See* Nondestructive testing (NDT)
Negative creep, 113, 829
NETL. *See* National Energy Technology Laboratory (NETL)
Neutron radiographic testing, 239
New Policies Scenario, 11–12
NextGenPower project, 827–831
  casting, 830
  creep, fatigue, and creep/fatigue interaction, 829–830
  creep properties, 828f
  by DNV KEMA, 827
  fireside corrosion, 829
  forged rotor for, 579
  forging precipitation hardening Ni alloys, 830
  highlights of results, 830–831
  material choice, 828–829
  material selection, 830
  mechanical issues, 829
  overview and partnership of project, 827f
  rotor forging, 830
  rotor welding, 579–586
  SP1 boiler and pipework, 827
  spin-off, 831
  steam-side oxidation, 829
NG. *See* Narrow gap (NG)
NG-GTA. *See* Narrow gap gas tungsten arc (NG-GTA)
Nickel alloys (Ni-based alloys), 100, 101f, 363, 391–392, 469, 519–520, 530, 552, 556–557, 563, 609–614, 695t, 745, 747, 838
  as candidate materials for A-USC blades, 189–192, 190t, 191f
  development, 442
  Ni alloy 625, 602
  superalloys, 423, 783
    TOS1X, 423
  testability of thick-walled components from, 808–809
  weldments between martensitic steels and, 619
Nil strength temperature (NST), 534–535
Nimonic 105, 191–192
Nimonic 263. *See* Alloy 263
Nimonic 80A, 184–186, 186f
Niobium (Nb), 414, 461
Nippon Steel & Sumitomo Metal Corporation (NSSM), 423
Nitride-free steel, 93–95
Nitrogen concentration, 332–333
Nominal alloy compositions, 696t
Noncondensing turbines, 38
Nondestructive analyses, 198
Nondestructive evaluation (NDE), 232–233
Nondestructive examination (NDE), 232–233
  methods for cast nickel-based alloys, 810
Nondestructive inspection (NDI), 232–233
Nondestructive testing (NDT), 625–627, 197, 232–243, 299–313, 311t–312t, 817–818
  AE, 233–234, 234f
  dye penetrant, 233
  eddy-current testing, 234–235, 235f
  gas back protection, 302
  hardness, 236–237, 236f
  heating and cooling assembly, hydrogen control, 302–304, 303f
  HI, 237, 237f
  infrared thermography, 238–239
  LINAC, 242–243, 242f–243f

Nondestructive testing (*Continued*)
MPI, 235–236, 236f
preheating and interpass, 304–313, 304t
RT, 239–240
testability of thick-walled components, 808–809
ultrasonic phased array systems, 241–242
UT, 240–241, 240f
weld metal shape, 302
welding methods, 302
Nonrenewable resource, 18
North Rhine-Westphalia Power Plant at 700°C (NRWPP700), 805–808
NRWPP700. *See* North Rhine-Westphalia Power Plant at 700°C (NRWPP700)
NSSM. *See* Nippon Steel & Sumitomo Metal Corporation (NSSM)
NST. *See* Nil strength temperature (NST)
NTPC. *See* National Thermal Power Corporation (NTPC)
Nuclear power plant, 1, 2f

O

Oak Ridge National Laboratory (ORNL), 476, 498–500, 518, 691
OCDO. *See* Ohio Coal Development Office (OCDO)
OECD. *See* Organisation for Economic Co-operation and Development (OECD)
OEMs. *See* Original equipment manufacturers (OEMs)
Ohio Coal Development Office (OCDO), 689, 691
Oil recovery and storage, 669f
Optical microscopy, 200–201
Optimized alloy *vs*. C-263, 592
Optimized C-263 grade, 591
Organic maturity, 643
Organisation for Economic Co-operation and Development (OECD), 15–16, 716
Original equipment manufacturers (OEMs), 176
ORNL. *See* Oak Ridge National Laboratory (ORNL)
Orowan stress, 328
Ostwald ripening of carbides, 361
Over-tempering, 131
Oxidation, 281, 376, 704–705
in dry air, 482–484
oxidation resistance
by pretreatment, 363–367, 364f–365f
in steam, 407–408
Sanicro 25 SEM images, 410f
steam, 482–484, 593–598
atmospheres, 528–530
resistance of austenitic stainless steels, 409f
in water vapor, 528–530
Oxyfuel system, 671f
oxy-fuel coal combustion, 834
oxyfuel combustion systems, 670

P

p-h diagram. *See* Pressure-enthalpy diagram (p-h diagram)
P91 steel, 79
P92 steel, 83, 87f, 88
PAGB. *See* Prior austenite grain boundary (PAGB)
Particle strengthening, 93
Particle testing (PT), 309–310
“Partner Steam Power Plant” for regenerative power generation, 835
parts per million (ppm), 220–221
PBHT. *See* Post-bend heat treatment (PBHT)
Peaking power plants, 5
Penetrant testing. *See* Dye penetrant inspection
PESR. *See* Ar-protected atmosphere (PESR); Protective gas electro slag remelting (PESR)
Petroleum, 18–19
PH steels. *See* Precipitation hardenable steels (PH steels)
17–4 PH turbine blades, 181–183
Phase equilibrium software, 472–473
Phase stability diagram for alloy 740H, 470–474
Phase transition, 44
γ′-Phase, 548
stability, 518
and coarsening behavior, 517–518
PHT. *See* Preliminary heat treatment (PHT)
Physical metallurgy of alloy 263, 571–572
Pilot testing rig for China’s 700°C A-USC coal-fired demo plant, 726–727

"Pinning effect", 133
Pipe
  bending, 492
  fitting, 44, 45f
  manufacturing, 488–489
  system, 84
Pipeline monitoring process, 813
Planer dislocation structure, 406–407
Plant erection, 247–249
PnP program. *See* Prototype Nuclear Process Heat program (PnP program)
POEMA project, 834
Post AD700 project, 814–815
Post-bend heat treatment (PBHT), 105
Post-combustion
  capture, 668–670
  scrubbing technology, 670f
Post-weld heat treatment (PWHT), 630, 100, 111–112, 131, 250, 305–307, 306t, 307f, 351–354, 354f, 354t, 632
Powdered coal. *See* Pulverized coal
Power Austenite, 377–387
  alloying concept and microstructure sigma, 377–381
  creep strength, 381–383
  fireside corrosion behavior, 384–387
Power generation trend, 10–17
  age distribution of existing power plants, 16f
  electricity production from coal, 12f
  low carbon scenario, 16f
  size of challenge is clear, 13f
Power Plant (PP), 5–6, 24–25
PP. *See* Power Plant (PP)
ppm. *See* parts per million (ppm)
Practical limit, 813
Pre-combustion capture, 667–668, 669f
Pre-engineering study, 805–808
Precipitate stability, 88–89
Precipitation hardenable steels (PH steels), 180–183, 182t, 183f
Precipitation hardening, 186, 191–192, 328–329, 328t, 329f, 511, 574
Precipitation-strengthened nickel alloys, 621
Preheating and interpass, 304–313, 304t
  nondestructive testing, 309–313, 311t–312t
  PWHT, 305–307, 306t, 307f
  weldment testing, 307–309, 310f
Preliminary heat treatment (PHT), 163–164
Pressure-enthalpy diagram (p-h diagram), 22, 23f
Pretreatment, oxidation resistance improvement by, 363–367, 364f–365f
Prior austenite grain boundary (PAGB), 214, 272, 323
Protective gas electro slag remelting (PESR), 157
Prototype Nuclear Process Heat program (PnP program), 547
PT. *See* Particle testing (PT)
Pulverized coal, 7
  PC power plants, 733–734
    capacity in Japan, 733f
  pulverized coal-fired boiler, 7
PWHT. *See* Post-weld heat treatment (PWHT)

Q

QHT. *See* Quality heat-treatment (QHT)
Quality assurance, 299–313
  gas back protection, 302
  heating and cooling assembly, hydrogen control, 302–304, 303f
  preheating and interpass, 304–313, 304t
  weld metal shape, 302
  welding methods, 302
Quality heat-treatment (QHT), 159
Quality of steam, 22

R

R-41 alloy, 511–513, 517–518
R&D programs
  on materials for USC and A-USC power plants, 773–775
  overview and chronology, 774f
Radiographic testing (RT), 239–240, 239f, 308
"Rank" of coal, 644
Rankine cycle, 6, 7f
Raw material production, 187
Regenerative power generation, "Partner Steam Power Plant" for, 835
Reheat cracking, 111–112, 551, 564, 612–613, 829

Reheat turbines, 38
Reheaters (RHs), 24–25, 31–33, 34f, 53, 699–700, 720
  materials for, 720
  tubing, 102
Relaxation annealing, 559–560
Relaxation cracking. *See* Reheat cracking; Stress relief cracking
Remelting, 486–487
Repair welding, 278–279, 617–619
  weldments between
    martensitic steels and nickel alloys, 619
    weldments between USC martensitic steels and A-USC austenitic steels, 617
Research Fund for Coal and Steel (RFCS), 773
Residential electricity use, 654
Residual storage, 672
RFCS. *See* European Research Fund for Coal and Steel (RFCS); Research Fund for Coal and Steel (RFCS)
RHs. *See* Reheaters (RHs)
Rifled tubes, 27, 28f
Rig, 416
Room and pillar mining, 647
Rotor welding. *See also* Welding
  for NextGenPower project, 579–586
    full-scale rotor welding A263 + COST F Ø1000 mm, 586
    heterogeneous welding, 584–586
    homogenous welding, 581–584, 584f
    production of trial 1000-mm rotor, 582f
  welding technologies, fabrication issues, NDT, 625–627
Rotor(s), 704
  forging, 830
  forging and welding, 830
  material requirements, 144–147, 145f
Round robin test. *See* Base test
RT. *See* Radiographic testing (RT)
Russian SC technology, 762–763
  Kashirskaya thermal power plant, 763f

S

SA. *See* Solution-annealed (SA)
SAGBO. *See* Stress-assisted grain boundary oxidation (SAGBO)
Sand casting process, 122
Sand system, 122
Sanicro25 steels, 375–376, 605–609, 791
  creep and rupture behaviors, 397–405
  creep strength, 413, 413f
  fabricability, 413–416
  field experiences, 416–417
  future trends, 417–418
  high-strength austenitic material, development of, 392–393
  high-temperature corrosion and steam oxidation behavior, 407–410
  low-cycle fatigue properties, 405–407
  microstructure, 394–397
  standard and code cases for, 400–403
  weldability of, 410–413
SAVE 25 alloy, 375
SAW. *See* Submerged arc welding (SAW)
SC technology. *See* Supercritical technology (SC technology)
Scanning electron microscope (SEM), 202–203, 470–472, 594
Scanning probe microscopy, 200–201
Scanning transmission electron microscope (STEM), 211, 212f
SCC. *See* Stress corrosion cracking (SCC)
Schaeffler diagram, 99–100, 100f
Schottky emitter, 204
SCPC plants. *See* Supercritical pulverized coal plants (SCPC plants)
SE. *See* Secondary electrons (SE)
Secondary electrons (SE), 202, 204
Secondary hardening, 112–113, 113f
Secondary ion mass spectrometry (SIMS), 221–222, 221f, 348–350
  XPS, 222, 223f
Secondary phase formation, 516–517
Secondary refinement, 130
Sectorial scanning, 241–242
SEM. *See* Scanning electron microscope (SEM)
Sendai nuclear power plant, 736
Sensitization, 103–105, 104f–105f
  austenitic steels used in boiler applications, 106t–107t
Service degradation, 70–74
  creep degradation, 70–71, 72f
  steam oxidation, 71–74
700°C technology, 822
  steam technology, 783
Shaft arrangements. *See* Casing

Sheet alloys, 489
Shielded metal arc welding (SMAW), 66–67, 139, 289–293, 293f, 619–621
Shop-floor welding, 496–497
Short-term strength behavior, 281, 282f
SHs. *See* Superheaters (SHs)
Sigma-phase, 377
  embrittlement, 109
  precipitation, 108–109, 110f
  sigma stabilizing elements, 378
  strengthened concept, 377–387
    alloying concept and microstructure sigma, 377–381
    creep strength, 381–383
    fireside corrosion behavior, 384–387
SIMS. *See* Secondary ion mass spectrometry (SIMS)
Single-flow rotors, 39, 39f
SIPH. *See* Strain-induced precipitation hardening (SIPH)
6°C Scenario (6DS), 12
Slow strain rate tensile test (SSRT), 560
Small complex mode forgings, 494
Small forged components, 492–493
Small-scale tests, 813
SMAW. *See* Shielded metal arc welding (SMAW)
SMC. *See* Special Metals Corp. (SMC)
Soft annealing, 559–560
Solar energies, 143
Solar thermal electric plants, 3, 4f
Solid solution
  alloys, 511
  hardening, 326–328, 327f
  solid solution–strengthened alloys, 135
Solid-particle erosion (SPE), 704–705
Solid-state contraction, 123
Solidification
  cracking, 604, 609, 628
  ferritic grades, 255
Solid–liquid transition zone, 253–254
Solution-annealed (SA), 414, 476
Solution-strengthened alloys, 191
Solution-strengthening elements, 574
South Africa, power sources in, 766–767
  Eskom power plant mix, 766t
South Korean CF power plants, 763–764, 764f
  installation plan at Taean thermal power plant, 765f
  regional changes of installed capacity of coal power plants, 765f
SPE. *See* Solid-particle erosion (SPE)
Special Metals Corp. (SMC), 697, 727
Spiral furnace tube, 25–26, 28f
Spooled welding wire, 489
Sputtering, 220
SRF. *See* Stress reduction factor (SRF)
SSRT. *See* Slow strain rate tensile test (SSRT)
Stainless steels, 178–183
  12% Cr steels, 178–180, 179t, 180f
  9–12% Cr steels, 180–183, 182t, 183f
  PH steels, 180–183, 182t, 183f
Standard and code cases for Sanicro 25, 400–403
State-of-the-art technology
  CB2 type 9% Cr steel, 132–133
  MarBN steels, 133, 134f
  state-of-the art field-emission guns, 204
Static oxidation behavior in air, 527–528
Steam, 407–408
  line, 33, 36f
  path accuracy, 193
  power plants, 77, 733–734
  steam-side oxidation, 71–74, 408, 593–598, 699–701, 829
    resistance, 100, 101f
    tests, 438–441, 742, 743f
    TP 310HCbN, 408
  valves, 33–38, 36f–38f
Steam turbine, 6, 38, 42f, 702–704
  applications, 121–126
  attemperator, 44, 44f
  candidate materials for steam turbine rotors, 747, 748t
  casing, 39–40
  condenser, 44, 45f
  economizer, 41–43, 43f
  fabrication of welded rotors for, 251–252, 251f–252f
  pipe fitting, 44, 45f
  rotors in Europe, materials for, 155–168
    COST E and COST F rotor forgings, 155–162
    COST FB2, 162–168
  700°C-class, 745
  1000-MW-class, 751, 751f
  turbine blades, 41, 43f

Steam/water diagrams in boiler calculations, 19–24
h-s diagram, 24, 24f
p-h diagram, 22, 23f
T-Q diagram, 19–20, 21f
T-s diagram, 20–22, 21f–22f
Steel(s), 132, 197. *See also* Martensitic steels for rotors; Stainless steels
grades in code and mechanical properties, 57–60
steel HR3C, 375
Steels Tempaloy A-3 and NF 709, 375
STEM. *See* Scanning transmission electron microscope (STEM)
Strain-age cracking, 192
susceptibility, 532–533
Strain-induced precipitation hardening (SIPH), 100, 105–108, 108f
Stress corrosion cracking (SCC), 109–111, 111f, 283–284, 284f, 486, 562
Stress reduction factor (SRF), 286
Stress relaxation cracking, 504, 559–561
Stress relief cracking, 111–112, 284, 504
Stress-assisted grain boundary oxidation (SAGBO), 562
Strip mining, 648f
Structural storage, 672
Sub-boundary hardening, 330–331, 330f
Subbituminous coal, 18, 643
Subcritical pulverized coal plants (SubCPC plants), 8
Submerged arc welding (SAW), 297–299, 298f, 300t, 614
welding, 632t
Substitutional solute atoms, 326
Super 304HCu, 375
Superalloys, 197, 469
for A-USC, 774–775
development in MHPS, 443–460
alloy design strategy, 443–444
FENIX700 alloy, 444
LTES700R alloy, 446–447
USC141 alloy, 449–453
USC800 alloy, 453–460
EU superalloys development research programs for A-USC, 789–811
pipe, 488
Supercritical carbon dioxide, corrosion in, 486
Supercritical pulverized coal plants (SCPC plants), 8
Supercritical technology (SC technology), 756
Superheaters (SHs), 24–25, 31–33, 32f, 34f, 53, 699–700, 720
materials for, 720, 800–801
test section, 825–826
tubing, 102
Surface analysis. *See also* Microstructural analyses
AES, 219–220
EMP, 220–221
glow discharge optical emission spectroscopy, 220
SIMS, 221–222
XRD, 223, 224f
Surface hardening, 193–194
Surface mining, 647–648

T

T-Q diagram. *See* Temperature-heat diagram (T-Q diagram)
T-s diagram. *See* Temperature-entropy diagram (T-s diagram)
T. I. G. processes, 578
T23 steel, 53–57, 62–64
benefit, 70
effect of cooling rate, 65f–66f
creep rupture properties, 71f
high-strength, 67–68
microstructural changes, 72f
microstructures, 65f
welding, 66–67
T24 steel, 53–57, 62–64
benefit, 70
continuous cooling transformation diagrams for, 64f
high-strength, 67–68
welding, 66–67
Tachibanawan power station, 734, 734f
Tandem-compound turbines, 39, 40f
Tantalum (Ta), 461
TBCs, innovative, 193
Tectonic movements, 643
TEM. *See* Transmission electron microscopy (TEM)
Tempaloy AA-1 steels, 605–609
Temper embrittlement, 284

Temperature-entropy diagram (T-s diagram), 20–22, 21f–22f
Temperature-heat diagram (T-Q diagram), 19–20, 21f
Tempered martensitic microstructure and creep deformation, 337–338, 338f
Tempering, 231, 231f
Tensile properties
  HAYNES 282 alloy, 519–521
  for tubes and pipes, 476
Test facility (TF), 825
Tetragonal Z-phase crystal, 90, 92f
TF. *See* Test facility (TF)
Thermal efficiency, 733–734, 736–737
Thermal expansion coefficient (CTE), 446
Thermal fatigue, 102, 102t, 103f
Thermal power plant, 19, 20f, 99
  best technology, 45–46, 47f
  boiler, 24–38
  station types, 1–6
    classification by heat source, 1–4
    classification of power plants by duty, 5–6
  steam turbine, 38
  steam/water diagrams in boiler calculations, 19–24
Thermal shock, 813–814
Thermal stability, 515–518
  secondary phase formation, 516–517
  stability and coarsening behavior of γ′ phase, 517–518
Thermie AD700 technology, 391
Thermie program, 487–488
Thermo-Calc software, 199, 224–226, 225f–226f, 339–341, 392–393, 472–473
Thermogenic processes, 18–19
Thermomechanical fatigue tests (TMF tests), 284, 556
Threshold stress, 328
Ti-6Al-4V, 183–184
Ti-Al couple for Nimonic C-263, 226
TIG. *See* Tungsten inert gas (TIG)
Time-of-flight (ToF), 349–350
Titanium, 548. *See also* Heat-resistant alloys
  density, 183
  Ti-6Al-4V, 183–184
TMF tests. *See* Thermomechanical fatigue tests (TMF tests)
ToF. *See* Time-of-flight (ToF)
TOS 110 steel, 93–95
TOS1X alloy, 460–465, 748–749. *See also* HAYNES 282 alloy; INCONEL alloy 740H
  creep rupture strength, 748f
  TOS1X, 461
  TOS1X-2, 461–465
  Toshiba alloy design strategy, 460–461
Toshiba alloy design strategy, 460–461
Toughness, 630
TP310MoCbN, 408–410
TP347HFG steels, 375, 605–609
Transmission electron microscopy (TEM), 209–210, 210f–211f, 394–395, 470–472, 550–551
Trial components manufacturing, 579–586
  NextGenPower project
    forged rotor for, 579
    rotor welding for, 579–586
  pipe for ENCIO project, 579
Tube bending, 491–492
Tubing manufacturing, 487–488
Tungsten (W), 427–428, 698
Tungsten inert gas (TIG), 66–67, 294, 607
  welding, 410–411
Turbine blades, 41, 43f
  alloys, 178–187
  blades, 175
  coatings, 193–195
  fir-tree roots, 176f
  hammer-forging, 177f
  highly alloyed steels, 177
  roots, 175–176
  tensile and fatigue strengths, 176–177
  trends in USC steam turbine blading, 189–192
  in USC power plants, 175
Turbine components, 802
Turbine materials. *See also* Boiler materials
  castings for casings and valve bodies, 702–704
  coatings, 704–705
  oxidation, 704–705
  rotors, 704
Turbine materials subgroup, AD700 R&D program, 792–793
Turbine rotors, 165
Turbine test sections, 826

Turkey, power sources in, 767–769
  installed capacity and electricity generation, 769f
  location of Turkish coal mines, 768f
  planned coal power plants, 770f
Two-flow rotors, 39–40, 39f
2°C Scenario (2DS), 12
Type IV cracking, 83–84, 85f, 268f, 603
Type IV fracture suppression in HAZ of welded joints, 351–358, 352f
  schematics of welded joints, 353f
  thermal cycle conditions of simulated-HAZ specimens, 353f

U

Udimet 520, 187
Udimet U-520, 187
Ultra-high vacuum (UHV), 222
Ultra-mega power projects (UMPPs), 756
Ultra-supercritical power plants (USC power plants), 6, 8, 53, 121, 143–144, 175, 247, 323, 773. *See also* Advanced ultra-supercritical technology (A-USC technology)
  applications
    casting materials for, 126–128
    martensitic 9–12% Cr rotor steels for, 147–155
    material requirements for, 121, 122f
  boilers, 547
  coal-fired plants, 764
  components, 247–249
  pressure technology, 764
  pulverized coal plants, 8
  R&D programs on materials for, 773–775
  steam turbine blading, trends
    chemical optimizations of 9–12% Cr steels, 189
    nickel-based superalloys, 189–192
  DMW of USC steels, 276–277
  weldments between A-USC austenitic steels and USC martensitic steels, 617
Ultrasonic inspection, 625
Ultrasonic phased array systems, 241–242, 241f
Ultrasonic testing (UT), 240–241, 240f–241f, 309–310
UMPPs. *See* Ultra-mega power projects (UMPPs)
Under-tempering, 131
Underground mining, 647
United States Department of Energy (US DOE), 689
UNSN06617, 403
US A-USC materials consortium, 689–693
US Department of Energy (DOE), 536
US DOE. *See* United States Department of Energy (US DOE)
US DOE/OCDO A-USC materials technology R&D program. *See also* Chinese 700°C A-USC development program; Indian A-USC program
  A-USC materials technology future, 708–709
  boiler materials, 697–702
  component test facility, 707–708
  CURC-EPRI roadmap combustion, 690f
  economy of high-strength US A-USC alloy developments, 706–707
  materials selection, 693–694
  turbine materials, 702–705
  US A-USC materials consortium, 689–693
USC power plants. *See* Ultra-supercritical power plants (USC power plants)
USC141 alloy, 443, 449–453
USC800 alloy, 443, 453–460
UT. *See* Ultrasonic testing (UT)

V

Vacuum arc remelting (VAR), 486–487
Vacuum degassing (VD), 163
Vacuum induction melting (VIM), 444, 486–487
Valves, 801–802
  welding, 619–625
VAR. *See* Vacuum arc remelting (VAR)
"Varestraint" weldability test. *See* Variable Restraint weldability test
Variable Restraint weldability test, 533–534
VD. *See* Vacuum degassing (VD)
Very high-pressure turbine (VHPT), 751
VHPT. *See* Very high-pressure turbine (VHPT)
VIM. *See* Vacuum induction melting (VIM)
VIM/ESR/VAR ingot, 579
Visual testing (VT), 309–310

VM12-SHC tube weldments
mechanical properties, 608t
temperature control during welding, 608f
VT. *See* Visual testing (VT)

W

Waspaloy alloys, 192, 511–513, 517–518
Waste heat from industrial processes, 3, 4f
Water cooling wall materials, 719–720
Water quenching (WQ), 571–572
Water wall, 25–30
assembling in plants, 27f
design differences, 26f
increasing steam conditions, 30f
panel, 27f
tubes, 27f
WB2 specification, 623–625
Weld metal, 111
CB2 SMA weld metal composition, 624t
chemical compositions for Inconel 617 and alloy 263, 613t
development principles for creep-resistant USC steels, 279–280
shape, 302
Weld procedures, 83–84
Type IV cracking, 83–84
Weld repair(s), 130–131, 139f, 535
over-tempering, 131
PWHT, 131
under-tempering, 131
Weld solidification cracking, 533–534
Weld strength factors (WSF), 286, 603
Weld strength reduction factors (WSRFs), 287f, 701–702
for USC grades, 288t
Weldability, 83–84, 130, 410–413, 532–536
alloy 263, 578–579
creep strength of welded Sanicro 25 tube material, 413, 413f
dissimilar welding capabilities, 536
heat-affected zone liquation cracking, 534–535
heavy section weldments, 536
Sanicro 25, 410–413
strain-age cracking susceptibility, 532–533
Type IV cracking, 83–84
weld repairs after long-term thermal exposures, 535
weld solidification cracking, 533–534
and welding metallurgy
austenitic grades, 605–609
evaluated compositions of alloy 740H, 610t
mechanical properties of VM12-SHC tube weldments, 608t
nickel alloys, 609–614
welding of A-USC ferritic steels, 602–605
Welded fabrication of USC components, 247–252
fabrication of casings, valves, and cast components, 252, 253f
headers fabrication, 249–250, 249f
manifold, 249–250, 249f
membrane walls fabrication, 250–251, 250f–251f
metallic materials, 247–249
USC plants components, 247–249
welded pipework, 249–250, 249f
welded rotors for steam turbines fabrication, 251–252, 251f–252f
welded tube assemblies fabrication, 250
welding, 247–249
Welded joints, type IV fracture suppression in HAZ of, 351–358, 352f
schematics of welded joints, 353f
thermal cycle conditions of simulated-HAZ specimens, 353f
Welded rotor(s), 745
fabrication for steam turbines, 251–252, 251f–252f
Welded Sanicro 25 tube material, creep strength of, 413, 413f
Welding, 104–105, 247–249, 496–504, 532–536, 563–564. *See also* Advanced ultra-supercritical technology (A-USC technology)
arc welding consumables development, 614
A-USC ferritic steels, 602–605
and bending techniques, 432–433
boiler systems, 627–632
development behaviors for matching filler metals, 615t
dissimilar metal welding, 503, 617–619
dissimilar welding capabilities, 536
experience in other industrial fields, 602

Welding (*Continued*)
fabricated components, 501–502
gas back protection, 302
heat-affected zone liquation cracking, 534–535
heating and cooling assembly, hydrogen control, 302–304, 303f
heavy section weldments, 536
metallurgy of USC materials, 252–285
Ac1 transformation, 257f
austenitic steel grades, 274–275, 275f
CCT diagram, 256f
damage of weldments, 281–285
dendritic solidification, 254f
DMW of USC steels, 276–277
high-alloyed martensitic grades, 261–274
low-alloyed steel grades, 258–261
martensitic transformation, 257f
repair welding, 278–279
subzones of HAZ, 254f
tempering behaviors, 258f
weld metal development principles for creep-resistant USC steels, 279–280
methods, 302
next-generation A-USC fossil-fired power plants, 601
overlay, 281
preheating and interpass, 304–313, 304t
procedures, 299–313
procedures and best practices, 496–497
and properties of welds, 63–68
rotors, 625–627
strain-age cracking susceptibility, 532–533
stress relaxation cracking, 504
stress relief cracking, 504
technologies for USC power plants materials
arc welding technology and consumables for USC materials, 287–299
electron beam and arc fusion dissimilar metal welding, 314f
NDT, 299–313
quality assurance, 299–313
radiography, 313f
verification of signals, 315f
welded fabrication of USC components, 247–252
welding metallurgy of USC materials, 252–285
welding procedures, 299–313
weldments design, codes and standards, approvals, 285–287
weldments testing, 299–313
valves, casings, and cast components, 619–625
weld metal shape, 302
weld repairs after long-term thermal exposures, 535
weld solidification cracking, 533–534
weldability and welding metallurgy
austenitic grades, 605–609
compositions of alloy 740H, 610t
mechanical properties of VM12-SHC tube weldments, 608t
nickel alloys, 609–614
welding of A-USC ferritic steels, 602–605
weldment
properties, 497–501
between USC martensitic steels and A-USC austenitic steels, 617
Welding Procedure Specification (WPS), 307–308
Weldment(s)
damage, 281–285
creep, 284–285, 285f
ductility and toughness, 281–282, 282f
hydrogen delayed cracking, 283–284, 284f
oxidation, 281
short-term strength behavior, 281, 282f
stress corrosion cracking, 283–284, 284f
stress relief cracking, 284
temper embrittlement, 284
thermo-mechanical fatigue, 284
welding overlay, 281
design, codes and standards, approvals, 285–287, 286f–287f
between high-Cr martensitic grades, 276–277
between low-Cr and high-Cr grades, 277
between low-Cr bainitic grades, 276
between martensitic and austenitic grades, 277, 278f
properties, 497–501

creep rupture properties, 498–501
long time aged properties, 501
testing, 299–313, 310f
gas back protection, 302
heating and cooling assembly, hydrogen control, 302–304, 303f
preheating and interpass, 304–313, 304t
weld metal shape, 302
welding methods, 302
Wet steam, 22
WG1, 838–839
WG3A, 837–838
WG3B, 838
WG3C, 838
Widmannstätten type, 376
Wilshire approach, 523–524
Wind energies, 143
World coal production and consumption, 655–657
WPS. *See* Welding Procedure Specification (WPS)
WQ. *See* Water quenching (WQ)
Wrought 617 nickel alloy, 602
WSF. *See* Weld strength factors (WSF)
WSRFs. *See* Weld strength reduction factors (WSRFs)

X

X-ray crystallography, 224f
X-ray diffraction (XRD), 205, 223, 224f
X-ray photoelectron spectroscopy (XPS), 222
X-weld creep data, 116, 116f
X20 steel, 83
X20CrMoV121 steel, 78, 84
XEDS. *See* Energy-dispersive X-ray spectroscopy (EDS)
XPS. *See* X-ray photoelectron spectroscopy (XPS)
XRD. *See* X-ray diffraction (XRD)

Z

Z-phase, 89–93, 91f, 94t, 170, 331–332
formation, 113
strengthened steels for USC power plants, 784–785
Z-steel, 628
Z-Ultra project, 784
Zig-zag form, 406–407
ZL3 steel, 93

This page intentionally left blank

The transition from conventional subcritical to supercritical thermal power plants greatly increased power generation efficiency. Now the introductions of ultra-supercritical (USC) and, in near future, advanced ultra-supercritical (A-USC) designs, operating at higher temperatures and pressures, but necessitate advanced materials, will give further efforts to reduce fossil fuel consumption and associated carbon dioxide emissions with CCS technologies adoption. *Materials for Ultra-Supercritical and Advanced Ultra-Supercritical Power Plants* provides a comprehensive overview of the current and future stronger high-temperature materials martensitic and austenitic steels, and superalloys required for key components, like membrane wall tubes, high-pressure steam piping and headers, superheater/reheater tubes, forged rotors, cast components (casing and valves), bolting and blading for steam turbines in USC and A-USC power plants. Chapters on international research directions complete the volume.

This book is an essential reference text for professional engineers, students and researchers in academia working on high-temperature materials for USC and A-USC power plants.

Dr Augusto Di Gianfrancesco, Materials and Technologies consultant, was employed at the Centro Sviluppo Materiali (CSM), Rome, Italy since February 1983 until December 2014. He holds Senior Metallurgist and Project Leader positions on "High Temperature Materials". He was head of creep and metallography laboratories and responsible for R&D activities on steels and superalloys for high temperature applications in power generation plants. He was also member of Management Committee of EU Program COST 522-536, co-founder of the European Creep Collaborative Committee and of the Italian Working Group on Creep Resistant Materials. In addition he has been member of the International Board of the 5th, 6th &7th EPRI International Conferences on Advances in Materials Technology for Fossil Power Plants, METAL2013-16, the 6th International Conference on Creep, Fatigue and Creep-Fatigue Interaction, and vice chairman of the 3rd ECCC Conference held 2014 in Rome. He is author and/or co-author of more than 280 technical reports and more than 100 papers presented in national and international conferences or magazines.

ISBN 978-0-08-100552-1



WP
WOODHEAD PUBLISHING
ELSEVIER